AFRL-VA-WP-TR-2003-3002

ANALYSIS AND SUPPORT INITIATIVE FOR STRUCTURAL TECHNOLOGY (ASIST)

Delivery Order 0016: USAF Damage Tolerant Design Handbook: Guidelines for the Analysis and Design of Damage Tolerant Aircraft Structures

Peggy C. Miedlar, Alan P. Berens, Allan Gunderson, and J.P. Gallagher

By:
University of Dayton Research Institute
300 College Park
Dayton, OH 45469

For:
Anteon Corporation
5100 Springfield Pike, Suite 509
Dayton, OH 45431

NOVEMBER 2002

Final Report for 01 April 2000 – 03 January 2002

AIR VEHICLES DIRECTORATE
AIR FORCE MATERIEL COMMAND
AIR FORCE RESEARCH LABORATORY
WRIGHT-PATTERSON AIR FORCE BASE, OH 45433-7542

NOTICE

USING GOVERNMENT DRAWINGS, SPECIFICATIONS, OR OTHER DATA INCLUDED IN THIS DOCUMENT FOR ANY PURPOSE OTHER THAN GOVERNMENT PROCUREMENT DOES NOT IN ANY WAY OBLIGATE THE U.S. GOVERNMENT. THE FACT THAT THE GOVERNMENT FORMULATED OR SUPPLIED THE DRAWINGS, SPECIFICATIONS, OR OTHER DATA DOES NOT LICENSE THE HOLDER OR ANY OTHER PERSON OR CORPORATION; OR CONVEY ANY RIGHTS OR PERMISSION TO MANUFACTURE, USE, OR SELL ANY PATENTED INVENTION THAT MAY RELATE TO THEM.

THIS REPORT HAS BEEN REVIEWED BY THE OFFICE OF PUBLIC AFFAIRS (ASC/PA) AND IS RELEASABLE TO THE NATIONAL TECHNICAL INFORMATION SERVECE (NTIS). AT NTIS, IT WILL BE AVAILABLE TO THE GENERAL PUBLIC, INCLUDING FOREIGN NATIONS.

THIS TECHNICAL REPORT HAS BEEN REVIEWED AND IS APPROVED FOR PUBLICATION.

ARVIND NAGAR
Aerospace Engineer
Analytical Structural Mechanics Branch
Structures Division

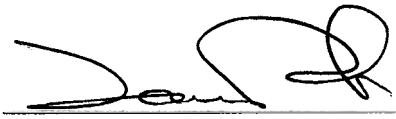

JAMES W. ROGERS JR., MAJ, USAF
Chief, Analytical Structural Mechanics Branch
Structures Division

JEFFREY S. TURCOTTE, LTC, USAF
Chief
Structures Division

Do not return copies of this report unless contractual obligations or notice on a specific document require its return.

REPORT DOCUMENTATION PAGE

Form Approved
OMB No. 0704-0188

1. REPORT DATE *(DD-MM-YY)*	2. REPORT TYPE	3. DATES COVERED *(From - To)*
November 2002	Final	04/01/2000 – 01/03/2002

4. TITLE AND SUBTITLE

ANALYSIS AND SUPPORT INITIATIVE FOR STRUCTURAL TECHNOLOGY (ASIST)

Delivery Order 0016: USAF Damage Tolerant Design Handbook: Guidelines For the Analysis and Design of Damage Tolerant Aircraft Structures

5a. CONTRACT NUMBER
F33615-98-D-3210

5b. GRANT NUMBER

5c. PROGRAM ELEMENT NUMBER
62201F

6. AUTHOR(S)

Peggy C. Miedlar, Alan P. Berens, Allan Gunderson, and J.P. Gallagher

5d. PROJECT NUMBER
2401

5e. TASK NUMBER
02

5f. WORK UNIT NUMBER
9A

7. PERFORMING ORGANIZATION NAME(S) AND ADDRESS(ES)

By
University of Dayton Research Institute
300 College Park
Dayton, OH 45469

For
Anteon Corporation
5100 Springfield Pike, Suite 509
Dayton, OH 45431

8. PERFORMING ORGANIZATION REPORT NUMBER
UDR-TR-2002-00019
AFRL-ASIST-16-01

9. SPONSORING/MONITORING AGENCY NAME(S) AND ADDRESS(ES)

Air Vehicles Directorate
Air Force Research Laboratory
Air Force Materiel Command
Wright-Patterson AFB, OH 45433-7542

10. SPONSORING/MONITORING AGENCY ACRONYM(S)
AFRL/VASM

11. SPONSORING/MONITORING AGENCY REPORT NUMBER(S)
AFRL-VA-WP-TR-2003-3002

12. DISTRIBUTION/AVAILABILITY STATEMENT
Approved for public release; distribution is unlimited.

13. SUPPLEMENTARY NOTES
This document updates a 1982 version of the AFWAL-TR-82-3073, Volumes 1 and 2 (AD number: ADA153161). An electronic version of this TR is available on the Internet at http://www.dtdesh.wpafb.af.mil/. Report contains color.

14. ABSTRACT

This is an electronic version of the revised *U.S. Air Force Damage Tolerant Design Handbook*. The technical content of the 2002 edition is enhanced by the addition of new developments in the areas of corrosion, widespread fatigue damage, and probabilistic methods. New sample problems are included which illustrate the stress intensity factor calculation, fatigue crack life prediction, residual strength risk assessment, resistance curves, inspection intervals, and analysis of aircraft areas, including longeron, wing spars, windshield doubler, fuselage skin, lap joints, layered structure, and flat panels. The revised handbook has 11 sections. An overview of MIL-HDBK-1530 ASIP Guidance and design guidelines specified in the *Joint Service Specification Guide* (JSSG-2006), and an overview of sustainment in aging aircraft, have been included in Section 1. The handbook provides guidance for analysis and design of damage tolerant aircraft structures.

15. SUBJECT TERMS
aircraft structures, structural integrity, damage tolerant design, fatigue crack growth, life prediction, residual strength

16. SECURITY CLASSIFICATION OF:			17. LIMITATION OF ABSTRACT:	18. NUMBER OF PAGES	19a. NAME OF RESPONSIBLE PERSON (Monitor)
a. REPORT	b. ABSTRACT	c. THIS PAGE			Arvind Nagar
Unclassified	Unclassified	Unclassified	SAR	716	19b. TELEPHONE NUMBER *(Include Area Code)* (937) 904-6777

HES&S 31-15093-1

Standard Form 298 (Rev. 8-98)
Prescribed by ANSI Std. Z39-18

Table of Contents

List of Examples

List of Figures

List of Tables

Section 1
Introduction

In the early 1970's, the United States Air Force (USAF) developed a damage tolerance philosophy to help eliminate the type of structural failures and cracking problems that had been encountered on various military aircraft. Air Force review of structural failures had revealed that the safe life philosophy did not protect against designs that were intolerant to defects that could be introduced during manufacturing or during in-service use. From the standpoint of flight safety, it was found prudent to assume that new airframe structures could contain initial damage (e.g. scratches, flaws, burrs, cracks, etc) and that not all cracks would be found during inspections of older airframes. Accordingly, a damage tolerance philosophy was formulated based on the demonstration of structural safety under the assumption that pre-existing damage would be present at critical locations of all structurally significant details. The intent was to ensure that the maximum possible initial damage would not grow to a size that would endanger flight safety during the service life of the aircraft. Damage tolerance was formally adopted by the Air Force as part of the Airplane Structural Integrity Program (ASIP) [MIL-STD-1530, 1972] and was implemented originally through MIL-A-83444, Airplane Damage Tolerance Requirements. The Air Force now implements damage tolerant design through the recommended practices of the Department of Defense Joint Services Specification Guide, JSSG-2006 [1998].

The primary purpose of this handbook document is to provide guidelines and state-of-the-art analysis methods that should aid engineering personnel in complying with the intent of the USAF Airplane Damage Tolerant Guidelines for metallic structures. A secondary purpose is to provide specific background data and justification for the detailed guidelines. The handbook has been structured to provide a clear and concise summary of the Damage Tolerant Requirements and the supporting data and rationale behind the critical assumptions. Where appropriate, analysis methods, test techniques, and NDI methods are provided with suggested and/or recommended practices, limitations, etc. so stated. In the Handbook, pertinent paragraphs of JSSG-2006 will be referenced.

The remaining subsections of Section 1 provide:

a) an historical perspective on the evolution of the Air Force approach to structural integrity;

b) an overview of the Air Force Aircraft Structural Integrity Program as implemented through MIL-HDBK-1530;

c) an overview of USAF damage tolerance design guidelines as specified in the Joint Service Specification Guide (JSSG-2006); and,

d) an overview of sustainment in aging aircraft.

The topics covered in Sections 2 through 11 are given in Table 1.0.1. Relevant sample problems are presented in each Section. Additional sample problems are included in the Sample Problem section of the Handbook. For the convenience of the user, links to the appropriate USAF structural specifications are contained as an Appendix to this handbook. Any conflict or discrepancy in information contained in this handbook and/or the Joint Service Specification

Guide is unintentional and in all cases, the governing document is the current version of the Guide.

This new version of the Handbook is presented as a web-based document, allowing easy access for all users from any location. The web page will allow timely updates as new methodologies emerge and technologies advance. Finding information will be easier with the search capabilities available in electronic documents. Hyperlinks are provided for sub-sections, figures, tables, and references within the handbook, as well as to other related web sites. Links are provided to websites where referenced papers can be found, software can be downloaded, and additional in-depth information is provided. Advantages of this are to give the user the most accurate, up-to-date information without reprinting the Handbook.

In addition to the web pages, each Section of the Handbook, as well as the Sample Problems, is available as a file in .pdf format, that can be downloaded and printed.

Table 1.0.1. Summary of Sections of Damage Tolerance Design Handbook

Section	Title	Description
2	Fundamentals of Damage Tolerance	Basic elements of the methodology for damage tolerant analysis.
3	Damage Size Considerations	Appropriate NDI practice, state-of-the-art procedures, demonstration programs to qualify NDI, in service NDI practice and specific examples illustrating how damage is assumed to exist in structures.
4	Residual Strength	Theory, methods, assumptions, material data, test verification, and gives examples for estimating the final fracture strength or crack arrest potential of cracked structures.
5	Analysis of Damage Growth	Current practice for estimating the rate of crack growth as a function of time, cyclic and sustained load occurrence; gives examples indicating limitations of methods, use of material data and suggested testing to support predictions and establish confidence.
6	Example Damage Tolerance Analyses	Detailed analysis of typical structural examples illustrating methodology and assumptions required.
7	Damage Tolerance Testing	Methods and recommended tests to verify methods, full-scale testing to verify residual strength and slow crack growth rates.
8	Force Management/ Sustainment Engineering	Force structural maintenance (FSM) planning and methods available to account for usage variations for individual aircraft based on a crack growth model.
9	Structural Repairs	Factors that should be considered when designing a repair, in order to ensure that the basic damage tolerance present in the original structure is not degraded by the repair.
10	Guidelines for Damage Tolerant Design and Fracture Control Planning	Methods and procedures for development and implementation of a damage tolerance control plan as required in MIL-HDBK-1530.
11	Summary of Stress Intensity Factor Information	Stress intensity factors

1.1 Historical Perspective on Structural Integrity in the USAF

The current design philosophy of U.S. Air Force aircraft has come about through a long series of evolutionary advances. Each advance followed the identification of a problem area that the then-current design criteria did not envision or comprehend. The changes in design philosophy also followed the advances in materials usage, from wood and fabric of the Wright Brothers era, to the all-metal (predominately aluminum) aircraft of World War II.

The early fabric-covered aircraft from the Wright Brothers era used spans, ribs and bulkheads of wood and laminated wood for the main load-carrying structural members. Professor Nicholas Hoff [1955] documented the fact that "the Wright Brothers performed a stress analysis of their first power machine and conducted static tests far in excess of the load that is required of it in flight."

This systematic, strength-based approach so dominated the early design methodology that it was used as the primary method for the next 50 years. Of special interest from a materials viewpoint, the selection of wood as the main structural material was based on technology of the day. Wood also has a very high fatigue strength compared to its tensile strength and is remarkably insensitive to notches.

With the continual development of higher performance aircraft, both in speed and maneuvering capabilities, through the twenties and early thirties, it was clear that the fabric-skinned aircraft were out of their element. This ushered in the age of aluminum as the primary aircraft structural material. The early aluminum aircraft fared well from a structural standpoint, due in part to designer's conservative nature associated with using a new material. The yeoman work done by the C-47 in WWII (military designation for the DC-3) attests to the success of the Wright's concept of strength-based design methods.

After WWII, the first major new Air Force aircraft design was the all-jet-powered B-47. This was a swept-wing, medium-range, strategic bomber which, in the 1950s, was a lynchpin in the post-WWII "Cold War" strategy of "massive nuclear retaliation." Aircraft production of the three models totaled 2,041 by three different manufacturers: Boeing, Douglas, and Lockheed [Negaard, 1980]. No aircraft usage life was predicted for the B-47, although the calendar phase-out was set for 1965.

The growth in aircraft gross weight and engine thrust are documented from the various models in Table 1.1.1. Many performance-oriented changes required structural strengthening and equipment changes, as well as additional fuel capacity to increase the range. The original B-47 was designed as a high-altitude bomber. However, in the last half of 1957, the Strategic Air Command, with Air Proving Ground approval, began using the bomber extensively at low altitudes. One of the low-level missions included a "structure-wrenching" low-altitude bombing system maneuver (LABS) for delivery of nuclear weapons [Patchin, 1959]. It was also called a toss-bomb maneuver and incorporated a strenuous "pop-up" bombing run. The mission training was typically performed at altitudes under 1000 feet, which added increased load excursions due to atmospheric turbulence, coupled with the increased refueling requirements and the unique load cycles imposed by that maneuver. The B-47 fleet had markedly changed the expected loading spectrum.

Table 1.1.1. B-47 Aircraft Production Models

Model	Gross Weight (Lbs.)	Thrust per Engine (Lbs.)	Thrust Growth Versions
B-47A	125,000	4,000	5,200
B-47B	185,000	5,800	5,800
B-47E	206,700	6,000	

Complicating Issues: water injection takeoffs, 17% increase in takeoff power
JATO rocket-assisted takeoff mechanisms
"LAB" Maneuvers (Toss bomb arc)

The history of the Air Force Structural Integrity Program (ASIP) started with the B-47. Fortunately, the AF Flight Dynamics Laboratory (now AFRL/VA) documented these beginnings through an Aeronautical Structures IAC report compiled by Gordon Negaard [1980]. Much of this historical synopsis was gleaned from that report.

On March 13, 1958, two B-47Bs broke up in flight in separate incidents. The first was a B-47B, which disintegrated at 15,000 feet with the initial failure occurring on the lower wing skin at Butt Line 45 – the aircraft had 2,070 hours. The second aircraft, a TB-47B, was at 23,000 feet when the lower wing skin failed at Butt Line 35 – this aircraft had 2,418 hours total flight time.

The investigations on these accidents were still underway when three more in-flight accidents occurred. A B-47E disintegrated in midair with only 1,129 hours, another B-47E exploded at 13,000 feet with only 1,265 hours, and yet another B-47E failed shortly after takeoff with a total aircraft flight time of 1,419 hours.

The immensity of the problem with the B-47 fleet caused massive infusion of personnel and funding to uncover the origins of fatigue failures and prepare and apply "fixes" for them. Technologies had to be developed to define the loads environment that the aircraft saw: number of takeoffs, landings, high-"g" pullups, rolling pullups, low-attitude maneuvers, and gust/turbulent weather loading.

A test spectrum of the applied loads had to be devised which matched the actual usage as closely as possible. The decision was made to run three concurrent fatigue test programs at Boeing Wichita, Douglas Tulsa, and at the NACA laboratory in Langley, Virginia. After about one month of testing, the Boeing test aircraft failed both fuselage upper longerons at Station 508 – one month later, the same fate occurred in the Douglas test aircraft.

Both the Boeing and Douglas test aircraft were repaired with improved longerons that had an additional reinforcement. Subsequently, lower wing failures occurred in all three aircraft and were repaired, then major fuselage cracking occurred and the cyclic testing stopped in February 1959.

The B-47 fatigue testing program accomplished a great deal towards identifying the problems associated with using a strength-based design criteria. It identified a series of very critical design areas on the B-47 which had to be repaired before release of the aircraft for full flight. It also served as a keystone for the fledgling Aircraft Structural Integrity Program (ASIP). This program was also aided by a policy directive by General Curtis LeMay, Air Force Vice Chief of Staff, which cut through the "red tape". This directive emphasized the importance of the structural integrity program and called for the complete and active support and cooperation of all Air Force elements [Negaard, 1980].

Throughout all the testing was an underlying learning experience for the Air Force structural engineers. A technical memorandum, WCLS-TM-58-4 [1958], set the baseline design requirements for fatigue life, expressed in flight hours and landings, for all Air Force aircraft that the program was to cover. A follow-on document to this memo entitled "ARDC-AMC Program Requirements for the Structural Integrity Program for High Performance Aircraft" dated 15 February 1959, delineated the breakout of responsibilities of eleven sub-program areas:

- Static test
- Flight load summary
- Fatigue test
- Low-altitude gust environment
- Mission profile data
- Interim service load
- VGH life history recording
- Eight-channel service load recording
- Sonic fatigue
- High-temperature structure
- Design criteria

General Curtis LeMay formally approved this joint command document and directed its "implementation on a priority basis." [Negaard, 1980].

The next several years saw minor changes in the basic ASIP document, but a major increase of supporting specifications were published to aid in the implementation. These included the Military Specification 8800 series of specifications that sought to clarify and document all aspects of the original ASIP guidelines. Table 1.1.2 lists the specifications of the MIL SPEC 8800 series that are most pertinent to the Damage Tolerance Design Handbook. Most were released 18 May 1960.

Table 1.1.2. Pertinent 8800 Series Specifications of 1960

Spec No.	Title
MIL-A-8860	Airplane Strength and Rigidity General Specification for
MIL-A-8861	Airplane Strength and Rigidity Flight Loads
MIL-A-8862	Airplane Strength and Rigidity Landing and Ground Handling Loads
MIL-A-8863	Airplane Strength and Rigidity Additional Loads for Carrier-Based Landplanes
MIL-A-8865	Airplane Strength and Rigidity Miscellaneous Loads
MIL-A-8866	Airplane Strength and Rigidity Reliability Requirements, Repeated Loads, and Fatigue
MIL-A-8867	Airplane Strength and Rigidity Ground Tests
MIL-A-8868	Airplane Strength and Rigidity Data and Reports
MIL-A-8869	Airplane Strength and Rigidity Special Weapons Effects
MIL-A-8870	Airplane Strength and Rigidity Vibration, Flutter, and Divergence
MIL-A-8871 (8 Oct. 1968)	Airplane Strength and Rigidity Flight and Ground Operations Tests

Even with the added attention on fatigue design issues, the learning process had many hesitations. During the full-scale fatigue test of the F-105D at Wright Field, the main wing carry-through frame at fuselage station (F.S.) 442 failed at less than 20% of one lifetime [Brammer, 1963]. After review of the data and the load spectrum, a replacement fuselage with specially-machined attachment lugs to reduce the stress concentration was inserted and the testing continued with a much-reduced load spectrum. This frame subsequently failed at 4653 flight hours, or 116% of one lifetime (the testing requirement was for four lifetimes.) A much beefier, five-piece frame was then inserted into the test fuselage and the testing resumed. The finalizing structural failure was a crack that initiated in the turtledeck on the upper fuselage and fractured down to the lower longerons. It was an ignominious end to a troubled test series.

In contrast, full-scale fatigue testing on the F-104G/MAP aircraft [Boensch, 1964] went through the entire four-lifetime test program with no major cracking observed (1963-1964). Following a fifth lifetime of 100% lateral gust loading, the airframe was cycled to 100% of the subsonic pull-up maneuver at 5 g's for an additional 775 cycles, at which time a catastrophic failure of the left wing occurred. The conclusions from the test were that the F-104G/MAP aircraft had adequate fatigue life without modification based on the usage spectrum tested.

On 12 June 1969, the definitive establishment document from ASIP occurred with the publication of Air Force Regulation 80-13. This document contained all the technical aspects of the ASIP programs, added a Phase VI on inspections, and assigned ASIP responsibilities to Headquarters USAF, Air Force Systems Command, Air Force Logistics Council and the using commands. It also included the implementation authority for the program.

On December 22, 1969, a catastrophic accident occurred when an F-111 lost a wing while on a training flight. Both pilots were killed and evidence pointed to the conclusion that they never had a chance to eject. The failure was found to originate at the lower wing pivot plate of this swing-wing fighter/bomber. The origin, shown in Figure 1.1.1 [Rudd, et al., 1979], occurred at a forging lap incorporated during the primary metal-working operation. Because of the proximity to a vertical reinforcement rib, it was not discovered in any of the production-level inspections.

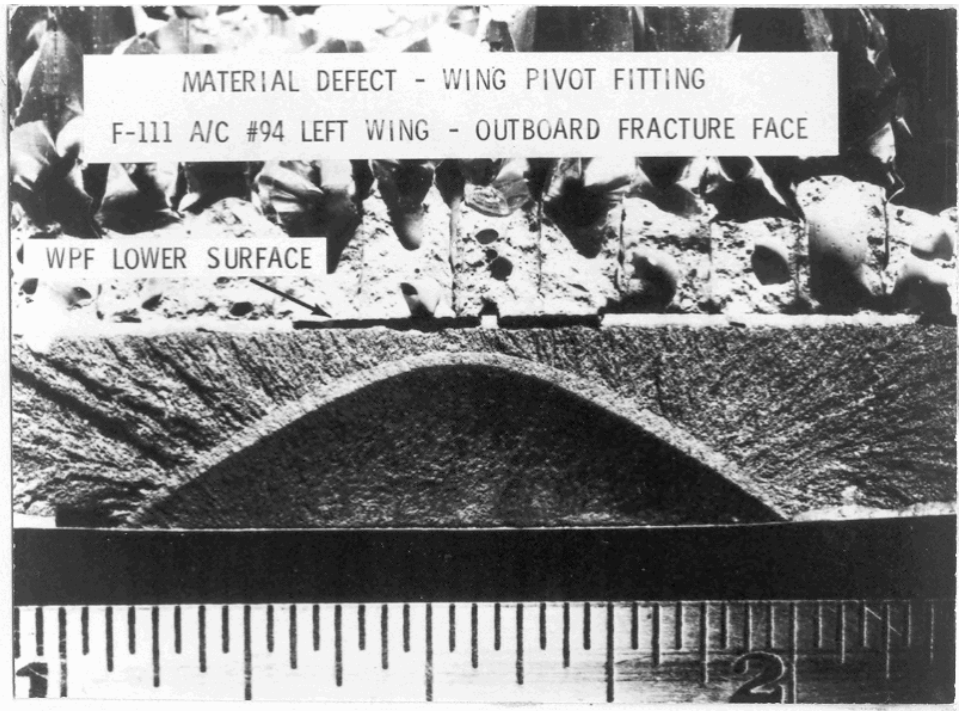

Figure 1.1.1. Origin of the F-111 Wing Defect [Rudd, et al., 1979]

This accident brought about the largest single material investigation ever, focused on D6AC steel. In addition to the database formed, a concept for releasing the aircraft for flight was based on a cold-proof test along with state-of-the-art NDI.

A Scientific Advisory Board assembled for the F-111 investigation subsequently recommended that a damage-tolerant design methodology be used for all future weapons systems. In September 1972, these new design concepts were incorporated into an ASIP document, MIL-STD-1530, Aircraft Structural Integrity Program, Airplane Requirements. MIL-STD-1530 incorporated all the applicable prior documents and also instituted the requirement that each aircraft system have an ASIP force structural maintenance master plan that identifies inspection and modification requirements and estimates the economic life of the airframe. This version of the ASIP document was also the most specific; it called out the Service Life Requirements clearly, as shown in Table 1.1.3.

Table 1.1.3. Service Life Requirements from MIL-STD-1530 [1972]

	Years of Service	Flight Hours	Number of Flights	Landings[(1)]	Fuselage Pressurization
Fighter					
Air Superiority					
Long-Range	15	8,000	6,000	8,000	8,000
Short-Range	15	6,000	8,000	10,000	8,000
Ground Attack	15	8,000	8,000	10,000	8,000
Bomber	25	15,000	3,000	5,000	5,000
Tanker	25	20,000	5,000	7,500	7,500
Cargo[(2)]					
Medium and Heavy	25	50,000	12,500	25,000	15,000
Assault	25	15,000	12,500	20,000	15,000
Utility	25	25,000	15,000	20,000	20,000
AEW&C[(3)]	20	40,000	4,000	8,000	6,000
Trainer					
Primary	25	15,000	15,000	40,000	15,000
Navigational	25	25,000	6,000	10,000	7,500

This table constitutes minimum structural design criteria and should not be used to interpret operational use (such as hours per flight)

[(1)]Full stop landings are assumed equivalent to the number of flights. Remainder are touch and goes

[(2)]Includes STOL & VTOL

[(3)]Includes command post systems

This was a period of rapid growth in both technical concepts for materials understanding and the development of methodologies for implementing the ASIP program. The Military Specification, Airplane Damage Tolerance Requirements, MIL-A-83444 (USAF), was issued in July, 1974 and presented detailed damage tolerance requirements as a function of design concept and degree of inspectability. In 1975, MIL-STD-1530A was issued to update and revise the process. The fatigue and fracture control plan of MIL-STD-1530 was replaced by the damage tolerance control plan of MIL-A-83444 and a durability control plan. An added section on chemical/thermal environment required contractors to also include these concerns in their design. After the publication of MIL-STD-1530A, AF Reg. 80-13 was updated. Since the technical responsibilities were now expressed in MIL-STD-1530A, Reg. 80-13 concentrated on the overall policy and responsibilities of the appropriate commands with respect to establishing, implementing, and utilizing the ASIP programs.

In February 1985, the ASIP requirements of MIL-A-83444 were revised in format and updated in content in MIL-A-87221 (USAF), General Specifications for Aircraft Structures. MIL-A-87221 was directed at specific design requirements for aircraft systems and presented guidance for demonstrating that the requirements were met. MIL-A-87221 (USAF) was superseded in June 1990 by AFGS-87221A in which the same format for requirements and verification guidelines were retained.

As part of the overall government acquisition reform initiative, the ASIP requirements were interpreted as ASIP guidelines with the issuance in November 1996 of MIL-HDBK-1530, "General Guidelines for Aircraft Structural Integrity Program." Further, the latest version of the structural requirements and verification guidelines were stated in the Department of Defense

Joint Service Specification Guide: Aircraft Structures, JSSG-2006. This guide is intended for all DoD departments and agencies and is predicated on a performance-based, business-environment approach to product development. JSSG-2006 was first released 30 October 1998 and is an evolving document.

In this Damage Tolerance Design Handbook, specific references to design requirements and verification guidance are from JSSG-2006 [1998].

1.2 Overview of MIL-HDBK-1530 ASIP Guidance

Overall guidance for the Aircraft Structural Integrity Program (ASIP) is contained in MIL-HDBK-1530. This program for ensuring the structural integrity of an aircraft system throughout its design life is based on the damage tolerance philosophy and provides a series of time related tasks from initial design through the operational life of a fleet. According to Lincoln [2000], "The introduction of damage tolerance principles by the USAF in their structural inspection program in the early seventies virtually eliminated fatigue as a safety issue in their aircraft."

The objectives of ASIP are to:

a) Establish, evaluate, and substantiate the structural integrity (airframe strength, rigidity, damage tolerance, and durability) of the airplane.

b) Acquire, evaluate, and utilize operational usage data to provide a continual assessment of the in-service integrity of individual airplanes.

c) Provide a basis for determining logistics and force planning requirements (maintenance, inspections, supplies, rotation of airplanes, system phase-out, and future force structure).

d) Provide a basis to improve structural criteria and methods of design, evaluation, and substantiation of future systems.

These objectives are met through five time-phased tasks that cover the structural design, development, and management of an aircraft structure. The ASIP tasks with major elements are presented in Table 1.2.1 from MIL-HDBK-1530. The first three tasks are concerned with the development of the ASIP Master Plan for the structure and the design information, design analyses, development tests, and full scale tests. The last two tasks list the recommended procedures for ensuring damage tolerance and durability of individual aircraft during fleet operations of the weapon system. These latter tasks are defined as force management and are an integral part of the ASIP Master Plan.

The Force Structural Maintenance Plan of Task IV of ASIP is the basis for the estimation of the maintenance costs that the fleet will incur during the period of its design service life. The timing of maintenance actions is based on predicted crack growth in the design load and environmental stress spectrum. Deviations due to individual aircraft usage are accounted for by the tracking program of Task V. However, as an aircraft ages, the force structural maintenance plan may have to be modified due to unanticipated usage, widespread fatigue cracking, corrosion, or accidental damage. Inspection schedules may also require changes due to extending airframe life beyond initial life goals.

The process of maintaining aging aircraft in an operational state is known as sustainment. This topic is addressed in Subsection 1.4.

Table 1.2.1. ASIP Tasks from MIL-HDBK-1530

Task I	Task II	Task III	Task IV	Task V
Design Information	Design Analysis and Development Tests	Full Scale Testing	Force Management Data Package	Force Management
ASIP Master Plan Structural Design Criteria Damage Tolerance & Durability Control Process Selection of Materials, Processes & Joining Methods Design Service Goal and Design Usage Mass Properties	Material & Joint Allowables Load Analysis Design Service Loads Spectra Design Chemical/Thermal Environment Spectra Stress Analysis Damage Tolerance Analysis Durability Analysis Aeroacoustics Analysis Vibration Analysis Flutter Analysis Nuclear Weapons Effects Analysis Non- Nuclear Weapons Effects Analysis Design Development Tests Mass Properties Analysis	Static Tests Durability Tests Damage Tolerance Tests Flight & Ground Operations Tests Aeroacoustic Tests Flight Vibration Tests Flutter Tests Interpretation & Evaluation of Test Results Weight & Balance Testing	Final Analyses Strength Summary Force Structural Maintenance Plan Loads/Environment Spectra Survey Individual Aircraft Tracking Program	Loads/Environment Spectra Survey Individual Aircraft Tracking Data Individual Aircraft Maintenance Times Structural Maintenance Records Weight and Balance Records

1.3 Summary of Damage Tolerance Design Guidelines

USAF damage tolerance design guidelines are specified in Joint Service Specification Guide JSSG-2006 [1998]. The guidelines apply to all safety of flight structure, i.e., structure whose failure could cause direct loss of the aircraft, or whose failure, if it remained undetected, could result in the loss of aircraft. The guidelines stipulate that damage is assumed to exist in each element of new structure in a conservative fashion i.e., critical orientation with respect to stress field and in a region of highest stress. The structure must successfully contain the growth of the initial assumed damage for a specified period of service, and must maintain a minimum level of residual static strength both during and at the end of this period.

1.3.1 Summary of Guidelines

The damage tolerance design guidelines are illustrated in Figure 1.3.1 in a diagrammatic form. Since residual static strength generally decreases with increased damage size, the residual strength and growth guidelines are coupled through the maximum allowable damage size, i.e. the damage size growth limit established by the minimum-required residual strength load. The safe growth period (period of unrepaired service usage) is coupled to either the design life requirement for the air vehicle or to the scheduled in-service inspection intervals. While the specific guidelines of JSSG-2006 may seem more complex than described in Figure 1.3.1, all essential elements are as illustrated. The remainder of Section 1.3 will describe these individual elements.

A structure can be qualified under one of two categories of defined damage, either Slow Crack Growth or Fail Safe. In the Slow Crack Growth category, structures are designed such that initial damage will grow at a stable, slow rate under service environment and not achieve a size large enough to cause rapid unstable propagation. In the Fail Safe category, structures are designed such that propagating damage is safely contained after failing a major load path by load shift to adjacent intact elements or by other damage arrestment features.

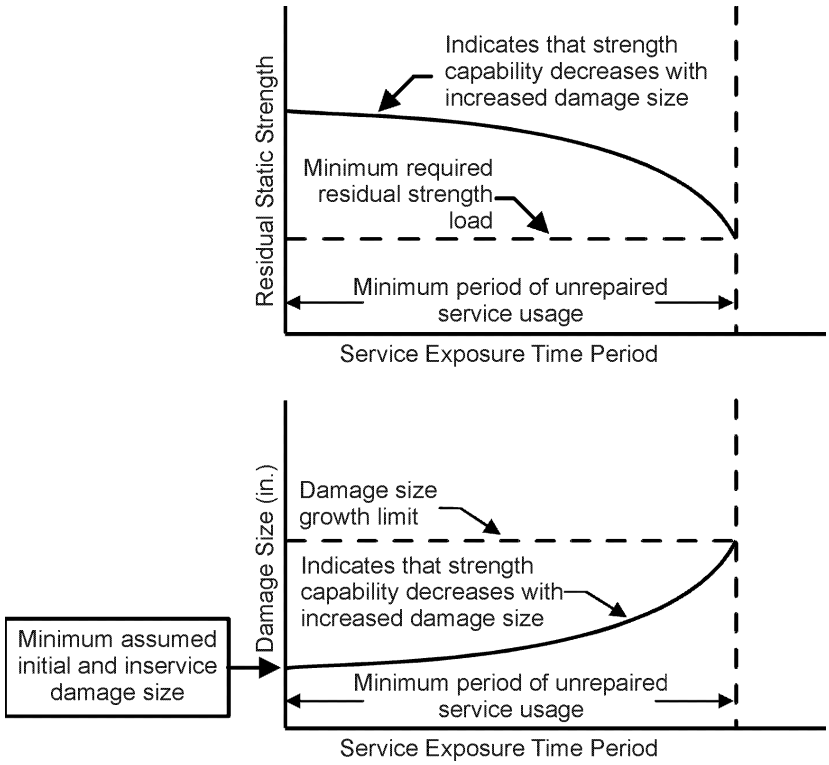

Figure 1.3.1. Residual Strength and Damage Growth Guidelines

In Slow Crack Growth qualified structure, damage tolerance (and thus safety) is assured only by the maintenance of a slow rate of growth of damage, a residual strength capacity and the assurance that sub-critical damage will either be detected at the depot or will not reach unstable dimensions within several design life times.

In Fail Safe qualified structure, damage tolerance (and thus safety) is assured by the allowance of partial structural failure, the ability to detect this failure prior to total loss of the structure, the ability to operate safely with the partial failure prior to inspection, and the maintenance of specified static residual strength through this period. Section 1.3.2 discusses the design categories.

Each structure must qualify within one of the designated categories of in-service inspectability (referred to as "The Degree of Inspectability" in JSSG-2006), including the option to designate Slow Crack Growth qualified structure as "in-service non-inspectable." The various degrees of inspectability refer to methods, equipment, and other techniques for conducting in-service inspections as well as accessibility and the location of the inspection (i.e., field or depot). These degrees of inspectability are discussed in Section 1.3.3.

The selection of the most appropriate damage tolerance category under which to qualify the structure is the choice of the designer/analyst. The choice of degree of in-service inspectability is somewhat limited, however, to those described in JSSG-2006. The inspection guidelines have been developed based upon past and present experiences and are felt to be reasonable estimates of future practice.

The intent of the guideline is to provide for at-least design limit load residual strength capability for all intact structure, i.e., for sub-critical damage sizes in slow crack growth structure and damage sizes less than a failed load path in fail safe qualified designs. This requirement allows for full limit load design capability and thus unrestricted aircraft usage. The imposition of the requirement constrains structure qualified as Slow Crack Growth to either depot level inspectable or in-service non-inspectable.

As described in Section 1.3.2, fail safe structure must meet both the intact structure and remaining structure guidelines. Slow crack growth structure will meet either the depot level inspectable or the non-inspectable structure guidelines. For each structure, evaluation of the following parameters is required:

- Design Category
- Degree of In-Service Inspectability
- Inspection Intervals
- Initial Damage, In-Service Damage and Continuing Damage Assumptions
- Minimum Required Residual Strength
- Damage Size Growth Limits
- Period of Unrepaired Service Usage
- Remaining Structure Damage Sizes

Each of these are described in the following sections, and Section 1.3.7 shows several examples.

1.3.2 Design Category

As specified in JSSG-2006 paragraph 3.12, all safety of flight structure must be categorized as either Slow Crack Growth or Fail Safe.

Slow Crack Growth structure consists of those design concepts where flaws or defects are not allowed to attain the critical size required for unstable rapid crack propagation. Safety is assured through slow crack growth for specified periods of usage depending upon the degree of inspectability. The strength of slow crack growth structure with sub-critical damage present shall not be degraded below a specified limit for the period of unrepaired service usage.

Fail Safe structure is designed and fabricated such that unstable rapid propagation will be stopped within a continuous area of the structure prior to complete failure. Safety is assured through slow crack growth of the remaining structure and detection of the damage at subsequent inspections. Strength of the remaining undamaged structure will not be degraded below a specified level for the period of unrepaired service usage.

In the development of the guidelines, it was recognized that multiple load path and crack arrest type structure have inherent potential for tolerating damage by virtue of geometric design features. On the other hand, it is not always possible to avoid primary structure with only one major load path, and therefore some provisions are necessary to ensure that these situations can be designed to be damage tolerant. It is the intent of the guidelines to encourage the exploration of the potentials for damage tolerance in each type of structure. Single load path or monolithic

structures must rely on the slow rate of growth of damage for safety and thus, the design stress level and material selection become the controlling factors.

Single load path “monolithic” structures must be qualified as Slow Crack Growth. However, the guidelines allow flexibility for qualification of multiple load path cases. The decision may be made to qualify multiple load path structure as Slow Crack Growth, instead of Fail Safe, if sufficient performance and life cycle costs advantages are identified to offset the burdens of the inspectability levels for Fail Safe structure. Therefore, the method of construction may not agree with the design category selected, i.e. all multiple load path structure is not Fail Safe. When deciding on the design category option, the most important factor to consider is that once a design category is chosen, the structure must meet all the guidelines in the guidelines that cover that category.

The mere fact that a structure has alternate load paths (local redundancy) in some locations does not necessarily qualify it as Fail Safe. Examples are helpful in illustrating this point. Examples 1.3.1 and 1.3.2 illustrate the fact that a structure is often locally redundant (usually good design practice), but in an overall sense may have some restriction such that one is not able to take advantage of the localized redundancy in order to qualify the structure as Fail Safe.

Considerable judgment is required for the selection of potential initial damage locations for the assessment of damage growth patterns and the selection of major load paths. The qualification as Fail Safe is thus a complex procedure entailing judgment and analysis. Because of this, the choice is often made to qualify the design as Slow Crack Growth regardless of the type of construction. As stated in JSSG-2006 A3.12.2.3 Requirement Lessons Learned "There are currently no aircraft in the Air Force inventory which have been qualified as fail-safe crack arrest structure under Air Force criteria".

EXAMPLE 1.3.1 Identifying Non-Redundant Structure – Lug Example of Slow Crack Growth Structure

The lug fitting illustrated here has multiple lug ends at the pinned connection. Failure or partial failure of one of the lugs (A) would allow the load to be redistributed to the remaining sound structure. Localized redundancy is often beneficial, and in this case is good design practice. However, the fitting cannot be qualified as Fail Safe Multiple Load Path structure since the occurrence and growth of damage at a typical location (B) would render the structure inoperative. The only means of protecting the safety of this structural element would be to qualify it as Slow Crack Growth.

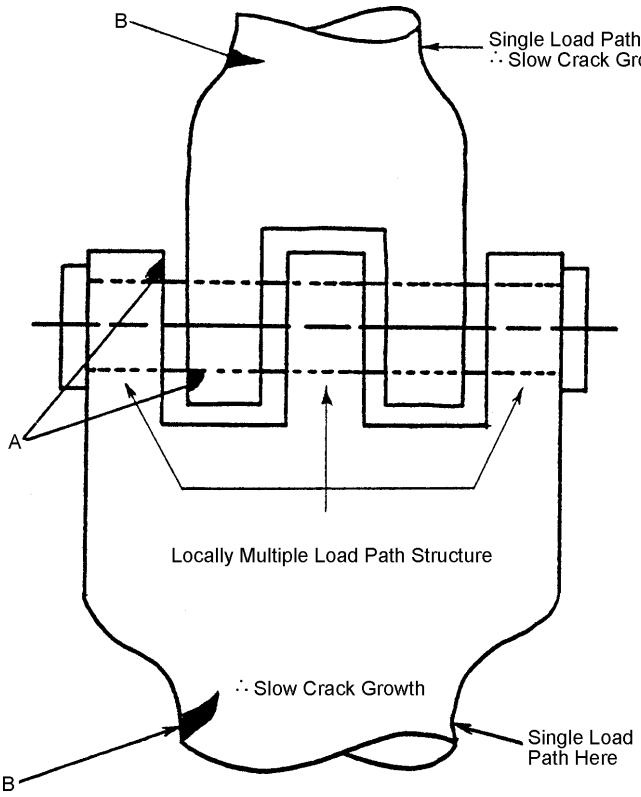

EXAMPLE 1.3.2 Choice Options for Redundant Structure – Wing Box Example

As shown here, a wing box is attached to the fuselage carry through structure by multiple fittings. The upper and lower skin is one piece for manufacturing and cost reduction. The substructure consists of multiple spars spaced to attach to the individual attachment fittings. A case could be made to qualify this structure as Fail Safe Multiple Load Path. Depending upon the amount of bending carried by the spars, it would be possible to design the structure such that damage in the skin would be arrested at a spar prior to becoming critical. The design might also tolerate failure of one spar cap and a portion of the skin, prior to catastrophic failure. The attachment system could be designed to satisfy Fail Safe guidelines with one fitting failed.

On the other hand, if the skin was the major bending member with a design stress of sufficient magnitude to result in a relatively short critical crack length, then the skin and spar structure could only be qualified as Slow Crack Growth structure.

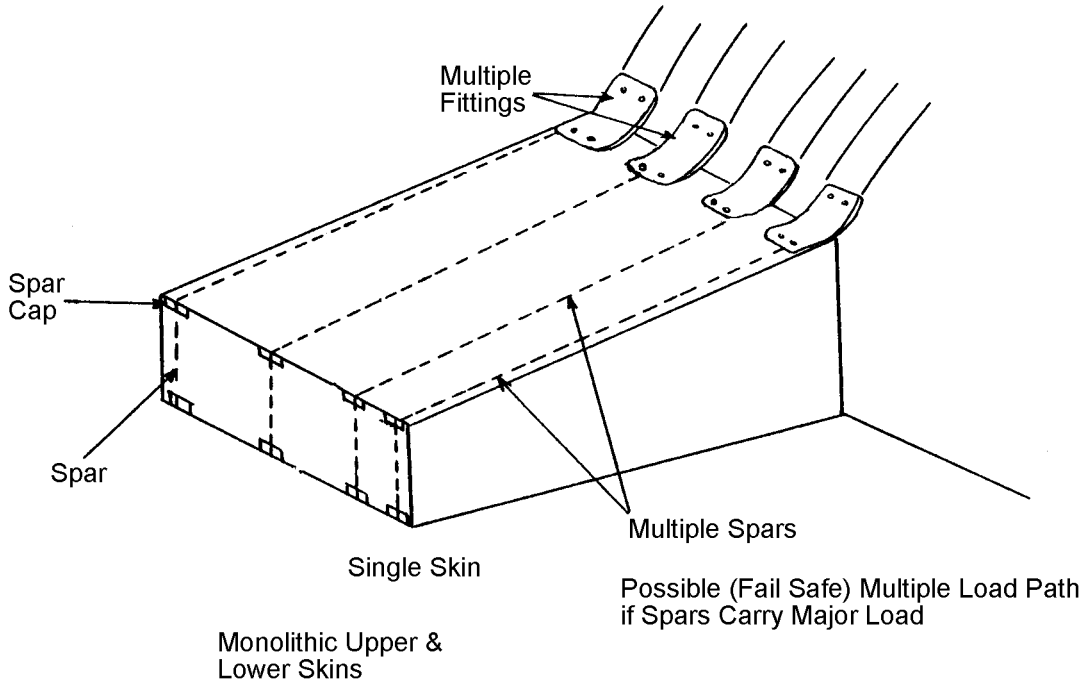

1.3.3 Inspection Categories and Inspection Intervals

For each individual aircraft system, the Air Force is obligated to specify the planned major depot and base level inspection intervals to be used in the design of the aircraft. Typically, these intervals will be approximately 1/4 of the design service life. The types and extent of inspection (i.e., equipment, accessibility, necessity for part removal, etc.) required at each of these major inspections is dependent upon the specific aircraft design and modifications resulting from development and full-scale tests or service experience. The Air Force wants its contractors to design a damage tolerant structure that will minimize the need for extensive non-destructive depot or base level inspections. Primary emphasis should therefore be placed on obtaining designs for which significant damage sizes can readily be found by visual inspection. However, where periodic inspections are required to satisfy the damage tolerance guidelines, the contractor must recognize that the USAF will probably conduct the inspections. The in-service damage sizes associated with the inspection categories of JSSG-2006 paragraph 3.12 reflect the estimated capability of the Air Force to find damage.

Guidelines for degree of inspectability are contained in JSSG-2006 paragraph 6.1.15. The degree of inspectability of safety of flight structure is established in accordance with the following definitions:

- In-flight evident inspectable - If the nature and extent of damage occurring in flight will result directly in characteristics which make the flight crew immediately and unmistakably aware that significant damage has occurred and that the mission should not be continued.
- Ground evident inspectable - If the nature and extent of damage will be readily and unmistakably obvious to ground personnel without specifically inspecting the structure for damage.
- Walkaround inspectable - If the nature and extent of damage is unlikely to be overlooked by personnel conducting a visual inspection of the structure. This inspection normally shall be a visual look at the exterior of the structure from ground level without removal of access panels or doors without special inspection aids.
- Special visual inspectable - If the nature and extent of damage is unlikely to be overlooked by personnel conducting a detailed visual inspection of the aircraft for the purpose of finding damaged structure. The procedures may include removal of access panels and doors, and may permit simple visual aids such as mirrors and magnifying glasses. Removal of paint, sealant, etc. and use of NDI techniques such as penetrant, X-ray, etc., are not part of a special visual inspection.
- Depot or base level inspectable - If the nature and extent of damage will be detected utilizing one or more selected nondestructive inspection procedures. The inspection procedures may include NDI techniques such as penetrant, X-ray, ultrasonic, etc. Accessibility considerations may include removal of those components designed for removal.
- In-service non-inspectable structure - If either damage size or accessibility preclude detection during one or more of the above inspections.

The specified frequency of inspections for each of the inspectability levels is indicated in Table 1.3.1 and is based on estimates of typical inspection intervals. As previously mentioned, the typical depot or base level frequency is once every one quarter of the design lifetime but may be

otherwise specified in the appropriate contractual document. Special visual inspection requires Air Force approval before being considered as a design constraint but, if approved, shall not be required more frequently than once per year. The justification for this restriction is cost and maintenance schedule guidelines.

Table 1.3.1. Summary of In-Service Inspections from JSSG-2006 Appendix Table X

Degree of Inspectability	Typical Inspection Interval
In-Flight evident inspectable	One flight*
Ground evident inspectable	One day (two flights)*
Walk-around inspectable	Ten flights*
Special visual inspectable	One year
Depot or base level inspection	¼ Design service lifetime
In-Service non-inspectable structure	One design service lifetime

* Most damaging mission

The design of some aircraft components for intermediate special visual inspections, typically once per year, may be advantageous from a performance or cost standpoint and may be used by the contractor in satisfying the guidelines. Normally, special visual inspections will not be specified by the Air Force in the design and development stage but may be dictated, subsequent to design, by the results of testing or service experience.

The assumed Air Force depot or base level inspection capabilities depend on the type of inspection performed. In special cases where potential benefits justify it, the contractor may recommend to the Air Force that specific components be removed from the aircraft and inspected during scheduled depot or base level inspections. If approval is given, the recommendations may be incorporated during design. In these cases, the assumed initial damage sizes subsequent to the inspection shall be the same as those in the original design providing the same inspection procedures are used and certified inspection personnel perform the inspection.

Conventional NDI procedures such as X-ray, penetrant, magnetic particle, ultrasonic, and eddy current are generally available for depot or base level inspections. Such inspection procedures will be performed as dictated by the specific aircraft design inspection guidelines, or as modified because of subsequent tests and service experience. In establishing the design inspection guidelines, the contractor should attempt to minimize the need for such NDI, and should not plan on nor design for general fastener pulling inspections.

1.3.4 Initial Damage Assumptions

To insure that the airframe will have adequate residual strength capability throughout its service life, initial flaws are assumed to exist in the structure. The airframe should have adequate residual strength in the presence of flaws for specified periods of service usage. These flaws are assumed to exist initially in the structure as a result of material and structure manufacturing and processing.

JSSG-2006 paragraph A3.12.1 assumes that any fastener hole in the structure can be marginal and can have an initial damage equivalent to a 0.005 inch radius corner flaw. Thus, the guidelines requires assuming that this flaw exists at each fastener hole within the structure at the

time of manufacture. Since the 0.005 inch size is based on limited data, the contractor may provide data representing his own manufacturing quality and negotiate with the Air Force for a smaller size of the apparent initial flaw to represent marginal hole quality.

The most critical location for the initial flaw should be determined by reviewing all elements of the structure and considering features such as edges, fillets, holes, and other high stressed areas.

1.3.4.1 Intact Structure Primary Damage Assumption

The basic premise in arriving at the initial damage sizes is the assumption that the as-fabricated structure contains flaws of a size just smaller than the maximum undetectable flaw size found with the NDI procedures used on the production line. These flaw size shapes which are intended to be covered by the initial flaw size assumptions include radial tears, drilling burrs, and rifle marks at fastener holes as well as forging defects, welding defects, heat treatment cracks, forming cracks, and machining damage at locations other than fastener holes.

Table 1.3.2 and Figure 1.3.2 summarize the initial damage assumptions as specified in JSSG-2006 paragraph A3.12.1 and Table XXX. For slow crack growth and fail safe primary element structure, the assumed initial flaw at holes and cutouts is a 0.05 inch through the thickness flaw at one side of the hole if the material thickness is equal to or less than 0.05 inch. For thicker materials (> 0.05 inch), the assumed initial flaw is a 0.05 inch radius corner flaw.

At locations other than holes, the assumed initial flaw is a semi-circular surface flaw with a length of 0.25 inch and depth of 0.125 inch, or, for material thickness less than 0.125 inch, a through thickness flaw of 0.25 inch length.

These assumptions - relative to the size, shape and location - were based on a review of existing NDI data. The crack length values given in Figure 1.3.2 and Table 1.3.2 were selected as most appropriate for the types of cracks considered and for the two design categories.

Table 1.3.2. Initial Flaw Assumptions for Metallic Structure, JSSG-2006 Appendix Table XXX

Category	Critical Detail	Initial Flaw Assumption*
Slow crack growth and Fail Safe primary element	Hole, Cutouts, etc.	For $t \leq 0.05$”, 0.05” through thickness flaw For $t > 0.05$”, 0.05” radial corner flaw
	Other	For $t \leq 0.125$”, 0.25” through thickness flaw For $t > 0.125$”, 0.125” deep x 0.25” long surface flaw
	Welds, embedded defects	TBD

* - Flaw is oritented in the most critical direction

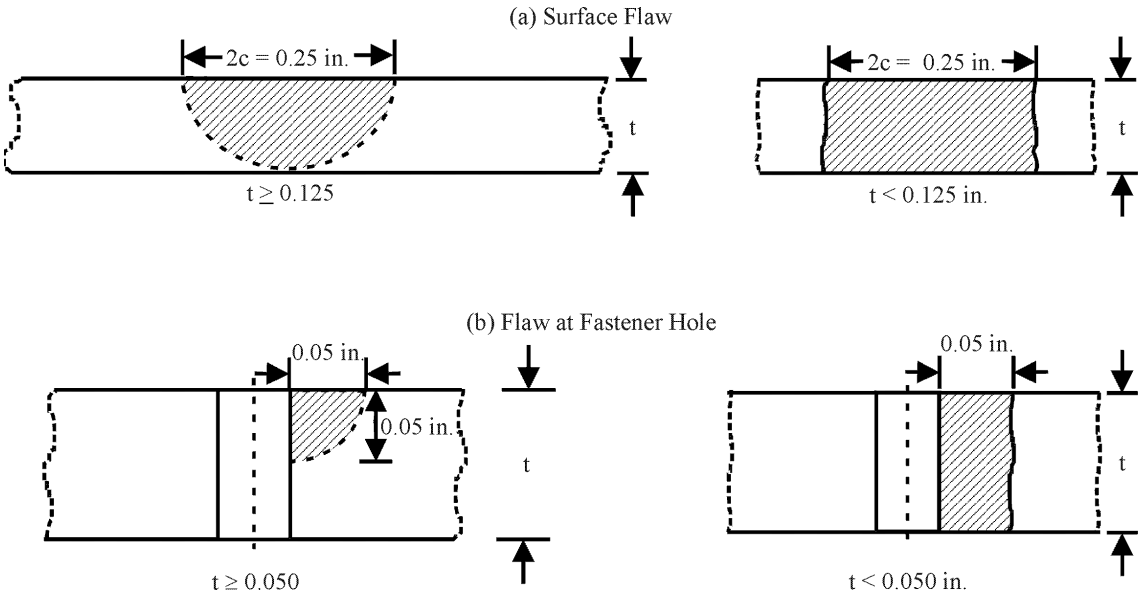

Figure 1.3.2. Summary of Initial-Flaw Assumption for Intact Structure

The Slow Crack Growth initial damage sizes are based on NDI probability of detection (POD) data (90 percent probability of detection with 95 percent confidence). The 0.050 inch crack size for holes and cutouts is based on POD data obtained in the lab using eddy current inspection with fastener removed. The surface flaw size, 0.250 inch long by 0.125 inch deep, was obtained from Air Force sponsored inspection reliability programs where several techniques were used including ultrasonic, dye penetrant and magnetic particle. In these programs, most techniques were found to be sensitive to both surface length and flaw depth and thus the NDI capability must be judged in terms of the flaw shape rather than simply surface length or crack depth.

1.3.4.2 Continuing Damage

In applying JSSG-2006 paragraph 3.12 to a built-up structure, it is noted that cyclic growth behavior of primary damage may be influenced by the geometry of the structure or the arrangement of the elements. In order to provide an orderly and progressive path for the crack that eventually causes the structure to fail, the continuing damage assumptions were incorporated. There are three cases where the continuing damage assumptions are made in order to keep the crack moving; these cases are described with examples.

Figure 1.3.3 describes a skin-stringer construction where equivalent initial (primary) damage is assumed to exist in both elements of the hole marked A. According to JSSG-2006 paragraph A3.12.1, all other holes are secondary cracking sites (marked B) and contain the small imperfections equivalent to the 0.005 inch radius corner flaw. As the primary damage progresses in both the skin and stringer, eventually the radial crack in the stringer will extend to the edge of the stringer, shown in Figure 1.3.3 - cracking sequence (ii). At this time, a new crack, equivalent to the 0.005 inch radial crack flaw plus the growth prior to the primary element failure, is assumed to exist on the diametrically opposite side of the failed hole, as shown in Figure 1.3.3 - cracking sequence (iii). This continues the growth process until the complete stringer fails, shown in Figure 1.3.3 - cracking sequence (iv).

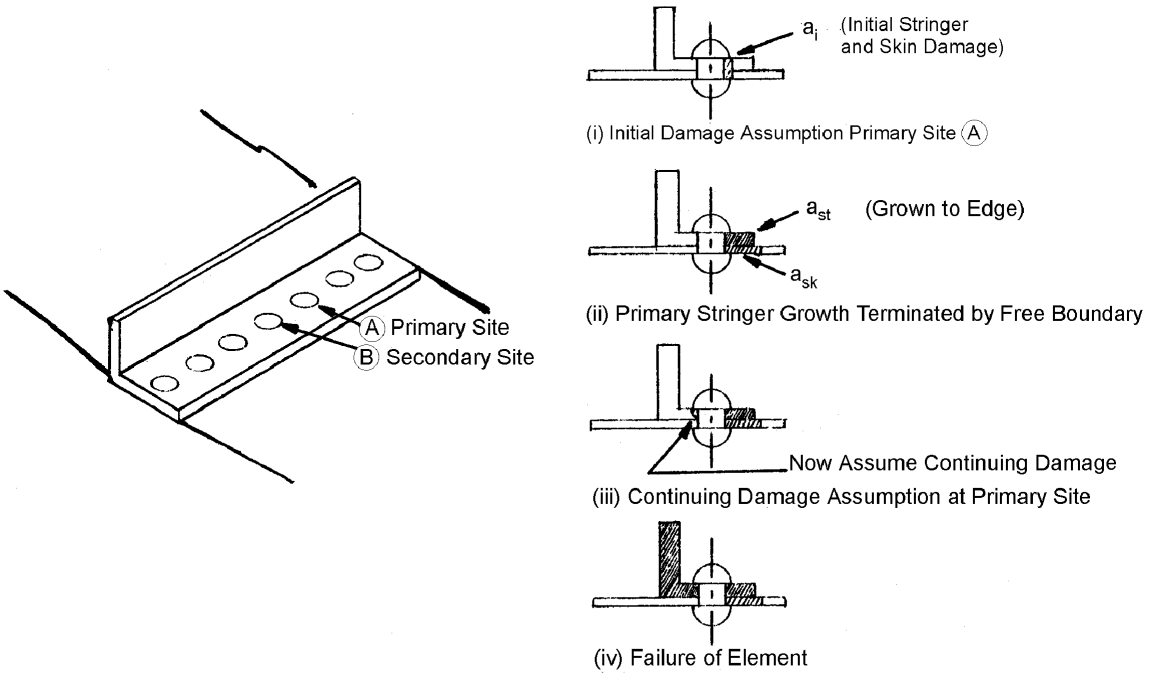

Figure 1.3.3. Example of Continuing Damage Growth Terminated at Free Edge and Terminated by Failure of Member

Under the condition that the primary damage terminates due to a member or element failure, such as the stringer illustrated in Figure 1.3.3, the designer is required to assume that continuing damage is present. The continuing damage is assumed to be present at the most critical location in the remaining element or structure. The continuing damage is either a corner crack that starts from an initial small imperfection of 0.005 inch or a surface flaw with length of 0.02 inch and depth of 0.01 inch, plus the amount of growth which occurs prior to element failure.

Figure 1.3.4 illustrates several choices for potential critical locations where continuing damage might be assumed subsequent to the failure of the stringers. Secondary Site 1 is assumed to be an adjacent hole, and the crack growth is in the skin and opposite in direction to the primary skin crack. Such a situation would eventually result in a stepwise shift in the crack growth path. Most logically, this type of damage could be assumed to exist at the primary damage site in the skin on the diametrically opposite side of the hole once the stiffener fails. Secondary Site 2 is located in the skin and would provide a path for link-up with the primary crack. Secondary Site 3 is located in a parallel stringer-skin hole and would also allow for possible link-up with the primary crack.

The type of continuing damage assumption that the designer must make when the assumed primary damage enters into and terminates at a fastener hole is described in Figure 1.3.5. The continuing damage in this case is a crack on the opposite side of the hole entered by the primary crack. The continuing damage crack is taken as the crack that has grown from an initial small imperfection of a 0.005 inch radial corner crack through the time period that it takes the primary damage to terminate at the hole.

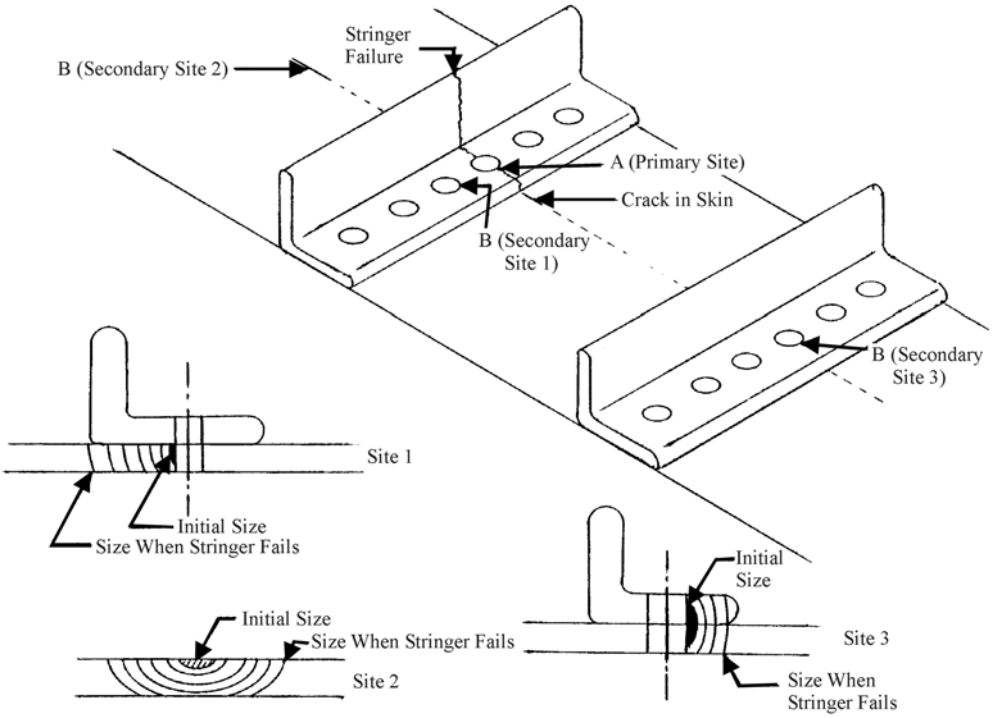

Figure 1.3.4. Example of Continuing Damage Types and Locations Assumed When Primary Damage Terminates Due to Element Failure

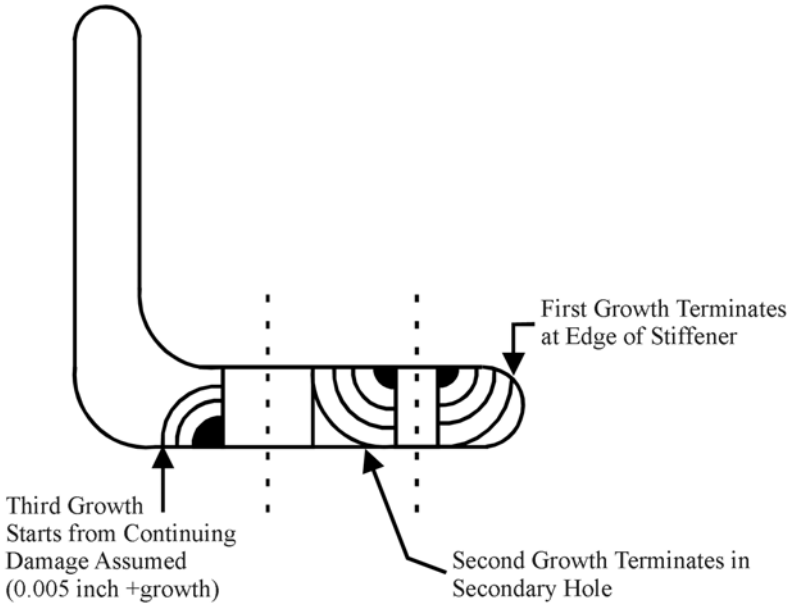

Figure 1.3.5. Continuing Crack Assumed at Opposite Side of Hole When Primary Crack Terminates at a Hole

1.3.4.3 Fastener Policy

In practice, the growth of flaws from fastener holes can be retarded by the use of interference fit fasteners, special hole preparation such as cold work, and to some degree, by joint assembly procedures like friction due to joint clamp-up. Because these procedures delay flaw growth, the slow crack growth lives (or intervals) can be significantly longer than those obtained from structure containing conventional low torque clearance fasteners

Experience has shown that to achieve the beneficial effects of these techniques consistently, exceptionally high quality process control is required during manufacture. However, this is not always obtained. As a result, it is thought unwise to consider all interference or hole preparation systems effective in retarding crack growth.

As stated in JSSG-2006 paragraph A3.12.1.g, to maximize safety of flight and to minimize the impact of manufacturing errors, the damage tolerance guidelines should be met without considering the beneficial effects of specific joint design and assembly procedures such as interference fit fasteners, cold expanded holes, and joint clamp-up.

Exceptions to this policy can be considered. The limits of the beneficial effects used in design should be no more than derived from assuming a 0.005 inch corner flaw as initial damage in an as-manufactured, non-expanded hole containing a neat fit fastener in a non-clamp-up joint.

1.3.4.4 In-Service Inspection Damage Assumptions

The basic rationale used to write assumed sizes following an in-service inspection is essentially the same as for the case of intact structure. Once it is established that reliance on in-service inspection is required to ensure safety, the damage size assumed to exist after an in-service inspection is that associated with the appropriate level of NDI capability, as opposed to that associated with initial manufacturing inspection capability. In special cases where specific part removal at the depot is economically warranted, the contractor may recommend that this action be taken. In this case, the assumed damage subsequent to part removal and inspection may be smaller than that associated with in-service inspection capabilities. It may in fact be the same as in the original design, providing the same inspection procedures as used in production are used and certified inspection personnel perform the inspection.

Figure 1.3.6 and Table 1.3.3 summarize the in-service post inspection damage sizes as a function of conditions and thickness, from JSSG-2006 Table XXXII. With fasteners installed and sufficient accessibility to the location, the maximum undetectable damage size is 0.25 inch of uncovered length at fastener holes. Depending upon part thickness, this damage may be a through or part-through flaw. The flaw size was established based on limited available inspection reliability data where the inspection was performed on the assembled aircraft as opposed to the part level inspection performed during production fabrication. These assumptions are considered to be applicable for penetrant, magnetic particle, and ultrasonics. Because of lack of sensitivity, X-ray is not considered appropriate for detecting tight fatigue cracks and thus is not applicable to these flaw size assumptions.

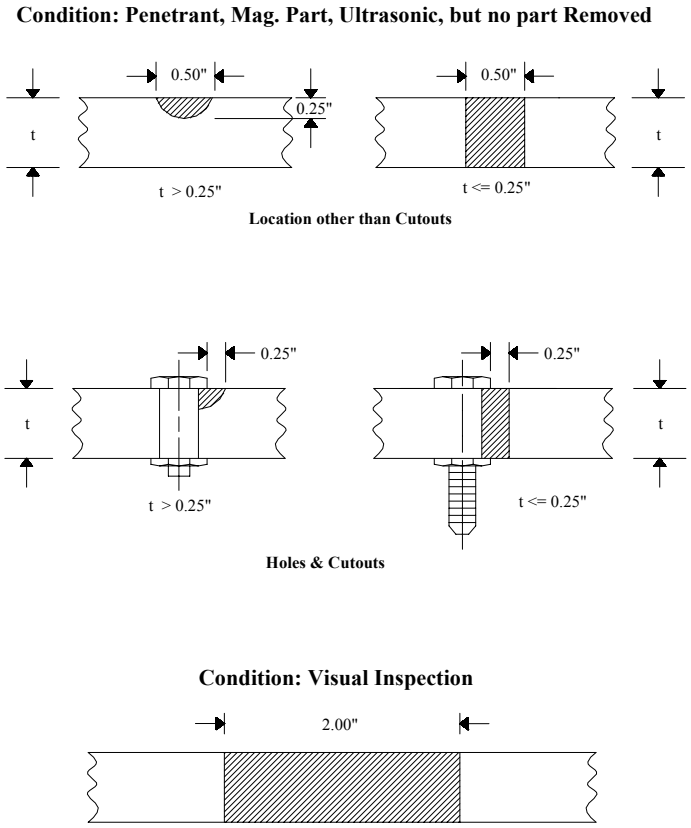

Figure 1.3.6. Summary of Initial-Flaw Sizes for Structure Qualified as In-Service-Inspectable

Table 1.3.3. In-Service Inspection Initial Flaw Assumptions

Accessibility	Inspection Method	Initial Flaw Assumption
Off-aircraft or on-aircraft with fastener removal	Same as initial	Same as initial
On-aircraft without fastener removal	Penetrant, magnetic particle, ultrasonic, eddy current	For $t \leq 0.25$”, 0.25” through thickness flaw at holes; For $t \leq 0.25$”, 0.50” through thickness flaw at other locations; For $t > 0.25$”, 0.25” radial corner flaw at holes; For $t > 0.25$”, 0.25” deep x 0.50” long surface flaw at other locations
On-aircraft with restricted accessibility	Visual	For slow crack growth, non-inspectable For fail-safe structure, primary load path failed

At locations other than holes or cutouts, a flaw size of surface length 0.50 inch is assumed to be representative of depot level capability. Where visual inspection is performed on the assembled aircraft, the minimum assumed damage is an open through the thickness crack having an uncovered length of 2 inches. This value was established based on visual inspection reliability data derived from inspection of large transport type aircraft during fatigue testing and subsequent teardown inspection, shown in Figure 1.3.7.

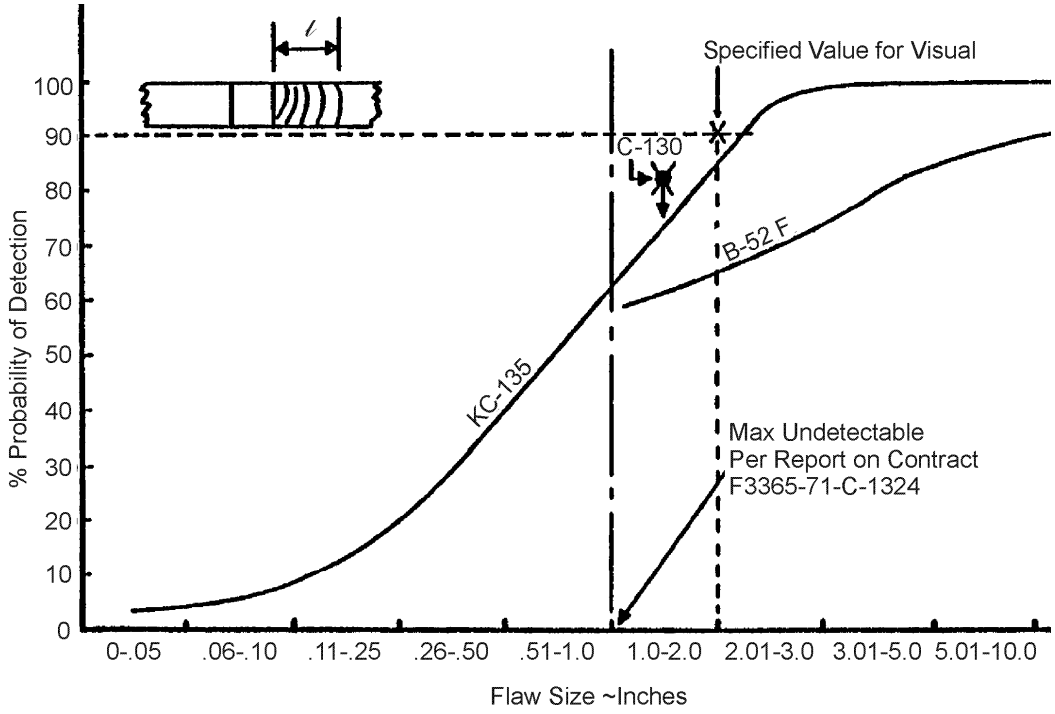

Figure 1.3.7. Development of Minimum NDI Detection for Visual Inspection

1.3.4.5 Demonstration of Initial Flaw Sizes Smaller Than Those Specified

The choice of smaller initial damage must be justified either through an NDI demonstration or a proof test. The NDI demonstration program is described in JSSG-2006 paragraph 4.12.1.a. The program must be formulated by the contractor and approved by the Air Force and must verify that, for the particular set of production and inspection conditions, flaws will be detected to the 90% probability level with 95% confidence.

Where no other means of NDI is available or where it is cost effective, the proof test can be an effective means of screening structure for flaws. Proof testing generally has been successful for the more brittle materials which exhibit plane strain fracture behavior (e.g. high strength steels) and for small structural components. The application of proof testing to complete airframe structure in the USAF has been somewhat limited. The notable exception has been the cold proof tests (-40° F) of the F-111 aircraft to clear the D6AC steel wing carry-through and appendage components for flight usage.

In general, proof testing has only been used on major airframe components as a last resort to allow operation (usually restricted) until extensive modifications are made to the structure (e.g. wing reskin modification of the B-52D). In deriving estimates of the initial flaw size associated with the proof test conditions, approved upper-bound fracture toughness values shall be used for

the materials under proof test conditions. Section 3 also presents more information on the proof test concept.

1.3.5 Residual Strength Guidelines

The residual strength capability is defined as the amount of static strength available at any time during the service exposure period considering that damage is initially present and grows as a function of service exposure time. The strength degrades with increased damage size, as shown in Figure 1.3.8. The intent of JSSG-2006 paragraph 3.12.2 is to provide residual strength capability for intact structure of at least design limit load at all times throughout the service life of the structure. The requirement to maintain limit load capability is considered necessary to allow unrestricted operational usage.

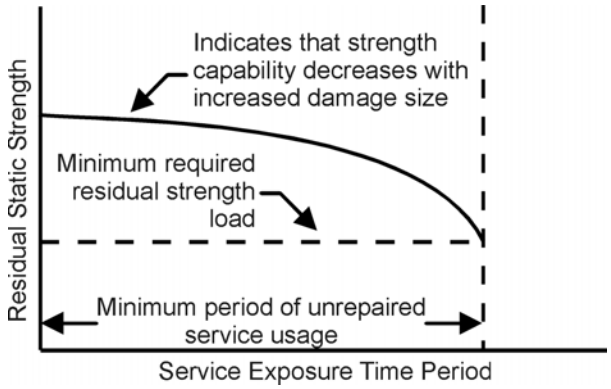

Figure 1.3.8. Residual Strength Diagram

The residual strength guidelines are specified in terms of the minimum internal member load P_{xx} that must be sustained. The magnitude of P_{xx} depends upon the service exposure time of the structure between inspections and the overall degree of inspectability. The load P_{xx} is intended to represent the maximum load that the aircraft might encounter during the time interval between inspections.

The required P_{xx} is at least design limit load for all intact structure whether the structure is being qualified as Slow Crack Growth or Fail Safe. The required P_{xx} is also at least design limit load when the only planned safety inspections are at the depot (i.e., the depot or base-level inspection category).

In addition, all Fail Safe Structure must be designed to be at least depot level inspectable, and P_{xx} over this inspection interval must be at least limit load. This restriction is obvious since the only means to protect the safety is not to allow damage growth to degrade the strength of the structure to less than design limit load. Where partial failure is allowed and subsequent detection of failed load path is required, the limit load requirement on intact structure has two benefits. First, it is the only way that the operational force can be maintained with unrestricted capability; and second, when coupled with the intact structure damage growth guidelines, it provides assurance that, under normal situations, early nuisance cracking will not occur as a result of lower stress.

1.3.5.1 Fail-Safe Structure at Time of Load Path Failure

For Fail Safe Structure, there is a requirement that the remaining structure at the time of a single load path failure must be capable of withstanding a minimum load P_{yy}. This load P_{yy} is at least the load that causes the load path failure, plus an additional increment to account for the dynamic conditions of the breaking member. While most data and analyses indicate that the dynamic magnification factor associated with the member failure is probably very small, the current guidance in JSSG-2006 requires that a 1.15 dynamic factor be applied to the redistributed incremental load unless another value is determined by test or analysis. For non-metallic structure, the dynamic factor should be verified by testing. Figure 1.3.9 illustrates the change in residual strength guidelines as a result of a load path failure.

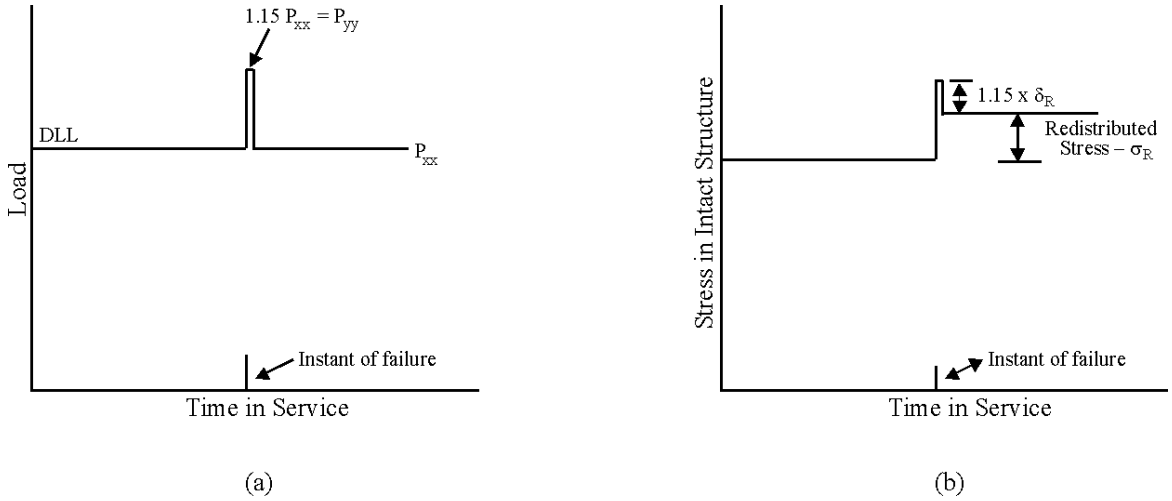

Figure 1.3.9. Schematic Residual Strength Guidelines for Fail Safe Structure

1.3.5.2 Determining the Residual Strength Load for Remaining Structure

The magnitude of the required residual strength load depends upon the exposure time in service because the longer the exposure time, the greater the probability of encountering a high load. Accordingly, the value of required P_{xx} load increases with an increase in the inspection interval or period of unrepaired service usage (allowable crack growth period). For the short service exposure times between inspections for the In-Flight Evident, Ground Evident and Walk Around Visual categories, the probability of encountering limit load conditions is low and thus the required P_{xx} may be significantly below design limit load. For the longer exposure times between depot or base level inspections, the probability of encountering limit load is much higher, and therefore for Depot Level and Non-Inspectable categories, the minimum required P_{xx} must be at least limit load, but P_{xx} need not be greater than 1.2 times the maximum load in one lifetime.

The value of P_{xx} is established from load spectra data derived from a mission analysis of the particular aircraft considering average usage within each mission segment. Unless otherwise stated, MIL-A-8866 is the basic source of load factor data for the various classes of aircraft. Since safe operation depends upon the residual strength capability and since any individual aircraft may encounter loads in excess of the average expected during the particular exposure time, the P_{xx} load required is larger than the average derived value.

One way to determine the level of P_{xx} required is to hypothetically increase the service exposure time for the aircraft between inspections by a factor of M. This is the method used in JSSG-2006. The values of M are specified in JSSG-2006 Table X, and summarized in Table 1.3.4. For example, under the ground-evident level inspectability category, the P_{xx} load is the maximum load expected to occur once in 100 flights (M x inspection interval = one flight x 100).

Table 1.3.4. Inspection Interval Magnification Factors from JSSG-2006 Table X

P_{xx}	Degree of Inspectability	Typical Inspection Interval	Magnification Factor M
P_{FE}	In-Flight Evident	One Flight	100
P_{GE}	Ground Evident	One Flight	100
P_{WV}	Walk-Around Visual	Ten Flights	100
P_{SV}	Special Visual	One Year	50
P_{DM}	Depot or Base Level	¼ Lifetime	20
P_{LT}	Non-Inspectable	One Lifetime	20

* P_{xx} = Minimum average interval member load that will occur once in M times the inspection interval. Where P_{DM} or P_{LT} is determined to be less than the design limit load, the design limit load shall be the required residual strength load level. P_{xx} need not be greater than 1.2 times the maximum load in one lifetime if greater than design limit load.

The basis for the specified M values is somewhat arbitrary although it is felt that the loads derived by this method are not unreasonably conservative. The basis for $M = 100$ is exceedance data for transport type aircraft, where it has been observed that shifting exceedances by approximately two decades (i.e., $M = 100$) magnifies the value of load factor (or stress) by approximately 1.5 (Figure 1.3.10). It was recognized that for fighter data, exceedances approaching or exceeding design limit values are probable but that extrapolation of the basic exceedances curve very far beyond limit load factor (n_z) is often meaningless and unwarranted due to physical limitations of the vehicle and crew. Furthermore, in most cases actual service data is somewhat sparse for this region of the curve. Therefore, (1) an upper limit was required on P_{xx} for fighter aircraft and (2) the value of M should be less for longer inspection intervals in order that unreasonable factors would not be imposed should the actual derived P_{xx} be less than the specified upper limit. The values of M equal to 20 and 50 are arbitrary but probably not unreasonable. Where the derived P_{xx} is larger that that associated with the design limit conditions, P_{xx} can be taken as 1.2 times the maximum load expected to occur in one design lifetime.

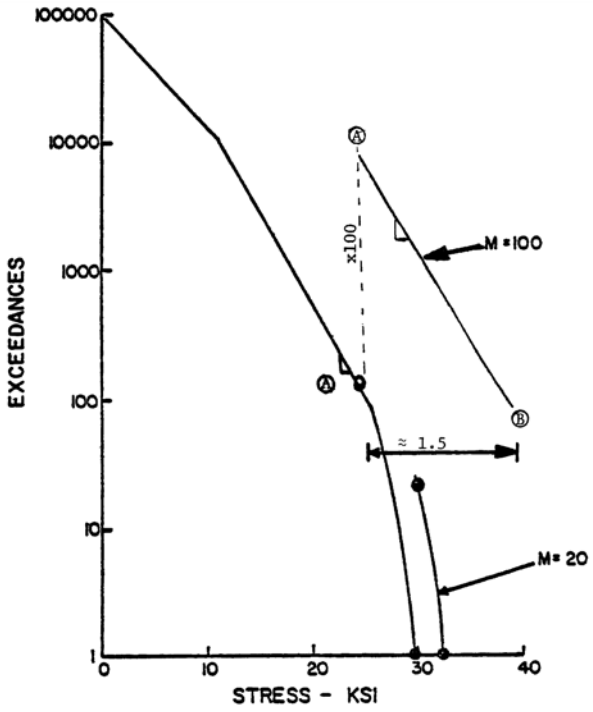

Figure 1.3.10. Illustration of Procedure to Derive *M* Factor to Apply to Exceedance Curve

EXAMPLE 1.3.3 Derivation of P_{xx} From Exceedance Data for Non-Inspectable Structure

The procedure for obtaining P_{xx} is illustrated using the exceedance plot shown here. This figure presents the average exceedance data for one design lifetime. The point A represents the maximum load expected in one lifetime; this is shown to be larger than the limit load (Point E). For the core of a non-inspectable structure, the twenty lifetime (M_x inspection interval) exceedance curve is obtained by shifting the exceedance curve from point A to point B and extrapolating to point C. The twenty lifetime exceedance curve yields P_{xx} (derived) at C. The required load P_{xx} then is either the value derived at C or 1.2 × (load at point A) i.e., the load at point D, whichever is smaller. In this case, P_{xx} (= P_{LT}) is the load at point C.

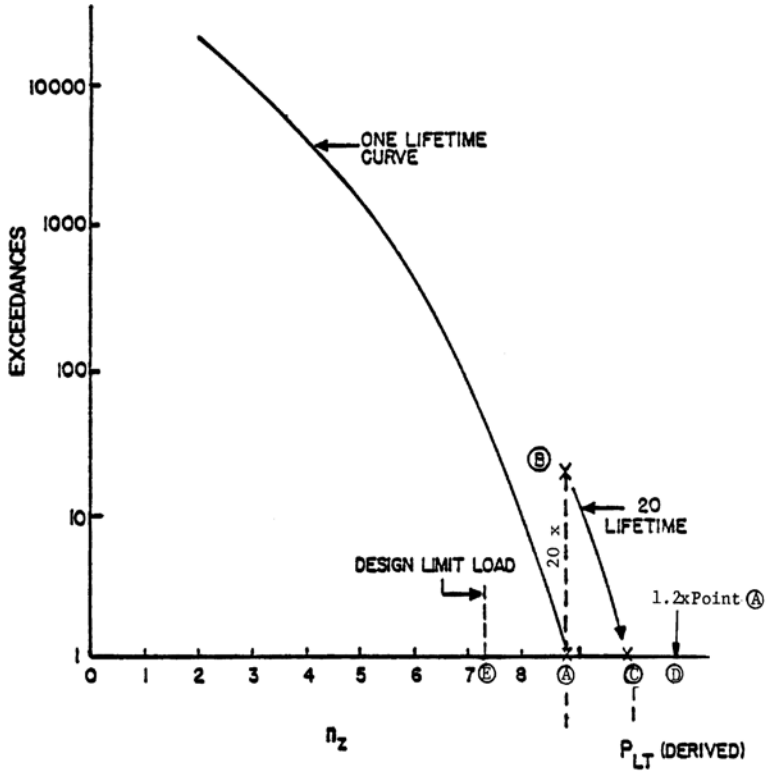

1.3.6 Required Periods Of Safe Damage Growth

All safety of flight structure are required to maintain the required residual strength in the presence of damage for a specified period of unrepaired service usage. During the period of safe damage growth, the initial damage, which is presumed to exist in the structure, will not grow to a critical size and cause failure of the structure.

The required period of safe damage growth is a function of design category (either slow crack growth or fail safe) and the degree of inspectability as defined in Section 1.3.3. In order to cover various uncertainties associated with crack growth during service usage that may not be adequately accounted for in the analyses or laboratory test, the structure must withstand a period of service usage longer than the planned inspection interval. The periods of unrepaired service usage for the inspectability categories is given in JSSG-2006 Table XXXIII and repeated in Table 1.3.5.

Table 1.3.5. Minimum Periods of Unrepaired Service Usage for In-Service Inspectable Structures

Degree of Inspectability	P_{xx}	Minimum Period of Unrepaired Service Usage
In-Flight Evident	P_{FE}	Return to base
Ground Evident	P_{GE}	Two flights of most damaging design mission
Walk-Around Visual	P_{WV}	5 × Inspection interval (= 5×10 flights)
Special Visual	P_{SV}	2 × Inspection interval (= 2× one year)
Depot or Base Level	P_{DM}	2 × Inspection interval (= 2× ¼ lifetimes)

1.3.6.1 Slow Crack Growth Structure

For slow crack growth structure, the required period of unrepaired service usage is two service usage lifetimes. A factor of two is applied to cover various uncertainties associated with crack growth during service usage, such variability in material properties, manufacturing quality and inspection reliability.

1.3.6.2 Fail Safe Multiple Load Path Structure

Fail safe structure must be able to withstand a specified period of service usage after a primary load path failure. The period of unrepaired service usage depends upon the type and frequency of inspection for the structure.

An initial inspection interval is established to insure detection of any premature primary element failure. The initial inspection interval is dependent on the particular geometry and degree of inspectability, as given in Table 1.3.5. The initial inspection interval should not be greater than one half of the time to primary load path failure from the specified initial flaw for primary elements plus one half of remaining time to failure of adjacent structure from its flaw size at the time of primary element failure. These initial flaw sizes are specified in Section 1.3.4.

Subsequent inspection intervals are also based on the degree of inspectability of the primary element as given in JSSG-2006 Table XXXIV and repeated in Table 1.3.6.

1.3.6.3 Fail Safe Crack Arrest Structures

Fail safe crack arrest structure must be able to withstand a specified period of service usage after a primary load path failure. The period of unrepaired service usage depends upon the inspectability level for the structure. The degrees of inspectability for fail safe crack arrest structure are the same as for fail safe multiple load path structures.

The initial inspection intervals are given in Table 1.3.5, and subsequent inspection intervals are given in Table 1.3.6.

Table 1.3.6. Subsequent In-Service Inspection Intervals for Fail-Safe Structures

Primary Element Degree of Inspectability	P_{xx}	**Subsequent Inspection Intervals**
In-Flight Evident	P_{FE}	Each flight of most damaging design mission
Ground Evident	P_{GE}	Two flights of most damaging design mission
Walk-Around Visual	P_{WV}	Ten flights of most damaging design mission
Special Visual	P_{SV}	One year
Depot or Base Level	P_{DM}	One half of the remaining time to failure of the adjacent structure from the flaw size specified for adjacent load paths at the time of primary element failure; or, if the adjacent structure is inspected, one half of the remaining time to failure of the adjacent structure from in-service inspection flaw size for the adjacent structure as specified. In either case, the primary element is assumed to be failed.

1.3.7 Illustrative Example Of Guidelines

These examples are based on the lower wing structure shown in Figure 1.3.11. The structure is comprised of multiple skin and stringer elements. The skin panels 1–5 are considered the major load paths. At each spanwise splice, a major splicing stringer is located and the construction is such that the load paths are independent, i.e., no common manufacturing tie exists between the skin panels.

The design service life is assumed to be 40,000 hours for these examples.

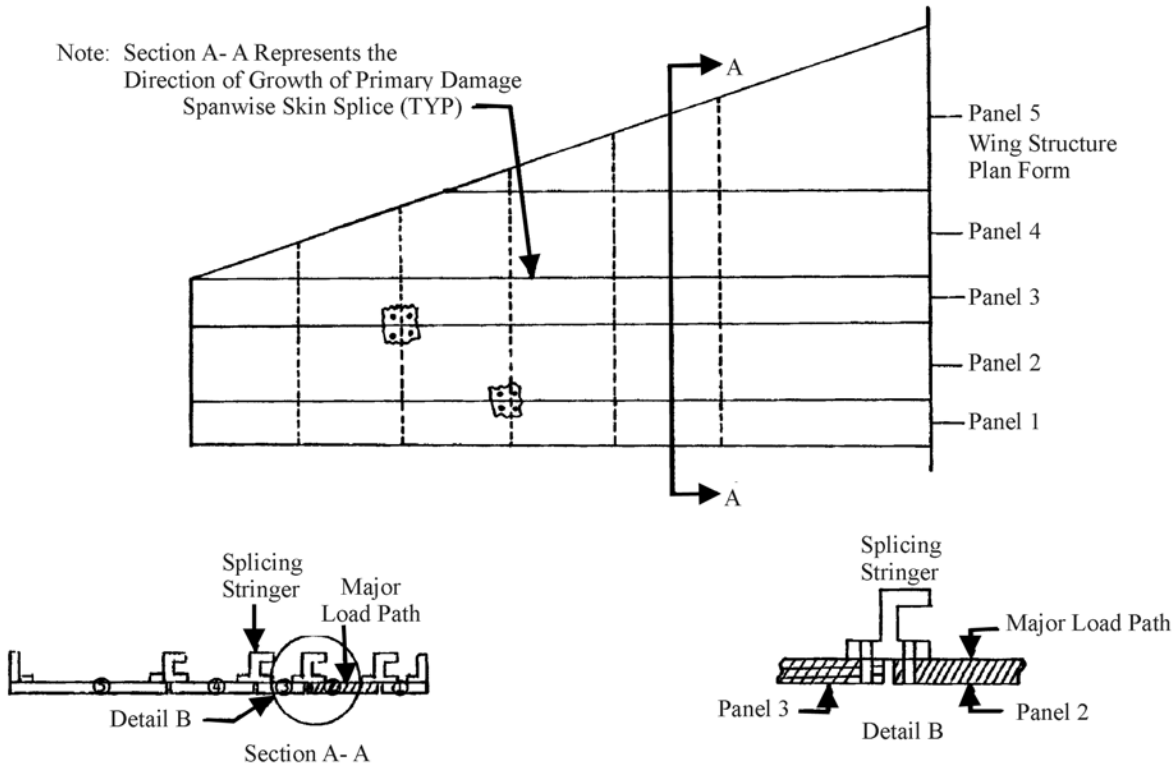

Figure 1.3.11. Structural Example of Lower Wing Skin

1.3.7.1 Slow Crack Growth Structure

The choice of structural design concept for this example is Slow Crack Growth Structure. The steps required to satisfy this requirement are outlined in the following sections. Panel ② is chosen to be the critical load path for purposes of illustration

1.3.7.1.1 Initial Flaw Sizes Assumed to Result from Manufacturing

The assumed flaws for the slow crack growth type structure are described in Section 1.3.4. Thus, an 0.050 inch corner flaw is assumed to exist at the critical fastener hole joining panel ② and the splicing stringer, as shown in Figure 1.3.12. For this example, it is assumed that a common drilling operation was employed to prepare the hole with the primary damage, and therefore the same size crack is assumed in both elements. Also, as explained in Section 1.3.4, initial flaws equivalent in stress-intensity factor level to an 0.005 inch radius corner flaw shall be assumed to exist in each hole of each element in the structure, such as shown in Figure 1.3.12.

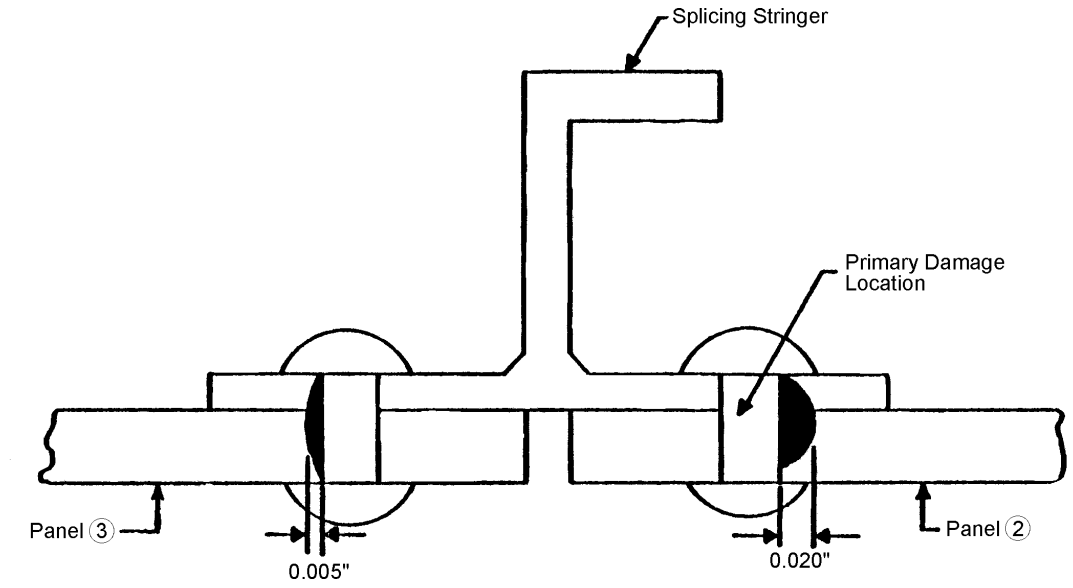

Figure 1.3.12. Illustration of Initial Flaws for Structure Qualified as Fail-Safe Multiple Load Path

1.3.7.1.2 Choice of Inspection Category

There are only two inspection categories that are available to the designer for Slow Crack Growth Structure: in-service non-inspectable and depot level inspectable. The choice of inspection category directly impacts the guidelines for residual strength and for damage growth limits. For purposes of this discussion, both categories are presented.

1.3.7.1.3 In-Service Non-Inspectable Category

For this example case, no special in-service and no depot level inspections will be required to protect the integrity of the lower wing structure shown in Figure 1.3.11. The implication is that no inspections are desired; however, there are cases in which the flaw size at failure is so small that such a flaw might easily be overlooked during an inspection. Thus, the in-service non-inspectable category covers those cases where inspections are neither desirable nor practical.

Residual Strength Load, P_{xx}

From Table 1.3.4, the required level of residual strength P_{xx} for non-inspectable structure is P_{LT}. This is the maximum load that could occur in one lifetime. Example 1.3.3 describes the method for establishing this load level.

Analysis Guidelines

The slow crack growth and residual strength guidelines for this category are illustrated in Figure 1.3.13. This figure specifically shows that the initial manufacturing damage is restricted from growing to critical size and causing failure of the structure due to the application of P_{LT} in two (2) design service lifetimes. Note that the damage limit is the ultimate failure of the wing. Engineering judgement may dictate that a more reasonable limit and, perhaps, an easier situation to adhere to, would be to establish the limit at some intermediate point, such as the failure of the primary load path panel ②. This might be accomplished in design at very little expense to overall weight.

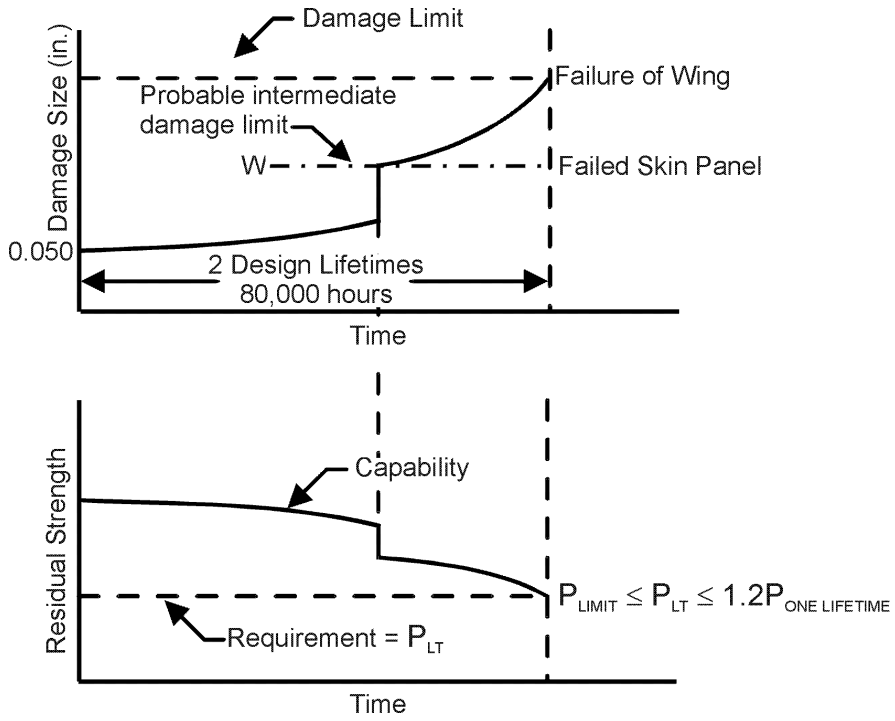

Figure 1.3.13. Illustration of Damage-Growth and Residual-Strength Guidelines for Example Problem Qualified as Slow Crack Growth Non-Inspectable

1.3.7.1.4 Depot Level Inspectable Category

For this example case, the damage which is presumed to exist in the structure after completion of the depot or base level inspection is given in Table 1.3.3.

In-Service Flaw Assumptions Following Inspection

The capability of inspection in the field is generally less than at the depot. The sizes of damage assumed to exist following inspection are specified in Table 1.3.2. For this example, assume that penetrant or ultrasonics will be used at the depot both exterior and interior to the lower surface. If this type of inspection is conducted, the damage likely to be found will be much smaller than the failed skin panel. From Table 1.3.3, the minimum damage size to be assumed at the hole is a through crack of 0.25 inch uncovered length. The locations of the 0.25 inch flaw in both the skin and the splicing stringer should be selected on the basis of inspectability but should be the location most critical to subsequent growth. Assume for purposes of illustration, that the damage is as indicated in Figure 1.3.14. The 0.005 inch flaw away from the primary damage site represents the initial manufacturing type damage as explained in Section 1.3.4.

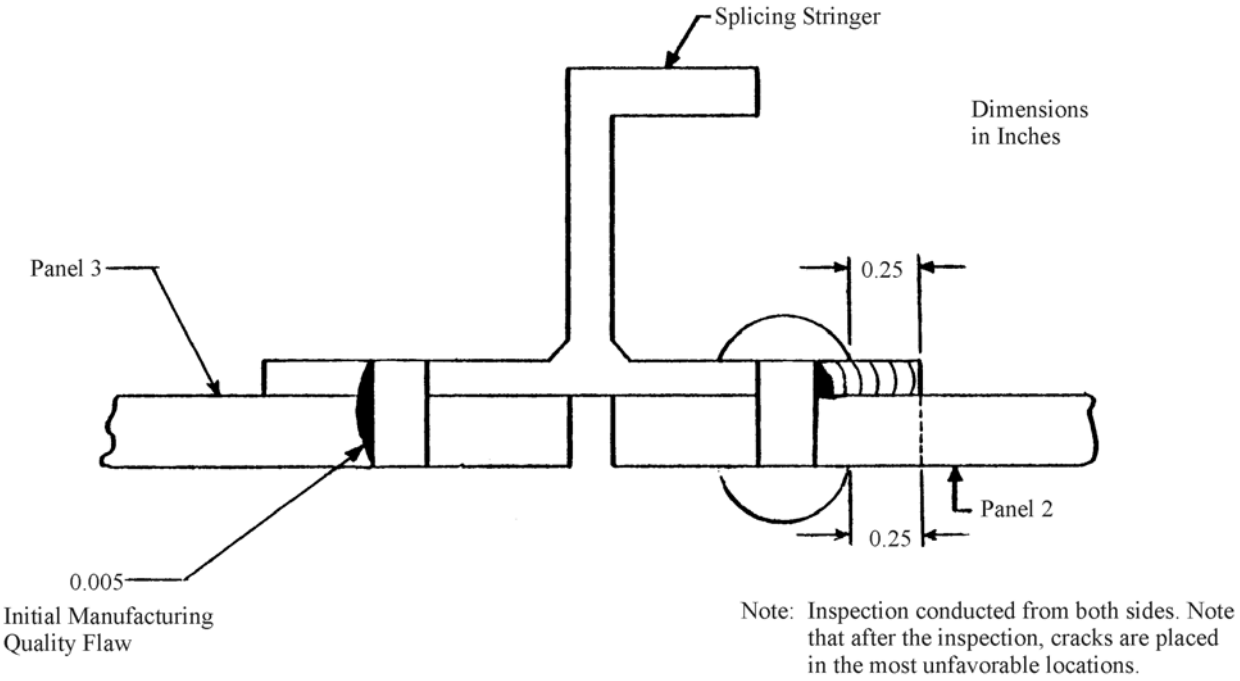

Figure 1.3.14. Illustration of Primary Damage Following a Depot-Level Penetrant or Ultrasonic Inspection

Residual Strength Load, P_{xx}

The required level of residual strength P_{xx} for the depot or base level inspection category is P_{DM}, as shown in Table 1.3.4. This is the maximum load that would occur in the planned ¼ lifetime (10,000 hour) inspection interval. The method for establishing this particular load level follows the method outlined in Example 1.3.3 where the one life time exceedance curve is multiplied by a factor of 5 rather than 20.

Analysis Guidelines

Figure 1.3.15 illustrates the slow crack growth and residual strength guidelines for this category, as established by JSSG-2006 paragraph A3.12.2. This figure specifically shows that the post-inspection damage is restricted from growing a crack to critical size and thereby causing failure of the structure due to the application of P_{DM} in two times the inspection interval (½ lifetime, 20,000 flight hours).

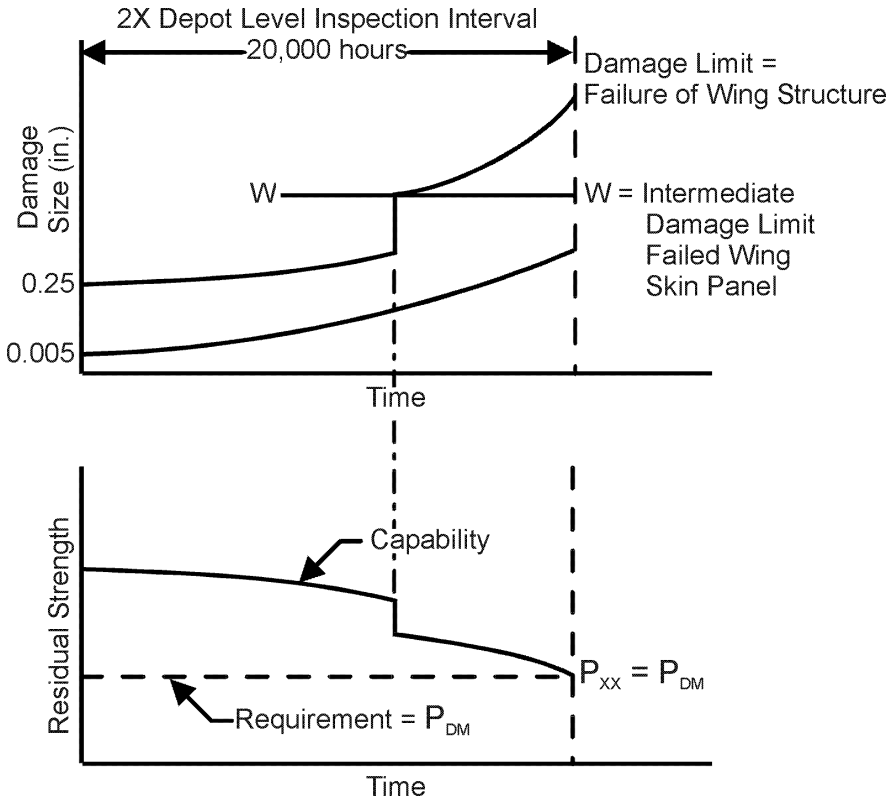

Figure 1.3.15. Illustration of Damage-Growth and Residual Strength Guidelines for Example Problem Qualified as Depot-Level-Inspectable

1.3.7.2 Fail Safe Structure

This example of fail safe structure is based on the lower wing structure shown in Figure 1.3.11. The structure is assumed to be a Fail Safe Multiple Load Path Structure and the steps required to satisfy this requirement will be outlined. The structure will be designed to be Fail Safe by virtue of being able to sustain the failure of one major load path or skin panel and still maintain the residual strength and remaining structural guidelines. For illustration purposes, panel ② was chosen as the critical load path. Although the loss of panel ② is critical from a remaining structure point of view, every panel must be designed to meet the intact guidelines.

1.3.7.2.1 In-Service Inspection Consideration

Since the design is intended to satisfy the Fail Safe Multiple Load Path category, an in-service inspection plan is required. It is assumed that the lower surface will be periodically inspected in the field by a walk-around-visual-type examination, generally unaided. The frequency of these inspections is approximately every ten flights. In addition, the structure will undergo a depot level inspection at approximately ¼ design lifetime intervals of every 10,000 hours. During manufacture, inspections by conventional methods will be conducted and a fracture control program will be instituted.

1.3.7.2.2 Initial Flaw Considerations

Flaws assumed to result from manufacturing and/or material conditions are specified in JSSG-2006 paragraph A3.12.2 for Fail Safe Structure. The primary damage at a fastener hole (Figure

1.3.16) is an 0.05 inch corner flaw. Since the drilling operation is common to the skin and splicing stringer, the 0.05 inch flaw must be assumed in both members. Panel ② is considered for this example because it was previously chosen to be the critical load path. Note that only one primary damage site is assumed for each load path (e.g. along the path of expected damage, along a wing section). Also, it is not necessary to consider the interaction of flaws from adjacent primary sites. Each analysis of primary damage is conducted independently. At each hole other than the assumed primary site, an 0.005 inch radius corner flaw is assumed to represent average or typical manufacturing quality. The effect of interactions between the 0.005 inch flaws and the primary flaws must be considered when conducting the analysis.

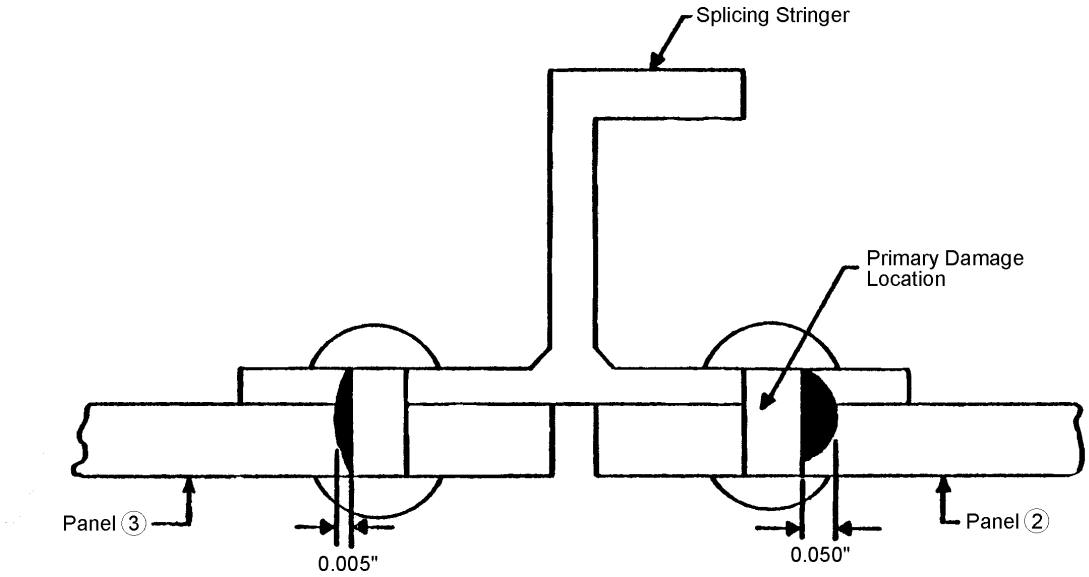

Figure 1.3.16. Initial-Flaw Assumptions for Example Case Qualified as Fail Safe

1.3.7.2.3 In-Service Flaw Assumptions Following Inspection

The capability of inspection in the field is generally less than at the depot. The sizes of damage assumed to exist following inspection are specified in JSSG-2006 paragraph A3.12.1. For this example, assume that penetrant or ultrasonics will be used at the depot both exterior and interior to the lower surface. If this type of inspection is conducted, the damage likely to be found will be much smaller than the failed skin panel. From JSSG-2006 Table XXXII the minimum damage size to be assumed is a through crack of 0.25 inch uncovered length. The locations of the 0.25 inch length both in the skin and in the splicing stringer should be selected on the basis of inspectability but should be the location most critical to subsequent growth. Assume for purposes of illustration, that the damage is as indicated in Figure 1.3.17. The 0.005 inch flaw away from the primary damage site represents the initial manufacturing type damage as specified in JSSG-2006 paragraph A3.12.1.

1.3.7.2.4 Adjacent Structure Damage Following the Failure of the Major Load Path

Figure 1.3.18 illustrates the condition of the structure following the complete failure of the primary load path (skin panel ②) represented by the cross hatched area. The condition of the remaining structure is as specified in JSSG-2006 paragraph A3.12.1c(2) since this is an example

of independent structure. Each fastener hole in the structure is assumed to contain the 0.005 inch typical manufacturing hole quality flaw. The Δa_2 increment is the growth of these typical flaws from the time of manufacture until the point at which the load path is assumed to have failed. The increment Δa_2 will be discussed later.

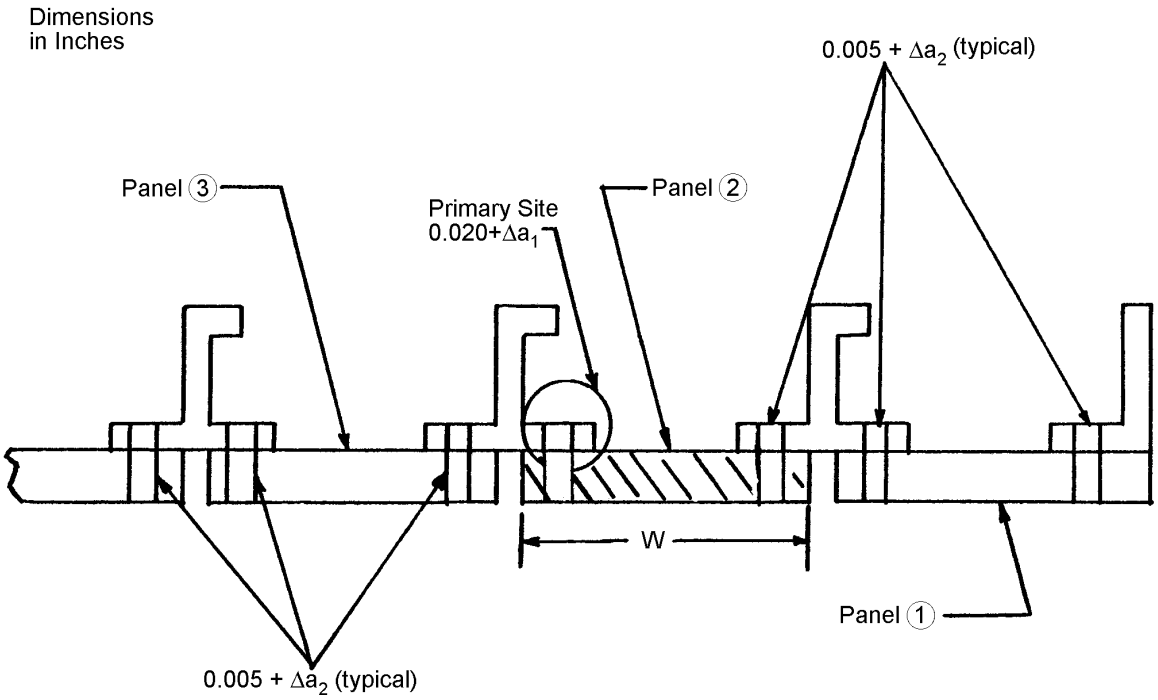

Figure 1.3.17. Illustration of Primary Damage Assumptions Following the Failure of Major Load Path (Panel 2)

1.3.7.2.5 Analysis of Intact Structure–Residual Strength Guidelines and Damage Growth Limits

The specific set of guidelines for intact structure depends upon the capability of the depot level inspection. Since this example has assumed the situation where the normal inspection can detect less than a failed load path, this case will be examined first.

The intact requirement is that the in-service damage, assumed to be present following the depot level inspection (Figure 1.3.17), shall not grow and cause failure of the major load path (panel ②) before the next opportunity to discover the damage, i.e., the next inspection.

Since this is merely a one-time design requirement, not specifically intended for safety, it is not necessary to account for prior service at the time at which the requirement was imposed. Thus, the structure is considered as "new" and no incremental growth Δa due to prior service is computed. Figure 1.3.18 illustrates schematically the residual strength and growth guidelines that must be met for the intact structure.

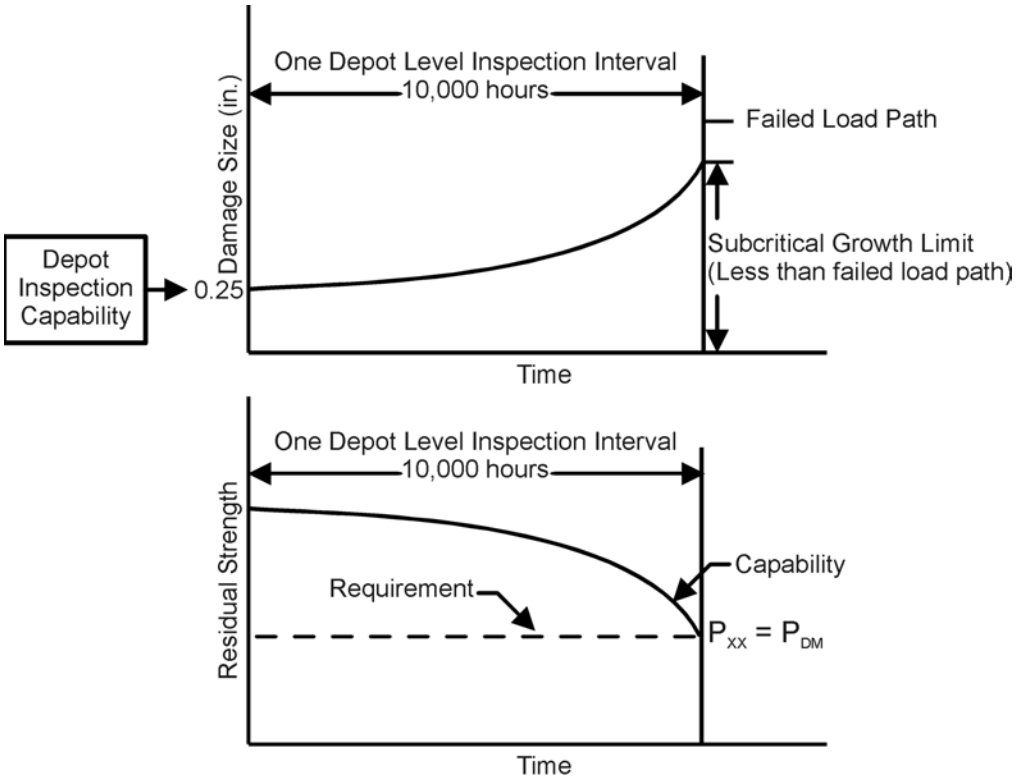

Figure 1.3.18. Illustration of Damage-Growth Limits and Residual-Strength for Intact Structure Following Depot or Base-Level Inspection for Less-Than-Failed Load Path

1.3.7.2.6 Analysis of Intact Structure (Alternate Requirement)

If the depot level inspection is incapable of finding damage less than a failed load path, then the requirement for intact structure is given in JSSG-2006 paragraph A3.12.1c. This states that initial manufacturing damage shall not grow to the size required to cause load path failure due to the application of P_{LT} in one design lifetime. The initial damage assumption for this case is illustrated in Figure 1.3.16. The schematic of the growth and residual strength guidelines are illustrated in Figure 1.3.19.

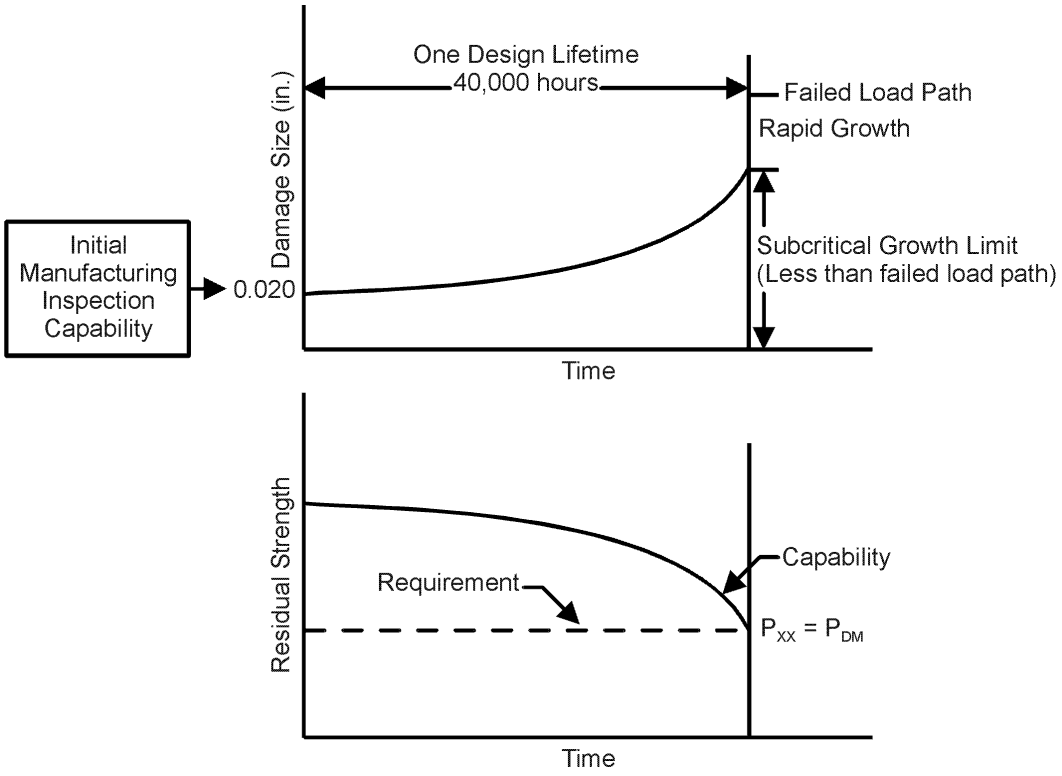

Figure 1.3.19. Illustration of Damage-Growth Limits and Residual Strength; Intact Structure for When Depot Inspection Cannot Detect Less-Than-Failed Load Path

1.3.7.2.7 Discussion of Intact Structure Analysis

Although the structure in the example was assumed to be depot level inspectable for less than a failed load path, the intact structure requirement associated with this set of conditions might have been more difficult to meet than would be the case if the structure were not inspectable for less than a failed load path. In the latter case, it would be satisfactory for the designer to qualify the structure under the alternate requirement described in Section 1.3.7.2.6. As is often the case, the designer may choose to qualify the structure in the easiest (analysis) manner.

1.3.7.2.8 Analysis of Remaining Structure Subsequent to Load Path Failure

The fail safe characteristics of this structure, i.e., the ability to fail panel ② and fly safely until the failed panel is detected, depends upon the residual strength capability at the time of and subsequent to load path failure and the capability of and frequency of in-service inspections. The remaining structure guidelines are specified in JSSG-2006 paragraph A3.12.2.2.

As stated earlier, the fail safety will be supported by walk-around-visual inspections for damage sizes on the order of a failed load path. Generally, the walk-around-visual inspection can be aided by detectable signs such as fuel leakage. At any rate, the minimum inspection capability for this example will be considered to be a failed load path.

The damage as illustrated in Figure 1.3.17 shall not grow to a size such as to cause loss of the wing due to the application of P_{VW} in 5 times the inspection interval (10 flights), i.e. in 50 flights. This is illustrated in Figure 1.3.20. The load $P_{xx} = P_{yy}$ will generally be less than the design limit

condition and P_{yy} (as discussed in Section 2.5) will always be equal to or greater than that associated with the design limit condition.

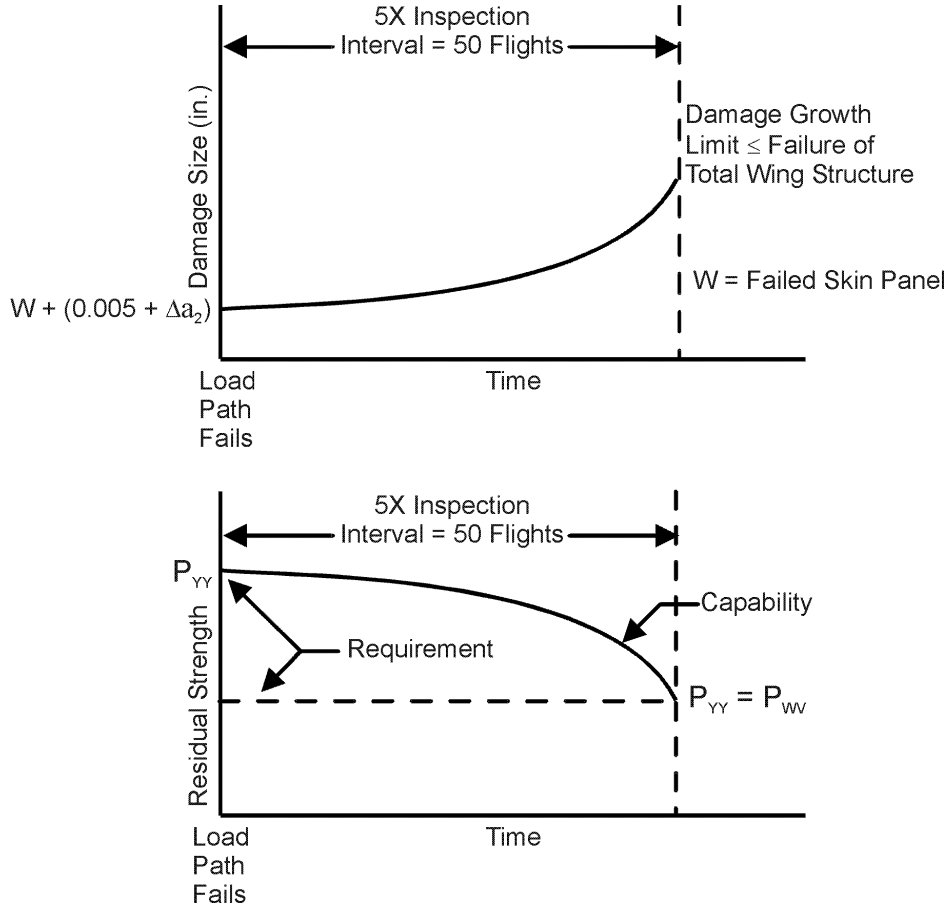

Figure 1.3.20. Illustration of Damage-Growth Limits and Strength Guidelines; Remaining Structure Subsequent to Load-Path Failure

1.3.7.2.9 Derivation of Residual Strength Load

In the analysis of the intact structure, the critical damage limit is failure of the skin panel ②. The mode of failure was slow growth of either depot level inspection type damage or initial manufacturing damage (Figure 1.3.18 and 1.3.19, respectively). In each case, the damage is assumed to grow in a stable manner until the critical damage size in the skin panel is reached. The critical damage size for this case would be that size at $P_{xx} = P_{DM}$ or $P_{xx} = P_{LT}$ where P_{xx} is bounded by

$$P_{limit} \leq P_{xx} \leq 1.2P_{one\ lifetime}$$

For a balance fail safe design, the remaining structure must be capable of withstanding the effects of the major load path failing, including the redistribution of load to adjacent members at the time of load path failure. This is the basis for the requirement that the remaining structure must support the P_{yy} residual strength load. The load P_{yy} is dependent upon the design allowable for the first panel (Panel ② in this case).

Assume for example that the P_{xx} allowable for first panel failure is exactly P_{limit}. The remaining structure must be capable of supporting P_{limit} with adjacent panels carrying the increment or that portion originally carried by panel ② at P_{limit}. This is illustrated in Figure 1.3.21 where the amount of load in panel ② at the limit design condition, i.e. P_2 is redistributed after it is multiplied by 1.15 to account for dynamic effects ($\Delta P_1+\Delta P_2+ \Delta P_3+ \Delta P_4+ \Delta P_5$). The total redistribution increment then is

$$1.15P_2 = \left(\Delta P_1 + \Delta P_3 + \Delta P_4 + \Delta P_5\right)$$

The residual strength capability of the remaining structure is then checked against this condition; the P_{yy} requirement for panel ③ is $P_{yy}^3 = P_{yy}^3 + \Delta P_3$.

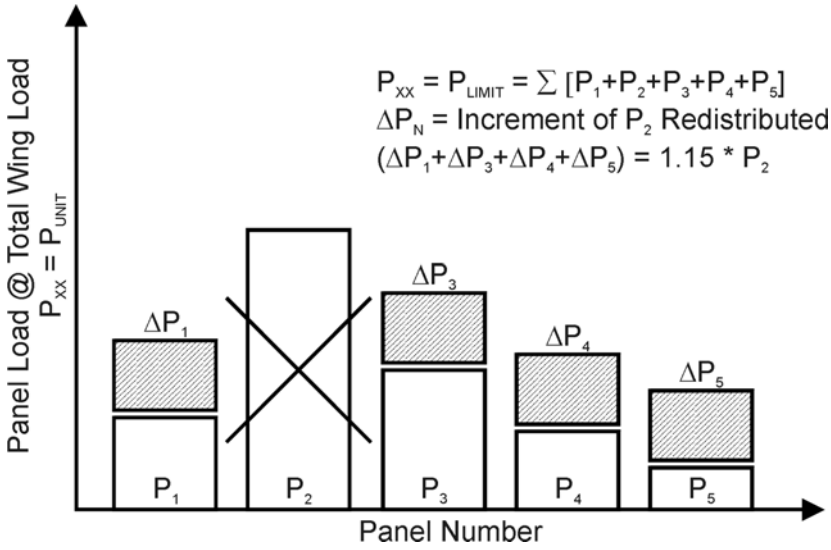

Figure 1.3.21. Illustration of Redistributed Panel Load P_2 to Adjacent Structure

1.3.7.2.10 Incremental Damage Growth Δa

The remaining structure analysis of damage growth and residual strength considers damage in the adjacent structure at the time of load path failure which has grown an amount Δa from the time of manufacture (Figure 1.3.19). Since the structure must met the single design lifetime requirement, it becomes necessary to establish at what point during the lifetime the failure of the load path is assumed to take place so that the proper amount of growth Δa can be computed to represent growth during this time segment.

Figure 1.3.22 illustrates the growth of the 0.005 inch manufacturing type damage from time zero for one design lifetime. In this example, the walk-around-visual inspection is used to detect the failure of the major load path and the inspection interval is 10 flights. JSSG-2006 Table XXXIII requires a factor of 5 on this interval and thus the damage growth life requirement is 50 flights. Therefore, the maximum amount of Δa and the condition to be met would be growth for one design lifetime minus 50 flights.

For any other in-service inspection interval the amount Δa would be computed in a similar manner. For example, if the walk-around-visual inspection was not conducted and fail safety was dependent upon discovery of damage at the scheduled 10,000 hour depot level inspection, then the increment of growth Δa would be one design lifetime minus 2x 10,000 hours, as in Figure 1.3.23.

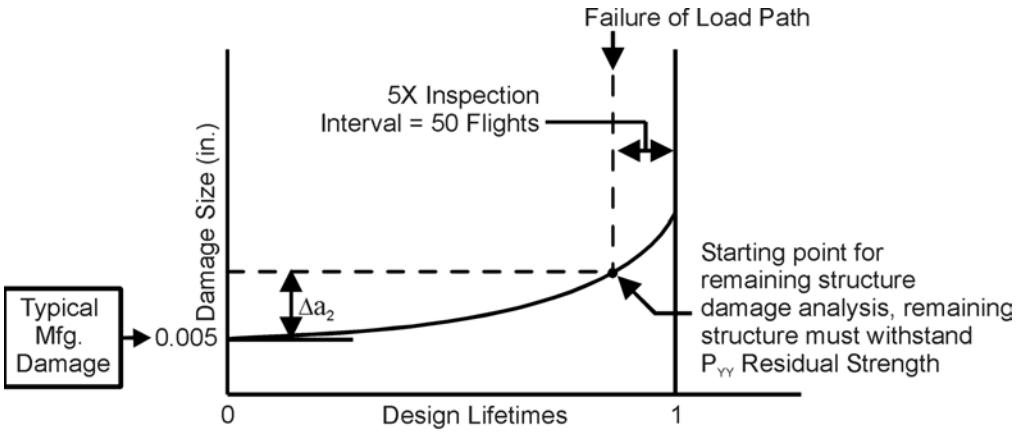

Figure 1.3.22. Development of Increment of Growth Δa_2 for Walk-Around-Visual Inspectable Damage

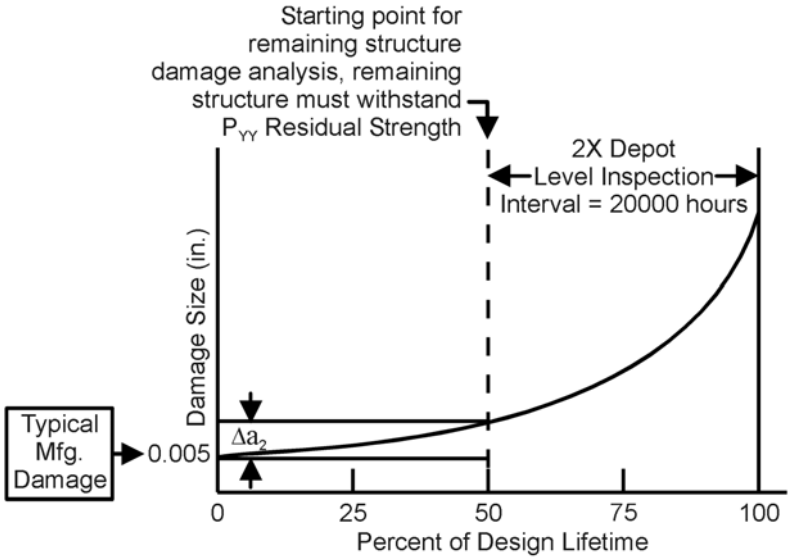

Figure 1.3.23. Development of Increment of Growth Δa_2 for Depot-Level-Inspectable Damage

1.3.7.2.11 Alternative-Analysis of Remaining Structure Subsequent to Load Path Failure

As indicated in 1.3.7.2.10, the designer may choose to depend upon the depot level inspection instead of the walk-around visual. This would be a satisfactory alternative and for this situation

the assumption would be made that the major load path failed between depot level inspections and that the aircraft would be designed to operate safely with the failed load path until the next depot inspection. Figure 1.3.24 illustrates this case.

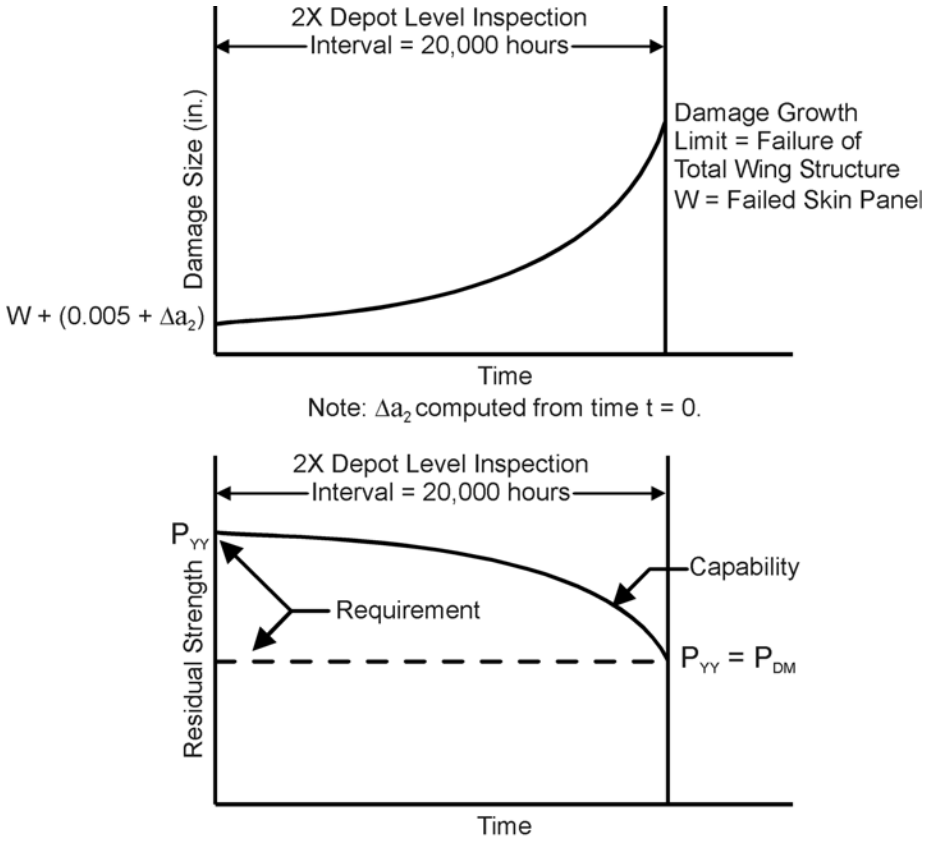

Figure 1.3.24. Illustration of Damage Growth and Residual-Strength Guidelines for Remaining Structure-Depot-Level-Inspectable

1.3.7.2.12 Summary and Comments

This example has illustrated the steps required to qualify the structure under the category of Fail Safe Multiple Load Path Structure. For this category, an intact structure requirement (prior to load path failure), a residual strength requirement at the time of load path failure, and a remaining structure damage growth and residual strength requirement had to be met.

The requirement to qualify the structure generally requires a complex set of analyses, and in the early design stage may be impractical. The design could be made to satisfy Slow Crack Growth Structure guidelines, either non-inspectable or depot level inspectable, while still maintaining some level of fail safety, but not necessarily meeting the guidelines specifically. This approach would generally be satisfactory and usually requires a lesser amount of analysis, particularly for computing residual strength and the growth increment.

1.4 Sustainment/Aging Aircraft

The life of an aircraft is determined by its operational capabilities and maintenance costs rather than its initial design life goal. The guidelines of MIL-HDBK-1530 call for a Force Structural Maintenance Plan (FSMP) that is the basis of planned maintenance actions for a fleet. If unanticipated structural problems are identified due to design deficiencies or unplanned usage, the FSMP is updated using the deterministic damage tolerance methods of MIL-HDBK-1530. However, the effects of usage and time will cause fatigue cracks and corrosion damage to initiate and grow, compromising structural integrity of the fleet. Because of the uncertain nature of the sizes of the cracks that are in the fleet and the need to evaluate the interaction of cracks in multiple elements, the assessment of the effect of a population of fatigue cracks is typically made using probabilistic risk analysis. When such widespread fatigue cracking, corrosion, or use beyond the original life goals cause the deterministically based maintenance plan to be changed to ensure adequate structural integrity, the fleet is considered to be aging [Lincoln, 2000].

Sustainment is the process by which an aging aircraft fleet is maintained in an operational state. Sustainment encompasses both the actual maintenance of the structures and the analyses and tests needed to plan the maintenance tasks. As such, damage tolerance analyses are an integral part of sustainment.

1.4.1 Widespread Fatigue Damage

Widespread fatigue damage (WFD) is considered a primary threat to structural safety on aircraft. The National Materials Advisory Board report on the aging of USAF aircraft [Tiffany, et al., 1997] summarized this with the statement - "The onset of WFD in a structure is characterized by the simultaneous presence of small cracks in multiple structural details; where the cracks are of sufficient size and density, the structure can no longer sustain the required residual strength load level in the event of a primary load-path failure or a large partial damage incident." Thus, the presence of small cracks can reduce the safe load carrying capability of a fail-safe structure below its design requirement.

The objective of WFD studies is to determine when (in-service time) the crack population reaches the size and density to invalidate the initial design assumptions. Most older transport aircraft were designed (or later checked) using fail-safe damage tolerant design assumptions whereby if a discrete event (major local damage by fatigue or ballistic penetration) caused a rather large crack to form in the structure. And then the design loads were set to preclude loss of the aircraft due to the nature of the redundant structure. The assumption was that the discrete damage could occur anytime during the design lifetime of the aircraft. The discrete damage was assumed to be of such a size that it would be evident either in flight or during routine inspections. The design rules required that the structure could withstand this level of damage (with some growth) during an additional period of operation that was based on some multiple of the inspection period. This design approach assumed that only the discrete damage was present and that only this damage was allowed to grow. If the crack population in the surrounding structure could influence the stress intensity factors associated with this discrete damage event, then the initial design considerations were violated and it would be necessary to determine when this crack population became a threat to the behavior of the discrete damage.

Subsets of WFD are Multi-Site Damage (MSD) and Multiple-Element Damage (MED). MSD refers to the cracking scenario where cracks are developing in the same structural element

(fuselage joint) and MED refers to the cracking scenario where cracks are simultaneously developing in several elements (skin, spars, etc.) in a structural component (wing). Multi-Site Damage has been found to be an important consideration in the continued safe operation of aircraft [Steadman, et al. 1999].

1.4.2 The Effect of Environment and Corrosion

In-service environments can have a broad range of effects on aircraft structural behavior. In some situations, the in-service environment might affect neither the residual strength nor the crack growth life of a structural element or component. However, this is not normally the case.

Typically, the environment and choice of the structural material will change the rates at which cracks nucleate and grow, and can cause cracks to nucleate in locations where the risk for cracking damage without the environment is negligible. As a result of using military aircraft past their initial planned design life (about 20-25 years), new categories of structural integrity problems caused by environmental attack have been identified. Developing a damage tolerant design guidelines handbook that covers corrosion damage and environmental attack requires a more systematic approach for presenting approaches and methods that engineers can use to control the risk of structural failure.

Stress corrosion cracking (SCC) is a particularly deleterious form of environmental attack that will create opportunities for cracks to nucleate and grow to failure, even under limited fatigue loading conditions (mechanism requires constant tensile stress conditions, and low material resistance to this kind of attack). SCC has caused extensive (and expensive) problems due to the limited resistance of older forging alloys initially used in the C-141, KC-135, B-52, C-130 and C-5 aircraft. These problems have been recognized and, as materials have been developed for service in the newer KC-10 and C-17 aircraft, the problem has been controlled. Besides potentially causing SCC problems, the environment frequently will accelerate or enhance the fatigue process by creating corrosion sites (pits, exfoliation damage, surface roughness, etc.) where fatigue cracks will develop, accelerate the crack nucleation process, and then accelerate the rate at which these fatigue cracks grow. In fuselage lap joints, the crevice corrosion that occurs will result in pressure build up between the layers, sometimes to the point where rivet heads will pop off and the joint will look pillowed, such as shown in Figure 1.4.1.

Figure 1.4.1. Photo of Lap Joint Illustrating the Localized Pillowing Caused by Crevice Corrosion Occurring between the Two Layers

There are several different features of corrosion that can be used to characterize the severity and extent of damage. These corrosion metrics include thickness loss, pitting, surface roughness and pillowing, deformation in the metal caused by the excess corrosion by product produced between layers (see Figure 1.4.1). Corrosion can grow in exposed areas, under paint, around fasteners, between layers of skin, and inside structural components. Depending on the type of corrosion, it can grow in depth and area. It can grow along grain boundaries. Growth rates are influenced by environmental and load factors. The impact that each of these characteristics have on structural integrity continues to be the subject of current research, but will depend upon the structure within which the corrosion is located.

Stress corrosion cracking is another form of corrosion damage found in aircraft structures. As stated in Tiffany, et al. [1996], "Stress corrosion cracking (SCC) is an environmentally induced, sustained-stress cracking mechanism." Of particular interest is the identification of the operational need to reevaluate, possibly during ASIP durability and damage tolerant assessments, SCC-susceptible components to look for potential safety risks.

Currently the ALCs are operating under a maintenance philosophy that has been termed "find it – fix it". Under this mode of operation, when corrosion is detected, it must be dealt with by either repairing the damage, or replacing the component with the damage. Corrosion is considered an economic issue at this time, but the costs associated with maintaining the aircraft in accordance with this philosophy are escalating. Correspondingly, the readiness of the fleet is adversely affected. To respond to this trend, the Air Force is pursuing the technologies necessary to implement a corrosion management maintenance philosophy. This so-called "Anticipate and Manage" mode of operation attempts to make disposition decisions based on the impact of the damage to structural integrity. This requires knowing the condition of the corrosion damage through nondestructive inspection, understanding the corrosion growth rates as affected by the environment, and predicting the future corrosion condition using models of corrosion growth. The present and future states of corrosion can then be used in structural integrity calculations to determine remaining strength and life. Disposition may now include

flying the aircraft with known corrosion present, among other alternatives. Economical disposition can then be made while maintaining safety of the aircraft.

Other areas of ongoing research include understanding corrosion growth mechanisms, corrosion inhibition and arrest, coating technology and the replacement of chromate in coating systems.

1.5 References

AFGS-87221A (1990, June). "Air Force Guide Specification – General Specifications for Aircraft Structures".

Air Force Regulation 80-13 (1984, October). "Aircraft Structural Integrity Program".

Air Force Regulation 80-13 (1976, July). "Aircraft Structural Integrity Program".

F.D. Boensch (1964, August). "Fatigue Test Program, F-104G/MAP Aircraft", Report No. FDL TDR 64-97, AFFDL, WPAFB, OH.

D.E. Brammer (1963, July). "Structural Fatigue Test Program, F-105D Airplane", Report No. ASD-TDR-63-505, AFFDL, WPAFB, OH.

N.J. Hoff (1955, January). "From the Structural Standpoint". *Journal of the Royal Aeronautical Society* (Vol 59).

JSSG-2006 (1998, October). "Joint Service Specification Guide, Aircraft Structures". Department of Defense.

J.W. Lincoln (2000), "Aging Systems and Sustainment Technology" *Structures Technology for Future Aerospace Systems,* Ahmed K. Noor, Editor, Volume 188, Progress in Astronautics and Aeronautics.

H.B. Lowndes, Jr., et al. (1958, June). "Detail Requirements of Structural Fatigue Certification Program". WCLS-TM-58-4.

MIL-A-83444 (1974, July). "Military Specification – Airplane Damage Tolerance Requirements", USAF.

MIL-A-87221 (1985, February). "Military Specification – General Specifications for Aircraft Structures", USAF.

MIL-HDBK-1530 (1996, November). "Military Handbook – General Guidelines for Aircraft Structural Integrity Program", USAF.

MIL-STD-1530 (1972, September). "Military Standard – Aircraft Structural Integrity Program, Airplane Requirements", USAF.

MIL-STD-1530A (1975, December). "Military Standard – Aircraft Structural Integrity Program, Airplane Requirements", USAF.

G.R. Negaard (1980, June). "The History of the Aircraft Structural Integrity Program". Report No. 680.1B, Aerospace Structures Information and Analysis Center, AFFDL/FBR, WPAFB, OH.

J.L. Rudd, T.M. Hsu, H.A. Wood (1979). "Part-Through Crack Problems in Aircraft Structures", *Part-Through Crack Fatigue Life Prediction*. J.B. Chang (Ed.). ASTM STP 687, American Society for Testing and Materials, pp.168-194.

D. Steadman, A. Carter, R. Ramakrishnan (1999, September). "Characterization of MSD in an In-Service Fuselage Lap Joint", *Proceedings on CD of the Third Joint FAA/DoD/NASA Conference on Aging Aircraft*, Albuquerque, New Mexico.

C. Tiffany, et al (1977). "Aging of U.S. Air Force Aircraft – Final Report", Committee on Aging of U.S. Air Force Aircraft, National Materials Advisory Board, Commission on

Engineering and Technical Systems, National Research Council, NMAB-488-2, National Academy Press, Washington D. C.

Section 2
Fundamentals of Damage Tolerance

The basic elements of damage tolerant methodology are introduced in this section. The concept of crack growth behavior, from an initial flaw to failure, is introduced, with a discussion of some of the factors that affect the rate growth. The fundamentals of fracture mechanics, residual strength and life prediction methodology are presented. Many computer programs have been developed for life prediction calculations, and these are discussed in subsection 2.6.

2.1 Introduction To Damage Concepts and Behavior

Past experience with tests of structures under simulated flight loading has indicated that the time to initiation of cracks from most structural details such as sharp corners or holes is relatively short and that the majority of the life (i.e., 95%) is spent growing the resultant cracks to failure. Likewise, analyses of in-service fractures, cracking instances, etc. have indicated that a major source of cracks is the occurrence of initial manufacturing defects such as sharp corners, tool marks and the like. Thus, it is now common practice to consider the damage accumulation process as entirely crack growth, with zero time to initiate the crack. Although this assumption may seem unduly severe, recent studies have shown the approach feasible, of minimal detriment to weight, cost, etc., but most important, the consideration of initial damage in the form of cracks or equivalent damage is absolutely necessary to ensure structural safety.

This subsection will detail the fundamentals of life prediction based on crack growth. The crack length will be the measure of damage and the crack growth rate will define the rate of damage accumulation.

2.1.1 Damage Growth Concepts

Figure 2.1.1 presents a schematic of typical growth behavior for a crack being observed in a structural element as it moves from an initial damage size to a damage size that causes structural failure (loss of structural safety). Note that the x-axis measures either the elapsed time (t) during which loading is applied or the number of loading events (N) applied, and the y-axis measures the corresponding length of crack observed in the structure. Typically, the elapsed time is given in operational flight hours and the number of loading events is counted (grossly) by the number of the aircraft's flights.

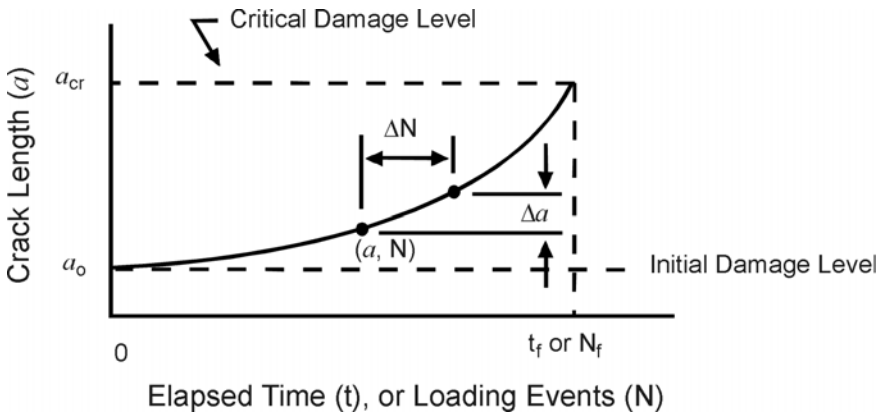

Figure 2.1.1. Schematic of Observed Crack Growth Behavior for a Typical Structural Cracking Problem

The crack grows in response to the cyclic loading applied to the structure. Any crack will grow a given increment (Δa) in a given number of loading events (ΔN), the rate being measured by $\Delta a/\Delta N$. When the crack length reaches a critical value (a_{cr}), the growth becomes unstable, thereby inducing failure.

When the crack (a) reaches the critical length, the measure of loading (t or N) reaches the structural life limit (t_f or N_f). The structural life limit is a measure of the maximum allowable service time (or number of accumulated service events) associated with driving the crack from its initial length (a_o) to the critical length (a_{cr}). It is the objective of the Damage Tolerant Requirements to ensure that cracks do not reach levels that could impair the safety of the aircraft during the expected lifetime (t_s or N_s) of the aircraft, i.e., t_f (N_f) must be greater than t_s (N_s).

As can be noted from Figure 2.1.1, when the crack is small, it grows very slowly. As the crack gets longer, the rate of growth increases until the crack reaches the critical size a_{cr}, whereupon fracture of the structural element ensues. While the subcritical crack growth process occurring for $a \leq a_{cr}$ may take twenty to thirty years of service, the fracture process is almost instantaneous. Studies of the failure process indicate a very close relationship between the length of crack at failure and the load or stress that induces the onset of rapid fracture.

Typically, this relationship between crack length and failure strength level is as shown in Figure 2.1.2. The cracked element strength is referred to as the residual strength (σ_{res}) since this represents the remaining strength of a damaged structure. By considering the basic elements of Figures 2.1.1 and 2.1.2 collectively, a residual strength diagram can be developed as a function of elapsed time (or loading events).

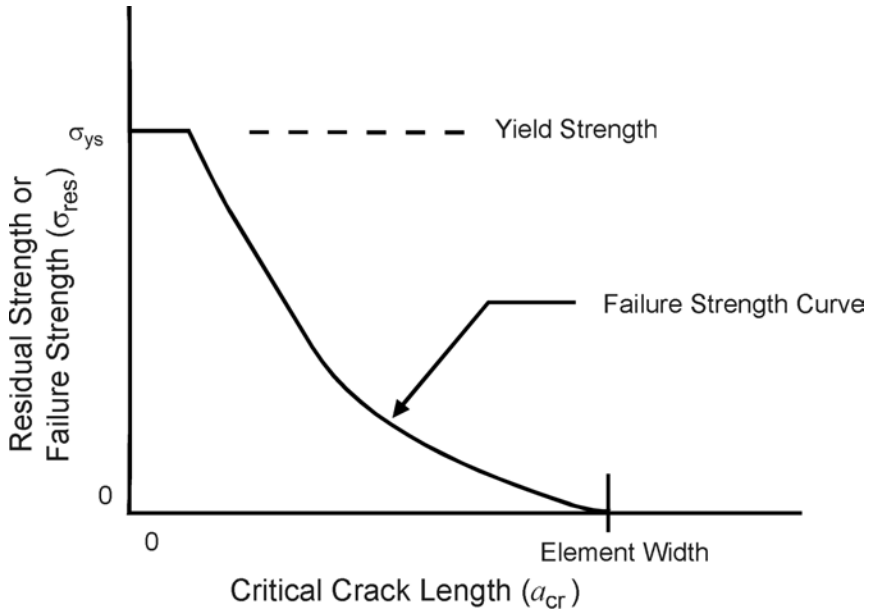

Figure 2.1.2. Schematic of Relationship Between Failure Strength and Crack Length for a Typical Single Element Type Structure

A residual strength diagram is presented in Figure 2.1.3; this diagram shows that while the structure is young ($t << t_f$) the residual strength capacity is basically unimpaired because the crack is both small and doesn't grow much with time. As the structure starts to age, the residual strength capacity is shown to decrease and just prior to failure, the rate of decrease in residual strength capacity is accelerating because now the crack is rapidly becoming very large. When

the residual strength capacity equals the level of the maximum stress in the operational history, failure occurs.

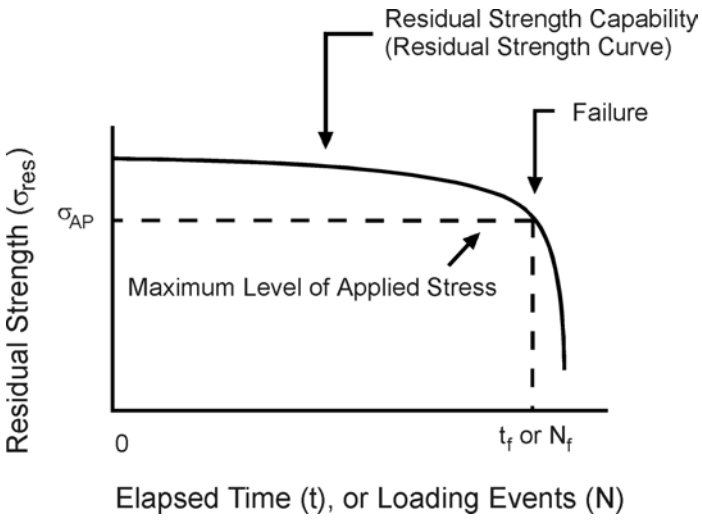

Figure 2.1.3. Residual Strength Diagram Relationship Between Residual Strength Capacity and Elapsed Time

As implied by the residual strength diagram, a ten to twenty percent change in the maximum applied stress in the operational history would not normally affect the allowable structural life significantly, assuming that the subcritical crack growth process (Figure 2.1.1) was unaffected. Normally, when the loads in the operational history change, the subcritical crack growth process changes its pattern of growth and this in turn affects the residual strength diagram and the allowable structural life.

2.1.2 Damage Growth Behavior/Effects

As discussed above, the crack length a_o will grow to a_{cr} in some life t_f, and as the crack grows the residual strength capability decreases. Experiments have shown that several parameters affect the crack growth life; the most important of these being the initial crack size, a_o, the load history, the material properties, and the structural properties. The isolated effect of each parameter on the crack growth behavior and the residual strength curves will be discussed in turn using the baseline conditions identified in Figure 2.1.4. The interrelation of these parameters will be developed in the discussion of life prediction methodology (Section 2.4).

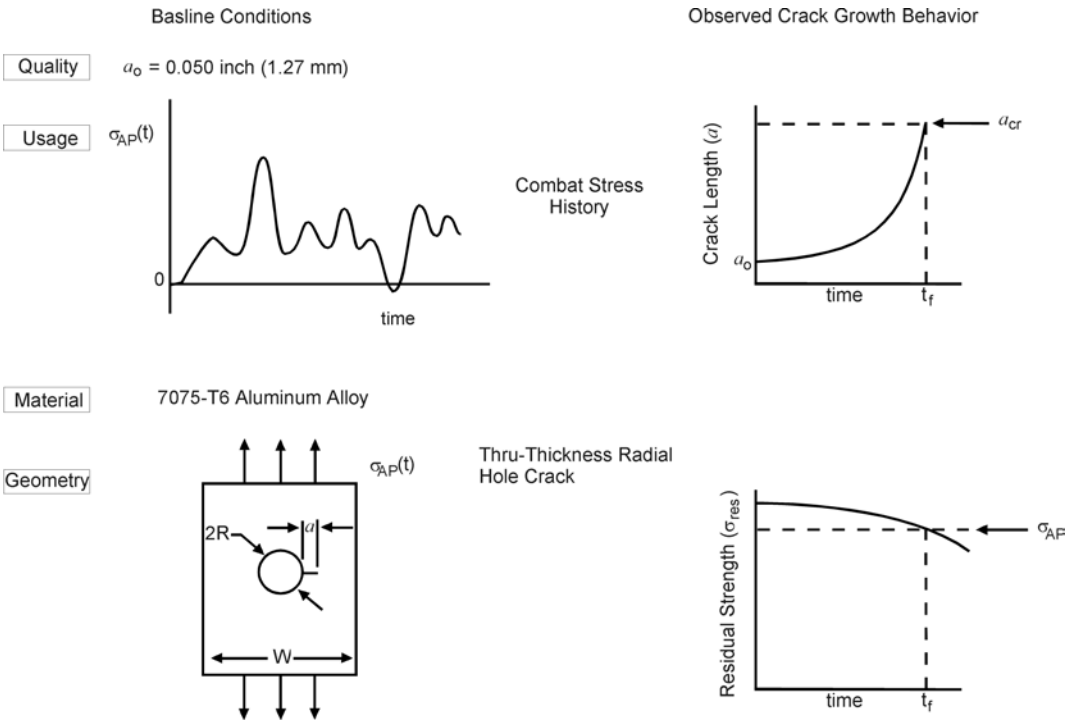

Figure 2.1.4. Description of Baseline Conditions for Observed Crack Growth Behavior

Initial Crack Size – A Measure of Quality

The effect of initial crack size is significant. Given a configuration and loading, the smaller the initial crack size, the longer the life and the higher the residual strength capacity at any time. These observations are displayed in Figure 2.1.5a and b, respectively. Note that the shape of the crack growth curve (for a given configuration and loading) remains essentially constant for any given crack growth increment.

Thus, given the crack growth curve for the smaller initial crack, it is possible to construct the crack growth curve for the baseline condition. This can be accomplished by shifting the crack growth curve with a smaller initial crack horizontally to the left until the curve intersects the vertical axis at the baseline initial crack size. Also, note that the residual strength curve for the baseline condition can be constructed from the curve obtained for the smaller initial crack size.

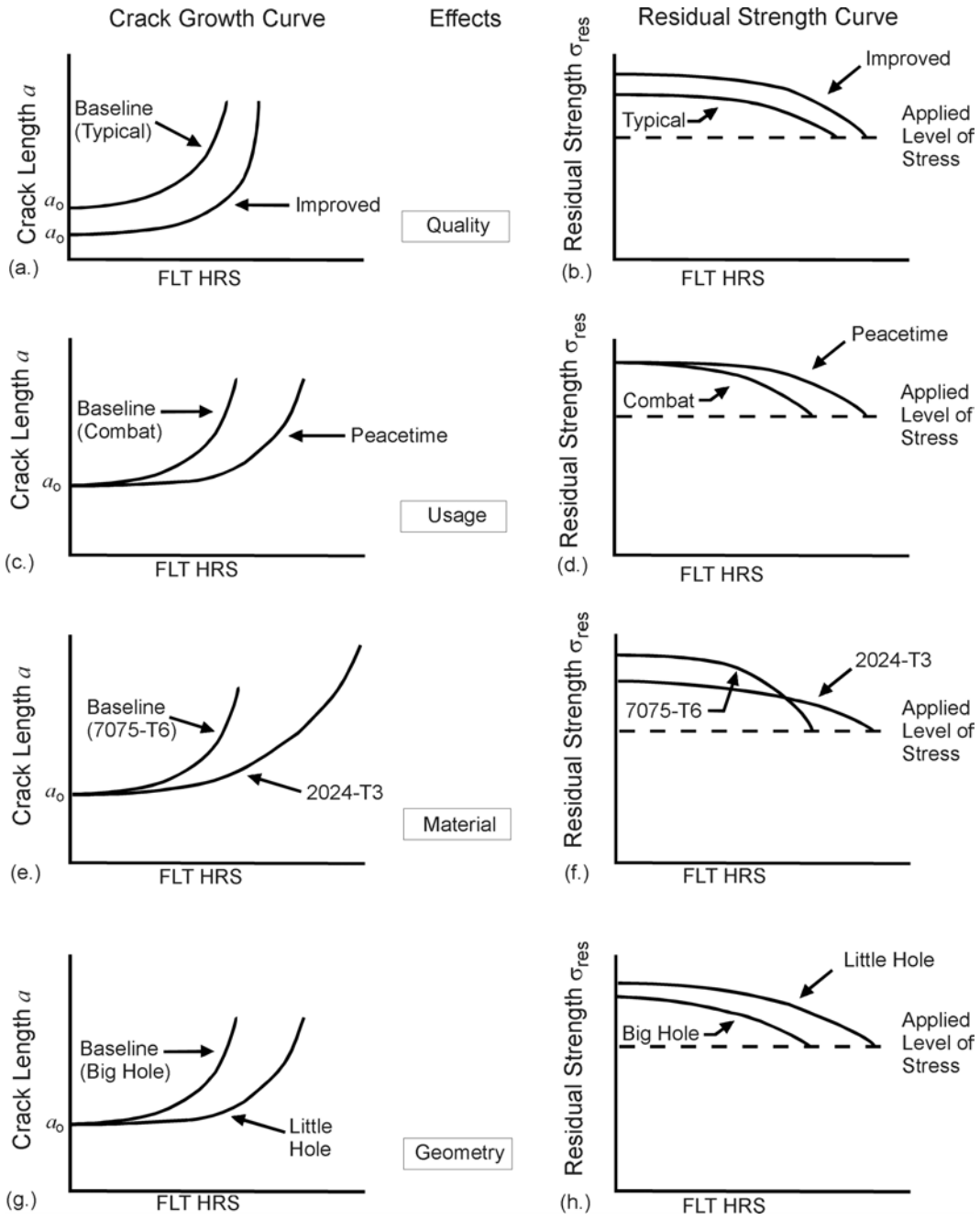

Figure 2.1.5. Schematic Summary of the Effects of Quality, Usage, Material, and Geometry on Both the Crack Growth and Residual Strength Curves

Stress History - A Measure of Usage and Location

As an aircraft flies different missions and different maneuvers, it experiences different loadings. The magnitude and sequence of aircraft loadings are noted to have a significant effect on the rate at which cracks grow. The stress history describes the magnitude and sequence of stresses at one location that results from the sequence of missions or maneuvers that an aircraft flies. Figure 2.1.5c and d illustrate the effect that stress history (usage) can have on the crack growth behavior

and residual strength capacity, respectively. While it was not shown, a change in stress history will normally also change the applied stress level at which fracture occurs.

The stress history experienced at each location on the aircraft will also differ due to changes in bending moment, twisting moment, shear loading, etc., given a particular crack configuration (e.g., a crack growing from a fastener hole on a wing). The loading spectra for a lower surface location is typically more severe than a corresponding upper surface location; and, therefore, the life for the lower surface will be significantly shorter than that of the upper surface all other conditions being equal.

Material Properties - A measure of Material Resistant to Cracking

Experimentally, it has been shown that for the same loading condition (i.e., the same number and amplitude of stress cycles) cracks will grow faster in certain alloys than in others. The crack growth rate $(\Delta a/\Delta N)$ can be derived experimentally for each material. Given the same load and geometric conditions, the alloy having the slower growth rate characteristics (i.e. 2024-T3) will have a longer life (t_f) as shown in Figure 2.1.5e. This material also has some inherent resistance to fracture. The higher this inherent resistance, the higher the residual strength capacity for any crack length. This effect is described in Figure 2.1.5f.

If the cracks are so small that the fracture process is controlled by gross yielding, then the residual strength curve is controlled by a net section failure criterion rather than a fracture criterion. In this case, the material with the highest yield strength would have the highest residual strength in the region of the curve controlled by the behavior of the small cracks.

Structural Properties - A Measure of Geometry

The most complex of the parameters affecting crack growth behavior are the structural properties. The structural properties involve such things as crack configuration, load transfer through fasteners, fastener hole size, part thickness, etc. A substantial amount of experimental work has been performed to characterize the geometrical effects on life. The effect of a change of hole radius on the crack growth behavior and on the residual strength capacity is shown in Figure 2.1.5g and h. The structure with the smaller hole, and thus the smaller stress concentration is noted to have the longer life and higher residual strength.

Summary of Effects

As discussed above, there are four major parameters that affect the crack growth life and residual strength capacity of structures. These parameters are in the realm of quality (initial crack size), usage (loading history), material (material properties), and geometry (structural properties). Figure 2.1.6 has been prepared to summarize the parameters' effect on life and to illustrate various presentation schemes that might be employed to compare effects.

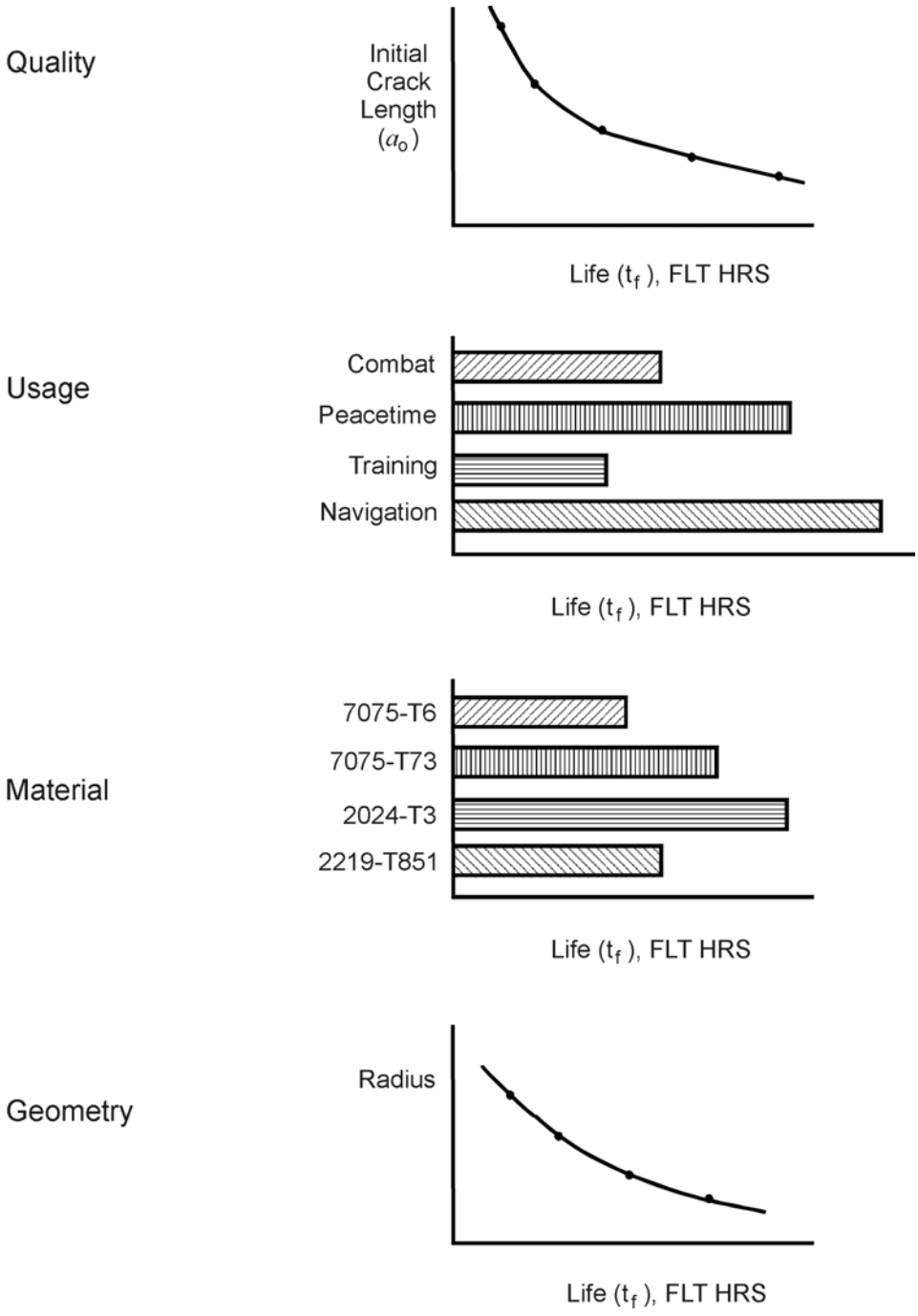

Figure 2.1.6. Summary of Schemes Which Illustrate the Sensitivity of Life to Various Structural Parameters

2.2 Fracture Mechanics Fundamentals

Fracture Mechanics is that technology concerned with the modeling of cracking phenomena. Bulk (smooth specimen) properties are not normally useful in design for determining a material's tolerance to cracks or crack-like defects, because material tolerance to flaws resides in a material's ability to deform locally. Since the source of fractures can be identified with the lack of material tolerance to cracks, it seems only natural that attention should be focused on the crack tip region where the material must resist crack extension. This section will introduce the principal features of a mechanical model that characterizes a crack movement in structural components fabricated from materials having low tolerance to flaws.

Some basic information that a designer should be familiar with prior to the utilization of remaining sections of this handbook is presented. This subsection will define the meaning and use of the fracture mechanics model for the control of fracture and sub-critical crack growth processes.

The application of a fracture mechanics model to solve crack problems came about through the following realization: component fractures that result from the extension of small crack-like defects are failures that depend on localized phenomena. Consider the three independent modes of crack extension that are illustrated in Figure 2.2.1. The tensile opening mode, Mode 1, represents the principal action observed and this is the type of separation that we design against. While fractures induced by shear stresses can occur, these fractures are rather infrequent. There are hypotheses available for describing the combined influence of two (or three) modes of crack extension but these will not be discussed until Section 4. In general, since improvement of a material's Mode 1 fracture resistance will also improve the resistance to the combined mode action, the development of concepts throughout the Handbook will emphasize Mode 1 crack extension behavior.

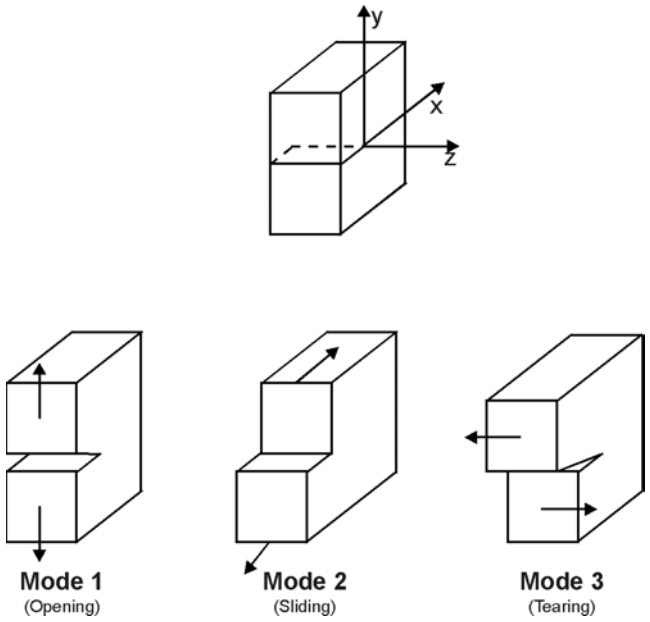

Figure 2.2.1. The Three Modes of Crack Extension

A linear elastic analysis of a cracked body provides a good first approximation to the localized stress state in materials that fracture at gross section stresses below the yield strength. No additional refinements in the analysis are necessary if the gross section stresses at failure are below $0.7\sigma_{ys}$. The elastic analysis when modified to account for restricted amounts of stress relaxation due to crack tip plastic deformation provides an adequate description of fracture that occurs above $0.7\sigma_{ys}$.

2.2.1 Stress Intensity Factor – What It Is

The model referred to above is called the linear elastic fracture mechanics model and has found wide acceptance as a method for determining the resistance of a material to below-yield strength fractures. The model is based on the use of linear elastic stress analysis; therefore, in using the model one implicitly assumes that at the initiation of fracture any localized plastic deformation is small and considered within the surrounding elastic stress field. Application of linear elastic stress analysis tools to cracks of the type shown in Figure 2.2.2 shows that the local stress field (within $r < a/10$) is given by [Irwin, 1957; Williams, 1957; Sneddon & Lowengrub, 1969; Rice, 1968a]:

$$\sigma_x = \frac{K}{\sqrt{2\pi r}} cos\frac{\theta}{2}\left[1 - sin\frac{\theta}{2} sin\frac{3\theta}{2}\right]$$

$$\sigma_y = \frac{K}{\sqrt{2\pi r}} cos\frac{\theta}{2}\left[1 + sin\frac{\theta}{2} sin\frac{3\theta}{2}\right] \qquad (2.2.1)$$

$$\sigma_{xy} = \frac{K}{\sqrt{2\pi r}} sin\frac{\theta}{2}\left[cos\frac{\theta}{2} cos\frac{3\theta}{2}\right]$$

The stress in the third direction are given by $\sigma_z = \sigma_{xz} = \sigma_{yz} = 0$ for the plane stress problem, and when the third directional strains are zero (plane strain problem), the out of plane stresses become $\sigma_{xz} = \sigma_{yz} = 0$ and $\sigma_z = \nu\,(\sigma_x + \sigma_y)$. While the geometry and loading of a component may change, as long as the crack opens in a direction normal to the crack path, the crack tip stresses are found to be as given by Equations 2.2.1. Thus, the Equations 2.2.1 only represent the crack tip stress field for the Mode 1 crack extension described by Figure 2.2.2.

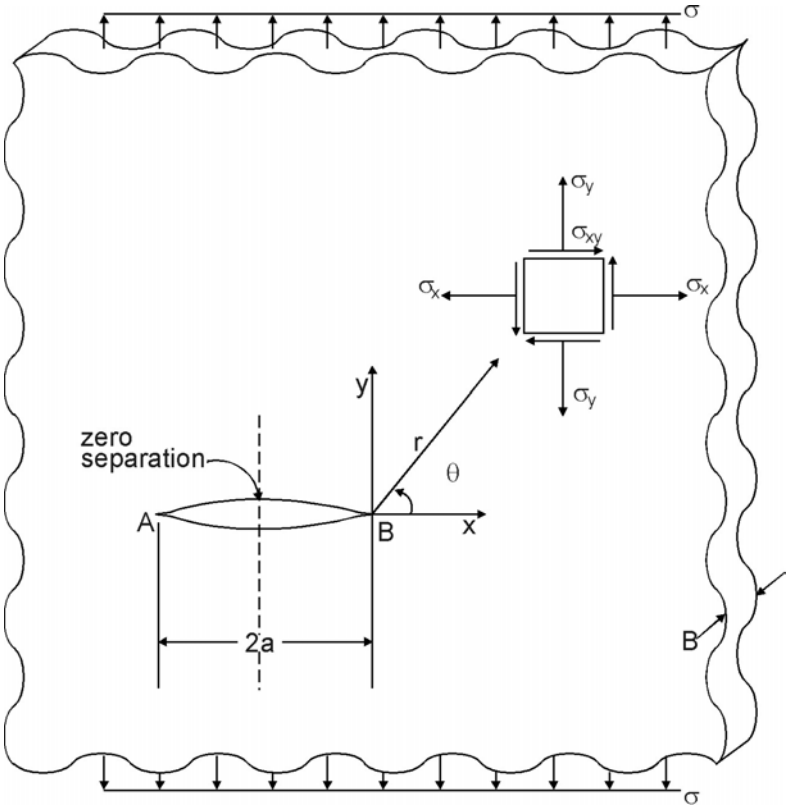

Figure 2.2.2. Infinite Plate with a Flaw that Extends Through Thickness

Three variables appear in the stress field equation: the crack tip polar coordinates r and θ and the parameter K. The functions of the coordinates determine how the stresses vary with distance from the right hand crack tip (point B) and with angular displacement from the x-axis. As the stress element is moved closer to the crack tip, the stresses are seen to become infinite. Mathematically speaking, the stresses are said to have a square root singularity in r. Because most cracks have the same geometrical shape at their tip, the square root singularity in r is a general feature of most crack problem solutions.

The parameter K, which occurs in all three stresses, is called the stress intensity factor because its magnitude determines the intensity or magnitude of the stresses in the crack tip region. The influence of external variables, i.e. magnitude and method of loading and the geometry of the cracked body, is sensed in the crack tip region only through the stress intensity factor. Because the dependence of the stresses (Equation 2.2.1) on the coordinate variables remain the same for different types of cracks and shaped bodies, the stress intensity factor is a single parameter characterization of the crack tip stress field.

The stress intensity factors for each geometry can be described using the general form:

$$K = \sigma\beta\sqrt{\pi a} \tag{2.2.2}$$

where the factor β is used to relate gross geometrical features to the stress intensity factors. Note that β can be a function of crack length (a) as well as other geometrical features

It is seen from Equation 2.2.2 that the intensity of the stress field and hence the stresses in the crack tip region are linearly proportional to the remotely applied stress and proportional to the square root of the half crack length.

A structural analyst should be able to determine analytically, numerically, or experimentally the stress-intensity factor relationship for almost any conceivable cracked body geometry and loading. The analysis for stress-intensity factors, however, is not always straightforward and information for determining this important structural property will be presented subsequently in Section 11. A mini-handbook of stress-intensity factors and some methods for approximating stress-intensity factors are also presented in Section 11.

2.2.2 Application to Fracture

Can the magnitude or intensity of this crack tip pattern be used to characterize the material instability at fracture? The formulation of such a hypothesis for measuring a material's resistance to fracture was developed by G.R. Irwin and his co-workers at the Naval Research Laboratories in the 1950's [Irwin, 1957; Irwin & Kies, 1954; Irwin, et al., 1958].

The hypothesis can be stated:

> if the level of crack tip stress intensity factor exceeds a critical value, unstable fracture will occur.

The concept is analogous to the criterion of stress at a point reaching a critical value such as the yield strength. The value of the stress-intensity factor at which unstable crack propagation occurs is called the fracture toughness and is given the symbol K_c. In equation form, the hypothesis states:

$$\text{if } K = K_c, \tag{2.2.3}$$

then catastrophic crack extension (fracture) occurs.

To verify the usefulness of the proposed hypothesis, consider the results of a wide plate fracture study given in Figure 2.2.3 [Boeing, 1962]. These data represent values of half crack length and gross section stress at fracture. The stress-intensity factor for the uniformly-loaded center-cracked finite-width panel is given by:

$$K = \sigma\left[\pi a \sec\frac{\pi a}{W}\right]^{1/2} \tag{2.2.4}$$

where W is the panel width. Application of Equation 2.2.4 given in Figure 2.2.3 followed by averaging the calculated fracture toughness values (except for those at the two smallest crack lengths) gives the average fracture toughness curve shown. This example illustrates that the fracture toughness concept can be used to adequately describe fractures that initiate at gross sectional stress below 70% of the yield strength.

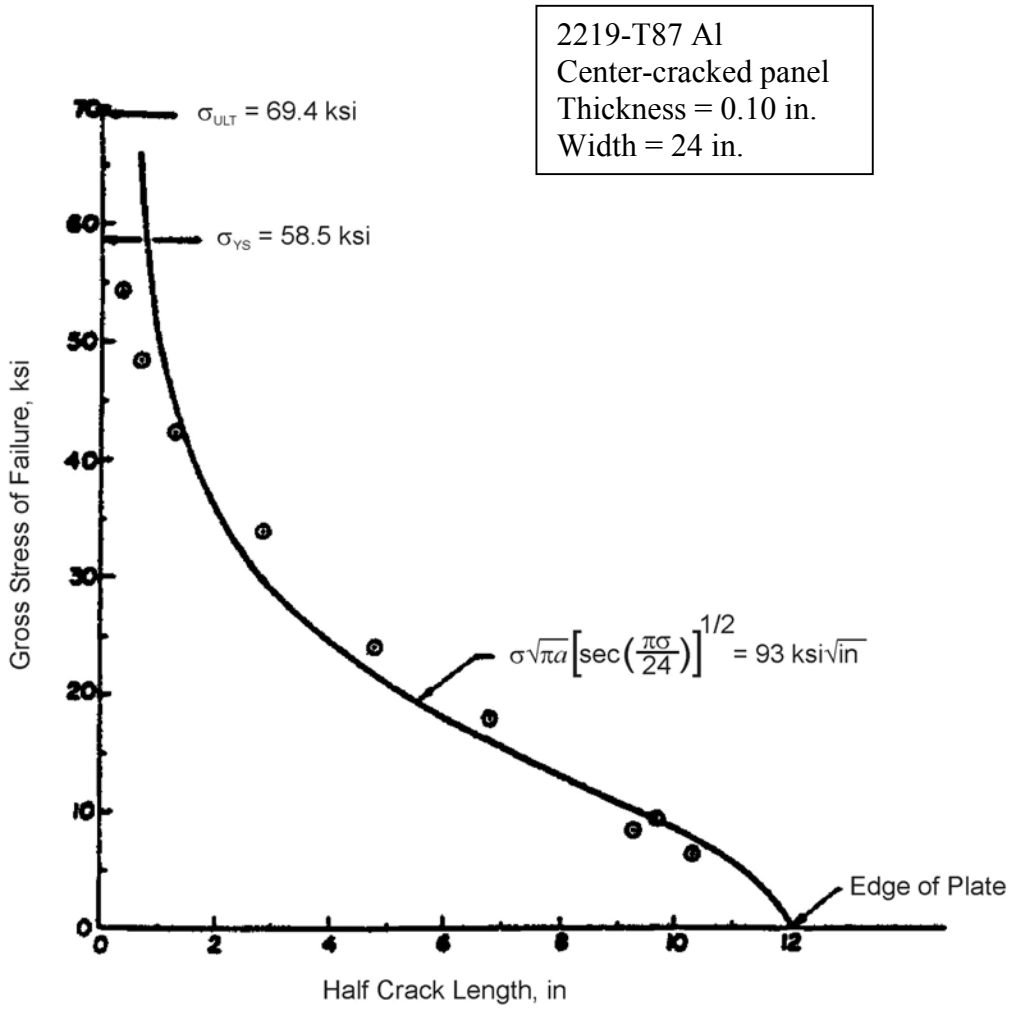

Figure 2.2.3. Results of a Wide Plate Fracture Study Compared with a Fracture Toughness Curve Calculated Using the Finite Width Plate Stress Intensity Factor Equation, Equation 2.2.4 (Data from Boeing [1962])

Note that since plastic deformation is assumed negligible in the linear elastic analysis, Equation 2.2.3 is not expected to yield an accurate approximation where the zone of plastic deformation is large compared to the crack length and specimen dimensions. Figure 2.2.3 shows that the relationship derived on the basis of the Equation 2.2.3 hypothesis does not describe the crack growth behavior for small cracks in plastic stress fields.

2.2.3 Fracture Toughness - A Material Property

Fracture toughness (K_c) is a mechanical property that measures a material's resistance to fracture. This parameter characterizes the intensity of stress field in the material local to the crack tip when rapid crack extension takes place. Similar to other microstructurally sensitive material properties, fracture toughness can vary as a function of temperature and strain rate. But, unlike the yield strength, K_c will be strongly dependent on the amount of crack tip constraint due to component thickness. The reason why thickness has to be considered in fracture analysis is due to its influence on the pattern of crack tip plastic deformation. The two thickness limiting crack tip plastic deformation patterns are shown in Figure 2.2.4. For "thin" plane stress type components, a 45 degree through the thickness yielding pattern develops; in "thicker" plane strain components of the same material, the hinge-type plastic deformation pattern predominates [Hahn, & Rosenfield, 1965]. Section 4 and 7 discuss the effect of thickness and other factors on fracture toughness.

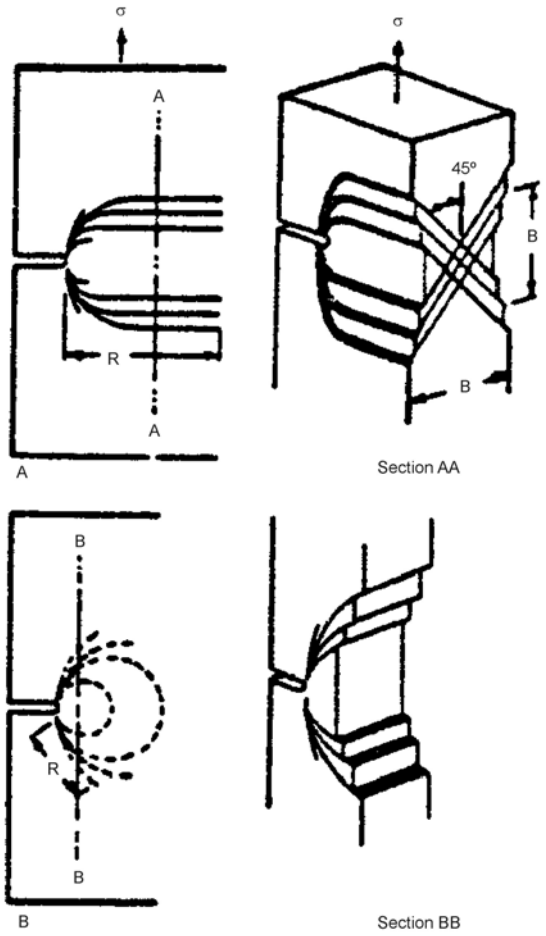

Figure 2.2.4. Yield Zone Observed on the Surface and Cross Section of a Cracked Sheet Under Uni-axial Tensile Loading in: A-Plane Stress, 45 degree Shear Type; B-Plane Strain, Hinge Type

The linear elastic fracture mechanics approach can only be expected to characterize fracture when the region in which plastic deformation occurs is contained within the elastic crack tip stress field. When the crack tip plastic deformation is unrestricted by elastic material around the crack, the engineer must resort to using elasto-plastic techniques to predict the critical crack size at fracture. Presently, it is not possible to say if these techniques will lead to the same type of single parameter characterization of fracture discussed above.

2.2.4 Crack Tip Plastic Zone Size

It is recognized that plastic deformation will occur at the crack tip as a result of the high stresses that are generated by the sharp stress concentration. To estimate the extent of this plastic deformation, Irwin equated the yield strength to the y-direction stress along the x-axis and solved for the radius. The radius value determined was the distance along the x-axis where the stress perpendicular to the crack direction would equal the yield strength; thus, Irwin found that the extent of plastic deformation was

$$r_y = \frac{1}{2\pi}\left(\frac{K}{\sigma_{ys}}\right)^2 \qquad (2.2.5)$$

Subsequent investigations have shown that the stresses within the crack tip region are lower than the elastic stresses and that the size of the plastic deformation zone in advance of the crack is between r_y and $2r_y$. Models of an elastic, perfectly plastic material have shown that the material outside the plastic zone is stressed as if the crack were centered in the plastic zone. Figure 2.2.5 describes a schematic model of the plastic zone and the stresses ahead of the crack tip. Note that the real crack is blunted as a result of plastic deformation.

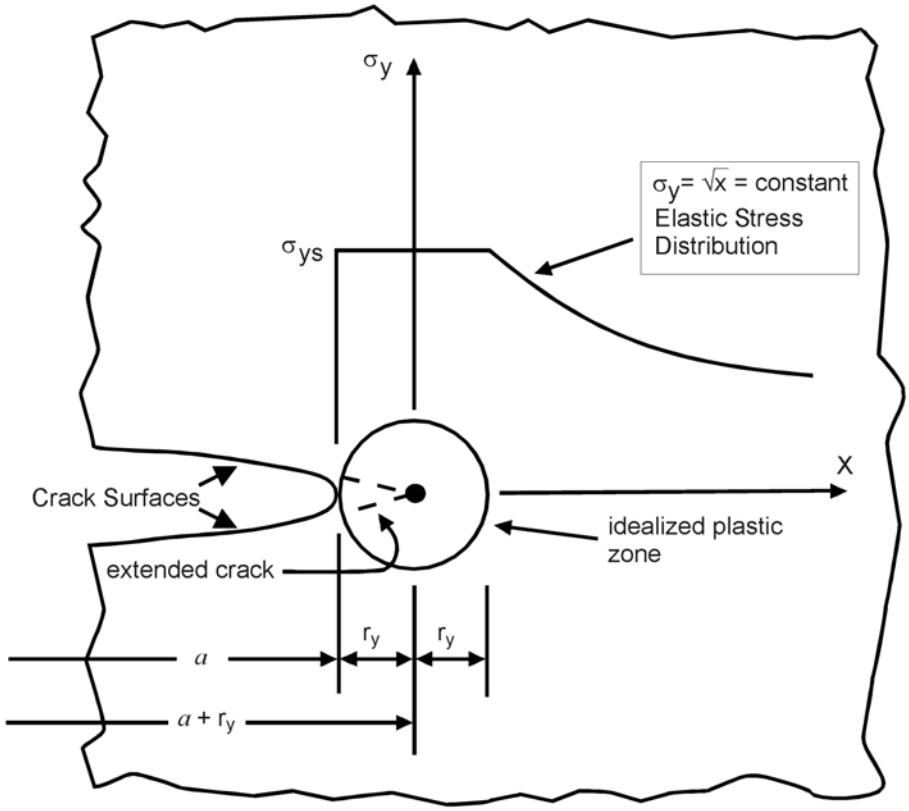

Figure 2.2.5. Small-Scale Yield Model for Restricted Crack Tip Plastic Deformation

If the extent of the plastic zone as estimated by Equation 2.2.5 is small with respect to features of the structural geometry and to the physical length of the crack, linear elastic fracture mechanics analyses apply. Sometimes, the concept of contained yielding, as illustrated in Figure 2.2.5, is referred to as small scale yielding. Most structural problems of interest to the aerospace community can be characterized by linear elastic fracture mechanics parameters because the extent of yielding is contained within a small region around the crack tip.

2.2.5 Application to Sub-critical Crack Growth

The only quantifiable measure of sub-critical damage is a crack. Cracks impair the load-carrying characteristics of a structure. As described above, a crack can be characterized for length and configuration using a structural parameter termed the stress intensity factor (K). This structural parameter was shown to interrelate the local stresses in the region of the crack with crack geometry, structural geometry, and level of load on the structure. In a manner similar to Irwin, who utilized the stress intensity factor for fracture studies, Paris and his colleagues at Lehigh University and at the Boeing Company developed a crack mechanics approach to solve sub-critical crack growth problems [Paris, et al., 1961; Donaldson & Anderson, 1961; Paris, 1964].

The concepts that Paris and his colleagues developed were based upon a similitude hypothesis: if the crack tip stress state and its waveform are the same in a given time period for two separate geometry and loading conditions, then the crack growth rate behavior observed by the two cracks should be the same for that time period. This hypothesis is a direct extension of Equation 2.2.3 to the problem of sub-critical crack growth. The equation representing the sub-critical crack growth hypothesis is simply:

$$\frac{\Delta a}{\Delta t} = f(K(t))$$

or (2.2.6)

$$\frac{\Delta a}{\Delta N} = f(K(t))$$

That is, a material's rate of crack growth is a function of the stress intensity factor. The stress intensity factor is shown to explicitly depend on time in order to indicate the influence of its waveform on the crack growth rate. The value of the hypothesis stated by Equation 2.2.6 is that the material behavior can be characterized in the laboratory and then utilized to solve structural cracking problems when the structure's loading conditions match the laboratory loading conditions. A general description of the procedure utilized will be presented in Section 2.5. Section 5 is devoted to a complete description of the detailed methodology available to a designer for estimating the crack growth life of a structural component using a material's crack growth rate properties.

A verification of Paris' Hypothesis was first conducted using fatigue crack growth data generated under constant amplitude type repeated loading. The parameters that pertain to constant amplitude type loading are presented in Figure 2.2.6. Figure 2.2.6a describes a repeating constant amplitude cycle with a maximum stress of σ_{max}, a minimum stress of σ_{min}, and a stress range of $\Delta\sigma$. The stress ratio (R) is given by the ratio of the minimum stress to the maximum stress. In describing constant amplitude stress histories, it is only necessary to define two of the above four parameters; typically $\Delta\sigma$ and R or σ_{max} and R are used. A stress history is converted into a stress-intensity factor history by multiplying the stresses by the stress-intensity-factor coefficient (K/σ). As can be noted from the figure, the coefficient is evaluated at the current crack length a_i and the stress-intensity-factor history is shown to be a repeating cyclic history in Figure 2.2.6b. The terms K_{max}, K_{min} and ΔK define the maximum, the minimum and range of stress-intensity factor, respectively. Strictly speaking, the stress-intensity factor history given in Figure 2.2.6b should not be shown constant but reflective of the changes in the stress-intensity-factor coefficient as the crack grows. For small changes in crack length, however, the stress-intensity factor coefficient does not change much, so the portrayal in Figure 2.2.6b is reasonably accurate for the number of cycles shown.

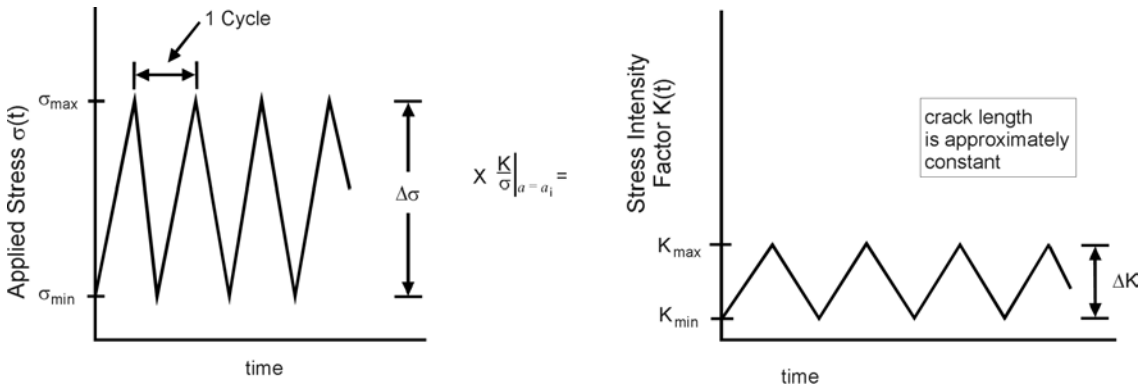

Figure 2.2.6. Parameters that Define Constant Amplitude Load Histories for Fatigue Crack Growth. The Figure also Illustrates the Transformation between Stress History Loading and Stress-Intensity-Factor Loading at One Crack Length Position

The fatigue crack growth rate behaviors exhibited by a plate structure subjected to two extreme loading conditions (but at the same nominal stress level) are compared in Figure 2.2.7 [Donaldson & Anderson, 1961; Anderson & James, 1970]. These loading conditions are referred to as wedge loading and remote loading. In the remote loaded structure, the rate of crack length change accelerates as the crack grows. An opposite growth rate behavior is exhibited by the wedge loaded structure. These two extreme loading conditions provide a good test for the application of the fracture mechanics approach to the study of fatigue crack growth rates. If the approach can be used to describe these opposite growth rate behaviors, then it should be generally applicable to any other type of structure or loading.

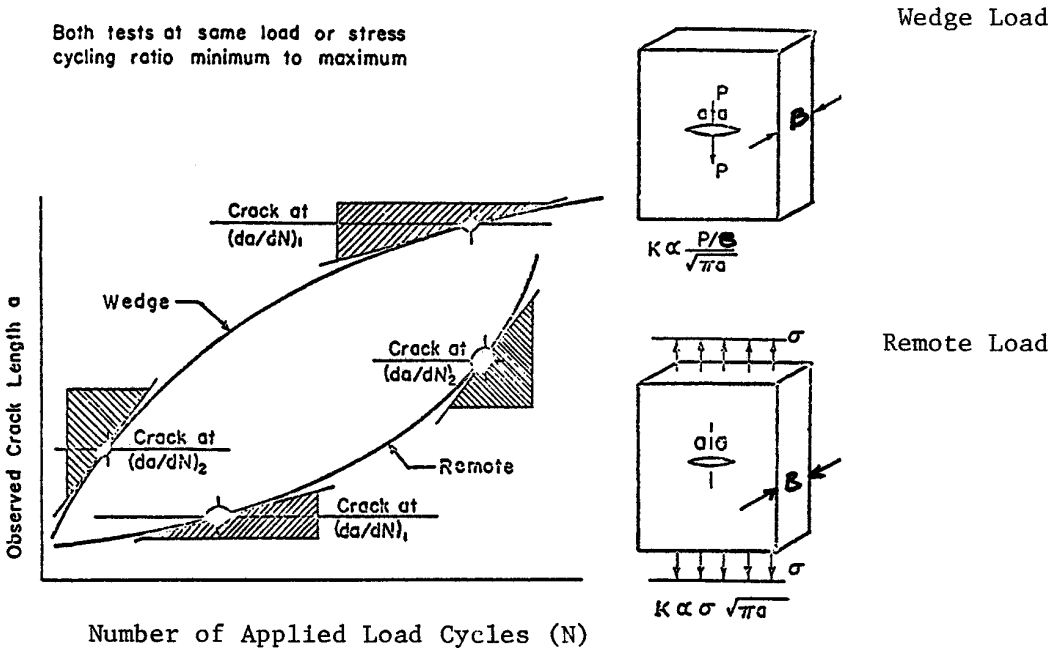

Figure 2.2.7. Description of Crack Growth Behavior Observed for Two Very Different Structural Geometries

Paris, et al. [1961], suggested that the appropriate stress intensity parameter for fatigue crack propagation should be the difference between the maximum and minimum stress-intensity factors in a cycle of fatigue loading. This difference in the stress-intensity factors is the stress intensity range *(*ΔK) and it measures the alternating intensity of the crack tip stress field responsible for inducing reversed plastic deformation. The stress-intensity range as a function of crack length is obtained from the static stress-intensity-factor formulas where the range in stress (load) replaces the static stress (load). Section 2.5 provides a more extensive description of the calculation procedures for stress-intensity-factor parameters that are used to describe sub-critical crack growth.

Approximate expressions for the small crack in a wide plate are shown in Figure 2.2.7. The reader will note that the stress-intensity factor for the remotely loaded wide plate increases with crack length while just the reverse is observed to occur for the wedge loaded wide plate.

Drawing tangents to the cyclic crack length curves given in Figure 2.2.7 provides estimates of the cyclic (fatigue) crack growth rates at various crack lengths $\left(\frac{da}{dN} \cong \frac{\Delta a}{\Delta N}\right)$. Calculation of corresponding stress-intensity ranges for these same crack lengths provides the data plotted in Figure 2.2.8 [Donaldson & Anderson, 1961; Anderson & James, 1970]. Note that at the same stress-intensity range *(*ΔK), the same crack growth rate (*da/dN*) is observed, even though both the form of the stress-intensity equations and the cycle-crack length curves are very different.

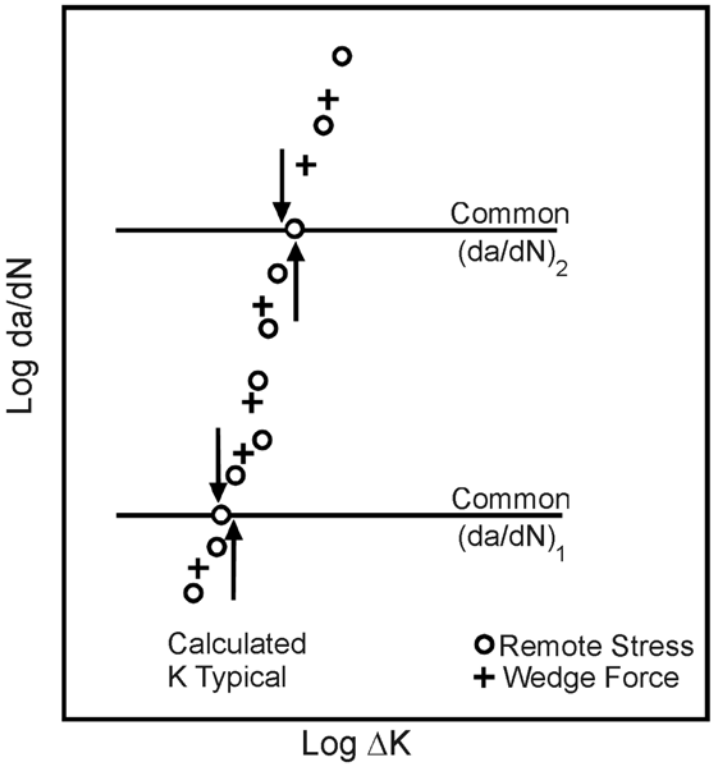

Figure 2.2.8. Comparison of Crack Growth Rate Results for the Two Structural Geometries. The Coincidence of the Data Shows that the Hypothesis of Equation 2.2.6 is Correct

The general fatigue cracking behavior pattern exhibited by most structural materials is shown in Figure 2.2.9. The shape of the curve is sigmoidal with no crack growth being observed below a given threshold level of stress-intensity range and rapid crack propagation occurring when the maximum stress-intensity-factor in the fatigue cycle approaches the fracture toughness of the material. In the sub-critical growth region, numerous investigators have indicated that the rate of cyclic growth (*da/dN*) can be described using a power law relation

$$\frac{da}{dN} = C(\Delta K)^p \qquad (2.2.7)$$

where C and p are experimentally developed constants. Fatigue crack propagation data of the type shown in Figure 2.2.9 can be conveniently collected using the conventional specimen geometries where load is controlled and the crack length is measured optically (20x) as a function of applied cycles. The details of the methodology employed to generate such curves are covered in Section 7.

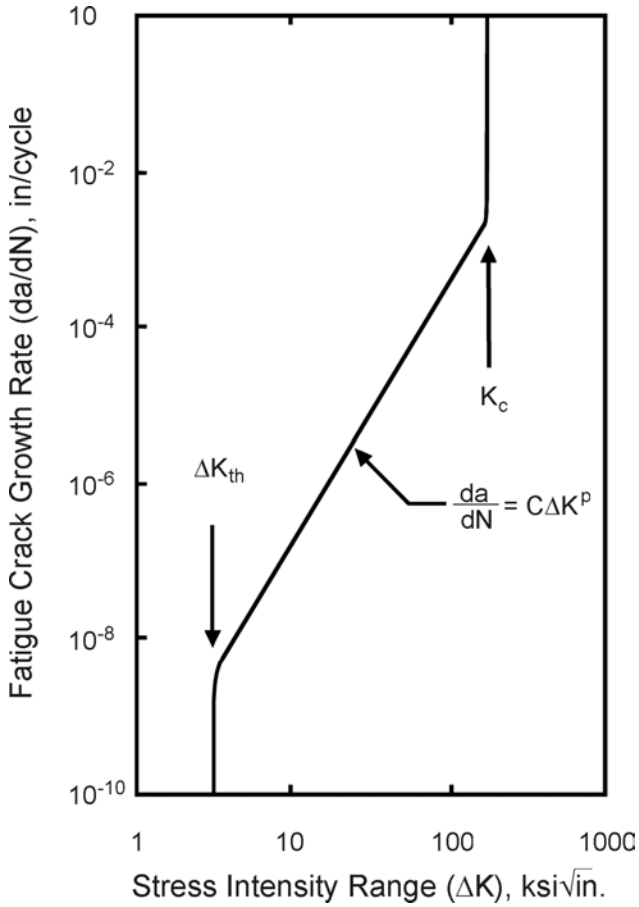

Figure 2.2.9. Schematic Illustration of the Fatigue Crack Growth Rate as a Function of Stress Intensity Range

The application of sub-critical crack growth curves to the design of a potentially cracked structure only requires that the differentiation process be reversed. In other words, given crack growth rate data of the type shown in Figure 2.2.9, the designer integrates the crack growth rate as a function of the stress-intensity factor for the structure through the crack growth interval of interest.

Other investigations have demonstrated that sub-critical crack growth processes that result from variable amplitude loading, stress corrosion cracking, hydrogen embrittlement and liquid metal embrittlement can in general be described using Equation 2.2.6. The sub-critical cracking of structural materials has been successfully modeled with fracture mechanics tools primarily because the plastic deformation processes accompanying cracks are localized and thereby controlled by the surrounding stress field. As suspected, the magnitude in the elastic crack tip stress field is found to correlate well with the rate of sub-critical crack advance.

2.2.6 Alternate Fracture Mechanics Analysis Methods

In the other subsections of Section 2, the emphasis has been on developments of linear elastic fracture mechanics (LEFM) specifically based on the crack tip characterizing parameter *K*, the stress-intensity factor. This parameter has provided the major damage tolerance design tool for aerospace engineers since the early sixties. It was discovered and justified for its universal capability for describing the magnitude of the crack tip stress field by Irwin [1957; 1960] and Williams [1957]. Irwin discovered this relationship through his studies of the energy balance equation associated with fracture. Prior to 1957, fracture research concentrated on extending the original energy balance equation given by Griffith [1921] In 1957, Irwin [1960] linked the "driving force", *G*, in the energy balance equation to the stress-intensity factor, *K*, and suggested how the stress-intensity factor could be used as the driving force for crack tip behavior. Subsequent to Irwin's initial stress-intensity factor analysis, and as a result of the

success of the LEFM approach for solving major fracture problems, interest in the energy approach to fracture waned.

In the late sixties, Rice [1968b] published a paper that again heightened the interest in the energy approach. Rice's specific contribution was to develop an integral, the *J*-integral, which could be used to account for observed non-linear behavior during the fracture process. This integral also has the useful property that it reduces to the elastic "driving force", *G*, when the localized plastic deformation is well contained by the elastic crack tip stress field. Because many of the materials utilized in aerospace structures have exhibited typical LEFM behavior, aerospace engineers have not assumed a leadership role in the development of the *J*-integral technology.

Engineers interested in the damage tolerance analysis of more ductile pressure vessels and welded steel structures have provided the major developments here. Aerospace applications are being recognized each day, however, for this technology, e.g., residual strength analysis of tough materials and sub-critical crack growth behavior of aircraft gas turbine engine structures.

Another analysis approach for characterizing the level of the local stress-strain behavior at the tip of a crack was initiated in Britain in the early sixties. Wells [1961] suggested that the localized behavior at the tip of the crack was controlled by the amount of crack opening, which was referred to as the crack opening displacement, COD. The value of the technology built on the COD concept, like that of the *J*-Integral technology, is that it allows for the coupling of the LEFM analysis and its results to the solution of problems in which the behavior approaches unconstrained yielding.

The subsections below further describe the analysis methodologies based on the three fracture mechanics parameters: the strain energy release rate (driving force - *G*), the *J*-Integral (*J*), and the crack opening displacement (COD), respectively. Each subsection outlines the analytical basis for the parameter and provides the principal equations that tie the parameter to the LEFM parameter *K*. Further information on these parameters can be obtained by the references cited in the text.

2.2.6.1 Strain Energy Release Rate

Paris [1960] gave one of the better descriptions of the fracture energy balance equation associated with the stability of a cracking process in a set of notes prepared for a short course given to the Boeing Company in 1960. Paris simply described the process of determining if a crack would extend as a comparison between the Rate of Energy Input and the Rate at which Energy was absorbed or dissipated. This comparison is similar to performing as analysis based on the Principle of virtual work. In equation form, Paris indicated

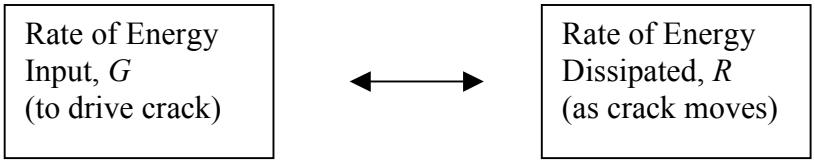

(2.2.8)

where the left hand side of Equation 2.2.8 represents the input rate (as a function of crack area *A*) and the right hand side represents the dissipation rate. If the input rate, the driving force *G*, is equal to the dissipation rate, the resistance *R*, then the crack is in an equilibrium (stable) position, i.e., it is ready to grow but doesn't. If the driving force exceeds the resistance, then the crack grows, an unstable position. Since a crack will not heal itself, if the resistance is greater than the driving force, then the crack is also stable.

The basis for Equation 2.2.8 was further described [Paris, 1960] so that the components are identified as:

$$G = \frac{dX}{dA} + \frac{dG}{dA} \lessgtr \frac{dS}{dA} + \frac{dQ}{dA} = R \qquad (2.2.9)$$

where < and = imply stability while > implies instability.

The driving force (input work rate, *G*) components are:

$\frac{dX}{dA}$ = the work done by external forces on the body unit increase in crack area, dA.

$\frac{dG}{dA}$ = the elastic strain energy released per unit increase in dA.

And the resistance (rate of dissipation, R) components are:

$\frac{dS}{dA}$ = surface energy absorbed in creating a new surface area, dA.

$\frac{dQ}{dA}$ = plastic work dissipated throughout the body during an increase in surface area, dA.

While Equation 2.2.9 is most general and covers fractures that initiate in either brittle or ductile materials, it is not always possible to estimate the individual component terms. For linear elastic materials, the terms can be estimated; and in fact, this was accomplished by Griffith [1921] forty years before Paris presented the above general work rate analysis in 1960. Before any further discussion of the work preceeding that of Paris, however, several additional points need to be made about Equation 2.2.9. First, the component terms of the input energy rate will be defined relative to a specific structural geometry and loading configuration: the uniaxially loaded, center cracked panel shown in Figure 2.2.10. Then the input energy rate (G) will be related to the elastic strain energy.

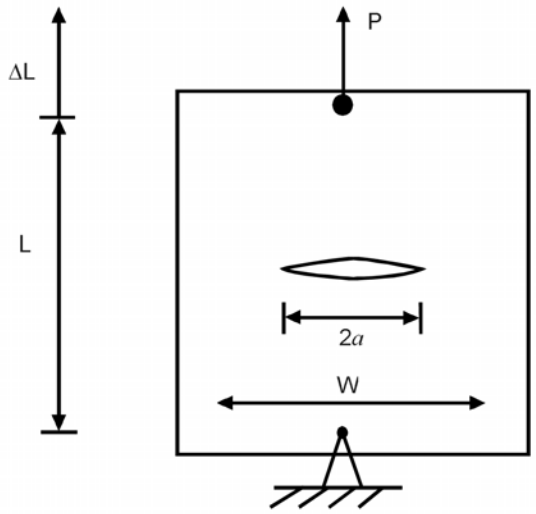

Figure 2.2.10. Finite Width, Center Cracked Panel, Loaded in Tension with Load P

The two components of the energy input rate (G) are given by

$$\frac{dX}{dA} = \frac{PdL}{dA} \tag{2.2.10}$$

the boundary force per increment of crack extension; and by

$$\frac{dG}{dA} = \frac{-dV}{dA} \tag{2.2.11}$$

the decrease in the total elastic strain energy of the plate. With these additional definitions, it can be seen that G is equal to the negative of the rate of change in the potential energy of deformation (U_σ), i.e.,

$$G = \frac{-dU_\sigma}{dA} \tag{2.2.12}$$

2.2.6.1.1 The Griffith-Irwin Energy Balance

The earliest analysis along the above lines was conducted by Griffith [1921] in 1920. Griffith used the crack geometry and loading configuration shown in Figure 2.2.11 and assumed that the stress would be constant during any incremental growth of the crack. Griffith also neglected the plastic work term in Equation 2.2.9 since he was trying to test his fracture hypothesis with a brittle material, glass. Griffith's analysis showed that the input work rate (G) was equal to the negative of the derivative of potential energy of deformation (U_σ) as shown by Equation 2.2.12, and the resistance (R) was equal to the rate of increase in potential energy due to surface energy (U_T) during crack extension:

$$R = \frac{dS}{dA} = \frac{dU_T}{dA} \tag{2.2.13}$$

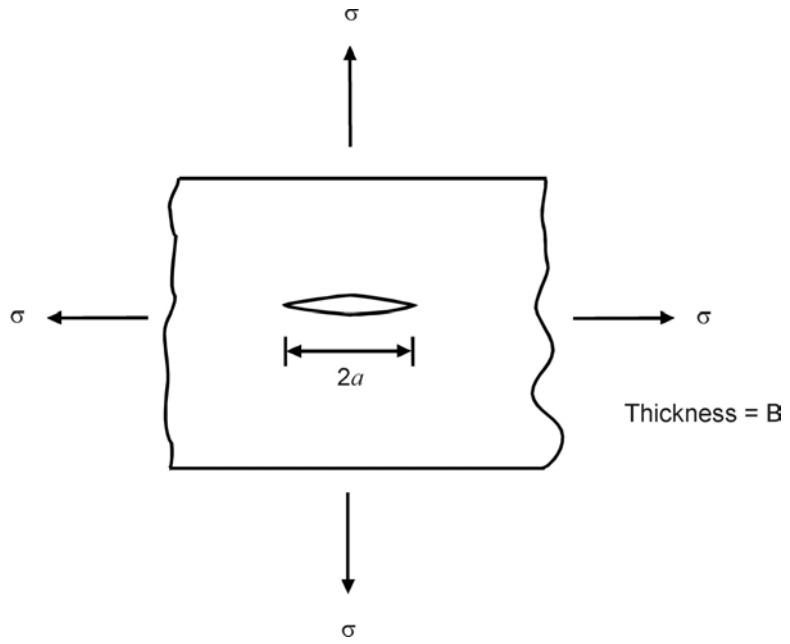

Figure 2.2.11. Griffith Crack and Loading Configuration, Uniformly Loaded, Infinite Plate with a Center Crack of Length 2a

The potential energy of deformation (U_σ) was found to be

$$U_\sigma = \frac{\pi\sigma^2 a^2 B}{E} \tag{2.2.14}$$

while the potential energy due to surface tension (U_T) was given by

$$U_T = 4aTB \tag{2.2.15}$$

with surface tension T, and for plate thickness B.

The crack area A is given by

$$A = 2aB \tag{2.2.16}$$

So the energy balance equation becomes

$$G = \frac{-dU}{dA} = \frac{\sigma^2 \pi a}{E'} = 2T = \frac{dS}{dA} = R \tag{2.2.17}$$

where E′ is dependent on the stress state in the following way

$$E' = \begin{cases} E/(1-\nu^2), \text{ for plane strain} \\ E, \text{ for plane stress} \end{cases} \tag{2.2.18}$$

Solving Equation 2.2.17 for the critical stress (σ_{cr}) associated with the point at which the crack (a) would grow, one finds

$$\sigma_{cr} = \sqrt{\frac{2TE'}{\pi a}} \tag{2.2.19}$$

Later, Irwin [1948] and Orowan [1949] incorporated the effects of crack tip plasticity into the analysis by taking the plastic dissipation term in Equation 2.2.9 as a constant, i.e. they assumed that

$$\frac{dQ}{dA} = q \tag{2.2.20}$$

so that the resistance in Equation 2.2.17 was defined as the combination of surface energy absorbed and plastic work dissipated. Thus, the Griffith-Irwin-Orowan energy balance equation became

$$G = \frac{\sigma^2 \pi a}{E'} = 2T + q = R \tag{2.2.21}$$

and the critical stress was

$$\sigma_{cr} = \sqrt{\frac{(2T + a)E'}{\pi a}} \tag{2.2.22}$$

Both Irwin and Orowan noted that the plastic dissipation rate for metals was at least a factor of 1000 greater than the surface energy absorption rate so that Equation 2.2.22 could be approximated by

$$\sigma_{cr} = \sqrt{\frac{qE'}{\pi a}} \tag{2.2.23}$$

Irwin also noted that the driving force or input energy rate G was directly related to the square of the magnitude of the crack tip stress field for the Griffith center crack geometry (Figure 2.2.11), i.e., that

$$G = \frac{\sigma^2 \pi a}{E'} = \frac{K^2}{E'} \tag{2.2.24}$$

Later, Irwin [1960] reported this result to be general for any cracked elastic body based upon a virtual work analysis of the stresses and displacements associated with crack tip behavior during an infinitesimal crack extension.

2.2.6.1.2 The Relationship between G, Compliance, and Elastic Strain Energy

If one defines the relationship between the force (P) applied to the structure shown in Figure 2.2.10 and the deformation it induces in the direction of load as

$$\Delta L = C \cdot P \tag{2.2.25}$$

where

$$C = C(A) \tag{2.2.25a}$$

is the compliance, the inverse structural stiffness, which varies as a function of crack length (area). With the definitions given by Equation 2.2.25, the elastic strain energy (V) can be written as

$$V = \frac{P.\Delta L}{2} = \frac{CP^2}{2} \tag{2.2.26}$$

The change in V simultaneous to dA and dP is

$$dV = \frac{\partial V}{\partial A}\Big|_P dA + \frac{\partial V}{\partial P}\Big|_A dP \tag{2.2.27}$$

which leads to

$$dV = \frac{P^2}{2}\frac{\partial C}{\partial A}dA + CPdP \tag{2.2.28}$$

Similar operations on changes in dL $(=d(\Delta L))$ lead to

$$PdL = P^2\frac{\partial C}{\partial A}dA + PCdP \tag{2.2.29}$$

So that the input energy rate (G) based on Equation 2.2.9 becomes

$$G = \frac{dX}{dA} + \frac{dG}{dA} = \frac{P^2}{2}\cdot\frac{\partial C}{\partial A} + (0)\cdot\frac{dF}{dA} \tag{2.2.30}$$

Showing that the input energy rate is independent of the variation of force during any incremental crack extension. Thus, Equation 2.2.30 reduces to

$$G = \frac{P^2}{2}\frac{\partial C}{\partial A} \equiv \frac{\partial V}{\partial A}\Big|P = constant \tag{2.2.31}$$

Equation 2.2.31 provides the basis for experimentally evaluating the crack driving force using compliance measurements and clearly shows that the rate of energy input is identically equal to the change in elastic strain energy considering the loading force constant. When one conducts a similar analysis with the displacement (Δ) and crack area (A) as independent variables, one finds that

$$G = -\frac{\partial V}{\partial A}\Big|\Delta L = constant \tag{2.2.32}$$

which means that the input energy rate is the negative of the areal derivative of elastic strain energy considering the displacement constant during crack extension. This is the so-called fixed displacement condition. The term strain energy release rate was assigned to G, the input energy rate, when it was realized that for cracked elastic bodies Equation 2.2.30 and 2.2.31 were generally applicable.

Figure 2.2.12 describes the change in elastic strain energy that occurs when a crack grows under fixed load and fixed displacement conditions. It can be noted that the difference between the change in elastic strain energy for the two cases is the infinitesimal area $\frac{1}{2}dP * \Delta L$, shown cross-hatched in Figure 2.2.12a. For the case of the fixed load condition (Figure 2.2.12a), the elastic strain energy is seen to increase as the crack grows; the gain in elastic strain energy is greater than the indicated loss (by a factor of 2). For the case of the fixed displacement condition (Figure 2.2.12b), the elastic strain energy is seen to decrease as the crack grows; only a loss is indicated.

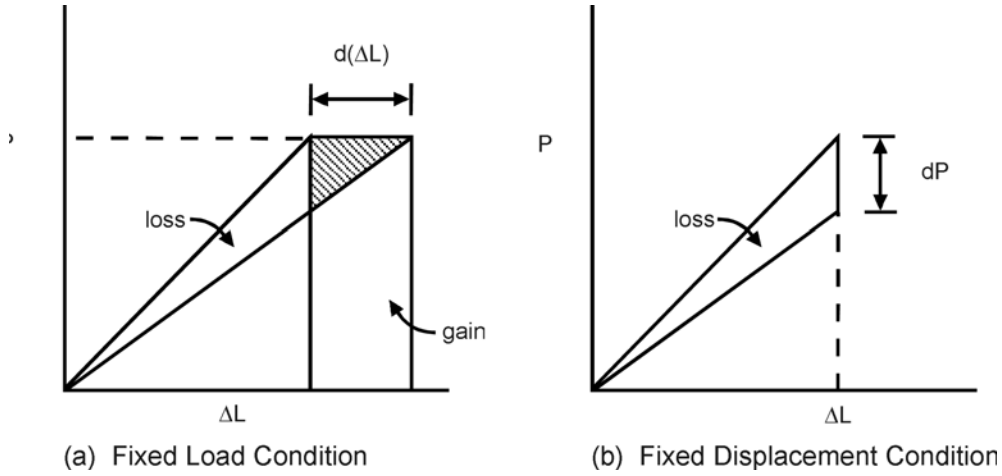

Figure 2.2.12. Load-Displacement Diagrams for the Structure Illustrated in Figure 2.2.10. The Diagram Shows the Changes that Occur in the Elastic Strain Energy as a Crack Grows Under the Two Defined Conditions

Some important observations presented in the subsection are:

(a) the general form of Equation 2.2.24 can be utilized to relate G and K;

(b) G is equal to the negative rate of change in the potential energy of deformation (Equation 2.2.12); and

(c) G is related to the areal rate of change in compliance (Equation 2.2.31).

Note that by combining Equations 2.2.24 and 2.2.12 or 2.2.31 the analyst and/or experimentalist have energy-based methods for obtaining estimates of the stress-intensity factor. These combinations are discussed in Section 11.2.1.4 (see, for example, Equation 11.2.25).

2.2.6.2 The J-Integral

In 1968, Rice [1968b] published a paper describing a path independent integral (J) which was noted to be equal to the negative of the change in potential energy of deformation occurring during the infinitesimal growth of a crack in a nonlinear elastic material, i.e. he showed that

$$J = -\frac{\partial U_\sigma}{\partial A} \tag{2.2.33}$$

Rice's path independent integral J was defined by [Rice, 1968a; 1968b]

$$J = \int_\Gamma \left(W dy - \vec{T} \cdot \frac{\partial \vec{u}}{\partial x} ds \right) \tag{2.2.34}$$

where Γ is any contour surrounding the crack tip, traversing in a counter clockwise direction (see Figure 2.2.13), W is the strain energy density, $\vec{\Gamma}$ is the traction on Γ, and $\vec{u}$ is the displacement on an element along arc s.

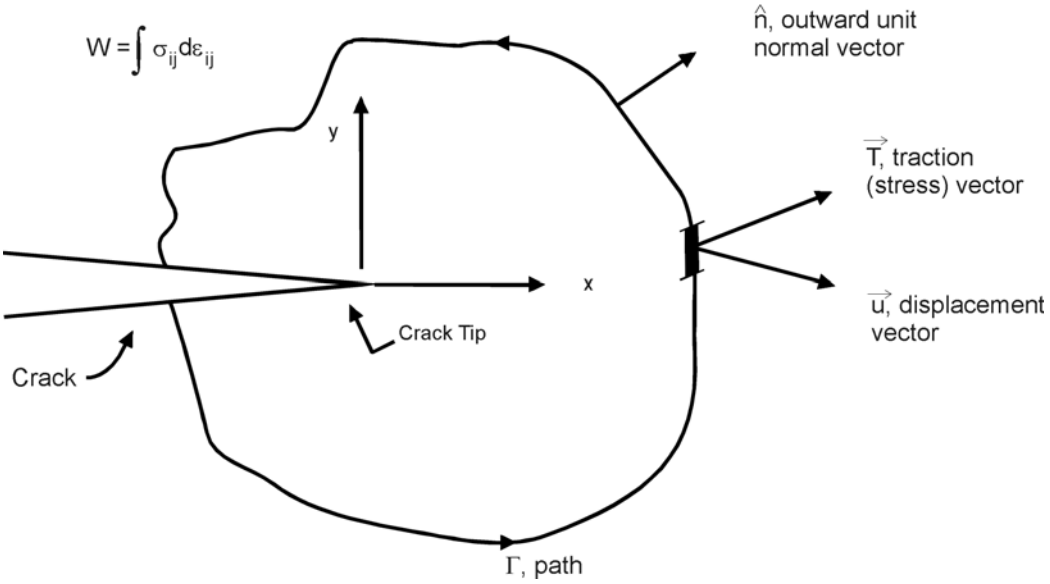

Figure 2.2.13. *J*-Integral Parameters Illustrated

Before elaborating on a detailed description of the parameters involved in the calculation of the *J*-Integral, it is useful to note that Equation 2.2.33 is the nonlinear elastic equivalent of Equation 2.2.12. Thus, for linear elastic materials, *J* reduces to the value of the strain energy release rate, *G*, i.e.

$$J = G \tag{2.2.35}$$

and the *J*-integral is related to the stress-intensity factor through the expression

$$J = \frac{K^2}{E'} \tag{2.2.36}$$

where E' is given by Equation 2.2.18.

Equations 2.2.35 and 2.2.36 are noted to be valid only when the material is behaving in a linear elastic fashion. When values of the *J*-Integral are determined via Equation 2.2.34 using finite element methods applied to linear elastic cracked structures, Equation 2.2.36 provides the engineer with a simple energy-based method for obtaining stress-intensity factors as a function of crack length.

In the first subsection below, the calculations associated with developing the *J*-Integral for an elastic-plastic material are detailed. In the second subsection, some engineering approximation methods for calculating the J-Integral are outlined.

2.2.6.2.1J-Integral Calculations

This subsection outlines the calculation of parameters involved in the *J*-Integral. Consideration is given to *W*, $\vec{T}, \vec{u}$, $\vec{T}, \vec{u}$ and Γ as well as the choice of material stress-strain behavior.

The strain energy density W in Equation 2.2.34 is given by

$$W = \int \left[\sigma_{xx} d\varepsilon_{xx} + \sigma_{xy} d\gamma_{xy} + \sigma_{xz} d\gamma_{xz} + \sigma_{yy} d\varepsilon_{yy} + \sigma_{yz} d\gamma_{yz} + \sigma_{zz} d\varepsilon_{zz}\right] \tag{2.2.37}$$

and for generalized plane stress

$$W = \int \left[\sigma_{xx} d\varepsilon_{xx} + \sigma_{xy} d\gamma_{xy} + \sigma_{yy} d\varepsilon_{yy}\right] \tag{2.2.38}$$

In Equation 2.2.34, the second integral involves the scalar product of the traction stress vector $\vec{T}$ and the vector $\frac{\partial \vec{u}}{\partial x}$ whose components are the rate of change of displacement with respect to x. The traction vector is given by

$$\vec{T} = T_x \hat{i} + T_y \hat{j} = \left(\sigma_{xx} \cdot n_x + \sigma_{xy} n_y\right)\hat{i} + \left(\sigma_{yx} \cdot n_x + \sigma_{yy} \cdot \sigma_{yy} n_y\right)\hat{j} \tag{2.2.39}$$

and the displacement rate vector is given by

$$\frac{\partial \vec{u}}{\partial x} = \frac{\partial u}{\partial x}\hat{i} + \frac{\partial v}{\partial x}\hat{j} \tag{2.2.40}$$

where u and v are the displacements in the x and y directions, respectively.

Typically, when evaluating the J-Integral value via computer, rectangular paths such as the one illustrated in Figure 2.2.14 are chosen. Noted on Figure 2.2.14 are the values of the outward unit normal components and the ds path segment for the four straightline segments. For loading symmetry about the crack axis (x-axis), the results of the integration on paths 0-1, 1-2 and 2-3 are equal to the integrations on paths 6-7, 5-6 and 4-5, respectively. Thus, for such loading symmetry, one can write

$$\begin{aligned} J = 2\left\{\int_6^7 \left[W - \sigma_{xx}\frac{\partial u}{\partial x} - \sigma_{xy}\frac{\partial v}{\partial x}\right]dy + \int_5^6 \left[\sigma_{xy}\frac{\partial u}{\partial x} + \sigma_{yy}\frac{\partial v}{\partial x}\right]dx\right\} \\ + \int_4^5 \left[W - \sigma_{xx}\frac{\partial u}{\partial x} - \sigma_{xy}\frac{\partial v}{\partial x}\right]dy \end{aligned} \tag{2.2.41}$$

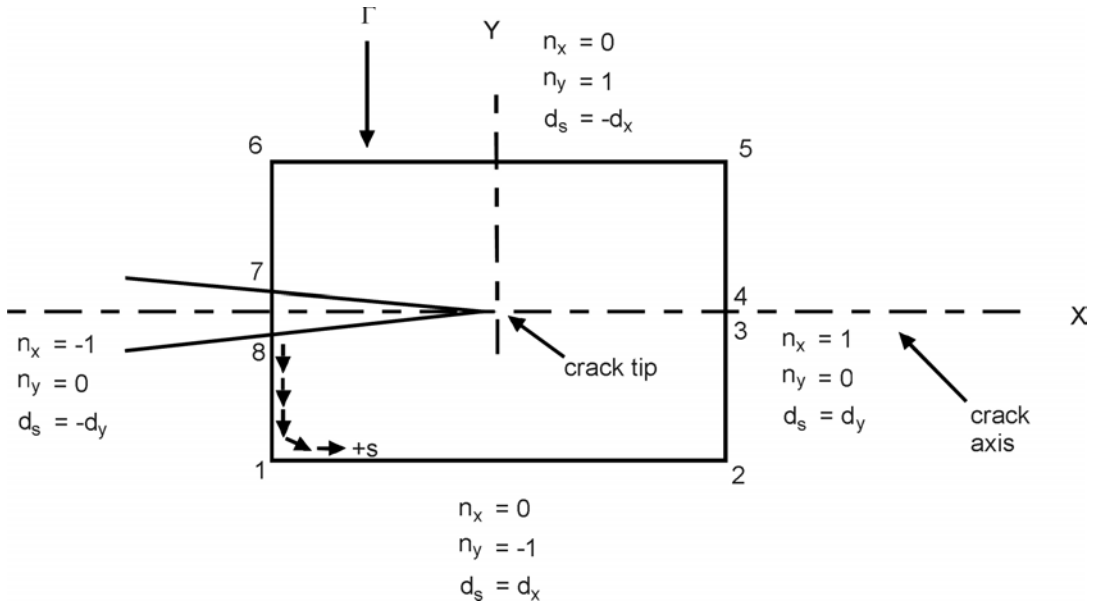

Figure 2.2.14. Rectangular Path for *J* Calculation

For paths of the type shown in Figure 2.2.14, the *J*-Integral can be evaluated by the integrations indicated in Equation 2.2.41. The strain energy density *W*, appearing in Equation 2.2.41, is given by Equation 2.2.37, or by Equation 2.2.38 for plane stress conditions. To integrate according to Equations 2.2.37 or 2.2.38, a relationship between stresses and strains is required. For material exhibiting plastic deformations, the Prandtl-Reuss equations provide a satisfactory relationship. For the case of plane stress, when the Prandtl-Reuss relations are introduced into Equation 2.2.38, Equation 2.2.38 becomes

$$W = \frac{1}{2E}\left[\sigma_{xx} + \sigma_{yy}\right]^2 + \frac{(1-\upsilon)}{E}\left[\sigma_{xy}{}^2 - \sigma_{xy}\sigma_{yy}\right] + \int \bar{\sigma} d\bar{\varepsilon}_p \qquad (2.2.42)$$

where $\bar{\sigma}$ and $\bar{\varepsilon}_p$ are the equivalent stress and equivalent plastic strain, respectively. The strain energy density will have a unique value only if unloading is not permitted. If loading into the plastic range followed by unloading is permitted, then W becomes multi-valued. It follows that *J* is also multi-valued for this occurrence.

The statements made in the preceding paragraph would appear to seriously limit the use of *J* as a fracture criterion since the case of loading into the plastic range followed by unloading (i.e., the case for which *J* is multi-valued) occurs when crack extension takes place. On the basis of a number of examples, Hayes [1970] deduced that monotonic loading conditions prevail throughout a cracked body under steadily increasing load applied to the boundaries, provided that crack extension does not occur. Thus, valid *J* calculations can be performed for this case.

2.2.6.2.2 Engineering Estimates of J

While the J-Integral was developed for nonlinear elastic material behavior, it has been extensively studies for its direct application to describing elastic-plastic material behavior [Begley & Landes, 1972; Verette & Wilhem, et al., 1973; Landes, et al., 1979; Paris, 1980; Roberts, 1981]. Its nonlinear elastic foundation has provided engineers with some techniques which allow them to focus on the combination of linear-elastic and plastic-strain hardening behavior and then to separate these two components for further study of the plastic behavior. The *J*-Integral for an elastic-plastic material is taken as the sum of two components parts: the linear elastic part (J_{el}) and the plastic-strain hardening part (J_{pl}), i.e.,

$$J = J_{e\ell} + J_{p\ell} \qquad (2.2.43)$$

which when used in conjunction with Equation 2.2.36 becomes

$$J = \frac{K^2}{E'} + J_{p\ell} \tag{2.2.44}$$

Engineering estimates of J then focus on the development of the plastic-strain hardening part J_{pl}. Recently, Shih and coworkers have published a series of reports and technical papers [Shih & Kumar, 1979; Kumar, et al., 1980; Shih, 1976; Kumar, et al., 1981] detailing how the J_{pl} term can be calculated from a series of finite element models that consider changes in material properties for the same structural geometry. The following briefly describes the Shih and coworkers method for estimating J_{pl}.

First, the material is assumed to behave according to a power hardening constitutive (σ - ε) law of the form

$$\frac{\varepsilon}{\varepsilon_o} = \alpha\left(\frac{\sigma}{\sigma_o}\right)^n \tag{2.2.45}$$

where α is a dimensionless constant, $\sigma_o = E\varepsilon_o$, and n is the hardening exponent. For $n = 1$, the material behaves as a linearly elastic material; as n approaches infinity, the material behaves ore and more like a perfectly plastic material. For a generalization of Equation 2.2.45 to multiaxial states via the J_2 deformation theory of plasticity, Ilyushin [1946] showed that the stress at each point in the body varies linearly with a single load such as σ, the remotely applied stress, under certain conditions.

Ilyushin's analysis allowed Shih and Hutchison [1976] to use the relationship for crack tip stresses under contained plasticity, i.e. to use [Hutchinson, 1968; Rice & Rosengren, 1968]

$$\sigma_{xx} = \sigma_o\left(\frac{J_{pl}}{r\sigma_o\varepsilon_o}\right)^{\frac{1}{1+n}}\tilde{\sigma}_{xx}\left(\theta, \frac{1}{n}\right) \tag{2.2.46}$$

and similar equations for σ_{yy}, σ_{xy}, etc., to relate the crack tip parameters uniquely to the remotely applied load. Note that J_{pl} term in Equation 2.2.46 acts as a (plastic) stress field magnification factor similar to that of the stress-intensity factor in the elastic case. The form of the relationship that Shih and Hutchinson postulated is given by

$$\frac{J_{pl}}{\sigma_o\varepsilon_o a_o} = \left(\frac{\sigma}{\sigma_o}\right)^{n+1} \cdot \hat{J}\left(\frac{a}{b}, n\right) \tag{2.2.47}$$

where $\hat{J}$ is a function only of relative width (a/b) and n. An alternate form of Equation 2.2.47 that has been previously used in computer codes [Kumar, et al., 1980; Kumar, et al., 1981; Weerasooriya & Gallagher, 1981] is

$$J_{pl} = \alpha\sigma_o\varepsilon_o a \cdot f_1\left(\frac{a}{b}\right) \cdot h_1\left(\frac{a}{b}, n\right) \cdot \left(\frac{P}{P^T_o}\right)^{n+1} \tag{2.2.48}$$

where P is the applied load (per unit thickness), P^T_o is the theoretical limit load (per unit thickness), f_1 is a function only of geometry and crack length, while h_1 depends on geometry, crack length, and the strain hardening exponent n. Shih and coworkers [Kumar, et al., 1980; Kumar, et al., 1981] have tabulated the functions for a number of geometries for conditions of plant stress and plane strain. From the reference tabulated data [also see Weerasooriya & Gallagher, 1981], these functions can be obtained by interpolation for any value within the a/b and n limits given; thus, the plastic (strain hardening) component of Equation 1.3.44 can be computed for any given applied load P from Equation 2.2.48.

EXAMPLE 2.2.1 *J* Estimated for Center Crack Panel

Figure 2.2.10 describes the geometry for this example wherein the width W is set equal to $2b$ and the load P is expressed per unit thickness. Using Equation 2.2.44 to describe the relationship between the elastic and plastic components, we have

$$J = \frac{K^2}{E'} + J_{pl}$$

From elastic analysis, the stress-intensity factor is known to be (see section 11):

$$K = \left(\frac{P}{2b}\right)\sqrt{\pi a \sec\left(\frac{\pi a}{2b}\right)}$$

For the strain hardening analysis, Equation 2.2.48 is employed, i.e., we use

$$J_{pl} = \alpha\sigma_o\varepsilon_o a \cdot f_1\left(\frac{a}{b}\right) \cdot h_1\left(\frac{a}{b}, n\right) \cdot \left(\frac{P}{P_o^T}\right)^{n+1}$$

For a center crack panel, the function f_1 is given by [Kumar, et al., 1980; Kumar, et al., 1981]

$$f_1\left(\frac{a}{b}\right) = \frac{2b - 2a}{2b}$$

and the limit load (per unit thickness) is given by either

$$P_o^T = \frac{4}{\sqrt{3}}\sigma_o(b - a)$$

for plane strain or by

$$P_o^T = 2\sigma(b - a)$$

for plane stress. The supporting data for calculating the function h_1 is supplied by the following tables for plane strain conditions and plane stress conditions. The other functions (h_2 and h_3) contained in these tables support displacement calculations. As indicated above, data are available for estimating the *J*-integral according to this approach for a number of additional (simple geometries). See Kumar, et al. [1981] and Weerasooriya & Gallagher [1981] for further examples.

Table of Values of h_1, h_2, and h_3 for the Plane Strain CCP in Tension
[Shih, 1979; Kumar, et al., 1980; Weerasooriya & Gallagher, 1981]

a/b		n = 1	n = 2	n = 3	n = 5	n = 7	n = 10	n = 13	n = 16	n = 20
1/4	h_1	2.535	3.009	3.212	3.289	3.181	2.915	2.625	2.340	2.028
	h_2	2.680	2.989	3.014	2.847	2.610	2.618	1.971	1.712	1.450
	h_3	0.536	0.911	1.217	1.639	1.844	1.554	1.802	1.637	1.426
3/8	h_1	2.344	2.616	2.648	2.507	2.281	1.969	1.709	1.457	1.193
	h_2	2.347	2.391	2.230	1.876	1.580	1.276	1.065	0.890	0.715
	h_3	0.699	1.059	1.275	1.440	1.396	1.227	1.050	0.888	0.719
1/2	h_1	2.206	2.291	2.204	1.968	1.759	1.522	1.323	1.155	0.978
	h_2	2.028	1.856	1.600	1.230	1.002	0.799	0.664	0.564	0.466
	h_3	0.803	1.067	1.155	1.101	0.968	0.796	0.665	0.565	0.469
5/8	h_1	2.115	1.960	1.763	1.616	1.169	0.863	0.628	0.458	0.300
	h_2	1.705	1.322	1.035	0.696	0.524	0.358	0.250	0.178	0.114
	h_3	0.844	0.937	0.879	0.691	0.522	0.361	0.251	0.178	0.115
3/4	h_1	2.072	1.732	1.471	1.108	0.895	0.642	0.461	0.337	0.216
	h_2	1.345	0.857	0.596	0.361	0.254	0.167	0.114	0.081	0.051
	h_3	0.805	0.700	0.555	0.359	0.254	0.168	0.114	0.081	0.052

Table of Values of h_1, h_2, and h_3 for the Plane Stress CCP in Tension
[Shih, 1979; Kumar, et al., 1980; Weerasooriya & Gallagher, 1981]

a/b		n = 1	n = 2	n = 3	n = 5	n = 7	n = 10	n = 13	n = 16	n = 20
1/4	h_1	2.544	2.972	3.140	3.195	3.106	2.896	2.647	2.467	2.196
	h_2	3.116	3.286	3.304	3.151	2.926	2.595	2.288	2.081	1.814
	h_3	0.611	1.010	1.352	1.830	2.083	2.191	2.122	2.009	1.792
3/8	h_1	2.344	2.533	2.515	2.346	2.173	1.953	1.766	1.608	1.431
	h_2	2.710	2.621	2.414	2.032	1.753	1.473	1.279	1.134	0.988
	h_3	0.807	1.195	1.427	1.594	1.570	1.425	1.267	1.133	0.994
1/2	h_1	2.206	2.195	2.057	1.809	1.632	1.433	1.300	1.174	1.000
	h_2	2.342	2.014	1.703	1.299	1.071	0.871	0.757	0.666	0.557
	h_3	0.927	1.186	1.256	1.178	1.040	0.867	0.758	0.668	0.560
5/8	h_1	2.115	1.912	1.690	1.407	1.221	1.012	0.853	0.712	0.573
	h_2	1.968	1.458	1.126	0.785	0.617	0.474	0.383	0.313	0.256
	h_3	0.975	1.053	0.970	0.763	0.620	0.478	0.386	0.318	0.273
3/4	h_1	2.073	1.708	1.458	1.208	1.082	0.956	0.745	0.646	0.532
	h_2	1.611	0.970	0.685	0.452	0.361	0.292	0.216	0.183	0.148
	h_3	0.933	0.802	0.642	0.450	0.361	0.292	0.216	0.183	0.149

In the application of Equation 2.2.44 to structural material problems, it has been found [Bucci, et al., 1972] that better correlation with experimental results is obtained if one uses the plasticity enhanced, effective crack length (a_e) in plane of the physical crack length (a) in the elastic component expressions. The effective crack length utilized by Bucci, et al. [1972] was based on the Irwin plastic zone size correction, i.e. the effective crack length was given by

$$a_e = a + r_y \tag{2.2.52}$$

where

$$r_y = \frac{1}{x\pi}\left(\frac{K}{\sigma_o}\right)^2 \tag{2.2.53}$$

with $x = 2$ for plane stress and $x = 6$ for plane strain. K represents the stress-intensity factor.

2.2.6.3 Crack Opening Displacement

The crack opening displacement (COD) parameter was proposed to provide a more physical explanation for crack extension processes. [Wells, 1961; Burdekin & Stone, 1966] The philosophy was based on a crack tip strain based model of cracking that would allow for the occurrence of elastic-plastic material behavior. The initial modeling, however, was based on elasticity solutions of crack tip displacements. Equation 2.2.54 describes the x and y displacements (u and v, respectively) in the crack tip region of an elastic material:

$$u = \frac{K}{2G}\left(\frac{r}{2\pi}\right)^{1/2} cos\frac{\theta}{2}\left[\kappa - 1 + 2sin^2\frac{\theta}{2}\right] \tag{2.2.54a}$$

$$v = \frac{K}{2G}\left(\frac{r}{2\pi}\right)^{1/2} sin\frac{\theta}{2}\left[\kappa + 1 - 2cos^2\frac{\theta}{2}\right] \tag{2.2.54b}$$

where $\kappa = 3 - 4\nu$ for plane strain and $\kappa = (3 - \nu)/(1 + \nu)$ for plane stress, and where G is the shear modulus ($G = 0.5E/(1 + \nu)$). If the angle θ is chosen to be 180° (π), the displacements are those associated with crack sliding (u component) or opening (v component). Under mode 1 (symmetrical) loading, the case covered by Equation 1.3.54, the sliding displacement term is noted to be identically zero; and all displacement is perpendicular to the crack, i.e. only opening is observed. Based on Equations 2.2.54 and 2.2.18 and the definition of shear modulus (G), the displacement of the crack relative to its longitudinal axis (x axis) is

$$v = 4\frac{K}{E'}\left(\frac{r}{2\pi}\right)^{1/2} \tag{2.2.55}$$

The relative movement of the crack faces is the COD and it is twice the value obtained by Equation 2.2.55, i.e.

$$COD = 2v \tag{2.2.56}$$

One immediate observation is that COD will vary as a function of position along the crack, and that the COD at the crack tip, i.e. at $r = 0$, is zero. In the quasi-elastic-plastic analysis performed by Wells, the crack was allowed to extend to an effective length (a_e), one plastic zone radius larger than the physical crack length (a); the crack opening displacement was then determined at the location of the physical crack tip. Figure 2.2.15 describes the model used to define the crack tip opening displacement (CTOD). The Wells modeling approach leads one to

$$CTOD = 8\frac{K}{E'}\left(\frac{r_y}{2\pi}\right)^{1/2} \tag{2.2.57}$$

which after some simplification gives the CTOD as

$$CTOD = \frac{4}{\pi}\frac{K^2}{E'\sigma_o} \tag{2.2.58}$$

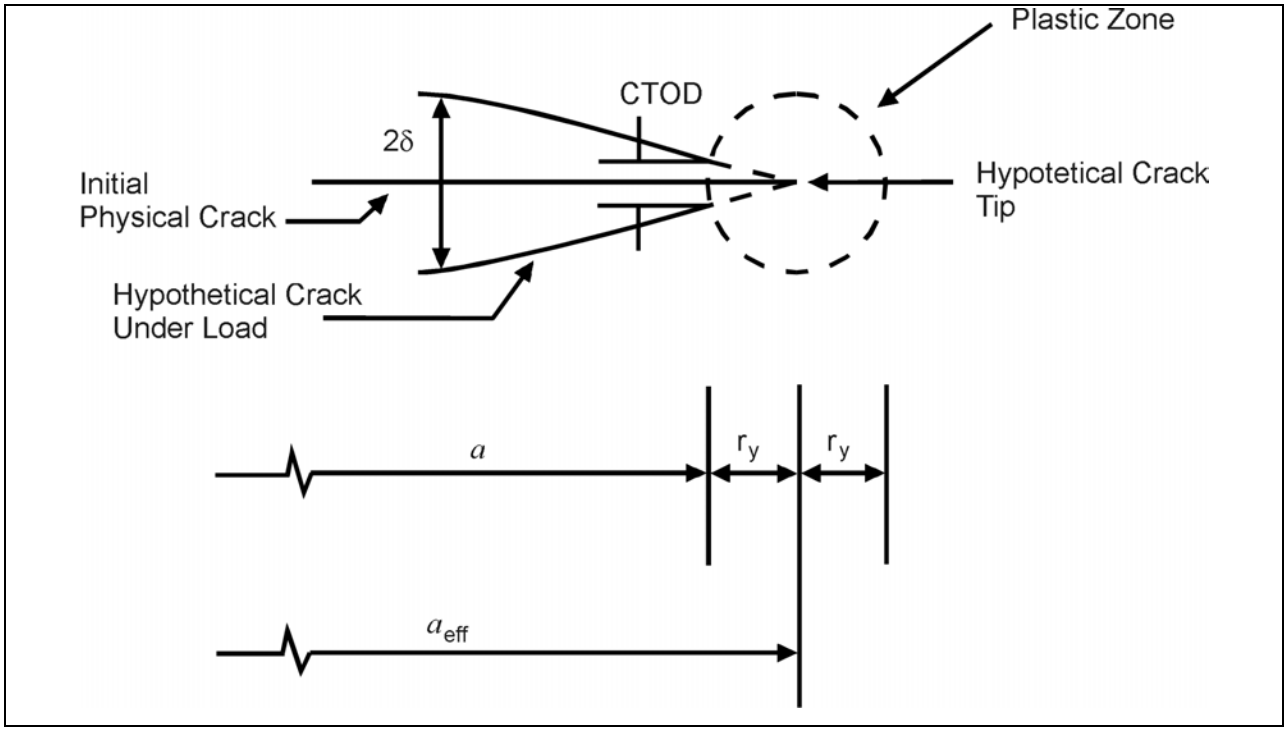

Figure 2.2.15. Description of Model Used to Establish the CTOD Under Elastic Conditions

It is immediately seen that the CTOD is directly related to the stress-intensity factor for elastic materials; thus, for elastic materials, fracture criteria based on CTOD are as viable as those based on the stress-intensity factor parameter. The other relationships developed between *K* and *G* or *J* in this section allow one to directly relate *G* and *J* to the CTOD in the elastic case.

In the late 1960's, Dugdale [1960] conducted an elasticity analysis of a crack problem in which a zone of yielding was postulated to occur in a strip directly ahead of the crack tip. The material in the strip was assumed to behave in a perfect plastic manner. The extent of yielding was determined such that the singularity at the imaginary crack tip (see Figure 2.2.16) was canceled due to the balancing of the remote positive stress-intensity factor with the local yielding negative stress-intensity factor. The Dugdale quasi-elastic-plastic analysis provided an estimate of the relative displacement of the crack surfaces for a center crack (crack length = 2*a*) in an infinite plate subjected to a remote tensile stress (σ) and having a yield strength equal to σ_o, the CTOD is

$$CTOD = \frac{8a\sigma_o}{\pi E'}\ell n\left(sec\left(\frac{\pi\sigma}{2\sigma_o}\right)\right) \tag{2.2.59}$$

at the tip of the physical crack tip (*a*) and the extent of the plasticity ahead of the crack is

$$\omega = a\left[sec\left(\frac{\pi\sigma}{2\sigma_o}\right) - 1\right] \tag{2.2.60}$$

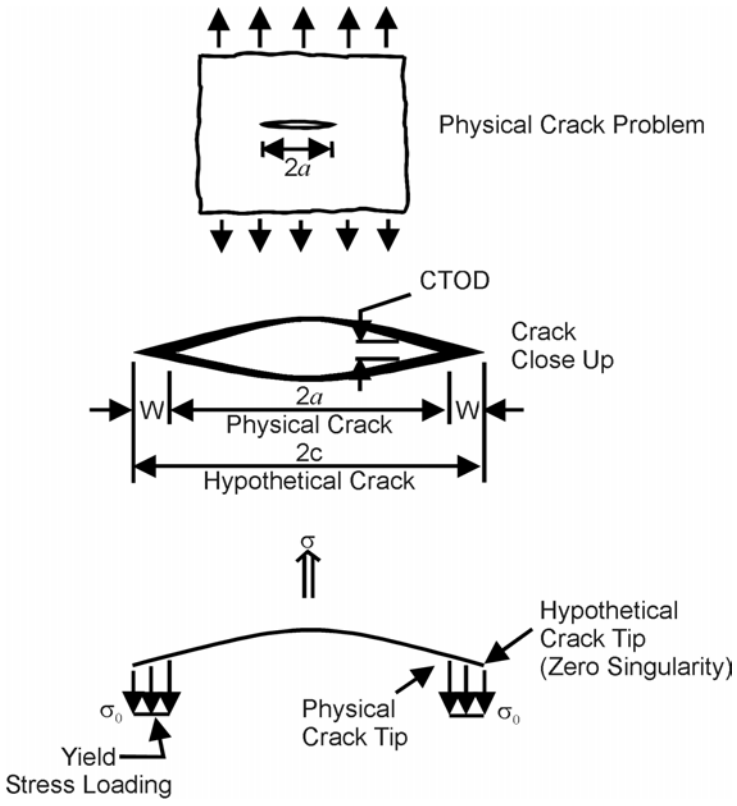

Figure 2.2.16. Dugdale Type Strip Yield Zone Analysis

For the case of small scale yielding, i.e., when σ/σ_0 is low, the CTOD and extent of plasticity (ω) reduce to

$$CTOD \cong \frac{\sigma^2 \pi a}{E' \sigma_o} = \frac{K^2}{E' \sigma_o} \tag{2.2.61}$$

and

$$\omega \cong \frac{\pi}{8} \frac{K^2}{\sigma_o 2} \tag{2.2.62}$$

It can first be noted that the extent of the plasticity (ω) is only about 20% higher than would be predicted using the Irwin estimate of the plastic zone diameter ($2r_y$). The level of CTOD estimated by Equation 2.2.61 also compares favorably with that given by Equation 2.2.58; Equation 2.2.61 gives an estimate that is about 30 percent lower than Equation 2.2.58. Numerous other studies have shown that the CTOD is related to the stress-intensity factor under conditions of small scale yielding through

$$CTOD = \alpha \frac{K^2}{E' \sigma_o} \tag{2.2.63}$$

where the constant α ranges from about 1 to 1.5. Experimental measurements [Bowles, 1970; Roberson & Tetelman, 1973] have indicated that α is close to 1.0, although there is substantial disagreement about the location where CTOD should be measured.

One difficulty with elastic analyses is that the crack actually remains stationary and thus one must reposition the crack through a quasi-static crack extension so that the CTOD for the actual crack can be assessed. During loading, cracks in ductile materials tend to extend through a slow tearing mode of cracking prior to reaching the fracture load

level. In these cases, the amount of opening that occurs at the initial crack tip represents one measure of the crack tip strain; but, this parameter depends not only on load, initial crack length and material properties, it also depends on the amount of crack extension from the initial crack tip. Rice and co-workers [Rice, 1968b; Rice & Tracey, 1973] attempted to provide an alternate choice of locating the position where CTOD would be measured. They found that when the CTOD was determined for the position shown in Figure 2.2.17, the CTOD and J integral were related (for ideally plastic materials) by

$$CTOD = d_n \frac{J}{\sigma_o} \tag{2.2.64}$$

For the case of plane stress behavior, d_n is unity and for plane strain behavior, d_n is about 0.78.

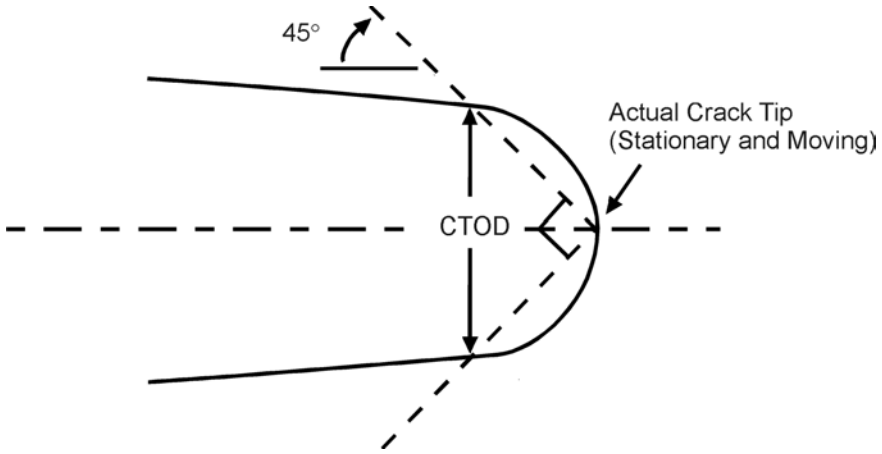

Figure 2.2.17. Definition of the Crack Tip Opening Displacement (CTOD)

For strain hardening materials controlled by Equation 2.2.45, Shih and co-workers [Shih & Kumar, 1979; Shih, 1979] have shown that Equation 2.2.64 relates J and CTOD if the constant d_n is replaced with a function that is strongly dependent on the strain hardening exponent and mildly dependent on the ratio σ_o/E. Thus, there is a direct relationship between CTOD and J throughout the region of applicability of the J-Integral and CTOD can likewise be considered a measure of the magnitude of the crack tip stress-strain field.

2.3 Residual Strength Methodology

The strength of a structure can be significantly affected by the presence of a crack and is usually substantially lower than the strength of the undamaged structure. To prevent catastrophic failure, one must evaluate the load carrying capacity that will exist in the potentially cracked structure throughout its expected service life. The load carrying capacity of a cracked structure is the residual strength of that structure and it is a function of material toughness, crack size, crack geometry and structural configuration.

The determination of residual strength for uncracked structures is straightforward because the ultimate strength of the material is the residual strength. A crack in a structure causes a high stress concentration resulting in a reduced residual strength. When the load on the structure exceeds a certain limit, the crack will extend. The crack extension may become immediately unstable and the crack may propagate in a fast uncontrollable manner causing complete fracture of the component.

In general, unstable crack propagation results in fracture of the component. Hence, unstable crack growth is what determines the residual strength. In order to estimate the residual strength of a structure, a thorough understanding of the crack growth behavior is needed. Also, the point at which the crack growth becomes unstable must be defined and this necessitates the need for a failure criterion. There are several criteria available; these criteria are tailored to represent the ability of a material to resist failure.

A material's toughness depends on thickness. When the thickness is such that the crack tip plastic zone size is on the order of the plate thickness, the toughness reaches a maximum value, $K_{c(max)}$. With increasing thickness of the plate, the plastic zone size reduces and thus the toughness gradually decreases, from $K_{c(max)}$ to K_{Ic}. When the thickness is large enough that the crack tip deformation is not affected by the thickness, plane strain conditions prevail at the crack tip. The toughness in the plane strain regime is virtually independent of thickness. For increasing thickness, the toughness asymptotically approaches the plane strain fracture toughness, K_{Ic}.

The critical K_{cr} for abrupt fracture mode is denoted as K_{Ic} for plane strain conditions and K_c for plane stress conditions; the conditions for plane stress or plane strain are determined by experiment. The test requirements necessary for generating K_{Ic} and K_c are discussed in Section 7.

When the crack extends by a tearing mode of fracture, which typically occurs in thin metal sheets or in tough materials, the crack extension is essentially slow and stable. The failure condition for tearing fractures depends on the crack growth resistance (K_R) behavior of the material and the applied stress-intensity factor K, which in turn depends on the crack and structural configurations.

The crack growth resistance curve (K_R) has shown good promise for materials where limited (small-scale) yielding occurs in front of the crack tip. Difficulties in estimating crack tip plasticity under large-scale yielding conditions, led Wilhem [1974] to an alternate failure criterion based on the J-integral [Rice, 1968]. For a basic introduction to the J-integral see Section 11.

An important element in the process of predicting residual strength of a structure experiencing ductile tearing is having a criterion that predicts the onset and rate of this phenomenon. Tests and

numerical simulations have been performed to assess the critical crack tip opening angle ($CTOA_c$) criterion for predicting residual strength of structures containing MSD. Section 4 section details the theoretical background behind the $CTOA_c$ criterion, and describes experimental and computational investigations into it.

2.4 Life Prediction Methodology

Currently, within the Air Force, airframe life predictions are based on a crack growth damage integration package that uses a data base and analysis to interrelate the following six elements:

a) The initial flaw distribution which accounts for size variations and location of cracks in a given structure;

b) aircraft usage describing the load spectra data base;

c) constant amplitude crack growth rate material properties accounting for stress ratio and environmental effects;

d) crack tip stress intensity factor analyses which account for crack size, shape, and structural interactions;

e) damage integrator model which assigns a level of crack growth for each applied stress application and accounts for load history interactions; and

f) the fracture or life limiting criterion which establishes the end point of the life calculation.

Prior to describing each of the above itemized elements in separate subsections, the damage integrating equation will be introduced to show how the various elements interact. As expressed in a numerical form, the damage integrating equation is

$$a_{cr} = a_o + \sum_{j=1}^{t_f} \Delta a_j \qquad (2.4.1)$$

where Δa_j is the growth increment associated with the j^{th} time increment. The purpose of Equation 2.4.1 is to determine the life t_f. The various elements affect the quantities in Equation 2.4.1 in the following manner:

1. a_{cr} is determined interrelating elements b, d, and f.

2. a_o is determined using element a.

3. Δa_j is determined by interrelating elements a, b, c, d, and e.

2.4.1 Initial Flaw Distribution

A measure of initial quality in a component of service hardware is given by the distribution of initial crack sizes as illustrated in Figure 2.4.1. For predictions of safety limits, the initial cracks larger than the nondestructive inspection (NDI) detectability limit are of principal concern. Current specifications detail NDI limits and require verification/certification of contractor capability to detect cracks smaller than the specified NDI limits. Normally, such certification is demonstrated with curves of the type shown in Figure 2.4.2. The program of certification for a contractor's quality control inspector/inspection techniques allows the USAF to assess the probability and confidence limits associated with detecting a given crack. Section 3 will present a state-of-the-art summary of the technology and equipment that supports the establishment of initial flaws via nondestructive tools.

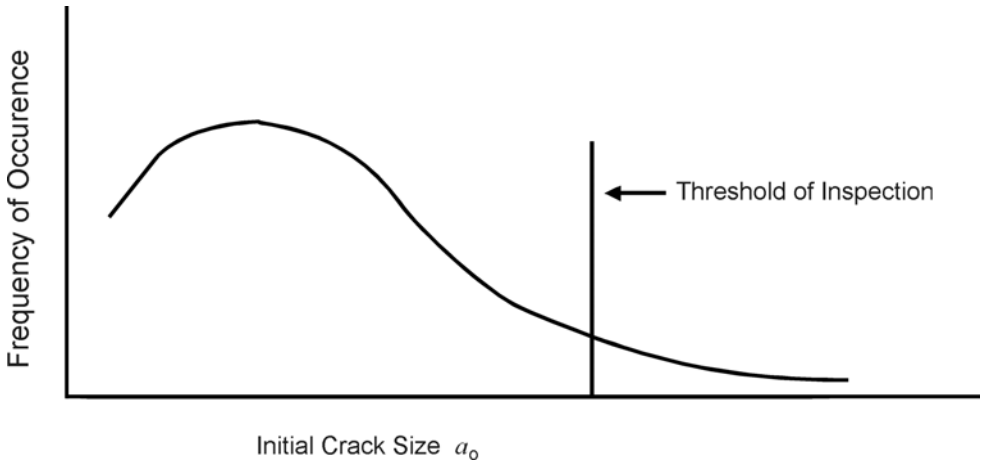

Figure 2.4.1. Distribution of Initial Crack Size for a Given Type of Crack (e.g., Radial Cracks Growing from Fastener Holes)

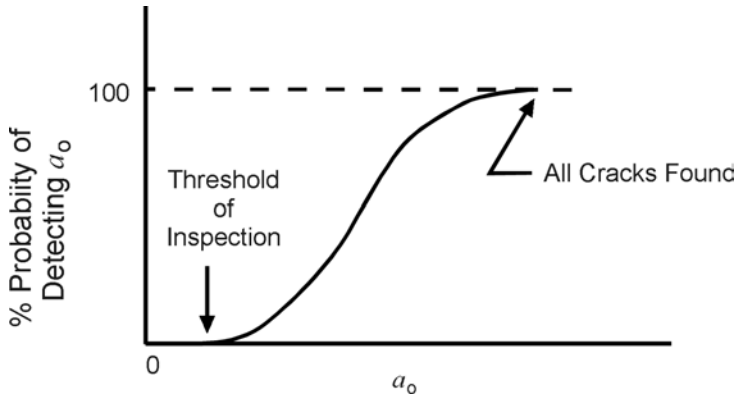

Figure 2.4.2. Certification of NDI Capability

Results generated by the F-4 Independent Review Team (IRT) provided a method of characterizing the initial flaw population (apparent initial quality) based on full-scale fatigue test-induced cracking behavior [Lozano, et al., 1974]. Given the measurable flaw distribution in a structure at some time subsequent to test startup, the initial flaw population can be backtracked by analysis. The "back" extrapolation of the flaw population is conducted using the damage integration package. The process is schematically illustrated in Figure 2.4.3. Subsequently, the initial flaw distribution established as illustrated in Figure 2.4.3 can be used to estimate influence of load factors, mission profiles, and usage changes on the life of service hardware. The F-4 IRT study also provided an evaluation of statistical methods for describing the large crack length extremes for initial flaw distributions established in this manner. The resulting distribution of F-4 initial cracks is shown in Figure 2.4.4 [Lozano, et al., 1974; Pinchert, 1976].

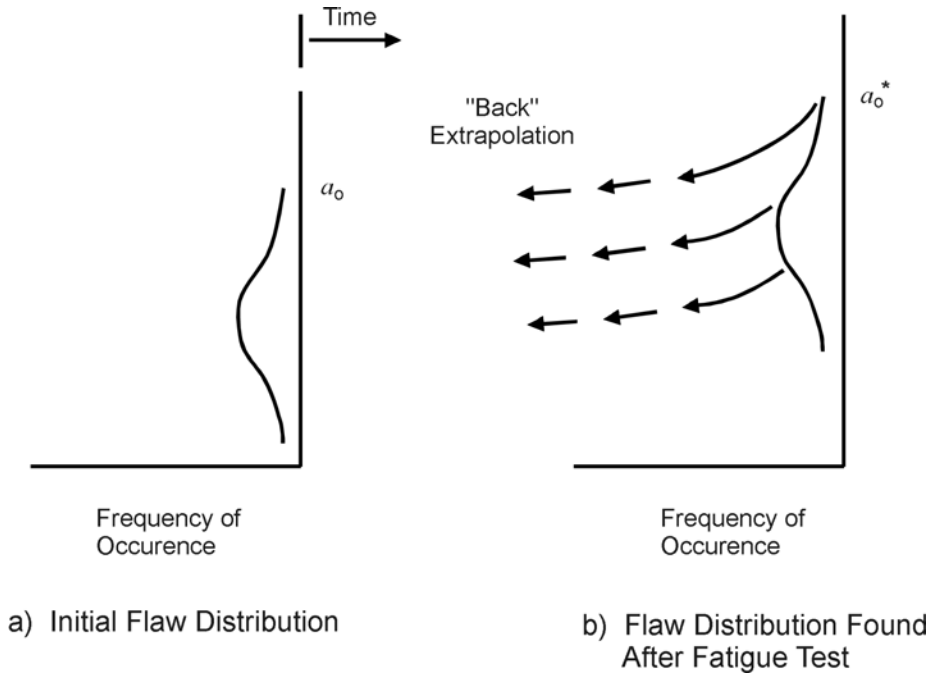

Figure 2.4.3. Determining Initial Quality by Back Calculation

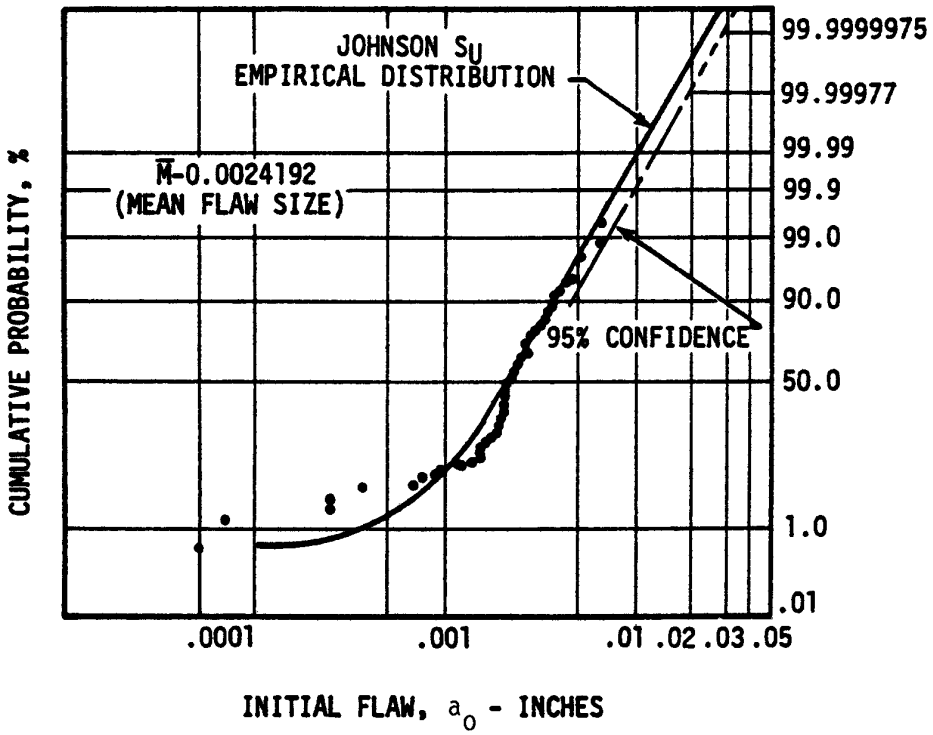

Figure 2.4.4. Initial Flaw Distribution for F-4 Based on Back Calculation

2.4.2 Usage

The sum of the load levels that a structure is expected to experience is determined by a projection of the amount of usage expected over the life in the various possible missions; e.g., hours in training, air-to-air combat, reconnaissance, weapons delivery, etc. The mission mix includes the relative amounts of time spent in each mission. The most basic information needed is the load factor exceedances at the center of gravity (CG) of the aircraft. This information is illustrated in Figure 2.4.5. For new designs, this data is derived from actual measured exceedances from operational aircraft flying similar missions. The USAF specifications contain such data. The Air Force Guidelines Handbook for developing Load/Environmental Design Spectra [Giessler, et al., 1981] summarizes the techniques that are currently being utilized to develop the loading and environmental spectra based on these data for various types of structures.

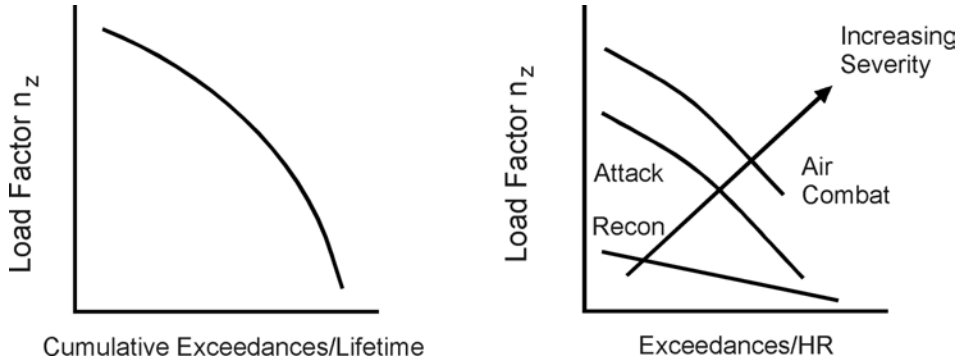

Figure 2.4.5. Typical Load Factor Exceedance Information Indicating Usage

The specific sequence of loads applied to the structure is necessary to the crack growth damage accumulation analysis. Current practice is to simulate the overall life on a flight-by-flight basis. Each flight in the design, analysis, or test load spectrum consists of a series of cycles that combine the deterministic and probabilistic events describing the type of mission. The deterministic events include takeoff and landing, and certain basic maneuver loads during each flight. Probabilistic events such as gusts or rough field taxiing occur periodically. Although it is possible to estimate the number of times these events occur, their position in the load sequences is determined in a probabilistic manner.

In developing the load spectrum for crack growth damage analysis, it is necessary to determine the stress history for each critical area on the airframe. This is accomplished by determining the relationship between the load history derived above and the stress response. Figure 2.4.6 schematically illustrates the load factor to stress history transformation.

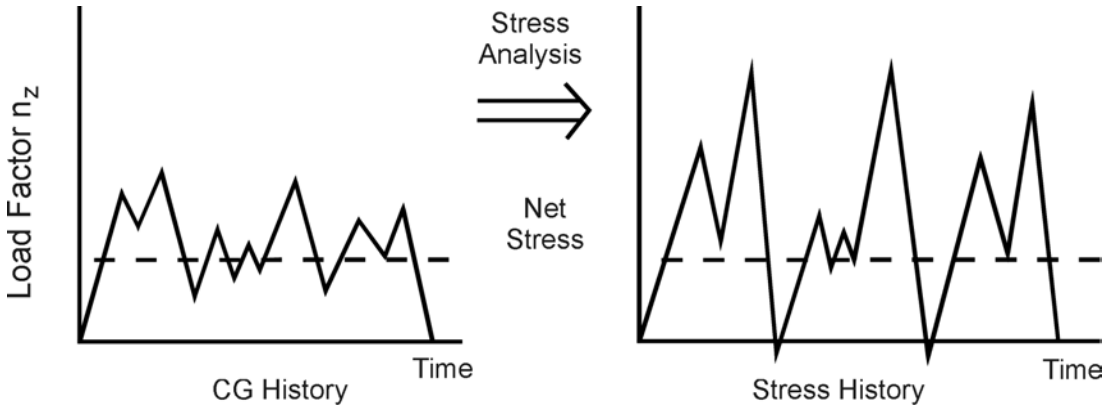

Figure 2.4.6. Load Factor to Stress History Transformation

Differences in crack growth resulting from mission mix can be significant. A fighter aircraft that is used primarily for air-combat or air-combat training typically accumulates more damage than one that is used for the same number of hours on a reconnaissance-type mission.

2.4.3 Material Properties

The material properties enter the damage integration package in the form of constant amplitude crack growth rate data. Crack growth data are generated in the laboratory under constant cyclic loading on simple specimens with accepted characterizing stress intensity factors. Crack growth rate data are developed and correlated on the basis of growth rate (*da/dN*) as a function of stress intensity factor range, ΔK, ($\Delta K = K_{max} - K_{min}$), as defined in Figure 2.4.7. The ASTM defines $K_{min} = 0$ and thus $\Delta K = K_{max}$ whenever $R < 0$ ($R = \sigma_{min}/\sigma_{max}$); see Section 5.1 for additional discussion.

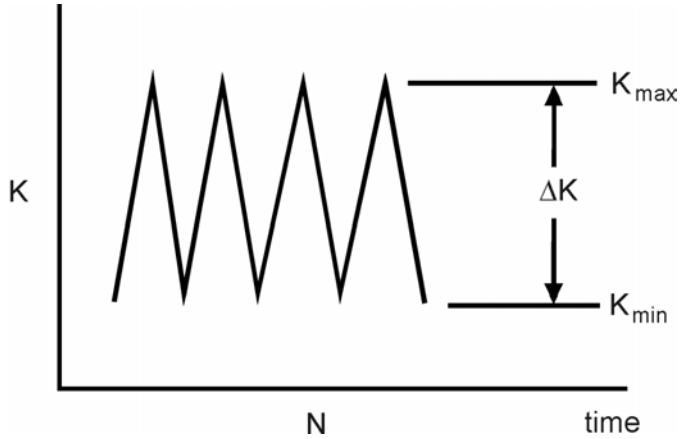

Figure 2.4.7. Stress-Intensity Factors – Cyclic Loading

For a given ΔK, the crack growth rate increases with increasing stress ratio, R for $R > 0$. Hence, the constant amplitude crack growth rate properties for a given material or alloy consist of a family of curves as illustrated in Figure 2.4.8. The crack mechanics approach described in Section 2.2.1 considers that for a given ΔK, R combination, there is a *da/dN* that is independent

of geometry. Thus, the damage integration package has available a growth rate for each ΔK determined for the given crack configuration and loading.

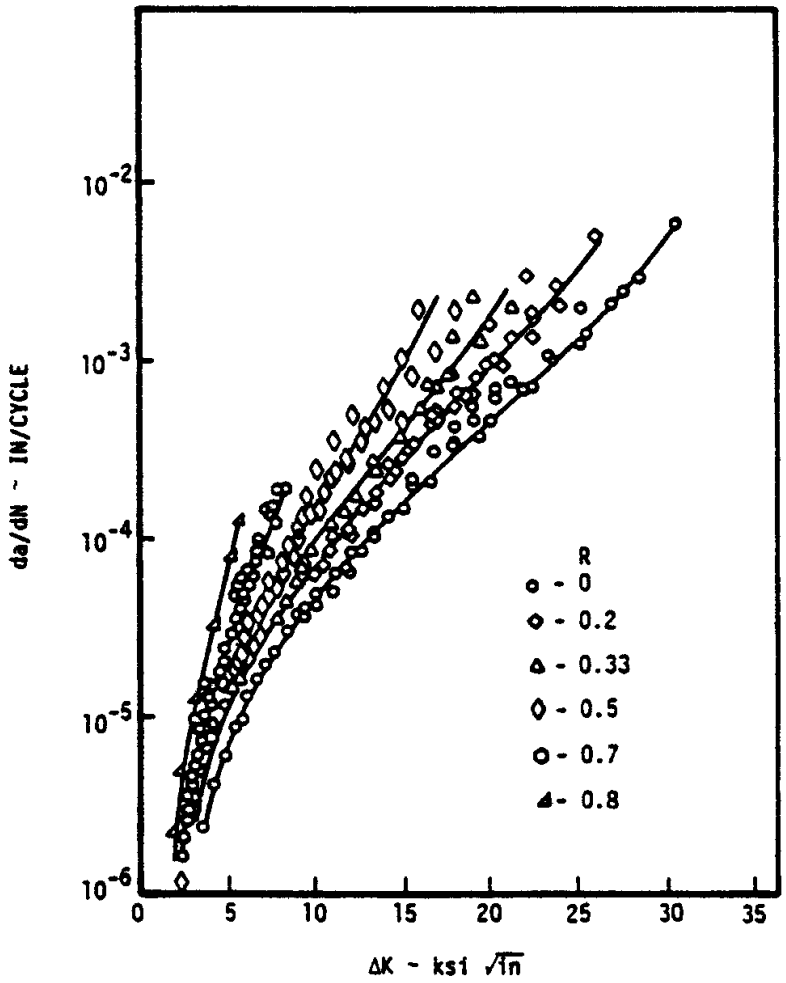

Figure 2.4.8. Constant Amplitude Crack Growth Rate Data for 7075-T6 Aluminum.

When necessary, thermal or chemical environment and time (frequency of loading) effects are also included in the crack growth rate data generated for use with the damage integration package.

Section 7 presents a summary of the currently available procedures and techniques which are used to establish crack growth rate data.

2.4.4 Crack Tip Stress Intensity Factor Analysis

The crack tip stress intensity factor (K) interrelates the crack geometry, the structural geometry, and the load on the structure with the local stresses in the region of the crack tip. The stress intensity factor takes the form

$$K = \beta\sigma\sqrt{\pi a} \tag{2.4.2}$$

where

β - geometric term for structural configuration, can be a function of crack length

σ - stress applied to the structure

a - crack length

It can be seen that any number of combinations of the parameters β, a, and σ can given rise to the same K. The crack growth analysis rests on the experimentally verified proposition that a given K gives rise to a certain crack growth rate, regardless of the way in which the parameters were combined to generate that K.

A considerable body of data exists which defines experimental and mathematical solutions for stress intensity factors for various structural configurations. A review of the procedures for obtaining stress intensity factors is covered, and the K solutions for a number of practical structural geometries are presented in Section 11.

Since stress enters Equation 2.4.2 in a linear sense it is appropriate to express the geometrical part of the stress intensity factor by using the stress intensity factor coefficient, K/σ. Figure 2.4.9 illustrates two typical solutions expressed in this manner. For a through-the-thickness crack in a plate of infinite extent, the value of β is unity and K becomes

$$K = \sigma\sqrt{\pi a} \qquad (2.4.2a)$$

Equation 2.4.2a provides one way of normalizing more complex K solutions in terms of the infinite plate solution. Figure 2.4.10 depicts a typical solution of this type.

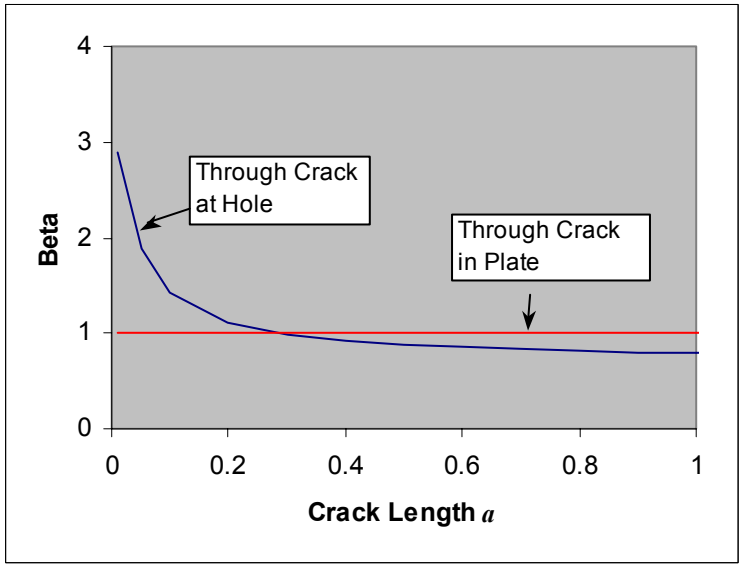

Figure 2.4.9. Stress-Intensity-Factor Coefficients Showing Influence of Hole on K

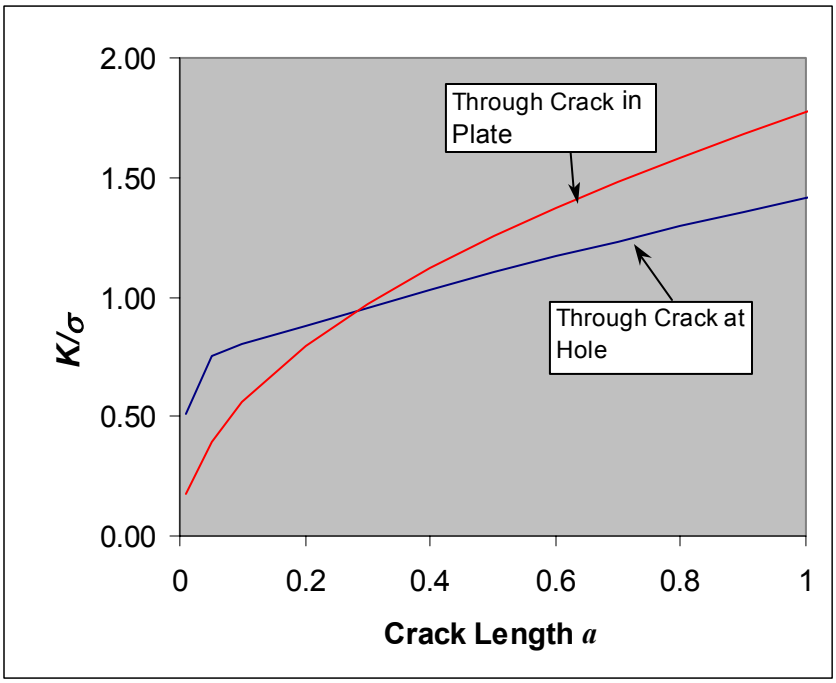

Figure 2.4.10. Influence of Hole on Geometric Correction Factor

Through-the-thickness cracks are handled quite well analytically. However, for corner cracks and semi-elliptical part-through cracks, such as illustrated in Figure 2.4.11, K varies from point to point around the crack perimeter. This variation allows the crack shape to change as it grows, which leads to a complex three-dimensional problem. The determination of β and K/σ for these complex cases have received a substantial amount of attention (see Section 11).

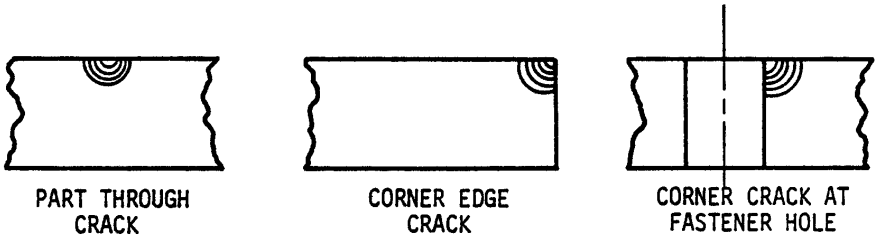

Figure 2.4.11. Complex Crack Geometries

2.4.5 Damage Integration Models

Rewriting Equation 2.4.1 such that the integration is conducted between the initial crack length (a_o) and any intermediate crack length (a_K) between a_o and the critical crack length results in

$$a_K = a_o + \sum_{j=1}^{t} \Delta a_j \qquad (2.4.3)$$

where $t(N)$ is the elapsed time (number of load cycles) corresponding to growing the crack a_o to the intermediate crack length a_K. The next cycle of the applied stress (the $N+1$ cycle) induces a

crack length growth increment Δa_{N+1}. The damage integration model provides the analysis capability to determine this crack length growth increment. The growth increment Δa_{N+1} is equated to the constant amplitude crack growth rate, which in turn is determined from a function of stress intensity factor range (ΔK) and stress ratio (R), i.e.,

$$\Delta a_{N+1} = \frac{da}{dN}\Big|_{N+1} = f(\Delta K_{N+1}, R_{N+1}) \qquad (2.4.4)$$

The stress intensity factor range and stress ratio in Equation 2.4.4 are determined by using the maximum and minimum stresses in the N+1 cycle of the given stress history and evaluating the stress intensity factor coefficients associated with the given structural geometry at the crack length a_K. Subsequent to the direct calculation of the two crack tip parameters ΔK and R, and prior to their insertion in Equation 2.4.4, ΔK and R are modified to account for the effect of prior load history using retardation models. Retardation models account for high-to-low load interaction effects, i.e., the phenomena whereby the growth of a crack is slowed by application of a high load in the spectrum. Failure to account for high-to-low load interaction via a retardation model leads to conservative (~2 to 5 times shorter) life.

There are numerous functional forms of Equation 2.4.4 and numerous models describing retardation. The following list describe the general scheme of the crack growth calculation.

Step 1 - Knowing crack length a_K, determines the stress intensity factor coefficient, K/σ.

Step 2 - For the given stress cycle, $\Delta\sigma$, and the coefficient K/σ, determine the stress intensity factor cycle, ΔK, and stress ratio R.

Step 3 - Utilizing the retardation model, modify the stress-intensity cycle ΔK and R to account for previous load history.

Step 4 - Determine the growth rate for the stress-intensity factor cycle to establish the crack growth increment.

Section 5 provides a current state-of-the-art summary of the procedures and techniques that are used in damage integration models.

2.4.6 Failure Criteria

The interrelationship between critical crack length, loading, and residual strength of a structure was first discussed in Section 2.2 using Figure 2.2.3. Based on the information presented in Section 2.3.1, the residual strength (σ_{res}), the load-carrying capacity of the cracked structure, can be shown to monotonically* decrease with increasing crack length in the following manner:

$$\sigma_{res} = K_c/f(a) \qquad (2.4.5)$$

where

K_c = the material resistance to fracture, termed fracture toughness, and

$f(a) = \beta(a)\sqrt{\pi a}$, the structural property, termed the stress intensity factor coefficient.

* monotonic implies that the rate of change does not change sign.

When the residual strength decays to the level of the maximum stress in the service load history, fracture of the structure occurs. The crack length associated with fracture (i.e., a_{cr}) is normally determined by solving Equation 2.4.5 for crack length, assuming that the residual strength equals the maximum stress in the stress history. Note that the rate of growth of a crack is directly related to the rate of loss of residual strength through Equation 2.4.5, thus justifying the selection of the crack to quantify structural fatigue damage.

The critical crack length (a_{cr}) is thus a function of material, structural geometry, and loading. As shown in Figure 2.4.12, the relative effect of a_{cr} on life is typically small (i.e., when $a_{cr}/a_o \geq 5$). The primary advantage of designing for a large critical crack length is the increased inspectability it provides. A large critical crack length increases the probability of locating the crack before it becomes critical, thereby enhancing aircraft safety.

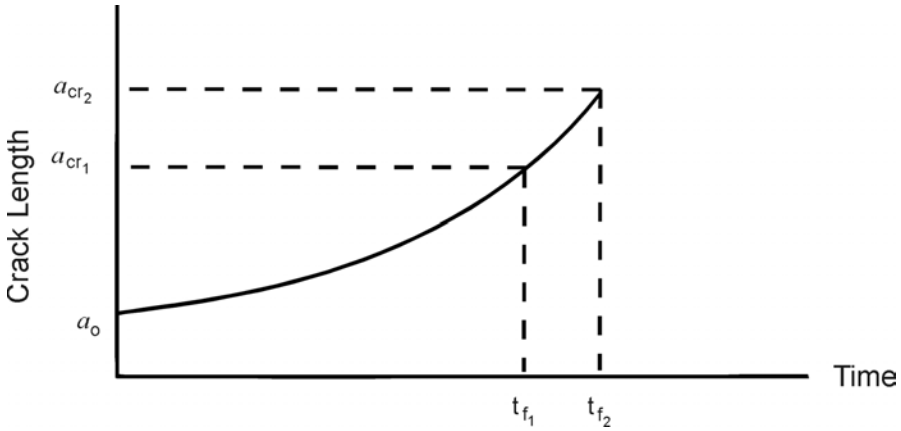

Figure 2.4.12. Effect of Critical Crack Size on Life

Determination of the critical crack size via Equation 2.4.5 would ordinarily be sufficient for safety limits; however, durability considerations often dictate that the final crack size, a_f, be chosen smaller than a_{cr} to represent rework of repair limits. A choice of a_f along these lines is shown in Figure 2.4.13.

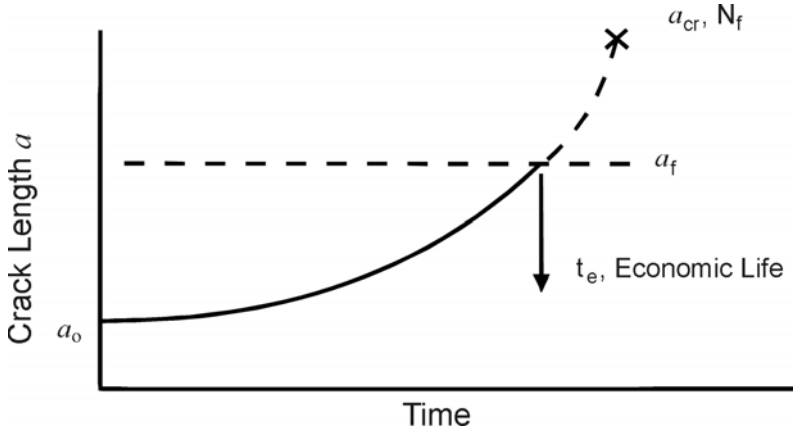

Figure 2.4.13. Economic Final Crack Size

Section 4 provides a summary of available residual strength estimating techniques and procedures that are generally applicable to all different types of structures and materials. Section

7 presents the experimental methods and procedures used to generate toughness data and residual strength data.

2.5 Deterministic Versus Probablistic Approaches

The ASIP design guidance of MIL-HDBK-1530 and JSSG-2006 is based on deterministic analyses. The growth of the largest, single flaw that might be in the most critical location of a structural element is predicted using a sequence of stresses from expected operational use of the aircraft. Maintenance actions for the element are conservatively scheduled from damage tolerance analyses of the predicted time for the flaw to grow to a critical size. This design philosophy has worked well. However, cracking scenarios can arise in an aging fleet that are not amenable to analyses based on the growth of a monolithic crack. For example, widespread fatigue damage can produce complex cracking scenarios in which the structural conditions of the elements in a load path are unknown and conservative assumptions would lead to unacceptable inspection intervals. In these scenarios, structural risk analyses are being used to assess the structural integrity of the load path.

In a probabilistic risk analysis, structural integrity is characterized in terms of the single flight probability of failure of the load path. This probabilistic evaluation of strength versus stress is dynamic since strength degrades as fatigue cracks in the load path grow and the condition of the structure might change during maintenance actions. In a risk analysis, the condition of the structure is modeled in terms of distributions of damage at the critical locations and fracture mechanics tools are used to predict the growth of the damage distributions as a function of flight hours. Probability of failure as a function of flight hours is calculated from the distribution of strength at time T and the expected distribution of stress that will be experienced at time *T*. Maintenance actions would be scheduled at intervals that provide an acceptably small failure probability. Lincoln [2000] has suggested that 10^{-7} is an acceptable upper bound on single flight failure probability for Air Force applications.

There are a number of approaches to defining and modeling the stochastic contributors to a probabilistic evaluation of a structure and for calculating the probability of failure. The simplest of models involves only the distributions of strength and stress. For two or three stochastic contributors in the model, the failure probability can be made using direct double or triple integration. If there are more than three random components, fracture probability must be calculated using a Monte Carlo simulation or a failure function (FORM/SORM) approach, [Madsen, 1987]. Examples of the use of risk analysis in airframe structures can be found in Lincoln [1997], Cochran, et al., [1991], and Berens, et al. [1998]. Examples of the use of probabilistic analyses in engine structures can be found in Yang and Chen [1985], Harris [1987], and Roth, [1992].

2.6 Computer Codes

2.6.1 Structural Analysis

FRANC2D/L is a highly interactive finite element program for the small deformation analysis of two-dimensional structures. As such, it is useful for engineering calculations or for instruction in finite element and fracture courses. Linear elastic fracture mechanics analyses can be performed with automatic remeshing as the crack grows. The layered capability allows the user to model riveted and adhesively bonded structures, such as lap joints and bonded repairs. Elastic-plastic material behavior is also available. This allows the user to model tearing with the critical crack tip opening angle approach. This provides the full capability of growing a fatigue crack and calculating residual (tearing) strength as a function of crack length.

FRANC2D/L is an extension of FRANC2D, which was originally written by Paul Wawrzynek at Cornell for the analysis of crack growth. A key concept in his work was the use of a winged-edge data structure to describe the geometry. This greatly facilitates automatic remeshing during crack growth.

2.6.2 Life Prediction

2.6.2.1 NASGRO Fracture Analysis Software

NASGRO Fracture Analysis Software is a suite of programs based on fracture mechanics principles. NASGRO can be used to analyze crack growth, perform assessments of structural life, compute stresses, and process and store fatigue crack growth properties. The package includes a large set of crack growth rate and fracture data.

NASGRO was originally developed at NASA Johnson Space Center to perform fracture control analysis on NASA space systems. Later, after the NASA/FAA/USAF Aging Aircraft Program was formed and began supporting the development effort, NASGRO was developed further for use in damage tolerance analysis of aircraft, including that required for FAA certification.

The software is comprised of the following three modules:

- NASFLA - Life Assessment
- NASBEM - 2-D Boundary Element
- NASMAT - Database of da/dN & fracture test results

NASFLA is part of the NASGRO 3.0 suite of programs Stress Intensity Factor -These are computed for the crack geometry and loading chosen from the NASFLA library of models, and displayed in tabular or graphical form.

NASBEM is part of the NASGRO 3.0 suite of programs. It is a two-dimensional boundary element program used to perform the following analyses:

- Stress Intensity Factors - These can be calculated for any geometry and loading. Tables of stress intensity factors and corresponding crack lengths can be generated for use by the NASFLA module in performing life assessments.
- Stress Fields - These can be calculated for any collection of points in the two-dimensional uncracked object being modeled including its boundary.

NASMAT is used to store, retrieve and curve fit crack growth and fracture toughness data. It has a database containing over 9000 sets of data. This includes over 3000 sets of fatigue crack growth data and over 6000 fracture toughness data points. These data can be searched, plotted, and fitted to either the NASGRO crack growth rate equation or a user specified growth rate equation, or they can be entered into a growth rate table.

Additional information on the NASGRO software can be found at:

http://nasgro.swri.edu

2.6.2.2 AFGROW Fracture Analysis Software

Additional information on theAFGROW software can be found at:

http://fibec.flight.wpafb.af.mil/fibec/afgrow.html

2.6.2.3 Cracks2000 Structural Integrity Software

The CRACKS2000 program is based on the Linear Elastic Fracture Mechanics (LEFM) approach for estimating the fatigue life of a component with a crack. The LEFM approach uses the stress intensity factor parameter, as the driving factor for crack growth. The Cracks2000 program has considerable flexibility in the analytical modeling of crack growth analysis problems.

The program can solve both constant amplitude and variable amplitude crack growth analysis problems, with the user choosing the stress intensity factor, the type of loading spectrum, the type of retardation model, and the type of crack growth rate behavior description.

Cracks2000 has fifty-one stress intensity factors solutions. There are closed form equations for stress intensity factor solutions for 25 geometries. Many of these solutions are the early Newman-Raju solutions, which are retained for comparisons with older analysis. For the latest stress intensity factor solutions, tables of β-factors are generated from the equations; the tables are used for the life analysis, and can be printed and plotted for β-factors comparison

Additional information on the Cracks2000 software can be found at:

http://www.udri.udayton.edu/cracks/

or contact

Ms. Peggy C. Miedlar
University of Dayton Research Institute
300 College Park
Dayton, Ohio 45469-0120

Phone: (937) 229-4417

email: miedlar@udri.udayton.edu

2.6.3 Risk/Probability

PRobability Of Fracture (PROF)

PROF is a computer program that was specifically written to interface with the data that are available as a result of ASIP. PROF runs in the Windows environment using an Excel spreadsheet interface with ASCII data files and two C^{++} calculation modules. The two calculation modules estimate the probability of failure as a function of flight hours due to either fatigue crack growth at a stress riser and the probability of failure due to discrete source damage in a load path.

The PROF input requirements for estimating failure probability due to fatigue crack growth are:

- crack growth versus flight hours (a versus T) for the expected stress sequences;
- a versus K/σ at the stress riser;
- distribution of critical stress intensity factors at the stress riser;
- distribution of maximum stress per flight experienced at the stress riser;
- distribution of crack sizes at the stress riser;
- probability of detection as a function of crack size, POD(a), function for the inspection system used at inspections;
- distribution of equivalent crack sizes at repaired stress risers; and
- flight hour intervals between inspections.

PROF projects the crack size distribution using the a versus T relation from the deterministic damage tolerance analysis of ASIP. At an inspection, PROF changes the distribution of crack sizes in accordance with the POD(a) function and the equivalent repair crack sizes. The post-inspection/repair crack size distribution is then projected for the next usage interval. Single flight probability of failure is calculated using the Irwin abrupt fracture criterion. That is, the failure probability is calculated as the probability that the maximum stress intensity factor (combination of the distributions of maximum stress per flight and crack sizes) during the flight exceeds the critical stress intensity factor. This probability is obtained from a triple integration over input distributions.

For failure probability due to discrete source damage, PROF requires the additional input of residual strength as a function of crack size in the remaining critical elements of the load path. The residual strength characterization replaces the stress intensity factor input. PROF again grows the crack size distributions with modifications, as necessary, at inspections. Single flight failure probability is calculated from the distribution of maximum stress per flight, crack size distribution at the critical element and residual strength as a function of crack size. This probability is obtained from a double integration over input distributions.

The output of PROF is stored in an Excel workbook and provides both the single flight failure probability as a function of flight hours and the crack size distributions before and after an inspection. The availability of the crack size distributions permits changing the analysis due to known changes in usage. Further, multiple runs of PROF permit analyzing more complex scenarios such as multiple element damage. See Sample Problems UDRI-2, UDRI-3 and UDRI-4

for examples of the use of PROF for risk analysis of discrete source damage, multiple element damage and corrosion damage scenarios, respectively.

PROF is proprietary to the University of Dayton but is freely available for United States government applications. PROF can be obtained for United States government applications from

Mr. David Banaszak
AFRL/VASM
Wright-Patterson Air Force Base, Ohio 45433

Phone: (937) 255-6104

email: David.Banaszak@wpafb.af.mil

For applications not directly related to the United States government, a license for the use of PROF can be arranged. Contact

Dr. Alan Berens
University of Dayton Research Institute
300 College Park
Dayton, Ohio 45469-0120

Phone: (937) 229-4417

email: berens@udri.udayton.edu

DARWIN

Design Assessment of Reliability WIth INspection (DARWIN) is a risk analysis program for calculating the probability of failure in turbine engine disks. With a graphical user interface for problem setup and output, DARWIN integrates finite element analysis, fracture mechanics, non-destructive inspection, random defect occurrence and location, and other random variables to assess the risks of rotor fracture. Risk calculations incorporate both Monte Carlo and failure function/fast integration methods.

See www.darwin.swri.org

2.7 Achieving Confidence In The Life Prediction Methodology

As discussed in Section 2.4, airframe life predictions are based on a crack growth damage package that interrelates the following six elements: a) initial flaw distributions, b) aircraft usage, c) basic crack growth material properties, d) crack/structural properties, e) damage model, and f) fracture or life limiting criteria.

Since life predictions for service hardware are based on the crack growth damage integration package, the confidence in a life prediction value must be based on a measure of the ability for a given package to predict measured phenomena. To support evaluation of the damage integration package, laboratory tests are conducted which simulate the basic features of cracked hardware. Predictions are then compared to measured crack growth behavior. The confidence normally associated with life predictions using a damage integration package is derived from the ability of the package to predict the laboratory generated crack growth behavior.

Verification of the package is normally conducted in steps progressing from predictions of laboratory-generated fatigue crack growth data (for which all test conditions are reasonably well characterized and documented) to predictions of service-experienced cracking behavior. Verifying the package in steps allows for immediate deletion of inaccurate or erroneous assumptions made in developing or improving a given element of the package. Since the package will be used to make life predictions where unknowns (e.g. spectra, structural load interactions) prevail, it is essential that confidence be established for each level of prediction capability that has been achieved.

A change of any fundamental element within the package (e.g., retardation model) generally requires a resubstantiation of this confidence for the revised package. An extension of capability, i.e., more complex geometry, would require only a substantiation for that level of complexity. This approach must be taken because of the substantiated influence of each of the variables associated with the individual elements.

Only when cracking is evident from service inspections can there be the necessary information to verify that the damage integration package is performing satisfactorily. The difficulty of assessing the confidence level associated with the life prediction derived from the damage integration package results from extrapolating the use of the package from a simple data base to the more complex service hardware case.

Figures 2.7.1 through 2.7.3 are provided as examples to show how elements within a package are verified. All figures show the correlation between predicted and measured life. Figure 2.7.1 provides an evaluation of a new retardation model in which the database was a measure of the cyclic delay subsequent to an overload. Figure 2.7.2 compares the predictions developed with the AFWAL-Willenborg-retardation model (damage integration package to laboratory test data) which show the influences of spectra and crack geometry changes. Figure 2.7.3 shows the evaluation of a AFWAL modified damage integration package which accounts specifically for C-5A spectra changes on life observed when the crack geometry is a radial corner crack growing from an open or plugged hole.

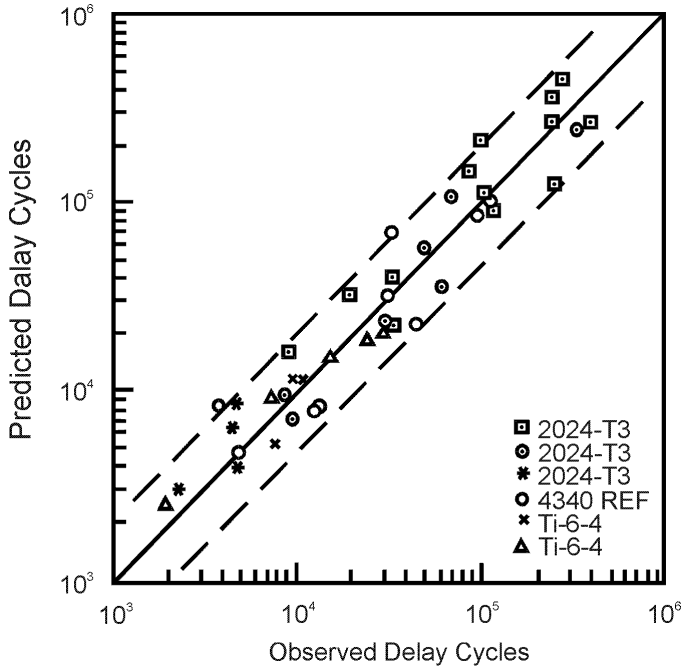

Figure 2.7.1. Single Overload Correlation with Modified Wheeler Retardation Model

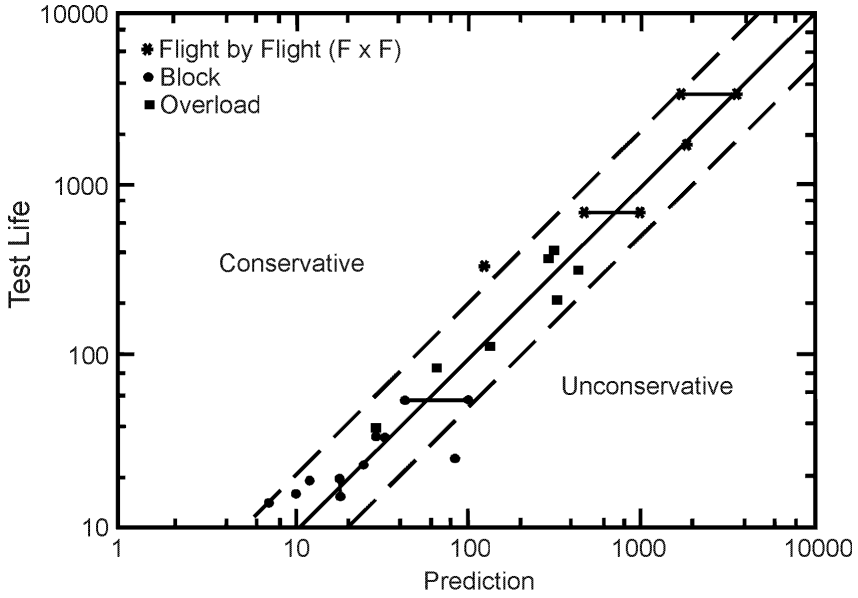

Figure 2.7.2. Spectrum Correlation Using the AFWAL Willenborg-Retardation-Model (Damage Integration Package)

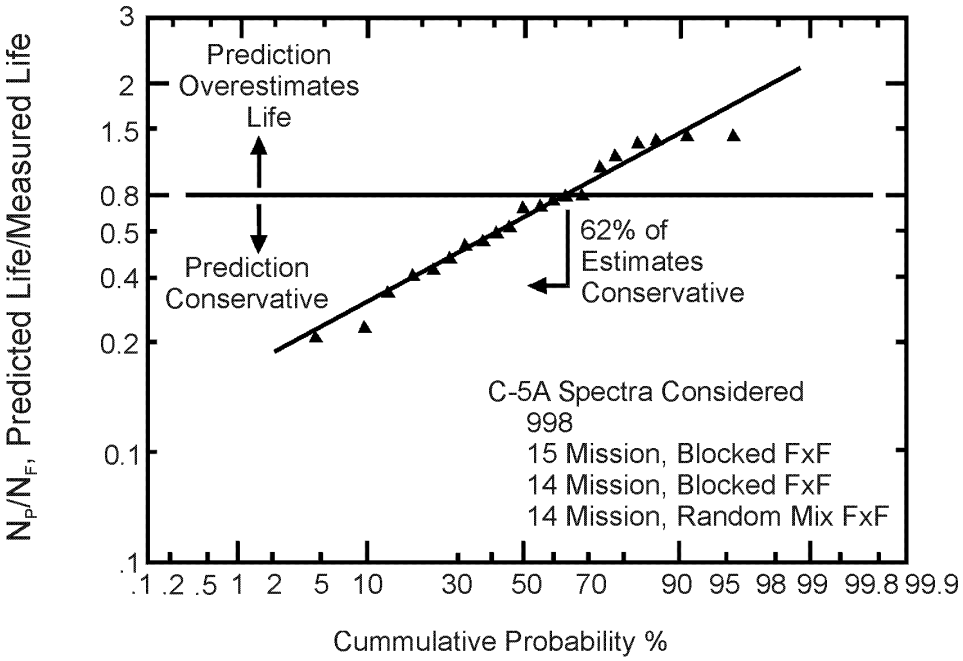

Figure 2.7.3. Prediction Capability of Damage Integration Package (Based on 21 Laboratory Tests Conducted at AFWAL/FIB)

2.8 References

W.E. Anderson and L.E. James (1970, April). "Estimating Cracking Behavior of Metallic Structure". *Journal of the Structural Division, Proceedings, American Society of Civil Engineers,* (Vol. 98), *No. 4*, p. 773. See Rice, 1968 in Section 4.

J. A. Begley and J. D. Landes (1972). "The J-Integral As a Fracture Criterion". *Fracture Toughness,* ASTM STP 514, pp. 1-20.

Boeing Co. (1962, June). "Fracture Resistance Data Summary," D2-20947.

C.Q. Bowles (1970). "Strain Distribution and Deformation at the Crack Tip in Low Cycle Fatigue". AMMRC-CR-70-23, Army Material and Mechanical Research Center, Waterown, MA.

R.J. Bucci, P.C. Paris, J.D. Landes, and J.R. Rice (1972). "J-Integral Estimation Procedures". *Fracture Toughness,* ASTM STP 514, pp. 40-69.

F.M. Burdekin and D.E.W. Stone (1966). "The Crack-Opening-Displacement Approach to Fracture Mechanics in Yielding". *Journal of Strain Analysis,* pp. 145-153.

D.R. Donaldson and W.E. Anderson (1961, September). "Crack Propagation Behavior of Some Airframe", p. 375.

D.S. Dugdale (1960). "Yielding of Steel Sheets Containing Slits". *Journal of Mechanics and Physics of Solids* (Vol. 8), pp. 100-104.

F.J. Giessler, S.J. Duell, and R.F. Cook. (1981, February). *Handbook of Guidelines for the Development of Design Usage and Environmental Sequences for United States Air Force Aircraft*. AFWAL-TR-80-3156.

A.A. Griffith (1921). "The Phenomena of Rupture and Flow in Solids". *Phil. Trans. Roy. Soc. London, A221*, pp. 163-197.

G.T. Hahn and A.R. Rosenfield (1965). "Local Yielding and Extension of a Crack Under Plane Stress". *Acta Metallurgical* (Vol. 13, No. 3), p. 293.

D.J. Hayes (1970). "Some Applications of Elastic-Plastic Analysis to Fracture Mechanics". Ph.D. Thesis, Imperial College.

J.W. Hutchinson (1968). "Plastic Stress and Strain Fields at the Crack Tip". *Journal of Mechanics and Physics of Solids*, pp. 13-31; pp. 337-347.

A.A. Ilyushin (1946). "The Theory of Small Elastic-Plastic Deformations". *Prikadnaia Matematika.* P.M.M. (Vol. 13), p. 347.

G.R. Irwin (1948). "Fracture Dynamics". *Fracturing of Metals*. ASM, pp. 147-166.

G.R. Irwin and J.A. Kies (1954). "Critical Energy Rate Analysis of Fracture Strength". *Welding Journal* (Research Supplement, Vol. 33), p. 193s.

G.R. Irwin (1957). "Analysis of Stresses and Strains Near the End of a Crack Traversing a Plate". Trans. ASME, *Journal of Applied Mechanics* (Vol. 24), p. 361.

G.R. Irwin, J.A. Kies, and H.L. Smith (1958). "Fracture Strengths Relative to Onset and Arrest of Crack Propagation". *Proceedings ASTM* (Vol. 58), p. 640.

G.R. Irwin (1960). “Fracture Mechanics”. *Structural Mechanics*. J. N. Goodier and N. J. Hoff (Eds.). Pergamon Press, pp. 557-594.

V. Kumar, M.D. German, and C.F. Shih (1980). “Estimation Technique for the Prediction of Elastic-Plastic Fracture of Structural Components of Nuclear Systems”. Combined Second and Third Semiannual Report, Feb. 1979 to Jan. 1980 for EPRI, General Electric Company, SRD-80-094.

V. Kumar, M.D. German, and C.F. Shih (1981, July). “An Engineering Approach for Elastic-Plastic Fracture Analysis”. EPRI-NP-1931, Electric Power Research Institute.

J.D. Landes, J.A. Begley, and G.A. Clarke (Eds.) (1979). *Elastic-Plastic Fracture*. ASTM STP 668.

R.J. Lozano, G.S. Parker, and R.J. Werdes, (1974, June). “F-4 Fatigue and Damage Tolerance Assessment Program – Vol. 1”. MCAIR MDC A2883, McDonnell Douglas, St. Louis, Missouri.

E. Orowan (1949). “Fracture and Strength of Solids”. *Rep. Prog. Physics* (Vol. 12), pp. 185-232.

P.C. Paris (1960, March). “A Short Course in Fracture Mechanics”. The Boeing Airplane Company.

P.C. Paris, M.P. Gomez, and W.E. Anderson (1961, January). “A Rational Analytic Theory of Fatigue”. *The Trend in Engineering*. University of Washington (Vol. 13, No. 1), p. 9.

P.C. Paris (1964). “The Fracture Mechanics Approach to Fatigue”. *Fatigue and Interdisciplinary Approach*. Proceedings, Tenth Sagamore Conference, Syracuse, N.Y.: Syracuse University Press, p. 107.

P.C. Paris (Ed.) (1980), *Fracture Mechanics: Twelfth Conference*. ASTM STP 700.

R.E. Pinchert (1976, September). “Damage Tolerant Assessment of F-4 Aircraft”. Presented at the American Institute of Aeronautic and Astronautics Aircraft Systems and Technology Meeting, Dallas, Texas.

J.R. Rice (1968a). “Mathematical Analysis in the Mechanics of Fracture”. H. Liebowitz (Ed.). *Fracture* (Vol. II). New York: Academic Press, pp. 191-308.

J.R. Rice (1968b). “A Path Independent Integral and the Approximate Analyses of Strain Concentration by Notches and Cracks”. *Journal of Applied Mechanics*. ASME, 35, pp. 379-386.

J.R. Rice and G. F. Rosengren (1968). “Plane Strain Deformation Near a Crack Tip in Power-Law Hardening Material”. *Journal of Mechanics and Physics of Solids*, pp. 1-12.

J.R. Rice and D. M. Tracey (1973). “Computational Fracture Mechanics”. *Numerical and Computer Methods in Structural Mechanics.* S.J. Fenves, et al. (Eds.). Academic Press, N.Y., pp. 585-623.

J.N. Roberson and A.S. Tetelman (1973). “The Critical Crack-Tip Opening Displacement and Microscopic and Macroscopic Fracture Criteria for Metals”. UCLA RE 7360. University of California, Los Angeles, CA.

R. Roberts (Ed.) (1981), *Fracture Mechanics: Thirthteenth Conference.* ASTM STP 743.

C.F. Shih (1976). "J-Integral Estimates for Strain Hardening Materials in Antiplane Shear Using Fully Plastic Solutions". *Mechanics of Crack Growth*. ASTM STP 590, pp. 3-22.

C.F. Shih and J.S. Hutchinson (1976). "Fully Plastic Solutions and Large Scale Yielding Estimates for Plane Stress Crack Programs". *Journal of Engineering and Materials and Technology* (Vol. 98), pp. 289-295.

C.F. Shih (1979, April). "Relationship Between the J-Integral and the Crack Opening Displacement for Stationary and Extending Cracks". General Electric Co. TIS Report No. 79CRDO75.

C.F. Shih and V. Kumar (1979, June). "Estimation Techniques for the Prediction of Elastic-Plastic Fracture of Structural Components of Nuclear Systems". First Semiannual Report, July 1978-January 1979 for EPRI Contract RP 1237-1, General Electric Co., Schenectady, N.Y.

I.N. Sneddon and M.Lowengrub, (1969). *Crack Problems in the Classical Theory of Elasticity*. New York: John Wiley and Sons, Inc.

R. Verette and D.P. Wilhem (1973, May). "Development & Evaluation of Methods of Plane Stress Fracture Analysis". *Review and Evaluation of Structural Residual Strength Prediction Techniques*. AFFDL-TR-73-42.

T. Weerasooriya and J.P. Gallagher (1981, July). "Determining Crack Tip Field Parameters for Elastic-Plastic Materials via an Estimation Scheme". AFWAL-TR-81-4044. Air Force Wright Aeronautical Laboratories.

A.A. Wells (1961, September). "Unstable Crack Propagation in Metals-Cleavage and Fast Fracture". *Proceedings of the Cranfield Crack Propagation Symposium, 1*, pp. 210-230.

M.L. Williams (1957). "Stress Distribution at the Base of a Stationary Crack". Trans. ASME, *Journal of Applied Mechanics* (Vol. 24), p. 109.

Section 3
Damage Size Characterizations

The damage tolerance approach to structural integrity assumes that cracks are present in all critical locations and demonstrates that these cracks will not grow undetected to a critical length during a period of service usage. Since the rate of crack growth depends on the crack length, the structural service lives or periods between inspections are greatly influenced by the crack lengths assumed at the beginning of a usage period. From the safety viewpoint, these initial crack lengths must be longer than any equivalent damage that could be present in the structure after passing quality inspections. From a practical viewpoint, however, the degree of conservatism introduced by assuming long cracks must be limited to reach realistic usage lives or periods of operation without inspections. This trade-off results in great emphasis being placed on quantifying the damage sizes that may be present in the structure at the beginning of an operational period.

The distribution of crack lengths in any given structure can be considered to consist of the composite of the several distributions shown in Figure 3.0.1. The material as received from the vendor will contain very small flaws or defects such as inclusions, cracks, porosity and surface pits, scratches, and machine marks. These inherent material flaws are considerably below the detection capability of the non-destructive inspection (NDI) and should be sufficiently small to not grow appreciably in service. These small flaws form the basis of the continuing damage crack size assumption and are characterized by a single crack length, a_i, which is assumed to be an upper bound on the distribution.

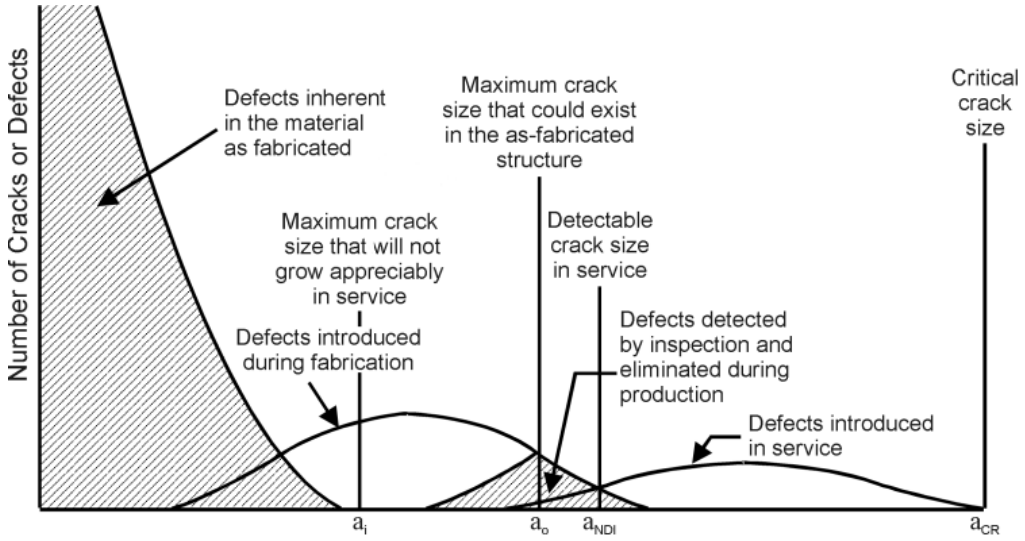

Figure 3.0.1. The Effect of Defects Distribution in Structural Integrity Planning [Walker, et al., 1979]

A distribution of larger defects can exist as a result of the fabrication process or as large inherent flaws. The production quality control process is designed to detect and eliminate as many of these cracks as possible but those which are not detected will propagate due to fatigue mechanisms during service. The largest crack size that could remain undetected in the newly fabricated structure after the final inspection is designated as a_o. This crack length provides the starting

point for crack growth projections which demonstrate adequate service life or the necessity for an in-service inspection.

Cracks smaller than a_o will propagate in service operations and others, due to fatigue crack initiation, corrosion, and foreign object damage, will be initiated. If any of these cracks can propagate to critical size, a_{cr}, before the end of the service life, they must be detected and repaired at scheduled maintenance intervals. The largest crack size that can remain undetected after an inspection is designated as a_{NDI} and becomes the initial crack size for the next usage period. Figure 3.0.2 is a schematic of the projected crack growth of the critical crack lengths and illustrates the resetting of the potential crack to a_{NDI} after the inspection. In this figure, the inspection was scheduled at one-half the usage time required for an initial crack (a_o or a_{NDI}) to grow to critical.

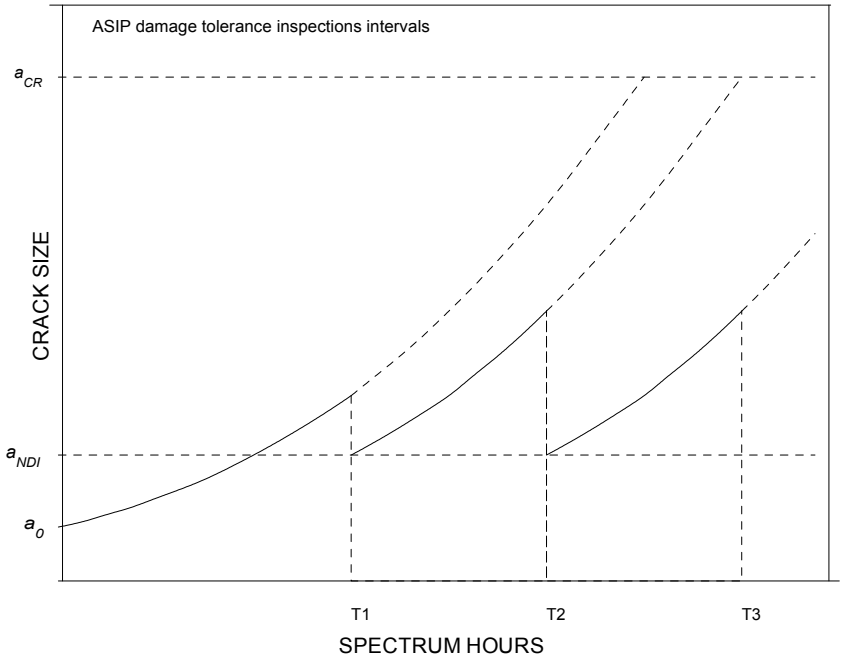

Figure 3.0.2. Crack Growth-Life Curve after Second Inspection

JSSG-2006 specifies the type and size of cracks that must be assumed during design. These are summarized in Section 1.3.4. The assumed crack sizes depend on:

1) the design concept (slow crack growth or fail safe);
2) inspectability level (inspectable or non-inspectable) with and without component removal; and
3) continuing damage after initial primary damage.

In the current version of the Specification Guide, smaller initial crack sizes (a_o) may be assumed for slow crack growth structures based on the contractors demonstrated capability to eliminate all cracks greater than the smaller value. This demonstration may be based on an NDI system or on a proof test. These qualification processes are shown schematically in Figure 3.0.3(a) and 3.0.3(b).

The continuing damage crack size assumption can also be reduced if the contractor can demonstrate an improved manufacturing quality. One method for such a demonstration is based

on the determination of the distribution of equivalent initial flaws as shown schematically in Figure 3.0.3(c).

Since NDI, proof testing, and the equivalent initial quality method can be applied under the current airplane damage tolerance requirements and may receive greater emphasis in future specifications, they are reviewed in the following subsections. Section 3.1 describes the major NDI methods currently in use and discusses statistically based demonstrations program for measuring NDI capability. Sections 3.2 and 3.3 describe and give examples of the proof test and equivalent initial quality methods, respectively.

a) Inspection:
NDE Demonstration

b) Structure:
Proof Test

c) Manufacturing:
Equivalent Initial
Quality

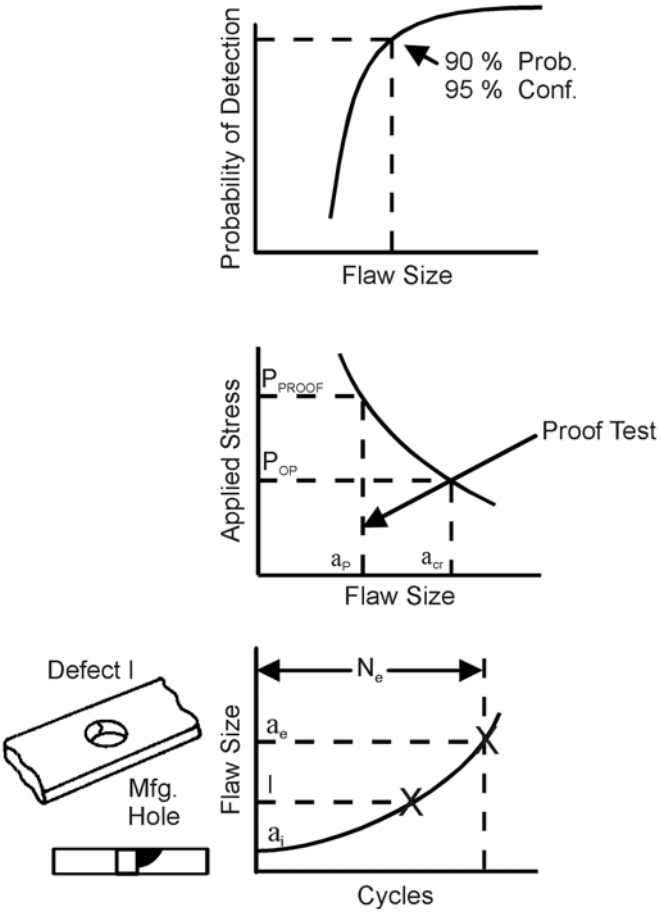

Figure 3.0.3. Various Qualification Processes

3.1 NDI Demonstration Of Crack Detection Capability

Non-destructive inspection (NDI) methods are commonly used to determine the condition of a structure during production and at in-service inspections. Detailed descriptions of the principles and use of these methods are generally available (see, for example, Nondestructive Testing Handbook, Volume Ten [1996]). The objectives of this subsection are to briefly describe and compare the common NDI methods and to discuss the statistically based demonstration programs that are required to quantify the detection capability of an NDI system. A distinction between inspections for cracks and for corrosion is made for capability evaluations even though the physical principles of the techniques are common.

3.1.1 NDI Methods

There are six commonly-used NDI techniques, and two others are expected to receive widespread acceptance and application. These eight methods are visual, liquid penetrant, eddy current, ultrasonic, magnetic particle, radiography, thermographic and acoustic emission inspections. Each of these is briefly described in the following paragraphs.

3.1.1.1 Visual Inspection

In a sense, all inspections in which the find/no find decision is made by a human are visual. However, in categorizing NDI methods, visual inspections are generally interpreted as inspections in which the inspector is aided, at most, by optical devices, such as magnifying glasses and mirrors. In the context of JSSG-2006, the in-flight evident, ground evident, walk-around evident, and special visual inspections are all visual inspections and play an important role in the maintenance of structural integrity through damage tolerance.

Visual inspections are the most common and the most economical of the inspections to perform. However, visual inspections are also the least reliable in terms of the size of the cracks that can be detected. Since the efficacy of visual inspections is highly dependent on the alertness and acuity of the inspector, an additional level of human factors is introduced in discerning the physical attributes of a crack from its environment.

3.1.1.2 Liquid Penetrant Inspection

Liquid penetrant inspection is a non-destructive method for finding discontinuities that are open to the surface of parts fabricated from essentially nonporous materials. After cleaning the surface, the penetrant is applied and will seep or be drawn into various types of minute surface openings. The excess penetrant is removed and a developer is applied which highlights the cracks under ultraviolet light. The process is well-suited for the detection of all types of surface cracks, laps, porosity, shrinkage area, laminations, and similar discontinuities.

Indications of cracks can be found regardless of size, configuration, internal structure, or chemical composition of the workpiece being inspected and regardless of the orientation of the crack to the workpiece.

Liquid penetrant inspections are relatively simple and inexpensive (as compared to the other NDI methods) and can be applied to a broad range of materials. Very small cracks can be found. However, they can only detect surface cracks and their effectiveness can be adversely influenced by surface coatings, surface roughness, and porosity. Extreme care is required in pre- and post-inspection cleaning and, in some cases, etching may be required prior to inspection.

3.1.1.3 Eddy Current Inspection

The principles of electromagnetic induction are used in eddy current inspections to detect surface and near-surface cracks in electrically-conductive metals. When an electrically-conductive material is subjected to an alternating magnetic field, small circulating electric currents are generated in the material. Since these eddy currents are affected by variations in conductivity, magnetic permeability, mass, and material homogeneity, the conditions that affect these characteristics can be sensed by measuring the eddy current response of the material. In practice, eddy currents are induced in the part to be inspected with a coil carrying an alternating current. The induced eddy currents generate their own magnetic field, which interacts with the magnetic field of the exciting coil, and changes the impedance of the exciting coil. By measuring the impedance of the exciting coil, or a separate indicating coil, the inspector can infer the presence of cracks in the material.

An important use of the eddy current NDI method has been in the detection of fatigue or stress corrosion cracks around fastener holes after the cracks have grown beyond the fastener head. Special bolt hole probes have also been devised for use after the fastener has been removed for locating cracks emanating from the wall of the fastener hole. This inspection process has been automated to remove operator influence, speed inspections, and produce a permanent inspection record.

Eddy current methods do not require contact with the specimen or clean up, and are generally faster than liquid penetrant and radiographic methods. Although eddy current methods can detect both surface and subsurface cracks, the depth of inspection below the material surface is limited (approximately 0.25 in.). Since eddy currents are influenced by many material variables, masked or false indications can easily be caused by sensitivity to part geometry, lift-off, edge effects and permeability variations. Finally, eddy current methods require well-trained operators to man the test instruments and reference standards are necessary.

3.1.1.4 Ultrasonic Inspection

Ultrasonic inspection uses high frequency sound waves as a probing medium to detect subsurface, as well as surface cracks. The sound waves travel through the part with attendant energy loss and are reflected at material-crack interfaces. Ultrasonic inspection devices detect cracks by monitoring one or more of the following: (a) reflection of energy from interfaces or discontinuities within the metal; (b) time of transit of a sound wave through the test piece; and (c) attenuation of the beams by absorption and scattering within the test piece.

Ultrasonic inspection is one of the most widely used NDI methods. Cracks, laminations, shrinkage cavities, bursts, flakes, pores, bonding faults, and other discontinuities that act as metal-gas interfaces can be detected. Inclusions and other non-homogeneity in the metal being inspected can also be detected by causing partial reflection or scattering of the wave, even though they may not act as a metal-gas interface. Although the primary application of ultrasonic inspection in metals is the detection and characterization of internal cracks, it is also used to detect surface cracks, define bond characteristics, measure extent of corrosion and, (much less frequently) determine physical properties such as structure, grain size, and elastic constants. The penetrating power of ultrasound waves allows the detection of cracks deep within a part. Due to the sensitivity of the instruments, very small cracks can be detected but, if the gain is set too high, at the expense of many false indications. Ultrasonic methods provide greater accuracy than other NDI methods in determining the position of internal cracks, estimating their size, and characterizing their orientation, shape and nature. The limitations of ultrasonic methods are governed by the requirement for experienced technicians, the difficulty in developing inspection procedures, the need for reference standards

for equipment calibration, and the physical limitations of the hardware. Since couplants (light oil or water) are needed to provide effective transfer of ultrasonic wave energy between transducers and material, parts that are rough or irregular in shape are difficult to inspect. Similarly, parts that are very small are difficult to inspect. Finally, since discontinuities in a shallow layer immediately below the surface may not be detectable, inspection results of very thin components are questionable.

3.1.1.5 Magnetic Particle Inspection

Magnetic particle inspection is effective in the detection of surface and near-surface cracks in ferromagnetic parts. The inspection is accomplished by inducing a magnetic field in the part and applying either a dry magnetic powder or a liquid suspension of iron particles to the surface being inspected. Defects in the part cause local bipolar perturbations in the magnetic field which attract the magnetic particles, producing visible indications by color contrast or by fluorescence under "black light". The magnetically-held particles form the outline of the discontinuity and generally indicate its location, size, shape, and extent to an experienced inspector.

The magnetic particle method is a relatively fast and inexpensive method for locating small and shallow surface cracks in ferromagnetic materials. Discontinuities that do not break the surface are detectable, but deeper cracks must be larger to be found. Elaborate pre-cleaning is not necessary, but thin coatings of paint or other non-magnetic coverings, such as plating, adversely affect the sensitivity of this inspection technique. Following the inspection, the material must often be de-magnetized, and post-cleaning to remove the clinging magnetic particles is usually necessary. This NDI method can be used only on ferromagnetic materials, which include most of the iron, nickel and cobalt alloys. Many of the precipitation-hardening steels, such as 17-4PH, 17-7PH, and 15-4PH stainless steels, are magnetic after aging. Non-ferromagnetic materials that cannot be inspected by this method include aluminum, magnesium, copper, and titanium alloys and austenitic stainless steels.

3.1.1.6 Radiographic Inspection

Radiographic NDI is based on the differential absorption of penetrating radiation by the structure being inspected. In conventional radiography, the object is bombarded by a beam of X-rays and the portion of the radiation that is not absorbed by the object impinges on a sheet of film. The unabsorbed radiation exposes the film emulsion similar to the way light exposes film in photography. Development of the film produces an image that is a two-dimensional "shadow picture" of the entire volume of the object. Variations in density, thickness, and composition of the object being inspected cause variations in the intensity of the unabsorbed radiation and appear as variations in shades of gray in the developed film. Evaluation of the radiograph is based on a comparison of the differences in photographic density with known characteristics of the object or with standards derived from radiographs of similar objects of acceptable quality.

Radiographic inspection provides the capability to probe the internal characteristics of materials and components. It can disclose structural weaknesses, assembly errors, and mechanical malfunctions, as well as revealing voids, long cracks, and other material anomalies. Radiography is, however, expensive, slow, and not sensitive to detecting certain type cracks. Cracks cannot be detected unless they are parallel to the radiation beam. Tight cracks in thick sections cannot usually be detected even when properly oriented. Laminations are almost always non-detectable. Minute discontinuities such as inclusions in wrought material, flakes, microporosity and microfissures cannot be detected unless they are sufficiently segregated to produce a detectable gross effect. Finally, due to the hazards of exposure to X-rays, strict controls are required to prevent biological damage to the inspectors.

3.1.1.7 Thermographic Inspection

Thermographic inspection uses relative differences in heat transmission to detect internal features and defects, such as delaminations in layered materials. In active thermography, heat is applied to the object under test and surface temperatures are monitored by an infrared camera as the heat propagates through the object. In the reflection method, heat is applied to the surface that is monitored; relatively warm areas indicate possible internal defects. In the transmission method, heat is applied to the opposite side of a panel from a detector, and relatively cooler areas will indicate areas of poor thermal transmission. Heat may be applied by a laser, warm air, heat lamps, flash lamps, or other methods. While heating is most common, cooling may also be used to create thermal transients within the material. Passive thermography, with no external heat source, may be used if thermal contrasts are produced within the object under test by other means, such as electrical heating at a poor solder joint.

Thermographic methods are most appropriate for use with materials that have low thermal conductivity, such as ceramics and polymers. Heat propagates more slowly in these materials, which decreases the image acquisition rate needed from the infrared camera. In addition, interference with the thermal excitation can obscure near-surface data, with "near-surface" measured in time of thermal transmission, so that much less data is lost when the heat is propagating slowly. High emissivity surfaces radiate heat better and, therefore, produce better sensitivity. Coatings, such as a flat black paint, may be applied to low emissivity or reflective surfaces to increase emissivity. Flaws, such as delaminations that are perpendicular to the propagation of thermal energy through the object, are the best candidates for detection by thermography. Other flaws that disrupt heat flow, such as fluids trapped in honeycomb materials, can also be detected with relative ease. The resolution of this method decreases with depth, because the thermal energy is conducted in all directions, not just directly through the material. Surface flaws, such as cracks, may be detected if heat can be forced to propagate along the surface of the material. Thickness or composition variations may be detected by transmission thermography.

Thermography has a long history, but has not achieved the widespread use of other methods, such as ultrasonic, eddy current, and radiography. Disadvantages of this method include the expense of equipment, the reliance on surface emissivity, and the generally low signal-to-noise ratio. Advantages include area inspection nature of the technology, speed, noncontact nature, and versatility. Currently, thermographic methods are used for delamination detection in layered composites, coatings evaluation, honeycomb inspection, thermal barriers, bond evaluation, and thickness evaluation. Improvement in the sensitivity of infrared detectors and better thermal sources indicate that the use of thermographic methods will increase as the supporting technologies continue to mature.

3.1.1.8 Acoustic Emission Inspection

Acoustic emission (AE) is the term used for dynamic stress waves that are created within a material due to the application of a force. Some examples are the sound of fibers breaking when a piece of wood is bent, high-frequency stress waves created when a crack grows in a metal structure undergoing mechanical fatigue, and the pulse of stress waves emanating from the impact site of a meteorite colliding with a spaceship hull. AE differs from most of the other NDI methods in that no directed energy is put into the test object. Whole-body forces create the localized stress waves that propagate through the test object to AE sensors.

AE NDI is done by placing multiple acoustic sensors on the object being inspected and then recording and correlating the signals generated when stress waves reach the sensors. The sensors typically are responsive to acoustic frequencies between 50 kHz and 1 MHz. The lower limit is important in order to limit acoustic noise, although it should be noted that common objects such as jingling car keys or grinding wheels produce acoustic energy above 100 kHz. The upper limit is strongly dependent on the bandwidth of the AE sensor. Occasionally, AE tests utilize sensors with the upper limit extending into the 2-3 MHz range. The sensors are connected to AE instruments that amplify, filter, store, and process the signals produced by the sensors. Typical results from AE tests are the number of AE "events" recorded; the energy, time, and duration of each event; and the location of the event within the test object.

Some advantages of AE NDI are: 1) the method is sensitive to stress waves emanating from anywhere within the test object; the sensors do not have to be focused or scanned across the object; 2) triangulation of the time of detection of the stress wave at different sensors allows identification of the location of the emission, and 3) sensors can be placed on objects with very limited access.

Disadvantages of AE NDI are: 1) the instrumentation is expensive, 2) appropriate signal processing to eliminate unimportant signals can be complicated, 3) large amounts of data often are generated, creating data storage problems.

3.1.1.9 NDI Methods Summary

Figure 3.1.1 summarizes and compares attributes of the five principal non-visual NDI methods that are in widespread use. This subjective comparison describes the types of defects that can be characterized, the structural applications, the advantages, and limitations of each of the methods. For damage tolerance considerations, the key characteristic of an NDI system is the size of the flaws that can be missed when the system is applied in the field. Quantifying inspection capability in terms of flaw size is referred to as inspection or NDI reliability. Because of the many differences in material and geometry of structural details and the many approaches to the application of any of the methods, there is no single characterization of capability in terms of a reliably-detected crack size for any of the methods. Further, because of the difficulty and cost of quantifying NDI reliability, relatively few capability demonstrations have been conducted. Only very general statements can be made comparing the NDI reliability of the five methods.

Because of the random nature of inspection response to flaws of ostensibly the same size, NDI capability is characterized in probabilistic terms and estimated using statistical methods. In particular, NDI reliability is quantified in terms of the probability of detection as a function of flaw size, POD(a). There is no practical flaw size for which there is 100 percent assured detection. For damage tolerance applications in the aircraft industry, it has become customary to characterize inspection capability in terms of the crack size for which there is a 90 percent probability of detection, the a_{90} crack size. To reflect the statistical uncertainty in the estimate of a_{90}, a 95 percent confidence bound can be calculated yielding the $a_{90/95}$ crack size characterization of capability. There is 95 percent confidence that at least 90 percent of all cracks of size $a_{90/95}$ will be detected. The reliably detected crack size for a system is usually taken to be either a_{90} or $a_{90/95}$. Note that cracks smaller than $a_{90/95}$ are readily detected by the NDI systems since POD(a) functions for production inspections increase over a relatively large crack size region. Typically, the 50 percent detectable crack size is less than half the a_{90} crack size for a non-automated inspection. Subsection 3.1.2 describes in considerable detail the approach to demonstrating NDI reliability for an application.

Method	Measures or Defects	Applications	Advantages	Limitations
Magnetic Particles	Surface and slightly subsurface defects; cracks, seams, porosity, inclusions Permeability variations Extremely sensitive for locating small, tight cracks	Ferromagnetic materials, bar, forgings, weldments, extrusions, etc.	Advantage over penetrant in that it indicates subsurface defects, particularly inclusions Relatively fast and low cost May be portable	Alignment of magnetic field is critical Demagnetization of parts required after tests Parts must be cleaned before and after inspection Masking by surface coatings
Liquid Penetrant	Defects open to surface of parts; cracks, porosity, seams, laps, etc. Through-wall leaks	All parts with non-absorbing surfaces (forgings, weldments, castings, etc.) Note: Bleed-out from porous surfaces can mask indications of defects	Low cost Portable Indications may be further examined visually Results easily interpreted	Surface films, such as coatings, scale, and smeared metal may prevent detection of defects Parts must be cleaned before and after inspection Defect must be open to surface
Ultrasonic (0.125 MHz)	Internal defects and variations, cracks, lack of fusion, porosity, inclusions, delaminations, lack of bond, texturing Thickness or velocity Poisson's ratio, elastic modulus	Wrought metals Welds Brazed joints Adhesive-bonded joints Nonmetallics In-service parts	Most sensitive to cracks Test results known immediately Automating and permanent recording capability Portable High penetration	Couplant required Small, thin, complex parts may be difficult to check Reference standards required Trained operators for manual inspection Special probes
Eddy Current (200 Hz to 6 MHz)	Surface and subsurface cracks and seams Alloy content Heat treatment variations Wall thickness, coating thickness Crack depth Conductivity Permeability	Tubing Wire Ball bearings "Spot checks" on all types of surfaces Proximity gage Metal detector Metal sorting Measure conductivity in % IACS	No special operator skills required High speed, low cost Automation possible for symmetrical parts Permanent record capability for symmetrical parts No couplant or probe contact required	Conductive materials Shallow depth of penetration (thin walls only) Masked or false indications caused by sensitivity to variation, such as part geometry, lift-off Reference standards required Permeability variations
Radiography (X-rays-film)	Internal defects and variations; porosity, inclusions; cracks; lack of fusion; geometry variations; corrosion thinning Density variations Thickness, gap and position Misassembly Misalignment	Castings Electrical assemblies Weldments Small, thin, complex wrought products Nonmetallics Solid propellant rocket motors Composites	Permanent records; film Adjustable energy levels (5 kv-25 mev) High sensitivity to density changes No couplant required Geometry variations do not effect directions of X-ray beam	High initial costs Orientation of linear defects in part may not be favorable Radiation hazard Depth of defect not indicated Sensitivity decreases with increase in scattered radiation

Figure 3.1.1. Summary and Comparison of Principal Nondestructive Testing Methods [Walker, et al., 1979]

Table 3.1.1 presents approximate lower limits of reliably-detected crack sizes for the NDI methods in common use in the aircraft industry. These limits are achievable on some structures by well-trained inspectors working in a good production environment. Because the crack sizes of Table 3.1.1 represent the limits of the methods, such capabilities must be demonstrated before use in a damage tolerance based inspection schedule. Note that most routine inspections are not designed for these target crack sizes.

Table 3.1.1. Approximate Limits of Reliably Detectable Crack Sizes

Method		Location	Dimension	Size (in.)
Eddy Current	Manual	Near Surface	Length	0.030-0.040
	Semi-Automated	Near Surface	Length	0.020-0.030
	Automated	Near Surface	Length	0.005-0.010
Ultrasonic	Manual	Subsurface	FBH*	0.032-0.064
	Automated	Subsurface	FBH*	0.016-0.032
Fluorpenetrant	Manual	Surface	Length	0.075-0.100
	Automated	Surface	Length	0.060-0.075
Magnetic Particle	Manual	Near Surface	Length	0.010-0.020

*FBH – capability based on flat bottom holes

There have been a number of demonstrations of NDI reliability for different structures and NDI methods. An early compilation of such results can be found in Yee, et al. [1974], but the analysis methods for POD data were still evolving at that time and the quoted $a_{90/95}$ values in this report are not compatible with those of more recent vintage. A major study sponsored by the United States Air Force was that of a program known as "Have Cracks, Will Travel" [Lewis, et al., 1978]. This study evaluated inspection capability at Air Force facilities and demonstrated the need for improving NDI reliability. More recently, Rummel and Matzkanin [1997] have produced a data book that lists POD results for aluminum and titanium flat plates and panels and steel turbine engine bolt holes. Among others, this data book contains the results of NDI demonstrations produced by the Aging Aircraft NDI Development and Demonstration Center at Sandia National Laboratories (see for example Spencer & Schurman [1995] and those of an AGARD round robin [Fahr, et al., 1995]). A number of POD evaluations have been performed on the Retirement for Cause Eddy Current Inspection System (RFC/ECIS) for the inspection of turbine engine components but the results of these evaluations have not been released.

Another quantitative comparison of the various NDI methods is represented by the default reliably detected crack sizes that can be used in structural design. See, for example, NASA/FLAGRO Version 2.03, in which such default crack sizes are listed for 24 different crack types and the five common NDI methods. As an example of such default reliably detected crack sizes, Figure 3.1.2, from Rummel & Matzkanin [1997] and NASA/FLAGRO Version 2.03, presents one of the crack types and the corresponding default crack sizes.

CC01

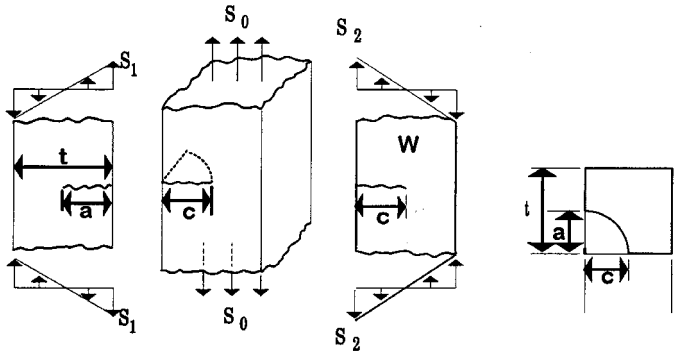

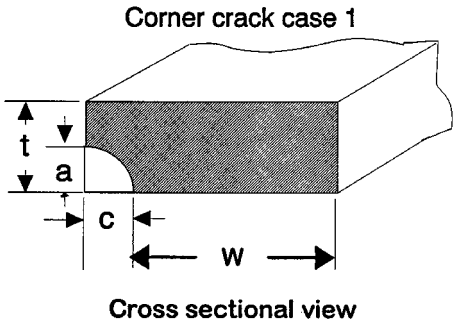

Crack Case	NDE Inspection Technique or Flaw Size Criterion	Thickness Range (in.)	Crack depth, a	Size (in.) crack length, c
CC01, (edge)	EC	t > 0.075	0.075	0.075
	P	t > 0.100	0.100	0.100
	MP	t > 0.075	0.075	0.075
	U	t > 0.100	0.100	0.100

Notes:
EC = eddy current (ET) MP = magnetic particle (MT)
P = dye/fluorescent penetrant (PT) U = ultrasonic (UT)

Figure 3.1.2. Standard NDE Flaw Sizes for STS Payloads – Edge Corner Cracks [Rummel & Matzkanin, 1997]

3.1.2 NDI Capability Evaluation for Cracks

While all of the NDI systems are capable of finding "small" cracks, damage tolerance analyses are based on the largest crack that might be in the structure after an inspection. Thus, the focus of NDI capability evaluation for damage tolerance is the largest crack that might be missed at an inspection. NDI techniques do not always produce a correct indication when applied by inspectors to cracks of the same size. The ability and attitude of the operator, the geometry and material of the structure, the environment in which the inspection takes place, and the location, orientation, geometry and size of the crack all influence the chances of detection. When considering the efficacy of an NDI system as a function of only crack size, uncertainty is introduced as a result of

ignoring the other factors. This uncertainty is quantified in terms of the probability of detection (POD) of cracks of a fixed size. POD(a) is defined as the proportion of all cracks of size a that will be detected by the NDI system when applied by representative inspectors to the population of structural elements in a defined environment. At present, demonstrating the capability of an NDI system for a specific application requires a carefully controlled experiment with a valid statistical analysis of the resulting data. Figure 3.1.3 presents an example POD(a) function with a 95 percent confidence bound for a liquid penetrant inspection of turbine engine blades. Each data point represents the proportion of times cracks of the indicated size were detected.

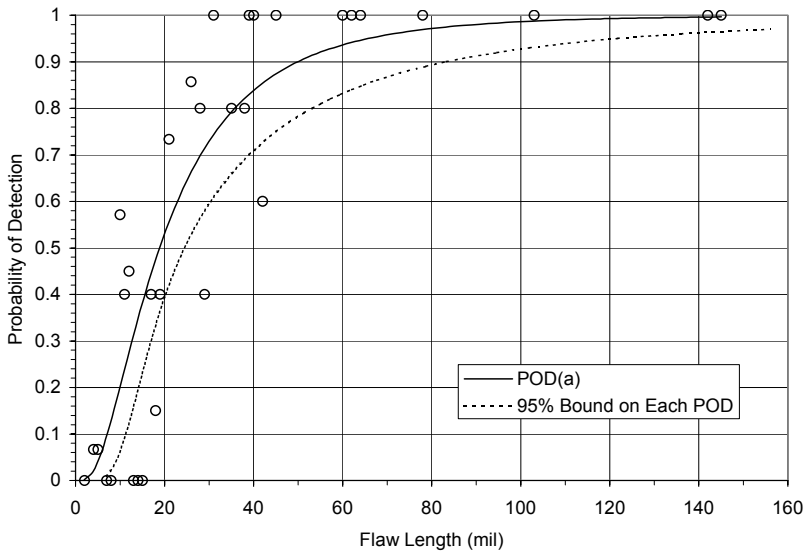

Figure 3.1.3. Example POD(a) Curve with Confidence Bound for Liquid Penetrant Inspections

The statistically-based characterization of NDI capability has two significant ramifications. First, for a given NDI application, the true probability of detection as a function of crack size (or for a single crack size) will never be known exactly. The capability of an NDI system can only be demonstrated by inspecting representative structures with known crack sizes. The true POD(a) function is estimated from the responses to the inspection stimuli or by the observed percentages of correct positive indications. The estimated POD(a) is subject to the statistical variation that can result from all of the uncontrolled factors that lead to variability in positive indications for all cracks of a particular size. However, statistical methods (which depend on the experimental procedure) are available which yield confidence limits on the true probability of detection. Protection against making a wrong decision on the basis of a set of non-typical results is provided by the confidence limits.

Second, in the real-world structural integrity problem, no inspection procedure will provide 100 percent assurance that all cracks greater than some useful size will be detected. Current NDI capabilities at the short crack lengths of interest in aircraft applications dictate that a reliably detectable crack size, can only be specified in terms of a size for which a high percentage of cracks will be detected. To reflect the statistical uncertainty, a confidence bound is often placed on this estimate of crack size. Such single crack size characterizations of NDI capability are expressed in terms of the crack sizes for which there is at least a given POD at a defined level of confidence (the POD/CL crack size). Such characterizations provide a stand-alone measure of the NDI system that is valid for applications represented by the demonstration test conditions. For example, JSSG-2006 states that smaller initial crack sizes can be used for slow crack growth

structures if it can be shown that there is 95 percent confidence that at least 90 percent of all cracks of the smaller size will be detected by the manufacturers' NDI system.

There are three major limitations associated with the POD/CL type characterization:

1) The choice of particular POD and confidence limits has been made on a rather arbitrary basis. For example, 90/95 values were selected for JSSG-2006 recommended crack sizes even though there is no real interest in a crack length that is detected only 90 percent of the time. Rather, 90/95 limits were selected because higher POD or confidence limit values would have required much larger sample sizes in the demonstration programs for the analysis methods being used. The 95 percent confidence limit is assumed to provide the required degree of conservatism.
2) A POD/CL limit is not a single, uniquely defined number but, rather, is a statistical or random quantity. Any particular POD/CL estimate is only one realization from a conceptually-large number of repeats of the demonstration program. Berens & Hovey [1981] showed there can be a large degree of scatter in these POD/CL estimates and the scatter depends on the POD function, analysis method, POD value, confidence level and number of cracks in the demonstration program.
3) The POD/CL characterization is not related to the size of cracks that may be present in the structure after an inspection. To calculate the probability of missing a large crack requires knowledge of both POD(a) for all cracks sizes and the distribution of the sizes of the cracks in the population of structural details being inspected.

MIL-HDBK-1823 and Berens [1988] present in considerable detail an acceptable approach to demonstrating NDI capability in terms of a POD/CL characterization. Other approaches are also in use. After a brief description of the design of NDI capability experiments, the following paragraphs present a description of the analyses that are in current use for calculating POD/CL limits.

3.1.2.1 Basic Considerations in Quantifying NDI Capability

There are two distinct strategies for quantifying NDI capability for damage tolerance analyses. These are: a) estimating POD(a) as a function of crack size and b) demonstrating capability for a fixed crack size. To estimate a POD(a) function, the structural details to be inspected would comprise a range of crack sizes in the expected domain of increasing POD. A parametric equation is assumed for the POD(a) function, the parameters of the equation are estimated from the inspection results, and the statistical properties of the estimates are used to place a confidence limit on the selected detection probability. To demonstrate capability for a fixed crack size, only cracks of the size of interest are inspected. The proportion of the cracks that are detected is the estimate of POD (for cracks of that size) and binomial theory is used to place a lower confidence bound on the detection probability. Because of the greater utility of the POD(a) function, the approach based on estimating the entire function is preferred by many, including the Air Force [MIL-HDBK-1823]. The fixed crack size approach is used by NASA for qualifying the inspection capability of vendors [Salkowski, 1993]. It might be noted that a binomial approach to estimating POD as a function of crack size was extensively considered in the 1970's, but later abandoned. Very large numbers of cracked specimens were needed to ensure an adequate sample size within reasonably small intervals of crack size.

The analysis of data for demonstrating capability at a fixed crack size using the binomial approach will be discussed, but the major thrust of the capability evaluation is focused on estimating the POD(a) function. Similar considerations apply to the planning of both types of capability demonstrations.

Inspection results are recorded in two distinct formats and the format determines the analysis method to be used in modeling the POD(a) function. When the results of an inspection are expressed only in terms of whether or not a crack was detected, the data are known as find/no find, hit/miss, or pass/fail data. Such dichotomous inspection results are represented by the data pair (a_i, Z_i) where a_i is the size of the i^{th} crack and Z_i represents the outcome of the inspection of the i^{th} crack: $Z_i = 1$ for the crack being found (hit or pass) and $Z_i = 0$ for the crack not being found (miss or fail). Examples of such data would be the results of visual, magnetic particle, or fluorescent penetrant inspections or any inspection for which the magnitude of the response to the inspection stimulant was not recorded. POD(a) analysis for data of this nature is often called hit/miss or pass/fail analysis. Maximum likelihood estimates of the parameters of the POD(a) model are obtained from the (a_i, Z_i) data. Asymptotic properties of the maximum likelihood estimates are used to calculate the confidence bound on the estimate of the reliably detected crack size.

When the results of the inspection are based on the quantified magnitude of a response to the inspection stimulus and the response is recorded, the POD(a) function can be estimated from the statistical scatter in the response magnitudes as a function of crack size. The data pair comprising size and signal response are designated as (a_i, $\hat{a}_i$) in which $\hat{a}_i$ is the response to the inspection stimulus for the i^{th} crack. If $\hat{a}_i$ is greater than a pre-set threshold, $\hat{a}_{th}$, a crack is indicated. Data of this nature are often referred to as $\hat{a}$ vs a (a-hat vs a). Data from automated eddy current systems are of this nature. Data from ultrasonic and liquid penetrant inspections have also been recorded and analyzed in the $\hat{a}$ vs a format. The parameters of the POD(a) function are estimated from the scatter in $\hat{a}$ values about the mean response to cracks of size a. Maximum likelihood is used to estimate the parameters and to place confidence bounds on the estimate of the reliably detected crack size when desired [MIL-HDBK-1823; Berens, 1988].

The demonstration of NDI capability is a consumer or quality concern. The primary objective of such demonstrations for a particular application is to estimate the POD(a) function and, consequently, the reliably detected crack size, say a_{NDI}. For damage tolerance considerations, a_{NDI} is commonly accepted to be the crack sizes designated as a_{90} or $a_{90/95}$. The a_{90} crack size is defined as the size for which POD(a_{90}) = 0.90 and $a_{90/95}$ is the upper (conservative) 95% confidence bound on the estimate of a_{90}. (The estimate of the a_{90} crack size is often referred to as the $a_{90/50}$ crack size under the wrong assumption that the estimate of a_{90} is the median of the sampling distribution of the estimates.)

NDI reliability experiments have also been conducted to optimize the inspection protocol and to ensure process control. System optimization with respect to POD(a) would have the objective of determining system configurations that produce acceptable a_{90} or $a_{90/95}$ values. The design of system optimization programs is of a different character and beyond the scope of demonstrating the capability of the system.

3.1.2.2 Design of NDI Capability Demonstrations

NDI capability is typically quantified through a capability demonstration program. The concept for such a demonstration is to mimic the real inspection as closely as possible on representative specimens that contain cracks of known sizes that span the range of increase of the POD(a)

function. A comprehensive description for the execution of such a demonstration program and the analysis of the resulting data is presented in MIL-HDBK-1823 (see also Berens [1988] and Berens [2000]). The analysis of the data from an NDI demonstration uses the maximum likelihood estimates of the parameters of the POD(a) model and the asymptotic properties of such estimates. This subsection briefly reviews the design and execution of a generic capability demonstration.

An NDI reliability demonstration comprises the execution of a test matrix of inspections on a set of specimens with known crack locations and sizes. The inspection results, either $\hat{a}$ or hit/miss, are then analyzed to estimate the parameters of the POD(a) function and the reliably detected crack size for the inspection application. The specimens are inspected under a test protocol that simulates as closely as practical the actual application conditions. Establishing test protocols for eddy current, fluorescent penetrant, ultrasonic and magnetic particle inspection systems are discussed in MIL-HDBK-1823.

The objectives and costs of an NDI demonstration determine the matrix of inspections to be performed. From the analysis viewpoint, there are two major categories of concerns that must be addressed in establishing the experimental design. These are: a) the generality of inferences that can be made from the controlled and uncontrolled inspection and material parameters; and, b) the number and sizes of cracks and the number of uncracked inspection sites in the specimens.

Controlled and Uncontrolled Factors

To demonstrate capability for an application, it is assumed that: a) the complete protocol for conducting the inspection is well defined for the application; b) the inspection process is under control; and, c) all other factors which introduce variability in an inspection decision are reasonably representative of the application. The representativeness of these other factors limits the scope of the POD(a) characterization and is addressed by controlling the factors during the inspection or by randomly sampling the factors to be used in the demonstration. The methods of accounting for these factors are important aspects of the statistical design of the demonstration and significantly influence the statistical properties of the estimates of the POD(a) function parameters.

The important classes of the factors that introduce variation in crack detectability are:

a) the inherent degree of repeatability of the magnitude of the NDI signal response when a specific crack is independently inspected many times with all controllable factors held constant;
b) the material and geometrical properties of the specimens and the differences in the physical properties of cracks of nominally identical "size";
c) the variation introduced by different hardware components in the inspection system; and,
d) the summation of all the human factors associated with the particular population of inspectors that might be used in the application.

The effects of these factors are present in every NDI reliability demonstration and they should be explicitly considered in the design of the demonstration and the interpretation of the results.

Little can be done about the variation of the response to the NDI excitation at the demonstration stage when inspections are repeated under fixed conditions. This variation might be reduced if the system was modified or better optimized but that is a different objective. Repeat inspections under identical conditions will provide a measure of the inherent variability that is a lower bound on the variability to be expected in applications of the system.

The character of the cracks in the structure being inspected will have a significant influence on the inspection outcome. There are two elements of crack character that impact the demonstration: the physical characteristics of the specimens containing the cracks and the physical properties of the cracks in the specimens. The inspection system will be designed to detect cracks of a defined size range at a location in a structural element defined at least by a material type and geometrical configuration combination. A fixed set of specimens containing cracks will be inspected and these specimens either must be of this combination or the assumption must be made that differences in inspection response in the specimens is identical to that obtained in the real application.

The cracks in the specimens must be as close as possible to the cracks that will be in the real structures and of sizes that span the region of interest for the POD(a) analysis. The assumption of equivalent response to the real inspection is implied when the results of the demonstration are implemented. Experience with the inspection will dictate the degree of acceptance of the assumption. For example, EDM notches are not good substitutes for eddy current inspections of surface fatigue cracks but may be the only possible choice for subsurface ultrasonic inspections.

Inspection capability is expressed in terms of crack size but not all cracks of the same "size" will produce the same magnitude of inspection response. In general, the specimens used in NDI reliability demonstrations are very expensive to obtain and characterize in terms of the sizes of the cracks in the specimens. Each set of specimens will be inspected multiple times if other factors are being considered in the demonstration. From a statistical viewpoint, this restriction on the experimental design limits the sample size to the number of cracks in the specimen set. Multiple independent inspections of the same crack only provide information about the detection probability of that crack and do not provide any information about the variability of inspection responses between different cracks. Stated another way, k inspections on n cracks is not equivalent to inspections of $n \bullet k$ different cracks, even if the inspections are totally independent. The number and sizes of cracks will be addressed later.

Accounting for the variability due to differences in inspection hardware must first be considered in terms of the scope of the capability evaluation. Each component of the inspection system can be expected to have some, albeit small, effect on inspection response. The combinations of particular components into sub-systems and complete inspection stations can also be expected to influence the response. Recognizing that individual hardware combinations might have different POD(a) capabilities, a general capability objective must be set. Each combination can be characterized, each facility comprising many combinations can be characterized, or many facilities can be characterized. Ideally, the available hardware combinations would be randomly sampled for the scope of the desired characterization and a weighted average of responses would be used to estimate the POD(a) function. On a practical level this is seldom done for ostensibly identical equipment. (Note that an analogous problem exists when accounting for the human factors which will be discussed in the following.) More commonly, capability demonstrations are performed on combination of hardware and the assumption is made that the characterization would apply to all combinations. That is, the POD(a) differences between combinations are assumed to be negligible.

The above is directed at a complete individual inspection system (however defined), but the variability of interchangeable components of a system can often be directly assessed. For example, experience has shown that different eddy current probes produce different responses when all other factors are constant. If a single probe is used to demonstrate the capability of an eddy current system, the estimated POD(a) function applies to the relevant inspections using that probe.

However, if the POD characterization is to be used for in-service inspections using any such probe, an assumption is required that the probe is representative of the entire population. If a larger demonstration is affordable, the inspections could be performed using a random sample of probes from the available population. The analysis method must then account for the fact that multiple inspections of each crack were made with the different probes. The resulting characterization would better represent an inspection for a randomly selected probe.

Accounting for the variation from more than one source is more complex. Care must taken to ensure that the multiple sources are balanced in the analysis of the data and that the correct analysis procedures are used. For example, in the early evaluations of an automated eddy current system for turbine engine disks (the ECIS system for the ENSIP/RFC applications), there was considerable interest in the inherent variability in response from repeated, identical inspections and from different probes with their associated re-calibration changes. (Other factors were initially considered but were later ignored after it was shown that they had no affect on POD(a) for the system.) The specimen sets would be inspected three times: twice with one probe and once with a second probe. The data from the three inspections, however, could not be combined in a single analysis since such an analysis would skew the results toward the probe with double representation. Thus, one analysis would be performed to estimate the inherent repeat variability and a second analysis would be performed to estimate the probe to probe variation. The results would then be combined to arrive at the POD(a) function that accounted for both sources of variation. It might be noted in this context that the repeat variability was negligible as compared to the variability that results from re-calibration and probe changes. The demonstration plan was later modified to better estimate the more significant between probe variation by performing the third inspection with a third probe.

Factorial-type demonstrations are an efficient approach to simultaneously account for several significant factors. However, such demonstrations for more than a couple of factors require many inspections of the specimen set. More sophisticated statistical experimental designs might be employed but the actual choice of such a design and the analysis of the data are driven by the specific objectives of a particular experiment. Discussion of such designs is beyond the scope of this discussion.

Human Factors

When the inspector plays a significant role in the find/no find decision, he or she is an integral component of the NDI system. In such common inspection scenarios, human factors can contribute significantly to the variability in inspection results. In this context, human factors refer to both the dynamic capabilities of individual inspectors and the user friendliness of the inspection tools in the environment of the application. Experiments have been conducted to quantify some of the environmental effects of human factors and data from some demonstration experiments have been interpreted in terms of the level of training and experience of the inspectors (see, for example, Spencer & Schurman [1994]). However, the effects and interactions of human factors on inspection results have not been characterized. Rather, to the extent possible, NDI systems are automated to minimize the effect attributed to the inspector.

In a non-automated inspection, many human factors potentially influence the inspection decision and they cannot all be accounted for in a capability demonstration. At some level, the representative inspection assumption will be required. Given that the mechanical aspects of the NDI system and inspection environment are held constant, differences between inspectors can cause a biased

capability characterization if ignored. Again, the objective of the capability characterization must be stated in advance. If each inspector is being evaluated, a separate POD(a) function for each is estimated. If a single POD(a) function is wanted for an entire facility, the inspectors in the demonstration must be randomly sampled in proportion to the percent of such inspections each performs. Alternatively, inspectors might be categorized by, say, capability as implied by certification level. A random sample of the inspectors from each level could be selected to arrive at a composite POD(a) for the level and a weighted average would be calculated based on the percent of inspections performed by each level. An example of designing such a demonstration is given in Hovey, et al. [1989]. Example results from the evaluation of a population of inspectors can also be found in Davis [1988].

3.1.2.3 Sample Size Requirements

Sample sizes in NDI reliability experiments are driven more by the economics of specimen fabrication and crack characterization than by the desired degree of precision in the estimate of the POD(a) function. Reasonable appearing POD(a) functions can often be obtained from applying the maximum likelihood analysis to an inspection of relatively few specimens. Totally unacceptable results can also be obtained from inspecting specimens containing too few cracks or from inspection results that are not reasonably represented by the assumptions of the models. Therefore, it must be recognized that the confidence bound calculation for a POD(a) analysis is based on asymptotic (large sample) properties of the estimates and that there are minimal sample size requirements that must be met to provide a degree of reasonable assurance in the characterization of the capability of the system.

Larger sample sizes in NDI reliability experiments will, in general, provide greater precision in the estimate of the POD(a) function. However, the sample size is determined from the number of cracks in the experiment and there is an information content coupling with the crack sizes that must also be considered. The effect of this coupling manifests itself differently for the $\hat{a}$ versus a and hit/miss analyses.

Sample sizes for the binomial analysis that is used to demonstrate a capability at a single crack size are dictated strictly by the selected value of the target POD and the degree of confidence.

Sample Size Requirements for $\hat{a}$ versus a Analysis

When the crack decision is made on the basis of a recorded response, $\hat{a}$, to the inspection stimulus, the data are known as $\hat{a}$ versus a inspection results and a better POD(a) analysis is available. An example of $\hat{a}$ versus a data from a capability demonstration is presented in Figure 3.1.4. When the inspection response is greater than a pre-set detection threshold, a crack is indicated for the site. In a capability demonstration, the minimum signal threshold is set as low as possible with respect to noise. Detection thresholds are later set that will yield a desired a_{90} value with an acceptable rate of extra indications. Extra indications are crack indications at sites with no known cracks. Extra indications can be the result of noise or large responses from insignificant cracks. However, they can also result from anomalies that do not impair structural integrity.

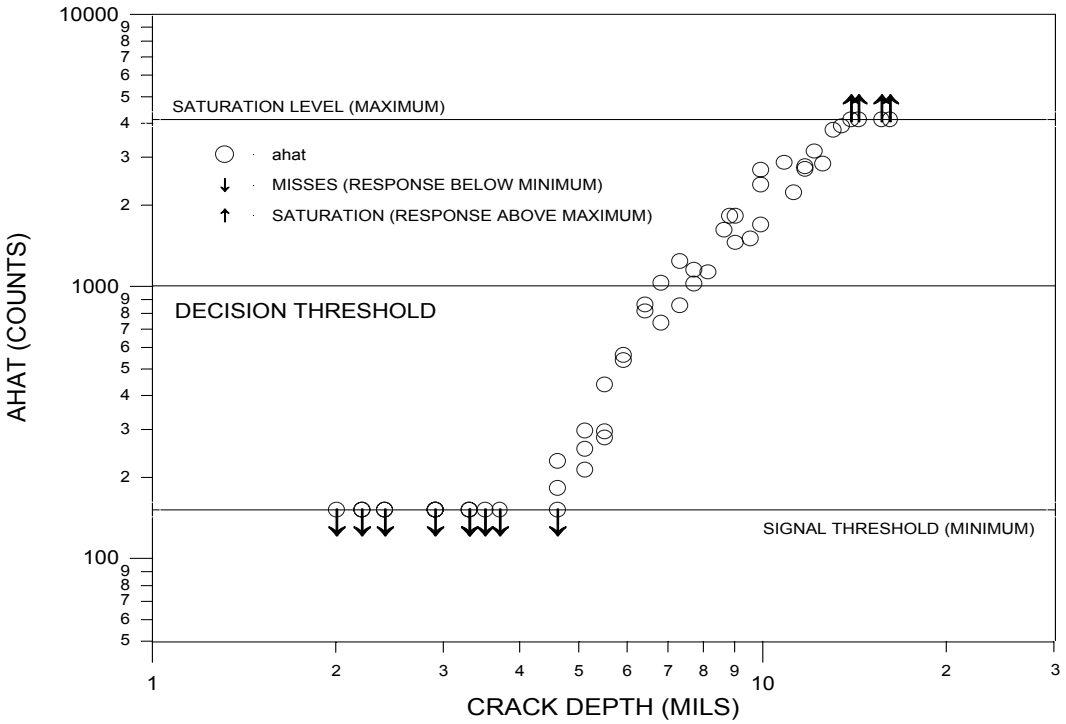

Figure 3.1.4. Example Plot of $\hat{a}$ versus a Data

The recorded signal response, $\hat{a}$, provides significantly more information for analysis than a simple crack or no crack decision of a hit/miss inspection response. The POD(a) model is derived from the correlation of the $\hat{a}$ versus a data and the assumptions concerning the POD(a) model can be tested using the signal response data. Further, the pattern of $\hat{a}$ responses can indicate an acceptable range of extrapolation. Therefore, the range of crack sizes in the experiment is not as critical in an $\hat{a}$ versus a analysis as in a hit/miss analysis. For example, if the decision threshold in Figure 3.1.4 was set at 1000 counts, only the cracks with depths between about 6 and 10 mils would provide information that contributes to the estimate of the POD(a) function. The larger and smaller cracks are always found or missed and would have provided little information about the POD(a) function in a hit/miss analysis. In the $\hat{a}$ analysis, however, all of the recorded $\hat{a}$ values provided full information concerning the relation between signal response and crack size and the censored values at the signal minimum and maximum limits provided partial information. The parameters of the POD(a) function are derived from the distribution of $\hat{a}$ values about the median response for cracks of size a. Assumptions necessary for characterizing this distribution are readily evaluated with the $\hat{a}$ versus a data.

Because of the added information in the $\hat{a}$ data, a valid characterization of the POD(a) function with confidence bounds can be obtained with fewer cracks than are required for the hit/miss analysis. It is recommended that at least 30 cracks be available for demonstrations whose results can be recorded in $\hat{a}$ versus a form. Increasing the number of cracks increases the precision of estimates. Perhaps, more importantly, increasing the number of cracks provides a broader population of the different types of cracks that the inspection will address. Therefore, the demonstration specimen test set should contain as many cracked sites as economically feasible. The analysis will provide parameter estimates for smaller sample sizes but the adequacy of the asymptotic distributions of the estimates is not known.

Sample Size Requirements for Pass/Fail Analysis

In a hit/miss capability demonstration, the inspection results are expressed only in terms of whether or not the crack of known size was detected. There are detection probabilities associated with each inspection outcome and the analysis assumes that the detection probability increases with crack size. Since it is assumed that the inspection process is in a state of control, there is a range of crack sizes over which the POD(a) function is rising. In this crack size range of inspection uncertainty, the inspection system has limited discriminating power in the sense that detecting or failing to detect would not be unusual. Such a range might be defined by the interval ($a_{0.10}$, $a_{0.90}$), where a_p denotes the crack size that has probability of detection equal to p; that is, POD(a_p) = p. Cracks smaller than $a_{0.10}$ would then be expected to be missed and cracks greater than $a_{0.90}$ would be expected to be detected.

In a hit/miss capability demonstration, cracks outside the range of uncertainty do not provide as much information concerning the POD(a) function as cracks within this range. Cracks in the almost certain detection range and almost certain miss range provide very little information concerning probability of detection. In the hit/miss demonstration, not all cracks convey the same amount of information and the "effective" sample size is not necessarily the total number of cracks in the experiment. For example, adding a large number of very large cracks does not increase the precision in the estimate of the parameters of the POD(a) function.

Ideally, all of the cracks in a hit/miss demonstration would have 80 percent of their sizes in the ($a_{0.10}$, $a_{0.90}$) range of the POD(a) function. However, it is not generally possible to have a set of specimens with such optimal sizes for all demonstrations. The demonstrations are being conducted to determine this unknown range of sizes for the NDI system being evaluated. Further, because of the high cost of producing specimens, the same sets of specimens are often used in many different demonstrations. To minimize the chances of completely missing the crack size range of maximum information and to accommodate the multiple uses of specimens, the sizes of cracks in a specimen set should be uniformly distributed between the minimum and maximum of the sizes of potential interest. A minimum of 60 cracks should be distributed in this range, MIL-HDBK-1823, but as many as are affordable should be used. This minimum sample size recommendation was the result of subjective considerations as to the number needed to make the asymptotic assumptions reasonable, experience in applying the model to data, and the results of analysis from a number of simulated POD demonstrations [Berens & Hovey, 1981; Berens & Hovey, 1984; and Berens & Hovey, 1985].

Sample Size Requirements for Binomial Analysis

When capability is to be demonstrated by using specimens with cracks of the same size and the binomial analysis, the number of cracks in the specimens can be determined exactly from the POD level and the desired degree of confidence. The best (maximum likelihood) estimate of the POD at the crack length of interest is the proportion of cracks in the specimen set that are detected. A lower bound on the estimate is then calculated for the desired confidence level using binomial distribution theory. For example, to demonstrate that there is 95 percent confidence that at least 90 percent of all cracks of the size under consideration will be detected requires at least 29 cracks of that size. If all 29 cracks are detected, the maximum likelihood estimate of POD is 1.0 and the lower 95 percent confidence bound is slightly greater than 0.9. If any crack is missed, the lower confidence bound on the estimate of POD is less than 0.9. Sample sizes for the binomial analysis will be discussed further in the subsection on analysis methods.

It must be emphasized that the sample size is determined by the number of different cracks, not the number of inspections. Different cracks can respond differently to inspection stimuli. Multiple inspections of the same crack are not independent and, therefore, cannot be treated as independent samples from the population of cracks of the given size. There is a tendency to re-inspect specimens to increase the sample size. For example, if one of 29 cracks is not detected, the inspection does not qualify for an $a_{90/95}$ capability at that size. The specimen set cannot be re-inspected with the expectation of passing the test for a sample size of 58. New specimens with different cracks must be used or the analysis is not valid.

Uncracked Inspection Sites

In the context of the preceding discussion, sample size refers to the number of known cracks in the specimens to be inspected during the capability demonstration. The complete specimen set should also contain inspection sites that do not contain any known cracks. If the inspection results are of the hit/miss nature, at least twice as many uncracked sites as sites are recommended. The uncracked sites are necessary to ensure that the NDI procedure is truly discriminating between cracked and uncracked sites and to provide an estimate of the false call rate. If the NDI system is based on a totally automated $\hat{a}$ versus a decision process, many fewer uncracked sites will be required. If any $\hat{a}$ values are recorded at the uncracked sites, their magnitude would provide an indication of the minimum thresholds that might be implemented in the application.

3.1.2.4 POD Analysis

As noted there are two approaches to quantifying NDI capability – fitting a model that expresses probability of detection as a function of crack size and demonstrating a POD capability for a particular crack size. Data from the single crack size demonstration approach are analyzed using a straightforward binomial distribution analysis. Fitting a POD(a) model to the results of an NDI demonstration depends on the nature of the data (hit/miss or $\hat{a}$ versus a), the function chosen to represent POD(a), and the method for fitting the parameters of the function and determining the confidence bound on the reliably detected crack size. Experience with $\hat{a}$ versus a data from eddy current inspections has shown that a cumulative normal equation provides a reasonable model for the POD(a) function when transformations of crack size or inspection signal response are considered. Further, Berens and Hovey [1981], showed that the lognormal cumulative distribution provided as good or better a model than the eight others that were considered. Accordingly, the Air Force has generally adopted the cumulative normal distribution function as the model for POD(a) analyses. Note that the cumulative lognormal model is the cumulative normal model after crack size is transformed. The log odds equation is also often used to fit NDI data. The log odds equation and the cumulative lognormal equation are essentially indistinguishable.

A computer program, POD Version 3, is recommended by MIL-HDBK-1823 for the analysis of both $\hat{a}$ versus a and hit/miss POD(a) analyses (see also Berens [2000]). The program calculates the maximum likelihood estimates of the cumulative normal model as well as confidence bounds on estimates of a_p. The program permits transformations of the data. Since the default analysis is based on the natural logarithm transformation, the default analysis is for the cumulative lognormal POD(a) function. In POD Version 3, data are input through an Excel spreadsheet and output is provided as separate tables and graphs in the spreadsheet.

The following paragraphs present a general description of the analysis methods.

$\hat{a}$ Versus a Analysis

All NDE systems make find/no find decisions by interpreting the response to an inspection excitation. In some inspections, the response is a recordable metric, $\hat{a}$, that is related to the flaw size. Find/no find decisions are made by comparing the magnitude of $\hat{a}$ to the decision threshold value, $\hat{a}_{dec}$. The $\hat{a}$ versus flaw size analysis is a method of estimating the POD(a) function based on the correlation between $\hat{a}$ and flaws of known size, a. The general formulation of the $\hat{a}$ versus a model is expressed as

$$\hat{a} = f(a) + \delta \tag{3.1}$$

where $f(a)$ represents the average (or median) response to a crack of size a and δ represents the sum of all the random effects that makes the inspection of a particular crack of size a different from the average of all cracks of size a. In principle, any f(a) and distribution of δ that fit the observations can be used. However, if f(a) is linear in a,

$$\hat{a} = B_0 + B_1 a + \delta \tag{3.2}$$

and δ is normally distributed with constant standard deviation, σ_δ, then the resulting POD(a) function is a cumulative normal distribution function. Monotonic transformations of $\hat{a}$ or a can be analyzed in this framework. In fact, the model has been shown to fit a large number of cases in which a logarithmic transformation of both a and $\hat{a}$ was applied.

As an example consider the formulation of the $\hat{a}$ versus a analysis that has been used exclusively in the evaluation of the RFC/ENSIP automated eddy current inspection system. The relation between $\hat{a}$ and a is expressed in terms of the natural logarithms of $\hat{a}$ and a.

$$ln\,\hat{a} = B_0 + B_1 \bullet ln\,a + \delta \tag{3.3}$$

where δ is Normal (0, σ_δ). For a decision threshold of $\hat{a}_{dec}$,

$$POD(a) = \Phi\left[\frac{ln\,a - \mu}{\sigma}\right] \tag{3.4}$$

where $\Phi(z)$ is the cumulative standard normal distribution function and

$$\mu = \frac{ln\,\hat{a}_{dec} - B_0}{B_1} \tag{3.5}$$

$$\sigma = \sigma_\delta / B_1 \tag{3.6}$$

The calculation is illustrated in Figure 3.1.5. The parameters of the $\hat{a}$ versus a model (B_0, B_1, and σ_δ) are estimated from the data of the demonstration specimens. The probability density function of the ln $\hat{a}$ values for a 13 mil crack depth is illustrated in the figure. The decision threshold in the example is set at $\hat{a}_{dec}$ = 165. The POD for a randomly selected 13 mil crack would be the proportion of all 13 mil cracks that would have an $\hat{a}$ value greater than 165, i.e. the area under the curve above 165. In this example, the decision threshold was selected so that POD(13) = 0.90. The estimate of the POD(a) function and its 95 percent confidence bound for the decision threshold of 165 counts is presented in Figure 3.1.6. It might be noted that when all cracks have a recorded response between the signal minimum and maximum, the maximum likelihood estimates are identical with those obtained from a standard regression (least squares) analysis. However, when

crack response is below the signal minimum or above the maximum (saturation level of the recorder), more sophisticated calculations are required to obtain parameter estimates and the confidence bound. For complete details of the maximum likelihood calculations and more discussion of the $\hat{a}$ versus a analysis, see MIL-HDBK-1823, Berens [1988], and Berens [2000].

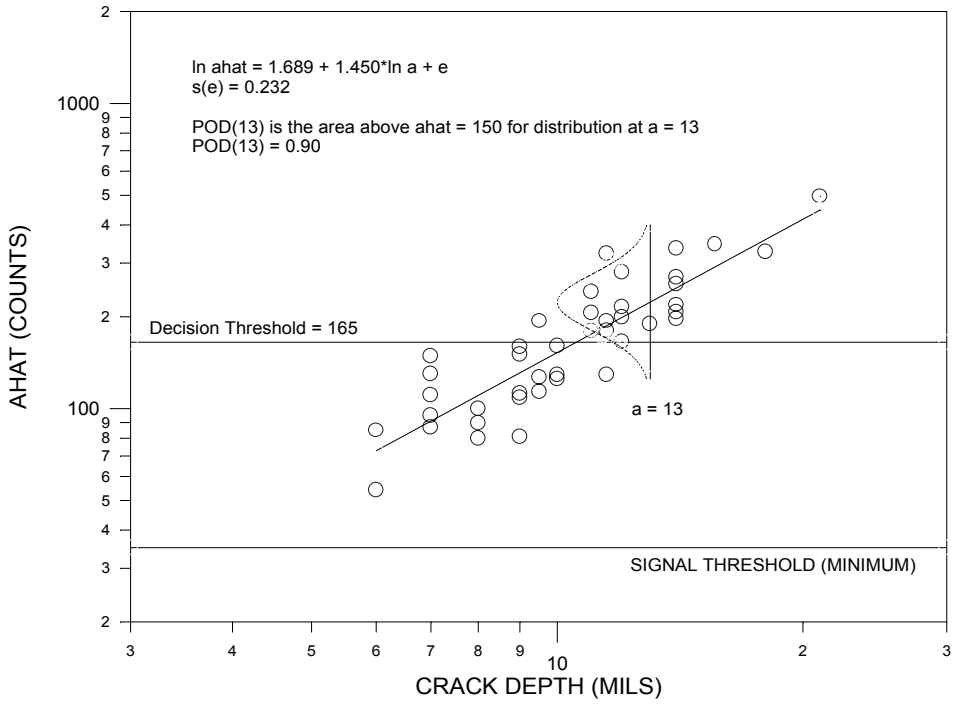

Figure 3.1.5. Example POD(a) Calculation from $\hat{a}$ versus a Data

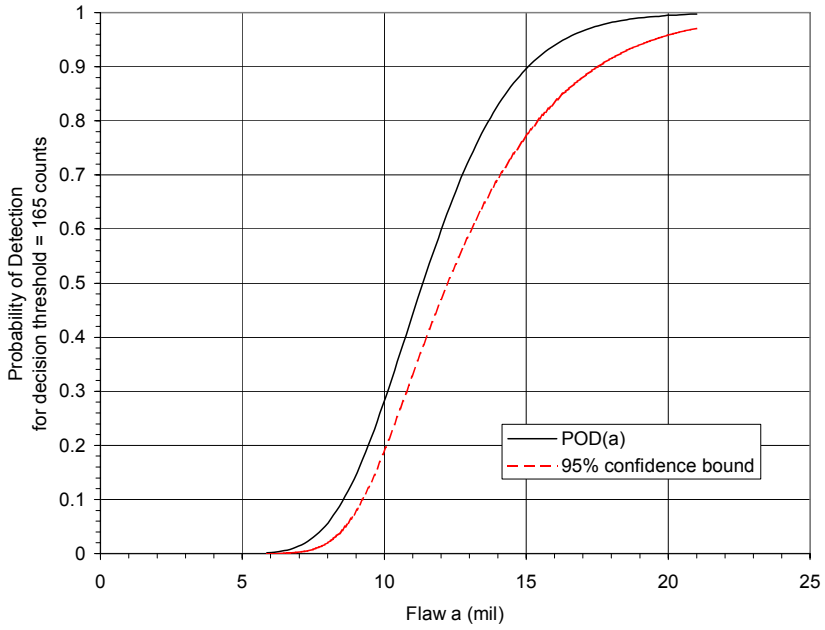

Figure 3.1.6. POD(a) Function with 95 Percent Confidence Bound for an Example $\hat{a}$ versus a Analysis

The preceding formulation of the $\hat{a}$ versus a model is based on three assumptions:

a) the mean of the log responses, ln $\hat{a}$, is linearly related to log crack size, ln a;

b) the differences of individual ln $\hat{a}$ values from the mean response have a normal distribution; and,

c) the standard deviation of the residuals, σ_δ, is constant for all a.

These assumptions can be tested using the results of the data from the demonstration. When the assumptions are not acceptable, current practice is to restrict the analysis to a range of crack sizes for which the assumptions are acceptable.

These assumptions can be easily checked and statistical tests for all three assumptions are built into the standard analysis of the POD Version 3 computer program of MIL-HDBK-1823.

If the ln $\hat{a}$ versus ln a relation is not linear, it may be possible to use other transformations of either the signal response or the crack size. If the three assumptions are reasonably valid for other transformations of the data, the above analysis can be applied using the different transformation. The inverse transformation of the results provides the answers in the correct units. Data sets have been observed in which no transformation was required and the fit was made directly to $\hat{a}$ versus a data (i.e. without the logarithmic transform). Other data sets have been analyzed in which the three assumptions were acceptable when the analysis was performed in terms of ln $\hat{a}$ versus $1/a$. It should be noted that extreme caution must be exercised when extrapolating the results beyond the range of crack sizes in the data. The POD Version 3 computer program has been designed to perform the POD analyses using transformations other than the logarithmic. The logarithmic transform of both crack size and inspection response is the default transform.

Hit/Miss Analysis

The results of an inspection system are often recorded only as a decision as to the presence (hit, find, or pass) or absence (miss, no find or fail) of a crack. The available data from the capability demonstration of such inspections comprise data pairs of crack size and the inspection result. The parameters of a POD(a) model for such data can be estimated using maximum likelihood as follows:

Let a_i represent the size of the i^{th} crack and Z_i represent the result of the inspection: $Z_i = 1$ if the flaw was found (hit) and $Z_i = 0$ if the flaw was not found (miss). Assume POD(a_i) is the equation relating probability of detection to flaw size for the inspection. The likelihood of obtaining a specific set of (a_i, Z_i) results when inspecting the specimens is

$$L(\theta) = \prod [POD(I)]_i^Z [1 - POD(a_i)]_i^{1-Z} \tag{3.7}$$

where $\theta = (\theta_1, \theta_2, \ldots, \theta_k)$ is a vector of the parameters of the POD(a) function. Values of $\theta_1, \theta_2, \ldots, \theta_k$ are determined to maximize L(θ). For typical POD(a) models, it is more convenient to perform the analyses in terms of logarithms.

$$ln\, L(\theta) = \sum Z_i \, ln\, POD(a_i) + \sum (1 - Z_1) \, ln[1 - POD(a_i)] \tag{3.8}$$

The maximum likelihood estimates are given by the solution of the k simultaneous equations:

$$\frac{\delta \, ln(\theta)}{\delta \theta_i} = 0, \quad i = 1, \ldots, k \tag{3.9}$$

In general, an iterative solution will be required to solve Equations 3.9.

Any monotone increasing function between zero and one can be used for POD(a). However, an early study of data with multiple inspections per crack [Berens & Hovey, 1981] indicated that the log odds or, equivalently, the cumulative lognormal models were more generally applicable than the others investigated. Further, the assumptions leading to a cumulative log normal model for the POD(a) function for $\hat{a}$ versus a data have often been verified for eddy current data. The log odds and cumulative lognormal models are equivalent in a practical sense in that the maximum difference in POD(a) between the two for fixed location and scale parameters is about 0.02 which is well within the scatter from repeated determinations of a POD(a) capability.

POD Version 3, the computer program recommended by MIL-HDBK-1823, is based on a cumulative normal equation but allows transformations of the crack size. The default transform of POD Version 3 is the natural logarithm transform so that the program will fit the cumulative lognormal equation by default. However, the program also provides a solution based on the log odds equation. Other models for the POD(a) function may be appropriate but, if preferred, would require a different computer implementation.

Repeating Equation 3.4, the cumulative log normal equation for the POD(a) functions is:

$$POD(a) = \Phi\left(\frac{\ln a - \mu}{\sigma}\right) \tag{3.10}$$

where $\Phi(z)$ is the standard normal cumulative distribution function. The log odds model for the POD(a) function is:

$$POD(a) = \left\{1 + exp-\left[\left(\frac{\pi}{\sqrt{3}}\right)\frac{(\ln a - \mu)}{\sigma}\right]\right\}^{-1} \tag{3.11}$$

Equation 3.10 or 3.11 is substituted in Equations 3.7 through 3.9 for POD(a). $\hat{\mu}$ and $\hat{\sigma}$ are determined so as to maximize $L(\mu, \sigma)$, the likelihood of obtaining the observed inspection results. Note that POD(μ) = 0.5 for both models. σ is a scale parameter that determines the degree of steepness of the POD(a) function. A negative value of σ is not contradictory but, for a negative σ, the POD(a) function will decrease with increasing a.

There are occasions when Equations 3.9 do not converge. No solution will be obtained if the sizes of found cracks do not overlap with the sizes of missed cracks. Little information is obtained from cracks that are so large they are always found or so small they are always missed. More overlap is needed for the cumulative lognormal model than for the log odds model. It is also possible to obtain negative estimates of σ from erratic data sets. Results of this nature are due to the wrong range of crack sizes in the demonstration or to an inspection process that is not under proper control. When the crack sizes in the specimens are not in the range of increase of the POD(a) function, the effective sample size is smaller and the effect is reflected in larger standard deviations of the sampling distributions of the parameter estimates and, thus, wider confidence bounds.

Damage tolerance analyses are driven by the single crack size characterization of inspection capability for which there is a high probability of detection. Typically, the one number characterization of the capability of the NDE system is expressed in terms of the crack length for which there is 90 percent probability of detection, a_{90}. But a_{90} can only be estimated from a

demonstration experiment and there is there is sampling uncertainty in the estimate. To cover this variability, an upper confidence bound can be placed on the best estimate of a_{90}. The use of an upper 95 percent confidence bound, the $a_{90/95}$ crack size has become the de facto standard for this characterization of NDE capability. The use of $a_{90/95}$ is intended to be conservative from the viewpoint of damage tolerance analyses.

In the hit/miss analysis of POD Version 3 a single value of POD(a), say 0.90, is selected and an upper confidence bound, say 95 percent is calculated for the POD value. This procedure is known as a point by point confidence bound. These are valid confidence bounds for any one POD value but not for the entire POD(a) curve.

The confidence bounds for the estimates of a_{90} are calculated using the asymptotic normality properties of the maximum likelihood estimates [Berens, 2000]. Figure 3.1.7 presents an example of a fit to hit/miss data from a semi-automated, directed eddy current inspection.

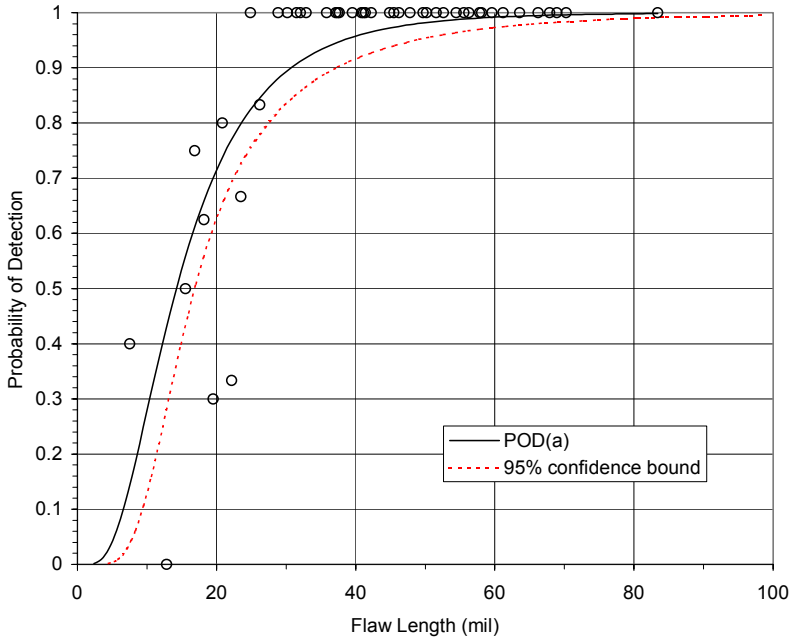

Figure 3.1.7. Example POD(a) for a Semi-Automated, Directed Eddy Current Inspection

Binomial Analysis for Cracks of Fixed Size

Because of the individual physical differences between cracks, cracks of the same size will have different detection probabilities for a given NDI system. However, a single POD for all cracks of that size can be postulated in terms of the probability of detecting a randomly selected crack from the population of all cracks of the given size. In this formalism, the proportion detected in a random sample of the cracks is an estimate of POD for that size and binomial distribution theory can be used to calculate a lower confidence bound on the estimate. Given a sample of inspection results from cracks of a target size, say a_{NDI}, the inspection system is considered adequate if the lower confidence bound on the proportion of detected cracks exceeds the desired POD value.

The theory of the binomial analysis is as follows. Given independent inspection results from specimens containing n cracks of size a_{NDI}, the target reliably detected crack size. Assume that r

of the cracks are detected. If POD is the true (but unknown) probability of detection for the population of cracks, the number of detections is modeled by the binomial distribution. The probability of r detections in n independent inspections of cracks of size a_{NDI} is:

$$P(r) = \frac{n!}{(n-r)!} POD^r (1 - POD)^{n-r} \tag{3.12}$$

The unbiased, maximum likelihood estimate of POD is

$$\overline{POD} = r / n \tag{3.13}$$

The 100(1-γ) percent lower confidence bound, POD_{CL}, on the estimate of POD is obtained as the solution to the equation:

$$\gamma = \sum_{i=r}^{n} \frac{n!}{(n-1)!\,i!} POD_{CL}{}^{i} (1 - POD_{CL})^{n-i} \tag{3.14}$$

The interpretation of POD_{CL} as a lower confidence bound is as follows. If the demonstration was completely and independently repeated a large number of times, 100(1-γ) percent of the calculated lower bounds would be less than the true value of POD. There is 100(1-γ) percent confidence that POD_{CL} from a single demonstration will be less than the true value.

Solutions to Equation 3.14 are tabulated in Natrella [1963] for 90, 95, and 99 percent confidence limits and selected sample sizes. General solutions expressed in terms of the incomplete beta function and the normal approximation to the binomial distribution can be found in many statistical references, for example, Mood [1950]. Minimum values of n and r which yield predefined values of POD_{CL} and confidence level, 100(1-γ), are often quoted. Selected values can be found in Packman, et al. [1976].

For example, consider a demonstration that there is 95 percent confidence that at least 90 percent of all cracks of size a_{NDI} will be detected by a given inspection system. To achieve the desired level of confidence and POD would require results as given in Table 3.1.2.

Table 3.1.2. Minimum Number of Detections Require to Conclude that POD > 0.90 with 95 Percent Confidence

Number of Cracks of Size a_{NDI}	Number of Cracks Detected
29	29
46	45
61	59
75	72
89	85
103	98

If there were 28 cracks in the demonstration and all 28 were detected, the lower 95 percent confidence bound on the estimate of POD would be 0.899. If less than 28 were detected, the lower confidence bound would be even lower. Since the minimum number of specimens that

can yield a 90 percent POD at 95 percent confidence is 29, this approach to capability demonstration has been referred to as the "29 out of 29" method.

There are several objections to the use of this approach to quantifying inspection capability:

1) This demonstration approach to capability provides only minimal and reasonably gross POD information for the single crack size used for the inspections. Steep POD(a) functions are generally considered superior to flat POD(a) functions and a single crack size capability demonstration provides no information regarding POD(a) steepness.

2) Passing or failing the demonstration provides no discrimination of degree of detectability at the high POD levels. For example, consider the 29 finds out of 29 cracks criterion for demonstrating the 90/95 capability. If the true POD is less than 0.9, there is up to a 5 percent chance that the demonstration will conclude that the true POD is 0.9 or greater. Conversely, if the true POD is 0.995, there is a 15 percent chance that at least one crack out of 29 will be missed and the demonstration will fail to conclude that there is 95 percent confidence that the POD is greater than 0.9. At POD = 0.976, there is about a fifty-fifty chance of concluding the POD is greater than 0.9. POD(a) tends to be relatively flat above 0.9 and there could easily be a very large crack size difference between, say, a 0.9 capability and 0.995 capability. Even when crack detection is absolutely certain for the given size, only a 90/95 capability can be claimed after the demonstration.

3) When attempting to demonstrate a 90/95 capability and one crack out of 29 is missed, the demonstration must be repeated with at least additional 17 cracks. Since demonstrations are planned with the expectation of meeting the criteria, the need for additional specimens can create significant problems.

For these reasons, quantifying inspection capability in terms of the entire POD(a) function has evolved as the preferred method [MIL-HDBK-1823].

It might be noted that attempts have been made to use a binomial approach to the analysis of demonstration data comprising a range of crack sizes [Yee, et al., 1976]. These approaches have been generally abandoned but a Bayesian approach to such analyses is being considered [Bruce, 1998].

3.1.3 NDI Capability Evaluation for Corrosion

The impact of corrosion on the sustainment costs of an aging fleet is significant, particularly for transport aircraft. The presence of corrosion indicates a failure of the corrosion protection system and necessitates some sort of action in the maintenance plan. Regardless of the corrosion control maintenance strategy, NDI plays an important role in its implementation and the need exists to quantify the corrosion detection capability of the inspection system.

Several types of corrosion are typically found in aging airframes – uniform, pitting, intergranular, exfoliation, crevice (uniform and pitting), and stress corrosion cracking. Adaptations of the standard NDI methods discussed in Subsection 3.1.1 can be used to detect the various types of corrosion damage and new inspection methods are evolving. Although there is a need to quantify the corrosion detection capability of an NDI system, at present there is no commonly accepted procedure for doing so. Approaches to characterizing corrosion detection capability can be found in Alcott [1994], Howard and Mitchell [1995], Roach [1997], Komorowski, et al. [1998],

and Hoppe, et al. [2000]. This subsection discusses two of the major problems in quantifying NDI capability for detecting corrosion and describes the method of Hoppe, et al. [2000].

3.1.3.1 Corrosion Metrics

When characterizing the NDI capability for detecting cracks, the natural metric for measuring crack damage was the linear crack dimension used in damage tolerance analyses. The selection of the appropriate metric for corrosion damage, however, is not immediately apparent. There are different types of corrosion damage and different metrics can be used to quantify the damages. For example, in hidden corrosion in lap joints and doublers on fuselage structures there are several possible metrics: thickness loss, pit depth and/or frequency, surface roughness, and joint pillowing. When inspecting for intergranular and exfoliation corrosion, around fasteners, useful metrics might be the maximum radial distance that the corrosion extends from the fastener hole or the corrosion area about each fastener. In some sense, each metric plays a role in the effect that the corrosion defect has on the structure. Consequently, it is important to consider all of the metrics for a given application. Each corrosion type must be considered separately, but the important aspect of the metric is that it measures corrosion severity. Ideally, the metric should be based on an "effect of defects" study; however, in practice the important metrics are generally known, and, in order to keep the assessment focused, it becomes necessary to select only one metric at a time for detection assessment. If it is absolutely essential to include an evaluation of more than one metric, then multiple evaluations must be performed (one evaluation per metric).

There is a necessary relation between the corrosion metric and the NDI technique. Obviously, the NDI technique must be responsive to changes in the corrosion damage metric. For example, in inspecting for hidden corrosion in lap joints, eddy current is responsive to thickness loss but may not be sufficiently responsive to pit depth. If pit depth is a critical parameter, a different NDI technique would be needed.

3.1.3.2 Corrosion Specimen Selection and Design

In the case of a crack detection assessment, representative cracks can be grown quite successfully in the laboratory. Since methods of corrosion growth are not well established, most notably for hidden corrosion, at present it is necessary to include real aircraft pieces with real corrosion in the specimen sets to be used in NDI capability demonstrations. Finding specimens with appropriate levels of corrosion is not a trivial problem. Potential specimens can be obtained from obsolete aircraft and from depots. While such specimens may contain real corrosion, they are not necessarily representative for a particular application. Further, a "good" NDI system for detecting hidden corrosion would be needed to select the specimens with varying degrees of corrosion damage. On the other hand, this situation does not eliminate the need for engineered and manufactured specimens. These specimens provide a level of control not available with the aircraft specimens. The type, location, and size of the defect (as measured by the chosen metric) can be controlled. The particulars of the engineered specimens must be determined from the specific metric chosen and the application. For thickness loss between layers, engineered specimens might include machined out areas of various depths and lateral dimensions. Experiment objectives also impact specimen designs. For example, a spatial resolution test would require a specially designed and manufactured specimen.

3.1.3.3 Example of Evaluating the Capability of an Eddy Current Inspection to Detect Hidden Corrosion in Lap Joints

The following example presents the results of an evaluation of an eddy current inspection for corrosion damage in C/KC-135 lap joints taken from Hoppe, et al. [2000]. For the example, the corrosion damage metric was taken to be thickness loss as thickness loss is an important criteria in judging severity of corrosion damage and eddy current is sensitive to thickness loss in the top layer of the lap joint.

Both real and engineered specimens were used for the capability demonstration. Several pieces from C/KC-135 and Boeing 707 fuselages were acquired. The specimens represented areas of interest on the aircraft and were expected to contain representative amounts of crevice corrosion. The specimens included fuselage lap joint and doubler sections that were anticipated to contain corrosion, as determined by disassembly of adjacent pieces of the skin. The specimens also included areas of little or no corrosion. The specimens that were selected incorporated the type, material, size and spacing of fasteners, thickness and lay-up of skins, presence of substructure, and specimen curvature variability that were expected to be experienced in typical aircraft inspections.

An engineered specimen was designed and manufactured for measuring the spatial resolution of the eddy current system. Spatial resolution of the system was necessary in to order to ascertain inspection regions of complete independence of the eddy current response. This specimen was constructed with several sets of lines of different widths machined in to the back surface of the front layer of an assembly of aluminum layers.

Specimens of a skin configuration were inspected using the eddy current system. NDI responses were recorded at independent sites within each specimen producing an inspection output profile of the specimen. Because thickness loss due to corrosion is variable within a specimen, the responses at the independent sites represent different samples of response at different thickness losses. The process is illustrated in Figure 3.1.8. The eddy current output at a point, *P*, in a response image is a function of the corrosion in a small region (or cell), *C*, on the specimen. The set of non-overlapping cells represents the collection of independent inspection opportunities from which probability of detection as a function of thickness loss can be calculated.

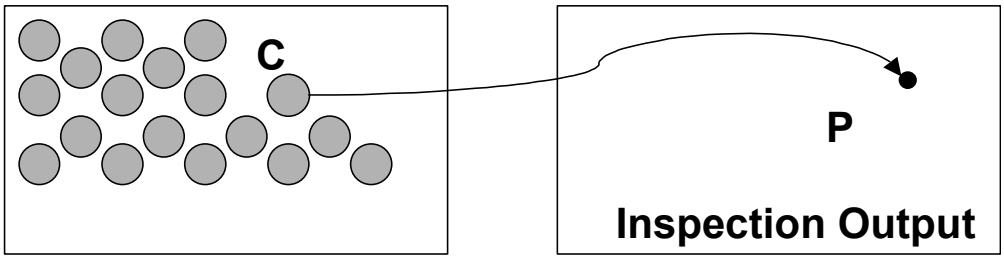

Figure 3.1.8. Schematic Diagram of Specimen and Inspection Output Images

After completion of the inspection of a specimen, the actual corrosion profile of the specimen was determined. The specimens were carefully disassembled by drilling out the fasteners and prying apart the layers. Corrosion products were chemically removed using a high concentration nitric acid exposure protocol. Measurement of remaining thickness was accomplished using calibrated topographic radiography. The inspection system output images and actual thickness

loss profiles were registered to specimen features, such as fasteners and lap joint edges, in order to relate measured to actual thickness loss across each specimen.

Data pairs of real and EC measured thickness loss were generated for the independent inspection cells. The data pairs are plotted analogously to the $\hat{a}$ versus a plot of crack detection POD estimation. Figure 3.1.9 is an example of thickness loss versus EC response for one of the structural configurations. The scatter of the EC responses about the mean trend determines the POD as a function of thickness loss. Figure 3.1.10 shows the POD function for a threshold chosen to yield 90 percent detection for a 10 percent thickness loss. Also shown in Figure 3.1.10 is the 95 percent confidence bound on the POD function.

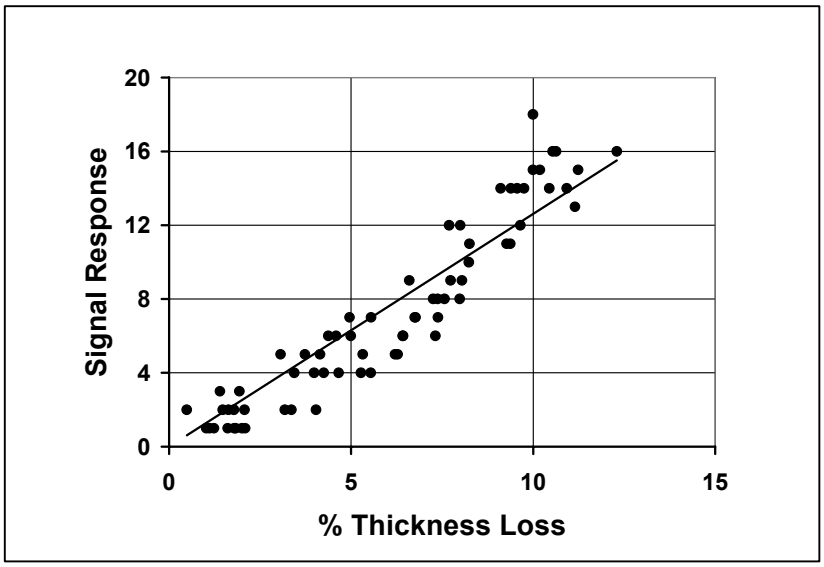

Figure 3.1.9. Example Eddy Current Response for Cells of Different Thickness Loss

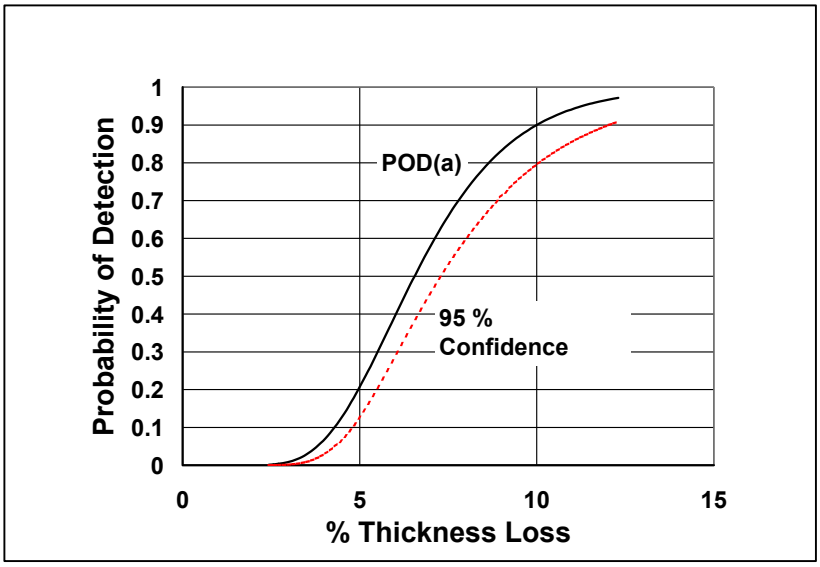

Figure 3.1.10. POD versus Percent Thickness Loss with Response Detection Threshold Set to Yield POD of 90 percent at 10 percent Loss

3.2 Equivalent Initial Quality

The requirements of JSSG-2006 specify that initial flaws shall be assumed to exist as a result of manufacturing and processing operations. Small imperfections, equivalent to a 0.005 in. radius corner crack, resulting from these operations shall be assumed to exist in each hole of each element in the structure. These assumed cracks provide the basis for the fastener policy requirements as well as the continuing damage and remaining damage assumptions. However, if the contractor has developed initial quality data on fastener holes, these data may be submitted to the procuring activity for review and serve as a basis for negotiating a different size than the specified 0.005 in. radius corner flaw.

One method of accounting for the initial quality is to represent the quality in terms of an equivalent fatigue crack of a particular size and shape. Such a method of quantifying the initial quality is the Equivalent Initial Quality Method [Rudd & Gray, 1976; Rudd & Gray, 1978; Pinckert, 1976; Dumesnil, et al., 1977; and Potter, 1978]. The Equivalent Initial Quality method for characterizing manufacturing quality is described in the Subsection 3.2.1 and demonstrated by example in Subsection 3.2.2.

The concept of a distribution of flaw sizes for a population of structural details that will experience equivalent stresses in operational usage has been applied in more general contexts than characterizing initial quality. In particular, this concept plays a central role in a probabilistic approach to characterizing structural durability and in structural risk analyses. These uses of flaw size distributions will be briefly discussed in Subsection 3.2.3

3.2.1 Description of Equivalent Initial Quality Method

The Equivalent Initial Quality Method is presented for fastener holes since this is the most prevalent source of cracking in aircraft structures [Rudd & Gray, 1978]. Quality may be defined as a measure of the condition of the structure relative to imperfections, flaws, defects, or discrepancies that are either inherent in the material or introduced during manufacturing of the structure. The approach is to quantify these imperfections by representing them with fatigue cracks of a particular size and shape, such as the corner cracks illustrated in Figure 3.2.1. Also illustrated in Figure 3.2.1 are some of the parameters that can contribute to the initial quality of fastener holes. If an initial quality representation is performed for each of a number of fastener holes, an equivalent initial quality statistical distribution can be used to quantify the quality of the fastener holes produced by certain manufacturing and processing procedures [Potter, 1978].

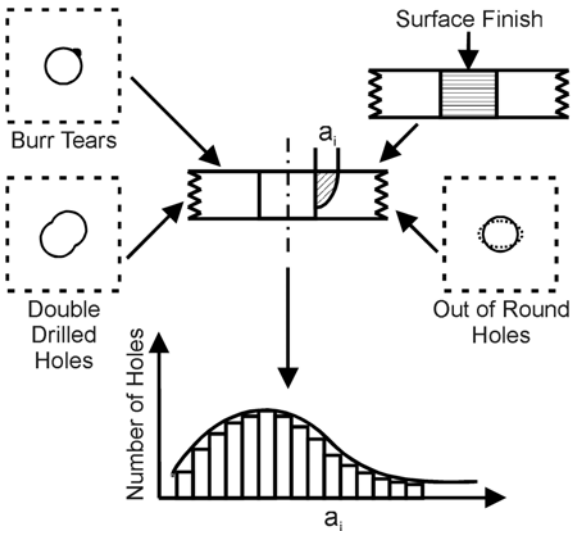

Figure 3.2.1. Parameters that Affect Fastener-Hole Initial Quality [Rudd & Gray, 1978]

The initial quality representation, defined as the equivalent initial quality, can be obtained in the following manner. Consider a piece of structure with a fastener hole containing the defect of characteristic dimension l (Figure 3.2.2). This defect results in fatigue crack initiation and propagation when subjected to some known load history. Upon failure of the structure, a fractographic examination of the fracture surface is performed to obtain as much of the crack growth curve as possible. Analytical crack propagation analyses are performed until there is good agreement between the analytical prediction and the fractographic test data. The initial crack length (crack length when the load history is first applied), a_i, of the analytical crack growth curve that correlates best with the fractographic test data is defined as the equivalent initial quality. Hence, a_i is said to be the analytical equivalent of the actual defect of characteristic dimension, l, if each results in a crack size a_e after N_e cycles of the same load history have been applied. Hence, fastener holes that contain actual crack lengths less than a_e after N_e cycles have been applied are of better quality than those that contain actual crack lengths equal to or greater than a_e after N_e cycles.

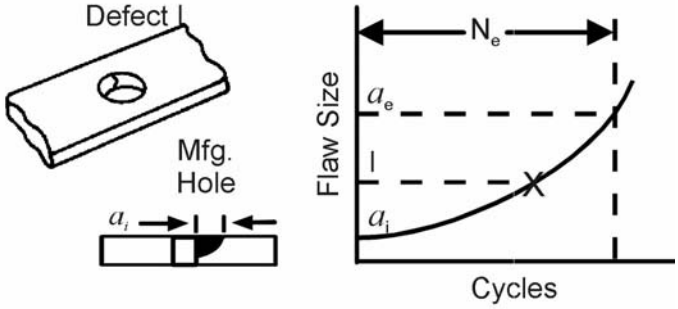

Figure 3.2.2. Definition of Equivalent Initial Quality [Rudd & Gray, 1978]

3.2.2 Example Application of Equivalent Initial Quality Method

Although Equivalent Initial Quality Method studies have been conducted on the F-4C/D [Pinckert, 1976], F-4E(S) [Pinckert, 1976], and A-7D [Dumesnil, et al., 1977], only a summary

of the quality assessment program by Rudd & Gray [1978] on the A-7D will be reviewed here. The remaining paragraphs in this subsection are taken directly from Rudd & Gray [1978]:

The purpose of the A-7D quality assessment was to establish the manufacturing quality (a_i) of the A-7D aircraft. This was accomplished using the Equivalent Initial Quality Method. The method was applied to a sample problem involving an A-7A wing fatigue test failure. Next, specimens were cut from an A-7D production aircraft and tested to failure under a selected block loading. The fracture surfaces were then fractographically examined and the equivalent initial quality was established.

A photograph of the failure area of a full-scale fatigue test of an A-7A wing was used as a sample problem to check out the Equivalent Initial Quality Method. The wing had been subjected to a 10-level, blocked, low-high stress spectrum. Fractographic measurements were taken from the photograph (Figure 3.2.3), making it possible to generate a large portion of the crack growth curve. Crack propagation analyses were performed using the computer routine EFFGRO and the Wheeler Retardation Model until the analytical crack growth curve correlated well with the fractographic test data. This correlation is presented in Figure 3.2.4, which indicates that the manufacturing quality of the test hardware at the failure location was equivalent to an initial crack of length $a_i = 0.00109$ in. This excellent correlation of the analytical crack growth prediction with the fractographic test supported the validity of the Equivalent Initial Quality Method for this particular problem.

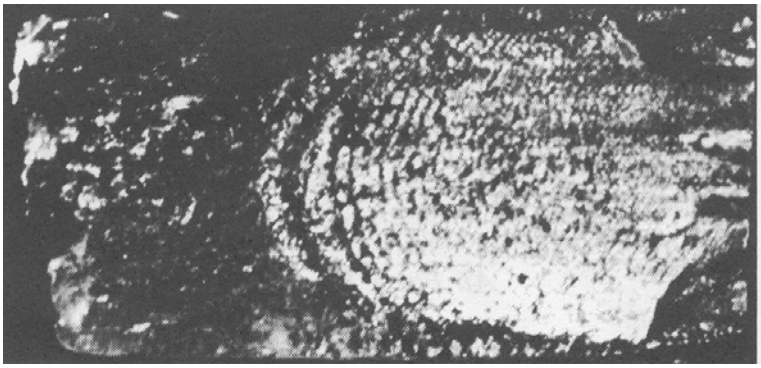

Figure 3.2.3. A-7A Wing Fatigue Test Fracture Surface [Rudd & Gray, 1978]

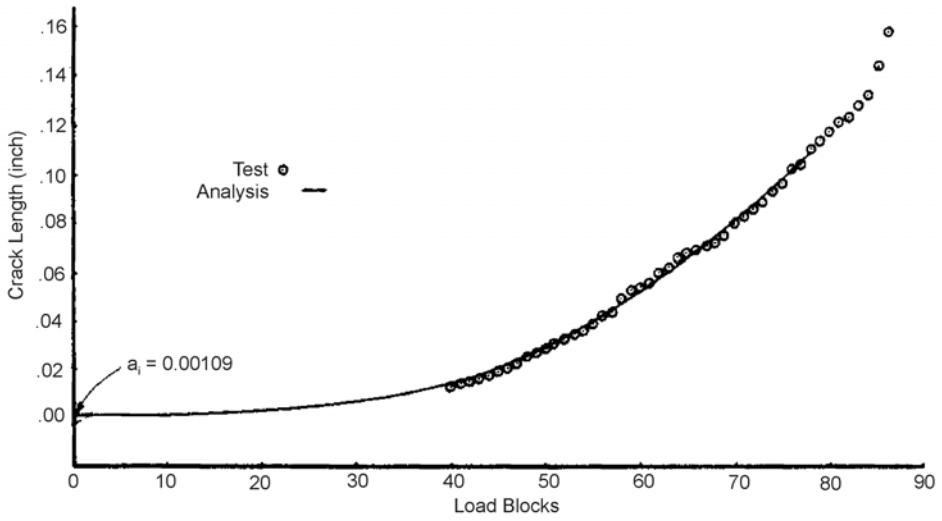

Figure 3.2.4. Equivalent Initial Quality Results for A-7A Wing [Rudd & Gray, 1978]

The Equivalent Initial Quality Method was next used to establish the A-7D quality assessment. This assessment was accomplished using test specimens cut from the lower wing skin of an A-7D production aircraft that had been used as a gunfire target. Because this particular aircraft had low flight time (691.9 hours), the probability of cracking in the wings was very low. The location of each specimen in the lower wing skin is illustrated in Figure 3.2.5. Each specimen was made of 7075-T6 aluminum and contained multiple holes. The geometric details for each specimen are presented in Table 3.2.1, indicating that the thickness ranged from approximately 3/16 in. to 1/4 in. and the nominal values of the width and hole diameter were 3 in. and 1/4 in., respectively. The specimens contained two types of holes – countersunk holes (wet-wing region) and straight-shank holes (dry-wing region).

The test specimens were subjected to a fatigue stress spectrum consisting of 5,000 cycles with a maximum stress of 20 ksi and a stress ratio of 0.1 followed by 100 cycles with a maximum stress of 30 ksi and a stress ratio of 0.1. The block spectrum was chosen because it produced test lives of reasonable length (less than 20 blocks) and fracture surfaces that were readily readable.

Table 3.2.2 contains a summary of the number of fastener holes involved, the number of flaws detected, the number of flaws fractographically examined, the crack length range at the time of specimen failure (a_f), and the range of the equivalent initial quality (a_i). All but two of the 44 holes contained double flaws. One of these two holes contained one crack, while no crack was detected in the other hole. This resulted in a total of 85 flaws, of which 44 were examined fractographically. The flaws were arbitrarily chosen for fractographic examination at magnifications ranging from 30x to 400x using a universal measuring microscope. The equivalent initial quality range for all the holes was found to be 0.00015 - 0.0022 in. A statistical distribution of the A-7D equivalent initial quality was obtained.

Table3.2.1. Geometric Details of A-7D Quality Assessment Specimens [Rudd & Gray, 1978]

Specimen	Thickness [a]	Width [a]	Hole Diameter [a]
101	0.226	2.93	0.253 [b]
201	0.226	2.93	0.253 [b]
301	0.217	3.00	0.253 [b]
401	0.231	3.00	0.253 [b]
501	0.183	2.90	0.253 [c]
502	0.176	3.00	0.253 [c]
601	0.263	3.00	0.253 [c]
602	0.264	3.00	0.253 [c]

[a] Dimensions in inches
[b] Countersunk hole
[c] Straight-shank hole

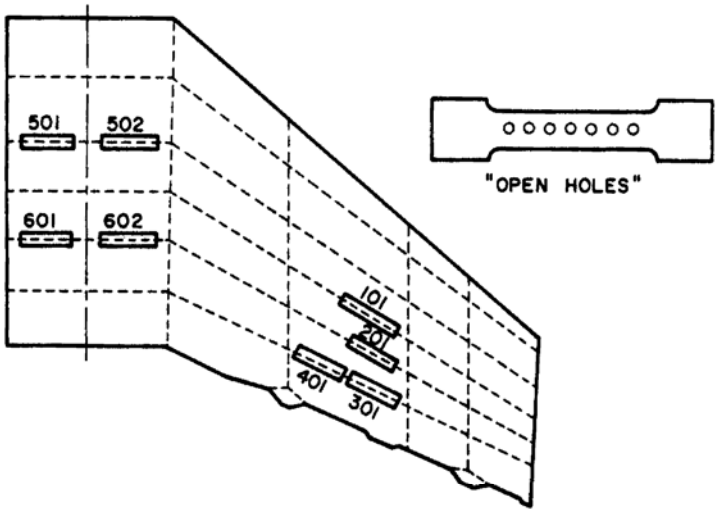

Figure 3.2.5. A-7D Quality-Assessment Specimen Locations [Rudd & Gray, 1978]

Table 3.2.2. A-7D Quality Assessment Test Results [Rudd & Gray, 1978]

Specimen	No. Holes	No. Flaws	a_f^a Range [a]	Flaws Tracked	a_i [a] Range
101	7	14	0.05-0.75	14	0.0004-0.0022
201	6	12	<0.01-1.10	12	0.0004-0.0012
301	4	8	0.01-0.65	1	0.0003
401	3	6	0.02-0.50	1	0.0002-0.0014
501	8	14	0.00-0.60	1	0.0007
502	8	16	<0.01-0.62	6	0.0006
601	4	8	0.02-0.50	8	0.00015-0.0009
602	4	7	0.00-1.05	1	0.0006
Total	44	85		44	

[a] Dimensions in in.

The fractographic examinations revealed the origins of the flaws for both the straight-shank holes and the countersunk holes as illustrated in Figure 3.2.6. There is equal possibility of flaw occurrence along the bore of the hole for the straight-shank hole, while the most frequently occurring flaw location for the countersunk hole is at the inside radius of the small-diameter portion of the hole. Typical flaw origins for each type of hole are shown on the fracture surfaces of Figure 3.2.7. Also illustrated in Figure 3.2.7 is the readability of the fracture surfaces for the selected stress spectrum, with the dark marking bands resulting from the application of the high-load (maximum stress of 30 ksi) portion of the specimen.

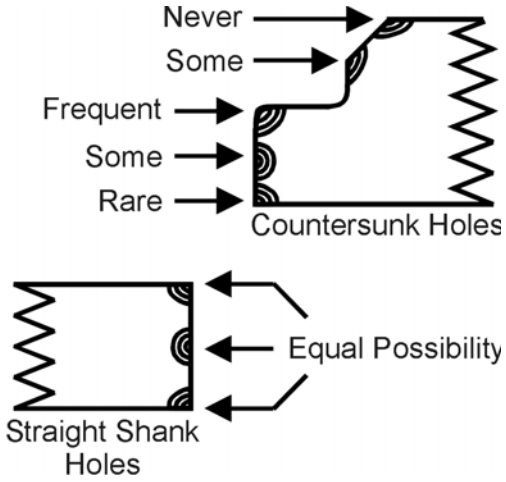

Figure 3.2.6. A-7D Flaws Origins [Rudd & Gray, 1978]

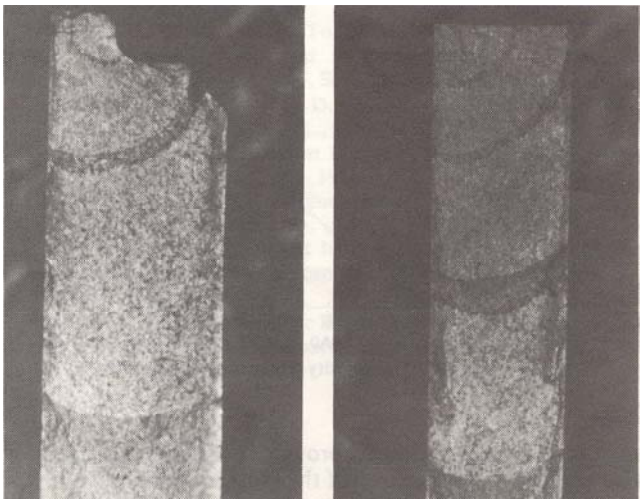

Figure 3.2.7. Fracture Surfaces for Countersunk (Left) and Straight-Shank (Right) Holes [Rudd & Gray, 1978]

Metallurgical investigations of the A-7D flaw origins revealed that the flaws were the result of two different sources-anodize pitting and mechanical sources. The majority of the flaws (86.4%) initiated from anodize pits in the following manner. Insoluble microconstituents were exposed along the bore of the hole during the hole-drilling operation. The anodizing ate away the microconstituents and caused pitting. The exposed pits were then filled with aluminum oxide, resulting in flaw initiation. The remaining flaws (13.6%) were due to the mechanical damage. Although anodizing provided corrosion protection, it also resulted in the majority of the fatigue cracks.

All but two of the holes contained double flaws, of which none were through-the-thickness flaws. The selected stress spectrum marked the fracture surfaces extremely well, making it possible to determine the crack length within each loading block. Hence, it was possible to fractographically determine the equivalent initial quality for each flaw examined.

Figure 3.2.8 presents the probability density of occurrence versus the equivalent initial quality for the A-7D aircraft. It should be noted that the A-7D equivalent initial quality was determined by fractography alone, since it was possible to measure the crack length during the application of the first block of loading.

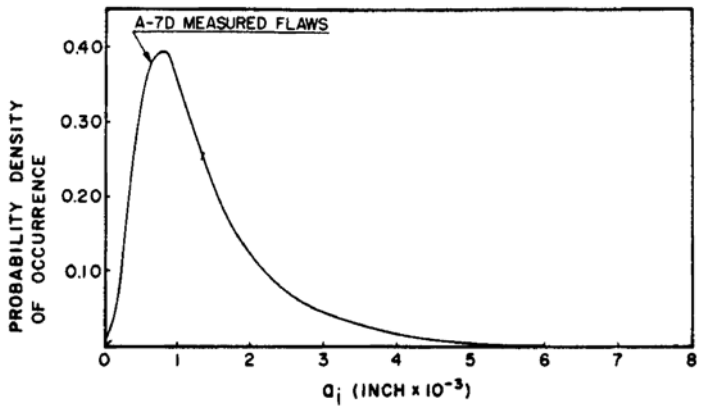

Figure 3.2.8. Probability Density of Occurrence of A-7D Equivalent Initial Quality [Rudd & Gray, 1978]

The probability density of occurrence (Figure 3.2.8) was used to determine the cumulative probability of occurrence for the A-7D aircraft. Figure 3.2.9 presents the cumulative probability of occurrence versus the equivalent initial quality for the A-7D and F-4 C/D aircraft. Also presented in Figure 3.2.9 is the cumulative probability of occurrence with 95% confidence for each aircraft. For example, Figure 3.2.9 indicates that with 95% confidence, 99.9% of the A-7D flaws have an equivalent length less than 0.007 in. This means that one out of a thousand flaws have an equivalent length greater than 0.007 in.

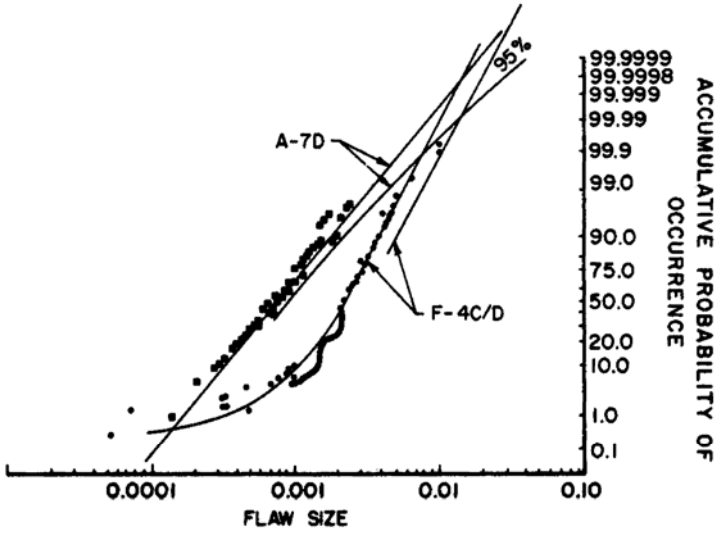

Figure 3.2.9. Cumulative Probability of Occurrence of A-7D Equivalent Initial Quality [Rudd & Gray, 1978]

3.2.3 Other Applications of Equivalent Flaw Size Distributions

The concept of a distribution of flaw sizes to model the physical condition of a population of structural details extends to areas other than manufacturing quality. In particular, characterizing

damage in terms of crack sizes has been applied to the demonstration of structural durability and the evaluation of structural failure probabilities in risk analyses.

3.2.3.1 Durability Analysis

A probabilistic approach to characterizing structural durability has been extensively explored by Manning and Yang [1987, 1989]. For the durability analysis, the growth of a distribution of equivalent initial flaw sizes for a population of structural elements is calculated as a function of flight hours in the expected usage environment. Durability is then characterized in terms of either the expected number of cracks that will exceed a fixed size as a function of flight hours or in terms of the distribution of flights to reach a crack of given size. These concepts are illustrated in Figure 3.2.10, from Manning & Yang [1989], in which:

- EIFSD represents the equivalent initial flaw size distribution of initial quality;
- $p(i, \tau)$ represents the distribution of number of cracks of a size larger than x;
- $F_{T(x)}(\tau)$ represents the distribution of service time to reach a crack of size x.

The EIFSD must be projected forward based on a crack growth methodology that is compatible with that used to produce the EIFSD. Manning and Yang recommend a combined deterministic crack growth analysis (DCGA) and stochastic crack growth analysis (SCGA) for projecting the EIFSD.

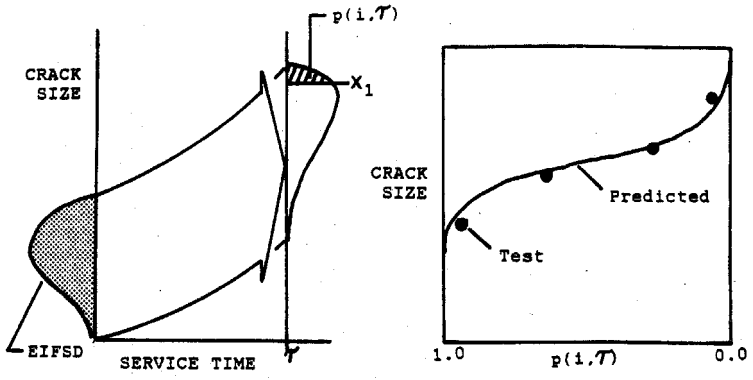

a) Probability of Crack Exceedance at Service Time τ

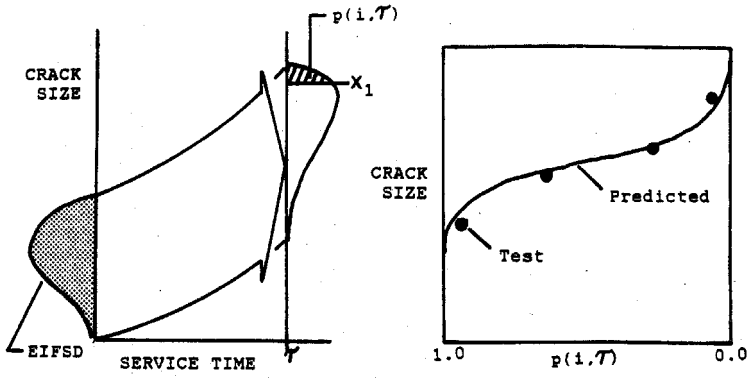

b) Cumulative Distribution of Service Time at Crack Size x_1

Figure 3.2.10. Schematic Using the Equivalent Initial Crack Size Distribution (EIFSD) for Durability Analysis

3.2.3.2 Risk Analysis

A number of structural risk assessments have been performed in which damage in the structural detail is modeled in terms of the distribution of cracks or equivalent cracks. Examples of such risk analyses can be found in Lincoln [1985], Berens, et al. [1991], Alford, et al. [1992] and Lincoln [1997]. If the risk analysis calculations start with a virgin structure the crack sizes are equivalent initial cracks. If the risk analysis is being performed for in-service or aging aircraft, the crack size distribution is usually obtained either from the sizes of the cracks discovered during fleet inspections or from tear down inspections of structures removed from the fleet. The cracks detected during fleet inspections would have experienced different total service times and would have to be translated to a common service age to obtain a representative crack size distribution for the population of details. The cracks from tear down inspections may be from one or many airframes. In either case, the crack sizes usually need to be translated to a common or different service age. Typically, to locate the crack sizes at a common number of flight hours, the crack sizes are translated using a fracture mechanics based crack size versus flight hour curve for expected or observed usage. This process is illustrated in Figure 3.2.11. After all cracks have

been translated to a common service age, a crack size distribution can be established for use in calculating probability of failure as a function of flight hours.

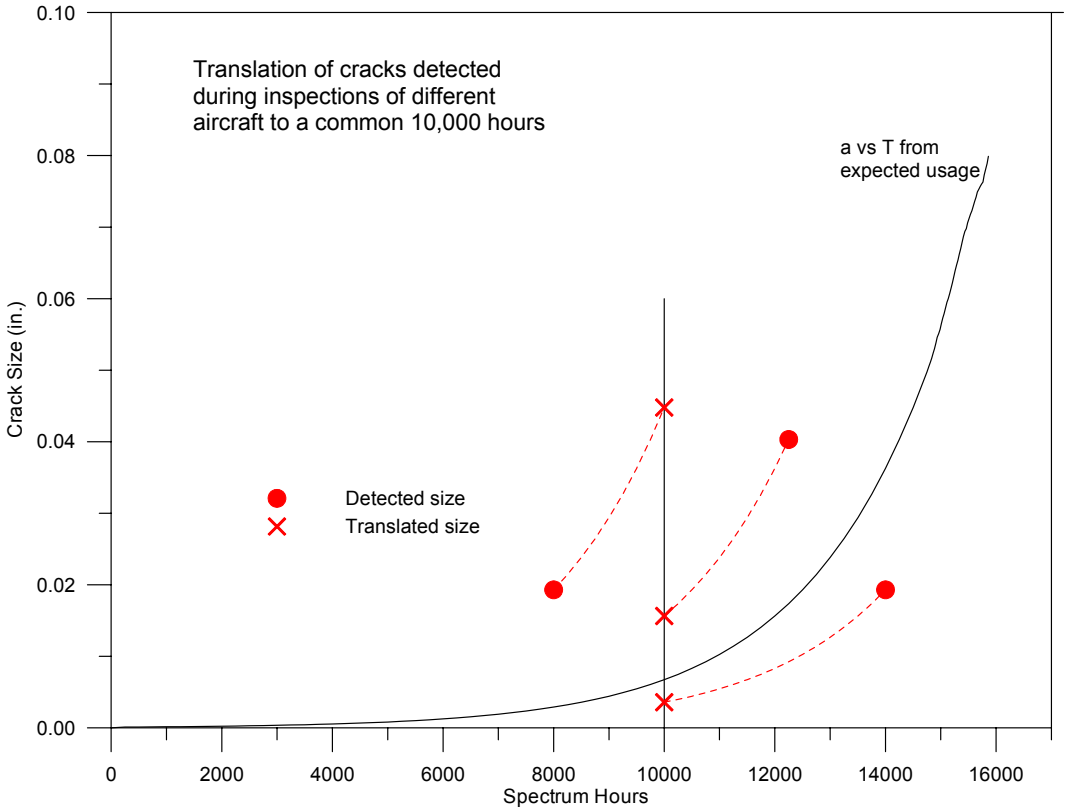

Figure 3.2.11. Schematic Demonstrating the Translation of Crack Sizes to a Common Size Using Predicted *a* versus T

3.3 Proof Test Determinations

Tiffany and Masters [1965] first suggested that the conventional structural proof test could be used to inspect for crack damage that would eventually lead to catastrophic failure. These techniques were first applied to rocket motor cases and tankage as a result of numerous missile launch failure at Cape Canaveral. Air Force acceptance of this proof test philosophy has been stimulated by the inability of alternate non-destructive inspection tools to reliably detect cracks of near-critical size. The Air Force in the recent past has employed the proof test as a means of determining the maximum possible initial flaw that could exist in the structural subsystems identified in Table 3.3.1. Note that almost all of the examples cited represent the application of the proof stress techniques as an In-service Inspection. Buntin [1971], Cowie [1975], Horsley, et al. [1976], Gunderson [1974] and Albrectsen & Aitken-Case [1976] document the Table 3.3.1 and other Air Force uses of the crack-inspection proof test. White, et al. [1979] documents the recent Navy proof test of an A-7 arresting hook; this proof test is periodically repeated to ensure the continuing structural integrity of the component.

The proof test concept for all applications has been to size or eliminate the life degrading damage so that the structure would maintain its required level of structural integrity throughout a defined period of usage. However, due to substantially different technical requirements, the proof testing techniques employed in each case were different. The technical requirements that establish the type of tests conducted have been structural geometry, material properties, type of crack damage present in the structure, as well as the crack growth mechanism.

Table 3.3.1. Proof Testing of Aircraft Structures

System	Subsystem	Damage	Special Techniques
F-111	Lower surface of inner wings and pivot fittings	Potential forging defects propagated due to fatigue in D6AC steel	Upwing bending at -40° F after every 1,000 hours of flight
B-1A	F-101 (Development) engine combustor case	Pores and inclusion stringers in circumferential butt welds in Inconel 901 alloy	Internal pressure to 200% operating pressure
B-52D	Center and inner wing structure	Fatigue and stress corrosion cracks nucleated during southeast Asia service in 7075-T6 and 7079-T6 aluminum alloy structure	Down and up-wing bending at ambient temperature
C-141	Main Landing gear (cylinder)	Hydrogen entrapped during refurbishment	500 hours of continuous static loading to initiate and propagate cracks to failure
A-7	Carrier arresting hook (Navy)	Fatigue cracking initiated during service	Repeat periodically

3.3.1 Description of the Proof Test Method

Tiffany and Masters [1965] utilized the proof test as a means of guaranteeing that a potentially cracked structure would not fail during a defined period of operation. This guarantee results from the fact that all the cracks remaining in a proof-loaded structure must be smaller than those cracks which would have failed the structure during the proof test. Since the proof test loadings are typically larger than the maximum operating conditions, the post proof-tested structure's cracks are also expected to be substantially smaller than the cracks which would cause failure under operating loads.

Figure 3.3.1 schematically illustrates a stress-crack length diagram that defined the levels of loading (proof stress and operational maximum stress) and the corresponding crack lengths associated with structural failure by fracture. It can be noted from Figure 3.3.1 that all cracks larger than a_i will cause the structure to fail during the proof test loading, thus guaranteeing a "minimum" safe crack growth interval between a_i and the crack size (a_{op}) at which the operating conditions will cause failure. The interval established is the minimum safe interval because the structure may initially have cracks that are substantially smaller than the guaranteed initial size (a_i).

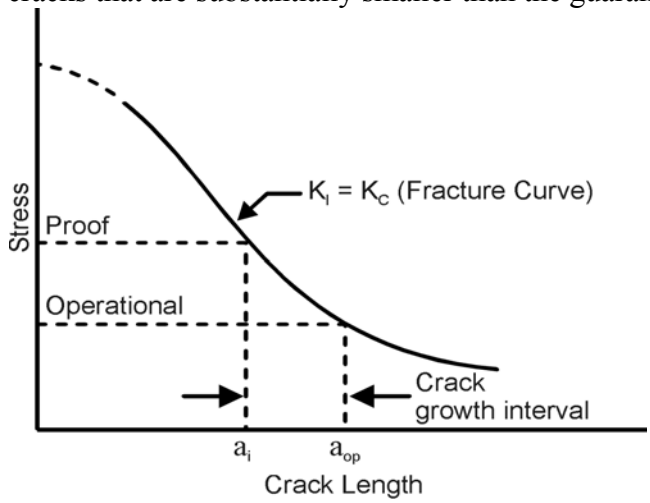

Figure 3.3.1. Fracture Critical Curve Defining Relationship Between Stress and Crack Length Associated with Fracture

Tiffany and Masters [1965] designed the proof test conditions so that all cracks initially present in the structure and of sufficient size that they could grow to failure during the planned service operating period would fail the structure during the proof test. If the operating conditions and the crack growth mechanisms are known, then a crack growth life calculation can be performed to establish the minimum safe crack growth interval during which failure will not occur during service. The minimum safe crack growth interval extends from the largest allowable initial crack size (a^*_i) and the crack size (a_{op}).

Figure 3.3.2 describes the interrelationship between the crack growth life and residual strength behavior of a structure and the stress-crack size diagram. As indicated in Figure 3.3.2 (right-hand side), the life limit associated with the crack growth process and the decay of the residual strength capability is lower than the service life requirement. An increase in the proof stress if required,

therefore, to decrease the corresponding crack size (a_i) to the maximum allowable crack size (a^*_i) and thus ensure a safe period of operation. Note that the stress-crack size diagram indicates that all cracks greater than a_i, present at the time of the proof test, will cause structure failure. Thus, the proof test ensures that when the structure enters service, its initial cracks will be no larger than the size associated with the proof test conditions.

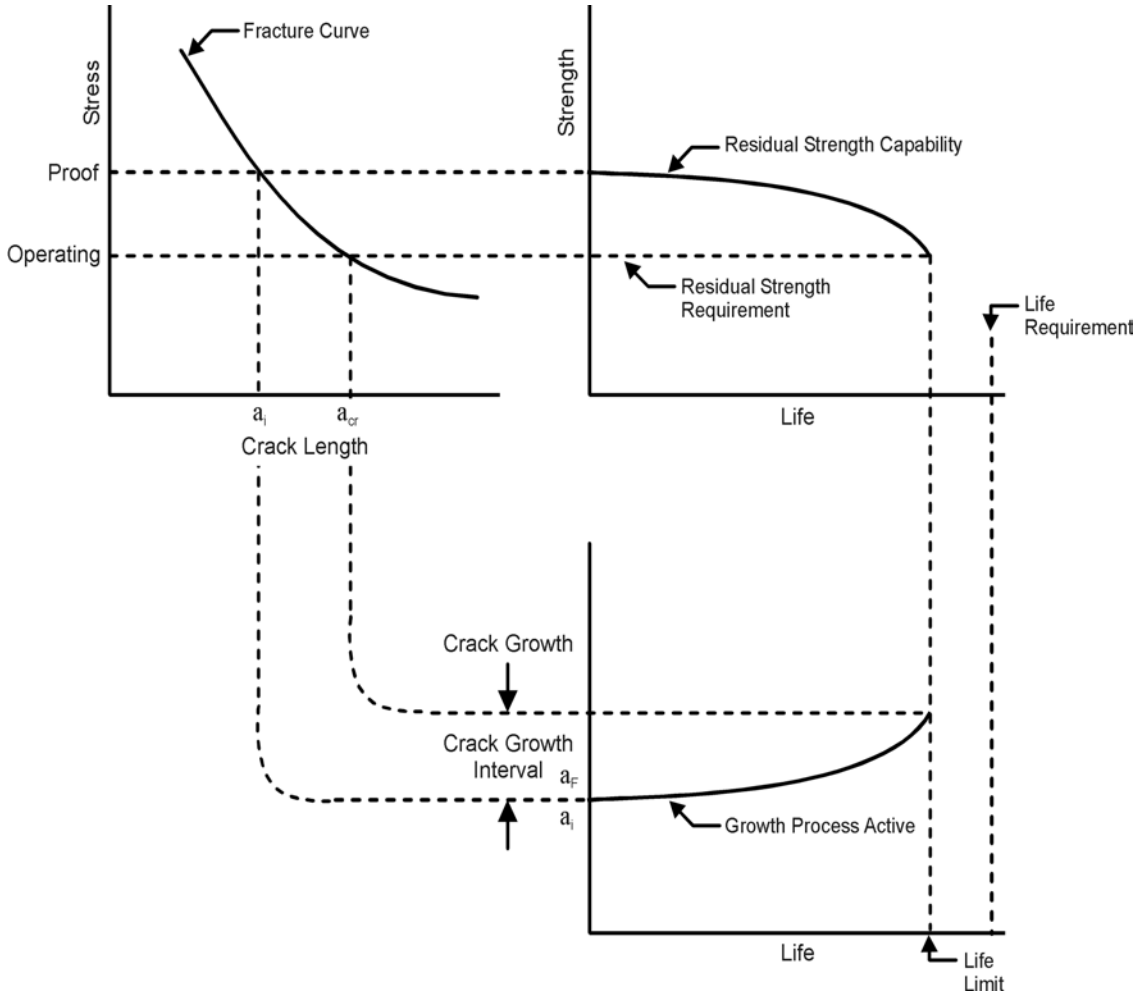

Figure 3.3.2. Schematic Illustrating the Relationship Between the Proof Test Diagram, the Residual Strength Capability and Crack Growth Life Interval

The levels of proof test stress and the material's fracture toughness combine to establish the maximum initial crack size guaranteed by the proof test. Because material and stress variations will exist throughout any proof loaded structure, the designer of a proof test must be aware of several important material variations which could significantly affect the post-proof test crack size distribution. These important material variations are caused by changes in temperature, loading rate, thickness, and yield strength. Figure 3.3.3 schematically describes how fracture toughness varies as a function of these parameters. Note that temperature and loading rate can affect some materials (some steels and titanium alloys are particularly susceptible) while other materials are unaffected. Aluminum alloys and many nickel-bases alloys exhibit almost no variation in fracture toughness as a function of temperature and strain rate).

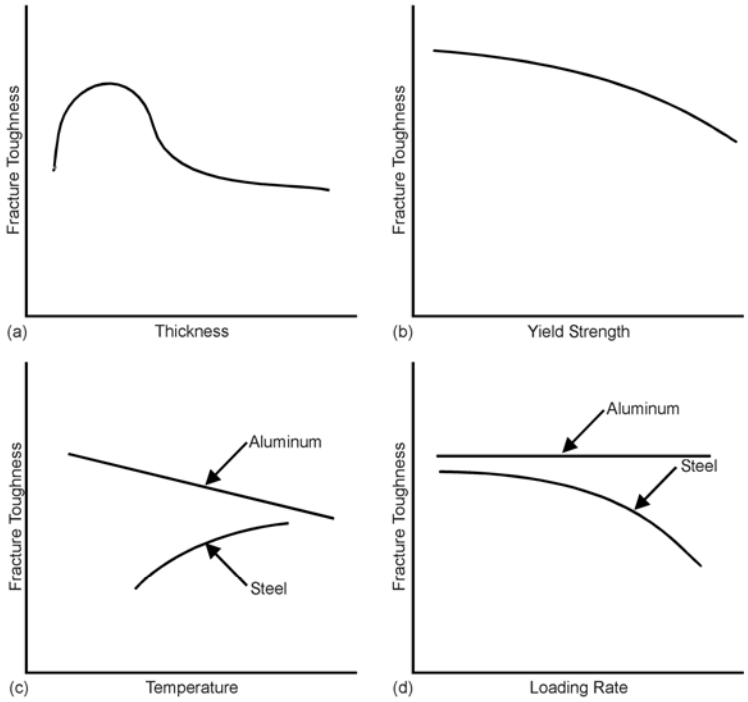

Figure 3.3.3. Fracture Toughness Varies as a Function of (a) Thickness, (b) Yield Strength, (c) Temperature, and (d) Loading Rate

Figure 3.3.4 provides an example of how a material's response to external stimuli can be utilized to increase the minimum safe crack growth interval. In Figure 3.3.4, a material's known response to temperature is utilized to select a low temperature condition for conducting the proof test. The lower fracture toughness exhibited at the low temperature is shown to extend the minimum safe crack growth interval substantially beyond what would have been expected for the same proof stress at the operating temperature conditions.

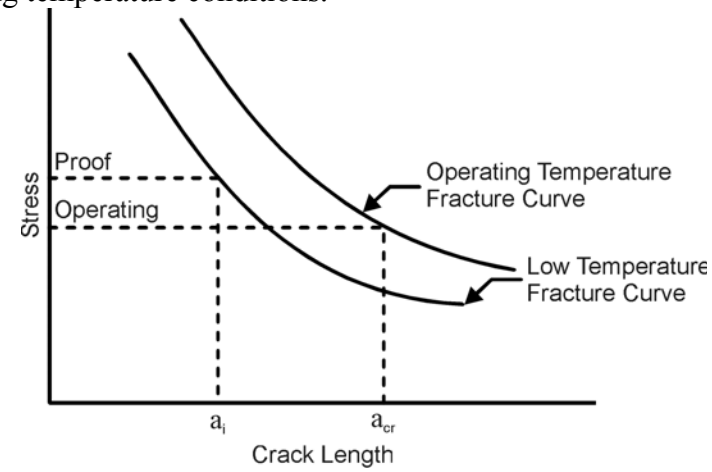

Figure 3.3.4. Using a Material's Low Temperature Fracture Sensitivity to Decrease Initial Crack Size and thus Increase the Minimum Safe Crack Growth Interval for a Given Proof Stressing Condition

As stated by JSSG-2006 A.3.12.1, "the minimum assumed initial flaw size shall be the calculated critical size at the proof test stress level and temperature using procuring activity approved upper-bound of the material fracture toughness data." The concept of using an approved upper-bound for the fracture toughness ensures a worst case assumption for the maximum allowable initial crack size (see Figure 3.3.5) and the minimum safe crack growth interval (see Figure 3.3.6). Figure 3.3.6 summarizes the JSSG-2006 requirements for establishing the minimum safe crack growth interval for the NDE proof test conditions.

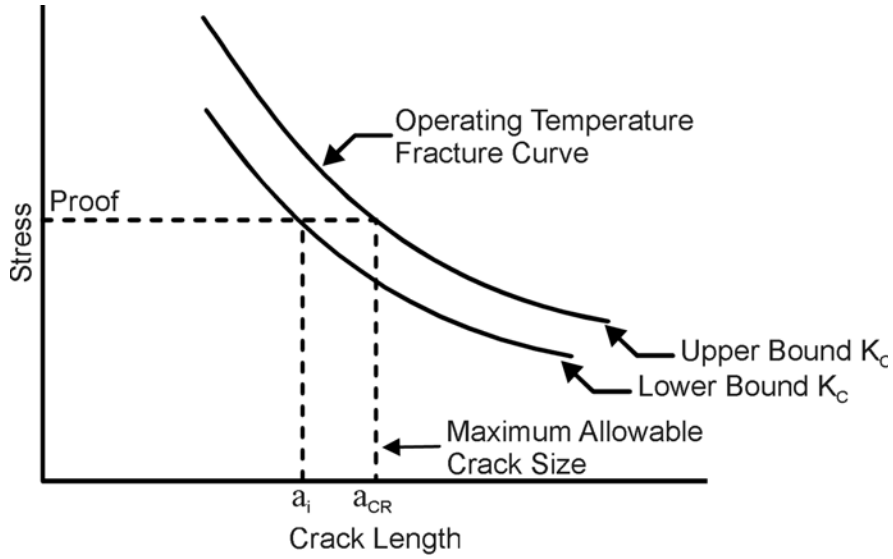

Figure 3.3.5. Influence of Fracture Toughness Variation on the Maximum Allowable Crack Size

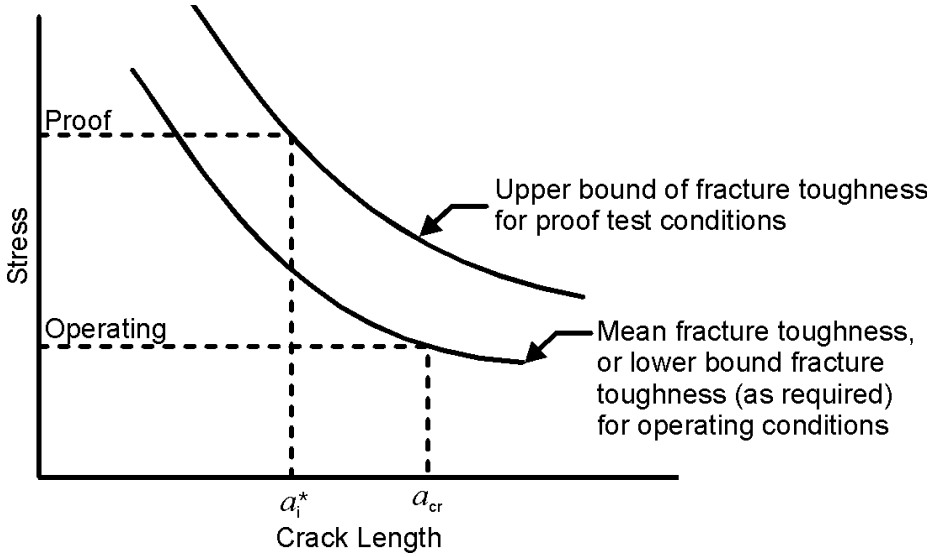

Figure 3.3.6. Description of Procedure Used to Establish Initial Crack Size and the Minimum Safe Crack Growth Interval According to JSSG-2006, A.3.12.1

There are no design allowables for fracture toughness of aerospace materials. Figure 3.3.7 presents a portion of MIL-HDBK-5G data that define typical plane strain fracture toughness for aluminum alloys. The fracture toughness values presented are averages, coefficients of variation and the

minimum and maximum values obtained from the test data collected for the individual alloys and heat temperature conditions shown. The supporting text in MIL-HDBK-5G notes that the fracture toughness values given do not have the statistical reliability of the typical mechanical properties (yield strength, elastic modulus, etc.) that are usually present in MIL-HDBK-5 properties. The lack of a definition of the fracture toughness upper-bound required by JSSG-2006 would be overcome if the upper-bound is estimated by a statistical definition that is agreed to by the procuring agency. An example of such a bound might be a tolerance limit on the distribution of fracture toughness values.

TABLE 3.1.2.1.6. *Values of Room-Temperature Plane-Strain Fracture Toughness of Aluminum Alloys*[a]

Alloy/Temper	Product Form	Orientation[b]	Product Thickness Range, inches	Number of Sources	Sample Size	Specimen Thickness Range, inches	K_{Ic}, ksi $\sqrt{in.}$				
							Max.	Avg.	Min.	Coefficient of Variation	Minimum Specification Value
2014-T651	Plate	L-T	≥0.5	1	24	0.5-1.0	25	22	19	8.4	
2014-T651	Plate	T-L	≥0.5	2	34	0.5-1.0	23	21	18	6.5	
2014-T652	Hand Forging	L-T	≥0.5	2	15	0.8-2.0	48	31	24	21.8	
2014-T652	Hand Forging	T-L	≥0.8	2	15	0.8-2.0	30	21	18	14.4	
2024-T351	Plate	L-T	≥1.0	2	11	0.8-2.0	43	31	27	16.5	
2024-T851	Plate	L-S	1.4-3.0	4	11	0.5-0.8	32	25	20	17.8	
2024-T851	Plate	L-T	≥0.5	11	102	0.4-1.4	32	23	15	10.1	
2024-T851	Plate	T-L	0.4-4.0	9	80	0.4-1.4	25	20	18	8.8	
2024-T852	Forging	T-L	2.0-7.0	3	20	0.7-2.0	25	19	15	15.5	
2024-T852	Hand Forging	L-T	-----	4	35	0.8-2.0	38	28	19	18.4	
2024-T852	Hand Forging	T-L	-----	2	17	0.7-2.0	22	18	14	14.4	
2124-T851	Plate	L-T	≥0.8	13	497	0.5-2.5	38	29	18	10.4	24
2124-T851	Plate	T-L	0.6-6.0	10	509	0.5-2.0	32	25	19	9.7	20
2124-T851	Plate	S-L	≥0.5	6	489	0.3-1.5	27	21	16	9.8	18
2219-T851	Plate	L-T	-----	4	67	1.0-2.5	38	33	30	7.2	
2219-T851	Plate	T-L	≥1.0	6	108	0.8-2.5	37	29	20	10.1	
2219-T851	Plate	S-L	≥0.8	3	24	0.5-1.5	26	22	20	9.6	
2219-T851	Forging	S-L	-----	1	85	1.0-1.5	34	25	19	12.1	
2219-T8511	Extrusion	T-L	-----	1	19	1.8-2.0	34	29	23	12.3	
2219-T852	Forging	S-L	-----	2	60	0.8-2.0	35	25	20	12.1	
2219-T852	Hand Forging	L-T	-----	2	32	1.5-2.5	46	38	30	9.7	
2219-T852	Hand Forging	T-L	≥1.5	2	28	1.5-2.5	30	27	22	8.4	
2219-T87	Plate	L-T	≥1.5	3	11	0.8-2.0	34	27	25	9.3	
2219-T87	Plate	T-L	-----	1	11	1.0	22	22	19	3.9	
7049-T73	Die Forging	L-T	1.4	3	21	0.5-1.0	34	30	27	7.4	
7049-T73	Die Forging	S-L	≥0.5	3	46	0.5-1.0	26	22	18	9.7	
7049-T73	Hand Forging	L-T	≥0.5	2	28	0.5-1.0	37	30	23	12.1	
7049-T73	Hand Forging	T-L	2.0-7.1	2	27	1.0	28	22	18	12.5	
7049-T73	Hand Forging	S-L	1.0	2	24	0.8-1.0	22	19	14	14.2	
7050-T7351	Plate	L-T	1.0-6.0	2	31	1.0-2.0	43	35	28	11.3	
7050-T7351	Plate	T-L	2.0-6.0	1	29	1.5-2.0	35	30	25	8.5	
7050-T7351	Plate	S-L	2.0-6.0	1	30	0.8-1.5	30	28	25	4.6	
7050-T74	Die Forging	S-L	0.6-7.1	3	12	0.6-2.0	27	24	21	8.8	

Figure 3.3.7. Table of Fracture Toughness Data from MIL-HDBK-5G

3.3.2 Examples

Two examples are now presented to illustrate how the proof test might be used. The first example describes how a proof stress condition might be chosen to find specific crack sizes. The second example describes a typical situation whereby the proof test must be designed to guarantee a service life interval.

EXAMPLE 3.3.1 Proof Test Stress-Crack Length Relationships

For the radially-through-thickness cracked structure illustrated here, answer the following questions:

(a) What proof stress (σ_p) is required at room temperature to guarantee that the maximum crack size is less than 0.05 inches? Also, define the ratio of proof to operating stress conditions ($\alpha = \sigma_p/\sigma_{op}$).

(b) For a proof test conducted at -40°F, define the proof stress and proof stress ratio associated with finding a crack with a length 0.05 in.

(c) If the proof test ratio is 1.5, what is the minimum flaw size that will be detected at room temperature?

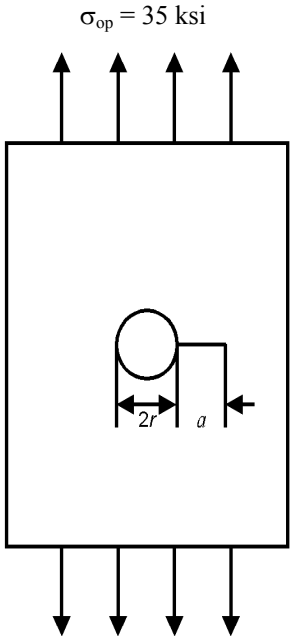

Material Properties

σ_{YS} = 70 ksi
K_{IC} = 40 ksi √in at 75°
K_{IC} = 35 ksi √in at -40°

STRESS INTENSITY FACTOR SOLUTION

$K = \sigma\sqrt{\pi a}\,F(a)$
where

$$F(a) = \frac{0.8734}{0.3246 + \frac{a}{r}} + 0.6762$$

SOLUTION:

The equation that governs the solution to all three questions is the Irwin fracture criterion, i.e.,

$$K = K_{IC}$$

where

$$K = \sigma\sqrt{\pi a}\cdot F(a/r)$$

with *F(a/r)* and the material properties defined above.

To address the questions parts a and b, the equations are solved for the proof stress σ_p, i.e.

$$\sigma_p = \frac{K_{IC}}{\sqrt{\pi a}\cdot F(a/r)}$$

for the given K_{IC} conditions at temperature and for a 0.05 inch long crack, i.e. a in this equation is 0.05 inch. So, for room temperature, the proof stress is

$$\sigma_p = \frac{40}{\sqrt{\pi(0.05)} \cdot (2.34)} = 43.1 ksi$$

and for -40° F the proof stress is

$$\sigma_p = \frac{35}{\sqrt{\pi(0.05)} \cdot (2.34)} = 37.7 ksi$$

In both cases, the proof stress is well below the yield strength; however, it might be noted that localized yielding at stress concentrations could occur at these levels. The proof stress ratios (α) are 1.23 and 1.08 for the room temperature and -40°F proof test conditions, respectively. To address the third part of the question, it is necessary to solve the equations for crack length (a), i.e.

$$a = \frac{1}{\pi}\left(\frac{K_{IC}}{\sigma_p}\right)^2 \left[\frac{1}{F(a/r)}\right]^2$$

Because this equation involves crack length in the function F in a complicated fashion, the equation is solved iteratively for the given material and stress conditions, i.e. K_{IC} = 40 ksi √in and σ_p = 1.50 x (35) = 52.5 ksi. Thus,

$$a = \frac{1}{\pi}\left(\frac{40}{52.5}\right)^2 \left[\frac{1}{F\left(\frac{a}{r}\right)}\right]^2$$

A series of several trials are shown in the following table, where a match of the right and left side of the equation is achieved when $a \cong 0.0245$ inches. Thus, 0.049 inch long cracks can be found for a proof test ratio of 1.50.

Trial And Error Solution

***a* (left-hand side)**	***a/r***	***F(a/r)***	***a* (right-hand side)**
0.020	0.08	2.835	0.0230
0.025	0.10	2.733	0.0247
0.030	0.12	2.641	0.0265
0.0255	0.102	2.723	0.0249
0.0245	0.098	2.743	0.0246

In the above solutions, it is seen that in some cases the proof stress is sufficiently large such that yielding can be expected at the edge of the hole and other stress concentration sites. The reader is cautioned that linear elastic fracture mechanics (LEFM) techniques such as applied in these equations should not be utilized when extensive local yielding occurs except to obtain first-order estimates of the crack length. From a proof test standpoint, the LEFM estimates of the minimum crack length will be actually larger than those screened by loading the structure to the proof condition, assuming load control conditions, and thus conservative.

EXAMPLE 3.3.2 Proof Test Conditions to Guarantee Life

The pressure vessel shown here has a semicircular surface crack of unknown size located in the longitudinal direction. This vessel is subjected to an on-off pressure loading condition of the type illustrated below and is made of a structural steel with the mechanical properties shown.

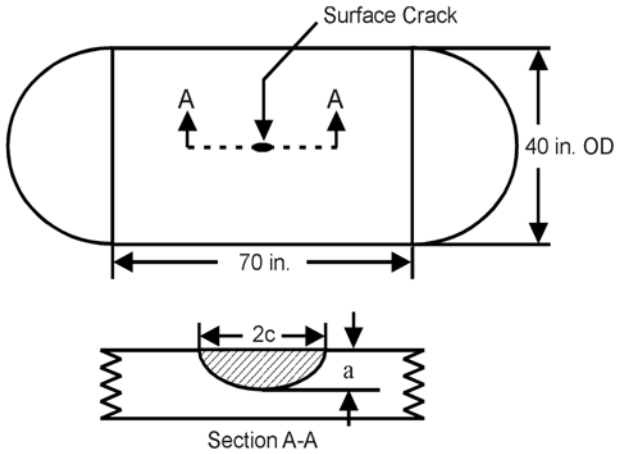

Pressure Vessel Structure with Semicircular Surface Crack

For economic purposes, it has been decided that the structure will only be inspected yearly and the inspection procedure has been chosen to be a proof test. You have been asked to select the proof pressure level that will guarantee that this vessel will not fail during the interval between proof test inspections subject to the crack/loading/material property assumptions.

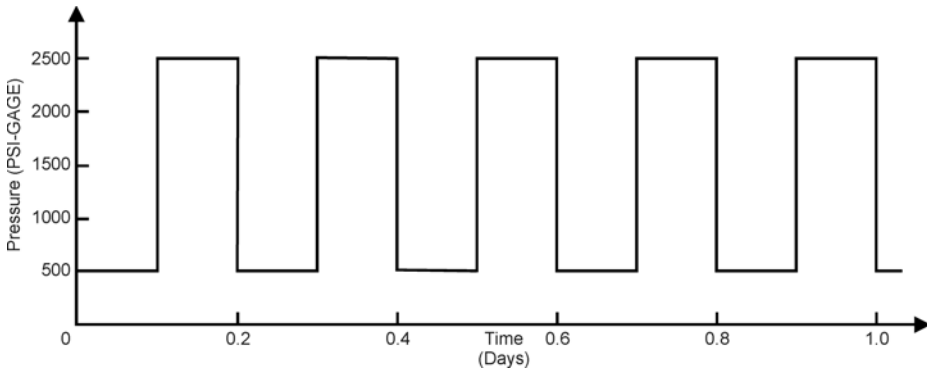

Pressure/Time Loading Cycle

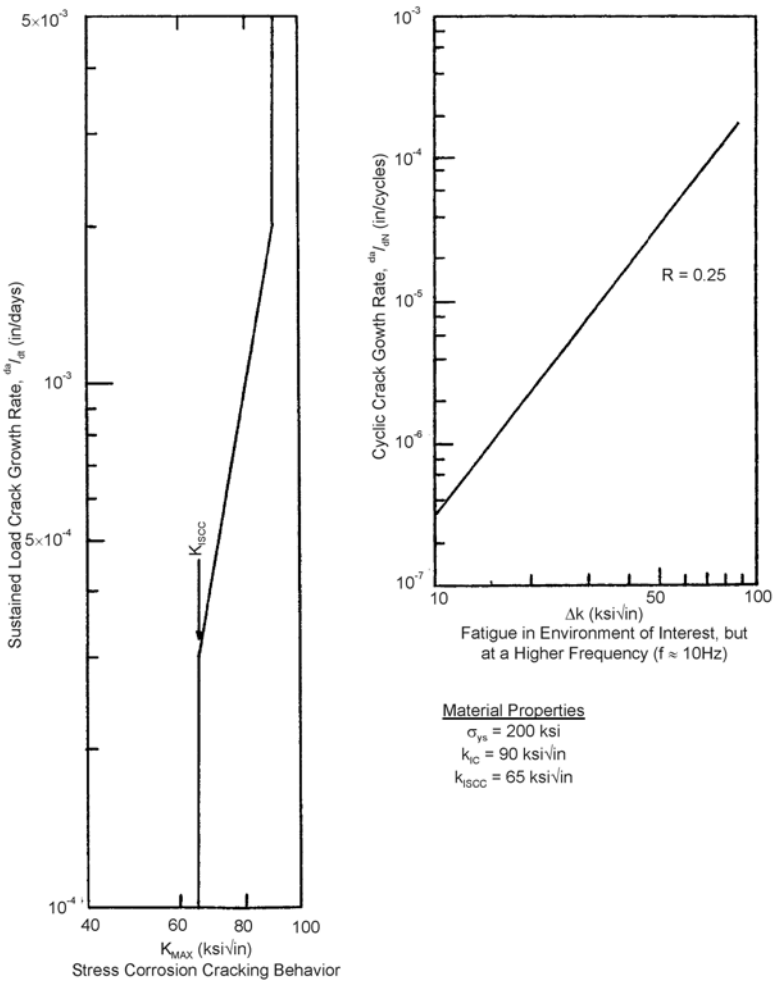

Material Properties for Steel Pressure Vessel

SOLUTION:

It is first necessary to calculate the gross stress in the section of the structure where the crack is located. From any standard strength of materials text, it is determined that for a pressure (p) of 2,000 psi, the maximum operating stress (σ) for the vessel with an outside diameter of 40 inch and a thickness (B) of 0.4 inch is given by

$$\sigma_{\max} = \frac{pD}{2B} = \frac{(2000)(40)}{2(0.4)} = 100{,}000\,psi$$

or 100 ksi, and the range of stress is

$$\Delta\sigma = 0.75\sigma_{max} = 75ksi$$

For the semicircular crack partly through the vessel wall, the stress-intensity factor is given by

$$K = 1.12\left(\frac{2}{\pi}\right)\sigma\sqrt{\pi a}$$

neglecting the back surface correction factor. Assume for illustrative purposes that the equation can be considered a reasonable estimate of the true stress-intensity factor at all depths through the thickness. As a first step, determine if the structure will leak before it breaks by calculating the stress-intensity factor for the condition where the crack depth is equal to the thickness. Thus, with σ = 100 ksi and a = 0.4 in.,

$$K = 1.12\left(\frac{2}{\pi}\right)(100)\sqrt{\pi(0.4)}$$
$$= 79.9ksi\sqrt{in}$$

which is less than K_{IC} = 90 ksi√in and thus the vessel might leak before fracturing. Consider, however, the potential cracking situation that occurs if the semicircular crack penetrates the wall and immediately transitions to a through thickness crack as shown. An analysis indicates that $K \cong$ 112 ksi√in, which is greater than K_{IC}. Thus, given this situation, the vessel will fail catastrophically.

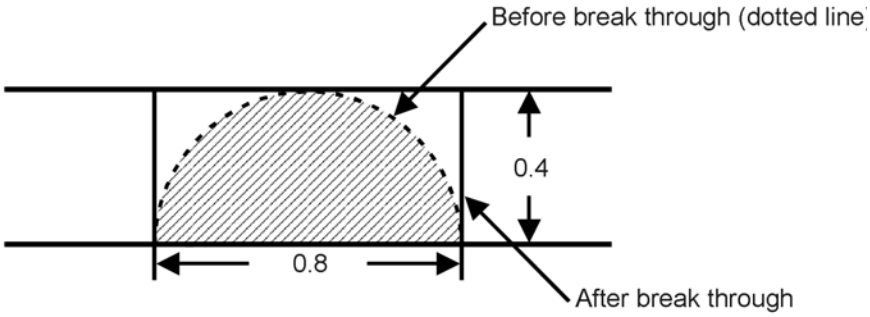

Change in Crack Geometry to Through-Thickness Crack After the Semicircular Crack Grows to the Inside Wall

To establish the crack size associated with the proof test, one must conduct a life analysis which works from the final crack size (a = 0.4 inch) backwards until the one-year life interval (a two-year life interval with the factor of two life margin) is guaranteed. The life analysis that is conducted illustrates an incremental crack length method that uses the iterative equation

$$Life = \sum_{i=1}^{n}\left[\frac{\Delta a_i}{\left.\frac{da}{dt}\right|_i}\right](days)$$

where the increments of crack length (Δa_i) and crack growth rate values ($da/dt/_i$) are chosen to be compatible.

On the basis of the given material data, one must assume that both a fatigue and a stress-corrosion cracking mechanism are active (see Section 5 for discussion on these mechanisms). The fatigue crack growth rate behavior can be described using the power law

$$\frac{da}{dN} = 3.3x10^{-10}\Delta K^{2.959}(in/cycle)$$

On the basis of the material data, this equation is restricted to the range $10 \leq \Delta K \leq 90$ ksi $\sqrt{in}$, and to the stress ratio (R) of 0.25, which is compatible with the given loading cycle.

The stress-corrosion cracking rate data can be described with the power law:

$$\frac{da}{dt}\Big|_{cor} = 9.24x10^{-15} K_{\max}^{\ 5.798} (in/day)$$

which is valid for sustained loading conditions when K_{max} is between the threshold of stress corrosion cracking (K_{Iscc} = 65 ksi √in) and the fracture toughness level (K_{IC} = 90 ksi √in).

As a first approximation of the effect of combined stress corrosion action and fatigue crack growth, the linear summation hypothesis of Wei-Landes is suggested (see Section 5):

$$\frac{da}{dt}\Big|_{total} = \frac{da}{dt}\Big|_{cor} + \frac{da}{dt}\Big|_{fat}$$

where the time based fatigue crack growth rate is obtained from

$$\frac{da}{dt}\Big|_{fat} = f \cdot \frac{da}{dN}$$

whereby the cycle-dependent component from the power law equation is multiplied by the cyclic frequency (f). It is also to be noted that the stress-corrosion cracking rate contribution for a day in service is one-half that established by the da/dt equation since the vessel is only loaded to the maximum pressure only half the time.

There are a number of ways that the *Life* equation can be used to establish the crack length-life relationship. The method for this example will be to choose equal increments of K_{max} between the crack size at failure and the other crack lengths established to obtain the Δa_i values. The next table describes the relationships between the maximum stress-intensity factor and the crack length, the crack length increment, the average values of the maximum stress-intensity factor ($\overline{K}_{max}$) and stress-intensity factor range ($\overline{\Delta K}$).

Crack Interval Table

K_{max} (ksi √in)	55	60	65	70	75	80
a (inch)	0.189	0.225	0.264	0.307	0.352	0.400
Δa (inch)	0.036	0.039	0.043	0.045	0.048	
$\overline{K}^{*}_{\max}(ksi\sqrt{in.})$	57.5	62.5	67.5	72.5	77.5	
$\overline{\Delta K}^{*}(ksi\sqrt{in.})$	43.1	46.9	50.6	54.4	58.1	

*Average values for the interval

The calculations of crack length a in this table are directly related to K_{max} through the equation

$$a = \left[\frac{K_{\max}}{1.12\left(\frac{2}{\pi}\right)\sigma_{\max}\sqrt{\pi}} \right]^2$$

which when solved for a typical value of K_{max}, say 55 ksi √in, the crack length becomes

$$a = \left[\frac{55}{1.12\left(\frac{2}{\pi}\right)100\sqrt{\pi}} \right]^2 = 0.189 inch$$

The difference in crack lengths *(Δa)* comes from subtracting the two corresponding crack lengths. The values of $\overline{K}_{max}$ are computed by averaging the two corresponding K_{max} values, e.g. 62.5 ksi √in = 0.5 (60 + 65). The values of $\overline{\Delta K}$ are computed from the relationship $\Delta K = (1-R) K_{max}$, where R is the stress ratio (0.75).

The next table presents the fatigue crack growth rate contribution and the following table presents the stress corrosion cracking contribution.

Fatigue Crack Growth Rate Contribution

$\overline{\Delta K}$ **(ksi √in)**	$\frac{da}{dN}$ **(in/cycle)**	$\left.\frac{da}{dt}\right\|_{fat} = \frac{5 cycles}{day} x \frac{da}{dN}$
43.1	2.26 x 10 $^{-5}$	1.13 x 10 $^{-4}$
46.9	2.91 x 10 $^{-5}$	1.46 x 10 $^{-4}$
50.6	3.64 x 10 $^{-5}$	1.82 x 10 $^{-4}$
54.4	4.51 x 10 $^{-5}$	2.25 x 10 $^{-4}$
58.1	5.48 x 10 $^{-5}$	2.74 x 10 $^{-4}$

Stress-Corrosion Cracking Rate Contribution.

$\overline{K}_{max}$ *(ksi* $\sqrt{in}$ *)*	$\frac{da}{dt}$ (in/day)	$\left.\frac{da}{dt}\right\|_{cor}$ (in/day)
57.5	0*	0
62.5	0*	0
67.5	3.73 x 10 $^{-4}$	1.86 x 10 $^{-4}$
72.5	5.65 x 10 $^{-4}$	2.82 x 10 $^{-4}$
77.5	8.3 x 10 $^{-4}$	4.16 x 10 $^{-4}$

* $\overline{K}_{max}$ is below K_{Iscc} and therefore no growth occurs

In the Fatigue Crack Growth Rate Table, the $\Delta\overline{K}$ values are taken from the Crack Interval Table and cover each of the consecutive intervals of crack length. From the *da/dN* equation the crack growth fatigue rate for a stress-intensity range of 43.1 is

$$\frac{da}{dN} = 3.3x10^{-10}(43.1)^{2.959} = 2.26x10^{-5}\frac{in}{cycle}$$

The calculations of $\left.\frac{da}{dt}\right|_{fat}$ follow directly from multiplying the fatigue crack growth rates by the frequency of load application (5 cycles/day).

In the Stress-Corrosion Cracking Rate Table, the $\overline{K}_{max}$ values are taken from Crack Interval Table and cover each of the consecutive intervals of crack length. From the *da/dt* equation, the sustained load stress corrosion cracking growth rate is

$$\frac{da}{dN} = 9.24x10^{-15}(67.5)^{5.798} = 3.73x10^{-4}\,in/day$$

The calculations of the corrosion contribution to the total *da/dt* equation are also given in the table. These come directly from the fact that the structure is only loaded into the range where stress corrosion cracking occurs for one-half of the time (on-off cycling) so the $\left.\frac{da}{dt}\right|_{cor}$ numbers are one-half those given in the middle column.

The total contribution to cracking behavior is calculated from the total *da/dt* equation, and the individual crack increments in the *Life* equation are used to establish the time that it takes to grow the crack through the successive intervals. The appropriate calculations are reported in the next table.

Estimating the Time To Growth Through Successive Intervals.

Δa (inch)	**$\left.\frac{da}{dt}\right\|_{total}$ (in/day)**	**Δt (days)**	**A (inch)**	**$t = \Sigma\Delta t$ (days)**
0.036	1.13 x 10^{-4}	318.6	0.189	861.1
0.039	1.46 x 10^{-4}	267.8	0.225	542.5
0.042	3.68 x 10^{-4}	114.9	0.264	274.7
0.045	5.07 x 10^{-4}	89.5	0.307	159.8
0.048	6.9 x 10^{-4}	70.3	0.352	70.3
			0.400	0

The crack length increment (Δa) and the crack length (a) values given in this table come from the Crack Interval Table. The total crack growth rate $\left(\left.\frac{da}{dt}\right|_{total}\right)$ values come from the total *da/dt*

equation, where the individual contributions come from the Fatigue Crack Growth Rate and Stress-Corrosion Cracking Rate Tables, e.g.

$$\left.\frac{da}{dt}\right|_{total} = 5.07x10^{-4}\,\frac{in}{day} = 2.25x10^{-4} + 2.82x10^{-4}$$

for Δa = 0.045 inch and a between 0.307 and 0.352 inch. The increment of time required to propagate the crack through this interval is obtained from

$$\Delta t = \left.\frac{\Delta a}{\frac{da}{dt}}\right|_{total} = \frac{0.045in}{5.07x10^{-4}\,\frac{in}{day}} = 89\,days$$

The total time that it takes to grow through successive intervals is obtained by summing the results from this equation for each interval using the *Life* equation.

The data from the table that relates crack length (a) to the total time (t) to failure shows that the proof test must find a crack length between 0.189 and 0.225 inch to guarantee the integrity of the vessel with a factor of two life margin. The crack length versus total time to failure data have been graphically displayed in the next figure, where it can be seen that for one year of growth the crack length is 0.245 inch (and for a factor of two life margin the crack length is 0.20 inch). The required proof stress for the 0.20 inch long crack length is obtained from the Irwin criterion:

$$\sigma_p = \frac{K_{IC}}{1.12\left(\frac{2}{\pi}\right)\sqrt{\pi a}} = \frac{90}{1.264\sqrt{(0.2)}}$$

which is about 80 percent of the yield strength and therefore, the proof pressure (p_p) must be at least

$$p_p = \frac{2\sigma_p B}{D} = \frac{2(159{,}200)(0.4)}{40}$$

to ensure that all semicircular cracks longer than 0.2 inch are removed from the center section of the vessel prior to operation.

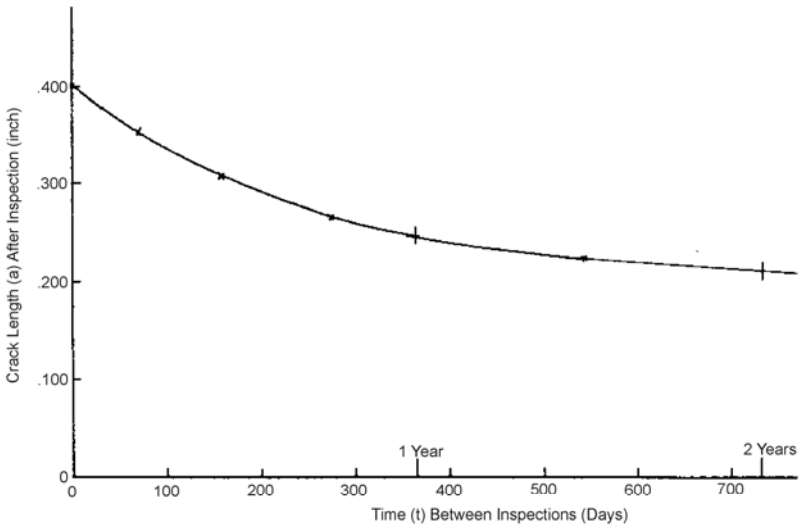

Graphical Procedure for Interpreting Crack Length

3.4 References

U. Albrectsen and P. Aitken-Case (1976, March). *Briefing Charts on C-141 Loading Gear Proof Test Conditions*. Ogden Air Logistics Center/MMIRCL, Hill Air Force Base.

J. Alcott (1994). "An Investigation of Nondestructive Inspection Equipment: Detecting Hidden Corrosion on USAF Aircraft." *Materials Evaluation* (Vol. 52, No. 1), pp.64-73.

R.E. Alford, R.P. Bell, J.B. Cochran, and D.O. Hammond (1992). "C-141 WS 405 Risk Assessment." WL-TR-92-4045. *Proceedings of the 1991 USAF Structural Integrity Program Conference*, San Antonio, Texas.

A.P. Berens and P.W. Hovey (1981, November). *Evaluation of NDE Reliability Characterization*. AFWAL-TR-81-4160. Air Force Wright Aeronautical Laboratories, Wright-Patterson Air Force Base, Ohio 45433.

A.P. Berens and P.W. Hovey (1984, April). "*Flaw Detection Reliability Criteria, Volume I, Methods and Results*," AFWAL-TR-84-4022. Air Force Wright Aeronautical Laboratories, Wright-Patterson Air Force Base, Ohio 45433.

A.P. Berens and P.W. Hovey (1985). "The Sample Size and Flaw Size Effects in NDI Reliability Experiments." *Review of Progress in Quantitative Nondestructive Evaluation,* (Vol. 4B). Edited by D.O. Thompson and D.E. Chimenti. Plenum Press, pp. 1327-1334.

A.P. Berens (1988). "NDE Reliability Data Analysis." *ASM Metals Handbook, Volume 17, 9th Edition: Nondestructive Evaluation and Quality Control*. ASM International, Materials Park, Ohio, pp. 689-701.

A.P. Berens, P.W. Hovey, and D.A. Skinn (1991, October). "*Risk Analysis for Aging Aircraft Fleets*." WL-TR-91-3066. Wright Laboratory, Wright-Patterson Air Force Base, Ohio 45433.

A.P. Berens (2000, January). "*Probability of Detection (POD) Analysis for the Advanced Retirement for Cause (RFC)/Engine Structural Integrity Program (ENSIP) Nondestructive Evaluation (NDE) System Development, Volume 1 – POD Development*." AFRL-ML-WP-TR-2001-4010, Air Force Research Laboratory, Wright-Patterson Air Force Base, OH, 45433.

D.A. Bruce (1998). "NDI Reliability Estimation from Small Samples and In-Service Experience." *Airframe Inspection Reliability under Field/Depot Conditions*." RTO Meeting Proceedings 10, NATO, Research and Technology Organization, Neuilly-Sur-Seine Cedex, France.

W.D. Buntin (1971, October). *Concept and Conduct of Proof Test of F-111 Production Aircraft*. Paper presented to the Royal Aeronautical Society, London, England.

W.D. Cowie (1975, April). Turbine Engine Structural Integrity Program (ENSIP), AIAA. *Journal of Aircraft,* (Vol. 12, No. 4). Special Issue, pp. 366-369.

M.K. Davis (1988). "Proficiency Evaluation of NDE Personnel Utilizing the Ultrasonic Methodology." *Review of Progress in Quantitative Nondestructive Evaluation,* (Vol. 7B). Edited by D.O. Thompson and D.E. Chimenti. Plenum Press, pp. 1777-1789.

C.E. Dumesnil, S.D. Aratki, R.P. Wilson, C.P. Martin, D.J. White, and O.L. Hooks (1977, January). *A-7D ASIP Part I, Damage Tolerance and Fatigue Assessment Program*. Vought Corp., Report No. 2-53440/7R-5928 (Vol. I).

A. Fahr, D. Forsyth, M. Bullock, W. Wallace, A. Ankara, L. Kompotiatis, and H.F.N. Goncalo (1995). *POD Assessment of NDI Procedures Using a Round Robin Test*. AGARD-R-809, NATO Advisory Group for Aerospace Research and Development, Neuilly-Sur-Seine Cedex, France.

A.W. Gunderson (1974, October). *Fracture Mechanics Tests and Analyses of the AEDC APTU Storage Vessel Material*. AFML-TR-74-133. Air Force Materials Laboratory, Wright-Patterson Air Force Base, Ohio 45433.

W.C. Hoppe, N. Schehl, C. Buynak, J.P. Gallagher, and A.P. Berens (2000). "From Cracks to Corrosion: The Evolution of a Probability of Detection Approach that Quantifies Corrosion Damage in Aging Aircraft." *2000 USAF Aircraft Structural Integrity Conference Proceedings*, San Antonio, Texas.

J.J. Horsley, D.F. Bryan, and J.E. Fuller (1976, February). *B-52D Proof Load Program, Laboratory Crack Growth Tests*. The Boeing Company, Wichita Division, Document No. D3-9700, (Restricted Publication).

P.W. Hovey, W.H. Sproat, and P. Schattle (1989). "The Test Plan for the Next Air Force NDI Capability and Reliability Assessment Program." *Review of Progress in Quantitative Nondestructive Evaluation* (Vol. 8B). Edited by D.O. Thompson and D.E. Chimenti. Plenum Press, pp. 2213-2220.

JSSG-2006, Joint Service Specification Guide, Aircraft Structures, Department of Defense, 30 October 1998.

J.P. Komorowski, D.S. Forsyth, D.L. Simpson, and R.W. Gould (1998). "Probability of Detection of Corrosion in Aircraft Structures." RTO-MP-10. *RTO Meeting Proceedings 10, Airframe Inspection Reliability under Field/Depot Conditions.* NATO Research and Technology Organization, Neuilly-Sur-Seine Cedex, France.

W.H. Lewis, B.D. Dodd, W.H. Sproat, and J.M. Hamilton (1978). *Reliability of Nondestructive Inspections – Final Report*. Report No. SA-ALC/MEE 76-6-38-1. United States Air Force, San Antonio Air Logistics Center, Kelly Air Force Base, Texas.

J.W. Lincoln (1985). "Risk Assessment of an Aging Military Aircraft." *Journal of Aircraft* (Vol. 22, No. 8).

J.W. Lincoln (1997). "Risk Assessments of Aging Aircraft." *Proceedings of the First Joint DOD/FAA/NASA Conference on Aging Aircraft*, Ogden, UT.

S.D. Manning and J.N. Yang (1987, July). "*Advanced Durability Analysis, Volume I – Analytical Methods*." AFWAL-TR-86-3017. Air Force Wright Aeronautical Laboratories, Wright-Patterson Air Force Base, Ohio 45433.

S.D. Manning and J.N. Yang (1989, February). "*USAF Durability Design Handbook: Guidelines for the Analysis and Design of Durable Aircraft Structures*." AFWAL-TR-88-3119. Air Force Wright Aeronautical Laboratories, Wright-Patterson Air Force Base, Ohio 45433.

MIL-HDBK-1823 (1999, 30 April). Department of Defense Handbook, "Nondestructive Evaluation System Reliability Assessment."

MIL-HDBK-5G (1994, November). Military Handbook, Metallic Materials and Elements for Aerospace Vehicle Structures (Vol. 1), pp. 3-11.

A.M. Mood (1950). *Introduction to the Theory of Statistics*. McGraw-Hill Book Company, Inc., New York.

"Fatigue Crack Growth Computer Program 'NASA/FLAGRO', Version 2.03" (1994). National Aeronautics and Space Administration, JSC-22267A.

Natrella, M.G. (1963), *Experimental Statistics*, Handbook 91, National Bureau of Standards.

Nondestructive Testing Handbook, Volume Ten, Second Edition, Nondestructive Testing Overview (1996). Stanley Ness and Charles N. Sherlock, Technical Editors, Patrick O. Moore and Paul M. McIntire, Editors. American Society for Nondestructive Testing, Inc.

P.F. Packman, S.J. Klima, R. Davies, J. Malpani, J. Moyzis, W. Walker, B.G.W. Yee, and D.P. Johnson (1976). Reliability of Flaw Detection by Nondestructive Inspection. *ASM Metal Handbook* (Vol. 11), 8th Edition. Metals Park, Ohio, pp. 214-224.

R.E. Pinckert (1976, 26-27 September). *Damage Tolerance Assessment of F-4 Aircraft*. AIAA-76-904. Presented at AIAA Aircraft Systems & Technology Meeting, Dallas, Texas.

J.M. Potter (1978). Advances in Fastener Hole Quality through the Application of Solid Mechanics. *Proceedings of the Army Symposium on Solid Mechanics*, *Case Studies on Structural Integrity and Reliability*. AMMRC-MS 78-3. Watertown, MA.

D. Roach (1998, 24-28 March). "Development of a Corrosion Detection Experiment to Evaluate Conventional and Advanced NDI Techniques." 41st Sampe Symposium, pp 265-278.

J.L. Rudd and T.D. Gray (1978). "Quantification of Fastener-Hole Quality." *Journal of Aircraft* (Vol. 15, No. 3).

J.L. Rudd and T.D. Gray (1976, September). *Equivalent Initial Quality Method*. AFFDL-TM-76-83-FBE. Air Force Flight Dynamics Laboratory, Wright-Patterson Air Force Base, Ohio 45433.

W.O. Rummel and G.A. Matzkanin (1997). *Nondestructive Evaluation (NDE) Capabilities Data Book*. Nondestructive Testing Information Analysis Center, (NTIAC), Austin Texas.

C. Salkowski (1993). "NDT and the Aging Orbiter." FAA Inspection Reliability Workshop, Atlantic City, NJ.

F.W. Spencer and D.L. Schurman (1994, March). "Reliability Assessment at Airline Inspection Facilities, Volume III: Results of an Eddy Current Inspection Reliability Experiment." DOT/FAA/CT-92/12, III. FAA Technical Center, Atlantic City, NJ.

C.F. Tiffany and J.N. Masters (1965). Applied Fracture Mechanics. *Fracture Toughness Testing and Its Application*. ASTM STP 381. American Society for Testing and Materials, Baltimore, MD, pp. 249-277.

E.K. Walker, J.C. Ekvall, and J.E. Rhodes (1979). "Design for Continuing Structural Integrity." *Structural Integrity Technology*. ASME, NY.

White, et al. (1979, May). *Fatigue Life Evaluation of the A-7E Arresting Gear Hook Shank*. Vought Report No. 2-30400/9R-52133, Vought Corporation, Dallas, TX.

B.G.W. Yee, F.H. Chang, J.C. Couchman, G.H. Lemon, and P.F. Packman (1976). *Assessment of NDE Reliability Data*. NASA CR-134991. National Aeronautics and Space Administration, Lewis Research Center, Cleveland, Ohio.

Section 4
Residual Strength

The strength of a structure can be significantly affected by the presence of a crack and is usually substantially lower than the strength of the undamaged structure. To prevent catastrophic failure, one must evaluate the load carrying capacity that will exist in the potentially cracked structure throughout its expected service life. The load carrying capacity of a cracked structure is the residual strength of that structure and it is a function of material toughness, crack size, crack geometry and structural configuration.

4.1 Introduction

The basic concept in damage tolerance design is to ensure the safety of the structure throughout the expected service life. To provide the required safety, a structure must be designed to withstand service loads even when cracks are present or when part of the structure has already failed; i.e., the structure has to be damage tolerant. The overriding philosophy is to maintain a minimum required residual strength so that catastrophic failure of the structure is prevented.

Figure 4.1.1 identifies the major sequence of events that ultimately define the residual strength requirements. As can be noted from the figure, once a safety-of-flight-critical element is identified, either its structural configuration or its degree of inspectability will establish the allowable structural design concept and the inspection level categories. Every safety-of-flight-critical element must be qualified in at least one design concept category and in one inspection category. Each allowable combination of design concept and inspection category is coupled in JSSG-2006 to a residual strength requirement, a service life requirement, and a requirement to assume a level of initial damage.

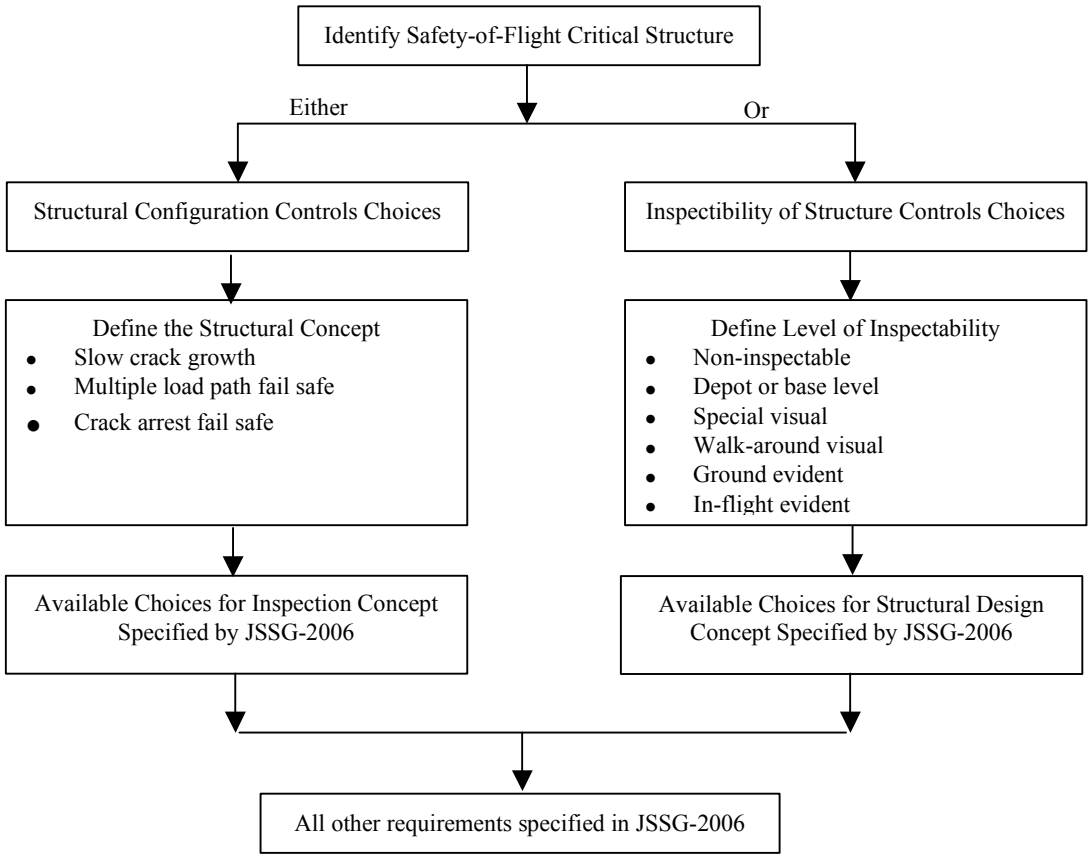

Figure 4.1.1. The Structural Configuration or Degree of Inspectability Controls the Subsequent Choices of Design Concept and Inspection Level

Figure 4.1.2 illustrates the residual strength and the service life interval requirements as well as a residual strength capability curve. The residual strength capability curve defines the level of

load that the structure can withstand without failing in the presence of a growing crack. To account for the change in residual strength capacity as a function of time, it is necessary to determine the crack size as a function of time. The crack-growth-life curve and its various properties are shown schematically in Figure 4.1.3. Shown are the various technology and specification requirements needed to define the crack growth curve which, in turn, establishes the life limit.

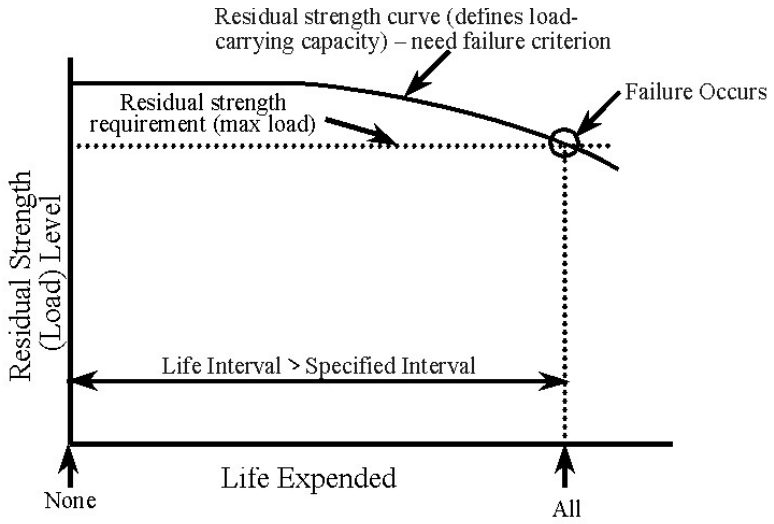

Figure 4.1.2. Relationship Between the Life Expended and Residual Strength Capability Showing a Monotonic Decrease in Load Carrying Capacity Due to Damage

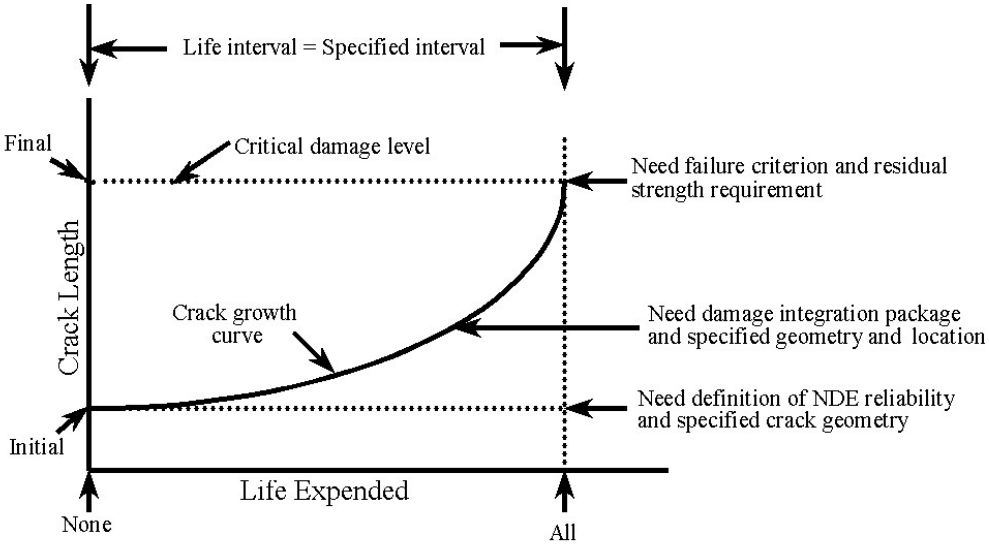

Figure 4.1.3. Relationship Between Crack Length and Life Expended Showing a Monotonic Increase in Crack Length Up Until Failure

As can be seen from Figure 4.1.2, when the residual strength of the structure falls below the maximum stress in the service load history, failure can be expected. To avoid such a failure, a thorough understanding of the problem is essential. Significant advances have been made in recent years in procedures for analyzing damaged structures. Assessments now consider residual strength, damage growth, interactive multiple damage sites and quantitative structural maintenance and in-service evaluations.

The application of existing fracture mechanics solution techniques has yielded effective methods for analyzing the residual strength of the cracked structure. The necessary theories and methods for determining the residual strength capability of cracked structures are presented in this section. Prior to presenting this information in the following sections, a few remarks are made about the residual strength requirements for the two damage tolerant design categories: slow crack growth structure and fail-safe structure.

4.1.1 Slow Crack Growth Structure

In a slow crack growth structure, the damage tolerance must be assured by the maintenance of a slow rate of crack growth, a residual strength capacity, and the assurance that subcritical damage will either be detected at the depot or will not reach unstable dimensions within the design lifetime of the structure. The residual strength curve for a structure which is inspected periodically is schematically shown in Figure 4.1.4. As a result of the inspections, the initially assumed cracks do not grow to a critical size and the structure is restored to its original load carrying capability when an inspection capability equal to that of the manufacturer's is employed.

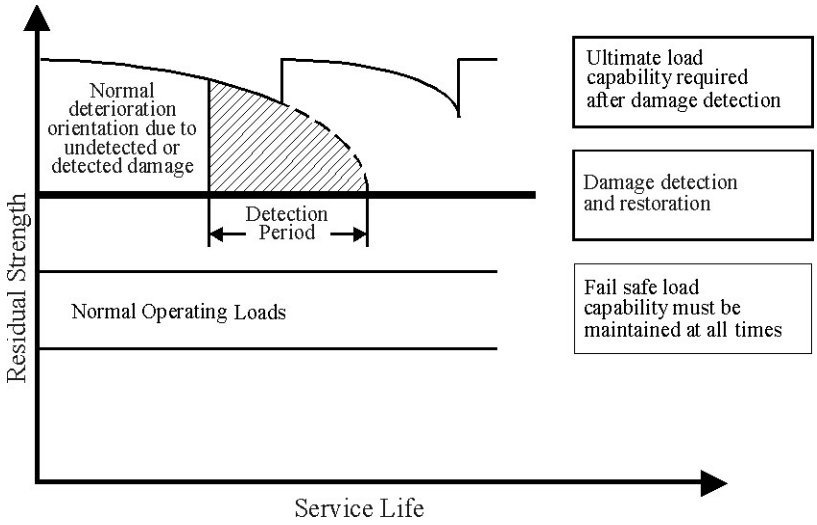

Figure 4.1.4. Strength Criteria for Periodically Inspected Damage Tolerant Structure

Single-load-path "monolithic" structure must be qualified in this category; the residual strength estimation procedure for this type of structure is fairly straightforward. Built-up (multiple-load-path) structure can be qualified either in this category or in the fail-safe category.

4.1.2 Fail-Safe Structure

The residual strength requirement of a fail-safe structure is to assure damage tolerance following a partial failure of the structure. Damage tolerance is maintained through detection of this failure prior to total loss of the structure and sufficient residual strength capability for operating safely within the partial failure prior to inspection. The fail-safe structure is typically a built-up structure with multiple load paths or crack arrest features in its design. In the event of failure of a structural member, its load must be transferred to and withstood by the remainder of the structure, which also contains crack damage, without causing the loss of whole structure. The residual strength of the built-up structure must be determined under such critical circumstances so that the fail-safe design requirements are met.

The analysis of residual strength capability for built-up structure requires the estimation of the critical stress level at which the partial failure occurs, as well as an understanding of the capability of the total structure to withstand this partial failure at and subsequent to the time of failure. The required load associated with the time subsequent to failure is based on the inspection category and, the partially-failed structure must be able to maintain this load until the time of inspection.

4.2 Failure Criteria

The determination of residual strength for uncracked structures is straightforward because the ultimate strength of the material is the residual strength. A crack in a structure causes a high stress concentration resulting in a reduced residual strength. When the load on the structure exceeds a certain limit, the crack will extend. The crack extension may become immediately unstable and the crack may propagate in a fast uncontrollable manner causing complete fracture of the component.

Figure 4.2.1 illustrates the results obtained from a series of tests conducted on a lug geometry containing a crack. The lug geometry shown in Figure 4.2.1a is a single-load-path structure. Figure 4.2.1b indicates that the cracks in each of the three tests extended abruptly at a critical level of load, which is noted to be a function of a crack length. The crack length-critical load level data shown in Figure 4.2.1b provide the basis for establishing the residual strength capability curve. The locus of critical load levels as a function of crack length is shown in Figure 4.2.1c, where the residual strength capability of the lug structure is shown to decrease with increasing crack length.

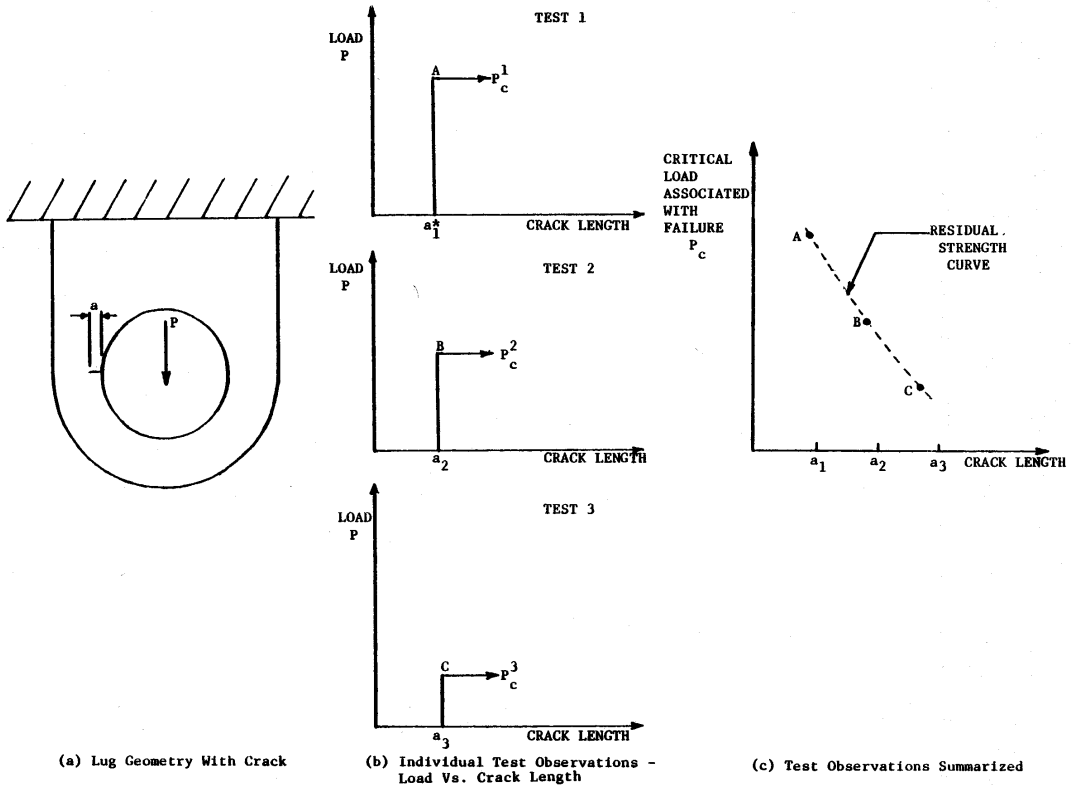

Figure 4.2.1. Description of Crack Geometry and Residual Strength Results

Considering the preceding in terms of applied stress (σ) rather than load gives the σ versus a and σ_c versus a_c plots as shown in Figure 4.2.2 a and b. Schematically, the plots exhibit the same abrupt fracture behavior as the curves presented in Figure 4.2.1. As also shown in Figure 4.2.2c and 4.2.2d, crack extension can first occur at a load level that is well below the fracture critical level. The point A′ corresponds to the start of slow and stable extension of the crack. The unstable rapid extension leading to total failure occurs at point A. This kind of behavior is

observed typically in thin metal sheets or in tough materials. When different crack lengths are considered, the σ_c versus a_c plot will contain two distinct curves, as shown in Figure 4.2.2d. The curve A′B′C′ corresponds to the start of slow and stable crack extension and the curve ABC corresponds to failure.

In general, unstable crack propagation results in fracture of the component. Hence, unstable crack growth is what determines the residual strength. In order to estimate the residual strength of a structure, a thorough understanding of the crack growth behavior is needed. Also, the point at which the crack growth becomes unstable must be defined and this necessitates the need for a failure criterion. There are several criteria available; these criteria are tailored to represent the ability of a material to resist failure.

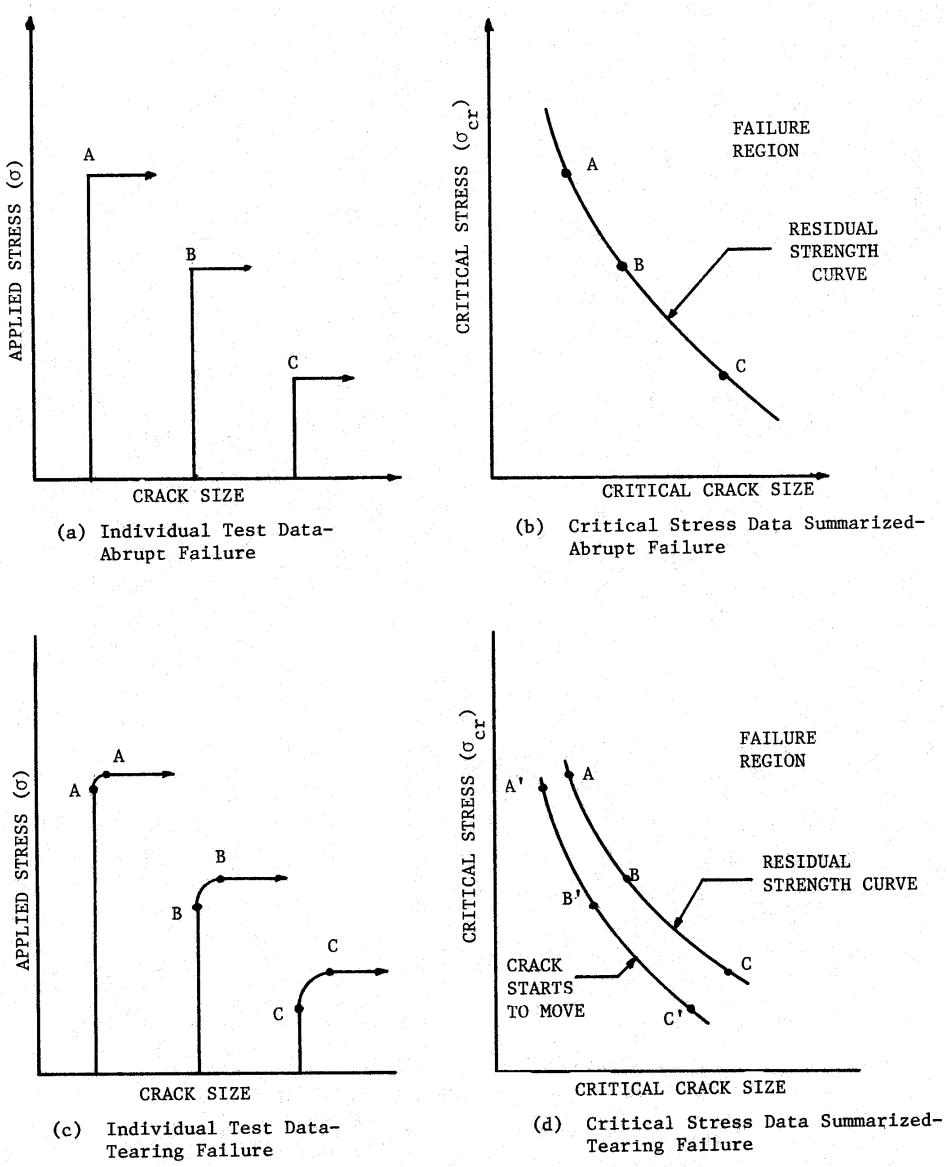

Figure 4.2.2. Fracture Data Described as a Function of Crack Length

4.2.1 Ultimate Strength

The simplest failure criterion assumes that failure occurs at the ultimate (or yield) strength of the material. Thus, the failure criterion becomes simply

$$\sigma_f = F_{tu} \tag{4.2.1}$$

where σ_f is the fracture stress and F_{tu} is the ultimate strength. This criterion is applicable primarily to uncracked structures and is included here for completeness. In past analyses of failure of built-up structure, the residual strength of stiffeners was based upon this criterion. When the main panel between the stiffeners fails due to catastrophic crack growth, the panel loads are transferred to the stringers (or stiffeners). The transferred loads may increase the stress level in the stringer so it is high enough to reach the value of σ_f, causing stiffener failure.

4.2.2 Fracture Toughness – Abrupt Fracture

In a cracked structure, as discussed in Section 2, the stress intensity factor (K) interrelates the local stresses in the region of the crack tip with crack geometry, structural geometry, and the level of load on the structure. When the applied load level increases, the K value also increases and reaches a critical value at which time the crack growth becomes unstable, as shown in Figure 4.2.3.

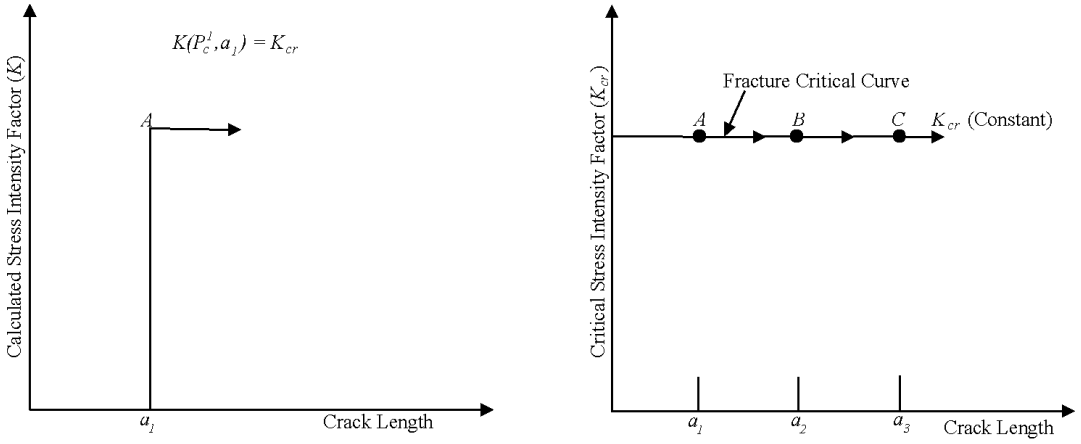

(a) Stress Intesity Factor Calculated as a Function of Load and Crack Length

(b) Critical Stress Intesity Factor Levels Described as a Function of Crack Length

Figure 4.2.3. The Fracture Mechanics Basis for Establishing Residual Strength

This critical level of K, which is independent of the crack length, is a material property called fracture toughness. The fracture toughness is a measure of the material's resistance to unstable cracking. Several test procedures are available to evaluate the fracture toughness. Also, various theoretical and numerical solution techniques are available, as discussed in Section 2, which can be used to estimate the (applied) stress intensity factor, K, for a given structure.

The failure criterion (Irwin's Criterion) states that abrupt fracture occurs when the crack-tip stress-intensity factor reaches or exceeds the fracture toughness of the material. The corresponding applied stress at failure is called the fracture strength. The failure criterion becomes simple

$$K \geq K_{cr} \tag{4.2.2}$$

where K_{cr} is the material's fracture toughness.

The critical K_{cr} for abrupt fracture mode is denoted as K_{Ic} for plane strain conditions and K_c for plane stress conditions; the conditions for plane stress or plane strain are determined by experiment. The test requirements necessary for generating K_{Ic} and K_c are discussed in Section 7.

The Damage Tolerant Design (Data) Handbook [Skinn, et al., 1994] contains a large quantity of fracture toughness data. Examples of the formats associated with individual test data for 7075 aluminum alloy are shown in Figures 4.2.4 and 4.2.5 for plane strain and plane stress fracture toughness values, respectively.

TABLE 8.9.2.1

1 of 36

ALUMINUM 7075 K_{Ic}

CONDITION	PRODUCT FORM	PRODUCT THICK (in.)	TEST TEMP (°F)	SPEC OR	YIELD STR (Ksi)	SPECIMEN WIDTH (in.) W	SPECIMEN THICK (in.) B	SPECIMEN DESIGN	CRACK LENGTH (in.) A	2.5 * (K_{Ic}/TYS)^2 (in.)	K_{Ic} (K_{Ic} (Ksi * $\sqrt{in.}$))	K_{Ic} MEAN	K_{Ic} STAN DEV	DATE	REFER
T6	Forging	0.50	R.T.	L-T	79.0	1.000	0.500	CT	0.534	0.23	24.20	24.3	0.1	1973	86213
		0.50			79.0	1.000	0.500	CT	0.523	0.24	24.40			1973	86213
T6	Forging	0.89	R.T.	T-L	67.2	0.500	0.249	NB	0.265	0.21	19.70	20.9	1.7	1973	86213
		0.89			70.0	0.500	0.249	NB	0.273	0.25	22.10			1973	86213
T6	Forging	0.50	R.T.	S-L	65.4	1.000	0.499	CT	0.493	0.17	17.00	16.8	0.4	1973	86213
		0.50			65.4	1.000	0.500	CT	0.510	0.16	16.70			1973	86213
		0.50			65.4	1.000	0.500	CT	0.496	0.16	16.40			1973	86213
		0.50			65.4	1.000	0.500	CT	0.505	0.17	17.20			1973	86213
T6	Forging	0.75	82	L-T	69.9	2.000	0.500	CT	1.025	0.44	29.20	---	---	1973	86213
T6	Forging	0.89	82	T-L	57.4	1.500	0.749	CT	0.785	0.32	20.40	19.4	1.7	1973	86213
		0.89			57.4	1.500	0.749	CT	0.762	0.32	20.40			1973	86213
		0.75			67.6	1.000	0.500	CT	0.511	0.17	17.50			1973	86213
T6	Forging	0.89	84	T-L	68.0	1.500	0.750	CT	0.792	0.24	21.20	20.6	0.8	1973	86213
		0.89			68.0	1.500	0.750	CT	0.798	0.22	20.00			1973	86213
T6	Extrusion	2.00	R.T.	T-L	72.0	1.500	0.750	CT	0.797	0.19	20.00	19.9	0.2	1973	86213
		2.00			73.6	1.500	0.749	CT	0.798	0.18	19.70			1973	86213
		2.00			73.6	1.500	0.748	CT	0.791	0.19	20.10			1973	86213
T6	Extrusion	2.00	R.T.	S-L	67.0	1.500	0.748	CT	0.791	0.19	18.50	18.5	0.2	1973	86213
		2.00			67.0	1.500	0.750	CT	0.798	0.19	18.30			1973	86213
		2.00			67.2	1.500	0.749	CT	0.808	0.19	18.70			1973	86213
T6	Forged Bar	---	R.T.	C-L	68.6	1.500	0.750	CT	0.750	0.20	19.60	19.5	0.2	1972	82879
		---			68.6	1.500	0.750	CT	0.750	0.20	19.30			1972	82879

Figure 4.2.4. Plane-Strain Fracture Toughness (K_{Ic}) Data for 7075 Aluminum in the Format of the Damage Tolerant Design (Data) Handbook [Skinn, et al., 1994]

TABLE 8.9.2.2

1 of 81

ALUMINUM 7075 K_C

CONDITION HEAT TREAT	PRODUCT FORM	PRODUCT THICK (in.)	TEST TEMP (°F)	SPEC OR	YIELD STR (Ksi)	SPECIMEN WIDTH (in.) W	SPECIMEN THICK (in.) B	CRACK LENGTH INIT (in.) $2a_o$	CRACK LENGTH FINAL (in.) $2a_f$	GROSS STRESS ONSET (Ksi) σ_o	GROSS STRESS MAX (Ksi) σ_{max}	K_{app} K_{app} (Ksi$\sqrt{in}$)	K_{app} MEAN	K_{app} STAN DEV	K_C K_C (Ksi$\sqrt{in}$)	K_C MEAN	K_C STAN DEV	DATE	REFER
BUCKLING OF CRACK EDGES RESTRAINED																			
T6	Sheet	0.10	R.T.	L-T	75.9	1.500	0.100	0.500	0.570	---	44.90	42.76*	---	---	46.72*	---	---	1962	62306
T6	Sheet	0.10	R.T.	L-T	75.9	3.500	0.100	0.500	0.760	---	53.70	48.20*	---	---	60.44*	---	---	1962	62306
		0.10			75.9	3.500	0.100	0.770	1.140	---	46.40	52.61			66.49*			1962	62306
T6	Sheet	0.10	R.T.	L-T	75.9	6.000	0.100	2.000	2.450	---	33.50	63.81	---	---	73.42	---	---	1962	62306
T6	Sheet	0.09	R.T.	L-T	75.9	12.000	0.090	1.040	1.460	---	46.60	59.84	64.6	3.2	71.22	71.9	2.8	1969	75599
		0.09			75.9	12.000	0.090	2.340	2.860	---	33.70	66.17			74.04			1969	75599
		0.09			75.9	12.000	0.090	1.060	1.560	---	44.80	58.09			70.87			1969	75599
		0.09			75.9	12.000	0.090	1.400	1.860	---	43.60	65.20			75.65			1969	75599
		0.09			75.9	12.000	0.090	3.880	4.720	15.30	25.20	66.55			76.00			1969	75599
		0.09			75.9	12.000	0.090	2.800	3.460	---	29.90	64.90			73.51			1969	75599
		0.09			75.9	12.000	0.090	1.100	1.440	---	44.00	58.14			66.77			1969	75599
		0.09			75.9	12.000	0.090	1.560	1.880	---	41.20	65.17			71.89			1969	75599
		0.09			75.9	12.000	0.090	4.500	5.460	11.40	22.50	65.60			75.82			1969	75599
		0.09			75.9	12.000	0.090	1.080	1.420	---	46.10	60.35			69.45			1969	75599
		0.09			75.9	12.000	0.090	1.820	1.920	---	40.00	68.61			70.58			1969	75599
		0.09			75.9	12.000	0.090	3.180	3.600	---	28.20	65.90			71.04			1969	75599
		0.09			75.9	12.000	0.090	3.060	3.580	---	28.20	64.43			70.80			1969	75599
		0.09			75.9	12.000	0.090	2.040	2.320	---	35.60	64.89			69.57			1969	75599
		0.09			75.9	12.000	0.090	2.620	3.500	---	29.80	61.88			73.29			1969	75599

* NOTE: NET SECTION STRESS EXCEEDS 80% OF YIELD STRENGTH. VALUE NOT INCLUDED IN MEAN OR STANDARD DEVIATION.

Figure 4.2.5. Plane-Stress Fracture Toughness (K_c) Data for 7075 Aluminum in the Format of the Damage Tolerant Design (Data) Handbook [Skinn, et al., 1994]

In general, a material's toughness depends on thickness, as shown in Figure 4.2.6. When the thickness is such that the crack tip plastic zone size is on the order of the plate thickness, the toughness reaches a maximum value, $K_{c(max)}$. With increasing thickness of the plate, the plastic zone size reduces and thus the toughness gradually decreases, from $K_{c(max)}$ to K_{Ic}. When the thickness is large enough that the crack tip deformation is not affected by the thickness, plane strain conditions prevail at the crack tip. The toughness in the plane strain regime is virtually independent of thickness. For increasing thickness, the toughness asymptotically approaches the plane strain fracture toughness, K_{Ic}.

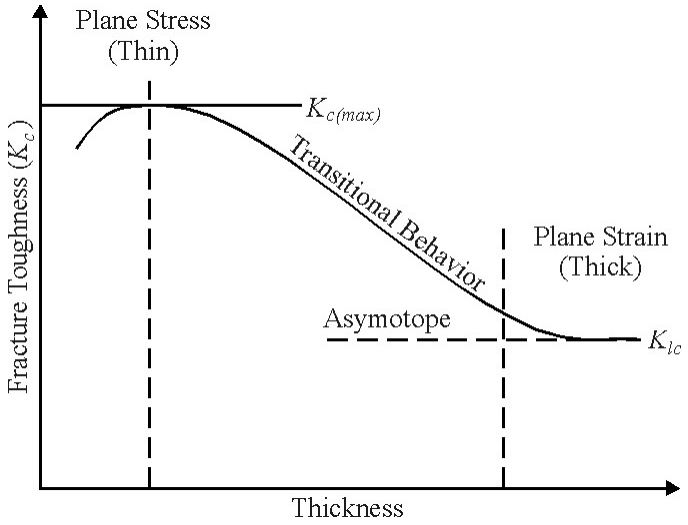

Figure 4.2.6. Fracture Toughness as a Function of Thickness

4.2.3 Crack Growth Resistance – Tearing Fracture

As illustrated in Figures 4.2.2c and d, when the crack extends by a tearing mode of fracture, which typically occurs in thin metal sheets or in tough materials, the crack extension is essentially slow and stable. The failure condition for tearing fractures depends on the crack growth resistance (K_R) behavior of the material and the applied stress-intensity factor K, which in turn depends on the crack and structural configurations. Figure 4.2.7 describes the observations that lead to the development of the crack growth resistance curve (K_R vs. Δa). Figure 4.2.7 a and b present the tearing behavior as a function of applied stress and the corresponding stress-intensity factor, respectively. Figure 4.2.7c presents the crack growth resistance curve that is a composite of the three stress-intensity factor curves shown in Figure 4.2.7b. Note that the composite was created by using the amount of physical crack movement observed in each case as the independent variable. As implied by the data points on the crack growth resistance curve in Figure 4.2.7c, the stress-intensity factor level associated with material failure is not necessarily constant.

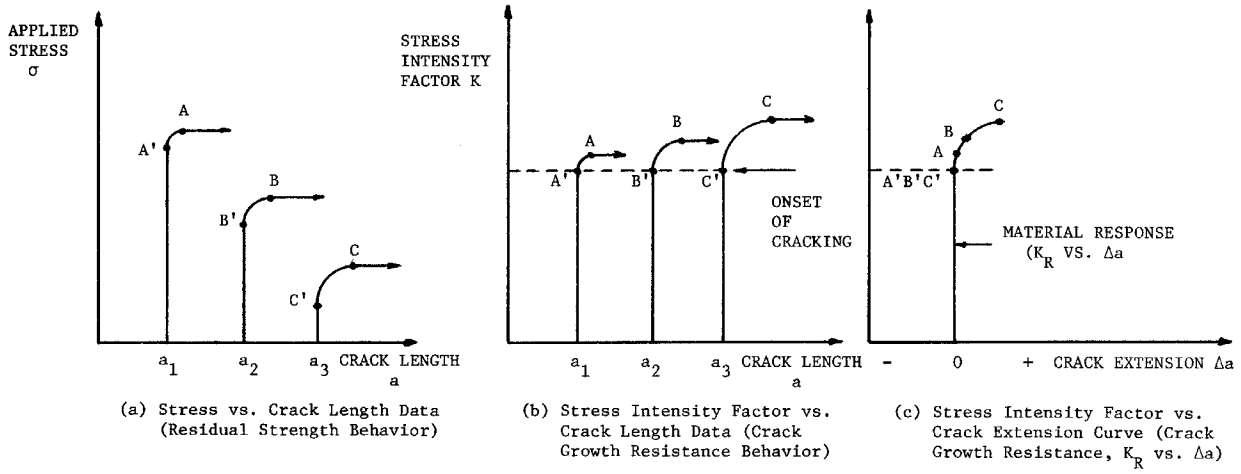

Figure 4.2.7. Schematic Illustration of Tearing Fracture Behavior and the Development of a Crack Growth Resistance Curve (R-Curve)

Shown in Figure 4.2.8 is a resistance curve for a 7475 aluminum alloy described as a function effective crack length [Margolis, et al., 1975]. The effective crack length is the sum of the physical crack length and the plastic zone size corresponding to the current crack length and loading conditions.

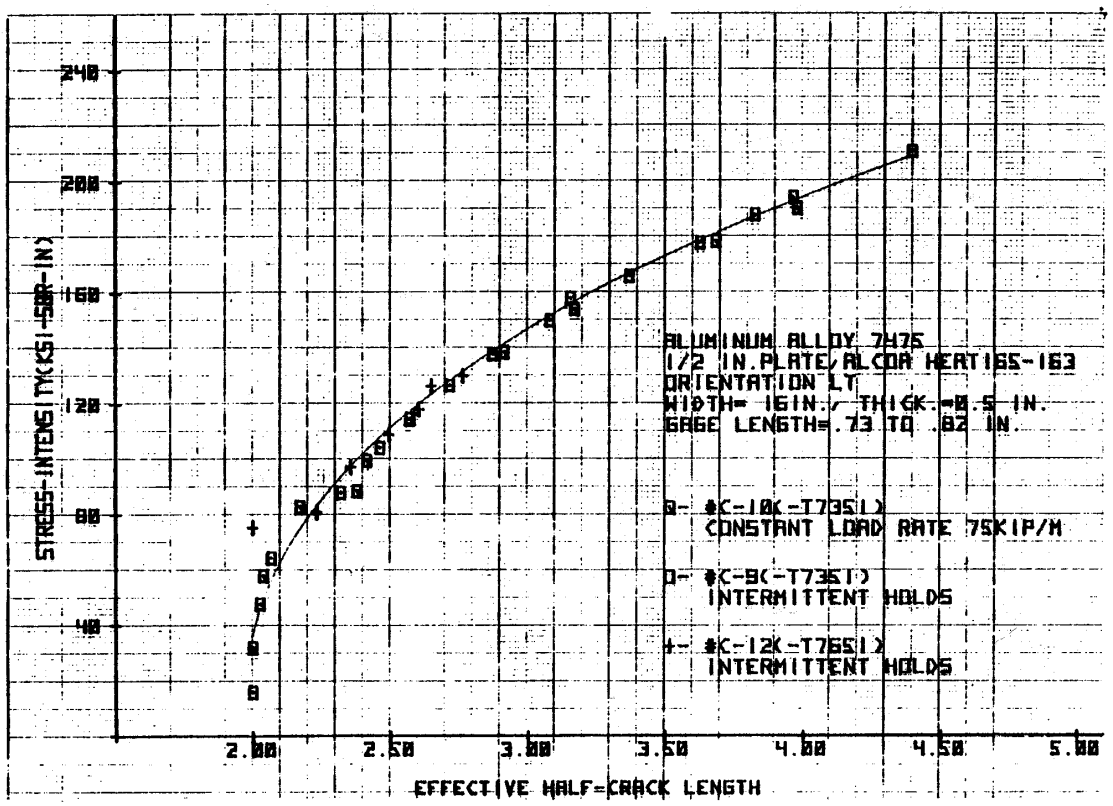

Figure 4.2.8. K_R Curve from 7475 Alloy, 16 Inch Wide Panels, 0.5 Inch Thick [Margolis, et al., 1975]

Indeed, while the shape of the resistance curve is basically independent of crack length or other geometrical effects, the fracture level is a function of crack length (see Figure 4.2.9). To account for this variation in fracture critical level, a two parameter failure criterion was required. However, before introducing the two parameter criteria that are used for more accurate estimates, approximate single parameter criteria for tearing failures are presented.

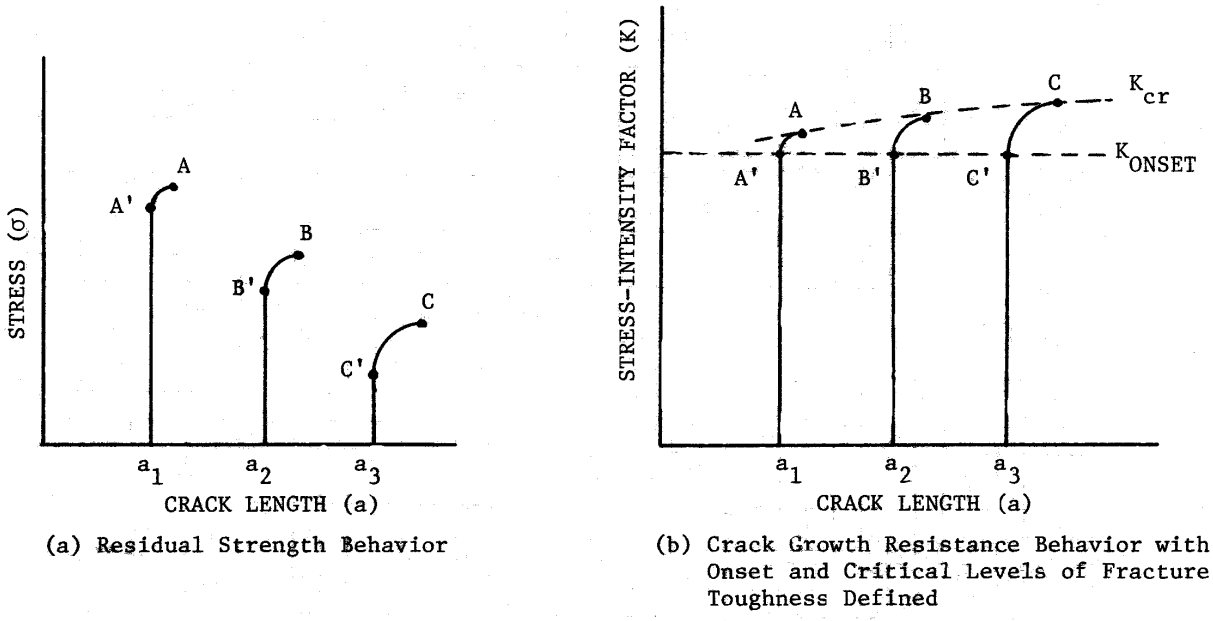

Figure 4.2.9. Schematic Illustration of Tearing Fracture Behavior Which Further Defines the Change in Critical Level of Fracture Toughness as a Function of Crack Length (also see Figure 4.2.7)

4.2.3.1 The Apparent Fracture Toughness Approach

Due to the complexity of the two parameter fracture criteria for tearing fracture behavior, engineers sometimes obtain preliminary estimates for the residual strength using a single parameter fracture toughness criterion. Figure 4.2.10 describes the stress-crack length levels associated with the onset of cracking ($K = K_{ONSET}$) and fast fracture ($K = K_{cr}$) conditions for a tearing material. Intermediate between the two curves established from material observations is a third curve referred to as the apparent fracture curve. The apparent fracture toughness (K_{APP}) is established from the same data employed to derive K_{ONSET} and K_{cr}. The calculation procedure uses the onset (or initial) crack length (a_i) and the final recorded stress level (σ_{cr}) for the tests conducted. Thus, K_{APP} represents a fracture toughness level bounded by the onset and fast fracture levels.

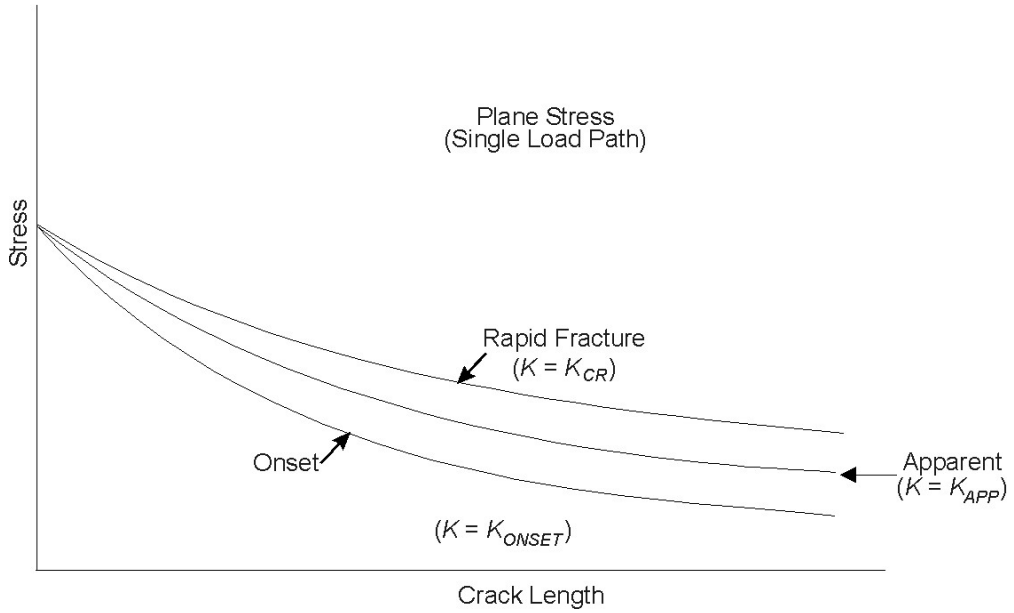

Figure 4.2.10. Description of the Three Fracture Toughness Criteria that are Utilized to Estimate Residual Strength Under Tearing Fracture Conditions

For lower bound estimates of the residual strength for fast fracture of a tearing material, one could equate the level of applied stress-intensity factor (K) to the apparent fracture toughness (K_{APP}), i.e., assume that fracture occurs when

$$K = K_{APP} \tag{4.2.3}$$

in order to determine the critical level of stress. Equation 4.2.3 is an abrupt failure criterion for a tearing fracture.

4.2.3.2 The Resistance (R) Curve Approach

If the crack tip plastic zone size is estimated to be on the order of the structural thickness but substantially smaller than other geometrical variables (crack length, ligament size, height, etc.), a linear elastic fracture mechanics analysis can still be sensibly used to predict the catastrophic cracking event. The failure criterion for tearing type fractures under these conditions states that fracture will occur when (1) the stress-intensity factor K reaches or exceeds the material's fracture resistance K_R and (2) the rate of change of K (with respect to crack length) reaches or exceeds the rate of change of K_R (with respect to crack length). Physically, the criterion means that at failure, the energy available to extend the crack equals or exceeds the material resistance to crack growth. The failure criterion becomes simply,

$$K \geq K_R; \quad \frac{\partial K}{\partial a} \geq \frac{\partial K_R}{\partial a} \tag{4.2.4}$$

The corresponding applied stress, σ_f, at this point is defined as the fracture stress that determines the residual strength of the cracked structure. The criterion presented in Equation 4.2.4 is noted to be a two-parameter criterion rather than the single parameter criteria that was presented in paragraph 4.2.3.1. To interpret the meaning of this criterion, first consider the structural parameters that are a function of the geometry and stress, i.e. K and $\frac{\partial K}{\partial a}$.

In general, the estimation of K involves the relationship $K = \sigma\beta\sqrt{\pi a}$ as given in Section 2; using this equation, the variation of K with respect to crack length (a) can be obtained for various values of stress (σ) as shown in Figure 4.2.11a. Shown in Figure 4.2.11b is the variation of K_R with respect to the crack extension (Δa) that was developed for the given material using the procedures outlined in Figure 4.2.7. Since this R-curve is assumed to be independent of the initial crack length, it can be superimposed on the plot of K versus a as shown in Figure 4.2.11c. The tangency point between the applied stress intensity factor curve (K vs. a) and the R-curve (K_R vs. Δa) determines the commencement of unstable crack propagation. In general, the accurate method of determining the tangency point involves the numerical solution based on the experimentally obtained R-curve. Using a least squares determined polynomial expression for R-curve and knowing an expression for K in terms of crack length, the common tangent point can be obtained by equating the functional values ($K = K_R$) and also the first derivatives with respect to the crack length $\left(\frac{dK}{da} = \frac{dK_R}{da}\right)$ of these two expressions.

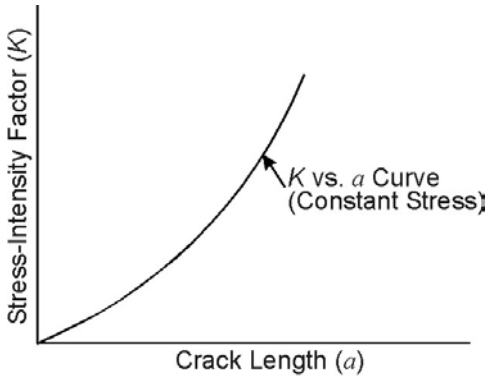

(a) Driving Force

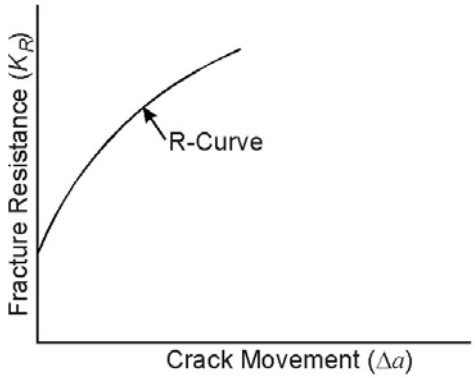

(b) Resistance to Crack Growth

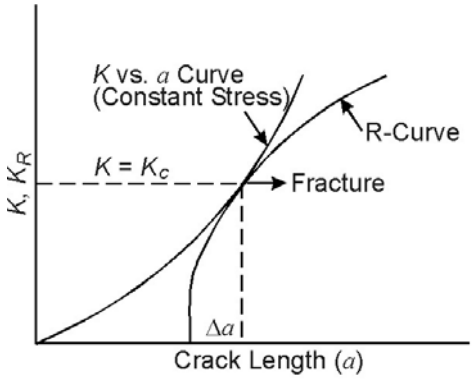

(c) Establishment of Critical Conditions

Figure 4.2.11. Schematic Illustration of the Individual and Collective Parts of a K_R Fracture Analysis

The slow stable tear is dependent on a structural configuration in which the plastic zone at the crack tip is no longer negligible but not enormous. Krafft, et al. [1961], Srawley & Brown [1965], and McCabe [1973] explain the dependence of the *R*-curve on structural configuration as well as with test procedures used to evaluate the *R*-curve. See Section 7 for additional information on test procedures and the Damage Tolerant Design (Data) Handbook [Skinn, et al., 1994] for a summary of available data.

4.2.3.3 The *J*-Integral Resistance Curve Approach

The crack growth resistance curve (K_R) has shown good promise for materials where limited (small-scale) yielding occurs in front of the crack tip. Difficulties in estimating crack tip plasticity under large-scale yielding conditions, led Wilhem [1974] to an alternate failure criterion based on the *J*-integral [Rice, 1968]. For a basic introduction to the *J*-integral see Section 11.

Wilhem's *J*-integral criterion is similar to the K_R-curve criterion; it states that failure will occur when the following conditions are met:

$$\sqrt{J} \geq \sqrt{J_R}; \frac{d\sqrt{J}}{da} \geq \frac{\partial\sqrt{J_R}}{\partial a} \qquad (4.2.5)$$

where J is the value of the applied *J*-integral and J_R is the value of the *J*-integral representing the material resistance to fracture. The applied stress (σ_f) corresponding to Equation 4.2.5 is defined as the fracture stress. Since the effect of large-scale yielding can be appropriately incorporated through a suitable elastic-plastic model in the estimation of *J*-integral, it becomes an effective parameter for predicting failure under plane stress conditions where the plastic zone size is significantly large.

The crack resistance curve for the tearing failure is now represented by $\sqrt{J_R}$ vs. Δa curve instead of K_R vs. Δa curve. The use of $\sqrt{J_R}$ rather than J_R is justified by the fact that $\sqrt{J}$ is directly related to the stress-intensity factor for elastic behavior through the equation

$$J = K^2/E' \qquad (4.2.6)$$

where E' is the elastic modulus (E) for plane stress conditions and $E/(1-\nu^2)$ for plane strain conditions.

For different levels of applied load, the *J*-integral can be computed using finite element techniques for the structure of interest for a series of different crack sizes; the $\sqrt{J}$ versus crack length curve is illustrated in Figure 4.2.12a for a constant level of applied stress. It is noted that this curve will incorporate the influence of material properties (yield strength and strain hardening exponent) through the finite element analysis. In a manner similar to the stress-intensity factor type resistance curve, i.e. the K_R curve. The resistance curve based on $\sqrt{J_R}$ can be experimentally obtained [Griffis & Yoder, 1974; Verette & Wilhem, 1973]. A $\sqrt{J_R}$ versus crack movement (Δa) curve, i.e. the *J*-integral resistance curve, is schematically illustrated in Figure 4.2.12b. The failure criterion is also based on the tangency conditions between the $\sqrt{J}$ versus crack length curve and the $\sqrt{J_R}$ versus crack movement curve. To obtain this condition, the $\sqrt{J_R}$ vs. Δa curve can be superimposed on the plot of $\sqrt{J}$ vs. a curve such that at some crack length these two curves are tangent to each other as shown in Figure 4.2.12c. The corresponding crack length then defines the critical crack size of the structure for the fracture stress, σ_f.

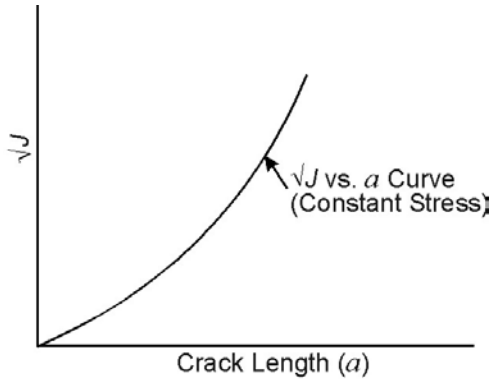

(a) Driving Force

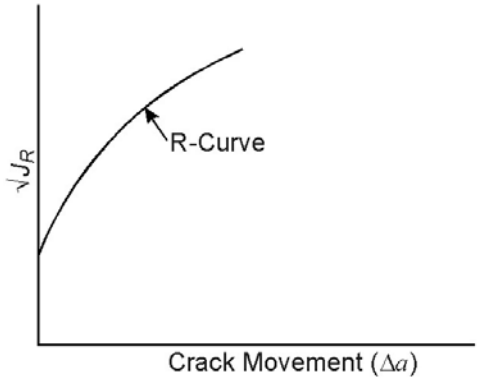

(b) Resistance to Crack Growth

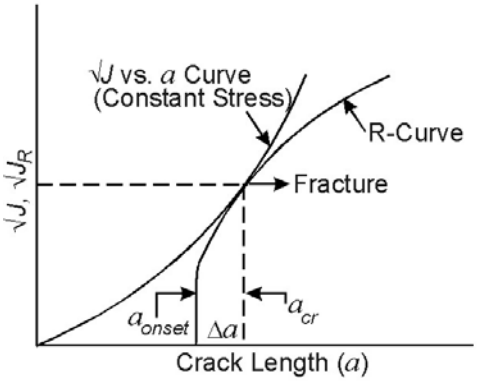

(c) Establishment of Critical Conditions

Figure 4.2.12. Schematic Illustration of the Individual and Collective Parts of a J_R Fracture Analysis

4.3 Residual Strength Capability

To establish the residual strength capability of a given structure under certain loading conditions, prediction techniques must be developed with a thorough understanding of the complexities involved in evaluating the residual strength. For monolithic or single load path structures which must be classified as slow crack growth structures, the estimation of residual strength capability is straightforward. In multiple load path, built-up structures, whether classified as slow crack growth or fail-safe structures, the strength analysis can become complicated due to the complex geometric construction of the built-up components. In general, the prediction techniques are based on the critical value of the stress-intensity factor for a given geometry and loading. Using fracture toughness failure criteria as explained earlier, the decay in critical stress can be obtained in terms of crack size.

As described by Figure 4.1.2, the residual strength capability is a function of service time for a given structure. This is because the residual strength capability depends on the size of the crack in the structure and the crack grows as a function of time. Thus, to obtain a residual strength capability curve (Figure 4.1.2), one needs two types of data: (a) the relationship between crack length and time, and (b) the relationship between fracture strength (σ_f) and crack length. Section 5 is devoted to obtaining the crack length-time relationship and the remainder of this section is devoted to presenting methods and procedures for obtaining the fracture strength-crack length (σ_f vs. a) relationship. It is to be noted that the σ_f vs. a relationship is independent of time and has been referred to in the general literature as the residual strength diagram. This section presents useful information about residual strength diagrams for single load path and for multiple load path structures.

4.3.1 Single Load Path Residual Strength Diagrams

For a single load path structure, such as an unstiffened panel, the residual strength diagram under plane strain conditions, consists of a single curve as shown in Figure 4.3.1. The procedure for developing the residual strength diagram involves the calculation of the critical stress σ_f, for the critical crack length a_c, using the relationship

$$K_{cr} = \sigma_f \beta \sqrt{\pi a_c}$$

where K_{cr} is the known value of fracture toughness of the material. (K_{cr} may be equal to K_{Ic} or K_c depending on the problem.) The plot of σ_f vs. a_c then provides the necessary residual strength diagram required in design analysis for the simple configuration.

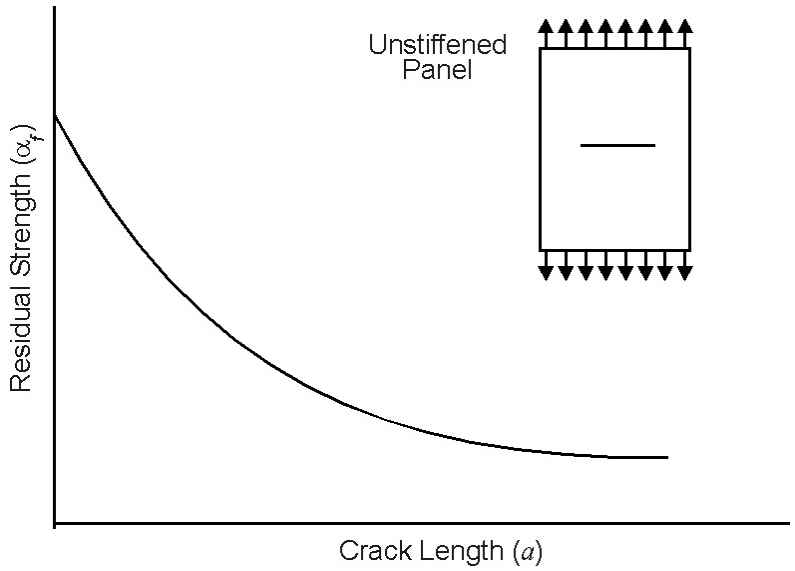

Figure 4.3.1. Residual Strength Diagram for Abrupt Failure of a Single Load Path Structure

The available fracture mechanics solution techniques, as given in Section 11, can be employed in the calculation of the crack-tip stress-intensity factor K to construct the residual strength diagram. Depending on the complexity of the structure, K can be calculated either numerically or through closed form solutions. These techniques, in conjunction with an appropriate failure criterion, can then be used to determine the residual strength capabilities of a given structure.

In general, the construction of a residual strength diagram involves three steps:

(a) The development of the relationship between the applied stress σ, the crack length parameter a, and the applied stress-intensity factor K for the given structural configuration (see Section 11).

(b) The selection of an appropriate failure criterion based for the expected material behavior at the crack tip (see Section 4.2.1).

(c) The fracture strength (σ_f) values for critical crack sizes (a_c) are obtained utilizing the results of the first two steps and residual strength diagram (σ_f vs. a_c) for the given structural configuration is plotted.

To understand these three steps for constructing a residual strength diagram, the following example is considered. The example considers a wide thin panel with a central crack that has a simple relationship for the stress intensity factor. This example illustrates the importance of the stress-intensity factor for constructing the residual strength diagram.

EXAMPLE 4.3.1 Unstiffened Center Crack Panel

Construct the residual strength diagram for the wide unstiffened panel shown here, assuming that the structure is made from 7075-T6 aluminum sheet material, with a fracture toughness of 40 ksi $\sqrt{in}$.

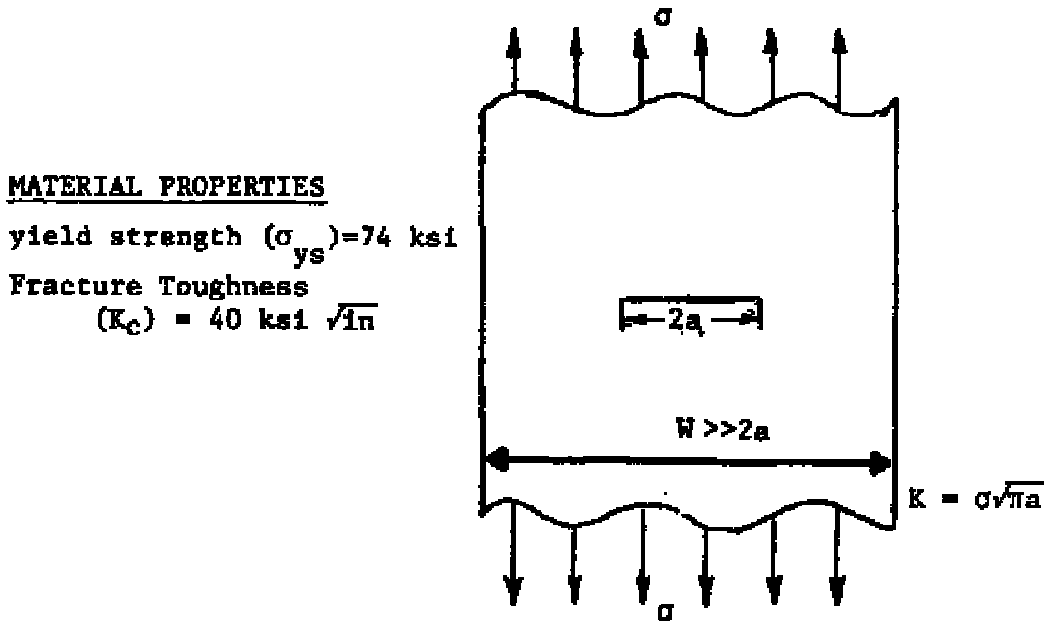

SOLUTION:

Step 1. Define the stress-intensity factor relationship. From Section 11, the stress intensity factor for a wide unstiffened, center crack panel is given by

$$K = \sigma\sqrt{\pi a}$$

Step 2. Define the failure criterion. For this problem, it is assumed that an abrupt fracture occurs and the condition that defines the fracture is

$$K = K_{cr} = K_c = 40 \ ksi\sqrt{in}$$

Step 3. Utilize the results of the first two steps to derive a relationship between fracture strength (σ_f) and critical crack size (a_c), the σ_f vs. a relationship is given by

$$\sigma_f \sqrt{a_c} = 40/\sqrt{\pi}$$

For a half crack size (a_c) of 2.0 inch, the fracture strength (σ_f) is about 16 ksi. Other (σ_f vs. a_c) values can be similarly obtained. Once a sufficient number of values are available, the residual strength diagram can be developed, or one could also attack the problem in the graphic manner that is explained using the following:

Step 1. Construct a plot of K vs a by using the equations in Step 1 for various values of stress and crack lengths.

Step 2. Superimpose the horizontal line $K = K_{cr} = 40$ ksi $\sqrt{in}$ on the diagram. This line represents the critical stress intensity, i.e., fracture toughness, for this material and is independent of crack length.

Step 3. Complete the residual strength diagram. Utilize the intersection points of the horizontal line with curves where the failure criterion is satisfied, i.e. where $K_{cr} = \sigma_f \sqrt{\pi a_c}$. The values of the respective stresses and the crack sizes at these points are termed to be the failure stresses and the critical crack sizes for the given structure, i.e., the unstiffened panel. The residual strength diagram is finally constructed by plotting the σ_f vs. a_c curve.

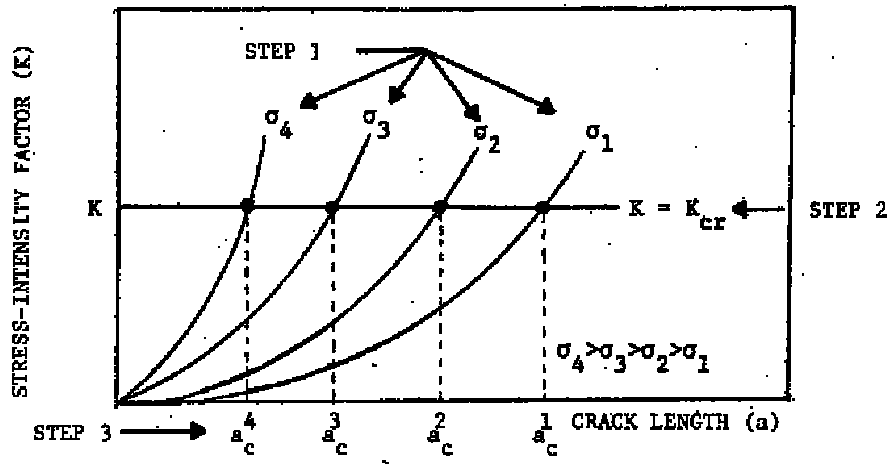

(a) Stress-Intensity Factor as a Function of Crack Length for Constant Values of Stress

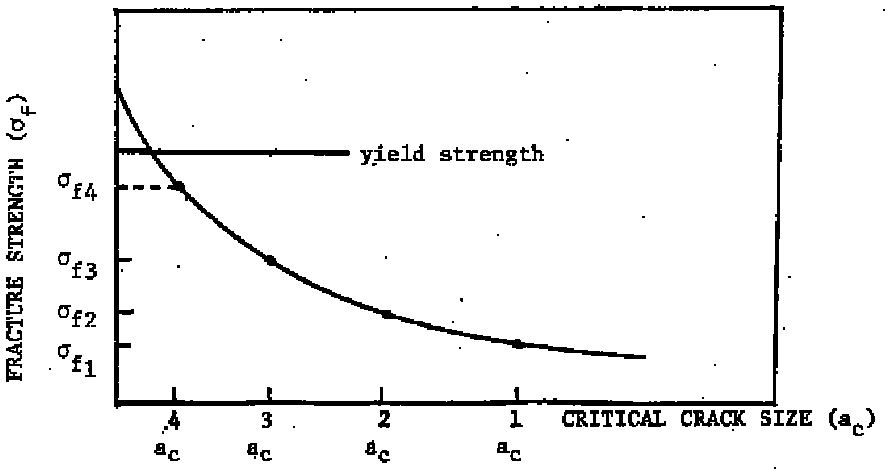

(b) Residual Strength Diagram

4.3.2 Built-Up Structure Residual Strength Diagrams

In single load path structures, the residual strength analysis involved only one failure criterion for a given structural geometry. In built-up structures, due to the complex geometrical configuration, one or more failure criterion may have to be considered in the determination of residual strength for the whole structure. The following paragraphs examine these aspects of the residual strength analysis of built-up structures.

It was explained earlier that safety can be achieved by designing aircraft structure either as slow crack growth or as fail-safe. The latter case can further be classified into two cases: Multiple Load Path and Crack Arrest. Typically, both Multiple Load Path and Crack Arrest structures are built-up structures. In Section 1.3, the definitions and requirements for these two types of built-up structure are discussed. For completeness, the structure shown in Figure 4.3.2 is analyzed to further explain the features inherent in multiple load path, built-up structure.

As long as the central member is not failed, all three elements carry a share of the total load P. In the event of failure of the center member, the total load P (actually $1.15P$) must be transmitted by the other two members at the instant of failure, if the structure is to stay intact.

The residual strength capability for the multiple load path structure shown in Figure 4.3.2 can be explained with Figure 4.3.3. When one element fails, Figure 4.3.3 shows that the remaining parallel members are able to carry the required load without failure. The residual capability is shown to degrade as the crack in the central member extends and as the cracks in the remaining elements fail. Figure 4.3.3 shows the discontinuous change in the strength capability as a result of element failures. Since the load levels in other members dramatically increase, if the load P must be maintained, the remaining members will have short lives. Thus, the second member may fail after the time (t_2). The residual strength capability is shown to drop below the safe level somewhere in time between t_1 and t_2. The duration of the time interval between the failure of the first element and the failure of the structure may be short or long depending on the "type of failure" of the first member and the load requirements subsequent to this failure. This time interval is available for the detection of the failure of the first member and the repair of the structure.

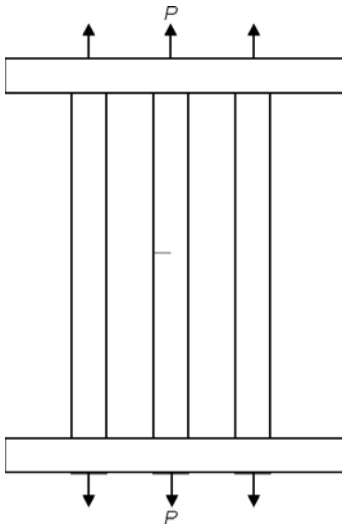

Figure 4.3.2. Multiple Load Path (Built-up) Structure with a Crack in the Central Member

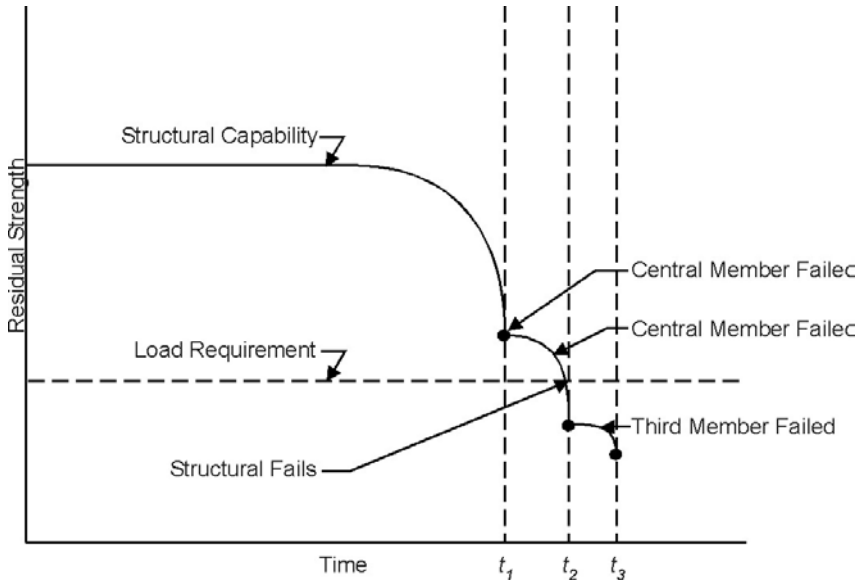

Figure 4.3.3. Reduction of Residual Strength During Successive Failure of Members in the Structure Shown on Figure 4.3.2

The failure stress or the critical flaw size level of the central member (any one of the parallel members) can be estimated by treating the problem in a manner similar to the single load path structure. Using a fatigue crack growth analysis, the crack propagation curve is obtained from the minimum detectable crack size to the critical crack length as illustrated in Figure 4.3.4. In multiple load path structure, partial failure of the structure can occur during its operating period. But this failure must be detected at an inspection before catastrophic failure of the entire structure occurs. A suitable inspection schedule must include analysis of structural characteristics along with the operational requirements for the intervals between inspections.

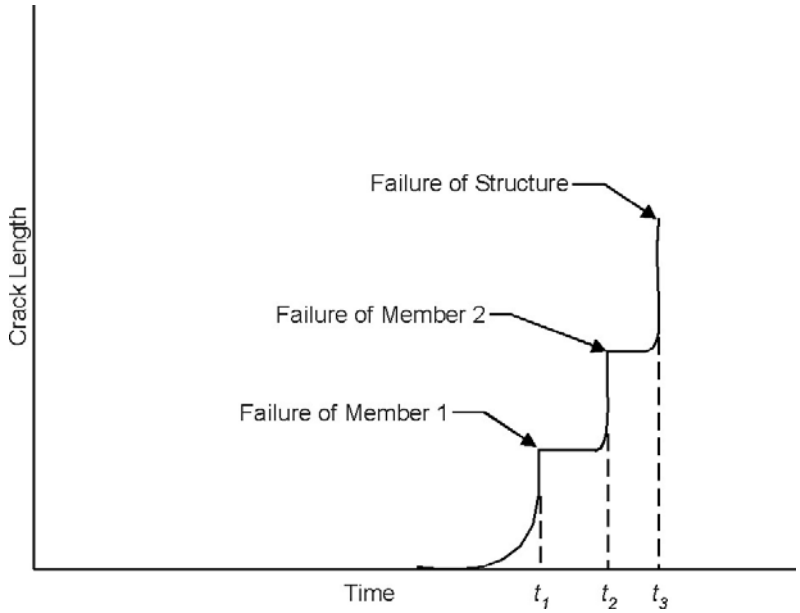

Figure 4.3.4. Crack Growth for Multiple Load Path Structure Shown in Figure 4.3.2

To illustrate the analysis involved in the estimation of residual strength of complex structures, consider an axially loaded skin-stringer combination with longitudinal stiffening as shown in Figure 4.3.5. Assuming that the fasteners are rigid, the displacements of adjacent points in skin and stringers will be equal. (If skin and stringers are made from the same material, the stresses in the two will also be equal for the case of no crack.) Let a transverse crack develop in the skin. This will cause larger displacement in the skin, and the stringers must follow this larger displacement. As a result, they take load from the skin, thus decreasing the skin stress at the expense of higher stringer stress. Consequently, the displacements in the cracked skin will be smaller than in an unstiffened plate with the same size of crack. This implies that the skin stresses are lower and that the stress-intensity factor is lower. The closer the stringers are to the crack, the more effective is the load transfer.

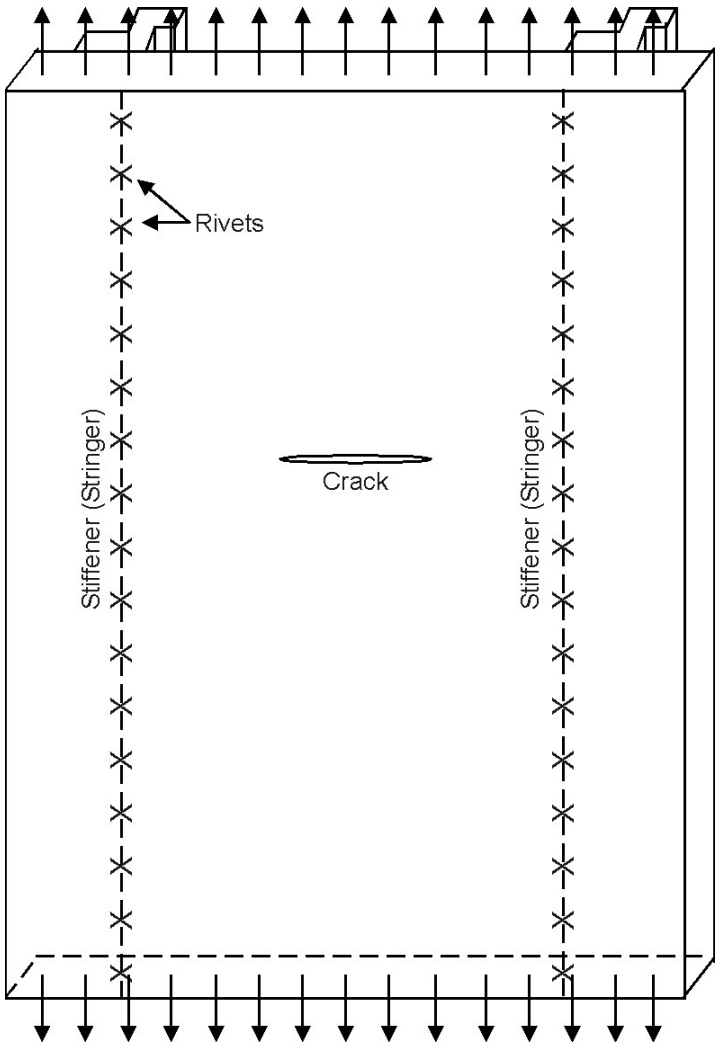

Figure 4.3.5. Skin-Structure Built-Up Structure

If the stress-intensity factor for a small crack in an unstiffened panel is approximated by $K = \sigma\sqrt{\pi a}$, the stress-intensity factor for the stiffened plate will be $K = \beta\sigma\sqrt{\pi a}$. The reduction

factor, $\beta = K/\sigma\sqrt{\pi a}$, will decrease when the crack tip approaches a stringer. Since the stringers take load from the skin, the stringer stress will increase from σ to $L\sigma$, where L increases as the crack tip approaches the stringer. Obviously, $0 < \beta \leq 1$, and $L \geq 1$. These values depend upon stiffening ratios, the stiffness of the attachment, and the ratio of crack size to stringer spacing. As will be shown subsequently, β and L can be readily calculated; at this point it is sufficient to note that β and L vary with crack length as shown in Figure 4.3.6.

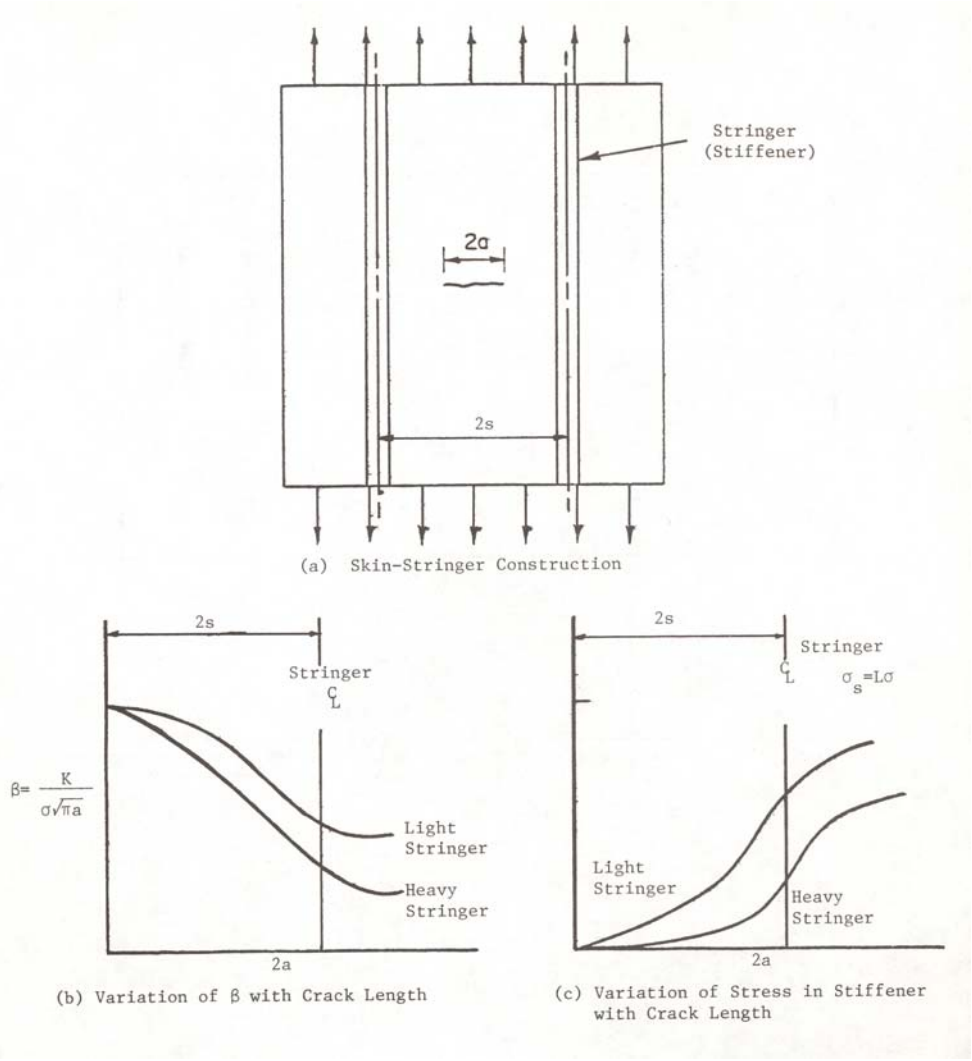

Figure 4.3.6. Variation of B and L with Crack Length in Stiffened Panel with a Crack Between the Stiffeners

Due to the complexity of stiffened skin structure, the construction of a residual strength diagram is considerably more difficult. Consider first the condition where an abrupt failure in the skin occurs. When the crack is small as compared to the stiffener spacing, the residual strength of the skin is not influenced by the stiffeners and the initial portion of the diagram follows the plot for an unstiffened panel (see point A in Figure 4.3.7). Once the crack size is long enough that the skin cannot sustain the applied load any further, the stringer will take some of the load from the skin, thus decreasing the skin stress. Consequently, the crack-tip stress-intensity factor will be

lower due to the reduced stress and so the residual strength of the skin structure will increase with crack length as shown in Figure 4.3.6. As the crack size increases further toward the stiffener location, the load transferred from the skin to the stiffener also increases significantly, thus reducing the stress-intensity factor. The residual strength of the stiffened panel continues to increase as shown in the figure for longer cracks. It can also be noted from the figure that the residual strength diagram for an unstiffened panel would have followed the dotted line, i.e., the continuous decay in the residual strength as the crack size increases. This is because there is no inherent feature present in the single load path structure to decrease the crack tip stress-intensity factor.

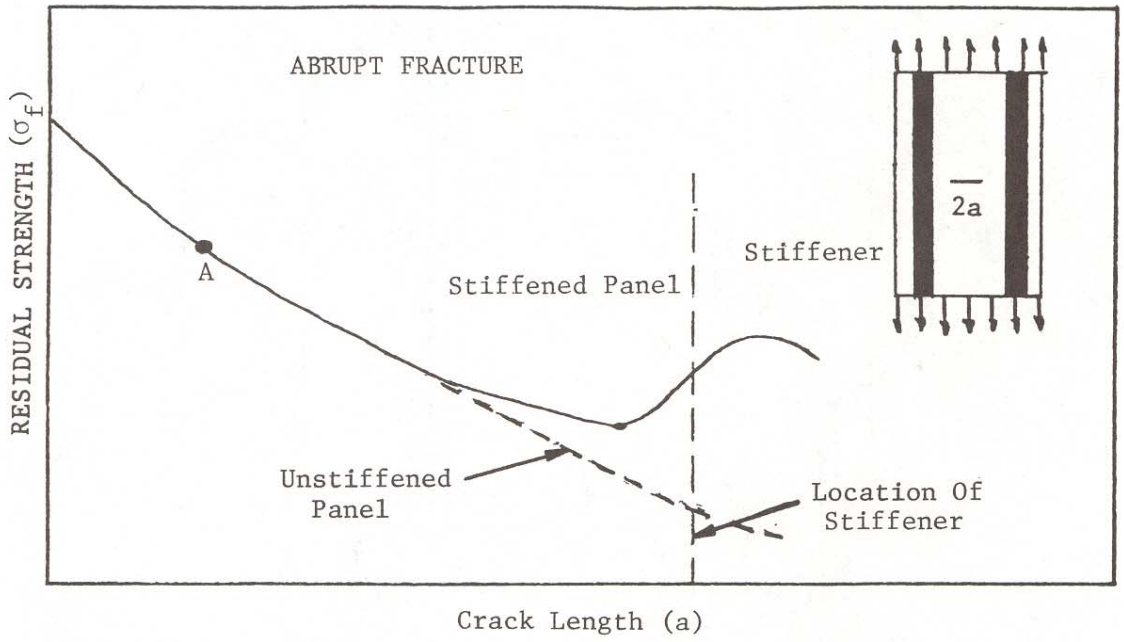

Figure 4.3.7. Residual Strength of the Cracked Panel as a Function of Crack Length for Built-Up Skin-Stiffened Structure Compared with Unstiffened Panel. Abrupt Failure Criterion Used to Determine Residual Strength

The residual strength diagram for the skin-stiffened structure is repeated in Figure 4.3.8 where several additional points of interest are defined for the analyst. For a structure with a crack of length a_A, the residual strength is identified as point A. Since point A is associated with a failure stress that is above the peak stress (σ_{peak}), the crack extends abruptly and completely fails the panel. If the structure contains a crack of length a_C, in the range between a_B and a_D, the crack extends abruptly but then arrests at crack length a_E, where the residual strength available is greater than the applied (failure) stress. This crack extension and arrest feature of skin-stringer construction greatly facilitates meeting inspection requirements for fail-safe structures.

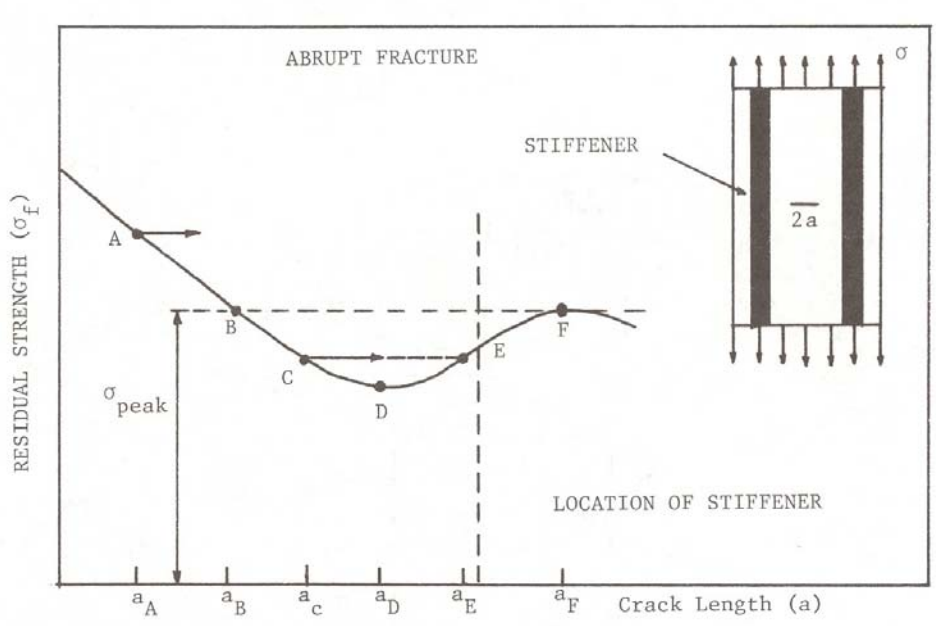

Figure 4.3.8. Residual Strength of the Cracked Panel as a Function of Crack Length for Built-Up Skin Stiffened Structure. Only Skin Failure Mode Considered. Abrupt Failure Criterion Used to Determine Residual Strength

Before the panel fails completely, the failure stress level at point C/E must be increased to the level associated with point F, i.e. to σ_{peak}. As the stress is increased above the level of point E, the crack extends from a_E to maintain an equilibrium between the input stress and the residual strength. When the stress reaches σ_{peak}, the crack has extended to a_F, at which point the crack abruptly extends causing failure of the panel. A schematic illustrating the load crack length diagram observed during an abrupt crack extension/arrest situation in a skin-stringer structure is presented in Figure 4.3.9. Thus, it is seen that the residual strength curve ABCDEF shown in Figure 4.3.8 can be replaced for all practical purposes with a curve that connects points ABF.

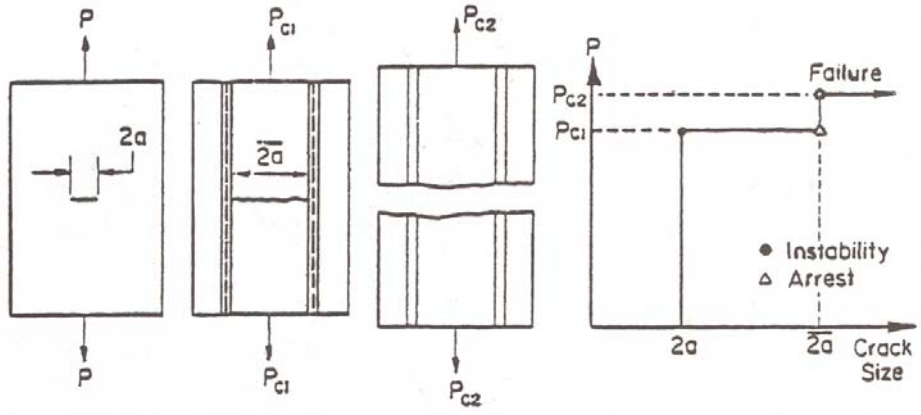

Figure 4.3.9. Load-Crack Length Behavior Observed in Skin-Stiffened Construction with Arrest Features

In the design of fail-safe structure, a frequent objective is to design the structure for limiting or arresting unstable crack growth so that catastrophic failure can be prevented. A number of arrest techniques are described in Bluhm [1969], Romauldi & Sanders [1959-1960] and Broek [1974]. The fundamental concept in crack arrest design is to provide within the structure a means to reduce the crack tip stress intensity factor. This concept requires the use of additional stiffening members such as stiffeners, reinforcing rings, etc., to produce a decrease in the stress. These are inherently present in built-up structures, such as aircraft wings, fuselages, etc..

In general, the residual strength analysis of a structure with crack arrest capabilities may involve more than one failure criterion. For instance, in a stiffened skin structure or an aircraft wing, the analysis should consider stringer failure, fastener failure, and skin crack failure criteria. Built-up panels loaded to fail-safe levels tend to exhibit substantial local deformations of critical elements. Failure criteria are thus dependent also on elastic-plastic deflection allowables for both fastener and skin/stringer elements. Gunther and Wozumi [1982] provide additional details on the residual strength analysis of complex panels based on the ultimate stringer strain.

The residual strength diagram for the structure that exhibits slow crack growth behavior will contain two curves as shown in Figure 4.3.10. The lower curve corresponds to the critical level of stress at which slow crack extension starts. The onset of slow tearing is then described by this lower curve. The upper curve provides the critical stress level at which the unstable rapid crack extension occurs. When the crack approaches the stiffener, as explained earlier, the residual strength levels, corresponding to the onset of slow cracking and the rapid extension, start increasing.

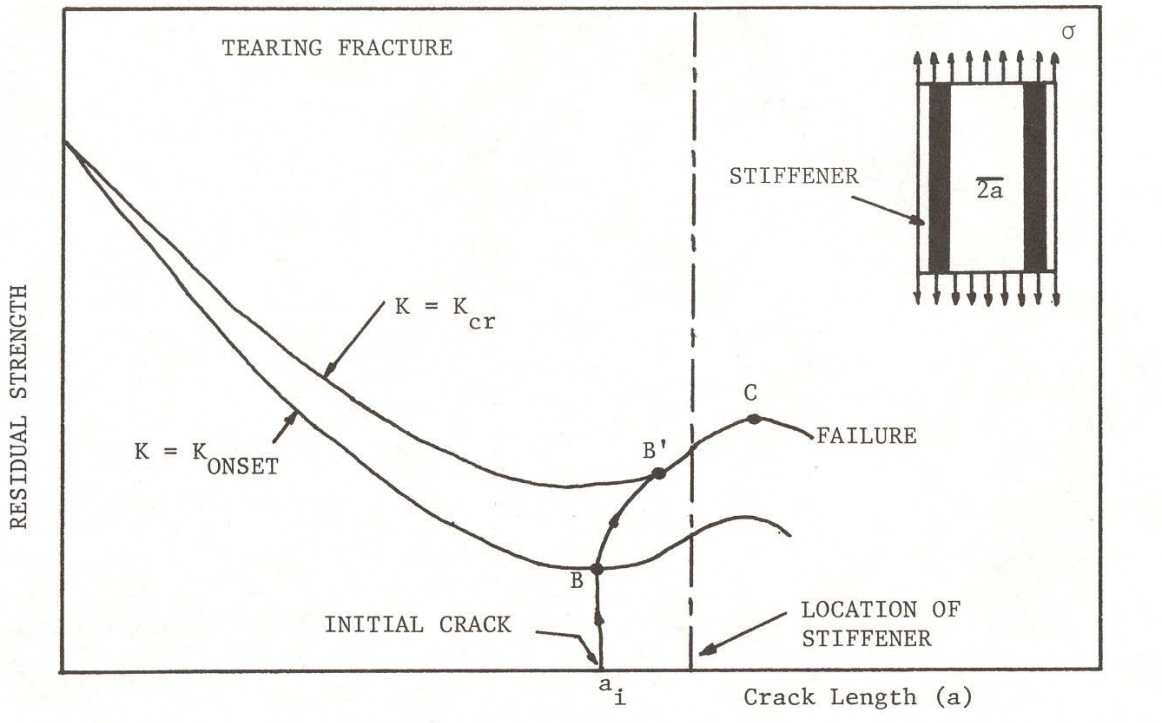

Figure 4.3.10. Residual Strength of Cracked Panel as a Function of Crack Length for Built-up Skin-Stringer Structure. Tearing Failure Criterion Used to Determine Residual Stress

For a crack length a_i, as shown in Figure 4.3.10, the slow crack extension begins at point B. This stable extension continues up to point B′ where the rapid failure is supposed to occur. However, due to the continuous rise in the residual strength of the stiffened panel, the stable crack extension continues to occur beyond point B′ and up to point C. Since the residual strength of the panel starts reducing at this point, any further increase in the applied load will lead to the rapid unstable crack extension.

The construction of the residual strength diagram follows the three steps presented in Section 4.3.1. Due to the complexity of the structural geometry, however, estimating requires the calculation of the loads that are transferred to the stiffening or secondary members from the main load carrying member of the structure. Depending upon the complexity, the K vs. a curves can be obtained either through an appropriate numerical method or through the method of superposition. The methods for constructing residual strength diagrams and for the residual strength capability analyses are further discussed in the following sections with various example problems.

4.4 Single Load Path Structure

For a single load path structure, the only means to protect the safety is to prevent the damage growth from degrading the strength of the structure to less than the design limit load. This applies for all structures classified as slow crack growth, regardless of the type of construction (such as single load path or multiple load path). The residual strength capability of the structure depends mainly on the material's resistance to fracture.

4.4.1 Abrupt Fracture

For materials that exhibit abrupt failure, the start of slow crack extension will be followed immediately by the onset of rapid fracture. The residual strength capability then requires a strict evaluation of the initial flaw sizes in the structure. The allowable initial crack length necessary to maintain the required residual strength will be less than a_f; the design limit load must also be such that the stress level in the structure is less than σ_i, as shown in Figure 4.4.1. The residual strength diagram can be evaluated as described earlier through the plot of σ_f vs. a_c using the relationship $K = \sigma\beta\sqrt{\pi a}$ for the structural geometry of interest and also employing the failure criterion based on a critical fracture toughness value, K_{cr}. The margin of safety as shown in Figure 4.4.1 allows for undetected cracks or for subcritical crack growth such that the initial crack size will not become greater than a_f.

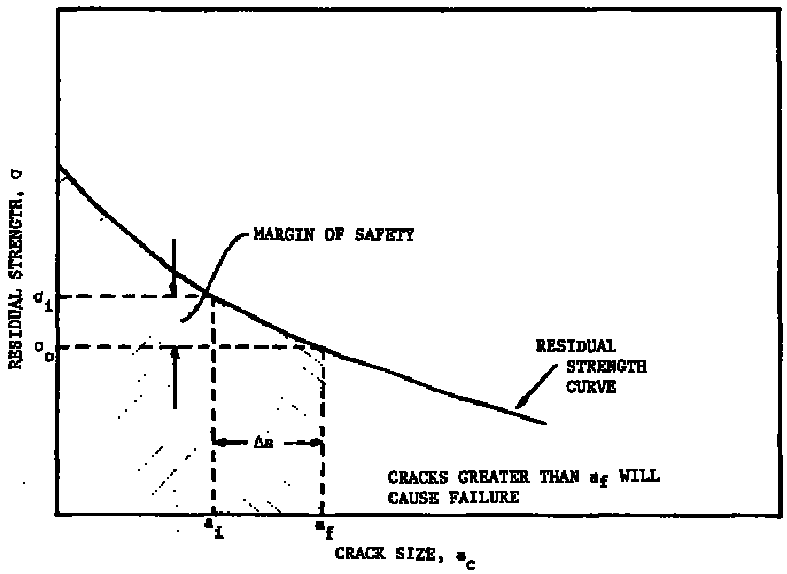

a_f = critical flaw size for the maximum operating load.
a_i = observed initial crack length.
Δa = available additional length. (allowance for undetected initial crack size and for subcritical crack growth).
σ_i = residual strength level for an initial crack a_i.
σ_o = maximum operating stress level.

Figure 4.4.1. Residual Strength Diagram Showing Defining Cracks and Residual Strength Parameters

The following example problem is presented to demonstrate the application of the steps in constructing the residual strength diagram and also to analyze the structure for its residual strength capabilities. This example demonstrates the basic concepts involved in the residual strength capabilities of a single load path structure.

EXAMPLE 4.4.1 Residual Strength of Center Cracked Panel

Develop the residual strength diagram for the cracked finite width panel shown here. The panel is 20 inches wide and 0.375 inches thick with a length of 60 inches. The yield strength (σ_y) for this material is 78 ksi and the fracture toughness (K_{Ic}) is 40 ksi √in. The inspection procedure is a viual inspection capable finding a crack ($2a$) 2 inches long.

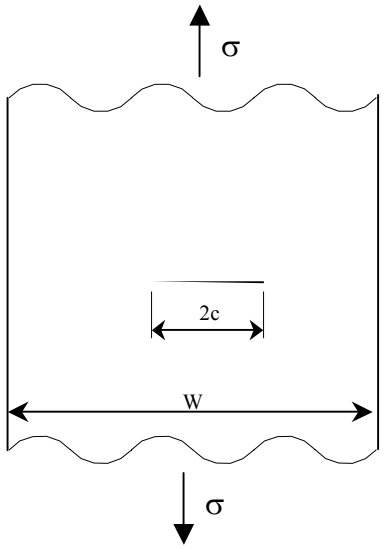

SOLUTION:

For the center-cracked geometry configuration shown, the stress-intensity factor K expresses by the relationship (see Section 11.3):

$$K = \sigma\sqrt{\pi a \sec\left(\frac{\pi a}{W}\right)}$$

Since we have an explicit expression for K, using the fracture toughness failure criterion (plane strain), the residual strength diagram can be obtained directly. The corresponding equation is

$$\sigma_f = K_{Ic} \Big/ \left(\sqrt{\pi a_c \, sec\left(\frac{\pi a_c}{W}\right)}\right)$$

where K_{Ic} = 40 ksi $\sqrt{in}$ and W = 20 inch are given as data and σ_f can be obtained for any selected crack length. The σ_f vs. a_c curve, which is the required residual strength diagram, can now be plotted.

The residual strength σ_f of the panel can be estimated from the equation that is described in the following diagram. From this figure, for the given operating stress level (20 ksi), the critical crack size a at which unstable crack extension would occur can be estimated as 1.2 inches. Thus, to avoid a fracture type failure of the panel, the structure should not develop a crack of this size. Assume that based on an established visual inspection schedule, the simple rectangular aluminum panel, uniformly loaded in tension as shown, could develop a 2.0 inch long, central through-the-thickness crack (normal to loading) before detection. This crack length is slightly smaller than the critical crack size ($2a$) of 2.4 (2 x 1.2 inch) under the operating conditions so that the margin of safety is small when this inspection process is employed.

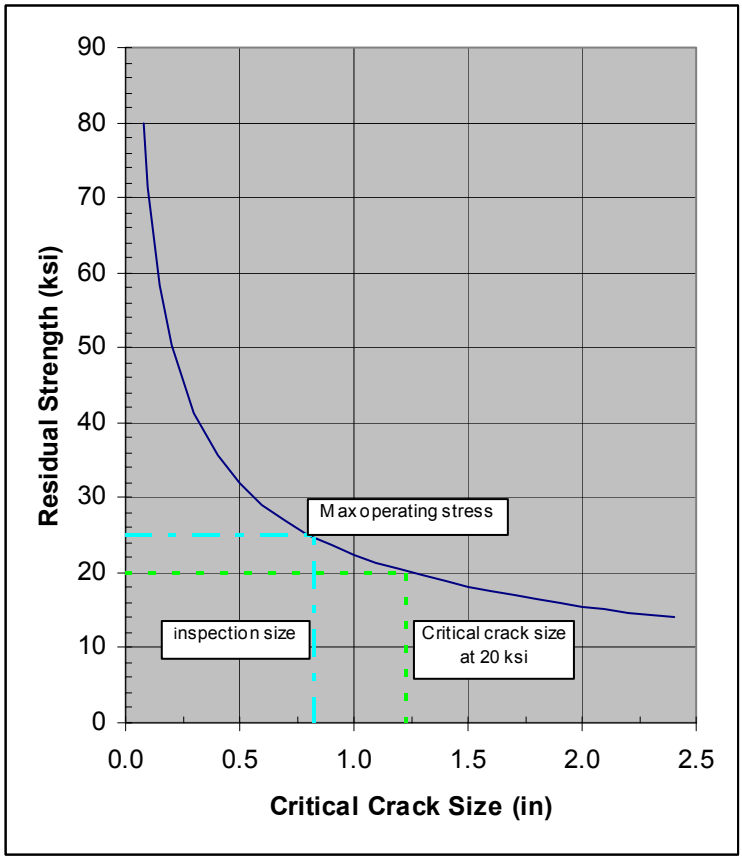

Residual Strength Diagram Determining Critical Crack Size at 20 ksi Operating Level

To establish the required residual strength level to fit the inspection schedule, the designer must reduce the crack-tip stress-intensity factor for the same applied load. One method is to transfer portions of the load to a stiffening member. Another method is to reduce the operating load level below the failure level corresponding to the inspection crack size, although this is not always practiced.

4.4.2 Tearing Fracture

Materials with medium or high fracture toughness exhibit a type of subcritical crack extension behavior prior to reaching the maximum load carrying capacity of the structure. When a limited amount of yielding occurs in front of the crack tip, the initial extension of an existing crack in these materials will be slow and stable threshold values of the stress-intensity factor (K_{ONSET}).

To understand this behavior, consider an unreinforced, center-cracked panel. The stress-intensity factor (K) at the crack tip increases linearly with the value of the normal tensile stress component acting on the structure for a stationary crack. As the K level increases, some point (point A) will be reached at which the crack length will begin to extend as shown in Figure 4.4.2. The crack will extend gradually as the load continues to increase, until reaching the critical size at which the crack extension becomes unstable (point B in Figure 4.4.2). The point of crack initiation and instability are determined by the appropriate failure criteria.

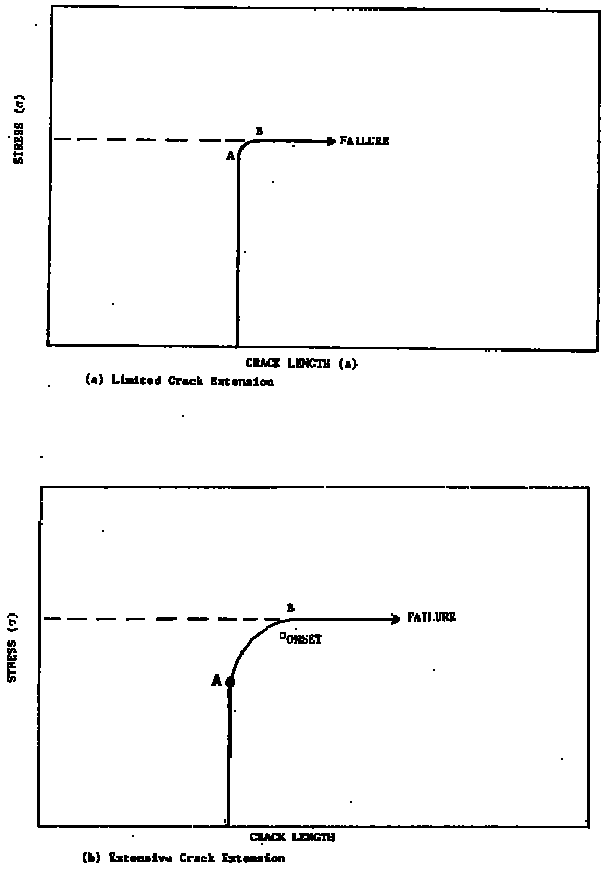

Figure 4.4.2. Diagrams Showing Onset of Unstable Crack Growth for Conditions of Limited or Extensive Crack Extension

When the subcritical growth of the crack, as shown in Figure 4.4.2a between the points A and B, is not significant, the fracture toughness criterion K_{CR} values can be used in the analysis. In this case, fracture is assumed to occur immediately after the start of crack extension as under abrupt failure conditions. However, for materials exhibiting substantial crack growth between points A and B as shown in Figure 4.4.2b, the crack resistance curve approach can be used in the residual

strength analysis. The crack resistance (R) curve approach might be based on either K_R vs. Δa or $\sqrt{J_R}$ vs. a. The K_R vs. Δa curve is normally used when the fracture strength is associated with stress levels below net section yield conditions; in other words, when limited crack tip plasticity occurs prior to fracture. The $\sqrt{J_R}$ vs. a curve is used for those conditions where the fracture strength is expected to result in gross yielding.

In the calculation of residual strength when the cracked structure exhibits a tearing instability, one normally follows these steps:

1. Obtain K_{eff} $\left(= \beta\sqrt{\pi(a+r)}\right)$ values for the structure for various crack lengths and applied stresses using a suitable plastic zone model (e.g. Dugdale Model). Evaluation of the K values involves methods described in Section 11. Plot K versus a curves for various applied stresses as shown in Figure 4.4.3a.
2. Obtain the experimentally determined R-curve (K_R versus Δa) for the sheet material (Figure 4.4.3b).
3. Determine the point of instability from the K curves of the structure and the K_R curves of the material as shown schematically in Figure 4.4.3c.
4. Obtain different values for the fracture strength and the corresponding crack lengths from step 3 and plot these points to establish the failure strength (σ_f) crack length (a_c) curve. This provides the necessary residual strength diagram of the structure.

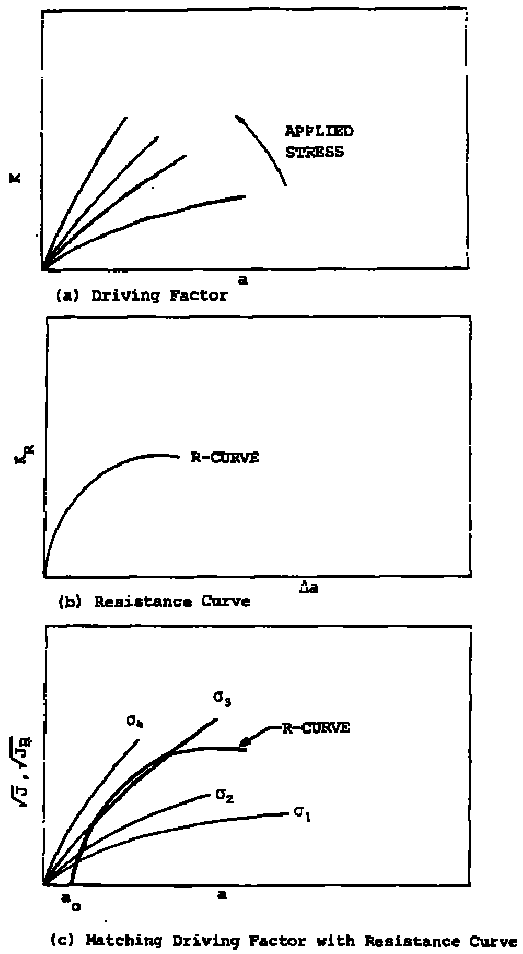

Figure 4.4.3. Steps Associated with Calculating Residual Strength of Cracked Structures with Tearing Fractures

The residual strength diagram for intermediate or high fracture toughness materials can be constructed by using either the K_R curve or the $\sqrt{J_R}$ method. To understand the use of the *R*-curve failure criteria in evaluating the residual strength, consider the following example in which failure criterion based on the K_R curve is applied.

EXAMPLE 4.4.2 Residual Strength of Tearing Radial Hole Crack

Construct the residual strength diagram for a large and relatively thin (0.063 in.) plate of 7075-T73 aluminum alloy having a through crack emanating (radially) from a hole with a diameter (D) equal to one inch, such as illustrated here. Assume the material inhibits a limited amount of crack tip yielding. Also calculate the crack length associated with a fracture strength associated with a crack length of 2.0 inch.

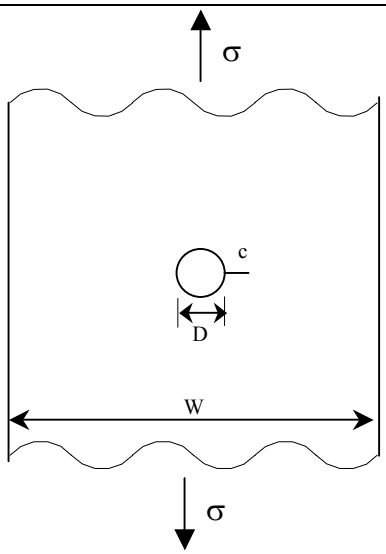

SOLUTION:

As the first step, the appropriate expression for the stress-intensity factor is obtained from Section 11:

$$K = \sigma\beta\sqrt{\pi c}$$

and β is given in Section 11.

The following figure describes the variation in stress-intensity factor with crack length and stress level.

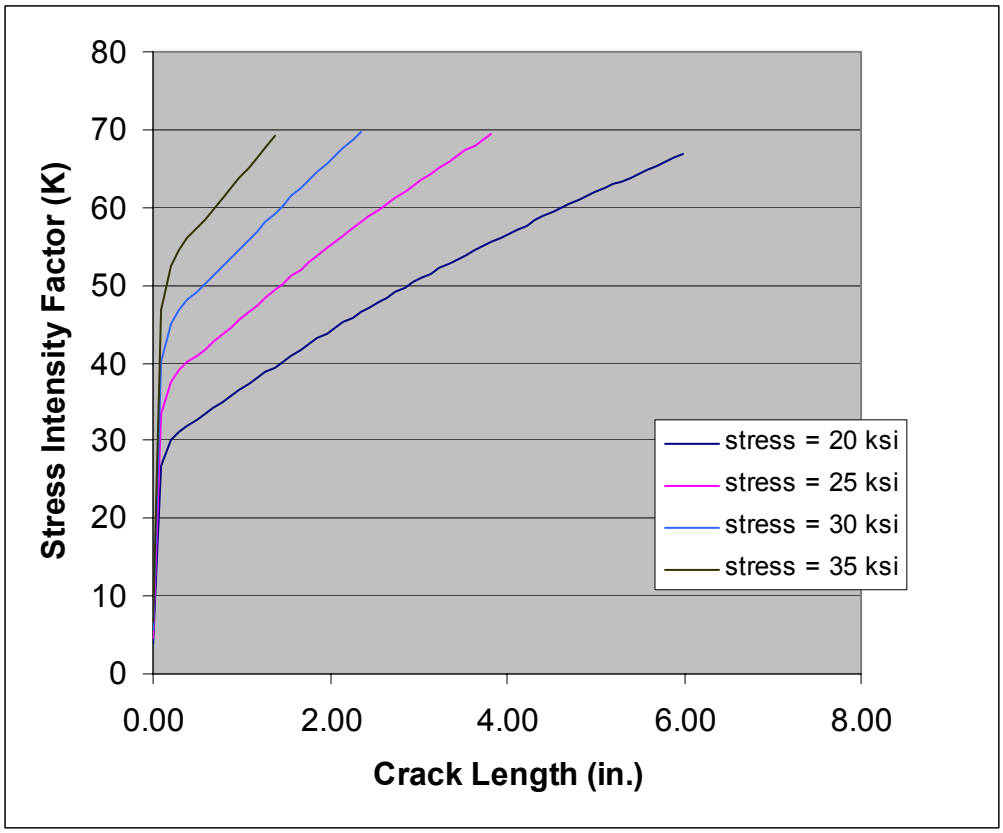

Stress-Intensity Factor Relationship for Various Values of Applied Stress

The next step is to consider the appropriate failure criterion. The given geometry is a thin sheet and the material exhibits limited crack tip yielding behavior. Therefore, the *R*-curve method based on K_R values can be applied to evaluate the fracture strength.

For the given 7075-T73 aluminum alloy material (0.063 inch thick), an experimentally obtained R-curve is shown here. By superposing the *R*-curve onto the plot obtained in step one, as explained in Section 4.2.1, the points where the *R*-curve is tangent to the *K*-curves are obtained.

At these points the failure criterion, i.e. K - K_R and $\frac{\partial K}{\partial a} = \frac{\partial K_R}{\partial a}$, is satisfied. The corresponding stress σ_c is the critical (fracture) stress at which the initiation of rapid fracture will occur. From a diagram like this, we can obtain the critical initial sizes of the crack and the respective fracture stresses.

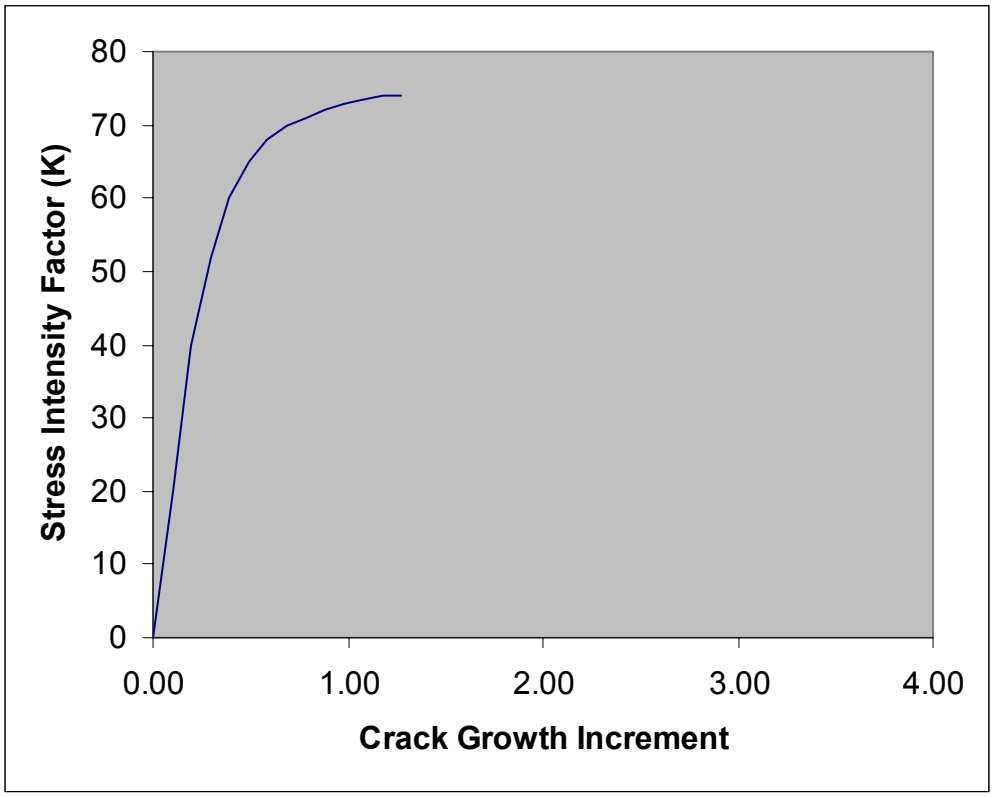

Resistance Curve for 7075-T73 Aluminum for a Thickness of 0.063 Inches

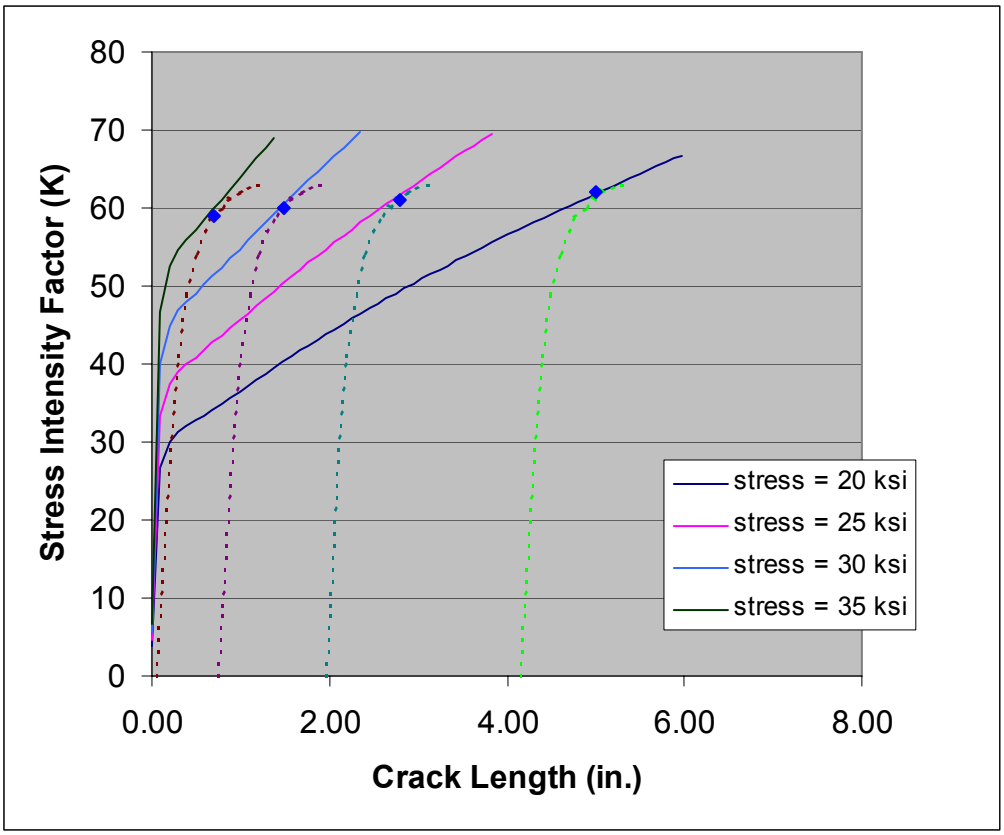

Matching the *R*-Curve and Stress-Intensity Factor Curves

The final step is to plot the σ_f vs. a_c curve. The required residual strength diagram is shown next for the 7075-T73 aluminum plate with a crack emanating radially from a hole. It can be seen from this figure that the critical crack size for a 20 ksi operating stress level is equal to 4.0 inches. As can also be seen from the figure, for an observed crack of 2.0 inches, the residual strength available is 27 ksi.

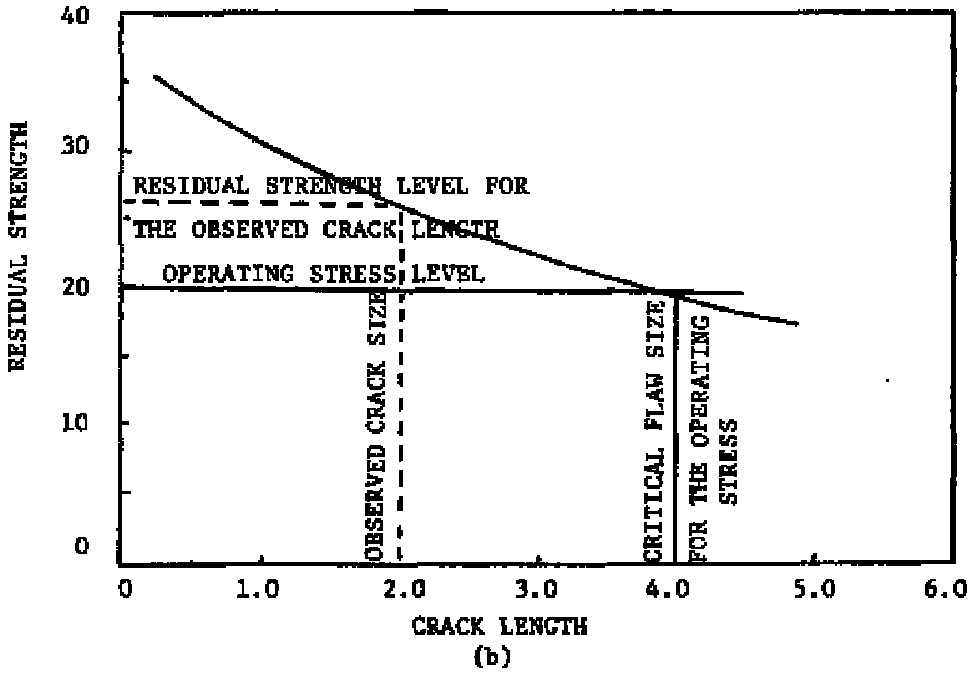

Residual Strength Diagram Obtained for Structure in Example 4.4.4

4.5 Built-Up Structures

Built-up structures normally require more than one failure criterion to determine the residual strength of the total structure. The development of the residual strength diagram of a given structure will involve the analysis of failures of each part of the load support system.

The structural configuration essentially determines the complexity of the residual strength analysis. Typical structural parameters which must be considered for skin-stiffened structure are:

- Type of Construction
  - Monolithic (unreinforced/forgings)
  - Skin (longerons, stringer)
  - Integrally stiffened
  - Planked
  - Layered (honeycomb/laminated)
- Panel Geometry
  - Planform
  - Curvature
  - Stiffener spacing and orientation
  - Attachments (spar caps, webs, frames, etc.)
- Details of Construction
  - Stiffener geometry (hat, Z-channel, etc.)
  - Attachment details (bolted, riveted, welded, etc.)
  - Fastener flexibility
  - Eccentricity

Ideally, the residual strength analysis will take all these parameters into consideration. In practice, many are treated empirically and others are not considered except in extremely detailed analyses. This section provides details of the analysis methods used for built-up skin stringer structure and the effects of many of the structural parameters listed above. In the order of their presentation, the subsections provide: overviews of the analysis for edge stiffened and for centrally stiffened skin structure, the analysis methods used to determine the stress-intensity factor in the skin structure and the loading transferred to the stringers, the analysis of stiffener failure, the analysis of fastener failure, the analysis methodology and an example.

4.5.1 Edge Stiffened Panel with a Central Crack

The residual strength diagram of a simple panel with two stringers and a central crack can be constructed as follows. Consider first a crack in plane stress, which starts propagating slowly at $\sigma_o = K_{onset} / \sqrt{\pi a_o}$ and becomes unstable at $\sigma_c = K_c / \sqrt{\pi a_c}$ in a sheet without stringers as shown in Figure 4.5.1a.

When the panel is stiffened with stringers, the stress-intensity factor is reduced to $K = \beta\sigma\sqrt{\pi a}$ where $\beta < 1$. As a result, both the stress for slow stable crack growth, σ_o, and the stress for

unstable crack growth, σ_f, are altered to give $\sigma_o = K_{onset} / \beta\sqrt{\pi a_o}$ and $\sigma_{cf} = K_c / \beta\sqrt{\pi a_c}$, respectively.

Hence, these events take place at higher stresses in the stiffened panel than in the unstiffened panel. This means that the lines in Figure 4.5.1a are raised by a factor $1/\beta$ for the case of the stiffened panel, as depicted in Figure 4.5.1b. Since β decreases as the crack approaches the stringer, the curves in Figure 4.5.1b turn upward for crack sizes on the order of the stringer spacing.

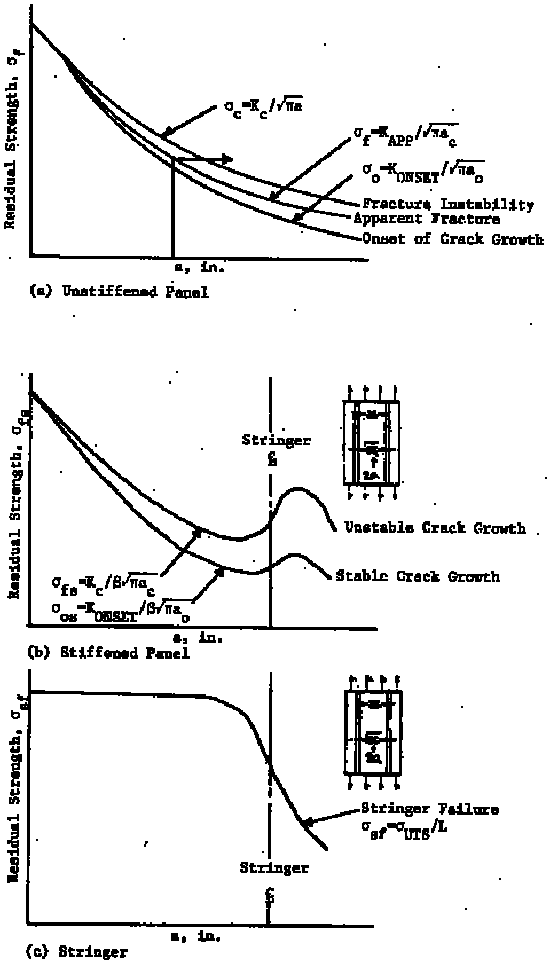

Figure 4.5.1. Elements of Residual Strength Diagram

The possibility of stringer failure should be considered also. The stringer will fail when its stress reaches the ultimate tensile stress (σ_{UTS}). As the stringer stress is $L\sigma$, where σ is the nominal stress in the panel away from the crack, failure will occur at σ_{sf}, given by $L\sigma_{sf} = \sigma_{UTS}$. Using L, a measure of the load transferred to the stringer, the panel stress at which stringer failure occurs is shown in Figure 4.5.1c. The stringer may yield before it fails. This means that its capability to take overload from the cracked skin decreases. As a result, β will be higher and L will be lower. The stress-intensity analysis should account for this effect.

Figure 4.5.2 shows the residual strength diagram of the stiffened panel. It is a composite of the critical conditions shown in Figure 4.5.1. In the case when the crack is still small at the onset of

instability ($2a << 2s$, where $2s$ is stringer spacing), the stress condition at the crack tip will hardly be influenced by the stringers and the stress at unstable crack growth initiation will be the same as that of an unstiffened sheet of the same size (Point B in Figure 4.5.2). When the unstably growing crack approaches the stiffener, the load concentration in the stiffener will be so high that the stiffener fails (Point C) without stopping the unstable crack growth (line BC).

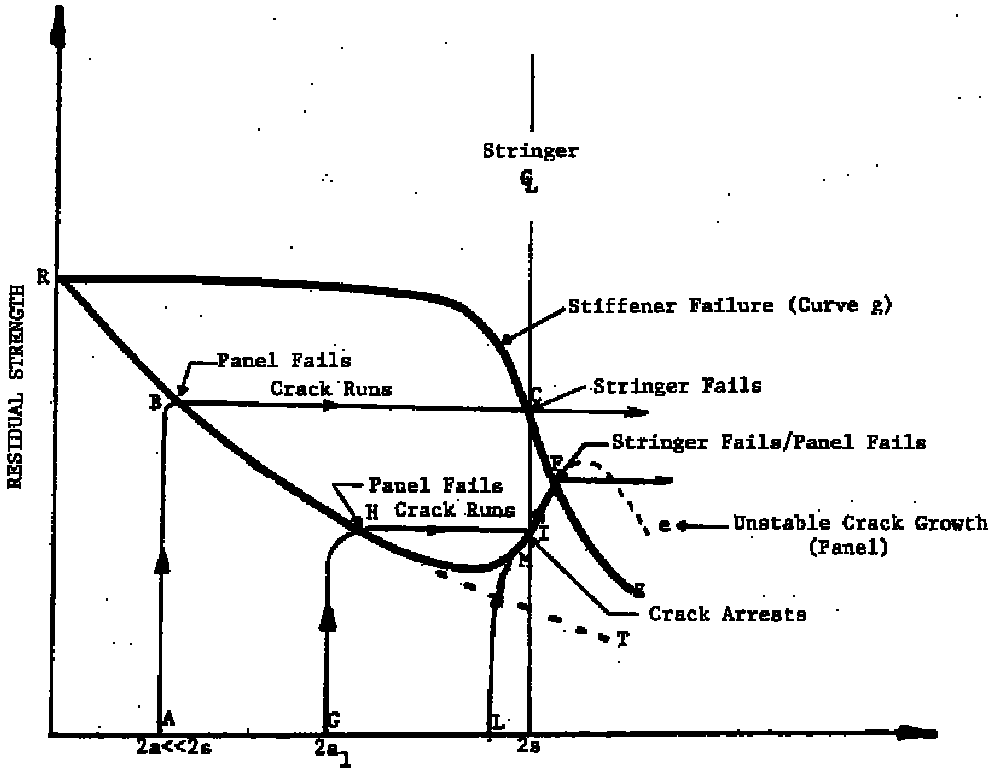

Figure 4.5.2. Residual Strength Diagram for a Stiffened Panel

When the panel contains a crack extending almost from one stiffener to the other ($2a \cong 2s$), the stringer will be extremely effective in reducing the peak stress at the crack tips (β small), resulting in a higher value of the stress at crack growth initiation. With increasing load, the crack will grow stably to the stiffener (line LMIF) and due to the inherent increase of stiffener effectiveness, the crack growth will remain stable. Fracture of the panel will occur at the same stress level corresponding to the point F due to the fact that the stiffener has reached its failure stress and the stress reduction in the skin is no longer effective after stringer failure.

For cracks of intermediate size ($2a = 2a_1$), there will be unstable crack growth at a stress slightly above the fracture strength of the unstiffened sheet (point H), but this will be stopped under the stiffeners at I. After crack arrest, the panel load can be further increased at the cost of some additional stable crack growth until F, where the ultimate stringer load is reached.

Since β and L depend upon stiffening ratio, the residual strength diagram of Figure 4.5.2 is not unique. Figure 4.5.2 shows the case where stringer failure is the critical event. For other stiffening ratios, skin failure may be the critical event as depicted in Figure 4.5.3. Due to a low stringer load connection, the curve e and g do not intersect. A crack of size $2a_1$ will show stable growth at point B and become unstable at point C. Crack arrest occurs at D from where further

slow growth can occur if the load is raised. Finally, at point E, the crack will again become unstable, resulting in panel fracture. It is, therefore, obvious then that a criterion for crack arrest has to involve the two alternatives of stringer failure and skin failure, and these depend upon the relative stiffness of sheet and stringer.

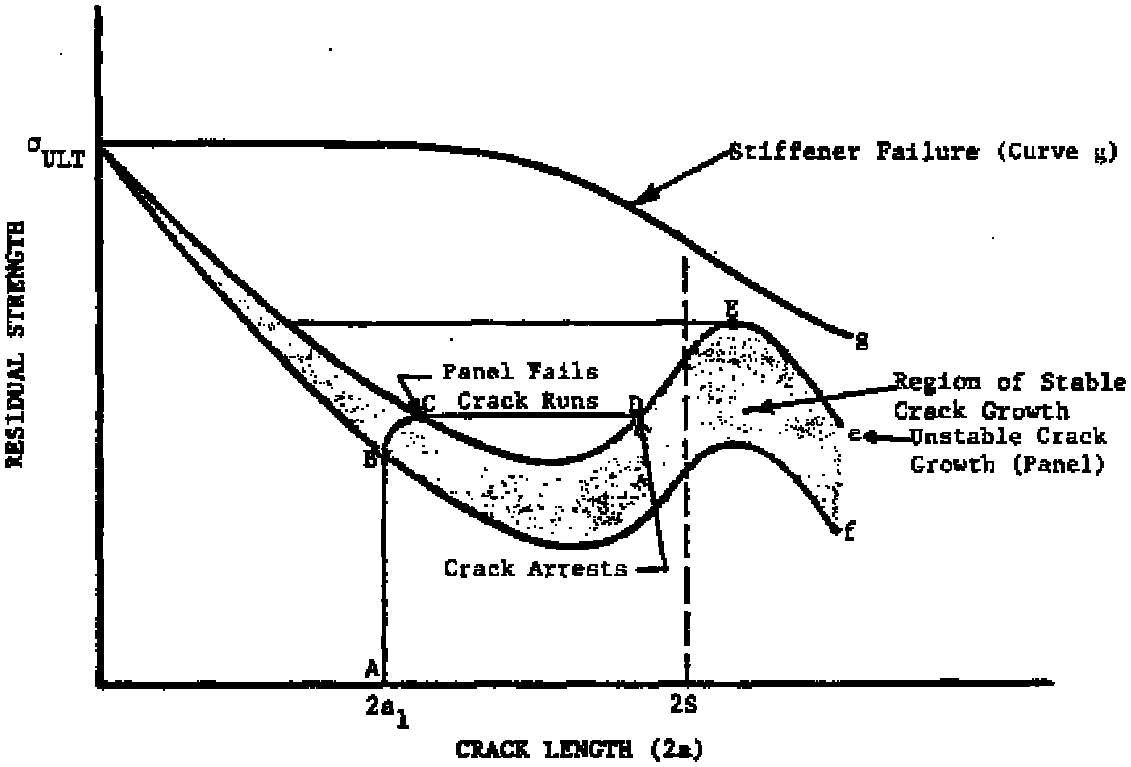

Figure 4.5.3. Panel Configuration with Heavy Stringers; Skin-Critical Case

The foregoing clearly shows that for crack arrest it is not essential that the crack run into a fastener hole. Crack arrest basically results from the reduction of stress-intensity factor due to load transmittal to the stringer.

For the particular case depicted in Figure 4.5.4, the residual strength is not determined by stringer failure solely but also by fastener failure (point K). A crack of length $2a_1$ will show slow growth from E to F and instability from F to G. After crack arrest at G, further slow growth occurs until at point K the fasteners fail. The latter could cause panel failure, but this cannot be directly determined from the diagram.

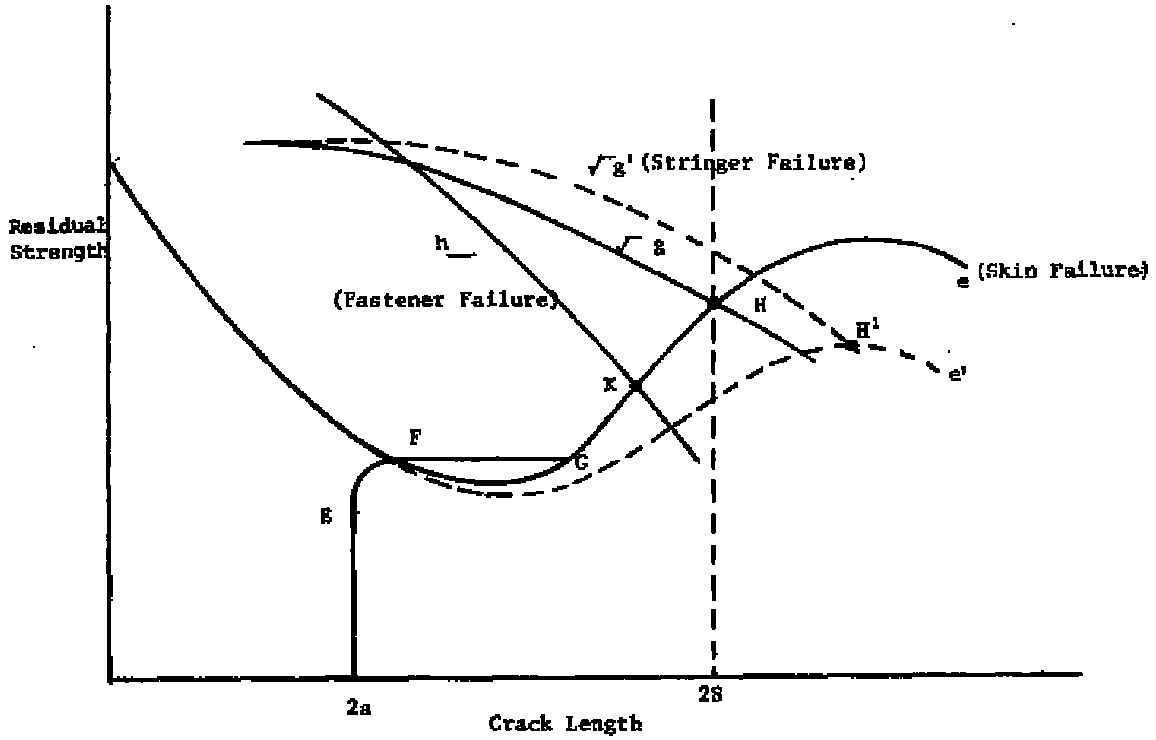

Figure 4.5.4. Criterion for Fastener Failure

In fact, a new residual strength diagram must now be calculated with omission of the first row of rivets at either side of the crack. Fastener failure will affect load transmittal from the skin to the stringer: line e will be lowered, line g will be railed. The intersection point H′ of the new lines g′ and e′ may still be above K and hence, the residual strength will still be determined by stringer failure at H′.

In reality, the behavior will be more complicated due to plastic deformation. Shear deformation of the fasteners, hole deformation, and plastic deformation of the stringers will occur before fracture takes place. Plastic deformation always reduces the ability of the stringer to take load from the skin that implies that line g in actuality will be raised and line e will be lowered. The intersection of the two lines (failure point) will not be affected a great deal, however, (compare points H and H′ in Figure 4.5.4). For this reason the residual strength of a stiffened panel can still be predicted reasonably well, even if plasticity effects are ignored. Nevertheless, a proper treatment of the problem requires that plasticity effects be taken into account.

4.5.2 Centrally and Edge Stiffened Panel with a Central Crack

In the previous subsection, the cases considered pertain to cracks between two stiffeners. In practice, however, cracks frequently start at a fastener hole and then there will be a stringer across the crack which will have a high load concentration factor. The problem can be dealt with in a manner similar to a crack between stringers, using either analytical or finite-element procedures. A schematic residual strength diagram for this case is presented in Figure 4.5.5. Apart from the residual strength curve g for the edge stiffeners, there will now be an additional residual strength curve k for the central stiffener.

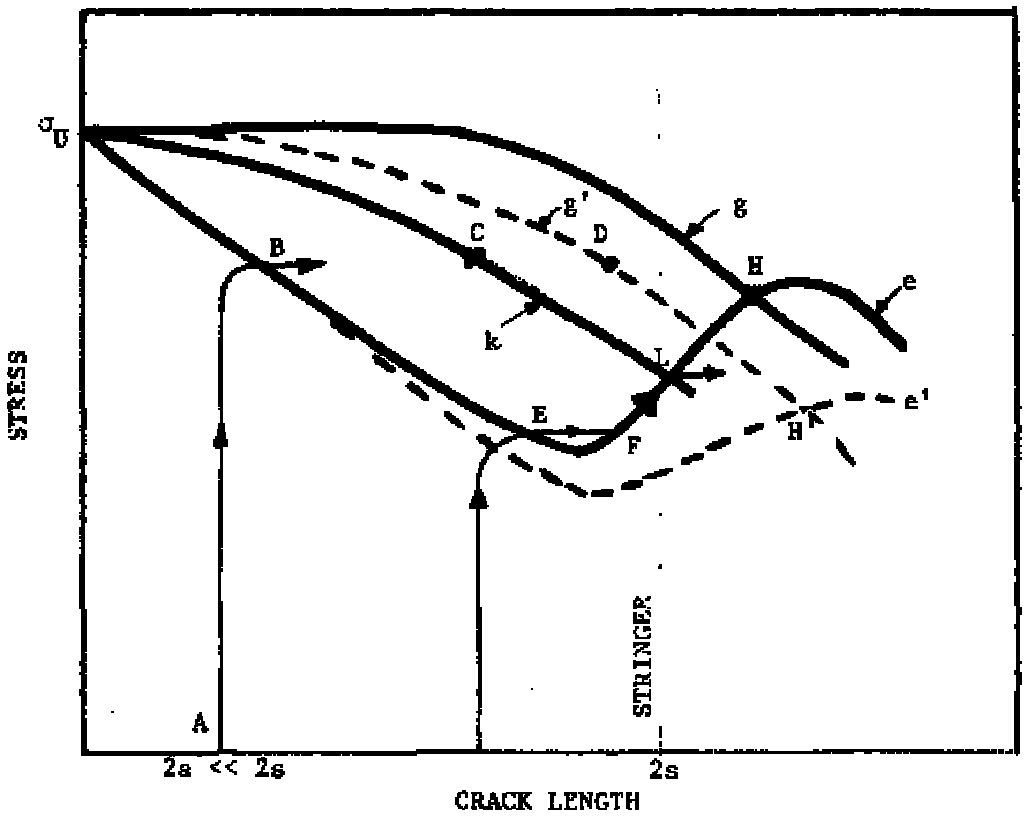

f: Residual Strength Curve of Skin Alone
g: Residual Strength Curve of Two Edge Stiffeners
k: Residual Strength Curve of Central Stiffener (Failing).
g': Residual Strength Curve of Two Edge Stiffeners After the Failure of Central Stiffener

Figure 4.5.5. Residual Strength Diagram for a Panel with Three Stiffeners and a Central Crack Emanating from a Rivet Hole

For the case where the crack in the skin is small ($2a << 2s$), the first failure in the structure is noted to occur at point B in Figure 4.5.5 where the skin fails and the crack starts to run. When the crack reaches a size such that point C is reached, the central stiffener residual strength has dropped to the operating stress level and then the central stringer fails, immediately causing

additional loading to be transferred to the edge stiffeners and the skin structure. The effect of losing the capability of the central stringer is noted in Figure 4.5.5 with a repositioning of the residual strength curves from the edge stiffeners (from curve g to curve g′) and skin structure (from curve e to curve e′). As the crack in the skin structure continues to grow after causing the ultimate tensile strength failure in the central stringer at point C, it reaches a size that causes the ultimate tensile strength failure of the two edge stringers at point D, at which point all potential arrest capability is lost and the structure is lost.

For the case of longer cracks, Figure 4.5.5 shows that skin cracks may start running (line EF), arrest (point F), and tear along curve FL as the stress is increased. At point L, the crack has reached a length that has resulted in sufficient stress being transferred to the central stringer so that this stiffener now fails. Again, this failure causes a redistribution of stress in the entire structure so that a new set of residual strength diagrams are required to determine the consequences associated with failing the central stringer. The new edge stringer and skin structure residual strength curves are presented by curves g′ and e′, respectively.

Due to the high load concentration, the middle stringer will usually fail fairly soon by fatigue and, therefore, lines e′ and g′, with the middle stringer failed, will have to be used and the residual strength is determined by point H′. (Note that e′, g′, and H′ will have different positions in the absence of the middle stringer; a failed central stringer will induce higher stresses in both the skin and the edge stiffeners.) The foregoing discussion provides the concepts required to establish a complete residual strength diagram.

4.5.3 Analytical Methods

In this subsection analytical procedures are presented for the residual strength capability analyses. Methods for evaluating the unknown fastener force and the stress-intensity factors for the stiffened panel are presented. Since the equations for the solution procedures have been based on linear elastic fracture mechanics, the failure criterion used in these analyses are also based on fracture toughness values for abrupt fracture conditions and K_R resistance curve data for tearing fracture conditions.

Analysis methods for stiffened panels have been developed independently by Romualdi, et al 1957], Poe [1970, 1971], Vlieger [1973], Swift and Wang [1969], Swift [1971], Creager and Liu [1971], and Wilhem and Ratwani [1974].

Application of the stress intensity factor parameter, β, and the stringer load concentration factor, L, were proposed by Vlieger [1973] and Swift and Wang [1969].

From the residual strength capability analysis as discussed in the preceding subsections, it is evident that the construction of residual strength diagrams for built-up structures also requires the estimation of the stress-intensity factor K. A number of approaches for determining K have been developed. Solutions for complicated structural geometries can sometimes be obtained from the basic stress field solutions combined with displacement compatibility requirements for all the structural members involved. This approach has been shown by several investigators to be useful in the analysis of built-up sheet structure. While the analysis is based on closed form solutions, the actual analyses are computerized for efficient solutions. The essentials of this technique are described below.

In calculating β and L, two methods can be used. There are the finite-element method and an analytical method based on closed-form solutions. The analytical method has advantages over the finite-element method in that the effect of different panel parameters on the residual strength of a certain panel configuration can be easily assessed, so that the stiffened panel can be optimized with respect to fail-safe strength. It allows direct determination of the residual-strength diagram. In the case of the finite-element method, a new analysis has to be carried out when the dimensions of certain elements are changed because a new idealization has to be made. An advantage of the finite-element analysis, on the other hand, is that such effects as stringer eccentricity, hole deformation, and stringer yielding can be incorporated with relative ease. Details of the calculations can be found in the referenced papers.

The procedure for analytical calculation is outlined in Figure 4.5.6. The stiffened panel is split up into its composite parts, the skin and the stringer. Load transmission from the skin to the stringer takes place through the fasteners. As a result, the skin will exert forces F_1, F_2, etc., on the stringer, and the stringer will exert reaction forces F_1, F_2, etc. on the skin. This is depicted in the upper line of Figure 4.5.6.

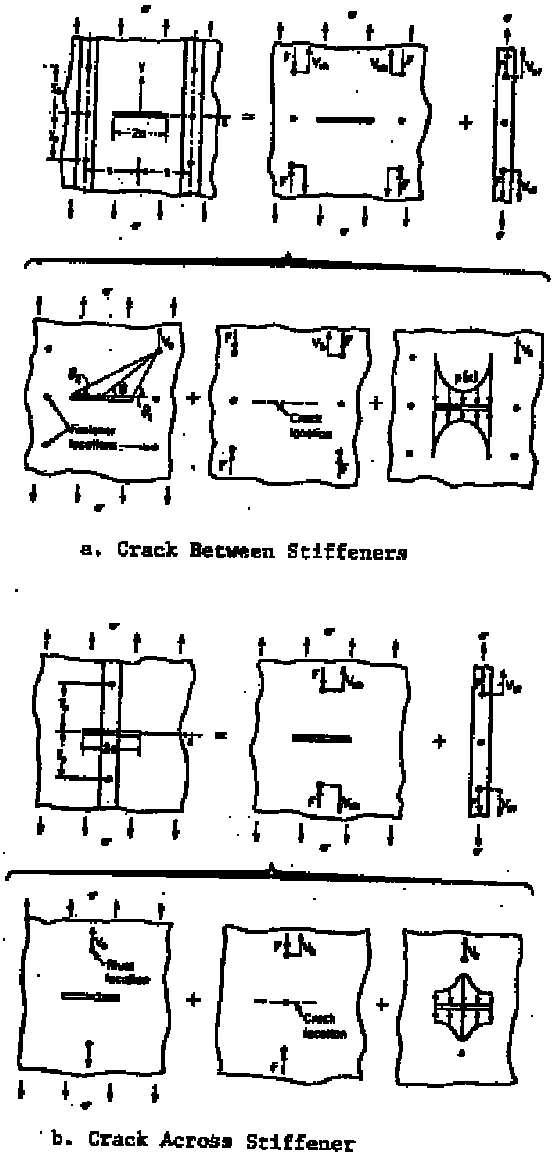

Figure 4.5.6. Analysis of Stiffened Panel

The problem is now reduced to that of an unstiffened plate loaded by a uniaxial stress, σ, and fastener forces $F_1 \ldots F_n$. This case can be considered as superposition of three others, shown in the second line of Figure 4.5.6. Namely:

a. A uniformly loaded cracked sheet.

b. A sheet without a crack, loaded with forces $F_1 \ldots F_n$.

c. A cracked sheet with forces on the crack edges given by the function $p(x)$. The forces $p(x)$ represent the load distribution given by Love [1944]. When the slit CD is cut, these forces have to be exerted on the edges of the slit to provide the necessary crack-free edges.

The three cases have to be analyzed individually. For case a, the stress-intensity factor is $K = \sigma\sqrt{\pi a}$. For case b, $K = 0$. The stress intensity for case c is a complicated expression that

has to be solved numerically. However, once the K value for case c is determined, the stress-intensity factor for the whole stiffened panel can be obtained by adding the K values for cases a and b.

The determination of K requires calculations of fastener forces $F_1, F_2 \ldots F_n$. To calculate these forces, the displacement compatibility conditions which require equal displacements in sheet and stringer at the corresponding fastener locations, can be used. These compatibility requirements deliver a set of n (n = number of fasteners) independent algebraic equations from which the fastener forces can be obtained. These equations can be solved numerically using Gauss-Seidal or Gauss-Jordan iterative methods.

The number of fasteners to be included in the calculation depends somewhat upon geometry and crack size. According to Swift [1974] and shown in Figure 4.5.7, 15 fasteners at either side of the crack seems to be sufficient to get a consistent result. Similar results were obtained by Sanga [1974]. Swift's analysis provides a detailed description of how to incorporate nonelastic behavior in this kind of analysis. The method can account for (1) stiffener flexibility and stiffener bending, (2) fastener flexibility, and (3) biaxiality. Stringer yielding, fastener flexibility, and hole flexibility are lumped together in an empirical equation for fastener deflection.

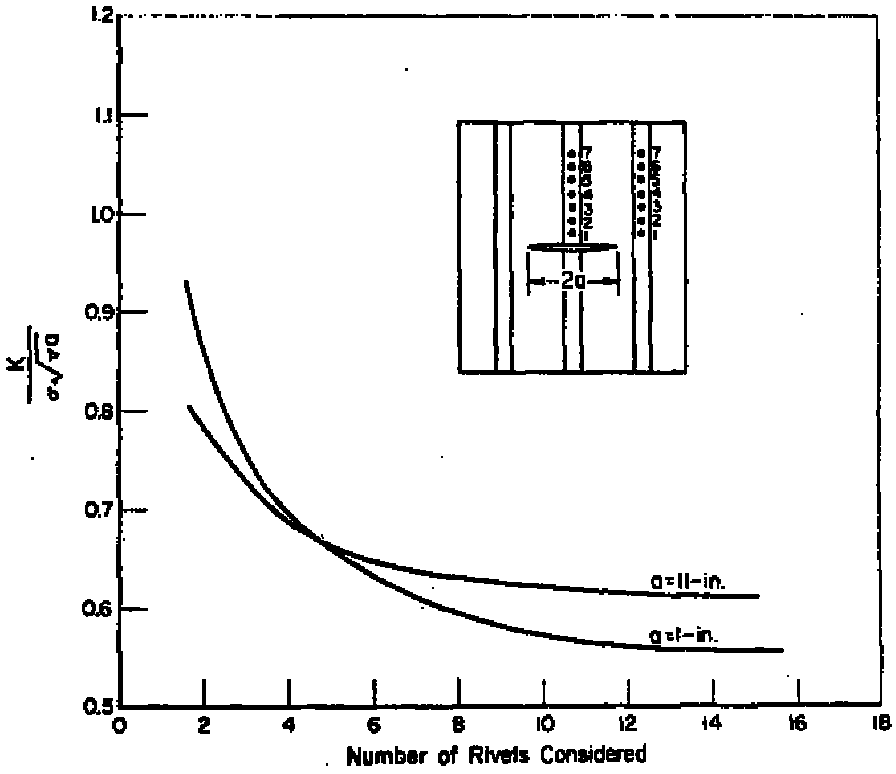

Figure 4.5.7. Effect of Number of Fasteners Included in Analysis on Calculated Stress-Intensity Factor

The effect of fastener flexibility and stiffener bending on β and L is shown in Figure 4.5.8. Although the effects are quite large, the vertical position of the crossover of critical stress-intensity factor curve and stringer stress curve is not affected too much (compare points A and B in Figure 4.5.8). The level of the crossover determines the residual strength, as pointed out in the

previous subsections. This explains why the residual strength can be reasonably well predicted if the flexibility of the fasteners is neglected.

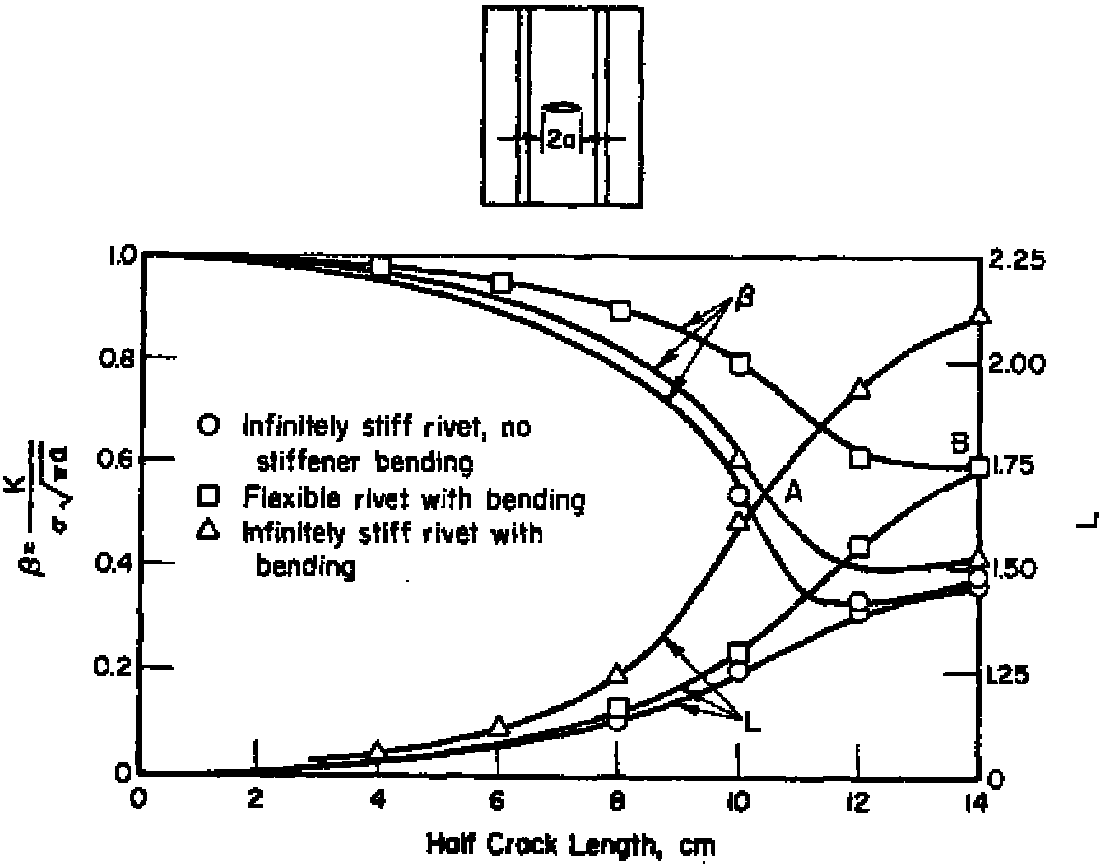

Figure 4.5.8. Skin-Stress-Reduction β and Stringer-Load-Concentration L as Affected by Fastener Flexibility and Stiffener Bending

In the case of adhesively bonded stiffeners, the displacement compatibility approach was used to calculate the fastener loads $F_1, F_2 \ldots F_n$. The adhesive was considered by dividing it into a series of discrete segments. The forces $F_1, F_2 \ldots F_n$ correspond to the segments shown in Figure 4.5.9. Using an appropriate computational method as explained for riveted fastener, the unknown fastener forces can be evaluated. The method of superposition results in an expression in terms of a complex integral for the stress-intensity factor. A typical residual strength diagram for a bonded structure as compared to the riveted structure is shown in Figure 4.5.10. The required expressions and the solution techniques are discussed in the example problem for a riveted skin-stringer combination with a central crack in the skin.

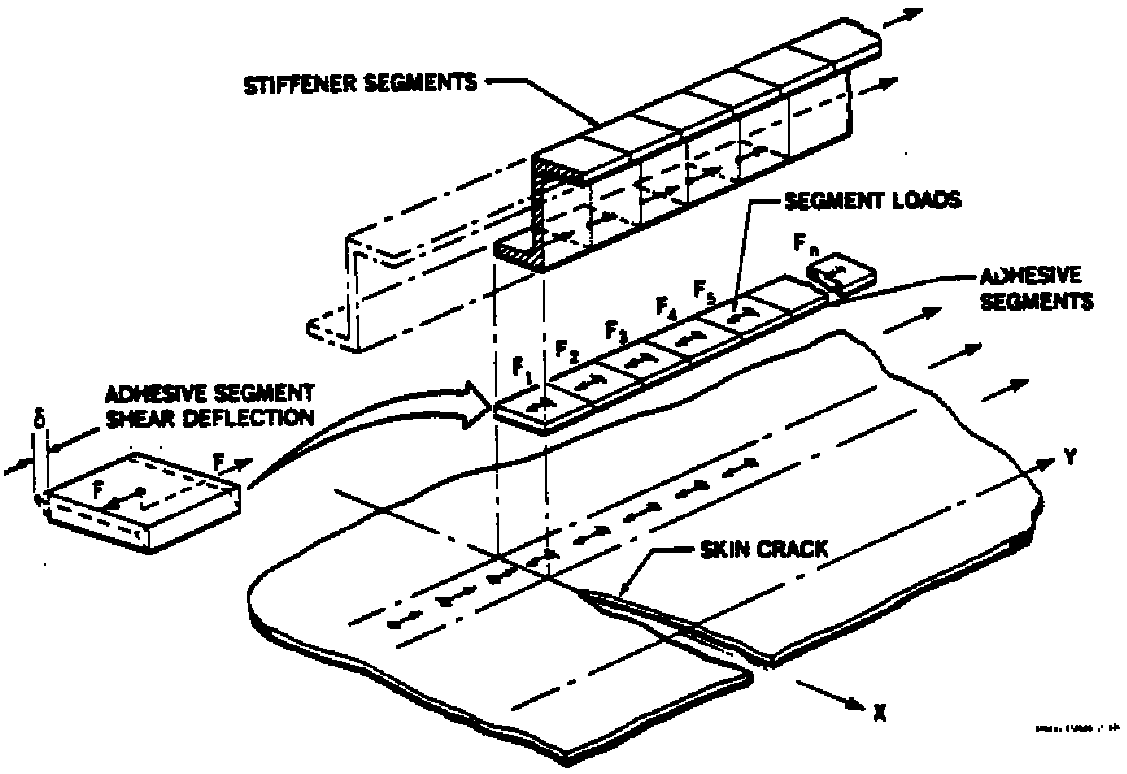

Figure 4.5.9. Bonded Fastener Divided into Discrete Segments

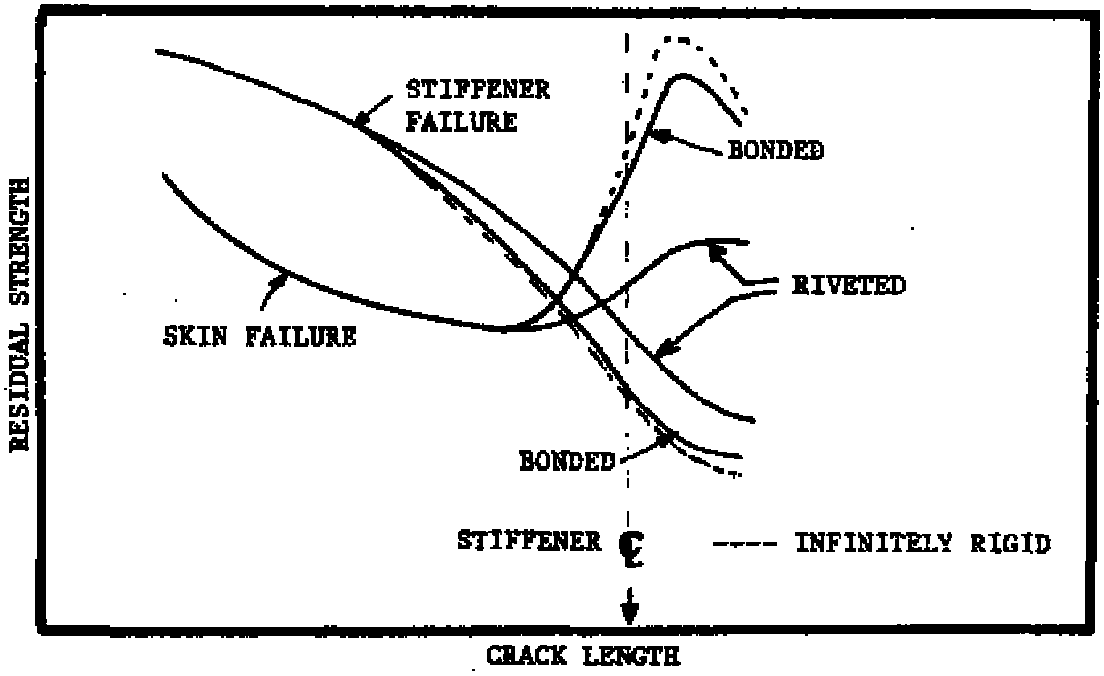

Figure 4.5.10. Residual Strength Diagram Comparing Riveted and Bonded Structures

4.5.4 Stiffener Failure

Stiffener failures are based on the following three stiffener conditions:

1. Intact stiffener (no cracks),
2. Partially failed stiffener (with cracks),
3. Totally failed stiffener.

The failure criterion for the intact stiffener is based on the ultimate strength criterion. As mentioned earlier, the ratio between the stiffener load in the cracked region (P_{max}) and the remote region from the crack (P) is defined as the load concentration factor L_s or

$$L_s = \frac{P_{\max}}{P} = \frac{P_{\max}}{\sigma A_s} \tag{4.5.1}$$

where σ is the uniform stress in the skin at the loaded end of the panel and A_s is the stiffener cross sectional area. Failure of the stiffener will occur when the value of P_{max} is equal to the ultimate strength of the stiffener (P_{ult}), or when

$$P_{max} = P_{ult} = \psi \sigma_{ult} A_s \tag{4.5.2}$$

where σ_{ult} is the ultimate tensile strength of the stiffener material and $\psi \leq 1$ is a factor accounting for load eccentricity and notch effects in the stiffener. For a uniform stress distribution in the panel remote from the crack the stress in the stringer will equal the nominal stress σ in the skin, i.e.,

$$P = \sigma A_s \tag{4.5.3}$$

Combining equations 4.5.1 to 4.5.2, yields the following stiffener failure criterion:

$$\sigma = \psi \frac{\sigma_{ult}}{L_s} \tag{4.5.4}$$

When the stress in the stringer reaches the value of $\psi \sigma_{ult}$, the stringer will fail. The parameter ψ is determined by tests.

When load eccentricity and not effects are not considered for a stringer, ψ equals one. The stiffener failure curve obtained using Equation 4.5.4 is shown in Figure 4.5.11. The initial portion of the residual strength curve is flat because the load concentration factor L_s is equal to one for small skin crack lengths. As the skin crack increases in size, L_s becomes significantly greater than one and the stringer carries a large portion of the total structural load which eventually leads to stringer yielding and failure. The portion of the curve in Figure 4.5.11 corresponding to $L_s > 1$ shows the gradual reduction of the residual strength.

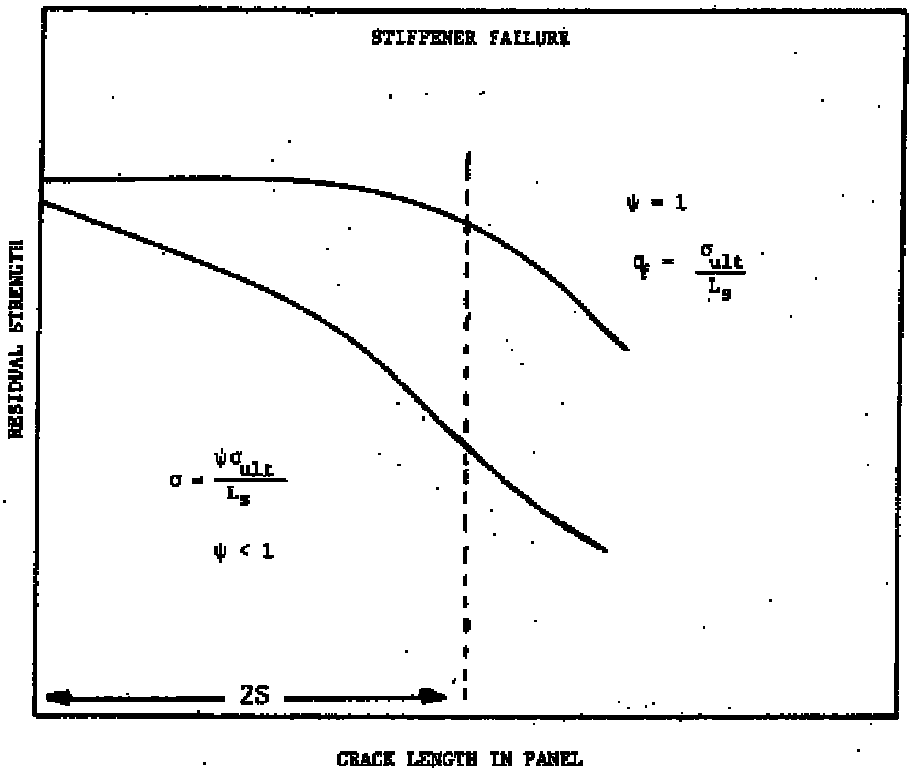

Figure 4.5.11. Residual Strength Diagram for Stiffener

When the load eccentricity and notch effects in the stiffener are considered, the parameter ψ in Equation 4.5.4 is less than one. The residual strength corresponding to a case where $\psi < 1$ is shown in Figure 4.5.11. The curve CD does not have the initial flaw portion exhibited by the case $\psi = 1$. Instead, the residual strength starts decreasing even for small skin crack lengths. The residual strength diagram for the stringer can be constructed knowing the values of L_s and ψ. Determining L_s requires numerical solution techniques that are discussed in the example presented in subsection 4.5.7.

According to JSSG-2006 requirements, cracks are assumed in all load carrying members. This means that all structural elements, stringer included, are assumed to be damaged. The residual strength diagram for the stringer will involve using the fracture mechanics approach of predicting unstable crack growth. The critical stress for a partially cracked stringer is given by $\sigma_f = \frac{K_{cr}}{L_s \beta_s \sqrt{\pi a_s}}$ where K_{cr} is the appropriate fracture toughness, β_s is the stringer geometric parameter, and a_s is the stringer crack size. When the crack in the panel approaches the stringer, the load transmitted to the stringer will become large ($L_s >> 1$) and thus the critical stress level required to fail the stringer rapidly decreases as shown by curve CE in Figure 4.5.11. Curve CE corresponds to the total failure of the stringer. This may happen when a large crack emanates from a stringer rivet hole. Total failure of the stiffener occurs before the skin crack approaches the stiffeners.

The residual strength diagram for the stiffened panel in this case would, in fact, be approximately that of the unstiffened panel.

The foregoing discussion presented analysis of a riveted built-up structure. However, built-up structures exist in which the stringer is adhesively bonded to the skin. The load transfer from the skin to the stringer is more effective in the bonded structure due to the increased rigidity in the stiffener. The corresponding load transfer parameter L_s will have higher values as shown schematically in Figure 4.5.12a. Due to the effective load transfer from the skin to the stiffener, the applied stress-intensity factor will be reduced when the panel crack approaches the stiffener. Figure 4.5.12b illustrates the levels of stress-intensity factor that occur for riveted and bonded stiffeners. The figure also shows that the bonded stiffener is subjected to higher loads due to the effective load transfer; the higher load causes the stiffener failure of the bonded structure to be more critical than that of the riveted structure. Figure 4.5.13 compares the decay of residual strength for these two types of structures. The residual strength of the bonded stiffener decreases faster than the riveted stiffener. In the determination of the residual strength diagram, the parameter L_s is usually calculated by numerical methods. The steps to obtain L_s are discussed later in this section.

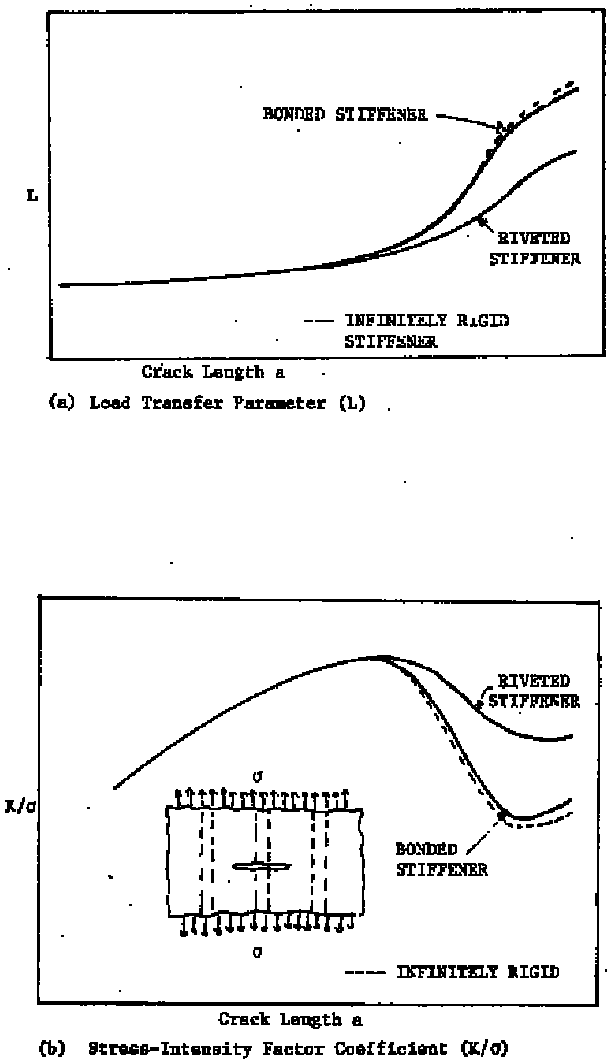

Figure 4.5.12. Comparison of *Ls* and K/σ for Riveted and Bonded Structures

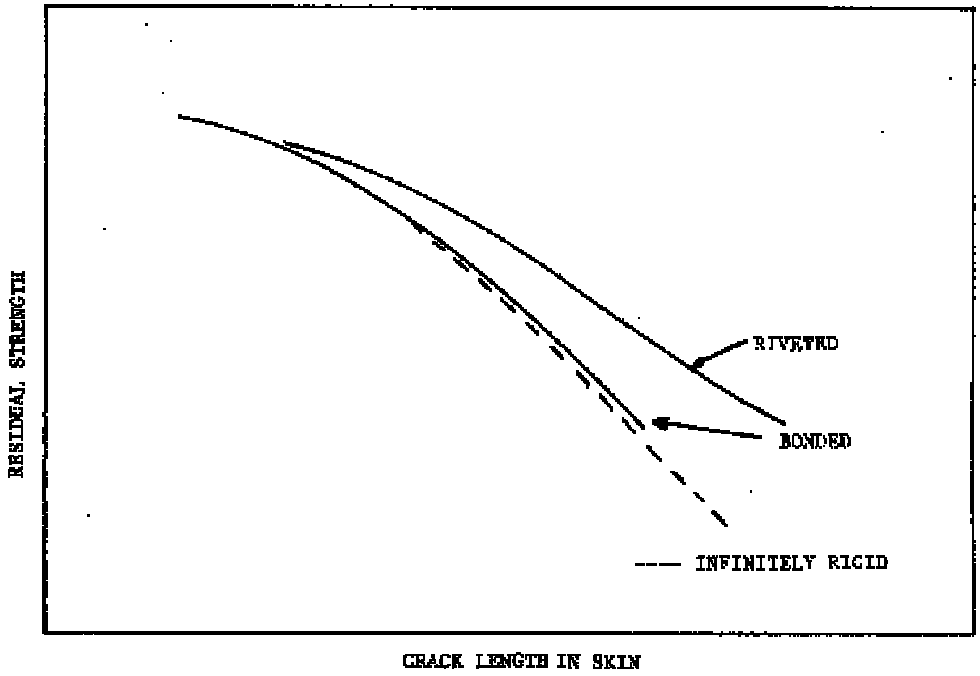

Figure 4.5.13. Comparison of Residual Strength for Riveted and Bonded Stiffeners

4.5.5 Fastener Failure

In subsections 4.5.3 and 4.5.4, the discussion focused on skin and stiffener failures. A third mode of failure involves the fasteners. This paragraph will discuss the failure of the fastener system. Load is transmitted from the skin to the stringers through fasteners. If the fastener loads become too high, fastener failure may occur by shear. Fastener failure will reduce the effectivity of the stringer; and therefore, the residual strength of the panel will drop. The highest loads (F) in the stringer/skin connections will occur in the fasteners adjacent to the crack path. Fastener failure will occur when the fastener forces F transmitted by the fasteners adjacent to the crack exceed the critical shear load of the fastener. The fastener failure criterion is given by

$$F = \pi/4\, d^2\, \tau_{ult} \qquad (4.5.5)$$

where d is the fastener diameter and τ_{ult} is the ultimate shear stress of the fastener material. It is emphasized that fastener failure need not necessarily cause total failure of the panel. Once the fastener failure criterion is met, however, the values of L_s and β will change since the loads transferred to the stiffener and skin changes. Once the fastener fails, the values of β and L_s will be recalculated in order to proceed further with the residual strength analysis. The load that causes the fasteners to fail by shear can be calculated from Equation 4.5.5; the corresponding nominal stress in the panel then gives the residual strength curve for the fasteners as shown in Figure 4.5.14. At zero crack length, and for the case where the skin and stringers are made from common materials, the fasteners do not carry any load; the curve therefore tends to increase rapidly for $a \rightarrow$o. The fastener forces F_i can be computed through the displacement compatibility between the stiffener and the panel. The necessary steps involved in the computation of F_i are discussed in the example presented in subsection 4.5.7.

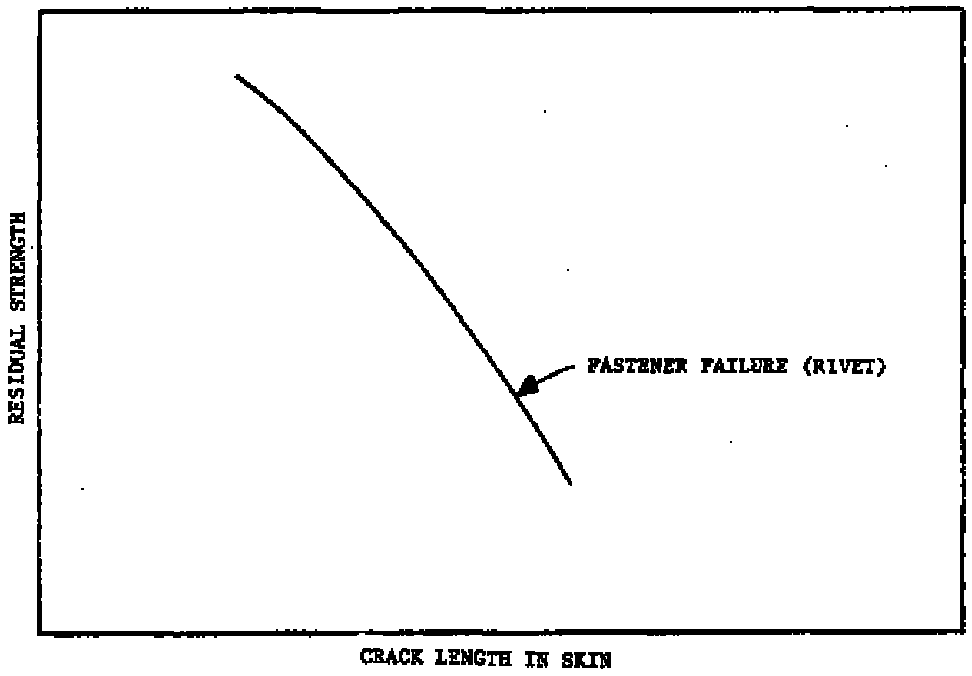

Figure 4.5.14. Residual Strength Diagram for the Fasteners in a Built-Up Structure

In the case of adhesively bonded structures, the adhesive (fastener) failure criterion is based on a maximum adhesive strain value. The residual strength analysis is fairly complicated (see, for example, reference 24). Based on the displacement compatibility between the panel and the stiffener, the adhesive segment strain deflection can be numerically computed for different amounts of disbond. Figure 4.5.15a shows the adhesive strain versus gross stress for various levels of adhesive delamination. The vertical line AB represents average failure strain of the adhesive. The intersection points between the line AB and the curves give the critical gross stress versus amount of adhesive failed as shown in Figure 4.5.15b. The corresponding curve ABC can be used for panel failure analysis. The area above the curve defines the failure of adhesive.

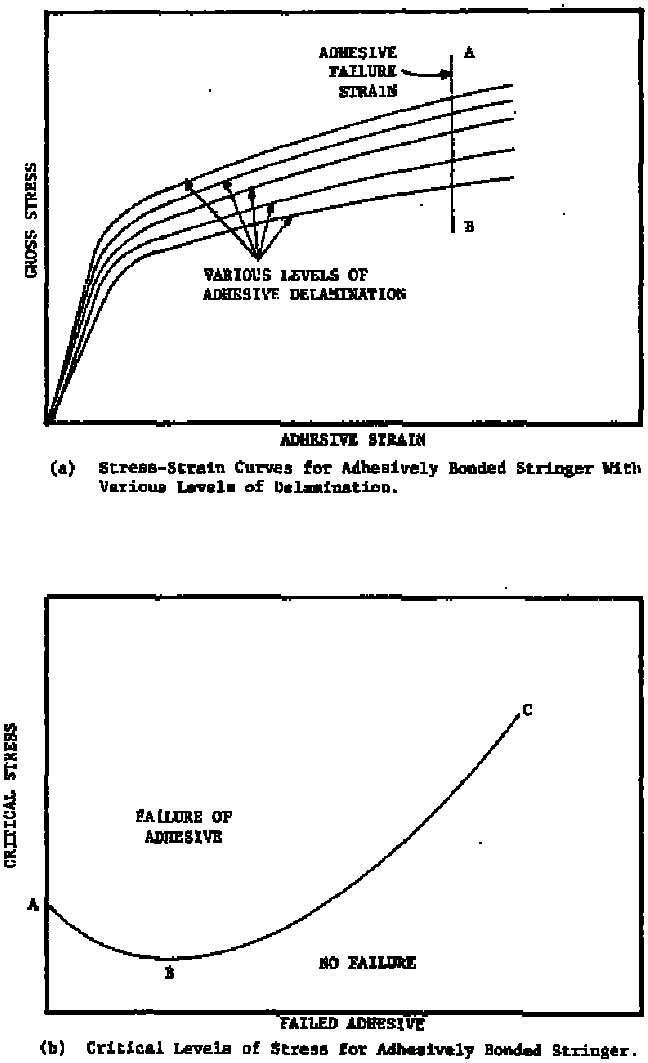

Figure 4.5.15. Gross Stress and Critical Stress Diagram for Adhesively Bonded Stringer

4.5.6 Methodology Basis for Stiffened Panel Example Problem

The residual strength analysis of an edge stiffened, centrally cracked skin structure of the type shown in Figure 4.5.16 can be performed by following the general steps described in the preceding subsections.

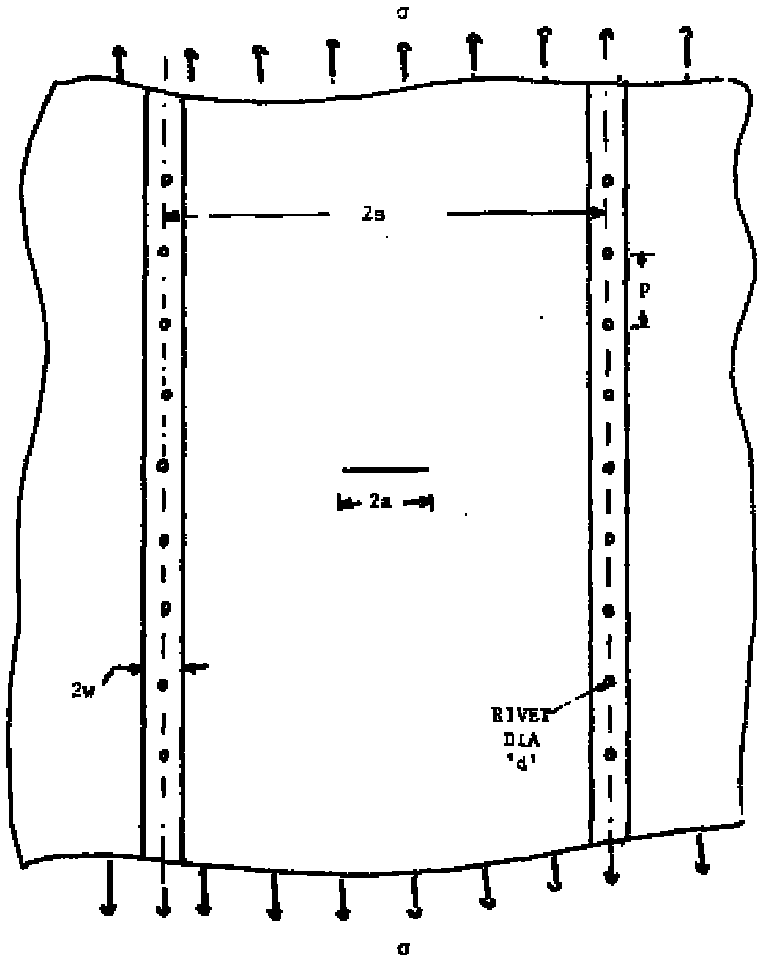

Figure 4.5.16. Riveted Panel with a Central Crack Between Two Stringers

In this subsection, the specific details are covered which are associated with conducting the stress-intensity factor analysis as well as the analysis to determine the stresses in the stringers and fastener loads. To simplify the detailed calculations, it is assumed that only one fastener (rivet) on either side of the crack is active, as shown in Figure 4.5.17 and that this rivet is assumed to be rigid. Thus, there is only one unknown fastener force F transferred between the stringers and the skin by this rivet.

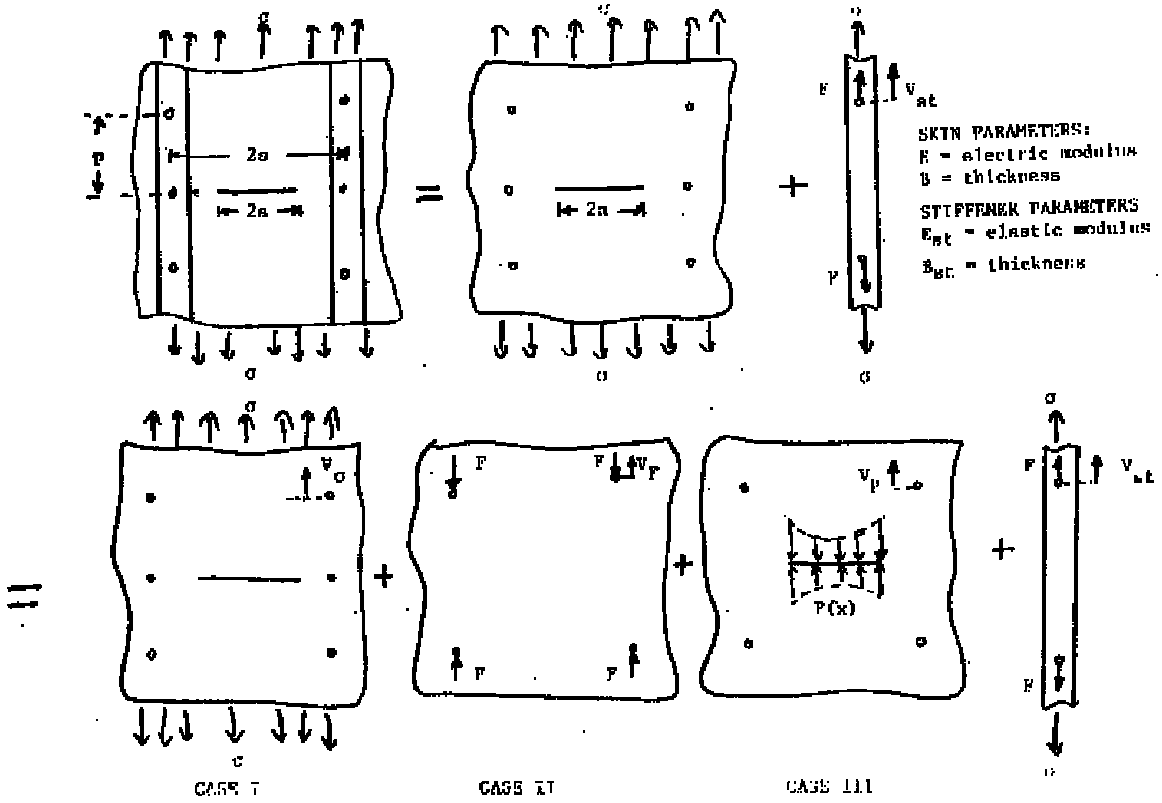

Figure 4.5.17. Stiffened Structure Broken into Components

Typically, the analysis proceeds by splitting up the structure shown in Figure 4.5.16 into its component parts as shown in Figure 4.5.17. The unknown force F can be calculated from the displacement compatibility condition between the skin and the stringer. The complicated expressions which correspond to the displacements V_σ, V_F, and V_P due to the applied stress, σ, the fastener force F and the distributed pressure $P(x)$, respectively, can be obtained using a procedure suggested by Westergaard [1939] and by Love [1944]. The detailed discussions on the methods of obtaining the required relationships are presented by Broek [1974]. The necessary relationships for V_σ, V_F, V_p and V_{st} (displacement in the stringer) are given as:

$$V_\sigma = \frac{\sigma}{E} f_\sigma \tag{4.5.6}$$

$$V_F = \frac{-F}{EB} f_F \tag{4.5.7}$$

$$V_p = \frac{-F}{EB} f_p \tag{4.5.8}$$

$$V_{st} = \frac{F}{E_{st} B_{st}} f_{st} + \frac{\sigma}{E_s} p \tag{4.5.9}$$

where

$$f_\sigma = \sqrt{\rho_1\rho_2}\left\{2\sin\left[\frac{\theta_1+\theta_2}{2}\right]\frac{(1+\upsilon)pr}{\rho_1\rho_2}\cos\left[\theta\frac{\theta_1+\theta_2}{2}\right]\right\}+\upsilon p \tag{4.5.10}$$

$$f_F = \frac{(1+\upsilon)}{4\pi}\left\{(3-\upsilon)\left[\ell n\frac{d}{4p}1\right]+(1+\upsilon)\left[2-\frac{s^2}{s^2+p^2}\right]+(3-\upsilon)\ell n\left(\frac{s^2}{s^2+p^2}\right)\right\} \tag{4.5.11}$$

$$f_P = \frac{\overline{P}}{\pi a}\left\{2\left[\sqrt{\rho_1\rho_2}\sin\left(\frac{\theta_1+\theta_2}{2}\right)-p\right]-(1+\upsilon)p\left[\frac{r}{\sqrt{\rho\rho_{21}}}\cos\left(\theta-\frac{\theta_1+\theta_2}{2}\right)-1\right]\right\} \tag{4.5.12}$$

where

$$\overline{P} = \left\{\tan^{-1}\left(\frac{a+s}{p}\right)+\tan^{-1}\left(\frac{a-s}{p}\right)+\frac{p(1+\upsilon)}{2}\left[\frac{a+s}{p^2+(a+s)^2}+\frac{a-s}{p^2+(a-s)^2}\right]\right\} \tag{4.5.13}$$

and

$$f_{st} = -\frac{(1+\upsilon)}{4\pi}\left\{\left[(3-\upsilon)\left(\ell n\frac{d}{4y_o}-1\right)+(1+\upsilon)\right]+\right.$$

$$\left.2\sum_{n=1}^{\infty}\left[(3-\upsilon)\ell n\frac{nw}{\sqrt{n^2w^2+4p^2}}+(1+\upsilon)\left(\frac{4p^2}{n^2w^2+4p^2}\right)\right]\right. \tag{4.5.14}$$

The geometric variables r, ρ_1, ρ_2, θ_1, θ_2 and θ are shown in Figure 4.5.18. The displacement compatibility condition requires equal displacements in corresponding points of sheet and stringer; it yields the following equation to calculate the unknown fastener force F.

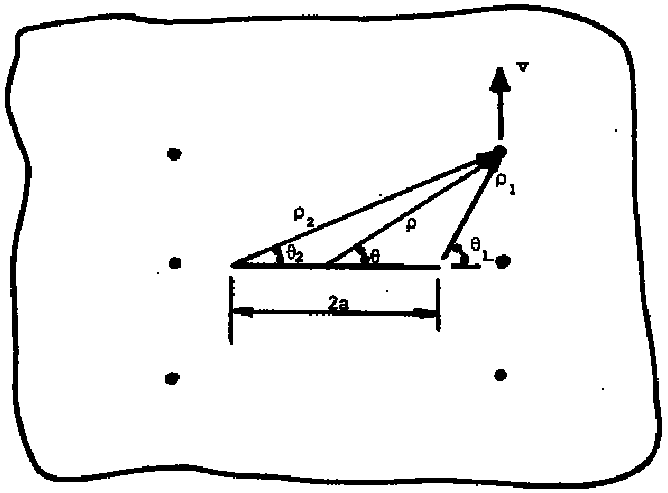

Figure 4.5.18. Geometrical and Displacement Parameters Relative to the Crack Tip

$$V_\sigma + V_F + V_p = V_{st} \tag{4.5.15}$$

substituting the expressions 4.5.6 - 4.5.9 for V_σ, V_F, V_p, and V_{st} in the above relationship, and reassembling, we get

$$F = \sigma\lambda \text{ where } \lambda = \left\{ \frac{\frac{f_\sigma}{E} - \frac{p}{E_{st}}}{\frac{f_F + f_p}{EB} + \frac{f_{st}}{E_{st}B_{st}}} \right\} \tag{4.5.16}$$

The next step is to obtain an expression for the stress-intensity factor for the entire stiffened panel configuration. Using superposition, the stress-intensity factor is obtained as the sum of the stress-intensity factors for the three cases shown in Figure 4.5.17. It can easily be seen that for Case I: $K = \sigma\sqrt{\pi a}$ and for Case II: $K = 0$. The stress-intensity factor (K) for Case III is a fairly complicated expression and it is given by,

$$K_{III} = -2\sqrt{\frac{a}{\pi}}\frac{1}{\pi}\frac{F}{Bp}\left[\frac{(3+\upsilon)}{2}I_1 + (1+\upsilon)I_2\right] \tag{4.5.17}$$

where

$$I = {}_1\int_o^a \frac{d\bar{x}}{\sqrt{\bar{a}2\bar{x}2}}\left\{\frac{1}{(1+(\bar{x}-\bar{s})^2} + \frac{1}{(1+(\bar{x}+\bar{s})^2)}\right\} \tag{4.5.18a}$$

and

$$I_2 = \int_o^a \frac{d\bar{x}}{\sqrt{\bar{a}2-\bar{x}2}}\left\{\frac{(\bar{x}-\bar{s})^2}{(1+(\bar{x}-\bar{s})^2)^2} + \frac{(\bar{x}+\bar{s})^2}{(1+(\bar{x}+\bar{s})^2\_^2}\right\} \tag{4.5.18b}$$

where $\bar{a}, \bar{x}$ *and* $\bar{s}$ are normalized with respect to the rivet pitch. The estimation of K_{III} requires solution of the above integrals by numerical methods. Replacing the fastener force F by the expression and rearranging the expression for K_{III}, the stress-intensity factor K for the stiffened panel then becomes

$$K = \sigma\sqrt{\pi a} - \sigma\sqrt{\pi a}\lambda_1\lambda_2 \tag{4.5.19}$$

where

$$\lambda_1 = \frac{(3+\upsilon)}{2}I_1 + (1+\upsilon)I_2 \tag{4.5.20a}$$

and

$$\lambda_2 = \frac{2\lambda}{\pi^2 Bp} \tag{4.5.20b}$$

The stress-intensity factor K can be finally expressed in the following form,

$$K = \sigma\beta\sqrt{\pi a} \tag{4.5.21}$$

where

$$\beta = \left(1 - \lambda_1\lambda_2\right) \tag{4.5.22}$$

To calculate K for a given stiffened panel the values of F_σ, f_F, f_p, f_{st}, and λ_1 have to be obtained. These variables are numerically calculated and plotted as shown in Figures 4.5.19 to 4.5.23 for various values of $\bar{s}, \bar{a}, and\ \bar{d}$. For the given example data, we can now construct the residual strength diagram using the values obtained from these plots.

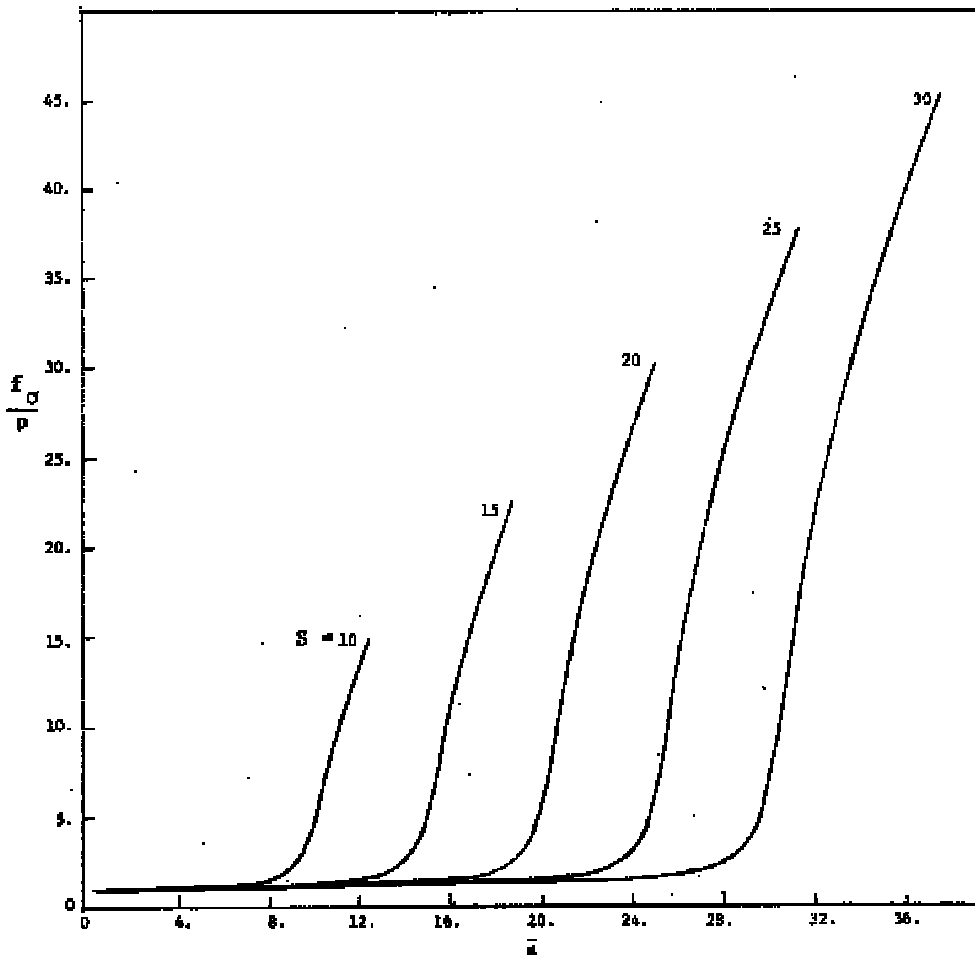

Figure 4.5.19. Normalized Panel Displacement Function (f_s /p) Due to Applied Stress vs. Normalized Crack Length (a/p) for Various Stringer Spacing (s=S/p)

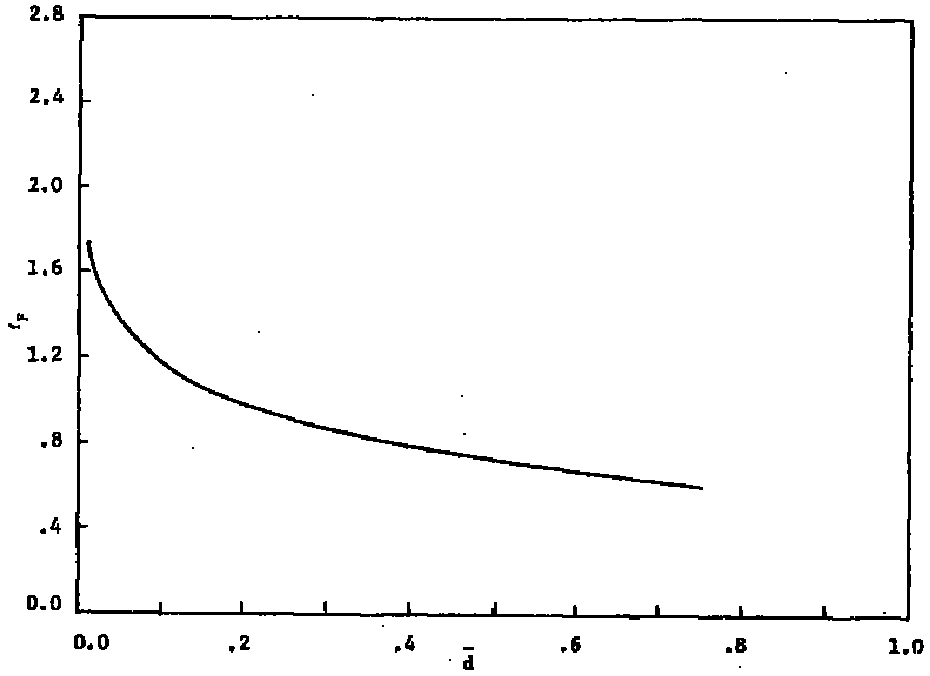

Figure 4.5.20. Panel Displacement Function Due to Fastener Force vs. Normalized RivetDiameter (*d/p*) for All Stiffener Spacings

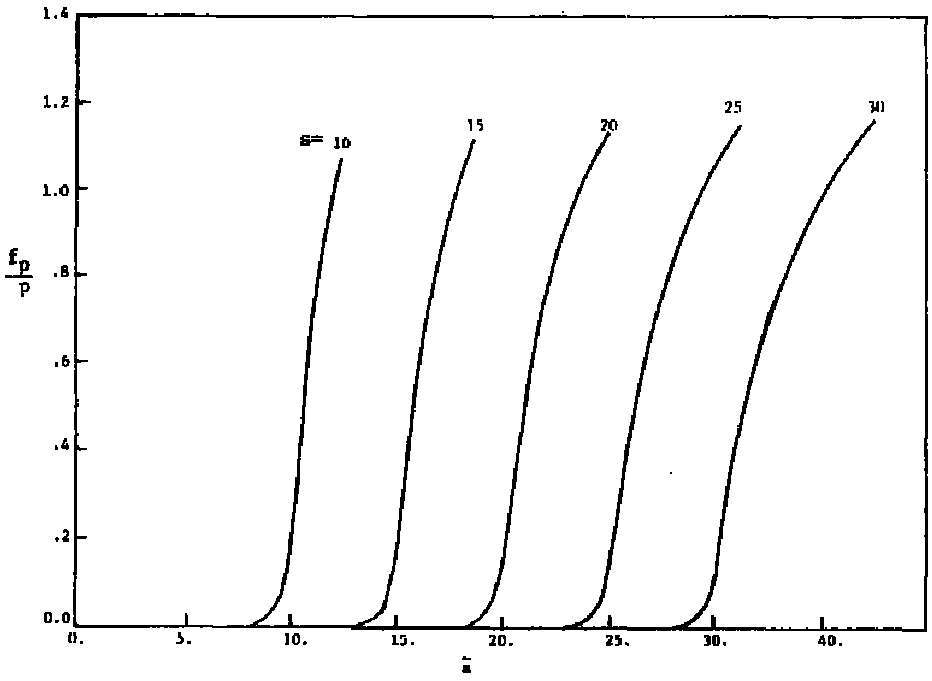

Figure 4.5.21. Normalized Panel Displacement Function (F_p /*p*) Due to Crack Distributed Pressure Along Crack vs. Normalized Crack Length (*a/p*) for Various Stringer Spacings (*s=s/p*)

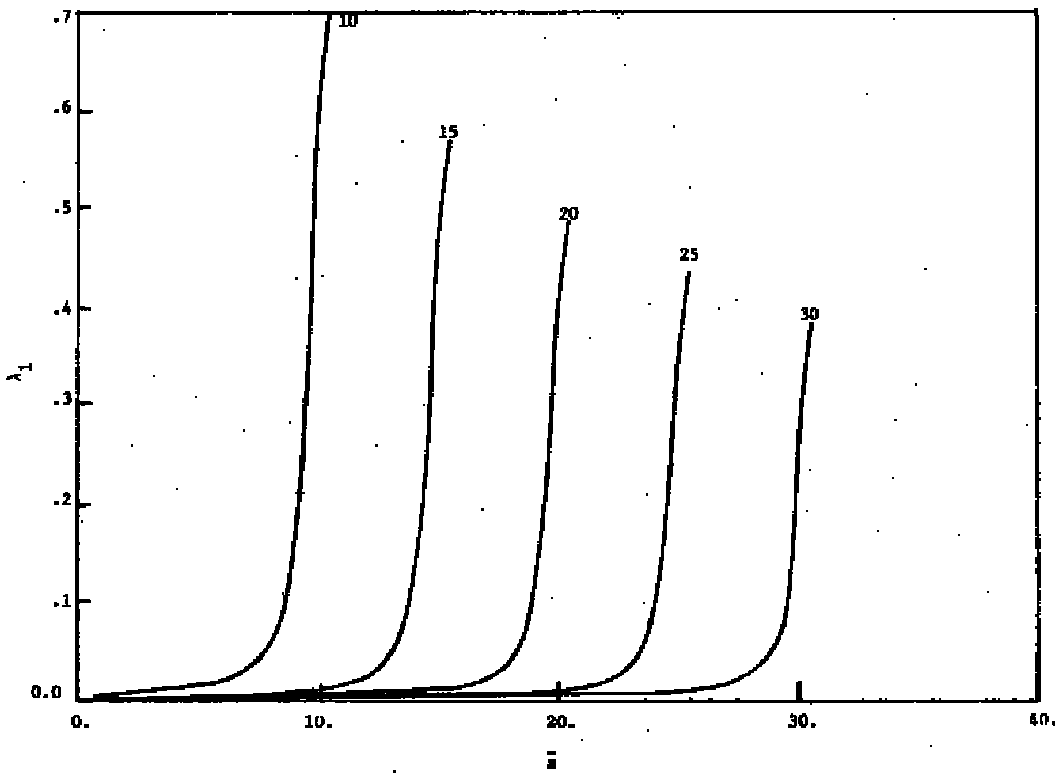

Figure 4.5.22. Stringer Displacement Function vs. Normalized Rivet Diameter (*d/p*) for Various Half-Stringer Widths

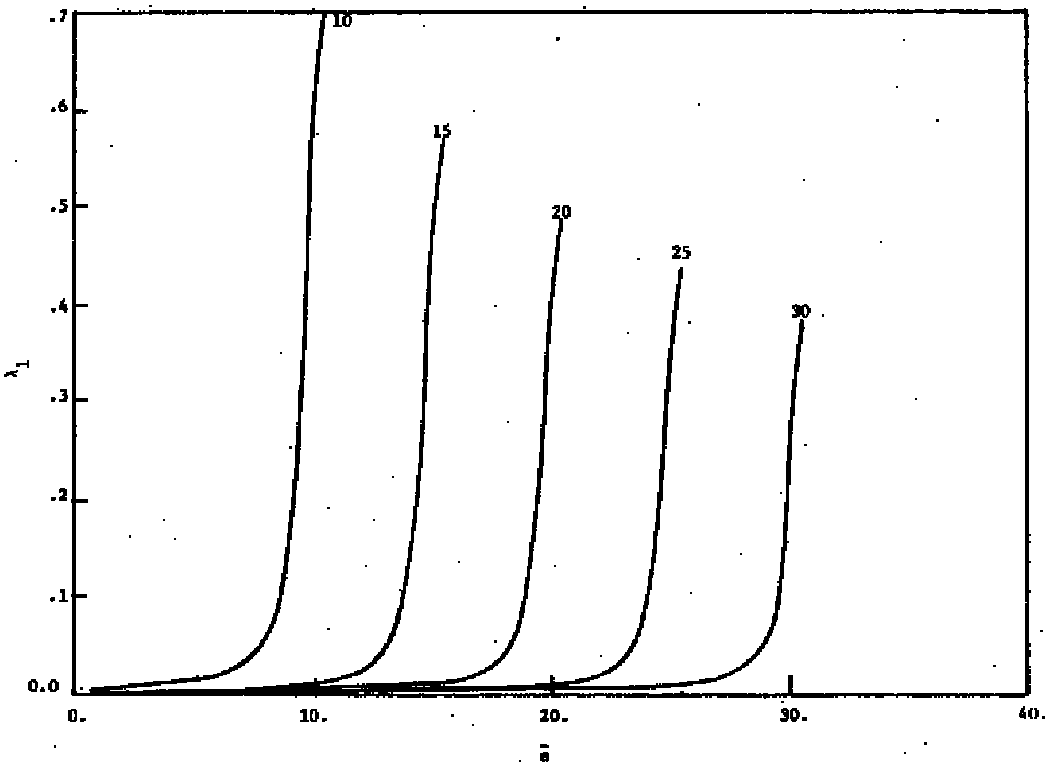

Figure 4.5.23. Parameter λ_1 Vs. Normalized Crack Length (a/p) for Various Normalized Stringer Spacings (s/p)

EXAMPLE 4.5.1 Residual Strength Analysis of Stiffened Panel

Determine the residual strength capabilities of a stiffened panel of 7075 aluminum with a central crack between the two stringers as shown in Figure 4.5.24.

For a critical crack size ($2a$) of 4.0 inch, what is the fracture strength and for an operating stress of 20 ksi, what is the critical crack size?

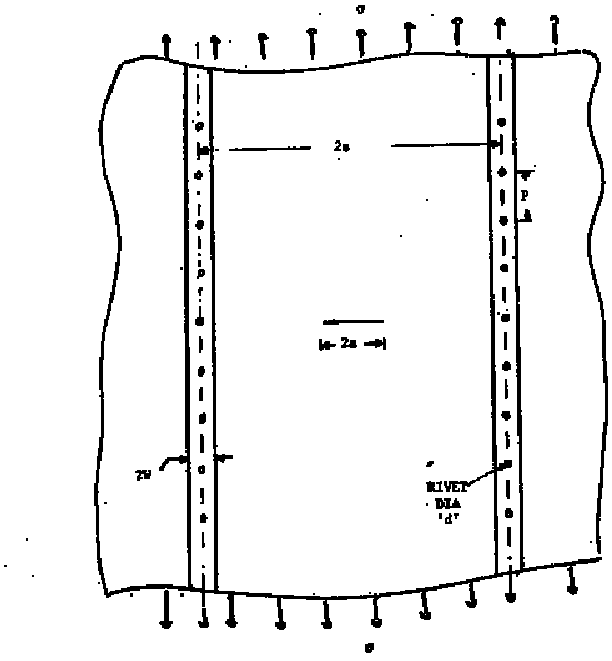

given the following data:

Maximum operating stress: 20 Ksi
Stiffener spacing (2s): 40 inch
Stiffener width (w): 0.5 inch
Stiffener thickness (B_{st}): 0.063 inch
Panel thickness (B): 0.063 inch
Rivet pitch (p): 1 inch
Rivet diameter (d): 3/16 inch
Material: 7075-T6 Aluminum
Fracture toughness: 65 Ksi$\sqrt{\text{inch}}$
Ultimate Strength: 78 Ksi

Structural Geometry and Material Properties for Example 4.5.1

SOLUTION:

The first step is to obtain the stress-intensity factor by means of Equation 4.5.21 that involves the parameters λ_1 and λ_2. For various crack lengths, these two variables can be calculated using Equation 4.5.20. The calculations involve the values of f_σ, f_F, f_p, f_{st} and λ which are obtained from the plots for various values of $\bar{a}$ for the given $\bar{s} = 20$ and $d/p = 3/16$. Knowing the values of λ_1 and λ_2, the geometric parameter β can be estimated from Equation 4.5.22. It is then straightforward to obtain the K vs. a plot by substituting the sets of values of a and β in the stress-intensity factor equation ($K = \sigma\beta\sqrt{\pi a}$) for a particular value of the applied stress σ. The

corresponding K vs. a plot is shown for σ = 5, 10, and 15 ksi. This figure shows that the stress-intensity factor decreases rapidly when the crack approaches the stringer. The figure also shows the effect of stringer to panel thickness ratio on the stress-intensity factor.

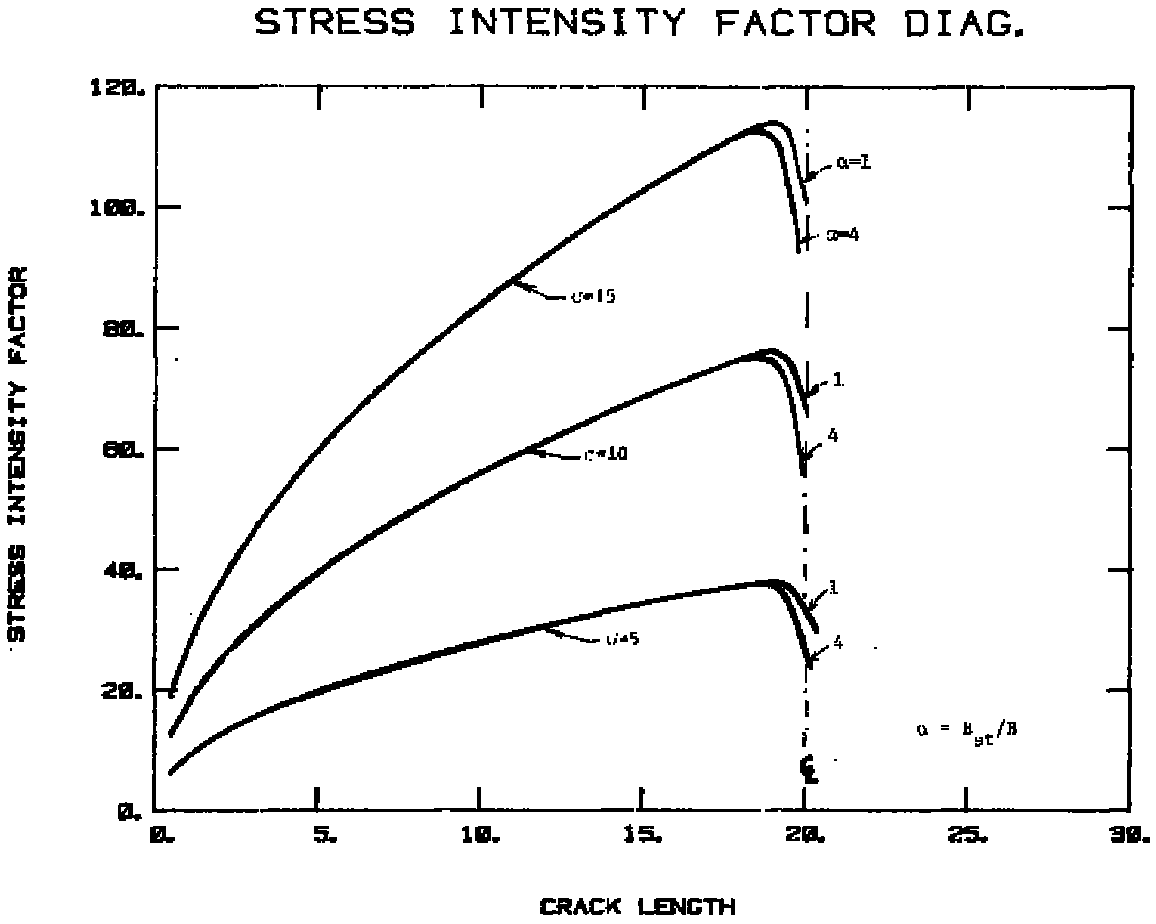

Stress Intensity Factor Diagram for Panel and Riveted Stringers

The next step is to apply a failure criterion to evaluate the fracture stresses, σ_{cr}, for various crack sizes. Assuming that the material exhibits negligible subcritical crack growth, the fracture toughness failure criterion ($K = K_{cr}$) based on the plane stress condition can then be applied. For $K = K_c$ in Equation 4.5.12, σ_f can be evaluated for a particular crack size and the corresponding β which was obtained through Equation 4.5.22. The residual strength diagram, i.e., the plot of σ_f vs. a_c for the given data (K_c = 65 ksi $\sqrt{in}$), is shown in the following figure.

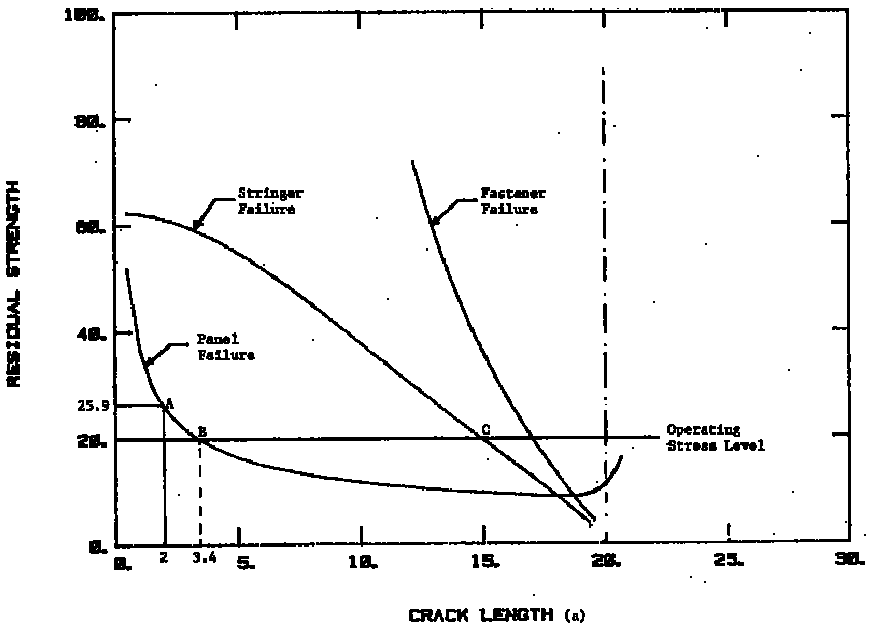

Residual Strength Diagram for Panel and Riveted Stringers (Light Stringers)

The residual strength curves of the fastener and stiffeners are obtained by combining the equations for fastener failure and the equations stringer failure. The corresponding equations are given by:

$$\sigma_f = \frac{\pi d^2 \tau_{ult}}{4\lambda} \text{ (Fastener)}$$

and

$$\sigma_f = \psi \frac{\sigma_{ult}}{\left(1 + \frac{\lambda}{A_s}\right)} \text{ (Stringer)}$$

where λ is a function of *a,* and the values of λ for various crack lengths can be obtained using the Equation 4.5.16. To obtain this Equation 4.5.24, note that the maximum stringer load (P_{max}) is the source of the fastener force ($F = \sigma\lambda$) and the remote stringer force (σA_s). The composite residual strength diagram as shown in the figure above contains the three failure curves corresponding to panel, stringer, and fastener. The stringer failure curve corresponds to $\alpha = 1$ (light stringer).

For the crack length given ($2a = 4$ inches), the corresponding residual strength is found from the figure for a half crack length (a) of 2 inches. Point A in this figure identifies the skin failure condition which occurs at a stress level of 25.9 ksi. For the operating stress level of 20 ksi, the panel can be effective without catastrophic failure for cracks with length less than the critical crack (a_{cr}) of 3.4 inch (note $2a_{cr} = 6.8$ inch). If the panel develops a crack less than a_{cr}, it will not fail by unstable crack growth. However, for any other crack size which is equal or

greater than the a_{cr} (3.4 inch), the residual strength level will fall below the operating stress level, leading to the rapid extension of the crack. Nevertheless, the structure has to be fully analyzed for its crack arrest capabilities when it develops cracks of length greater than a_{cr}.

Assume that the panel develops a crack of size a_{cr}. At point B in the figure, the crack extends rapidly. When the rapidly extending crack becomes 15 inches, the stress level in the stiffener (point C) reaches its critical value and the stiffener fails. Due to the stiffener failure, the stiffener becomes ineffective, leading to the total failure of the panel without any crack arrest possibilities.

In the next figure, the stiffener failure curve is plotted for a strong stiffener with $\alpha = 4$ (the stiffener thickness if "assumed" four times the panel thickness). If the panel develops a crack size a_{cr}, the crack will extend rapidly from point D to point E as shown in the next figure. At point E, the fastener fails, leading to an ineffective stringer (loads are no longer transferred to the stringer). Thus, the failure of the panel is unavoidable and the unstable crack growth without effective crack arrest leads to the total failure of the structure.

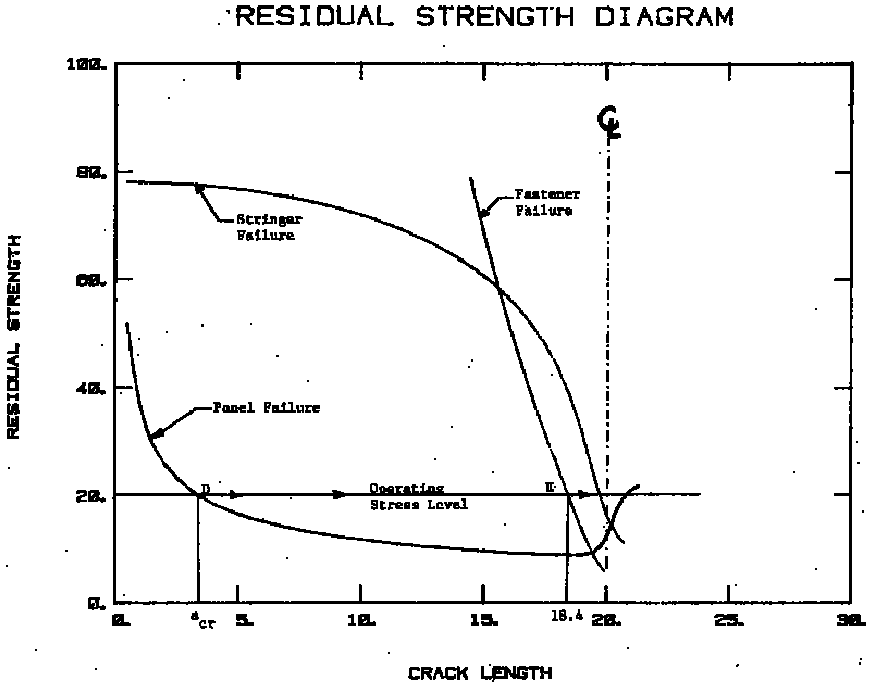

Residual Strength Diagram for Panel and Riveted Stringers (Heavy Stringers)

4.5.7 Tearing Failure Analysis

When the cracked thin sheet structure of high fracture toughness material is considered, the solutions based on linear elastic behavior for the calculation of residual strength are no longer valid due to the large scale yielding at the crack tip. For fail-safe structures with crack arrest capabilities, the residual strength analysis becomes complicated. However, using the R-curve based on $\sqrt{J_R}$ concept as the failure criterion Ratwani and Wilhem [1974] developed a step-by-step procedure for predicting the residual strength of built-up skin stringer structure composed of tough material exhibiting tearing type fractures.

The residual strength prediction procedure is briefly outlined here to show step-by-step, the required data and analysis. It should not be assumed that by reading this step-by-step procedure that the uninitiated can perform a residual strength prediction. It is strongly recommended that the details of the preceding subsections and Ratwani and Wilhem [1974] be examined prior to attempting a structural residual strength analysis based on the following ten procedural steps:

Step 1. Model the structure for finite-element analysis or use an existing finite-element modeling remembering –

a. That structural idealizations are typically two-dimensional,

b. That no out-of-plane bending is permitted,

c. To use a proper fastener model (a flexible fastener model for riveted or bolted structure, or a shear spring model for bonded structure).

d. To use material property data from skin and substructure of interest (i.e., E, E_{ty} and F_{tu}),

e. To select the most critical crack location (normally highest stressed area),

f. To take advantage of structural symmetry.

Step 2. Select one crack length ($2a$ or a) of interest (based on inspection capability or detailed damage tolerance requirement). Based on this "standard" crack length, five other crack lengths are selected for a Dugdale type elastic plastic analysis. These crack lengths should be selected such that crack length to stiffener spacing ($2a$) ratios vary between 0.15 to 1.1 remembering –

a. That the greatest variation in J values will take place near reinforcements, and

b. To select at least one crack size shorter than "standard".

Step 3. With the finite-element model (from Step 1) and assumed crack lengths (from Step 2), perform an analysis assuming Dugdale type plastic zones for each crack size remembering –

a. To select the first increment of plastic zone length at 0.2 inches and sufficient successive increments (normally 6) to reach Bueckner-Hayes calculated stresses up to 85 percent to F_{ty}.

b. To make judicious selection of plastic zone increments so as to take advantage of overlapping a_e (effective crack length) (e.g., 3.2, 3.5, 4.2, 5.0 inches for a 3 inch physical crack and 4.2, 4.5, 5.0 inches, etc., for a 4 inch physical crack). If overlapping is done, those cases where the crack surfaces are loaded throughout

the crack length will be common for two or more physical crack sizes hence the computer programs need be run only once (e.g. 4.2 and 5.0 inches) thus reducing computer run times.

Step 4. From Step 3, obtain stresses in stiffeners for Dugdale analysis and elastic analysis. Plot stiffener stresses as function of applied stress.

Step 5. From the crack surface displacement data of Step 3, plot $\sqrt{J}$ (obtained by Bueckner-Hayes approach) versus applied stress to F_{ty} ratio for each crack size.

Step 6. From Step 5, cross plot the data in the form of $\sqrt{J}$ versus crack size (a) at specific values of applied stress to F_{ty} ratio.

Step 7. Employing the data of Step 4 and the "standard" crack size determine, gross panel stress to yield strength ratio, σ/F_{ty} at ultimate strength (F_{tu}) for the stiffener material - assuming zero slow crack growth. This information will be used subsequently to determine if a skin or stiffener critical case is operative.

Step 8. Obtain crack growth resistance data for skin material (see Volume II of reference 26) remembering --

a. To use thickness of interest (i.e., if the skin material is chemically milled, use the experimentally obtained R-curve for the same chemically milled material)

b. Use proper crack orientation (LT, TL, or off angle) corresponding to anticipated direction structural cracking.

Step 9. Plot $\sqrt{J}$ versus Δa_{PHY} curve as shown in Figure 4.5.24 from the data obtained in Step 8.

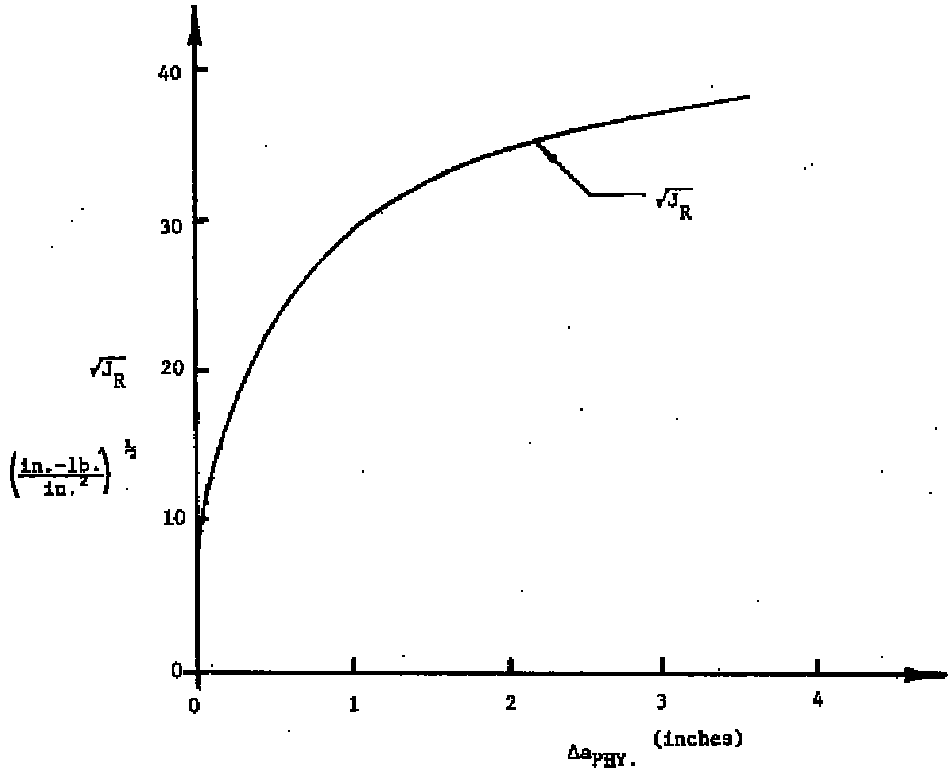

Figure 4.5.24. Square Root of J_r Resistance Curve

Step 10. Determine structural residual strength. On the $\sqrt{J}$ versus crack size (a) plots obtained in Step 6 for the structure, overlay the $\sqrt{J_R}$ versus Δa_{PHY} material plot of Step 9 at the initial crack length of interest as shown in Figure 4.5.25. Determine if –

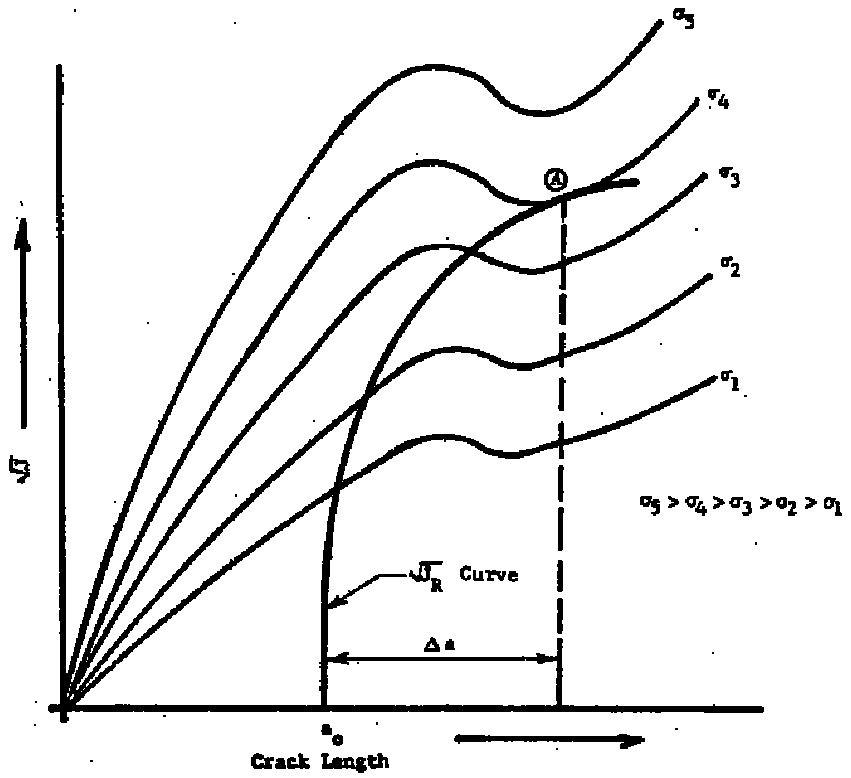

Figure 4.5.25. Failure Analysis Based on J critical Curve

At the gross panel stress obtained from Step 7, significant slow tear ($\geq$ 0.25 inch) will occur as indicated from the intersection of the $\sqrt{J_R}$ versus Δa_{PHY} curve with the constant σ/F_{ty} curve at a stringer ultimate strength (see Step 7). Interpolation will probably be necessary between values of constant σ/F_{ty}. Then proceed as follows:

If significant slow tear occurs (> 0.25 inch) the structure can be considered to be skin critical (at that particular crack length). Tangency of $\sqrt{J_R}$ versus Δa_{PHY} and $\sqrt{J}$ versus a_{PHY} at constant applied stress can be used to determine extent of slow tear and residual strength at failure as a percentage of F_{ty}

If significant slow tear does not occur (Δa_{PHY} < 0.25 inch) the structure will normally be stiffener critical. To determine a conservative value of residual strength (for that crack length) use the Dugdale curve of Step 4 and stiffener ultimate strength.

4.5.8 Summary

The most important factor to consider in residual strength prediction of a cracked built-up structure is to decide whether the structure is skin or stiffener critical. Normally, a short crack length is likely to be a skin critical case and a long crack length a stiffener critical case. However, there is no clear cut demarcation between the two cases. Factors such as percentage stiffening, spacing of stringers, lands in the structure, and other structural details will influence the type of failure. Hence, a good technique is to determine the residual strength of a given structure based on both skin critical and stiffener critical cases. The minimum fracture stress of

the two will then represent the residual strength of the structure and should be considered to be the governing case.

4.6 References

J.I. Bluhm (1969). "Fracture Arrest". *Fracture* (Vol. V). H. Liebowitz (Ed.). Academic Press, pp. 1-63.

O.L. Bowie (1956). "Analysis of an Infinite Plate Containing Radial Cracks Originating at the Boundary of an Internal Circular Hole". *Journal of Mathematics and Physics, 35,* pp. 60-71.

D. Broek (1974). *Elementary Engineering Fracture Mechanics*. Noordhoff.

M. Creager and A.F. Liu (1971). "The Effect of Reinforcements on the Slow Stable Tear and Catastrophic Failure of Thin Metal Sheet". AIAA paper, pp. 71-113.

D.A. Skinn, J.P. Gallagher, A.P. Berens, P.D. Huber, and J. Smith (1994). *Damage Tolerant Design (Data) Handbook.* WL-TR-94-4052. Wright Laboratory, Air Force Materiel Command, Wright-Patterson Air Force Base, Ohio.

D.E. McCabe (Ed.) (1973). *Fracture Toughness Evaluation by R-Curve Method.* ASTM STP 527. American Society for Testing and Materials.

W.T. Fujimoto (1976, May 4-7). "Determination of Crack Growth and Fracture Toughness Parameters for Surface Flaws Emanating from Fastener Holes". *MCAIR Report A4093.* Presented at the AIAA/ASME/SAE Structures, Structural Dynamics and Materials Conference, Valley Forge, PA.

A.F. Grandt (1975). "A General Stress-Intensity Factor Solution for Through-Cracked Fastener Holes", *International Journal of Fracture, 11*.

C.A. Griffis and G.R. Yoder (1974, April). "Application of the J-Integral to Crack Initiation in a 2024-T351 Aluminum Alloy". Naval Research Lab Report 7676.

C.K. Gunther and J.T. Wozumi (1982). "Critical Failure Modes in Cracked Mechanically Fastened Stiffened Panels". *Design of Fatigue and Fracture Resistant Structures*, P.R. Abelkis and C.M. Hudson (Eds.). ASTM STP 761, American Society for Testing and Materials, pp. 310-327.

JSSG-2006 (1998, October). "Joint Service Specification Guide, Aircraft Structures". Department of Defense.

J.M. Krafft, A.M. Sullivan, and R.W. Boyle (1961). "Effect of Dimensions on Fast Fracture Instability of Notched Sheets", Cranfield Crack Propagation Symposium (Vol. 1), pp. 8-28.

A.E.H. Love (1944). *A Treatise on the Mathematical Theory of Elasticity*, New York, Dover (4^{th} Ed.), p. 209.

W.S. Margolis and F.C. Nordquist (1975). "Plane Stress Fracture Toughness (K_c) of Aluminum Alloy 7475 - 1/2 Inch Plate, Tempers - T7651 and T7351 and of Aluminum Alloy 2024 - 1/8 Inch Sheet - T81 and T62 Temper". General Dynamics, Fort Worth Div., F-16 Air Combat Fighter Technical Reports TIS GA2300, CDRL A031, USAF Contract F33657-75-C-0310.

C.C. Poe (1970). "The Effect of Riveted and Uniformly Space Stringers on the Stress-Intensity Factor of a Cracked Sheet". Air Force Conference on Fatigue and Fracture, 1969. AFFDL-TR-70-144.

C.C. Poe (1971). “Fatigue-Crack Propagation in Stiffened Panels”. ASTM STP 486, pp. 79-97.

M.M. Ratwani and D.P. Wilhem (1974, December). “Development and Evaluation of Methods of Plane Stress Fracture Analysis, A Technique for Predicting Residual Strength of Structure”. AFFDL-TR-73-42.

J.R. Rice (1968, June). “A Path Independent Integral and the Approximate Analyses of Strain Concentration by Notches and Cracks”. *Journal of Applied Mechanics*, ASME (Vol. 35), pp. 379-386.

J.P. Romauldi and P.H. Sanders (1959-1960). “Fracture Arrest by Riveted Stiffeners”. *Proceedings of Fourth Midwest Conference on Solid Mechanics*. University of Texas Press.

J.P. Romauldi, J.T. Frasier, and G.R. Irwin (1957). “Crack-Extension Force Near a Riveted Stringer”. NRL Memo Report No. 4956.

R.V. Sanga (1974). “The 747 Fail-Safe Structural Program”. *Fail-Safe Aircraft Structures* (Vol. II). I CAF Symposium (1973). RAE RE 73 183, pp. 3.1/1-3.1/66.

J.E. Srawley and W.F. Brown (1965). “Fracture Toughness Testing Method”. ASTM STP 381, pp. 133-195.

T. Swift (1971).“Development of the Fail-Safe Design Features of the DC-10”. ASTM STP 486, pp. 164-214.

T. Swift (1974) “The Effects of Fastener Flexibility and Stiffener Geometry on the Stress Intensity in Stiffened Crack Sheet”. *Prospects of Fracture Mechanics*, G.C. Sih and D. Broek (Eds.). Nordhoff, (1974), pp. 419-436.

T. Swift and D.Y. Wang (1969). “Damage Tolerant Design Methods and Test Verification of Fuselage Structure”. Air Force Conference on Fatigue and Fracture, AFFDL-TR-70-144, pp. 653-683.

R. Verette and D.P. Wilhem (1973, May). “Development & Evaluation of Methods of Plane Stress Fracture Analysis, Review and Evaluation of Structural Residual Strength Prediction Techniques”. AFFDL-TR-73-42.

H. Vlieger (1973). “The Residual Strength Characteristics of Stiffened Panels Containing Fatigue Cracks”. *Engineering Fracture Mechanics, 5*, pp. 447-478.

H.M. Westergaard (1939). “Bearing Pressures and Cracks, Transactions, American Society Mechanical Engineers”. *Journal of Applied Mechanics* (Vol. 6), pp. 49-53.

D.P. Wilhem (1970, February). “Fracture Mechanics Guidelines for Aircraft Structural Application”. AFFDL-TR-69-111, Air Force Flight Dynamics Laboratory.

D.P. Wilhem (1974, June). “An Improved Technique for Residual Strength Prediction – A Modified Crack Growth Resistance Approach”. Paper presented at Conference on Prospects of Fracture Mechanics, Delft University, The Netherlands.

Section 5
Analysis Of Damage Growth

The airplane damage tolerance design requirements of JSSG-2006 specify that cracks shall be assumed to exist in all primary aircraft structure. These cracks shall not grow to a size to cause loss of the aircraft at a specified load within a specified period. Showing compliance with these requirements implies that the rate of growth of the assumed flaws must be predicted. This section covers basic crack growth terms, variable amplitude loading, retardation, stress sequence development, small crack behavior, and crack growth predictions.

5.1 Basic Information

Crack growth is a result of cyclic loading due to gusts and maneuvers (fatigue cracking), or of the combined action of sustained loading and environment (stress-corrosion cracking), or both. The most common crack growth mechanisms are fatigue crack growth and environment-assisted (corrosion) fatigue crack growth. Certain aircraft parts, especially high-strength forgings, may be liable to stress-corrosion cracking. Since there is a design threshold for stress corrosion, proper detail design and proper material selection can minimize or prevent stress corrosion. Fatigue cracking is difficult to prevent, but it can be controlled.

To predict crack growth behavior such as illustrated in Figure 5.1.1, the following information must be available:

- The stress-intensity factor, described as a function of crack size, for the relevant structural and crack geometry;
- The stress (load) – time history, described for the structural location component or structure under consideration;
- The baseline crack growth properties (constant amplitude crack growth rate data), described as a function of the stress intensity factor, for the material and for the relevant environment;
- A damage integration routine that integrates the crack growth rate to produce a crack growth curve, and uses the proper stress-time history, the proper stress intensity formulation, and an appropriate integration rule.

This section provides guidelines to arrive at crack growth estimates, and points out where deficiencies in knowledge and analysis methods lead to inaccuracies.

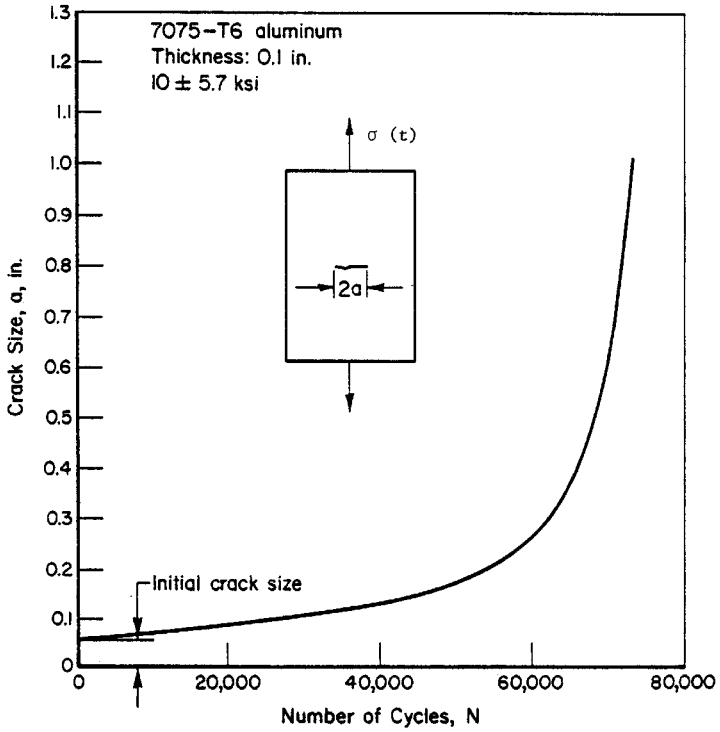

Figure 5.1.1. Typical Crack Growth-life Curve

5.1.1 Fatigue-Crack Growth and Stress-Intensity

Consider the constant-amplitude fatigue loading shown in Figure 5.1.2a. The following parameters are defined:

σ_m – mean stress

σ_a – stress amplitude

$\Delta\sigma$ – stress range

σ_{max} – maximum stress

σ_{min} – minimum stress

R – stress ratio: $R = \dfrac{\sigma_{min}}{\sigma_{max}} = \dfrac{\sigma_m - \sigma_a}{\sigma_m + \sigma_a} = 1 - \dfrac{\Delta\sigma}{\sigma_{max}}$.

The cyclic stress can be fully characterized (apart from the frequency) by any combination of two of these parameters. The stress range, $\Delta\sigma$, and the stress ratio, R, are the two most commonly used. Note that in a constant-amplitude test each of these parameters has a constant value with respect to time.

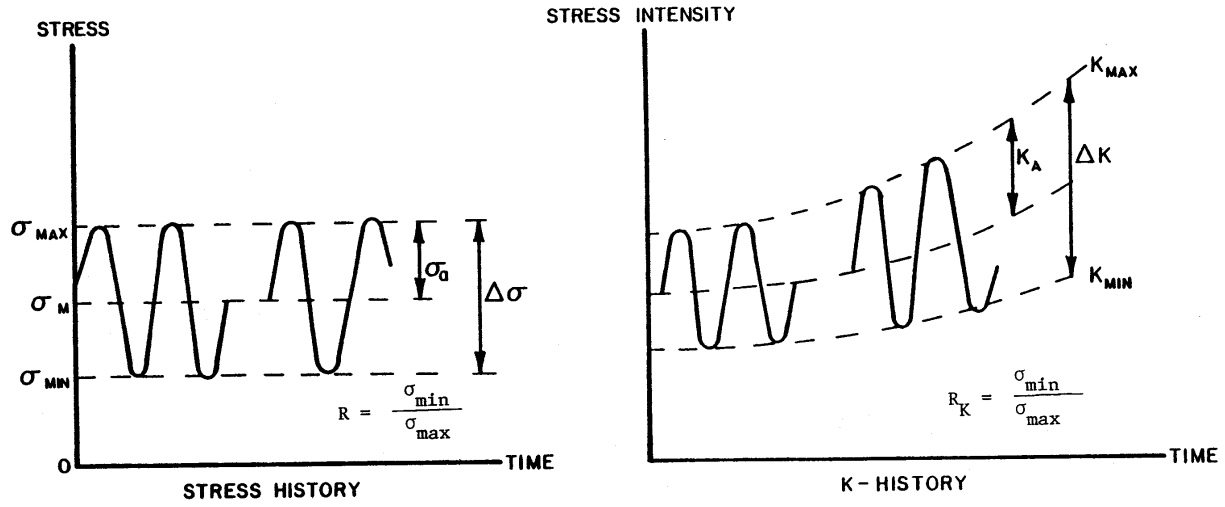

Figure 5.1.2. Definition of Terms for Fatigue Crack Growth and Stress Intensity

The stress history can be converted into a stress intensity factor history at a given crack length by multiplying the stress history by the stress intensity factor coefficient, as shown in Figure 5.1.2b. The following parameters are defined:

K_{max} – maximum stress intensity factor $= \beta\sigma_{max}\sqrt{\pi a}$

K_{min} – minimum stress intensity factor $= \beta\sigma_{min}\sqrt{\pi a}$

K_m – mean stress intensity factor $= \beta\sigma_m\sqrt{\pi a}$

K_a – amplitude of the stress intensity factor $= \beta\sigma_a\sqrt{\pi a}$

ΔK – range of the stress intensity factor $= \beta\Delta\sigma\sqrt{\pi a}$

R_K – cycle ratio: $R_K = \dfrac{K_{min}}{K_{max}}$

The above calculation schemes for stress intensity factor parameters, while being the most straightforward algebraically, have an operational quality about them. For example, it is theoretically difficult to define a negative stress intensity factor that happens if the stress becomes compressive. In this case, the crack closes and the crack tip stress field loses its singularity character; thus, the stress intensity factor ceases to have meaning. The operational quality of the negative stress intensity factors calculated for compressive stress situations has been given a lot of consideration by the aerospace industry and by ASTM, specifically its subcommittee on sub-critical crack growth (ASTM E24.04). ASTM has chosen to provide the following definitions when the minimum stress (σ_{min}) is less than zero:

$K_{min} = 0$ if $\sigma_{min} < 0$ $\qquad\qquad$ $\Delta K = K_{max}$ if $\sigma_{min} < 0$

The reader should be aware of the ASTM definition of ΔK because that convention is used in the Damage Tolerant Design (Data) Handbook [1994] for the presentation of crack growth rate data when part of the fatigue cycle is compressive, i.e., when $\sigma_{min} < 0$ ($R < 0$). The algebraic definition of ΔK is used in the current version of MIL-HDBK-5. Before negative stress ratio ($R < 0$) data are used, it is important to establish the operational definition of ΔK. The reader should note that the behavior of the material under negative stress ratio conditions is itself independent of the operational definition of ΔK.

In the elastic case, the stress-intensity factor alone is sufficient to describe the stress field at the tip of a crack. When the plastic zone at the crack tip is small compared with the crack size, the stress-intensity factor gives a good indication of the stress environment of the crack tip. Two different cracks that have the same stress environment (equal stress-intensity factors) will behave in the same manner and show the same rate of growth.

Since two parameters are required to characterize the fatigue cycle, two parameters are required to characterize crack growth rate behavior. The crack growth rate per cycle, *da/dN*, can be generally described with functional relation of the type:

$$\frac{da}{dN} = f(\Delta K, R) \quad or = g(K_{max}, R) \qquad (5.1.1)$$

where a is the crack length, N is the number of cycles, and R is the stress ratio associated with the stress cycle.

EXAMPLE 5.1.1 Meaning of *da/dN* Equation

For a wide center crack panel subjected to constant amplitude loading conditions, Equation 5.1.1 implies that the crack growth rate of a 2-inch long crack subjected to a remote loading of $\Delta\sigma = 10$ ksi for $R = 0$ will be identical to the rate of growth of a 0.5-inch long crack subjected to a remote loading of $\Delta\sigma = 20$ ksi for $R = 0$. The rates for the two different crack length - loading conditions will be the same because the stress-intensity factor range (ΔK) and the stress ratio (R) are the same in both cases.

Typically, fatigue crack growth rate data is described using plots of *da/dN* versus ΔK on double-logarithmic scale graph paper. Figure 5.1.3 presents fatigue crack growth rate data for 7075 aluminum in the graphical format that is used in the Damage Tolerant Design (Data) Handbook [1994]. Figures 5.1.4 and 5.1.5 describe example composite *da/dN* data plots for 7075 aluminum as a function of ΔK (algebraic definition) for different stress ratio (R) values [MIL-HDBK-5H, 1998]. Both Figures 5.1.4 and 5.1.5 provide mean trend curves that represent the function $f(\Delta K, R)$ in Equation 5.1.1. On the basis of these figures, it can be seen that $f(\Delta K, R)$ is not a simple function. Figure 5.1.6 is a schematic illustration of fatigue crack growth rate behavior from the threshold region (below 10^{-8} inch/cycle) to the onset of rapid cracking in the fracture toughness region (above 10^{-3} inch/cycle). As can be seen from Figures 5.1.3 - 5.1.6, the behavior exhibits a sigmoidial shape suggesting that there might be asymptotes at the two extreme regions.

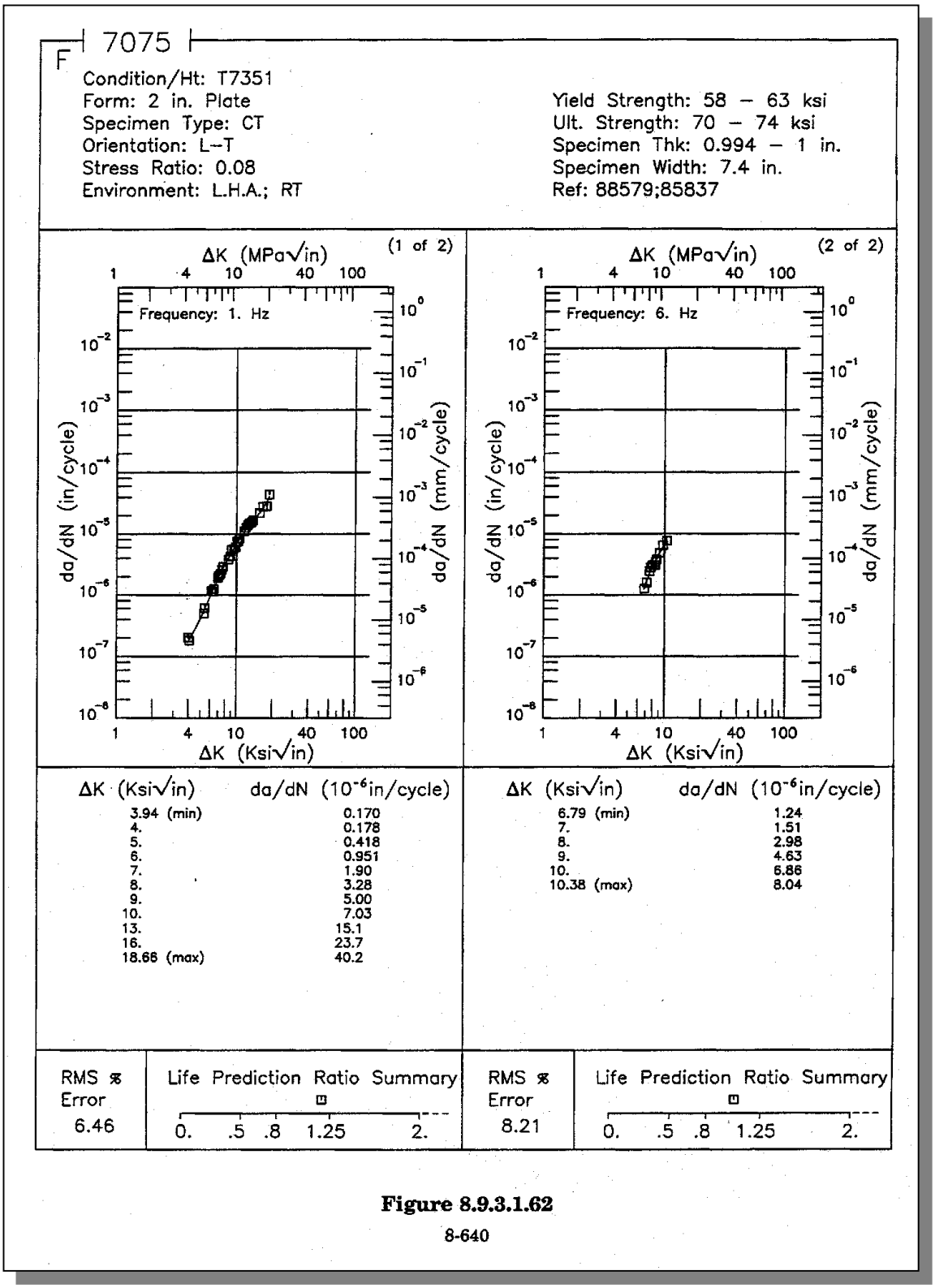

Figure 5.1.3. Fatigue Crack Growth Rate Data Presentation Format Used in the Damage Tolerant Design (Data) Handbook [1994]. Data Presented for Two Stress Ratios for 7057-T7351 Aluminum Alloy

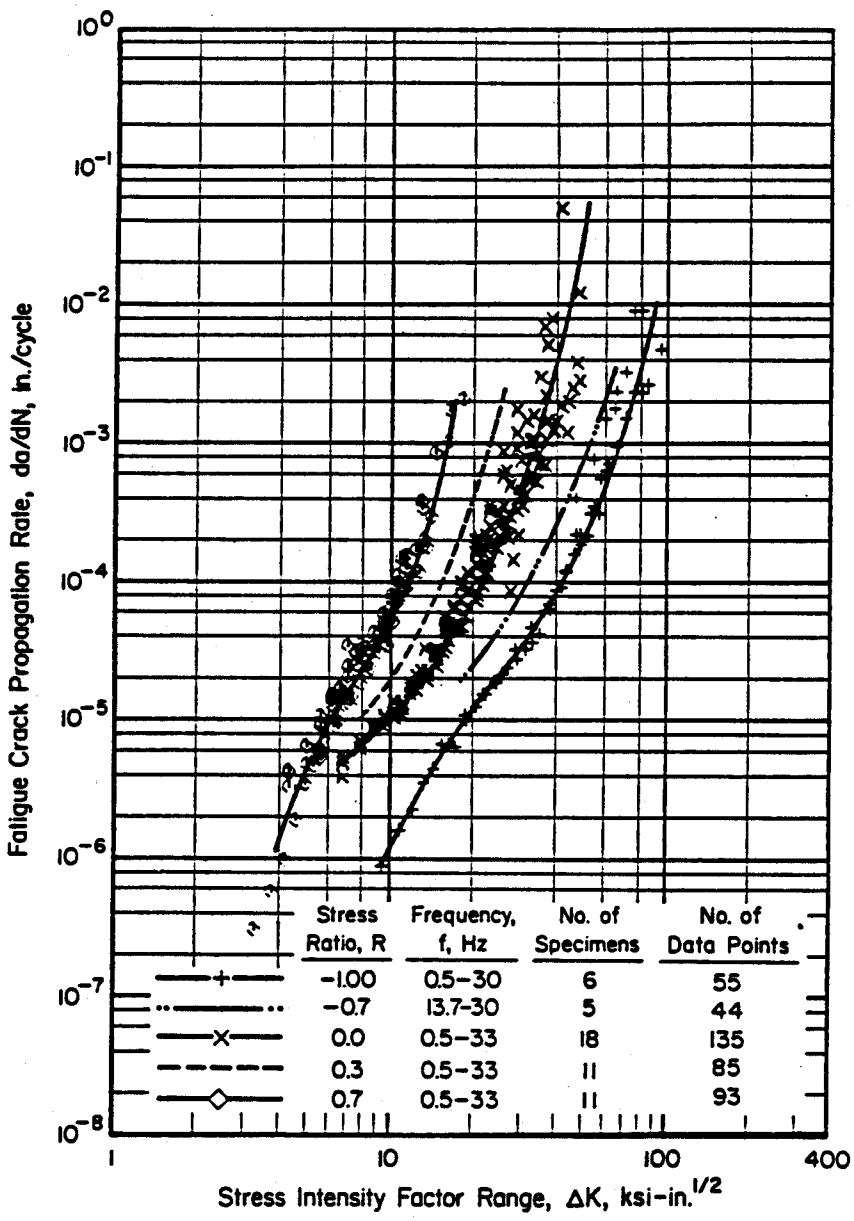

Figure 5.1.4. Sample Fatigue Crack Growth Rate Data for 7075-T6 Aluminum Alloy Sheet From MIL-HDBK-5H [1998]

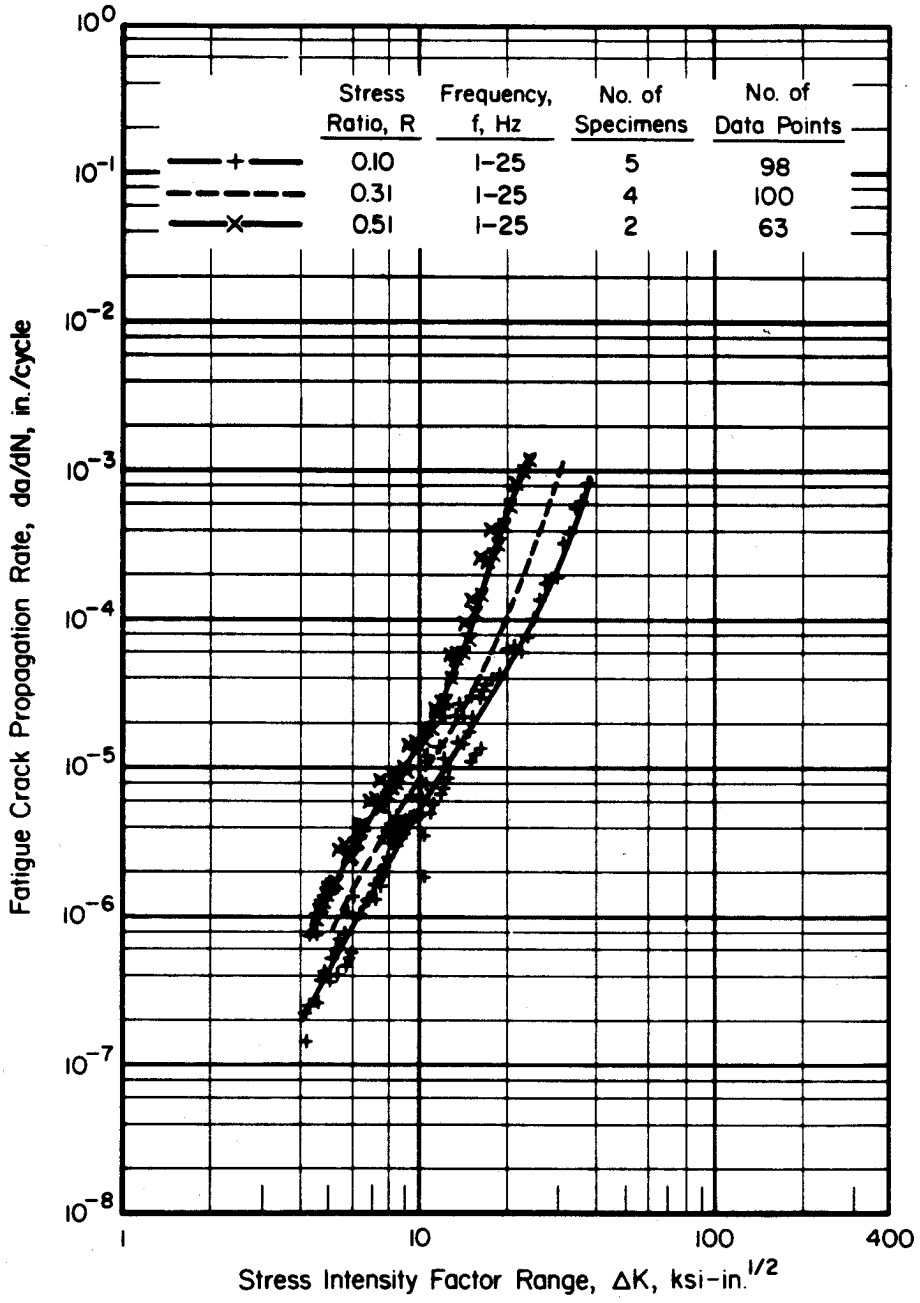

Figure 5.1.5. Sample Fatigue Crack Growth Rate Data for 7075-T7351 Aluminum Alloy Plate From MIL-HDBK-5H [1998]

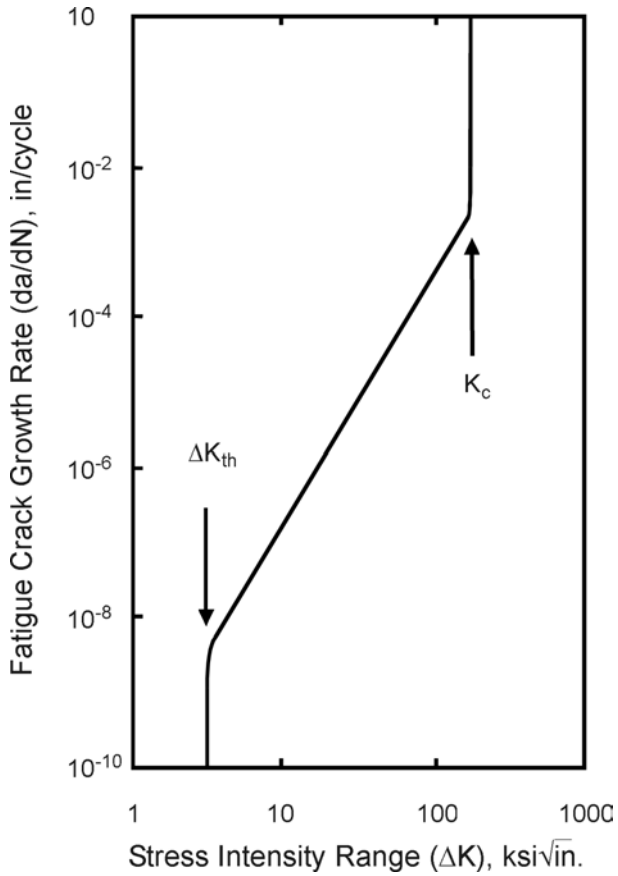

Figure 5.1.6. Schematic of Fatigue Crack Growth Rate Behavior

5.1.2 Fatigue Crack-Growth Rate (FCGR) Descriptions

Many descriptions of the function *f(ΔK, R)* in Equation 5.1.1 have been proposed. In the early literature [Pelloux, 1970; Erdogan, 1967; Toor, 1973; Gallagher, 1974], most of the descriptions were either based on physical models of the crack growth process (referred to as "laws") or on equations that appeared to describe the trends in the data. Currently, the fatigue crack growth rate (FCGR) descriptions are carefully selected to provide accurate mean trend descriptions of the specific data collected to support a materials evaluation or structural design. Before introducing these more accurate FCGR descriptions, the Paris power law [Paris, 1964], the Walker equation [Walker, 1970], and Forman equations [Forman, et al., 1964] will be reviewed.

The Paris power law equation was initially proposed to describe the crack growth rate behavior in the central region for specific values of stress ratio. This equation is given by the general form:

$$\frac{da}{dN} = C\Delta K^{p} \qquad (5.1.2)$$

where C and p are experimentally determined constants. Equation 5.1.2 is still extensively used to develop first order approximations of life behavior when only limited amounts of data are available. The reader is cautioned that Equation 5.1.2, as well as any other FCGR description, should not be extrapolated beyond its limits of applicability without a great deal of care and

experience. Greater life prediction errors can result from data extrapolation errors than almost all other design methodology errors combined.

The Walker equation provided one of the first simple equations that accounted for the stress ratio shift. It is a subtle modification of Equation 5.1.2 and is given by

$$\frac{da}{dN} = C\left[(1-R)^m K_{max}\right]^p \qquad (5.1.3)$$

where C, m, and p are empirical constants. The exponent m typically ranges from 0.4 to 0.6 for many materials. Because Equation 5.1.3 is a power law, it has been noted to be most useful in describing the central region of the growth rate behavior.

The Forman equation was initially proposed to describe both the central and high crack growth regions of the behavior. To account for the acceleration of the cracking rates as the stress-intensity factors levels approached critical, the Paris power law equation was divided by a factor that would reach zero when the stress-intensity factor reached a critical level. The general form of the Forman equation is:

$$\frac{da}{dN} = \frac{C\,\Delta K^p}{(1-R)K_c - \Delta K} \qquad (5.1.4)$$

where C, p, and K_c are experimentally evaluated for the given material and thickness. Equation 5.1.4 can be rearranged to yield:

$$\frac{da}{dN} = \frac{C\,(1-R)^{p-1}.K^p{}_{max}}{K_c - K_{max}} \qquad (5.1.5)$$

which shows that the equation has the capability to describe multiple stress ratio data sets.

The empirical constants in Equations 5.1.2 - 5.1.4 are typically derived using least square fitting procedures. Note that the simplicity of Equations 5.1.2 and 5.1.3 allow for a graphical fit to the data on log-log coordinate paper and the direct evaluation of the constants from the graph. The usefulness of Equations 5.1.2 - 5.1.4 comes from the ease in which their constants can be evaluated from available data, as well as the direct application of the equations to simplified life integration calculations. When considering the general expression for crack growth life (N_f)

$$N_f = \int_{a_o}^{a_f} \frac{da}{f(\Delta K, R)} \qquad (5.1.6)$$

it is seen that the function f is simple for Equations 5.1.2 - 5.1.4.

One modeling procedure that has consistently shown itself to range among the most accurate FCGR descriptions for predicting lives is the table look-up scheme . For life prediction purposes, many aircraft companies have gone to a table look-up scheme in which they describe crack growth rate as a function of ΔK for specific values of fatigue crack growth rate or vice versa, i.e., da/dN is described for specific values of ΔK.

Table 5.1.1 summarizes the mean trend FCGR behavior of the 2219-T851 aluminum alloy employed by the ASTM Task Group E24.04.04. Within the main body of Table 5.1.1, da/dN are presented as a function of pre-chosen ΔK levels for specific levels of stress ratio (or environment, etc.). In the rows directly above and directly below the main body of the table, the data extreme

values are defined. In the bottom rows of the table, statistical summaries that define the accuracy of the mean trend (tabular) description relative to the FCGR data and with respect to life prediction (life prediction ratios based on original a vs. N data). The RMSPE (root mean square percentage error) is a statistic that measures the deviation of fatigue crack growth rate data from the table; and, it is somewhat akin to the coefficient of (life) variation.

The mean trend data presented in the Damage Tolerant Design (Data) Handbook [1994] can be directly utilized with table look-up algorithms in crack growth life prediction computer codes. These data might also be utilized with least square fitting procedures to generate wider ranging predictive schemes that account for the effects of stress ratio, frequency, environment, temperature, and other controlling conditions.

The Damage Tolerant Design (Data) Handbook provides crack-growth data for a variety of materials. The data are presented in the form of graphs and tables, as shown in Figure 5.1.3. Multiple parameter equation fitting should not be attempted if only limited sets of data are available. In case limited data sets have to be used, a comparison should be made with similar alloys for which complete data are available, and curves may be fitted through the limited data sets on the basis of this comparison.

Table 5.1.1. Example Fatigue Crack Growth Rate Table (2219-T851 Aluminum)

$\Delta K\left(ksi\sqrt{in}\right)$			$da/dN \times 10^6$ **inches/cycle**				
			R_1=-1.0	**R_2=0.1**	**R_3=0.3**	**R_4=0.6**	**R_5=0.8**
ΔK_{min} at:	R_1	1.09	0.00730				
	R_2	2.55		0.00336			
	R_3	2.11			0.00369		
	R_4	1.38				0.00351	
	R_5	1.17					0.00112
		1.3	0.0167				0.00429
		1.6	0.0351			0.0176	0.0251
		2.0	0.0676			0.0569	0.0689
		2.5	0.127		0.0451	0.0911	0.128
		3.0	0.216	0.0166	0.152	0.139	0.228
		3.5	0.336	0.0639	0.246	0.218	0.431
		4.0	0.488	0.171	0.355	0.339	0.809
		5.0	0.884	0.566	0.691	0.753	2.60
		6.0	1.37	1.14	1.30	1.46	7.83
		7.0	1.91	1.93	2.28	2.50	46.3
		8.0	2.47	3.09	3.60	3.95	
		9.0	3.08	4.78	5.14	6.07	
		10.0	3.80	7.04	6.86	9.38	
		13.0	7.16	17.0	14.4	38.4	
		16.0	13.2	36.2	30.9		
		20.0	28.3	126.0			
ΔK_{max} at:	R_1	20.7	32.0				
	R_2	24.7		887.0			
	R_3	19.3			81.3		
	R_4	15.8				146.0	
	R_5	7.01					47.4
RMSPE			2.2	80.4	8.6	6.4	6.1
Life prediction ratio summary							
0.0-0.5			1	1 3	1	2	2
0.5-0.8							
0.8-1.25							
1.25-2.0							
>2.0							

ASTM Task Group E24.04.04 on FCGR descriptions conducted two analytical round robin investigations of the utility of various FCGR descriptions that describe crack growth behavior [Miller, et al., 1981; Mueller, et al., 1981]. These round robin investigations have clearly demonstrated that FCGR descriptions which are classified as "good" from a life analysis standpoint must adequately represent the mean trend of the FCGR data. Figure 5.1.7 outlines a general procedure whereby the FCGR behavior is first described by least square regression analysis (Figure 5.1.7a) and then the regression equation, in conjunction with the stress-intensity factor analysis for the test geometry, is used in integral form to obtain an estimate of the fatigue crack growth life N_f (Figure 5.1.7b). In Figure 5.1.7a, the mean trend behavior is described along with bounds on the regression equation. Those descriptions which fail to model the mean trend of the FCGR data, either because they are preconceived to have a specific form (sinh, power law, Forman, etc.) or due to a lack of care in performing the regression analysis, lead to life prediction errors that are biased or exhibit significant scatter.

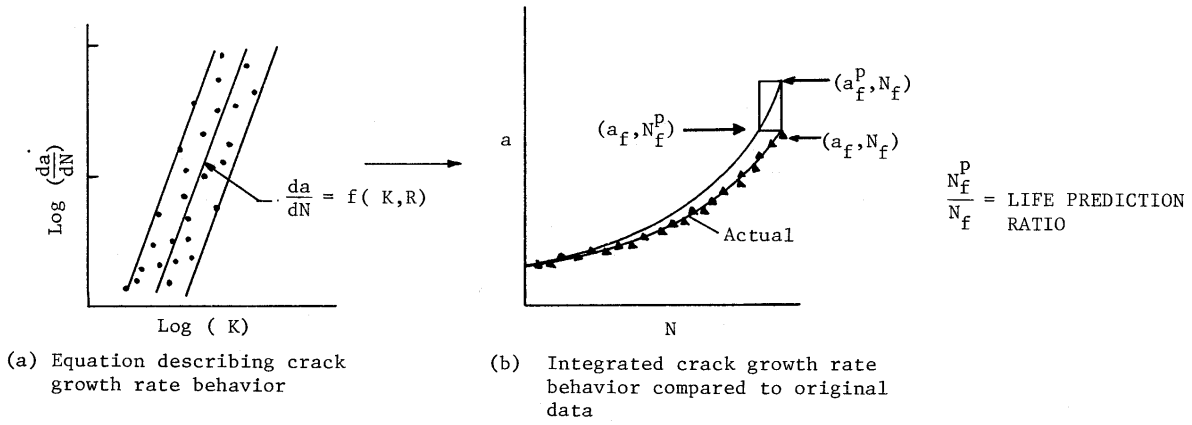

(a) Equation describing crack growth rate behavior

(b) Integrated crack growth rate behavior compared to original data

Figure 5.1.7. Description of FCGR Data Fitting and the Comparison of Predicted to Actual Behaviors

To support the first round robin, FCGR data from compact and center crack test geometries fabricated from 0.25 inch thick 2219-T851 aluminum alloy were supplied to the participants. The tests were conducted between threshold and fracture toughness levels for five separate stress ratios (-1, 0.1, 0.3, 0.5, and 0.8). A number of individuals from government, industry, and academia participated in the round robin (see Table 5.1.2) and chose to evaluate the ten (10) descriptions defined in Table 5.1.3. Each participant was given FCGR data and asked to describe the mean trend of the behavior using equations or other procedures. The participants then integrated their mean trend analysis to establish predicted life values. They were each given the initial and final crack sizes as well as the loading conditions for these life predictions of center crack specimens and compact specimens.

Table 5.1.2. Active Participants and their Organizations for Round Robin Investigation [Miller, et al., 1981]

Name	Affiliation
C.G. Annis F.K. Haake	Pratt & Whitney Aircraft
J. Fitzgerald	Northrop Corporation
J.P. Gallagher* M.S. Miller	University of Dayton Research Institute
S.J. Hudak, Jr. A. Saxena	Westinghouse R & D Center
J.M. Krafft	Naval Research Laboratory
D.E. Macha	Air Force Materials Laboratory
L. Mueller+	Alcoa Laboratories
B. Mukherjee M.L. Vanderglas	Ontario Hydro
J.C. Newman	NASA Langley Research Center

*Chairman, ASTM Task Group E24.04.04 on FCGR Descriptions (1975 - 80)
+Chairman, ASTM Task Group E24.04.04 on FCGR Descriptions (1980 - 83)

One of the procedures utilized to evaluate the ten descriptions was to summarize the sixteen (16) life prediction ratios (life predicted divided by life measured, N^P_f/N_f, see Figure 5.1.7b) associated with each description. The means and standard deviations for the life prediction ratios associated with each participant/FCGR description is presented in Table 5.1.4.

Table 5.1.3. FCGR Descriptions for Round Robin Investigation

Participant/FCGR Description No.	Form
(1)	$\frac{da}{dN} = C_1 \overline{\Delta K}^{C_2}$
(2)	$\frac{da}{dN} = P_1 \frac{(\Delta K - \Delta K_t)^{P_2}}{(\Delta K_c - \Delta K)^{P_3}}$
(3)	$\frac{1}{da/dN} = \frac{A_1}{(\Delta K)^{n_1}} + A_2 \left[\frac{1}{(\Delta K)^{n_2}} - C' \right]$
(4)	$\frac{da}{dN} = C(K_{\max})^m \left[(K_{\max} + K_e)(1 - R_{eff}) + {}^*K \right]^2$
(5)	$\log_{10}\left(\frac{da}{dN} \right) = P_1 \exp(P_2 x) + P_3 \exp(P_4 x) + P_5$
$(6)^+$	$\frac{da}{dN} =_{10} \{C_1 sihn[C_2(\log \Delta K + C_3)] + C_4\}$
$(7)^+$	$\frac{da}{dN} =_{10} \{C_1 sihn[C_2(\log \Delta K + C_3)] + C_4\}$
(8)	$\frac{da}{dN} = e + (v - e)\left[-\ln\left(1 - \frac{\Delta K}{K_b} \right) \right]^{1/k}$
(9)	Tensile ligament instability model
(10)	Table lookup procedure

+ The hyperbolic sine model is listed twice because two separate organizations chose to evaluate this description.

The life prediction ratio (LPR) numbers in Table 5.1.3 can be interpreted by comparing the mean LPR to 1.0 and the standard deviation to 0.0. A mean LPR less than 1.0 implies a conservative prediction. A further interpretation of the results of the round-robin are also presented in Table 5.1.3 with the percentage of life prediction ratios that fall within the ranges of 0.80 and 1.20 and of 0.90 and 1.10. Note that five descriptions were able to achieve LPR numbers between 0.80 and 1.20 for at least 80 percent of the number of predictions made.

Table 5.1.4. Comparison of FCGR Descriptions

Participant/FCGR Description No.	Mean	Standard Deviation	Percent of All Predictions Within:	
			± 20% of 1.0	± 10% of 1.0
1	0.95	0.27	53.3	20.0
2	0.72	0.16	33.3	20.0
3	1.00	0.27	86.7	26.7
4	0.76	0.15	38.5	15.4
5	0.96	0.12	100.0	73.3
6	0.97	0.24	73.3	53.3
7	2.32	5.81	80.0	66.7
8	0.99	0.10	89.5	57.9
9	1.05	0.32	31.3	18.8
10	0.96	0.12	100.0	80.0

5.1.3 Factors Affecting Crack Growth

Unlike tensile strength and yield strength, fatigue crack growth rate (FCGR) behavior is not a consistent material characteristic. The FCGR is influenced by many uncontrollable factors. As a result, a certain amount of scatter occurs. Therefore, crack growth predictions should be based on factors relevant to the conditions in service.

Among the many factors that affect crack propagation, the following should be taken into consideration for crack growth properties:

Material production:

- Type of product (plate, extrusion, forging)
- Heat treatment
- Orientation with respect to grain direction
- Manufacturer and batch
- Thickness

Environmental conditions:

- Environment
- Temperature
- Frequency

No attempt will be made to illustrate the effects of all these factors with data, particularly because some factors have largely different (and sometimes opposite) effects on different materials. Rather, some general trends will be briefly mentioned.

Several factors pertaining to the material production affect crack growth. The crack propagation characteristics for a particular alloy differ for plates, extrusions, and forgings. The latter may exhibit large anisotropy, which may have to be considered in the growth of surface flaws and corner cracks, which grow simultaneously in two perpendicular directions. Closely related to this are other processing variables, particularly the heat treatment.

An alloy of nominally the same composition but produced by different manufacturers may have quite different crack propagation properties [Schijv & DeRijk, 1966]. This is illustrated in Figure 5.1.8. The differences are associated with slight variations in composition, inclusion content, heat treatment (precipitates), and cold work. Similar variations in crack growth occur for different batches of the same alloy produced by the same manufacturer. Data presented in Figure 5.1.9 show that growth rates can vary with sheet thickness [Broek, 1963; Broek, 1966; Raithby & Bibb, et al., 1961; Donaldson & Anderson, 1960; Smith, et al., 1968].

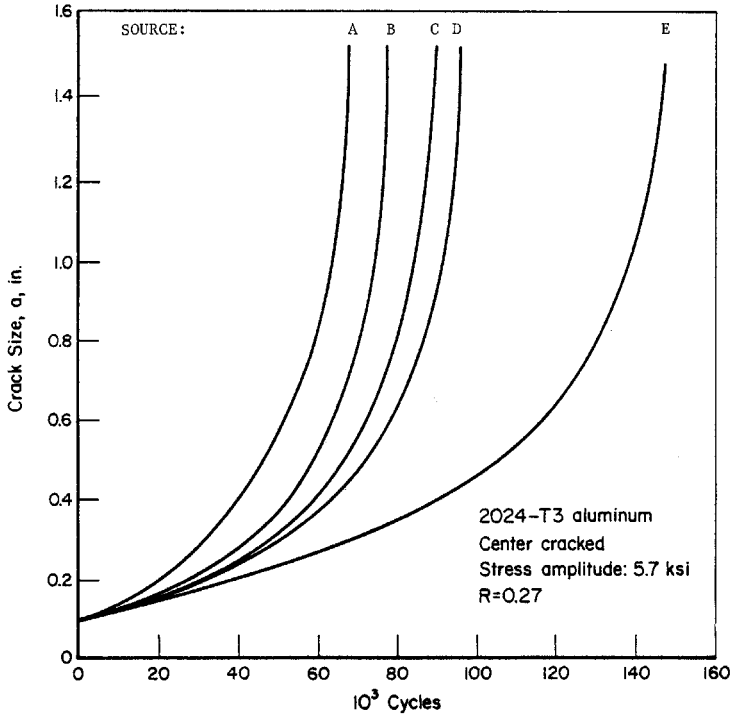

Figure 5.1.8. Possible Variation of Crack Growth in Materials from Different Sources [Schijve & DeRijk, 1966]

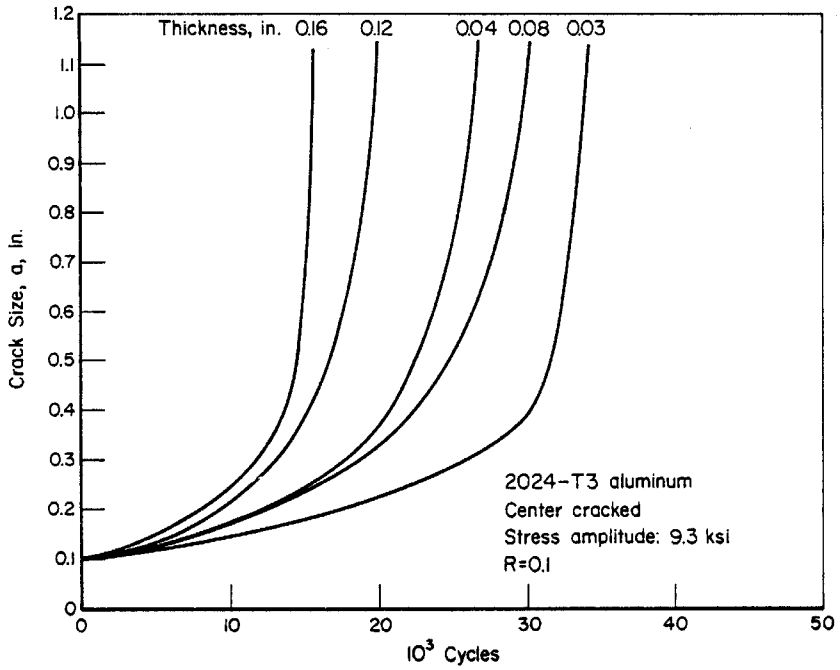

Figure 5.1.9. Example of Effect of Thickness on Crack Growth [Broek, 1963]

In view of the factors that influence crack growth properties, predictions of crack growth should be based on material data that pertain to the product form. Spot checks may be necessary to account for variability in heats and/or manufacturer.

The factors pertaining to environmental conditions are associated with the environmental circumstances. A lightly corrosive environment (humid air) gives rise to higher crack growth rates than a dry environment [Hartman, 1965; Piper, et al., 1968; Bradshaw & Wheeler, 1969; Dahlberg, 1965; Meyn, 1971; Meyn, 1968; Achter, 1967; Wei, 1970; Hartman & Schijve, 1970; Shih & Wei, 1974]. The effect is illustrated in Figure 5.1.10. Although opinions differ in explaining the environmental effect, there is concurrence that the principal factor is corrosive action, which is time and temperature dependent. The effect of cyclic frequency [Piper, et al., 1968; Meyn, 1971; Hartman & Schijve, 1970; Schijve & Brock, 1961] is related to the environmental effect, with slower cyclic frequencies usually associated with accelerated fatigue crack growth rates.

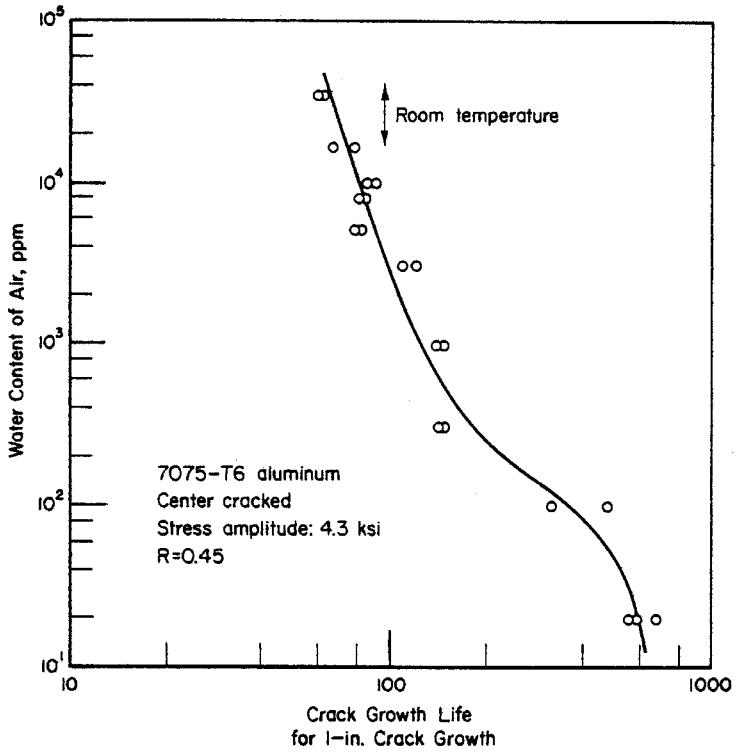

Figure 5.1.10. Effect of Humidity on Fatigue Crack Propagation [Hartman, 1965]

At low temperatures, the reaction kinetics are slower and the air contains less water vapor. This may reduce crack propagation rates in certain alloys [Broek, 1972; Tobler, et al., 1974]. Figure 5.1.11 shows the influence of low temperature on crack growth for 7075-T6 alloy compared with growth at normal temperatures [Broek, 1972]. Temperatures higher than ambient may increase crack growth rates [Schijve & DeRijk, 1963; Lachnaud, 1965].

In view of the effect of environment on crack growth, the data used for life predictions should represent the effect of the expected environment and temperature.

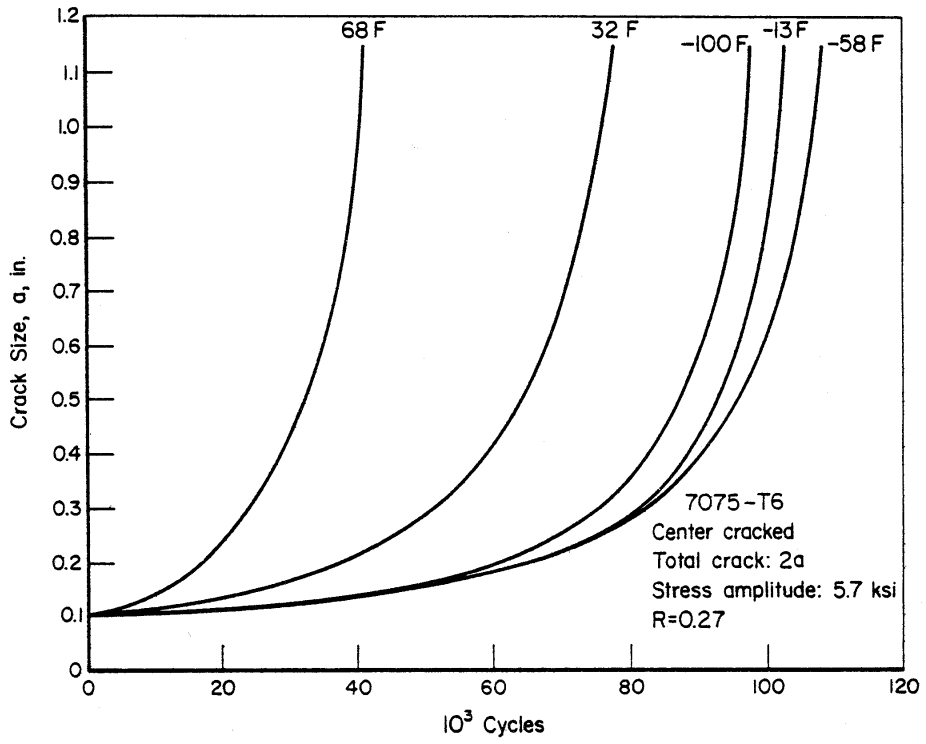

Figure 5.1.11. Example of Temperature Effect on Crack Growth [Broek, 1972]

5.1.4 Use of Data and Data Scatter

Fatigue-crack-propagation data for a variety of materials can be found in data handbooks. In many cases, because of unique material condition, thickness and environment, the data for a particular application will have to be generated in the manner prescribed by Section 7.

As indicated by the results presented in the previous section, accurate mean trend FCGR descriptions result in accurate fatigue crack life descriptions. People have worried in the past about trying to account for the substantial amount of scatter that exists in the crack growth rate data. The amount of crack growth between crack measurements and the accuracy of this incremental crack growth measurement determines a large part of the scatter. Another inherent reason for data scatter is due to the differentiation techniques that one uses to reduce the data.

Figure 5.1.12a shows a hypothetical example of the crack growth-life behavior observed in a single laboratory test; Figure 5.1.12b represents the FCGR data derived from this test. An asterisk in Figures 5.1.12a and b indicates outlying data points. The mean trend curves faired through the data are directly related to each other; the integral of the curve in Figure 5.1.12b gives the curve in Figure 5.1.12a for the test conditions. If more tests are run and all the data compiled, the plot is as shown in Figure 5.1.12c; each test might have a few outlying data points, but the compilation has many outlying points. When all data points, including the outliers, are plotted, the data exhibit a wide scatter-band, noted as the apparent scatter-band, shown in Figure 5.1.12c. However, as previously seen from Figures 5.1.12a and b, the outlier points did not significantly affect the crack growth curve or the mean trend FCGR curve. When considered collectively, the outlying data points in Figure 5.1.12c can be misleading since they do not represent the mean trend behavior of any specimen. If the wide scatter-band were considered for

a crack growth prediction, the upper bound would predict a consistent high growth rate for each crack size (whereas it happened only incidentally as shown in Figure 5.1.12a). As a result, the diagram would reflect a large apparent scatter in crack growth lives (Figure 5.1.12d), whereas the real scatter in crack growth lives is much smaller.

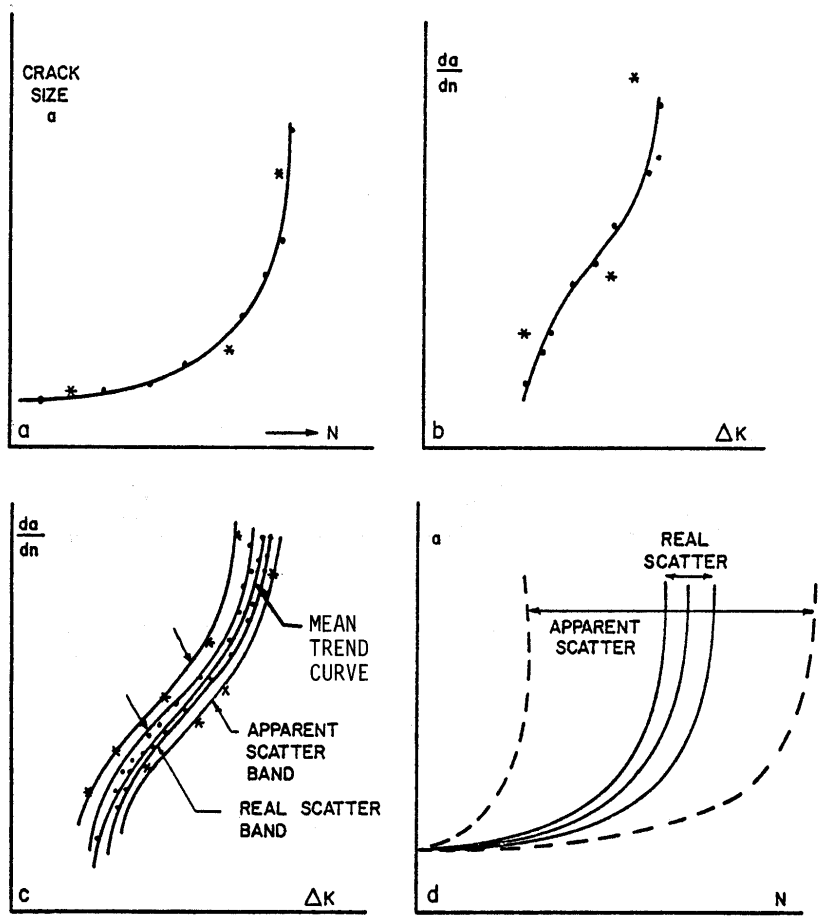

Figure 5.1.12. Crack Growth Data Scatter for Identical Conditions

As indicated by the above remarks, worrying about the random (within specimen) scatter in fatigue crack growth rates is really not that important from a life estimation standpoint. What has been found from analyses of multiple specimen data sets is that the width of the scatter-bands associated with specimen to specimen mean trend variations in FCGR is closely related to the variability in crack growth-life behavior. The scatter-band associated with specimen to specimen variations is identified in Figures 5.1.12c and d as the real scatter-band since it focuses on the variability in crack growth-life behavior.

The coefficient in variation of crack growth lives is sometimes similar in magnitude to the root mean square (percentage) error associated with fatigue crack growth rate modeling. When conservative estimates in crack growth lives are desired, the upper bound of the real scatter-band (identified in Figure 5.1.12c) determined on the basis of four or more specimens should be used.

5.1.5 Stress-Corrosion Cracking and Stress Intensity

Many engineering materials exhibit some cracking behavior under sustained loading in the presence of an environment (thermal and/or chemical). The type of cracking behavior for many chemical environments is referred to as stress-corrosion cracking behavior. The mechanism for this attack process has been attributed to the chemical reactions that take place at the crack tip and to diffusion of reactive species (particularly hydrogen) into the high stressed region ahead of the crack. The cracking process has been noted to be a function of time and it is highly dependent on the environment, the material, and the applied stress (or stress-intensity factor) level.

For a given material-environment interaction, the stress-corrosion-cracking rate has been noted to be governed by the stress-intensity factor. Similar specimens with the same size of initial crack but loaded at different levels (different initial K values) show different times to failure [Brown, 1968; Sullivan, 1972; Chu, 1972], as shown in Figure 5.1.13. A specimen initially loaded to K_{Ic} fails immediately. The level below which cracks are not observed to grow is the threshold level that is denoted as K_{Iscc}.

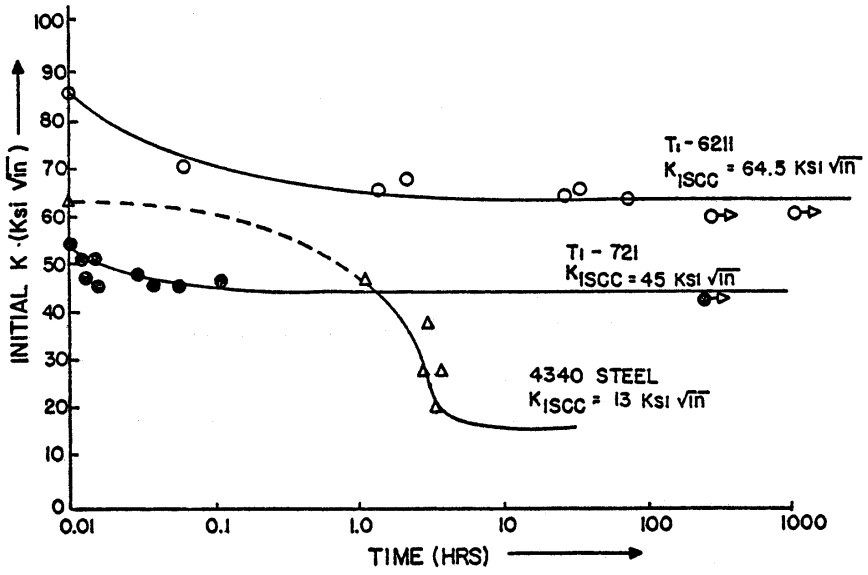

Figure 5.1.13. Stress Corrosion Cracking Data [Brown, 1968]

If the load is kept constant during the stress-corrosion-cracking process, the stress-intensity factor will gradually increase due to the growing crack. As a result, the crack-growth rate per unit of time (da/dt) increases according to

$$\frac{da}{dt} = f(K) \qquad (5.1.7)$$

When the crack has grown to a size so that K becomes equal to $K_{Ic,}$ the specimen fails. This is shown schematically in Figure 5.1.14. In typical tests, specimens may be loaded to various initial K's such as K_1, K_2, and K_3. The time to failure is recorded giving rise to the typical data point (t_1, K_1). During the test, K will increase, as a result of crack extension, from its initial value to K_{Ic}, when final failure occurs. The times t_2 and t_3 represent the time to failure for higher K's such as K_2 and K_3.

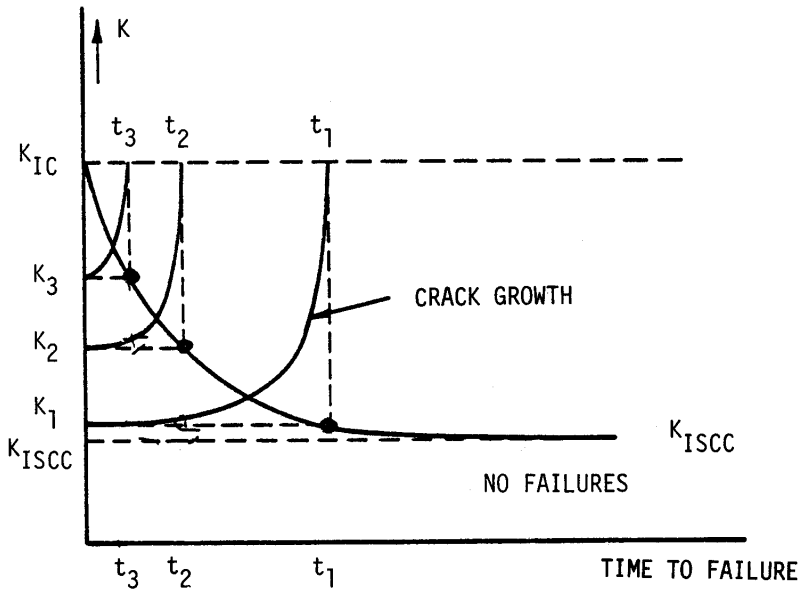

Figure 5.1.14. Stress Corrosion Cracking

The stress-corrosion threshold and the rate of growth depend on the material and the environmental conditions. Data on K_{Iscc} and *da/dt* can be found in the Damage Tolerant Design (Data) Handbook [1994] . Typical examples of K_{Iscc} and *da/dt* data presentation formats are shown in Figures 5.1.15 and 5.1.16.

TABLE 7.5.3.3

(1 of 2)

K_{Iscc} SUMMARY FOR ALUMINUM ALLOY 2024

Condition/ Heat Treat	Prod Form	Test Temp (°F)	Spec Or.	Yield Str (Ksi)	Environment	Specimen			Prod Thk (in)	Crack (in)	K_Q (Ksi√in)	K_{Iscc} (Ksi√in)	Test Time (min)	Test Date	Reference
						Thick (in)	Design	Width (in)							
T351	P	R.T.	S-L	47	3.5% NaCl	1	DCB	5	1	---	50	10	---	1969	78313
				42.4	Industrial Atm	1	CT	2	2.5	---	21.2	10	---	1973	86688
					Salt-Dichromate-Acetate	1	CT	2	2.5	---	21.2	9	---	1973	86688
					Seacoast Atm	1	CT	2	2.5	---	21.2	10	---	1973	86688
T352	F	R.T.	S-L	43.3	Seawater	0.7	DCB	1.4	6	---	27.6	23*	---	1972	82675
T851	P	R.T.	L-T	59.8	3.5% NaCl	1.25	TDCB	5	3.2	---	18.6	21.5	---	1971	84360
					Air 78% RH	1.25	TDCB	5	3.2	---	18.6	22.7	---	1971	84360
					Dist Water	1.25	TDCB	5	3.2	---	18.6	22	---	1971	84360
					JP-4 Fuel	1.25	TDCB	5	3.2	---	18.6	21.6	---	1971	84360
			S-L	61.8	Industrial Atm	1	CT	2	2.5	---	16.7	16	---	1973	86688
					Salt-Dichromate-Acetate	1	CT	2	2.5	---	16.7	15	---	1973	86688
					Seacoast Atm	1	CT	2	2.5	---	16.7	16	---	1973	86688
T852	F	R.T.	L-T	53	S.C.S.	1	DCB	5.5	3	---	34	22.1	64920	1976	RI006
						1	DCB	5.5	3	---	34	34*	61680	1976	RI006
				58	S.T.W.	1	DCB	5.5	3	---	37	22.5	76140	1976	RI006
						1	DCB	5.5	3	---	37	>23.5	76140	1976	RI006
						1	DCB	5.5	3	---	37	22.5	76140	1976	RI006

Figure 5.1.15. Kiscc Data as Present by the Manage Tolerant Design (data) Handbook [1994]

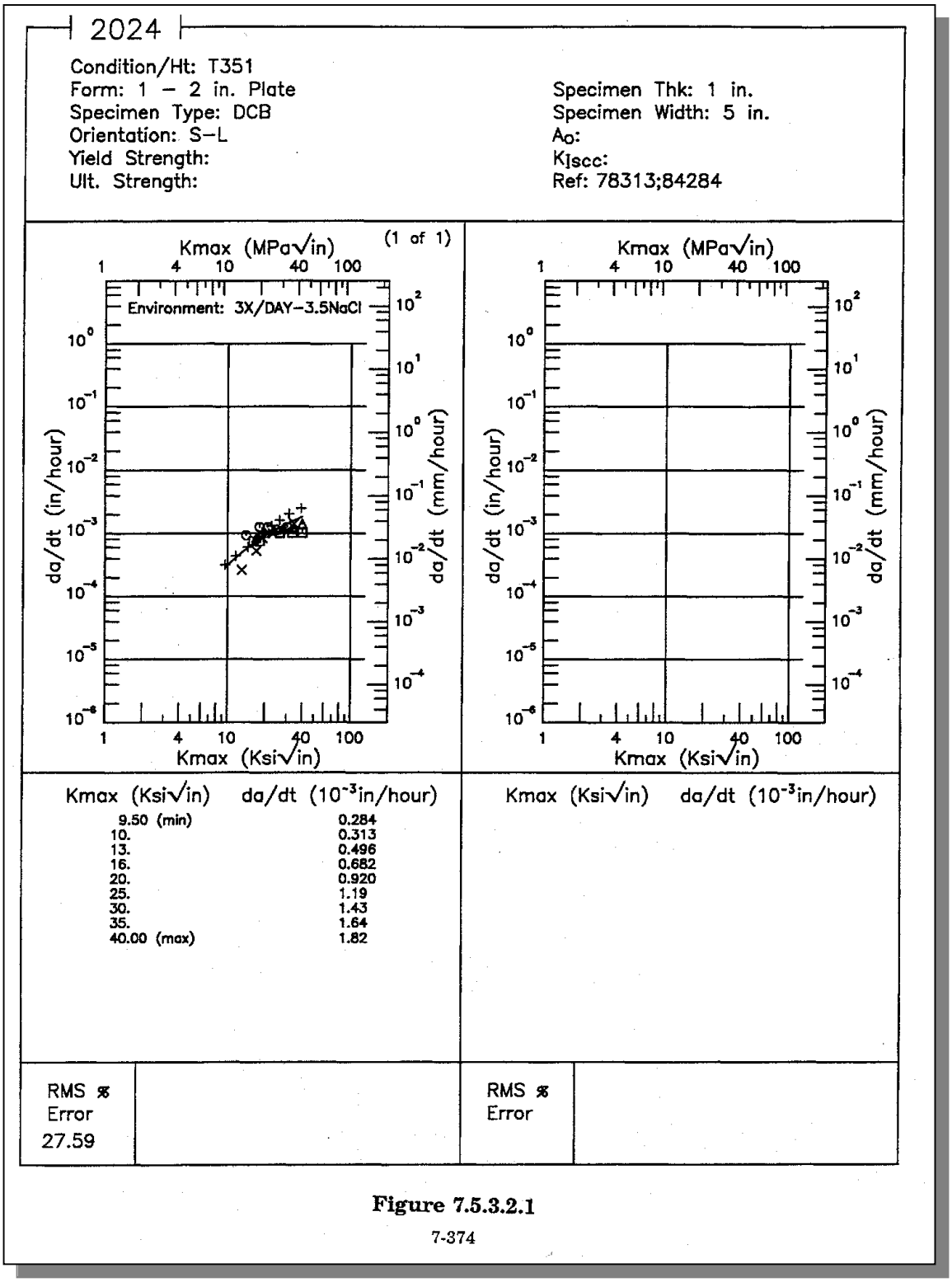

Figure 5.1.16. Stress Corrosion Cracking Rate Data for 2024-T351 Aluminum as Presented by the Damage Tolerant Design (Data) Handbook [1994]

As illustrated in Figure 5.1.17, a component with a given crack fails at a stress given by

$$\sigma_c = \frac{K_{Ic}}{\beta\sqrt{\pi a}}$$

It will exhibit stress-corrosion-crack growth when loaded to stresses in excess of

$$\sigma_{scc} = \frac{K_{Iscc}}{\beta\sqrt{\pi a}}$$

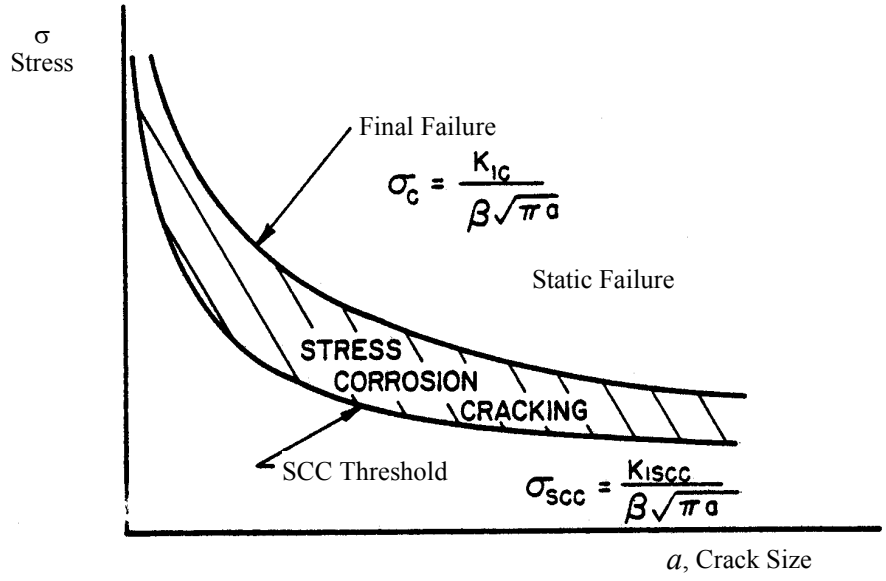

Figure 5.1.17. Stress Required for Stress Corrosion Cracking

In service, stress-corrosion cracks have been found to be predominantly a result of residual stresses and secondary stresses. Stress-corrosion failure due to primary loading seldom occur because most stress-corrosion cracks favor the short transverse direction (S-L), which is usually not the primary load direction. In many materials, the long transverse (T-L) and longitudinal (L-T) directions are not very susceptible to stress corrosion.

Prevention of stress corrosion cracking is preferred as a design policy over controlling it as is done for fatigue cracking. This means that stress-corrosion critical components must be designed to operate at a stress level lower than

$$\sigma_{scc} = \frac{K_{Iscc}}{\beta\sqrt{\pi a_i}}$$

in which a_i is the initial flaw size as specified in the Damage Tolerance Requirements of JSSG-2006. However, if stress corrosion can occur, it must be accounted for in damage tolerance analyses by using an integral form of Equation 5.1.7.

Stress-corrosion cracking may occur in fatigue-critical components. This means that in addition to growth by fatigue, cracks might show some growth due to stress corrosion. In dealing with this problem, the following should be considered:

- Stress-corrosion cracking is a phenomenon that basically occurs under a steady stress. Hence, the in-flight stationary stress level (l g) is the governing factor. Most fatigue cycles are of relatively short duration and do not contribute to stress-corrosion cracking. Moreover, the cyclic crack growth would be properly treated already on the basis of data for environment-assisted fatigue-crack growth. When stress corrosion cracking is expected, the stress corrosion cracking rate should be superimposed on the fatigue crack growth rate [Wei & Candes, 1969; Gallagher & Wei, 1972; Dill & Saff, 1978; Saff, 1980].
- Stress-corrosion cracking is generally confined to forgings, heavy extrusions, and other heavy sections, made of susceptible materials. Thus, the problem is generally limited to cases where plane strain prevails.
- The maximum crack size to be expected in service is $a_c = K_{Ic}^{\ 2} / \pi\beta^2\sigma^2$, where σ equals σ_{LT} or σ_{DM}, depending upon the inspectability level (see Section 1.3).

If stress-corrosion cracking is not expected at any crack size, the l-g stress, σ_{lg}, should be lower than $\sigma_{scc} = K_{Iscc} / \beta\sqrt{\pi a_c}$. With a_c given as above, it follows that complete prevention of stress corrosion extension of a fatigue crack requires selection of a material for which:

$$K_{Iscc} > \frac{\sigma_{\mathrm{lg}}}{\sigma_{LT}(or\,\sigma_{DM})} K_{Ic} \qquad (5.1.8)$$

5.2 Variable-Amplitude Loading

Baseline fatigue data are derived under constant-amplitude loading conditions, but aircraft components are subjected to variable amplitude loading. If there were not interaction effects of high and low loads in the sequence, it would be relatively easy to establish a crack-growth curve by means of a cycle-by-cycle integration. However, interaction effects of high and low loads largely complicate crack-growth under variable-amplitude cycling.

In the following sections these interaction effects will be briefly discussed. Crack growth-prediction procedures that take interaction effects into account will be presented in Section 5.2.3.

5.2.1 Retardation

A high load occurring in a sequence of low-amplitude cycles significantly reduces the rate of crack-growth during the cycles applied subsequent to the overload. This phenomenon is called retardation. Figure 5.2.1 shows a baseline crack-growth curve obtained in a constant-amplitude test [Schijve & Broek, 1962]. In other experiments, the same constant-amplitude loading was interspersed with overload cycles. After each application of the overload, the crack virtually stopped growing during many cycles, after which the original crack-growth behavior was gradually restored.

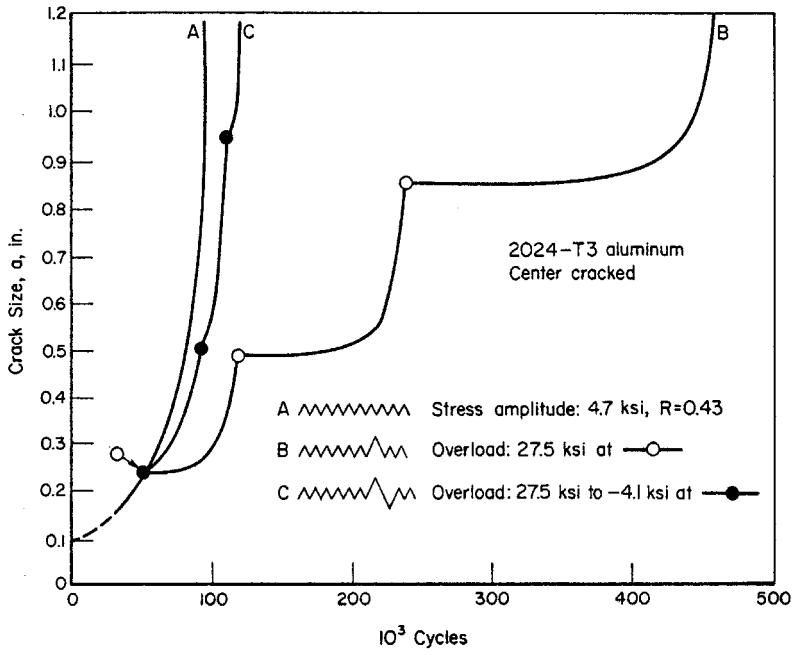

Figure 5.2.1. Retardation Due to Positive Overloads, and Due to Positive-Negative Overload Cycles [Schijve & Broek, 1962]

Retardation results from the plastic deformations that occur as the crack propagates. During loading, the material at the crack tip is plastically deformed and a tensile plastic zone is formed. Upon load release, the surrounding material is elastically unloaded and a part of the plastic zone experiences compressive stresses. The larger the load, the larger the zone of compressive stresses. If the load is repeated in a constant amplitude sense, there is no observable direct effect of the residual stresses on the crack-growth behavior; in essence, the process of growth is steady state. Measurements have indicated, however, that the plastic deformations occurring at the crack tip remain as the crack propagates so that the crack surfaces open and close at non zero (positive) load levels. These observations have given rise to constant amplitude crack-growth models referred to as closure models [Elber, 1971] after the concept that the crack may be closed during part of the load cycle.

When the load history contains a mix of constant amplitude loads and discretely applied higher level loads, the patterns of residual stress and plastic deformation are perturbed. As the crack propagates through this perturbed zone under the constant amplitude loading cycles, it grows slower (the crack is retarded) than it would have if the perturbation had not occurred. After the crack has propagated through the perturbed zone, the crack growth rate returns to its typical steady state level.

Two basic models have been proposed to describe the phenomenon of crack retardation. The first model is based on the concept of the compressive residual stress perturbation and the second on the concept of plastic deformation with enhanced crack wedging and more closure.

If the tensile overload is followed by a compressive overload, the material at the crack tip may undergo reverse plastic deformation and this reduces the residual stresses. Thus, a negative overload in whole or in part annihilates the beneficial effect of tensile overloads, as is also shown by curve C in Figure 5.2.1.

Retardation depends upon the ratio between the magnitude of the overload and subsequent cycles. This is illustrated in Figure 5.2.2. Sufficiently large overloads may cause total crack arrest. Hold periods at zero stress can partly alleviate residual stresses and thus reduce the retardation effect [Shih & Wei, 1974; Wei & Shih, 1974], while hold periods at load increase retardation. Multiple overloads significantly enhance the retardation. This is shown in Figure 5.2.3.

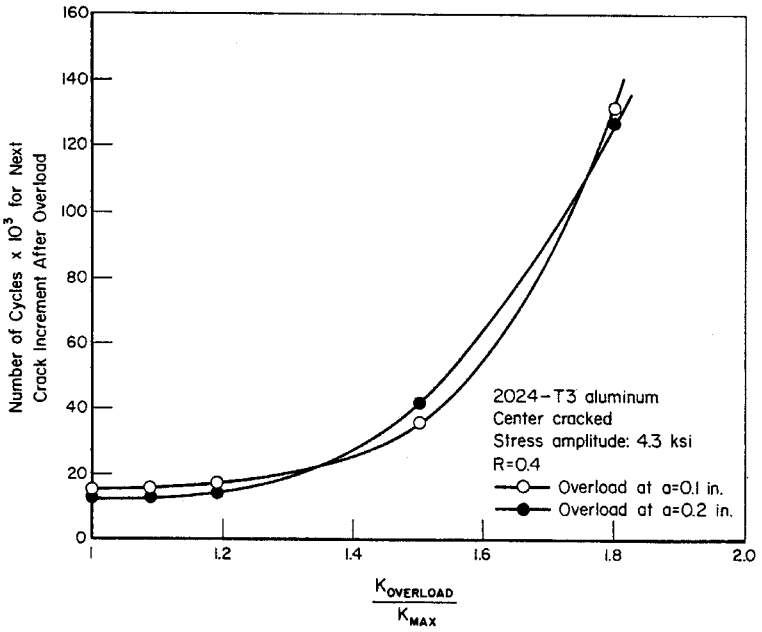

Figure 5.2.2. Effect of Magnitude of Overload on Retardation [Shih & Wei, 1974]

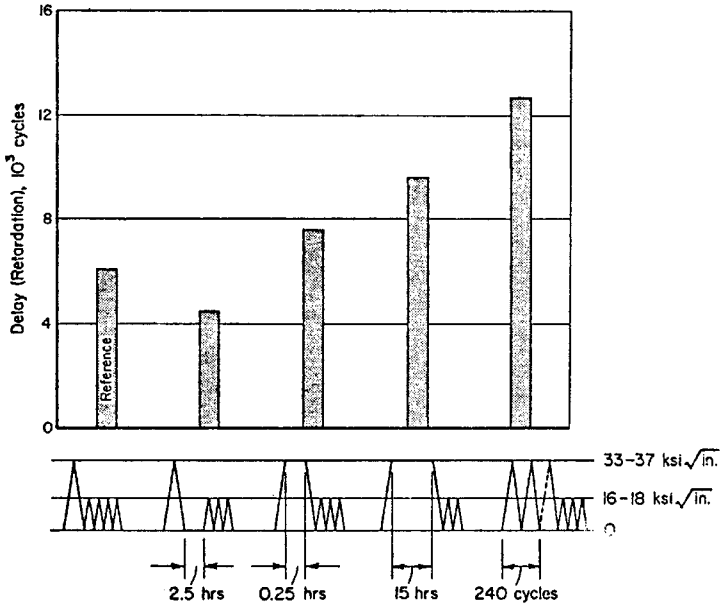

Figure 5.2.3. Retardation in Ti-6V-4Al; Effect of Hold Periods and Multiple Overloads [Wei & Shih, 1974]

5.2.1.1 Retardation Under Spectrum Loading

An actual service load history contains high- and low- stress amplitudes and positive and negative "overloads" in random order. Retardation and annihilation of retardation becomes complex, but qualitatively the loading produces behavior that is similar to a constant-amplitude history with incidental overloads. The higher the maximum stresses in the service load history, the larger the retardation effect during the low-amplitude cycles. Negative stress excursions reduce the retardation effect and tend to enhance crack-growth. These effects have been documented in various sources [Schijve, 1972; Schijve, 1970; Wood et al., 1971; Porter, 1972; Potter, et al., 1974; Gallagher et al., 1974; Wood, et al., 1971]; a few examples are now presented.

When the magnitude of the higher loads are reduced (or clipped) without eliminating the cycle, i.e., higher loads are reset to a defined lower level, the cracking rates are observed to speed up as shown in Figure 5.2.4 [Schijve, 1972; Schijve, 1970]. Figure 5.2.4 describes the crack growth life results for a study in which a (random) flight-by-flight stress history was systematically modified by "clipping" the highest load excursions to the three levels shown.

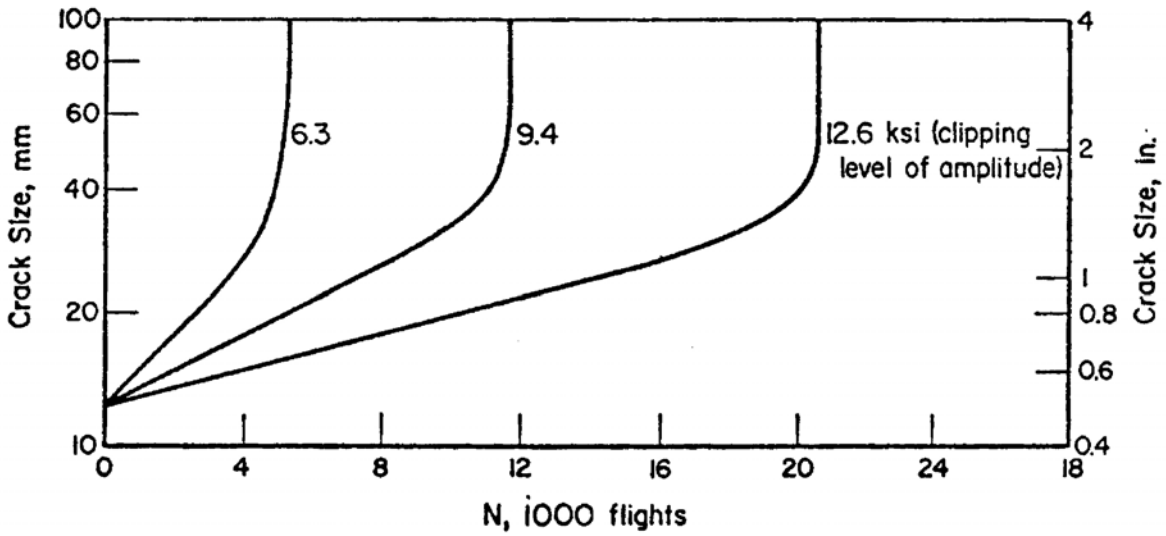

Figure 5.2.4. Effect of Clipping of Higher Loads in Random Flight-by-Flight Loading on Crack Propagation In 2024-T3 Al Alloy [Schijve, 1972; Schijve, 1970]

In Schijve [1970; 1972], it was also observed that negative stress excursions reduce the retardation effect and omission of the ground-air-ground (G-A-G) cycles (negative loads) in the tests with the highest clipping level resulted in a longer crack growth life for the same amount of crack growth.

Figure 5.2.5 shows the importance of load sequence. The crack-propagation life for random load cycling is shown at the top. Ordering the sequences of the loads, low-high, low-high-low, or high-low increases the crack-growth life, the more so for larger block sizes. Hence, ordering should only be permitted if the block size is small. Low-high ordering gives more conservative

results than high-low ordering. In the latter case, the retardation effect caused by the highest load is effective during all subsequent cycles.

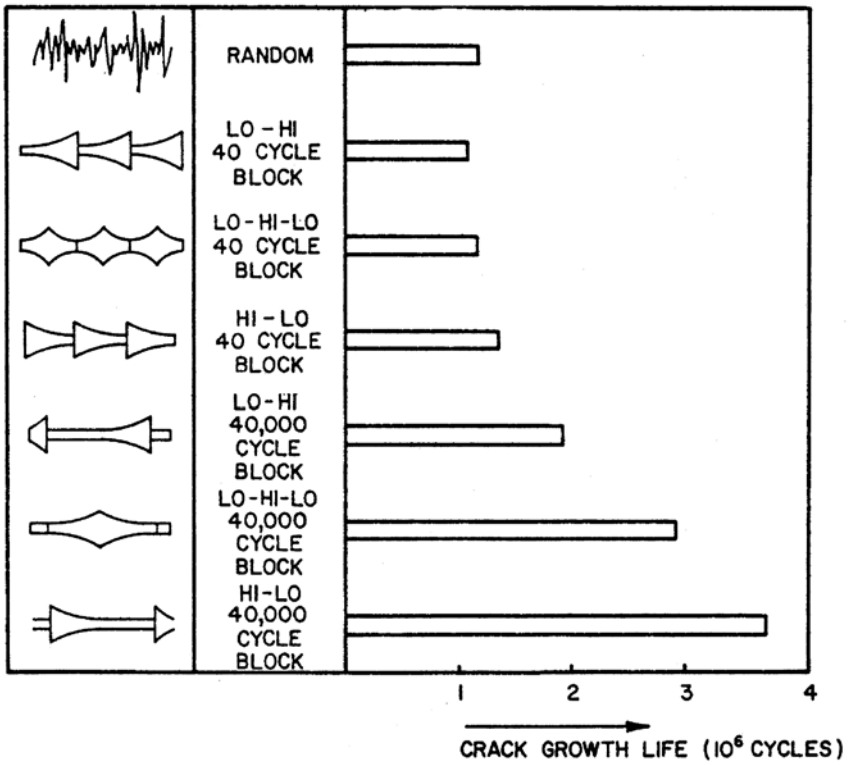

Figure 5.2.5. Effect of Block Programming and Block Size On Crack Growth Life All Histories Have Same Cycle Content; Alloy: 2024-T3 Aluminum [Shih & Wei, 1974]

5.2.1.2 Retardation Models

Some mathematical models have been developed to account for retardation in crack-growth-integration procedures. All models are based on simple assumptions, but within certain limitations and when used with experience, each model will produce results that can be used with reasonable confidence. The two yield zone models by Wheeler [1972] and by Willenborg, et al., [1971], and a crack-closure model by Bell & Creager [1975] will be briefly discussed. Detailed information and applications of closure models can be found in Bell & Creager [1975], Rice & Paris [1976], Chang & Hudson [1981], and Wei & Stephens [1976].

Wheeler Model

Wheeler defines a crack-growth reduction factor, C_p:

$$\left(\frac{da}{dN}\right)_r = C_p f(\Delta K) \tag{5.2.1}$$

where $f(\Delta K)$ is the usual crack-growth function, and (da/dN) is the retarded crack-growth rate. The retardation factor, C_p is given as

$$C_p = \left(\frac{r_{pi}}{a_{oL} + r_{poL} - a_i} \right)^m \qquad (5.2.2)$$

where (see Figure 5.2.6):

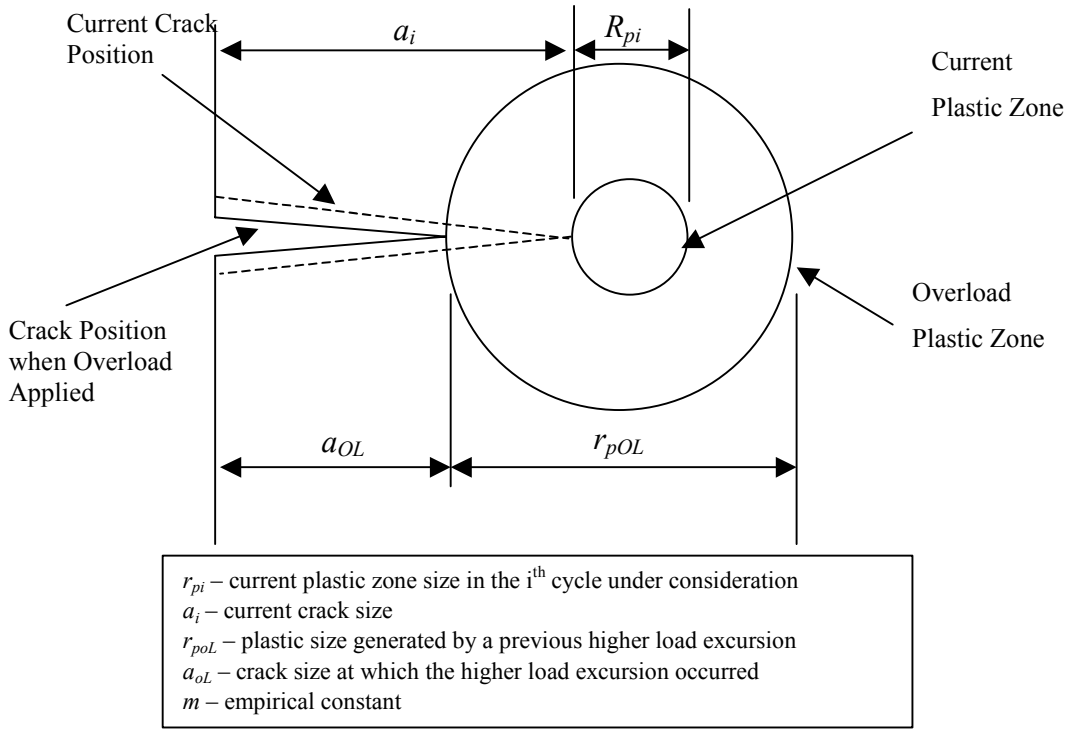

Figure 5.2.6. Yield Zone Due to Overload (r_{poL}), Current Crack Size (a_i), and Current Yield Zone (r_{pi})

There is retardation as long as the current plastic zone (r_{pi}) is contained within a previously generated plastic zone (r_{poL}) ; this is the fundamental assumption of yield zone models.

Some examples of crack-growth predictions made by means of the Wheeler model are shown in Figure 5.2.7. Selection of the proper value for the exponent m will yield adequate crack-growth predictions. In fact, one of the earlier advantages of the Wheeler model was that exponent m could be tailored to allow for reasonably accurate life predictions of spectrum test results. Through the course of time, it has become recognized, however, that the exponent m was dependent on material, crack size, and stress-intensity factor level as well as spectrum. The reader is cautioned against using the Wheeler model for service life predictions based on limited amounts of supporting test data and more specifically against estimating the service life of structures with spectra radically different from those for which the exponent m was derived. Estimates made without the supporting data required to tailor the exponent m can lead to inaccurate and unconservative results.

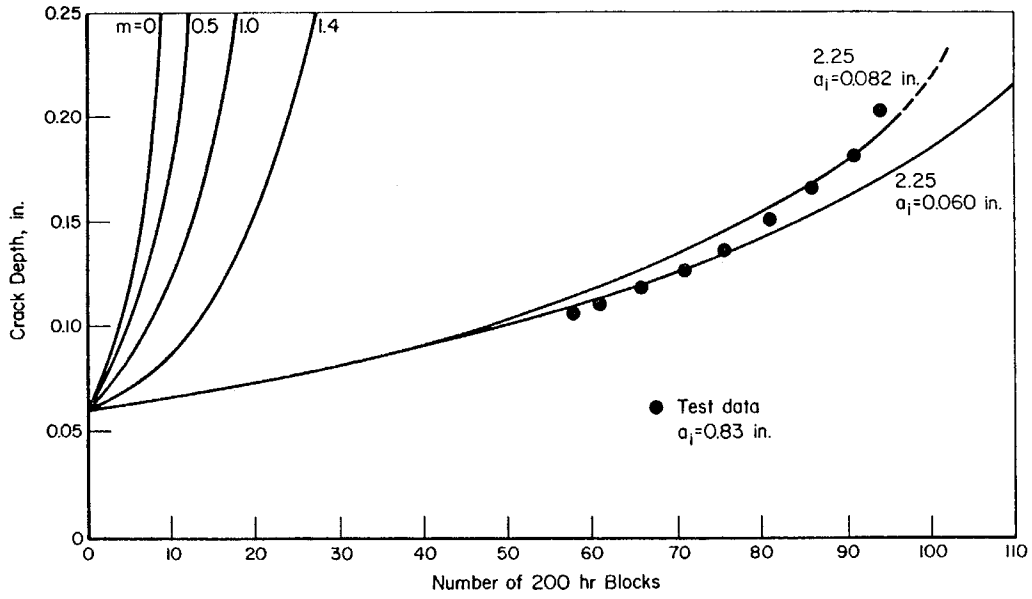

Figure 5.2.7. Crack Growth Predictions by Wheeler Model Using Different Retardation Exponents [Wood, et al. 1971]

Willenborg Model

The Willenborg model also relates the magnitude and extent of the retardation factor to the overload plastic zone. The extent of the retardation is handled exactly the same as that of the Wheeler model. The magnitude of the retardation factor is established through the use of an effective stress-intensity factor that senses the differences in compressive residual stress state caused by differences in load levels. The effective stress-intensity factor (K^{eff}_i) is equal to the typical remote stress-intensity factor (K_i) for the ith cycle minus the residual stress-intensity factor (K_R):

$$K_i^{eff} = K_i - K_R \tag{5.2.3}$$

where in the original formulation [Willenborg, et al., 1971; Gallagher, 1974; Gallagher & Hughes, 1974; Wood, 1974]

$$K_R = K_R^W = K_{max}^{oL}\sqrt{1-\frac{a_i - a_{oL}}{r_{poL}}} - K_{max,i} \tag{5.2.4}$$

in which (see Figure 5.2.6):

a_i – current crack size

a_{oL} –- crack size at the occurrence of the overload

r_{poL} – yield zone produced by the overload

K^{oL}_{max} – maximum stress intensity of the overload

$K_{max,i}$ – maximum stress intensity for the current cycle.

The equations show that retardation will occur until the crack has generated a plastic zone size that reaches the boundary of the overload yield zone. At that time, a_i-a_{oL}= r_{poL} and the reduction becomes zero.

Equation 5.2.3 indicates that the complete stress-intensity factor cycle, and therefore, its maximum and minimum levels ($K_{max,\,i}$ and $K_{min,\,i}$), are reduced by the same amount (K_R). Thus, the retardation effect is sensed by the change in the effective stress ratio calculated by

$$R_{eff} = \frac{K^{eff}_{min,i}}{K^{eff}_{max,i}} = \frac{K_{min,i} - K_R}{K_{max,i} - K_R} \tag{5.2.5}$$

since the range in stress-intensity factor is unchanged by the uniform reduction. Thus, for the ith load cycle, the crack growth increment (Δa_i) is:

$$\Delta a_i = \frac{da}{dN} = f\left(\Delta K, R_{eff}\right) \tag{5.2.6}$$

For many of the early calculations with the Willenborg model, it was assumed that R_{eff} was never less than zero and that $\Delta K = K^{eff}_{\max,i}$ when R_{eff} was calculated to be less than zero. Recent evidence, however, supports the calculations of R_{eff} as given by Equation 5.2.5 and the use of a negative stress ratio cut-off in the crack growth rate calculation (Equation 5.2.6) for more accurate modeling of crack growth behavior.

Another problem that was identified with the original Willenborg model was that it was always assigned the same level of residual stress effect independent of the type of loading. In particular, it can be noted (through the use of Equation 5.2.3 and 5.2.4) that the model predicts that $K^{eff}_{\max,i} = 0$, and therefore crack arrest, immediately after overload if $K^{oL}_{max} = 2\,K_{max,i}$. That is, if the overload is twice as large as (or larger than) the following loads, the crack arrests. To account for the observations of continuing crack propagation after overloads larger than a factor of two or more, Gallagher & Hughes [1974] introduced an empirical (spectra/material) constant into the calculations. Specifically, they suggested that

$$K_R = \phi K^W_R \tag{5.2.7}$$

where ϕ is given by

$$\phi = \frac{1 - \dfrac{K_{\max,th}}{K_{\max,i}}}{S^{oL} - 1} \tag{5.2.7a}$$

There are two empirical constants in Equation 5.2.7a: $K_{max,\,th}$ is the threshold stress-intensity factor level associated with zero fatigue crack growth rates (see Section 5.1.2), and S^{oL} is the overload (shut-off) ratio required to cause crack arrest for the given material. The type of underload/overload cycle, as well as the frequency of overload cycle occurrence, affects this ratio. Results of some life predictions made using what has become to be called the "Generalized" Willenborg model are presented in Figure 5.2.8 [Engle & Rudd, 1974]. Compressive stress levels were ignored in this analysis.

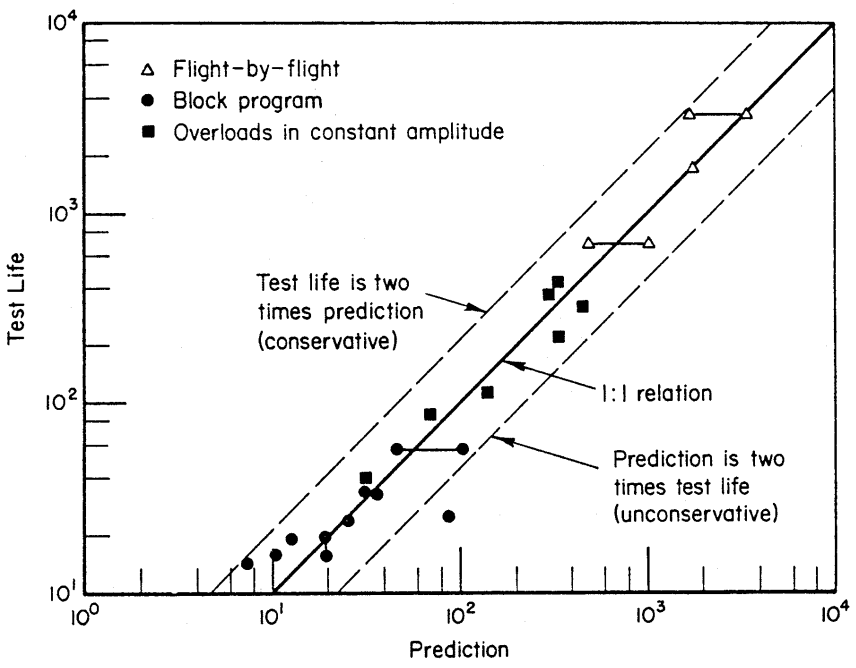

Figure 5.2.8. Predictions of Crack Growth Lives with the Generalized Willenborg Model Compared to Test Data [Engle & Rudd, 1974]

Closure Models

One of the earliest crack-closure models developed for aircraft structural applications is attributed to Bell & Creager [1975]. The closure model makes use of a crack-growth-rate equation based on an effective stress-intensity range ΔK_{eff}. The effective stress intensity is the difference between the applied stress intensity and the stress intensity for crack closure. Some examples of predictions made with the model are presented in Figure 5.2.9. The final equations contain many experimental constants, which reduces the versatility of the model and make it difficult to apply. Recent work by Dill & Saff [1977] shows that the closure model can be simplified to the point of practicality while retaining a high level of accuracy in life prediction.

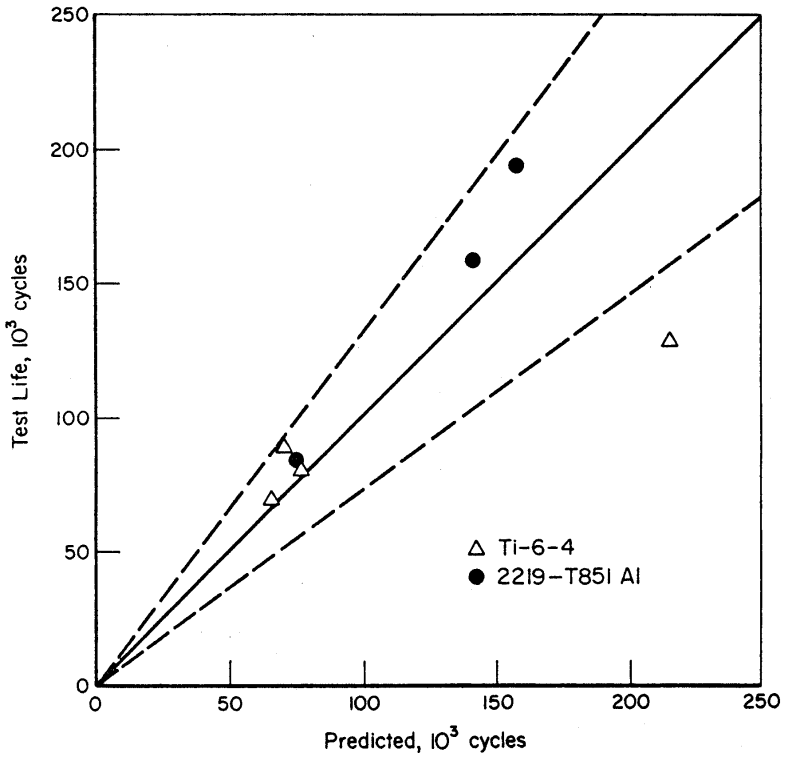

Figure 5.2.9. Predictions by Crack Growth Closure Model as Compared with Data Resulting From Constant-Amplitude Tests with Overload Cycles [Bell & Creager, 1975]

Crack-growth calculations are the most useful for comparative studies, where variations of only a few parameters are considered (i.e., trade-off studies to determine design details, design stress levels, material selection, etc.). The predictions must be verified by experiments. (See Analysis Substantiation Tests in Section 7.3). Example calculations of crack-growth curves will be given in Section 5.5.

Other factors contributing to uncertainties in crack-growth predictions are:

- Scatter in baseline *da/dN* data,
- Unknowns in the effects of service environment,
- Necessary assumptions on flaw shape development,
- Deficiencies in *K* calculation,
- Assumptions on interaction of cracks,
- Assumptions on service stress history.

In view of these additional shortcomings of crack-growth predictions, the shortcomings of a retardation model become less pronounced; therefore, no particular retardation model has preference over the others. From a practical point of view, the Generalized Willenborg model is easier to use since it contains a minimum number of empirical constants.

5.2.2 Integration Routines

The determination of a crack growth increment due to any particular stress history depends upon an integration of the growth rate relation such as given by equations 5.1.2 - 5.1.4. Four general methods are available for this purpose.

The first approach is based on extensive spectrum crack growth data. Tests that incorporate the important stress levels, part geometry, crack shape details and loading sequences are run to determine the effect of the particular variables of interest on the component life.

A second approach, and one used extensively, is the cycle-by-cycle crack growth analysis where crack rates are integrated over the crack length of interest as a function of stress and crack length [Gallagher, 1976; Brussat, 1971].

A third approach is based on the statistical stress-parameter-characterization. The actual service stress histories are replaced with equivalent constant amplitude stress histories for the analytical prediction of component life [Smith, et al., 1968].

A fourth approach, recently developed, utilizes a crack-incrementation scheme to analytically generate "mini-block" crack growth rate behavior prior to predicting life. It combines some features of the first three methods [Gallagher, 1976; Brussat, 1971; Gallagher & Stalwaker, 1975].

The application of the second through fourth approaches requires methods for integrating the crack growth rate relations requires the knowledge of the following items:

- An initial flaw distribution
- The aircraft loading spectrum
- Constant amplitude crack growth rate material properties
- Crack tip stress-intensity factor analysis
- A damage integrator model relating crack growth to applied stress and which accounts for load-history interactions
- The criteria which establishes the life-limiting end point of the calculation

These items are described in detail in Section 1.5 of this handbook. The basic damage integrating equation is also presented as equation 1.5.1 but is repeated here:

$$a_{cr} = a_o + \sum_{j=l}^{t_f} \Delta a_j \qquad (1.5.1R)$$

where Δa_j is the growth increment associated with the j^{th} time increment, a_o is the initial crack length, a_{cr} is the critical crack length and t_f is the life of the structure. The determination of t_f is the objective of this equation.

Of the integration methods described above, the second and third are most frequently used. The generation of the data required for the first method is very expensive and is only recommended for extremely critical parts.

Cycle-by-cycle method

The second method, the cycle-by-cycle integration method, uses a type of integrating relation whereby the effect of each cycle is considered separately. This is generally the least efficient method, but if the spectrum under consideration cannot be considered as statistically repetitive, it may be the most accurate of the analytical methods. This method is covered in detail in subsection 5.2.3.

Statistical Stress-Parameter Characterization

The third method, using a statistical characterization of a crack growth parameter is based on the similarity of certain variable amplitude crack growth behavior to the constant amplitude function relationship:

$$\frac{da}{dF} = C\left(\overline{K}\right)^p \tag{5.2.8}$$

where (da/dF) is the flight-by-flight crack growth behavior and $\overline{K}$ is a stress-intensity factor parameter that is derived using the product of a statistically characterizing stress parameter ($\overline{\sigma}$) and the stress-intensity factor coefficient (K/σ), i.e.,

$$\overline{K} = \overline{\sigma} \cdot (K/\sigma) \tag{5.2.9}$$

The statistically characterizing parameters that have been employed in the past to some success are derived using a root mean square (RMS) or similar type analysis of the stress range or stress maximum. The crack growth behavior of both fighter and transport aircraft stress histories have been described using various forms of equation 5.2.8.

One might imply from equations 5.2.8 and 5.2.9 that the use of a single stress characterizing parameter for stress histories would allow one to utilize equivalent constant amplitude histories to derive the same crack growth rate behavior. Unfortunately, relating constant amplitude behavior to variable amplitude behavior has not been that successful.

The damage integration Equation (1.5.1R) is now expressed for the flight as

$$a_k = a_o + \sum_{j=1}^{N_f} \Delta a_j \tag{5.2.10}$$

where N_f is the number of flights corresponding to crack length a_k, and Δa_j is computed from Equation 5.2.8 evaluated for the given conditions. The parameters C and p of Equation 5.2.8 are determined by a least squares curve fit to previously determined data. The value that comes from employing the third method comes from the fact that a somewhat limited variable amplitude data base might be extended to cover other crack lengths, structural geometry, or stress level differences.

Crack-Incrementation Scheme

The fourth approach provides an analytical extension of the cycle-by-cycle analysis to predict flight-by-flight crack growth rates. In essence, this approach combined some of the best features of the other three methods. The basic element in this analysis is what is referred to as a mini-block which is taken to be a flight (includes takeoff, landing and all intermediate stress events) or

a group of flights. The approach hinges on the identification of the statistically repeating stress group that approximates the loading and sequence effects for the complete spectrum.

The basic damage integration equation can be written in the mini-block form to compute the crack increment (Δa) due to application of N_G flights:

$$\Delta a = a_k - a_o = \sum_{j=1}^{N_G} \sum_{i=1}^{N_j} \left(\Delta a_i\right) \qquad (5.2.11)$$

where there are N_j stress cycles in the j[th] flight. The most direct method for applying the equation is called the simple crack-incrementation-mini-block approach. Successive crack increments are obtained at successively larger initial-crack-lengths. Figure 5.2.10 illustrates this method. The resulting values of $\Delta a/\Delta F$ and the corresponding K_{max} values are fit with a curve of the desired type, usually similar to Equation 5.2.8, which can now be used to compute life.

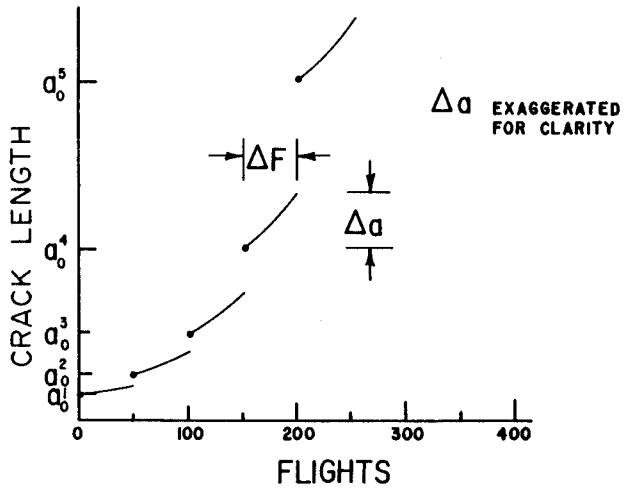

Figure 5.2.10. Simple Crack-Incrementation Scheme Used to Determine Crack Growth Rate Behavior [Gallagher, 1976]

An alternate method, called the statistical crack-incrementation-mini-block approach, is illustrated in Figure 5.2.11. This method allows evaluation of the effect of mini-block group-to-group variation in the crack growth rate behavior. A number of different mini-block groups are used at each initial crack length. A curve can be fit through the mean $\Delta a/\Delta F$ vs. $\overline{K}_{\max}$ values and the variation of $\Delta a/\Delta F$ at each K_{max} can be observed. Confidence limits can be determined for each set of data.

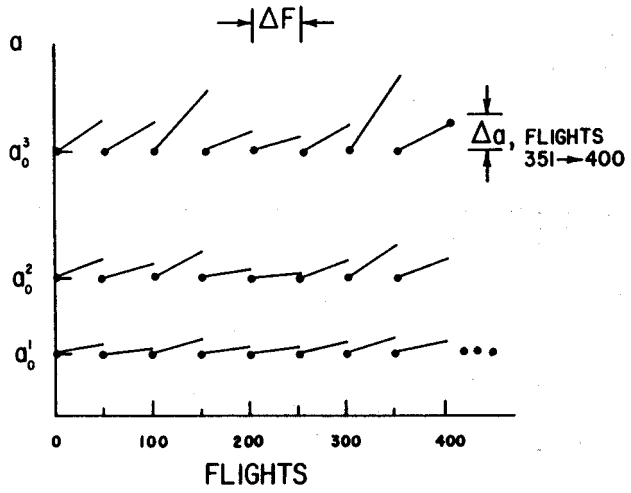

Figure 5.2.11. Statistical Crack-Incrementation Scheme Used to Determine Spectrum Induced Variations in Crack Growth-Rate Behavior [Gallagher, 1976]

The fourth approach provides a more efficient integration scheme than the cycle-by-cycle analysis. However, its use is determined by the type of stress history that has to be integrated.

Summary

In summary, there are a number of integration schemes available. These schemes all employ modeling approaches based on either limited or extensive variable amplitude databases so that the analyst might properly account for loading and sequence effects in the most direct and most accurate manner.

5.2.3 Cycle-by-Cycle Analysis

Several computer programs are available for general uses that include one or more of the retardation models in a crack-growth-integration scheme. These are discussed in Section 1.7. The user has the option of using any of the retardation models discussed in the previous section. Most airframe companies, however, have their own in-house computer program for performing variable-amplitude fatigue life calculations.

In general, the crack-growth-damage-integration procedure consists of the following steps, schematically outlined in Figure 5.2.12.

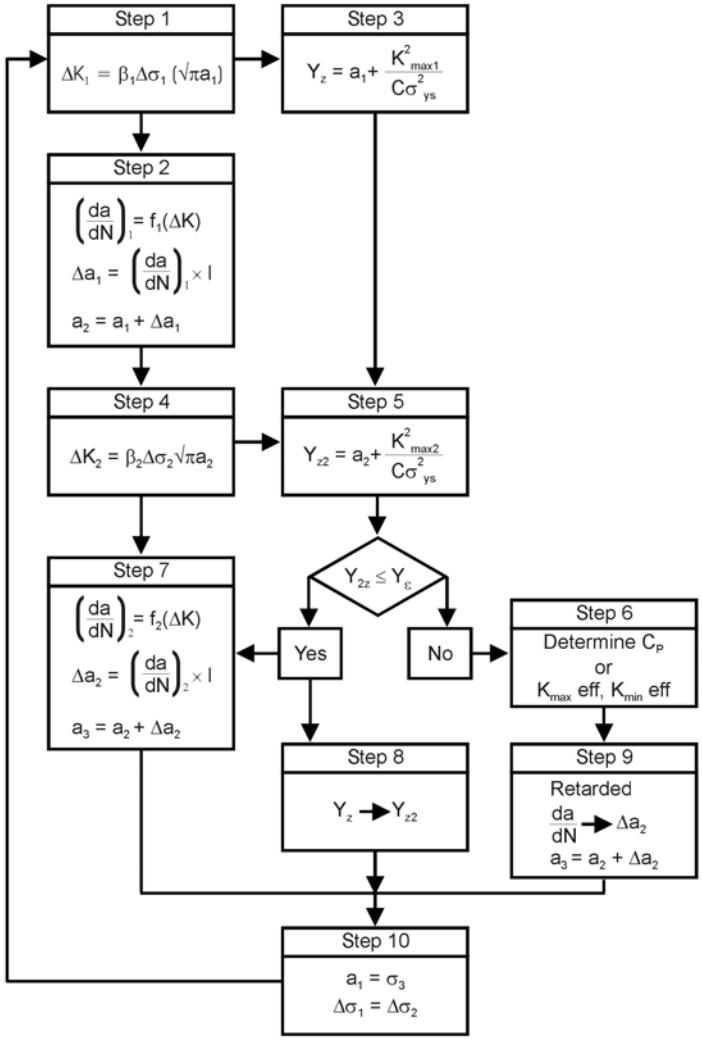

Figure 5.2.12. Steps Required for Crack Growth Integration

Step 1. The initial crack size follows from the damage tolerance assumptions as a_1. The stress range in the first cycle is $\Delta\sigma_1$. Then determine $\Delta K_1 = \beta\Delta\sigma_1\sqrt{\pi a_1}$ by using the appropriate β for the given structural geometry and crack geometry. Computer programs generally have a library of stress-intensity factors or schemes for tabular data input for determining the appropriate β.

Step 2. Determine $(da/dN)_1$, at ΔK_1 from the da/dN -ΔK baseline information, taking into account the appropriate R value. The da/dN - ΔK baseline information may use one of the crack growth equations discussed in Section 5.1.2. The computer program may contain options for any of these equations, or it may use data in tabular form and interpolate between data points. The crack extension Δa_1 in cycle 1 is

$$\Delta a_1 = \left(\frac{da}{dN}\right)_1 \times 1 \cdot$$

The new crack size will be $a_2 = a_1 + \Delta a_1$

Step 3. The extent of the yield zone in Cycle 1 is determined as

$$Y_2 = a_{oL} + r_{pL}$$

where $a_{oL} = a_1$

$$r_{pL} = \frac{1}{2\pi}\left(\frac{K_{\max,1}}{\sigma_{ys}}\right)^2 \quad \text{for plane stress}$$

$$\text{or } r_{pL} = \frac{1}{4\sqrt{2\pi}}\left(\frac{K_{\max,1}}{\sigma_{ys}}\right)^2 \quad \text{for plane strain.}$$

Step 4. The crack size is now a_2. The stress range in the next cycle is $\Delta\sigma_2$. Calculate ΔK with

$$\Delta K_2 = \beta\Delta\sigma_2\sqrt{\pi a_2}\ .$$

Step 5. Calculate the extent of the yield zone

$$Y_{22} = a_2 + r_{p2}\ .$$

Step 6. If $Y_{22} < Y_2$:

When using the Wheeler model, calculate C_p according to Equation 5.2.2.

When using the Generalized Willenborg model, calculate K_{max}^{eff} or K_{min}^{eff} and R_{eff} according to Equations 5.2.3, and 5.2.5.

Go to Step 9, skipping steps 7 and 8.

Step 7. If $Y_{22} \geq Y_2$, determine $(da/dN)_2$ from ΔK_2. Determine the new crack size a_3

$$a_3 = a_2 + \Delta a_2 = a_2 + \left(\frac{da}{dN}\right)_2 \times 1.$$

Step 8. Replace Y_2 by Y_{22}, which is now called Y_2. Replace $a_{oL} = a_1$ with $a_{oL} = a_2$. Go to Step 10, skipping Step 9.

Step 9. When using the Wheeler model, determine the amount of crack growth on the basis of ΔK_2 from the da/dN - ΔK data. Find the new crack size from

$$a_3 = a_2 + \Delta a_2 + C_p\left(\frac{da}{dN}\right)_2 \times 1.$$

When using the Generalized Willenborg model, determine the amount of crack growth using the ΔK and R_{eff} value determine in Step 6 from the da/dN - ΔK data. Determine the new crack size as

$$a_3 = a_2 + \Delta a_2 = a_2 + \left(\frac{da}{dN}\right)_2 \times 1$$

Step 10. Repeat Steps 4 through 9 for every following cycle, while for the i^{th} cycle replacing a_2 by a_i and a_3 by a_i+1.

This routine of cycle-by-cycle integration is not always necessary. The integration is faster if the crack size is increased stepwise in the following way.

- At a certain crack size, the available information is a_i, a_{oL}, Y_2.
- Calculate Δa_i for the i_{th} cycle in the same way as in Steps 4 through 9.
- Calculate Δa_{j+1}, . . . , Δa_j, . . . , Δa_n for the following cycles but let the current crack size remain a_i constant. This eliminates recalculation of β every cycle.
- Calculate Y_{2k} for every cycle. If $Y_{2k} > Y_2$, then replace Y_2 by Y_{2k} and call it Y_2. Then replace a_{oL} by a_i and call it a_{oL}.
- Sum the crack-growth increments to give:

$$\Delta a = \sum_{k=i}^{j} \Delta a_k \cdot$$

- Continue increasing j until Δa exceeds a previously determined size or until $j = n$ and the cycles are exhausted. Then increment the crack size by

  $a = a_i + \Delta a$,

  and repeat the procedure.

A reasonable size for the crack-growth increment is $\Delta a = 1/20\ a_i$; this choice of increment typically keeps the change in K small. It can also be based on the extent of the yield zone, e.g., $\Delta a = 1/10\ (Y_2 - a_i)$. The advantage of the incremental crack-growth procedure is especially obvious if series of constant-amplitude cycles occur. Since the crack size (a_i) is fixed, the stress intensity does not change. Hence, each cycle produces the same amount of growth. This means that all n constant-amplitude cycles can be treated as one cycle to give

$$\Delta a = n \frac{da}{dN}$$

The integration scheme is a matter of individual judgment, but may be dictated by available computer facilities.

5.3 Small Crack Behavior

Damage tolerant structural design requires that a pre-existing, initial crack at a critical location in a structural detail must not reach the critical size required to maintain the minimum load bearing capability during its design life. The design life of a damage tolerant structure, i.e., the number of flights required to grow an initial crack to a critical size, is calculated from the crack growth relations discussed in Section 5.5. The initial crack size assumptions for structural details are discussed in Section 1. For structures with close tolerance fasteners, the initial primary damage size is 0.05 inch. A crack size of .005 inch for continuing damage at the holes is recommended. These assumptions for initial crack lengths are based on NDI capability of the designer. With improved NDI techniques, cracks smaller than 0.05 inch can be detected. The small crack growth behavior discussed here provides guidelines for crack growth analysis if an initial crack smaller than 0.05 inch is assumed in the damage tolerant design of structural members.

5.3.1 Small Crack Growth Analysis

The design guidelines and linear elastic fracture mechanics based life prediction methods discussed in this Handbook are applicable to long cracks only. From mechanics considerations, the development of crack occurs in three distinct stages: crack initiation, small crack development and long crack progression. Crack initiation (and nucleation) is not discussed in this Handbook because of the required assumption of a pre-existing structural crack. A long crack has a dominant singularity in the continuum domain. A crack is considered small when it is smaller than the long crack. For a small crack, the similitude rules break down. The crack size is comparable to one or few grains, the plastic zone size is not small compared to the size of the crack and the assumption of a linearly elastic material at the crack tip region is not realistic.

It has been experimentally observed that small crack growth behavior is different from the behavior of long cracks. However, the upper limit of the crack size below which the small crack effects start and the conventional long crack growth behavior resumes is not well established. The crack lengths from .040 in. to .070 in. have been proposed. The following observations of small crack behavior from experimental data have been reported in the literature.

1. It has been demonstrated from the crack growth data under both the constant amplitude loads and the spectrum loads that the small crack growth rates are higher than those for long cracks. Higher crack growth rates result in non-conservative predictions of fatigue life.
2. A small crack can grow even when the applied stress intensity factor is well below the threshold limit. The threshold stress intensity factor range is dependent on the stress ratio.
3. The experimental results show that the small crack effects are more pronounced at extreme values of stress ratios.
4. The behavior of small cracks initiated at holes is different from the behavior of small cracks in un-notched materials.

Because of these differences, an understanding of the mechanics of small crack growth and mechanisms of cracking in the small crack regime is necessary. The structural designer should have the appropriate design tools to incorporate the effects a small crack may have on crack growth rate and resulting life prediction. The small crack effects are present either because the similitude rule for LEFM application to crack growth breaks down or inappropriate evaluation of the damage parameters such as the stress intensity factor K or the J-integral used for steady state

crack growth rate prediction. The similitude rules are a set of requirements on structural crack geometry and the mode and extent of crack-tip deformation of a material under loading. A discussion of similitude rules is presented by Leis, et.al.[1986].

The small crack effects have been observed in both notched and un-notched specimens. The un-notched small crack growth behavior has been attributed to crack grain boundary interaction effects not accounted for in the fracture mechanics based predictions of small crack growth. In the case of long cracks, the crack growth in the plastic wake is averaged over many grains. It has been argued by Leis, et al. [1986] and Blom, et al. [1986] that the difference in crack growth at notches is not due to the breakdown of similitude rules but inaccurate calculations of the stress intensity factors.

Based on observations of small crack growth in 2024-T3, Blom [Blom, et al., 1986] reported that the short crack effects are due to plasticity induced crack closure and roughness induced closure effects. He also concluded that in this material a crack should be al least four grains in length before qualifying as a long crack. In Newman's [1992] study of small cracks in 2024-T3 and 7075-T6 specimens, the crack closure transients have been found to be the cause of crack growth effects. There is transient behavior of crack opening stress as the crack progresses from small crack size to long crack. At higher stress ratios (stress ratios over 0.5), the crack may be assumed to be open and thus has no significant effect on crack opening stress. At higher negative stress ratios (i.e. at R=-2), the effects have been found to be more significant. A fatigue crack growth analysis computer code "FASTRAN" based on plasticity induced closure has been developed and currently available at NASA Computer Management and Software Information Center.

Nagar [2002] studied small fatigue crack growth behavior at pin-loaded holes in structural joints where small cracks are often observed. Experiments were conducted on 2024-T3 specimens with 0.003 inch single, thru-radial cracks. The rectangular panel specimens with a radial crack at the loaded hole and doublers of varying stiffness were joined by close fit titanium pins. The doublers provided the variation in load transfer rates at the fasteners holes. The loads of constant amplitude with marker bands and spectrum loads were applied to the specimens.

A comparison of structural joint small crack growth data with FASTRAN predictions show that FASTRAN predicts small crack behavior under constant amplitude loading reasonably well. However, the plasticity induced closure based predictions by FASTRAN do not correlate with the small crack growth data under periodic over loads (marker bands) as well. The predictions of small crack life under spectrum loads (EIFS) were even farther off. In general, the crack growth rates are lower than predicted. Thus there is a question whether FASTRAN can be employed reliably to predict small crack growth in joints with loading histories.

The experimental strain data developed during this program also indicated that the load transfer rates for steel doublers can not be predicted using the same technique as used in NASTRAN which have been used for calculations of fastener load transfer with aluminum doublers. This study was conducted under a co-operative FAA/Air Force/Boeing program and the details are available in an Air Force Research Laboratory Report [Nagar, 2002].

5.4 Stress Sequence Development

In order to predict the crack-growth behavior of an aircraft structure, the designer needs to know the sequence of stress cycles applied during the life of the structure. This stress history for a new design is developed from the service life requirements and the mission profile information specified by the procurement activity. Based on this information a repeated load history due to ground handling, flight maneuvers, gusts, pressurization, landing, store ejection, and any other load source is developed. The stress history at any given point is then determined from the applicable load/stress relations. Giessler, et al. [1981] describes this procedure in detail.

This section will outline the necessary steps and illustrate the development of a simplified stress sequence for the purpose of showing the effect of various sequence characteristics on crack-growth behavior. Understanding of these effects is of great importance in determining the damage tolerance of a structure.

5.4.1 Service Life Description and Mission Profiles

The load sequence developer works from the service life requirement summary and the mission profiles as given by the aircraft procurement documents. The service life data contains the total flight hours, expected calendar year life, number of missions to be flown, identification of mission types, and number of touch and go and full stop landings. The mission profile description provides the time variation of the airspeed, altitude, and gross weight such as illustrated in Figure 5.4.1. Each mission is divided into segments, as shown, which can be easily characterized by the type and frequency of the various load sources.

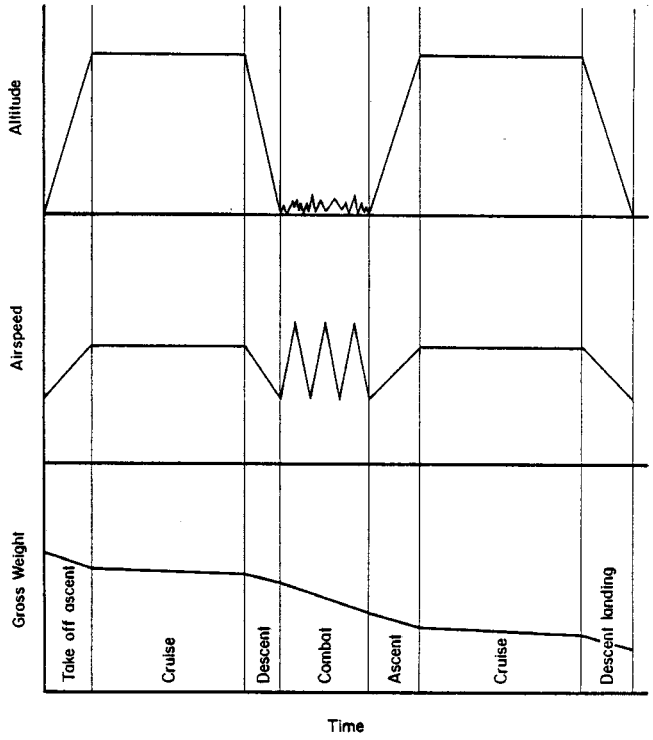

Figure 5.4.1. Mission Profile and Mission Segments

The load spectrum for each mission segment is characterized by a table of occurrences of a load parameter. The commonly used parameter is the normal load factor at the aircraft center-of-gravity, n_z. Such a table can be presented as an exceedance plot, which shows the number of occurrences that exceed specified values during a specified time period.

MIL-A-8866 presents tabular exceedance data for six classes of aircraft, broken out by mission segment. The number of identified segments varies from three to seven. These tables give the number of exceedances per 1,000 mission hours. The total number of exceedances is on the order of 10^5 - 5 x 10^5. Figure 5.4.2 shows a plot of the composite maneuver spectrum for the six classes of aircraft. This composite was made by summing the exceedances of the mission segments for each class of aircraft.

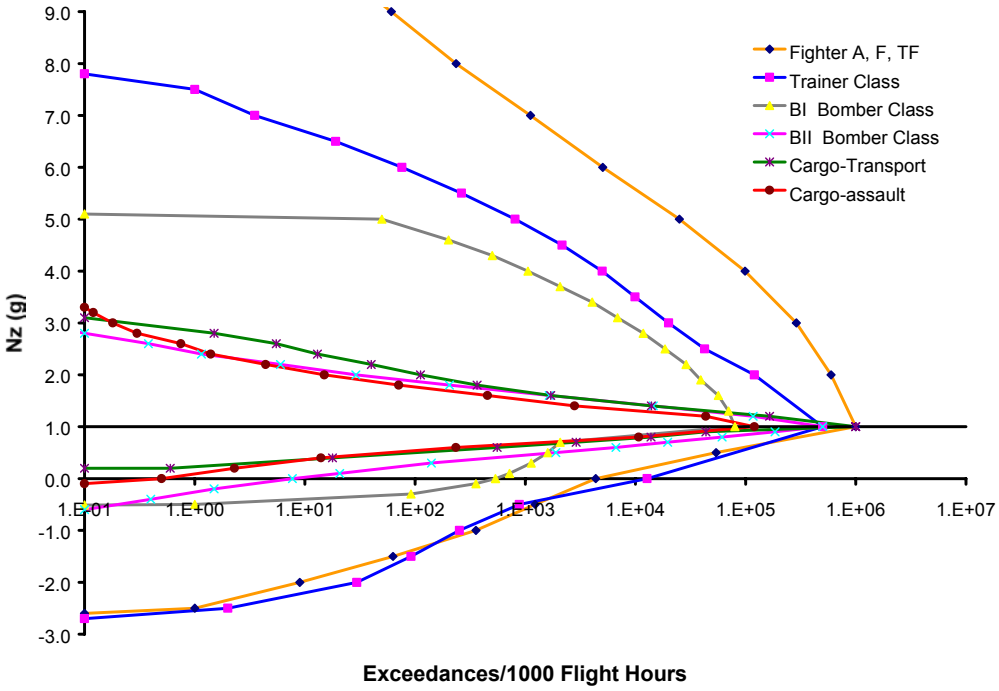

Figure 5.4.2. Maneuver Spectra According to MIL-A-8866

These three basic pieces of information, the service life summary, the mission profiles, and the load factor spectra are converted into the loads history and the stress history at critical locations on the aircraft. This procedure is briefly described in the next section.

5.4.2 Sequence Development Techniques

The preparation of a flight-by-flight load sequence is done in five essential steps:

1. Prepare the representative life history mission ordering.
2. Define mission segment flight conditions.
3. Determine the number of maneuver and gust load cycles at each load level in each mission segment.
4. Order the maneuver and gust load cycles within each mission segment.

5. Place load cycles from other sources within each mission segment.

Giessler, et al. [1981] presents detailed instructions to accomplish these steps; however, brief descriptions are presented here for completeness.

The establishment of the mission sequence for the life history of the aircraft is usually done in a deterministic manner and is based on past observations of similar type aircraft. It is reasonable to assign missions in blocks as flying assignments usually follow specific groupings of missions as various flying skills are being stressed. Missions occurring relatively few times are usually interspersed throughout the sequence either singly or in small numbers. It is recommended that the severest missions be somewhat evenly spaced throughout the sequence. It is common to treat the sequence as a repeating block. Each block would contain all mission types and represent some proportion of the total flight history. Blocks of five hundred or one thousand flight hours have been found to be convenient. For example: for a 6,000 hour aircraft life, a 500 hour block would be repeated twelve times to obtain the total sequence.

Each mission is divided into segments for ease in defining the loading cycles. This division is specified in the mission profile. The same ordering of mission segments is used each time a mission occurs. This division is useful in two ways: it facilitates the identification of load spectra and it provides for the definition of the flight condition parameters. The flight condition parameters are the values of airspeed, altitude, gross weight, configuration, and time used for each mission segment. These conditions are selected from the mission profile to give a set of representative loading conditions for each segment. These are combined with the load level indicator to compute the loads.

The determination of the number and severity of loads assigned to each mission segment is based on a spectrum of a load level indicator. For most applications this is the normal load factor, n_z. This spectrum is obtained from analysis of previous usage of similar aircraft in the case of a design specification, or from current usage of the aircraft being analyzed in the case of an update to the design analysis. Some of the concerns that need to be considered when applying this information will now be discussed.

The load information for an aircraft structure is usually in the form of an exceedance spectrum. The spectrum is an interpretation of in-flight measurements of center-of-gravity accelerations or stresses at a particular location. The interpretation consists of a counting procedure, which counts accelerations (or stresses) of a certain magnitude, or their variation (range). Information on the various counting procedures can be found in Schijve [1963] and VanDÿk [1972].

Typical exceedance spectra are given in Figure 5.4.3 for a transport wing, bomber wing, and fighter wing. The ordinate represents the normal load factor, n_z. The abscissa represents the number of times a level on the vertical axis is exceeded. For example, using the transport spectrum in Figure 5.4.3, level A is exceeded n_1 times and level B is exceeded n_2 times. This means that there will be n_1-n_2 events of a load between levels A and B. These loads will be lower than B, but higher than A. The exact magnitude of any one of the n_1-n_2 loads remains undetermined.

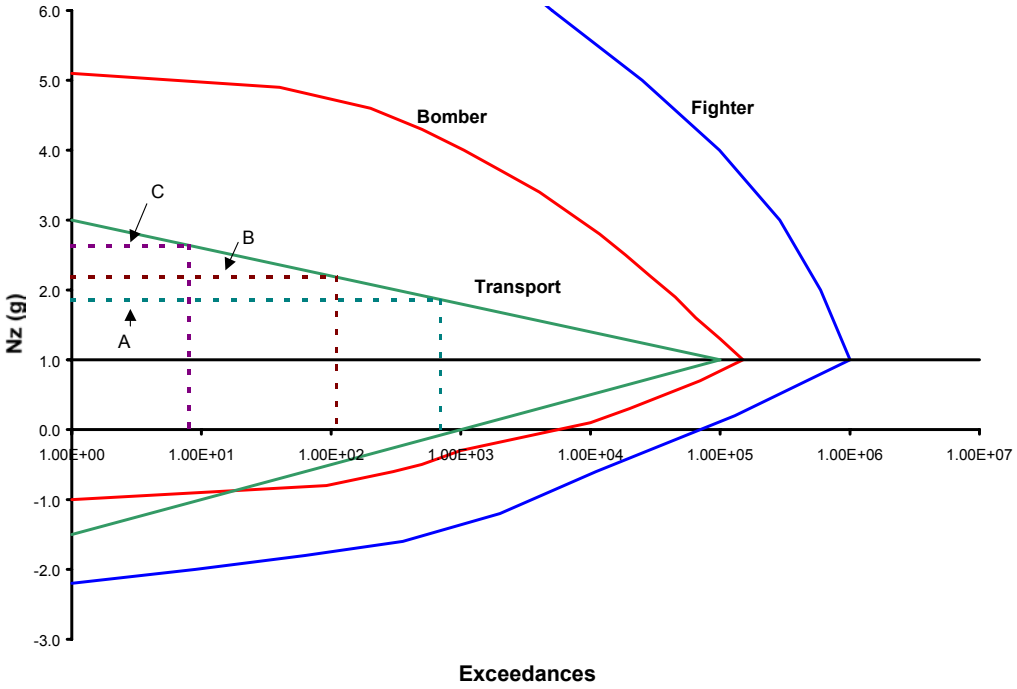

Figure 5.4.3. Exceedance Spectra for 1000 Hours

One can define an infinite number of load levels between A and B. However, there are only n_1-n_2 occurrences, which means that while the number of load levels to be encountered is infinite; not every arbitrary load level will be experienced. Strictly speaking each of the n_1-n_2 occurrences between A and B could be a different load level. If one chose to divide the distance between A and B into n_1-n_2 equal parts, ΔA, each of these could occur once. Mathematically, a level $A+\Delta A$ will be exceeded n_1-1 times. Hence, there must be one occurrence between A and $A+\Delta A$. In practice, such small steps cannot be defined, nor is there a necessity for their definition.

If measurements were made again during an equal number of flight hours, the exceedance spectrum would be the same, but the actual load containment would be different. This means that the conversion of a spectrum into a stress history for crack-growth analysis will have to be arbitrary because one can only select one case out of unlimited possibilities.

Going to the top of the spectrum in Figure 5.4.3, level C will be exceeded 10 times. There must be a level above C that is exceeded 9 times, one that is exceeded 8 times, etc. One could identify these levels, each of which would occur once. In view of the foregoing discussion this becomes extremely unrealistic. Imagine 10 levels above C at an equal spacing of ΔC, giving levels C, $C+\Delta C$, $C+2\Delta C$, etc. If level C is exceeded 10 times, all of these exceedances may be of the level $C+3\Delta C$ for another aircraft.

As a consequence, it is unrealistic to apply only one load of a certain level, which would imply that all loads in the history would have a different magnitude. Moreover, if high loads are beneficial for crack growth (retardation), it would be unconservative to apply once the level $C+\Delta C$, once $C+2\Delta C$, etc., if some aircraft would only see 10 times C.

Hence, the maximum load level for a fatigue analysis should be selected at a reasonable number of exceedances. (This load level is called the clipping level). From crack-growth experiments

regarding the spectrum clipping level, it appears reasonable to select the highest level at 10 exceedances per 1,000 flights. This will be discussed in more detail in later sections. (Note that the maximum load used in the fatigue analysis has no relation whatsoever to the P_{xx} loads for residual strength analysis).

The same dilemma exists when lower load levels have to be selected. Obviously, the *n* loads in 1,000 hours will not be at *n* different levels. A number of discrete levels has to be selected. This requires a stepwise approximation of the spectrum, as in Figure 5.4.4. As shown in the following table, the number of occurrences of each level follows easily from subtracting exceedances.

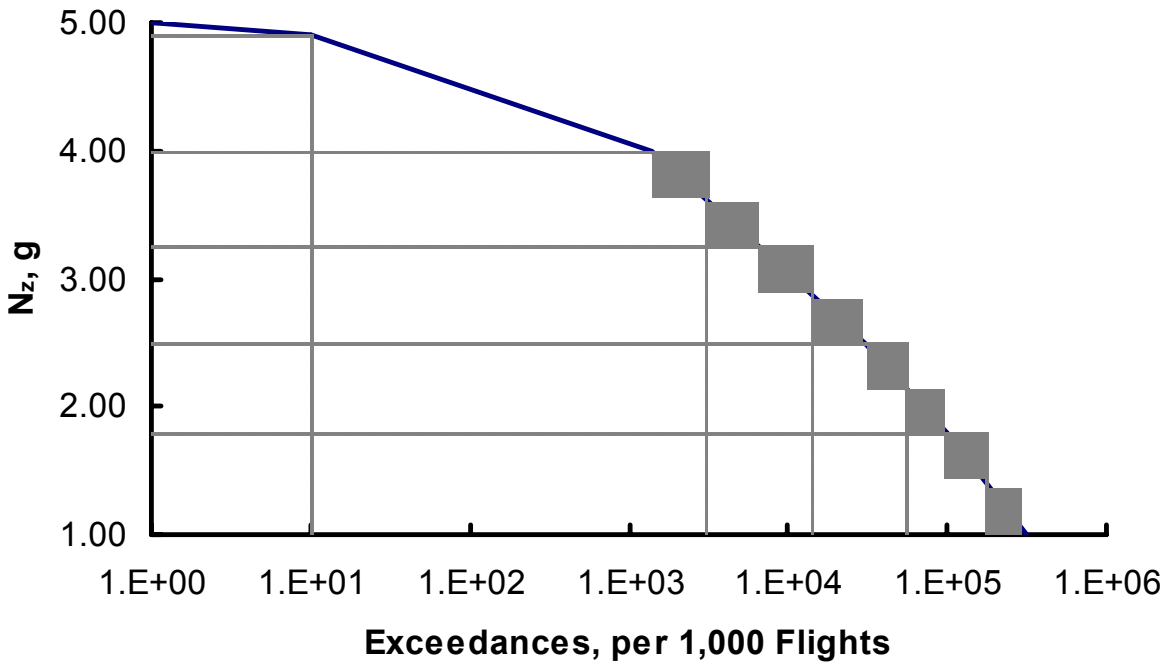

Figure 5.4.4. Stepped Approximation of Spectrum

Table 5.4.1. Occurrences Calculated from the Exceedances of Figure 5.4.4

Level	Exceedances	Occurrences
L_1	n_1	n_1
L_2	n_2	n_2-n_1
L_3	n_3	n_3-n_2
L_4	n_4	n_4-n_3
L_5	n_5	n_5-n_4

The more discrete load levels there are, the closer the stepwise approximation will approach the spectrum shape. On the other hand, the foregoing discussion shows that too many levels are unrealistic. The number of levels has to be chosen to give reliable crack-growth predictions.

Figure 5.4.5 shows results of crack-growth calculations in which the spectrum was approximated in different ways by selecting a different number of levels each time. If the stepped approximation is made too coarse (small number of levels) the resulting crack-growth curve differs largely from those obtained with finer approximations. However, if the number of levels is 8 or more, the crack-growth curves are identical for all practical purposes. A further refinement of the stepped approximation only increases the complexity of the calculation; it does not lead to a different (or better) crack-growth prediction. Crack-growth predictions contain many uncertainties anyway, which means that one would sacrifice efficiency to apparent sophistication by taking too many levels. It turns out that 8 to 10 positive levels (above the in-flight stationary load) are sufficient. The number of negative levels (below the in-flight stationary load) may be between 4 and 10.

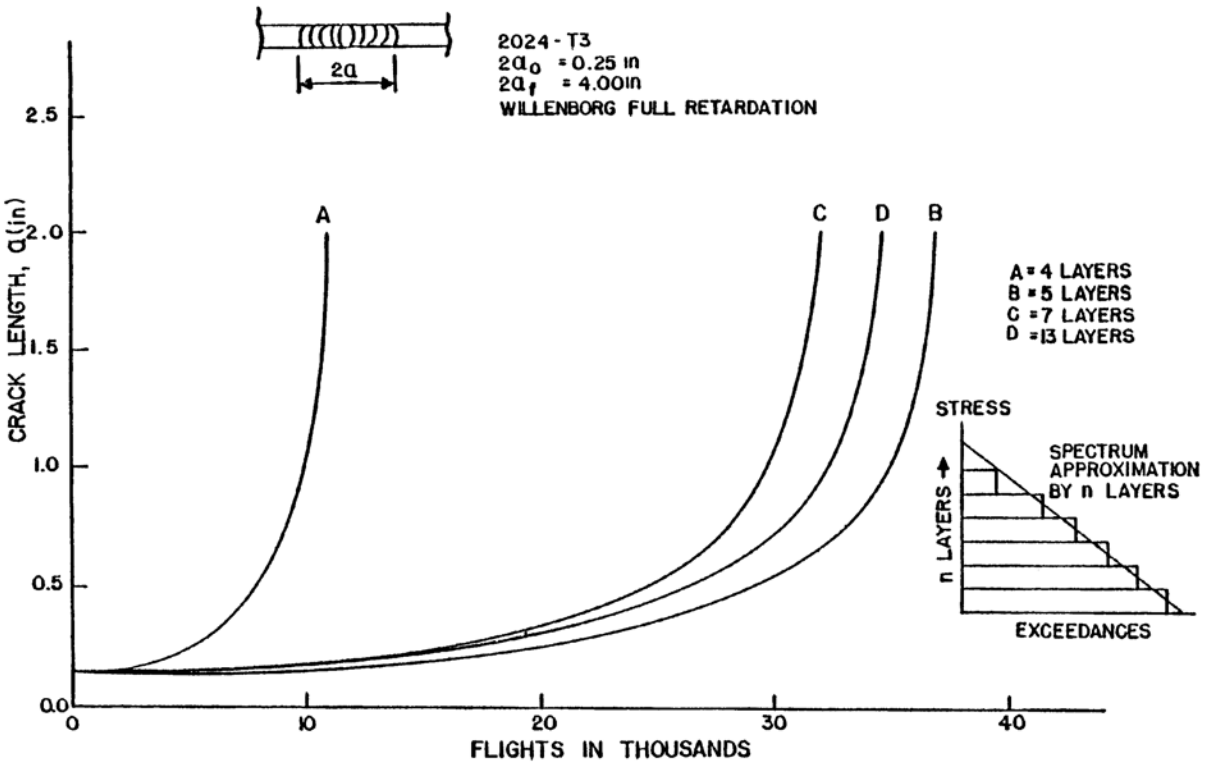

Figure 5.4.5. Fatigue-Crack Growth Behavior Under Various Spectra Approximations

Selection of the lowest positive level is also of importance, because it determines the total number of cycles in the crack-growth analysis. This level is called the truncation level. Within reasonable limits the lower truncation level has only a minor effect on the outcome of the crack-growth life. Therefore, it is recommended that this lower truncation level be selected on the basis of exceedances rather than on stresses. A number in the range of 10^5 - 5 x 10^5 exceedances per 1,000 flights seems reasonable. This will be discussed in more detail in Section 5.5.

EXAMPLE 5.4.1 Constructing Occurrences from Exceedance Information

This example illustrates how a stepped approximation can be constructed. Consider the positive load factor spectrum shown in Figure 5.4.4.

First select the maximum level as the load which is exceeded 10 times in 1,000 flights. This is done by constructing a line from the 10 exceedance level to the curve and then constructing the horizontal to intersect the vertical axis. This gives L_1= 4.9 g. Next construct a vertical from the 10^5 exceedance value. This line is extended until the area A_5 equals B_5. The horizontal line defining the top of A_5 is extended to the vertical axis defining the level L_5. In this case L_5 = 1.8g.

Now the interval from L_5 to L_1 is divided into as many parts as desired. They may be equal or not. Current fighter aircraft practice uses 0.5 g intervals. After the vertical divisions are selected, horizontal lines are extended at L_2, L_3, and L_4 such that the enclosed areas (A_2, B_2), (A_3, B_3) and (A_4, B_4) are approximately equal. At that point the verticals are constructed to define n_2, n_3, and n_4. This now gives the results:

Level	n_z	Exceedance	Occurrences
L_1	4.9	10	10
L_2	4.0	1400	1,390
L_3	3.25	6500	5,100
L_4	2.5	30,000	23,500
L_5	1.8	100,000	70,000
Total			100,000

This procedure is only used to construct the steps after the L_1 level. The L_1 level is taken as the intersection with the curve. It is seen that, as the exceedance plot tails off the high levels on n_z, to construct equal areas becomes difficult if not impossible. In the present example, in order to keep the exceedance value of 10 for the high level, L_1 could not extend beyond 5.0 g and the lower limit of the range could not go below 4.75 g. Now the range from 4.75 g to L_2 would need to be added to the number of levels. This would add high level occurrences that may not be realistic. It should be remembered that the exceedance plot is a curve faired through observed data and that the high level values are usually the result of very few observations.

This method of approximating the spectrum associates the level L_5 with the occurrence represented by a range extending on either side of L_5 and similarly for L_1 which was discussed above. An alternate procedure is to select the ranges first and then to associate the occurrences with the mid-point of the ranges.

After the levels and number of occurrences of the load indicator are determined for each mission segment, the actual loads are computed using the previously defined flight conditions and the specific load equations for the aircraft. Cycles are formed by combining the positive loads with the mean or negative loads. As there are more positive loads than negative loads, most cycles

are formed with the mean, or 1.0g steady flight condition, as the minimum value of the cycle. The assignment of the negative load cycles is usually on a random basis.

The sequencing of these load cycles is the next step. In order to achieve a realistic effect on the crack-growth analysis, care must be taken in establishing this sequence. Some guidelines are given below.

a) Deterministic loads are placed directly in the sequence. Obviously, the ground load of the ground-air-ground (G-A-G) cycle will occur at the beginning and at the end of each flight. Similarly, maneuver loads associated with take-off will be at the beginning of the flight.

b) Probabilistic loads due to gusts and maneuvers have to be arbitrarily assigned and sequenced. The assignment of the loads in a particular mission segment is made on a random basis to all flights containing that mission segment. This results in each flight of a particular mission having a different selection of loads. If a repeating block approach is used, then each flight in the block would be different. Sequencing of the assigned loads within a segment can be either random or deterministic. A deterministic low-high-low sequence has been shown by Schijve [1970, 1972] to be very similar to random loading for a gust spectrum. This sequence is also realistic for the combat maneuvering segments of fighter aircraft. Thus, the low-high-low sequence is recommended if programmed sequencing is considered rather than random sequencing.

c) After determination of all the mission stresses, simplifications are sometimes possible. Usually the stresses will be given in tabular form. They will show an apparent variability. For example, if an acceleration, n_2, is exceeded 10,000 times, this will not result in the exceedance of 10,000 times of a certain stress level, since n_2 causes a different stress in different missions or mission segments. However, if a stress exceedance spectrum is established for the various missions on the basis of the tabular stress history, it may turn out that two different missions may have nearly the same stress spectrum. In that case, the missions can be made equal for the purpose of crack-growth predictions.

d) Placement of non-probabilistic load sources which occur a specified number of times in a flight is made on a deterministic basis. One such method is to place them after a certain number of occurrences of the probabilistic loads. This is reasonable for a random sequencing, however, if the sequencing has been low-high-low, then following the same method and placing these miscellaneous cycles in the proper location is suggested.

While the above discussions were primarily directed toward development of wing loadings, similar methods are used to obtain the load sequencing for other parts of the aircraft. Only the significant loading conditions will change.

5.4.3 Application of Simplified Stress Sequences for Design Studies

In the early design stage, not much is known about the anticipated stress histories. An exceedance spectrum based on previous experience is usually available. However, material selection may still have to be made, and operational stress levels may still have to be selected. Hence, it is impossible and premature to derive a detailed service life history as discussed in Section 5.4.2. Yet, crack-growth calculations have to be made as part of the design trade-off studies. The designer wants to know the effect of design stress, structural geometry, and material

selection with respect to possible compliance with the damage-tolerance criteria, and with respect to aircraft weight and cost. Such studies can be made only if a reasonable service stress history is assumed. The following example shows how much a history can be derived in a simple way, if it is to be used only for comparative calculations.

EXAMPLE 5.4.2 Construction of a Simple Stress Sequence

Consider the exceedance spectrum for 1,000 flights shown below. Instead of selecting stress levels for the discretization, it is much more efficient in this case to select exceedances. Since a large number of levels is not necessary in this stage, six levels were chosen in the example. The procedure would remain the same if more levels were to be selected.

The exceedances in the example were taken at 10 (in accordance with Section 5.4.2); 100; 1,000; 10,000; 100,000; and 500,000 (in accordance with Section 5.4.2). Vertical lines are drawn at these numbers, and the stepped approximation is made. This leads to the positive excursion levels, S_1-S_6, and the negative excursion levels, L_1-L_6 , as shown below. The stress levels and exceedances are given in columns 1 and 2 of the table; subtraction gives the number of occurrences in column 3.

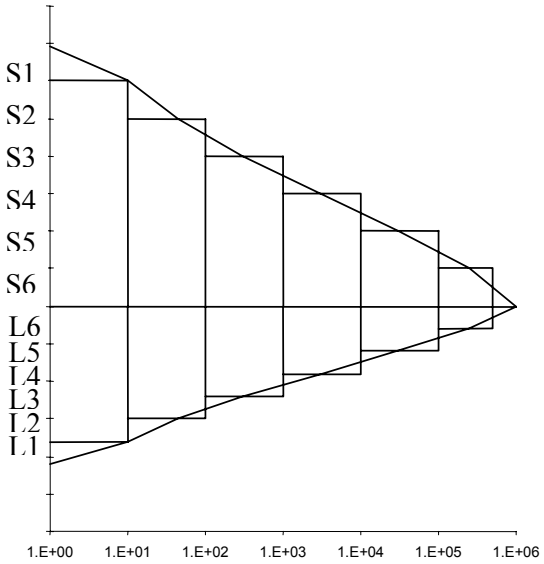

The highest stress level is likely to occur only once in the severest mission. Therefore, a mission *A* spectrum is selected, as shown in column 4, in which S_1 occurs once, and lower levels occur more frequently in accordance with the shape of the total spectrum. In order to use all 10 occurrences of level S_1, it is necessary to have 10 missions *A* in 1,000 flights. The number of cycles used by 10 missions *A* is given in column 5. The occurrences from these missions are subtracted from the total number of occurrences (column 3) to give the occurrences in the remaining 990 flights (column 6).

The next severest mission is likely to have one cycle of level S_2. Hence, the mission *B* spectrum in column 7 can be constructed in the same way as the mission *A* spectrum. Since 60 cycles of S_2 remain after mission *A*, mission *B* will occur 60 times in 1,000 flights. The 60 missions *B* will use the cycles shown in column 8, and the cycles remaining for the remaining 930 flights are given in column 9.

Composite			Mission A			Mission B		
1 Level	2 Exceedances	3 Occurrences	4 Occurr.	5 10 x	6 Remain (= 3-5)	7 Occurr.	8 60 x	9 Remain (= 6-8)
S_1	10	10	1	10	--	--	--	--
S_2	100	90	3	30	60	1	60	--
S_3	1,000	900	15	150	750	3	180	570
S_4	10,000	9,000	48	480	8,520	17	1,020	7,500
S_5	100,000	90,000	300	3,000	87,000	200	12,000	75,000
S_6	500,000	400,000	1,900	19,000	381,000	1,500	90,000	291,000

Composite		Mission C			Mission D		
1 Level		10 Occurr.	11 570 x	12 Remain (= 9-11)	13 Occurr.	14 360 x	15 Remain (= 12-14)
S_1		--	--	--	--	--	--
S_2		--	--	--	--	--	--
S_3		1	570	--	--	--	--
S_4		10	5,700	1,800	5	1,800	--
S_5		100	57,000	18,000	50	18,000	--
S_6		400	228,000	63,000	175	63,000	--

Level S_3 will occur once in a mission *C*, which is constructed in column 10. There remain 570 cycles S_3, so there will be 570 missions *C*. These missions will use the cycles given in column 11, and the remaining cycles are given in column 12.

Mission	Number of Times	Repeat
D	6	Repeat 33 times
B	1	
C	19	
B	1	
D	6	
A	1	

There will be 10 missions *A*, 60 missions *B*, and 570 missions *C* in 1,000 flights, meaning that 360 flights remain. By dividing the remaining cycles in column 12 into 360 flights, a mission *D* spectrum is defined, as given in column 13. Consequently, all cycles have been accounted for.

A mission mix has to be constructed now. With mission *A* occurring 10 times per 1,000 flights, a 100-mission block could be selected. However, a smaller block would be more efficient. In the example, a 33-mission block can be conceived, as shown below. After 3 repetitions of this block (99 flights) one mission *A* is applied.

Mission	Number of Times	Repeat
D	6	Repeat 33 times
B	1	
C	19	
B	1	
D	6	
A	1	

The cycles in each mission are ordered in a low-high-low sequence. The negative excursion L_1-L_6 are accounted for by combining them with the positive excursions of the same frequency of occurrence: L_1 forms a cycle with S_1, L_2 with S_2, etc.

To arrive at the stresses an approximate procedure has to be followed also. Given the flight duration, an acceleration spectrum (e.g., the 1,000 hours spectra given in MIL-A-8866B) can be converted approximately into a 1,000 flight spectrum. Limit load will usually be at a known value of n_z, e.g., 7.33g for a fighter or 2.5g for a transport. As a result, the vertical axis of the acceleration diagram can be converted into a scale that gives exceedances as a fraction of limit load. This is done in Figure 5.4.6 for the MIL-A-8866B spectra of Figure 5.4.2. A comparison of these figures will clarify the procedure.

Once the spectrum of the type of Figure 5.4.6 is established, design trade-off studies are easy. Selecting different materials or different design stress levels S_1-S_6 and L_1-L_6 can be determined and the flight-by-flight spectrum is ready. Selection of a different design stress level results in a new set of S_1-S_6., and the calculations can be re-run.

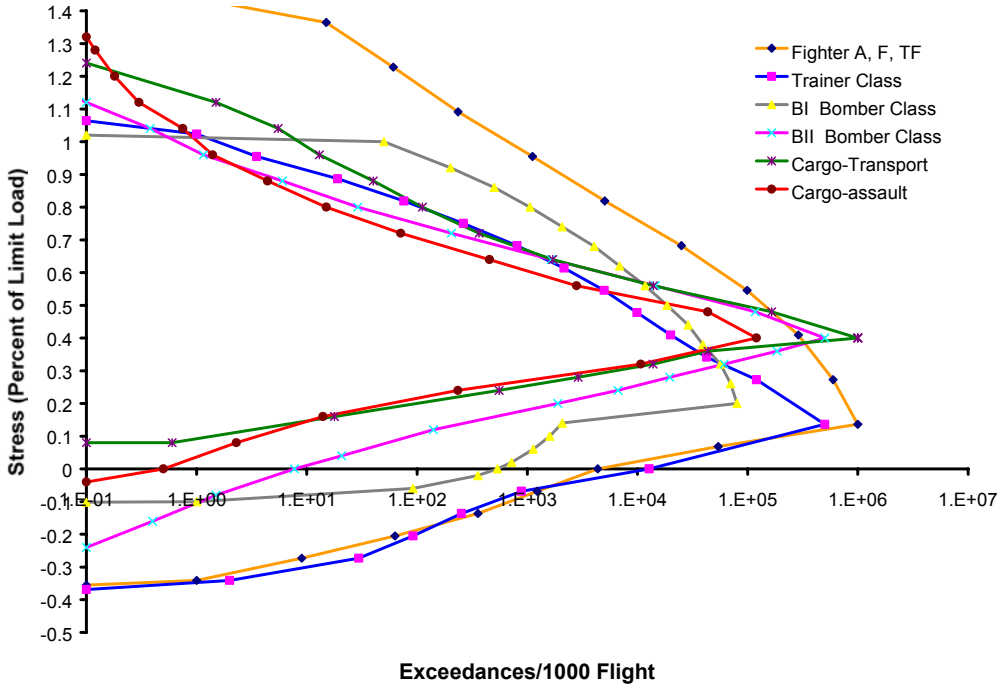

Figure 5.4.6. Approximate Stress Spectrum for 1000 Flights Based on MIL-A-8866B (USAF)

This shows the versatility of the spectrum derivation shown in Example 5.4.2. It is a result of choosing exceedances to arrive at the stepped approximation of the spectrum, which means that the cycle content is always the same. If stress levels were selected instead, a change in spectrum shape or stress levels would always result in different cycle numbers. In that case, the whole procedure to arrive at the spectrum in Example 5.4.2 would have to be repeated, and many more changes would have to be made to the computer program.

Example 5.4.2 shows only a few levels. The spectrum could be approximated by more levels and more missions could be designed, but the same procedure can be used. In view of the comparative nature of the calculations in the early design stage, many more levels or missions are not really necessary.

Note: The stress history derived in this section is useful only for quick comparative calculations for trade-off studies.

The stress history developed in Example 5.4.2 was applied to all the s spectra from MIL-A-8866B (shown in Figure 5.4.6) to derive crack-growth curves. These results will be discussed in Section 5.5.3.

5.5 Crack Growth Prediction

The analysis procedure for crack-growth prediction requires the following steps:

1. Find baseline crack growth data (Section 5.1)
2. Select a retardation model; select and apply an integration routine (Section 5.2)
3. Establish a stress history and mission mix (Section 5.4)
4. Determine the stress-intensity factor (Section 11)

Each of these steps was discussed in general terms in one of the foregoing sections. However, there are some detail problems that need consideration. These detail problems are the subject of Section 5.5.

5.5.1 Cycle Definition and Sequencing

In Section 5.2, the retardation phenomenon was discussed. Retardation caused by high stress excursions can have a large effect on crack growth. As a result, the sequence of low and high stresses can be critical. Independent of retardation, however, there is another sequence effect that is related to the cycle definition necessary for a crack growth calculation.

If a flight-by-flight stress history is developed for damage tolerance analysis or tests, it will be given as a sequence of load levels. Each of the cases, *a*, *b*, c, and *d* in Figure 5.5.1, could be considered as a series of details in such a sequence. Each case is a stress excursion of 8δ between levels A and B containing a dip of increasing size from *a* to *d*. In case *a*, the dip might be so small that for practical purposes it can be neglected. The cycle then can be considered as a single excursion with a range ΔK_1 of size 8δ. In cases *b* through *d*, the dips are too big to be neglected. Normal crack growth calculations might consider each of these cases as a sequence of two excursions, for example case *b* would be made up of two excursions, one with a range ΔK_2, the other with a range ΔK_3, each of size 5δ.

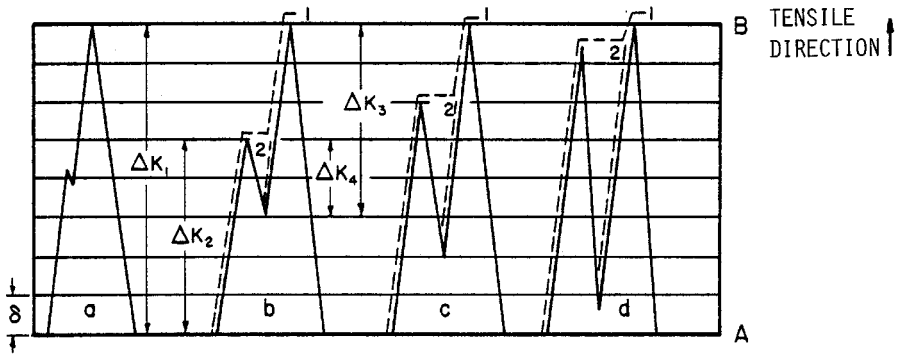

Figure 5.5.1. Definition of Cycles

Table 5.5.1. Calculation of Crack Growth For Figure 5.5.1

Range Calculated Crack Growth (Δa)				
a	$\Delta a_a =$	$C(\Delta K_1)^4 =$	$C(8\delta)^4 =$	$4096\ C\delta^4$
b	$\Delta a_b =$	$C(\Delta K_2)^4 + C(\Delta K_3)^4 =$	$2C(5\delta)^4 =$	$1250\ C\delta^4$
c	$\Delta a_c =$		$2C(6\delta)^4 =$	$2592\ C\delta^4$
d	$\Delta a_d =$		$2C(7.5\delta)^4 =$	$6328\ C\delta^4$
Range-Pair Calculated Crack Growth (Δa)				
a	$\Delta a_a =$	$C(\Delta K_1)^4 =$	$C(8\delta)^4 =$	$4096\ C\delta^4$
b	$\Delta a_b =$	$C(\Delta K_1)^4 + C(\Delta K_4)^4 =$	$C(8\delta)^4 + C(2\delta)^4 =$	$4112\ C\delta^4$
c	$\Delta a_c =$		$C(8\delta)^4 + C(4\delta)^4 =$	$4352\ C\delta^4$
d	$\Delta a_d =$		$C(8\delta)^4 + C(7\delta)^4 =$	$6497\ C\delta^4$

If the four cases were treated this way, the calculated crack extension based on range excursions would be as given Table 5.5.1, where, for simplicity, the crack growth equation is taken as $da/dN = C(\Delta K)^4$ and the R ratio effect is ignored. As indicated in this table, the damage estimates for cases *b* and *c* are considerably less than the crack damage estimated for case *a*. This is very unlikely in practice, since the crack would see one excursion from A to B in each case. Therefore, cases *b*, *c*, and *d* should be more damaging than case *a* in view of the extra cycle due to the dip. Although the effect of cycle ratio was neglected, the small influence of R could not account for the discrepancies.

It seems more reasonable to treat each case as one excursion with a range of ΔK_1 plus one excursion of a smaller range (e.g., ΔK_4 in case *b*) which follows the philosophy of range-pair counting. If this is done, the ranges considered would be as indicated by the dashed lines in Figure 5.5.1. The crack growth calculation based on range-pair counting is shown at the bottom of Table 5.5.1, indicating an increasing amount of damage going from *a* to *d*.

Another cycle definition is obtained by rainflow counting [VanDÿk, 1972; Dowling, 1972]. The method is illustrated in Figure 5.5.2. While placing the graphical display of the stress history vertical, it is considered as a stack of roofs. Rain is assumed to flow from each roof. If it runs off the roof, it drips down the roof below, etc., with the exception that the rain does not continue on a roof that is already wet. The range of the rain flow is considered the range of the stress. The ranges so obtained are indicated by AB, CD, etc., in Figure 5.5.2. Figure 5.5.3 shows how cycle counting methods may affect a crack growth prediction.

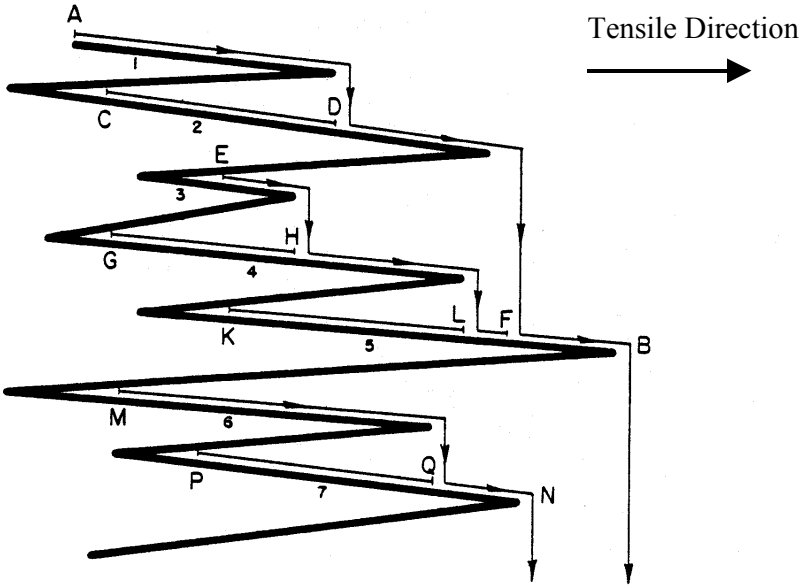

Figure 5.5.2. Rain Flow Count

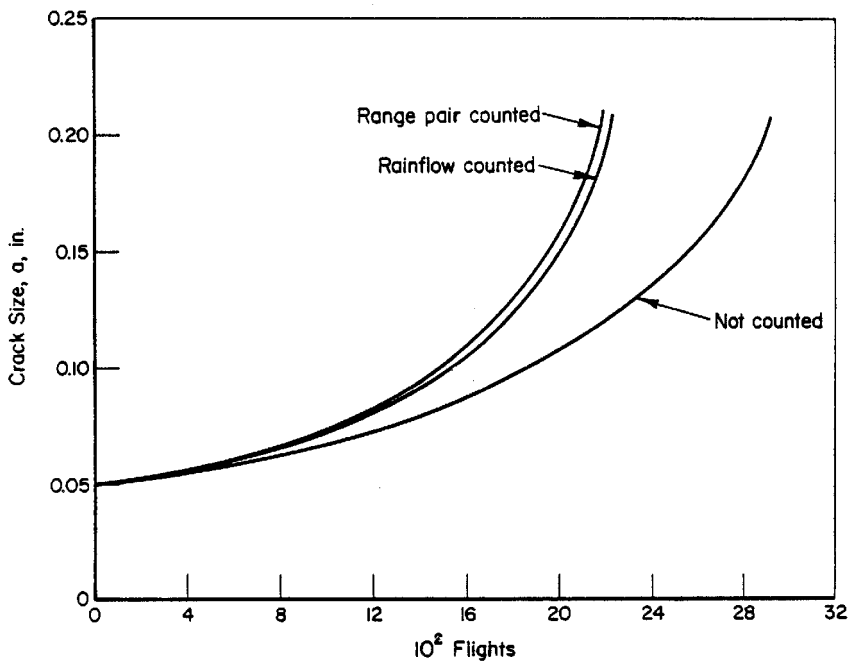

Figure 5.5.3. Calculated Crack Growth Curves for Random Flight-by-Flight Fighter Spectrum [VanDÿk, 1972]

Several other counting methods exist, and they are reviewed in Schijve [1963] and VanDÿk [1972]. Counting methods were originally developed to count measured load histories for

establishing an exceedance diagram. Therefore, the opinions expressed in the literature on the usefulness of the various counting procedures should be considered in that light. The counting procedure giving the best representation of a spectrum need not necessarily be the best descriptor of fatigue behavior.

It is argued that ranges are more important to fatigue behavior than load peaks. On this basis, the so-called range-pair count and the rainflow count are considered the most suitable. However, no crack growth experiments were ever reported to prove this.

The use of counting procedures in crack growth prediction is an entirely new application. An experimental program is required for a definitive evaluation. Calculated crack growth curves show that the difference in crack growth life may be on the order of 25-30 percent. It should be noted that counting is not as essential when the loads are sequenced low-high-low in each flight. The increasing ranges automatically produce an effect similar to counting.

For the time being, it seems that a cycle count will give the best representation of fatigue behavior. Therefore, it is recommended that cycle counting per flight be used for crack growth predictions of random sequences. Care should be taken that the stress ranges are sequenced properly to avoid different interaction effects (note that K_{max} determines retardation and not ΔK). As an example, consider again Figure 5.5.2. The proper sequence for integration is: CD, GH, KL, EF, AB, PQ, MN. In this way, the maximum stress intensity (at B) occurs at the proper time with respect to its retardation effect, and the maximum stress-intensity of cycle AB will cause retardation for cycles PQ and MN only.

5.5.2 Clipping

Apart from the sequencing problems addressed in the previous section, there is a sequence problem associated with retardation. In Section 5.4, it was pointed out that sequencing of deterministic loads should be done in accordance with service practice; probabilistic loads can be sequenced randomly, but a low-high-low order per flight is acceptable. This can be concluded from data of the type presented in Figure 5.2.5.

The sequencing effect due to retardation is largely dependent on the ratio between the highest and lowest loads in the spectrum and their frequency of occurrence. As a result, it will depend upon spectrum shape. Compare, for example, the fighter spectrum with the transport spectrum in Figure 5.4.6. The relatively few high loads in the transport spectrum may cause a more significant retardation effect than the many high loads in the fighter spectrum.

The selection of the highest loads in the load history is critical to obtain a reliable crack growth prediction. It was argued in Section 5.4 that it is not realistic to include loads that occur less frequently than about 10 times in 1,000 flights, because some aircraft in the force may not see these high loads. This means that the spectrum is clipped at 10 exceedances. No load cycles are omitted. Only those higher than the clipping level are reduced in magnitude to the clipping level. The effect of clipping on retardation and crack growth life was illustrated in Figure 5.2.4.

The question remains whether proper selection of a realistic clipping level is as important for a crack-growth prediction as it is for an experiment. In this respect, it is important to know which retardation model is the most sensitive to clipping level. As pointed out above, the sensitivity may also depend upon spectrum shape. The effects can be determined by running crack growth

calculations for different clipping levels, different spectrum shapes, and with two retardation models.

Calculations were made for the six spectra shown in Figure 5.4.6, by using the flight-by-flight history developed in Example 5.4.2. The cycles in each flight were ordered in a low-high-low sequence. Figure 5.5.4 shows the crack growth curves for the full spectra using the Willenborg model, and Figure 5.5.5 shows the curves using the Wheeler model. The crack configuration was a corner crack from a hole, as indicated in the figures. A limit load stress of 35 ksi was used for all spectra, and the material was 2024-T3 aluminum.

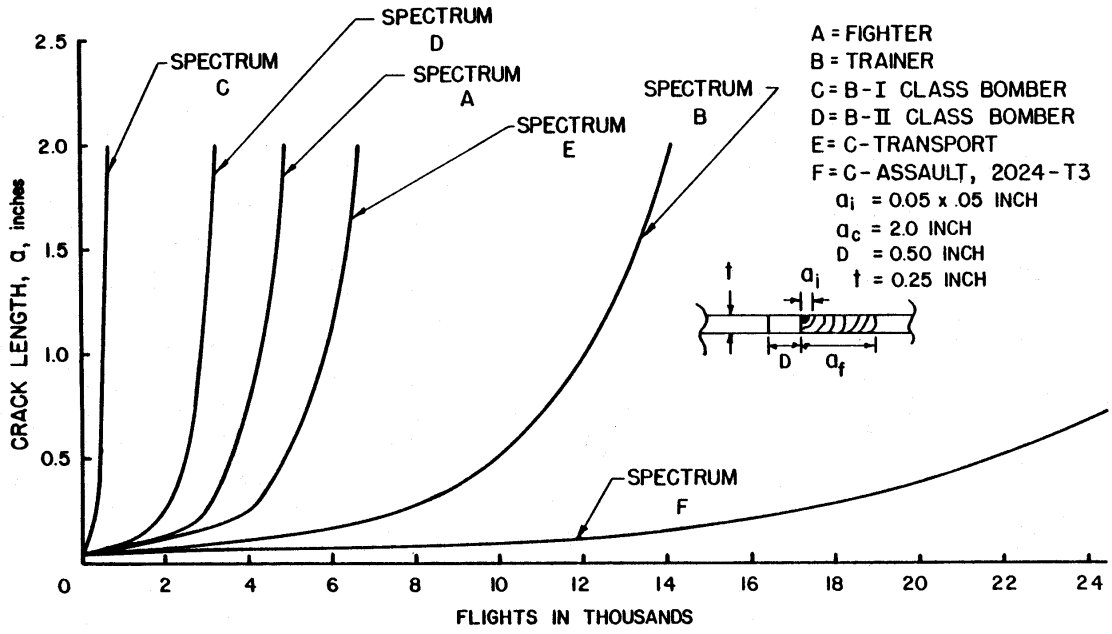

Figure 5.5.4. Spectrum Fatigue Crack Growth Behavior Willenborg Retardation Model

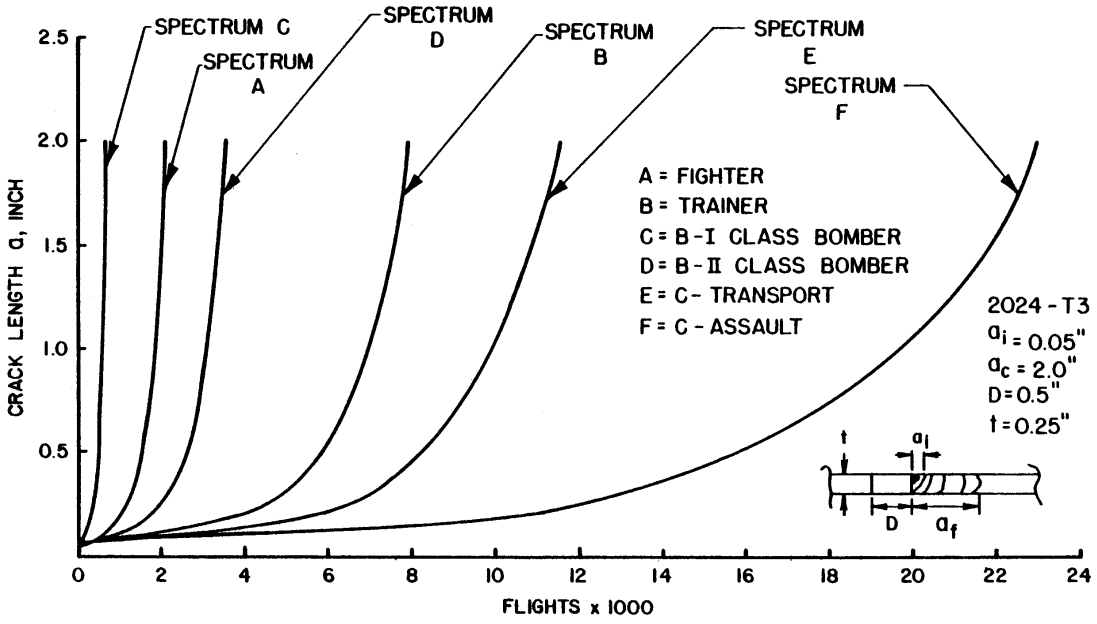

Figure 5.5.5. Spectrum Fatigue Crack Growth Behavior Wheeler Retardation Model

Subsequently, four significantly different spectra (A, B, C, and E) were selected. Crack growth curves were calculated using the clipping levels S_2, S_3, S_4, and S_5 in Example 5.4.2. The resulting crack growth curves for one spectrum are presented in Figure 5.5.6. Also shown is a curve for a linear analysis (no retardation). The crack growth life results for all spectra are summarized as a function of clipping level in Figure 5.5.7. Test data for gust spectrum truncation are also shown. Some characteristic numbers are tabulated in Table 5.5.2 for the four spectra as a function of crack growth model.

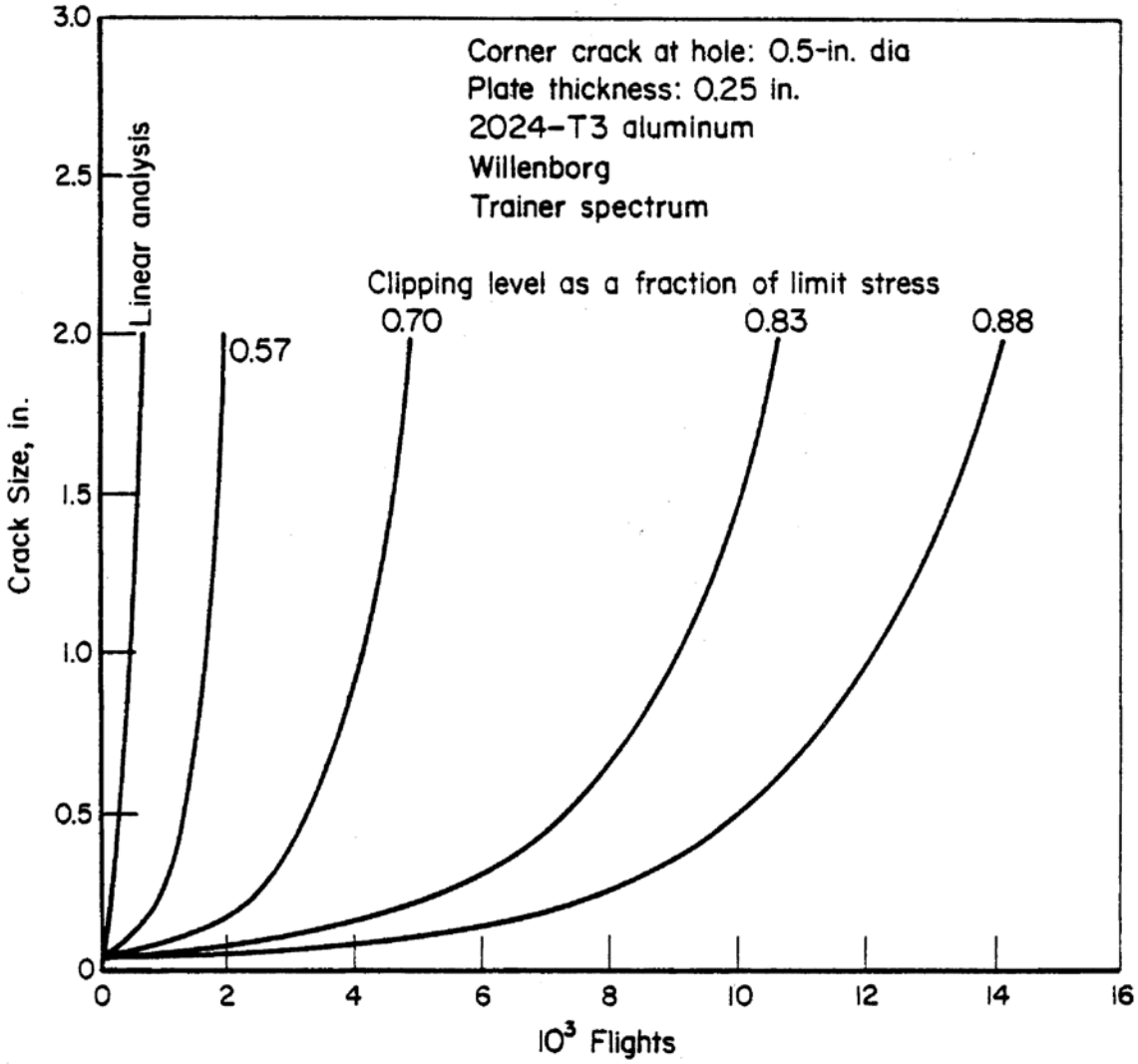

Figure 5.5.6. Effect of Clipping Level on Calculated Crack Growth for Spectrum B-Trainer

Table 5.5.2. Characteristic Value for the Four Spectra of Figure 5.5.6

Symbol	Spectrum	Linear Analysis (Flights)	Retardation Life (Flights)	
			Willenborg Fully Retarded	Wheeler m = 2.3
A ▲ Willenborg △ Wheeler	Fighter	270	4,900	2,100
B ● Willenborg ○ Wheeler	Trainer	460	14,200	7,900
C ■ Willenborg □ Wheeler	B-1 Class Bomber	140	700	700
D ▼Willenborg ▽ Wheeler	C Transport	1,270	6,700	11,600

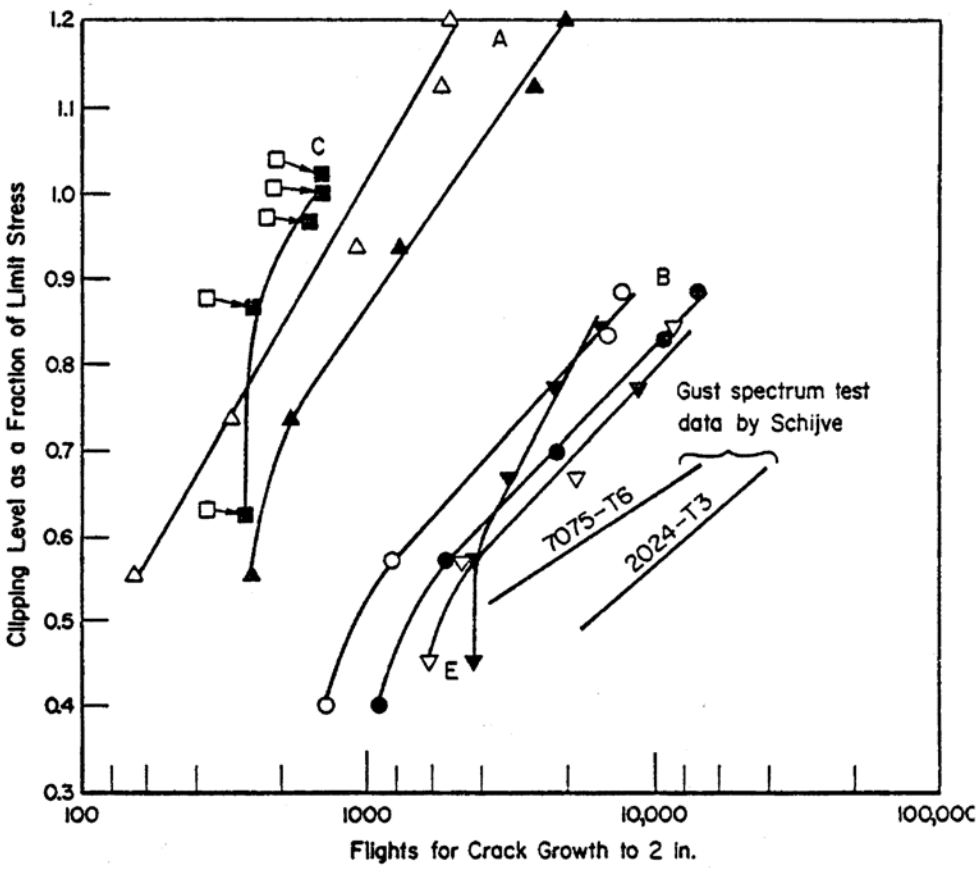

Figure 5.5.7. Effect of Clipping for Various Spectra

Figures 5.5.4 through 5.5.7 allow the following observations:

- The two retardation models predict largely different crack growth lives for all spectra, except C. The differences are not systematic. Since there are no test data for comparison, the correct answers are not known.
- With one exception, the two models essentially predict the same trend with respect to clipping levels. This shows that they both have equal capability to treat retardation.
- The steep spectra (fighter, trainer) are somewhat more sensitive to clipping level. Apparently, the damage of the high cycles outweighs their retardation effect.
- With extreme clipping, the analysis attains more the character of a linear analysis, indicating that the largest amount of damage in the linear analysis comes from the large number of smaller amplitude cycles.
- Bringing the clipping level down from 10 exceedances per 1,000 flights (top data points in Figure 5.5.7) to 100 exceedances per 1,000 flights (second row of data points in Figure 5.5.7) reduces the life by only 15 percent or less for all spectra.

In addition, crack growth calculations were made to re-predict the gust spectrum test data shown in Figure 5.5.7. The results are presented in Figure 5.5.8 where the calculated results are shown to be very conservative. However, with one exception, they would all fall within the scatter-band of Figure 5.2.4. The baseline data used were worst case upper-bound *da/dN* data. This can easily account for a factor of two in growth rates. If the growth rates were reduced by a factor of two, the calculations would be very close to the test data (dashed line in Figure 5.5.8).

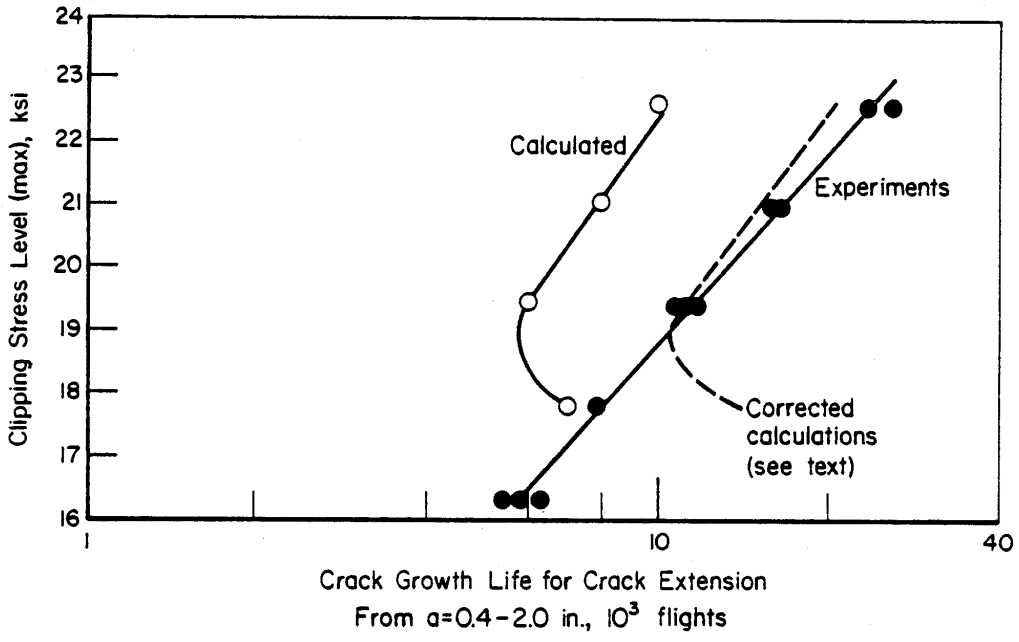

Figure 5.5.8. Calculated and Experimental Data for Gust Spectrum Clipping [Schijve, 1970; 1972]

One important thing has been disregarded so far. As shown in Figure 5.2.1, compressive stresses reduce retardation (compare curves B and C). Omission of the ground-air-ground (GAG) cycle in the experiments by Schijve (1970) shown in Figure 5.5.8 increased the life by almost 80 percent. Apart from the GAG cycle, there are other compressive stresses in the spectrum. All compressive stress effects were ignored in the crack growth calculations with the retardation models used for this analysis.

The top clipping level in Figure 5.5.8 is at 5 exceedances per 1,000 flights, the second level is at 13 exceedances per 1,000 flights. From these results and Figure 5.5.7, it appears that an exceedance level of 10 times per 1,000 flights will combine reasonable conservatism with a realistically high clipping level. This supports the arguments given previously to select the clipping level at 10 exceedances per 1,000 flights for both calculations and experiments. The effect of clipping level should be calculated for a small number of representative cases to show the degree of conservatism.

5.5.3 Truncation

Truncation of the lower load levels is important for the efficiency of crack growth calculations. Truncation means that cycles below a certain magnitude are simply omitted. The argument is that low stress excursions do not contribute much to crack growth, especially in view of the retardation effect. Since there are so many cycles of low amplitude, their omission would speed up experiments and crack growth calculations.

Figure 5.5.9 shows some experimental data regarding the effect of truncation. The lowest load levels of a complete stress history were simply omitted, without a correction of the stress history. These data might be somewhat misleading, because truncation was not carried out properly. Figure 5.5.10 shows the improper and the correct procedure for truncation.

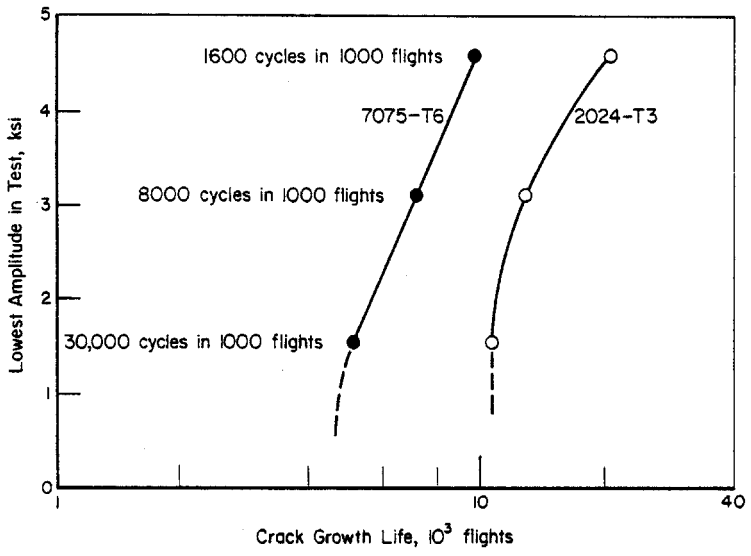

Figure 5.5.9. Effect of Lowest Stress Amplitude in Flight-by-Flight Tests Based on Gust Spectrum [Schijve 1970; 1972]

The left half of Figure 5.5.10 illustrates the truncation procedure used for the experiments in Figure 5.5.9. In the example, the 580,000 cycles of level S_8 would simply be omitted, thus reducing the total cycle content from 700,000 to 120,000. Proper truncation requires that the lower spectrum approximation step be reconstructed, as indicated in the right half of Figure 5.5.10. The hatched areas in the figure should be made equal. This means that the number of S_7 cycles would increase from 80,000 to 260,000, and the total cycle content would be reduced from 700,000 to 300,000. This increase of 180,000 cycles of S_7 would be substituted for 580,000 cycles of S_8. In this way, the effects of lower level truncation are less than suggested by the experimental data in Figure 5.5.9.

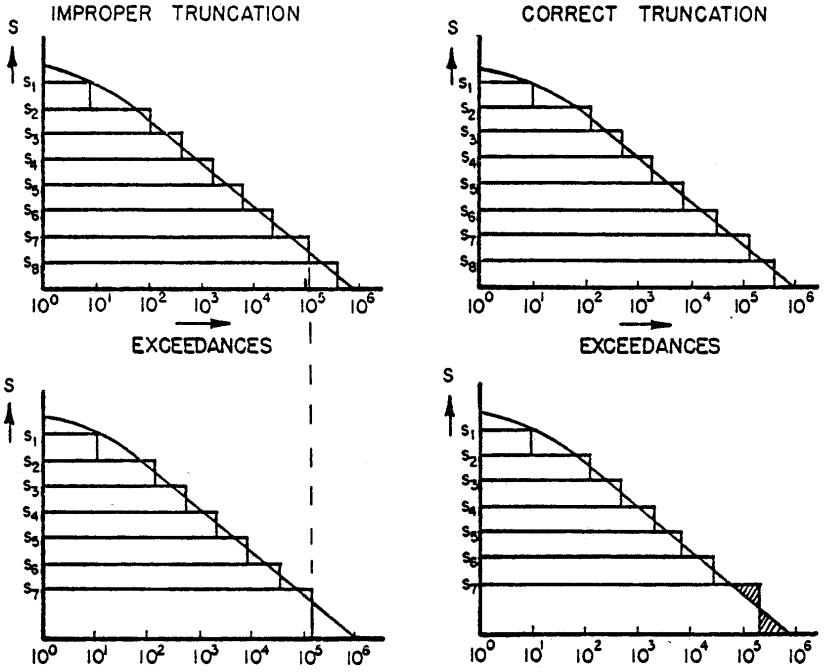

Improper Truncation		
Level	**Exceedances**	**Occurrences**
S_1	10	10
S_2	100	90
S_3	600	500
S_4	2,000	1,400
S_5	8,000	6,000
S_6	40,000	32,000
S_7	120,000	80,000
S_8	700,000	580,000

Correct Truncation		
Level	**Exceedances**	**Occurrences**
S_1	10	10
S_2	100	90
S_3	600	500
S_4	2,000	1,400
S_5	8,000	6,000
S_6	40,000	32,000
S_7	300,000	260,000

Figure 5.5.10. Improper and Correct Truncation

In Section 5.4 it was recommended that the truncation level be selected at 10^5 - $5x10^5$ exceedances per 1,000 flights, depending upon how steep the exceedance curve is at its extreme point. That recommendation is reiterated here.

5.5.4 Crack Shape

The most common crack shape in crack growth analysis is the quarter-circular corner flaw at the edge of a hole. Stress-intensity factor solutions for this case are presented in Section 11. For use in crack growth analysis, these solutions present some additional problems. The stress-intensity factor varies along the periphery of the crack. Since crack growth is a function of the stress-intensity factor, crack extension also will vary along the crack front. If this is accounted for in a calculation, the flaw shape at a hole changes from quarter-circular to quarter-elliptical.

For the calculation, it would be sufficient to include two points of the crack front, e.g., the crack tip at the surface and the crack tip at the edge of the hole. The stress-intensity factor is calculated at these points, and the amount of crack growth determined. There will be a different amount of growth along the surface than along the edge of the hole. For an initially quarter-circular crack of size a_i, the new crack will have a size $a_i+\Delta a_s$ along the surface, and a size $a_i+\Delta a_h$ along the hole. For the next crack growth increment the crack may be considered a quarter-elliptical flaw with semi-axes $a_i+\Delta a_s$, and $a_i+\Delta a_h$.

There are three reasons why the above procedure may not give the accuracy expected for crack growth life estimating:

- The variation of stress-intensity factor along a corner flaw front at the edge of a hole is not accurately known.
- The differences in stress-intensity factor cause differences in growth and flaw shape development. If this is so, the difference in crack growth properties in the two directions (anisotropy) should be accounted for too.
- The differences in growth rates and stress-intensity factor levels also give different retardation effects.

When the flaw size becomes equal to the plate thickness, the flaw will become a through-thickness-crack with a curved front for which stress-intensity solutions are readily available. Cracks usually have a tendency to quickly become normal-through-thickness cracks once they reach the free surface (Figure 5.5.11). Therefore, it is recommended to conservatively assume the crack to become a normal-through-thickness-crack of a size equal to the thickness immediately after it reaches the free surface ($a = B$, Figure 5.5.11).

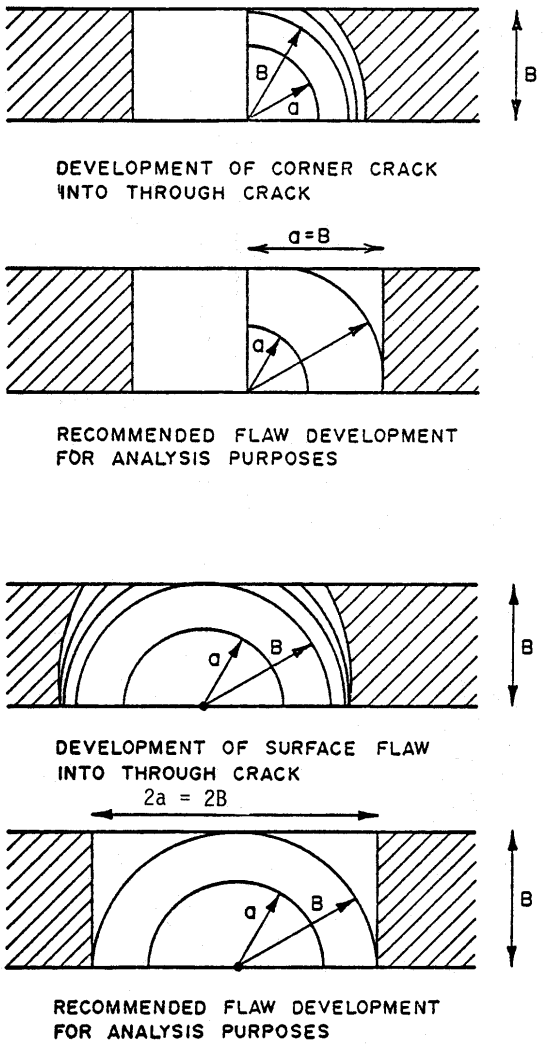

Figure 5.5.11. Development of Flaws

5.5.5 Interaction of Cracks

For the initial flaw assumptions, JSSG-2006 paragraph A3.12.1 states: "Only one initial flaw in the most critical hole and one initial flaw at a location other than a hole need be assumed to exist in any structural element. Interaction between these assumed initial flaws need not be considered." Obviously, interaction between these cracks can be disregarded because these cracks are not assumed to occur simultaneously, although each of them may occur separately. However, more than one initial flaw may occur if due to fabrication and assembly operations two or more adjacent elements can contain the same initial damage at the same location. Note that each of the adjacent elements has only one flaw. JSSG-2006 paragraph A3.12.1 further states: "For multiple and adjacent elements, the initial flaws need not be situated at the same location, except for structural elements where fabrication and assembly operations are conducted such that flaws in two or more elements can exist at the same location."

The previous statement that interaction between assumed initial flaws need not be considered is not repeated here because these cracks will interact as they occur simultaneously. In principle, the damage tolerance calculation should consider this interaction. However, a rigorous treatment of this problem is prohibitive in most cases. Consider, e.g., a skin with a reinforcement as in Figure 5.5.12. Because of assembly drilling, both holes should be assumed flawed (Figure 5.5.12a). If both elements carry the same stress, there will be hardly any load transfer initially. Hence, the stress intensities for both flaws will be equal, implying that initially both will grow at the same rate.

If the two cracks continue to grow simultaneously in a dependent manner, their stress-intensity factors (K) will eventually be different (e.g., K of the reinforcement would increase faster if only for the finite size effect). This means that in a given cycle the rate of growth would be different for the two cracks resulting in different crack sizes. Since it cannot be foreseen prior how the crack sizes in the two members develop, it would be necessary to develop K-solutions for a range of crack sizes and a range of crack size ratios in the two members.

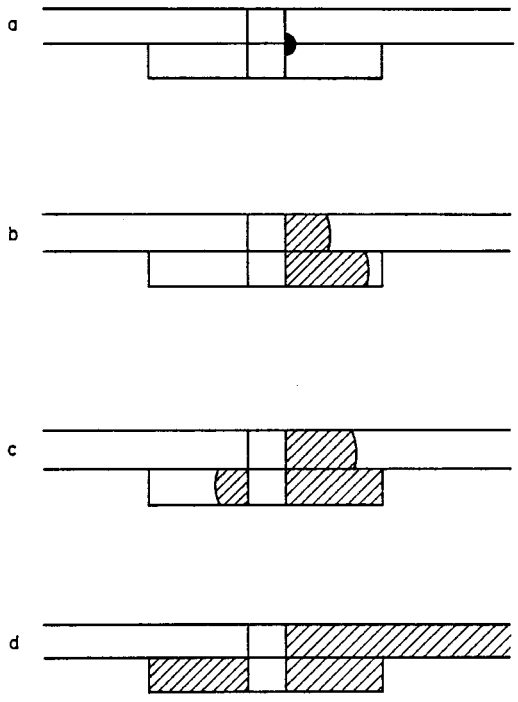

Figure 5.5.12. Interaction of Cracks

EXAMPLE 5.5.1: Interacting Cracks

Assume the crack size in the skin is a_s, the crack size in the reinforcement a_r. For a given value of a_r, the K for the skin crack would be calculated as a function of a_s. This calculation would be repeated for a range of a_r sizes. The same would be done for the reinforcement crack and a range of a_s values. For any given combination of a_r and a_s, the two stress-intensity factors then can be found by interpolation.

Although the consequences of crack interaction should be evaluated, routine calculations may be run without interaction of cracks [Smith, et al., 1975; Smith, 1974]. Obviously, the calculation procedure is much simpler if interaction can be ignored. However, the procedure may give unconservative results.

If either element remained uncracked, the stress-intensity factor in the cracked element would be much lower because there would be load transferred from the cracked element to the uncracked element. Obviously, the stress-intensity factor in the cracked skin of Example 5.5.1 would be the lowest. The cracks could be grown as if the other element was uncracked and crack growth would be slower.

Finally, the reinforcement could be totally cracked. Interaction must be taken into account, i.e., the crack in the skin would be treated now for the case of a failed reinforced panel (e.g., stringer reinforced structure with middle stringer failed).

This means that two analysis have to be made for a K-determination, one with the reinforcement uncracked, one with the reinforcement failed. If the two independent crack growth analyses show that the reinforcement has failed, the analysis of the skin is changed appropriately.

5.6 References

M.R. Achter (1967). "Effect of Environment on Fatigue Cracks". *Fatigue Crack Propagation*. ASTM STP 415, pp. 181-204.

P.D. Bell and M. Creager (1975). "Crack-Growth Analysis for Arbitrary Spectrum Loading". AFFDL-TR-74-129.

A.F. Blom, et al. (1986). "Short Fatigue Crack Growth Behavior in Al 2024 and Al 7475". EGF Publication 1, Mechanical Engineering Publications, London, pp. 37-66.

F.J. Bradshaw and C. Wheeler (1969). "Effect of Environment and Frequency on Fatigue Cracks in Aluminum Alloys". *International Journal of Fracture Mechanics, 5*, pp. 255-268.

D. Broek (1972). "Residual Strength and Fatigue-Crack Growth in Two Aluminum Alloy Sheets Down to -75°C". National Aerospace Institute, NLR TR-M-72096.

D. Broek (1966). "Fatigue-Crack Growth; Effect of Sheet Thickness". *Aircraft Engineering, 38*, (11), pp. 31-33.

D. Broek (1963). "The Effect of Sheet Thickness on the Fatigue-Crack Propagation in 2024-T3 Sheet". National Aerospace Lab. Report NLR-TR-M-2129, Amsterdam.

B.F. Brown (1968). "The Application of Fracture Mechanics to Stress Corrosion Cracking". *Metals and Materials, 2*; *Metal Reviews, 13*, pp. 171-183.

T.R. Brussat (1971). "An Approach to Predicting the Growth to Failure of Fatigue Cracks Subjected to Arbitrary Uniaxial Cyclic Loading, Damage Tolerance in Aircraft Structures". ASTM STP 486, American Society for Testing and Materials, pp. 122-143.

J.B. Chang and C.M. Hudson (Eds.) (1981). "Methods and Models for Predicting Fatigue Crack Growth Under Random Loading". ASTM STP 748, American Society for Testing and Materials.

H.P. Chu (1972). "Fracture Characteristics of Titanium Alloys in Air and Seawater Environment". *Engineering Fracture Mechanics, 4*, pp. 107-117.

E.P. Dahlberg (1965). "Fatigue-Crack Propagation in High Strength 4340 Steel in Humid Air". *ASM Trans 58*, pp. 46-53.

H.D. Dill and C.R. Saff (1977). "Analysis of Crack Growth Following Compressive Loads Based on Crack Surface Displacements and Contact Analysis". *Cyclic Stress-Strain and Plastic Deformation Aspects of Fatigue Crack Growth*. ASTM STP 637, American Society for Testing and Materials, pp. 141-152.

H.D. Dill and C.R. Saff (1978, November). "Environment-Load Interaction Effects on Crack Growth". AFFDL-TR-78-137, Air Force Flight Dynamics Laboratory.

D.R. Donaldson and W.E. Anderson (1960). "Crack-Propagation Behavior of Some Airframe Materials". *Cranfield Symposium* (Vol. II), pp. 375-441.

N.E. Dowling (1972). "Fatigue Failure Predictions for Complication Stress-Strain Histories". *Journal of Materials*, ASTM, pp. 71-87.

W. Elber (1971), "The Significance of Crack Closure". ASTM STP 486, pp. 230-242.

R.M. Engle and J.L. Rudd (1974). "Analysis of Crack Propagation Under Variable-Amplitude Loading Using the Willenborg Retardation Model". AIAA Paper No. 74-369.

R.M. Engle, Jr. (1970). "CRACKS, A FORTRAN IV Digital Computer Program for Crack Propagation Analysis". AFFDL0TR-70-107, Air Force Flight Dynamics Laboratory.

F. Erdogan (1967). "Crack-Propagation Theories". NASA-CR-901.

R.G. Forman, V.E. Kearney, and R.M. Engle (1967). "Numerical Analysis of Crack Propagation in a Cyclic-Loaded Structure". *Journal Basic Engineering*, ASME (Vol. 89), Series D, pp. 459-464.

J.P. Gallagher (1974a). "A Generalized Development of Yield Zone Models". AFFDL-TR-FBR 74-28.

J.P. Gallagher (1974b). "Fatigue-Crack-Growth Rate Laws Accounting for Stress Ratio Effects". ASTM E24-04-04, Report 1.

J.P. Gallagher (1976, November). "Estimating Fatigue-Crack Lives for Aircraft: Technique." *Experimental Mechanics* (Vol. 16), No. 11, pp. 425-433.

J.P. Gallagher and H.D. Stalnaker (1975, September), "Predicting Flight-by-Flight Fatigue Crack Growth Rates". *Journal of Aircraft*, AIAA (Vol. 12), No. 9, pp. 699-705.

J.P. Gallagher and T.F. Hughes (1974). "Influence of the Yield Strength on Overload Affected Fatigue-Crack-Growth Behavior of 4340 Steel". AFFDL-TR-74-27.

J.P. Gallagher, H.D. Stalnaker, and J.L. Rudd (1974). "A Spectrum Truncation and Damage Tolerance Study Association with the C-5A Outboard Pylon Aft Truss Lugs." AFFDL-TR-74-5.

J.P. Gallagher and R.P. Wei (1972). "Corrosion Fatigue Crack Propagation Behavior in Steels". *Corrosion Fatigue: Chemistry, Mechanisms, and Microstructure*. A.J. McEvily and R.W. Staehle (Eds.), National Association of Corrosion Engineers, pp. 409-423.

F.J. Giessler, S.J. Duell, and R.F. Cook (1981, February). "Handbook of Guidelines for the Development of Design Usage and Environmental Sequences for USAF Aircraft". AFWAL-TR-80-3156, Air Force Wright Aeronautical Laboratories.

L.R. Hall and W.L. Engstrom (1974). "Fracture and Fatigue-Crack-Growth Behavior of Surface Flaws Originating at Fastener Holes". AFFDL-TR-74-47

A. Hartman (1965). "On the Effect of Water Vapour and Oxygen on the Propagation of Fatigue Cracks in an Aluminum Alloy". *International Journal of Fracture Mechanics, 1*, pp. 167-188.

P. Hartman and J. Schijve (1970). "The Effects of Environment and Frequency on the Crack-Propagation Laws for Macrofatigue Cracks". *Engineering Fracture Mechanics 1*, pp. 615-631

JSSG-2006 (1998, October). "Joint Service Specification Guide, Aircraft Structures". Department of Defense.

R. Lachnaud (1965). "Fatigue Strength and Crack Propagation in AV2GN Alloy as a Function of Temperature and Frequency". *Current Aeronautical Fatigue Problems*. J. Schijve (Ed.). Pergamon, pp. 77-102.

B.N. Leis, M.F. Kanninen, A.T. Hopper, J. Ahmad and D. Broek (1986). "Critical Review of the Fatigue Growth of Short Cracks". Engineering Fracture Mechanics, (Vol. 23).

D.A. Meyn (1971). "Frequency and Amplitude Effects on Corrosion Fatigue Cracks in a Titanium Alloy". *Materials Trans. 2*, pp. 853-865.

D.A. Meyn (1968). "The Nature of Fatigue-Crack Propagation in Air and Vacuum for 2024 Aluminum". *ASM Trans. 61*, pp. 52-61.

MIL-HDBK-5H (1998, December). Military Handbook, Metallic Materials and Elements for Aerospace Vehicle Structures.

M.S. Miller and J.P. Gallagher (1981). "An Analysis of Several Fatigue Crack Growth Rate (FCGR) Descriptions". *Fatigue Crack Growth Measurement and Data Analysis*. S.J. Hudak, Jr. and R.J. Bucci (Eds.). ASTM STP 738, American Society for Testing and Materials, pp. 205-251.

L. Mueller, et al. (1981, October). ASTM Task Group E24-04.04 presentations during ASTM Committee Week held in St. Louis, MO.

A. Nagar (2002). "Small Crack Growth at Pin Loaded Holes", AFRL-VA-WP-TR-2001-3008.

J.C. Newman (1992). "Fracture Mechanics Parameters for Small Cracks". *Small Crack Test Methods*. ASTM STP 1149, American Society for Testing and Materials.

P.C. Paris (1964). "The Fracture Mechanics Approach to Fatigue, Fatigue – An Interdisciplinary Approach". Syracuse University Press, pp. 107-132.

R.M.N. Pelloux (1970). "Review of Theories and Laws of Fatigue-Crack Propagation". AFFDL-TR-70-144, pp. 409-416.

D.E. Piper, S.H. Smith, and R.V. Carter (1968). "Corrosion Fatigue and Stress Corrosion Cracking in Aqueous Environment". *Metals Engineering Quarterly, 8*, pp. 3.

T.R. Porter (1972). "Method of Analysis and Prediction for Variable Amplitude Fatigue-Crack Growth". *Engineering Fracture Mechanics 4*.

J.M. Potter, J.P. Gallagher, and H.D. Stalnaker (1974). "The Effect of Spectrum Variations on the Fatigue Behavior of Notched Structures Representing F-4E/S Wing Stations". AFFDL-TM-74-2 FBR.

R.D. Raithby and M.E. Bibb (1961). "Propagation of Fatigue Cracks in Wide Unstiffened Aluminum Alloy Sheet". R.A.E. TN Structures 305.

J.R. Rice and P.C. Paris (Eds.) (1976). "Mechanics of Crack Growth". ASTM STP 590, American Society for Testing and Materials.

C.R. Saff (1980, December). "Environment-Load Interaction Effects on Crack Growth in Landing Gear Steels". NADC-79095-60. Naval Air Development Center, Warminister, PA.

J. Schijve (1972). "The Accumulation of Fatigue Damage in Aircraft Materials and Structures". AGARDograph No. 157.

J. Schijve (1970). "Cumulative Damage Problems in Aircraft Structures and Materials". *The Aeronautical Journal, 74*, pp. 517-532.

J. Schijve (1963). "The Analysis of Random Load Time Histories With Relation to Fatigue Tests and Life Calculations". *Fatigue of Aircraft Structures*. Barrois and Ripley (Eds.), McMillen, pp. 115-149.

J. Schijve and D. Broek (1962). "Crack Propagation Based on a Gust Spectrum with Variable-Amplitude Loading". *Aircraft Engineering, 34*, pp. 314-316.

J. Schijve and D. Broek (1961). "The Effect of the Frequency on the Propagation of Fatigue Cracks". NLR TR-M-72096. National Aerospace Institute.

J. Schijve and P. DeRijk (1966). "Fatigue-Crack Propagation in 2024-T3 Alclad Sheet Materials of Seven Different Manufacturers". NLR TR-M-2162. National Aerospace Lab.

J. Schijve and P. DeRijk (1963). "The Effect of Temperature and Frequency on Fatigue-Crack Propagation in 2024-T3". NLR TR-M-2138.

T.T. Shih and R.P. Wei (1974). "Load and Environment Interactions in Fatigue-Crack Growth". *Prospects of Fracture Mechanics*, Noordhoff, pp. 237-250.

D.A. Skinn, J.P. Gallagher, A.P. Berens, P.D. Huber, and J. Smith (1994). *Damage Tolerant Design (Data) Handbook.* WL-TR-94-4052. Wright Laboratory, Air Force Materiel Command, Wright-Patterson Air Force Base, Ohio.

S.H. Smith (1974). "Fatigue-Crack-Growth Behavior of C-5A Wing Control Points" ASD-TR-74-18.

S.H. Smith, T.R. Porter and W.D. Sump (1968). "Fatigue-Crack Propagation and Fracture Toughness Characteristics of 7079 Aluminum Alloy Sheets and Plates in Three Aged Conditions". NASA CR-996.

S.H. Smith, F.A. Simonen, and W.S. Hyler (1975). "C-141 Wing Fatigue Crack Propagation Study". Final Report to Warner Robins ALC; BCL Report G-2954-1.

A.M. Sullivan (1972). "Stress-Corrosion-Crack Velocity in 4340 Steel". *Engineering Fracture Mechanics, 4*, pp. 65-76.

R.L. Tobler, et al. (1974). "Fatigue and Fracture Toughness Testing at Cryogenic Temperatures". Report by Cryogenics Division, NB 3.

P.M. Toor (1973). "A Review of Some Damage Tolerance Design Approaches for Aircraft Structures". *Engineering Fracture Mechanics, 5*, pp. 837-880.

G.M. VanDÿk (1972). "Statistical Load Data Processing". *Advanced Approaches to Fatigue Evaluation*. NASA SP-309, pp. 565-598.

E.K. Walker (1970). "The Effect of Stress Ratio During Crack Propagation and Fatigue for 2024-T3 and 7075-T6 Aluminum". *Effects of Environment and Complex Load History on Fatigue Life*. M.S. Rosenfeld (Ed.). ASTM STP 462, American Society for Testing and Materials, pp. 1-14.

R.P. Wei (1970). "Some Aspects of Environment-Enhanced Fatigue-Crack Growth". *Engineering Fracture Mechanics 1*, pp. 633-651.

R.P. Wei and J.D. Landes (1969). "Correlation Between Sustained Load and Fatigue Crack Growth in High Strength Steels, Materials Research and Standards". ASTM, Vol. 9, pp. 25

R.P. Wei, and R.I. Stephens (1976). "Fatigue Crack Growth Under Spectrum Loads". ASTM STP 595, American Society for Testing and Materials.

R.P. Wei and T.T. Shih (1974). "Delay in Fatigue-Crack Growth". *International Journal Fracture, 16*, pp. 77-85.

O.E. Wheeler (1972). "Spectrum Loading and Crack Growth". *Journal Basic Engineering, 94D*, pp. 181.

J.D. Willenborg, R.M. Engle, and H.A. Wood (1971). "A Crack-Growth Retardation Model Using an Effective Stress Concept". AFFDL-TM-71-1 FBR.

H.A. Wood (1974). "Important Aspects of Crack-Growth Prediction for Aircraft Structural Applications". *Prospects of Fracture Mechanics*. Shi, VanElast, Broek (Eds.), Noordhoff, pp. 437-457.

H.A. Wood and T.L. Haglage (1971). "Crack-Propagation Test Results for Variable-Amplitude Spectrum Loading in Surface Flawed D6ac Steel". AFFDL-TM FBR 71-2.

H.A. Wood, R.M. Engle, and T.L. Haglage (1971). "The Analysis of Crack Propagation Under Variable-Amplitude Loading in Support of the F-111 Recovery Program". AFFDL-TM-71-3 FBR.

Section 6
Examples of Damage Tolerant Analyses

The basic ingredients for damage tolerance analysis are the residual strength calculation and the crack growth prediction. These two subjects were dealt with in two previous sections. This section will show how crack growth and residual strength analysis are combined in a damage tolerance analysis of an actual structure in the various stages of design. Guidelines will be given on how to demonstrate compliance with the Airplane Damage Tolerance Design Requirements of JSSG-2006. The various options to qualify a structure will be reviewed.

In the next subsection, the general scheme for a damage-tolerance analysis will be given in the form of a stepwise procedure. Thereafter the option of inspectable versus non-inspectable qualification will be considered; the advantages and disadvantages of each will be summarized. Then an example will be given to show the consequences of selecting a certain qualification option. Finally, a number of example problems will be presented to illustrate the application of damage-tolerance analysis.

6.1 Damage Tolerance Analysis Procedure

For intact structure the analysis procedures for Slow Crack Growth and Fail Safe structure are essentially the same. An initial flaw is assumed and its growth is analyzed until failure of the member or load path occurs (or instability and arrest in Fail Safe Crack Arrest structure).

For intact structure, there are two options for the qualification of each type of structure: depot-level inspectable or non-inspectable. The differences are in the assumed initial flaws and the required crack growth life to instability. These requirements are explained in detail in Section 1.3.

After load path failure (or instability and arrest), the damage will be of sufficient size to afford more frequent inspection. As a result, there are more options for qualification of the structure with remaining structure damage depending upon the inspectability of the remaining structure damage. The options are: flight evident, ground evident, walkaround visual, special visual, and depot level. The required crack-growth life with remaining structure damage present depends upon the inspection interval, which increases from one (1) flight to ¼ lifetime. Obviously, these requirements do not apply to slow crack growth structure.

Crack arrest can only occur if there is load transfer from the cracked part to other members (e.g., separate member or reinforcements in the case of Fail Safe structure). However, load transfer does not automatically classify a structure as Fail Safe structure. Only if such load transfer can be shown to give crack arrest, and if the remaining structure requirements can also be met, can the structure be qualified as Fail Safe structure. In all other cases the structure is considered as Slow Crack Growth structure and should be qualified on the basis of Slow Crack Growth requirements.

The crack growth analysis for all types of structures requires the following steps:

Step 1. Determine the stress-intensity factor (K) as a function of crack size for each member involved. Possible load transfer must be considered, because it may affect K and this crack growth. (See Section 11).

Step 2. Obtain or derive the stress history for the location under consideration. (See Section 5).

Step 3. Obtain baseline crack-growth data (da/dN as a function of ΔK and R) for all the materials involved, e.g., the skin and the reinforcement members might be fabricated from different materials. (Section 7 summarizes data collection programs).

Step 4. Using the results of Steps, 1, 2, and 3, calculate the crack-growth curve for each element, using one of the retardation models described in Section 5. Start with a 0.05 inch flaw. The result will be as shown schematically in Figure 6.1.1.

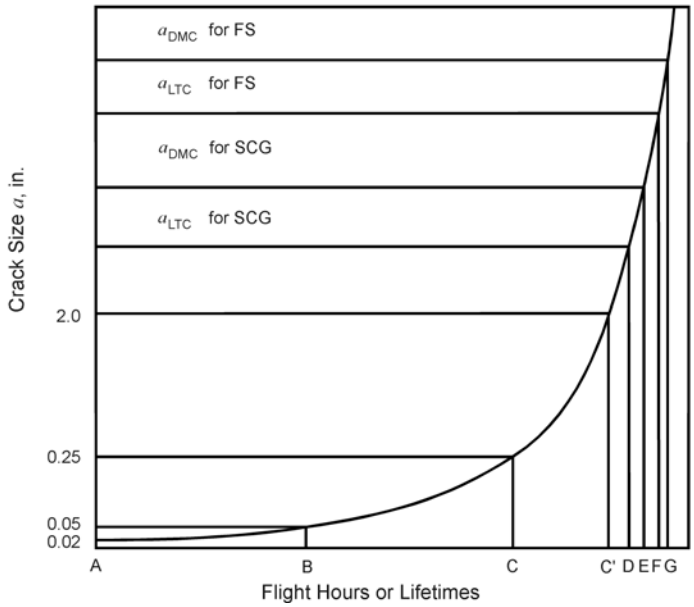

Figure 6.1.1. Diagrammatic Crack Growth Curve (SCG = Slow Crack Growth, FS = Fail Safe)

Step 5. By using the results of the residual strength analysis (Section 4), plot the critical (first instability) crack sizes, a_{DMC} and a_{LTC} , for depot level inspectability (fail safe load P_{DM}) and non-inspectable (fail safe load P_{LT}). These are shown in Figure 6.1.1.

NOTE: Since P_{DM} (and P_{LT}) differ for slow crack growth and for fail safe categorized structure, four critical crack sizes may have to be considered.

Step 6. For slow crack growth structure, check Figure 6.1.1 to determine:

I. whether BD is equal to or greater than 2 design lifetimes.

II. whether CE (or C'E) is equal to or greater than ½ design lifetime.

If only I is satisfied, the structure is qualified as slow crack growth, non-inspectable. If only II is satisfied, the structure is qualified as slow crack growth, depot level inspectable structure. If both I and II are satisfied, it is optional to qualify the structure as non-inspectable, or inspectable. It should be qualified as non-inspectable to avoid costly inspections. If neither I nor II is satisfied, there are three options:

- redesign or lower stress levels until either I or II is satisfied.
- make the structure dismountable and require a special non-destructive inspection. In that case the post-inspection flaw may be assumed 0.05-inch instead of 0.25-inch. Then BE should be equal to ½ lifetime for qualification as slow crack growth, depot level inspectable structure.
- demonstrate that cracks smaller than 0.25-inch can normally be detected, and show that crack growth from this size to critical covers ½ lifetime for qualification as slow crack growth, depot level inspectable structure.

To check for potential qualification as Fail Safe structure continue with the following steps:

Step 7. Check (Figure 6.1.1) to determine:

I. whether AF is equal to or greater than 1 design lifetime.

II. whether CG (or C'G) is equal to or greater than ¼ design lifetime.

If either or both of the two conditions are satisfied the structure might qualify as fail safe structure with the same possibilities as in Step 6. However, classification still depends upon the following steps. If neither condition is satisfied, either redesign or reduce stress levels. (Note that the structure would certainly not satisfy Slow Crack Growth requirements.)

Step 8. Determine the size of the arrested crack from the residual strength analysis (Section 4).

Step 9. Determine the remaining structure damage as specified in JSSG-2006, the Airplane Damage Tolerance Requirements. First calculate the stress-intensity factor as a function of crack size. The growth of this damage is calculated in the same way as that of the initial damage following Steps 1 through 4.

- for independent structure, a flaw of 0.005 inch should be assumed in the adjacent (uncracked) member. The remaining structure damage is of the size to which this flaw has grown prior to instability and arrest or member failure.
- two adjacent members in Fail Safe dependent structure have a common source of cracking, so that both have a 0.02 inch initial flaw. If one member fails, the remaining structure damage in the adjacent member is obviously of the size to which the 0.02-inch initial flaw has grown prior to instability of the crack in the first member.
- in Fail Safe structure, the crack may arrest in a hole. In that case the remaining structure damage is simply a 0.005 inch flaw at the other side of the hole, plus its growth prior to instability. If the crack does not arrest in a hole, remaining structure damage has to be mutually agreed upon by the USAF and the contractor.

Step 10. Determine the total damage size by combining the results of Steps 8 and 9. Determine the stress-intensity factor of this damage as a function of its further growth.

Step 11. Calculate the post-arrest crack propagation curve, using the stress-intensity factors determined in Step 10 and follow the same procedure as in Steps 2, 3, and 4.

Step 12. By using the results of the residual strength analysis (Section 4) plot the critical crack size for the applicable level of remaining structure inspectability; five levels are available. If the life satisfied the requirement for the selected inspection, the structure qualifies as Fail Safe structure provided that the residual strength of the remaining structure at the moment of arrest is adequate. If neither of these requirements is met, the structure does not qualify. In that case, there are two options:

- redesign (e.g., detail design of adjacent structure) or lower stress level.
- try to qualify the structure as Slow Crack Growth structure by following Steps 1 through 6 (larger initial flaw sizes and longer crack lives are specified in that case).

The following example illustrates, in a much simplified example, the interaction of these decisions and some of the information which can be obtained from the basic crack growth analysis. This example is illustrative only and many of the simplifying assumptions would not be valid for actual design purposes.

A Simplified Example

It is not immediately obvious whether it is always advantageous to qualify a structure as non-inspectable. This subsection intends to illustrate in which cases higher design stresses can be allowed if the non-inspectable qualification is selected, and in which cases an inspectable qualification would allow higher design stresses. Subsequently, the other advantages and disadvantages of the two cases will be briefly considered.

For Slow Crack Growth structure the required crack-growth life for the non-inspectable case (2 lives from 0.05 inch to critical) is on the order of four times the required life for depot level inspectability (1/2 lifetime from 0.25 to critical). The same holds for Fail Safe structure (1 lifetime from 0.05-inch to critical, and ¼ lifetime from 0.25 to critical).

Crack-growth curves usually show a sharp rise towards the end of the life. This raises the question whether the structure would not always qualify as non-inspectable if it qualifies as depot level inspectable. For example, in Figure 6.1.1, if CG covers ¼ lifetime would not AF be at least 1 life; and similarly if CE covers ½ life would not BE at least cover 2 lives? If this were so, a depot-level inspectable structure would always qualify as non-inspectable. (A non-inspectable structure would not always qualify as depot level inspectable, however.) Then the inspectable case would be superfluous, since the non-inspectable qualification would always permit the higher design stress.

If the initial damage of 0.05 inch consists of through cracks in skin panels, it can easily be shown that the crack-growth life from initial flaw size to failure is always more than four times the life from 0.25 inch (through crack) to failure. However, this does not hold for the case of cracks at holes. In the following example, an approximate derivation shows in which cases depot-level inspectable qualification would allow higher stresses than non-inspectable structure, and vice versa. It should be emphasized that this example is only an approximation. The results should not be used as a basis for design; each new structure should be considered as a separate case, and be analyzed as such.

The stress-intensity factor for a cracked hole can be given as:

$$K = \beta\sigma\sqrt{\pi a}$$

For simplicity, a fourth power law for crack growth is assumed:

$$\frac{da}{dN} = \phi C(\Delta K)^4$$

where ϕ is an arbitrary retardation factor, used as an average for the whole spectrum (it would be different for different spectra, but this is irrelevant since ϕ will disappear during the derivation). The growth rate can be integrated to give the crack-growth life as:

$$N = \int_{a_i}^{a_c} \frac{da}{\phi C(\Delta K)^4} = \frac{1}{\pi^2 \phi C \sigma^4} \int_{a_i}^{a_c} \frac{da}{\beta^4 a^2} \qquad (6.1.1)$$

In this equation, a_i is the initial flaw size, a_c is the critical crack size, and β is a function of crack length and hole diameter. For the non-hole case where β was independent of crack length (for simplicity assume $\beta = 1$), it would follow that:

$$N = \frac{1}{\pi^2 \phi C \sigma^4}\left(\frac{1}{a_i} - \frac{1}{a_c}\right) \tag{6.1.2}$$

Also:

$$\frac{N_{LT}}{N_{DM}} = \frac{\dfrac{1}{a_{iLT}} - \dfrac{1}{a_{cLT}}}{\dfrac{1}{a_{iDM}} - \dfrac{1}{a_{cDM}}} \tag{6.1.3}$$

where the subscript *LT* refers to the non-inspectable case, and *DM* refers to the depot-level inspectable case.

Using the proper function for β for a radial crack at a hole, Equation 6.1.1 was evaluated to give the equivalent of Equation 6.1.3. For Slow Crack Growth structures, a_{iLT} = 0.05-inch and a_{iDM} = 0.25 inch. The critical cracks a_{cLT} and a_{cDM} were taken equal, because the last part of the crack-growth curve is very steep, (i.e., the difference in life would only be small if $a_{cLT} \neq a_{cDM}$). For Fail Safe structures, a_{iLT} = 0.25 inch. Also here a_{cLT} and a_{cDM} were taken equal.

On the basis of these numbers, the equations were numerically evaluated as a function of the critical crack size (a_c) for various hole sizes. The results are shown in Figures 6.1.2 for Slow Crack Growth and 6.1.3 for Fail Safe. The abscissa gives a_c; it could be converted into K_{Ic} (or K_c) since

$$a_c = \frac{K_{Ic}^2}{\pi \beta^2 \sigma_{DM}^2}$$

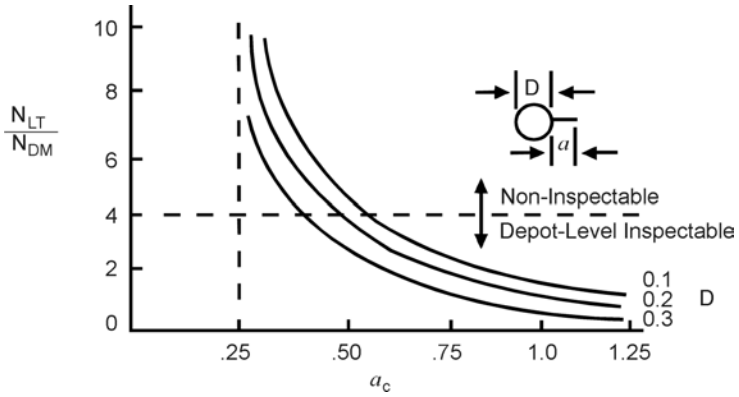

Figure 6.1.2. Design Curve for Slow Crack Growth Structure

For cracks at holes, the ratio N_{LT}/N_{DM} becomes smaller than 4 above a certain value of a_c (when the material has a sufficiently high toughness). The larger the hole diameter, the smaller the crack size at which N_{LT}/N_{DM}<4. In view of the small initial crack size (more life is spent in crack growth to 0.25 inch) these numbers are somewhat larger for Fail Safe structures (Figure 6.1.3).

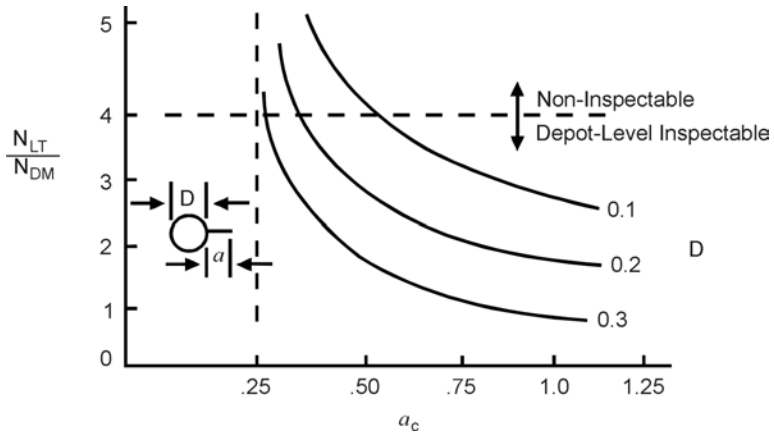

Figure 6.1.3. Design Curve for Fail Safe Structure

In the regime $N_{LT}/N_{DM} > 4$, it is easier to qualify the structure as non-inspectable. If the total life from a_i to a_c just covers two lifetimes (1 life for Fail Safe structure, the life from 0.25 to a_c will fall short of ½ life (¼ life for Fail Safe structure). The crack-growth life might be so long that it still qualifies as both inspectable and non-inspectable. That means that the structure is oversized.

As an example, consider a Slow Crack Growth structure with a_c = 0.35-inch and D = 0.2-inch. According to Figure 6.1.2 this would have $N_{LT}/N_{DM} \approx 6$. For the structure to qualify as depot-level inspectable, N_{DM} has to be at least ½ life. Then N_{LT} would be at least 3 lives (N_{LT}/N_{DM} = 6), whereas 2 lives would be adequate to qualify as non-inspectable. If crack-growth is assumed approximately inversely proportional to σ^4 (since $da/dN = C\Delta K^4$) the design stress could be increased by a factor of $(3/2)^{1/4} \approx 1.11$. The structure would still qualify as Slow Crack Growth, non-inspectable, but not any more as depot-level inspectable (N_{DM} would only be 1/3 life).

On the other hand, if the toughness were high enough to give a_c = 0.75 inch, an inspectable structure could be designed to a higher stress. For D = 0.2 inch, the ratio N_{LT}/N_{DM} would be on the order of 2.5 (Figure 6.1.2). If N_{LT} would still be equal to 2 lives, then N_{DM} would be 2/2.5 = 0.8 life. In order to qualify for depot-level inspectability, the stress could be raised by a factor of $(0.8/0.5)^{1/4}$ = 1.12. In that case, N_{DM} would be ½ life, but N_{LT} would only be 2.5 x 0.5 = 1.25 lives. Hence, qualification as non-inspectable would require 12 percent lower stress than qualification as depot-level inspectable.

Similar examples can be given for Fail Safe structure. The smaller initial crack sizes work slightly in favor of the non-inspectable qualification. It should be borne in mind, however, that the primary crack-growth requirements here may not be decisive for the design, because the remaining structure damage requirements have to be met also.

As might be expected, longer critical crack sizes favor qualification as depot-level inspectable at higher allowable stresses than qualification as non-inspectable. Longer critical crack sizes are also beneficial for the total crack-growth life. Therefore, qualification as non-inspectable is more easily attainable with high toughness materials.

A depot-level inspectable structure has advantages and disadvantages. Safety is ensured by sufficiently slow growth of cracks of inspectable sizes (large critical crack size) and by periodic inspections. However, the necessity of inspection is a burden to the operator, and it may make

the design less attractive. Besides, safety does depend on the adequacy of inspections. If a crack is not detected in a timely manner, failure will still occur.

Non-inspectable structures will generally be somewhat heavier. Safety is ensured by a sufficiently long crack-growth life. The inadequacies and deficiencies of the damage tolerance analysis (which are the same as for inspectable structure) are not partly compensated by periodic inspections. If the crack growth analysis would be a factor 2 in error, a catastrophic failure might still occur within one lifetime. This could be prevented if the structure were inspectable.

The latter considerations are less applicable to Fail Safe structures. Their safety is ensured by adequate remaining structure damage behavior, and by the fact that the large damage after load path failure (or instability and arrest) is easier to detect. Consequently, pre-instability requirements can be less stringent, and are more of economical significance than in the case of Slow Crack Growth structure.

6.2 Damage Development And Progression

Fatigue-crack-growth prediction is complicated by the assumptions that have to be made for the progression of damage through the structure (continuing damage and remaining structure damage). These damage assumptions are specified in JSSG-2006 Table XXX and will not be repeated here. This section will discuss interpretation of these requirements through a series of three examples of increasing complexity. The examples pertain to a Slow Crack Growth component, a Multiple Load Path Dependent, Fail Safe structure, and a Crack Arrest, Fail Safe structure, in this order. They are illustrations of the analysis procedure. No general rules can be given.

6.2.1 Slow Crack Growth Structure

The first example is a heavy-section spar cap (Figure 6.2.1a). The spar cap will be treated as Slow Crack Growth structure. The initial flaw has to be assumed at the most critical location. Assume that this is location A (Figure 6.2.1a). Due to assembly drilling the skin is assumed to be flawed also. If there is load transfer from the cracked spar cap to the skin, it should be taken into consideration. The damage development for the spar cap is shown schematically in Figure 6.2.1b, the change of the stress-intensity factor is shown schematically in Figure 6.2.1c.

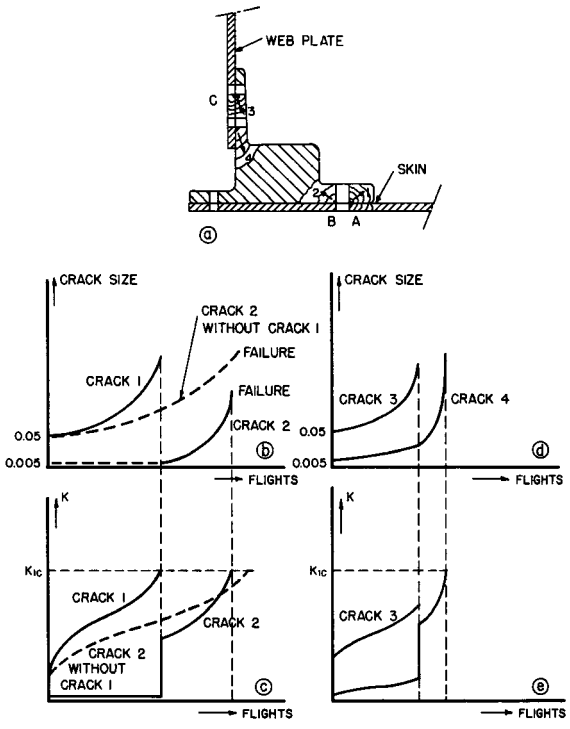

Figure 6.2.1. Damage Development in Slow Crack Growth Structure

Crack 1 starts as a 0.05 inch crack. It grows until the remaining ligament fails at $K = K_{Ic}$. The continuing damage is a 0.005 inch flaw at the other side of the hole (point B). Its prior growth need not be considered, since the primary damage terminated by ligament failure (JSSG-2006 paragraph A3.12.1e). Hence, it may be assumed to have been stationary thus far.

At ligament failure, crack 2 is suddenly introduced and the stress-intensity factor is determined by the total damage size, consisting of the failed ligament, the hole, and a 0.005 inch crack. This damage grows to failure by the growth of crack 2.

Now consider the case that B is the critical location (Figure 6.2.1a). In that case, crack 1 would be absent (ligament intact), but crack 2 would start at 0.05 inch (dashed lines in Figure 6.2.1b,c). Due to the absence of crack 1 it will grow slower.

Now assume that C is the most critical location. This case is depicted in Figure 6.2.1d, e. Crack 3 will start as a 0.05 inch crack, and terminates in the next hole. Continuing damage is a 0.005-inch crack at the other side of the hole, plus its prior growth, Δa, must be assumed (JSSG-2006 paragraph A3.12.1e). Contrary to the previous case, the 0.005 inch crack was growing previously. Its independent growth, Δa, has to be calculated. Due to this previous growth there is an increase of K. When crack 3 terminated in the next hole the stress-intensity factor of crack 4 jumps, because crack 3 and 4 together now constitute the total damage. Therefore, the growth of crack 4 will be much faster than before.

6.2.2 Multiple Load Path, Fail Safe Structure

The second example is academic, but illustrative. It is a multiple load path dependent beam consisting of members A, B, C (Figure 6.2.2a). Assume that crack 1 is the critical crack. (If the critical location was at the other side of the hole, damage development would be similar as in Figure 6.2.2). Due to assembly drilling the two members, A and B should both be assumed flawed. The damage development is shown in Figure 6.2.2b, c.

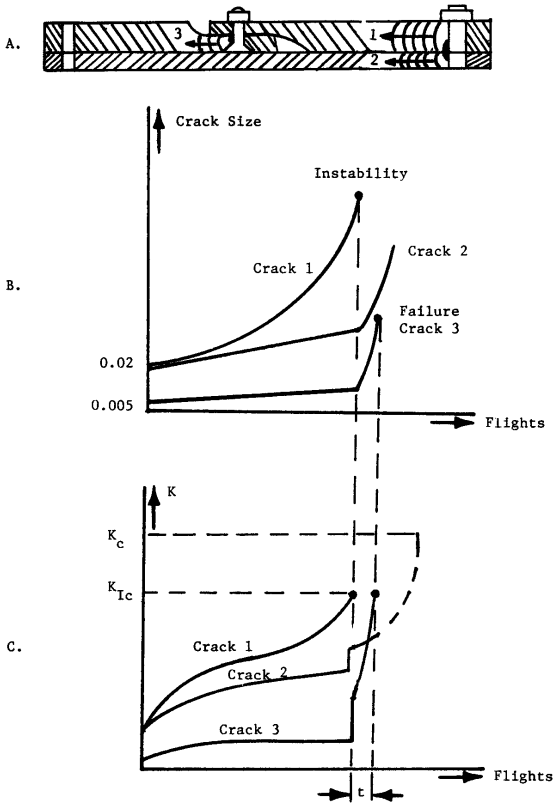

Figure 6.2.2. Damage Development in Multiple Load Path, Fail Safe Structure

Cracks 1 and 2 both start as 0.05 inch flaws. Crack 1 is assumed to grow faster, and when $K = K_{Ic}$ rapid crack propagation (instability) will occur at which point member A is assumed failed. Remaining structure damage has to be assumed in the adjacent member (crack in member C). It is a 0.005 inch crack plus its prior growth, Δa.

Due to member failure the stress-intensity factors of all cracks will show a jump. Therefore, cracks 2 and 3 will grow much faster than before: Final failure will occur when the stress-intensity factor (K) of crack 3 reaches K_{Ic}, or when K of crack 2 reaches K_c, whichever occurs first. (It is assumed that plane stress prevails in the thin member B). The period between failure of member A and final failure (indicated by t in Figure 6.2.2c) has to be adequate for one of the options of remaining structure damage inspection. Otherwise, the structure would not qualify as Multiple Load Path, Fail Safe structure.

6.2.3 Crack Arrest, Fail Safe Structure

The last example is Crack Arrest Fail Safe structure consisting of a skin with tear straps, as shown in Figure 6.2.3a. Due to assembly drilling, skin, tear strap and shear clip are assumed to have 0.02 inch corner flaws, giving rise to cracks 1, 2, and 3. Damage development is shown in Figure 6.2.3b. Stress-intensity factor (K) development is shown in Figure 6.2.3c. Corresponding points on the flights axes are indicated by A, B, C, and D.

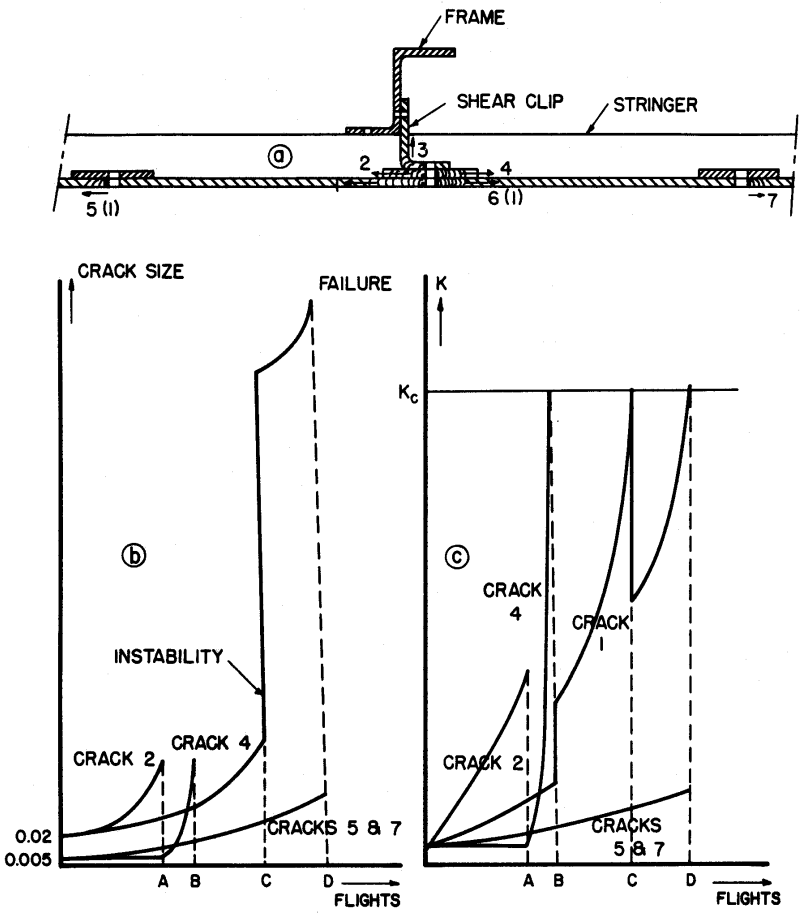

Figure 6.2.3. Damage Development in Crack Arrest Fail Safe Structure

First consider cracks 2 and 4 in the tear strap. When crack 2 terminates due to ligament failure, the continuing damage is a 0.005 inch crack 4 without prior growth. From point A onwards, growth of crack 4 will be rapid until the tear strap fails.

The independent previous growth of crack 1 was slow. However, upon tear strap failure there will be load transfer from the cracked tear strap to the skin. Consequently, there will be a sudden increase of the stress-intensity factor of the skin crack resulting in accelerated growth. When K of the skin crack reaches K_c, instability (rapid crack growth) will occur, and the crack will run to the left tear strap. Due to load transfer from the skin to the tear strap, K will drop (point C), and the instable crack will be arrested at the tear strap.

Subsequent damage development is strongly dependent upon remaining structure damage assumptions (which may be mutually agreed upon by the USAF and the contractor). In this particular example, the most logical damage would be a 0.005 inch crack at both 5 and 6 (only prior growth of 5 should be considered). At the moment of instability of crack 1, the shear clip will most likely be failed, because it was cracked already. Hence, there will be little load transfer to the frame. Therefore, it is most likely that crack 6 becomes unstable immediately in conjunction with crack 1, so that the skin crack would be from the left to the right tear strap. This case would be as in JSSG-2006 paragraph A3.12.1d. (A two-bay crack with the central strap failed). It is questionable whether also the frame should be assumed cracked. Upon failure of the shear clip, continuing damage requirements would strictly apply to the frame, at the next fastener hole (away from the primary damage source). The complexity of these assumptions is obvious.

Further growth of the skin crack (with continuing cracks 5 and 7) will take place until K_c is reached again. The period CD would have to be adequate, otherwise the structure would not qualify as Crack Arrest Fail Safe structure.

6.3 Slow Crack Growth Structure

The purpose of this example is to demonstrate the lowest level of damage tolerance analysis that can be undertaken. This example problem will be set up to use only a hand-held calculator for all calculations. Some simplifying assumptions to obtain engineering estimates will also be demonstrated.

EXAMPLE 6.3.1 Wing Attachment Fitting

Problem Definition

A training aircraft has been discovered to have cracks in the wing attachment fitting. A redesign and retrofit will be necessary. Cracks have been found in two aircraft that have been grounded. The problem is to determine inspection intervals for the remainder of the force until the modifications can be performed.

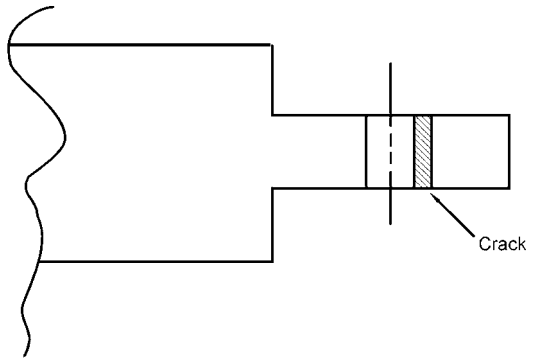

Wing Attachment Fitting

Material Property Data

The material for the attachment fitting is 7079 aluminum forging with the following properties:

$K_{Ic} = 22.5$ ksi$\sqrt{\text{in}}$

and a Forman equation describes the crack growth rate behavior:

$$\frac{da}{dN} = \frac{2.25\times10^{-7}(\Delta K)^{3.0}}{(1-R)*22.5-\Delta K}$$

Structural Loads and Stress History

Each aircraft is equipped with a counting accelerometer. The data has been collected and published in the form of n_z counts per 500 hours, as shown in the table.

The stress analysis for the aircraft gives the l-g stress as 7.0 ksi., and using this, the n_z values are converted to stresses. Assuming the 1-g stress is the minimum stress, the stress ratios R can be calculated. These values are also shown in the table.

Stress History for 500 Hours

n_z	Counts/500 Hours	S_{max} (ksi)	R
5.1	80	35.7	0.20
4.5	1200	31.5	0.22
3.5	2500	24.5	0.29
3	12500	21.0	0.33
2	22000	14.0	0.50

Initial Flaw Sizes

The structure is assumed to be slow crack growth structure. A special inspection program has demonstrated an initial flaw size inspection capability of 0.02 inches.

Geometry Model

The critical configuration is determined to be a radial through flaw at the edge of the hole. The stress-intensity factor for this geometry, while well known, is not amenable to closed form solutions. However, applying the approximation techniques discussed in Section 11 leads to an approximate expression for K as follows:

$$K = 3\sigma_{max}\sqrt{\pi a}$$

This equation represents a K solution for a through crack in a plate multiplied by the stress concentration factor, K_t, for a hole. Using this expression the initial K's for each load level are determined, as shown in the table.

Residual Strength Diagram

The residual strength diagram for this configuration is obtained simply by setting K in the above equation equal to K_{Ic} and solving for a, which gives:

$$a_{cr} = \frac{K_{I_c}^2}{9\pi\sigma^2}$$

Plotting this function gives the residual strength diagram, as shown.

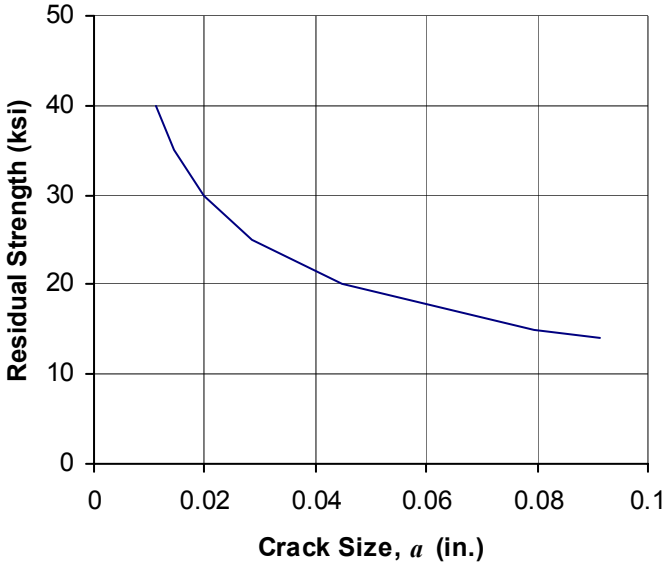

Residual Strength Diagram

Fatigue Crack Growth Analysis

The basic purpose of this analysis is simply to determine the life under the given stress history. Since the shape of the crack growth curve is not of prime importance because of the imminent retrofit, a damage index approach can be used to estimate the life. The Forman Equation may be integrated to give the life from an initial crack size to critical crack size for n_z level.

$$\int_0^{N_f} dN = \int_{a_0}^{a_f} \frac{(1-R)22.5 - \Delta K}{2.25\times10^{-7}(\Delta K)^{3.0}}\, da$$

Performing this integration gives:

$$N_{allow} = \frac{2}{2.25\times10^{-7}\pi(1-R)^2\sigma_{max}^2}\left[\frac{K_c}{K_o} - 1 - ln\frac{K_c}{K_o}\right]$$

This function is evaluated to give N_{allow} for each stress level in the history. The results are shown in the next table.

Using a fatigue damage analogy, a damage index (DI) is calculated for each stress level by dividing the number of counts in 500 hours by N_{allow}. For n_z = 5.1, the damage index is:

$$DI = \frac{80}{2320.9} = 0.034$$

The life is then obtained by dividing 500 hours by the sum of the damage indices:

$$Life = \frac{500}{\sum DI} = \frac{500}{1.03} = 486$$

Inspection Intervals

The life calculated from the previous analysis is 486 hours under the given usage. Based on the simplifying assumptions made in the analysis an inspection interval of 200 hours until the retrofits are made should be recommended.

Crack Propagation Analysis Using Linear Damage Indices

n_z	Count/500 Hours	S_{max} (ksi)	R	K_o (ksi√in)	N_{allow}	Damage Index
5.1	80	35.7	0.20	8.49	2320.92	0.034
4.5	1200	31.5	0.22	7.49	4260.63	0.282
3.5	2500	24.5	0.29	5.83	13957.88	0.179
3	12500	21.0	0.33	4.99	28875.60	0.433
2	22000	14.0	0.50	3.33	222173.42	0.100
						Sum = 1.027

6.4 Multiple Load Path Structure

The basic purpose of the example is to illustrate two facets of damage tolerance design. The first is that, while a structure may appear to fit one category of JSSG-2006 by virtue of its geometry, the loading and damage progression may force the structure to be qualified under another category. Secondarily, this example attempts to illustrate the use of some of the more advanced techniques described in Section 11.

EXAMPLE 6.4.1 Wing Spanwise Splice

Problem Definition

The problem is to determine the adequacy of the base or depot level inspection intervals for an existing cargo aircraft wing structure. The fracture critical location in the wing box has been described as the lower surface spanwise splice. In addition, an attempt will be made to qualify the structure as Multiple Load Path Fail Safe structure per JSSG-2006.

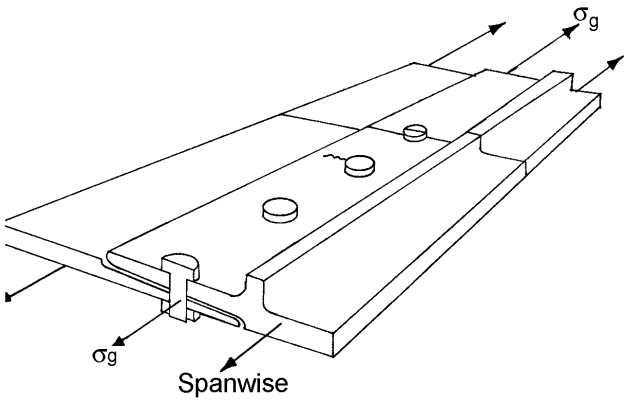

Spanwise Splice, Wing Lower Surface

Material Property Data

Spanwise splice material is 7075-T6511 extrusion

K_{Ic} = 25 ksi $\sqrt{in.}$

K_c = 50 ksi $\sqrt{in.}$

$$\frac{da}{dN} = \frac{2.74x10^{-10}(\Delta K)^{4.0}}{(1-R)50.0-\Delta K}$$ (Forman equation)

Structural Loads and Stress History

Input stresses are defined for a typical usage mission mix of 14 missions consisting of 12 logistics missions and 2 training missions with touch-and-go landings. Typical stresses for logistics and training missions are shown in the following tables. The mission mixes to be considered are:

a) Logistics missions only

b) Training missions only

c) Heavy logistics deliver and lightweight return

d) Mixture of logistics and training missions of typical usage.

Typical Logistics Mission Spectrum

Layer	Maximum Stress (ksi)	Minimum Stress (ksi)	Cycles per Layer
1	14.0	0.0*	1
2	14.0	12.6	325
3	16.0	10.0	32
4	17.6	8.6	2
5	19.3	6.3	1
6	17.6	8.6	2
7	16.0	10.0	32
8	14.0	12.6	325

*Actual minimum GAG stresses were approximately –12.0 ksi (compressive). Negative stresses were truncated to zero for analysis.

Typical Training Mission Spectrum

Layer	Maximum Stress (ksi)	Minimum Stress (ksi)	Cycles per Layer
1	8.0	0.0*	1
2	8.0	7.0	429
3	10.0	6.4	64
4	12.0	4.4	4
5	13.7	2.7	1
6	8.0	7.0	429
7	10.0	6.4	64
8	12.0	4.4	4
9	13.7	2.7	1
10	8.0	0.0*	1
11	8.0	7.0	429
12	10.0	6.4	64
13	12.0	4.4	4
14	13.7	2.7	1
15	8.0	0.0*	1
16	8.0	7.00	429
17	10.0	6.4	64
18	12.0	4.4	4
19	16.1	0.7	1
20	8.0	0.0*	1
22	10.0	6.4	64
23	12.0	4.4	4
24	13.7	2.7	1
25	8.0	7.0	429
26	10.0	6.4	64
27	12.0	4.4	4
28	8.0	0.0*	1
29	8.0	7.0	429
30	10.0	6.4	64
31	12.0	4.4	4

*Actual minimum GAG stresses were approximately –6.0 ksi (compressive). Negative stresses were truncated to zero for analysis.

Initial Flaw Sizes

The splice structure is assumed to be a multiple load path structure. It is dependent structure because of assembly drilling of fastener holes. The damage assumptions are:

- Initial - 0.02 inch radius corner crack at edge of hole toward free edge (each plank of splice) for Multiple Load Path Fail Safe qualification,
  - 0.05 inch for Slow Crack Growth qualification
- Continuing - 0.005 inch radius corner crack at diametrically opposite side of hole in each plank.

Geometry Model

The finite-element-modeling approach was selected since this type of joint might contain some load transfer. Two levels of finite-element models were developed for the structural splice. The large first level model contains ten fastener holes with fasteners and over-layed grid systems in the reduced splice area which are coupled through the centroid of each fastener. The second level model is a much finer grid model of a section of the first level model. Boundary nodal point and fastener displacements of the first level model were applied to the second level model for fracture mechanics analysis. The contact boundary conditions of the fastener and plate were those of a loose "neat-fit" pin.

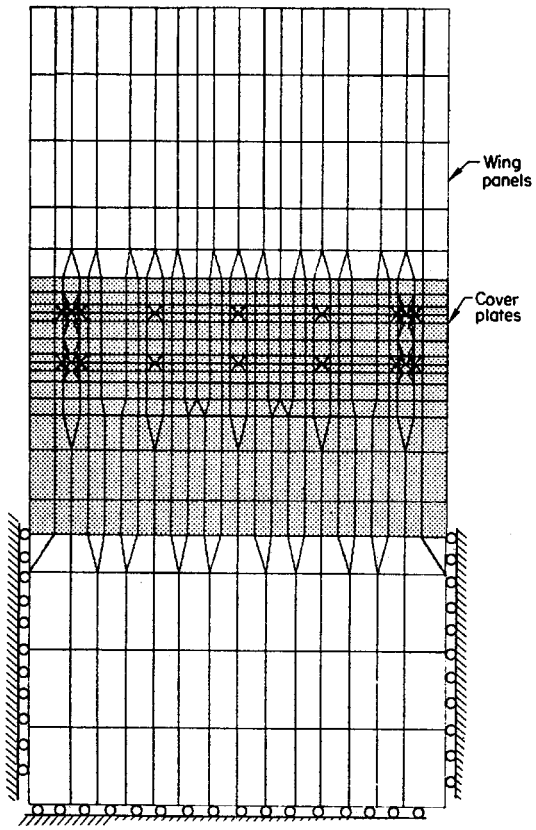

Joint Finite Element Model

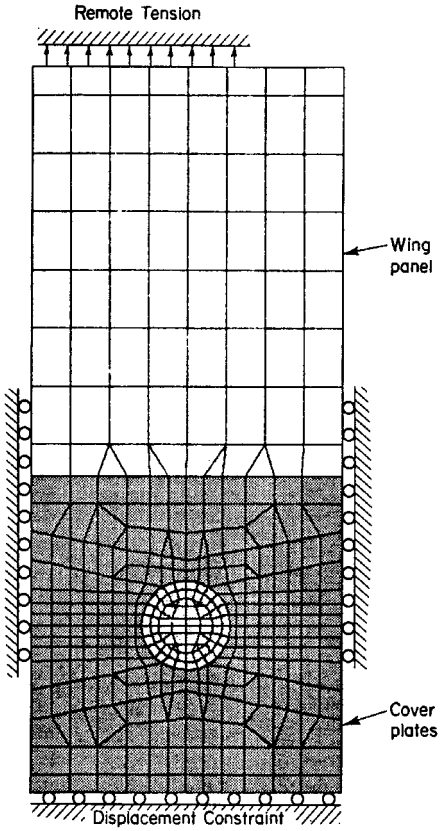

Criteria Hole Finite Element Model

The variation of stress-intensity factor (K) with crack size as derived from this analysis is shown in the plot. The work-energy and crack-opening displacement methods show essentially the same results. Details of this type of derivation are covered in Section 11.

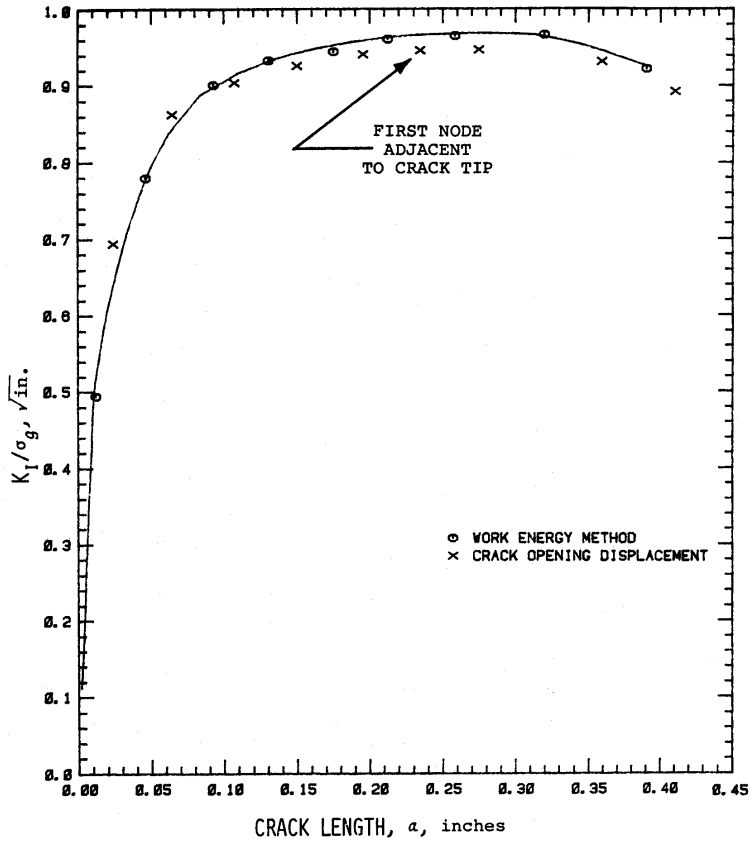

Stress Intensity Factor Coefficient as a Function of Crack Size (to Free Edge)

The basic stress analysis of this joint demonstrated that each member of the splice is equally stressed and there was no load transfer. This means that both planks, if cracked, will crack at the same rate and the two planks will become critical at the same time. Therefore, the structure will never meet Multiple Load Path Fail Safe structure requirements and must be analyzed as Slow Crack growth with corresponding initial damage sizes.

Residual Strength Diagram

The residual strength diagram was generated based on the following failure criteria:

- Corner crack instability based on K_{Ic}
- Through-the-thickness crack instability based on K_c

The residual strength in the large crack region is based on a through-the-thickness edge crack. The figure shows the residual strength diagram for the structure based on the above assumptions and the stress-intensity-factor analysis. The limit load stress level is assumed approximately 35 ksi.

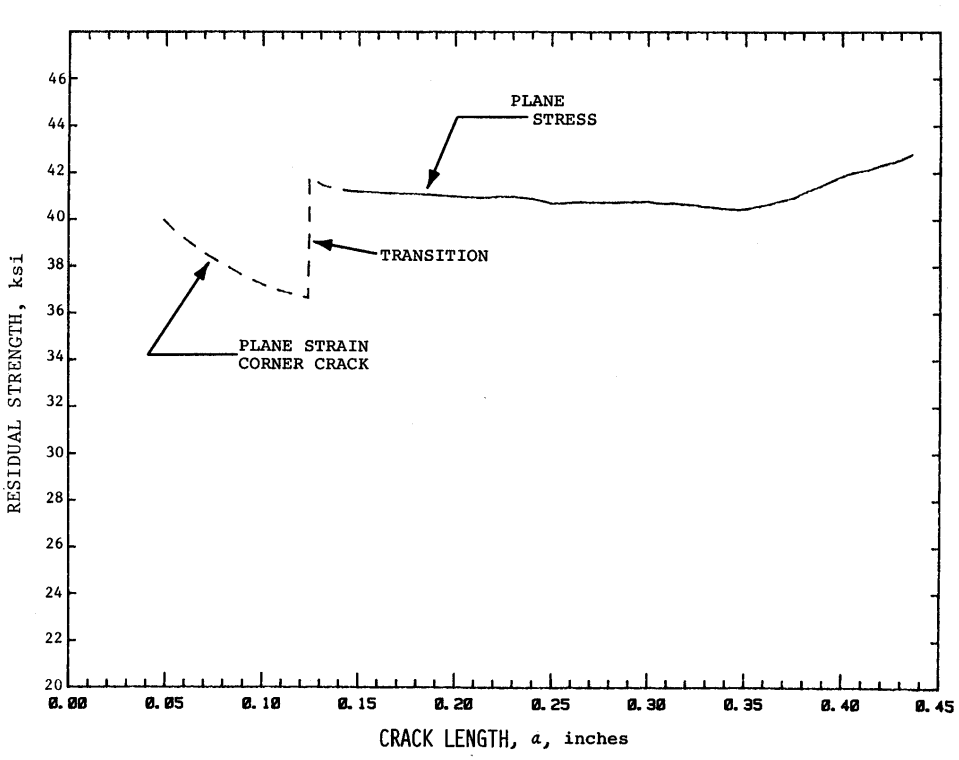

Residual Strength Curve of Spanwise Splice

Fatigue Crack Growth Analysis

The spectra used in the growth analysis consisted of the typical usage mix of 14 missions as mentioned previously. The stresses were ordered in a low-high-low sequence per mission. Other missions were logistics only, training only, or heavy logistics only. The mission mixes considered in the analysis were:

- Logistics mission only
- Training mission only
- Logistics and training missions (typical usage)
- Heavy logistics

The next figure shows the fatigue-crack-propagation behavior of the splice subjected to the four mission mix spectra starting from the initial 0.050 inch corner flaw at the edge of the hole.

There are two sets of curves in the figure. The linear curves represent linear solutions that ignore load interaction (retardation) effects. The linear solutions are seen to be conservative by at least a factor of three. Even more significant for life and inspection interval predictions is the fact that, when considering mission mix variations, linear analysis may not even rank the various stress histories correctly. The linear analysis shows the "logistics only" mission to be more severe than the various mission mixes. However, full consideration of load interaction effects shows this to be the most benign of the four variations considered.

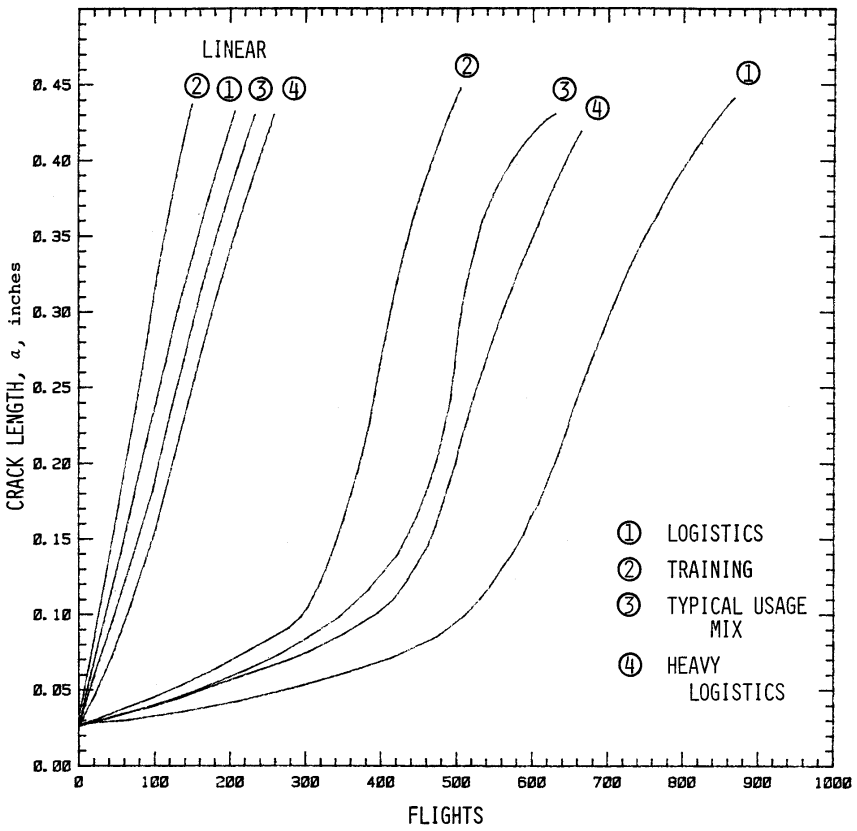

Fatigue Crack Propagation Behavior of Spanwise Splice Under Various Spectra

Inspection Intervals

Based on the spectrum loading fatigue-crack-propagation results, the qualification and the required inspection intervals can be determined. The original design life of the structure was 30,000 hours with a quarter life depot or base level inspection interval of 7500 hours.

For qualification as Slow Crack Growth Non-Inspectable structure, the analytical crack-growth life should be 2 lifetimes or 60,000 hours. For qualification as Slow Crack Growth Depot Level Inspectable structure, the crack-growth life from a 0.25 inch in-service flaw to critical should be 1/2 lifetime or 15,000 hours. These requirements cannot be met.

Based on an average training flight of 3.0 hours and an average logistics flight of 4.0 hours, the following inspection intervals could be recommended instead:

Training Missions = 645 hours

Logistics Missions = 1450 hours

Typical Usage Mix = 1875 hours

Heavy Logistics = 1375 hours

6.5 Fail Safe Multiple Load Path Structure

This example will be used to demonstrate the application of damage tolerance requirements at the early design stages of fail safe structure. This example will demonstrate the steps necessary to establish the crack arrest capability of the structure and present the trade-offs necessary to establish stringer spacing and sizing in built-up structure.

EXAMPLE 6.5.1 Skin Stringer Construction

Problem Definition

A transport wing is being designed to satisfy the requirements of JSSG-2006. Three basic geometries must be evaluated to determine the "optimum" crack arrest structure that will then be evaluated for life and inspection intervals. The wing will be designed for a 30,000-hour lifetime.

Candidate Geometries

The geometric quantities are shown below. The values of the geometry parameters for the three candidates are given in the table. The stiffening ratio u is calculated as:

$$u = \frac{A_{st}}{A_{total}} = \frac{A_{st}}{A_{st} + A_{bay}}$$

$2a$ – crack length
p – fastener spacing
W – bay width
A_{st} – stringer area
A_{bay} – bay area

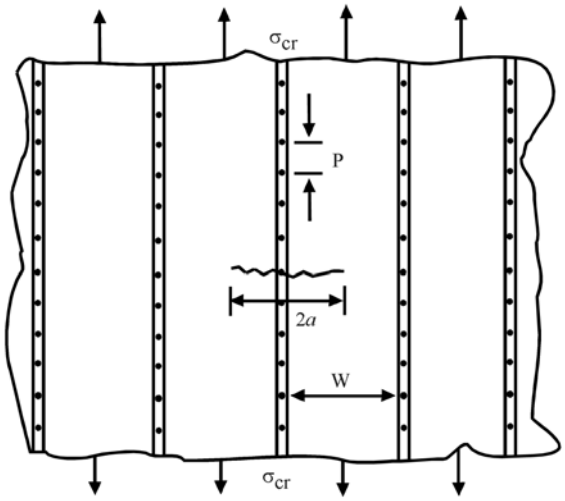

Skin-crack across stiffener

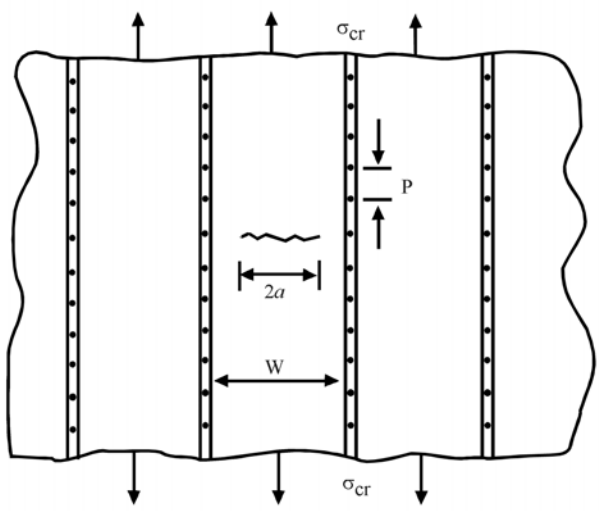

Skin Stiffener Panel Configuration

Skin-Stiffener Geometry

Skin Thickness (inch)	Z-Stiffener Cross-Section, A_{st} (inch^2)			Stiffening Ratio A_{st}/A_{total}
	Bay Width (w)			
	6.0 in.	8.0 in.	10.0 in.	
0.30	1.2	1.5	2.0	40
0.25	1.5	2.0	2.5	50
0.20	1.8	2.4	3.0	60

t_{st}/t_{sk} = 1.0, Fastener diameter D = 0.5 inch, 2D edge distance, 3D spacing

Material Property Data

The following material strength, fracture and fatigue-crack-propagation data are given as follows:

Skin Material:

2024-T3 sheet or plate

K_c = 90 ksi $\sqrt{in}$ (t = 0.2 - 0.3 inch)

$$\frac{da}{dN} = \frac{3.0 \times 10^{-6} (\Delta K)^{3.0}}{(1-R)83.0 - \Delta K}$$ (Forman equation)

Stiffener Material:

7075-T6 extruded Z-sections

F_{tu} = 77 ksi

F_{ty} = 67 ksi

Selection of "Optimum" Geometry

The structural configurations defined in the table were analyzed for residual strength and crack arrest capability. The results were determined for rigid fasteners. Complete residual strength diagrams were developed for each structural geometry: (a) stiffener failure due to skin crack, (b) skin failure with crack, and (c) fastener shear failure based on allowable per 1,000 pounds.

The three critical structural cracking conditions analyzed were as follows:

(1) A skin crack located symmetrically about a stiffener reinforcement

(2) A skin crack located symmetrically about a broken stiffener

(3) A skin crack located symmetrically at mid-bay between stiffeners

The next figure shows the critical stress or residual strength as a function of crack aspect ratios (a/w) for a skin crack across the stiffener. The residual strength of the skin, stiffener, and first fastener adjacent to the crack are shown. The skin critical stress is based on K_c and the stiffener critical stress is based on F_{tu}. The fastener parameter is σ_{cr}/Q_{cr} where σ_{cr} is the critical stress per Q_{cr} (Q_{cr} = 1000 lb). The curves shown are for 60% stiffening and were generated using methods described in Section 4.5. Similar curves would be generated for 40% and 50% stiffening. The results demonstrate an increase of residual strength with increasing percent stiffening. Residual strength decreases with increased stiffener spacing.

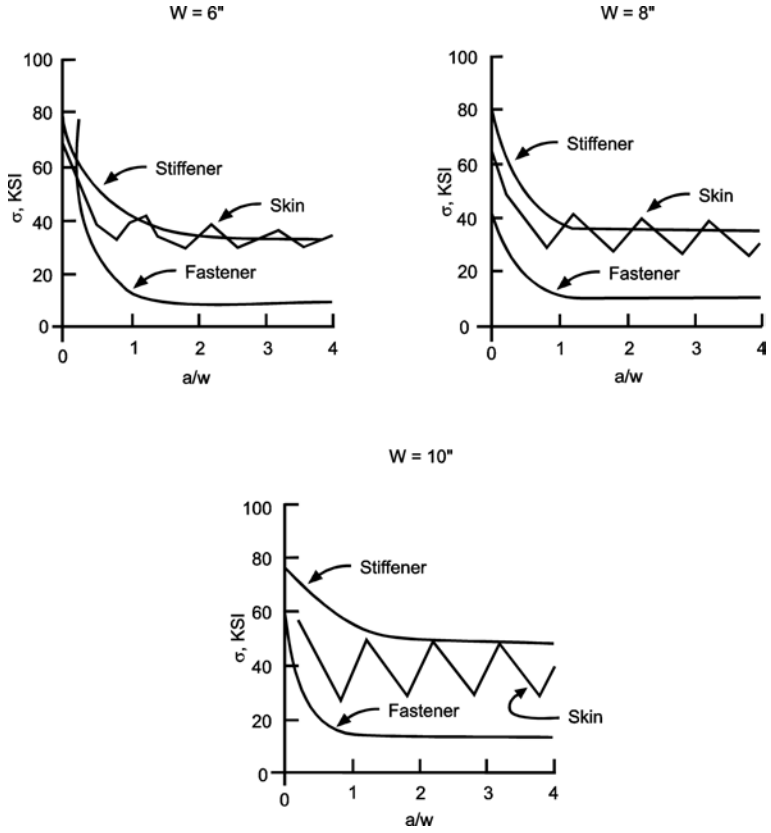

Residual Strength Diagram – Skin Crack Across Stiffener

The following figure shows the residual strength diagram for the skin stiffener panel for a crack located across a broken stiffener. The variation of residual strength with crack size is shown for the skin and the adjacent stiffeners at 40, 50 and 60 percent stiffening. The critical stress for the skin is based on K_c and the adjacent stiffener critical stress is based on F_{tu}. This structural crack condition is the most critical of the three cases. Since the stiffener is failed, the load transfer carrying capability of the stiffener is lost and actually causes the crack to open more and increase the skin stress intensity level. This case should be considered primary in Fail Safe Crack Arrest structural design.

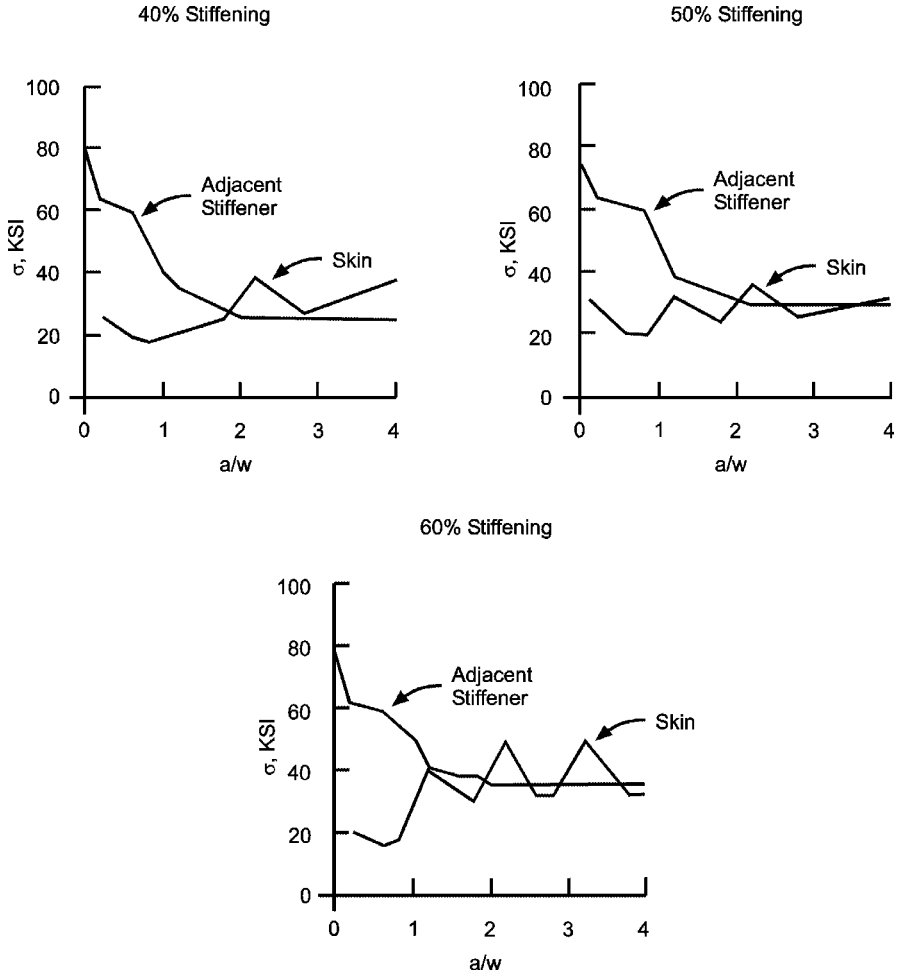

Residual Strength Diagram – Broken Stringer

The residual strength of the skin stiffened panels for a structural crack located at mid-bay are shown in the next figure. The structural geometries analyzed are the same as for a skin crack located across a stiffener. Again only the 60% stiffening curves are shown. The effect of increasing percent stiffening on increasing residual strength can be seen in the figures for each bay width. For a given percent stiffening, the residual strength of the structural panel decreases with increased bay width.

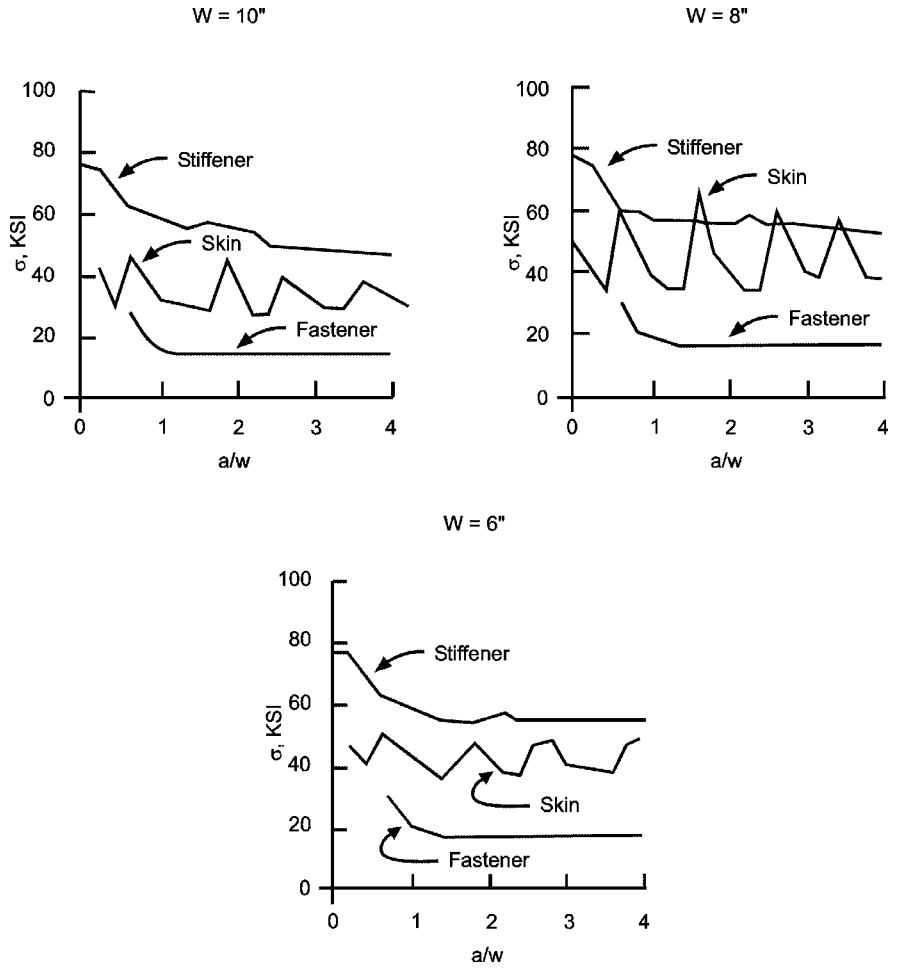

Residual Strength Diagram – Mid–Bay Skin Crack

In comparing the three cases analyzed and presented in the previous figures, the following conditions of structural instability are summarized:

(1) For a skin crack located symmetrically across a stiffener, the critical structural element is either the stiffener or skin.

(2) For a skin crack located symmetrically across a failed stiffener, the critical structural element is the skin.

(3) For a skin crack located symmetrically between stiffeners, the critical structural element is the skin.

The skin stiffener geometry results in crack-arrest capability. A skin crack that grows critical will be arrested provided the adjacent stiffeners are intact. Examination of the results of the trade study shows that the requirement to contain damage hinges on the ability of the stiffener to remain intact with a crack. Therefore, it was required to conduct fatigue-crack-propagation analysis of the skin stiffened panel for the following crack conditions:

(1) A skin crack located symmetrically about a stiffener.

(2) A crack in the stiffener with a crack in the skin.

The results of the trade study are summarized below in terms of crack arrest capability. The maximum allowable stress that can be applied to the structure for crack containment is presented as a function of bay width and percent stiffening. The "near-optimum" structural configuration selected for further analysis was:

Percent Stiffening = 60 percent

Bay Width = 7.0 inches

Fastener Diameter = 0.50 inch

3D spacing

2D edge distance

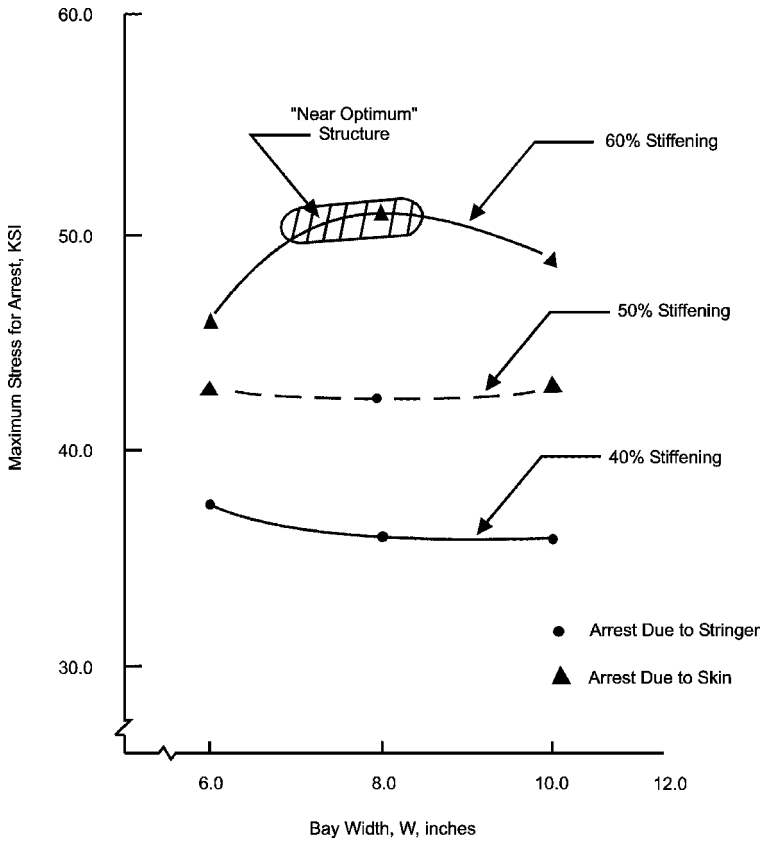

Arrest Capability of Structure (Results of Trade Study)

The selection of 60 percent stiffening was also enhanced by the crack arrest capability of the structure for a broken central stiffener situation.

Since the results of the trade study considered rigid fastener connections, the effect of fastener flexibility or deformation has to be evaluated. Using techniques described in Section 11.2 and Section 4.5, a model was developed to obtain the stress-intensity factor for this configuration. The stiffeners were simulated by a lumped stiffness finite-element mesh system. This system was over-layed on the finite-element mesh system of the skin. The mesh systems were connected through discrete nodes that simulated the fastener flexibility by "soft-springs". Crack progression was simulated by unzipping double nodes.

The variation of stress-intensity factor with through-the-thickness crack size is shown in the next figure. Comparison with the behavior of an unstiffened panel shows the decrease in stress-intensity level due to the load transfer at a given crack size. The stiffener stress concentration factor due to load transfer $(\sigma_g + \Delta\sigma_g)/\sigma_g$ and the first fastener loads are shown in the following figure.

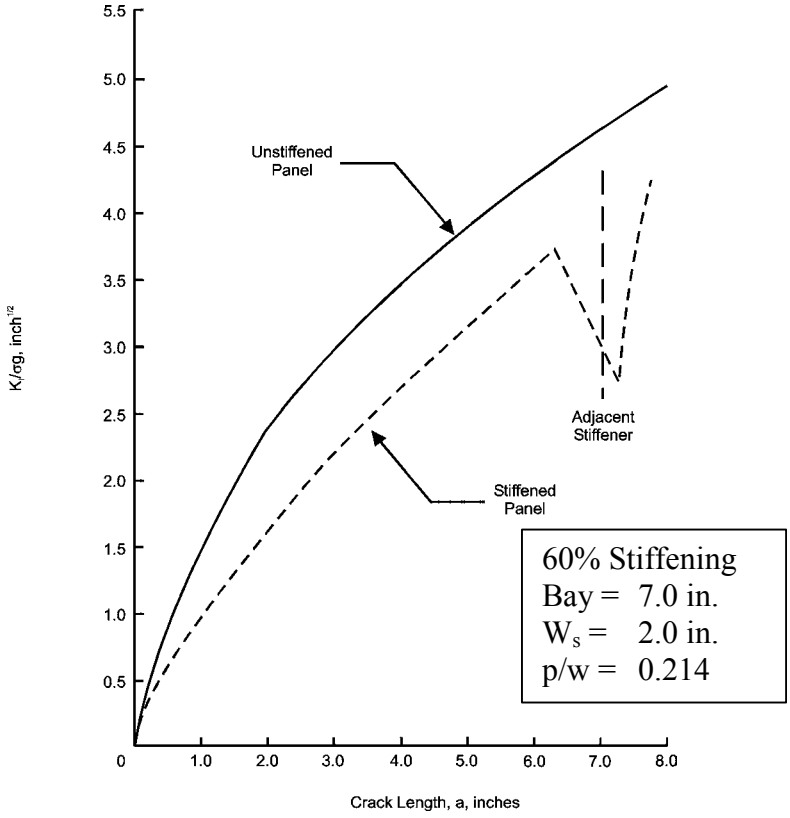

Stress Intensity Variation with Crack Length
(Crack Symmetric about Stringer)

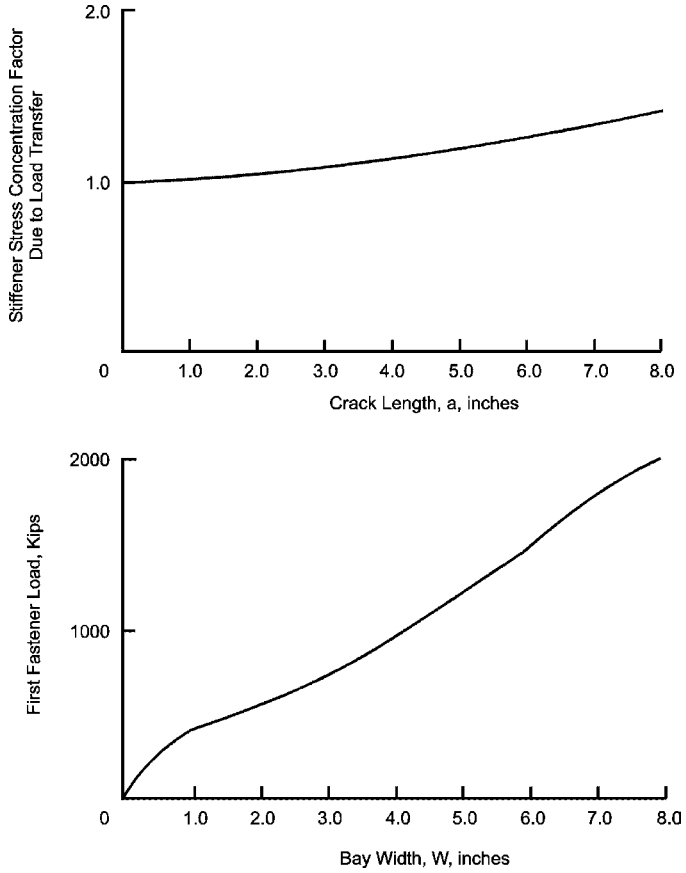

Stiffener Stress Concentration and Fastener Load Due to Load Stiffener

Damage Tolerance Analysis

In an effort to demonstrate the interrelationships between all the elements in the damage tolerance analysis, the results of all the analyses have been collected on a single figure. The most critical case is the crack in the skin with the central stringer broken. This is the case presented.

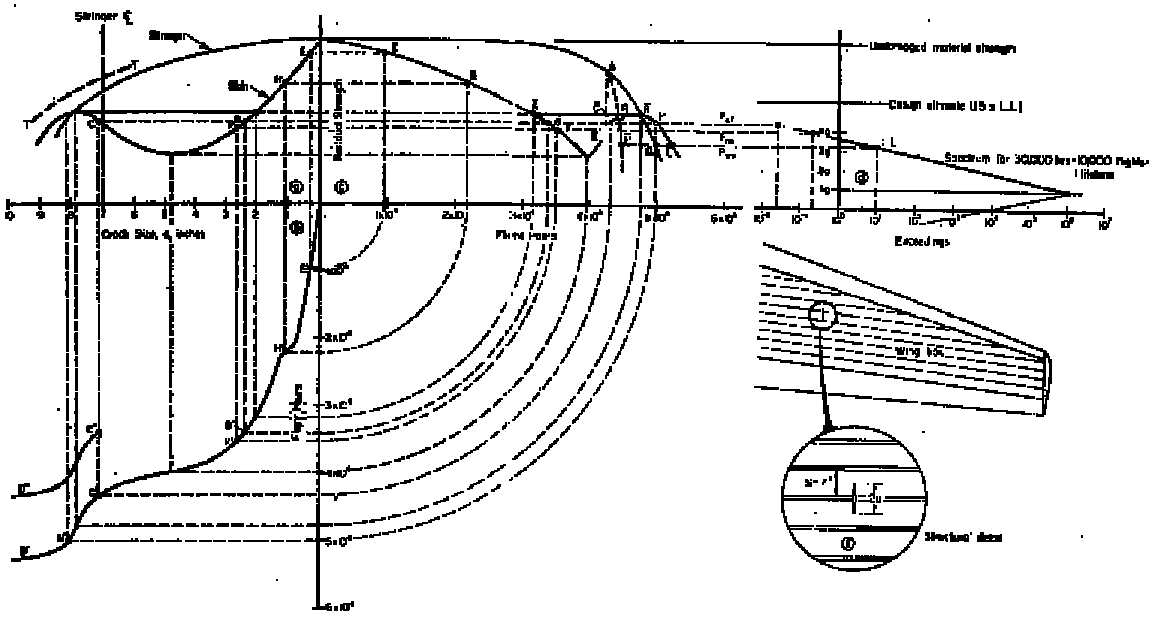

Damage Tolerant of Fail Safe Structure

The figures shows the residual strength diagram, the crack growth curve, the degradation of residual strength as a function of time, and the assumed load spectrum. The residual strength diagram and the crack growth curve are drawn in an unusual way, with the crack axis to the left and the cycle axis to the bottom. This has been done to get all plot properly positioned.

Initially, when the crack is small, the center stringer is still intact. Since the attachment holes in skin and stringer are assembly drilled, both holes are assumed initially flawed (0.05 flaw). This means that the center stringer will fail at a certain moment in time. The occurrence is shown in the crack growth curve, because it is important for the life. The residual strength diagram is only for the case with the center stringer failed, because that is the relevant situation. Corresponding points in the three diagrams are indicated by A, B, C; A', B', C'; A", B", C"; and $\overline{A}$, $\overline{B}$, $\overline{C}$,.

The assumed load spectrum is a gust exceedance spectrum for 30,000 flight hours, or 1 lifetime. Average flight time is supposed to be 3 hours, so the life is 10,000 flights. The vertical axis shows accelerations. It is assumed that the conversion to stresses is properly made, so that a point in the exceedance diagram corresponds with a point at the same level in the residual strength diagram. Limit load is assumed to be as the once-per-lifetime occurrence, which brings the design ultimate at the indicated level. The techniques described in Section 5.4.1.2 were used to develop the mission segment stress history from the load spectrum. This stress history was then used for the crack growth predictions.

The spectrum permits determination of the fail safe loads. It is assumed that the spectrum may be linearly extrapolated. Only P_{LT}, P_{DM}, and P_{WV} are indicated. The load P_{LT} is the highest load occurring in 20 lives, i.e., it has a frequency of occurrence of 5×10^{-2} in one lifetime. The Depot Level fail safe load occurs once in 5 lives, so it has a frequency of occurrence of 2×10^{-1} in one lifetime. Finally, P_{WV} occurs once in 1000 flights.

The damage tolerance requirement for intact structure concerns the growth of the initial flaw to instability, i.e., to the point at which an instability would first be possible at the given fail safe load. For a non-inspectable, intact, fail-safe structure, the initial 0.02-inch flaw may not cause

instability at P_{LT} in one lifetime. Instability at P_{LT} is first possible at $\overline{B}$. This point is at 34,000 hours which is just over one lifetime. Hence, the condition is satisfied. The instability would extend the crack from B to C. In the crack growth curve there would be a jump from B' to C", and crack growth would continue along C" D" parallel to C' D'. Instability need not occur at $\overline{B}$, since P_{LT} may not be encountered (P_{LT} could occur once in 20 lives; it may not be met at all in less than 20 lives). In that case, crack growth will continue along B' C' D'.

The possibility that the structure might qualify as Depot Level inspectable will now be considered. For Depot Level inspectability the crack growth period should be a quarter lifetime to instability at P_{DM}. The instability would first be possible at $\overline{F}$. The in-service damage depends on inspection. For normal NDI without removal of fasteners, the damage would be 0.25 inch through-the-thickness crack (a = 0.25 in.). The 0.25 inch crack is at E', the residual strength is at E. Thus, the period from $\overline{E}$ to $\overline{F}$ should be ¼ lifetime. Apparently, the structure could qualify for this.

For a close-visual, Depot-Level inspection, the in-service damage is a 2-inch crack (a = 1 inch). This crack occurs at H', with a residual strength at H. The period from $\overline{H}$ to $\overline{F}$ should cover ¼ lifetime, or 7,500 hours. Since it covers approximately 10,000 hours, the structure would still qualify as inspectable.

Apparently, there would be no problems in satisfying any one of the primary requirements for intact structure. Next consider the requirements to be met at and after instability. The residual strength at instability should be 1.15 P_{LT} or 1.15 P_{DM}, whichever is applicable.

The non-inspectable structure may show instability at $\overline{B}$. The crack will grow to $\overline{C}$ and be arrested. At that moment, the residual strength is still at $\overline{G}$. Hence, the level of $\overline{G}$ should be 1.15 times the level of $\overline{B}$. In reality, it is only 10 percent higher. Consequently, the structure does not qualify as non-inspectable after all.

The Depot-Level-inspectable structure may show instability at $\overline{F}$. The crack will be arrested at $\overline{K}$, the residual strength still being at $\overline{G}$. The level of $\overline{G}$ is 19 percent above $\overline{K}$, so that the structure would meet the requirement. Hence, the structure should be classified as Depot Level inspectable. Inspections should be called for either by NDI or close visual, since both are adequate as shown above.

The requirements for remaining structure damage call for adequate crack growth life after instability. A two-bay crack is assumed to be Walk-Around Visual detectable. In that case, the required residual strength is P_{WV}, the load occurring once in 1,000 flights. The remaining structure damage may not grow to critical at P_{WV} within 5 times the inspection interval, i.e. 50 flights. At P_{WV}, the skin crack would become critical at $\overline{L}$. However, the stringer becomes critical already at $\overline{M}$. At that point the skin crack extends to N' (or $\overline{N}$).

Instability may occur at $\overline{F}$ with arrest at $\overline{K}$. Hence crack growth from $\overline{K}$ to $\overline{N}$ should take at least 50 flights. According to the figure, this crack growth covers approximately 5,000 hours of 1,700 flights, which should be plentiful. However, at this point, the figure is deceiving, because the possibility of stringer failure by fatigue was ignored.

When the crack extends to $\overline{K}$, its propagation is slow, because of load transfer to the stringer. Therefore, the skin crack can easily meet the requirement. But the load transfer induces a high stress in the stringer, and from now on the stringer has to be assumed cracked also. This means that the line for stringer failure is likely to be modified from $\overline{GM}$ to $\overline{GP}$. This implies that a separate crack growth and residual strength analysis has to be carried out for the cracked stringer. For the purpose of illustration, suppose $\overline{GP}$ is the result of the analysis. Then the stringer will fail at $\overline{P}$. Hence, the crack growth life from $\overline{K}$ to $\overline{R}$ has to be 50 flights. This still can be met. Thus, the structure qualifies as a CAFS structure with Depot Level inspectability of the intact structure, and Walk-Around Visual inspectability of remaining structure damage.

One thing still has been neglected. If the stringer starts cracking, it will become more compliant. This means that load transfer will be somewhat reduced. As a result, the stringer life will be slightly longer, whereas crack growth in the skin will be slightly faster. Since the life from $\overline{K}$ to $\overline{R}$ is 500 flights (1500 hours), this correction will not affect the conclusion that the structure meets the requirements.

Summary

This particular example does not present the details of the analysis to the extent that others in this chapter and throughout the handbook do. The emphasis of this example is on interpreting the analysis. While the figure seems rather imposing at first glance, the interrelationships it displays are necessary to the full understanding of damage tolerance analysis.

Section 7
Damage Tolerance Testing

The purpose of this section is to describe tests that support the development of damage tolerant aircraft structures. These tests range from simple element tests used to collect basic material properties to the full-scale article tests used to verify the damage tolerant characteristics of the complete structure. For purposes of presentation, the damage tolerant tests have been subdivided into four categories: materials tests, quality control tests, analysis verification tests, and structural hardware tests.

7.1 Introduction

The materials tests provide the basic materials data for structural life analyses and for residual strength calculations. For the most part, these tests are conducted as early in the design phase as practical, in order to aid in the selection of materials and in the sizing of the structure. Materials data covered by this category of tests include fracture toughness and crack growth resistance properties, as well as basic tensile, compression, bearing and shear data.

The quality control tests provide data that support the initial quality design assessments or ensure the uniformity of the production product. Requirements for these tests are defined after the preliminary sizing and the identification of fracture critical parts have been accomplished. Quality control data covered by this category of tests include equivalent initial quality (EIQ), fracture toughness, tensile strength and notch tensile strength data.

The analysis verification tests provide data that define the accuracy of the damage tolerance analysis tools relative to their ability for predicting the crack growth behavior of the structure under operational conditions. These tests are typically conducted during the design analysis and development testing phase of the contract prior to testing the full-scale structure. Additional testing may also be required subsequent to the full-scale flight and ground tests to support interpretation and evaluation of cracking problems. Analysis verification tests include those tests that are used to verify stress-intensity factor calculations, residual strength methods, crack growth calculations and test spectrum truncation procedures.

The structural hardware tests have two functions: (a) to support the verification of the complete structural design, and (b) to define those areas of the structure that need additional attention. These tests are scheduled so that there is sufficient time to incorporate structural changes into production aircraft. In fact, production go-ahead is predicated on achieving one design lifetime of flight-by-flight loading in the full-scale durability test per JSSG-2006 paragraph 3.11.1. Structural hardware tests include joint tests, component tests, assembly tests, as well as full-scale structural tests.

Each of the following sections will describe one of the four categories of damage tolerant tests. Test procedures as well as data reduction methods will be outlined as appropriate. Where the test has been required by JSSG-2006, the appropriate paragraphs in this controlling document are cited.

7.2 Material Tests

The material tests provide the basic materials data for conducting structural crack growth life and residual strength analyses. The tests are relatively simple to conduct compared to many of the tests in the other categories. Typically, a large number of material tests are conducted in the early part of the design phase so that the appropriate materials can be selected to meet design objectives. The materials selection process may concentrate on specific design criteria relative to requirements of cost, weight, strength, stiffness, fracture toughness, corrosion resistance, and crack growth resistance to fatigue loading. The damage tolerance materials tests discussed in this section must, of course, be supplemented by other tests, e.g. tensile tests, exfoliation tests, etc., in order to ensure that preliminary material trade studies result in the appropriate choices for the given application. Typically, before the final bill of materials for the structure is signed off, additional in-depth structural tests must be accomplished to verify initial material choices and to identify additional criteria not initially considered.

Residual strength and crack growth life analyses are supported by a damage integration package that requires the definition of fracture toughness and crack growth rate properties for the materials being considered (See Section 2 for a discussion of the damage integration package). As indicated in Section 4 on Residual Strength and in Section 5 on Crack Growth, a material's crack growth behavior is a function of a wide number of different factors such as anisotropy, environment, loading rate, processing variables, product form, thickness, etc. The damage integration package accounts for these effects by utilizing data collected from specimens (a) that are representative of the material variables of interest, (b) that contain cracks which grow in the appropriate direction, and (c) that are loaded in the manner representative of operational conditions.

Standardization of test methodologies, data reduction and reporting procedures are to a large part responsible for the success of the current life prediction models. The predictive accuracy of any lifing model is only as good as the quality of the baseline crack growth and fracture data inputs. The American Society for Testing and Materials (ASTM) is the world leader in producing consensus testing standards to accurately identify materials behavior in general – and most important to the DTDH – have been the leader in developing procedures usable for damage tolerance applications. The ASTM Standards applicable to the DTDH are listed in Table 7.2.1.

The ASTM Book of Standards is published yearly to give all users of the test methods and analytical procedures the latest versions available. Within this section, whenever an ASTM Standard Test Method is referenced (i.e. ASTM E399), the ASTM Book of Standards for the current year should be consulted.

Table 7.2.1. ASTM Standards for Damage Tolerant Testing

Standard	Title	Specimens	Results
E399	Standard Test Method for Plane-Strain Fracture Toughness of Metallic Materials	C(T), SE(B), A(T), DC(T), A(B)	K_{Ic}
E561	Standard Practice for R-Curve Determination	M(T), C(T), C(W)	K_R
E647	Standard Test Method for Measurement of Fatigue Crack Growth Rates	M(T), C(T), ESE(T)	da/dN vs ΔK
E740	Standard Practice for Fracture Testing with Surface-Crack Tension Specimens	SC(T)	K_{Ie}
E812	Standard Test Method for Crack Strength of Slow-Bend Precracked Charpy Specimens of High Strength Metallic Materials	Charpy	σ_c
E1304	Standard Test Method for Plane-Strain (Chevron-Notch) Fracture Toughness of Metallic Materials	Chevron-notch	K_{IvJ}, K_{IvM}
E1457	Standard Test Method for Measurement of Creep Crack Growth Rates in Metals	C(T),	da/dt
E1681	Standard Test Method for Determining a Threshold Stress Intensity Factor for Environment-Assisted Cracking of Metallic Materials	MC(W), SE(B), C(T)	K_{IEAC}, K_{EAC}
E1820	Standard Test Method for Measurement of Fracture Toughness	SE(B), C(T), DC(T)	K_{Ic} , J_{Ic}, CTOD
E1823	Standard Terminology Relating to Fatigue and Fracture Toughness	All	NA
E1942	Standard Guide for Evaluating Data Acquisition Systems Used in Cyclic Fatigue and Fracture Mechanics Testing	All	NA

Each of the Standard Test Methods used for damage tolerance testing have a selection of test specimens that are preferred for each test. Figure 7.2.1 shows the most common types of specimens and includes the preferred specimen ratios of width/thickness (*W/B*) for each type. The thickness *B* is the dominant geometric consideration for determining if the specimen crack tip geometry is in a plane strain or a plane stress (or intermediate) condition. An asterisk denotes the most common *W/B* ratio for damage tolerance testing.

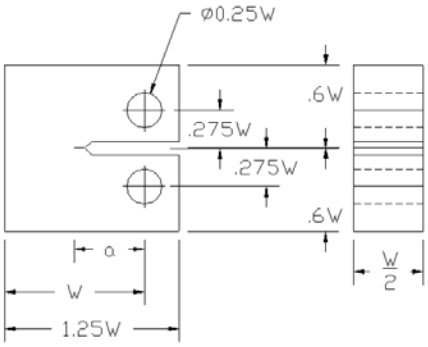

	K_{IC}	R	EAC	J_{IC}
W/B	2-4	Plane Stress	1-2	2-4

(a) Compact Tension Specimen

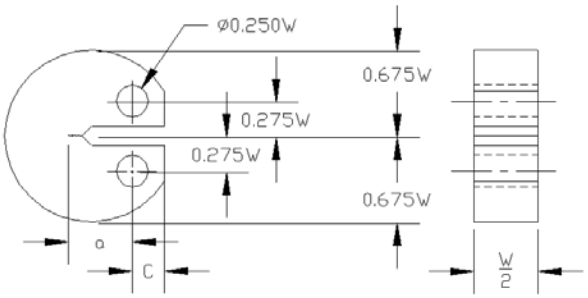

	K_{IC}	J_{IC}
W/B	2-4	2-4

(c) Disk-Shaped Compact Specimen DC(T)
Standard Proportions

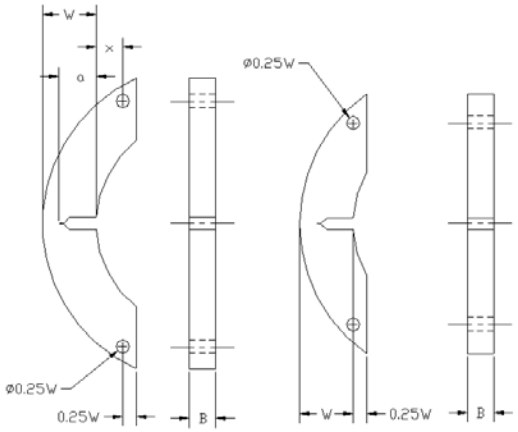

	K_{IC}
W/B	2-4

(b) Arc-Shaped Specimen Designs A(T)
Standard Proportions

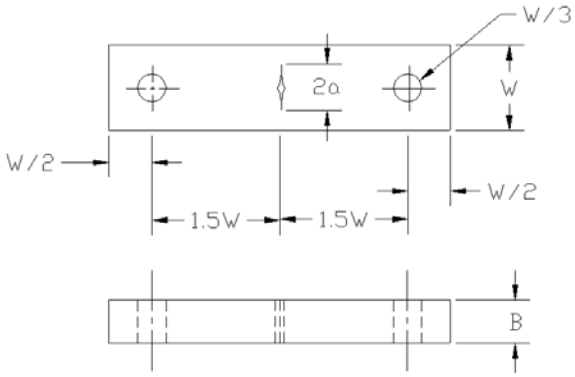

	R	EAC
W/B	Plane Stress	Var

(d) Standard Middle Tension Specimen
when W≤75 mm

Figure 7.2.1. Specimens for Damage Tolerance Testing

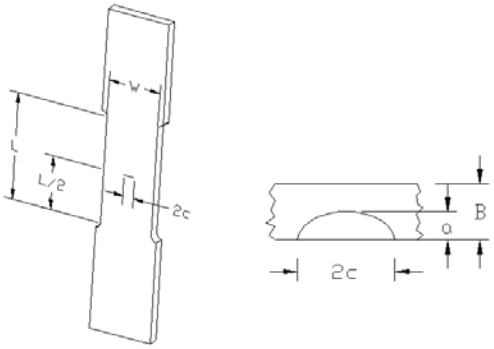

(e) Part-Through Crack

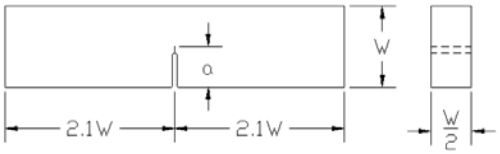

	K_{IC}	EAC	J_{IC}
W/B	1-4	1-2	1-4

(g) Bend Specimen SE(B) – Standard Proportions

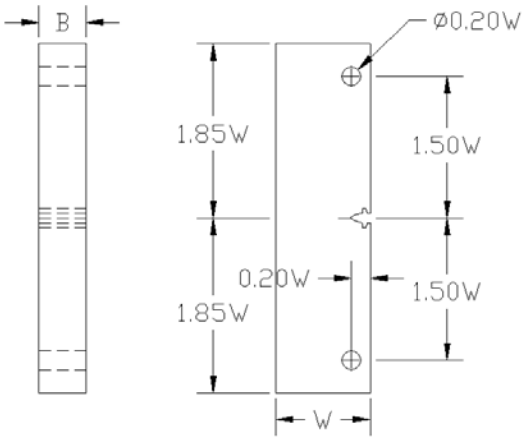

	FCG
W/B	4-20

(f) Standard Eccentricaly-Loaded Single Edge Crack Tension Specimen

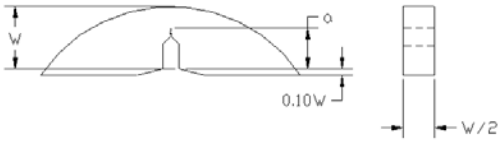

(h) Arc-Shaped Bend

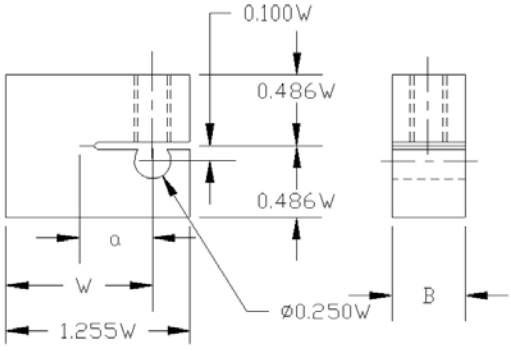

	EAC
W/B	1-2

(i) Bolt-Loaded Wedge-Opening-Loading MC(W) Specimen

Figure 7.2.1. Specimens for Damage Tolerance Testing (Continued)

As a result of the concerns about the effects of anistropy on material fracture toughness and crack growth resistance properties, standard nomenclature relative to directions of mechanical working (grain flow) has evolved. Figure 7.2.1 shows drawings of specimens which will be oriented in different directions relative to the product form. The orientation of the crack plane should be identified whenever possible in accordance with the systems shown in Figure 7.2.2.

For rectangular sections, the reference directions are identified in parts a and b of Figure 7.2.2 where an example of a rolled plate is used. The same system would be useful for sheet, extrusions, and forgings with non-symmetrical grain flow:

L – direction of principal deformation (maximum grain flow)
T – direction of least deformation
S – third orthogonal direction.

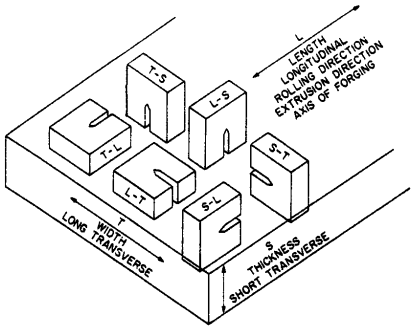

(a) Crack Plane Orientation Code for Rectangular Sections

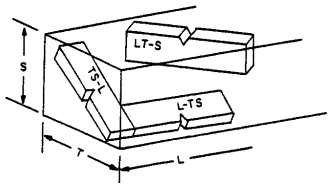

(b) Crack Plane Orientation Code for Rectangular Sections where Specimens are Tilted with Respect to the Reference Directions

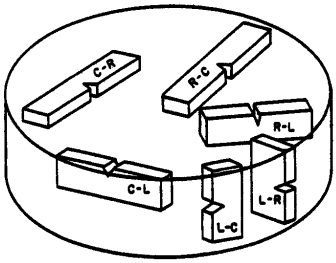

(c) Crack Plane Orientation Code for Bar and Hollow Cylinder

Figure 7.2.2. Crack Plane Orientation Code for Rectangular Sections and for Bar and Hollow Cylinders [ASTM 2001]

When reporting crack orientation in rectangular sections, the two letter code, such as T-L in Figure 7.2.2a, is used when both the loading direction and direction of crack propagation are aligned with the axes of deformation.

For specimens tilted with respect to two of the reference axes (Figure 7.2.2b), a three-letter code, e.g. L-TS, is used. The designation used can be interpreted by considering the codes as a composite pair in which the first element in the pair designates the direction normal to the crack plane and the second element designates the expected direction of crack propagation. The code T-L for a cracked specimen indicates that the fracture plane has a stress application normal in the T direction (width direction of the plate) and the expected direction of propagation in the L direction (in the longitudinal direction of the plate), see Figure 7.2.2a. The code L-TS means that the crack plane is perpendicular to the L direction (principal deformation) and the expected crack direction is intermediate between T and S, see Figure 7.2.2b.

For cylindrical sections where the direction of principal deformation is parallel with the longitudinal axis of the cylinder, such as for drawn bar stock and for extrusions or forged parts having a circular cross section, the specimen reference directions are described in Figure 7.2.2c. The three directions used here are:

L – directional of maximum grain flow (axial)
R – radial direction, and
C – circumferential or tangential direction

Interpretation of the specimen designations relative to the location of the crack plane and crack path is similar to that employed for the rectangular sections.

In the remainder of this section, attention will be given to those tests which are utilized to collect data that support the material selection function and the damage integration package. The first of these subsections covers those tests which are used to establish the fracture toughness of materials. The other subsections cover tests utilized to collect sub-critical crack growth data.

7.2.1 Fracture Toughness Testing Methods

Fracture toughness data have provided the basis for estimating the crack length-residual strength behavior of aerospace structures since the late fifties. Initial correlation tests for airplane skin-stringer type structures were typically conducted using wide, center crack panel tests of the skin material. It was soon realized that such tests were inappropriate for estimating the fracture behavior of thicker material/structure for a number of reasons. By the late sixties, ASTM had evolved a fracture toughness test for materials that fail by abrupt fracture. This test method eventually became the plane-strain fracture toughness (K_{Ic}) test standard, ASTM E399, in 1972.

Additional work by ASTM throughout the seventies resulted in several additional fracture toughness methods. One such method appropriate for tougher (or thinner) materials which fail by tearing fracture is ASTM Standard E561, which covers the development of the K_R resistance curve. The K_R resistance curve test has found wide acceptance in the aircraft industry since calculation procedures were already in place to utilize the data for residual strength estimates. Another recently-approved standard, ASTM E1820, covers the determination of fracture toughness using several methods. One such method applicable to materials which lack sufficient thickness for plane-strain fracture toughness (K_{Ic}) per ASTM E399 is the J-integral approach to determine the plane-strain toughness J_{Ic}.

7.2.1.1 Plane-Strain Fracture Toughness

The plane-strain fracture toughness (K_{Ic}) measures crack resistance to abrupt fracture under tri-tensile crack tip stress conditions where the constraint against crack tip deformation is maximized. As such, K_{Ic} data represent a lower bound on the fracture toughness that a material might experience under a wide range of cracking and geometric configurations. The ASTM E399 standard that covers plane-strain fracture toughness of metallic materials was developed to obtain values of fracture toughness using relatively thick specimens (thus maximizing the crack tip constraint) subjected to quasi-static loading conditions. The determination of K_{Ic} is also covered in the common fracture toughness method ASTM E1820.

A variety of specimen configurations are currently recommended for collecting K_{Ic} data, some of which are described in Figure 7.2.1. The compact tension [C(T)] and the single edge notched bend specimen [SE(B)] were initially the only specimens recommended for the measurements and most laboratories are well equipped to support these tests. The arc-shaped tension [A(T)], disk-shaped compact tension [DC(T)], and arc-shaped bend [A(B)] specimens have since been added as these configurations evolved to characterize the resistance of specific structural product forms, i.e. tube/pipe type structures and cylindrically shaped bar stock.

It should be noted that ASTM E399 uses linear elastic fracture mechanics as its basis for calculating fracture toughness. For this reason, specimen sizing requirements are predicated on maintaining a crack tip plastic zone size that is a small fraction of the planar dimensions of the specimen. The test method is also specific about ensuring that the thickness of a K_{Ic} specimen is substantially larger than the crack tip plastic zone size so that a crack tip tri-tensile stress state is established which maximizes the constraint on plastic deformation. Basically, the specimens are sized so that the dimensions of crack size (a), thickness (B), and remaining ligament size (W-a) are greater than the ratio of 2.5 $(K_{Ic}/\sigma_{ys})^2$, i.e., so that

$$a, B, (W-a) > 2.5\left(\frac{K_{Ic}}{\sigma_{ys}}\right)^2 \qquad (7.2.1)$$

where σ_{ys} is the 0.2 percent offset yield strength and the K_{Ic} value meets all the test criteria.

The procedures for determining fracture toughness outlined in ASTM E1820 are essentially identical to E399 for samples sufficiently thick to provide valid K_{Ic} measurements. The plane-strain crack toughness test is unusual in that there can be no advanced assurance that the fracture toughness established by a given test will be a valid K_{Ic} value. The fracture toughness calculated after a given test must be validated through a series of criteria checks that are thoroughly described in E399 and E1820. The principle advantage of E1820 is that one can analyze the test information using different criteria to come up with valid toughness measurements if the thickness is too thin for valid K_{Ic} values.

Schematic load-displacement curves representative of the type of behavior exhibited during a test to determine the plane-strain fracture toughness are shown in Figure 7.2.3. The collection of such load-displacement data is a requirement of most ASTM fracture related standards. The objective of this test record is to establish the load, P_Q, which will be used in the calculations of the test fracture toughness value (K_Q), and the level of maximum test load (P_{max}). The test fracture toughness (K_Q) is a conditional result that must be validated through checking the size requirements before accepting K_Q as a valid plane-strain fracture toughness (K_{Ic}) value. If K_Q is

a non-valid test result according to ASTM E399, K_Q should not be utilized as an estimate for K_{Ic} for design purposes since the value may be very non-conservative.

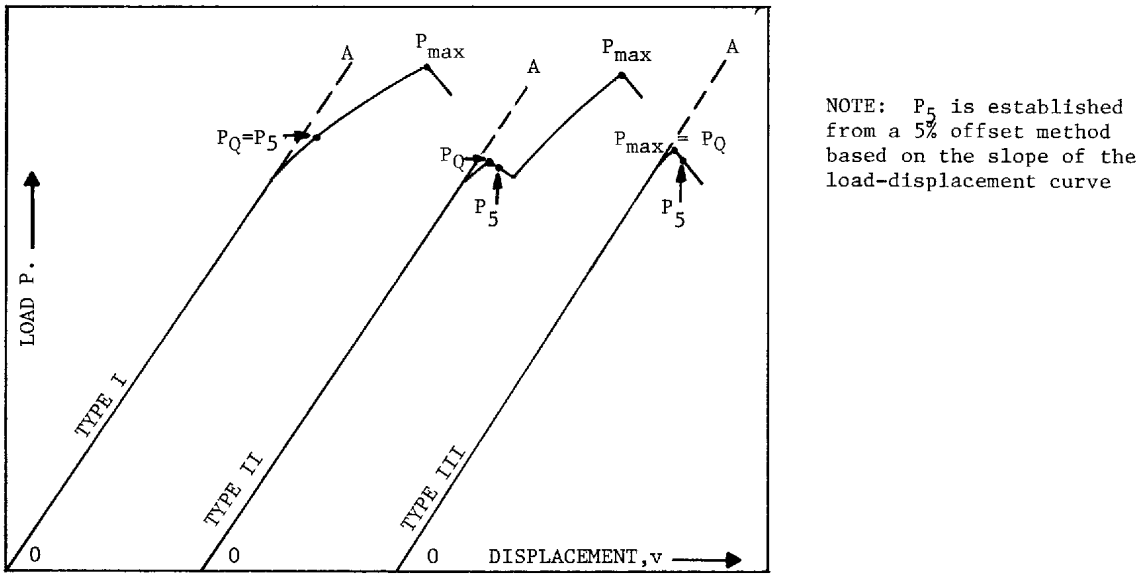

Figure 7.2.3. Principal Types of Load-Displacement Records [ASTM 2001]

7.2.1.2 R-Curve

The R-Curve measures crack resistance to tearing fracture for situations where the material thickness employed within a structure is below the requirement for plane-strain fracture toughness conditions. The R-curve describes the extent of crack movement from an initial starting condition as a function of the level of applied stress-intensity factor (K) and as such represents a complete history of quasi-static crack growth up until fracture occurs. It has been shown for several materials that the R-curve for a given thickness is independent of crack size and structural geometry [McCabe, 1973].

For the detailed reasons stated in Section 4 on Residual Strength, the R-curve is not as easily employed in design as abrupt fracture criteria. Early work on aerospace materials with thicknesses below that required for K_{Ic} was directed at obtaining the limits on the R-curve, i.e. on obtaining K_{ONSET}, associated with the K conditions at the start of crack movement, and K_c, associated with the K conditions at the moment of instability. After it was realized that the plane-stress fracture toughness (K_c) was a function of crack size and structural geometry as well as thickness, attention was focused on obtaining the complete history of the tearing fracture.

ASTM evolved a standard practice for determining the R-curve to accommodate the widespread need for this type of data. While the materials to which this standard practice can be applied are not restricted by strength, thickness or toughness, the test specimens utilized in tests must be of sufficient size to remain predominantly elastic throughout the duration of the test. The reason for the size requirement is to ensure the validity of the linear elastic fracture mechanics calculations. Specimens of standard proportions are required, but size is variable, to be adjusted for yield strength and toughness of the material considered.

The ASTM Standard E561 covers the determination of R-curves using middle cracked tension panel [M(T)], compact tension [C(T)], and crack-line-wedge-loaded [C(W)] specimens. The compact tension and middle cracked tension panel geometries are illustrated in Figure 7.2.1. A schematic illustrating the loading arrangement for the crack-line-wedge-loaded specimen is provided in Figure 7.2.4. The crack-line-wedge-loaded configuration and loading conditions are such that, as the crack grows, the stress-intensity decreases under fixed-displacement conditions. Such an arrangement facilitates collecting the complete R-curve using one specimen since the crack growth remains stable under decreasing K conditions. Load control conditions ensure that the stress-intensity factor will increase as the crack grows. This arrangement results in limiting the K_R versus crack extension (Δa) data to a level associated with the fracture of the test specimen.

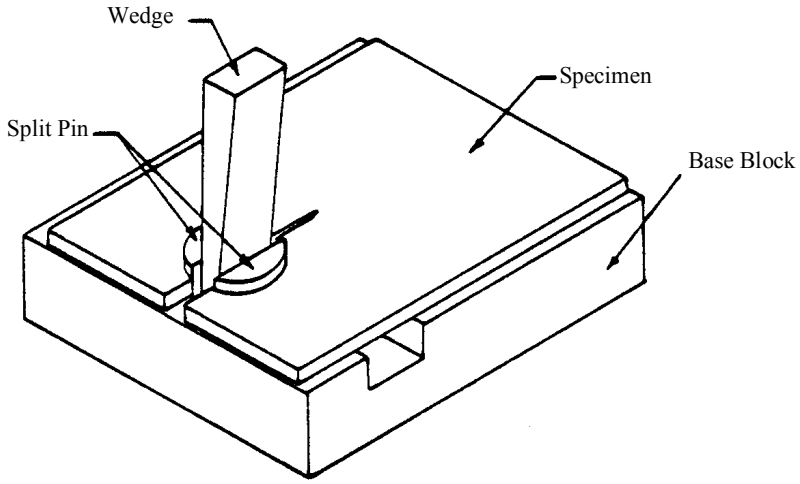

Figure 7.2.4. Crack-Line-Loaded Specimen with Displacement-Controlled Wedge Loading [ASTM 2001]

While the C(W) specimen had gained substantial popularity for collecting K_R curve data, many organizations still conduct wide panel, center cracked tension tests to obtain fracture toughness data. As with the plane-strain fracture toughness standard, ASTM E399, the planar dimensions of the specimens are sized to ensure that nominal elastic conditions are met. For the M(T) specimen, the width (W) and half crack size (a) must be chosen so that the remaining ligament is below net section yielding at failure. It is recommended in ASTM E561 that the M(T) specimen be sized so that the dimensions can be referenced to the plane stress plastic zone size (r_y).

$$r_y = \frac{1}{2\pi}\left(\frac{K}{\sigma_{ys}}\right)^2 \qquad (7.2.2)$$

where the specimen sizes are chosen on the basis of the maximum stress-intensity factor expected in the test. Table 7.2.2 provides a list of minimum recommended M(T) sizes for assumed K_{max} -to-yield strength ratios.

Table 7.2.2. ASTM E561-98 Recommended M(T) Dimensions

K_{max}/σ_{ys} ($in^{1/2}$)	Width (in.)	Crack Size (in.)	Specimen Length (in.)
0.5	3.0	1.0	9
1.0	6.0	2.0	18
1.5	12.0	4.0	36
2.0	20.0	6.7	30*
3.0	48.0	16.0	72*

* Panels wider than 12 in. will require multiple pin grips and the length requirement is relaxed to 1.5*W*

It should be noted that the initial crack length is sized to be *W*/3 to minimize the potential for net section yielding prior to a stress-intensity factor controlled fracture. Based on data collected from a number of aluminum panels with different widths, it appears that there is a tendency for the calculated fracture toughness K_c to increase with increasing panel width, as shown in Table 7.2.3. While it is difficult to generalize the observation based on these results to all materials, such data indicates that it is possible to develop conservative predictions of the plane-stress fracture toughness by using sub-size specimens.

Table 7.2.3. Room Temperature Plane-Stress Fracture Toughness Values for Several Aluminum Alloys Presented as a Function of Thickness and Width

Material	Crack Orientation	Buckling Restraint	Specimen Thickness (in.)	Specimen Width (in.)	Kapp (ksi $in^{1/2}$)	Kc (ksi $in^{1/2}$	No. of Measure.
2020-T6	L-T	No	0.063	2.0	29.6	34.6	5
				3.0	29.1	30.1	2
				15.8*	36.1	36.9	4
2020-T6	T-L	No	0.063	2.0	25.9	30.5	5
				3.0	26.9	27.8	2
				15.8*	34.5	34.5	5
2024-T81	T-L	No	0.063	2.0	35.6	--	9
				6.0	51.2	57.9	3
				9.0*	55.2	61.2	2
2024-T851	T-L	No	0.250	3.0	26.7	31.3	6
				4.0	38.0	47.1	7
				20.0*	38.6	48.4	12
7075-T6 clad	L-T	No	0.040	7.5	47.3	--	3
				9.0	51.4	55.0	12
				30.0*	64.9	85.6	6/2+
7075-T6 clad	L-T	Yes	0.080	5.9	53.5	60.1	9/6+
				11.8*	61.5	70.1	17
				23.6*	62.4	69.3	20
7075-T6 clad	L-T	No	0.090	3.0	49.4	--	11
				9.0*	64.5	70.0	16/12+
				20.0*	56.4	61.8	10
7075-T7351	L-T	Yes	0.250	8.0	59.7	--	13
				15.9	77.2	--	8
				36.1*	93.0	119.9	3/2+
7075-T7351	L-T	No	1.00	8.0	43.1	45.9	3
				16.0*	47.3	52.7	9
				20.0*	77.9	96.7	16/12+

*Width requirements meet ASTM E 561 requirements.
+First number represents number of Kapp calculations, the second represents Kc [ASTM 2001]

Another test condition important to consider during R-curve (or plane-stress fracture toughness) testing is the amount of buckling restraint that should be built into the test fixtures. Most tests are conducted either with no buckling restraint or with extensive fixturing that tends to maintain inplane loading by preventing buckling. With tests conducted with limited buckling restraint, the

spurious stress distributions created when buckling occurs (at the specimen edges or in the crack tip region) can lead to mechanical driving factors that either enhance or degrade the calculated levels of applied stress-intensity factor. The ASTM E561 method places restrictions on the amount of buckling exhibited during the R-curve test.

The data collected during an R-curve test includes load and crack size readings. The stress-intensity factor associated with a given increment of crack size, i.e. K_R, is calculated using the stress-intensity factor formula for the specimen, the applied force (P), and a plasticity enhanced crack size. The plasticity enhanced crack length is referred to as the effective crack (a_{eff}) and is calculated by adding the plane stress plastic zone radius (r_y), per Equation 7.2.2, to the current physical crack, i.e.

$$a_{eff} = a_0 + \Delta a + r_y \qquad (7.2.3)$$

where a_o is the initial crack length and Δa is the increment of crack movement.

Visual and non-visual methods of measuring crack size are available for collecting the data. Within ASTM E561, the details associated with making crack length measurements based on compliance (force-displacement) methods are fully described. In fact, for those situations where extensive crack tip plasticity can occur, the compliance methods are recommended since these methods yield an estimate of crack length that already accounts for a plasticity correction.

ASTM E561 recommends that the R-curve be presented using an effective crack increment ($\Delta a_{eff} = \Delta a + r_y$) so that the instability predictions can be directly made from the plots. Thus, the R-curve is a plot of $K_R = K(a_{eff}, P)$ versus Δa_{eff}. The test engineer must describe how Δa_{eff} and a_{eff} were calculated so that structural engineers using the data have a full report of the behavior.

7.2.1.3 Crack Initiation J-Integral

The J_{Ic} can be used as a toughness value at the initiation of crack tearing from a sharp fatigue crack in metallic materials. This toughness value can serve as a basis for screening tough materials or for evaluating materials utilized in sub-K_{Ic} thicknesses. Requirements for a valid J_{Ic} value according to ASTM E1820 are based on the ratio of the J_{Ic} to yield strength, i.e.,

$$B, b_0 > 25\left(\frac{J_Q}{\sigma_{ys}}\right) \qquad (7.2.4)$$

where B is thickness and b_0 is the initial ligament. The relationship between the J-integral and the stress-intensity factor was given in Section 11 as,

$$J = \frac{K^2}{E'} \qquad (7.2.5)$$

where $E' = E$, the elastic modulus, for plane stress, and $E' = E/(1-\nu 2)$ for plane strain, and ν = Poisson's ratio. Thus, using Equations 7.2.5 evaluated at the critical condition ($J = J_{Ic}$, $K = K_{JIc}$) and Equation 7.2.4, the thickness requirement becomes after some algebra

$$B > 25\left(\frac{\sigma_{ys}}{E'}\right)\left(\frac{K_{JIc}}{\sigma_{ys}}\right)^2 \qquad (7.2.6)$$

For the typical condition where the ratio of yield strength to elastic modulus (σ_{ys}/E) is below 0.1, J_{Ic} values can be obtained using specimens thinner than that required by the K_{Ic} standard (ASTM E399).

The K_{JIc} value in Equation 7.2.6, however, does not normally correspond to the K_{Ic} value that would be obtained using the plane-strain fracture toughness standard. The K_{Jic} value based on J_{Ic} measurements is typically lower and thus leads to conservative estimates of the ASTM E399 K_{Ic} value. The differences in K_{JIc} and K_{Ic} arise as a result of differences in the amount of allowable physical crack growth associated with the two standards; there is less growth allowed for the J_{Ic} value than for the K_{Ic} value.

While the use of a toughness standard for sub-K_{Ic} thickness specimens provides additional opportunities for characterizing material resistance to fracture, the J_{Ic} concept appears somewhat limited relative to the design of aerospace structures. A single test of a J_{Ic} type specimen might be similar in cost to a K_{Ic} type test; but a number of J_{Ic} type specimens must be tested to develop the required crack resistance data prior to estimating the J_{Ic} value. Through unloading compliance testing, it is possible to reduce the number of tests.

7.2.2 Sub-Critical Crack Growth Testing Methods

Since the early sixties, sub-critical crack growth data have provided the basis for estimating the crack growth behavior of structural components under service conditions. In the initial stages of damage tolerant design methodology and test development, the effects of stress ratio, environment and load sequencing were poorly understood. Thus, the initial damage integration packages did not account for these effects; furthermore, testing capability was for the most part limited to constant amplitude or to block loading. By the early seventies, understanding and capability had progressed to the point where evaluation of each major damage producing element in the service history could then be modeled by damage integration packages.

The ASTM Committee E08 on Fatigue and Fracture Testing also played an important part in developing standards for collecting data which could be used to support damage integration packages. Throughout the seventies, inter-laboratory testing programs were conducted which further refined the testing conditions that could be standardized by consensus. The AF Materials Laboratory funded development of a standard test method to ensure a stable methodology for information used in aircraft damage tolerance assessments [Hudak, et al., 1978]. In 1978, ASTM issued the first standard based on these developments, ASTM E647, on fatigue crack growth rate (*da/dN*) testing. Additional standards or additions to existing standards such as ASTM E1681 on environmentally assisted cracking testing (K_{IEAC}), on corrosion fatigue, on automated methods and on threshold testing have and continue to evolve. Methods for non-visual crack size monitoring such as compliance and electric-potential have been developed over the last 15 years and incorporated into nearly all of the fracture related standards.

7.2.2.1 Fatigue Crack Growth Rate Testing

Fatigue crack growth rate data that support standard damage integration packages of the type described in Sections 5.1 and 5.2 are based on constant amplitude testing of cracked specimens. Typically, multiple specimen tests are conducted at a number of fixed stress ratio (R) conditions so that the complete range of crack growth rate is covered for the mechanical and environmental variations of interest. For the most part, all tests of this type are covered by ASTM E647 on fatigue crack growth rate testing.

Test conditions that deal with the conditions essential for obtaining near threshold growth rates are further described by ASTM E647. Substantial care is necessary for correctly controlling the precracking operation and the stress-intensity-factor control conditions in the near threshold region of the fatigue crack growth rate curve (*da/dN* vs *ΔK*) [Yoder, et al., 1981; Wei & Novak, 1982]. Also, ASTM E647 must be supplemented with information relative to control of environmental conditions when these conditions affect behavior.

The ASTM E647 describes the test, as well as the data collection, reduction and reporting requirements. The test itself requires standard fatigue test capability and utilizes precracked specimens which have widely accepted stress-intensity factor solutions. The standard currently recommends three specimen configurations, the middle-cracked tension [M(T)], the compact tension [C(T)], and the eccentrically-loaded single edge tension [ESE(T)] specimen geometries, which are shown in Figure 7.2.1. While the M(T) specimen is generally recommended for all stress ratio conditions, it should be noted that the C(T) and the ESE(T) specimens can only be used for positive stress ratio conditions.

The primary control exercised during a test is the control of the fatigue forces that are being applied to the test sample. Most modern servocontrolled, electrohydraulic test machines that are periodically recalibrated using force cells traceable to the National Institute of Standards and Technology (NIST) will result in force control well within the ASTM E647 requirements. Force cells, of course, should be selected such that fatigue crack growth rate tests are being conducted using forces that are at the higher end of the load cell range to maximize force accuracy. Specific care should be taken to minimize force errors. Such errors can cause major errors in reported crack growth rate data since stress-intensity factor (*K*) is a linear function of force.

Fatigue crack growth rate data are derived from the crack length data (discrete pairs of crack length and cycle count data) and test load data. Significant errors in crack growth rate behavior can also result if systematic errors in crack length measurement occur since such errors directly affect the calculated stress-intensity factor parameters. ASTM E647 places strict requirements on the measurement of crack size and recommends a frequency of crack length measurement based on the gradient (rate of change) of the stress-intensity factor through the crack length interval in the given test specimen.

Figure 7.2.5 shows a schematic that illustrates the data reduction of a single test's crack length data to the fatigue crack growth rate format. The procedures that one uses to differentiate the crack length data have some effect on the individual *da/dN* vs *ΔK* discrete data points. To ensure some uniformity in this part of the data reduction process, ASTM E647 recommends that either the secant or the 7-point incremental polynomial methods be utilized. In fact, the standard includes a listing of a FORTRAN computer program that can be utilized to reduce the crack length data according to the 7-point incremental polynomial method. Other differentiation methods leading to the same data trends for a given test include 5, 7, 9 point incremental, linear, quadratic, and power law least squares fitting schemes and the three-point average incremental slope method utilized by MIL-HDBK-5. The specific differences that result from differentiating a set of crack length data using different methods are primarily associated with point-to-point data scatter in the *a* vs *N* data. Discussion of the impact of this scatter on design was covered in Section 5.1.

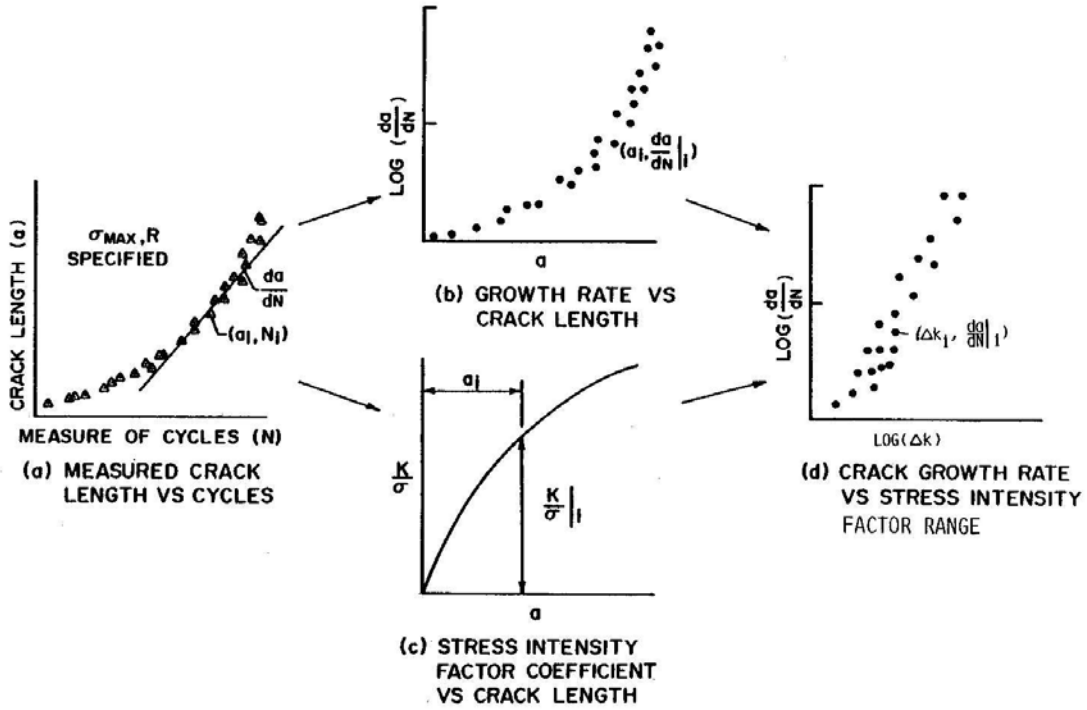

Figure 7.2.5. Fatigue Crack Growth Rate Data Reduction Procedure

ASTM E647 recommends that duplicate tests be conducted to establish the crack growth rate behavior for a given set of test conditions (constant and environment). However, if a complete definition of the growth rate behavior between threshold and fracture is required for a given set of test conditions, six constant load type tests with three different load levels might be required to cover the range. For determining general trends under a given set of test conditions, shortcut methods are available. These methods include:

- methods of periodically increasing the constant amplitude load (by less than 10 percent) as the crack grows, and
- methods of periodically modifying either the stress ratio or cyclic load frequency during a test.

These shortcut methods are designed so that only selected intervals of the fatigue crack growth rate data are generated, although a description of the complete *da/dN* vs *ΔK* curve is possible since the entire range of behavior is covered.

When shortcut methods are utilized to obtain a design database, it is recommended that a preliminary test program be conducted to verify the accuracy of these shortcut methods. The preliminary test program would be based on a sufficient number of both constant load amplitude and shortcut tests to justify the shortcut test methods, since changing test loads, stress ratio levels, cyclic load frequencies and environmental conditions can introduce crack growth transients. The crack growth transients of most concern are those that modify the interpretation of the mean trend behavior exhibited by the material under the test variations considered. The preliminary test program should determine the magnitude of the transient and the crack growth increment required to establish steady-state behavior after a new condition is introduced. The

approving agency should review the results of the preliminary test program relative to the impact of transient behavior and to the development of data reduction methods that exclude those intervals of crack length where transient behavior might be exhibited.

7.2.2.2 Stress Corrosion Cracking

Stress corrosion or environmentally-assisted cracking data which support standard damage integration schemes, as well as materials evaluation and selection studies, are based on either constant load or constant displacement type tests of fatigue cracked specimens placed in simulated service environments. There are two types of stress corrosion cracking data properties measured by such tests:

1) the threshold property (K_{IEAC}), which is the level of the stress-intensity factor associated with no cracking in the given environment, and
2) the crack growth rate resistance property (*da/dt* as a function of the static stress-intensity factor *K*).

ASTM E1681 covers determination of stress corrosion threshold. Figure 7.2.1 describes the three types of test specimen configurations utilized in the ASTM standard:

- a bolt-loaded, compact [MC(W)] specimen,
- a constant load single-edge specimen [SE(B)], and
- a compact tension specimen [C(T)].

As can be noted from the figure, the bolt-loaded MC(W) specimen is a self-loading specimen. The force loaded SE(B) and C(T) specimens must be placed in a test figure that supports the specimen while under load, which is typically applied using weights attached to one end of the specimen. (Note that ASTM E1681 does not describe *da/dt* testing, but does mention *da/dt* information may be obtained on such tests.)

As with other sub-critical crack growth resistance tests, the materials test engineer must pay particular attention to the pre-cracking, loading, and crack size measurement details. In addition, because the environment has a more important influence on the crack growth resistance of many materials, specific controls must be instituted here also.

Crack growth tests conducted in aqueous or similar deleterious environments lead to difficult crack length measurement problems since typically the direct use of visual techniques is restricted to conditions whereby the specimen is removed from the environment. Use of visual techniques under these conditions is acceptable if it can be shown that removing the specimen from the environment introduces no major crack growth transient effects. Collecting crack length data using electric potential difference (EPD) methodology and the relationships between crack size and potential voltage difference has gained credibility in recent years as a means of automating the measurement of crack size in both SE(B) and C(T) specimens. Since stress-corrosion cracking tests are conducted over longer periods of time (~ 10,000 hours) than other mechanical tests, stability of the crack size measurement system must be given a great deal of attention.

Differences of opinion exist between the experts relative to the use of either the increasing (constant load) or decreasing (constant displacement) stress-intensity factor (*K*) type specimens for collecting threshold stress corrosion cracking data. These differences result from the

influences of test conditions and of crack growth transients. Since the objective of the K_{IEAC} test is to obtain a threshold level of K associated with a preset growth rate limit, a series of tests should be conducted which would minimize these effects.

The K_{IEAC} results obtained using constant load specimens are influenced somewhat by the fact that the test time includes both the time associated with initiating the crack movement from the sharp precrack and that associated with subsequent propagation. For K_{IEAC} data collection programs using increasing K specimens, a number of tests should be conducted such that the precracked specimens are loaded above and below the level of the expected stress-intensity factor condition associated with zero crack movement. Subsequently, each unbroken specimen should be broken open and examined for evidence of crack movement during the test period. In all cases, the K_{IEAC} value is lower than the lowest value of the stress-intensity factor associated with the broken specimens. If no stress-corrosion cracking movement is observed when the unbroken specimens are examined, the K_{IEAC} is taken as the highest stress-intensity factor level associated with the unbroken specimen group. When stress-corrosion cracking movement is observed in the unbroken specimen group, the amount of crack movement should be divided by the test time in order to ascertain if the average growth rate associated with any test is below that required to obtain the K_{IEAC} value. The highest level of stress-intensity factor that yields an average growth rate below that required is taken as the K_{IEAC} value.

The K_{IEAC} results obtained using the bolt-loaded (K-decreasing type) specimen can be influenced by crack growth transients that occur after loading. (For additional information see the discussion in ASTM E1681 on stress relaxation influences in Section 5.1.7) For K_{IEAC} data collection programs using decreasing K specimens, a number of tests should be conducted such that the precracked specimens are loaded to levels that are slightly above (10 to 25 percent) the level of expected K_{IEAC}. High initial stress-intensity factor levels (relative to K_{IEAC}) result in a number of problems in determining K_{IEAC} accurately. These problems sometimes result from the fact that once the precrack starts to move it has a longer distance to travel before arresting as a result of the high initial K condition and the slowly decaying K gradient associated with the bolt-loaded conditions. Another problem associated with high initial K conditions is that cracks will sometimes initiate and arrest prematurely due to crack blunting (under first loading) and crack front tunneling. In the decreasing K specimen, as soon as crack movement occurs from the precrack, the crack front loses the sharpness of a fatigue crack; this sometimes results in a value of K_{IEAC} that is somewhat above that measured in the increasing K specimen.

Some of the problems in estimating K_{IEAC} using either constant-load (increasing K) and bolt-loaded (decreasing K) specimens are alleviated when crack growth measurements are continuously made throughout the test. Specifically, measurement of the first crack movement that occurs in constant-load specimens provide a better time basis for estimating the crack growth rate from unbroken specimens. Even periodic measurement of the crack length in the bolt-loaded C(T) specimens will increase the test engineer's confidence that transient or abnormal crack growth behavior has not occurred during the test. Crack growth rate data used for sensing a material's resistance to environmental attack is collected and reduced in a manner similar to fatigue crack growth rate data. The principal difference in an environmental attack testing program is that the loads or displacements are held constant during the test. K_{IEAC} is used primarily for ranking materials for sub-critical crack growth resistance in environments. Because fatigue testing is conducted extensively in similar environments during the design of airframe structures, a high level of interest continues in combining the time dependent rate

information with the cyclic dependent data into a common predictive model. It is therefore suggested that when such tests are necessary to support damage integration packages, that stress-corrosion cracking rate tests follow the basic guidelines of the fatigue crack growth rate tests in ASTM E647.

7.3 Quality Control Testing

The quality control tests provide data that (a) support the initial quality design assessments and non-destructive inspection (NDI) requirements, or (b) ensure the uniformity of the production product. Because many of these tests will be conducted during the production run they are fairly simple tests. Requirements for these tests are defined after the preliminary sizing and the identification of fracture critical parts. Quality control data covered by this category of tests include equivalent initial quality (EIQ) data, continuing assessment of the non-destructive evaluation (NDE) capability, and component prolongation tests for fracture toughness and crack growth resistance.

One sure method for minimizing damage tolerant problems due to the presence of the manufacturing induced rogue flaw is to take ample precautions on the production line to minimize the probability that such defects could be present in safety-of-flight structures. The manufacturer, during design, will typically suggest methods for ensuring strict production line control of material preparation, fabrication and joining techniques. The manufacturer's control can be periodically checked using the same type of testing and analysis approaches that were utilized in design to justify the choices of materials and defect sizes for the airframe's damage tolerant analysis.

Throughout the procurement cycle of several recent weapon systems, fracture toughness was controlled to specified design minimum levels for airframe safety-of-flight type structure. The particular fracture toughness property used for quality control was the plane-strain fracture toughness – K_{Ic}, (see Section 7.2). Since some manufacturing processes are such that they alter the microstructure of some materials (and thus the fracture resistance), it was believed necessary to monitor the behavior of material subjected to the gamut of processes that precede final assembly. In fact, the B-1A material quality control program was designed so that the fracture toughness was sampled for each fracture critical part after each major manufacturing process; such a sampling program provided an immediate indication if any process was detrimental to the fracture toughness.

In almost all the past cases where fracture toughness was controlled, ASTM E399 was employed to obtain a valid plane-strain fracture toughness (K_{Ic}) value. As a result of the difference in cost between a K_{Ic} test and other much simpler mechanical tests such as the tensile test, engineers have been giving attention to the development of tests that are both simple and representative of the fracture toughness property of interest. The double-edge notched specimen and the round edge-notched specimen are two notched geometries that have been examined. Both notched geometries are prepared with sharp root radii, i.e. radius < 0.002 inch, but do not contain fatigue precracks. A Chevron Notch Test for K_{IV} (ASTM E1304) can also be used as a K_{Ic} indicator.

For quality control purposes, the manufacturer might prepare a series of round-edge notched specimens and K_{Ic} specimens with the same microstructure (from the same lot of material) and determine the relationship between, for example, notched tensile strength and fracture toughness. The series of tests would be repeated for different microstructure (different lots of material) until every possible combination of microstructure was covered. The manufacturer would then formulate a global relationship between notched tensile strength and fracture toughness of this material. Using standard statistical techniques, the manufacturer could then establish the required level of notch tensile strength that should be measured during production in order to achieve the minimum allowable level of fracture toughness.

While the crack growth property is actually of greater concern than the fracture toughness property, controlling the level of subcritical crack growth resistance via a quality control test has not been attempted for any large weapon system due to the expense and complexity of the crack growth rate test. The Air Force funded one study to explore the possible development of an inexpensive crack growth test but the results of this program were mixed [Creager & Sommers, 1977]. With the advent of automated fatigue crack growth rate test methods, future quality control programs could incorporate a test for controlling the subcritical crack growth resistance of fracture critical parts.

7.4 Analysis Verification Testing

The analysis verification tests provide data that define the accuracy of the damage tolerance analysis tools relative to their ability to predict the crack growth behavior of the structure under operational conditions. In essence, these tests are conducted to verify individual or collective elements of the damage integration package that will be used to conduct damage tolerant life analysis studies. Analysis verification tests include those tests that are used to verify stress-intensity factor calculations, residual strength methods, crack growth calculations, and test spectrum truncation procedures. The tests range in difficulty from constant amplitude tests on fairly simple structural geometries to flight-by-flight load type tests conducted on structures that simulate isolated design features contained in full-scale structural components. These tests are typically conducted during the design analysis and development testing phase of the contract prior to testing the full-scale structure and major components. Additional testing may also be necessary subsequent to the results of the full-scale flight and ground tests to support interpretation and evaluation of cracking problems.

7.4.1 Structural Parameter Verification Techniques

The current analytical procedures for developing the stress-intensity factor (K) associated with two-dimensional structural geometries have been extensively verified. The verification of the tools required to solve three-dimensional structural geometry problems, however, is still receiving major attention. This subsection reviews the experimental techniques utilized to verify the analytical procedures for obtaining stress-intensity factors for two- and three-dimensional geometries.

For the two-dimensional crack geometries, the engineer has the opportunity to employ four different types of experimental tests to verify the stress-intensity factor solution for the given problem: compliance (displacement/load) measurements [Bubsey, et al., 1973], moiré fringe techniques [Kiu & Ke, 1975], photoelastic procedures [Kobayashi, 1973], and crack growth rate testing [James & Anderson, 1969]. In the realm of the three-dimensional problem, only two of the above tests can be relied upon: photoelastic procedures [Smith, 1975], and crack growth rate testing [Grandt & Sinclair, 1972; Grandt & Hinnerichs, 1974].

7.4.1.1 Compliance

The compliance measurement test is based on the relationship between compliance (C), which is a measure of stored energy in the structure, and the strain energy release rate (G). The relationship as discussed in Section 1.3 is:

$$G = \left(\frac{P^2}{2B}\right)\left(\frac{\partial C}{\partial a}\right) \tag{7.4.1}$$

where P is the applied load, B is the structural thickness, and a is a measure of crack length. The compliance in Equation 7.4.1 is associated with the displacement of the load points along the axis of loading. It should be noted that displacements not along the axis of loading cannot be used in the calculation of the strain energy release rate (G). Once the relationship between G and C has been established the stress-intensity factor (K) is calculated using:

$$K = \sqrt{GE'} \tag{7.4.2}$$

where $E' = E$, the elastic modulus, for plane stress problems and $E' = E/(1-\nu^2)$ for plane strain problems, ν is Poisson's ratio. Since the bulk of the material in any given structure is subject to plane stress conditions, the better correlations are obtained between analytically determined K solutions and compliance determined K solutions based on the plane stress formulation of Equation 7.4.2.

7.4.1.2 Moiré Fringe

The moiré fringe technique for obtaining the stress-intensity factor for a through-thickness crack (two-dimensional geometry) is based on the measurement of in-plane displacements (or strains) in the crack tip region. The moiré fringes, which leads to displacement or strain measurements, are developed as a result of an interference created by an optical mismatch of two grid patterns; one pattern is the model grid which is placed on the structure, the other is the reference grid which has the same pattern as the model grid in the unloaded condition. As the moiré fringes are converted to, say, displacement measurements in the crack tip region, the displacement (δ) of the crack surfaces close to the crack tip is related to the stress-intensity factor (K) through the relation (plane stress-linear elasticity assumed)

$$\delta = \frac{8K}{E}\left(\frac{r}{2\pi}\right)^{1/2} \qquad (7.4.3)$$

where E is the elastic modulus and r is the distance from the crack tip. Typically, measurements are made of the displacement as a function of distance from the crack tip; and, the collection of these results are used with a linear regression equation to estimate the value of K.

Continuing evolvement of the moiré interferometry techniques have produced methods for increased displacement sensitivity which are covered by a review paper by Post, et al. [2000] In a method called microscopic moiré interferometry, two techniques have evolved which are used sequentially: a) an immersion interferometer uses a fluid coupling media to produce virtual reference gratings of 4800 lines/mm – double the usual basic sensitivity, b) a complementary technique uses optical/digital fringe multiplication by fringe shifting, along with an efficient algorithm to generate an enhanced contour map of the displacement field. The two advances work in concert to result in an overall sensitivity multiplier as high as 24X.

Even planar surfaces are no longer a strict requirement for using moiré. Work by Boeman [1991] and later expanded by Mollenhauer [1997] have developed innovative methods for imaging the inner surfaces of bolt holes in composite plates.

Other variations include shadow moiré, which is useful for higher in-plane displacements, again as with regular moiré, increased sensitivities can be obtained using the optical/digital fringe multiplication techniques.

In work by Epstein and Dadkah [1993], applications to fracture mechanics solutions have been pursued. Moiré interferometry measures the stress intensity factor local to the crack-tip without relying on compliance calculations, a savings in instrumentation complications for both fracture and corrosion studies. Portable field units have been developed at Idaho National Engineering Lab for extending the use to maintenance and field activities.

A comprehensive review of experimental mechanics techniques and applications is included in Rastogi [2000].

7.4.1.3 Photoelasticity

Photoelastic techniques are based on the bi-refringent characteristics exhibited by transparent plastic materials of specific tailored compounds of plexiglas, polycarbonate, and epoxy resins. These plastics, under load, develop an isochromatic fringe pattern that can be directly related to the maximum shear stresses in the geometry being analyzed. The photoelastic materials can be selected to match with the expected elongation of the substrate material. In Table 7.4.1, the photoelastic test materials are bracketed into three levels by expected elongation range. The maximum measurable strain for a particular photoelastic coating depends upon its stress-strain curve and the linearity of photoelastic behavior.

Table 7.4.1. Coating Selection for Elongation Levels

Coating Material	Maximum Elongation	Typical Application
PS-1	5%	Testing on metals, concrete, glass, and hard plastics in the elastic and elastoplastic ranges
PS-8	3%	
PL-1	3%	
PL-8	3%	
PS-3	30%	Testing on soft materials such as rubber, plastics and wood
PL-2	50%	
PL-3	>50%	
PS-4	>40%	
PS-6	>100%	Testing on soft materials such as rubber, plastics and wood

Chart courtesy of Vishay Measurements Group, Inc.

The bi-refringent sensitivity is another important factor to consider when choosing a photoelastic coating [Vishay Measurements Group, Inc., 2001]. The overall sensitivity of the strain measurement system depends on:

- The sensitivity of the coating is expressed by the fringe value, ϕ. The fringe value represents the difference in principle strains, or the maximum shear strain, required to produce one fringe. The lower this parameter, the more sensitive the coating,
- The sensitivity of the polariscope system for examining the photoelastic pattern and determining the fringe order, N.

The primary difference between the approach used for two- and three-dimensional work is that two-dimensional models can be directly analyzed under load whereas the three-dimensional model must be reduced to a two-dimensional model before the crack tip fringe information can be recovered. To obtain the fringe results from the three-dimensional model, the isochromatic fringe pattern must first be frozen in place while the model is under load; the stress freezing is accomplished through a thermal treatment that takes the material above a critical temperature for a hold-time period which is followed by a slow cooling. Subsequent to the stress freezing operation, the three-dimensional model is sliced up to obtain a two-dimensional slice that

contains the crack segment of interest. This two-dimensional slice is then interrogated with normal photoelastic equipment (polariscope) to recover the imbedded fringe information.

A new development for building 3-D structural models is by using stereolithography (SLA). [TECH, Inc. 2001] SLA is a rapid prototyping process by which a product is created using an ultra-violet (UV) curable liquid resin polymer and advanced laser technology. Using a CAD package such as Pro/Engineer, SolidWorks, or other solid modeling software, a 3-D solid model is exported from the CAD package as an .stl file. The .stl file is then converted into thin layers. The sliced model, in layers, is then sent to the SLA machine. The SLA machine uses its laser to cure the shape of the 3-D CAD model on a platform in the vat of resin from the bottom up, one layer at a time. As each layer is cured, the platform is lowered the thickness of one layer so that when the part is completely built, it is entirely submerged in the vat. Stereolithography is capable of creating the most complex geometries quickly and precisely.

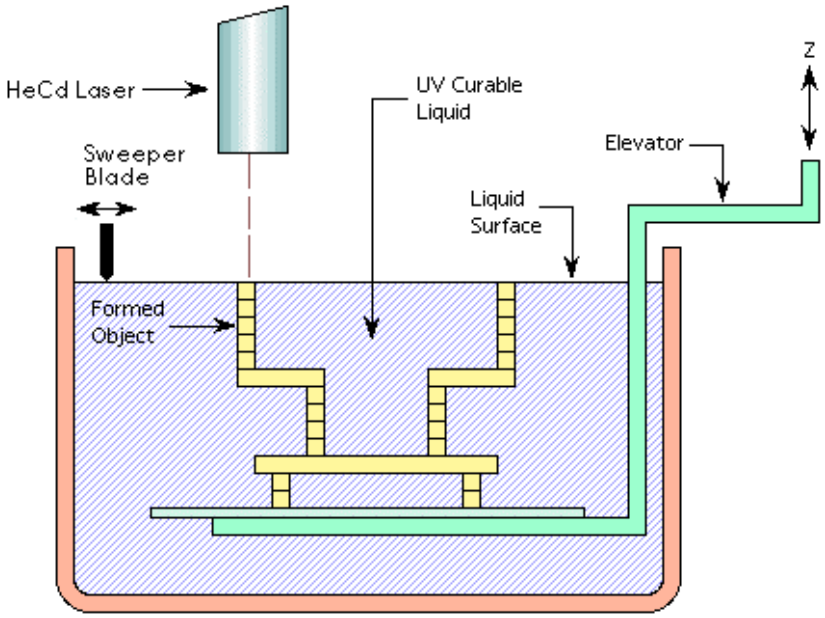

Figure 7.4.1. Stereolithography process diagram (Courtesy of TECH, Inc.)

The analysis of crack tip fringe information is the same for both the two- and three-dimensional models. For Mode 1 loading, the stress-intensity factor (K) is obtained using:

$$K = \sqrt{\pi r}\left(8\tau_{max}^2 - \sigma_0^2\right)^{1/2} - \sigma_0 \qquad (7.4.4)$$

where σ_o is an unknown pseudo-boundary stress, r is the distance directly above the crack tip on an axis perpendicular to the crack path, and τ_{max} is the maximum shear stress obtained from the stress-optic law

$$\tau_{max} = \frac{nf}{2B} \qquad (7.4.5)$$

with n the photoelastic fringe order, f the material fringe value, and B the thickness of the two-dimensional model or slice. The shear stress (τ_{max}) is typically analyzed using a truncated Taylor series that describes the behavior in the crack tip region, i.e.

$$\tau_{max} = \frac{A}{r^{0.5}} + \sum_{N=0}^{M} B_N r^{N/2} \qquad (7.4.6)$$

where Smith [1975] suggests N is chosen to be the lowest possible number that results in Equation 7.4.6 providing a good fit to the shear stress data. Figures 7.4.2 and 7.4.3 illustrate the two basic steps used in determining the stress-intensity factor from photoelastic experiments [Smith, 1975]. For both three-dimensional surface crack models considered, the thin two-dimensional slice that was analyzed for the crack-tip fringe pattern was taken through the point p. The slice was perpendicular to the crack plane and oriented so that the slice was through the thickness; thus the slice had the appearance of a single edge cracked geometry.

Figure 7.4.2 describes the shear stress distribution (points) and the corresponding least-squares derived truncated Taylor series expansion (curve) for the two surface crack geometries considered. Figure 7.4.3 illustrates how Equation 7.4.6 and 7.4.4 are combined to extrapolate the photoelastic data to the crack tip. Figure 7.4.3 portrays the stress-intensity factor based on photoelastic data (K_{AP}) as the ratio of the photoelastic result to the preexisting theoretical result. Note that the photoelastic result is calculated from Equation 7.4.4 where the pseudo boundary stress (σ_o) is taken as zero. This stress is accounted for through the N=0 term of Equation 7.4.6. The curves in Figure 7.4.3 are based on the truncated Taylor series solutions obtained from the data in Figure 7.4.2. In both cases shown, the extrapolations lead to reasonable estimates of the theoretical results and are somewhat typical of what one might expect from photoelastic estimates of the stress-intensity factor.

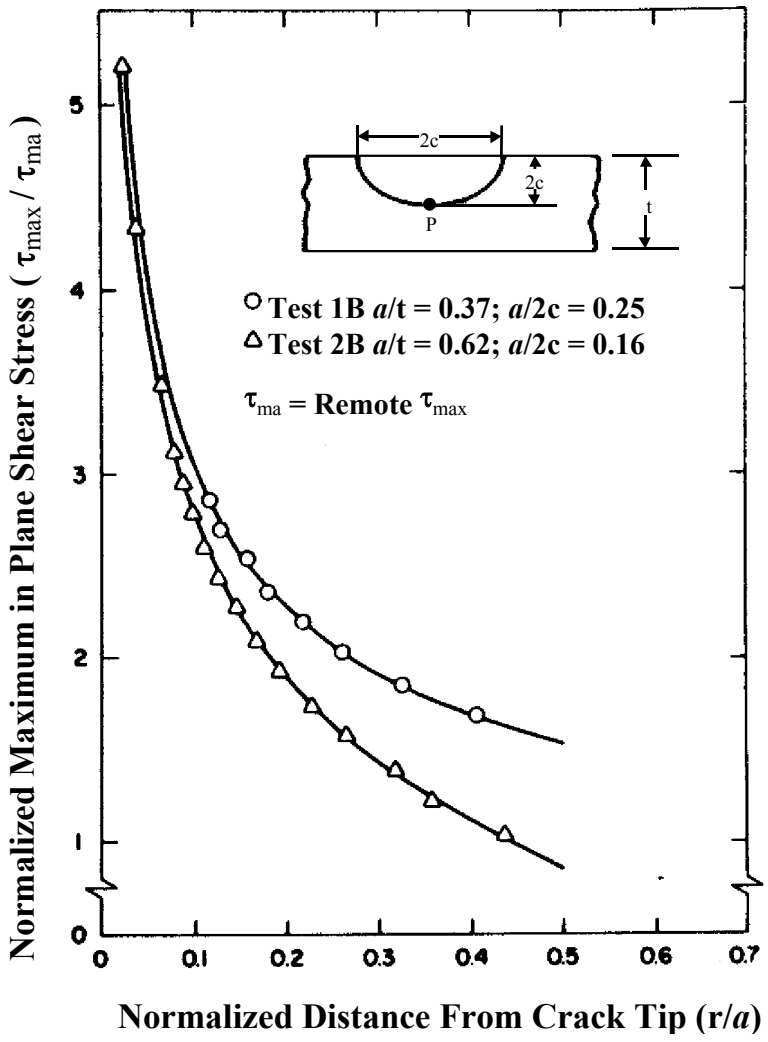

Figure 7.4.2. Typical Maximum Shear Stress Data Modeled with a Truncated Taylor Series Equation [Smith, 1975]

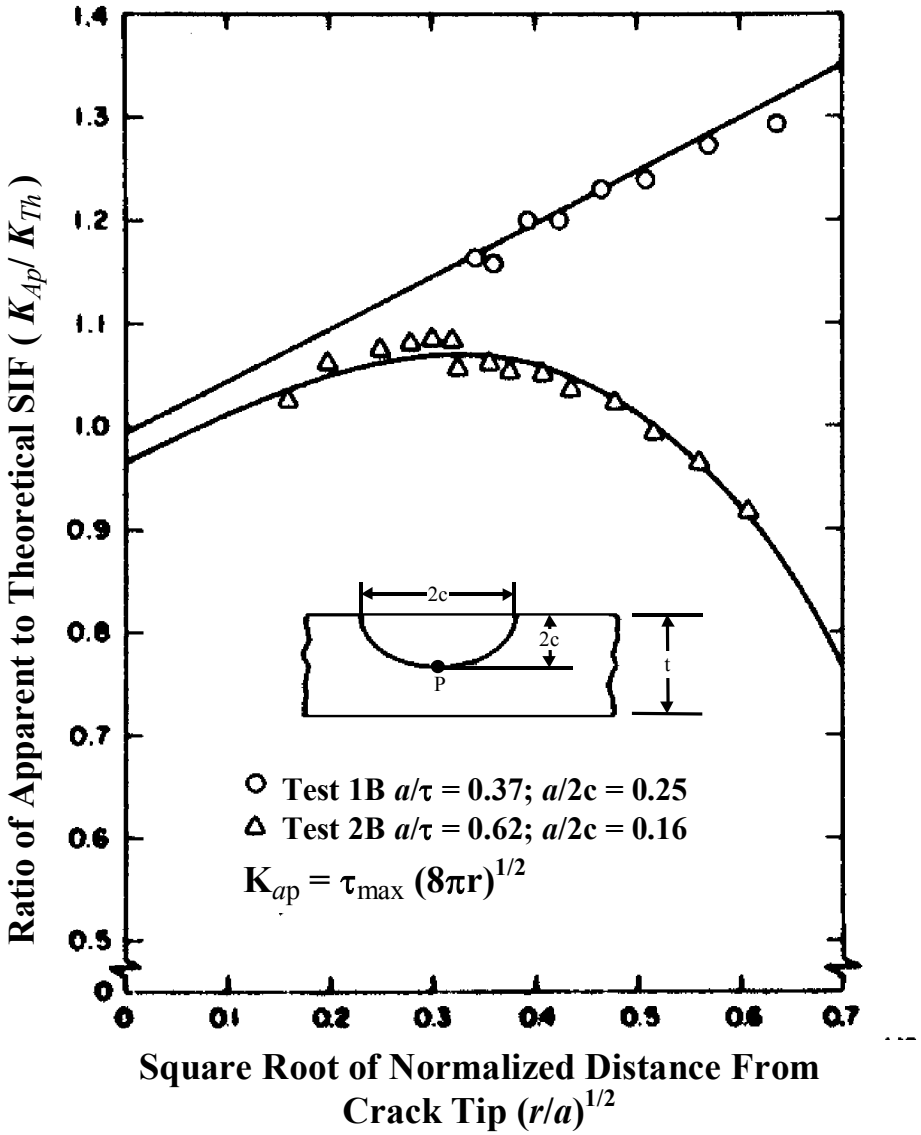

Figure 7.4.3. Extrapolation of Equation 7.4.4 Based on the Truncated Taylor Series Equation Results Presented in Figure 7.4.2 [Smith, 1975]

7.4.1.4 Crack Growth Rate

The basic hypothesis of the fracture mechanics approach to fatigue is that crack growth rate data can be described as a function of a stress-intensity factor (K) parameter associated with the fatigue loading. For constant amplitude loading, the parameter is the stress-intensity factor range (ΔK); and for steady-state variable amplitude loading histories, the parameter might be a root mean square value of the stress-intensity factor (K_{rms}). Once the basic hypothesis has been verified, crack growth data can be generated using relatively simple specimens; such data are independent of stress level, crack length, and structural test geometry, and thus can be related to the behavior of complicated structural geometries through the use of the stress-intensity factor.

The transferability of the crack growth rate data using the stress-intensity factor has provided a semi-inverse procedure for estimating the stress-intensity factor for complicated crack problems.

The semi-inverse procedure depends on the availability of two pieces of information:

- crack growth rate data for the structure for which the stress-intensity factor will be estimated, and
- crack growth rate versus stress-intensity factor type data collected for the material subjected to the same type of loading history to which the structural crack has been exposed.

The semi-inverse procedure relies on using the structure's crack growth rate (information item 1) to interpolate the material's crack growth rate/stress-intensity factor relationship (information item 2) to estimate the structure's stress-intensity factor. Figure 7.4.4 provides a schematic illustrating how the two information items are used to obtain the structure's stress-intensity factor relationship.

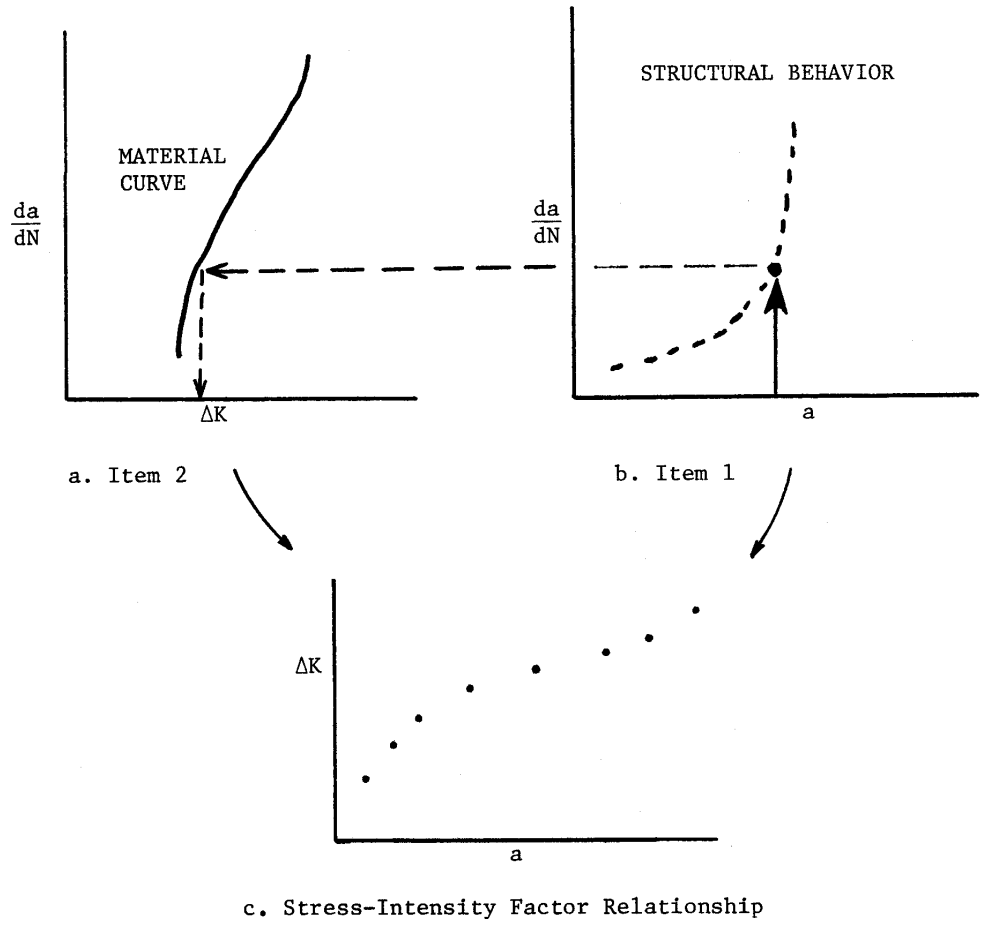

Figure 7.4.4. Semi-Inverse Fatigue Crack Growth Rate Determination of Stress-Intensity Factors

Grandt and coworkers [Grandt & Sinclair, 1972; Grandt & Hinnerichs, 1974] have applied the semi-inverse procedure to a number of problems of Air Force interest. Figure 7.4.5 describes the results for a radially cracked cold-worked hole that was subjected to two different levels of remote loading. It can be seen from the figure that the stress-intensity factor values obtained from the semi-inverse procedure (the data points) describe a relatively smooth function and closely approximate the analytical results marked linear superposition. Due to the cold-working operation, the stress-intensity factor is also seen to be substantially below that associated with the open hole configuration (curve marked Bowie), which well demonstrates the benefit of cold working.

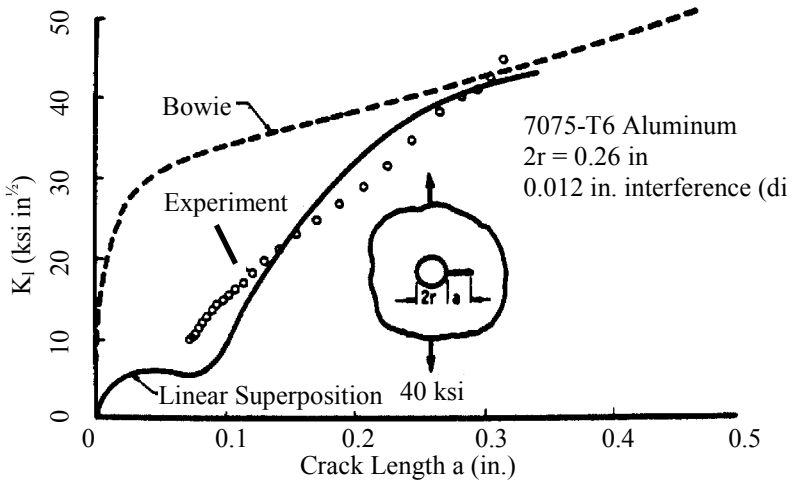

a. Remote Stress = 40 ksi, R = 0

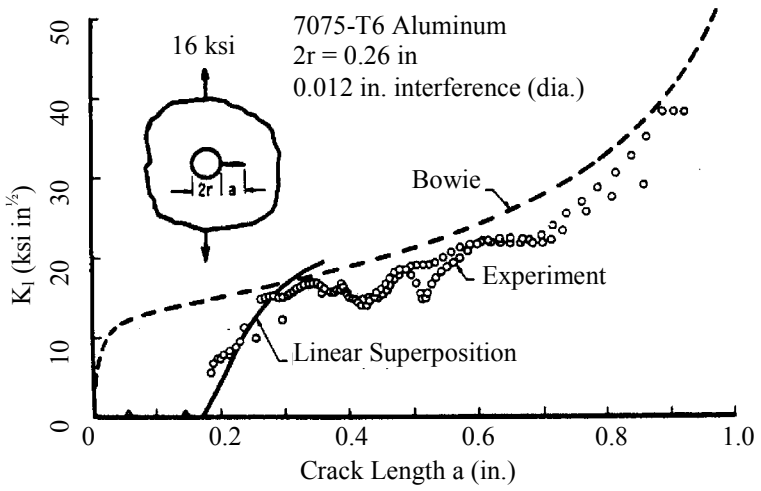

a. Remote Stress = 16 ksi, R = 0

Figure 7.4.5. Stress-Intensity Calibration for a 0.26 Inch Diameter Hole Cold-worked to Achieve a 0.012 Inch Diametrical Interference in 7075-T6 Aluminum Alloy (0.25 Inch Thick)

7.4.2 Residual Strength Methods-Verification

In Section 4, the residual strength analysis was discussed which requires a material model describing the fracture process, the specific materials data that support the model for the structural thickness and loading conditions, and the ability to derive the value of the controlling structural parameter (such as the stress-intensity factor) for the cracked structure. There are a series of residual strength tests that can be conducted during the course of the design analysis and development test activity (JSSG-2006 paragraph 4.12.2) that will support the verification of residual strength analysis capability in aircraft safety-of-flight critical structure. For example, a manufacturer could choose to conduct some constant amplitude fatigue crack growth rate tests

using radial-corner-cracked-hole type specimens or part-through thickness cracked type specimens in order to verify the stress-intensity factor analysis part of the damage integration package. Instead of cycling such constant amplitude tests to failure, the tests could be stopped prematurely and the specimens pulled to fracture. By monitoring these fracture tests and recording critical events as a function of load, the manufacturer can build a database that can be utilized to verify the applicability of various material (fracture) models proposed for the residual strength analysis.

An example illustrating some of the initial steps in verifying the applicability of a new type of fracture model can be obtained from a review of the work of Wang and McCabe [1976]. One of the first steps in verifying any residual strength analysis is to demonstrate the transferability of the data between simple cracked geometries.

Wang and McCabe considered the applicability of the R-curve (K_R) analysis to the prediction of residual strength of aircraft structures. At the time of their study, there was almost no documentation that supported the transferability of R-curve data. Wang and McCabe employed two types of crack-line-wedge-loaded compact [C(W)] specimens to provide the basic materials data and then performed a residual strength analysis on middle-crack tension [M(T)] panels. They also directly compared the R-curves from the two cracked geometries; Figure 7.4.6 describes one of their comparisons.

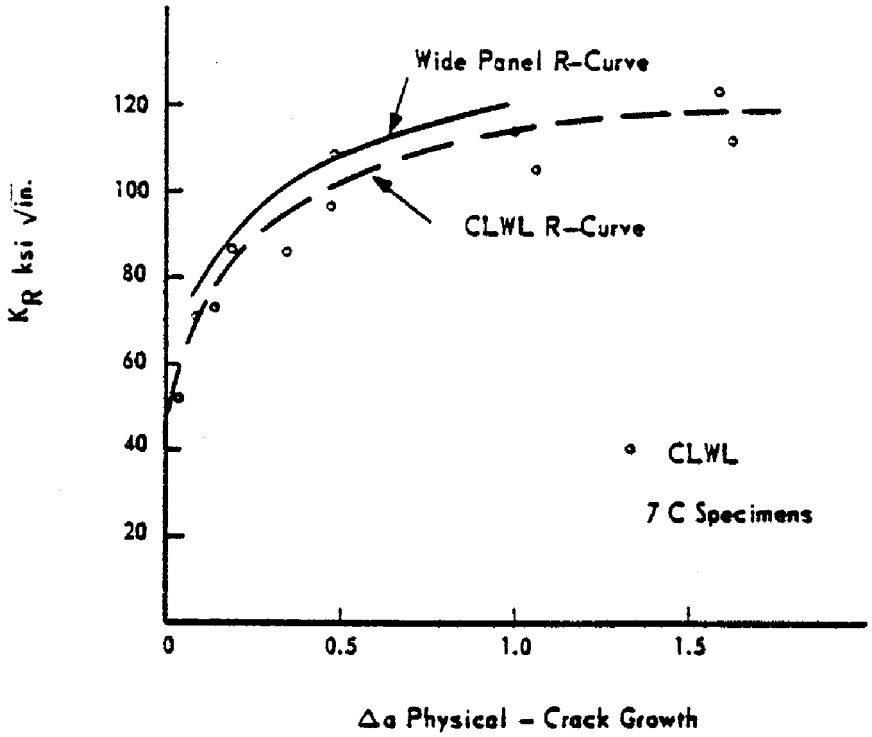

Figure 7.4.6. R-Curve Comparison for 7475-T61 Aluminum [Wang & McCabe 1976]

The Wang and McCabe residual strength results are summarized in Table 7.4.2 and in Figure 7.4.7. They were able to predict the gross stress at fracture, i.e. the residual strength, on the average to within 5 percent (on the conservative side) of the experimental results. Their most non-conservative prediction was only about 8 percent higher than the experimental value.

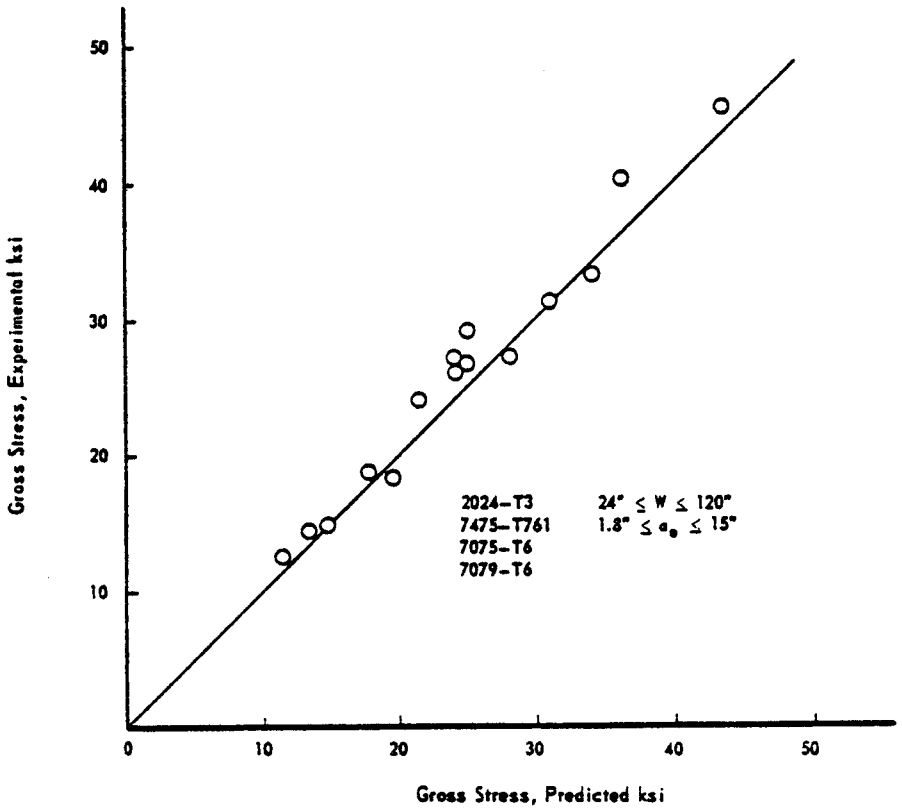

Figure 7.4.7. Summary of the Capability of the R-Curve Method for Predicting the Residual Strength of Center-Cracked Panels Using CLWL Specimen Data [Wang & McCabe 1976]

Table 7.4.2. Comparison Of CLWL Predicted Instability Conditions To Experimentally Determined Values In Middle-Cracked Panels.

			Half Crack Length (in)		Gross Stress, Fracture (ksi)		K_c ksi √in.		Net Section Stress, predicted ksi
Material	**Width (in.)**	**a_o (in.)**	**Predict**	**Exper.**	**Predict**	**Exper.**	**Predict**	**Exper.**	
2024-T3	24	4.0	5.64	4.79	24.9	26.7	121.9	116	46.6
	36	5.4	7.43	7.03	24.1	26.1	130.5	134	40.8
	120	10.0	12.57	13.46	21.6	24.22	139.5	162	27.3
	120	15.0	17.66	19.05	17.8	18.7	140.1	156	25.2
7475-T761	36	1.8	2.91	2.65	43.5	45.2	133.8	133	51.8
	36	3.6	4.85	4.75	34.1	33.1	139.4	135	46.6
	36	5.4	6.70	6.50	28.1	27.2	141.1	134	44.8
	48	4.8	6.12	5.90	31.1	31.2	142.2	139	41.7
	120	10.0	11.46	11.05	23.8	27.2	146.1	164	29.3
	120	15.0	16.50	16.05	19.5	18.1	147.3	133	26.9
7075-T6	30	4.87	5.28	5.23	13.4	14.35	59.2	63	20.7
	48	7.0	7.42	7.3	11.5	12.5	59.0	63	16.6
7079-T6	48	7.0	7.49	8.05	14.9	14.95	77.0	78	21.6
7475-T61	36	1.8	2.54	2.65	35.9	39.8	102.6	118	41.8
	48	4.8	6.13	5.7	25.1	29.25	114.8	129	33.7
	120	10.0	11.67	-	19.3	-	119.7	-	24.0

The next step in verifying the residual strength prediction model is through the testing of built-up (multiple-load-path) type structure. Such structures have the attributes of transferring load during crack propagation as well as of possibly arresting the running crack before a catastrophic failure of the complete structure occurs. As discussed in Section 11, the development of an accurate value of the structural parameter K, the stress-intensity factor, requires that the structural analyst properly account for load transfer, joint deformations, fastener effects, etc. As such, the testing of built-up structures can result in the verification of the stress-intensity factor (or other appropriate parameter) estimates as well as the material failure model and its supporting data.

As an example of results obtained to validate the use of a residual strength model for built-up structure with fracture arrest features, consider the work of Swift and Wang [Swift, 1971; Swift & Wang, 1970]. They tested extremely large flat panels with longerons and frames. The longerons were either T or hat sections. The frames were attached to the skin with shear clips; in some cases, extra tear straps were used as crack stoppers. Figure 7.4.8 describes a comparison of their predicted residual strength curves for four different configurations with the experimental results shown as points (initiation/arrest as appropriate). In most cases, the analysis was shown to be within 5 percent of predicting the experimental observation. Additional examples of residual strength verification tests for model transferability using single-load-path and built-up

structures can be found in Liu & Eckvall [1976], Verette, et al. [1973, 1977], Liebowitz [1974], and Potter [1982].

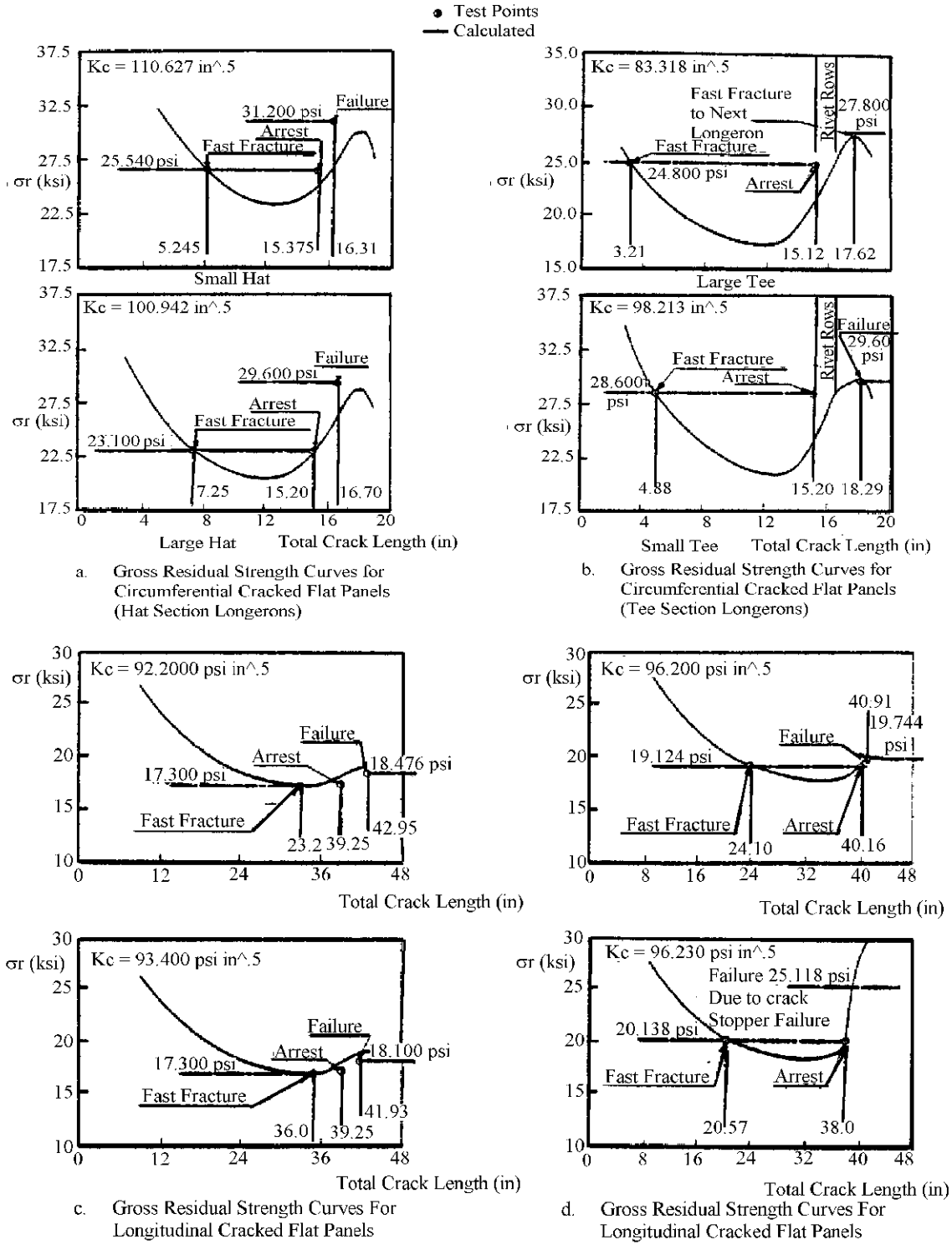

Figure 7.4.8. Test Results of Swift and Wang on 120 Inch Wide Panels with 7075-T73 Skin

A similar program was conducted by Dawicke, et al. [1999]. Under the auspices of the NASA Aircraft Structural Integrity (NASIP) and Airframe Airworthiness Assurance/Aging Aircraft (AAA/AA) programs, a residual strength prediction methodology has been experimentally verified for aircraft fuselage structures.

The fracture criteria selected for use on the (mostly) thin gage aluminum fuselage structure was the crack tip opening angle (COTA). A detailed description of the testing methodology used for determining the COTA is given in Dawicke [1997] and Dawicke & Sutton [1993]. The COTA was selected to handle the diverse loading problems of large scale yielding, and significant stable crack growth which limited the applicability of more normal linear elastic fracture mechanics. Two finite element codes were used in the program: a) ZIP3D was used for the simple laboratory specimens which did not exhibit large out of plane displacements, b) STAGS, which is a nonlinear shell analysis code, was used for the residual strength analysis for larger specimens with large out of plane displacements.

A typical fuselage skin material, 2024-T3, was used throughout the program. Specimen thicknesses were 0.040, 0.063, and 0.090 inches. The laboratory test results of the CTOA were used to predict the results from larger structural element and full scale structure validation tests. The final test in the series was a full size fuselage segment with combined internal pressure loading and axial tension loads to simulate fuselage body bending.

The CTOA fracture criteria projects that crack growth will occur when the included angle of the two crack surfaces (Figure 7.4.9) with respect to the crack tip reaches a critical value. The critical angle for a given material is nearly constant after growth exceeds the half thickness point, as shown in Figure 7.4.10. An increase in the thickness of the specimen causes a decrease in the CTOA, as shown in Figure 7.4.11.

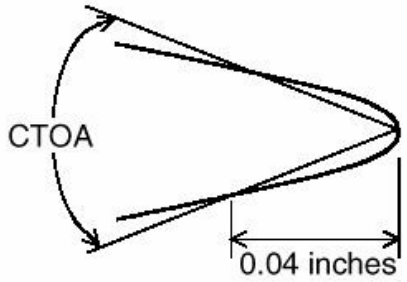

Figure 7.4.9. Schematic of the Definition of Critical Crack-Tip Opening Angle (CTOA) [Dawicke, et al., 1999]

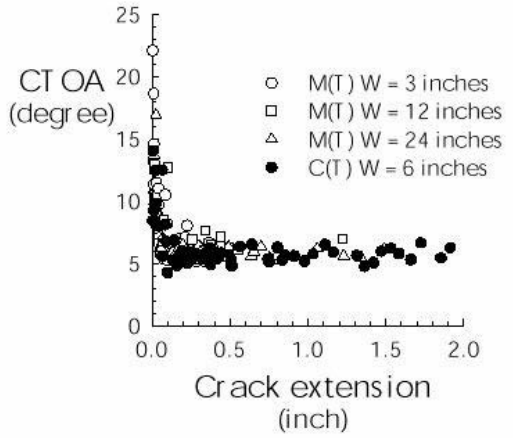

Figure 7.4.10. CTOA Measurements For 0.063-Inch-Thick, 2024-T3 Aluminum Alloy [Dawicke, et al., 1999]

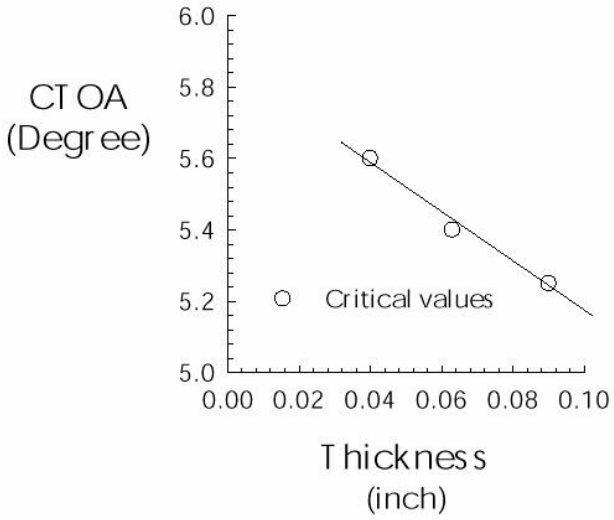

Figure 7.4.11. Influence Of Specimen Thickness On The Critical CTOA For 2024-T3 Aluminum Alloy [Dawicke, et al., 1999]

Another complexity that was introduced by using the STAGS 2D FEM was the necessity to account for the through-thickness constraint effects by using an approximation for the plane strain core (PSC). This approximation of the PSC height is nominally equal to or less than the specimen thickness (Figures 7.4.12 and 7.4.13).

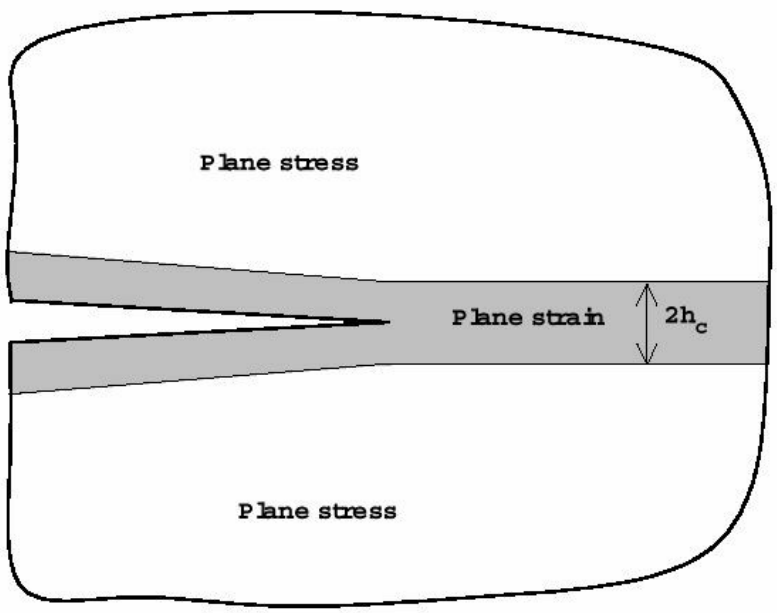

Figure 7.4.12. Illustration of the Plane Strain Core Around a Crack [Dawicke, et al., 1999]

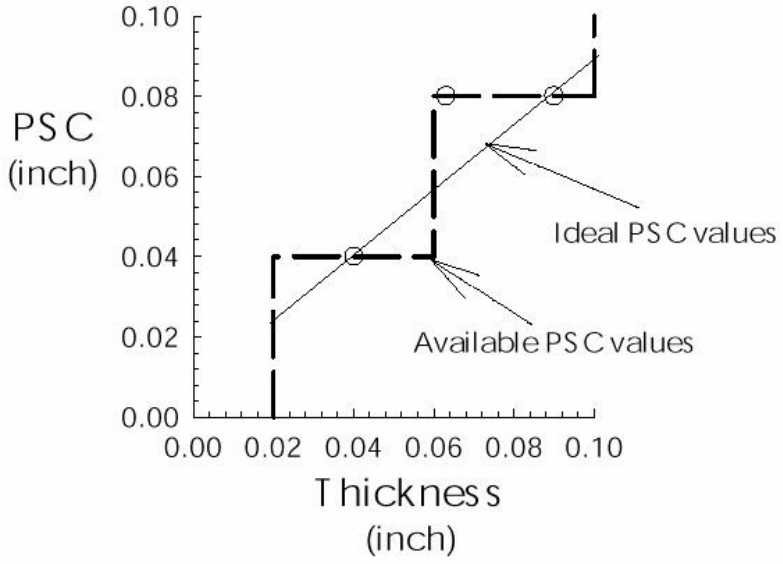

Figure 7.4.13. Plane Strain Core Heights (PSC) for the 0.04, 0.063, and 0.09-inch-thick 2024-T3 Aluminum Alloy Specimens [Dawicke, et al., 1999]

The report summarizes a successful application of the CTOA fracture criteria in conjunction with a 2D non-linear FEM model. The critical CTOA and the plane strain core (PSC) were acquired from small laboratory size specimens and the results were projected for wide panel (40 inches)

(Figure 7.4.14 and 7.4.15) and full scale fuselage structural components. For a specified thickness, the predicted value to the experimental test value was within 10% for all the program specimens.

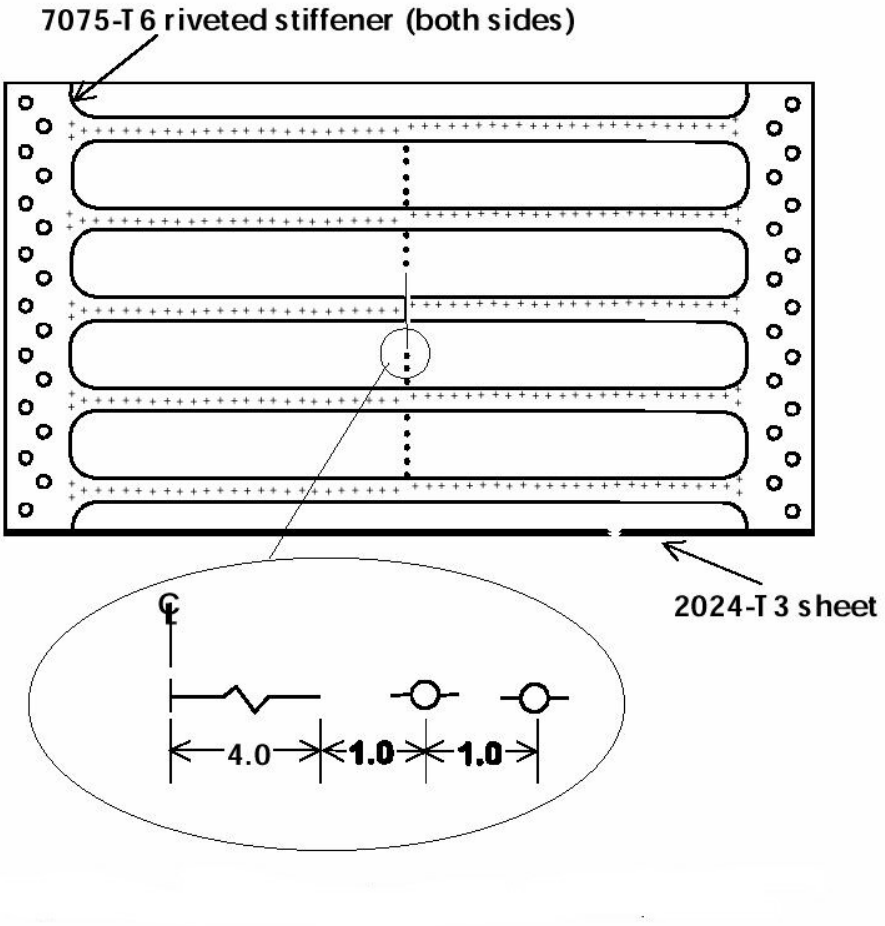

Figure 7.4.14. Stiffened Panel and MSD Crack Configuration [Dawicke, et al., 1999]

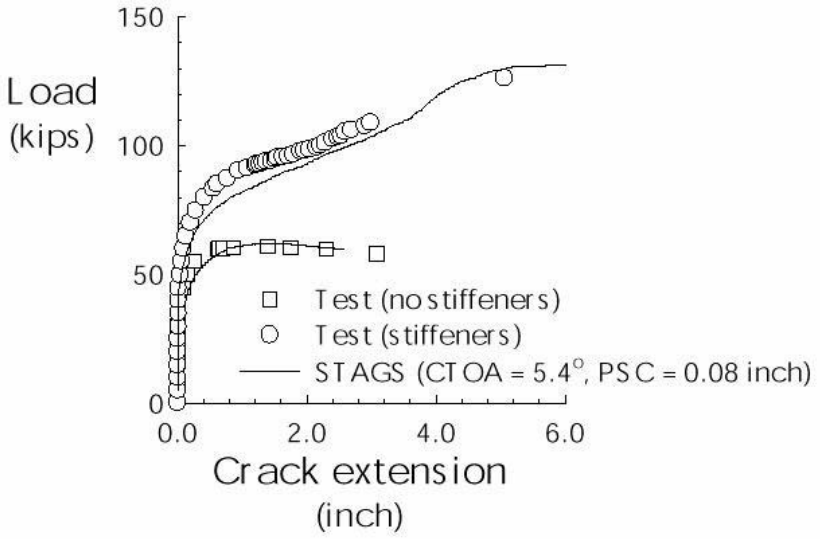

Figure 7.4.15. Fracture Test Results For 2024-T3, B=0.063-Inch-Thick, 40-Inch-Wide M(T) Specimens With and Without Stiffeners and STAGS Predictions Using CTOA=5.4° and PSC=0.08 Inch [Dawicke, et al., 1999]

The residual strength verification testing continues through both the design analysis and test development phase and the full-scale flight and ground test phase of an aircraft development contract (JSSG-2006 paragraph 4.12.2 and A4.12.2). For cost-effectiveness, it is useful to terminate a number of fatigue tests (used to verify the crack growth analysis or test spectrum design) with a controlled fracture test. Continuing a fatigue test until failure occurs may give incomplete or false information about the residual strength characteristics of the structure. Hence, it would not be appropriate to use fatigue failures to verify residual strength. The problems associated with attempting to verify residual strength analysis or characteristics using the information from fatigue test failures are summarized below:

1) The damage tolerance requirements specify residual strength loads, P_{xx}, which are all on the order of limit load. Stresses on the order of the limit load stress may occur seldom in the test stress history; they may not occur at all during the last part of crack growth. As a result, the cracks may grow much longer than the critical size associated with the stress level at the Pxx load. Then final failure will occur at a much lower stress.

2 Letting failure occur in the course of a crack growth test introduces a difficulty in determining the stress at fracture. If the loading is constant amplitude, it is reasonable to assume that fracture occurs at the peak stress. In variable-amplitude loading a series of low stress cycles may be followed by one high stress cycle during which fracture occurs. It is not certain now whether fracture took place at the peak or at a somewhat lower stress.

3) The critical crack size may be difficult to determine. Usually some crack growth has occurred since the last measurement. During the last cycles, crack growth

may accelerate fast. This usually means that the fracture surface is very similar to that of a static fracture. As a result, the size of the fatigue crack at which fracture occurred is not well delineated on the fracture surface.

4) The crack growth at low stresses may continue so long that fracture occurs at a crack size that is too long with respect to specimen dimensions. A rational comparison with other test data is complicated due to the remaining ligament requirements and could be misleading.

Therefore, it is useful to perform a controlled residual strength test near the end of the crack growth test. For this purpose, the critical crack size is estimated on the basis of the stress at the required P_{xx}. The test is discontinued when this crack size is reached. Then an appropriately instrumented fracture test is performed. In this respect, it is important that the specimen is of sufficient size. There can be no question about this when a complete component is tested. In that case, any size requirement is overruled.

7.4.3 Crack Growth Modeling-Verification

The basis of all crack growth calculations is the damage integration package discussed in Section 5, which includes the models and procedures used in estimating the effects of the load and environmental events in the operational history that must be verified. To model the impact that a variable amplitude load history has on the crack propagation characteristics of a structure, the damage integration package must be able to predict the effects of load amplitude, stress ratio (R), load sequences, and hold time events, as well as load frequency and waveshape in the case of a material sensitive to environmental effects.

Testing for verification of the crack growth models in the damage integration package should be conducted using middle-cracked panels. The middle-cracked panel geometry is characterized by widely accepted stress-intensity factor calibration and the results of spectrum tests with this geometry are easiest to correlate. It is recommended that the procedures outlined in Section 7.2 and in ASTM E647 relative to geometry, crack measurement, and pre-cracking be employed when using the middle-cracked panel specimen for non-constant amplitude loading.

Additional tests should be performed on specimens with radial corner cracked hole geometries and on specimens containing surface flaws in order to verify methods that describe the change in crack shape as the crack grows. It is important that corner-crack and surface-crack geometries be included in any crack growth verification test program in view of their relevance to the damage tolerance criteria. Radial corner-cracked-hole specimens and other part-through thickness specimens require special preparation techniques. Typically, the radial corner-cracked hole specimens are prepared in two steps. The first step is to introduce damage (EDM notch, saw cut, etc.) into a hole that is undersized and pre-crack the specimen until a crack of sufficient size appears. The second step is to enlarge the hole, remove the initial damage, and leave a crack with the required size in the specimen. It is necessary in the first step during pre-cracking to limit the stress-intensity factor levels so that the crack tip is not exposed to levels higher than what will be experienced during the test start up. Sometimes to preclude overload effects, the radial-cracked specimen is pre-cracked subsequent to the second step.

The surface flaw (part-through-crack) specimens are normally prepared along the lines suggested by ASTM E740. While the objective of this standard is to describe a fracture test of a part-

through-crack type structural geometry, the standard details damage preparation techniques as well as pre-cracking procedures.

Because each material responds differently to the same spectrum, and because each load history will cause different amounts of damage in different materials, a crack growth damage integration package will be based on a combination of models and experimentally established constants. Typically, the effects of load amplitude, stress ratio and load sequence are addressed through the use of a model that effectively combines a crack-growth-rate-based stress-ratio model with a crack-growth-retardation model which in turn accounts for the effect of tensile and compressive overloads, as well as multiple overload occurrences. The stress-ratio models as well as the retardation models are empirically based as was discussed in Section 5. The tailoring of the retardation model so that it adequately represents effects of a given spectrum and material is one of the more difficult tasks of the damage tolerant design analysis and test development activities.

The tailoring of the retardation model is based on crack growth life predictions of test results using reliable baseline (constant amplitude) crack growth rate data. In terms of developing a good correlation between prediction and test results, the following guidelines apply for each test. First and foremost, there should be a good estimate of the crack growth life based on the growth from crack initiation to test termination. Second, and normally just as important, the shapes of the predicted and test crack growth curves should match as closely as possible. Figure 7.4.16 illustrates these two points: predictions A and B would be considered bad, even though the life to failure was predicted correctly. Correlations are considered good if the prediction of all relevant points are within about 20 percent of the test data, as indicated by the shaded region of the figure. Typically, a number of tests with different conditions must be conducted before the damage integration package can be accepted with confidence. It is recommended that each crack growth test be summarized with crack growth life curves (predicted and test). The next several paragraphs describe a verification test program for an improved damage integration package.

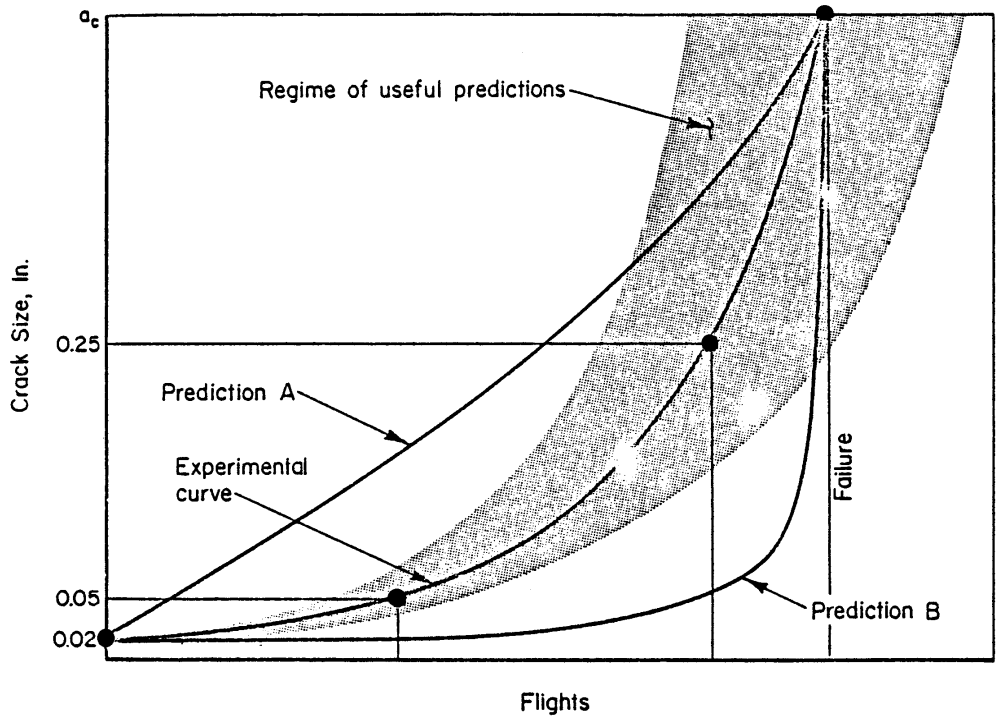

Figure 7.4.16. Comparison of Analytical and Experimental Crack Growth Curves

In a study for the (then) Flight Dynamics Laboratory, Chang [Chang, et al., 1978; Chang, et al., 1981; Chang, 1981] conducted a series of crack growth tests on 2219-T851 aluminum alloy that were used to verify the accuracy of an improved damage integration package imbedded within the computer code EFFGRO. In Chang, et al., [1981], Chang summarizes the results of ten constant amplitude tests (different stress ratios), 20 tests where single and periodic overloads were applied, and 30 tests where multiple overloads and block loading conditions were studied. In Chang [1981], Chang summarized thirteen tests where different flight-by-flight loading conditions were applied; eleven tests involved fighter histories, two tests involved transport type histories. Table 7.4.3 summarizes the test program and Chang's ability to estimate the crack growth lives for the various types of test conditions based on the life prediction ratio approach.

The life prediction ratio (N_{pred}/N_{test}) is the life determined from the prediction divided by the life from the test and is calculated for each test. Table 7.4.3 provides a collective summary of all the results that Chang developed, grouped in the same way that he presented the results as well as in larger groupings. For all the tests, the mean life prediction ratio is 0.987 and the standard deviation of this measure is 0.35; the lowest and highest life prediction ratios are 0.15 and 2.48, respectively. Table 7.4.4 shows how the life prediction ratio statistics (mean and standard deviation) can be used to estimate the error in a crack growth life calculation based on the improved model. Note from Table 7.4.4 that the damage integration package will predict lives that range between plus and minus (approximately) 60 percent of actual, 80 percent of the time.

Table 7.4.3. Summary of Chang's Improved Spectrum Prediction Results Based on Tables in Chang, et al.[1981] and Chang [1981]

Chang's Table No.	Number of Tests	Type of Load History	Life Prediction Ratios (N_{pred}/N_{test})		
			Mean ± Standard Deviation	Lowest Value	Highest Value
2*	10	Constant amplitude	1.340 ± 0.500	0.81	2.48
3*	19+	Single and periodic overload	0.783 ± 0.240	0.37	1.18
4*	30	Multiple overload and block	0.938 ± 0.30	0.15	1.60
2* and 3*	29	See above	0.974 ± 0.44	0.37	2.48
2*, 3* and 4*	59	All simple	0.956 ± 0.37	0.15	2.48
2++	13	Flight-by-flight	1.131 ± 0.22	0.80	1.46
2*,3*,4* and 2++	72	All	0.987 ± 0.35	0.15	2.48

+ one additional test reported but life estimate vague
* from Chang, et al. [1981]
++ from Chang [1981]

Table 7.4.4. Error Estimate in Life Prediction Ratio Based on Assumed Normal Distribution of All Chang's Results (72 Tests)

Probability of Maximum Error Occurring (%)	Formula For Estimating Errors	Life Prediction Data For Estimating Errors (See Table 7.4.2)	Lowest Error Expected (N_{pred}/N_{test})	Highest Error Expected (N_{pred}/N_{test})
±1	Mean ± 2.58 Std. Dev.	0.987 ± 2.58×0.35	0.084	1.89
±5	Mean ± 1.96 Std. Dev.	0.987 ± 1.96×0.35	0.301	1.67
±10	Mean ± 1.645 Std. Dev.	0.987 ± 1.645×0.35	0.411	1.56

By collectively evaluating the life prediction ratios for the individual tests, for selective test groupings, and for the total number of tests conducted, the engineer can evaluate both the effectiveness of the modeling approach as well as the accuracy of individual tests. Improvements in the more fundamental segments of the model might yield substantial improvements in all the life prediction ratios, whereas isolated modification of some empirical constants might only improve the predictability of a limited number of tests. It is recommended that life prediction ratio data such as illustrated in Table 7.4.3 provide the basis for justifying selection of damage integration packages. In fact, by using such schemes for different crack geometries or load transfer situations, the engineer will have the necessary confidence that crack

growth life predictions for more complicated cases can be made with the best possible reliability. See Saff & Rosenfeld [1982], Wozumi, et al. [1980], Rudd, et al. [1982], Dill, et al. [1980], Abelkis [1980] and Lambert & Bryan [1978] for other examples of test programs designed to verify the capability of a damage integration package.

In the design of a given airplane component, generality is not required if the damage integration package applies well to the spectrum and history of that component. The most applicable prediction method has to be found. The only basis for judgment of the applicability is a series of tests with the relevant spectrum and stress history. Therefore, it is recommended that some substantiation testing be performed as soon as there is reasonable certainty with respect to the spectrum shape. The experiments should be performed on a flight-by-flight basis, with landing loads included. A reasonable number of stress levels should be used as discussed in Section 5.3. The stress sequence within a flight should be representative for service usage (Section 5) or arranged in a lo-hi-lo sequence. Block loading should not generally be applied. Experiments should be run for a few different design stress levels and one or two clipping and truncation levels in order to evaluate the effect of these changes on crack growth behavior, and to justify proposed changes to the design spectrum for component and full-scale fatigue testing. Figure 7.4.17 describes the results of one comparative study [Dill, et al., 1980].

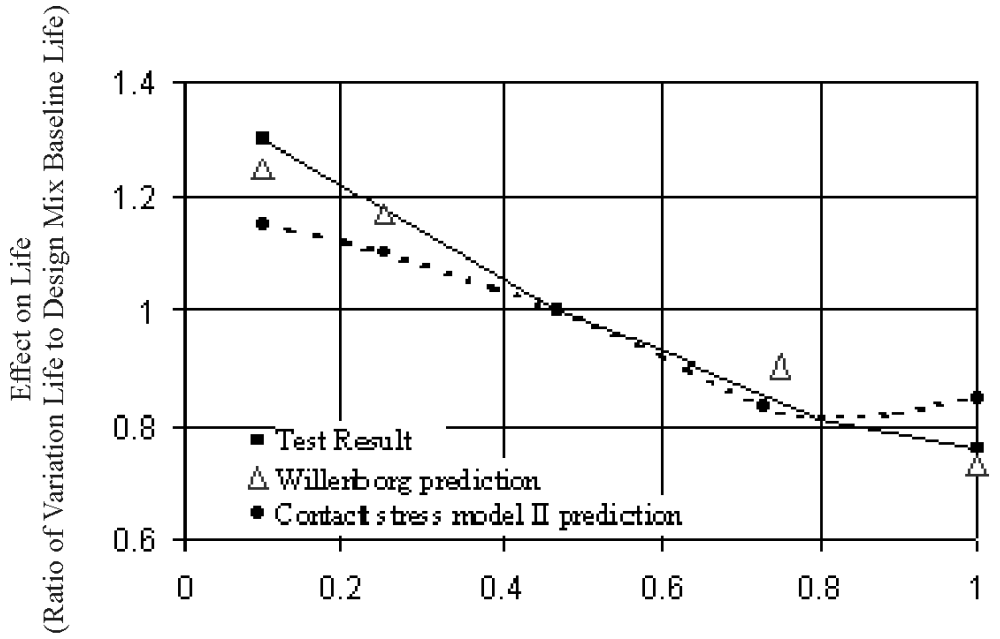

(a) Effect of Mission Mix on Crack Growth Life

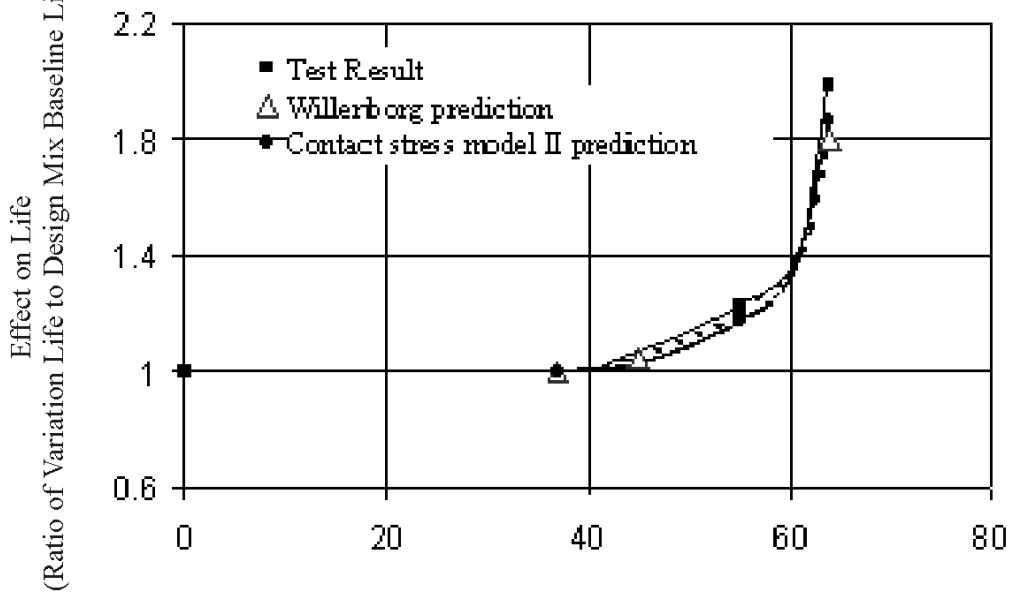

(b) Truncation Level
(Percent Limit Stress Level Below Which Loads are Truncated)

Figure 7.4.17. Effect of Spectrum Variations on Crack Growth Life Compared to Baseline (Design Mix) and to Two Damage Integration Packages [Dill, et al., 1980]

7.5 Structural Hardware Tests

The structural hardware tests have two functions: to support the verification of the complete structural design, and to define those areas of the structure that need additional attention. These tests are scheduled so that there is sufficient time to incorporate structural changes into production aircraft. In fact, production go-ahead is predicated on completing at least one design lifetime of flight-by-flight loading in the full-scale durability test (see JSSG-2006 paragraph A.4.11.1.2.2.b). Structural hardware tests include joint tests, component tests, assembly tests, as well as full-scale structural tests.

Examples of variables that may be considered for the study of different design concepts, design details and structural materials are:

- fastener systems
- type of joints and joint detail
- forged versus machined or built-up structure
- production method
- reinforcement or tear strap shape, size, and spacing
- multiple or single load path
- materials or combination of materials
- effect of design stress level

The testing of one or more of these variables will not be specifically addressed. Rather, a discussion of the essential conditions for design development testing for damage tolerance is presented in general.

7.5.1 Test Conditions

Structural hardware testing can be a form of comparative testing during the development phase. That means that the test conditions do not always have to be an exact simulation of service conditions as long as the variables considered are tested the same way. However, it is strongly recommended that service conditions be approximated as closely as possible. How closely the test conditions have to resemble service conditions depends upon the predictability of the effect of a change in conditions.

The following guidelines are applicable to structural hardware testing for damage tolerance. First, the specimen should contain the design and manufacturing details that are the subject of the investigation. The load should be properly distributed at the point of interest. Second, if the purpose is to validate a piece of structure for damage tolerance, then load sharing, load interaction, and load transfer among different members should be simulated or otherwise accounted for. Type of loading (bending, tension) should be as in service, or be such that the stress distribution at the critical location is as in the actual structure. Special care should be taken that no undesired bending is introduced due to load eccentricities. This requires intelligent grip design. It may also require some special structure to distribute the loads properly from these areas into the specimen. Third, the nominal stress at the critical location should be as in service. Experiments should be performed on a flight-by-flight basis with landing loads included. A reasonable number of stress levels should be used. The stress sequence within a flight should be representative

of service usage (see Section 5) or arranged in lo-hi-lo sequence. Block loading should not generally be applied.

7.5.2 Initial and Continuing Damage

In JSSG-2006 Tables XXX and XXXI, certain initial damage assumptions and continuing damage assumptions are prescribed. These assumptions form a basis for analysis but they cannot always be rigidly adhered to in damage-tolerance testing.

A 0.05 inch initial crack is assumed in slow-crack growth structure and in fail safe structures. If the specimens for design development testing are not provided with artificial defects, the cracks, once initiated, will grow through the sizes mentioned above. Crack-growth records would automatically cover the span of the requirements, provided the cracks can be detected. Otherwise the recorded crack-growth curve would have to be extrapolated backwards. If initial flaws are provided, it is recommended to make them the size assumed in the requirements or close to the size for analysis substantiation.

Continuing damage, from a testing standpoint, is more difficult to make as a result of the small initial sizes and the different growth requirements for different cases. Consider the example configuration shown in Figure 7.5.1 where A is the primary damage site, and B, C, D, & E are continuing damage sites. The four parts of the figure show (a) the initial damage assumed in the panel per JSSG-2006 paragraph 3.12.1 and Tables XXX and XXXI, (b) the initial damage and growth until the primary damage terminates at the edge, (c) the continuing damage that starts at B, the opposite side of the primary damage site which terminates in hole 2, and (d) the growth of continuing damage at C until termination at hole three. While the analysis can follow the assumptions required by JSSG-2006, it would be difficult (if not impossible) to manufacture the necessary continuing sizes either prior to test or after the primary damage (segment A) terminated at the edge. Therefore common practice is to put in the primary damage and continuing damage starter flaws as shown in Figure 7.5.1.a and let the specimen crack growth proceed without additional perturbations. Post test analysis of the crack growth data and fracture surface striation morphology will document this logic.

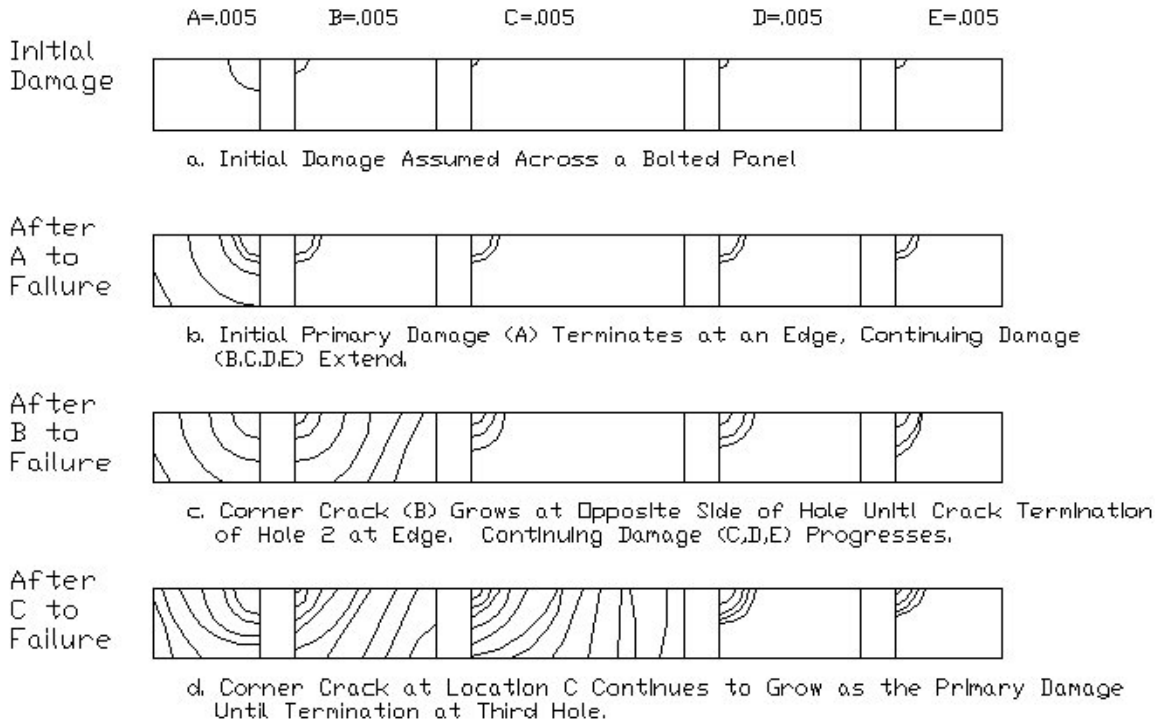

Figure 7.5.1. Primary and Secondary Damage Sites and Continuing Damage

In a AFRL/VA contracted study, Brussat et al. [1977] were able to show that the experimental fatigue lives of built-up structure with and without continuing damage flaws were about the same and that the primary crack damage chose the most effective path through the structure. Secondary cracks developed in a natural way during the test. Dormant periods when a crack ran into a hole could be estimated and subtracted if the results were used for a check of the analysis.

7.5.3 Residual Strength Testing

Residual strength tests of fail safe structure are of special importance. Interruption of a fatigue test at the critical crack size for intact structure is crucial. If the crack grows longer, the stress for rapid propagation is too low to give proper information on crack arrest capabilities and on the strength of the remaining structure at that stress (times the dynamic factor). Since these properties are essential for the qualification as fail safe structure, a proper evaluation is justified, even during design development tests.

After instability and arrest (or load path failure), if successful, fatigue testing should be continued. At that point the JSSG-2006 Damage Tolerance Requirements assume remaining structure damage. In testing, this poses the same problems as the continuing damage. Therefore, it is recommended that the remaining structure damage be developed in a natural way during damage tolerance testing; artificially induced damage may also be incorporated where necessary consistent with the initial flaw assumptions of the component. Again, fatigue cycling is discontinued when the (calculated) critical size for the remaining structure damage is reached. Then a final residual strength test is performed.

7.5.4 Damage Tolerance Test Articles

During the development cycle, the manufacturer will subject major assemblies and structural components to flight-by-flight fatigue loadings that approximate the operational environment. Some tests are specifically identified as damage tolerant tests or as durability tests, but other tests serve a dual function - first as a durability test (two lifetimes) and then as a damage tolerant test. Component durability tests or component dual function tests are normally scheduled to precede the full-scale durability test by a sufficient amount of time that would allow incorporating suggested structural modifications into the full-scale durability test article. The scheduling of the full scale damage tolerant test follows (and uses) the full scale durability test article.

The major assemblies and components selected for damage tolerant testing are chosen to provide further assurance that major elements will not fail during service and thus impact the operational readiness of the force due to safety-of-flight failures. Several examples of major assemblies and components selected during recent weapon system acquisition programs are listed in Table 7.5.1.

The damage tolerant articles will include artificially induced damage such as scratches, elox notches, sawcuts, and other types of non-crack damage, and are then subjected to an interval (about one-quarter lifetime) of flight-by-flight loading that is designed to initiate the desired starter cracks. The test interval subsequent to the precracking is up to one design lifetime with a P_{xx} loading applied at the end of the lifetime to verify residual strength capability. Crack growth should be monitored throughout the test. In-service inspection procedures should be employed whenever possible to evaluate the ability of these procedures to locate and measure the cracks.

Table 7.5.1. Major Assemblies and Components Tested to Support Damage Tolerant Design Verification

F–16	A–10	B–1A	KC–10
Wing/Fuselage Box Beam Components	Wing Lower Center Panel	Wing Carry Through Article*	Fuel Tank Panel and Fuselage Floor Beam Structure
Horizontal Tail Component	Engine/Nacelle Forward Support Frame Fuselage Support Lug	Aft Fuselage Article*	Aerial Refueling Boom
	Horizontal Tail Support Aft Frame Fitting and Attachment Lug		
	Nacelle Thrust Fitting Assembly		

* Damaged subsequent to durability test (2 lifetimes).

7.5.5 Evaluation and Interpretation of Test Results

Throughout the structural hardware test program, there is substantial attention given to cracking problems. Such problems, when they surface, identify areas where the design should be modified to ensure the soundness of the final product (see Figure 7.5.2). Each structural problem is analyzed to determine the specific cause of the problem so that appropriate candidate solutions can be incorporated into production aircraft.

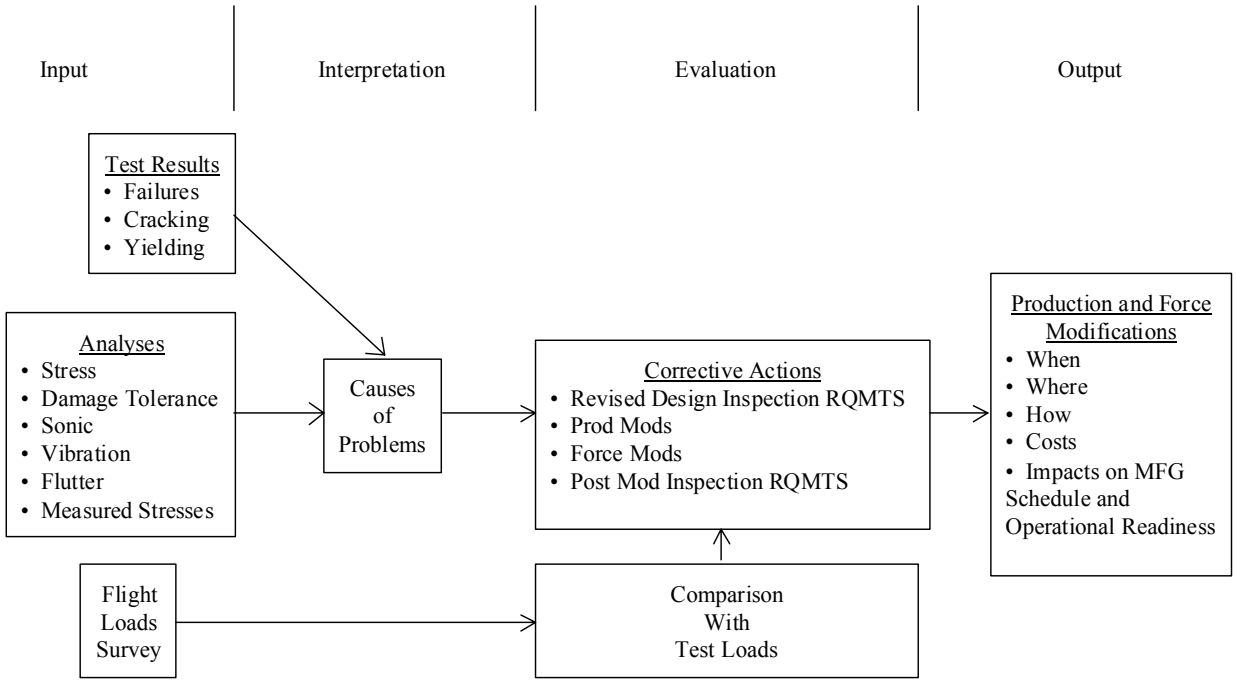

Figure 7.5.2. Summary of Interactions Resulting from Structural Failure Per JSSG-2006 Requirements

One final check on the adequacy of the structural design is the teardown inspection that follows the full-scale durability test (two lifetimes or economic life) and the damage tolerance test (one lifetime). The teardown inspection is required by JSSG-2006 paragraph 4.11.1.2.2.e to provide assurance that no critical area has been overlooked in the course of normal inspections, and to characterize the state of crack development in selected structural areas. In relation to the characterization of the state of crack development, the teardown inspection will typically include the sectioning of the structure for additional fatigue testing, residual strength testing, and/or microscopically tracking cracks back to the start of the durability test. The crack population at the end of the durability test and damage tolerance test becomes the basis for assessing the quality of the production structure through the use of the equivalent initial quality concept illustrated in Figure 7.5.3 (see Section 3 for more details).

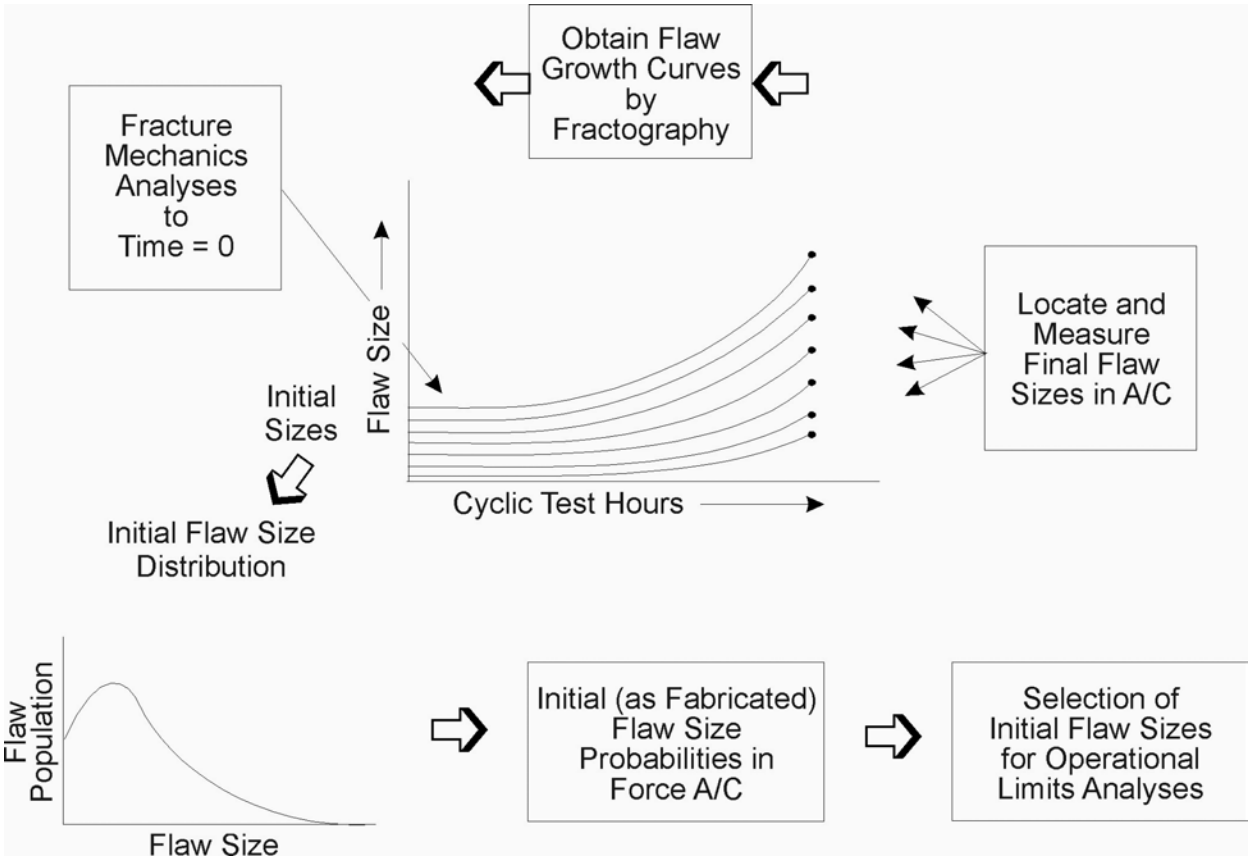

Figure 7.5.3. Equivalent Initial Quality Distribution Obtained by Backtracking Cracks Found in Durability Test Articles. Backtracking Procedures Involve Fractography and Fracture Mechanics Crack Growth Analyses

7.6 References

P.R. Abelkis (1980). "Effect of Transport Aircraft Wing Loads Spectrum Variation on Crack Growth". *Effect of Load Spectrum Variables on Fatigue Crack Initiation and Propagation*. D.F. Bryan and J.M. Potter (Eds.). ASTM STP 714, pp. 78-134. Also see AFFDL-TR-78-134 (1978, November).

ASTM, *2001 Annual Book of Standards*.

ASTM Subcritical Crack Growth Subcommittee E24.04 Internal Minutes and Stress-Corrosion Cracking Round-Robin Documentation (1974-1975).

A.P. Berens and P.W. Hovey (1981, December). "Evaluation of NDE Reliability Characterization". AFWAL-TR-81-4160 (Vol. 1), Air Force Wright Aeronautical Laboratories.

R.G. Boeman (1991). "Interlaminar Deformations on the Cylindrical Surface of a Hole in Laminated Composites: An Experimental Study, Center for Composite Materials and Structures Report 91-07". Virginia Polytechnic Institute and State University, Blacksburg, VA

T.R. Brussat, S.T. Chiu, and M. Creager (1977, December). "Flaw Growth in Complex Structures". AFFDL-TR-77-79 (Vols. 1, 2 and 3), Air Force Flight Dynamics Laboratory.

R.T. Bubsey, D.M. Fisher, M.H. Jones, and J.E. Srawley (1973). "Compliance Measurements, Chapter 4". *Experimental Techniques in Fracture Mechanics, 1*. A.S. Kobayashi (Ed.). Society for Exp. Stress Analysis, pp. 76-95.

J.B. Chang, J.H. Stolpestad, M. Shinozuka, and R. Vaicaitis (1978, March). "Improved Methods for Predicting Spectrum Loading Effects – Phase I Report (Vols. 1 and 2). AFFDL-TR-79-3036, Air Force Flight Dynamics Laboratory.

J.B. Chang (1981). "Round-Robin Crack Growth Predictions on Center-Cracked Tension Specimens Under Random Spectrum Loading". *Methods and Models for Predicting Fatigue Crack Growth Under Random Loading.* J.B. Chang and C.M. Hudson (Eds.). ASTM STP 748, pp. 3-40.

J.B. Chang and C.M. Hudson (Eds.) (1981). "Methods and Models for Predicting Fatigue Crack Growth Under Random Loading". ASTM STP 748.

J.B. Chang, R.M. Engle, and J. Stolpestad (1981). " Fatigue Crack Growth Behavior and Life Predictions for 2219-T851 Aluminum Subjected to Variable-Amplitude Loadings". *Fracture Mechanics: Thirteenth Conference*. R. Roberts (Ed.). ASTM STP 743, pp. 3-27.

M. Creager and A.W. Sommers (1977, November). "Development of a Crack Growth Rate Test for Quality Control". AFML-TR-77-193, Air Force Materials Laboratory.

T.W. Crooker, S.J. Gill, G.R. Yoder, and F.D. Bogar (1982, April). "Development of a Navy Standard Test Method for Fatigue Crack Growth Rates in Marine Environments". Presented at the ASTM Symposium on Environment-Sensitive Fracture: Evaluation and Comparison of Test Methods, held at the National Bureau of Standards, Gaithersburg, Maryland.

D.S. Dawicke and M.A. Sutton (1993, September). "Crack Tip Opening Angle Measurements and Crack Tunneling Under Stable Tearing in Thin Sheet 2024-T3 Aluminum Alloy". NASA CR-191523.

D.S. Dawicke (1997). "Residual Strength Predictions using a Crack Tip Opening Angle Criterion". *Proceedings of the FAA-NASA Symposium on the Continued Airworthiness of Aircraft Structures*. DOT/FAA/AR-92/2, pp.555-566.

D.S. Dawicke, J.C. Newman, Jr., J.H. Starnes, Jr., C.A. Rose, R.D. Youn; and B.R. Seshadri (1999, September). "Residual Strength Analysis Methodology: Laboratory Coupons to Structural Components". *Third Joint FAA/DoD/NASA Conference on Aging Aircraft*, Albuquerque, NM. http://techreports.larc.nasa.gov/ltrs/PDF/1999/mtg/NASA-99-3jcaa-dsd.pdf

H.D. Dill, C.R. Saff, and J.M. Potter (1980). "Effects of Fighter Attack Spectrum on Crack Growth". *Effect of Load Spectrum Variables on Fatigue Crack Initiation and Propagation*. D.F. Bryan and J.M. Potter (Eds.). ASTM STP 714, pp. 205-217. Also see AFFDL-TR-76-112 (1977, March).

P.R. Edwards, et al. (1981, October). "Fatigue Test Methodology". AGARD-LS-118. North Atlantic Treaty Organization, Advisory Group for Aerospace Research and Development.

J.S. Epstein and M.S. Dadkah (1993). "Moiré Interferometry in Fracture Research". J.S. Epstein (Ed.). *Experimental Techniques in Fracture*, pp. 427-508.

A.F. Grandt, Jr. and G.M. Sinclair (1972). "The Stress-Intensity Factors for Surface Cracks in Bending". *Stress Analysis and Growth of Cracks Part 1*, ASTM STP 513, pp. 37-58.

A.F. Grandt, Jr. and T.D. Hinnerichs (1974, September). "Stress-Intensity Factor Measurements for Flawed Fastener Holes". *Proceedings of the Army Symposium on Solid Mechanics, 1974: The Role of Mechanics in Design – Structural Joints*. AMMRC MC 74-8, Army Materials and Mechanics Research Center, pp. 161-176.

S.J. Hudak, Jr., A. Sexena, R.J. Bucci, and R.C. Malcolm (1978). "Development of Standard Methods of Testing and Analyzing Fatigue Crack Growth Rate Data - Final Report". AFML TR-78-40. Air Force Materials Laboratory, Wright-Patterson Air Force Base, Ohio.

G.R. Irwin (1960, August). "Plastic Zone Near a Crack and Fracture Toughness". *Proceedings Seventh Sagamore Ordnance Materials Research Conference*, MET E661-611/F.

L.A. James and W.E. Anderson (1969, April). "A Simple Experimental Procedure for Stress Intensity Factor Calibration". *Journal of Engineering Fracture Mechanics* (Vol. 1), pp. 565-568.

JSSG-2006 (1998, October). "Joint Service Specification Guide, Aircraft Structures". Department of Defense.

H.W. Kiu and J.S. Ke (1975). "Moiré Method, Chapter 4". *Experimental Techniques in Fracture Mechanics, 2*. A.S. Kobayashi (Ed.). Society for Exp. Stress Analysis, pp. 111-165.

A.S. Kobayashi (1973). "Photoelasticity Techniques, Chapter 6". *Experimental Techniques in Fracture Mechanics, 1*. A.S. Kobayashi (Ed.). Society for Exp. Stress Analysis, pp. 126-145.

G.E. Lambert and D.F. Bryan (1978, November). "The Influence of Fleet Variability on Crack Growth Tracking Procedures for Transport/Bomber Aircraft". AFFDL-TR-78-158, Air Force Flight Dynamics Laboratory.

H. Liebowitz (1974, January). "Fracture Mechanics of Aircraft Structures". AGARD-AG-176, North Atlantic Treaty Organization, Advisory Group for Aerospace Research and Development.

A.F. Liu and J.C. Ekvall (1976). "Material Toughness and Residual Strength of Damage Tolerant Aircraft Structure". *Damage Tolerance in Aircraft Structures*. ASTM STP 486, pp. 98-121.

D.E. McCabe (Ed.) (1973). "Fracture Toughness Evaluation by R-Curve Method". ASTM STP 527.

H. Mindlin and R.W. Landgraf (Eds.) (1976). "Use of Computers in the Fatigue Laboratory". ASTM STP 613.

D.H. Mollenhauer (1997). "Interlaminar Deformation at a Hole in Laminated Composites: A Detailed Experimental Investigation Using Moiré Interferometry". Ph.D. Thesis, Virginia Polytechnic Institute and State University, Blacksburg, VA.

D. Post, B. Han, and P. Ifju (2000). "Moiré Methods for Engineering and Science – Moiré Interferometry and Shadow Moiré ". P.K. Rastogi (Ed.). *Photomechanics, Topics Appl. Phys.* 77, pp.151-196.

D.L. Potter (1982). "Durability and Damage Tolerance Behavior of Adhesively Bonded Primary Structure". *Design of Fatigue and Fracture Resistant Structures*. P.R. Abelkis and C.M. Hudson (Eds.). ASTM STP 761, pp. 373-407.

P.K. Rastogi (Ed.) (2000). "Photomechanics". *Topics Appl. Phys.,* 77.

J.L. Rudd, T.R. Brussat, S.T. Chiu, and M. Creager (1982). "Experimental Evaluation of Initial Flaw Criticality and Analysis Methods for Damage Tolerant Air Force Aircraft". *Design of Fatigue and Fracture Resistant Structures*. P.R. Abelkis and C.M. Hudson (Eds.). ASTM STP 761, pp. 152-171.

C.R. Saff and M.S. Rosenfeld (1982). "Load-Environment Interaction Effects on Crack Growth in Landing Gear Steel". *Design of Fatigue and Fracture Resistant Structures*. P.R. Abelkis and C.M. Hudson (Eds.). ASTM STP 761, pp. 234-252.

D.A. Skinn, J.P. Gallagher, A.P. Berens, P.D. Huber, and J. Smith (1994). *Damage Tolerant Design (Data) Handbook.* WL-TR-94-4052. Wright Laboratory, Air Force Materiel Command, Wright-Patterson Air Force Base, Ohio.

C.W. Smith (1975). "Use of Three-Dimensional Photoelasticity and Progress Related Areas, Chapter 1". *Experimental Techniques in Fracture Mechanics, 2*. A.S. Kobayashi (Ed.). Society for Exp. Stress Analysis, pp. 3-58.

T. Swift (1971). "Development of the Fail-Safe Design Features of the DC-10". *Damage Tolerance in Aircraft Structures*. ASTM STP 486, pp. 164-214.

T. Swift and D.Y. Wang (1970). "Damage Tolerant Design-Analysis Methods and Test Verification of Fuselage Structure". *Air Force Conference on Fatigue and Fracture*, 1969. AFFDL-TR-70-144, Air Force Flight Dynamics Laboratory, pp. 653-683.

TECH, Inc. (2001) Website: www.techok.com

R.M. Verette, M.M. Ratwani, and D.P. Wilhem (1973, May; 1977, August). "Development and Evaluation of Methods of Plane Stress Fracture Analysis". AFFDL-TR-73-42, Air Force Flight Dynamics Laboratory, Part 1 and Part 2, Vol. 1.

Vishay Measurements Group, Inc. (2001). Website: www.measurementsgroup.com

D.Y. Wang and D.E. McCabe (1976). "Investigation of R-Curve Using Comparative Tests with Center-Cracked-Tension and Crack-Line-Wedge-Loaded Specimens". *Mechanics of Crack Growth*. ASTM STP 590, pp. 169-193.

R.P. Wei and S.R. Novak (1982, April). "Interlaboratory Evaluation of K_{Iscc} Measurement Procedures for Steels – A Summary". Presented at the ASTM Symposium on Environment-Sensitive Fracture: Evaluation and Comparison of Test Methods, held at the National Bureau of Standards, Gaithersburg, Maryland.

J.T. Wozumi, T. Spamer, and G.E. Lambert (1980). "An Engineering Model for Assessing Load Sequence Effects". *Effect of Load Spectrum Variables on Fatigue Crack Initiation and Propagation*. D.F. Bryan and J.M. Potter (Eds.). ASTM STP 714, pp. 128-142.

G.R. Yoder, L.A. Cooley, and T.W. Crooker (1981). "Procedures for Precision Measurement of Fatigue Crack Growth Rate Using Crack-Opening Displacement Techniques". *Fatigue Crack Growth Measurement and Data Analysis*. S.J. Hudak, Jr. and R.J. Bucci (Eds.). ASTM STP 738, pp. 85-102.

Section 8
Force Management/Sustainment Engineering

The maintenance of the damage tolerant capability of an aircraft after it enters service is the function of an activity called Force Management. Recommended guidance for accomplishing the force management objectives is contained in Tasks IV and V of MIL-HDBK-1530. As this activity can be considered to be the final phase of fracture control, a brief summary of the major force management elements is presented in the following. See Berens, et al. [1981] for a more extensive earlier discussion of Force Management.

Structural maintenance activities of a fleet are initially scheduled in accordance with the Force Structural Maintenance Plan (FSMP) of Task IV. Timing of maintenance actions (inspections, repairs, modifications, or retirement) is determined from predicted crack growth for the design environmental/stress usage. Task V calls for the initial FSMP to be updated as necessary to account for unexpected critical details and changes in usage. However, the effects of usage and time can eventually produce a degree of widespread cracking and corrosion that are not accounted for in the FSMP. Because of the uncertain nature of the sizes of cracks that might be in the fleet and the need to evaluate the interactive effects of cracks in multiple elements, the FSMP assessments of the effect of potential cracks at a single location can become inadequate. When the aircraft of a fleet are experiencing widespread fatigue cracking or corrosion, are being used beyond the original life goals, or have been repaired, a change in the initial approach to maintenance planning is required. The fleet is then said to be aging according to MIL-HDBK-1530. Structural integrity is maintained in an aging fleet through a process known as sustainment. Sustainment encompasses the actual structural maintenance as well as the analyses and tests needed to plan the maintenance tasks.

The ASIP force management concept is to monitor the usage of each aircraft and compare the computed damage accumulation, as described by a crack growth analysis, with the predicted damage accumulation of a baseline usage aircraft. The maintenance schedule of the monitored aircraft is modified as necessary to account for differences of usage from the baseline. This section discusses the major elements of force management. Since the force management techniques for sustainment analysis are still being developed, a general discussion of the damage tolerance sustainment issues is also presented.

8.1 Force Structural Management

Tasks IV and V of the ASIP guidelines of MIL-HDBK-1530 define the force management tasks for preserving the airworthiness of an aircraft throughout its design life. According to Berens, et al. [1981], force management is the "specification and direction of inspections, preventive maintenance, repairs, modifications, and damage assessments required to economically prevent structural failure and preserve the strength and rigidity of the individual airframe during its useful life." The basic objective of ASIP is to ensure operational safety and readiness of the aircraft. Force Management objectives are to:

1) Prevent structural failures through an effective maintenance program of inspections, repairs and modifications.
2) Preserve structural strength and rigidity through an effective preventive maintenance program of environmental protection and economic repair or replacement of deteriorating parts.
3) Minimize structural maintenance costs by eliminating unnecessary structural maintenance actions through effective application of data on test and operational failure modes and data on individual aircraft usage.
4) Provide a basis for planning of system phase-out and future force structure.

The guidelines of ASIP Task IV are directed at the manufacturer generated, force management data package that provides the design usage FSMP and the mechanism for collecting and analyzing data for updating the FSMP as required. Task V is directed at the implementation of the force management activities by the Air Force. Figures 8.1.1 and 8.1.2 from MIL-HDBK-1530 are functional flow diagrams of Tasks IV and V, respectively.

Under Task IV of ASIP, the airframe contractor devises a Force Management Plan that contains three essential parts: 1) the Force Structural Maintenance Plan (FSMP), 2) the Loads/Environment Spectra Survey (L/ESS), and 3) the Individual Aircraft Tracking (IAT) Program.

The initial FSMP presents the schedule for inspections and maintenance actions for aircraft that are accumulating damage according to the design loads spectra usage predictions. It is updated when the baseline operational load spectra are developed.

The L/ESS is a data collection and analysis program designed to provide the data to develop the baseline operational load spectra. A number of the force aircraft, usually about twenty percent, are fitted with data measuring and recording equipment. Parameters such as accelerations, angular rates, airspeed, altitude, weight and other load indicative quantities are obtained in a time history form as the aircraft are flown. The data are categorized by mission type and segment, and load histories are calculated for the critical areas of the aircraft. These are the same areas which were identified in the critical parts list and which will be subjected to subsequent inspection and possible repair or modification during maintenance actions. The new baseline operational damage accumulation rates based on the L/ESS data are used to update the FSMP.

The IAT program is also a data collection and analysis effort that is applied to each aircraft of the force. The minimum amount of data is collected that will allow the estimation of the damage being accumulated. Comparison with the baseline damage accumulation predictions allows modification of the FSMP to account for the differences in usage of each aircraft.

The planning for these three parts of the FSMP should begin with the initial design studies and the fracture control plan. Crack growth techniques used during the design are also those used in the IAT and FSMP portions of the program and should be formulated to permit easy incorporation. Studies made for evaluation of the effect of different load parameters on the loads computation and subsequently on crack growth calculations should be used in development of the parameter list for the L/ESS program. Accuracy requirements and parameter ranges should be selected to be commensurate with the methods of analysis.

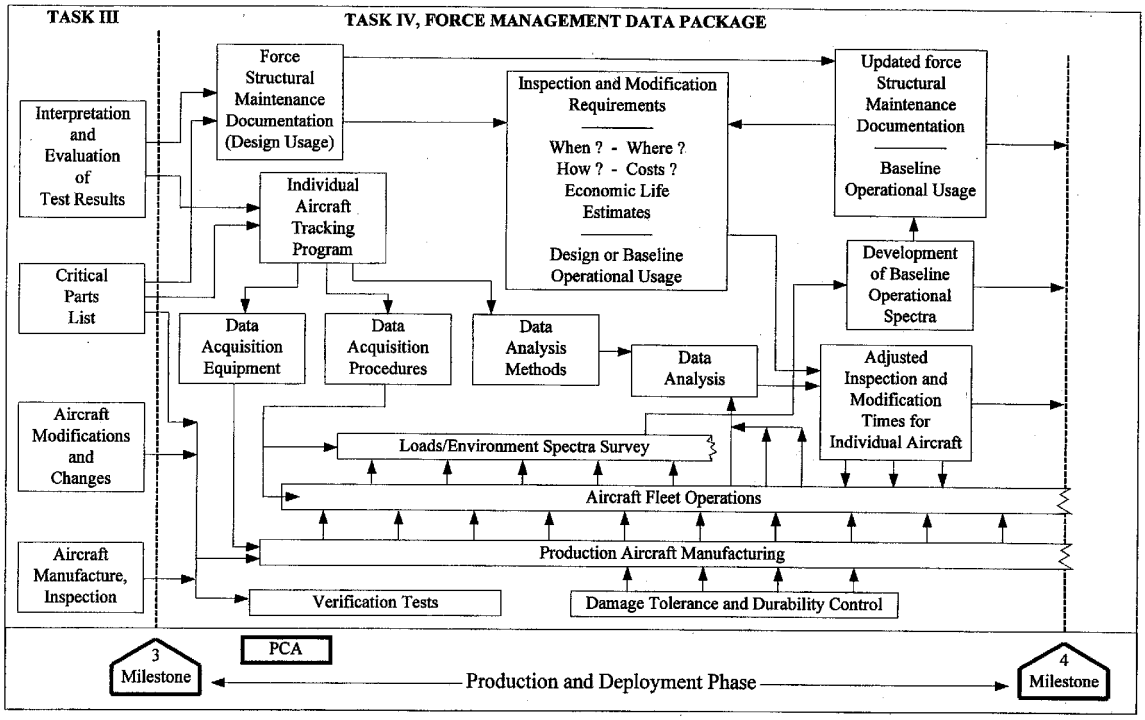

Figure 8.1.1. Functional Flow Diagram of ASIP Task IV from MIL-HDBK-1530

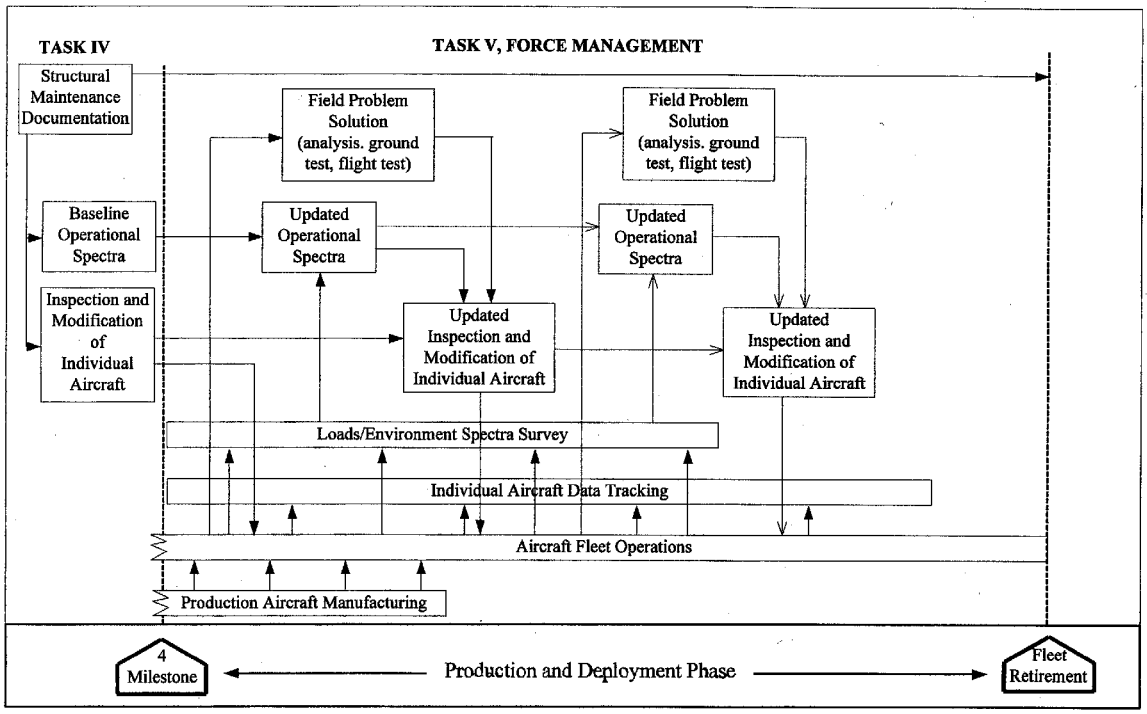

Figure 8.1.2. Functional Flow Diagram of ASIP Task V from MIL-HDBK-1530

The following subsections present general descriptive comments for the three major elements of force management. See Berens, et al. [1981] for more complete descriptions and discussions of these topics.

8.1.1 Force Structural Maintenance Plan (FSMP)

The FSMP is a schedule for performing the maintenance actions necessary to maintain structural integrity throughout the life of a fleet. In principle, the FSMP provides the Office of Primary Responsibility (OPR) sufficient detail for the establishment of budgetary, structural integrity and maintenance plans. The FSMP is initially based on design usage and is updated whenever significant changes occur in the fleet environment/stress histories. Such changes are detected through the data of the Loads/Environment Spectra Survey (L/ESS) elements. To maintain the airworthiness of the individual aircraft, the FSMP is keyed to the data generated under the Individual Aircraft Tracking (IAT) element. Figure 8.1.3 is a schematic from Berens, et al. [1981] depicting the relation between the damage tolerance analyses, the operational data collection and analysis programs and FSMP.

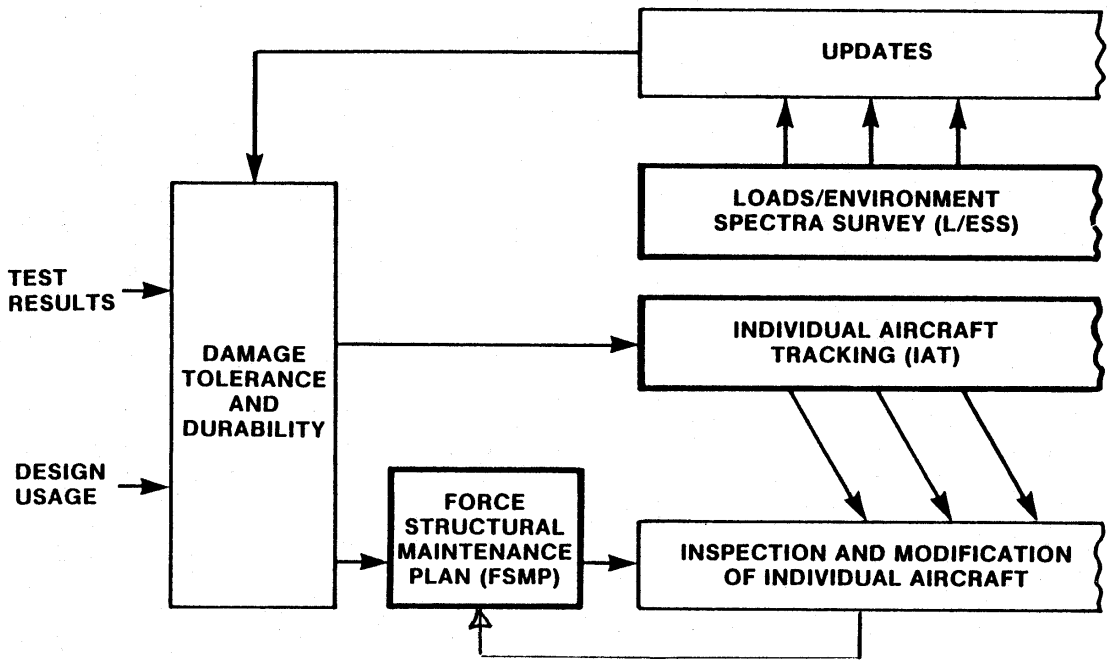

Figure 8.1.3 Relation of FSMP to IAT and L/ESS Elements of ASIP

The FSMP should contain:

1) all of the anticipated inspection, repair, and modification actions,
2) the critical locations and the crack sizes that trigger the required maintenance actions for individual airframes, and
3) supporting data required for the procedures of the Air Force Technical Order System.

The critical locations and critical crack sizes are the key items of the damage tolerance approach to structural integrity. Figure 8.1.4 is a generic schematic for the process of determining inspection intervals for a monitored location for three or more inspection cycles.

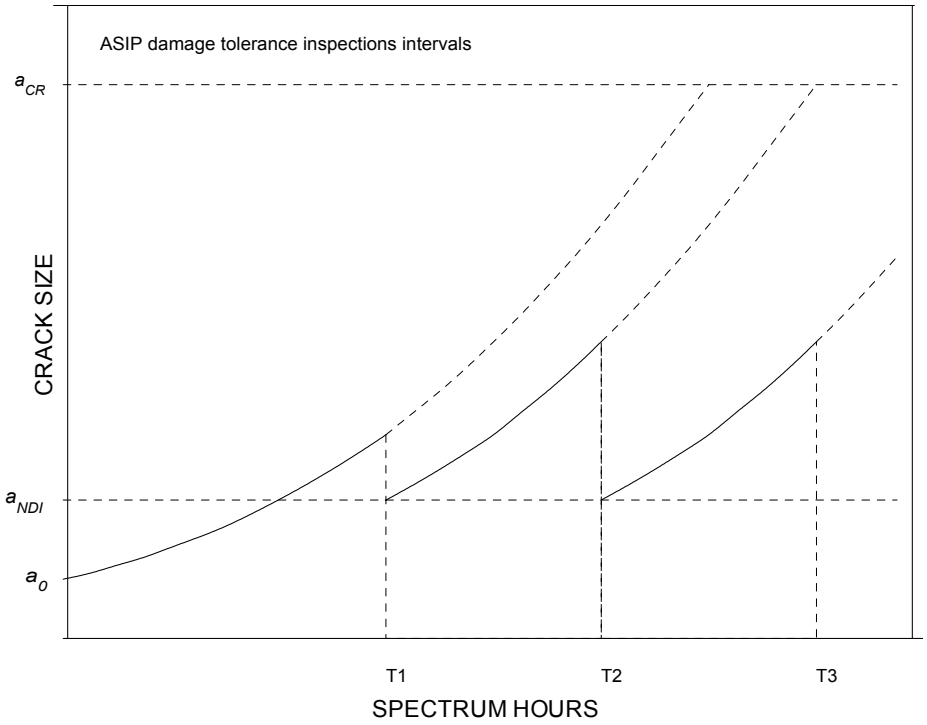

Figure 8.1.4 Schematic of Inspection Interval Determination

Inspections for safety are scheduled at one half of the flight hours for an assumed initial crack to grow to critical in the anticipated stress environment. For pristine structure, the initial crack size, a_0, is representative of flaws that might be in a structural detail as a result of manufacturing (see Section 1.3.4.1). After an inspection, the initiating flaw size, a_{NDI}, is the reliably detected crack size of the NDI method for the location. See Section 3.1. The crack size versus time curves are adjusted to account for variations in usage severity that are experienced by individual airframes.

The FSMP is based initially on the design loads spectrum, but as data is obtained from the L/ESS program a new operational baseline loads spectrum is developed and the FSMP is updated to reflect the operational usage.

The IAT program, also based originally on the design loads spectrum, is updated to reflect the L/ESS data. This update may involve changes in the IAT method but usually only includes changes in the crack growth rate in terms of the usage parameters being recorded by the IAT program.

Figure 8.1.5 from Berens, et al. [1981] shows the time sequence relation of these Force Management activities. The final activity is the airplane maintenance and the accumulation of these records.

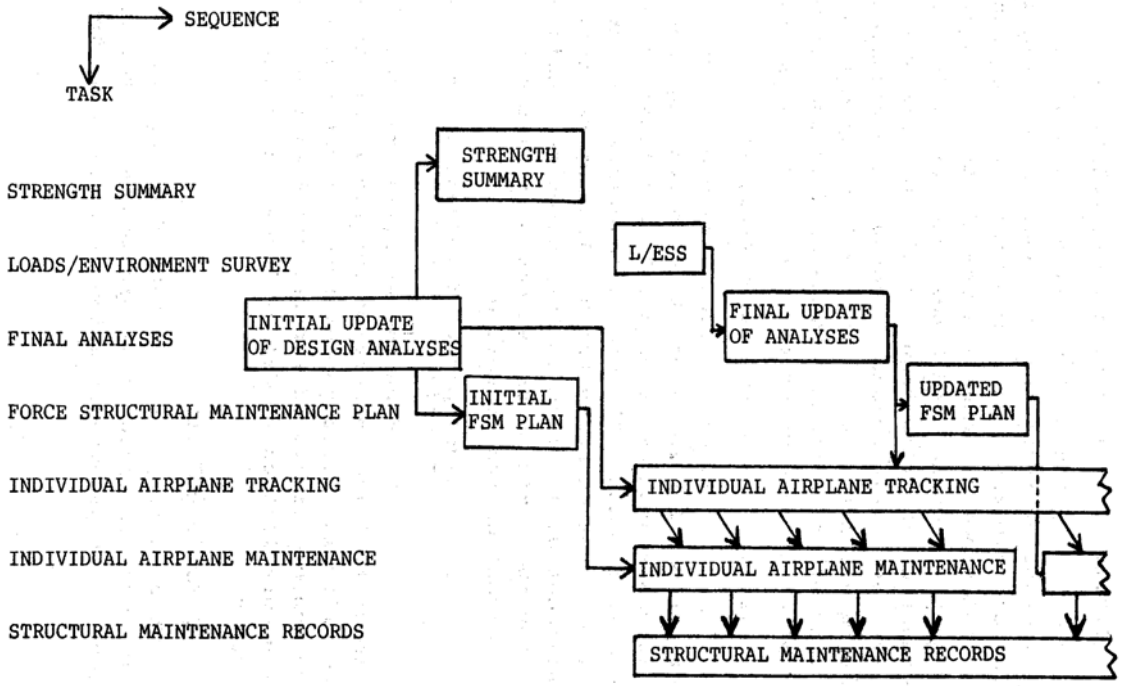

Figure 8.1.5 Sequence of Force Management Elements [Berens, et al., 1981]

The final FSM plan and all of the test results and analysis conducted during the design, manufacture, and testing of the aircraft form the final data package which is delivered to the Air Force. It substantiates the damage tolerance characteristics of the structure and describes how it may be maintained during the life of the aircraft.

A transition period normally occurs during which the contractor trains the user in all stages of the L/ESS, IAT, and FSM plan. It is essential that the user assume the same regard for the treatment of damage critical parts that was practiced during manufacture. The damage tolerance analysis is highly dependent on the size of the initial quality flaw. Manufacture processes and handling were watched so that quality was preserved. It is now the responsibility of the user to handle the aircraft in the same manner. Disregard for the structure could result in complete loss of all the previous efforts and could invalidate all of the tracking efforts.

It is the responsibility of the Air Force user to obtain the data from the L/ESS to be used in the baseline analysis update. Early collection of L/ESS data will lead to the most accurate use of the IAT data. Recognition of this operation as part of the fracture control plan should aid in the proper conduct of the task. Keeping the equipment in service and striving for the maximum amount of data return will lead to the most accurate final results. (This is, in part, also dependent on a selection of parameters that are easy to record.) Recording equipment and transducers should have a high reliability and be easy to use.

8.1.2 Loads/Environment Spectra Survey (L/ESS)

As noted earlier, the initial FSMP is based on the design load spectrum with its corresponding stress sequences at the critical locations. Experience has shown that the actual usage spectrum usually differs significantly from that anticipated at the design stage of development. Accordingly, ASIP calls for a data collection and analysis program to ascertain the baseline usage spectrum of

the fleet. The results of L/ESS provide the data for checking design load assumptions and for updating the FSMP through new crack growth curves of updated damage tolerance analyses. L/ESS does not directly impact decision making in the development of the FSMP.

The L/ESS objectives are met through the collection of time histories of sufficient parameters to characterize the magnitude, frequency, and order of the stresses being encountered at the monitored structural locations. MIL-HDBK-1530 recommends that 100 percent of operational aircraft be instrumented to measure relevant load parameters but that the data from 10 to 20 percent of the fleet be used to capture valid operational loads spectra. The assumption is made that the monitored flights are representative of all flights in a known stratification of usage such as type of mission or mission segment. The collected data are compared to the design spectrum and analyses are updated as needed. The L/ESS process continues through the life of the fleet so that data are available when change in usage dictates the need to update the damage tolerance analyses.

The L/ESS influences the FSMP through the damage tolerance analyses and analyses that feed the crack growth curves of the IAT. When sufficient data have been collected from the L/ESS to begin to define a spectrum, it can be compared with the design data that were used to generate the IAT analyses. Variations in the usage parameter distributions can be determined. Various comparisons can be made depending on the parameters being measured and analyzed in the tracking function. It is noted that the IAT parameters typically comprise a subset of the L/ESS parameters. Exceptions occur when strains are used as IAT parameters but not used in the L/ESS. Commonly, comparisons are made on the basis of differences in the load factor spectra. If the L/ESS is representative of the force usage, then the comparisons should be within sampling variation. If the spectra are significantly different, the L/ESS methods should be examined and possibly modified or the IAT methods should be examined and modified.

8.1.3 Individual Aircraft Tracking (IAT)

The Individual Aircraft Tracking (IAT) plan is an integral element of MIL-HDBK-1530. The plan is constructed by the airframe contractor as part of the Task IV, Force Management Data package. The plan is implemented by the Air Force under Task V, Force Management. The objective of IAT is to provide data on each aircraft that reflects differences in usage from that of the baseline spectra of the FSMP.

The basic concept of the IAT plan is as follows. The FSMP specifies the timing of required structural inspections and modifications and estimates the costs for repairs and inspections. These times and quantities are based on the FSMP crack growth curves as calculated from the relevant baseline (average) spectrum. Since the baseline stress histories that were used to generate these crack growth curves are not necessarily representative of the actual experience of individual aircraft, a method is needed to account for the individual differences. This is done in the IAT Program by collecting, processing and accumulating data descriptive of every flight of each airframe in a fleet. There is considerable variability in the degree of complexity of the necessary data systems required for different fleets of aircraft.

From the parameters measured in the IAT program, a crack growth increment per flight or per flight hour is computed and accumulated for each aircraft in the fleet. Comparing the observed crack growth plot with the predicted plot provides a determination of equivalent flight units for the current usage level. Figure 8.1.6 from Berens, et al. [1981] shows this comparison. The baseline usage life remaining until damage size a_f is reached is (t^*-t). The life t^* defined a specified maintenance action time. At any specific time, the total fleet can be viewed as having a distribution

of remaining life as expressed in terms of the baseline flight hours. Such information is then used for scheduling the maintenance activity.

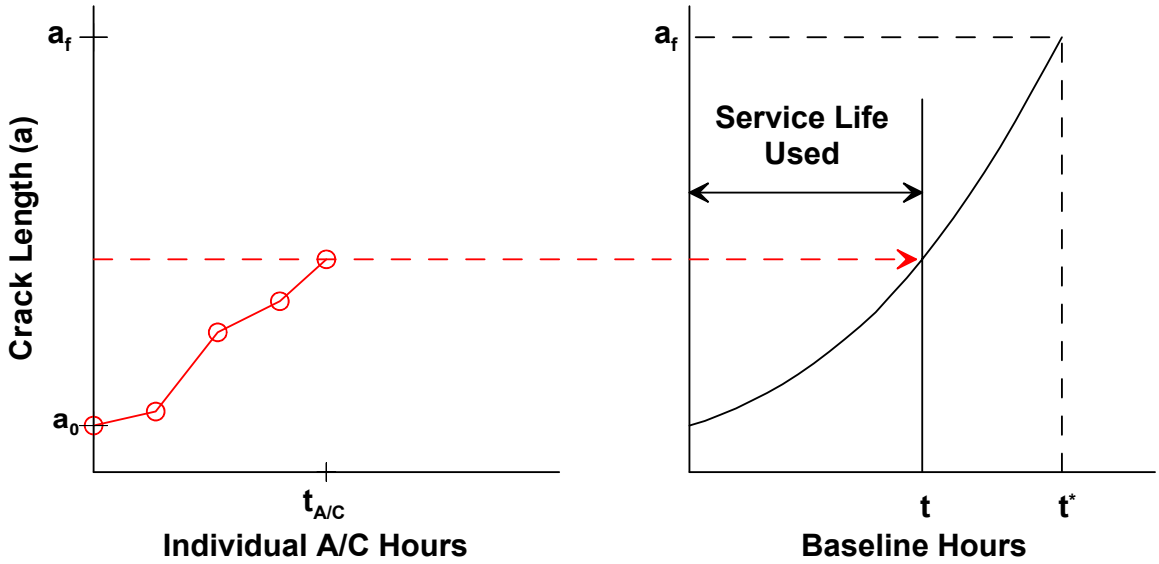

Figure 8.1.6. Relating Individual Aircraft Usage to FSM Plan Usage [Berens, et al., 1981]

Establishing the IAT plan involves the following steps:

1) the selection of the aircraft flight condition descriptions or parameters,
2) the development of a method to translate these parameters into incremental crack growth,
3) the translation of this crack growth into a measure of time which can be projected to a future date for the scheduling of some maintenance activity, and
4) the definition of a data processing system for maintaining and updating all of the analyses and record keeping.

There are many approaches to IAT as driven by the use and structural complexity of the fleet. Generally, in the past bomber/transport type aircraft have been tracked using crew reporting forms while attack/fighter/trainer aircraft have used load and flight parameters to reflect the more variable usage. See Clay, et al. [1978] for a description of the crack growth tracking methods developed during the 1970's. Many of these methods are still in use but the modern micro-processor based data recording systems are permitting the use of more sophisticated methods. See Selder & Liu [1997] for an example that calculates damage based on cycle-by-cycle crack growth analysis at each control point. These processors are also blurring the distinction between data collection for L/ESS and IAT.

8.2 Sustainment Engineering

A fleet of aircraft is considered to be aging when the FSMP must be modified due to: a) widespread fatigue damage, b) corrosion, c), repairs, or d) use beyond original life goals. Sustainment is the process by which the individual aircraft of an aging fleet are maintained in an airworthy state. Since both the actual maintenance actions and the analyses needed to plan the maintenance actions constitute sustainment, damage tolerance analyses will play a key role in scheduling the structural integrity related maintenance.

Currently, there are three structures related sustainment issues: widespread fatigue damage, corrosion, and repairs. The damage tolerance issues associated with repairs are discussed in Section 9. The following subsections briefly address widespread fatigue damage and corrosion. Research for methods for incorporating WFD and corrosion in the damage tolerance based FSMP is ongoing. Because of its role in assessing widespread fatigue and corrosion damage, a subsection (8.2.3) is also presented on structural risk analysis.

8.2.1 Widespread Fatigue Damage

The Technical Oversight Group for Aging Aircraft (TOGAA) of the Federal Aviation Administration adopted the following definition of widespread fatigue damage (WFD) for aging aircraft [Lincoln, 2000]:

> "The simultaneous presence of cracks at multiple structural details characterizes the onset of WFD. These cracks are of sufficient size and density whereby the structure will no longer meet its damage tolerance requirement (e.g. maintaining required residual strength after partial structural failure).
>
> Where damage tolerance is defined as follows:
>
> Damage tolerance is the attribute of a structure that permits it to retain its required residual strength for a period of unrepaired usage. It must be able to do this after it has sustained specified levels of fatigue, corrosion, accidental, or discrete source damage. Examples of such damage are (a) unstable propagation of fatigue cracks, (b) unstable propagation of initial or service induced damage, and /or (c) impact damage from a discrete source."

Current critical aircraft structures are designed to be damage tolerant. The structure is designed to withstand failures or discrete source damage for a defined period of operation during which the damage will be detected. For fail-safe designed structures, the analyses and tests for demonstrating fail-safety are based on the redundant or crack-stopping component to be essentially undamaged. However, if an aging airframe is experiencing WFD, the remaining structure in the load path may not be capable of stopping the propagation of the damage. Thus, WFD considerations shift the emphasis from the growth of a dominant, monolithic crack to the loss of fail-safety due to many small cracks. This shift in emphasis has major ramifications with respect to the application of the ASIP damage tolerance process.

A damage tolerance criterion for scheduling inspections for WFD would need to be based both on the size of the cracks to be reliably detected and on the number and location of the cracks in the crack-stopping structure. It has been shown that cracks on the order of 0.040 in. in the crack stopper can compromise fail-safety [Swift, 1987, 1992a, 1992b]. At present, the reliable detection of such small cracks, while possible, is cost prohibitive for the many details over the broad

expanse of structure that would need inspection. Further, the damage tolerance analysis process is essentially deterministic. The loss of fail-safety can occur as a result of many combinations of crack sizes and locations in the crack stopper of the propagating damage. The use of conservative, fixed-crack sizes in all of the crack stopper details would permit a deterministic analysis but would lead to unacceptably short inspection intervals. Therefore, maintenance planning for WFD cannot be done with the ASIP damage tolerance process.

Since the aircraft can perform normal flight operations with WFD, its presence can easily be overlooked. The problem for maintenance planning is to predict to onset of WFD so that repair, replacement, or retirement decisions can be made. At present, there is no standard method for predicting the onset of WFD but structural risk analysis has been used in the decision making process. The risk analysis objective is to determine the number of flight hours at which the probability of structural failure given a discrete source damage event exceeds a defined level. For example, in a risk analysis of the C-5A, probability of failure given the discrete source damage greater than 10^{-4} was judged to be an unacceptable level of fail safety [Lincoln, 2000]. Risk analysis is discussed in Section 8.2.3, but it might be noted that predicting the growth of small cracks can play an integral part of risk analyses.

There are two general scenarios for WFD that affect fail-safety. These are referred to as multiple-site damage (MSD) and multiple-element damage (MED). MSD is usually considered to be fatigue cracking in multiple details of the same structural element. A discrete source damage event (i.e. failure of an integral detail of an element) would raise stress levels in the remainder of the structural element. The discrete source damage event could be caused by an external disturbance or by the sudden linking of cracks in the element. An example of MSD leading to the loss of fail safety is provided by the failure in an Aloha Airlines Boeing 737 in April 1988. The failure occurred after the airframe had experienced 89,960 flights. Subsequent analyses have shown that the airframe had lost fail-safety at about 40,000 flights due to MSD (see NTSB [1989] and Lincoln [2000]).

In the MED scenario, fatigue cracking occurs in two or more multiple elements that support the same load path. Failure of selected combinations of the elements may not lead to system failure, but the effects of the failures may well lead to load and geometry effects that do influence the integrity of the remaining structure. An example of MED is provided by the fatigue cracking at WS-405 of the C-141 aircraft [Alford, et al., 1992].

8.2.2 Corrosion

Although corrosion is a major contributor to the costs of structural maintenance of aging aircraft, corrosion has not been a safety issue to date. Accordingly, corrosion has not been emphasized in ASIP. JSSG-2006 recognizes that corrosion can affect operational readiness through enhanced initiation of flaws that degrade damage tolerance, durability and residual strength. Corrosion prevention and control is addressed in Paragraph A.3.11.2 of JSSG-2006, but the emphasis here is on material selection and corrosion prevention systems. The guidance states that corrosion will not occur during the planned service life and usage because the corrosion prevention system will remain effective during the planned service life and usage. Planning for corrosion maintenance is a not formal part of the FSMP of MIL-HDBK-1530. In fact, there is no reference to corrosion in the Force Management Tasks IV and V of MIL-HDBK-1530. In Appendix B, “Additional Guidance for Aging Aircraft”, of MIL-HDBK-1530, corrosion is recognized as an aging aircraft issue. The guidance in Appendix B states that inspections for corrosion in aging aircraft should

be conducted. If corrosion is found, it should be removed. If, on rare occasion, the corrosion cannot be removed, the effect of the corrosion on structural integrity should be determined and the safety inspection schedule should be modified. This approach to maintenance is often referred to as "find it and fix it".

Corrosion is an economic burden in sustainment. Inspections for hidden corrosion are currently being performed during routine, depot level maintenance cycles. When corrosion is detected, the damage is repaired or the damaged component is replaced. Cost savings could be realized if the timing of corrosion maintenance actions could be optimized. However, at present there are no accepted analytical methods for predicting the initiation and growth of corrosion, so that a severity-of-damage type approach to scheduling inspections is not currently feasible. Such an "anticipate and manage" approach to corrosion maintenance is under development (see, for example, Peeler, et al. [2001], Brooks, et al. [2001], and Lang, et al. [2001]). This approach depends on knowing the condition of the corrosion damage through NDI, understanding the corrosion growth rates as affected by the environment, and predicting the future corrosion condition using models of corrosion growth. The present and predicted future states of the corrosion condition can then be used in structural integrity calculations to determine remaining strength and life. Disposition may now include flying the aircraft with known corrosion present, among other alternatives. Economical disposition can be made while maintaining aircraft safety.

For damage-based inspection scheduling, the capability of NDI systems must be characterized in terms of the damage metric being modeled. Refer to Section 3.1.3 for a discussion of characterizing the corrosion detection capability of NDI systems.

8.2.3 Structural Risk Analysis

The complex combinations of potential cracking within and between structural elements and the unknown state of the fatigue damage in aging aircraft essentially preclude the use of deterministic crack growth calculations for estimating the onset of WFD. Accordingly, structural risk analyses are being used to quantify structural capability. Current practice is to express structural risk in terms of the single-flight probability of failure as a function of experienced flights or flight hours from a reference age. According to Lincoln [2000], in the USAF, the acceptable upper bound on the single-flight failure probability is 10^{-7}. This degree of risk implies that less than one failure would be expected in any given fleet.

When an airframe enters service, estimates-of-failure probability would be based on the growth of monolithic cracks at the most severe, known critical locations and would be extremely small. Such estimates would be made on the basis of a probabilistic characterization of initial quality. Currently, the equivalent initial flaw size distribution is used to model the crack sizes at the critical locations. In the probabilistic approach to maintenance scheduling, inspections would be planned at intervals that keep the failure probabilities of the monolithic structures below 10^{-7}. In the aging aircraft scenarios, crack size distributions are obtained for the critical locations in the complete load path as the basis for the estimates of failure probability. Structural failure probability is then calculated as the conditional probability of inadequate strength given the condition of the elements in the load path. For example, assume there is a 10^{-3} probability of a discrete source damage event, such as a sudden fatigue crack linkup across two bays in a fuselage lap joint. To maintain an overall catastrophic failure probability less than 10^{-7}, the probability of failure in this damaged state must be less than 10^{-4}. In this example, loss of fail safety can be said to occur at the number of flight hours when the WFD reaches the state at which the probability of surviving

the discrete event exceeds 10^{-4}. The number of flight hours to reach such a state of fatigue cracking has been suggested as the definition of the onset of WFD [Lincoln, 1997].

There are several approaches that can be used to calculate single flight failure probability, but the USAF has available a computer program named PRobability Of Fracture (PROF) for risk analysis in aging aircraft. PROF is a computer program that runs in the Windows environment on a personal computer and was specifically written to interface with the data that is available as a result of ASIP. See Berens, et al. [1991] and Hovey, et al. [1998] for complete descriptions of the development of the program and its update to the Windows environment. Figure 8.2.1 is a schematic of the program for calculating probability of failure as a function of flight hours for a monolithic crack. The figure illustrates the types of data required to perform an analysis and the probability of failure (POF) output that is calculated as a function of flight hours. Another calculation module in PROF calculates probability of failure due to a discrete source damage event.

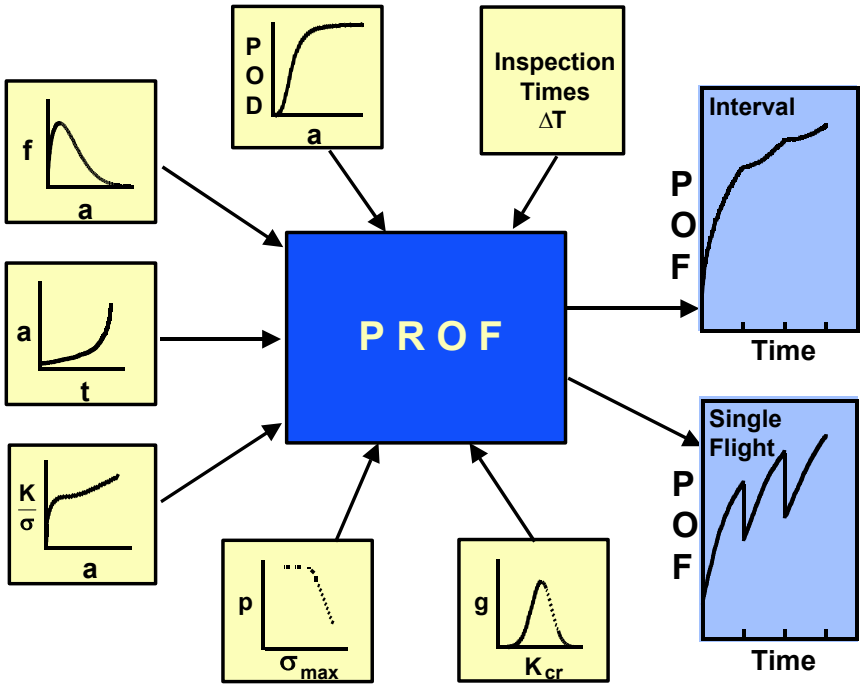

Figure 8.2.1 Schematic of the PROF Computer Program

Under ASIP, crack life predictions (*a* versus *T*) are available for every known critical location. This implies the availability of:

a) the flight by flight stress spectrum, from which the distribution of maximum stress per flight can be obtained;

b) stress intensity factors as a function of crack size, *a* versus K/σ; and,

c) fracture toughness, K_{cr}, from which a distribution of fracture toughness can be inferred.

The initiating crack size distribution can be obtained from inspection feedback, tear-down inspections, or equivalent initial flaw sizes. Probability of detection as a function of crack size,

POD(a), is from a characterization of the capability of the non-destructive inspection system used during the safety inspections.

The starting point of a PROF analysis can be representative of any arbitrary number of hours in the life of the fleet. PROF uses the deterministic a versus T curve to project the percentiles of the initiating crack size distribution as a function of flight hours. At defined flight hour increments, the single-flight probability of fracture is calculated from the distributions of crack size, maximum stress per flight, and fracture toughness. That is, the single-flight fracture probability is the probability that the maximum stress intensity factor (combination of the distributions of maximum stress per flight and crack sizes) during the flight exceeds the critical stress intensity factor.

At a maintenance cycle, the distribution of crack sizes is changed in accordance with the POD($\boldsymbol{a}$) function and the equivalent repair crack size distribution. It is assumed that all detected cracks are repaired and the equivalent repair crack size distribution accounts for the repaired cracks. PROF produces files of both the pre- and post-inspection crack size distributions. The availability of these distributions allows changing the analysis conditions at inspection times set by the analyst.

The a versus T, a versus K/σ, and crack size distributions are input to PROF in tabular form. Fracture toughness is modeled by a normal distribution and requires values for the mean and standard deviation. Maximum stress per flight is modeled by the Gumbel extreme value distribution and the parameters of the distribution can be obtained from a fit of either a flight-by-flight stress spectrum, or an exceedance curve of all of the stresses in the spectrum. The POD(a) function is modeled by a cumulative lognormal distribution with parameters μ and σ. Fifty percent of the cracks of size μ would be detected. The parameter, σ, determines the flatness of the POD(a) function with smaller values implying steeper POD(a) functions.

The module for the calculation of failure probability given discrete source damage also requires an evaluation of the residual strength in the presence of partial structural failure. Procedures for determining residual strength in the presence of discrete source damage for a number of representative aircraft skin structures can be found in Swift [1993].

Sensitivity studies have been performed on the application of PROF in representative problems [Berens, et al., 1991]. These studies have indicated that, although the absolute magnitudes of the fracture probabilities are strongly dependent on the input, relative magnitudes tend to remain consistent when factors are varied one at a time. Because of the indefinite nature of some of the input data, particularly the crack size information, absolute magnitudes of the fracture probabilities are suspect. However, it is believed that relative differences resulting from consistent variations in the better-defined input factors are meaningful.

A single run of PROF analyzes the growth of a crack for a single geometry, including crack type and shape. The analysis would apply to the population of structural details that both have this geometry and are subject to an equivalent stress spectrum. The output includes fracture probabilities for a single structural detail, for a single aircraft when there are multiple equivalent details, and for the entire fleet. The inspection intervals are set by the analyst, including the possibility for an immediate inspection at time zero.

More complex problems can be analyzed by combining the results of multiple runs. First, intermediate output can be used to initiate new runs for changed conditions. Examples of such analyses would include the introduction of corrosive thinning of the material, the effect of over-

sizing holes during repairs, and the effects of changing usage. The results from multiple runs for different details can also be combined to model more complex scenarios. Examples of such scenarios include the analyses of multi-element and multi-site damage.

There are four examples of the application of risk analysis in sustainment scenarios in the Sample Problem Section of the Handbook. The sample problems addressed are:

a) **Problem No. UDRI-2** – Structural Risk Assessment for a Discrete Source Damage Threat to the Fail Safety Capability of Stringer 7 in a Boeing 707 JSTARS Airframe.

b) **Problem NO. UDRI-3** – Structural Risk Assessment for the Multiple-Element Damage Scenario at WS 405 of a C-141 Airframe.

c) **Problem No. UDRI-4** – Comparative Risk Assessment of the Thinning Effect of Corrosion on a Representative Lap Joint.

d) **Problem No. NRC-3** – Effect of Discontinuity States on the Risk Assessment of Corroded Fuselage Lap Joints.

8.3 References

R.E. Alford, R.P. Bell, J.B. Cochran, and D.O. Hammond (1992). "C-141 WS 405 Risk Assessment". WL-TR-92-4045. *Proceedings of the 1991 USAF Structural Integrity Program Conference*, San Antonio, Texas.

A.P. Berens, D.S. Morcock, K.E. Brown, J.C. Davis, R.L. Johnson, C.E. Larson, and D.J. White (1981, April). "Handbook of Force Management Methods". AFWAL-TR-81-3079. Air Force Wright Aeronautical Laboratories, Wright-Patterson Air Force Base, Ohio, 45433.

A.P. Berens, P.W. Hovey, and D.A. Skinn, (1991). "Risk Analysis for Aging Aircraft Fleets, Volume 1 – Analysis". WL-TR-91-3066, Wright Laboratory, Wright-Patterson Air Force Base, OH, 45433, 1991.

C. Brooks, K. Honeycutt, and S. Prost (2001). "Monitoring the Robustness of Corrosion and Fatigue Prediction Models". *Proceedings of the 2001 USAF Structural Integrity Program Conference,* Williamsburg, Virginia.

L.E. Clay, N.H. Sandlin, D.S. Morcock, K.E. Brown, R.L. Johnson, and J.C. Davis (1978, December). "Force Management Methods Task I Report – Current Methods". AFFDL-TR-78-183. Air Force Wright Aeronautical Laboratories, Wright-Patterson Air Force Base, Ohio, 45433.

P.W. Hovey, A.P. Berens, and J.S. Loomis (1998). "Update of the Probability of Fracture (PROF) Computer Program for Aging Aircraft Risk Analysis, Volume 1 Modifications and User's Guide". AFRL-VA-WP-TR-1999-3030. Air Force Research Laboratory, Wright-Patterson Air Force Base, Ohio, 45469.

M. Lang, T. Hack, and V. Holzinger (2001). "Technology for Corrosion Management of Aging Aircraft". *Proceedings of the 2001 USAF Structural Integrity Program Conference,* Williamsburg, Virginia.

J.W. Lincoln (2000). "Aging Systems and Sustainment Technology". *Structures Technology for Future Aerospace Systems, Volume 188, Progress in Astronautics and Aeronautics*. Ahmed K. Noor, (Ed.).

J.W. Lincoln (1997). "Risks Assessments of Aging Aircraft". *Proceedings of the First Joint DoD/FAA/NASA Conference on Aging Aircraft*, Ogden, Utah.

NTSB/AAR-89/03 (1989). National Transportation Safety Board Aircraft Accident Report, Aloha Airlines, Flight 243, Boeing 737-200, N73711, near Maui, Hawaii, April 28, 1988.

D. Peeler, D. Raizenne, P. Sjoblom, J. Snide, and R. Rondeau (2001). "Transitioning of the Retrogression and Re-Aging (RRA) Process to USAF Hardware". *Proceedings of the 2001 USAF Structural Integrity Program Conference,* Williamsburg, Virginia.

R. Selder and Liu Ko-Wei (1997). "C-17A Individual Aircraft Tracking Program". *Proceedings of the 1997 USAF Structural Integrity Program Conference*, San Antonio, Texas.

T. Swift (1993). "WFD Monitoring Issues and Concern". *5th International Conference on Structural Airworthiness of New and Aging Aircraft,* Hamburg, Germany.

T. Swift (1992b). "Damage Tolerance Capability". *Fatigue of Airacraft Metals*. Delft University Press, *Proceedings of the Specialists' Conference Dedicated to the 65th Birthday of J. Schijve*. Delft, The Netherlands.

T. Swift (1992a). "Unarrested Fast Fracture". *Durability of Metal Aircraft Structures*, Atlanta Technology Publications, Proceedings of the International Workshop on Structural Integrity of Aging Aircraft.

T. Swift (1987). "Damage Tolerance in Pressurized Fuselages". *14th Symposium of the International Committee on Aeronautical Fatigue*, 11th Plantema Memorial Lecture, Ottawa, Canada, pp.1-77.

Section 9
Structural Repairs

The structural integrity of a force of operational aircraft is primarily ensured by implementing the periodic inspection and maintenance program defined in the Force Structural Maintenance (FSM) plan in the associated technical order (T.O.)-3 repair and -36 inspection manuals. In addition to this formal method of addressing known or potential cracking problems, the structural integrity of individual aircraft is also ensured through the timely identification of new cracking problems and by implementing repairs that will return cracked structure to a safe operational condition. This section is presented as a supplement to the other sections and only specifically addresses those guidelines applicable to ensuring that adequate damage tolerance exists in structural repairs. Adequate damage tolerance implies that cracks do not reduce the structure's load carrying capability below a predefined level throughout a required period of in-service usage.

9.1 Required Analysis

All repairs made to cracked structure, and all structure and structural changes made to in-service aircraft require some form of damage tolerance analysis. The degree of intensity of each analysis, however, depends on the consequences of failure in the repaired or modified structure if cracks are present. For example, the extent of the analysis of a repair to replace a compressively loaded fuselage member that is removed for corrosion damage would be minimal, while a force-wide modification to the tension-loaded, primary-load-path, lower wing skin structure of a fighter aircraft would require an in-depth evaluation of expected fatigue crack growth behavior.

The best categorization of what requires an in-depth damage tolerance analysis can be directly taken from the JSSG-2006 specification applicable to new structure. This specification requires that all safety-of-flight critical structure be designed using a damage tolerance analysis. This analysis ensures that cracks potentially present in this type of structure will not cause loss of the aircraft during flight for some predetermined period of in-service operation. The above suggests the first guideline for structural repairs and modifications, i.e., all structural repairs and modifications to safety-of-flight critical structure, must be subjected to in-depth damage tolerance analyses to ensure that the structure is not degraded as a result of the repair (or modification) below a level considered satisfactory for the subsequent in-service operational period contemplated.

A question arises relative to the definition of what constitutes safety-of-flight critical structure and their locations within the airframe. Based on the information required by MIL-HDBK-1530 for the support of force management operations, a critical parts list is prepared by the airframe contractor and appended to the Force Structural Maintenance (FSM) plan supplied to the Air Force. It is suggested then that clear definitions for safety-of-flight critical structure be provided with each aircraft's FSM plan along with the appendix that lists and illustrates safety-of-flight critical structure. If the manufacturer can conceive of potential problems associated with the repair or modification of special designed (or manufactured) safety-of-flight critical structure, then the manufacturer should identify such problems in the FSM plan with reference to additional details in the T.O.-3 repair manual.

The intensity of the analysis also varies as a function of the extensiveness of the change of the force. If the repair or modification can be incorporated into any given aircraft or will be applied to all aircraft in the force, than a more careful analysis of the impact of a crack potentially existing in the structure should be conducted. For one-of-a-kind repairs applied to an airframe in order to return the aircraft to a depot for more extensive repair, the type of damage tolerance analysis would be primarily of a residual strength type, without much consideration being given to variable amplitude fatigue loading.

There are two basic elements in damage tolerance analysis: a residual strength analysis and a sub-critical crack growth analysis. In the residual strength analysis, one develops a relationship between load carrying capability and crack length. In the sub-critical crack growth analysis, one determines a relationship between time-in-service and length for a given type of operation.

In a damage tolerance analysis, one obtains an estimate of the structural life to grow the initial crack damage in the structure to critical size. The residual strength analysis determines the critical crack size required to fail the structure; the sub-critical crack growth analysis is used to obtain the life estimate. One could also determine the decay in residual strength as the crack

extends under service loading by coupling the residual strength analysis with the sub-critical crack growth analysis. The first part of Figure 9.1.1 illustrates the relationship between residual strength and crack length, and the second describes the relationship between crack length and time-in-service. The third part of the figure couples the information in the first two parts to obtain the relationship between the decay in residual strength and time-in-service.

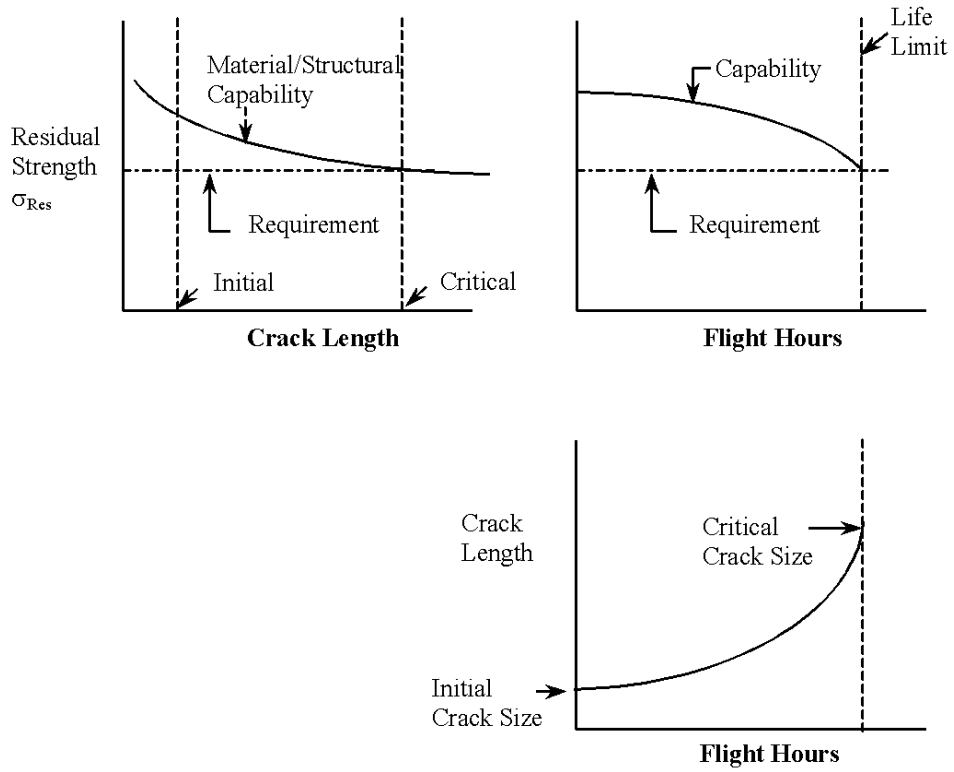

Figure 9.1.1. Relationship Between Residual Strength, Crack and Time-in-Service

As described in previous sections, the analyst needs the following structural/material information to conduct a damage tolerance analysis:

- Definition of quality – to obtain the initial crack length (a_0) for the sub-critical crack growth analysis.
- Definition of operational loading and environmental conditions – to establish the residual strength requirement and to grow the crack in the sub-critical crack growth analysis.
- Definition of the structural parameter that relates loading, global geometry, as well as crack size and geometry to crack tip conditions – this parameter makes it possible to relate laboratory behavior to in-service hardware.
- Definition of material properties that characterize resistance to fracture and to sub-critical crack growth – to provide the basis for estimating fracture level and the rate of crack growth in the structure.

- A damage summation model – to integrate the effects of variable amplitude loading and time dependant behavior in the sub-critical crack growth analysis.
- A fracture model – to provide the criteria for estimating the critical crack length.

For a safety-of-flight critical structural component, detailed analysis and understanding is required for the above structural/material information. Such detailed analysis is described in earlier sections. This section has been prepared to highlight what might be accomplished with both limited information and structural analysis capability. The method of approach in this section is to illustrate how approximate methods can reduce the complexity of a residual strength analysis or full-scale cycle-by-cycle sub-critical crack growth rate analysis. The approximate methods facilitate parameter studies that isolate those features of the structure, its material, the usage, the environment, or method of inspection, which control the level of damage tolerance associated with the structure, in an unrepaired or repaired condition.

The remainder of this section is organized to present (a) some general observations about usage characteristics for crack growth life estimates, (b) a detailed analysis of three transport wing stress histories and the effects of stress scaling, (c) fatigue life sensitivity analysis for stress effects, (d) fatigue life sensitivity for analysis for hole repair, (e) fatigue life sensitivity analysis for blend-out repairs, (f) a residual strength parametric analysis to establish limits for return to depot, (g) a detailed residual strength analysis of a cockpit longeron repair, and (h) a detailed residual strength analysis of a wing skin repair.

9.2 Usage Characterization for Simple Repairs

As explained in Section 9.1, there are two reasons for characterizing the usage for a damage tolerance analysis: (a) to establish the residual strength requirement and (b) to grow the crack in the sub-critical crack growth analysis. The maximum loading conditions and their frequency determine the loading (residual strength) requirement that the structural element must withstand without failure. Typically the more frequently occurring loading conditions are those responsible for growing a crack from its initial size to failure.

For a residual strength analysis of a structural repair, one would want to characterize the maximum loading condition that the structure might experience in its anticipated service life. A simple choice might be based on returning the load carrying capability of the cracked structure to the original ultimate load carrying capability of the structural member without a crack. Section 9.7 describes in more detail the methods for conducting a residual strength analysis.

For a sub-critical crack growth analysis, one is more typically interested in characterizing the average per flight loading conditions that will be experienced by the cracked or repaired structure. It is the relatively large, frequently occurring load excursions that drive the crack growth process. From a repair analysis standpoint, it is important that the analyst know what are the sources of large (and frequently occurring) stress excursions and have some indication of the maximum to minimum stress ratios as well as frequency of these excursions on a per flight (or per flight hour) basis.

The more critical the repair, the more important is the definition of the specifics of per flight average loading conditions for a life analysis. If one can identify those loading conditions that affect the rate at which cracks grow in a given structural member, then simple calculations can be made to obtain first order estimates of this member's structural life. While first order estimates can be questioned from an absolute sense, such estimates, when used in a relative sense, can provide the necessary guidance for designing a repair, or releasing an individual aircraft for flight.

In the following subsections, a sub-critical crack growth analysis approach, which was introduced in Section 5.2.5, is further described and justified for its application for repair analysis. In Section 9.3, an example analysis of three transport wing stress histories is utilized to illustrate how a generic stress history for a given structural member could be employed to estimate the life at any given location in that member.

9.2.1 Variable Amplitude Crack Growth Behavior

Many airframe loading conditions are sufficiently repetitive over a number of flight (~100 to 500 flights) that the crack growth damage accumulates in a relatively continuous manner. Figure 9.2.1 describes two examples of experimental crack growth data generated under typical flight-by-flight loadings involving multiple missions. Figure 9.2.1a represents the behavior experienced at a hole subjected to a fighter wing stress history and Figure 9.2.1b represents the behavior observed at a hole subjected to a bomber aircraft wing stress history. Both behaviors illustrate the regular and relatively continuous crack growth pattern exhibited by many flight-by-flight histories.

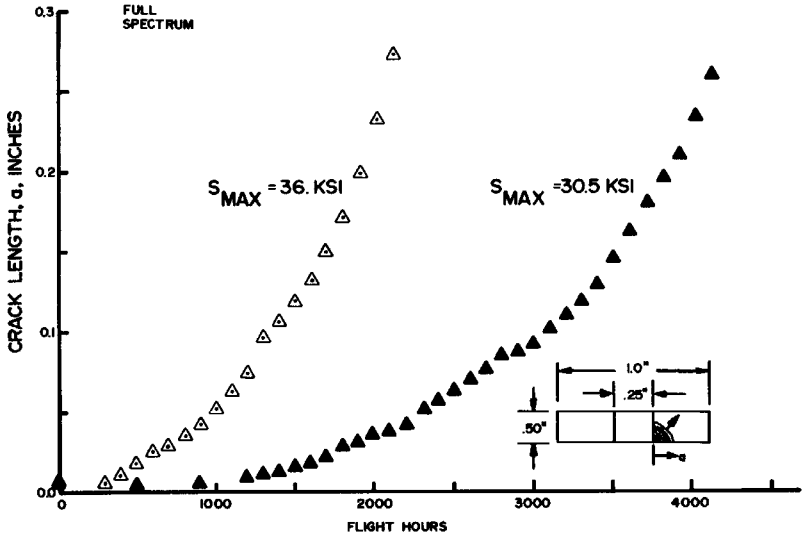

Figure 9.2.1a. Experimental Propagation Behavior of Corner Crack with Full F-4E/S Wing Spectrum (68000 cycles/1000 flight hours) Scaled to Two Stress Levels (36 and 30.5 ksi).

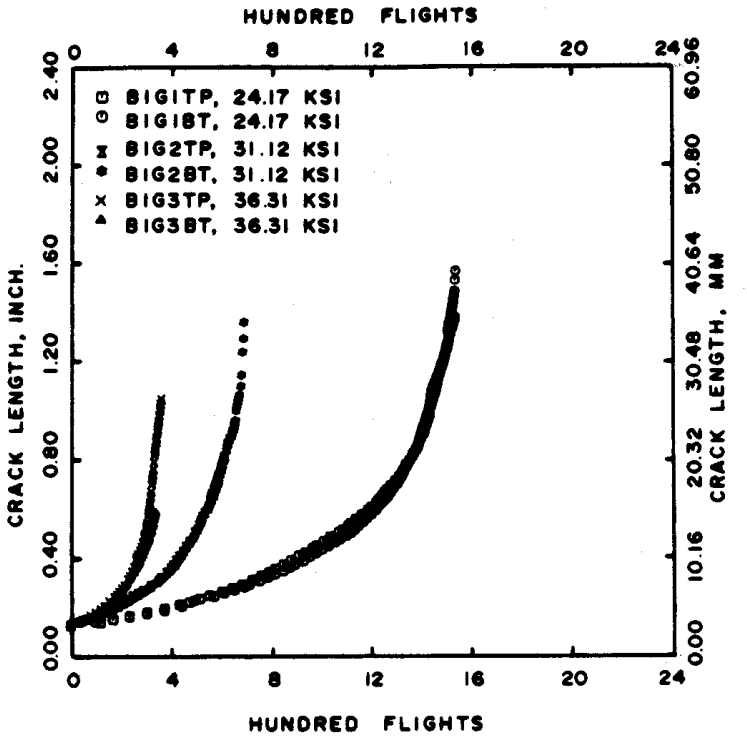

Figure 9.2.1b. Experimental Flight-By-Flight Fatigue Crack Growth Behavior for a B-1A Wing Spectrum Scaled to Three Levels (24.17, 31.12, and 36.31 ksi).

As a result of the regularity of such flight-by-flight induced crack growth behavior, there was a recognition as early as 1963 that aircraft stress histories can induce crack growth behavior similar to constant amplitude behavior. This early recognition has led to a number of schemes for utilizing limited information to characterize the behavior of cracks in aircraft structure. These schemes all focus on the translation of variable amplitude crack growth life data to variable amplitude crack growth "rate" data so that the simple analysis schemes for constant amplitude loadings can be used to establish life estimates. These replace the more complicated numerical, computer-based algorithms used for a load interaction, cycle-by-cycle analysis of the complete stress history.

The translation of the variable amplitude crack growth life data to that of variable amplitude crack growth rate data follows most of the procedures used to convert constant amplitude crack growth life data to constant amplitude crack growth rate data (see Subsection 7.2.2 and Figure 7.2.9, which is repeated as Figure 9.2.2). The major differences between describing variable amplitude rate behavior and constant amplitude rate behavior is in the choice of the rate variable and the characterizing stress history parameter. In variable amplitude descriptions, the crack growth rate may be described as rate per flight, rate per flight hour, or rate per cycle. Also, since the magnitude of the individual stress events in the stress history is a random variable the characteristic stress parameter that described the history is a statistical measure of the individual events in the history.

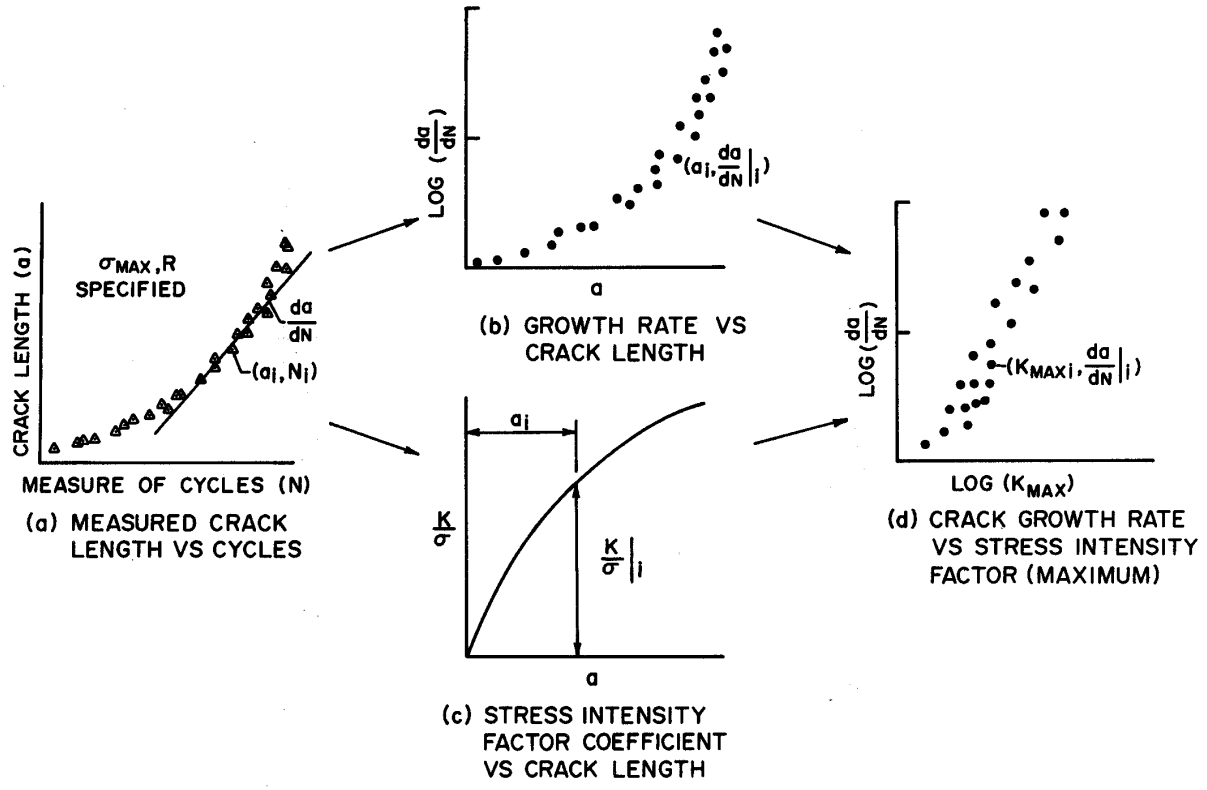

Figure 9.2.2. Method for Reducing Fatigue Crack Growth Life Data to Fatigue Crack Growth Rate Data

Figure 9.2.3 describes a variable amplitude crack growth rate behavior (*da/d*(*Flight*)) as a function of a spectra dependent characteristic stress-intensity factor ($\overline{K}$) for two transport wing histories. The *K* is calculated based on the formula

$$\overline{K} = \overline{\sigma} \cdot \left(\frac{K}{\sigma} \right) \tag{9.2.1}$$

where K/σ is the stress-intensity factor coefficient for the geometry and $\overline{\sigma}$ is the characteristic stress parameter, here chosen as the root mean square (RMS) of the maximum stresses in the history, i.e.

$$\overline{\sigma} = \overline{\sigma}_{\max} = \left[\sum_{i=1}^{N} \frac{\left(\sigma_{\max_i}\right)^2}{N} \right]^{\frac{1}{2}} \tag{9.2.2}$$

In equation 9.2.2, *N* is the number of stress events, and $\sigma_{max(i)}$ denotes the maximum stress for the i^{th} stress event.

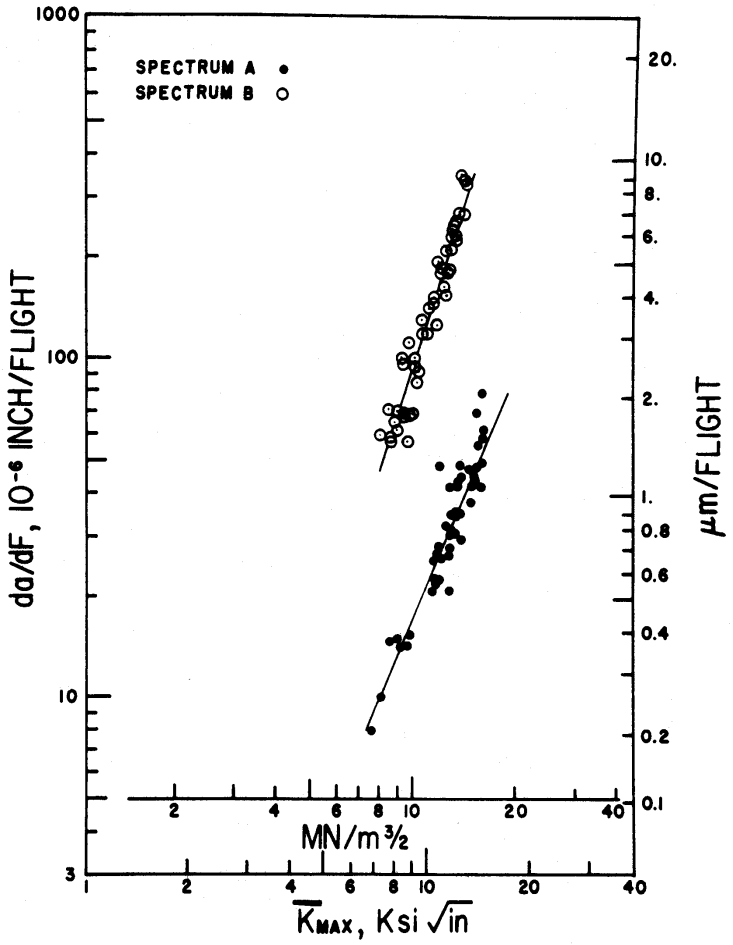

Figure 9.2.3. Fatigue Crack Growth Rate Data for Two Transport Spectra (A = Upper Wing, B = Lower Wing)

It is seen from Figure 9.2.3 that the crack growth rate (on a per-flight basis) behavior for the two spectra might be described by a power law equation of the form

$$\frac{da}{dF} = C\overline{K}^{p} \tag{9.2.3}$$

The corresponding image integration equation can be expressed as

$$F = \int_{a_0}^{a_f} \frac{da}{C\overline{K}^{p}} \tag{9.2.4}$$

or as

$$a = a_0 + \sum_{j=1}^{F} \Delta a_j \tag{9.2.5}$$

where F is the number of flights required to grow the crack from a_0 to a, and where Δa_j is evaluated for the current crack length using Equation 9.2.3. The coefficients C and p are evaluated using least squares procedures applied to data of the type shown in Figure 9.2.3.

The value of the data shown in Figure 9.2.3 and its description with a simple equation, e.g. Equation 9.2.3, is that parametric studies can be conducted in a relatively simple manner. Such parametric studies could cover other ranges of crack length for the same geometry, other structural geometries, and other stress magnification factors applied to the same spectra.

9.2.2 Other Methods for Generating Rate Descriptions

Translating experimental crack growth life data to flight-by-flight crack growth rate only provides one method for generating the flight-by-flight power law growth rate relationship given by Equation 9.2.3. The power law rate equation can also be generated using two different analytic methods. One popular analytical method is to calculate the RMS range and maximum parameters and to substitute these parameters into a constant amplitude - stress ratio equation. This method results in a single curve that describes the effects of this stress combination. The following example illustrates the procedure.

EXAMPLE 9.2.1 RMS Power Law Analysis

The constant amplitude crack growth equation for a particular alloy is given by

$$\frac{da}{dN} = 8.63x10^{-8} K_{eff}^{2.347}$$

where the effective stress-intensity factor has been determined to be of the form:

$$K_{eff} = \left[K_{\max} - \frac{3}{(1-R)^{0.35}} \right] \cdot (1-R)^{0.696}$$

When the values of maximum stress (σ_{max}) and stress range ($\Delta\sigma$) for a given constant amplitude loading are known, these values are used with the stress-intensity factor coefficient (K/σ) for the geometry of interest to generate K_{max},

$$K_{\max} = \sigma_{\max} \cdot \left(\frac{K}{\sigma} \right)$$

and with the stress ratio formula

$$R = 1 - \frac{\Delta\sigma}{\sigma_{\max}}$$

to generate the parameters defined in the growth equation. To obtain the power law relation that would result for a flight-by-flight spectrum, the RMS values are substituted into the equations.

If the RMS range ($\Delta\sigma$) is 4.45 ksi and maximum (σ_{max}) stresses for a given stress history are 12.30 ksi, the RMS stress ratio (R) is given by

$$\overline{R} = 1 - \frac{\Delta\overline{\sigma}}{\overline{\sigma}_{max}} = 1 - \frac{4.45}{12.30} = 0.640$$

and the RMS maximum stress-intensity factor is

$$\overline{K}_{\max} = \overline{\sigma}_{\max} \left(\frac{K}{\sigma} \right) = 12.3 \left(\frac{K}{\sigma} \right)$$

The growth rate is

$$\frac{da}{dN} = 8.63x10^{-8} \overline{K}_{eff}^{2.347}$$

where

$$\overline{K}_{eff} = \left[\overline{K}_{max} - \frac{3}{(1-0.640)^{0.35}} \right] \cdot (1-0.640)^{0.696} = \left[\overline{K}_{max} - 4.29 \right] \cdot 0.491$$

Notice that the rate *da/dN* is given on a per cycle basis so one must multiply this rate by the average number of cycles per flight or flight hour to obtain the corresponding average growth rate per flight or flight hour.

A method that substitutes RMS (or other statistically derived) parameters into constant amplitude equations has one major limitation. This limitation is that load interaction effects (retardation or acceleration) are ignored. Thus, the analyst must be wary of comparisons between spectra when using this method, since it will only provide first order approximations of spectra effects.

It is possible to account for load interaction effects with a cycle-by-cycle analysis, but as indicated above, the processing of the complete stress history requires extensive numerical analysis. An approach was suggested in the early 1970's for processing a limited portion of a stress history with a cycle-by-cycle analysis for the purpose of generating crack increments at several crack lengths. Most of the details for generating crack increments for such an analysis were discussed in subsection 5.2.5 relative to Figures 5.2.10 and 5.2.11. Figure 5.2.10 is repeated here as Figure 9.2.4, and the corresponding crack growth rate data is presented in Figure 9.2.5. The choice of methods that one might employ for the cycle-by-cycle analysis is dictated

by the success that a given analysis has had in predicting crack growth behavior of the type under consideration. In Section 9.3, a detailed example of an analytical analysis of the crack growth behavior (life and rate) of three transport wing stress histories is conducted. This example should provide additional insight into how the simplified rate method can be used to assess spectra and their differences.

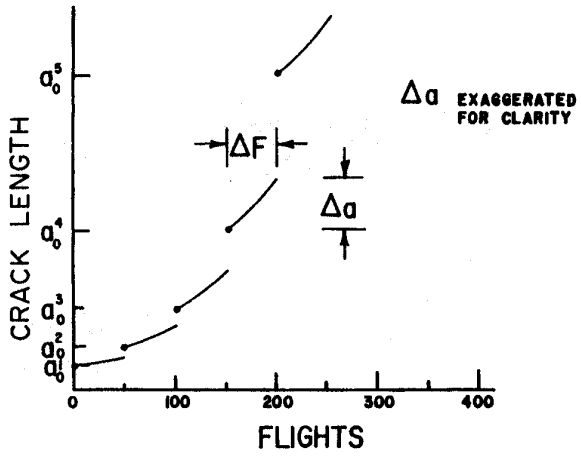

Figure 9.2.4. Crack Incrementation Scheme Based on Cycle-by-Cycle Crack Growth Analysis

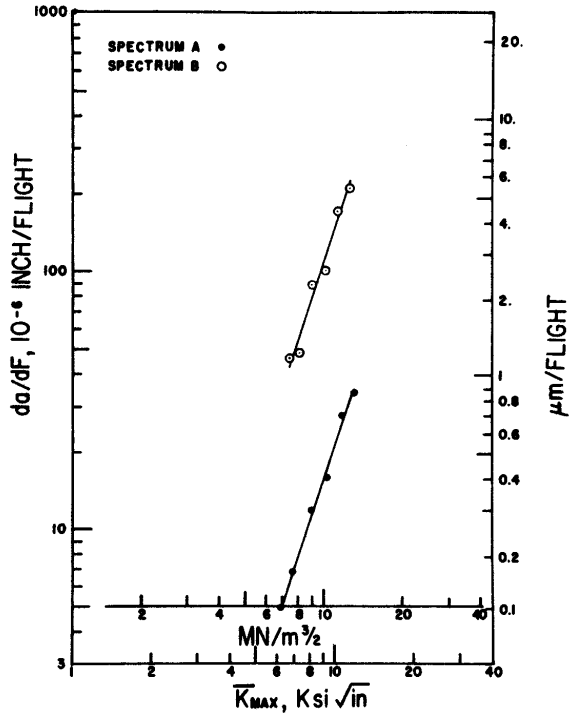

Figure 9.2.5. Crack Growth Rate Description of Crack Incrementation Data for Two Transport Wing Stress Histories (ΔF = 50 Flights)

9.2.3 Power Law Descriptions

A number of experimental and analytical investigations have revealed that the flight-by-flight crack growth rate behavior of military aircraft can be described with a power law relationship (Equation 9.2.3). Specifically, the stress histories considered were developed to facilitate the design of a new structure or an analysis of an in-service aircraft for force management purposes. As such, these stress histories represented an expected average usage based on a force wide composite mission mix; most of the stresses in these histories repeated after an application of a large block of flights or flight hours. None of the histories involved any major mission change during the expected life of the aircraft. For these histories, one might say that the operations today will be like the operation next year or five years from now.

Nevertheless, the generalized observations of power law flight-by-flight crack growth rate behavior here are immediately applicable to the study of parameters affecting structural repair. Thus, the results of these studies are summarized in Tables 9.2.1 and 9.2.2 for bomber/transport behavior and for fighter/attack/trainer behavior, respectively. Table 9.2.1 presents the coefficients for a crack growth rate per flight type equation, while Table 9.2.2 presents the coefficients for a crack growth rate per flight hour type equation.

The reader can note from Table 9.2.1 that the exponent p for bomber/transport aircraft wing stress histories only varies from about 3.0 to 3.5; Table 9.2.2 indicates a wider variation in the exponent for the aircraft and conditions indicated ($2.2 \le p \le 3.7$). Based on a close analysis of the results, it can be said that the largest variations in the exponent p are generated due to the wide variations in spectrum content (load magnitude and frequency).

Table 9.2.1. Bomber/Transport Behavior

Aircraft	History	Flights/Block	$\overline{\sigma}_{max}$ (ksi)	C^+	p	Aluminum Alloy
B1-B	Wing pivot	100	27.3	4.91×10^{-8}	3.025	2219-T851
C-5A	Upper wing	100	11.7	1.70×10^{-8}	3.111	7075-T651
C-5A	Lower wing	300	12.3	1.05×10^{-7}	3.183	7075-T651
B-52D	Lower wing	200	16.4	2.61×10^{-8}	3.529	7075-T651
KC-135	Proof test, Lower wing	200	17.8	5.97×10^{-9}	3.454	7178-T6
KC-135	Lower wing	200	18.4	1.01×10^{-8}	3.338	7178-T6

+ inch/flight, ksi $\sqrt{in}$

Table 9.2.2. Fighter/Attack/Trainer Behavior (Based on 1000 Flight Hour Block Spectra)

Aircraft	History	C^+	p	Aluminum Alloy
T-38	Lower wing (baseline)	2.66×10^{-8}	2.678	7075-T651
T-38	Lower wing (severe)	1.07×10^{-8}	3.152	7075-T651
T-38	Lower wing (mild)	5.32×10^{-9}	2.460	7075-T651
F-4	Lower wing (baseline)	1.68×10^{-8}	2.242	7075-T651
F-4	Lower wing (high stress baseline)	1.77×10^{-8}	2.242	7075-T651
F-4	Lower wing (severe)	1.76×10^{-8}	2.395	7075-T651
F-4	Lower wing (mild)	5.77×10^{-9}	2.395	7075-T651
F-16	Lower wing (mix)	6.92×10^{-10}	3.62	7475-T7351
F-16	Tail (mix)	1.33×10^{-10}	3.67	7475-T7351
F-16	Lower wing (air to air)	1.07×10^{-9}	2.905	7475-T7351
F-16	Lower wing (air to ground)	8.94×10^{-11}	3.464	7475-T7351

+ inch/flight, ksi $\sqrt{in}$

Before employing a flight-by-flight crack growth rate type analysis to estimate the life of a repair, the analyst should be concerned with the adequacy of such an analysis. The most important part of the analysis is the definition of the stress history that the repaired member will experience in the future. If the history is anticipated to be statistically repetitive as a function of time-in-service then the results from a flight-by-flight rate analysis will be comparable to a cycle-by-cycle analysis.

If the mission type or mix is expected to change significantly as a function of time, then projecting a predefined rate of crack growth without detailed consideration of how the damage will be changing could lead to non-conservative errors. One method for addressing mission type or mix changes is to utilize one rate curve before the time of change and another rate curve subsequently. A more exact method for addressing mission changes is by using a cycle-by-cycle crack growth analysis applied to the stress history that accounts for the changes.

Rate methods have one inherent problem: they tend to minimize the effects of the infrequently applied large loads. These large loads will cause retardation effects and tend to slow the growth process (if, in application, failure is not induced). Thus rate methods will normally predict somewhat shorter (more conservative) lives than the cycle-by-cycle analyses.

Based on Tables 9.2.1 and 9.2.2 the analyst should note that the crack growth rate equation is a function of material, location, and usage. An equation generated for the horizontal tail should not be used for the vertical tail (nor wing); an equation generated for air-to-ground operations should not be utilized for air-to-air operations.

9.3 Spectrum Analysis for Repair

As discussed in Section 9.2, the flight-by-flight crack growth rate behavior for many structural loading conditions can be defined using a power law that relates crack growth rate to a characteristic stress-intensity factor, i.e.

$$\frac{da}{dF} = C\overline{K}^{P} \qquad (9.3.1)$$

An example analysis is conducted using three transport wing stress histories to illustrate how such equations can be generated. Subsequent to the generation of the flight-by-flight crack growth rate equations, additional analysis is conducted to evaluate the effects stress level and structural location on the use of these equations for the structural repairs.

9.3.1 Definition of Stress Histories

The transport stress histories utilized for this example were developed during a force management update and represent the expected behavior at three separate locations on the lower wing surface. The force management update involved a complete durability and damage tolerant analysis of the airframe, as well as reassessment of past and future usage of the aircraft force. Stress histories were generated for durability and damage tolerant studies at those structural locations identified as potentially critical to the continuing safe operation of the force.

The lower wing stress histories chosen for this example analysis represent locations in the center wing (BL 70), in the inner wing (WS 733) and the outer wing. All three stress histories were developed assuming the same operation (mission mix) history. The operational history was considered to be represented by a block of 100 flights with a defined mission order. Eight (8) separate missions were identified as representative of service operations. Each mission in the 100-flight block averaged 4.8 hours per flight.

The 100-flight block of ordered missions repeated until the service life of 40,000 flight hours was exceeded; thus, more than 83 applications of the repeating 100-flight blocks were required to define a lifetime of operation. The mission order for the eight representative missions is defined by Table 9.3.1. For comparison purposes, Figure 9.3.1 presents the stress histories for mission one at three locations. The stress histories for the other seven missions could be defined in a similar manner.

Table 9.3.1. Mission Ordering for Transport Flight-by-Flight Spectrum

Order Per 20 Flight Group	Flights 1-20	Flights 21-40	Flights 41-60	Flights 61-80	Flights 80-100
1	4	6	7	6	5
2	1	7	7	1	4
3	1	7		6	1
6	7	2	3	7	1
5	6	1	6	6	1
6	4	4	2	5	8
7	5	3	6	3	2
8	2	8	7	7	3
9	5	5	3	4	8
10	8	4	8	2	6
11	2	3	8	3	7
12	8	1	7	6	5
13	2	6	3	5	6
14	7	6	1	6	6
15	1	3	8	7	6
16	6	8	5	7	5
17	7	6	7	6	1
18	7	1	6	2	5
19	2	2	2	5	4
20	7	4	4	4	7

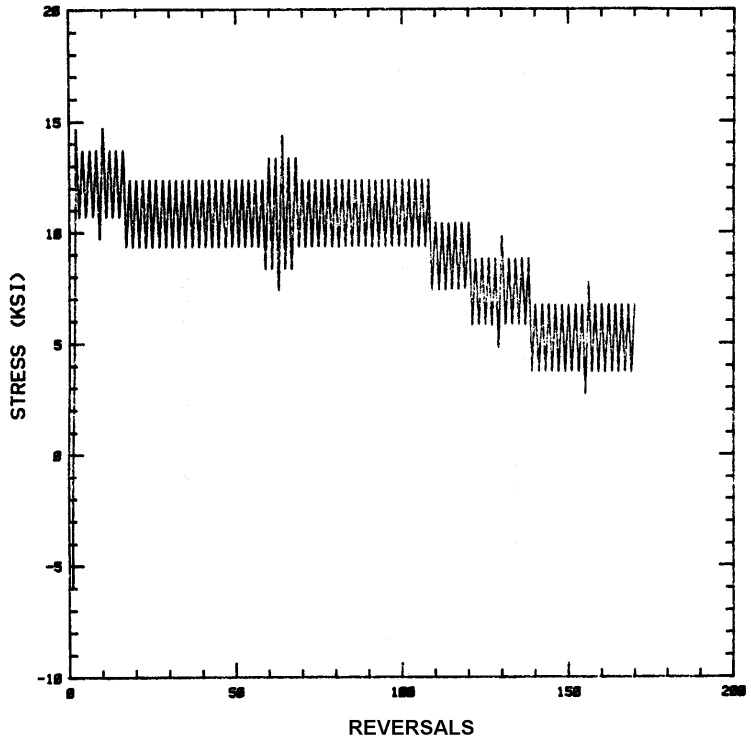

Figure 9.3.1a. Center Wing Stress History for Mission 1

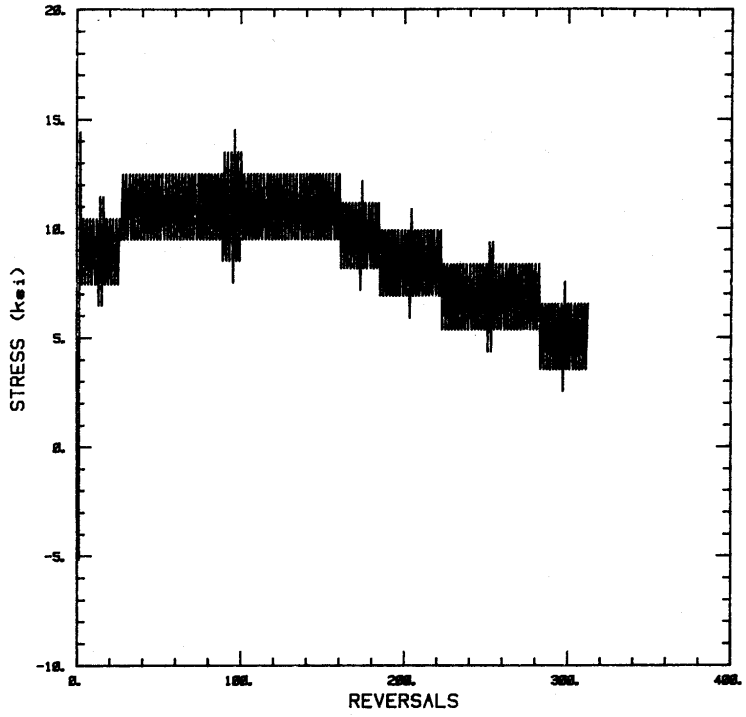

Figure 9.3.1b. Inner Wing Stress History for Mission 1

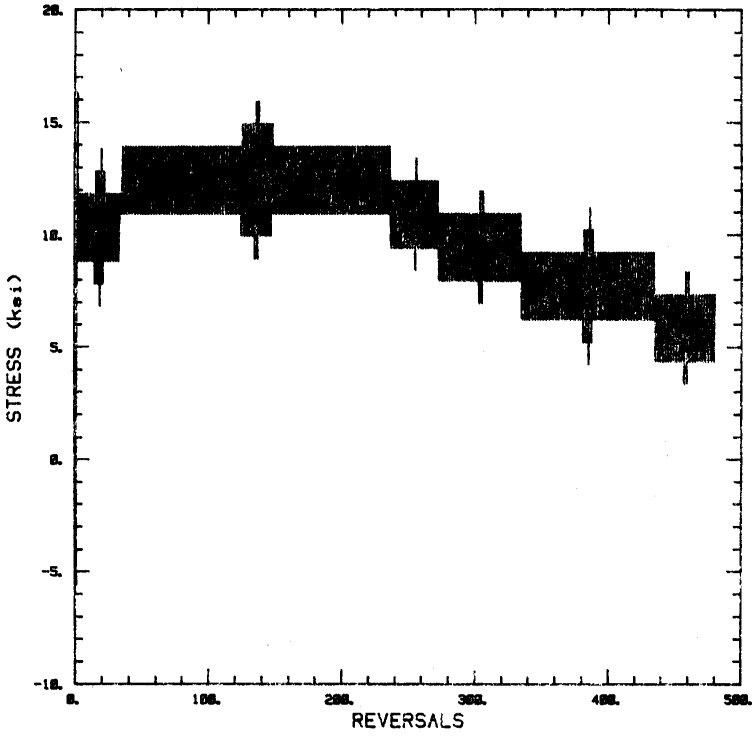

Figure 9.3.1c. Outer Wing Stress History for Mission 1

The stress history for each location is now defined except for the infrequently occurring maximum stresses. The infrequently occurring stresses in each mission were inserted into the history on a periodic basis as a replacement for the first maximum stress in the mission. The period of occurrence of these replacement load events was during the tenth, the one-hundredth, and the two-hundredth repeat occurrence of any of the individual eight missions. The replacement maximum stresses for mission 1 for the three locations are listed in Table 9.3.2. Each mission had a similar set of replacement stresses.

Table 9.3.2. Replacement Stresses for Mission 1 for the Three Wing Locations

Occurrence Frequency (per no. of mission repeats)	Center Wing (BL-70) Location (ksi)	Inner Wing (WS-733) Location (ksi)	Outer Wing Location (ksi)
1/1	14.64	14.43	16.34
1/10	16.16	16.16	18.36
1/100	17.96	17.96	20.79
1/200	18.6	18.60	21.56

9.3.2 Spectra Descriptions

The stress history uniquely defines the sequence and magnitude of the individual stress events applied at a specific location. While this information is essential for conducting a cycle-by-cycle crack growth analysis that accounts for load interaction, it is both difficult to use and interpret without computer programs that perform such analyses. One of the side benefits associated with describing flight-by-flight crack growth rates as a function of a characteristic stress-intensity factor is that one is forced into presenting stress history information simply. This subsection addresses two such schemes – the exceedance curve and an RMS characterization.

9.3.2.1 Exceedance Curve Descriptions

One normally generates a stress history for a given mission based upon exceedance information; however, the starting exceedance information is typically based in operational parameters, e.g. n_z, airspeed, weight, altitude, etc. for given mission functions. After a stress history has been generated for a collection of missions, it is recommended that stress exceedance curves be generated for the maximum stress, the minimum stress, and the positive (load-increasing) stress range associated with all stress events. The exceedance curves for the maximum, minimum, and range of the individual stress events in the three wing stress histories are presented in Figure 9.3.2.

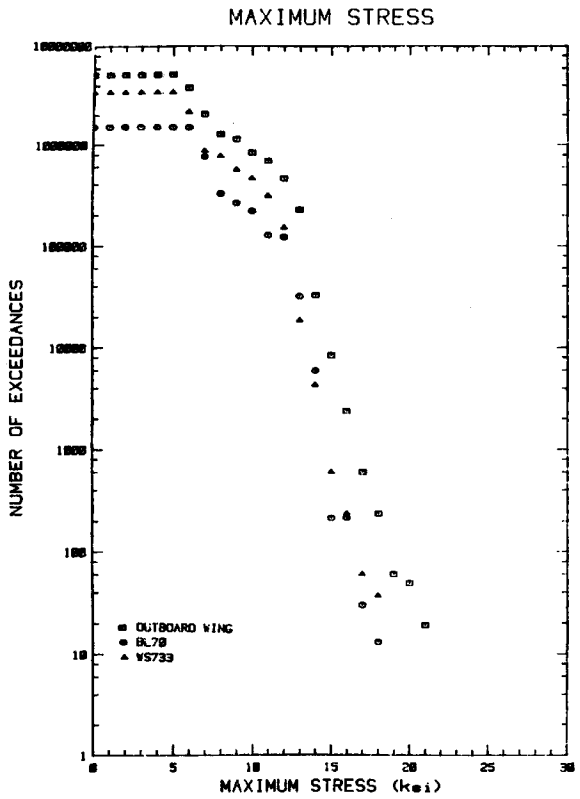

(a) Maximum Stress Exceedance

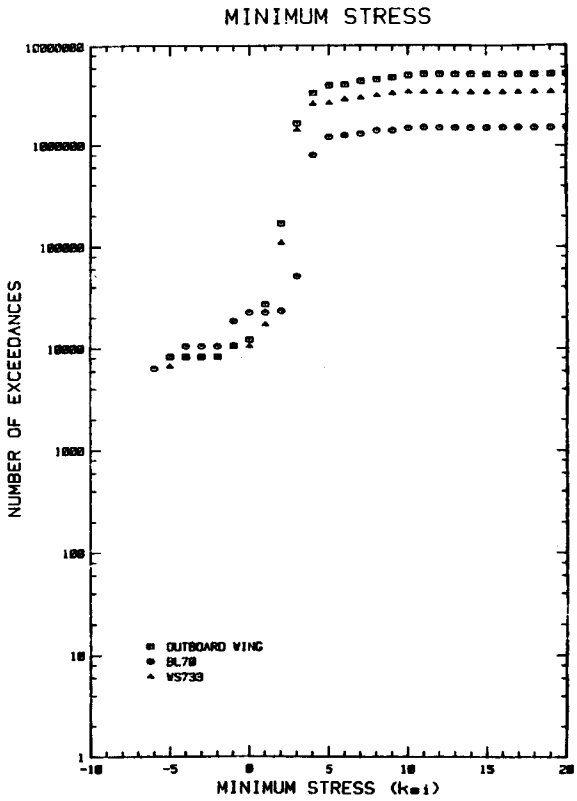

(b) Minimum Stress Exceedance

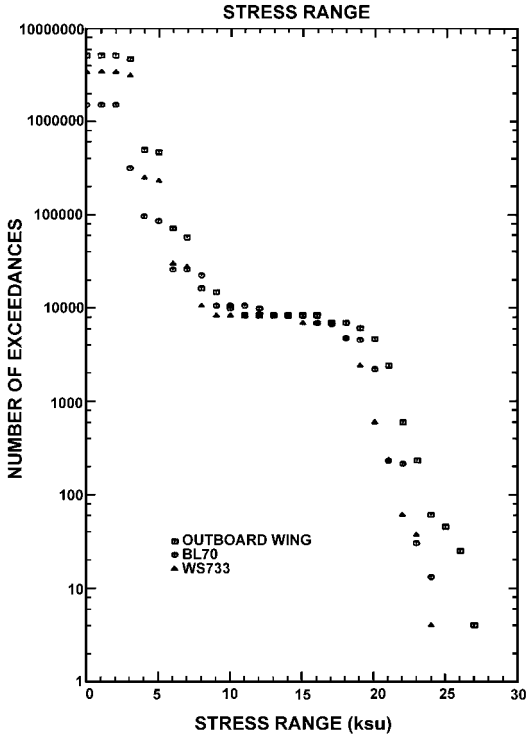

(c) Stress Range Exceedance

Figure 9.3.2. Exceedance Curves for the Three Transport Wing Stress Histories

The exceedance curves for each stress event characteristic are noted (from Figure 9.3.2) to be similar in shape but somewhat displaced relative to number of exceedances. The behavior observed might have been expected since all three locations are experiencing the same operational history. Both the minimum stress and stress range exceedance curves indicate a plateau around 8300 exceedances, which is the dividing line between once per flight occurrences and those that occur more frequently. Thus, because we are dealing with a transport aircraft, it can be noted that the once per flight ground-air-ground (GAG) cycle has a stress range typically larger than 16 ksi, while the gust/maneuver cycles have stress ranges less than 8 ksi.

In anticipating the level of damage that a stress history might generate, the exceedance curve becomes a useful tool. The highest stresses (all events) are noted to be present in the outboard wing (followed by the inner wing and then center wing). Also, for a given magnitude of any stress characteristic, the number of exceedances are the highest for the outboard wing location (followed by the inner wing and center wing). The implication is that, on a per flight basis, more damage is generated at the outer wing location then at the other two locations, all other things being equal (structural geometry, material, crack geometry, etc.).

The shape of the exceedance curve can also be used to determine if the stress history might be expected to introduce major perturbations in the crack growth behavior. If the exceedance curve associated with the maximum stress characteristic is relatively continuous from the infrequency of the once-per-flight event, then the flight-by-flight crack growth rate curve would also be expected to be relatively continuous. Except for the outboard wing location curve between 40-60 exceedances, Figure 9.3.2a shows that the maximum stress exceedance curves are relatively continuous. It is therefore expected that the flight-by-flight crack growth rate curves for the three wing histories will be relatively continuous (not show major effects of retardation).

9.3.2.2 RMS Descriptions

The presentation of complicated variable amplitude stress histories can be simplified by defining average or RMS values of the stress event characteristics, i.e. the maximum stresses and positive stress ranges of the history. The difference between the average value and the RMS value of a given characteristic is normally not more than 3 percent when one is considering stress histories with more than 1000 stress events. For average stress analysis, one uses

$$\sigma_{mean} = \sum_{i=1}^{N} \left(\frac{\sigma_i}{N} \right) \tag{9.3.2}$$

while for RMS analysis, one uses

$$\sigma_{RMS} = \left[\sum_{i=1}^{N} \frac{\sigma_i^2}{N} \right]^{\frac{1}{2}} \tag{9.3.3}$$

where σ_i is the characteristic (maximum stress or stress range) for the i^{th} stress event and N is the total number of stress events.

Similar analysis schemes have also been employed where the slope (p) of the crack growth rate power law expression (Equation 9.3.1) is used to calculate a representative stress, i.e.

$$\sigma_{REP} = \left[\sum_{i=1}^{N} \sigma_i^{\frac{p}{N}} \right]^{\frac{1}{p}} \qquad (9.3.4)$$

Experience has shown that such schemes (Equation 9.3.4) are not appreciably of more value than the average or RMS determined characteristics.

The RMS equation (Equation 9.3.3) was applied to the three transport wing stress histories to obtain RMS values for the maximum stress and stress range. The results are summarized in Table 9.3.3.

Table 9.3.3. Per Cycle Root Mean Square (RMS)Representative Stress Values for the Three Wing Stress Histories

Stress History	Maximum Stress (ksi)	Stress Range (ksi)	Cycles per 100 Flights
Center Wing (BL-70)	8.00	3.52	18268
Inner Wing (WS-733)	7.24	3.33	41174
Outer Wing	8.01	3.38	62562

Based on the RMS analyses presented in Table 9.3.3, it appears as if the three stress histories are quite similar on a per cycle basis (the stress ranges are within five (5) percent, and the maximum stresses are within ten (10) percent). Based on a constant amplitude analysis of these stress conditions, the damage per cycle would be expected also to be similar. From Table 9.3.3, one can note the number of cycles applied per 100 flight block differs substantially from stress history to stress history. If the RMS stresses are similar and the number of stresses per flight differ, then one would expect that the damage per flight would favor the stress history with the most stress events per flight.

One of the reasons that the RMS representative stresses can not be blindly used in a constant amplitude equation to accurately estimate crack growth behavior is because the damage is a non-linear function of the different events in the history. The analyst must understand where the damage is coming from and isolate on those events. For example, a transport wing stress history generates damage as a result of both GAG cycle loading and gust/maneuver cycle loading. A second analysis was therefore conducted on the three wing histories to obtain per flight characteristics for the GAG and gust/maneuver cycles. This analysis is presented in Table 9.3.4.

Table 9.3.4. Per Flight Root Mean Square Representative Stress Values for the Three Wing Stress Histories

Stress History	GAG Max Stress (ksi)	GAG Min Stress (ksi)	Gust/Manu. Max Stress (ksi)	Gust/Manu. Stress Range (ksi)	Number of Gust/Maneuver Cycles
Center Wing (BL-70)	12.23	18.64	7.97	3.35	182
Inner Wing (WS-733)	13.14	18.13	7.21	3.31	411
Outer Wing	14.73	20.01	7.99	3.29	625

Relative to the per flight RMS representative stress values for GAG and gust/maneuver cycles, the three stress histories are shown to be relatively similar. The magnitude of the GAG cycle appears to be increasing as the location moves outboard; this would indicate that the GAG cycle causes more damage per flight in the outboard wing than at the inner and center wing locations. We note that the largest number of gust/maneuver cycles occur at the outer wing location and this would also favor more damage per flight (due to gust/maneuver cycles) than the other two locations.

9.3.3 Crack Growth Analysis

To obtain a flight-by-flight crack growth rate equation (Equation 9.3.1), it is necessary to have either a crack growth life curve or the capability for generating such a curve. As described in Section 9.2, once a flight-by-flight crack growth life curve exists, it can be differentiated to obtain crack growth rates.

The simplest manner for differentiating a curve is by using the secant method, i.e.

$$\frac{da}{dF} = \frac{a_2 - a_1}{F_2 - F_1} \tag{9.3.5}$$

where (a_1, F_1) and (a_2, F_2) represent two different points on the crack growth life, crack length (a) versus flights (F) curve. The derivative is considered to be the slope of the curve at the mean crack length of the two points, ie.

$$a_{mean} = \frac{1}{2}(a_1 + a_2) \tag{9.3.6}$$

The mean crack length provides the ability to calculate the stress-intensity factor coefficient (K/σ) for the geometry associated with the crack growth life curve. To describe the crack growth rate as a function of stress-intensity factor, it is necessary to have either a formula or graph that relates stress-intensity factor to crack length for a known external loading condition. For example, if the stress-intensity factor is related to gross stress conditions (σ_{gross}) by the formula

$$K = \sigma_{gross} \cdot \beta\sqrt{\pi a} \tag{9.3.7}$$

Then the stress-intensity factor coefficient is

$$\frac{K}{\sigma_{gross}} = \beta\sqrt{\pi a} \qquad (9.3.8)$$

and Equation 9.3.8 is evaluated for $a = a_{mean}$ (Equation 9.3.6). Note that β is typically a function of crack length.

9.3.3.1 Generation of Crack Growth Curves

Crack growth life curves were generated for the three transport wing stress histories using a crack growth analysis computer code. The material chosen for the study was a 7075-T651 aluminum alloy; the associated constant amplitude crack growth rate curve was

$$\frac{da}{dN} = \frac{5x10^{-7}\left(K_{\max}(1-R)^{\frac{2}{3}}\right)^3}{K_C - K_{\max}} \qquad (9.3.9)$$

with K_C = 68 ksi $\sqrt{in}$ and R = -0.12. The Willenborg-Chang retardation model embedded within the software was used to account for load-interaction effects. These modeling choices affect the absolute accuracy of the crack growth predictions but not the implications of the analysis which are presented in a relative sense.

Rather than dealing directly with the actual structural geometries for the three wing locations, it was decided that the crack growth analysis would be applied for a common geometry for all three stress histories. This choice does not affect the crack growth rate analysis as will be further discussed below. The choice of common geometry for all three stress histories makes it possible to evaluate the relative effects of per flight and per cycle damage for the analyses. It was decided also to choose a simple geometry of a four (4) inch wide center cracked panel, giving a stress-intensity factor coefficient of

$$\frac{K}{\sigma} = \left(\pi a \cdot \sec\frac{\pi a}{W}\right)^{\frac{1}{2}} \qquad (9.3.10)$$

The initial and final crack length chosen for the configuration were 0.11 and 1.25 inch, respectively. Figure 9.3.3 summarizes the common configuration employed in this analytical study.

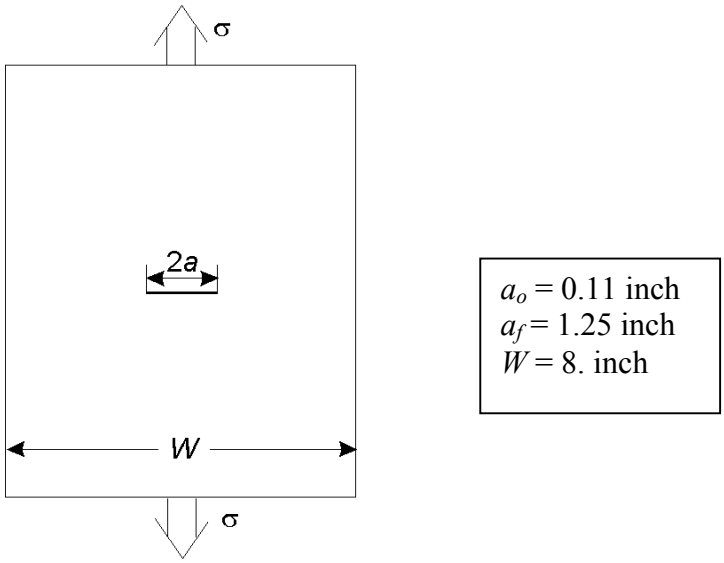

Figure 9.3.3. Common Geometry Used to Evaluate Stress History Effect on Crack Growth Behavior

Figure 9.3.4 presents both the crack growth life curve and its crack growth rate counterpart for the center wing stress history. The crack growth rate curve was generated by forming the secant defined slope for consecutive points on the life curve and relating this slope to the stress-intensity factor calculated using the mean crack length and the RMS maximum stress values (given in Table 9.3.3). The stress-intensity factor in Figure 9.3.4 is given by

$$K = \left(\sigma_{\max}\right)_{RMS} \cdot \left(\frac{K}{\sigma}\right) \qquad (9.3.11)$$

where $(\sigma_{max})_{\text{RMS}}$ = 8.0 ksi, and (K/σ) is given by Equation 9.3.10. The curve through the center of the points in Figure 9.3.4 is the mean trend curve that connects all the points.

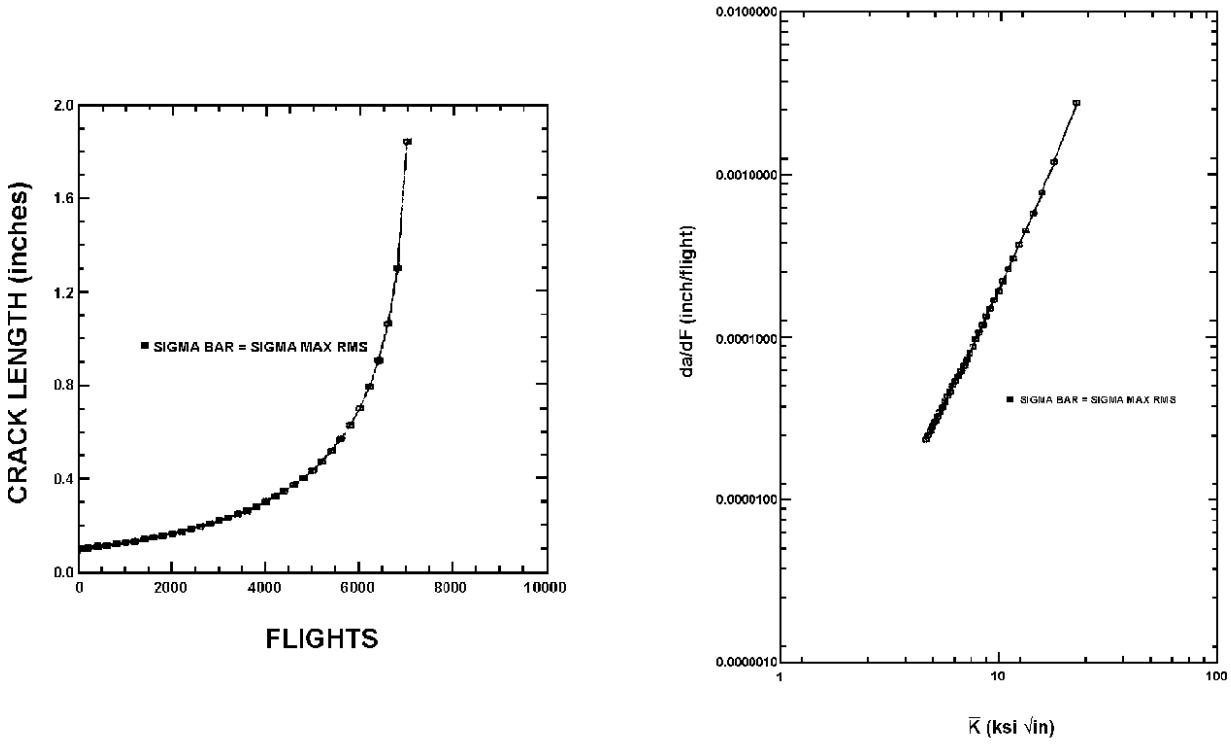

(a) Crack Growth Life Behavior (b) Crack Growth Rate Behavior

Figure 9.3.4. Crack Growth Behavior for the Center Wing Location

Figure 9.3.5 presents the crack growth life curves generated for the other two wing locations, again using the computer code. Figure 9.3.6 summarizes the crack growth rate behavior associated with all three stress histories. The inner and outboard wing crack growth rate data points were also generated by the secant method of analysis. The RMS maximum stresses used for the stress multiplier in Equation 9.3.11 were 7.24 and 8.01 ksi for the inner wing and the outer wing location, respectively.

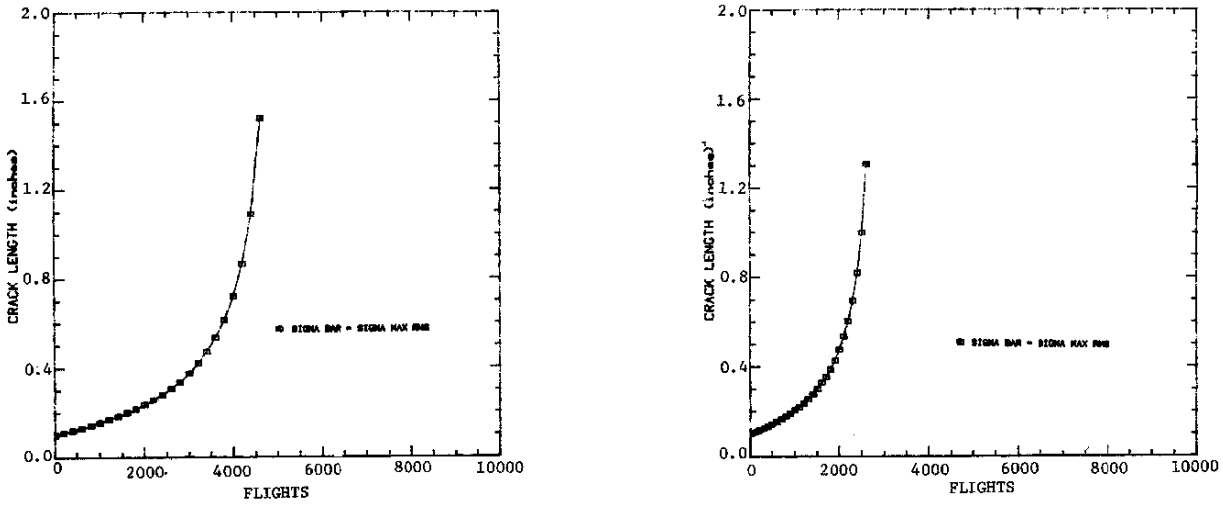

(a) Inner Wing (b) Outer Wing

Figure 9.3.5. Flight-by-Flight Crack Growth Life Behavior for Inner Wing (WS-733) and Outboard Wing Stress Histories

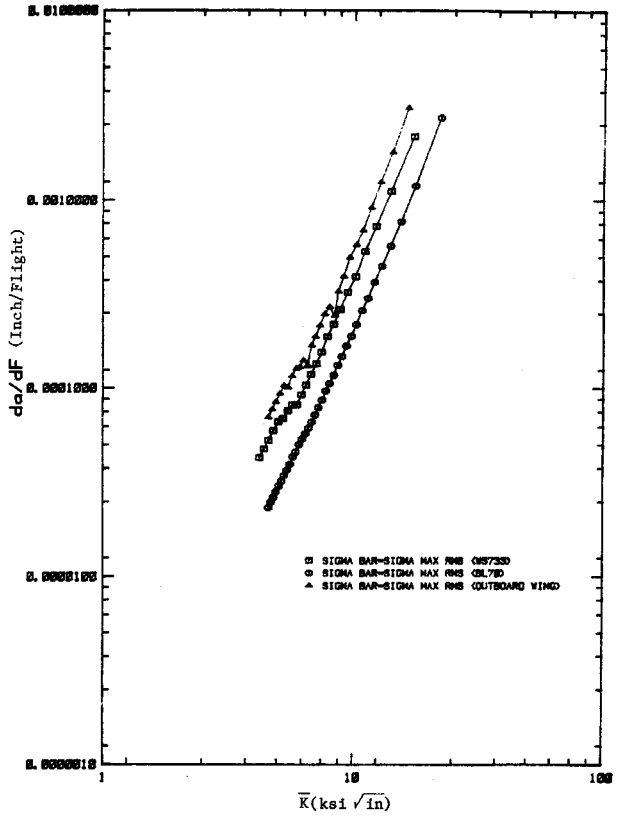

Figure 9.3.6. Flight-by-Flight Fatigue Crack Growth Rate Behavior for Three Transport Wing Histories

9.3.3.2 Analysis of Observed Behavior

A number of observations can be made from the data presented in Figures 9.3.4 through 9.3.6. First, the life is shortest and the rates are fastest for the outer wing stress history; this stress history is the most damaging from a crack growth point of view. The next most damaging history is the inner wing stress history; the least damaging history is associated with the center wing location. Second, the three crack growth rate curves appear to be almost parallel and relatively continuous throughout the range shown. There are discontinuities in the outer and inner wing curves which tend to locally depress the rate curves. These discontinuities are not severe and are associated with the exceptionally high but frequently occurring maximum stress events in the stress history.

As a result of the relatively continuous nature of the crack growth rate curves, least square procedures were applied to the data in Figure 9.3.6 in order to generate the constants in Equation 9.3.1. These constants are presented in Table 9.3.5 along with another set of constants derived using graphical procedures and the assumption that the crack growth rate curves were parallel. Figure 9.3.7 illustrates the degree of fit achieved by the curve established using least squares procedures for the outer wing data. The least squares determined power law curve is seen to adequately describe the outer wing data. The other two least squares power law curves provided similarly adequate descriptions of their respective crack growth rate data.

Table 9.3.5. Constants C and p for Equation 9.3.1

Stress History	Least Squares Method		Graphical Method	
	C	***p***	***C***	***p***
Center Wing (BL-70)	2.54×10^{-7}	2.93	3.35×10^{-7}	2.89
Inner Wing (WS-733)	7.29×10^{-7}	2.73	5.10×10^{-7}	2.89
Outer Wing	7.74×10^{-7}	2.86	9.05×10^{-7}	2.89

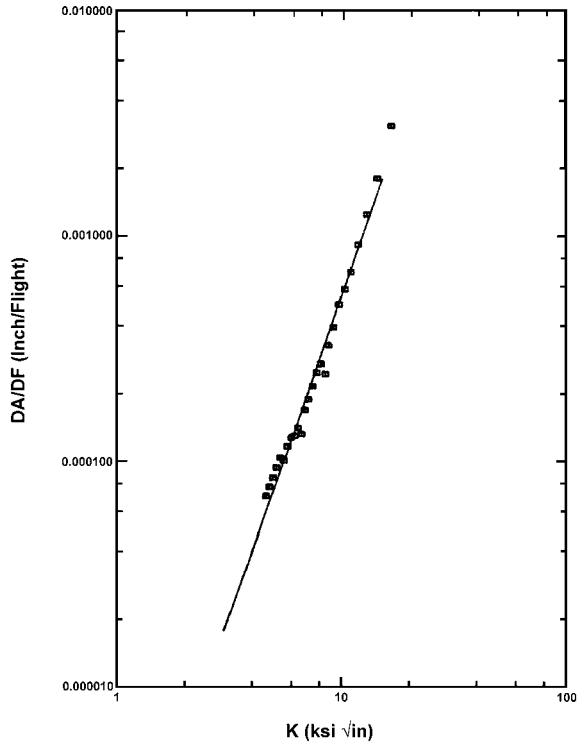

Figure 9.3.7. Comparison Between Outer Wing Data and the Least Squares Determined Curve

A second crack growth life analysis was conducted using the three transport wing stress histories scaled to a lower stress level; all stress events in the three histories were scaled to 0.903 of their original level (both tensile and compressive levels were scaled equally). The same computer software was employed for this second analysis, and all geometry and material properties were kept the same. The stress history mission mix and order (stress sequence) were the same as described in subsection 9.3.1. As expected, longer crack growth lives were associated with the lower stress magnitude stress histories. Table 9.3.6 summarizes the life predictions required to grow the crack between the previously defined limits of $2a_0 = 0.22$ inch and $2a_f = 1.60$ inch.

Table 9.3.6. Effect of Stress Magnification Factor on Crack Growth Lives (L) Calculated for a Center Crack ($2a$) Growing Between 0.22 and 1.60 inch

Stress History	**Lives for Two Stress Magnification Factor Values**		**Life Ratio** $L_{0.903}/L_1$
	L_1 **(Flights)**	$L_{0.903}$ **(Flights)**	
Center Wing (BL-70)	6220	8300	1.33
Inner Wing (WS-733)	4115	5345	1.30
Outer Wing	2385	3117	1.31

9.3.3.3 Interpertation and Use of Crack Growth Rate Curves

It can be noted from Table 9.3.6 that the ratios of crack growth lives for the two stress magnification factors are nearly the same (within 2 percent) for the three stress histories. The reason for this happening can be justified on the basis of the crack growth rate behavior. Consider Figure 9.3.8 where both the crack growth life and crack growth rate behavior associated with the scaled inner wing stress histories are described. Figure 9.3.8 shows that while the life behavior is different, the crack growth rate behavior can be described by a common curve. If the common crack growth rate curve is a power law equation (Equation 9.3.1) then its integral form, i.e.

$$F = \int_{a_0}^{a_f} \frac{da}{C\overline{K}^{\,p}} \tag{9.3.12}$$

can be written, using Equations 9.3.10 and 9.3.11, as

$$F = \frac{1}{C\left(\sigma_{max_{RMS}}\sqrt{\pi}\right)^{p}} \cdot \int_{a_o}^{a_f} \frac{da}{\left(a.sec\frac{\pi a}{W}\right)^{p/2}} \tag{9.3.13}$$

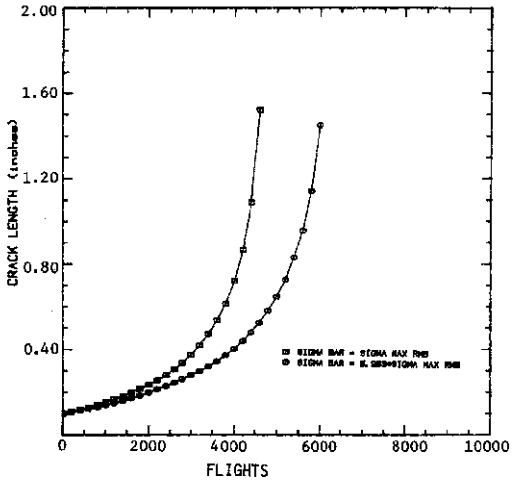

(a) Crack Growth Life Behavior

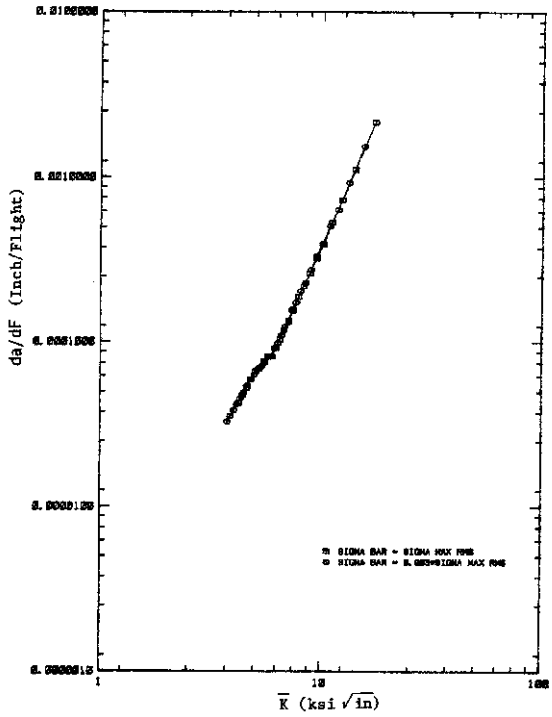

(b) Crack Growth Rate Behavior

Figure 9.3.8. Flight-by-Flight Crack Growth Behavior Exhibited for the Inner Wing (WS733) Stress History Scaled to two Different Stress Levels

If all the stresses in a stress history are scaled, then the σ_{max} characterizing stress will be scaled by the same factor. So, if the crack growth interval remains the same, the life ratio ($L_{0.903}$ / L_1 where $L_1 = F$ and $L_{0.903} = F$ with lower stress) is given by:

$$\frac{L_{0.903}}{L_1} = \frac{\left(\sigma_{\max_{RMS}}\right)^p}{\left(0.903 \cdot \sigma_{\max_{RMS}}\right)^p} = (0.903)^{-p} \qquad (9.3.14)$$

Since all other factors in Equation 9.3.13 are constant, note that the integral is only a function of geometry and once the geometry is defined the stress level does not influence its value.

Using Equation 9.3.14 and the power law exponents given in Table 9.3.5, the life ratio for the scaled stress histories is noted to vary between 1.32 and 1.35 (lowest value of exponent yield lowest life ratio). The life ratio estimate based on the crack growth rate power law exponent is noted to closely approximate the life ratios given in Table 9.3.6. Thus, if one can obtain an estimate of the crack growth rate power law exponent, then one can closely approximate the effect of stress scaling on the crack growth life behavior. Section 9.4 provides additional information on the use of this analysis approach for estimating the lives of structural repairs.

Independent of the above remarks, Equation 9.3.12 has an important application for directly estimating the structural life of cracked components. As an example of its use for conducting such analysis, we compared the results of the computer analysis with life estimates made using the data presented in Table 9.3.5 and Equation 9.3.13. These results are presented in Table 9.3.7, where it is seen that the power law life prediction ratios, which are conservative relative to the least squares procedure, result in estimates which more closely approximate the estimates for all three stress histories.

Table 9.3.7. Ratio of Power Law Life Predictions (L_{PL}) to Life Predictions (L_{CG}) (Ratio > 1, Unconservative)

Stress History	Stress Magnitude Factor =1			Stress Magnitude Factor =0.903		
	Flights	L_{PL}/L_{CG}		Flights	L_{PL}/L_{CG}	
		Least Squares	Graphical		Least Squares	Graphical
Center Wing (BL- 70)	6220	0.961	0.789	8300	0.773	0.632
Inner Wing (WS-733)	4115	0.752	0.769	5345	0.772	0.803
Outer Wing	2385	0.945	0.761	3117	0.977	0.790

Because the least squares determined coefficients are insensitive to the accuracy with which the crack growth rate data are described, it is suggested that the analyst comparatively review the least squares results in a graphical format such as Figure 9.3.7. One reason for choosing the

graphical method is to emphasize the (log-log) lower portion of the crack growth rate behavior. (The least squares procedure results in a "best" fit to all the data).

When flight-by-flight crack growth rate behavior is shown to be independent of stress scaling effects, the behavior will also be independent of the geometry used to collect the crack growth life data. This has been shown for a number of aircraft stress histories similar to those analyzed in this section.

One cautionary remark must be made relative to geometrical effects - if one reduces crack growth life data using a stress-intensity factor which is substantially in error of the actual stress-intensity factor for the geometry, then the transference of the crack growth rate data from one geometry to another will not be possible. In other words, take care in reducing crack growth life data from structural geometries where the stress-intensity factor is not well defined.

9.3.3.4 Analysis for Multiple Stress Histories

Air Logistics Center (ALC) engineers typically need to analyze structural locations within a component for which no stress history is available. Frequently, a stress analysis of these structural locations must be performed based on a strength of materials approach. One question asked repeatedly is: What is available that facilitates conducting a simple crack growth life analysis of these structural locations?

One method that has potential for a relatively large component is a wide area crack growth rate equation that describes the rate of damage growth within the area identified. This section provides an example of how a wide area crack growth rate equation might be generated and then utilized. The three transport wing stress histories provide the basis for this example.

To develop a wide area crack growth rate equation it is necessary to have crack growth life behavior described at a number of locations within the area of application. The mission mix and stress sequencing must be the same at all locations considered. It is anticipated that crack growth lives might be generated for ten or more locations experiencing loading conditions which produce similar contributions of damage. For the example, only three locations were analyzed for the entire wing; however, the approach and interpretation of results would be similar independent of the component and numbers of location.

As was shown in Figure 9.3.6, the flight-by-flight crack growth rate behavior associated with the three stress histories was different; the rate behavior of each was seen to be relatively continuous and parallel to the others. To obtain a wide area crack growth rate equation, the analyst must find a method for collapsing the rate curves into one master curve. This collapsing can only be accomplished (with confidence) if the analyst understands the relationship between the damage generation process and the stress events in the history. The damage may be generated primarily either by the gust/maneuver cycles or by the GAG cycles.

Figure 9.3.6 shows that the crack growth rates are ordered for the three histories according to the number of gust/maneuver cycles that occur per flight. The data in Figure 9.3.6 were therefore converted to a crack growth rate per cycle basis and replotted. Figure 9.3.9 describes the result of this scaling of crack growth rates. As is shown by Figure 9.3.9, the crack growth rates are found to collapse to tight scatter band with the inner wing location behavior forming the upper curve on the band.

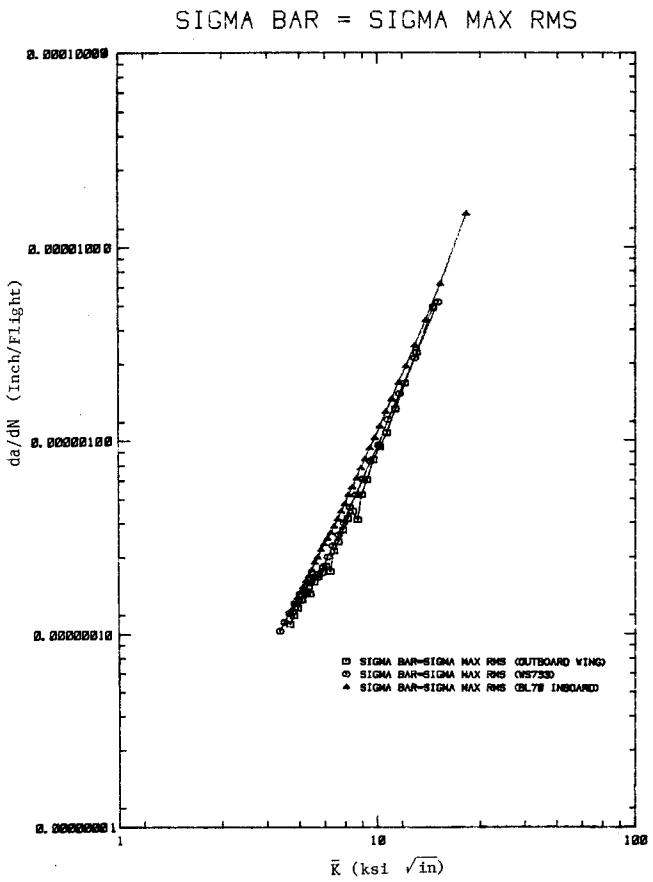

Figure 9.3.9. Cyclic Crack Growth Rate Behavior for Three Transport Wing Stress Histories

$$\overline{K} = \sigma_{\max_{RMS}} \cdot (K/\sigma)$$

The collapsing of crack growth rate data observed in Figure 9.3.9 does not always occur when the $\sigma_{max(RMS)}$ parameter is used as the stress history characterizing parameters. If the analyst uses a characterizing parameter that does not describe those events that create damage, one would not expect the crack growth rate data to collapse. Another good characterizing stress parameter for the three transport wing stress histories is the root mean square (RMS) stress range ($\Delta\sigma_{RMS}$). Figure 9.3.10 describes the cycle-by-cycle crack growth rate behavior for the three stress histories where the characterizing stress-intensity factor (K) was calculated using

$$\overline{K} = \Delta\sigma_{RMS}\left(\frac{K}{\sigma}\right) \qquad (9.3.15)$$

As Figure 9.3.10 illustrates, the characterizing stress-intensity factor given by Equation 9.3.14 also collapses the rate data. Additional choices of the characterizing stress maybe necessary when the damage contributions are not dominated by a single loading source.

Once a master crack growth rate curve exists, the curve can be used to integrate the crack growth rate curve at a specific location to produce a crack growth life curve. Figure 9.3.11 highlights the elements of the analysis.

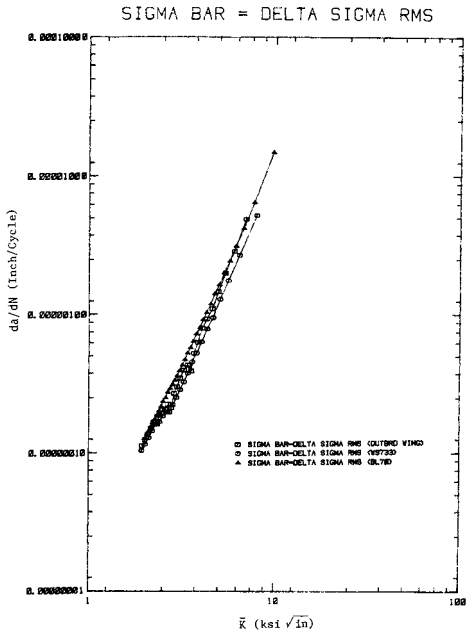

Figure 9.3.10. Cyclic Crack Growth Rate Behavior for Three Transport Wing Stress Histories

$$\overline{K} = \Delta\sigma_{RMS} \cdot (K/\sigma)$$

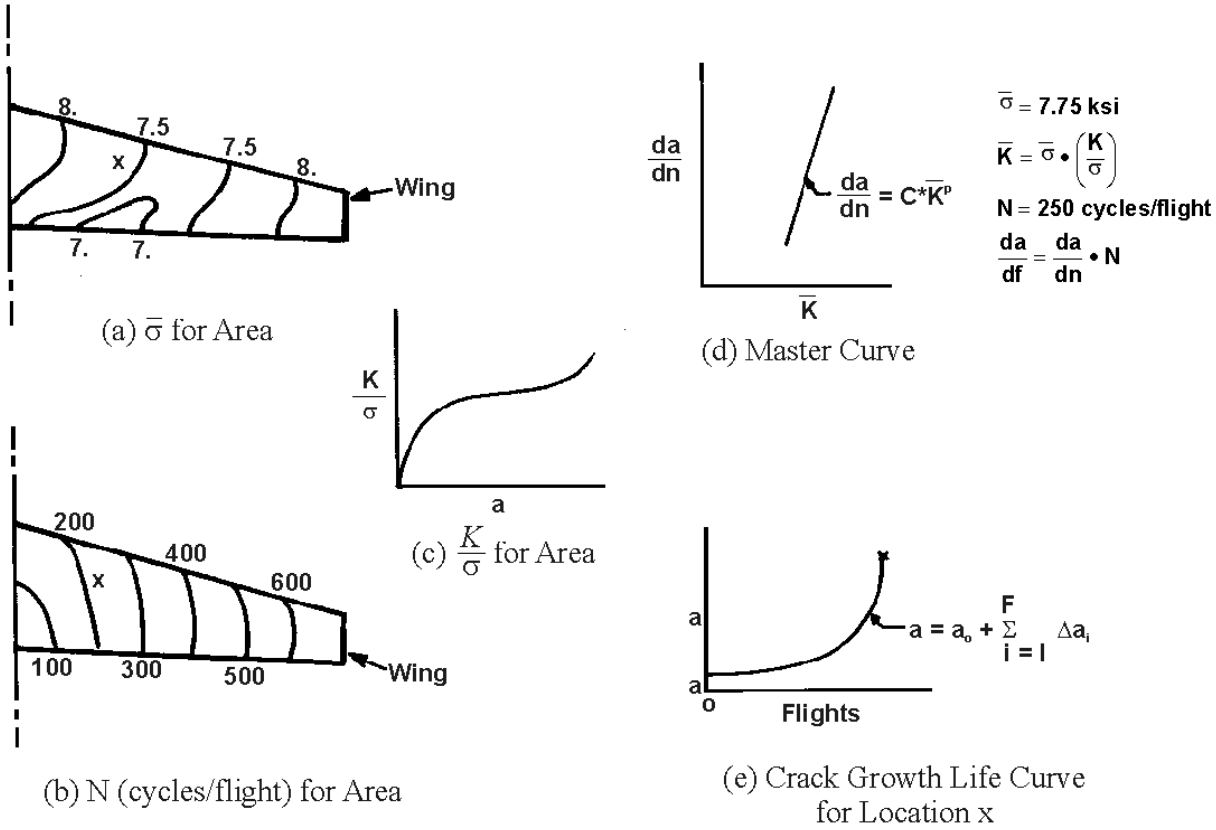

Figure 9.3.11. Schematic of Elements Required to Analyze for Crack Growth Life at Specific Locations

9.4 Life Sensitivity for Stress Effects

The fatigue crack growth life of structural components is significantly affected by the level of applied (repeating) stress and the initial crack size. This section addresses the effect of applied stress level on any structural component and provides examples whereby relative life estimates can be utilized to facilitate the damage tolerant analysis of structural repairs. Section 9.5 discusses the effect that initial crack size has on the crack growth life of a repaired hole.

The simple method for evaluating the effect of stress level on the fatigue crack growth life is based on the general form of Equation 9.3.14 and an available crack growth life curve for the structural geometry of interest. The general form of Equation 9.3.14 related the life (L_σ) at the current stress level (σ) to the life ($L_{x\sigma}$) at the new stress level ($x \cdot \sigma$) through the equation

$$\frac{L_{x\sigma}}{L_\sigma} = \left(\frac{1}{x}\right)^p = x^{-p} \qquad (9.4.1)$$

As explained in Subsection 9.3.3, Equation 9.4.1 will estimate life in a relative sense for any structural detail if (1) the crack growth life is known for a defined stress history and (2) the flight-by-flight crack growth rate behavior is described by the power law equation

$$\frac{da}{dF} = C\overline{K}^p \qquad (9.4.2)$$

Equation 9.4.1 does not allow one to calculate relative life for changes in crack interval, in crack geometry, or in mission mix (unless a master crack growth curve is available for different mission mixes). The above restrictions do not minimize the extensive usefulness of Equation 9.4.1.

Rewriting Equation 9.4.1 so that it relates the unknown crack growth life ($L_{x\sigma}$) to the known life results in

$$L_{x\sigma} = x^{-p} \cdot L_\sigma \qquad (9.4.3)$$

Equation 9.4.3, in essence, provides a scaling factor that would be applied to the complete crack growth life curve for any structural detail; Figure 9.4.1 illustrates this concept schematically. Note that the life scaling factor (x^{-p}) is independent of the shape of the crack growth life curve.

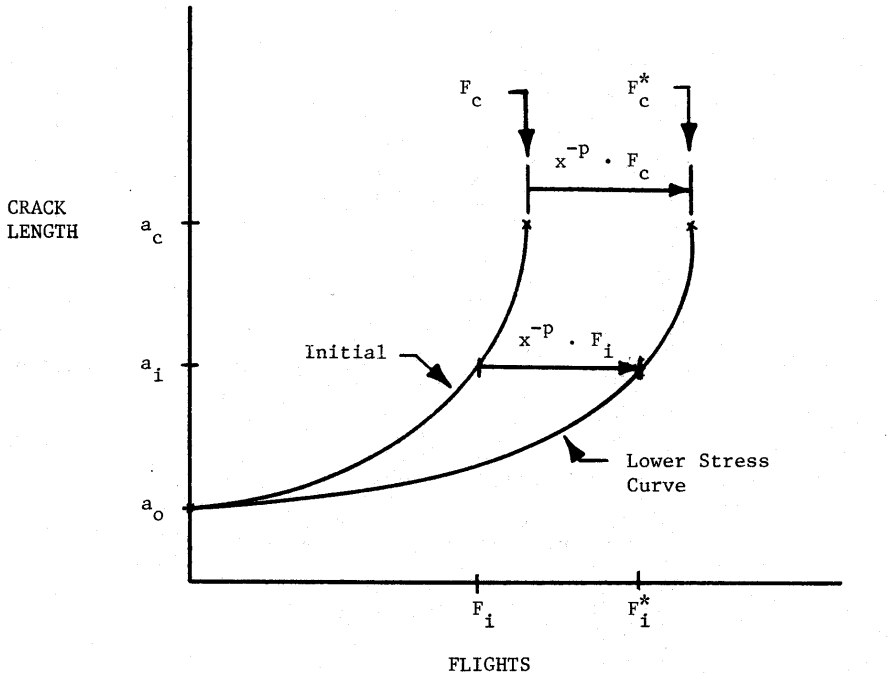

Figure 9.4.1. Schematic Describing the Use of Equation 9.4.3 to Scale the Crack Growth Life Curve Based on a Stress Level Change from σ to $x \cdot \sigma$ where $x < 1$

Due to the generality of the life scaling factor for constructing life estimates, it is instructive to evaluate this factor as a function of the stress scaling factor. The relationship is described in Table 9.4.1 for four different values of the crack growth rate exponent p. Table 9.4.1 shows that the smallest life scaling factors for $x < 1$ are associated with the lowest exponential value ($p = 2.2$). For $x < 1$, the new stress level is lower than the current level and as one would guess (see Table 9.4.1 and Figure 9.4.2), the greater the reduction in stress the longer the life (the higher the life scaling factors).

Table 9.4.1. Relationship Between Stress Scaling Factor x and Life Scaling Factor $L_{x\sigma}$ Defined for Values of the Crack Growth Exponent p

Stress Scaling Factor $x = \frac{\sigma_{new}}{\sigma_{current}}$	**Life Scaling Factor (for x^{-p})**			
	***p* = 2.2**	***p* = 2.5**	***p* = 3.0**	***p* = 3.0**
0.50	4.60	5.66	8.00	11.31
0.60	3.08	3.59	4.63	5.98
0.70	2.19	2.44	2.92	3.48
0.80	1.63	1.75	1.95	2.18
0.85	1.43	1.50	1.63	1.77
0.90	1.26	1.30	1.37	1.46
0.92	1.20	1.23	1.28	1.34
0.94	1.15	1.17	1.20	1.24
0.96	1.09	1.11	1.13	1.15
0.98	1.04	1.05	1.06	1.07
1.00	1.00	1.00	1.00	1.00
1.02	0.96	0.95	0.94	0.93
1.04	0.92	0.91	0.89	0.87
1.06	0.88	0.86	0.84	0.81
1.08	0.84	0.83	0.79	0.76
1.10	0.81	0.79	0.75	0.72
1.15	0.73	0.71	0.66	0.61
1.20	0.67	0.63	0.58	0.53
1.30	0.56	0.52	0.46	0.40
1.40	0.48	0.43	0.36	0.31
1.50	0.41	0.36	0.30	0.24

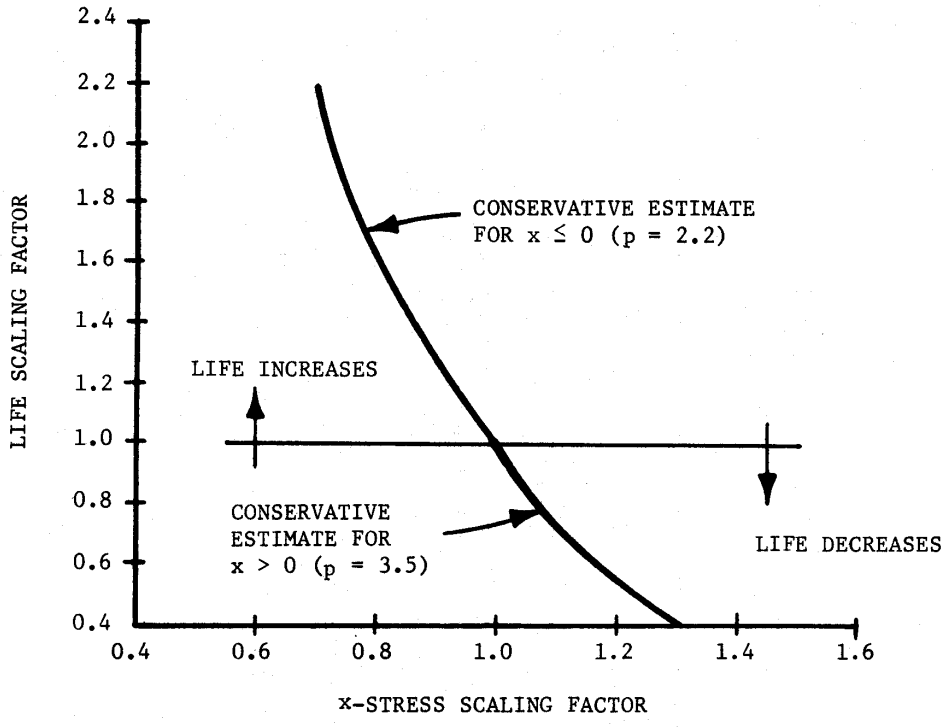

Figure 9.4.2. Life Scaling Factor (New Life / Current Life) as a Function of the Stress Scaling Factor (x = New Stress / Current Stress)

The life benefit achieved by reducing the general level of stress in a structural detail that has experienced crack problems can be estimated from Equation 9.4.3. If the power law exponent p is not available for this particular structural detail, it is recommended that a conservative estimate of p be made, i.e. for a stress reduction chose $p = 2.2$, and evaluate the increase in life on this basis.

EXAMPLE 9.4.1 Modify to Achieve Lower Stress Levels

The doubler shown below has been modified to reduce the general level of stress at the cracking site identified by ten (10) percent. The original doubler on a 6000 hour aircraft had a mean service life of 3400 flight hours to a crack size which would functionally impare the use of this aircraft. How much life will the replacement doubler have? No crack growth life curve exists for the doubler nor for the general area of the wing where it is located. A wide area master curve for the wing is described by a power law equation with exponent $p = 2.89$.

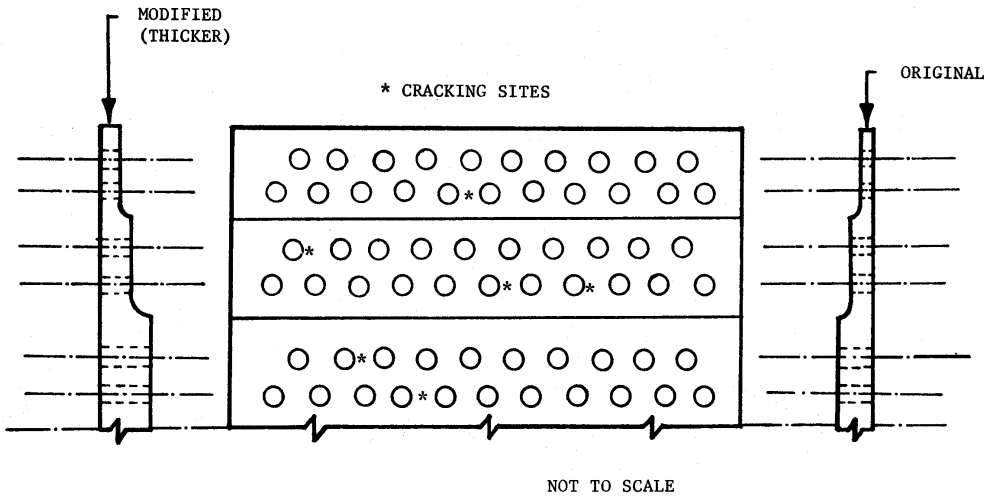

SOLUTION:

The aircraft is presumed to fly the same type of missions with the same frequency after the repair modification as before. Since a master crack growth rate curve is available for the wing, the analyst would evaluate the life of the repair using Equation 9.4.3 with a power law exponent of 2.89. The modification is expected to result in a new life (L_{new}) for a ten (10) percent reduction in stress level (the new stress level is 0.9 times the current stress level). The new life is given by

$$L_{new} = x^{-p} \cdot L_{current}$$

when $L_{current}$ is equal to 3400 flight hours, this reduces to

$$L_{new} = (0.9)^{-2.89} \cdot (3400)$$

$$= 1.356 \cdot 3400$$

$$= 4610 \text{ flight hours}$$

Thus, a first order estimate indicates the life of the replacement doubler will be 35 percent greater than the original doubler. If the original doubler are removed at 2500 hours and replaced with the doubler with the lower stress, it is anticipated that the replacement doubler will not fail during the remaining life of the aircraft (2500 + 4610 7110 hours > 6000 hour life requirement).

If no information on the crack growth rate behavior existed for this region where the doubler was located, then it is suggested that the equation be evaluated with $p = 2.2$. The result of this evaluation is 4285 hours, which still indicates that the replacement doubler will outlast the aircraft (2500 + 4285 = 6785 hours > 6000 hour life requirement).

As a cautionary note, it is important to recognize that the best estimate of the exponent p will result in the best life estimate. The exponent p is expected to vary as a function (due to material and stress event effects on damage) so if values of the exponent p are available for a given location in a component, it is more accurate to utilize the exponent p for that location.

Another direct application of Equation 9.4.4 comes from moving from a stress analysis control point where a complete crack growth life analysis is available to a new location where the cracking behavior is expected to be similar due to geometrical material conditions, but where only a strength of materials analysis is available. An example illustrates the approach here.

EXAMPLE 9.4.2 Local Stress Scaling

The figure describes a local area (Location A) of an aircraft structure that has been experiencing distress. Only the most critical hole (Location B) in the region was analyzed during a damage tolerance analysis; this analysis is summarized in the figure. The exponent p associated with the aircraft's standard operational missions is 3.2 for location B.

A strength of materials analysis was conducted to evaluate the difference in stress levels at the two location (A & B) for a given external loading; these stress levels are defined in the geometry. Provide an estimate of the life for the hole identified at Location A.

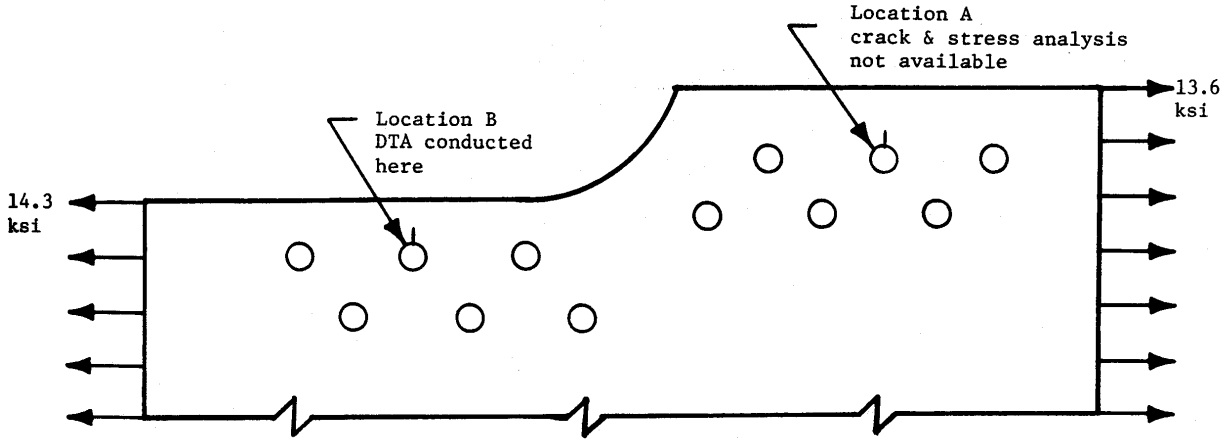

Description of Structural Geometry and Definition of
Analysis Location and of Crack Site

SOLUTION:

The crack at Location A is presumed to grow in the same manner illustrated for Location B. The stress history at Location A is identical to that at Location B except that the stresses are scaled to a lower level x given by

$$x = \frac{\sigma_A}{\sigma_B} = \frac{13.6}{14.3} = 0.951$$

So that the life (L_A) at Location A is found using Equation 9.4.3 and the crack growth life curve in Figure 9.4.5, which describes the life (L_B) to any given crack size for location B:

$$L_A = (0.951)^{-3.2}(L_B)$$

From the Location B crack life curve, the flights required to break the ligament and to fracture the component are 7300 and 12100 flights, respectively. From the equation, the corresponding lives at Location A are 8570 and 14210 flights, respectively, a 17 percent over that of location B.

If cracks are observed with a greater frequency at location A than at Location B, and if the crack sizes at location A are longer than that anticipated at location B for the same operational conditions, then the analyst might reverse the analysis, i.e. use the life ratios for specific crack sizes to obtain a better indication of the stresses at the distressed location.

EXAMPLE 9.4.3 Stress Estimated from Crack Behavior

Cracks have been noted during PDM in a number of aircraft at Location A show for Example 9.4.2. From the available inspection data, it appears that the cracks reach a length of 0.150 inches after about 3600 flights. The DTA established crack growth life curve indicated that 0.150 inch long cracks should not appear until 5800 flights. Estimate the stress level difference between location A and B. Also estimate the number of flights required to fail the ligament and the component.

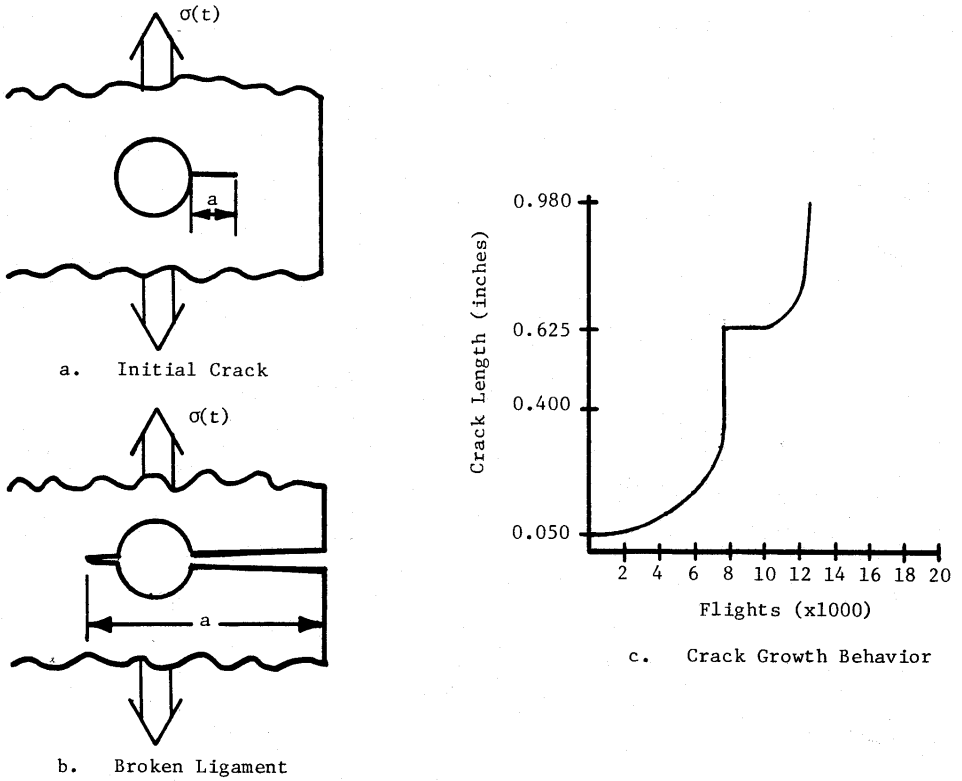

Details of Cracking Process at Location B and Life Curve

SOLUTION:

The method suggested for determining the stress level difference is with Equation 9.4.3, i.e.

$$L_A = x^{-p} \cdot L_B$$

where it's known that $L_A = 3600$, $L_B = 5800$, and $p = 3.2$. Solving for x, the stress ratio between Location A and B yields

$$x = \frac{(\sigma_A)}{(\sigma_B)} = \frac{(L_B)^{\frac{1}{p}}}{L_A}$$

and the stress ratio is

$$x = \frac{(5800)^{\frac{1}{3.2}}}{3600} = 1.16$$

So the stresses at the cracking site (Location A) are expected to be 16 percent greater than that at the DTA location (Location B).

Equation 9.4.6 can be now used to estimate the lives to grow the crack (at Location A) to fail the ligament and the component with x known, the lives are given by

$$L_A = (1.16)^{-3.2} L_B$$

And with L_B = 7300 and 12100 flights for the Location B critical conditions, L_A = 4540 and 7525 flights, respectively, to fail the ligament and the component at Location A.

9.5 Life Sensitivity Analysis for Hole Repair

Because holes are stress concentration sites, it is not surprising that a large number of holes are drilled oversize and repaired to remove crack indications identified during inspection. It is not possible to conduct a detailed damage tolerance analysis on every repair of this type; however, engineers can assess the life of many components before and after the hole is enlarged using Equation 9.3.1 and its integral counterpart Equation 9.3.12. Detailed evaluations should always be conducted for critical locations; in some cases, the detailed evaluations will become the building blocks for other simplified repair analyses.

Hole repairs are made to remove crack indications from the edge of the hole. Several example damage tolerance analyses are presented in this section to summarize the effect of oversizing the hole to remove some (but not all) of the crack damage. Practically speaking, the objective is to remove all the crack damage. But, because non-destructive evaluation (NDE) capability is what it is, the analyst can not presume that all traces of the crack are removed when the hole is oversized. From an economics and safety viewpoint, all traces of the crack should be removed and the aircraft restored to its original condition. When conducting a damage tolerance analysis to protect safety, it is wise to error on the conservative side in defining the initial crack size after a hole oversizing operation.

Before introducing the example analyses, it is instructive to review the integral counterpart of Equation 9.3.1, i.e. Equation 9.3.12, which is presented as Equation 9.5.1

$$F = \int_{a_o}^{a_f} \frac{da}{C\overline{K}^p} \tag{9.5.1}$$

or

$$F = \frac{1}{C\left(\overline{\sigma}\sqrt{\pi}\right)^p} \int_{a_o}^{a_f} \frac{da}{\left(\beta\sqrt{a}\right)^p} \tag{9.5.2}$$

The parameter β is the geometry correction factor that is normally a function of crack length. We again note that the integral

$$I = \int_{a_o}^{a_f} \frac{da}{(\beta\sqrt{a})^p} \tag{9.5.3}$$

is dependent of stress effects and is only dependent on the geometry of the structure and of the crack. So if the stress parameter, i.e., the stress history, is constant, then the impact of geometry changes on life can be assessed by studying the variation of I as the geometry changes. The following example will be used to illustrate this point.

EXAMPLE 9.5.1 Variation of Initial Crack Size on Life

A structural member made from D6AC steel has been experiencing cracking problems at a ¼ inch diameter weep hole. If the crack growth rate per flight hour is given by:

$$\frac{da}{d(FH)} = 1.6\times10^{-8}\overline{K}^{2.6}$$

then calculate the life required to grow a thru-thickness crack from several initial crack sizes to a 0.550 inch long radial crack. Assume the stress is 30 ksi.

SOLUTION:

The integral counterpart of the growth rate equation for this problem is

$$FH = \frac{1}{1.6\times10^{-8}(30\sqrt{\pi})^{2.6}}\int_{a_0}^{0.550}\frac{da}{(\beta\sqrt{a})^{2.6}}$$

where β is associated with the radially cracked hole geometry, (see Section 11):

$$\beta = 0.7071 + 0.7548y + 0.3415y^2 + 0.642y^3 + 0.9196y^4$$

where $y = \dfrac{1}{1+a/r}$

The life results for several initial crack lengths are presented in the following table.

Crack Growth Life as a Function of Initial Size for a_f = 0.550 inch

a_o (inch)	$\overline{\sigma}$ =30 ksi		$\overline{\sigma}$ =50 ksi	
	Life (L_{a_o}) **(Flight hours)**	**Life Ratio** $(L_{a_o}/L_{0.050})$	**Life** (L_{a_o}) **(Flight hours)**	**Life Ratio** $(L_{a_o}/L_{0.050})$
0.001	7715	1.48	2041	1.47
0.005	6720	1.29	1767	1.27
0.010	6364	1.22	1696	1.22
0.025	5806	1.11	1538	1.11
0.050	5220	1	1386	1
0.075	4796	0.92	1270	0.92
0.100	4395	0.84	1164	0.84
0.125	4023	0.77	1070	0.77

It is important to note that the life ratios generated by dividing all the life values by the life value associated with a_o = 0.050 inch is independent of stress level, as shown by the results for $\overline{\sigma}$ of 30 ksi and 50 ksi.

Equation 9.5.3 can also provide a simplified method for determining the effect of increasing the diameter of a cracked hole. Consider Figure 9.5.1, which defines the three stages associated with increasing the hole diameter to remove a pre-existing crack. One of the first steps in the analysis is to obtain an estimate of the initial structural life (this life is referred to as the DTA result or the Blueprint life). For purposes of this analysis, the DTA result is presumed available for the region of interest.

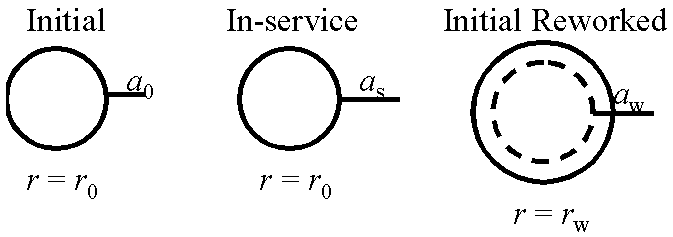

Figure 9.5.1. Three Stages in the Life of a Cracked Hole

As indicated in Example 9.5.1, the larger the initial crack size, the shorter the life. Thus, the decision of choosing the initial flaw size after over-sizing is an important one - both for economy and for safety. For consistency of analysis with JSSG-2006 requirements, it is recommended that crack sizes be no smaller than that associated with initial manufacturing. An example problem is presented later in the section to consider the influence that the initial post rework crack size has on the remaining structural life. First, let us consider the influence that the reworked oversized hole has on life relative to that of the initial hole.

EXAMPLE 9.5.2 Effect of Rework Hole Size on Life

In this example, the blueprint diameter is 0.250 inches and the final crack length is 0.550. For comparative purposes, the initial crack length (both manufacturer's and post rework) is 0.050 inches and is assumed to be a through-thickness crack. The figure shows a description of the geometrical conditions both initially and post-rework.

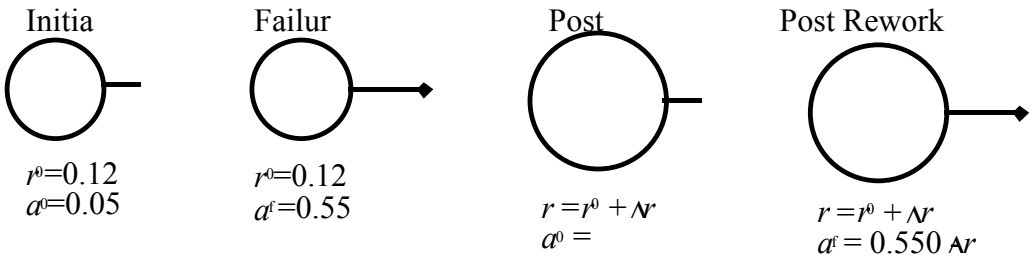

Geometrical Parameters Associated with Blueprint and Post Rework Crack Configurations

Present a comparative life analysis that defines the effect of enlarging the 0.250 inch diameter hole to larger sizes during repair of hole crack damage. Allow the crack growth rate exponent p to vary from 2.5 to 3.5. Assess the effect of the exponent p on the results.

SOLUTION:

Since a comparative analysis is being conducted, it is not necessary to know the stress level nor the crack growth rate constant C, i.e., only those parameters that affect the integral I of Equation 9.5.3 need be considered. The table presents the results of the calculations where the lives have been normalized to the Blueprint life ($I_{r\,=\,0.125}$), using

$$\frac{I_r - I_{r=0.125}}{I_{r=0.125}} * 100$$

where I_r is the value of Equation 9.5.3 for radius r.

Comparative Analysis To Determine the Effect Of Enlarging the Hole
(Initial Crack Length = 0.050 Inch)

Initial Hole Radius (inch)	**Rework Change in Radius (inch)**	**Final Crack Hole Radius (inch)**	**% Life Reduction**		
			p = 2.5	**p = 3.0**	**p = 3.5**
0.125	0	0.125	0	0	0
0.125	1/64	0.140625	9%	10%	14%
0.125	1/32	0.15625	17%	20%	20%
0.125	3/64	0.171875	23%	27%	29%
0.125	1/16	0.1815	27%	31%	35%
0.125	5/64	0.203125	34%	39%	46%
0.125	3/32	0.21875	38%	43%	53%
0.125	7/64	0.234375	41%	46%	59%
0.125	1/8	0.250	44%	49%	66%
0.125	9/64	0.265625	47%	53%	72%
0.125	5/32	0.28125	50%	56%	77%

9.6 Blend-Out Repairs

One of the accepted procedures for removing a small amount of crack damage in the field is through the use of blend-out repairs. These repairs are efficiently accomplished and for the most part, return the structure close to its original static strength and design crack growth life interval. This subsection addresses the type of fatigue crack growth life analysis one might conduct to ensure that a blend-out repair has not significantly degraded the anticipated service life of the structure.

There are two basic conditions that might degrade the life of the structure as a result of blend-out: (1) the accidental gouging, scraping, or otherwise damaging of the material during the repair and (2) the development of a stress concentration site. Both conditions must be actively avoided since both tend to accelerate the development of new cracks which could cause safety-of-flight problems.

As discussed in Section 9.5, one of the more difficult aspects of repair analysis is the definition of initial crack size utilized for life calculations. If the initial crack size assumed after repair is greater than or equal to the initial crack size assumed during design, then the structure life after repair is less than or equal to the initial design life. To determine the fractional loss (FL) in structural life, an engineer could utilize the ratio

$$FL = 1 - \frac{Life\,(Repair)}{Life\,(Blueprint)} \tag{9.6.1}$$

Alternately, the engineer could evaluate the loss in blueprint life by forming the life ratio:

$$LR = \frac{Life\,(Repair)}{Life\,(Blueprint)} \tag{9.6.2}$$

For comparison purposes, it would probably be advisable to calculate both the repair life and blueprint life based on the same initial crack length and thereby assess the effects of stress concentration introduced by the blend-out operation. To establish the crack growth life of the repair in an absolute sense would require that the choice of initial crack length be given careful engineering consideration.

Two examples have been prepared to illustrate the types of analyses that could be conducted to evaluate the damage tolerance of blend-out type repairs. Example 9.6.1 presents the calculations where the initial crack size for the repair is assumed to be equal to the crack size in as-manufactured structure. A sensitivity study is presented to demonstrate the impact that blend-out shape has on repair life. In Example 9.6.2, the crack size after repair is assumed to be smaller than that in the as-manufactured structure, and a sensitivity study is presented to illustrate the effect of crack size.

EXAMPLE 9.6.1 Blend-Out Repair - Effect of Shape

The angle transition component shown below periodically exhibits evidence of cracking in the location identified and the engineer has recommended a blend-out repair to remove all evidence of cracking. Based on the manufacturer's stress report, the tensile stress in the angle transition component is 27 ksi for the critical load condition. Evaluate the damage tolerance of the component assuming that the initial crack size in the repair and the as-manufactured structure are the same (a_o = 0.050 inch).

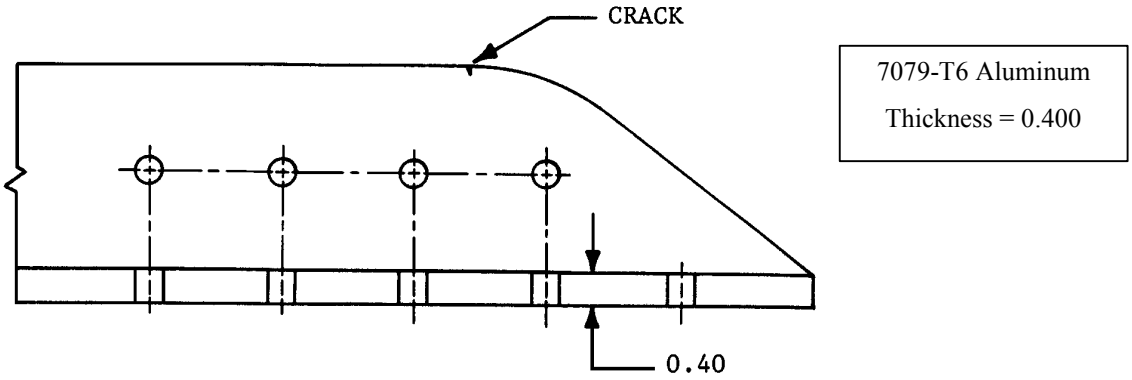

Geometry of Structure with Small Crack

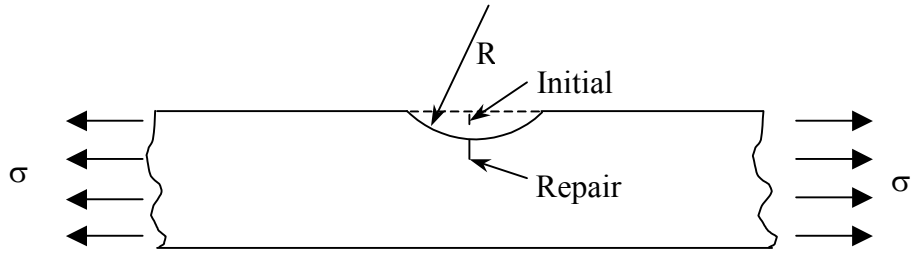

Geometry of Blend-Out Repair Assumed for Analysis

SOLUTION:

The damage tolerance evaluation will be based on an assessment of both the change in crack growth lives and the change in critical crack size. Based on a lack of both a stress history and a wide area crack growth rate equation (discussed in paragraph 9.3.3), an engineer might choose a worst case loading environment to conduct the evaluation. Since the stress condition is known (σ_{max} = 27 ksi), the engineer could approximate the loading with a once per flight maximum stress of 27 ksi applied in a constant amplitude manner. For simplicity, the minimum stress per flight is presumed to be zero so that the assumed loading is zero-tension (R = 0) constant amplitude with a stress maximum of 27 ksi.

To conduct the life analysis, the life equation based on continuous crack growth (consistent with the constant amplitude loading assumption) will be utilized, i.e., life will be calculated using

$$Life = \int_{a_o}^{a_f} \frac{da}{f(K)}$$

The function *f(K)* describes the crack growth rate for the material and loading condition; a_o and a_f are the initial and critical crack sizes, respectively. Three elements are necessary for the life calculation: (1) the function *f(K)*, (2) the stress-intensity factor relationship for the geometry, and (3) the critical crack size (a_f). Each element will be separated determined in the paragraphs below; subsequently, LIFE will be determined.

Function *f(K)* Established

The function *f(K)* describes crack growth rate as a function of a stress-intensity factor parameter (such as ΔK). As a result of the constant amplitude loading condition, the engineer would consult the Damage Tolerant Design (Data) Handbook [Skinn, et al., 1994] to find data consistent with the material and stress ratio conditions. The data in Figure 8.11.3.1 of the DTDH are considered representative of the 7079-T6 aluminum alloy. While it is possible to utilize the mean trend data given in tabular form, as presented in the figure, in conjunction with computer codes that employ table look-up schemes, it is instructive to plot the mean trend data and determine if a simple (power law) crack growth rate equation, i.e.

$$\frac{da}{dN} = C\Delta K^n$$

describes the behavior. Both the mean trend data for the $R = 0.05$ data set and a power law equation that describes these data are presented. The power law equation was determined (graphically evaluated) to be

$$\frac{da}{dN} = 5.84\text{x}10^{-10}\ \Delta K^{4.09}$$

Because the stress ratio (R) for the assumed loading ($R = 0$) and the data set ($R = 0.05$) are relatively close, no stress ratio correction factor is applied to Equation 9.6.5. If a stress ratio correction must be applied to a handbook data set, it is suggested that a Walker type correction be considered. The suggested Walker correction factor for aluminum alloys is given by

$$\frac{da}{dN_{R=R_{desired}}} = C_{dataset}\left[\left[\frac{1-R_{dataset}}{1-R_{desired}}\right]^{\frac{1}{2}}\Delta K\right]^n$$

where $R_{data\ set}$ and $R_{desired}$ are the stress ratios associated with the Handbook data set and the assumed loading, respectively, and where n is the power law exponent for the data set ($n = 4.09$ for the 7079-T6 aluminum data set). A quick evaluation of the Walker equation with the appropriate constants shows that the crack growth rate expression given by the power law equation is approximately 10 percent higher than a corresponding stress ratio corrected expression, and thus not overly conservative for a first order approximation.

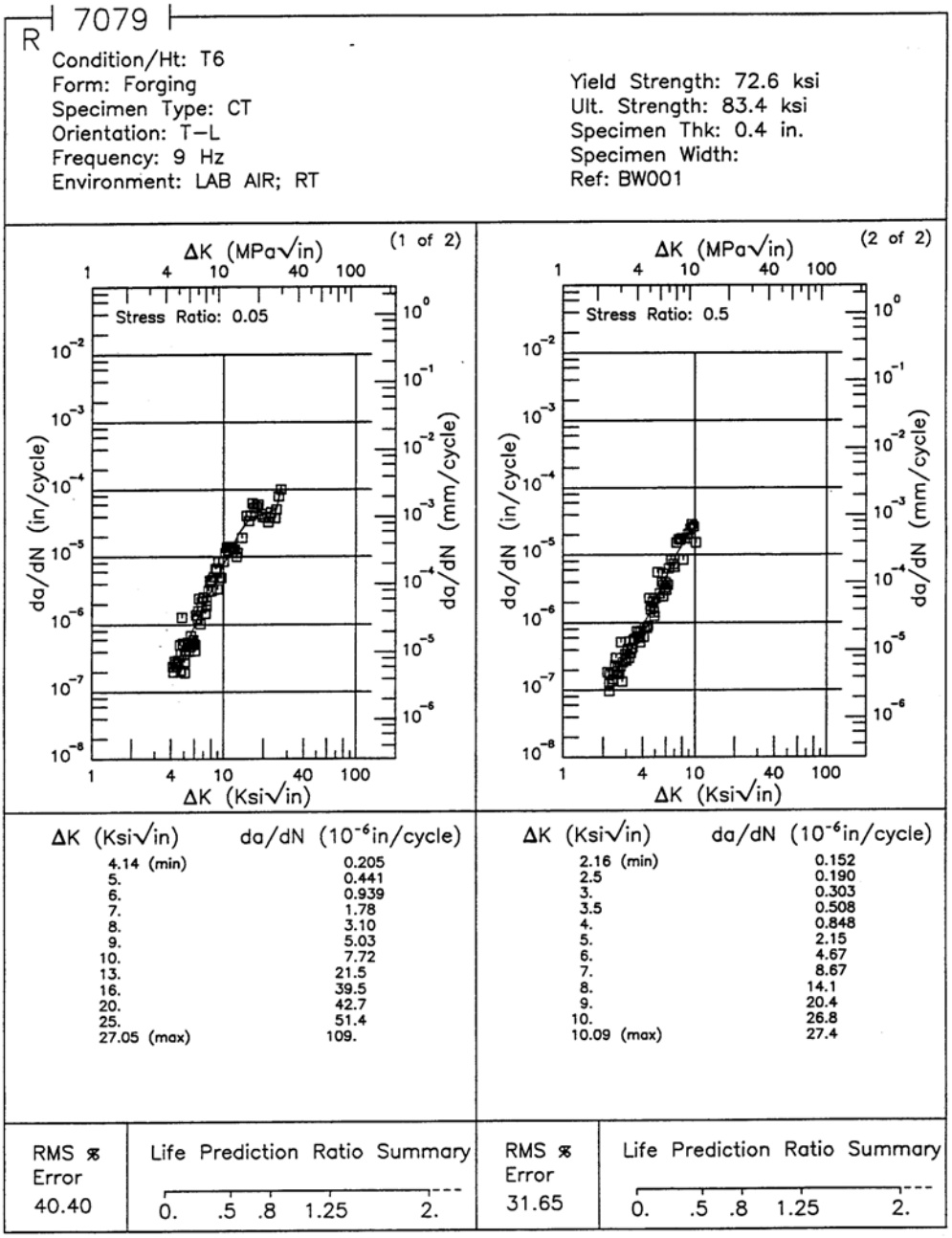

Figure 8.11.3.1.3

8-794

Data Page From the Damage Tolerant Design (Data) Handbook [Skinn, et al., 1994]
Used in Example 9.6.1

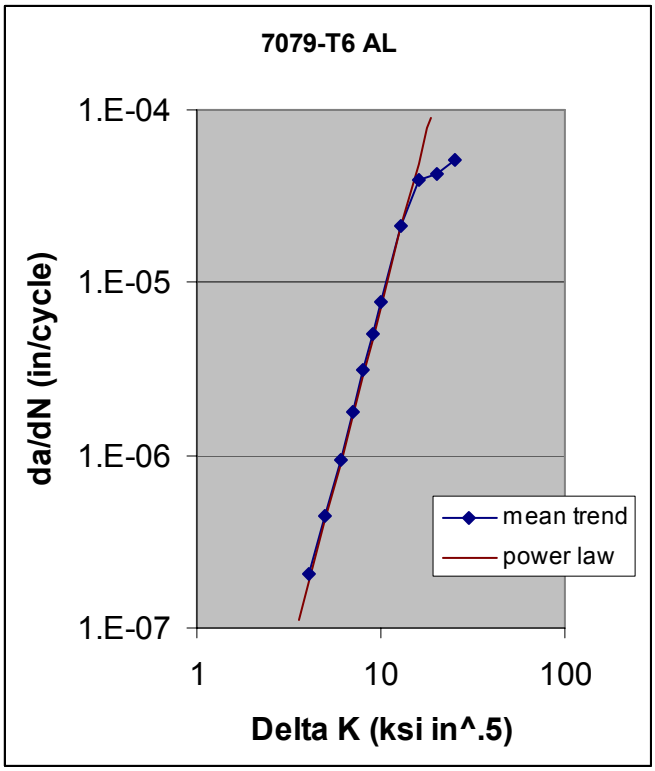

Data From Damage Tolerant Design (Data) Handbook Plotted and
Compared to Graphically Established Power Law Equation

Stress-Intensity Factor Establishment

The stress-intensity factor for the blend-out cracking problem can be solved without access to exact finite element stress analyses through the use of some work of Dowling [1979]. For the purpose of providing a methodology for estimating total fatigue life (crack initiation plus crack propagation lives) of notched structures, Dowling needed a transition crack length that separated the initiation life analysis from the crack propagation life analysis. His studies of the conditions controlling small crack growth behavior led him to the stress-intensity factor evaluation shown below. The point *M* identifies the condition where the short crack stress-intensity factor (K_s) is equal to the long crack solution (K_ℓ). Dowling noted that these two crack solutions provided reasonably accurate estimates of the finite element solution in their respective crack length regions. For crack initiation life analysis, Dowling restricted crack length size measured in smooth fatigue samples to sizes less than the crack length associated with the point *M* in the figure. This is because the stress concentration effect dominates in this region.

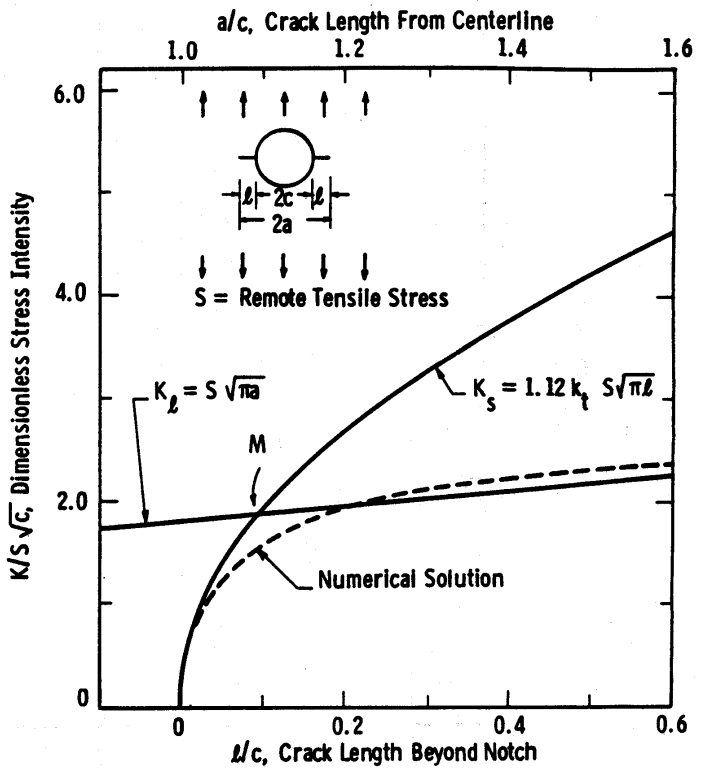

Short and Long Limiting Cases and Numerical Solution, for Crack Growing from a Circular Hole in an Infinite Plate (Newman)

For the purpose of analysis, the engineer could estimate the stress-intensity factor for the blend-out repair using a Dowling type approach where for small cracks, a short crack stress-intensity factor would apply, and for longer cracks, a long crack stress-intensity factor would apply. Thus, for the blend-out repair, the engineer could describe the stress-intensity factor as:

$$K = K_s \text{ if } a \le a_M$$
$$K = K_l \text{ if } a > a_M$$

with the short and long crack stress-intensity factors given by:

$$K_s = 1.12 k_t \sigma \sqrt{\pi a}$$

and

$$K_\ell = 1.12 \sigma \sqrt{\pi (a + d)}$$

where k_t is the stress concentration factor associated with the blend-out shape.

The equations are written in a form slightly different than those presented in the figure because (1) the geometry of the blend-out is more in line with an edge crack rather than a central crack (Dowling's solution) and (2) the crack length a is measured from the surface of the blend-out (see the figure for a definition of a and d).

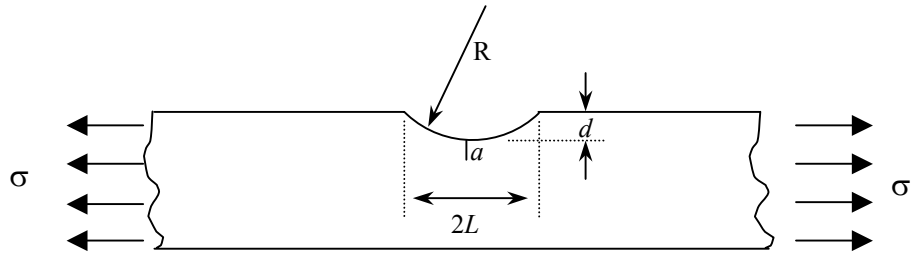

Geometry of Blend-Out with Edge Crack Present

Based on an analysis of these equations, one can see that the blend-out geometry affects the stress-intensity factor solutions through the stress concentration factor (k_t) and blend-out depth (d). An estimate of the stress concentration k_t for a blend-out repair is made using the solution of an elliptical cut out in a plate. For an ellipse oriented with the major axis in line with the direction of the stress axis, the stress concentration is given by [Mushhelishvili, 1954; Peterson, 1974]:

$$k_t = \frac{3 + 2M - M^2}{1 + 2M + M^2}$$

where

$$M = \frac{L - d}{L + d}$$

with L and d defined as the major and minor radii of the ellipse. As can be noted from the figure, L and d define a segment of a circle that we are approximating with a semi-ellipse. Thus, if one has a measure of L and d for a blend-out repair, one can estimate k_t and the corresponding short crack stress-intensity factor using the equations above.

Critical Crack Size, a_f

The critical crack size for both as-manufactured (blueprint) and repaired structure will be based on the Irwin hypothesis for abrupt failure, i.e., when

$$K = K_{cr}$$

failure occurs. The critical stress-intensity factor is obtained by estimating the stress-intensity factor range required to achieve a growth rate of 1000 microinches/cycle. Solving the power law equation in an inverse manner, i.e., solving

$$\Delta K = \left[\frac{1 \times 10^{-3}}{5.84 \times 10^{-10}} \right]^{\frac{1}{4.09}}$$

yields $\Delta K = 33.34$ ksi$\sqrt{\text{in}}$ As a lower bound to this estimate, one might choose $K_{cr} = 30$ ksi$\sqrt{\text{in}}$ for convenience. $K_{cr} = 30$ ksi$\sqrt{\text{in}}$ corresponds to a crack growth rate of 642 microinches/cycle. The stress-intensity factor for the blueprint structure is given by

$$K = 1.12\sqrt{\pi a}$$

whereas that for the repaired structure is given by

$$K = 1.12\sigma\sqrt{\pi(a+d)}$$

(Note that the long crack solution is being used for the repair). In both equations, a is measured from the surface. Solving for K_{cr} = 30 ksi√in and the above stress-intensity factor solutions yields

a_f = 0.325 inch for the blueprint critical size and

a_f = (0.325-d) inch for the repair critical size.

Life Estimating

While the LIFE equation could be used directly for life estimates of the as-manufactured (blueprint) structure, the stress-intensity factor analysis requires that the integral equation be broken into two intervals. For this repair analysis, LIFE is calculated using

$$LIFE = \int_{a_o}^{a_M} \frac{da}{f(K_s)} + \int_{a_M}^{a_f} \frac{da}{f(K_\ell)}$$

where the crack size a_M is associated with the transition between the short and long crack stress-intensity factor solutions. This crack size is obtained by equating the two solutions and solving for a_M, thus

$$K_s = K_\ell$$

in conjunction with the stress intensity equations results in

$$a_m = \frac{d}{k_t^{\,2} - 1}$$

Since for a blend-out repair k_t would be greater than 1.0 and hopefully less than 1.4, a_M will be greater than d.

Numerical Details of Blueprint Life

For an edge crack problem with the material crack growth rate response given by a power law expression, i.e. the LIFE equation can be written as

$$LIFE = \frac{1}{C(1.12\sigma\sqrt{\pi})^n}\left[\int_{a_o}^{a_f} \frac{da}{a^{\frac{n}{2}}}\right]$$

When integrated, this equation becomes

$$LIFE = \frac{1}{C(1.12\sigma\sqrt{\pi})^n}\left[\frac{1}{\left(1-\frac{n}{2}\right)} \cdot \left(a_f^{\,1-\frac{n}{2}} - a_o^{\,1-\frac{n}{2}}\right)\right]$$

Given the growth rate constants C and n, the critical crack size a_f, the given stress (σ = 27 ksi) and the given initial crack size (a_o = 0.050 inch), the crack growth life for the blueprint conditions is determined to be

$LIFE$ = 2910 cycles

of zero-tension loading.

Numerical Details of Repair Life

For the blend-out repair with the material crack growth rate response given by a power law expression, the *LIFE* equation can be expressed as:

$$LIFE = \frac{1}{C(1.12\sigma\sqrt{\pi})^n}\left[\frac{1}{k_t^{\,2}}\int_{a_o}^{a_M}\frac{da}{a^{\frac{n}{2}}} + \int_{a_M}^{a_f}\frac{da}{(a+d)^{\frac{n}{2}}}\right]$$

When integrated, this equation becomes

$$LIFE = \frac{1}{C(1.12\sigma\sqrt{\pi})^n}\left(\frac{1}{1-\frac{n}{2}}\right)\left[\frac{1}{k_t^{\,2}}\cdot\left(a_M^{\,1-\frac{n}{2}} - a_o^{\,1-\frac{n}{2}}\right) + \left((a_f+d)^{1-\frac{n}{2}} - (a_M+d)^{1-\frac{n}{2}}\right)\right]$$

Given the growth rate constants C (=5.84 x 10^{-10}) and n (=4.09), the critical crack size, the given stress (σ = 27 ksi), and the given initial crack size (a_o = 0.050 inch), one can estimate the LIFE for defined values of k_t and d. For example, when d and L are 0.08 inch and 1.0 inch, k_t is 1.16, a_f = 0.245 inch, a_M = 0.231 inch, and LIFE = 2033 cycles of zero-tension loading. This is approximately 30 percent lower than that given for the blueprint life.

Comparative Analysis of Shape Effect

To summarize the analysis for different blend-out shapes, the LIFE equation was repetitively solved for several different length ($2L$) and depth (d) conditions for a_o = 0.050 inch. These results are presented in the following table in the form of life ratios and utilize the blueprint life obtained above. Focusing on three crack depths (0.050, 0.100 and 0.150 inches) as representative, one can immediately note from the table that even for the more gradual blend-out case, the life is substantially reduced (to approximately 80, 65, and 50 percent, respectively) of the original life estimate.

The life ratios presented in the table show the close correlation between life and the stress concentration factor. These results only reinforce common sense since they show that the more gradual the blend-out, the closer to initial life one achieves.

Effects Of Blend-Out Shape On Crack Growth Life Ratio

Depth (d) inch	Length ($2L$) inch	k_t	Life Ratio	Condition
0.005	2	1.01	0.977	Gradual Blend–Out
0.010		1.02	0.954	
0.015		1.03	0.933	
0.020		1.04	0.911	
0.025		1.05	0.891	
0.030		1.06	0.870	
0.040		1.08	0.833	
0.050		1.10	0.796	
0.060		1.12	0.762	
0.080		1.16	0.699	
0.100		1.20	0.640	
0.120		1.24	0.584	
0.150		1.30	0.503	
0.200		1.40	0.366	
0.250		1.50	0.179	
0.010	1	1.04	0.911	Less Gradual Blend–Out
0.020		1.08	0.831	
0.050		1.20	0.638	
0.080		1.32	0.496	
0.100		1.40	0.421	
0.150		1.60	0.282	

EXAMPLE 9.6.2 Effect of Repair Initial Crack Size

To justify removing shallow cracks with blend-out repair procedures, Example 9.6.1 is extended by considering the effect of repair initial crack size. As a basis for comparison, the life ratio equation,

$$LR = \frac{Life\ (Repair)}{Life\ (Blueprint)}$$

will again be employed, and the blueprint (as-manufacturing) LIFE is calculated using

$$LIFE = \frac{1}{C(1.12\sigma\sqrt{\pi})^n}\left[\frac{1}{k_t^{\,2}}\int_{a_o}^{a_M}\frac{da}{a^{\frac{n}{2}}} + \int_{a_M}^{a_f}\frac{da}{(a+d)^{\frac{n}{2}}}\right]$$

with a_o = 0.050 inch. Thus, the blueprint LIFE is 2910 cycles, as calculated in Example 9.6.1.

The purpose of this example is to show that if only part of the crack remains after blend-out there can be substantial life improvement over that calculated for the blueprint LIFE.

The effect of repair initial crack size on crack growth life was calculated using

$$LIFE = \frac{1}{C(1.12\sigma\sqrt{\pi})^n}\left(\frac{1}{1-\frac{n}{2}}\right)\left[\frac{1}{k_t^{\,2}}\cdot\left(a_M^{\,1-\frac{n}{2}} - a_o^{\,1-\frac{n}{2}}\right) + \left((a_f+d)^{1-\frac{n}{2}} - (a_M+d)^{1-\frac{n}{2}}\right)\right]$$

whereas the initial crack size a_o was varied along with length ($2L$) and depth (d) of the blend-out.

The results are summarized in the following table as a function of the various geometric parameters considered. As expected, the table shows that initial repair crack size substantially affects the damage tolerant life of the blend-out. In fact, compared to the other parameters considered, it dominates. Based on this table, the importance of the variables on life is;

a_o - most significant,
k_t - significant, and
d - least significant.

Thus, during a blend-out repair, the objective is to remove as much of the damage as possible (and hopefully all) with a minimum amount of shape change.

Effect of Repair Initial Crack Size on Crack Growth Life Ratio

Repair Initial Crack Size (a_0) inch	**Depth (d) inch**	**Length ($2L$) inch**	**k_t**	**Life Ratio**
0.005	0.02	2.0	1.04	11.81
0.005	0.05	2.0	1.10	10.55
0.005	0.10	2.0	1.20	8.83
0.005	0.15	2.0	1.30	7.49
0.010	0.02	2.0	1.04	5.63
0.010	0.05	2.0	1.10	5.02
0.010	0.10	2.0	1.20	4.19
0.010	0.15	2.0	1.30	3.52
0.010	0.02	1.0	1.08	5.21
0.010	0.05	1.0	1.20	4.20
0.010	0.10	1.0	1.40	3.02
0.010	0.15	1.0	1.60	2.28
0.020	0.02	2.0	1.04	2.64
0.020	0.05	2.0	1.10	2.34
0.020	0.10.	2.0	1.20	1.94
0.020	0.15	2.0	1.30	1.61
0.050	0.02	2.0	1.04	0.91
0.050	0.05	2.0	1.10	0.80
0.050	0.10	2.0	1.20	0.64
0.050	0.15	2.0	1.30	0.50

9.7 Residual Strength Parametric Analysis

This section illustrates parametric analyses available to an engineer for evaluating the sensitivity of residual strength to geometric and material parameters. As discussed in Section 4, the residual strength relates load carrying capability to material toughness and crack size in a unique way for each structure. Two methods are generally available for describing the residual strength of a structure: the first is with a relationship between residual strength and crack length, and the second is with a relationship between residual strength and time. These relationships are summarized in Figure 9.7.1. The first relationship is best used to describe the effects of toughness or of global geometry. The second relationship is best used to describe the effects of crack growth resistance and of global geometry.

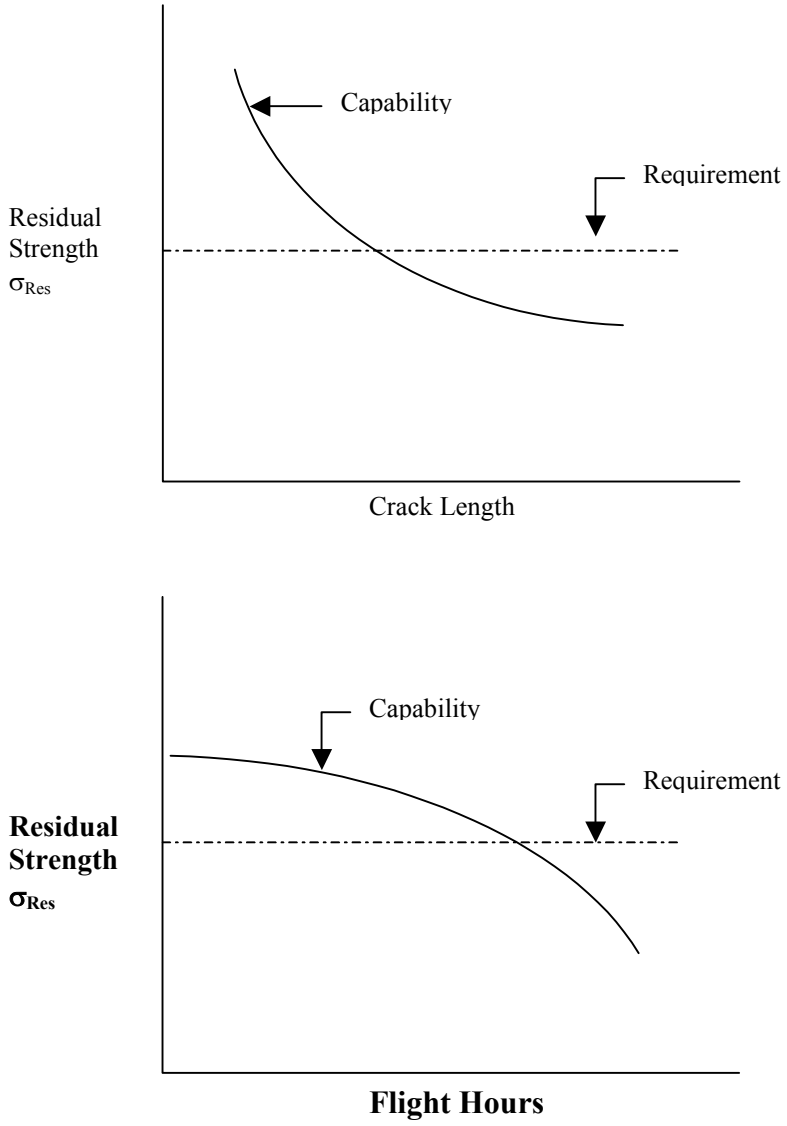

Figure 9.7.1. Types of Residual Strength Relationships

Constructing residual strength-crack length relationships are relatively straight forward. To do so requires both fracture toughness data for the material and a stress-intensity factor analysis for the cracked structure. Fracture toughness data can be found in the Damage Tolerant Design (Data) Handbook [Skinn, et al., 1994]. The stress-intensity factor for a given cracked structure can be obtained through the methods discussed in Section 11.

Constructing residual strength-life relationships requires the same information as above plus a description of the crack growth life behavior under the service loading. This additional information can be generated by integrating wide area crack growth rate equations or by summing incremental damage on a cycle-by-cycle basis. Cycle-by-cycle damage summation presumes (a) that a stress history is available for the cracked structure and (b) that constant amplitude fatigue crack growth rate data are available for the material. The additional complexity associated with generating residual strength-life relationships is one reason why residual strength data are normally only presented as a function of crack length.

A series of examples have been prepared to describe the effects of material properties, spectrum stress level, and structural geometry on the residual strength of relatively simple structures. The approach taken could be duplicated for other more complicated situations related to specific structural repairs.

For each example, the Irwin abrupt fracture criterion is employed to obtain the relationship between residual strength and crack size. Simply stated, failure is presumed to occur when the applied stress-intensity factor (K) is greater than or equal to the fracture toughness (K_{cr}) of the material, i.e.

$$K \geq K_{cr} \tag{9.7.1}$$

then failure occurs. Because the stress-intensity factor is a function of stress and crack size, Equation 9.7.1 provides the relationship between residual strength and critical crack length.

To facilitate a general overview of the residual strength-life relationship, the wide area crack growth rate equation methods developed in Section 9.3 are utilized. In this section, the wide area equation is expressed as

$$\frac{da}{dN} = C\overline{K}^{n} \tag{9.7.2}$$

where the crack growth rate (da/dN) is given appropriately as a function of cycles, flights, or flight hours depending on the given structural situation. Also, the characteristic stress-intensity factor ($\overline{K}$) in Equation 9.7.2 is related to the characteristic stress ($\overline{\sigma}$) through

$$\overline{K} = \overline{\sigma}\left(\frac{K}{\sigma}\right) \tag{9.7.3}$$

where (K/σ) is the stress-intensity factor coefficient (dependent only on geometric parameters, such as crack length and edge distances). The residual strength-life relationship is obtained by cross correlating the residual strength calculated from Equation 9.7.1 with the life calculated from

$$LIFE = \int_{a_o}^{a_{cr}} \frac{da}{C\overline{K}^{n}} \tag{9.7.4}$$

The cross correlation is accomplished using the same value of critical crack length (a_{cr}) for both the residual strength and life calculations.

Example 9.7.1 considers the effect of fracture toughness on both the residual strength-crack length and residual strength-life relationships. These relationships are established for an open hole with a through-the-thickness radial crack, and for a wide area crack growth rate equation defined as

$$\frac{da}{dN} = 1\times10^{-8}\overline{K}^{3.0} \qquad (9.7.5)$$

Examples 9.7.2, 9.7.3, and 9.7.4 consider how the characteristic stress level ($\overline{\sigma}$), the constant C, and the exponential constant n, respectively, affect the residual strength-life relationship. Subsequently, Examples 9.7.5 and 9.7.6 present the effect of geometrical and loading changes on the residual strength-crack length and residual strength-life relationships.

EXAMPLE 9.7.1 Effect of Fracture Toughness

Evaluated the residual strength relationships be as a function of fracture toughness for the structural geometry and loading described in the figure shown here.

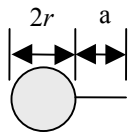

To determine the residual strength-crack length relationship, Equation 9.7.1 is utilized in conjunction with the stress-intensity factor coefficient obtained from Section 11. The stress-intensity factor coefficient for the tension-loaded, open-hole with a radial-through-the-thickness crack in a wide plate is given by:

$$\frac{K}{\sigma} = \sqrt{\pi a}\left(0.7071 + 0.7548y + 0.3415y^2 + 0.642y^3 + 0.9196y^4\right)$$

where $y = \left(\dfrac{1}{1+a/r}\right)$

$a_0 = 0.050$ inch
$r = 0.125$ inch
$K_{IC} = 30$ ksi $\sqrt{\text{in}}$
$\dfrac{da}{dN} = 1\times10^{-8}\overline{K}^{3.0}$

Solving Equation 9.7.1 in conjunction with this equation leads to the relationship between residual stress and critical crack size, thus

$$K_{cr} = \sigma_{cr}\sqrt{\pi a_{cr}}\left(0.7071 + 0.7548y + 0.3415y^2 + 0.642y^3 + 0.9196y^4\right)$$

where $y = \left(\dfrac{1}{1+a_{cr}/r}\right)$

Defining a series of critical crack sizes for a given value of K_{cr} is the easiest method for evaluating the relationship. The following plot describes the relationship between residual strength and crack length, evaluated in this manner, for several given values of K_{cr}. As the plot illustrates, a substantial difference exists between the residual strength curves at any crack

length; this difference is linearly related to the fracture toughness level. For a defined crack length, the equation gives a constant value of (K/σ), so an increase in K_{cr} leads to a similar increase in σ_{res}.

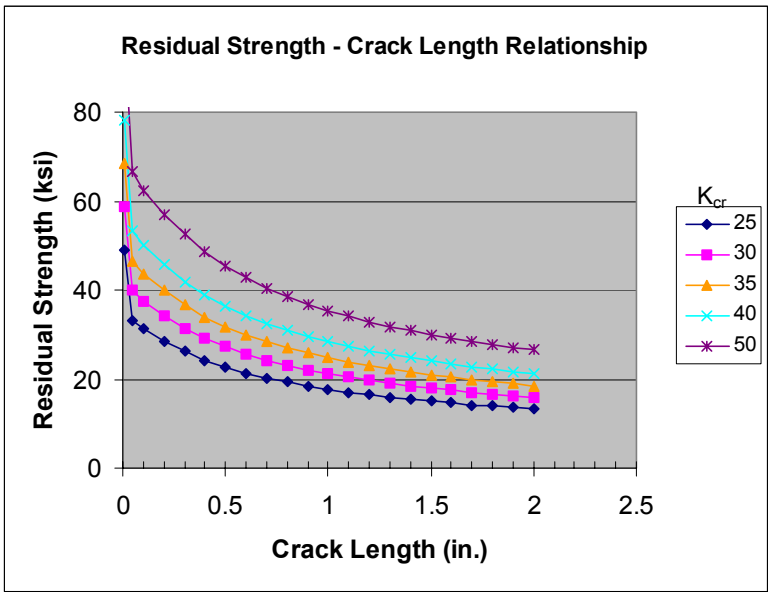

Effect of Fracture Toughness on the Residual Strength-Crack Length Relationship for a Radially Cracked Hole

Evaluating the difference between the residual strength curves based on a constant residual strength level illustrates that a greater improvement factor on critical crack size accompanies an increase in fracture toughness. For a requirement of σ_{res} = 40 ksi, the critical crack size for the K_{cr} = 30 ksi √in material is about 0.050 inch, whereas that for a K_{cr} = 50 ksi √in, the critical crack size is about 0.750 inch. As a first order approximation of the improvement factor, one might neglect the influence of the β factor and arrive at a simplified ratio

$$\frac{a_{cr}^{new}}{a_{cr}^{old}} = \left(\frac{K_{cr}^{new}}{K_{cr}^{old}} \right)^2$$

that illustrates the reason for the dramatic increase in critical crack length for fracture toughness improvements.

One function of an engineer is to provide the structure with sufficient fracture toughness in order to maintain the required residual strength throughout the anticipated service lifetime. A choice of high fracture toughness is appropriate when the engineer is attempting to ensure that potentially damaging cracks are large and easily inspectable prior to the loss of a residual strength requirement. To determine how rapidly the residual strength decays, it is necessary to perform a crack growth life calculation.

When the crack growth life calculation is based on the integral formulation of Equation 9.7.2 (a power law), i.e. on Equation 9.7.4, the shape of the crack growth-life curve is as shown here. This specific curve was obtained for a characteristic stress level ($\overline{\sigma}$) of 20 ksi and employed $C = 1 \times 10^{-8}$ and $n = 3.0$ as the constants in the growth rate equation. The initial crack length (a_o) was chosen as 0.050 inches.

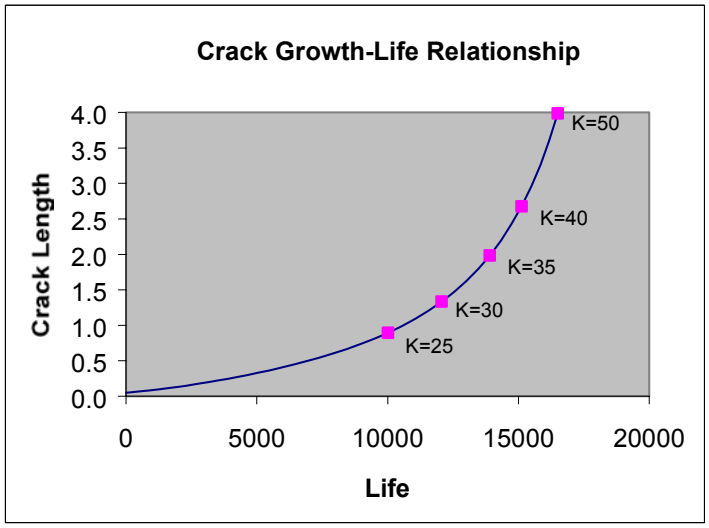

Crack Growth-Life Relationship for the Baseline Geometry

The curve has been marked to indicate the stress-intensity factor at various crack length levels. These levels correspond to the lower fracture toughness levels shown in the previous plot. One consequence of using a power law equation to describe crack growth rate behavior is that the crack growth life curve does not indicate a rapid increase as the stress-intensity factor approaches the fracture toughness level. From a practical standpoint, only a slight error in the life calculation occurs due to inaccurately modeling the crack growth rate in the fracture toughness regime.

When the crack length-life data are cross correlated with the residual strength-crack length data, one obtains the relationships between residual strength and life shown below. Each residual strength-life data point is associated with a common crack length that relates the data in the previous figures. The figure shows that the highest values of fracture toughness are again associated with the highest values of residual strength. The figure also shows that a material with high fracture toughness will maintain a high residual strength capability longer than one with low fracture toughness, all other conditions being equal. Interestingly, for the conditions given for this example, the residual strength capability decays in a linear fashion for most of the life. The only non-linearity occurs in the earliest part of life where the crack is in a severe stress-intensity factor gradient. Other factors which affect the extent of the nonlinear region will be discussed later.

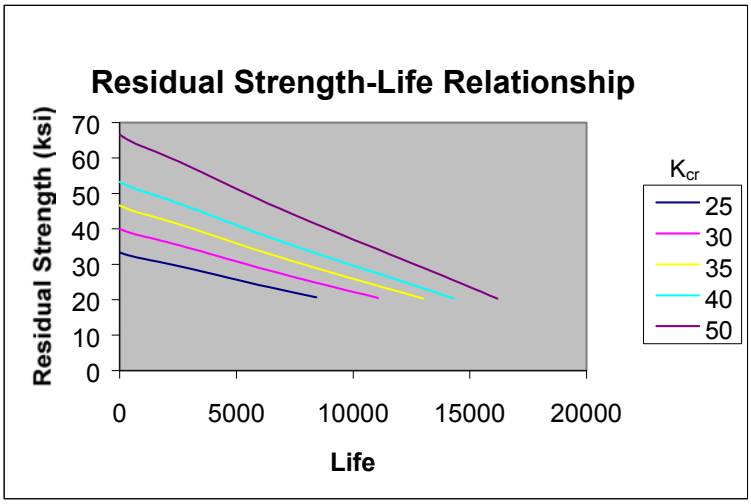

Effect of Fracture Toughness on the Residual Strength-Life Relationship

EXAMPLE 9.7.2 Effect of Characteristic Stress Level

Because the operational stress level significantly affects the crack length life of a structure, an engineer might wish to consider its effect on residual strength. For this evaluation, assume that the material is known to have a fracture toughness (K_{cr}) of 30 ksi √in and a crack growth rate behavior given by Equation 9.7.5 as:

$$\frac{da}{dN} = 1\times10^{-8}\overline{K}^{3.0}$$

The residual strength-crack length relationship will not be affected by the operational stress level; thus, the K_{cr} = 30 ksi √in curve in Example 9.7.1 describes the relationship for this example.

The corresponding crack growth-life curves for characteristic stress levels ($\overline{\sigma}$) of 15, 20, and 25 ksi are presented. As anticipated, the highest stress produces the fastest crack growth-life behavior. Based on Equation 9.7.4, the curves are related to each other by a life factor given by

$$\frac{L_2}{L_1} = \left(\frac{\overline{\sigma}_1}{\overline{\sigma}_2}\right)^n$$

where the lives L_1 and L_2 are calculated at the same crack length (any choice of a_{cr} applies) for characteristic stress levels $\overline{\sigma}_1$ and $\overline{\sigma}_2$.

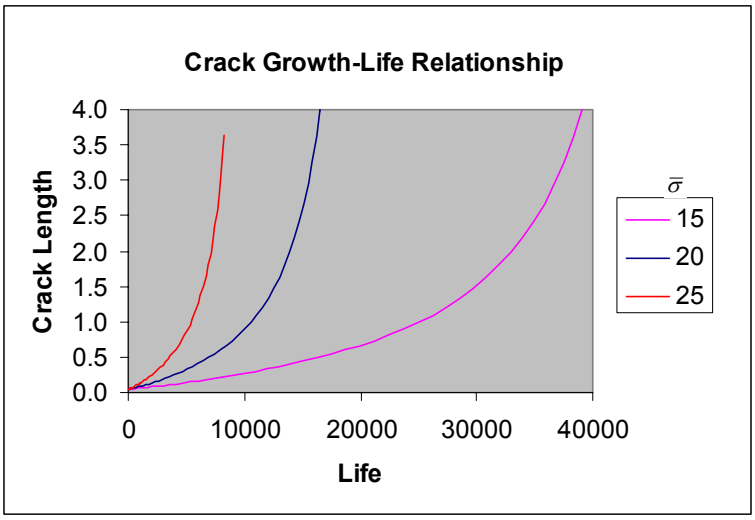

Effect of Stress Level on Crack Growth-Life Relationship

If one cross correlates the crack length-life behavior with the K_{cr} = 30 ksi √in residual strength-crack length behavior, then the residual strength-life behavior is as presented below. Note that the residual strength capability decays more slowly for the lower characteristic stress levels. As a method for predicting the residual strength-life behavior as a function of stress level, one could utilize the baseline curve identified for $\bar{\sigma}$ = 20 ksi and Equation 9.7.9 to provide the appropriate life factor (at any given residual strength level). For example, the $\bar{\sigma}$ = 15 ksi residual strength-life curve is displaced by a factor of

$$\frac{L_{15}}{L_{20}} = \left(\frac{20}{15}\right)^{3.0} = 2.37$$

from the $\bar{\sigma}$ = 20 ksi residual strength-life curve (check this at σ_{res} = 30 ksi where $L_{20} \cong 5400$ and where $L_{15} \cong 12800$.) Thus, one could construct residual strength-life curves as a function of characteristic stress levels by generating a baseline curve and applying the life factor.

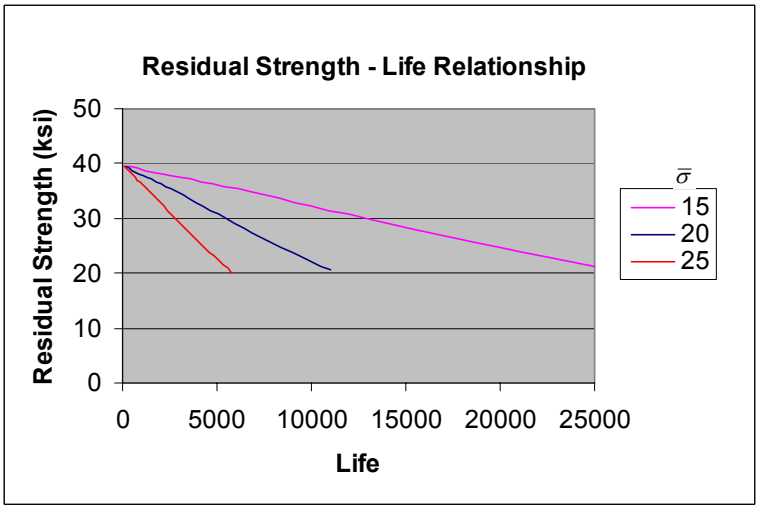

Effect of Stress Level on Residual Strength-Life Relationship

EXAMPLE 9.7.3 Effect of Pre-Exponential Constants

This example and Example 9.7.4 collectively consider the effect of modifying the material's crack growth rate response on the residual strength capability. In both examples, the baseline conditions stated in Example 9.7.1 are used unless otherwise specified.

It is noted that the crack growth rate resistance can be changed independent of the fracture toughness (fracture resistance), so that the residual strength-crack length relationship is again given by the K_{cr} = 30 ksi √in curve in Example 9.7.1.

In a somewhat decoupling fashion, the effect of varying the coefficients in the growth rate equation, (Equation 9.7.2)

$$\frac{da}{dN} = C\overline{K}^{n}$$

are considered separately. In this example, only the constant C is varied to reflect decreasing the crack growth rate response in a systematic manner from the baseline condition where $C = 1 \times 10^{-8}$. In Example 9.7.4, the effect of varying the exponent n is considered.

A change in the constant C is equivalent to shifting the crack growth rate curve to a new position but with the same slope. If the constant C is reduced by a factor of 2, i.e. C=0.5×10^{-8}, then the growth rate da/dN decreases by a factor of 2.

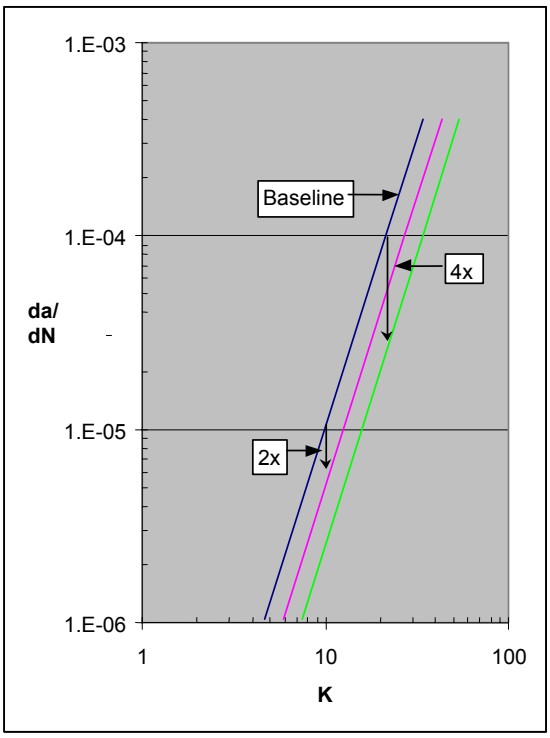

Variation of Crack Growth Behavior Resulting from
a Shift in the Power Law Curve

Based on an analysis of Equation 9.7.4, it is seen that the life difference that results from a change in C can be expressed as a life ratio

$$\frac{L_2}{L_1} = \frac{C_1}{C_2}$$

Thus, if a baseline crack growth-life curve and a baseline residual strength-life curve exist, new curves can be generated by factoring the lives from the baseline condition to the new material conditions using this equation.

The figure below describes the residual strength-life curves for the baseline and two lower values of the constant *C*. From the figure, it is seen that the increased crack growth resistance, i.e. lower *C* values, results in slower rates of residual strength decay. The new curves are exactly a factor of two and of four removed from the baseline curve.

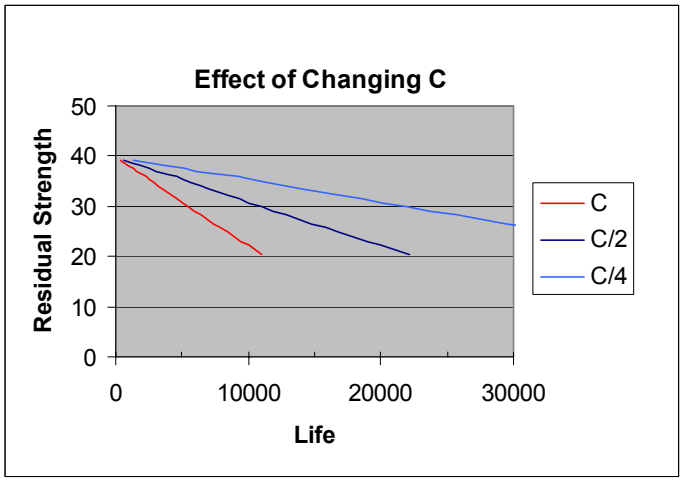

Effect of Constant *C* on Residual Strength-Life Relationship

Increasing the material's crack growth resistance has an immediate effect of increasing the number of flights (amount of flight hours) until the residual strength capability decays to the residual strength requirement.

EXAMPLE 9.7.4 Effect of Exponential Constant

In this example, the exponential constant (*n*) in Equation 9.7.2 is varied along with the constant *C* to reflect a defined rate of crack growth ($da/dN = 10 \times 10^{-6}$ in/cyclic unit) for a given characteristic stress-intensity factor level of $\overline{K}$ = 10 ksi √in. The baseline constants of $n = 3.0$ and $C = 1 \times 10^{-8}$ yield an equation which passes through the point $(10, 10 \times 10^{-6})$. This figure illustrates the three choices of *n* considered in this example.

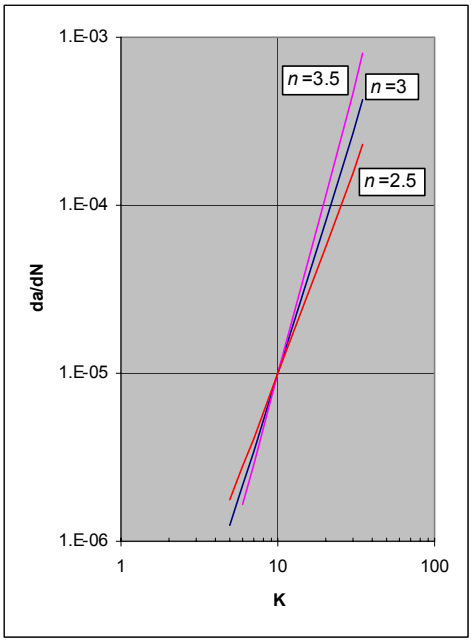

Crack Growth Curves Shown Passing Through Common Point

For this baseline geometry, fracture toughness level, and stress level, the characteristic stress-intensity factor varies between about 15 and 30 ksi √in as a result of the crack growth change. When the common point for the power law equations is located at a stress-intensity factor level that corresponds to a crack length within the crack length interval associated with the life calculation, one can not immediately interpret the effect of the crack growth rate behavior. However, based on the crack growth rate behavior defined in the figure, the curve with $n = 3.5$ will yield crack growth rates faster than the baseline throughout the crack length interval of interest. Thus, for the conditions stated, an engineer would expect a more accelerated crack growth behavior and a more rapidly decaying residual strength behavior for the $n = 3.5$ material than for the baseline. The following figures bear out this expectation.

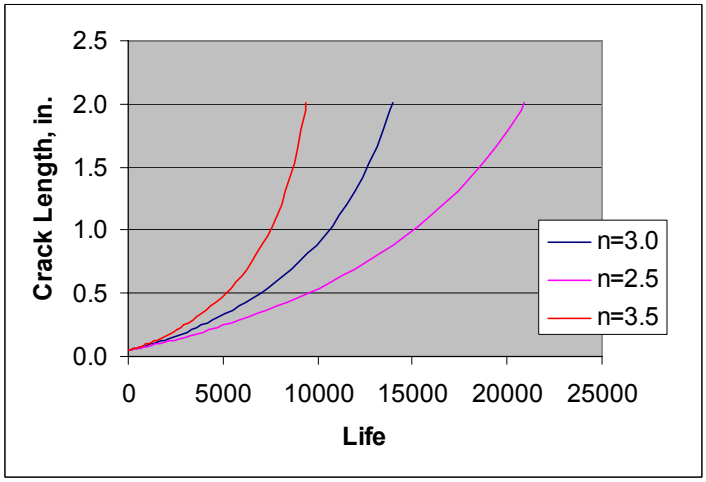

Effect of Exponent *n* on the Crack Growth Life Relationship

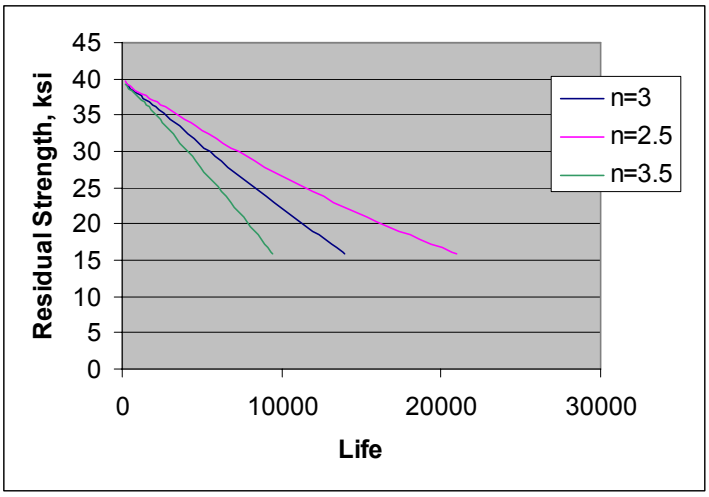

Effect of Exponent n on the Residual Strength-Life Relationship

One observation made in studying the residual strength-life behavior presented in the figure is that the decay in residual strength is slightly nonlinear in the long life region for the two non-baseline crack growth rate behaviors. For the $n = 2.5$ material, the residual strength-life curve is slightly concave up while the $n = 3.5$ material produces a slightly concave down shape. Thus, a second factor that produces nonlinear decay effects is the exponent n. Generally speaking, nonlinear decay effects would be expected when the crack growth rate behavior can not be described by a power law equation with $n = 3$. While the nonlinear behavior is evident, it is important to note that it is slight. As a result, local regions of the residual strength life curve can be easily described by linear line segments, and the procedures presented in Examples 9.7.1, 9.7.2, and 9.7.3 can be utilized to extrapolate from a segmented baseline curve.

The rate of decay in residual strength as a function of service loading has been shown by the above examples to be an important function of material behavior and of load level. The residual strength decay rate can also be significantly affected by geometric parameters and loading conditions. In Example 9.7.5, the effect of global and crack geometry is considered; and then in Example 9.7.6, the effect of localized fastener loading is evaluated.

EXAMPLE 9.7.5 Effect of Geometrical Parameters

Using the through-the-thickness, radially-cracked, open hole geometry (shown in Example 9.7.1) as the baseline geometry, two other geometrical configurations are considered: (1) the through-the-thickness, center-crack and (2) an open hole with a radial crack which transitions from a one-quarter-circular, corner-crack shape to a through-the-thickness-crack shape. In all cases, the width of the structure is considered sufficient so that it does not influence the results. Baseline material properties (K_{cr}, C, and n), initial crack length (a_o), and characteristic stress level ($\overline{\sigma}$) are as defined in Example 9.7.1 and apply to all three geometries. The center crack geometry does not have a central (starter) hole; its total initial length is $2a_o$. The radius (r) of the hole with the transitioning crack is 0.125 inch, the same as the baseline geometry.

The information presented at the introduction of this section described how the residual stress relationships could be developed using Equations 9.7.1 and 9.7.4 and the stress-intensity factor coefficient for the geometry. The only factor that changes as a function of geometrical parameters is the stress-intensity factor coefficient; Example 9.7.1 provides this coefficient for the baseline case. For the through-the-thickness, center crack configuration in an infinite plate, the stress-intensity factor coefficient is given by

$$\frac{K}{\sigma} = \sqrt{\pi a}$$

The case of the transitioning corner crack requires that the crack growth shape be known throughout the interval of crack growth. The stress intensity factor solution for this geometry is given in Section 11.

When the stress-intensity factor coefficients for the given geometries are utilized in conjunction with Equation 9.7.1, the residual strength-crack length relationships are determined (K_{cr}=30 ksi $\sqrt{in}$). As expected, the transitioning corner crack geometry exhibits residual strength that is greater than that of the through-the-thickness crack geometry (baseline) for shorter cracks. For crack lengths greater than 0.250 inch, the transitioning radial crack and baseline configurations exhibit the same residual strength (since the stress-intensity factor coefficients are the same here). One interesting feature of this plot is that the residual strength of the center crack configuration is higher than the radially cracked holes for short crack lengths but rapidly decreases with crack length and eventually falls below the residual strength exhibited by the cracked hole. One might puzzle through this observation by noting that the center crack has a total length of 2*a*, whereas the radially cracked hole has an equivalent length of (*a*+2*r*).

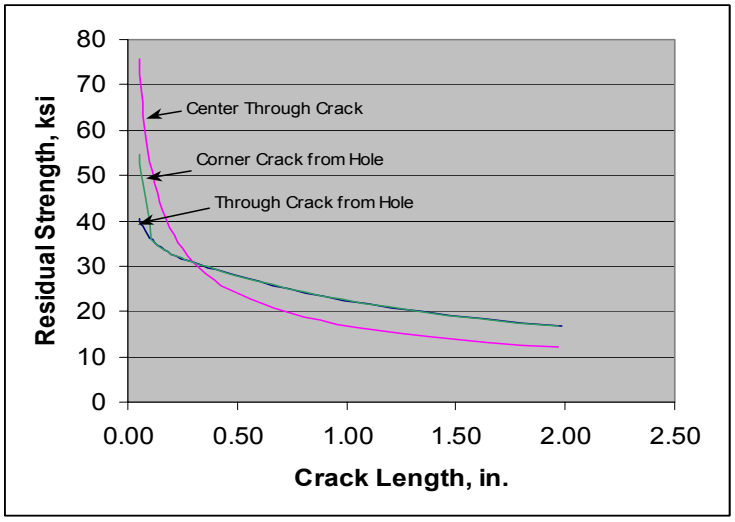

Effect of Geometry on the Residual Strength-Crack Length Relationship

Equation 9.7.4 was utilized to calculate the crack growth life relationships for the three geometries and these are shown below. Because the stress-intensity factor for the through-the-thickness radial crack is initially higher than those of the other two configurations, the baseline configuration exhibits the fastest crack growth behavior. The transitioning radial-corner-crack configuration initially exhibits slower crack growth behavior than the baseline but eventually these two crack growth curves become parallel (when the stress-intensity factor is the same, i.e. when $a > 0.250$ inch). The center crack configuration exhibits the slowest initial growth

behavior, and this is primarily because the stress-intensity factor for small crack lengths is substantially below that of the other two configurations.

By cross-correlating the information presented in these figures, one is able to construct the residual strength-life relationships shown in the next figure. As anticipated, the baseline configuration has the lowest residual strength capability and the center crack configuration exhibits the highest residual strength capacity. Both the baseline and center crack configurations are also shown to exhibit an extensive region of linear residual strength decay as a function of time-in-service. The nonlinear residual strength decay exhibited by the transitioning radial corner crack is attributed to the gradient in the stress-intensity factor coefficient for relatively short cracks and the transition to a through crack. Based on observations in this and other examples in Section 9.7, it would appear that one of the most important factors contributing to nonlinear behavior is the severity of stress-intensity factor gradient (as a function of crack length).

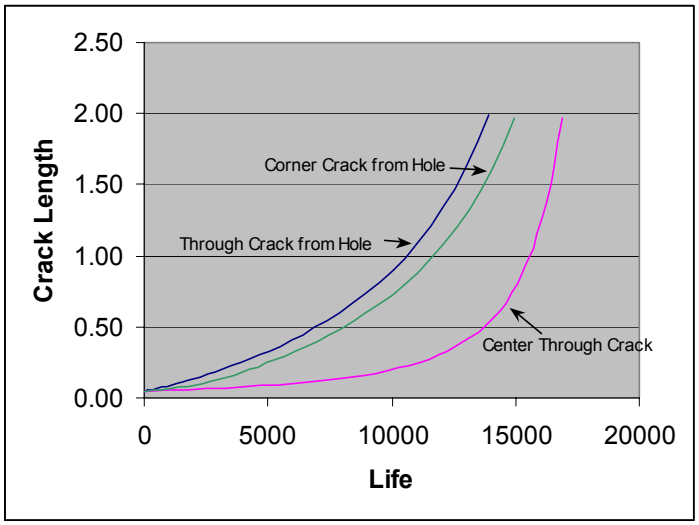

Effect of Geometry on the Crack Growth-Life Relationship

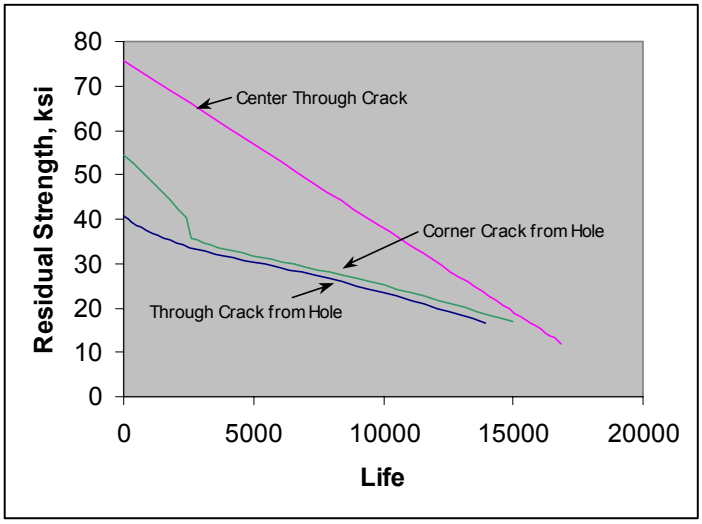

Effect of Geometry on the Residual Strength-Life Relationship

EXAMPLE 9.7.6 Effect of Hole Loading

As a means of evaluating the effect of fastener loading on the residual strength, this example combines the baseline remote loading configuration described in Example 9.7.1 with localized pin loading shown here. To calculate residual strength, the baseline material properties are utilized in Equations 9.7.1 and 9.7.4 along with the stress-intensity factor associated with the combined loading.

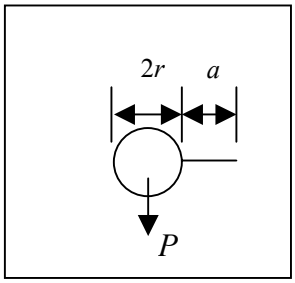

Because the structural response is linear elastic, stress-intensity factor solutions for the remote and localized loadings can be added to obtain the stress-intensity factor for the combined loading; thus,

$$K_{Total} = K_{remote} + K_{local}$$

where K_{remote} is obtained from the product of the remote stress ($\overline{\sigma}$) and the stress-intensity factor coefficient for a wide plate given in Example 9.7.1, so that:

$a_0 = 0.050$ inch
$r = 0.125$ inch
$K_{IC} = 30$ ksi $\sqrt{\text{in}}$
$\frac{da}{dN} = 1 \times 10^{-8} \overline{K}^{3.0}$

$$K_{remote} = \overline{\sigma}\beta_{remote}\sqrt{\pi a}$$

and $$\beta_{remote} = \left(0.7071 + 0.7548y + 0.3415y^2 + 0.642y^3 + 0.9196y^4\right)$$

where $$y = \left(\frac{1}{1 + a/r}\right)$$

K_{local} is the stress-intensity factor associated with the pin loading. From Section 11, this stress intensity factor is given by

$$K_{loacl} = \frac{P}{2rt}\beta_{PR}\sqrt{\pi a}$$

where

$$\beta_{PR} = \beta_{remote}\left(\frac{r}{W}\right) + G_1$$

and

$$G_1 = \left(0.078y + 0.7588y^2 - 0.4293y^3 + 0.0644y^4 + 0.651y^5\right)$$

As a method of comparing the effect of pin loading in conjunction with remote stress loading, the bearing to bypass ratio was used. The bearing to bypass ratio is the ratio between the bearing stress ($P/2rt$) and the remote stress $\overline{\sigma}$, i.e.

$$\frac{\sigma_{BR}}{\sigma_{BP}} = \frac{\frac{P}{2rt}}{\overline{\sigma}}$$

Various combinations of this ratio were chosen and the residual strength relationships were then generated using Equations 9.7.1 and 9.7.4. The residual strength-crack length relationships are shown for K_{cr}=30 ksi √in; and, the crack length-life are shown for $C=1\times10^{-8}$ and n=3.0. By cross-correlating this information, one can generate the residual strength-life relationships, as shown.

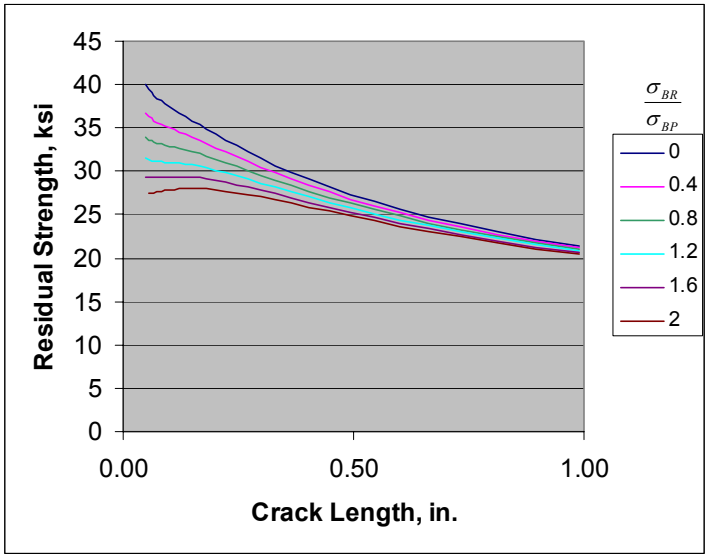

Effect of Pin Loading on the Residual Strength-Crack Growth Relationship

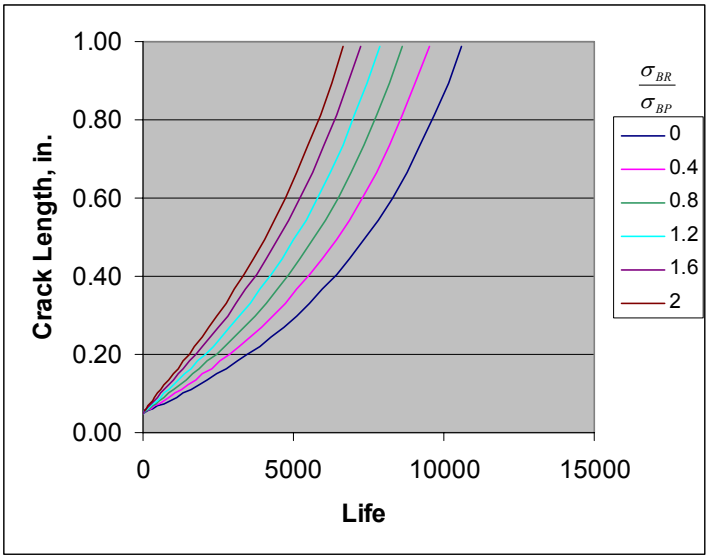

Effect of Pin Loading on the Crack Growth-Life Relationship

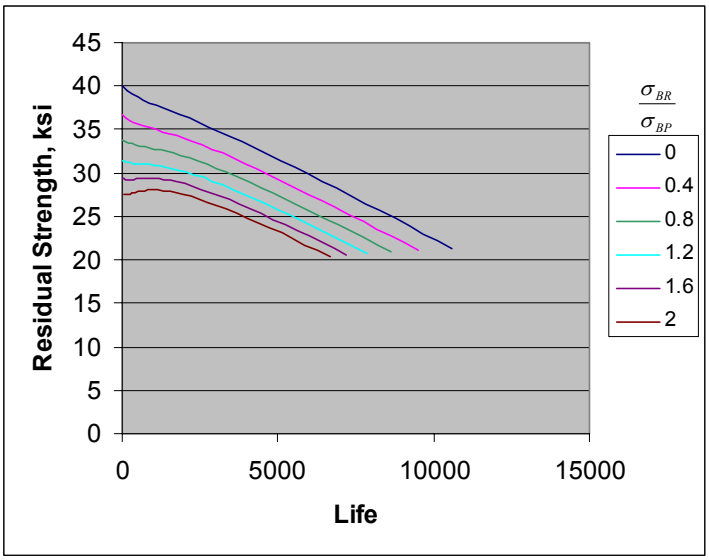

Effect of Pin Loading on the Residual Strength-Life Relationship

Based on the results presented in these figures, it would appear that bearing to bypass ratios less than 0.4 cause a relatively small change in the residual strength/crack length/life relationships. As the bearing to bypass ratio increases from 0 to 2, (a) the residual strength decays very rapidly in the short crack region, (b) a significant reduction occurs in the crack growth-life curves, and (c) the residual strength-life curves are progressively lower. The collective sum of these observations indicate that when substantial hole loading is present, it is necessary to account for the hole loading when assessing the residual strength and crack growth life behavior.

9.8 References

N.E. Dowling (1979). "Notched Member Fatigue Life Predictions Combining Crack Initiation and Propagation". *Fatigue of Engineering Materials and Structures* (Vol. 2), pp. 129-138.

G.E. Maddux, L.A. Vorst, F.J. Giessler, and T. Moritz (1970, February). *Stress Analysis Manual*. AFFDL-TR-69-42. Air Force Flight Dynamics Laboratory, Wright-Patterson Air Force Base, Ohio.

N.I. Muskhelishvili (1963). *Some Basic Problems of the Mathematical Theory of Elasticity.* Fourth, corrected and augmented edition, Moscow 1954. Translated from Russian by J.R.M. Radok, P. Noordhoff Ltd., Groningen, The Netherlands.

R.E. Peterson (1974). *Stress Concentration Factors.* Wiley-Interscience, New York, NY.

D.A. Skinn, J.P. Gallagher, A.P. Berens, P.D. Huber, and J. Smith (1994). *Damage Tolerant Design (Data) Handbook.* WL-TR-94-4052. Wright Laboratory, Air Force Materiel Command, Wright-Patterson Air Force Base, Ohio.

Section 10
Guidelines for Damage Tolerance Design and Fracture Control Planning

The attainment of trouble-free and damage tolerant design for safety-of-flight structure on aircraft is a continuing multiple element process which begins in the preliminary design phase and extends through manufacturing into the operational planning and use of the aircraft. The purpose of this process is to develop a planned approach to the control of fracture damage in the aircraft. Figure 10.0.1 illustrates the main elements of the process.

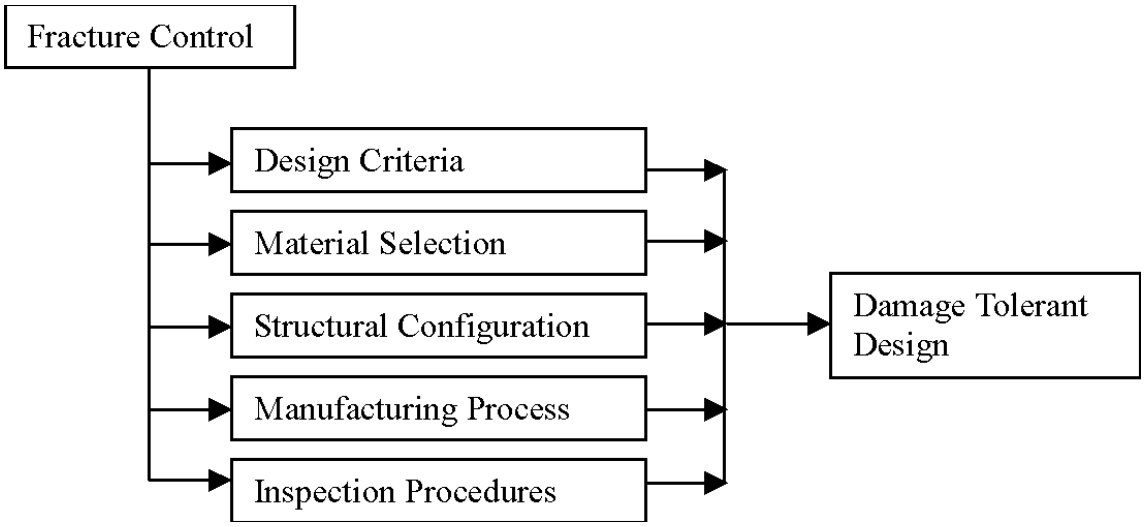

Figure 10.0.1. Elements of Damage Tolerant Design

The design criteria include the service loads history, the functional requirements, and the desired life of the structure. The initial damage assumptions to be used with each type of design concept and degree of inspectability are also specified in the criteria. These are discussed in detail in Section 1.3.

Material selection is a critical element of the process. Trade-off studies are conducted between competing materials and use a comparative property data is necessary in the selection process. Ultimate strength, yield strength, fracture toughness and stress corrosion resistance must be considered together with the expected aircraft environment. The crack growth rate as a function of stress-intensity factor is required.

The structural configuration development must consider the effects of design details on fracture control. The inspection level is defined and a list of critical parts is begun. Consideration of the inspection procedures to be used at each critical location is important. The analysis methods used and the stress-intensity factor computations are a function of the structural configuration and design details, and are set at this time. Testing methods for each critical part and assembly are also developed and incorporated into the damage tolerant design process.

Manufacturing processes must be selected for the critical parts such that they do not reduce the damage tolerance level required by the design. Control of processes and selection of inspection procedures to maintain process quality are the prime consideration of this element.

Procedures for inspecting the aircraft during operational maintenance and the development of the force structural management plan constitute the last element of the total damage tolerant design process.

This introduction of the elements illustrates the strong connections between design, testing, manufacturing, inspection and use in order to obtain and maintain the desired damage tolerant structure and to reduce the incidence of fracture related failures and loss.

The documents that outline the requirements for this activity and describe the various functions are military standards and specifications. MIL-HDBK-1530 establishes the requirements for aircraft structural integration program (ASIP) and JSSG-2006 describes the airplane damage tolerance design requirements.

Wood [1979] provides discussion of the ASIP technology. Tiffany [1978] presents extensive discussions of the durability and damage tolerance problem of USAF aircraft structures. In particular, the review by Mr. C.F. Tiffany, "Durability and Damage Tolerance Assessments of United States Air Force Aircraft," provides a thorough review of the background of this topic.

This section of the handbook describes these tolerant design elements in some detail, and when the described functions are followed, the resultant aircraft structure should have the required level of damage tolerance.

10.1 Design Loads Spectrum

The design load spectrum is used to determine the damage growth in each critical part during analysis and testing. It is based on the specified mission profile information and the required aircraft life. A description of the load sequence development is given in Section 5.3 of this handbook. A brief review is presented here. Giessler, et al. [1981] presents a detailed description of load sequence development methodology.

The load sequence is composed of the load cycles that can be expected to occur during the lifetime operation of the aircraft. They are the result of ground operations, such as towing, taxiing, turning, braking, take-off and landing, and of airborne operations of maneuvering, turbulence encounters, store ejection and refueling. The specification documents include the numbers of these loads to be anticipated at various levels during the aircraft life.

The design spectrum must be based on a reasonable estimate of the anticipated mission usage history. All load sources should be included and the anticipated severity should reflect on both previously observed data and on any performance advances being designed into the new aircraft. It has become somewhat of an axiom that the full maneuvering capability of the aircraft will be used during its operation. Thus, it is essential that the design load sequence be representative of the aircraft capability. Figure 10.1.1 from Buntin [1979] illustrates a basic procedure for the development of a design loads spectrum. This is an interactive program involving several different data sources and other design activities.

The design loads spectra usually progresses from a preliminary effort based on the initial aerodynamics to a final form based on the final aerodynamics and aircraft configuration.

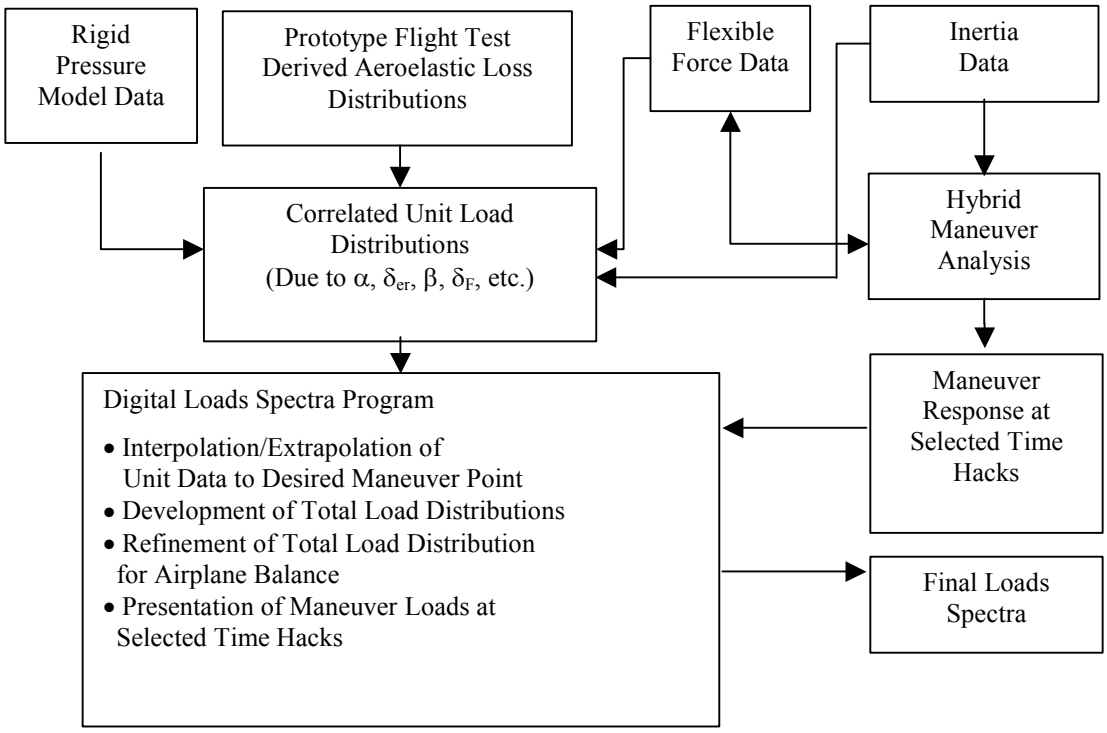

Figure 10.1.1. A Procedure for Development of Design Loads Spectra [Buntin, 1979]

10.2 Material Selection

The selection of materials for damage tolerant design is one of the most important functions. Materials must be evaluated and selected on both their static strength and their toughness and flaw growth characteristics. The properties used for these comparisons are:

- Yield strength, F_{ty}
- Ultimate strength, F_{tu}
- Fracture toughness, K_c or K_{IC}
- Stress corrosion factor, K_{Iscc}
- Crack growth rate, da/dN vs. ΔK

Figure 10.2.1 shows how some of these properties can be compared. In addition, typical crack growth characteristics for each material are analyzed.

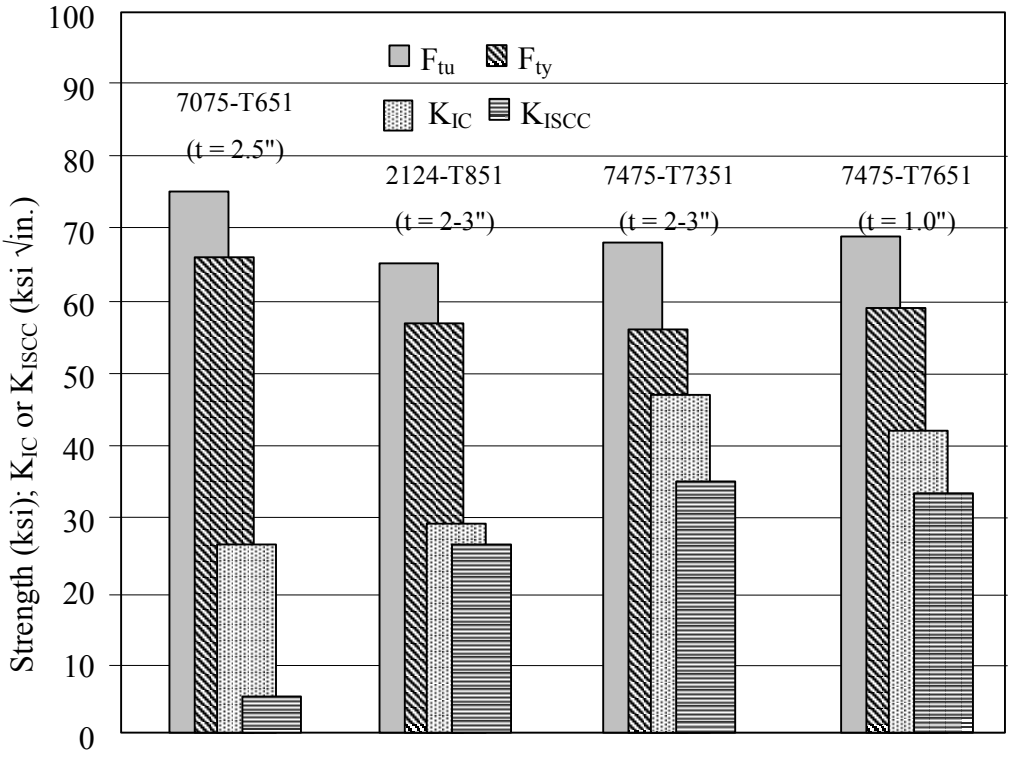

Figure 10.2.1. A Method of Presenting Comparative Material Data

10.2.1 Crack Growth Resistance and Fracture Toughness

The material properties used for the selection criteria must be obtained for conditions that correspond to those expected in the structural usage environment. Crack growth resistance as expressed in the *da/dN* data should be obtained from tests conducted using thickness similar to the anticipated structure applications and in similar environments. Some alloys are quite susceptible to corrosive media such as may be experienced in aircraft fuel bays or during operation near salt water. Effects of these variables are shown in Figure 10.2.2 [Circle & Conley, 1980].

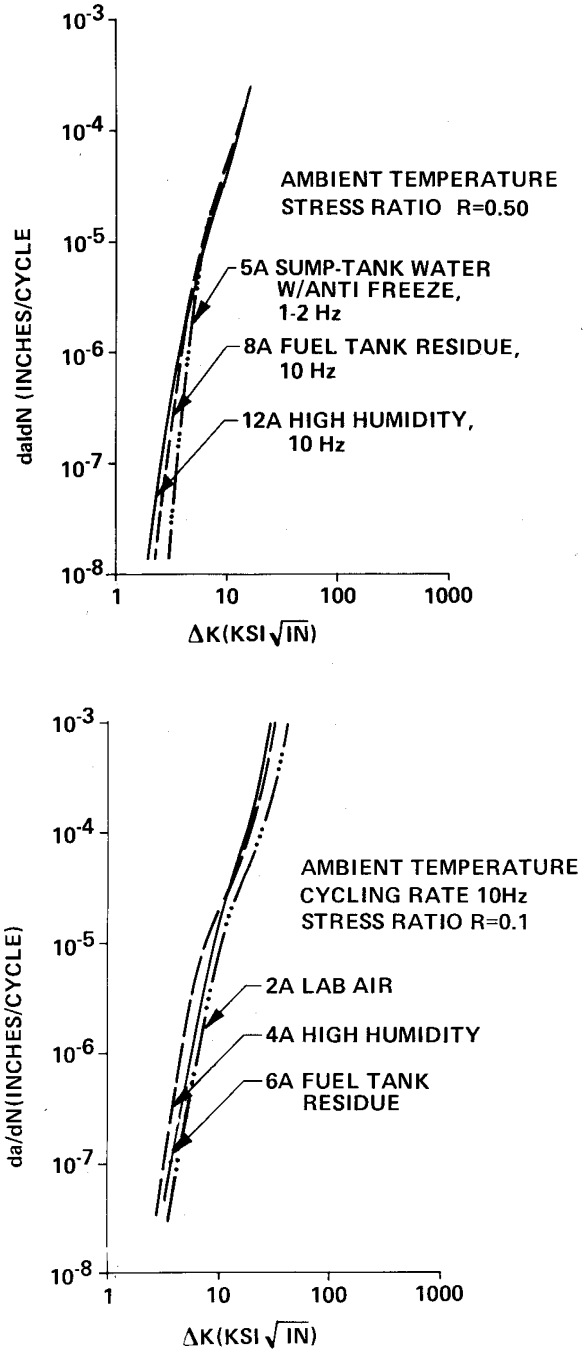

Figure 10.2.2. Illustration of Effects of Environment on Crack Growth Rates [Circle & Conley, 1980]

For ease of application in the design process, the crack propagation data is usually described by an empirical relationship, such as the Forman equation, given as:

$$\frac{da}{dN} = \frac{C(\Delta K)^n}{(1-R)K_c - \Delta K}$$

where

K_c - fracture toughness

ΔK - stress-intensity factor range

C, n - constants dependent on material, obtained from curve fitting techniques

It may be necessary to model the data in several parts over the ΔK range of interest in order to achieve adequate representation.

Ekvall, et al. [1982] presents a method for evaluation of weight savings due to the usage of advanced materials. The utilization of materials having improved damage tolerance characteristics as evidenced by a higher allowable stress value was shown to effect a weight savings from 1-3 percent for an improvement in allowable stress of 10-25 percent.

Simenz and Guess [1980] discusses material properties and characteristics of some new materials based on obtaining high strength with good durability and damage tolerance properties. This is mentioned to make the reader aware of current efforts to improve structural materials. Goals stated in this report are to increase the static strength, decrease the crack growth, and increase the temperature capability of aluminum alloy.

10.2.2 Material Property Control

Along with the selection of various materials for use on the structure, it is essential that a control system be established. Ehert [1979] describes such a system as including the areas of source selection, usage, evaluation, documentation, and tracking of all materials. The establishment of material control specifications is necessary to achieve the desired end result. It is suggested that a rating system be established for each material based on the expected usage. Ehert [1979] suggests a five-level system (A, B, C, U, X) which may be defined as:

- A - Acceptable for Usage
- B - Acceptable with Specific Controls
- C - Acceptable with Demonstration Evaluation
- U - Not Evaluated for a Given Usage
- X - Not Acceptable

The development of a material selection list includes all properties that are required for each material usage. A pre-release material approval is suggested as a screening device. This would be by a material review board that would pass on all selected materials.

After the approval of all selected materials, the next step is to assure that only approved materials are actually used and that they meet the requirements. An accountability procedure must be implemented. As a minimum, this system must do the following:

1. Identify the part
2. List all material data required

3. List all supplemental data related to part;
    a.) Test Data
    b.) Change Notices
    c.) Deviations
    d.) Process Specifications
    e.) Inspection Reports
    f.) Rework Required

This system should be easily accessible and usable throughout the design, manufacturing, and usage phases of the aircraft life cycle. It would provide the information necessary to solve any future problems and will be the basis for the next design. This system is directed toward fracture critical parts, but it is evident that such material control is necessary for all parts. If such is the case, then fracture critical parts can be easily identified and tracked as part of the total aircraft design and development.

As a part of this system, it is necessary to establish a material quality control program. Sample testing of all material which is identified for fracture critical parts should include verification of crack growth rate and toughness properties. Special handling instructions for this material to preserve initial quality should be implemented. Non-destructive testing techniques must be developed and incorporated into the manufacturing process to insure that manufacturing quality is maintained.

While such systems of material control are easily established by a prime contractor, it is also necessary to extend them to subcontractors and parts vendors who furnish fracture critical parts. All procurement specifications for such parts must include the same requirements for incorporation and maintenance of quality as practiced by the prime. Figure 10.2.3 from Ehert [1979] illustrates how such vendor interfaces can be achieved.

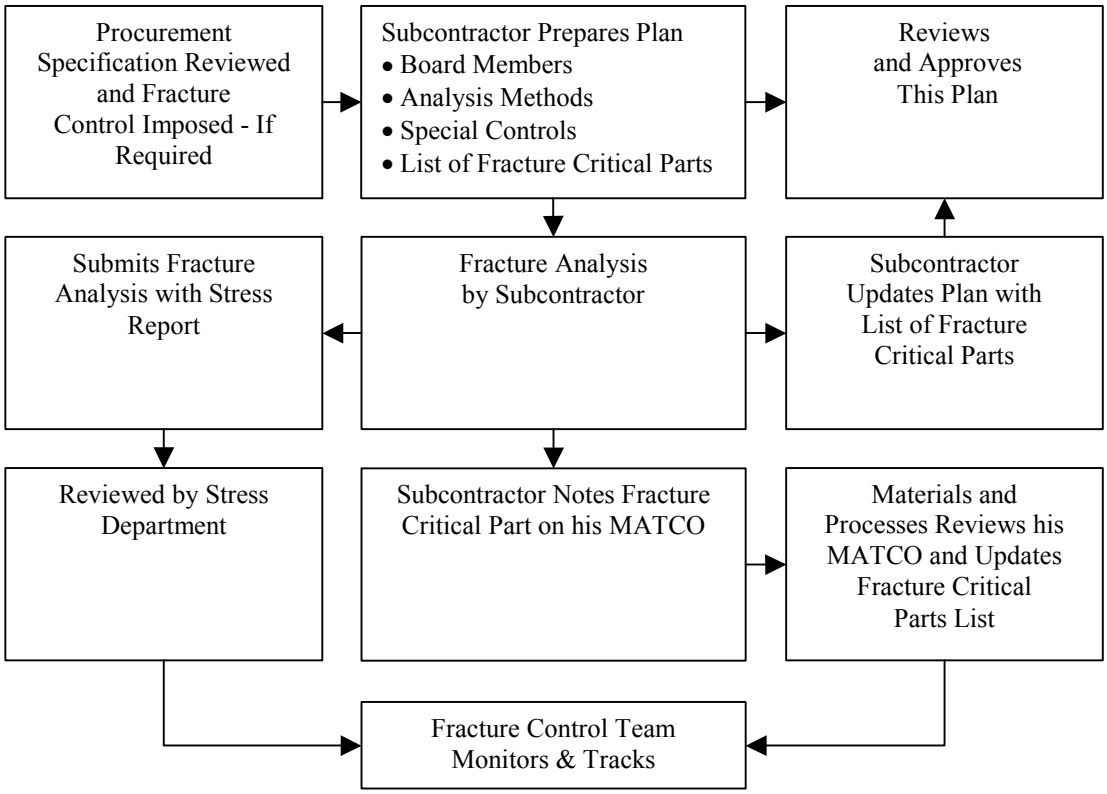

Figure 10.2.3. Fracture Control System for Subcontractors [Ehert, 1979]

10.3 Structural Configuration Analysis

The fracture control program must consider all of the design details incorporated into the structural configurations as possible critical items. It is as a part of this function that the critical parts list is developed and each part analyzed for its fracture propagation characteristics. The method to be used to inspect the critical parts must also be established. This will set the initial flaw size that is used in the analysis. Any testing which must be done to establish the damage tolerance of a part is also done during this phase of the development.

10.3.1 Critical Parts List

The development of the fracture critical parts list begins with the first design studies. This list is then maintained throughout the life of the aircraft. It identifies those parts that would cause loss of the aircraft or endanger personnel and cargo if they failed as a result of flaw propagation. The logic pattern and analysis necessary to identify critical parts is outlined in Figure 10.3.1 [Ehert, 1979].

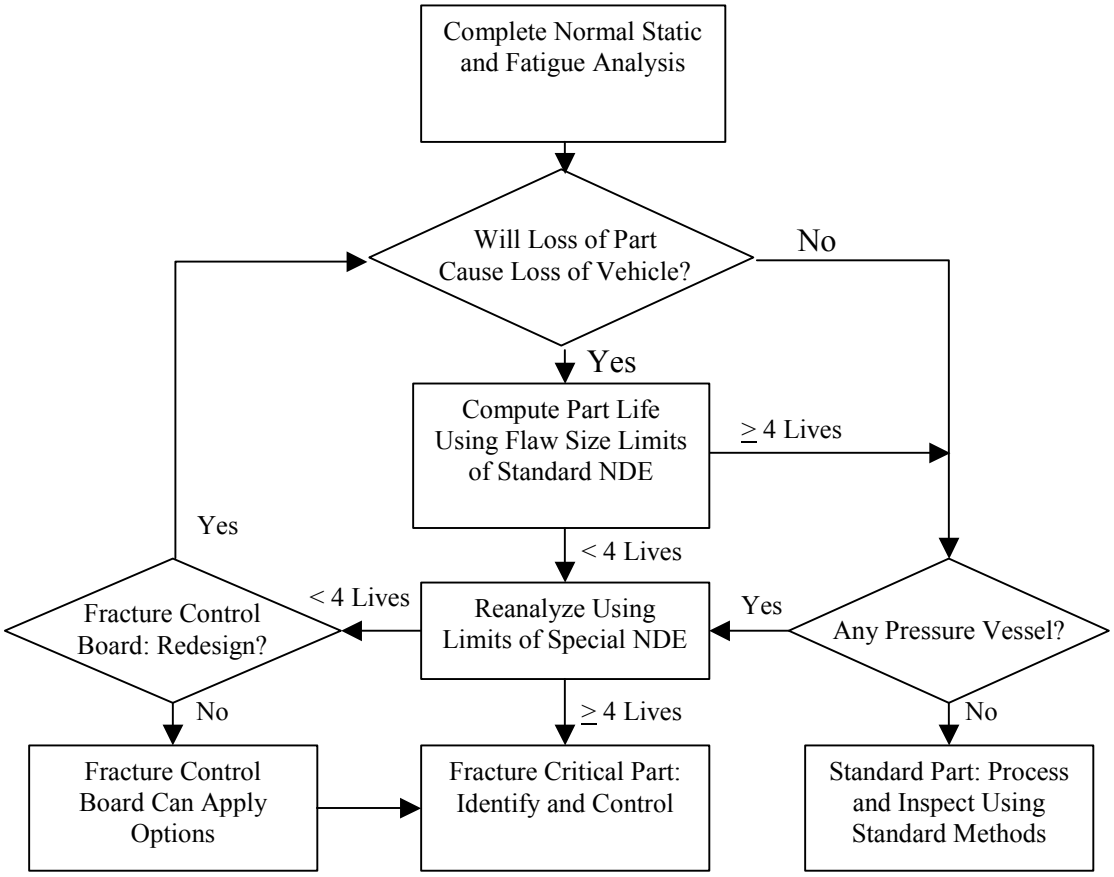

Figure 10.3.1. Illustration of Selection Logic for Fracture Critical Parts [Ehert, 1979]

Initially, the static analysis is used to identify the highly stressed areas of safety of flight items. A crack growth analysis using the best estimate of an initial flaw at the time of the analysis and the design load spectrum is run until either the required life has been exceeded without a predicted failure or until a failure is predicted in the part. Failure is usually related to a critical

crack size and the required residual strength load. This analysis is usually conducted as a part of the design trade studies used to select materials, select stress loads and to size the part. The factors affecting the selection of design stress levels are illustrated in Figure 10.3.2 [Walker, et al., 1979].

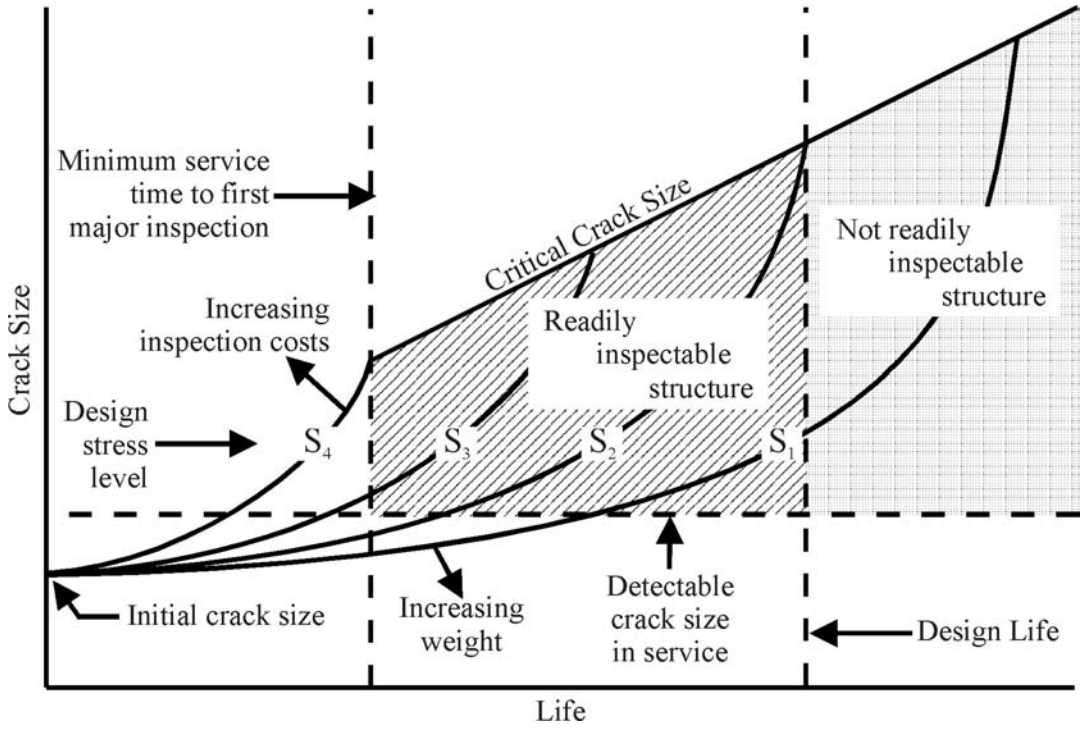

Figure 10.3.2. Selecting Design Stress Level to Meet Residual Strength Crack Growth and Inspectability Requirements [Walker, et al., 1979]

Redesign is done as necessary until the required life is attained. Figure 10.3.2 shows a decision point at four lifetimes. Actual life requirements will vary depending on the part; however, the logic is similar for all parts. The accurate determination of the component stress field for identification of critical areas is important. The best results can be achieved with fine grid finite element models.

Each part finally identified as a fracture critical part is then added to the list and identified for controlled handling during the manufacturing process. Establishment of this procedure early results in little disruption of standard procedures and makes the handling of fracture critical parts an integral part of the design and manufacturing process.

When the design load spectrum is developed to its final form, which should also be relatively early in the design process, the initial analysis of the most critical items should be repeated to determine if there are any changes in results. Any differences must be evaluated and redesign accomplished as indicated.

The selection of the manufacturing processes for the critical part should be made with care. Such things as surface finish, edge finish, location of parting planes, location of identification

marks, and amount of metal removal per part must be considered during the design. Considerations of these and other items are presented in publications such as Lunde [1976], Goranson, et al. [1981], and Watson [1979]. It is not considered appropriate to present a large number of details in this handbook, but a catalogue of acceptable and unacceptable design and machining details should be developed by the manufacturer as a guide to design and fabrication.

10.3.2 Inspection Method Development

The initial assumed flaw used in all crack growth computations is determined either by a specified minimum flaw based on standard inspection techniques or by a special minimum flaw which can be substantiated by special inspection techniques. Table 10.3.1 from Ehert [1979] lists an example of what may be expected from several inspection methods. These will vary with specific equipment.

During the development of the critical parts list, it is necessary to consider how each part will be inspected for flaws. This must be considered not only during the manufacturing process but also during the periodic inspections to be performed during the aircraft life. The results of the fracture analysis can be significantly affected by the inspection method and the selection of initial flaw sizes.

As improved inspection methods are incorporated into production use, it is to be expected that improved design will result. The trade-off between inspection costs and performance may also be considered.

Table 10.3.1. Examples Of NDE Capabilities [Ehert, 1979]

Inspection Method	Flaw Type	Standard NDE	Special NDE
Penetrant or magnetic particle	Surface flaw (Depth x length)	0.19 x 0.38 cm (0.075 x 0.150 in.) or equivalent area	0.083 x 0.127 cm (0.025 x 0.050 in.) or equivalent area
Ultrasonics	Embedded flaw (diameter)	0.254 cm (0.100 in.)	0.12 cm (0.047 in.)
Radiographic	Surface or embedded (depth x length)	0.7t x 1.4t Min length = 0.38 cm (0.150 in.)	0.6t x 1.2t Min length = 0.127 cm (0.050 in.)

t = thickness

10.3.3 Demonstration Test Development

The use of tests to demonstrate the existence of damage tolerant design is necessary when design details depart from past acceptable usage and when various environments are present for which data is not available. It is suggested that such testing begin early and start with element and small component tests. This testing should also use the flight-by-flight design load spectrum being used for analysis.

As the design progresses, large component tests of critical areas should be conducted. As much as possible, the anticipated environments should be a part of the test. As mentioned earlier, the influence of environment can be quite extensive on crack growth behavior.

10.4 Manufacturing Process

The realization of the design during the manufacturing process is where the fracture control plan reaches its ultimate test. It is now that a diverse group of participants must be brought into control to insure the production of the required quality.

Each manufacturing step of the fracture critical parts must be monitored and controlled. Procedures must be developed which provide strict accountability and sign-off from step to step but which also do not unduly hinder the normal flow of manufacturing processes. Two major items are involved at this point: (1) establishing the control of manufacturing quality, and (2) developing the methods for critical parts accountability.

10.4.1 Control of Quality of Processes

Three major items comprise the function of the manufacturing process quality control. They are:

(1) Definition of inspection requirements
(2) Demonstration of inspection methods
(3) Review of manufacturing process and inspections

The basic document for the manufacture of each fracture critical part is the process specification. It lists all of the processes that must be performed on the part. This forms the basis for selection of the inspection methods. Limits for acceptance are also a part of the process specification. The scheduling of inspections during the process must be considered. A trade-off between inspection cost, rework cost, and loss due to scrap must be made. This process may be more critical in a fracture critical part than in another part since there may not be as many rework options open. Thus, it may be more efficient to have more inspections than to risk losing a large amount of process time. Parts that do not pass an early inspection may be reclaimed through rework options still available at this time.

The demonstration of the efficiency of nondestructive process inspections can be made through destructive testing or through a more rigorous nondestructive inspection. This demonstration is made early in the program and may be subject to periodic checking over the life of the project. As experience is gained with the process, the inspection frequency may be decreased.

It should be noted that whenever either new process equipment is installed or inspection equipment is changed, the inspection procedure should be tightened until confidence is again attained. This also should include periodic review of the inspection process to insure that the quality of the inspection is being maintained.

10.4.2 Development of Critical Parts Accountability

The critical parts list is only the first step in the control process. It also includes the damage review procedure, material procurement and acceptance, handling of the part during manufacture, installation procedures, incorporation of design changes, and disposition of manufactured parts. This entire process is one of accountability. In order to do this, a method of serial numbering is used and a work routing sheet is suggested which identifies the source of the stock material used in the part during its manufacture and provides sign-off and transfer records for each process. In order for this process of control to be effective, the personnel involved during manufacture must have an awareness of the objective. They must realize the development of an individual commitment to achieve a damage tolerant aircraft. Goranson, et al. [1981] and Watson [1979]

present discussions of how damage tolerant design has been incorporated into transport aircraft design and construction.

10.5 References

A.P. Berens, D.S. Morcock, K.E. Brown, R.L. Johnson, J.C. Davis, C.E. Larson, and D.J. White (1981, April). "Handbook of Force Management Methods" AFWAL-TR-81-3079.

W.D. Buntin. (1979, May). "Durability and Safety in the F-16 Airframe." *Structural Integrity Technology,* J.P. Gallagher and T.W. Crooker, Eds., The American Society for Mechanical Engineers.

R.L. Circle and F.M. Conley (1980, May). "A Quantitative Assessment of the Variables Involved in Crack Propagation Analysis for In-Service Aircraft." *21st Structures, Structural Dynamics and Materials Conference*, AIAA, ASME, ASCE, AHS, Part I, p. 512-521.

R.M. Ehert (1979, May). "Material Control and Fracture Control Planning for the Space Shuttle Orbiter Program." *Structural Integrity Technology.* J.P. Gallagher and T.W. Crooker, Eds., The American Society of Mechanical Engineers.

J.C. Ekvall, J.E. Rhodes and C.G. Wald (1982). "Methodology for Evaluating Weight Savings from Basic Material Properties." *Design of Fatigue and Fracture Resistant Structures*, ASTM STP 761, P.R. Abelkis and C.M. Hudson, Eds., American Society for Testing and Materials, pp. 328-341.

F. J. Giessler, S. J. Duell and R.F. Cook (1981, February). "Handbook of Guidelines for the Development of Design Usage and Environmental Sequences for United States Air Force Aircraft." AFWAL-TR-80-3156.

U.G. Goranson, J. Hall, J.R. Maclin and R.T. Watanabe (1981). "Long Life Damage Tolerant Jet Transport Structures." *Design of Fatigue and Fracture Resistant Structures*, ASTM STP 761, P.R. Abelkis and C.M. Hudson, Eds., American Society for Testing and Materials, pp. 47-87.

T. Lunde (1976). "Fatigue and Stress Corrosion Guidelines." Lockheed-California Company.

R.F. Simenz and M.K. Guess (1970, July). "Structural Aluminum Materials for the 1980's." *Journal of Aircraft*, Vol. 17, No. 7, pp. 514-520.

C.F. Tiffany (Ed.) (1978, April). *Analysis of United States Air Force Aircraft Structural Durability and Damage Tolerance*, Notebook for AIAA Short Course.

E.K. Walker, J.C. Ekvall and J.E. Rhodes (1970, May). "Design for Continuing Structural Integrity." *Structural Integrity Technology*, J.P. Gallagher and T.W. Crooker, Eds., The American Society of Mechanical Engineers.

R.E. Watson (1979, May). "Structural Integrity Development of Commercial Aircraft." *Structural Integrity Technology*, J.P. Gallagher and T.W. Crooker, Eds., The American Society of Mechanical Engineers.

H.A. Wood (1979, May). "Structural Integrity Technology for Aerospace Applications." *Structural Integrity Technology*, J.P. Gallagher and T.W. Crooker, Eds., The American Society of Mechanical Engineers.

Section 11
Summary of Stress Intensity Factor Information

The stress intensity factor equation is the foundation on which fracture mechanics methodologies are built. This section will uncover some of the mystique behind the stress intensity factor development and also provide a catalogue of developed stress intensity factors for applications to future analyses.

11.1 Background of Stress Intensity Factors

The emergence of fracture mechanics as a tool for determining failure loads in materials has come a long way from the early work of A.A. Griffith who, in 1920 presented his treatise on the understanding of the fracture mechanism of glass, "The Phenomena of Rupture and Flow in Solids". Griffith's work was itself building on the earlier work by C.E. Ingliss summarized in "Stresses in a Plate due to the Presence of Cracks and Sharp Corners" [1913].

Many researchers followed and built on the original concepts, with a notable leader at the Naval Research Laboratory, Dr. G. R. Irwin, applying the concepts and improving the methodology from the energy based approach of Griffith to the stress intensity approach we use today. The Navy had a vested interest in this analysis technique to understand the fracture of steel ship plate material used in the World War II Liberty ships.

The 1950s and 1960s definitized the methodology by the standardization of some of the test methods and application techniques. What we now view in numerous handbooks as lists of stress-intensity factors (SIF) have each been "hammered out" by a succession of researchers to improve the accuracy and usefullness of the SIFs. Most of the advances have been under the guidance of one or more of the technical societies such as ASTM, ASM, and SAE.

11.2 Methodology For Determining Stress Intensity Factors

The linear elastic fracture mechanics approach to the analysis of cracked structures depends on the calculation of stress-intensity factors (K) for the typical crack geometries of interest.

The opening mode stress-intensity factor can always be expressed as

$$K_I = \beta\sigma\sqrt{\pi a} \tag{11.2.1}$$

where σ is the nominal stress remote from the crack and a is the crack size. The factor β is a function of crack geometry and of structural geometry. Since the dimension of K is ksi$\sqrt{}$in. or equivalent, β must be dimensionless. For a central crack of length, $2a$, in an infinite sheet, the stress-intensity factor may be written

$$K_I = \sigma\sqrt{\pi a} \tag{11.2.2}$$

Comparison with Equation 11.2.1 shows that for an infinite sheet β is unity. Thus, β may be considered as a correction factor relating the actual stress-intensity factor to the central crack in an infinite sheet. The correction factors for various geometrical conditions under a given load condition may be combined in the form of a product to account for the increase or decrease in the stress-intensity factor.

As the linear elastic fracture mechanics approach to engineering problems became a typical design approach, a widespread need for stress-intensity factor solutions for typical geometries arose. This need was met by a series of handbooks which presented available solutions in a compact format. Some of these handbooks include

- Handbook of Stress Intensity Factor (Sih, 1973),
- The Stress Analysis of Cracks Handbook (Tada, et al., 1973),
- Compendium of Stress Intensity Factors (Rooke & Cartwright, 1976),
- Stress Intensity Factors Handbook (Murakami, 1987)

The handbook solutions, which are typically fundamental, may be extended to more complex cases through the principle of superposition or by compound analysis. The handbook solutions are also quite useful for bounding exact solutions as discussed in Section 11.4. When the structural geometry and loading system is fairly complicated, engineers normally resort to numerical analysis procedures (e.g., finite element analysis) which have been proven for their accuracy in establishing stress-intensity factors.

11.2.1 Principle of Superposition

Because the linear elastic fracture mechanics approach is based on elasticity, one can determine the effects of more than one type of loading on the crack tip stress field by linearly adding the stress-intensity factor due to each type of loading. The process of adding stress-intensity factor solutions for the same geometry is sometimes referred to as the principle of superposition. The only constraint on the summation process is that the stress-intensity factors must be associated with the same structural geometry, including crack geometry. Thus, stress-intensity factors associated with edge crack problems cannot be added to that of a crack growing radially from a

hole. An example will illustrate the conditions under which one might linearly add stress-intensity factors.

EXAMPLE 11.2.1 Axial and Bending Loads Combined

An edge crack of length a is subjected to a combination of axial and bending loads as shown. The stress-intensity factor for the edge crack geometry subjected to the tensile load (P) is given by

$$K_P = \frac{P}{BW}\left(\sqrt{\pi a}\right) sec\,\beta \left(\frac{tan\,\beta}{\beta}\right)^{\frac{1}{2}} \left[0.752 + 2.02\left(\frac{a}{W}\right) + 0.37\left(1 - sin\,\beta\right)^3\right]$$

while that due to the bending moment (M) is given by

$$K_M = \frac{6M}{W^2 t}\left(\sqrt{\pi a}\right) sec\,\beta \left(\frac{tan\,\beta}{\beta}\right)^{\frac{1}{2}} \left[0.923 + 0.199\left(1 - sin\,\beta\right)^4\right]$$

with $\beta = \dfrac{\pi a}{2W}$

The stress intensity factor resulting from the combination of tensile and bending loads is given by the sum of K_P and K_M, so that

$$K_{TOTAL} = K_P + K_M$$

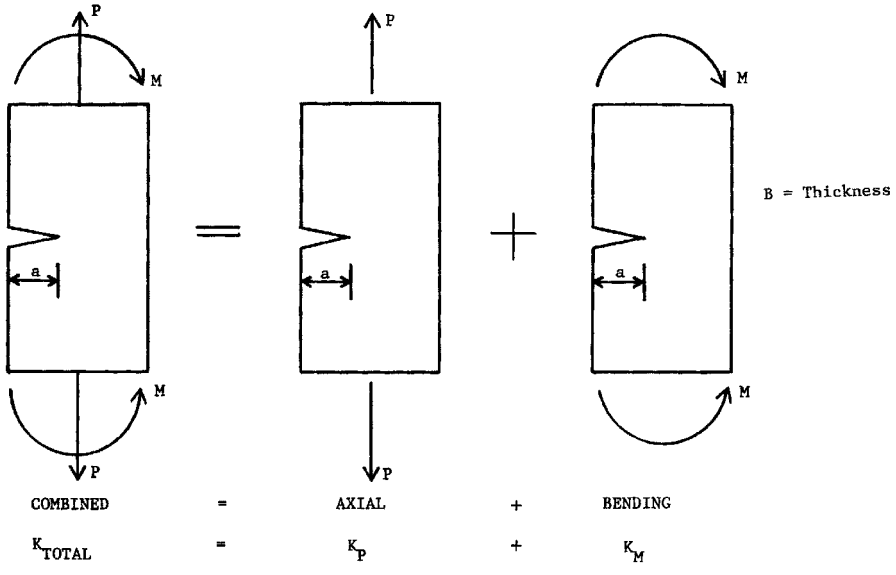

Edge Crack Geometry Loaded With Axial and Bending Loads

As shown by Example 11.2.1, if the geometry of the structure is described, the effect of each loading condition can be separately determined and the effect of all the loading conditions can be obtained by summing the individual conditions, i.e.,

$$K_{TOTAL} = K_1 + K_2 + K_3 + \ldots \qquad (11.2.3)$$

This particular property is quite useful in the analysis of complex structures. Example 11.2.2 (Wilhelm, 1970) further illustrates the principle of superposition.

EXAMPLE 11.2.2 Remote Loading and Concentrated Forces Combined

Many times in a particular aircraft design a part may develop cracks at rivet holes where the skin is attached to the frame or stringer. This situation is depicted in the figure below. It will be analyzed as a simple case in which the sheet is in uni-axial tension and the rivets above and below the crack are influential in keeping the crack closed. (Tests of panels with concentrated forces superimposed on the uniform tension loading simulate crack growth behavior in the presence of rivets.) The insert of the figure shows the local parameters necessary for determining the stress-intensity factors.

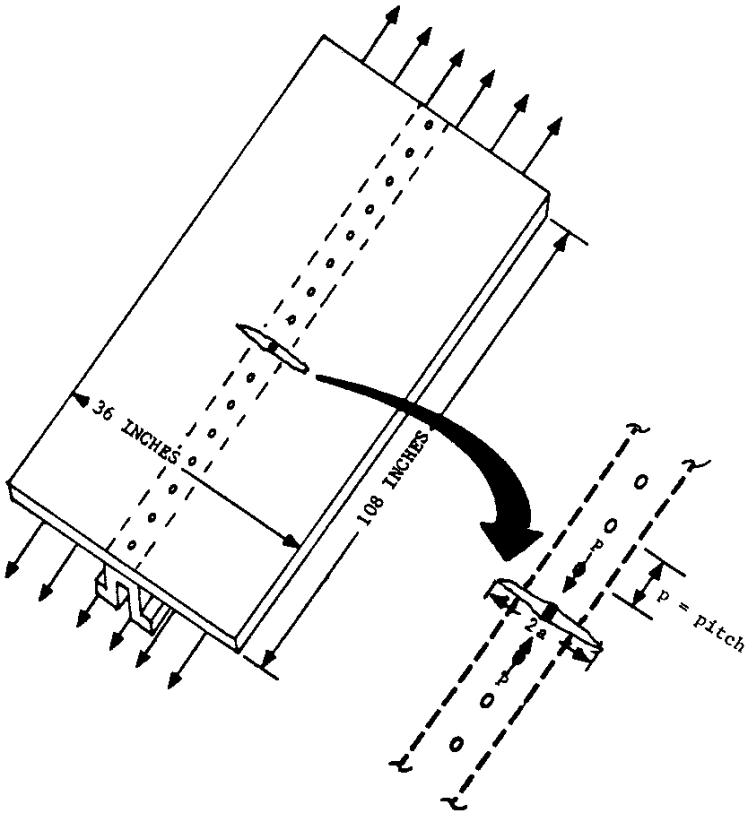

Crack at Rivet In a Riveted Skin-Stringer Panel (No Crack Buckling)

Assuming that a crack grows from the rivet hole, the total stress-intensity factor for this geometry is obtained using the linear superposition of stress-intensity factors. Closer examination of the figure indicates that the loading can be decomposed as shown in the next figure. The total stress-intensity factor is the sum of the remote loading and concentrated load induced stress-intensity factors.

Note: The concentrated force induced stress-intensity factor solution presented is only applicable if the concentrated forces are applied along the centerline of the sheet and at a distance greater than 3 or 4 times the hole diameter. Inasmuch as the concentrated forces are in an opposite direction to the uniform stress, and tend to close the crack, this stress-intensity is subtracted from the uniform extensional stress-intensity factor.

With knowledge of the stress-intensity solution for this geometry, it is possible to determine what effect the rivet closure forces have on the local stress field for similar problems.

Combined Uniform Tension Concentrated Force

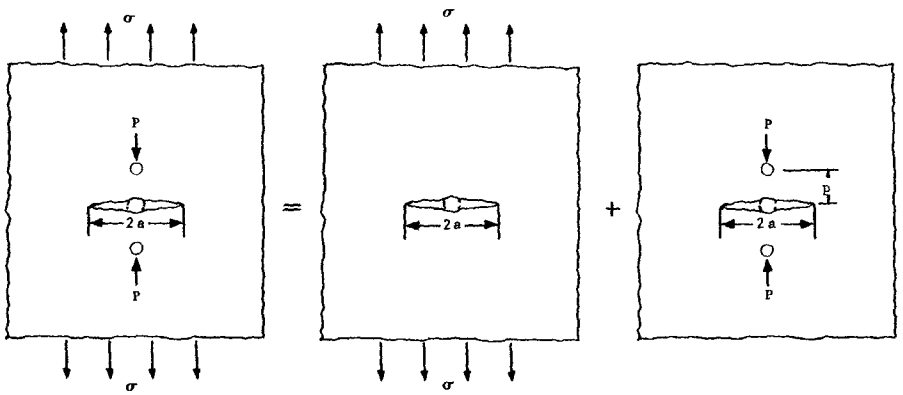

(a) (b) (c)

$$K_{Total} = K\left(=\sigma\sqrt{\pi a}\right) + K_P\left(\frac{-P\sqrt{\pi a}}{2\pi B}\frac{(3+\nu)p^2+2a^2}{\left(a^2+p^2\right)^{3/2}}\right)$$

Superposition of Stress intensities for Uniform Tension and Concentrated Force

In some cases, the additive property of the stress-intensity factor can be used to derive solutions for loading conditions that are not readily available. The process of deriving the stress-intensity factor for a center crack geometry, which is uniformly loaded with a pressure (p), shown in Figure 11.2.1, illustrates this feature. Figure 11.2.2 describes the process whereby the remotely loaded center crack geometry is decomposed into a set of two center crack geometries which have loading conditions, that when added, result in the canceling of the crack line loadings. The stress-intensity factor (K_I) for the plate loaded with the remote stress condition (σ) and the crack closing stresses (also equal to σ) is zero, i.e. $K_I = 0$, because the crack is clamped closed under such conditions. Thus, the equation for addition of stress-intensity factors

$$K_{TOTAL} = K_1 + K_2 \qquad (11.2.4)$$

reduces to

$$K_{TOTAL} = 0 + K_2 \tag{11.2.5}$$

so that the stress-intensity factor for a pressurized center crack with pressure (p) equal to σ is the same as that associated with remote loading, i.e.

$$K_2 = \sigma\sqrt{\pi a} = K_{TOTAL} \tag{11.2.6}$$

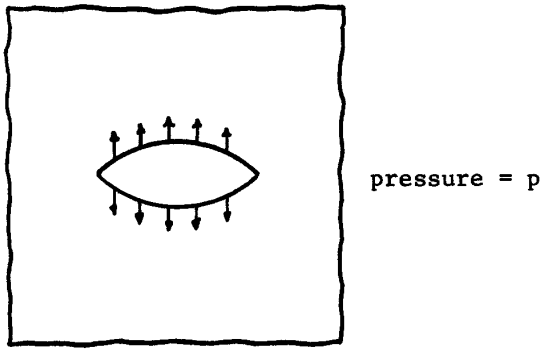

Figure 11.2.1. Internally Pressurized Center Crack

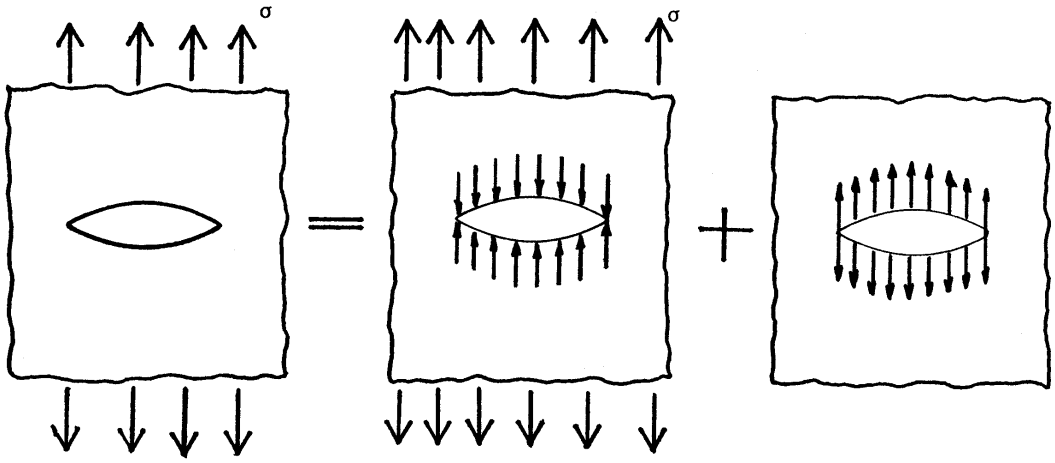

Remotely Loaded	=	Remotely Loaded With Crack Line Closing Stresses	+	Crack Line Opening Stresses
K_{Total}	=	K_1	+	K_2

Figure 11.2.2. Principle of Superposition Illustrated for Center Cracked Geometry

Sometimes, it is difficult to visualize how one arrives at the values of the crack closing stresses. Consider the uncracked body with the uniformly applied remote loading as shown in Figure 11.2.3a. Determination of the stresses along the dotted line lead to the observation that the stresses here are equal to the remote stress (σ). To obtain a stress-free condition along the dotted line, and thus simulate a cracked structural configuration, one must apply opposing stresses of

magnitude σ along the length of the dotted line as shown in Figure 11.2.3b. The stresses along the dotted line generated by the applied remote stresses are the opening stresses (Figure 11.2.3a). The equal but opposite stresses are the crack closing stresses. The reader should note that the stresses on the dotted line that are generated by the remote loading lead to the crack opening condition; these opening stresses lead to non-zero values for the stress-intensity factor (see Figure 11.2.2).

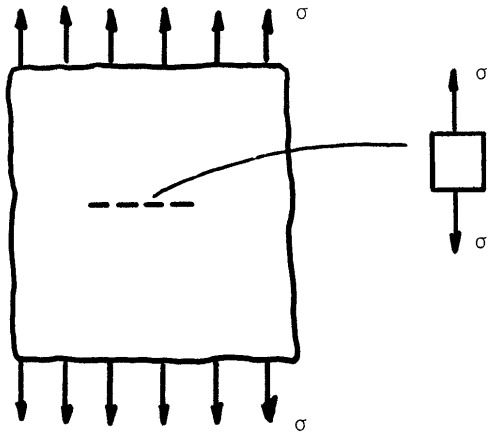

Figure 11.2.3a. Uniform Stresses Along Dotted Line Generated by Remote Loading

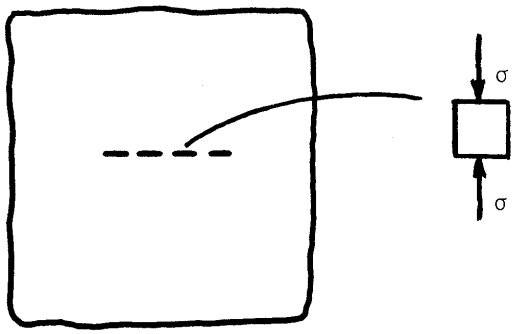

Figure 11.2.3b Opposing Stresses Applied Along the Dotted Line

Figure 11.2.4 presents the concept of linear superposition of elastic solutions in a slightly different way so that the reader has a full appreciation of the procedure. The structural element B is noted to be exactly the same as element A; the crack closing stresses exactly balance the effect of the remote stresses along the line so the structural element B still experiences uniform tension throughout. Structural element B is further decomposed into elements D and E. Note that the crack loading stresses shown on the structural element E are crack closing stresses and, therefore, result in a stress-intensity factor which is the negative of the remotely applied loading case, i.e. $K_E = -K_D$.

Remote Loading W/O Crack | Remote Loading With Crack | Crack Loading Stresses On Crack

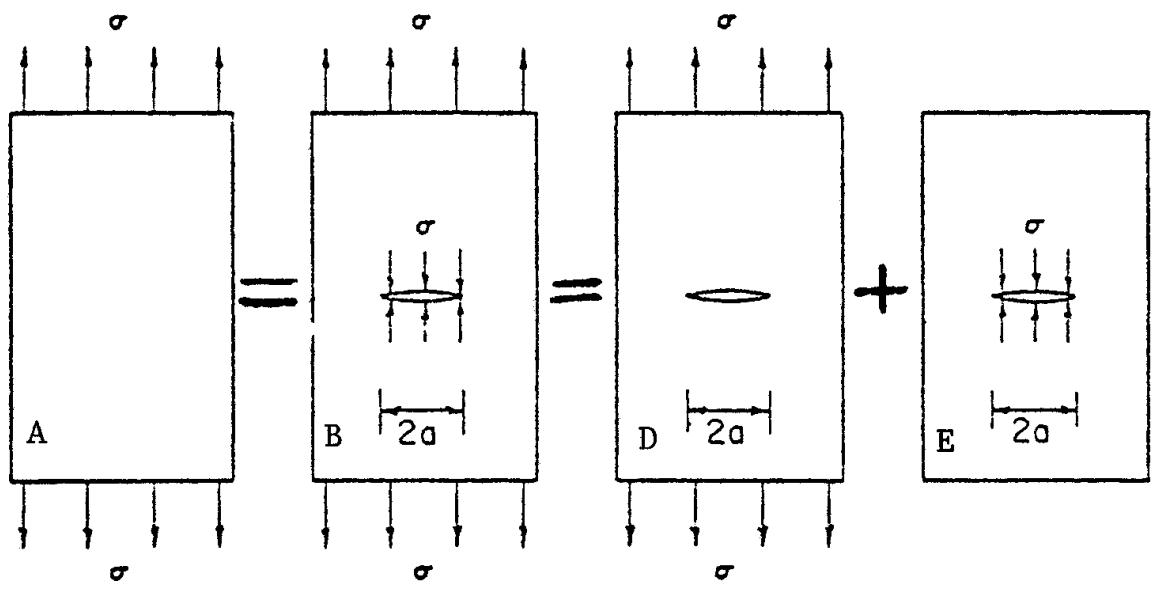

$K_A = 0$ $K_B = 0$ $K_B = K_D + K_E = 0$, $K_E = -K_D$

Figure 11.2.4. Illustration of Superposition Principle

Since K_D is known,

$$K_D = \sigma\sqrt{\pi a}$$

it follows that

$$K_E = -\sigma\sqrt{\pi a}$$

As we noted before, if the direction of stress in element E is reversed (becomes crack opening) then the stress-intensity factor is

$$K = \sigma\sqrt{\pi a}$$

The loading on structural element A in Figure 11.2.5 can be decomposed into the series of loadings shown. The stress-intensity factor for element A is obtained from the superposition of the three other loadings:

$$K_A = K_B + K_D - K_E \qquad (11.2.7)$$

Since it is obvious that the loadings in elements A and E will result in the same stress-intensity factor, i.e. $K_A = K_E$, the stress-intensity factor for element A becomes

$$K_A = 1/2\left[K_B + K_D\right] \qquad (11.2.8)$$

The stress-intensity factors for elements B and D are known, i.e.

$$K_B = \sigma\sqrt{\pi a} \qquad \text{and} \qquad K_D = \left[\frac{W}{2a}\right]\sigma\sqrt{\pi a}$$

and, therefore

$$K_A = 1/2\left[1+\frac{W}{2a}\right]\sigma\sqrt{\pi a} \tag{11.2.9}$$

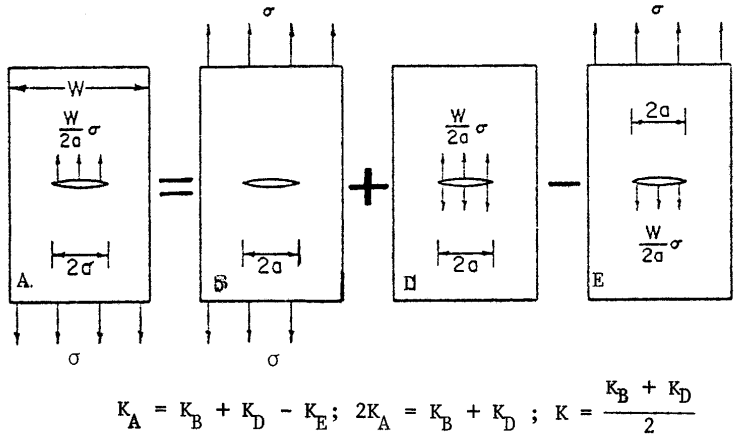

Figure 11.2.5. Application of Superposition Principle

Now a more complex example is presented using the principle of superposition applied in a two-step process. Shown in Figure 11.2.6 is a structural element (F) in which intermediate values of load transfer occur through a pin loaded hole. As shown, Step 1 consists of decomposing element F into two parts, such that in one part the pin reacts its entire load and the other part is remotely loaded. The stress-intensity factor for element F is the sum of those generated by the decomposed elements, i.e.,

$$K_F = K_A + K_B^{\sigma_2}$$

where the superscript denotes the loading.

Step 2 involves the determination of K_A. The pin reactive loading on element A is decomposed into the loading shown in Figure 11.2.6. Using the logic previously illustrated in Figure 11.2.5, K_A is determined as

$$K_A = 0.5\left(K_B^{\sigma} + K_D^{P}\right)$$

The stress-intensity factor for the loading on element F is

$$K_F = 0.5\left(K_B^{\sigma} + K_D^{P}\right) + K_B^{\sigma_2} \tag{11.2.10}$$

Note that while the stress-intensity factor solution formula for element B is the same in Steps 1 and 2, the stresses used in each calculation are different (as indicated by the superscripts).

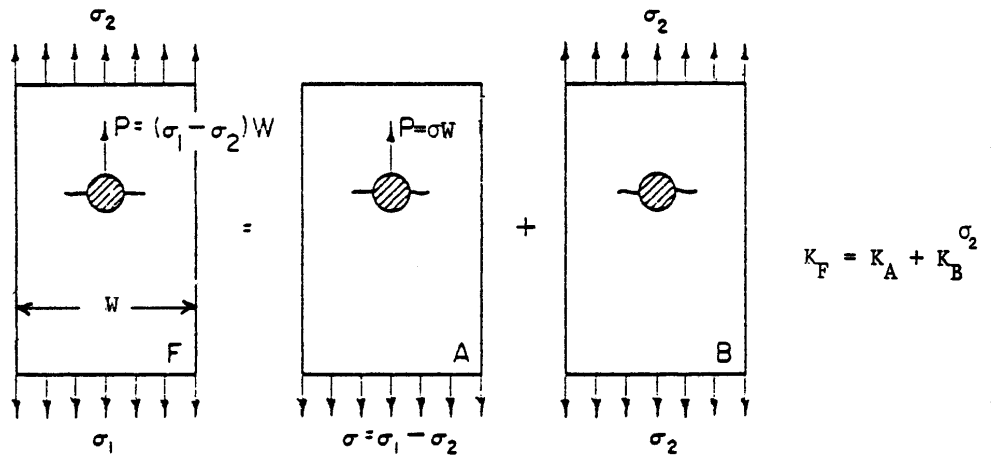

Step 1: Decompose loading so that pin reacts its entire load.

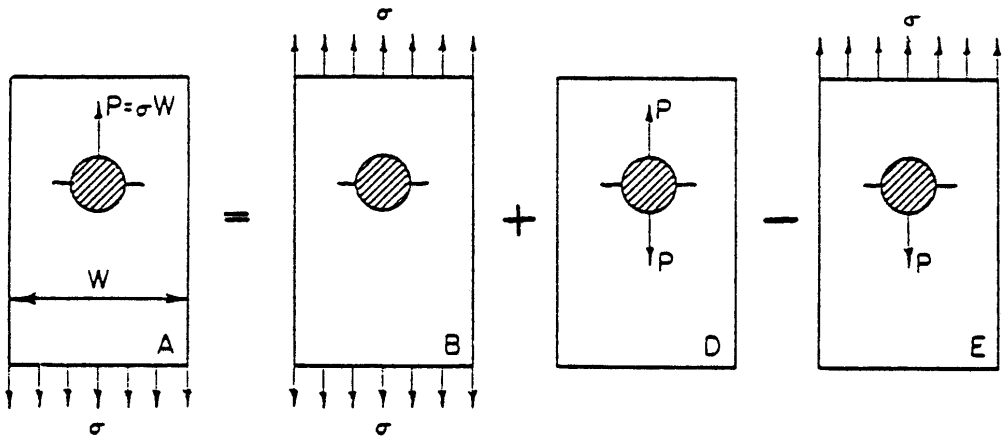

Step 2: Decompose pin reactive loading. $K_A = \dfrac{K_B^{\sigma_2} + K_D^P}{2}$

Figure 11.2.6. Stress Intensity Factor for Pin-Loaded Hole (Bearing By-pass Problem) Obtained by Superposition

11.2.2 Developing Stress Intensity Factor Solutions

There are a number of methods that are available for developing stress-intensity factor solutions for crack body problems. Review articles and textbook chapters that summarize these methods are provided in Sneddon & Lowengrub (1969), Rice (1968), Paris & Sih (1965), Sih (1973a, 1973b), Tada, et al. (1973), Rooke & Cartwright (1976), Wilhelm (1970), Parker (1981), Broek (1974) and Goodier (1969). The basic solutions for simple geometries can be derived by means of classical methods of elasticity which employ complex stress functions Sneddon & Lowengrub (1969), Rice (1968), Westergaard (1939) and Mushkelishvili (1953).

For finite size bodies containing cracks, the boundary conditions usually prohibit a closed form solution. In such cases, numerical solutions can be obtained using methods such as the finite element method, the boundary collocation technique [Gross, et al., 1964; Newman, 1971], or the boundary integral method [Cruse, 1972; Cruse & Besuner, 1975]. Solutions for multiple load path geometries can sometimes be obtained from basic stress field solutions combined with displacement compatibility requirements for all the structural members involved [Swift & Wang, 1969]. Section 4 describes this method and provides an example based on the displacement compatibility method.

There are also several experimental methods that have been used to obtain (or verify) the stress-intensity factor for cracked structural members. These experimental methods include: The compliance method, the photoelastic method [Smith, 1975; Kobayashi, 1973], the fatigue crack growth (inverse) method [James & Anderson, 1969; Grandt & Hinnericks, 1974; Gallagher, et al., 1974], and the interferometric method [Packman, 1975; Pitoniak, et al., 1974].

While a general knowledge of each stress-intensity factor solution method might be useful for attacking specific problems, detailed knowledge is required before any method can be applied to solve a given problem. Beyond what is described elsewhere in these guidelines, an engineer can also utilize two separate solution techniques to solve any two-dimensional structural geometry or loading situation without access to a damage tolerant specialist. One solution technique involves the generation of the stress for an uncracked body along the expected path of crack propagation. (The finite element method provides a powerful tool for generating stress at any point in an uncracked body). The second solution technique involves the generation of the stress-intensity factor solution via an integral calculation that employs the stresses obtained for the case of the uncracked body along the expected path of the crack. Two integral calculation technique types are available: the Green's function technique [Cartwright & Rooke, 1979, 1978; Cartwright, 1979; Hsu & Rudd, 1978; Hsu, et al., 1978] and the weight function technique [Cartwright & Rooke, 1978; Cartwright, 1979; Bueckner, 1971; Rice, 1972; Grandt, 1975]. These two crack-line loading techniques are reviewed in the following subsections.

11.2.2.1 Green's Function Technique

The Green's function technique takes advantage of the additive property of the stress-intensity factor and is based on generalized point load solutions of crack problems. For example, the point load solution for the central crack problem described in Figure 11.2.7 is given by:

$$K = \frac{P}{B}\frac{1}{\sqrt{\pi a}}\sqrt{\left(\frac{a+x}{a-x}\right)} \qquad (11.2.11)$$

This solution can be used to obtain the stress-intensity factor for stresses distributed over the crack faces by noting that the point load per unit thickness (*P/B*) in Equation 11.2.11 can be replaced by the product of the pressure stress *(σ(x))* and the distance over which it acts (*dx*). Thus, the stress-intensity factor for the distributed stresses applied to the crack becomes:

$$K = \int_{-a}^{+a} \frac{\sigma dx}{\sqrt{\pi a}} \frac{a+x}{\sqrt{a^2 - x^2}} \qquad (11.2.12)$$

The stress-intensity factor for the case of uniform opening stresses applied to the crack, where σ is a constant, is determined to be $K = \sigma\sqrt{\pi a}$, as was expected from the discussion of the method of superposition described previously.

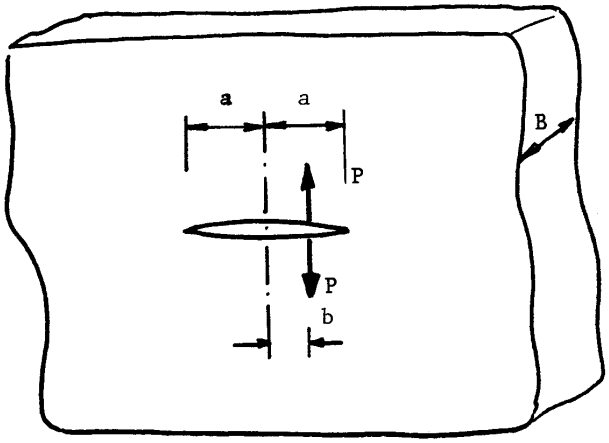

Figure 11.2.7. Point Load (*P*) Applied to the Crack Faces for a Central Crack Located in an Infinite Plate

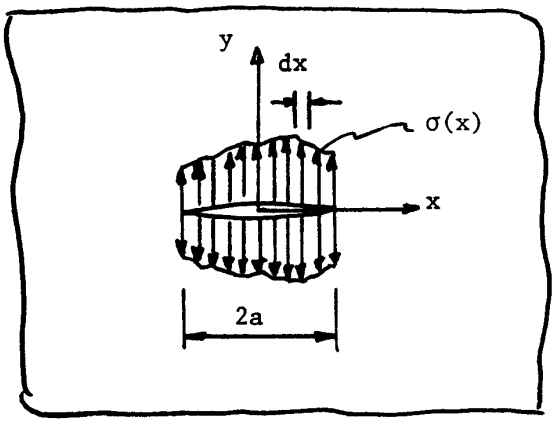

Figure 11.2.8. Distributed Loading Applied to Crack Faces of the Central Crack

Given a point force solution for a geometry of concern, it is then possible to define the summation process that would integrate the effects of stress loading over the crack faces. Integral equations such as that defined by Equation 11.2.12 utilize the stress solutions from the uncracked body problem. A number of point force stress-intensity factor solutions are presented in the tables given in Section 11.3 and an extensive review of the availability and application of Green's functions can be found in Cartwright & Rooke [1979]. Other reviews can be found in Cartwright & Rooke [1978] and Cartwright [1979].

One of the cases reviewed by Cartwright and Rooke [Cartwright & Rooke, 1979] is of particular interest to structural engineers. They presented the work by Hsu and Rudd [1978] on the development of a Green's function for a diametrically cracked hole. The Hsu and Rudd Green's function was based on a series of finite-element determined stress-intensity factor solutions for a symmetrical set of point forces of the type shown in Figure 11.2.9. The finite-element point force solutions were developed as a function of position for $X\,(=x/a) < 0.9$ and a limiting expression was given for $X > 0.9$. The Hsu and Rudd Green's function is shown in Figure 11.2.10 for several values of a/R; also shown are Green's functions for an edge crack and for a central crack. Note that all the Green's functions tend to infinity as X approaches 1. It should also be noted that the Green's functions presented are based on the following format

$$K = \frac{1}{\sqrt{\pi a}} \int_0^a \sigma(x) G(x,a) dx \qquad (11.2.13)$$

which has been widely used. Hsu and Rudd based their presentation of the Green's function on an approach taken by Hsu, et al. [1978], wherein the Green's function $G(x,a)$ in Equation 11.2.13 is obtained by multiplying the Hsu, et al. value G^H by π, i.e.

$$G(x,a) = \pi G^H(x,a) \qquad (11.2.14)$$

The complete table of $G^H(x,a)$ derived by Hsu, et al. can be found in Table 11.2.1. Other work by Hsu and co-workers on lug-type problems can be found in Section 11.3.

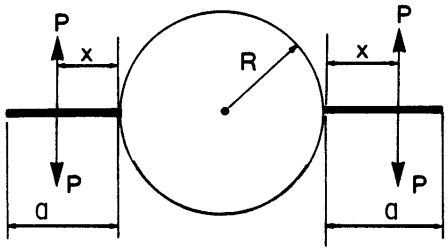

Figure 11.2.9. Diametrically Cracked Hole With Symmetrically Located Point Focus

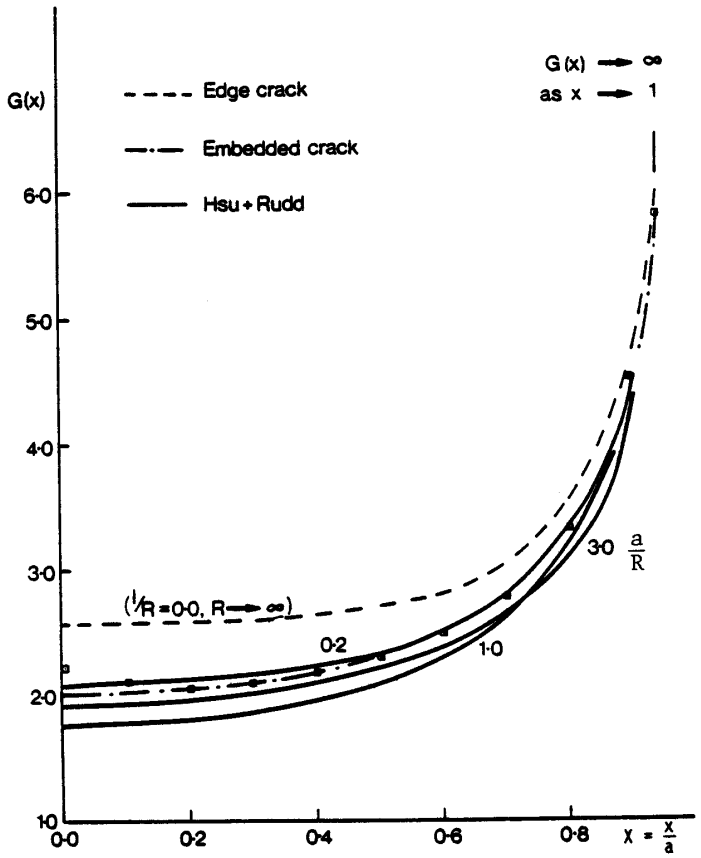

Figure 11.2.10. Green's Function for Geometry and Loading Described in Figure 11.2.9 [Cartwright & Rooke, 1979; Hsu & Rudd, 1978; Hsu, et al., 1978]

Table 11.2.1. Green's Function For A Double Crack Emanating From An Open Hole In An Infinite Plate [Hsu, et al., 1978]

x/a	a/r													
	.20	**.30**	**.40**	**.50**	**.60**	**70**	**80**	**.90**	**1.00**	**1.40**	**1.60**	**2.00**	**2.40**	**3.00**
.00	.664	.629	.603	.595	.568	.575	.572	.554	.548	.571	.582	.594	.600	.611
.10	.676	.639	.615	.604	.582	.583	.586	.569	.563	.587	.596	.603	.603	.615
.20	.688	.645	.628	.617	.599	.596	.600	.589	.578	.604	.612	.613	.609	.624
.30	.699	.658	.646	.633	.621	.613	.623	.610	.598	.627	.630	.625	.619	.639
.40	.718	.679	.671	.656	.651	.639	.655	.639	.624	.656	.653	.642	.635	.664
.45	.740	.691	.689	.671	.673	.657	.674	.658	.643	.674	.665	.654	.647	.680
.50	.760	.708	.712	.689	.698	.681	.701	.682	.668	.692	.678	.670	.662	.699
.55	.781	.732	.739	.712	.730	.711	.733	.708	.699	.709	.695	.692	.679	.723
.60	.802	.764	.762	.746	.770	.752	.766	.739	.737	.730	.725	.721	.702	.753
.70	.889	.868	.837	.838	.865	.867	.850	.827	.847	.819	.801	.811	.760	.842
.75	.960	.946	.907	.911	.913	.960	.912	.911	.929	.888	.859	.884	.817	.905
.80	1.071	1.089	1.044	1.030	.989	1.056	1.018	.995	1.021	.985	.955	.979	.904	.977
.85	1.234	1.254	1.245	1.211	1.141	1.252	1.177	1.187	1.192	1.130	1.130	1.120	1.042	1.101
.90	1.429	1.432	1.434	1.436	1.437	1.438	1.440	1.441	1.442	1.445	1.446	1.448	1.449	1.451

*For $x/a >$ 0.9, $G^H\left(a/r, x/a\right) = \frac{1}{\pi}\left[\frac{4\left(1+\frac{a}{r}\right)}{\left(1-\frac{x}{a}\right)\left(1+\frac{x}{a}+\frac{2r}{a}\right)}\right]^{1/2}$

There are two cautionary remarks that must be made about the use of Green's function techniques for solving crack problems. First, if all the loading across the crack tip is not tensile, and if the stress-intensity factor is positive at the crack tip of interest, the crack faces at some distance away from the crack tip may have (mathematically) merged in a nonphysical overlapping manner and the estimated stress-intensity factor might be unconservatively low. Accordingly, one should check to determine if the crack displacements all along the crack are positive and thus non-overlapping to ensure validity of the solution. Second, it is important in displacement boundary value problems to derive a Green's function that accounts for the requirement that there be zero displacement on those boundaries where displacement conditions are applied when estimating the stress-intensity factor from the uncracked geometry solution. Typically, neglecting this requirement for displacement boundary value problems produces a stress-intensity factor that is conservatively high. These two cautions apply equally well to the weight function technique.

11.2.2.2 The Weight Function Technique

The weight function technique can be derived using the definition of the strain energy release rate [Parker, 1981; Cartwright, 1979; Bueckner, 1971; Rice, 1972]. The stress-intensity factor is

obtained from the difference between the strain energy of a cracked structure and of the identical structure without a crack, and is given by:

$$K_I = \int_a \sigma(x) m(x,a) dx \tag{11.2.15}$$

where the function *m(x,a)* is the Bueckner weight function, a function which is unique for the given geometry and is independent of the loading from which it was derived. The weight function is defined as a function of

1) material properties,
2) a known stress-intensity factor (*K**) for the given geometry under a defined loading, and
3) the crack opening ν*(x,a) corresponding to *K**:

$$m(x,a) = \frac{H}{2K^*} \frac{\partial v^*}{\partial a}(x,a) \tag{11.2.16}$$

H is a material constant that is given by:

$$H = \frac{8\mu}{1+\kappa} \quad \begin{matrix} = \text{E for plane stress} \\ = \dfrac{E}{1-\nu^2} \text{ for plane strain} \end{matrix} \tag{11.2.17}$$

with μ = shear modulus and κ is defined as a function of the stress state and Poisson's ratio (ν)

$$\kappa = \begin{matrix} \dfrac{3-\nu}{1+\nu} \text{ for plane stress} \\ 3-4\nu \text{ for plane strain} \end{matrix} \tag{11.2.18}$$

For the infinite plate center crack problem *K**, ν^*, $\dfrac{\partial v^*}{\partial a}$, and *m* are given by the following equations:

$$K^* = \sigma\sqrt{\pi a} \tag{11.2.19}$$

$$v^*(x,a) = \left(\frac{1+\kappa}{4\mu}\right)\sigma\sqrt{a^2-x^2} \qquad \text{for } -a \le x \le a \tag{11.2.20}$$

$$\frac{\partial v^*}{\partial a} = \left(\frac{1+\kappa}{4\mu}\right)\sigma a \frac{1}{\sqrt{a^2-x^2}} \tag{11.2.21}$$

and

$$m(x,a) = \sqrt{\frac{a}{\pi}} \frac{1}{\sqrt{a^2-x^2}} \tag{11.2.22}$$

The stress-intensity factor associated with a symmetrical pressure loading of $\sigma(x)$ on the central crack faces is then given by

$$K = \sqrt{\frac{a}{\pi}} \int_{-a}^{+a} \frac{\sigma(x)}{\sqrt{a^2 - x^2}} dx \qquad (11.2.23)$$

The reader is cautioned to note that Equations 11.2.23 and 11.2.12 differ. However, both equations yield exactly the same stress-intensity factor solution when the pressure stress σ is a symmetrical function, i.e., the stress at $x = x_o$ is equal to the stress at $x = -x_o$ ($0 \le x_o \le a$). The reason that Equations 11.2.23 and 11.2.12 differ is that the Bueckner function in Equation 11.2.12 was derived for a symmetrical loading whereas the Green's function was derived for the more general case of unsymmetrical loading. Thus, when deriving the weight function one should seek to locate stress-intensity factor (K^*) and crack displacement (v^*) solutions which are representative of the loading symmetry associated with the problems that are to be solved.

A weight function for radially and diametrically cracked holes was developed by Grandt [1975] for through-thickness type cracks. His solution is given by

$$K = \frac{H}{K_B} \int_o^a \sigma(x) \frac{\partial \eta}{\partial a} dx \qquad (11.2.24)$$

where K_B represents the appropriate (radial or diametrical) Bowie stress-intensity factor (Sectoin 11.3), and the crack opening displacement η was obtained from finite-element solutions. The displacements η were described by the conic section equation:

$$\left(\frac{\eta}{\eta_o}\right)^2 = \frac{2}{2+m}\left(\frac{a-x}{a}\right) + \frac{m}{2+m}\left(\frac{a-x}{a}\right)^2 \qquad (11.2.25)$$

Here η_o is the displacement at the crack mouth (x=0) and m is the conic section coefficient from

$$m = \pi\left[\frac{H\eta_0}{2\sigma a Y}\right]^2 - 2 \qquad (11.2.26)$$

In this instance, Y is the Bowie geometric factor

$$Y = \frac{K_B}{\sigma\sqrt{a}} \qquad (11.2.27)$$

The finite-element results for the crack mouth displacement η_o were closely represented by the least squares expression

$$\eta_0 = R\sum_{i=o}^{6} D_i (a/R)^i \qquad (11.2.28)$$

where the coefficients D_i are given in Table 11.2.2.

Table 11.2.2. Least Squares Fit Of Finite Element Data For Crack Mouth Displacement [Grandt, 1975]

$$\eta_0 = R\sum_{i=o}^{6} D_i (a/R)^i$$

Coefficient	Single Crack	Double Crack
D_0	-1.567×10^{-6}	1.548×10^{-5}
D_1	6.269×10^{-4}	5.888×10^{-4}
D_2	-6.500×10^{-4}	-4.497×10^{-4}
D_3	4.466×10^{-4}	3.101×10^{-4}
D_4	-1.725×10^{-4}	-1.162×10^{-4}
D_5	3.485×10^{-5}	2.228×10^{-5}
D_6	-2.900×10^{-6}	-1.694×10^{-6}

Grandt has applied the weight function technique to a number of fastener-type cracked hole problems. Using finite-element descriptions of the stress along the expected crack path for a hole that has been cold-worked (loaded) to a 0.006 inch radial expansion and then unloaded, Grandt was able to derive the stress-intensity factor shown in Figure 11.2.11 for a remote stress loading of 40 ksi. Figure 11.2.11 also provides the stress-intensity factor solution for a remote stress loading of 40 ksi applied to a radially cracked hole without cold-working. The dramatic difference in stress-intensity factors from the two cases has been shown to translate itself into orders of magnitude difference in crack growth rate behavior.

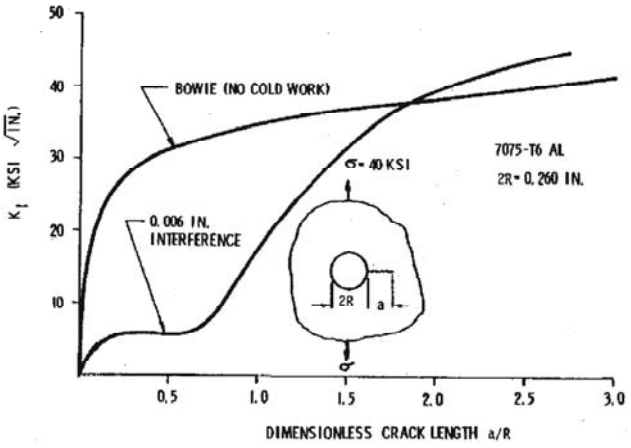

Figure 11.2.11. Stress-Intensity Factor Calibration for a Cold Worked Hole [Grandt, 1975]

11.2.3 Finite Element Methods

In all cases where an expression for the stress-intensity factor cannot be obtained from existing solutions, finite-element analysis can be used to determine *K* [Chan, et al., 1970; Byskov, 1970; Tracey, 1971; Walsh, 1971]. Certain aircraft structural configurations have to be analyzed by finite-element techniques because of the influence of complex geometrical boundary conditions or complex load transfer situations. In the case of load transfer, the magnitude and distribution

of loadings may be unknown. With the application of finite-element methods, the required boundary conditions and applied loadings must be imposed on the model.

Complex structural configurations and multicomponent structures present special problems for finite-element modeling. These problems are associated with the structural complexity. When they can be solved, the stress-intensity factor is determined in the same way as in the case of simpler geometry. This subsection deals with the principles and procedures that permit the determination of the stress-intensity factor from a finite-element solution.

Usually quadrilateral, triangular, or rectangular constant-strain elements are used, depending on the particular finite-element structural analysis computer program being used. For problems involving holes or other stress concentrations, a fine-grid network is required to accurately model the hole boundary and properly define the stress and strain gradients around the hole or stress concentration.

Within the finite-element grid system of the structural problem, the crack surface and length must be simulated. Usually, the location and direction of crack propagation is perpendicular to the maximum principal stress direction. If the maximum principal stress direction is unknown, then an uncracked stress analysis of the finite-element model should be conducted to establish the location of the crack and the direction of propagation.

The crack surfaces and lengths are often simulated by double-node coupling of elements along the crack line. Progressive crack extension is then simulated by progressively "unzipping" the coupled nodes along the crack line. Because standard finite-element formulations do not treat singular stress behavior in the vicinity of the ends of cracks, special procedures must be utilized to determine the stress-intensity factor. Three basic approaches to obtain stress-intensity factors from finite-element solutions have been rather extensively studied. These approaches are as follows:

a) Direct Method. The numerical results of stress, displacement, or crack-opening displacement are fitted to analytical forms of crack-tip-stress-displacement fields to obtain stress-intensity factors.

b) Indirect Method. The stress-intensity follows from its relation to other quantities such as compliance, elastic energy, or work energy for crack closure.

c) Cracked Element. A hybrid-cracked element allowing a stress singularity is incorporated in the finite-element grid system and stress-intensity factors are determined from nodal point displacements along the periphery of the cracked element.

These approaches can be applied to determine both Mode 1 and Mode 2 stress-intensity factors. Application of methods has been limited to two-dimensional planar problems. The state-of-the-art for treating three-dimensional structural crack problems is still a research area.

11.2.3.1 Direct Methods

The direct methods use the results of the general elastic solutions to the crack-tip stress and displacement fields. For the Mode 1, the crack tip stresses can always be described by the equations

$$\sigma_x = \frac{K_1}{\sqrt{2\pi r}}\cos\frac{\theta}{2}\left[1-\sin\frac{\theta}{2}\sin\frac{3\theta}{2}\right]$$

$$\sigma_y = \frac{K_1}{\sqrt{2\pi}}\cos\frac{\theta}{2}\left[1+\sin\frac{\theta}{2}\sin\frac{3\theta}{2}\right]$$

$$\sigma_z = 0 \qquad \text{for plane stress}$$

$$\sigma_z = \upsilon(\sigma_u + \sigma_y) \qquad \text{plane strain} \tag{11.2.29}$$

$$\tau_{xy} = \frac{K_1}{\sqrt{2\pi r}}\sin\frac{\theta}{2}\cos\frac{\theta}{2}\cos\frac{3\theta}{2}$$

$$\tau_{xz} = \tau_{yz} = 0$$

where r and θ are polar coordinates originating at the crack tip, and where x is the direction of the crack, y is perpendicular to the crack in the plane of the plate, and z is perpendicular to the plate surface.

If the stresses around the crack tip are calculated by means of finite-element analysis, the stress-intensity factor can be determined as

$$K_1 = \sigma_{ij}\frac{\sqrt{2\pi r}}{f_{ij}(\theta)} \tag{11.2.30}$$

where i and j are used to represent various permutations of x and y.

By taking the stress calculated for an element not too far from the crack tip, the stress intensity follows from a substitution of this stress and the r and θ of the element into Equation 11.2.30. This can be done for any element in the crack tip vicinity.

Ideally, the same value of K should result from each substitution; however, the stress field equations are only valid in an area very close to the crack tip. Also at some distance from the crack tip, nonsingular terms should be taken into account. Consequently, the calculated K differs from the actual K. The result can be improved [Chan, et al., 1970] by refining the finite-element mesh or by plotting the calculated K as a function of the distance of the element to the crack tip. The resulting line should be extrapolated to the crack tip, since the crack tip equations are exact for $r = 0$. Usually, the element at the crack tip should be discarded. Since it is too close to the singularity, the calculated stresses are largely in error. As a result, Equation 11.2.30 yields a K value that is more in error than those for more remote element, despite the neglect of the nonsingular terms.

Instead of the stresses, one can also use the displacements for the determination of K. In general, the displacements of the crack edge (crack-opening displacements) are employed. The Mode 1 and Mode 2 plane strain displacement equations are given by

$$u_1 = \frac{2K_1(1+\upsilon)}{E}\left[\frac{r}{2\pi}\right]^{1/2}\cos\frac{\theta}{2}\left(1-2\upsilon+\sin^2\frac{\theta}{2}\right) \tag{11.2.31}$$

$$v_1 = \frac{2K_1(1+\upsilon)}{E}\left[\frac{r}{2\pi}\right]^{1/2} \sin\frac{\theta}{2}\left(2-2\upsilon-\cos^2\frac{\theta}{2}\right)$$

and by

$$u_2 = \frac{2K_2(1+\upsilon)}{E}\left[\frac{r}{2\pi}\right]^{1/2} \sin\frac{\theta}{2}\left(2-2\upsilon+\cos^2\frac{\theta}{2}\right)$$

$$v_2 = \frac{2K_2(1+\upsilon)}{E}\left[\frac{r}{2\pi}\right]^{1/2} \cos\frac{\theta}{2}\left(2\upsilon-1+\sin^2\frac{\theta}{2}\right) \qquad (11.2.32)$$

respectively. The functions *u* and *v* represent the displacements in the *x* and *y* direction, respectively. The crack tip polar coordinates *r* and θ are chosen to coincide with the nodal points in the finite element mesh where displacements are desired. Since the above elastic field equations are only valid in an area near the tip of the crack, the application should be restricted to that area.

11.2.3.2 Indirect Methods

The indirect methods use relationships that exist between the stress-intensity factor (*K*) and the elastic-energy content (*U*) of the cracked structure. These relationships are developed in Section 1.3.2 along with a full discussion of the strain energy release rate (*G*) and compliance (*C*), i.e. the inverse stiffness of the system. The stress-intensity factor is related to these parameters by the following:

$$K^2 = G\overline{E} \qquad (11.2.33)$$

$$K^2 = \frac{\partial U}{\partial a}.\frac{\overline{E}}{B} \qquad (11.2.34)$$

$$K^2 = \frac{P^2}{2B}.\frac{\partial C}{\partial a}.\overline{E} \qquad (11.2.35)$$

where *B* is the plate thickness and $\overline{E}$ is the elastic modulus *E* in plane stress and is $E/(1-\nu^2)$ in plane strain.

The elastic energy content and the compliance of cracked structures are obtained for a range of crack sizes either by solving the problem for different crack sizes or by unzipping nodes. Differentiation with respect to crack size gives *K* from the above equations. The advantage of the elastic-energy content and compliance methods is that a fine mesh is not necessary, since accuracy of crack-tip stresses is not required. A disadvantage is that differentiation procedures can introduce errors.

The strain energy release rate relationship (Equation 11.2.33) was derived based on the use of the crack tip stress field and displacement equations to calculate the work done by the forces required to close the crack tip. The crack tip closing work can be calculated by uncoupling the next nodal point in front of the crack tip and by calculating the work done by the nodal forces to close the crack to its original size.

The concept is that if a crack were to extend by a small amount, Δa, the energy absorbed in the process is equal to the work required to close the crack to its original length. The general integral equations for strain energy release rates for Modes 1 and 2 deformations are

$$G_1 = \Delta a \xrightarrow{\lim} 0 \frac{1}{2\Delta a} \int_0^{\Delta a} \sigma_y(\Delta a - r, 0) v(r, \pi) dr,$$
$$G_2 = \Delta a \xrightarrow{\lim} 0 \frac{1}{2\Delta a} \int_0^{\Delta a} \tau_{xy}(\Delta a - r, 0) u(r, \pi) dr. \tag{11.2.36}$$

The significance of this approach is that it permits an evaluation of both K_1 and K_2 from the results of a single analysis.

In finite-element analysis, the displacements have a linear variation over the elements and the stiffness matrix is written in terms of forces and displacements at the element corners or nodes. Therefore, to be consistent with finite-element representation, the approach for evaluating G_1 and G_2 is based on the nodal-point forces and displacements. An explanation of application of this work-energy method is given with reference to Figure 11.2.12. The crack and surrounding elements are a small segment from a much larger finite-element model of a structure. In terms of the finite-element representation, the amount of work required to close the crack, Δa, is one-half the product of the forces at nodes c and d and the distance (v_c - v_d) which are required to close these nodes. The expressions for strain energy release rates in terms of nodal-point displacements and forces are (see Figure 11.2.12 for notations)

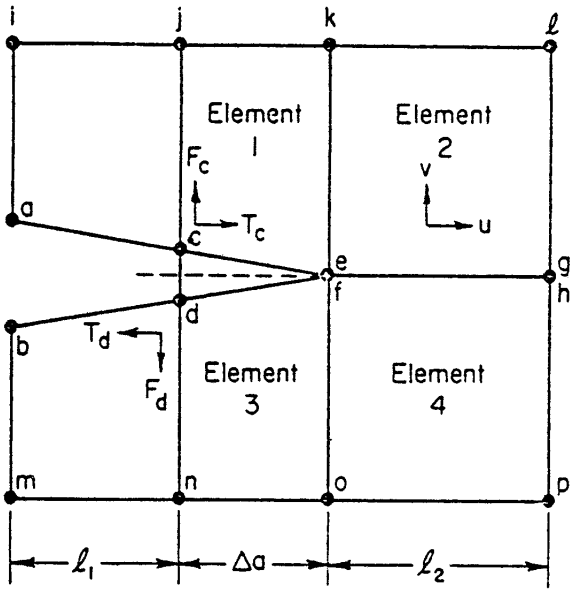

Figure 11.2.12. Finite-Element nodes Near Crack Tip.

$$G_1 = \Delta a \xrightarrow{\lim} 0 \frac{1}{2\Delta a} \overline{F_c}(v_c - v_d) \tag{11.2.37}$$

$$G_2 = \Delta a \xrightarrow{\lim} 0 \frac{1}{2\Delta a} \overline{T_c}\left(u_c - u_d\right)$$

11.2.3.3 Cracked Element Methods

This approach involves the use of a hybrid-cracked element that is incorporated into a finite-element structural analysis program. To date, only two dimensional crack problems can be solved with the cracked-element approach. Elements have been developed [Byskov, 1970; Tracey, 1971; Walsh, 1971; Gallagher, 1978; Jordon, et al., 1973; Atluri, et al., 1974; Hellen, 1979] that allow a stress singularity to occur at the crack tip.

The cracked element consists of boundary nodal points around the geometrical boundary of the element. The element is either contained within the complete finite-element model or is solved separately using the results of finite-element analysis. In either case, the crack surface is simulated by unzipping a double-noded line along the line of expected crack extension. This builds into the structural model the proper stiffness due to the presence of the crack. The variation of stress-intensity factors (K_1 and K_2) with crack length is determined by progressively unzipping the sets of coupled nodes.

Studies have been conducted on the variation of stress-intensity factors with cracked-element size and location [Jordon, et al., 1973; Atluri, et al., 1974]. These results define some definite guidelines in using cracked-element models. First, the distance from the crack tip to the cracked-element nodal points should be as constant as possible. Secondly, for long edge-cracks or cracks emanating from holes, the cracked element should only contain an area very near the crack tip.

11.3 Selected Stress Intensity Factor Cases

This section will present a catalog of stress-intensity factor solutions for some typical crack geometries. Many of these solutions are found in computer programs and handbooks. Tables 11.3.1 through 11.3.5 summarize the solutions that are presented. The solutions are categorized by the location of the crack, either embedded, in a plate (surface or edge), or at a hole, in Tables 11.3.1 through 11.3.3. Solutions for cracks in a cylinders and sphere are summarized in Table 11.3.4, and the ASTM standard specimens are listed in Table 11.3.5. Table 11.3.6 includes listings of the parameters used in the drawings and equations as well as their definitions.

Following these tables, the equations for the stress-intensity factor solutions are given. The solutions are presented in the same order as listed in the tables.

The remote loading solutions are presented in the form:

$$K_i = F_i \sigma \sqrt{\pi a} \qquad (11.3.1)$$

where the coefficient F_i is expressed as a function of geometry, and i indicates the loading type. Some of the cases considered can be used to develop more complex solutions through the methods of superposition and compounding

Table 11.3.1. Embedded Cracks

Description	Illustration	References
Embedded Crack in a Plate	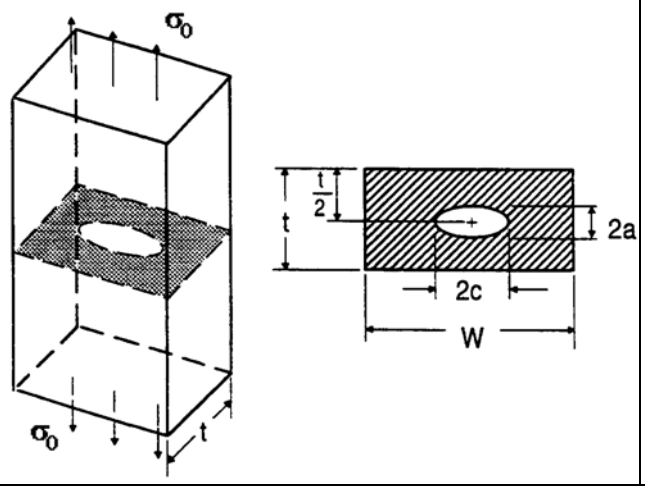	Newman & Raju [1984] Forman, et al. [1998]

Table 11.3.2. Cracks in a Plate

Description	Illustration	References
Surface Crack in Plate	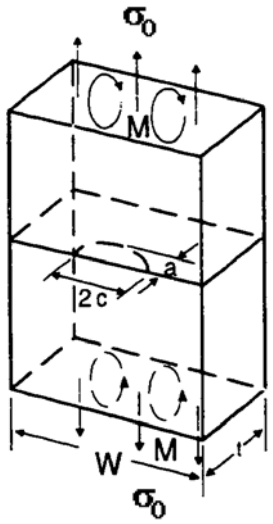	Newman & Raju [1984] Forman, et al. [1989]
Through Crack in the Center of a Plate	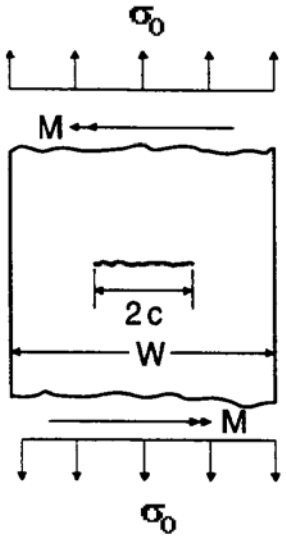	Fedderson [1966] Paris & Sih [1964] Roberts & Kibler [1971] Forman, et al. [1998]

Corner Crack at the Edge of a Plate	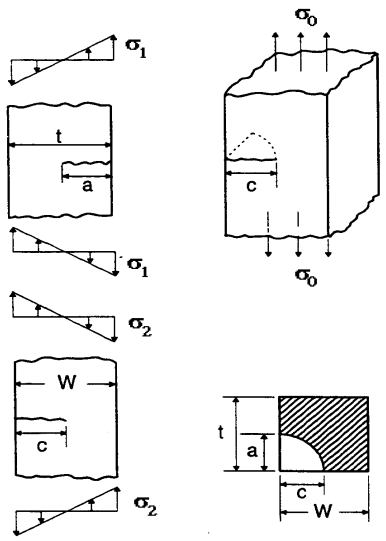	Raju & Newman [1988] Forman, et al. [1998]
Through Crack at the Edge of a Plate	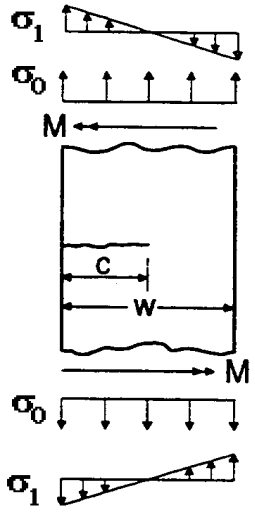	Tada, et al. [1973] Forman, et al. [1998]

Table 11.3.3. Cracks from Holes

Description	Illustration	References
Radial Corner Crack from a Hole	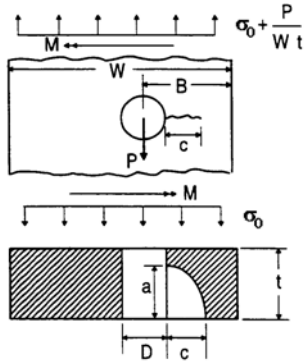	Newman & Raju [1984] Forman, et al. [1989]
Radial Through Crack from a Hole	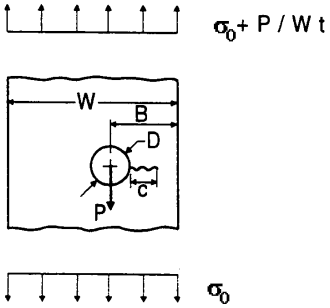	Shivakumar & Hsu [1977] Zatz, et al. [1981] Isida [1973] Forman, et al. [1989]
Corner Crack from a Hole in a Lug	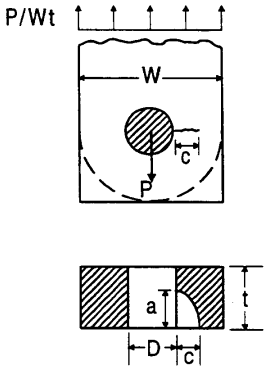	Newman & Raju [1984] Forman & Mettu [1992] Forman, et al. [1998]
Through Crack from a Hole in a Lug	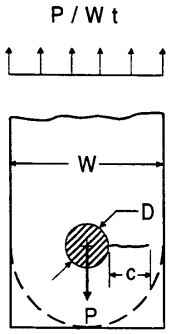	Shivakumar & Hsu [1977] Zatz, et al. [1981] Forman, et al. [1989]

Table 11.3.4. Cracks in Cylinders and Spheres

Description	Illustration	References
Surface Crack in a Solid Cylinder	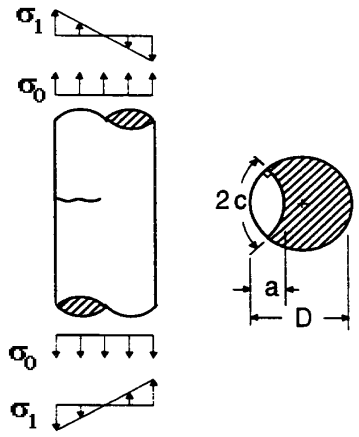	Forman & Shivakumar [1986] Forman, et al. [1998]
Longitudinal Surface Crack in a Cylinder	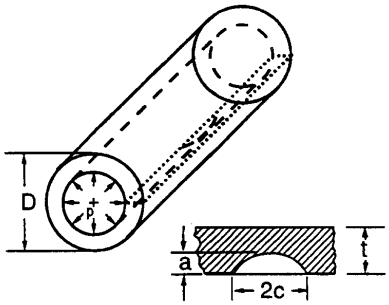	Newman & Raju [1979] Forman, et al. [1989]
Longitudinal Through Crack in a Cylinder	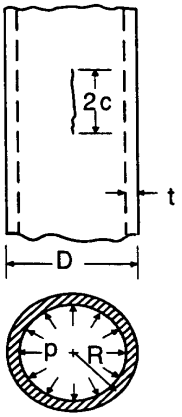	Newman [1976] Forman, et al. [1998]

Thumbnail Crack on a Hollow Cylinder	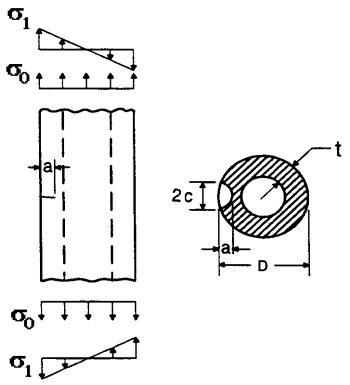	Raju & Newman [1984] Forman, et al. [1989]
Circular Through Crack in a Cylinder	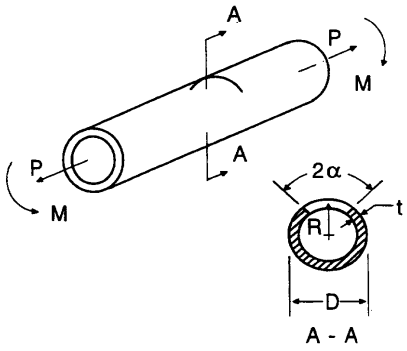	Forman, et al. [1985] Forman, et al. [1998]
Through Crack in a Sphere	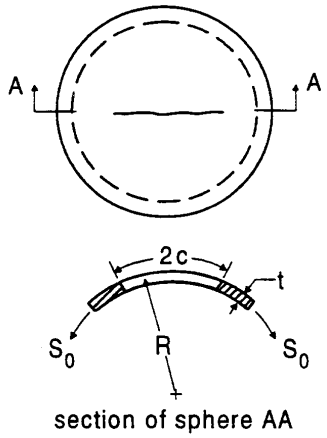	Erdogan & Kibler [1969] Forman, et al. [1998]

Table 11.3.5. ASTM Standard Specimens

Description	Illustration	References
Standard Center-Cracked Tension Specimen	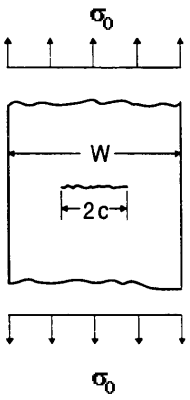	Fedderson [1966]
Standard Compact Specimen	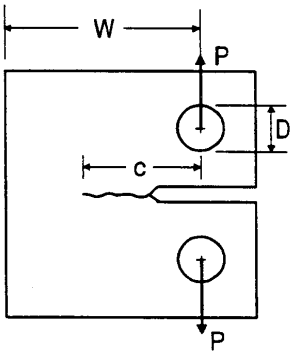	ASTM E399 [2000]
Standard Round Compact Specimen	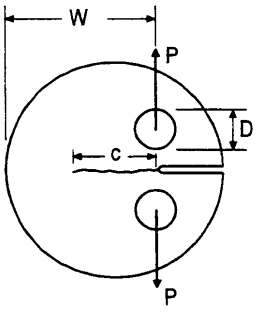	ASTM E399 [2000]
Standard Arc-Shaped Specimen	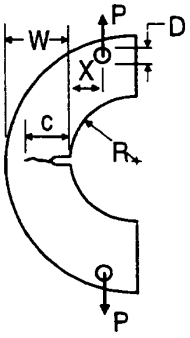	ASTM E399 [2000]

Standard Bend Specimen	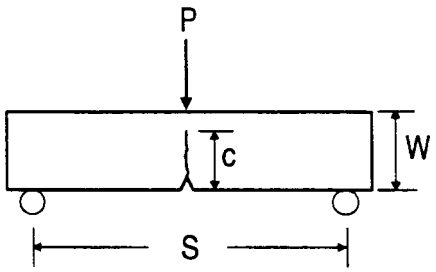	ASTM E399 [2000]

Table 11.3.6. Description of Parameters Used for SIF Solutions

Parameter	Description
a	Crack Depth
c	Crack Length
t	Thickness
W	Width
D	Hole diameter; cylinder diameter
B	Distance from hole center to edge of plate Thickness (ASTM standard solutions)
R	Cylinder radius
σ_0	Remote tension stress
σ_1 and σ_2	Bending stresses
σ_3	Bearing stress

Table 11.3.7. Stress Intensity Solutions for Embedded Cracks

Embedded Crack in a Plate	$K_0 = F_0 \sigma_0 \sqrt{\pi a}$ $F_0 = M_0 g f_\phi f_w f_x$ $M_0 = M_1 + M_2 (a/t)^2 + M_3 (a/t)^4$ $M_2 = \dfrac{0.05}{\left(0.11 + (a/c)^{\frac{3}{2}}\right)}$ $M_3 = \dfrac{0.29}{\left(0.23 + (a/c)^{\frac{3}{2}}\right)}$ $g = 1 - \left[\dfrac{(a/t)^4 \left(2.6 - 2(a/t)\right)^{\frac{1}{2}}}{\left(1 + 4(a/c)\right)} \right] \mid \cos \phi \mid$ $f_w = \left\{ \sec \left[\left(\dfrac{\pi a}{W} \right) \sqrt{\dfrac{a}{t}} \right] \right\}^{\frac{1}{2}}$ $\phi = 0^\circ \quad for \quad \dfrac{dc}{dN}$ $\phi = 90^\circ \quad for \quad \dfrac{da}{dN}$ See Tables 11.3.11 for f_ϕ and f_x equations

Table 11.3.8. Stress Intensity Solutions for Cracks in a Plate

Surface Crack in a Plate	*Tension* $K_0 = F_0 \sigma_0 \sqrt{\pi a}$ *Bending* $K_1 = F_1 \sigma_1 \sqrt{\pi a}$	$F_0 = M_0 g_1 f_\phi f_w f_x$ $F_1 = H_c F_0$ $f_w = \sqrt{sec\left(\frac{\pi c}{W}\sqrt{\frac{a}{t}}\right)}$ $\phi = 10^\circ \ for \ \frac{dc}{dN}$ $\phi = 90^\circ \ for \ \frac{da}{dN}$ See Table 11.3.12 for M_0, g_1, f_ϕ, and f_x equations
Through Crack in the Center of a Plate	*Tension* $K_0 = F_0 \sigma_0 \sqrt{\pi a}$ *Bending* $K_1 = F_1 \sigma_1 \sqrt{\pi a}$	$F_0 = \left\{ sec\left(\pi \frac{a}{W}\right)\right\}^{\frac{1}{2}}$ $F_1 = \frac{F_0}{2}$
Corner Crack at the Edge of a Plate	*Tension* $K_0 = F_0 \sigma_0 \sqrt{\pi a}$ *Bending* $K_1 = F_1 \sigma_1 \sqrt{\pi a}$	$F_i = f_x f_\phi f_a f_i$ $f_i = \left(\frac{a}{c}, \frac{a}{t}, \frac{c}{W}\right) \ for \ i = 0, 1, 2$ See Tables 11.3.12 for f_ϕ, f_a and f_x equations and Table 11.3.9 for f_i
Through Crack at the Edge of a Plate	*Tension* $K_0 = F_0 \sigma_0 \sqrt{\pi a}$ *Bending* $K_1 = F_1 \sigma_1 \sqrt{\pi a}$ $K_2 = F_2 \sigma_2 \sqrt{\pi a}$	$F_0 = sec\,\beta \left(\frac{tan\,\beta}{\beta}\right)^{\frac{1}{2}} \left[0.752 + 2.02\left(\frac{a}{W}\right) + 0.37\left(1 - sin\,\beta\right)^3\right]$ $F_1 = \frac{F_0}{2}$ $F_2 = sec\,\beta \left(\frac{tan\,\beta}{\beta}\right)^{\frac{1}{2}} \left[0.923 + 0.199\left(1 - sin\,\beta\right)^4\right]$ $\beta = \frac{\pi a}{2W}$

Table 11.3.9. Calculation of f_i for Corner Crack Solution

$$f_i = \left(\frac{a}{c}, \frac{a}{t}, \frac{a}{W} \right)$$ obtained from interpolating in f_0, f_1, f_2 tables as follows

1 Four data points, $f_i\{(a/c)_j, a/t, c/W\}|_{j=1,2,3,4}$, are calculated using cubic spline interpolation, where $(a/c)_j$ are listed tabular values of 0.2, 0.4, 0.5, 1.0, 2.0, 2.5, and 5.0, and, in general, $(a/c)_{j=1,2} < a/c$ and $(a/c)_{j=3,4} > a/c$.

2 $f_i(a/c)$ are then calculated from the above four data points using piecewise Hermite polynomial interpolation.

Table of F_0 Values

		c/W = 0.0		c/W = 0.1		c/W = 0.2		c/W = 0.5		c/W = 0.8		c/W = 1.0	
a/c	a/t	a-tip	c-tip	a-tip	c-tip	a-tip	c-tip	a-tip	c-tip	a-tip	c-tip	a-tip	c-tip
0.2	0.0	1.037	1.280	1.041	1.285	1.043	1.291	1.070	1.330	1.102	1.390	1.128	1.441
	0.1	1.078	1.311	1.083	1.318	1.087	1.322	1.116	1.355	1.145	1.408	1.169	1.452
	0.2	1.157	1.374	1.161	1.380	1.169	1.388	1.207	1.420	1.240	1.470	1.268	1.513
	0.5	1.515	1.752	1.536	1.787	1.571	1.833	1.732	1.993	1.944	2.243	2.124	2.448
	0.8	2.031	2.498	2.098	2.663	2.196	2.832	2.749	3.528	3.623	4.603	4.378	5.491
	1.0	2.475	3.286	2.578	3.585	2.749	3.931	3.790	5.340	5.523	7.514	7.026	9.311
0.4	0.0	1.073	1.173	1.077	1.177	1.082	1.183	1.130	1.244	1.201	1.314	1.254	1.365
	0.1	1.094	1.198	1.097	1.201	1.104	1.206	1.161	1.267	1.233	1.343	1.289	1.398
	0.2	1.131	1.241	1.135	1.246	1.147	1.257	1.227	1.337	1.306	1.417	1.375	1.488
	0.5	1.317	1.488	1.339	1.521	1.378	1.567	1.577	1.749	1.865	2.072	2.117	2.349
	0.8	1.636	1.985	1.691	2.069	1.780	2.198	2.318	2.781	3.239	3.816	4.066	4.723
	1.0	1.941	2.504	2.015	2.638	2.167	2.861	3.111	3.972	4.813	5.875	6.355	7.559
0.5	0.0	1.086	1.158	1.090	1.160	1.097	1.165	1.150	1.220	1.235	1.302	1.308	1.381
	0.1	1.102	1.179	1.106	1.180	1.113	1.185	1.178	1.245	1.271	1.339	1.350	1.424
	0.2	1.130	1.211	1.134	1.217	1.147	1.228	1.238	1.310	1.345	1.417	1.439	1.511
	0.5	1.272	1.414	1.294	1.446	1.335	1.492	1.550	1.684	1.879	2.045	2.161	2.355
	0.8	1.546	1.827	1.596	1.899	1.684	2.018	2.224	2.574	3.169	3.609	4.010	4.516
	1.0	1.801	2.260	1.871	2.368	2.021	2.558	2.931	3.568	4.595	5.380	6.163	7.059
1.0	0.0	1.138	1.138	1.142	1.141	1.145	1.144	1.236	1.192	1.416	1.343	1.601	1.523
	0.1	1.141	1.142	1.144	1.144	1.154	1.152	1.261	1.220	1.470	1.399	1.683	1.609
	0.2	1.144	1.145	1.152	1.154	1.172	1.172	1.309	1.267	1.565	1.486	1.801	1.685
	0.5	1.198	1.232	1.220	1.251	1.267	1.309	1.547	1.547	2.075	2.056	2.555	2.514
	0.8	1.364	1.413	1.399	1.470	1.486	1.565	2.056	2.075	3.171	3.171	4.196	4.162
	1.0	1.481	1.615	1.545	1.686	1.685	1.801	2.514	2.555	4.162	4.190	5.977	5.977

Table of F_1 Values

		c/W = 0.0		c/W = 0.1		c/W = 0.2		c/W = 0.5		c/W = 0.8		c/W = 1.0	
a/c	a/t	a-tip	c-tip	a-tip	c-tip	a-tip	c-tip	a-tip	c-tip	a-tip	c-tip	a-tip	c-tip
0.2	0.0	1.037	1.280	1.041	1.285	1.043	1.291	1.070	1.330	1.102	1.390	1.128	1.441
	0.1	0.939	1.287	0.940	1.289	0.945	1.294	0.975	1.336	1.029	1.400	1.077	1.458
	0.2	0.855	1.295	0.862	1.296	0.870	1.302	0.910	1.360	0.972	1.435	1.025	1.510
	0.5	0.683	1.475	0.689	1.486	0.706	1.520	0.820	1.632	0.956	1.829	1.070	1.990
	0.8	0.392	1.762	0.428	1.811	0.469	1.898	0.730	2.231	1.135	2.811	1.494	3.204
	1.0	0.056	2.050	0.093	2.129	0.165	2.266	0.572	2.793	1.264	3.745	1.883	4.577
0.4	0.0	1.073	1.173	1.077	1.177	1.082	1.183	1.130	1.244	1.201	1.314	1.254	1.365
	0.1	0.941	1.152	0.943	1.160	0.956	1.170	1.015	1.214	1.087	1.307	1.188	1.396
	0.2	0.820	1.148	0.828	1.157	0.842	1.168	0.911	1.212	0.997	1.333	1.124	1.455
	0.5	0.515	1.195	0.538	1.210	0.562	1.236	0.694	1.378	0.877	1.603	1.027	1.807
	0.8	0.194	1.340	0.217	1.360	0.247	1.400	0.488	1.705	0.903	2.243	1.255	2.739
	1.0	-0.026	1.490	-0.018	1.503	0.035	1.573	0.357	2.044	1.028	2.857	1.698	3.599
0.5	0.0	1.086	1.158	1.090	1.160	1.097	1.165	1.150	1.220	1.235	1.302	1.308	1.381
	0.1	0.946	1.130	0.952	1.139	0.965	1.148	1.027	1.192	1.117	1.297	1.233	1.417
	0.2	0.808	1.114	0.820	1.126	0.840	1.140	0.915	1.183	1.019	1.320	1.167	1.482
	0.5	0.475	1.124	0.490	1.140	0.526	1.164	0.660	1.313	0.873	1.573	1.055	1.831

	0.8	0.129	1.223	0.150	1.243	0.184	1.281	0.422	1.570	0.838	2.099	1.197	2.654
	1.0	-0.094	1.334	-0.079	1.343	-0.032	1.407	0.274	1.854	0.934	2.594	1.600	3.375
1.0	0.0	1.138	1.138	1.142	1.141	1.145	1.144	1.236	1.192	1.416	1.343	1.601	1.523
	0.1	0.965	1.087	0.977	1.097	0.993	1.111	1.094	1.176	1.288	1.348	1.488	1.573
	0.2	0.785	1.047	0.810	1.060	0.838	1.080	0.960	1.167	1.180	1.368	1.408	1.650
	0.5	0.345	0.982	0.375	1.000	0.419	1.033	0.590	1.194	0.942	1.574	1.270	2.012
	0.8	-0.070	0.961	-0.043	0.983	-0.006	1.031	0.228	1.280	0.698	1.831	1.189	2.551
	1.0	-0.352	0.964	-0.323	0.990	-0.279	1.043	-.005	1.407	0.637	2.028	1.154	2.992

Table of F_0 Values

		c/W = 0.0		**c/W = 0.1**		**c/W = 0.2**		**c/W = 0.5**		**c/W = 0.8**		**c/W = 1.0**	
a/c	**a/t**	**a-tip**	**c-tip**	**a-tip**	**c-tip**	**a-tip**	**c-tip**	**a-tip**	**c-tip**	**a-tip**	**c-tip**	**a-tip**	**c-tip**
0.2	0.0	1.037	1.280	1.006	1.054	0.976	0.822	0.900	0.138	0.800	-0.566	0.740	-1.033
	0.1	1.078	1.311	1.050	1.080	1.020	0.848	0.955	0.150	0.866	-0.550	0.805	-1.018
	0.2	1.157	1.374	1.119	1.123	1.090	0.896	1.039	0.190	0.952	-0.522	0.885	-0.996
	0.5	1.515	1.752	1.469	1.492	1.440	1.259	1.400	0.530	1.313	-0.276	1.250	-0.814
	0.8	2.031	2.498	1.997	2.282	2.009	2.081	2.124	1.447	2.200	0.614	2.300	0.058
	1.0	2.475	3.286	2.470	3.085	2.558	2.967	2.873	2.536	3.320	1.821	3.700	1.347
0.4	0.0	1.070	1.175	1.050	1.000	1.010	0.796	0.940	0.215	0.845	-0.335	0.769	-0.714
	0.1	1.095	1.198	1.070	1.015	1.037	0.812	0.970	0.242	0.875	-0.324	0.806	-0.700
	0.2	1.131	1.241	1.100	1.039	1.074	0.852	1.010	0.276	0.922	-0.284	0.859	-0.658
	0.5	1.317	1.488	1.281	1.288	1.271	1.112	1.250	0.563	1.196	-0.045	1.150	-0.419
	0.8	1.630	1.985	1.629	1.798	1.652	1.635	1.772	1.199	1.912	0.649	1.998	0.282
	1.0	1.941	2.504	1.970	2.318	2.044	2.167	2.376	1.861	2.778	1.548	3.177	1.194
0.5	0.0	1.086	1.158	1.055	0.989	1.020	0.789	0.942	0.244	0.854	-0.269	0.792	-0.625
	0.1	1.102	1.179	1.074	1.000	1.040	0.809	0.968	0.272	0.884	-0.255	0.825	-0.603
	0.2	1.130	1.211	1.100	1.025	1.070	0.846	1.004	0.310	0.930	-0.212	0.878	-0.561
	0.5	1.272	1.414	1.241	1.230	1.234	1.067	1.216	0.566	1.187	0.025	1.157	-0.311
	0.8	1.546	1.827	1.538	1.649	1.560	1.502	1.701	1.123	1.851	0.652	1.938	0.362
	1.0	1.801	2.260	1.851	2.075	1.926	1.939	2.271	1.685	2.680	1.435	3.068	1.132
1.0	0.0	1.138	1.138	1.087	0.965	1.047	0.785	0.982	0.345	0.961	-0.070	0.964	-0.352
	0.1	1.141	1.142	1.097	0.977	1.060	0.810	1.000	0.375	0.983	-0.043	0.990	-0.323
	0.2	1.144	1.145	1.111	0.993	1.080	0.838	1.033	0.419	1.031	-0.006	1.043	-0.279
	0.5	1.192	1.236	1.176	1.094	1.167	0.960	1.194	0.590	1.280	0.228	1.407	-0.005
	0.8	1.343	1.416	1.348	1.288	1.368	1.280	1.574	0.942	1.831	0.698	2.028	0.637
	1.0	1.523	1.601	1.573	1.488	1.650	1.408	2.012	1.270	2.551	1.189	2.992	1.154

Table 11.3.10. Stress Intensity Solutions for Cracks from Holes

Radial Corner Crack from a Hole	*Tension* $K_0 = F_0 \sigma_0 \sqrt{\pi a}$ *Bending* $K_1 = F_1 \sigma_1 \sqrt{\pi a}$ *Bearing* $K_3 = F_3 \sigma_3 \sqrt{\pi a}$	$F_0 = G_0 G_w$ $F_1 = G_1 G_w H_c$ $F_3 = \left(\frac{G_0 D}{2W} + G_1 \right) G_w$ See Tables 11.3.11 and 11.3.12 for additional equations
Radial Through Crack from a Hole	*Tension* $K_0 = F_0 \sigma_0 \sqrt{\pi a}$ *Bearing* $K_3 = F_3 \sigma_3 \sqrt{\pi a}$	$F_0 = G_0 G_w$ $F_3 = \left(\frac{G_0 D}{2W} + G_1 \right) G_w$ $G_w = \left[\frac{\sec \lambda \left(\sin \beta \right)}{\beta} \right]^{\frac{1}{2}}$ See Tables 11.3.11 and 11.3.12 for additional equations
Corner Crack from a Hole in a Lug	*Bearing* $K_3 = F_3 \sigma_3 \sqrt{\pi a}$	$F_3 = \left(\frac{G_0 D}{2W} + G_1 \right) G_w$ See Tables 11.3.11 and 11.3.12 for additional equations

Through Crack from a Hole in a Lug	*Bearing* $K_3 = F_3 \sigma_3 \sqrt{\pi a}$	$F_3 = \left(\frac{G_0 D}{2W} + G_1 \right) G_w G_L G_2$ $G_L = \left[\sec \left(\frac{\pi D}{2W} \right) \right]^{\frac{1}{2}}$ $G_w = \left(\sec \lambda \right)^{\frac{1}{2}}$ $G_2 = C_1 + C_2 \left(\frac{c}{b} \right) + C_3 \left(\frac{c}{b} \right)^2 + C_4 \left(\frac{c}{b} \right)^3$ $b = \frac{W - D}{2}$ $C_1 = 0.688 + 0.772 \left(\frac{D}{W} \right) + 0.613 \left(\frac{D}{W} \right)^2$ $C_2 = 4.948 - 17.318 \left(\frac{D}{W} \right) + 16.785 \left(\frac{D}{W} \right)^2$ $C_3 = -14.297 + 62.994 \left(\frac{D}{W} \right) - 69.818 \left(\frac{D}{W} \right)^2$ $C_4 = 12.35 - 58.664 \left(\frac{D}{W} \right) + 66.387 \left(\frac{D}{W} \right)^2$ See Tables 11.3.11 and 11.3.12 for additional equations

Table 11.3.11. Additional Equations Used for Calculating SIF at Holes

	Thru Cracks	**Part-thru Cracks**
λ	$\left(\frac{\pi}{2}\right)\left(\frac{D+a}{2B-a}\right)$	$\left(\frac{\pi}{2}\right)\left(\sqrt{\frac{a}{t}}\right)\left(\frac{D+a}{2B-a}\right)$
G_0	$f_0\left(z_0\right)$	$\frac{f_0\left(z_0\right)}{d_0}$
G_1	$f_1\left(z_0\right)$	$f_1\left(z_0\right)\left(\frac{g_p}{d_0}\right)$
G_2		$\frac{f_0(z_2)}{d_2}$
G_w		$M_0\ g_1\ g_3\ g_4\ f_w\ f_\phi\ f_x$
z	$\left(1+\frac{2a}{D}\right)^{-1}$	$\left[1+2\left(\frac{a}{D}\right)cos\left(\mu\phi\right)\right]^{-1}$
ϕ		$\phi = 10^\circ \ for\ \frac{dc}{dN}$ $\phi = 80^\circ \ for\ \frac{da}{dN}$

Table 11.3.12. Additional Equations Used for Calculating SIF for Cracks In a Plate and Cracks at Holes

Parameter	Equation	
$f_0(z)$	$0.7071 + 0.7548z + 0.3415z^2 + 0.642z^3 + 0.9196z^4$	
$f_1(z)$	$0.078z + 0.7588z^2 - 0.4293z^3 + 0.0644z^4 + 0.651z^5$	
M_0	$m_1 + m_2\left(\frac{a}{t}\right)^2 + m_3\left(\frac{a}{t}\right)^4$	
H_c	$H_1 + (H_2 - H_1)\sin^p \phi^3$	
H_1	$1 + G_{11}\left(\frac{a}{t}\right) + G_{12}\left(\frac{a}{t}\right)^2 + G_{13}\left(\frac{a}{t}\right)^3$	
H_2	$1 + G_{21}\left(\frac{a}{t}\right) + G_{22}\left(\frac{a}{t}\right)^2 + G_{23}\left(\frac{a}{t}\right)^3$	
$z_{0,1}$	$\left[1 + 2\left(\frac{a}{D}\right)\cos\left(\mu_{0,1}\,\phi\right)\right]^{-1}$	
$d_{0,1}$	$1 + 0.13z_{0,1}^2$	
μ_0	0.85	
μ_1	$0.85 - 0.25v^{0.25}$	
g_p	$\left(\frac{W+D}{W-D}\right)^{0.5}$	
β	$\frac{D}{B} - \frac{2D}{W}$	
	$\frac{a}{c} \le 1$	$\frac{a}{c} > 1$
f_x	$\left[1 + 1.464\left(\frac{a}{c}\right)^{1.65}\right]^{-\frac{1}{2}}$	$\left[1 + 1.464\left(\frac{c}{a}\right)^{1.65}\right]^{-\frac{1}{2}}$
f_ϕ	$\left[\left(\frac{a}{c}\cos\,\phi\right)^2 + \sin^2\phi\right]^{\frac{1}{4}}$	$\left[\cos^2\phi + \left(\frac{c}{a}\sin\,\phi\right)^2\right]^{\frac{1}{4}}$
f_a , M_1	1	$\sqrt{\frac{c}{a}}$
m_1	$1.13 - 0.09\left(\frac{a}{c}\right)$	$\left(\frac{a}{c}\right)^{-\frac{1}{2}} + 0.04\left(\frac{a}{c}\right)^{-\frac{3}{2}}$

m_2	$-0.54+\frac{0.89}{(0.2+(a/c))}$	$0.2(a/c)^{-4}$
m_3	$0.5-\frac{1}{(0.65+(a/c))}+14(1-(a/c))^{24}$	$-0.11\left(\frac{a}{c}\right)^{-4}$
g_1	$1+\left(0.1+0.35\left(\frac{a}{t}\right)^2\right)(1-sin\phi)^2$	$1+\left(0.1+\frac{0.35}{(a/c)}(a/t)^2\right)(1-sin\phi)^2$
g_3	$\left(1+0.04\left(\frac{a}{c}\right)\right)\left[1+0.1(1-cos\phi)^2\right]\left(0.85+0.15\left(\frac{a}{t}\right)^{\frac{1}{4}}\right)$	$\left(1.13-\frac{0.09}{\left(\frac{a}{c}\right)}\right)\left[1+0.1(1-cos\phi)^2\right]\left(0.85+0.15\left(\frac{a}{t}\right)^{\frac{1}{4}}\right)$
g_4	$1-0.7\left(1-\left(\frac{a}{t}\right)\right)\left(\left(\frac{a}{c}\right)-0.2\right)\left(1-\left(\frac{a}{c}\right)\right)$	1
p	$0.1+1.3\left(\frac{a}{t}\right)+1.1\left(\frac{a}{c}\right)-0.7\left(\frac{a}{c}\right)\left(\frac{a}{t}\right)$	$0.2+\frac{1}{(a/c)}+0.6\left(\frac{a}{t}\right)$
G_{11}	$-0.43-0.74\left(\frac{a}{c}\right)-0.84\left(\frac{a}{c}\right)^2$	$-2.07+\frac{0.06}{(a/c)}$
G_{12}	$1.25-1.19\left(\frac{a}{c}\right)+4.39\left(\frac{a}{c}\right)^2$	$4.35+\frac{0.16}{(a/c)}$
G_{13}	$-1.94+4.22\left(\frac{a}{c}\right)-5.51\left(\frac{a}{c}\right)^2$	$-2.93-\frac{0.3}{(a/c)}$
G_{21}	$-1.5-0.04\left(\frac{a}{c}\right)-1.73\left(\frac{a}{c}\right)^2$	$-3.64+\frac{0.37}{(a/c)}$
G_{22}	$1.71-3.17\left(\frac{a}{c}\right)+6.84\left(\frac{a}{c}\right)^2$	$5.87-\frac{0.49}{(a/c)}$
G_{23}	$-1.28+2.71\left(\frac{a}{c}\right)-5.22\left(\frac{a}{c}\right)^2$	$-4.32+\frac{0.53}{(a/c)}$

Table 11.3.13. Cracks in Cylinders and Spheres

Surface Crack in a Solid Cylinder	*Tension* $K_0 = F_0 \sigma_0 \sqrt{\pi a}$ *Bending* $K_1 = F_1 \sigma_1 \sqrt{\pi a}$	$F_0 = G\left[0.752 + 1.286\ \beta + 0.37\ Y^3\right]$ $F_1 = G\left[0.923 + 0.199\ Y^4\right]$ $G = 0.92\left(\frac{2}{\pi}\right) sec\ \beta \left[\frac{(tan\ \beta)}{\beta}\right]^{\frac{1}{2}}$ $Y = 1 - sin\ \beta$ $\beta = \left(\frac{\pi}{2}\right)\left(\frac{a}{D}\right)$
Longitudinal Surface Crack in a Cylinder	$K_0 = F_0 \sigma_0 \sqrt{\pi a}$	$F_0 = 0.97\ M_0 g_1 f_\phi f_c f_i f_x$ $f_c = \left[\frac{\left(1 + k^2\right)}{\left(1 - k^2\right)} + 1 - 0.5\sqrt{v}\right]\left[\frac{2t}{D - 2t}\right]$ $k = 1 - \frac{2t}{D}$ $f_i = 1.0 \quad for \quad internal \quad crack$ $f_i = 1.1 \quad for \quad external \quad crack$ $\phi = 10^\circ \quad for \quad \frac{dc}{dN}$ $\phi = 90^\circ \quad for \quad \frac{da}{dN}$ See Table 11.3.12 for M_0, g_1, f_ϕ, and f_x equations
Longitudinal Through Crack in a Cylinder	$K_0 = F_0 \sigma_0 \sqrt{\pi a}$	$F_0 = \left(1 + 0.52\ \lambda + 1.29\ \lambda^2 - 0.074\ \lambda^3\right)^{\frac{1}{2}}$ $\lambda = \frac{a}{\sqrt{Rt}}$

Thumbnail Crack on a Hollow Cylinder	*Tension* $K_0 = F_0 \sigma_0 \sqrt{\pi a}$ *Bending* $K_1 = F_1 \sigma_1 \sqrt{\pi a}$	$F_0 = G\left[\left(A_0 + B_0\left(\frac{a}{t}\right)\right)sin^2\,\phi + \left(C_0 + D_0\left(\frac{a}{t}\right)^2\right)cos^2\,\phi\right]$ $F_1 = G\left[\left(A_1 + B_1\left(\frac{a}{t}\right)\right)sin^2\,\phi + \left(C_1 + D_1\left(\frac{a}{t}\right)^2\right)cos^2\,\phi\right]$ $A_0 = 1.135 - 0.135\left(\frac{a}{c}\right)$ $B_0 = 0.5 - 0.663\left(\frac{a}{c}\right) + 0.266\left(\frac{a}{c}\right)^2 + \left(0.713 - 1.286\left(\frac{a}{c}\right) + 0.651\left(\frac{a}{c}\right)^2\right)\left(\frac{2t}{D}\right)$ $C_0 = 0.56 + 0.555\left(\frac{a}{c}\right)$ $D_0 = 0.876 - 0.465\left(\frac{a}{c}\right) - \left(0.86 - 0.217\left(\frac{a}{c}\right)\right)\left(\frac{2t}{D}\right)$ $A_1 = 1.093 - 0.1\left(\frac{a}{c}\right)$ $B_1 = 0.936 - 1.758\left(\frac{a}{c}\right) + 0.903\left(\frac{a}{c}\right)^2 - \left(\begin{array}{l}0.598 + \\ 0.417\left(\frac{a}{c}\right)\end{array}\right)\left(\frac{2t}{D}\right)$ $C_1 = 0.556 + 0.548\left(\frac{a}{c}\right)$ $D_1 = 0.943 - 0.518\left(\frac{a}{c}\right) - \left(\begin{array}{l}2.382 - 2.226\left(\frac{a}{c}\right) + \\ 0.9\left(\frac{a}{c}\right)^2\end{array}\right)\left(\frac{2t}{D}\right)$ $Y = 1 - 0.385\left(\frac{2t}{D}\right)\left(\frac{(a/t)}{(a/c)}\right)\left(\begin{array}{l}2.14\left(\frac{a}{c}\right) - 1.557\left(\frac{a}{c}\right)^2 + \\ 0.417\left(\frac{a}{c}\right)^3\end{array}\right)$ $f_x = \left[1 + 4.464\left(\frac{a}{c}\right)^{1.65}\right]^{-\frac{1}{2}} \qquad G = \frac{f_x}{Y}$ $\phi = 10^\circ \;\; for \;\; \frac{dc}{dN}$ $\phi = 90^\circ \;\; for \;\; \frac{da}{dN}$

Circular Through Crack in a Cylinder	*Tension* $K_0 = F_0 \sigma_0 \sqrt{\pi a}$ *Bending* $K_1 = F_1 \sigma_1 \sqrt{\pi a}$	$F_0 = \left(\frac{I_0}{2\pi\alpha} \right)^{\frac{1}{2}}$ $F_1 = \left(\frac{I_1}{2\pi\alpha} \right)^{\frac{1}{2}}$ $I_0 = \left[\sqrt{8}\left(f^2 - 1\right) + \frac{\pi\beta^2}{b} \right] \frac{\alpha^2}{k}$ $I_1 = \left[\sqrt{8}\left(g^2 - 1\right) + \frac{\pi\beta^2}{b} \right] \frac{\alpha^2}{k}$ $f = 1 + \frac{h\left(1 - \alpha \cot \alpha\right)}{2\alpha}$ $g = \left[1 + \frac{h\left(\alpha + \alpha \cot^2 \alpha - \cot \alpha\right)}{4} \right] \frac{\left(\sin \alpha\right)}{\alpha}$ $h = \frac{\sqrt{2}}{\left\{ \cot\left[\frac{\left(\pi - \alpha\right)}{\sqrt{2}} \right] + \sqrt{2} \cot \alpha \right\}}$ $b = \frac{\alpha}{2k}$ $k = \sqrt{\frac{t}{R}} \left[12\left(1 - \nu^2\right) \right]^{-\frac{1}{4}}$ $\beta = 1 + \left(\frac{\pi}{16} \right) b^2 - 0.0293\, b^3 \quad for \quad b \leq 1$ $\beta = \left(\frac{\sqrt{8b}}{\pi} \right)^{0.5} + \left(\frac{0.179}{b} \right)^{0.885} \quad for \quad b > 1$ $\alpha = c / R$
Through Crack in a Sphere	$K_0 = F_0 \sigma_0 \sqrt{\pi a}$	$F_0 = \sqrt{1 + 3\lambda^2}$ $\lambda = \frac{a}{\sqrt{Rt}}$

Table 11.3.14. Stress Intensity Solutions for ASTM Standard Specimens

Standard Center-cracked Tension Specimen	$K_0 = F_0 \sigma_0 \sqrt{\pi a}$ $F_0 = \left[sec\left(\frac{\pi a}{W} \right) \right]^{1/2}$
Standard Compact Specimen	$K_0 = F_0 \sigma_0 \sqrt{\pi a}$ $F_0 = D(\pi a W)^{-1/2} \left[\left(2 + \frac{a}{W} \right) \left(1 - \frac{a}{W} \right)^{-3/2} \right] G$ $G = 0.886 + 4.64\left(\frac{a}{W} \right) - 13.32\left(\frac{a}{W} \right)^2 + 14.72\left(\frac{a}{W} \right)^3 - 5.6\left(\frac{a}{W} \right)^4$
Standard Round Compact Specimen	$K_0 = F_0 \sigma_0 \sqrt{\pi a}$ $F_0 = D\left(\pi\, aW\right)^{-\frac{1}{2}} \left[\left(2 + \frac{a}{W} \right) \left(1 - \frac{a}{W} \right)^{-\frac{3}{2}} \right] G$ $G = 0.76 + 4.8\left(\frac{a}{W} \right) - 11.58\left(\frac{a}{W} \right)^2 + 11.43\left(\frac{a}{W} \right)^3 - 4.08\left(\frac{a}{W} \right)^4$
Standard Arc-Shaped Specimen	$K_0 = F_0 \sigma_0 \sqrt{\pi a}$ $F_0 = D\left(\pi\, aW\right)^{-\frac{1}{2}} \left[\frac{3X}{W} + 1.9 + 1.1\left(\frac{a}{W} \right) \right] GY$ $G = 1 + 0.25\left(1 - \frac{a}{W} \right)^2 \left[1 - \frac{R}{R+W} \right]$ $Y = \sqrt{\frac{a}{W}} \left(1 - \frac{a}{W} \right)^{-\frac{3}{2}} \left[3.74 - 6.3\left(\frac{a}{W} \right) + 6.32\left(\frac{a}{W} \right)^2 - 2.43\left(\frac{a}{W} \right)^3 \right]$
Standard Bend Specimen	$K_0 = F_0 \sigma_0 \sqrt{\pi a}$ $F_0 = \frac{\left[1.99 - \left(\frac{a}{W} \right) \left(1 - \frac{a}{W} \right) \left(2.15 - 3.93\left(\frac{a}{W} \right) + 2.7\left(\frac{a}{W} \right)^2 \right) \right]}{\sqrt{\pi} \left(1 + \frac{2a}{W} \right) \left(1 - \frac{a}{W} \right)^{\frac{3}{2}}}$

11.4 Approximate Solutions for Stress Intensity Factors

This subsection discusses the procedures that one can use to obtain approximate stress intensity solutions for complicated crack problems. Approximate solutions should only be used when the objective of the damage tolerant analysis is to bound the answer and when due care has been taken to understand all aspects of the cracking behavior. Most typically, the approximate solutions are derived using known (handbook) solutions that individually account for the effects of crack geometry, global geometry and loading. As noted in subsection 11.2.1, stress-intensity factors can be added for different types of loadings when the global and crack geometries are the same. This section will concentrate on those cases where the analyst must take existing solutions for several different geometries and estimate the stress-intensity factor for the geometry of interest. In those cases where the individual geometric effects can be accounted for by multiplication of factors, the analysis is referred to as compound analysis.

There are three geometric factors that normally must be accounted for in an approximate damage tolerant analysis: stress concentration, finite width and crack shape. The effects of all three factors on the stress-intensity factor can be established exactly using careful numerical analysis procedures. However, the solution of damage tolerant problems requires more than the accurate development of the stress-intensity factor. Frequently, the growth process causes the crack to constantly change its shape which significantly complicates the crack growth life analysis.

In order to describe how the three geometrical effects can be estimated, a series of examples are presented. In each case, the approximate solutions are based on known solutions. If the actual solution is available, it is compared to the approximate solutions.

11.4.1 Effect of Stress Concentration

The effect of stress concentration is fairly easy to estimate for small cracks because the stress-intensity factor for an elementary crack problem can be multiplied by the elastic stress concentration factor (k_t). Example 11.4.1 illustrates this point. For longer cracks initiating at stress concentrations, the crack will be propagating through the stress field created by the stress concentration and the influence of stress gradient should be taken into account. Example 11.4.2 discusses an approximate method for estimating the stress intensity factor for a crack moving through a stress field generated by a stress concentration.

EXAMPLE 11.4.1 A Small Edge Crack at a Stress Concentration Site

A geometrical description of the physical problem is provided in the figure, where a small edge crack is shown growing from the edge of a wing cutout. The stress-intensity factor for an edge crack (small with respect to the element width) is found in Table 11.3.8, and is given by

$$K = \beta\sigma\sqrt{\pi a}$$

$$\beta = sec\left(\frac{\pi a}{2W}\right)\left(\frac{tan\left(\frac{\pi a}{2W}\right)}{\left(\frac{\pi a}{2W}\right)}\right)^{\frac{1}{2}}\left[0.752 + 2.02\left(\frac{a}{W}\right) + 0.37\left(1 - sin\left(\frac{\pi a}{2W}\right)\right)^{3}\right]$$

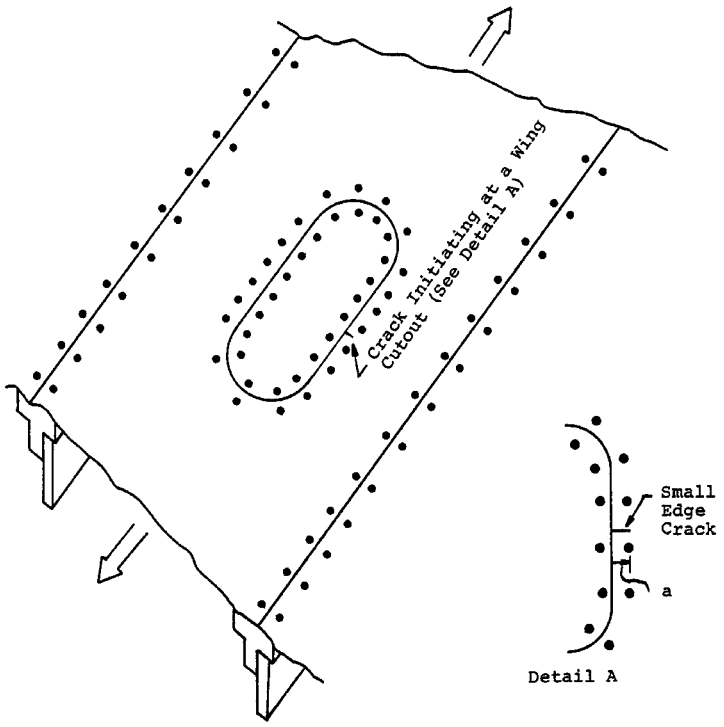

A Small Edge Crack Located at Stress Concentration

The stress term (σ) in the general equation typically represents the remote stress in the uniformly loaded edge cracked plate. This stress is also the stress that would exist along the line of crack propagation if no crack were present. As indicated by the figure, the stress along the line of crack propagation (assuming no crack for a moment) for the given structural configuration is the product of the remote stress and the stress concentration factor (k_t) associated with the cutout, i.e., the local stress is:

$$\sigma_{local} = \sigma \times k_t$$

For the given structural configuration, the stresses along the line of crack propagation more closely represent the type of loading that the small edge crack would experience if it were in a

uniformly loaded edge cracked plate subjected to the higher stresses given by the equation above. It is therefore suggested that the stress-intensity factor for the structural configuration given in the figure would be close to

$$K = (\sigma \times k_t)\beta\sqrt{\pi a}$$

In general, as long as one is dealing with small edge cracks in which the width or other geometrical effects are not important, the final equation provides a reasonable approximation to the stress-intensity factor for an edge crack in the vicinity of a stress concentration. See Example 11.4.2 for a discussion of stress gradient effects.

EXAMPLE 11.4.2 An Edge Crack Growing from a Stress Concentration Site

One difficulty in utilizing the Example 11.4.1 final equation for cracks that emanate from a stress concentration site is that the stress concentration normally generates its own stress field. The stress concentration stress field typically exhibits the highest stresses in the vicinity of the concentration and these high stresses decay as a function of distance from the stress concentration site. The question that needs to be answered is: If the stresses along the crack propagation path are not constant, as in the case of a uniformly loaded edge cracked plate, what stresses should be used to estimate the stress-intensity factor:

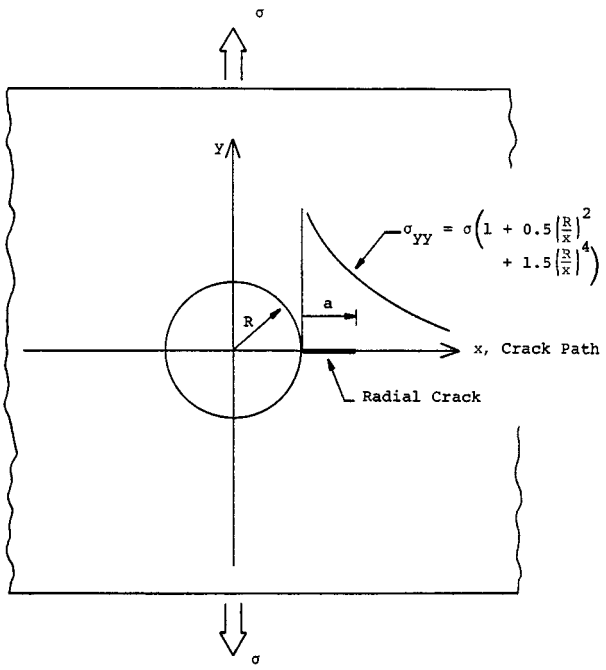

Distribution of Stresses Normal to the Crack Path for a Radial Crack Growing from an Uniaxially Loaded Hole in a Wide Plate

The stress distribution associated with an uncracked hole in a wide plate is shown in the figure. As can be seen, the (normal) stress drops off rapidly as a function of distance from the edge of the hole. An evaluation of the normal stress right at the edge of the hole, i.e., the local stress, leads one to the fact that

$$\sigma_{local} = \sigma \times 3$$

(which is obtained by letting $R/X = 1$ in the equation given in the figure). Thus k_t for the uniaxially loaded hole problem is three, i.e., $k_t = 3$ and the stress-intensity factor for a very small crack of length a at the edge of the hole is

$$K = (\sigma \times 3)\beta\sqrt{\pi a}$$

One estimate of the stress-intensity factor for a longer crack would be given by the equation above; but, this estimate would be high since the stresses along the crack propagation path are noted to be dropping.

11.4.2 Effect of Finite Width

As a crack tip approaches a free edge, its stress-intensity factor rapidly increases and tends to become infinite. One can look at the width contribution as a separate (multiplicative) β factor in the same way that the width contribution affects the solution of the center-crack remotely loaded geometry.

Recall that the stress-intensity factor for a loaded panel of finite width W is given by (see Table 11.3.8)

$$K = \sigma\sqrt{\pi a}\left(\sec\frac{\pi a}{W}\right)^{1/2} \tag{11.4.1}$$

which leads one to conclude that the (multiplicative) width effect β factor required to convert the infinite plate solution to the finite width solution is

$$\beta_W = \left(\sec\frac{\pi a}{W}\right)^{1/2} \tag{11.4.2}$$

Other width correction formulations yield similar results. Most SIF solutions have the width correction included in the formulation if it is necessary. If one is aware of the need the formulation should be checked before using it in an analysis.

11.5 Computer Codes

Many computer software programs have been developed for calculating stress intensity factors, often as part of a life assessment software. Some of these software programs are listed here.

11.5.1 NASGRO Fracture Analysis Software

NASGRO Fracture Analysis Software is a suite of programs based on fracture mechanics principles. NASGRO can be used to analyze crack growth, perform assessments of structural life, compute stresses, and process and store fatigue crack growth properties. The package includes a large set of crack growth rate and fracture data.

NASGRO was originally developed at NASA Johnson Space Center to perform fracture control analysis on NASA space systems. Later, after the NASA/FAA/USAF Aging Aircraft Program was formed and began supporting the development effort, NASGRO was developed further for use in damage tolerance analysis of aircraft, including that required for FAA certification.

The software is comprised of the following three modules:

- NASFLA - Life Assessment
- NASBEM - 2-D Boundary Element
- NASMAT - Database of da/dN & fracture test results

NASFLA is part of the NASGRO 3.0 suite of programs Stress Intensity Factor -These are computed for the crack geometry and loading chosen from the NASFLA library of models, and displayed in tabular or graphical form.

NASBEM is part of the NASGRO 3.0 suite of programs. It is a two-dimensional boundary element program used to perform the following analyses:

- Stress Intensity Factors - These can be calculated for any geometry and loading. Tables of stress intensity factors and corresponding crack lengths can be generated for use by the NASFLA module in performing life assessments.
- Stress Fields - These can be calculated for any collection of points in the two-dimensional uncracked object being modeled including its boundary.

NASMAT is used to store, retrieve and curve fit crack growth and fracture toughness data. It has a database containing over 9000 sets of data. This includes over 3000 sets of fatigue crack growth data and over 6000 fracture toughness data points. These data can be searched, plotted, and fitted to either the NASGRO crack growth rate equation or a user specified growth rate equation, or they can be entered into a growth rate table.

11.5.2 AFGROW Fracture Analysis Software

AFGROW Fracture Analysis Software is a suite of programs based on fracture mechanics

11.5.3 Cracks2000 Structural Integrity Software

The CRACKS2000 program is based on the Linear Elastic Fracture Mechanics (LEFM) approach for estimating the fatigue life of a component with a crack. The LEFM approach uses the stress intensity factor parameter, as the driving factor for crack growth. The Cracks2000

program has considerable flexibility in the analytical modeling of crack growth analysis problems.

Cracks2000 has fifty-one stress intensity factors solutions. There are closed form equations for stress intensity factor solutions for 25 geometries. Many of these solutions are the early Newman-Raju solutions, which are retained for comparisons with older analysis. For the latest stress intensity factor solutions, tables of β-factors are generated from the equations; the tables are used for the life analysis, and can be printed and plotted for β-factors comparison

Additional information on the Cracsk2000 software can be found at:

http://www.udri.udayton.edu/cracks/

or contact

Ms. Peggy C. Miedlar
University of Dayton Research Institute
300 College Park
Dayton, Ohio 45469-0120

Phone: (937) 229-4417

email: miedlar@udri.udayton.edu

11.6 References

S.N. Atluri, A.S. Kobayashi, and M. Nakagaki (1974, April). "Application of an Assumed Displacement Hybrid Finite-Element Procedure to Two-Dimensional Problems in Fracture Mechanics". AIAA Paper 74-390.

D. Broek (1974). Elementary Engineering Fracture Mechanics, Noordhoff International Publishing, Leyden.

H.F. Bueckner (1971). "Weight Functions for the Notched Bar". *Z. Angew Math. Mechanics* (Vol. 51), pp. 97-109.

E. Byskov (1970). "The Calculation of Stress-Intensity Factors Using the Finite-Element Method with Cracked Elements". *International Journal of Fracture Mechanics* (Vol. 6), pp. 159-167.

D.J. Cartwright (1979). "Stress-Intensity Factor Determination, Developments in Fracture Mechanics" (Chapter 2). G.G. Chell (Ed.), London, England: Applied Science Publishers Ltd., p. 29.

D.J. Cartwright and D.P. Rooke (1979). "Green's Functions in Fracture Mechanics, Fracture Mechanics – Current Status and Future Prospects". R.A. Smith (Ed.). Pergamon, pp. 91-123.

D.J. Cartwright and D.P. Rooke (1978). "Evaluation of Stress-Intensity Factors, A General Introduction to Fracture Mechanics" (Chapter 5). London, England: Mechanical Engineering Publications Ltd., p. 54.

S.K. Chan, I.S. Tuba, and W.K. Wilson (1970). "On the Finite-Element Method in Linear Fracture Mechanics". *Eng. Fracture Mechanics 2*, pp. 1-12.

T.A. Cruse (1972). "Numerical Evaluation of Elastic Stress Intensity Factors by the Boundary-Integral Equation Method, The Surface Crack: Physical Properties and Computational Solutions". J.L. Swedlow (Ed.). ASME, New York, pp. 153-170.

T.A. Cruse and P.M. Besuner (1975, April). "Residual Life Prediction for Surface Cracks in Complex Structural Details". *Journal of Aircraft* (Vol. 12, No. 4), pp. 369-375.

E399 (2000). ASTM Designation: "E399, Standard Test Method for Plane-Strain Fracture Toughness of Metallic Materials". *2000 Annual Book of ASTM Standards Section 3* (Vol. 03.01). American Society for Testing and Materials, Philadelphia.

F. Erdogan and J.J. Kibler (1969, September). "Cylindrical and Spherical Shells with Cracks". *International Journal of Fracture Mechanics* (Vol. 5, No. 3), pp. 229-237.

C.E. Fedderson (1966). Discussion to: "Plane Strain Crack Toughness Testing of High Strength Metallic Materials", by W.F. Brown, Jr. and J.E. Srawley. ASTM STP 410, Philadelphia, pp. 77-79.

R.G. Forman, J.C. Hickman and V. Shivakumar (1985). "Stress-Intensity Factors for Circumferential Through Cracks in Hollow Cylinders Subjected to Combined Tension and Bending Loads". *Engineering Fracture Mechanics*, (Vol. 21, No. 3), pp. 563-571.

R.G. Forman and V. Shivakumar (1986). "Growth Behavior of Surface Cracks in the Circumferential Plane of Solid and Hollow Cylinders" *Fracture Mechanics: Seventeenth*

Volume. J.H. Underwood, R. Chait, C.W. Smith, D.P. Wilhelm, W.A. Andrews and J.C. Newman (Eds.). ASTM STP 905, Philadelphia, pp 59-74.

R.G. Forman, V. Shivakumar, J.C. Newman, Jr. (1989). "Fatigue Crack Growth Computer Program – NASA/FLAGRO". JSC-22267, NASA/Lyndon B. Johnson Space Center, Houston, TX, August 1986, Revised March 1989.

R.G. Forman and S.R. Mettu (1992). "Behavior of Surface and Corner Cracks Subjected to Tensile and Bending Loads in a Ti-6Al-4V Alloy". *Fracture Mechanics:Twenty-Second Symposium (Volume I)*. H.A. Ernst, A. Saxena and D.L. McDowell (Eds.). ASTM STP 1131, Philadelphia, pp, 519-546.

R.G. Forman, V. Shivakumar, S.R. Mettu, J.C. Newman, Jr. (1998, September). "Fatigue Crack Growth Computer Program 'NASGRO' Version 3.00, Reference Manual". JSC-22267B, NASA/Lyndon B. Johnson Space Center, Houston, TX.

J.P. Gallagher, H.D. Stalnaker, and J.L. Rudd (1974, May). "A Spectrum Truncation and Damage Tolerance Study Associated with the C-5A Outboard Pylon Truss Lugs". AFFDL-TR-74-5.

R.H. Gallagher (1978). "A Review of Finite Element Techniques in Fracture Mechanics, Proceedings First International Conference on Numerical Methods in Fracture Mechanics". A.R. Luxmoore and D.R.J. Owen (Eds.). University College, Swansea, UK.

J.N. Goodier (1969). "Mathematical Theory of Equilibrium of Cracks, Fracture II". H. Liebowitz (Ed.). Academic Press, pp. 2-67.

A.F. Grandt, Jr. (1975, April). "Stress Intensity Factors for Some Through-Cracked Fastener Holes". *International Journal of Fracture*, (Vol. 11, No. 2), pp. 283-294.

A.F. Grandt, Jr. and T.D. Hinnericks (1974, September). "Stress Intensity Factor Measurements for Flawed Fastener Holes, Proceedings of the Army Symposium on Solid Mechanic". Cape Cod, MA, pp. 10-12.

B. Gross, J.E. Srawley, and W.F. Brown (1964). "Stress-Intensity Factors for Single-Edge Notch Tension Specimen by Boundary Collocation of a Stress Function". NASA TN-D-2395.

T.K. Hellen (1979). "Numerical Methods in Fracture Mechanics, Developments in Fracture Mechanics 1" (Chapter 5). G.G. Chell (Ed.). London, England: Applied Science Publishers Ltd., pp. 145-181.

T.M. Hsu and J.L. Rudd (1978). "Green's Function for Thru-Crack Emanating from Fastener Holes". *Fracture* (1977, Vol. 3A). D.M.R. Taplin (Ed.). Pergamon Press, p. 139.

T.M. Hsu, W.M. McGee, and J.A. Aberson (1978, April). "Extended Study of Flaw Growth at Fastener Holes". AFFDL-TR-77-83 (Vol. 1).

M. Isida (1973). "Laurent Series Expansion for Internal Crack Problems" in *Methods of Analysis and Solutions of Crack Problems*. G.C. Sih (Ed.). Noordhoof International Publishing, Leyden, pp. 56-130.

L.A. James and W.E. Anderson (1969). "A Simple Experimental Procedure for Stress Intensity Factor Calibration, Engineering Fracture Mechanics" (Vol. 1), pp. 565-568.

S. Jordon, J. Padlog, A.T. Hopper, E.F. Rybicki, L.E. Hulbert and M.F. Kanninen (1973, June). "Development and Application of Improved Analytical Techniques for Fracture Analysis Using MAGIC III". AFFDL-TR-73-61.

A.S. Kobayashi, Ed. (1973). "Photoelastic Techniques, Experimental Techniques in Fracture Mechanics 1". A.S. Kobayashi (Ed.). Society of Experimental Stress Analysis Monograph 1, pp. 126-145.

N.I. Mushkelishvili (1933). "Some Basic Problems of the Mathematical Theory of Elasticity". English translation, Noordhoff International Publishing, Leyden (1953).

J.C. Newman, Jr. (1971). "An Improved Method of Collocation for the Stress Analysis of Cracked Plates with Various Shaped Boundaries". NASA-TN-D-6376.

J.C. Newman, Jr. (1976, December). "Fracture Analysis of Surface and Through Cracks in Cylindrical Pressure Vessels". NASA TN D-8325.

J.C. Newman, Jr. and I.S. Raju (1979, July). "Stress-Intensity Factors for Internal Surface Cracks in Cylindrical Pressure Vessels". NASA-TM-80073.

J.C. Newman, Jr. and I.S. Raju (1984, April). "Stress-Intensity Factor Equations for Cracks in Three-Dimensional Finite Bodies Subjected to Tension and Bending Loads". NASA TM 85793.

P.F. Packman (1975). "The Role of Interferometry in Fracture Studies, Experimental Techniques in Fracture Mechanics 2" (Chapter 2). A.S. Kobayashi (Ed.). SESA, pp. 59-87.

P.C. Paris and G.C. Sih (1965). "Stress Analysis of Cracks". ASTM STP 381, pp. 30-81.

P.C. Paris and G.C. Sih (1964). "Stress Analysis of Cracks". ASTM STP 381, Philadelphia, pp. 30-81.

P.C. Paris, M.P. Gomez, and W.E. Anderson. (Jan 1961). "A Rational Analytic Theory of Fatigue, The Trend in Engineering" (Vol. 13, No. 1). University of Washington, p. 9.

A.P. Parker (1981). The Mechanics of Fracture and Fatigue, An Introduction. E. and F.N. Spon, Ltd., London, England.

F.J. Pitoniak, A.F. Grandt, L.T. Montulli, and P.F. Packman (1974). "Fatigue Crack Retardation and Closure in Polymethyl Methacrylate". Engineering Fracture Mechanics (Vol. 5).

I. S. Raju and J.C. Newman, Jr. (1984). "Stress-Intensity Factors for Circumferential Surface Cracks in Pipes and Rods Under Tension and Bending Loads". *Fracture Mechanics: Seventeenth Volume.* J.H. Underwood, R. Chait, C.W. Smith, D.P. Wilhelm, W.A. Andrews and J.C. Newman (Eds.). ASTM STP 905, Philadelphia, pp789-805.

I.S. Raju and J.C. Newman, Jr. (1988). "Stress Intensity Factors for Corner Cracks in Rectangular Bars". *Fracture Mechanics: Nineteenth Symposium*. T.A. Cruse (Ed.). ASTM STP 969, Philadelphia, pp.43-55.

J.R. Rice (1968). "Mathematical Analysis in the Mechanics of Fracture". *Fracture* (Vol. 2). H. Liebowitz (Ed.). New York: Academic Press, pp. 191-308.

J.R. Rice (1972). "Some Remarks on Elastic Crack-Tip Stress Fields". *International Journal of Solids and Structures* (Vol. 8), pp. 751-758.

R. Roberts and J.J. Kibler (1971). “Some Aspects of Fatigue Crack Propagation”. *Engineering Fracture Mechanics* (Vol. 2), pp. 243-260.

D.P. Rooke and D.J. Cartwright (1976). *Compendium of Stress Intensity Factors*. Her Majesty’s Station Office, London.

V. Shivakumar and Y.C. Hsu (1977, March). “Stress-Intensity Factors for Cracks Emanating from the Loaded Fastener Hole”. Presented at the International Conference on Fracture Mechanics and Technology, Hong Kong.

G.C. Sih (1973a). “Handbook of Stress Intensity Factors”. Institute of Fracture and Solid Mechanics, Lehigh University.

G.C. Sih (1973b). “Methods of Analysis and Solutions of Crack Problems”. Noordhoff International Publishing, Leyden.

C.W. Smith (1975). “Use of Three-Dimensional Photoelasticity and Progress in Related Areas, Experimental Techniques in Fracture Mechanics 2”. A.S. Kobayashi (Ed.). Society of Experimental Stress Analysis, Monograph 2, pp. 3-58.

I.N. Sneddon and M. Lowengrub (1969). *Crack Problems in the Classical Theory of Elasticity*. New York: John Wiley and Sons, Inc.

T. Swift and D.Y. Wang (1969). “Damage Tolerant Design Analysis Methods and Test Verification of Fuselage Structure”. Air Force Conference on Fatigue and Fracture, AFFDL-TR-70-144, pp. 653-683.

H.P. Tada, P.C. Paris and G. R. Irwin (1973). *The Stress Analysis of Cracks Handbook*. Del Research Corporation, Hellertown, PA.

D.M. Tracey (1971). “Finite Elements for Determination of Crack-Tip Elastic Stress-Intensity Factors”. *English Fracture Mechanics (Vol. 3)*, pp. 255-265.

P.F. Walsh (1971). “The Computation of Stress-Intensity Factors by a Special Finite-Element Technique”. *Journal of Solids and Structures (Vol. 7)*, pp. 1333-1392.

J.M. Westergaard (1939). “Bearing Pressures and Cracks”. *Journal Applied Mechanics (Vol. 61)*, pp. A49-53.

D.P. Wilhem (1970, February). “Fracture Mechanics Guidelines for Aircraft Structural Applications”. AFFDL-TR-69-111.

I. J. Zatz, H.L. Eidinoff and H. Armen, Jr. (1981). “An Application of the Energy Release Rate Concept to Crack Growth in Attachment Lugs”. AIAA Paper No. 81-0491.

Sample Problems

PROBLEM NO. FAC-1

Title: Computing Stress Intensity Factor Histories with the Finite Element Method and Interfacing with AFGROW and NASGRO

Objective:

To illustrate the process of using a finite element program, such as FRANC2D/L, to compute stress intensity factor histories accurately, so that they can be transmitted to AFGROW or NASGRO for fatigue crack growth rate (FCGR) and life predictions.

General Description:

This problem details the processes of using the finite element method to compute accurate relationships between stress intensity factors and crack length, and of communicating these relationships to AFGROW or NASGRO for further processing for FCGR and life predictions. Two problems are used for illustration: a typical detail in the standard library of AFGROW or NASGRO to confirm stress intensity factor accuracy, and a more complex problem for which no standard library solution is available.

Topics Covered:	Finite element analysis, stress intensity factor computation, non-standard geometry and/or boundary conditions, geometry factors for AFGROW or NASGRO
Type of Structure:	any single or multiple layer planar structure amenable to 2D or axisymmetric structural idealization

Relevant Sections of Handbook: Sections 2, 5, 11

Author: Dr. A. R. Ingraffea

Company Name: Fracture Analysis Consultants, Inc.

121 Eastern Heights Drive
Ithaca, NY 14850
607-257-4970

Contact Point: Dr. Paul Wawrzynek
Phone: 607-257-4970
e-Mail: wash@fracanalysis.com

Fracture Analysis
Consultants, Inc.

Overview of Problem Description

An essential task in predicting fatigue crack growth rate and remaining fatigue life is the accurate computation of a relationship between crack length and stress intensity factor. In Example 1 of this problem a finite element code is used to compute such a relationship on a relatively simple structural detail, Figure FAC-1.1. The pin load, *P*, is distributed as a normal pressure following a cosine function on the lower half-circumference of the hole. To assess the accuracy of the finite element calculations, they are compared to standard solutions stored in NASGRO for this detail.

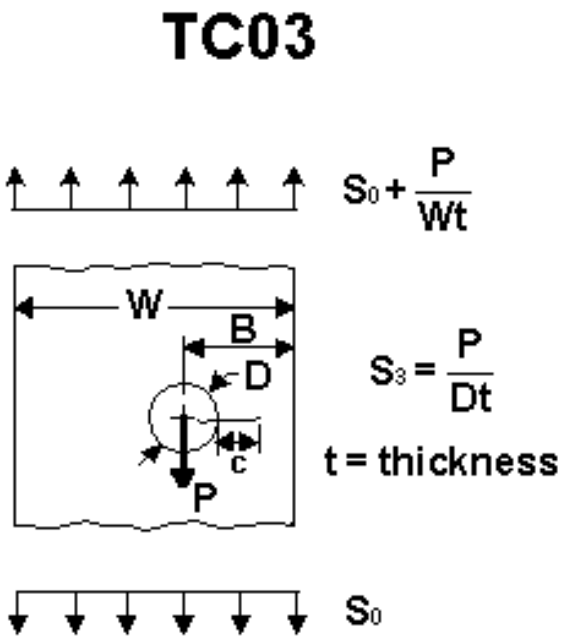

Figure FAC-1.1. ***Example 1*** *of this problem: a structural detail from standard library in NASGRO (Problem TC03) and AFGROW (Single Through Crack at Hole-Standard Solution). Here W =10, D = 1, B = 5, t = 1, S_o = 10, and P = 10, and c/D is varied from 0.09 to 1.35. All in kips and inches. Figure taken from NASGRO 3.*

Frequently, the structural detail of interest is not contained in standard libraries. In this case, either the actual detail must be idealized to resemble a standard solution, or a finite or boundary element model must be constructed. The finite element method can be used effectively in the role of general stress intensity factor calculator. The method can accommodate virtually any actual situation involving non-standard geometry and boundary conditions, and include multiple cracks, multiple materials, material anisotropy, and initial stresses.

As an example of this situation, a variant of the detail shown in Figure FAC-1.1 is studied in Example 2 of this problem, Figure FAC-1.2. This figure shows a simple lug under non-symmetric loading. A contact-fit pin is inserted in the hole, and the pin load, *P*, is distributed to the hole by way of an elastic contact analysis. A crack is initiated from a location of high tensile stress concentration along the lug bore, and then allowed to propagate in mixed mode.

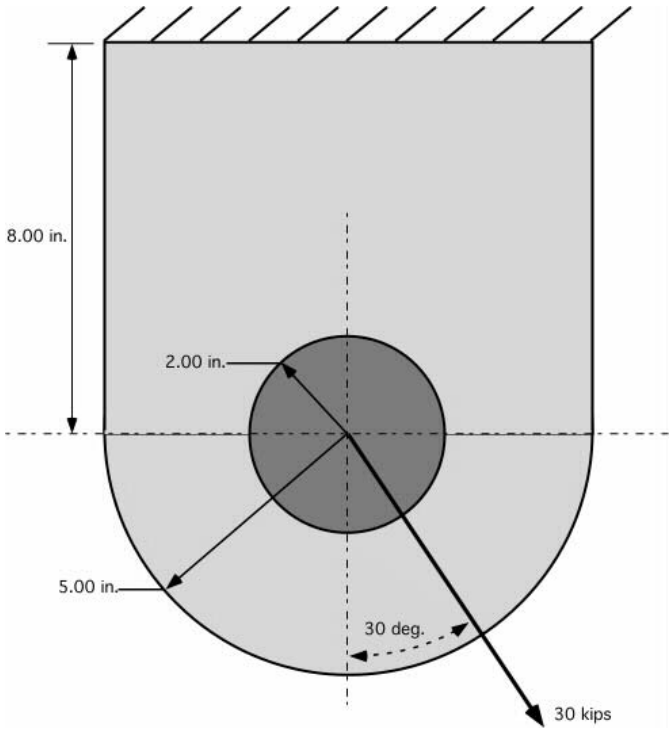

Figure FAC-1.2. ***Example 2*** *of this problem: a lug under unsymmetrical load. Lug and pin are both steel, E= 29,000ksi, ν=0.30, and frictionless, contact-fit of the pin in the lug is assumed. Thickness is 1.00 in.*

Computational Models: Example 1

Two finite element models shown in Figures FAC-1.3 and FAC-1.4 were used for Example 1 of this problem. The purpose of using two meshes is to show the degree of mesh refinement that is needed to achieve accurate values of stress intensity factors using at least quadratic order triangular and quadrilateral elements. There are about 2300 degrees-of-freedom in the initial, crack-free mesh shown in Figure FAC-1.3, hereafter called the coarse mesh.

There are about 9800 degrees-of-freedom in the initial, crack-free mesh shown in Figure FAC-1.4, hereafter called the refined mesh. The number of degrees-of-freedom in each model increases as the mesh is updated to accommodate crack growth.

The mesh is refined in the region of crack growth to the right of the hole in each case. A rule-of-thumb in creating the initial mesh in the region of expected crack growth is to make the average element size there smaller than (say one-half to one-quarter) the specified increment in crack length. Examples of this practice are shown in Figures FAC-1.3(b) and FAC-1.4(b) that show a detail of the mesh around a crack tip. FRANC2D/L automatically remeshes after each increment of crack growth. Figure FAC-1.5 shows a detail of the refined mesh after a few steps of crack growth.

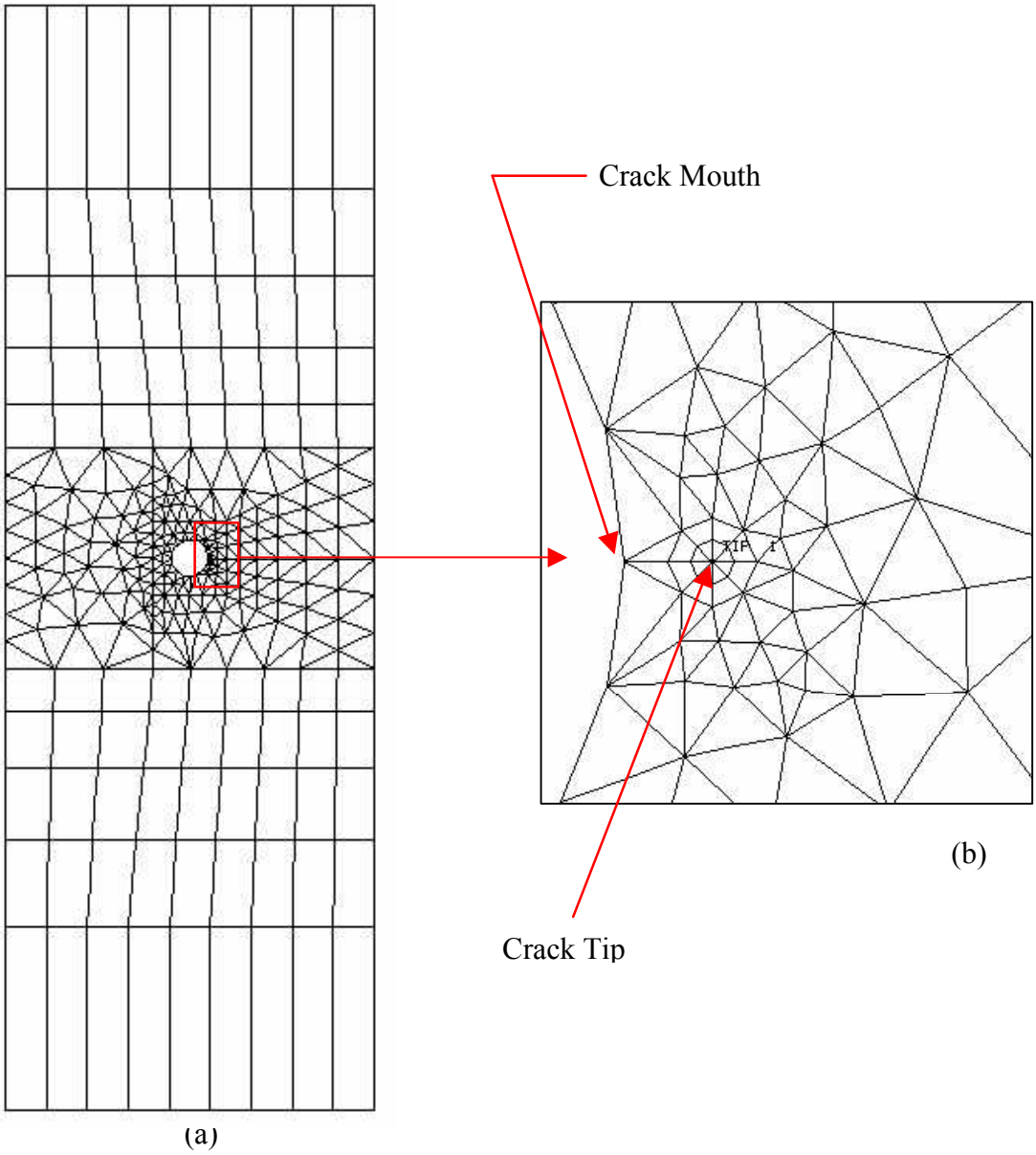

Figure FAC-1.3. ***Example 1****. (a) Coarse finite element model for structural detail shown in Figure FAC-1.1. (b) Detail of meshing near initial crack tip, c/D=0.09.*

Figures FAC-1.3(b) and FAC-1.4(b) show some other important details of meshing around a crack tip. These include the relative size, type, and distribution of elements immediately surrounding the crack tip. It is well known that mixed-mode stress intensity factors can be computed with excellent accuracy using the equivalent domain formulation of the elastic J-Integral (Nikishkov 1987). FRANC2D/L can automatically compute stress intensity factors with this technique. Other techniques, such as displacement correlation (Chan 1970) and modified crack closure (Rybicki 1977), are also available, but these have proven to be generally less accurate for a given discretization. This formulation of

the elastic J-Integral technique does not require extreme levels of mesh refinement in the vicinity of a crack tip.

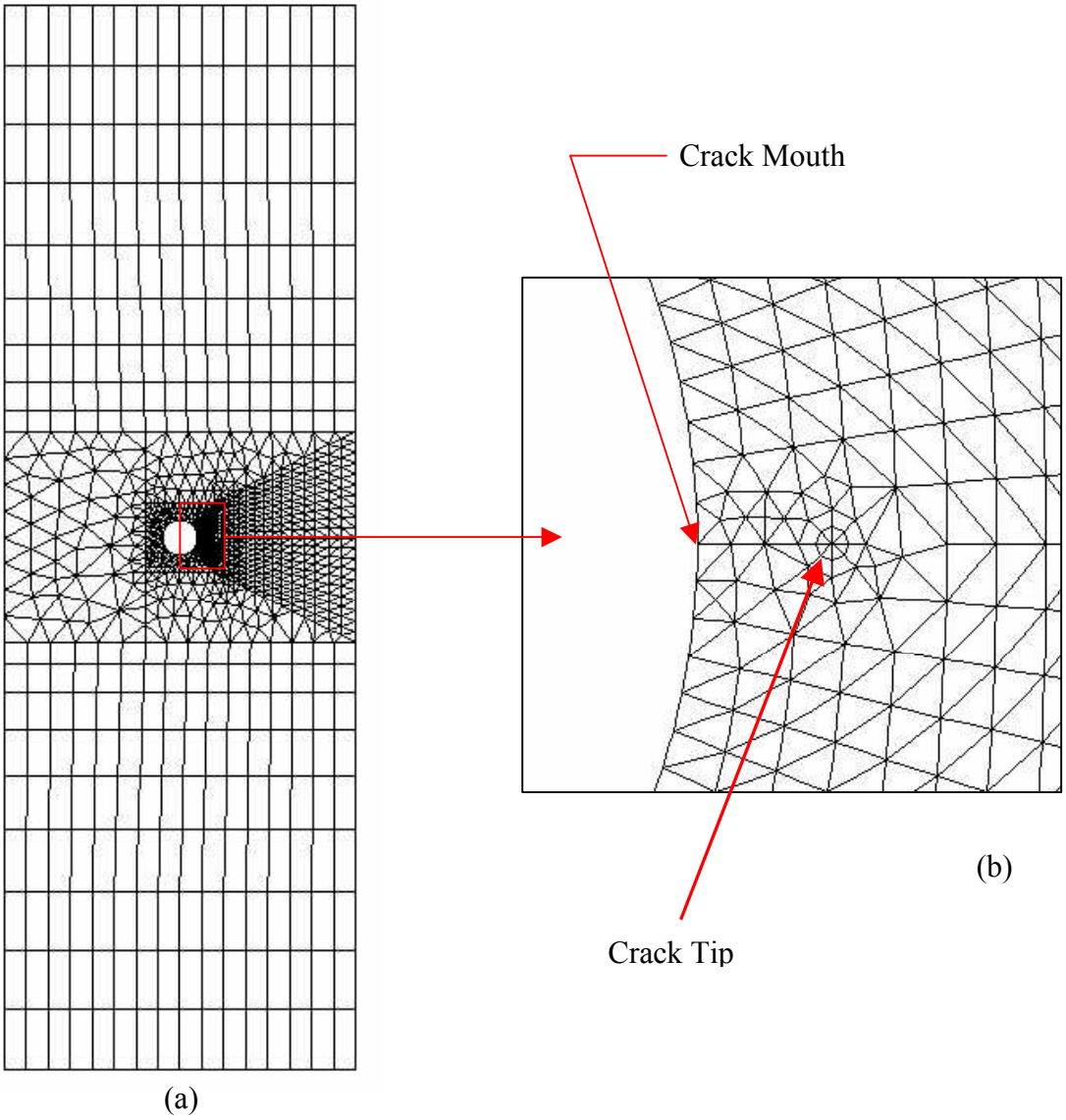

Figure FAC-1.4. ***Example 1****. (a) Refined finite element model for structural detail shown in Figure FAC-1.1. (b) Detail of meshing near initial crack tip, c/D=0.09.*

Experience has shown that the treatment shown in this example, a rosette of eight six-noded triangular elements immediately surrounding the tip, quarter-point versions of these elements, and element size ranging from a few to as much as 25 percent of crack length, will produce very accurate values of stress intensity factors. The use of quarter-point versions of these elements produces the singular stress field known to exist in linear elastic fracture mechanics, is automatically done in FRANC2D/L, and is well documented in the literature (Barsoum 1976).

Computational models like these require little effort to generate. An experienced finite element user can produce one in less than one-half hour of person-time using codes such as PATRAN[tm] or ProE[tm].

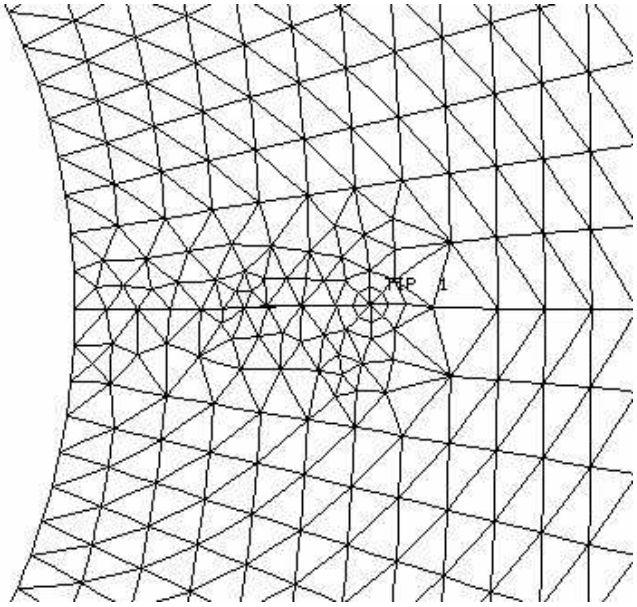

Figure FAC-1.5. ***Example 1****. Detail of refined finite element model for structural detail shown in Figure FAC-1.1 after a few steps of crack propagation, showing automatic remeshing.*

Computational Results: Example 1

Table FAC-1.1 shows a comparison between the stress intensity factor histories from NASGRO and finite element analysis for the coarse mesh. Each step of analysis took less than one second of total computer time on a PC running Windows 2000 on a 300MHz Pentium II processor. Shown are stress intensity factors due to the pin load, S_3, and the bypass load, S_0, and the total of these. The average difference in total stress intensity factor across the range of crack lengths analyzed was less than 1 percent.

Table FAC-1.2 shows a comparison between the stress intensity factor histories from NASGRO and finite element analysis for the refined mesh. Each step of analysis took about 10 seconds of total computer time on a PC running Windows 2000 on a 300MHz Pentium II processor. The average difference in total stress intensity factor across the range of crack lengths analyzed remained less than 1 percent, but did not improve over the results from the coarse mesh. This implies that the results from finite element analysis have converged to values acceptably close to those produced from the boundary element method used to generate the values in NASGRO. It also implies that relatively coarse meshes, such as those shown in Figure FAC-1.3, can be used to compute stress intensity factors accurately when used with the equivalent domain formulation of the elastic J-

Integral. Finally, the person-effort and computer time needed to produce an accurate stress intensity factor history for such 2D details are not overwhelming.

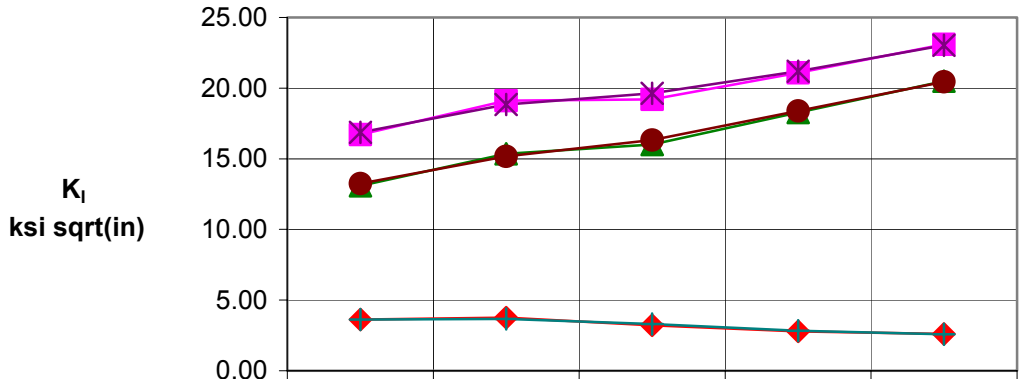

	0.09	0.23	0.45	0.9	1.35
K(Total) NASGRO	16.72	19.12	19.21	21.08	23.10
K(So) NASGRO	13.09	15.36	16.00	18.28	20.50
K(S3) NASGRO	3.63	3.76	3.21	2.79	2.60
K(Total) FRANC2D	16.87	18.85	19.64	21.2	23.02
K(S0) FRANC2D	13.24	15.18	16.33	18.38	20.44
K(S3) FRANC2D	3.63	3.67	3.31	2.82	2.59

c/D

Table FAC-1.1. ***Example 1****. Comparison between NASGRO and finite element analysis stress intensity factor histories for Example 1, using the coarse mesh shown in Figure FAC-1.3.*

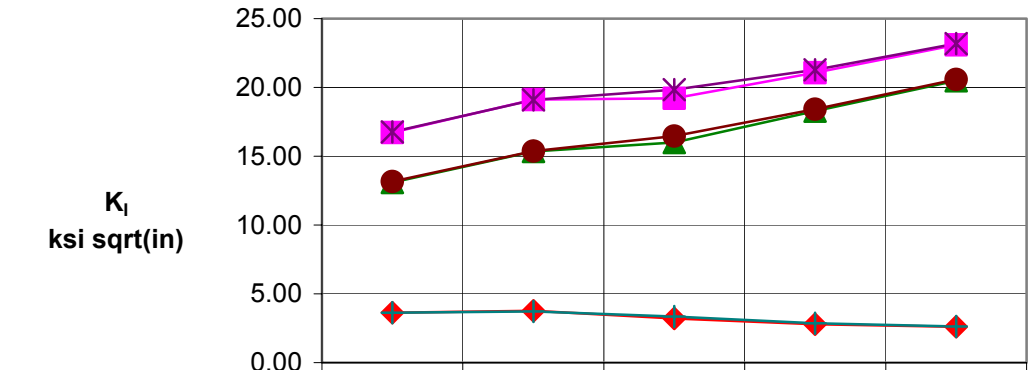

	0.09	0.23	0.45	0.9	1.35
K(Total) NASGRO	16.72	19.12	19.21	21.08	23.10
K(So) NASGRO	13.09	15.36	16.00	18.28	20.50
K(S3) NASGRO	3.63	3.76	3.21	2.79	2.60
K(Total) FRANC2D	16.77	19.1	19.83	21.27	23.19
K(So) FRANC2D	13.16	15.37	16.47	18.41	20.57
K(S3) FRANC2D	3.62	3.73	3.36	2.85	2.63

c/D

Table FAC-1.2. ***Example 1****. Comparison between NASGRO and finite element analysis stress intensity factor histories for Example 1, using the refined mesh shown in Figure FAC-1.4.*

Computational Models: Example 2

Figure FAC-1.6 shows the initial finite element model for the lug problem shown in Figure FAC-1.2. The lug and its frictionless, contact-fit pin are both steel. The elastic contact problem between the pin and the lug is solved in FRANC2D/L. Six-noded, zero-thickness interface elements with non-linear constitutive capability are inserted around the contact surface. This process is automated: the lug and pin are assigned different material property set numbers (but the same properties), and a feature in FRANC2D/L finds the closed curve defining the boundary between these two sets and automatically inserts interface elements along the entire curve.

The constitutive model used to represent the normal contact conditions is shown in Figure FAC-1.7. No tension is allowed across the contact, and a high compressive normal stiffness is assigned to minimize intrusion of the pin into the lug.

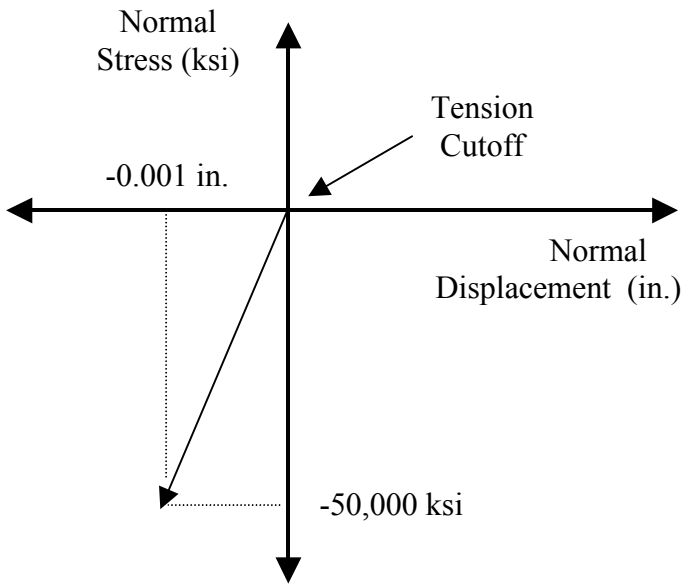

Figure FAC-1.7. ***Example 2****. Constitutive model for normal stress-displacement on the pin/lug contact surface.*

A non-linear solver is now needed, and FRANC2D/L uses a dynamic relaxation procedure (Underwood 1983). This is a relatively slow but extremely robust algorithm for solving nonlinear equilibrium equations. Figure FAC-1.8 presents the uncracked, deformed shape and shows that separation of the pin from the lug has occurred from about the 8 o'clock to the 2 o'clock positions, while non-overlapping contact occurs along the rest of the contact. Figure FAC-1.9 shows contours of major principal stress for the initial, uncracked configuration. This solution involved about 9200 DOF, and, with an error tolerance of 0.0005 on both equilibrium and displacement change between time steps, required about 5200 time steps and 2.5 minutes on a PC running Windows 2000 on a 1GHz Pentium III processor.

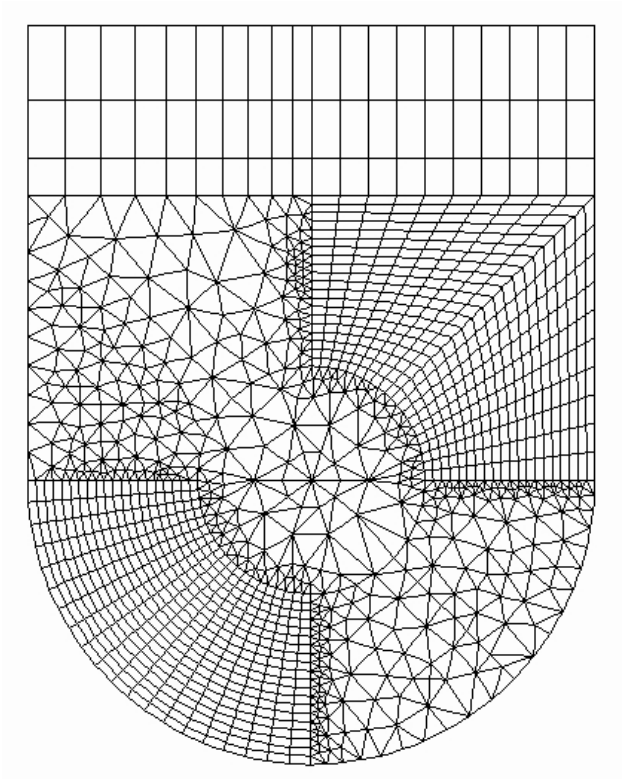

Figure FAC-1.6. ***Example 2****. Initial finite element mesh.*

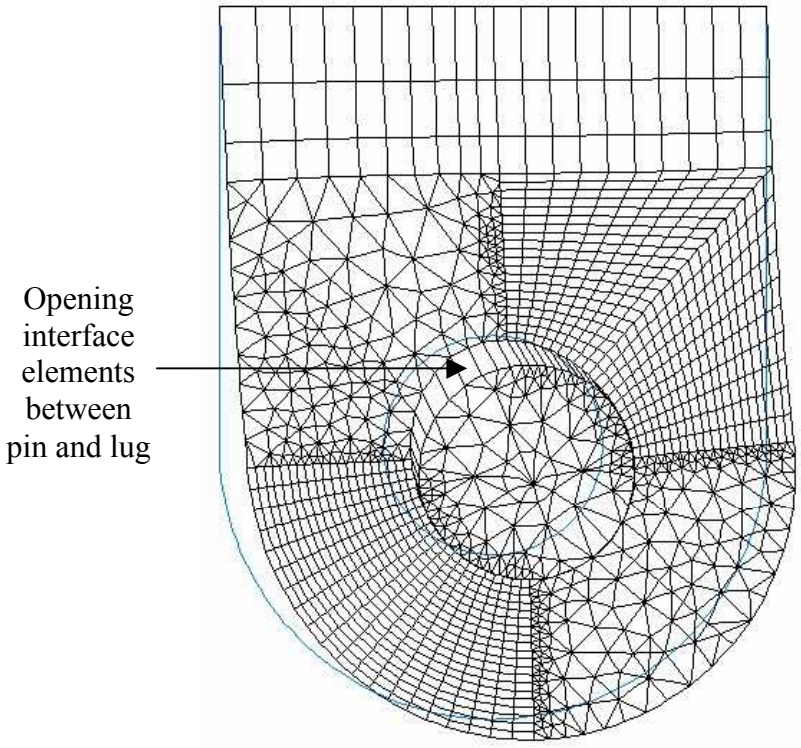

Figure FAC-1.8. ***Example 2****. Deformed shape of uncracked configuration. Amplification factor is 225.*

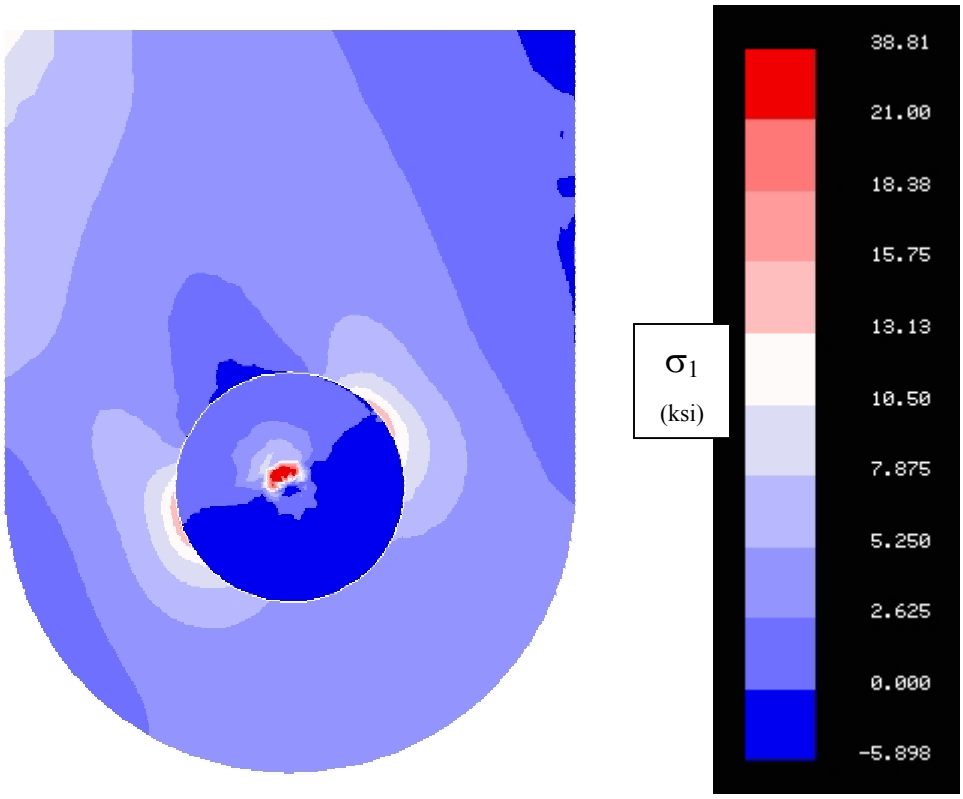

Figure FAC-1.9. ***Example 2****. Contours of major principal stress in uncracked condition.*

Computational Results: Example 2

Figure FAC-1.8 indicates that there are two locations of high stress concentration around the lug bore, as expected. A slightly higher concentration occurs in the lower left quadrant, at about the 8 o'clock position, and a short crack (0.067 in.) is initiated at the location of highest circumferential tensile stress near this point. Growth of this crack is then simulated by:

1. Computing K_I and K_{II} using the equivalent domain formulation of the elastic J-Integral;
2. Calculating the direction of crack growth using the maximum circumferential tensile stress theory (Erdogan 1963);
3. Extending the crack by 0.075 inch in this direction;
4. Resolving the finite element problem, including the non-linear contact between lug and pin;
5. Repeating steps 1-4 until the crack has extended about 2.5 inch at which point fatigue life or residual strength limits are likely to have been reached.

Figure FAC-1.10 shows the corresponding amplified displaced shape, while Figure FAC-1.11 shows the resulting stress intensity factor histories. Figure FAC-1.10 shows that the crack trajectory is not quite radial, and is responding to the asymmetrical loading and geometry. The trajectory is dictated here by the maximum circumferential tensile stress

theory that requires that K_{II} remain zero along the crack path. With a finite element model that discretizes the trajectory into finite, straight segments, there will always be residual, non-zero values of K_{II} computed at each crack tip location. If the segments are short enough, these residuals should be small compared to the K_I values. Figure FAC-1.12 shows that the values of K_{II} are oscillating around zero, and are indeed small, in this case, never reaching more than 3.5% of K_I. The highest values usually occur early in the trajectory while the finite element model is adjusting to the stress field that is evolving as a result of crack growth, as shown in Figure FAC-1.12. The key practical issue suggested here is the length of crack growth increment. This length should be sufficiently short to accurately discretize a curvilinear trajectory and provide enough data points for the accurate integration required for FCGR calculations, while not being so short that excessive computation times accrue. Here 32 increments were used. The number of DOF's grew to nearly 14,000 at the last increment, and a total of about 2 hours of computing time was required.

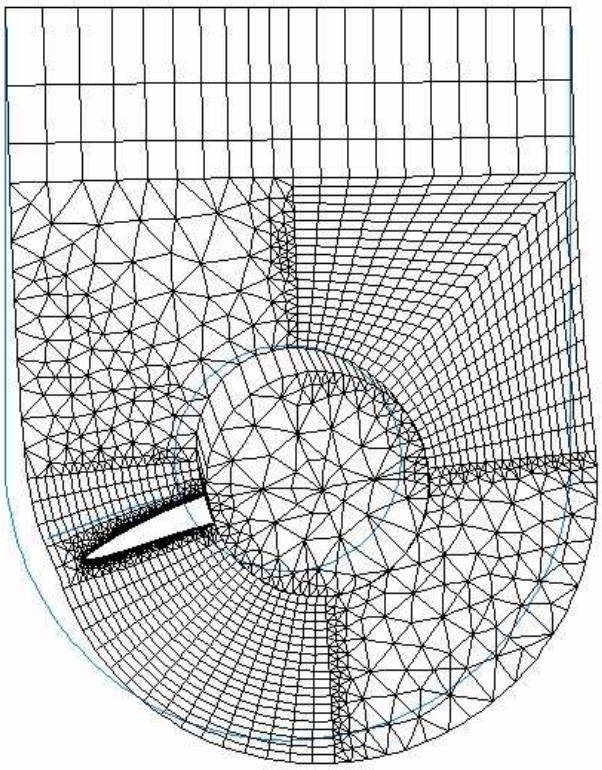

Figure FAC-1.10. ***Example 2****. Final deformed shape of single cracked configuration. Amplification factor is 150.*

As previously mentioned, a finite element code with fracture mechanics features can be thought of as a general stress intensity factor calculator. As such it can be used to attack practically interesting variants of problems. For example, it is possible that two fatigue cracks might initiate in this lug problem, one from each of the locations of initially high stress concentration. This possibility is also simulated here, under the assumptions that

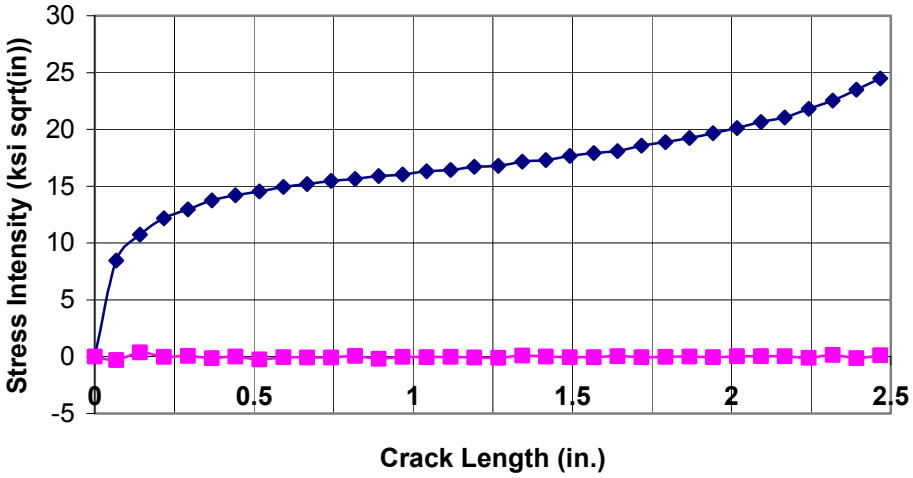

Figure FAC-1.11. ***Example 2****. Computed stress intensity factor histories. Single crack case.*

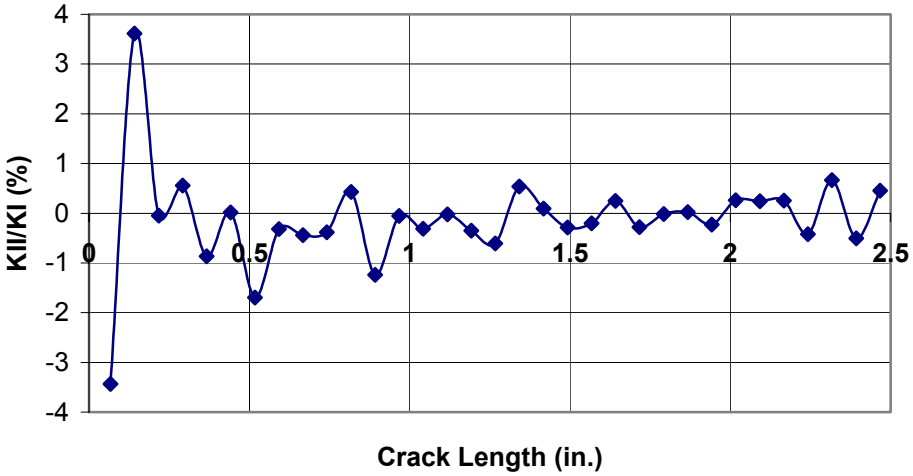

Figure FAC-1.12. ***Example 2****. History of computed ratio of stress intensity factors. Single crack case.*

the cracks initiate simultaneously, and that they have equal rates of growth. The resulting trajectories under these simplifying assumptions are shown in Figure FAC-1.13. The corresponding mode I stress intensity factor histories are given in Figure FAC-1.14. This figure shows that, even if initiation were simultaneous, rate of growth would not be equal; the left crack would have higher growth rate. However, even under these simplifying assumptions, Figure FAC-1.14 also shows that the growth rate of the left crack would be higher than it would be if it were the only crack to occur.

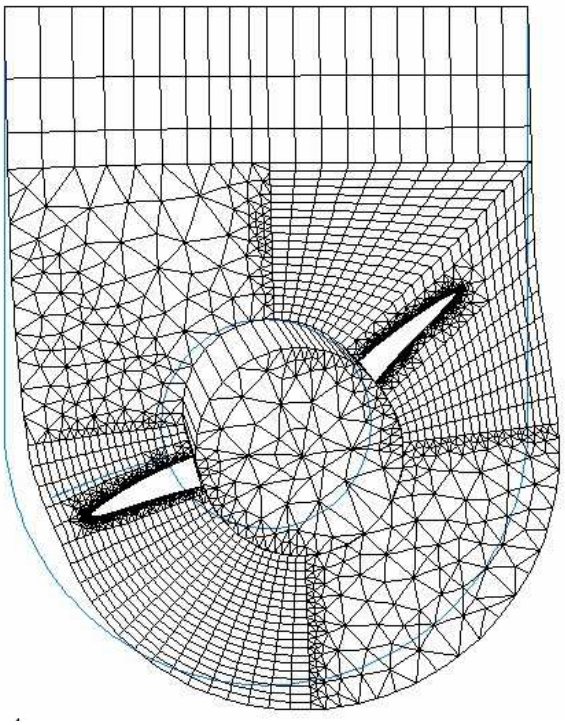

Figure FAC-1.13. ***Example 2****. Final deformed shape of multiply cracked configuration. Amplification factor is 100.*

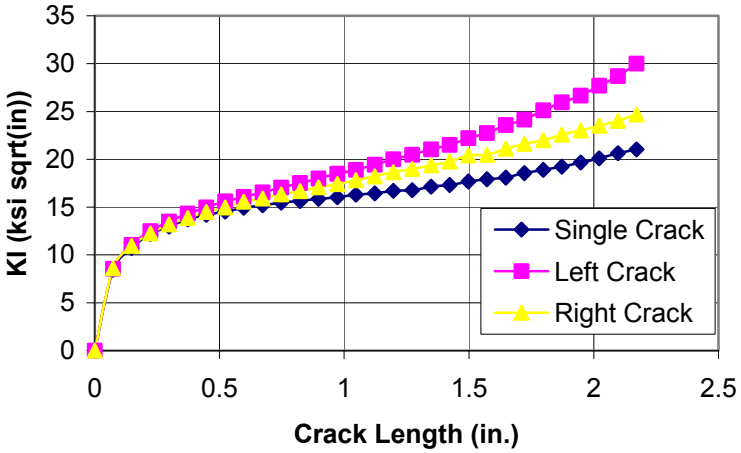

Figure FAC-1.14. ***Example 2****. Comparison of stress intensity factor histories for single and multiple crack cases.*

It is currently possible to couple the results of a stress intensity factor history analysis from finite element analyses *for a single crack* to FCGR simulators like NASGRO and AFGROW. This process is described next.

Interfacing with NASGRO and AFGROW

This section describes the process of interfacing the stress intensity factor history from finite element analyses with NASGRO (NASGRO 2000) or AFGROW (AFGROW 2000) to do FCGR and remaining life assessments.

Interfacing with NASGRO

In addition to its built in library of stress intensity factor solutions for many standard structural geometries, NASGRO offers the capability of performing crack growth analysis for non-standard geometries through its user defined data table (DT) approach. In this approach NASGRO requests stress intensity factor input in the form of a one-dimensional table (NASGRO:Reference Manual, Appendix C):

a/D	F_3
0.067	0.52
0.142	0.96
0.217	1.34
0.292	1.66
0.367	1.97
0.442	2.23

Table FAC-1.3. Portion of NASGRO stress intensity factor data table for a non-NASGRO-standard geometry. D= 4.0 in. and S_3 = 7.5 ksi.

NASGRO's general expression for stress intensity factors is,

$$K = \left[S_0F_0 + S_1F_1 + S_2F_2 + S_3F_3 + S_4F_4\right]\sqrt{\pi a} \qquad \text{NASGRO Eqtn. (2.2)}$$

where the stress quantities S_0, S_1 and S_2, S_3, and S_4 are for applied tension/compression, bending in the thickness and width directions, pin bearing pressures, and special cases, respectively. For Example 2 only S_3 is non-zero, so NASGRO expects a relationship of the form

$$K = S_3F_3\sqrt{\pi a}$$

where F_3 is the geometry correction factor for the present lug problem. The values of F_3 needed for the NASGRO data table are contained within the stress intensity factor values computed with FRANC2D/L, and can be explicitly obtained through

$$F_3 = \frac{K_{FRANC}}{S_3\sqrt{\pi a}}$$

Table FAC-1.3 contains a portion of the geometry correction factor history obtained from FRANC2D/L for Example 2 with a single crack. Herein D is the pin diameter, 4.0 in., and S_3 is the pin bearing stress

$$S_3 = P/Dt = 30 \text{ kips}/((4 \text{ in.})(1.0 \text{ in})) = 7.5 \text{ ksi}$$

Once stress intensity factor history data in this form has been supplied, all standard NASGRO fatigue crack growth capabilities become available for any cracked structural model for which FRANC2D/L is an appropriate modeling system.

Interfacing with AFGROW

In addition to its built in library of stress intensity factor solutions for many standard structural geometries, AFGROW offers the capability of performing crack growth analysis for non-standard geometries through its user-defined Beta Table approach (AFGROW: Users Guide). In this approach for a single through-crack, AFGROW requests stress intensity factor input in the form of a one-dimensional table of crack length versus stress intensity factor geometry correction, or beta, values, where beta is defined by

$$K_I = \beta\,\sigma\sqrt{\pi c}$$

and where σ is the relevant applied stress and c is crack length. The beta values are obtained from finite element results in the same way as the equivalent F_i values are obtained for NASGRO. Figure FAC-1.15 shows the User-Input Beta Table dialogue box in AFGROW with the first few beta values obtained for Example 2 with a single crack, and with σ set to unity.

Once stress intensity factor history data in this form has been supplied, all standard AFGROW fatigue crack growth capabilities become available for any cracked structural model for which FRANC2D/L is an appropriate modeling system.

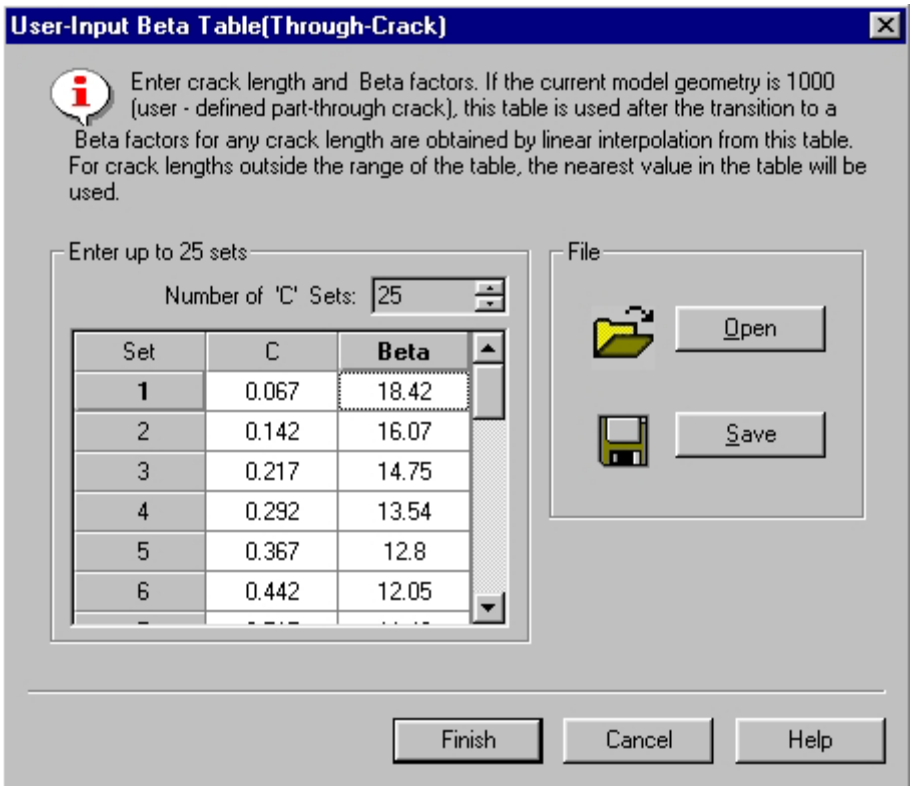

Figure FAC-1.15. AFGROW dialogue box for creating user-input beta table, showing portion of table for Example 2 with a single crack. Here σ has been set to unity.

References

AFGROW: Users Guide and Technical Manual, AFGROW for Win95/98/NT4/2K, Version 4.0001011.8, AFRL-VA-WP-TR-2000-XXXX, May 2000.

Barsoum, R.S. (1976), "On the use of Isoparametric Finite Elements in Linear Fracture Mechanics," *International Journal for Numerical Methods in Engineering,* Volume 10 (1976) pp 25-38.

Chan, S.K, Tuba, I.S., and Wilson, W.K., "On the Finite Element Method in Linear Fracture Mechanics," *Engineering Fracture Mechanics*, Volume 2 (1970) pp 1-17.

Erdogan, F., and Sih, G.C., "On the Crack Extension in Plates Under Plane Loading and Transverse Shear," *Journal of Basic Engineering, Volume* 85 (1963) pp 519-525.

NASGRO: Reference Manual, Fatigue Crack Growth Computer Program "NASGRO" Version 3.0, JSC-22267B, March 2000.

Nikishkov, G.P. and Atluri, S.N. (1987), "Calculation of Fracture Mechanics Parameters from an Arbitrary Three-Dimensional Crack by the Equivalent Domain Integration Method," *International Journal for Numerical Methods in Engineering*, Volume 24 (1987) pp 1801-1821.

Rybicki, E.R., and Kanninen, M. (1977), "A Finite Element Calculation of Stress Intensity Factors by a Modified Crack Closure Integral," *AIAA Journal* Volume 2, 1977.

Underwood, P., (1983)"Dynamic Relaxation", in *Computational Methods for Transient Analysis, Volume 1*. Belytchko T., and Hughes, J.R. Eds. North-Holland, Amsterdam, 1983.

PROBLEM NO. FAC-2

Title: Predicting Residual Strength of a Fuselage Section with/without MSD and with/without Corrosion

Objective

To illustrate the process of using the nonlinear finite element method to evaluate the residual strength of a built-up aircraft structure possibly containing multi-site fatigue damage and possibly having corrosion damage.

General Description:

This problem details the process of using the finite element method to predict the residual strength of a section of built-up fuselage structure. The section contains a lead fatigue crack, and might also contain MSD and corrosion damage. Stable growth of the lead crack is simulated based on the critical crack tip opening angle ($CTOA_c$) criterion. Methods for representing rivet stiffness and for local meshing are described. The process is applied to a section of K/C-135 fuselage, and strength assessment curves are generated for a number of configurations with no MSD, with MSD, and with MSD and corrosion conditions.

Topics Covered: Finite element analysis, stable tearing, MSD, corrosion damage, residual strength, non-linear fracture mechanics

Type of Structure: section of K/C-135 fuselage

Relevant Sections of Handbook: Sections 2, 4, 5, 11

Author: Dr. A. R. Ingraffea

Company Name: Fracture Analysis Consultants, Inc.

121 Eastern Heights Drive
Ithaca, NY 14850
607-257-4970
www.fracanalysis.com

Contact Point: Dr. Paul Wawrzynek
Phone: 607-257-4970
e-Mail: wash@fracanalysis.com

Fracture Analysis
Consultants, Inc.

Overview of Problem Description

A relatively simple built-up narrow body fuselage configuration is modeled. The example demonstrates an analysis to predict the residual strength of a pressurized fuselage, subjected to MSD and corrosion damage [Cope 1998]. The problem chosen for analysis is a three stringer wide, three-frame long K/C-135 fuselage panel. The panel section has a radius of curvature of 72 inches. It contains a lap joint at the central stringer. The lap joint is a typical three-row configuration with 3/16 inch diameter countersunk rivets. The other two stringers are spot-welded to the skin. The upper and lower skins are made of 0.04 inch thick, 2024-T3 aluminum alloy. The stringers and frames are made of 7075-T6 aluminum alloy. Frames are simply connected to the stringers by rivets. The panel configurations are shown in Figures FAC-2.1 and FAC-2.2. The frame and stringer dimensions are shown in Figure FAC-2.3.

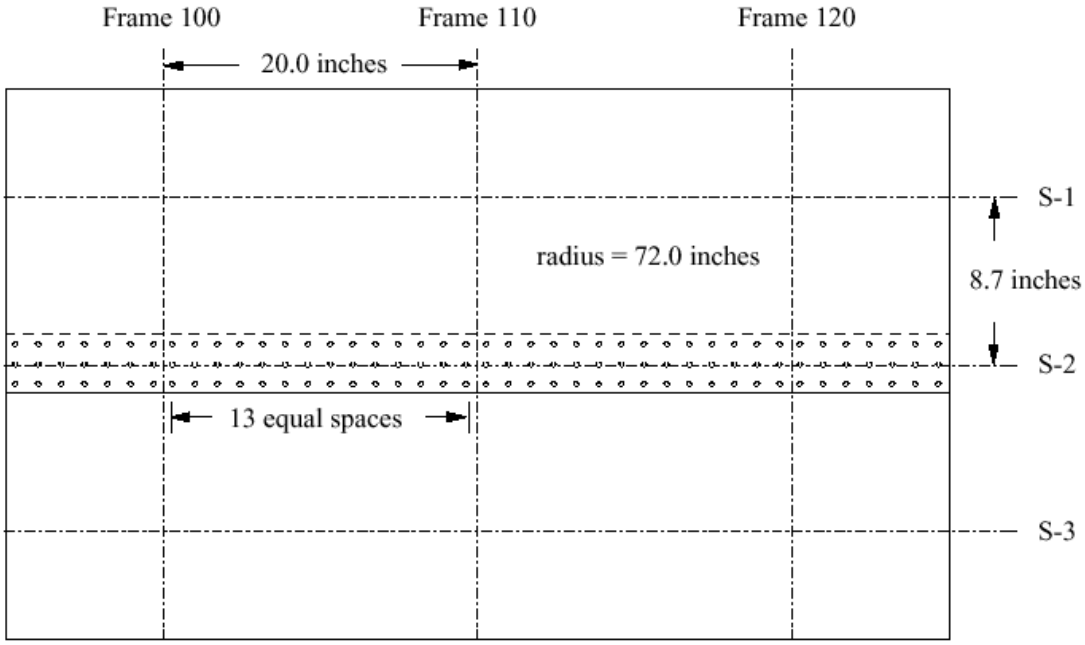

Figure FAC-2.1. Layout of K/C-135 fuselage section used in the present example.

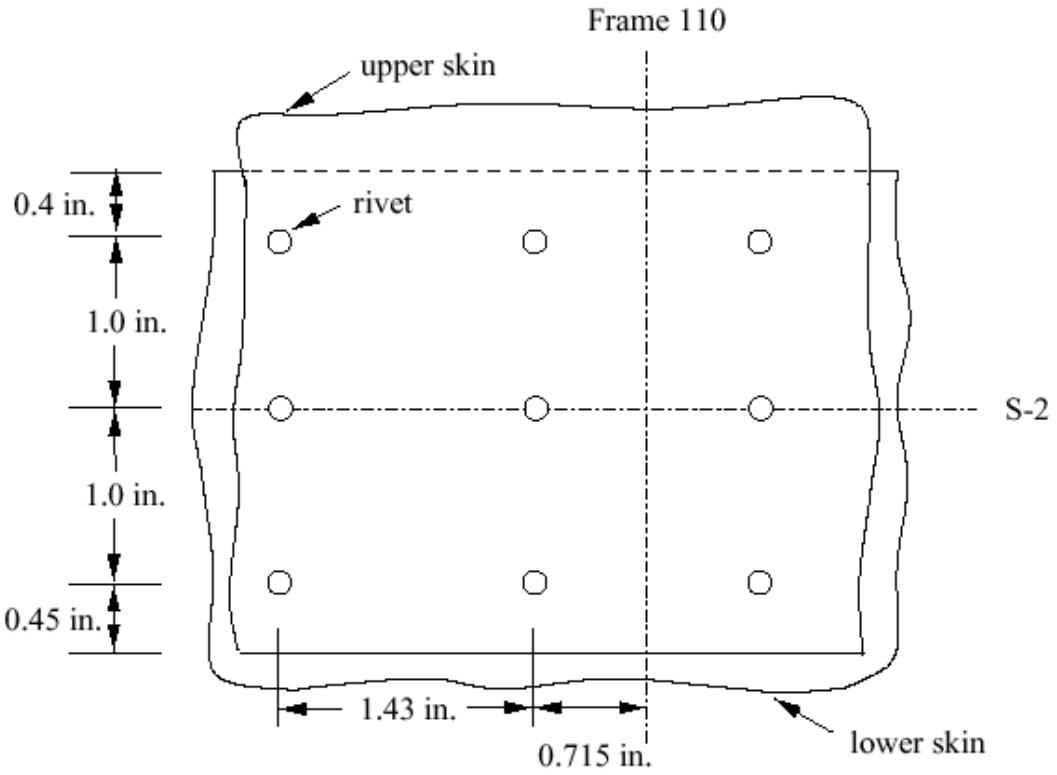

Figure FAC-2.2. Detail of lap joint rivet spacing used in the present example.

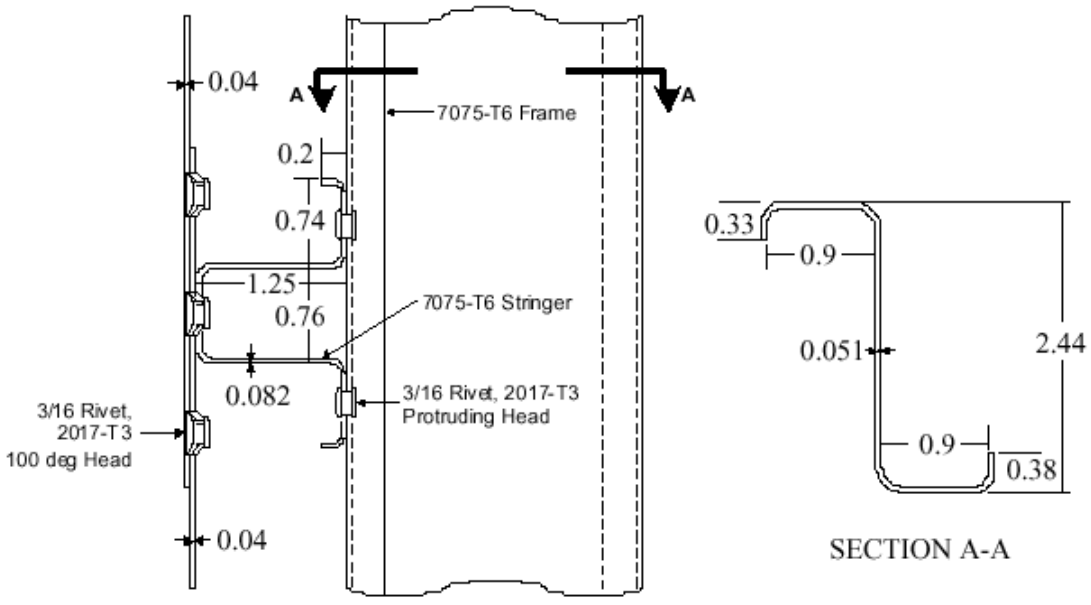

Figure FAC-2.3. Dimensions (all in inches) of stringer and frame used in the present example.

Computational Model

All structural components including skins, stringers, and frames are modeled by displacement-based, four-noded or five-noded Kirchoff shell finite elements [Rankin 1991]. The geometrical and mesh models were created using FRANC3D [www.cfg.cornell.edu], and all finite element computations were performed with STAGS [Rankin 1997]. Each node of a shell element has six degrees of freedom. A piecewise linear representation is used for the uniaxial stress-strain curves for 2024-T3 and 7075-T6 aluminum alloys (see Figures FAC-2.4 and FAC-2.5).

Symmetric boundary conditions are imposed on all the boundary edges to simulate a cylinder-like fuselage structure. Pressure loading is applied on all the external skins. Uniform axial expansion was allowed at one longitudinal end. On this boundary edge, an axial force equal to (PR/2)L was assigned where P is the applied pressure, R is the radius of the panel, and L is the arc-length of the edge. The kinematic boundary conditions (displacements and rotations) applied along the boundaries of this local model were extracted from a global model of the fuselage. Both geometric and material nonlinearities are included in the analysis. The former captures the out-of-plane bulging deformation and the latter captures the active plastic zone and the plastic wake during stable crack propagation.

The nonlinear solution algorithm consists of Newton's method. Large rotations are included in the nonlinear solution by a co-rotation algorithm applied at the element level [Nour-Omid 1991]. The Riks arc-length path following method is used to trace a solution past the limit points of a nonlinear response [Rankin 1997; Riks 1984].

Rivets are modeled by elastic-plastic spring elements that connect finite element nodes in the upper and lower skins. Each rivet is modeled with six degrees-of-freedom, corresponding to extension, shearing, bending and twisting of the rivet. The stiffness of each degree-of-freedom is defined by prescribing a force-deflection curve. The axial, flexural, and torsional stiffnesses of the spring elements are computed by assuming that the rivet behaves like a simple elastic rod with a diameter of 3/16 inch. The elastic shear stiffness of the rivet is computed by the following empirical relation developed by Swift [1984]:

$$K_{rivet} = \frac{ED}{[A + C(\frac{D}{t_1} + \frac{D}{t_2})]}$$

where E is the elastic modulus of the sheet material, D is the rivet diameter, t_1 and t_2 are the thicknesses of the joined sheets, and $A = 5.0$ and $C = 0.8$ for aluminum rivets. The initial shear yielding and ultimate shear strength of the rivets are assumed to occur at load levels of 510 lb and 725 lb, respectively. Once a rivet reaches its ultimate strength, it will break and lose its load carrying capacity. The force-deflection curve shown in Figure FAC-2.6 for shearing is intended to represent empirically the net shear stiffness of a

riveted sheet connection, accounting for bearing deformations and local yielding around the rivet [Young 1997; Swift 1984].

The critical crack tip opening angle ($CTOA_c$)[Dawicke 1994] is used to characterize elastic-plastic crack growth and to predict residual strength. For details on use of this criterion, see Problem FAC-4. The $CTOA_c$ used in this example was 5.7 degrees measured 0.04 inch behind the crack tip with a plane strain core height equal to 0.08 inch [Dawicke 1997]. Since no experimental crack growth data are available for this structure, this particular $CTOA_c$ value is estimated based on the 5.25 degrees found for 0.09 inch thick, 2024-T3 bare material. The plane strain core height is assumed to be twice the sheet thickness.

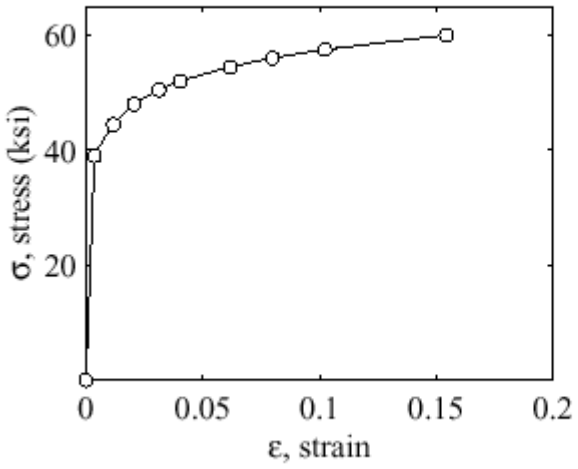

stress (ksi)	strain
0.0	0.0
39.0	0.003714
44.5	0.01172
48.0	0.02052
50.5	0.03131
52.0	0.04047
54.5	0.06199
56.0	0.07985
57.5	0.10254
60.0	0.15427

E = 1.05e+04 ksi
ν = 0.33

Figure FAC-2.4. Piecewise linear representation of uniaxial stress-strain relationship for 2023-T3 aluminum alloy used in the present example.

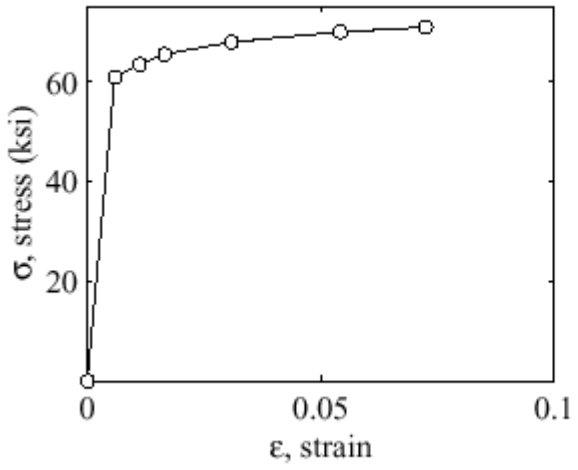

stress (ksi)	strain
0.0	0.0
61.0	0.00593
63.5	0.0112
65.5	0.01664
68.0	0.03093
70.0	0.05419
71.0	0.07257

E = 1.03e+04 ksi
ν = 0.33

Figure FAC-2.5. Piecewise linear representation of uniaxial stress-strain relationship for 7075-T6 aluminum alloy used in the present example.

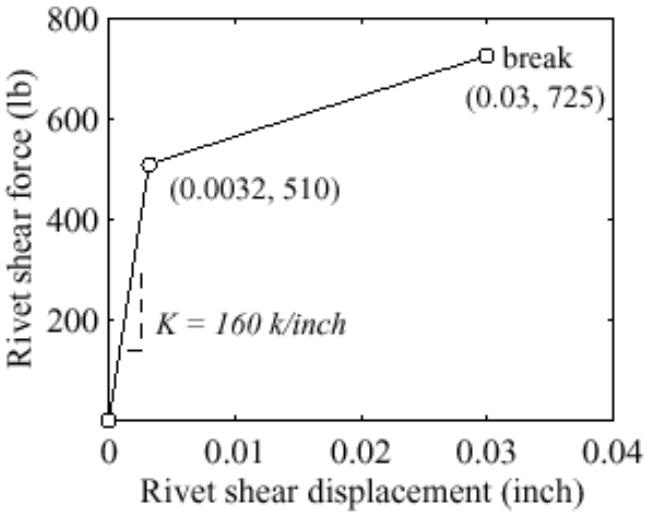

Figure FAC-2.6. Model for rivet shear stiffness and strength used in the present example.

Six different crack configurations with various lengths of lead and MSD cracks are studied. The initial configurations prior to crack growth are:

1. A 7.14 inch lead crack,
2. A 7.14 inch lead crack with 0.025 inch MSD cracks emanating from both sides of a fastener hole,
3. A 7.14 inch lead crack with 0.046 inch MSD cracks emanating from both sides of a fastener hole,
4. A 10 inch lead crack,
5. A 10 inch lead crack with 0.025 inch MSD cracks emanating from both sides of a fastener hole, and
6. A 10 inch lead crack with 0.046 inch MSD cracks emanating from both sides of a fastener hole.

The lead crack is located symmetrically about the central frame line. The MSD pattern is symmetric about the lead crack at the 3 rivets in front of the lead crack. The lead and MSD cracks are located along the upper rivet row in the upper skin of the joint. The crack configurations with a 10 inch initial lead crack are shown in Figure FAC-2.7. Since rivet holes are not modeled explicitly in the finite element model, a small crack with a length equal to the rivet diameter plus the MSD length is used to model the MSD crack. The finite element mesh for the model is shown in Figures FAC-2.8. Figure FAC-2.9 shows details of the near-tip mesh pattern with the 0.04 inch crack tip elements used there. In addition to the effects of MSD, material thinning due to corrosion damage is also studied. The effect of material thinning is modeled by a uniform reduction in thickness of the upper skin at the lap joint in the two center bays.

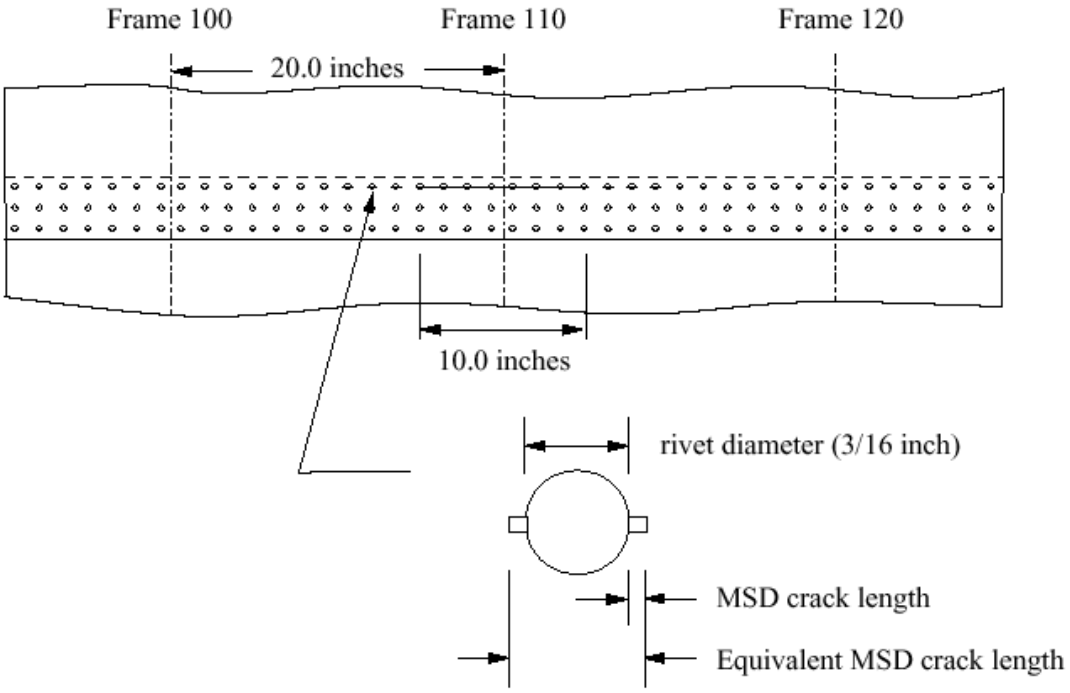

Figure FAC-2.7. Crack configurations for 10 inch lead crack and MSD.

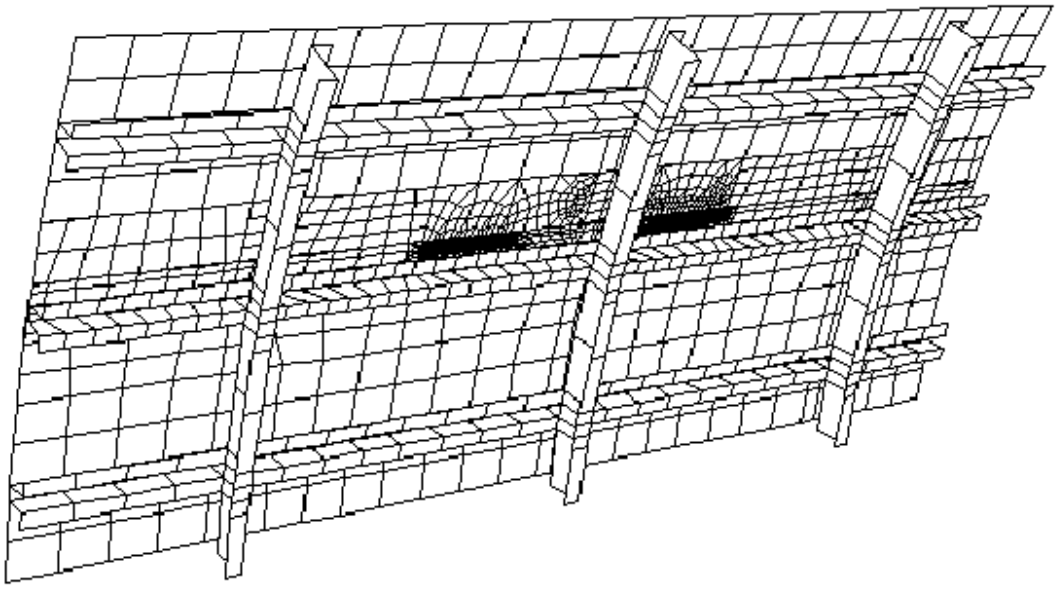

Figure FAC-2.8. Overall finite element mesh for present example.

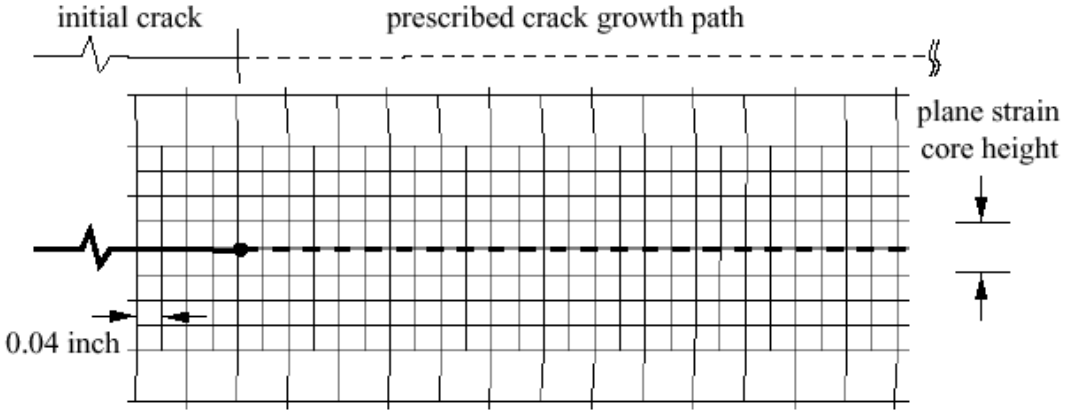

Figure FAC-2.9. Typical near-tip finite element meshing for present example.

Computational Results

Figure FAC-2.10 shows the predicted results of the operating pressure loading versus the total crack extension for all the cases conducted in this study. The predicted residual strengths summarized in Figure FAC-2.11 indicate:

- The MSD cracks significantly reduce the residual strength of the fuselage panel. A 21.8 to 28.0% loss of residual strength due to the presence of small MSD is observed.
- A 10% uniform thickness degradation due to corrosion damage reduces the residual strength by 3.4 to 9.0%. The coupling of MSD and corrosion damage leads to the most severe damage scenario.
- In general, increasing the lead and MSD crack lengths reduces the residual strengths. However, for the cases with a 10 inch initial lead crack, residual strength seems to be relatively insensitive to the MSD crack sizes.

The deformed structure at residual strength for the case with a 10 inch initial lead crack but without MSD and corrosion damage is shown in Figure FAC-2.12. Out-of-plane bulging is observed in the skin crack edges. Because of the stiffness of the stringer, the bulging at the lower crack edge is much smaller than the opposing edge. The unsymmetric, out-of-plane bulging thus leads to an anti-symmetric bending deformation field at the crack tips [Potyondy 1995].

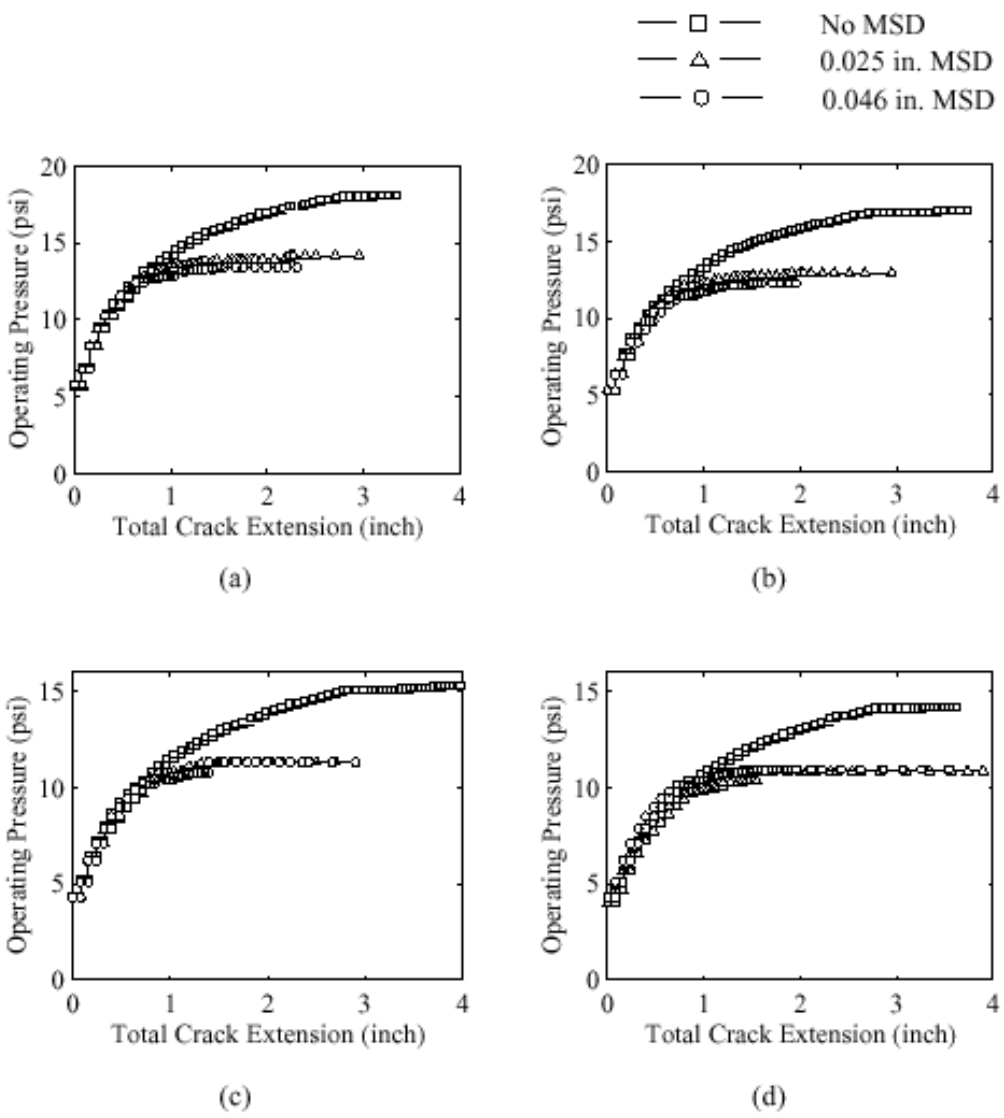

Figure FAC-2.10. Predicted operating pressure versus total crack extension for the present example: (a) 7.14 inch initial lead crack, (b) 7.14 inch initial lead crack with corrosion damage, (c) 10 inch initial lead crack, and (d) 10 inch initial lead crack with corrosion damage.

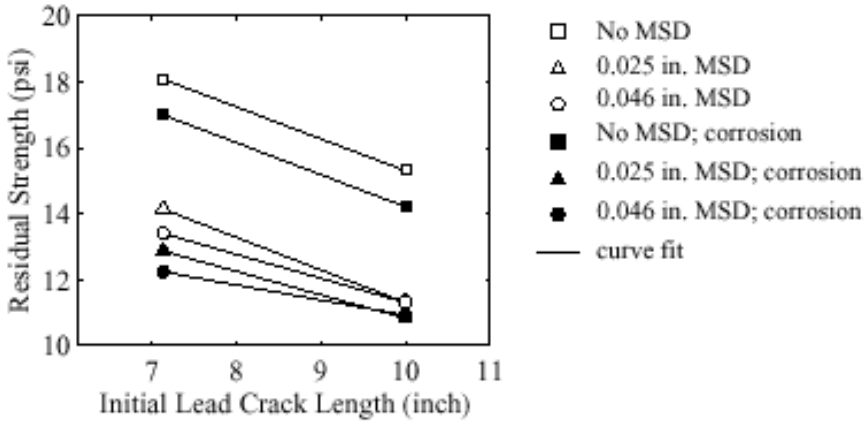

Figure FAC-2.11. Predicted residual strength versus initial lead crack length for present example.

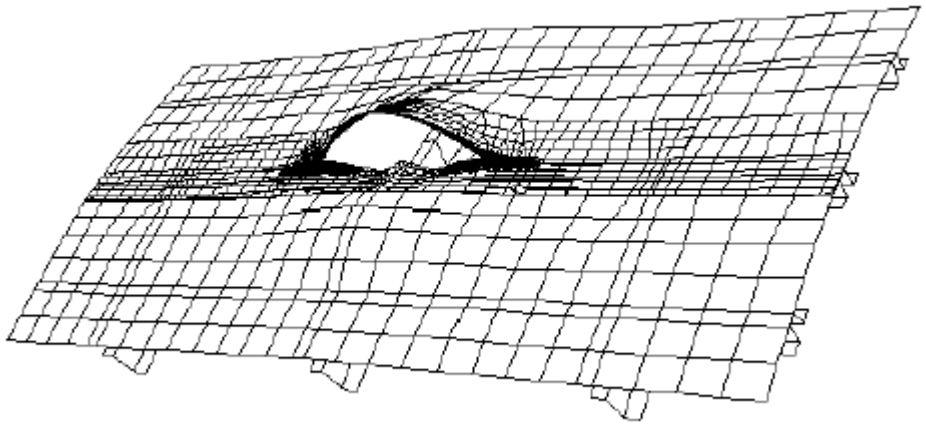

Figure FAC-2.12. Typical deformed shape of the present example (pressure = 15.3 psi, magnification factor = 5.0).

References

Cope, D., West, D., Luzar, J., Miller, G. Corrosion Damage Assessment Framework: Corrosion/Fatigue Effects on Structural Integrity. Technical Report D500-13008-1, The Boeing Defense and Space Group, 1998.

Dawicke, D., Piascik, R. and Newman, J. Prediction of Stable Tearing and Fracture of a 2000-Series Aluminum Alloy Plate Using a CTOA Criterion. In *Fracture Mechanics: 27th Volume, ASTM STP 1296*, Philadelphia, pp 90-104, 1997.

Dawicke, D.and Sutton, M. CTOA and Crack-tunneling Measurements in Thin Sheet 2024-T3 Aluminum Alloy. *Experimental Mechanics*, Volume 34, pp 357-368,1994.

Nour-Omid, B. and Rankin, C. Finite Rotation Analysis and Consistent Linearization Using Projectors. *Computer Methods in Applied Mechanics and Engineering*, Volume 93, pp 353-384, 1991.

D. O. Potyondy, P. A. Wawrzynek, and A. R. Ingraffea. Discrete Crack Growth Analysis Methodology for Through Cracks in Pressurized Fuselage Structures. *International Journal for Numerical Methods in Engineering*, Volume 38, pp 1611-1633,1995.

Rankin, C. and Brogan, F. The Computational Structural Mechanics Testbed Structural Element Processor ES5: STAGS Shell Element, 1991. NASA CR-4358.

Rankin, C., Brogan, F., Loden, W. and Cabiness, H. STAGS User Manual Version 2.4. Lockheed Martin Missiles & Space Co., Inc., Advanced Technology Center, 1997.

Riks, E. Some Computational Aspects of the Stability Analysis of Nonlinear Structures. *Computer Methods in Applied Mechanics and Engineering*, Volume 47, pp 219-259, 1984.

T. Swift. Fracture Analysis of Stiffened Structure. In *Damage Tolerance of Metallic Structures: Analysis Methods and Application, ASTM STP 842*, Philadelphia, pp 69-107, 1984.

R. D. Young, C. A. Rose, C. G. D'avila, and J. H. Starnes, Jr. Crack Growth and Residual Strength Characteristics of Selected Flat Stiffened Aluminum Panels. *Proceedings of the First Joint DoD/FAA/NASA Conference on Aging Aircraft,* Ogden, Utah, July 1997.

PROBLEM NO. FAC-3

Title: Crack Interaction and Multi-Site Damage

Objective

To illustrate the process of using the finite element method to calculate stress intensity factor histories for problems involving multiple, interacting cracks resulting from multi-site damage.

General Description:

This problem details the process of using the finite element method to calculate stress intensity factor versus crack length histories in a flat, unstiffened panel containing a number of holes, each of which is a site for crack growth. Such histories are needed to predict fatigue crack growth rates.

Topics Covered: Finite element analysis, stress intensity factor calculation, crack growth, crack interaction, MSD.

Type of Structure: flat, unstiffened panel containing multiple holes

Relevant Sections of Handbook: Example FAC-1, and Sections 2, 5, 11

Author: Dr. A. R. Ingraffea

Company Name: Fracture Analysis Consultants, Inc.

121 Eastern Heights Drive
Ithaca, NY 14850
607-257-4970
www.fracanalysis.com

Contact Point: Dr. Paul Wawrzynek
Phone: 607-257-4970
e-Mail: wash@fracanalysis.com

Fracture Analysis
Consultants, Inc.

Overview of Problem Description

Figure FAC-3.1 shows the configuration of flat, unstiffened panels tested by Luzar [1997] to examine effects of MSD on fatigue crack growth rates. 2024-T3 clad MSD panels were fabricated and tested to determine, among other objectives, fatigue crack growth values of uncorroded C/KC-135 airframe structure materials with MSD. All holes were EDM notched, and the finished EDM hole detail is shown in Figure FAC-3.1 also. The panel thickness (0.063-in.), fastener hole diameter (0.25-in.) and fastener pitch (1-in.) were selected as being representative of an actual aircraft lap joint configuration. Luzar [1997] discusses the criteria used to determine the panel width, the number of open holes, and the lead crack size in more detail. The as-tested configuration of the panels with end grips resulted in a pin-to-pin load height of 70 inches and a height to width ratio of 2.9. The grip end fixtures held the test panels in double shear resulting in all of the test loads being transmitted through joint friction. This loading arrangement has been demonstrated to produce uniform stress and displacement conditions throughout the test section.

In this example a finite element model (FEM) of a representative panel is created. The FEM includes initial MSD cracks emanating from each hole. Stress intensity factors are calculated for each crack tip, and these are used to predict relative rate-of-growth of each crack. The FEM naturally includes the effects of crack interaction, and comparisons are made between the growth rates of the cracks, and between these rates and those that would occur under the simplifying assumption of no-interaction.

Computational Model

A finite element model of the MSD panel, shown in Figure FAC-3.2, was created using the FRANC2D/L crack growth simulator [www.cfg.cornell.edu]. Due to symmetry, only one half of the panel was modeled. The model consisted of eight-noded and six-noded plane stress elements. The model geometry and boundary conditions matched those of the experimental test panel, as shown in Figure FAC-3.1. The EDM notches at the edges of each hole were modeled as simple cracks. Typical material properties for 2024-T3 clad aluminum, T-L orientation – Young's modulus of 10.6 Msi, Poisson's ratio of 0.33 - were used in the analysis. A uniform tensile displacement was applied at the top and bottom edges of the model to match the experiment set-up. The right hand edge of the model had free boundary conditions while the left hand edge (representing the vertical centerline) had a symmetry boundary condition. Figure FAC-3.3 shows a portion of the mesh near a pair of holes. Note the refined mesh around the cracks at the edges of each hole, and the use of a uniform template of elements around each crack tip. The elements in this template are ¼-point singular elements. See Problem FAC-1 for guidance on meshing for accurate stress intensity factor computations.

This FEM model was used to calculate stress intensity factors at each crack tip as a function of crack length. The crack growth simulation capability of FRANC2D/L was used for this purpose. After each analysis step, FRANC2D/L calculates the stress intensity factor (SIF) values at each crack tip using the J-integral method, determines the appropriate crack growth increment for each crack, extends each crack, remeshes around each new crack tip, and then perform the next solution step with the new mesh. This procedure was performed thirteen times in order to simulate incremental crack growth.

The initial crack length used in the analysis was 0.02 inches. The fastest growing crack was incremented at steps of 0.02 inches. All other crack growth increments were automatically calculated at each step using the crack tip SIF in a power law relation with an exponent of 3.9. The final maximum crack length was, therefore, 0.26 inches. However, the final length of each crack varied with its stress intensity factor history. The analysis was arbitrarily stopped at this point since the crack lengths had far exceeded those found in the test specimens.

The initial FEM model contained about 19000 degrees-of-freedom, the final mesh about 25000. Solution time on a 1GHz Pentium III PC was about one minute per crack growth step.

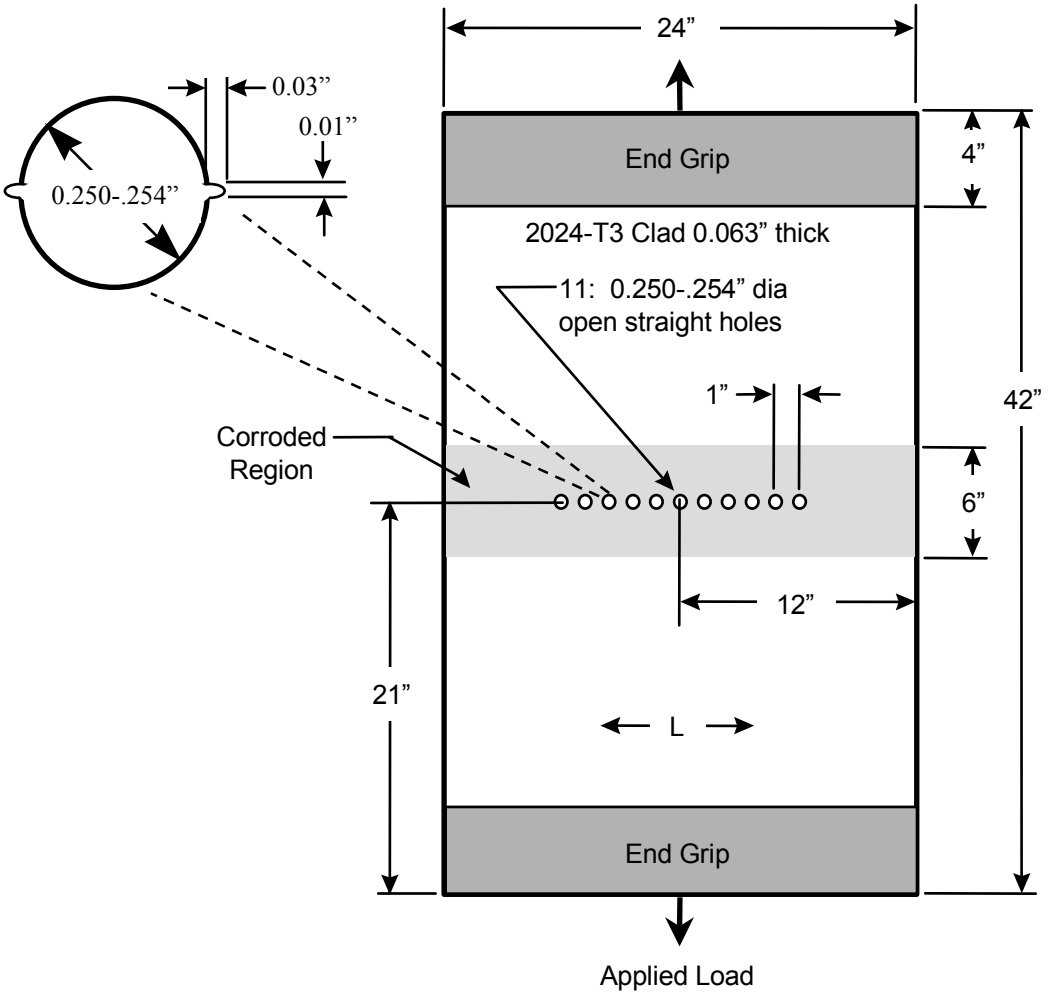

Figure FAC-3.1. MSD Panel Geometry used in this example. From Cope [1998].

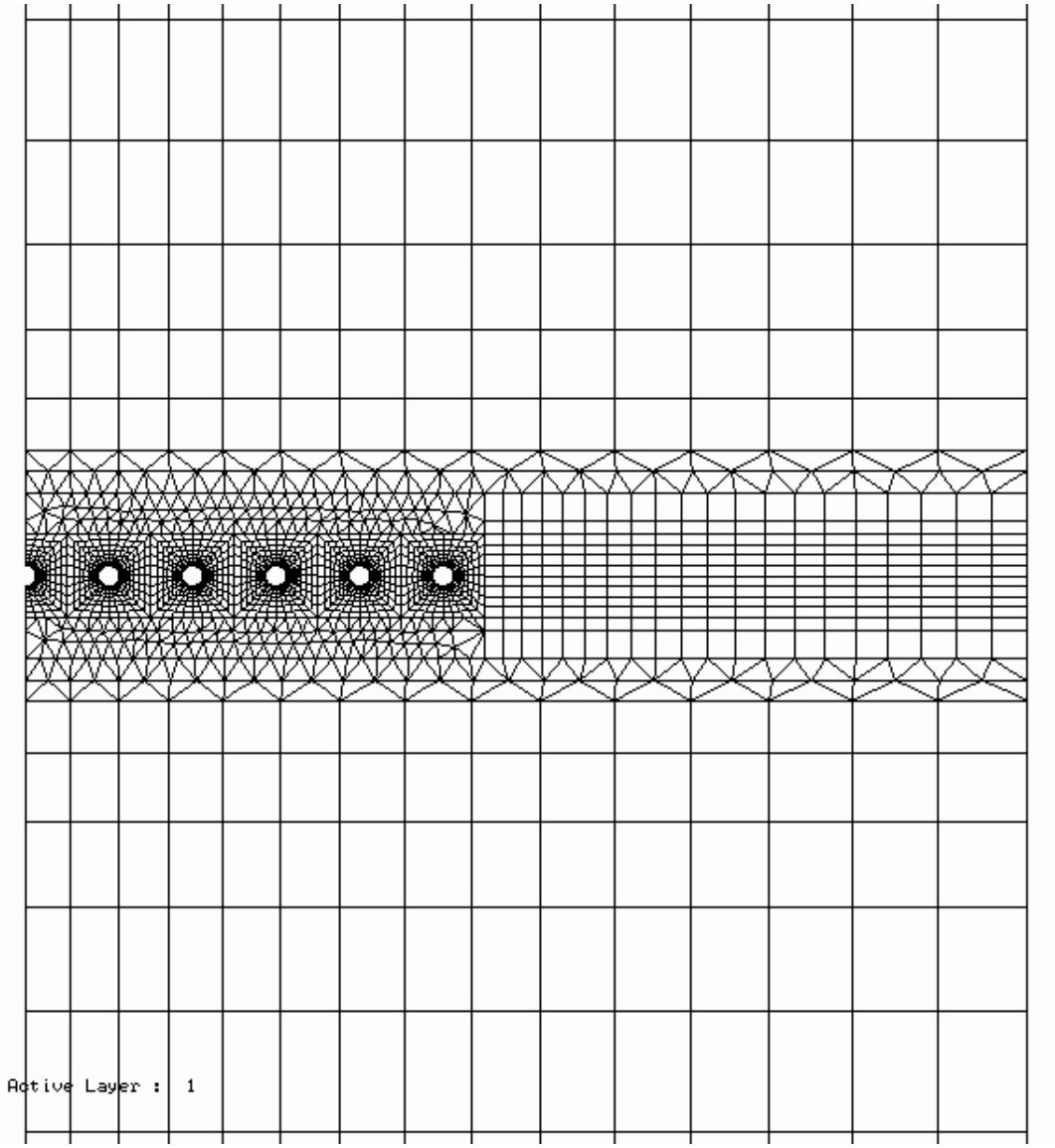

Figure FAC-3.2. Central portion of finite element model of flat plate with MSD.

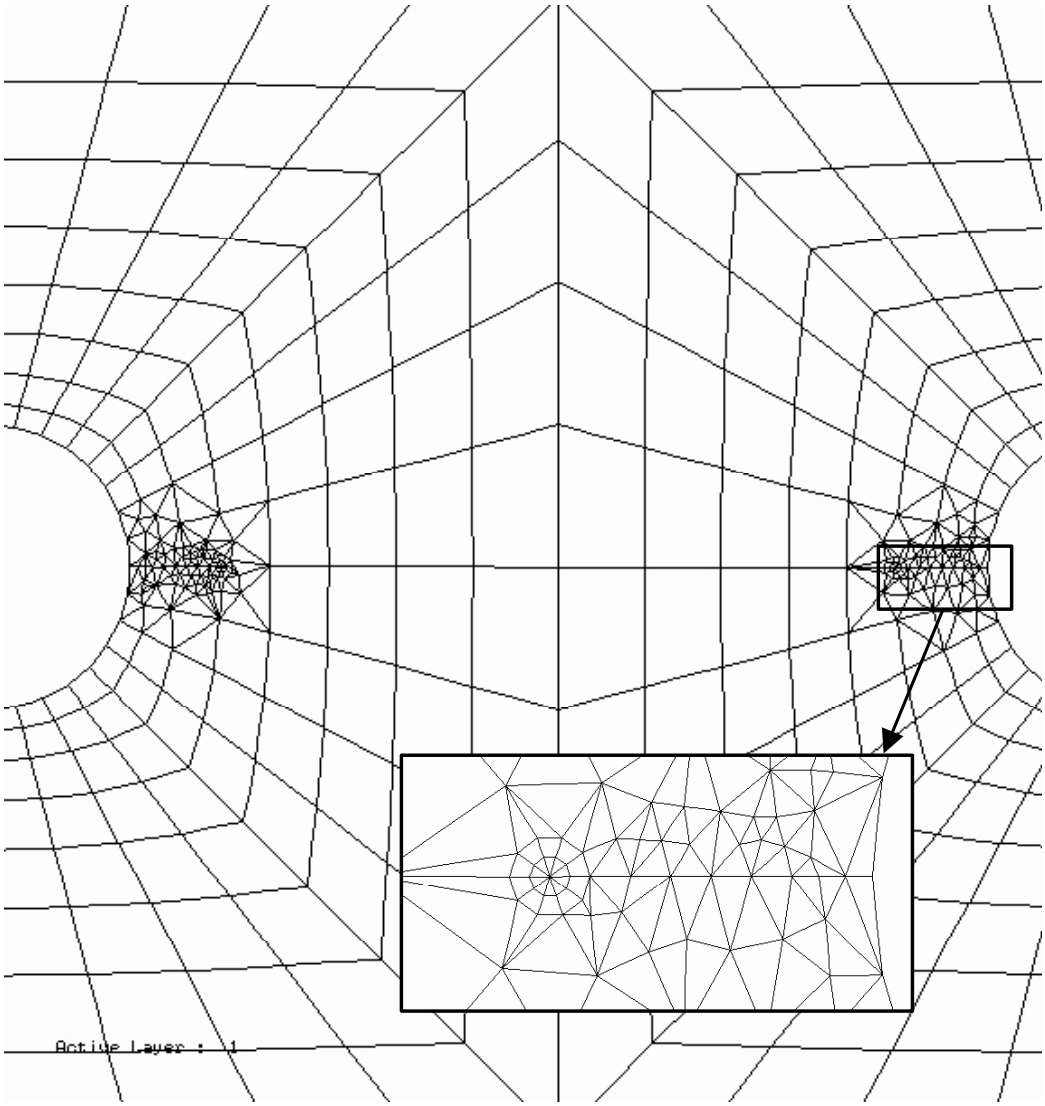

Figure FAC-3.3. Typical details of finite element model of flat plate with MSD. Near-hole meshing after four steps of crack propagation.

Computational Results

SIF histories of crack propagation were generated for each crack tip. As shown in Figure FAC-3.4, these histories were almost identical for the first 7 to 8 crack tips (numbered left to right), and for short crack lengths. There is a "falloff" of stress intensity for the rightmost 3 cracks, because of less interaction with surrounding cracks and holes. This falloff intensifies with crack growth, as would be expected with increasing crack interaction effect. At the 12^{th} growth step, the SIF for the rightmost crack tip is about

20% less than the average of the interacting crack tips. This means that this is the slowest growing crack, as seen in Figure FAC-3.4.

Another way of assessing the effects of crack interaction is shown in Figure FAC-3.5. Here the stress intensity factor histories for crack tip 1, where one expects strong interaction effects, and crack tip 11, where intensification from interaction is expected to be less than that for all other cracks, are compared to the benchmark solution for non-interacting cracks. This solution [Newman 1971] is for equal-length diametrically opposed cracks emanating from a single hole in an infinite plate. Figure FAC-3.5 shows very strong interaction effects present in this MSD problem with the stress intensity factor for crack 1 (and, therefore, the first 7 or 8 cracks) reaching a value more than 40% higher than that assuming no interaction.

The stress intensity factor histories shown in Figure FAC-3.4 can be used to predict fatigue crack growth rates by using them as input data for AFGROW of NASGRO, as shown in example problem FAC-1. Cope *et al*.[1998] used this procedure to produce a comparison between predicted and observed crack growth behavior in the problem shown in Figure FAC-3.1. This comparison is shown in Figure FAC-3.6.

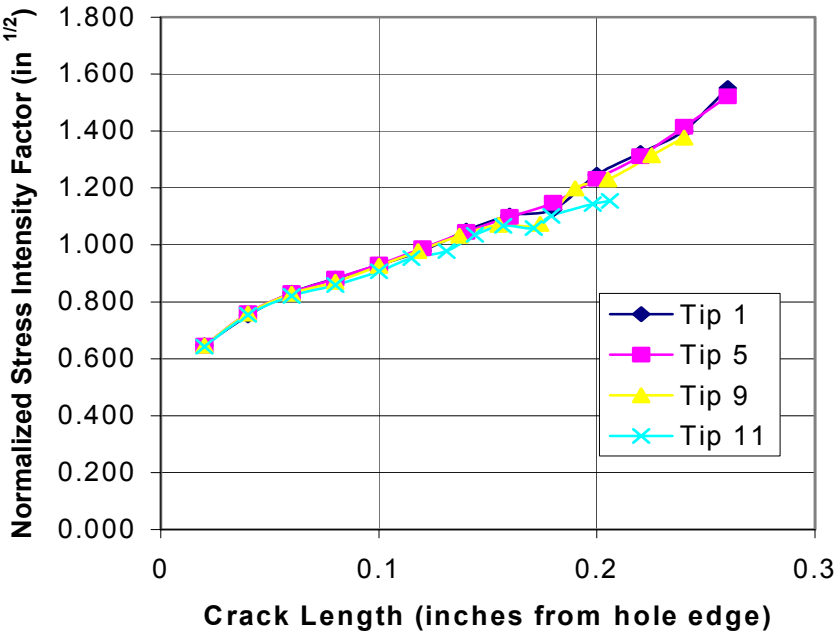

Figure FAC-3.4. Predicted normalized stress intensity factor histories for representative crack tips in this MSD problem. Crack tips are numbered from left to right.

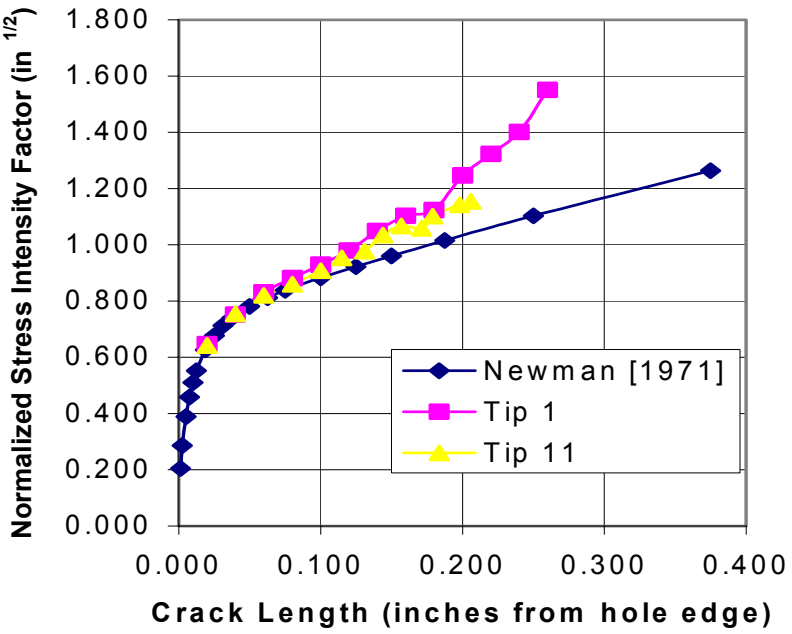

Figure FAC-3.5. Predicted normalized stress intensity factor histories for representative crack tips in this MSD problem compared to solution for non-interacting cracks. Crack tips are numbered from left to right.

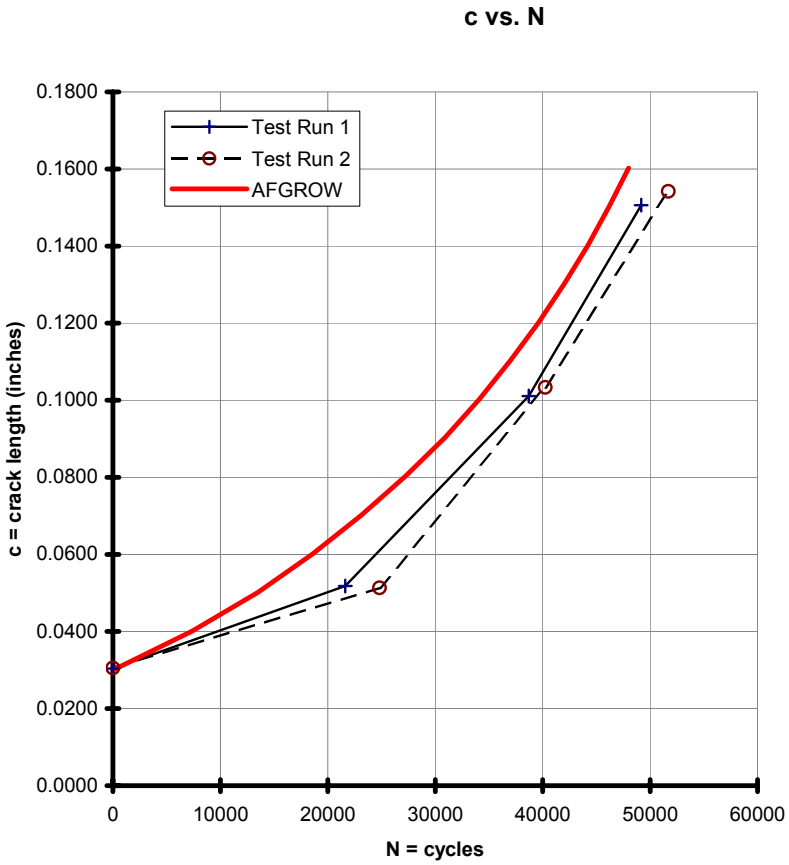

Figure FAC-3.6. Comparison between predicted and observed fatigue crack growth behavior for the problem shown in Figure FAC-3.1. From Cope et al. [1998].

References

Cope, D., West, D., Luzar, J., Miller, G. Corrosion Damage Assessment Framework: Corrosion/Fatigue Effects on Structural Integrity. Technical Report D500-13008-1, The Boeing Defense and Space Group, 1998.

Luzar, J.J. Pre-corroded Fastener Hole Multiple Site Damage Testing, Final Report, EA 96-135OTH-041, Boeing ISDS Post-Production/Derivative Aircraft Division, December 1997.

Newman, J. C. An Improved Method of Collocation for the Stress Analysis of Cracked Bodies with Various Shaped Boundaries. *NASA TN D-6376*, pp 1-45, 1971.

PROBLEM NO. FAC-4

Title: Predicting Ductile Tearing and Residual Strength of a Flat Sheet with/without MSD Objective:

To illustrate the process of using the nonlinear finite element method to predict stable, ductile tearing and to evaluate the residual strength of a flat sheet containing multi-site damage.

General Description:

This problem details the process of using the finite element method to predict the residual strength of a simple flat plate containing a single crack, or a lead crack with MSD. A criterion for stable, ductile tearing based on the crack tip opening angle ($CTOA_c$) is introduced. Bases for this criterion are discussed, and experimental and computational investigations of it are described and evaluated for guidelines in use. Example simulations are then detailed. These include one of an MT specimen containing a single crack, and five involving various configurations of MSD. Predictions of crack growth and linkup, of residual strength, and of effect of MSD on decrease in residual strength are presented.

Topics Covered: Finite element analysis, stable tearing, MSD, residual strength, non-linear fracture mechanics

Type of Structure: flat sheet with single crack or cracks with MSD

Relevant Sections of Handbook: Sections 2, 3, 4, 5, 11

Author: Dr. A. R. Ingraffea

Company Name: Fracture Analysis Consultants, Inc.

121 Eastern Heights Drive
Ithaca, NY 14850
607-257-4970
www.fracanalysis.com

Contact Point: Dr. Paul Wawrzynek
Phone: 607-257-4970
e-Mail: wash@fracanalysis.com

Fracture Analysis
Consultants, Inc.

Overview of Problem Description

An important element in the process of predicting residual strength of a structure experiencing ductile tearing is having a criterion that predicts the onset and rate of this phenomenon. Tests and numerical simulations have been performed to assess the critical crack tip opening angle ($CTOA_c$) criterion for predicting residual strength of structures containing MSD. The objectives of this problem are to describe the bases for this criterion and to present example simulations that employ it. The next section details the theoretical background behind the $CTOA_c$ criterion, and describes experimental and computational investigations into it. This section is followed by a review of findings of these investigations. Those readers wanting to go directly to a computational example application of this criterion can proceed directly to the **Computational Models** section.

The *$CTOA_c$ Criterion for Ductile Tearing*

The local slope of the crack tip opening profile, or CTOA, has been suggested to characterize ductile crack growth behavior [de Koning 1977]. Newman [1984], Rice and Sorensen [1978], and Kanninen and Popelar [1985] further defined the CTOA as the crack tip opening angle measured at a fixed distance behind the moving crack tip. The CTOA fracture criterion asserts that this angle maintains a constant value during stable crack growth for a given thickness of material.

The definition of CTOA as suggested by Newman [1984] is adopted for this problem. For Mode-I only deformations, CTOA is defined as, Figure FAC-4.1:

$$CTOA = 2\tan^{-1}\frac{\delta}{2d}$$

where d is the CTOD measured at a specific distance, d, behind the crack tip.

Stable crack growth is an inherent feature of elastic-plastic materials because of the occurrence of permanent plastic deformations during unloading [Rice 1975]. This effect can be demonstrated by global energy dissipation or by the local residual plastic deformations. Suppose two materials have the same uniaxial stress-strain curves; one is an idealized nonlinear elastic material and the other is an elastic-plastic material. For cases without crack growth, the same CTOA and strain concentration will occur in the two materials as illustrated in Figure FAC-4.2, STAGE 0. As the crack propagates in the nonlinear elastic material, deformation fields need to be readjusted and the same crack tip opening profile would occur for the new crack tip location. This is not the case for the elastic-plastic material because a large part of the energy is consumed by plastic dissipation with far less strain recovered during unloading. Thus, a smaller CTOA is obtained after crack growth (STAGE 1). Further increase of the applied loading is needed to open the crack (STAGE 2) and causes stable crack growth in the elastic-plastic material. Fracture instability will occur as the crack reaches a steady-state condition in which the crack continually advances without further increase in load. If the analysis is performed under displacement control, then a reduction in applied load is required to

maintain a constant CTOA for continuous crack growth. Hereafter, $CTOA_a$ is the crack tip opening angle measured immediately after propagation, STAGE 1. $CTOA_b$ is denoted as the increase in crack tip opening angle required to reach the critical value, $CTOA_c$. Thus, the condition

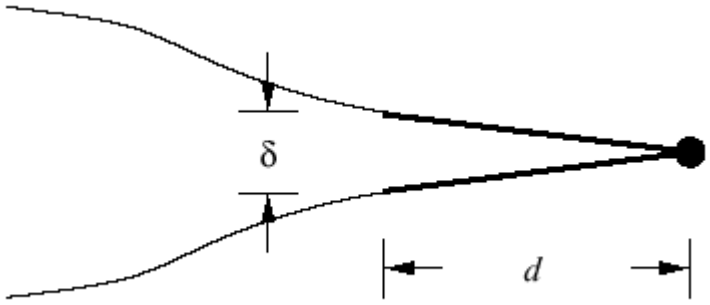

Figure FAC-4.1. Illustration of parameters used for CTOA definition.

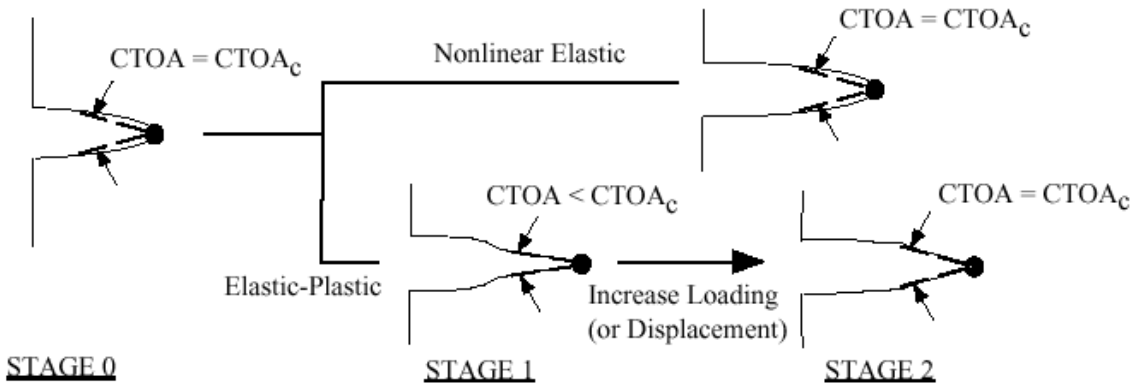

Figure FAC-4.2. Illustration of crack growth in nonlinear elastic and elastic-plastic materials.

$$CTOA_a + CTOA_b = CTOA_c$$

satisfies the fracture criterion for crack propagation, and the condition

$$CTOA_a = CTOA_c$$

indicates the occurrence of fracture instability for the analysis under load control. Another related factor for stable crack growth is the plastic wake effect caused by the residual plastic deformations [Newman 1984]. As the crack grows, the plastic zone behind the crack tip unloads to an elastic state leaving the appropriate plastic wake behind the advancing crack tip. This effect results in resistance to crack tip opening as

illustrated in Figure FAC-4.3. The dashed curves in the plastic wake region show what the crack opening profile would have been if residual plastic deformations had not been retained in the material behind the advancing crack tip. This phenomenon is also essential for simulating the initiation of stable crack growth associated with high fatigue stress prior to tearing [Dawicke 1994b].

Laboratory tests have been conducted on flat panels made of aluminum alloys to measure $CTOA_c$ values [Dawicke 1994a; Newman 1993]. Numerical simulations using these values have been conducted using two-dimensional [Newman, 1992, 1993; Dawicke 1994b, 1995, 1997a], thin-shell [Chen 1996, 1997, 1998], and three-dimensional [Dawicke 1996, 1998, 1997b] finite element elastic-plastic crack growth analyses. These activities are first reviewed to highlight important findings. The latest results are then used as a starting point for the example simulations.

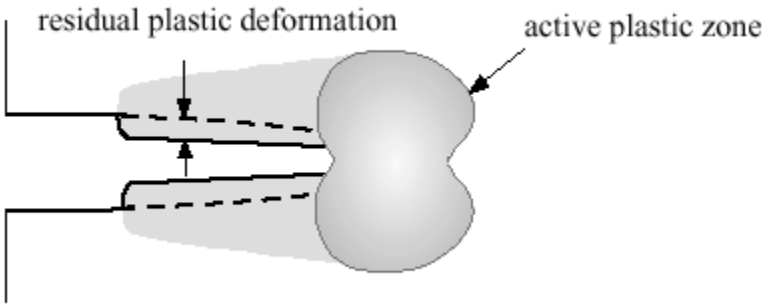

Figure FAC-4.3. Illustration of plastic wake effect caused by crack growth.

Review of Findings on $CTOA_c$ Criterion

A series of fracture tests has been conducted using a 2024-T3 aluminum alloy for MT, CT, blunt notch, THCT and MSD specimens. Newman *et al.* [1992] conducted tests on 0.05, 0.07, and 0.09 inch thick, 3.0 and 11.8 inch wide MT and blunt notch specimens as well as 0.09 inch thick, 10 inch wide THCT specimens. The blunt-notch specimen is similar to the MT specimen except that a small hole is drilled at both ends of the saw cut. It is intended to assess the suitability of elastic- plastic finite element analyses with the small-strain assumption to model large-scale plastic deformations. Good agreement between predicted and measured load versus notch-tip displacements substantiates the assumption. The critical values of CTOA were measured for the MT and THCT specimens to assert the specimen configuration independence of the fracture criterion. The THCT specimen had a stress intensity factor solution like that of a cracked, stiffened panel [Newman, 1995]. The measured $CTOA_c$ values showed higher angles at crack initiation, but reached the same constant value after a small transition period of crack growth. The agreement of $CTOA_c$ between MT and THCT specimens indicated that the $CTOA_c$ fracture criterion is independent of specimen configuration; this was further confirmed by a follow-up study with measurements from CT specimens [Dawicke 1995].

A 2D elastic-plastic finite element code, ZIP2D [Newman1974], and a 6.1 degree $CTOA_c$, computed at 0.01875 inch behind the crack tip, were used to simulate fracture behavior of the MT specimens [Newman 1992]. To model fatigue pre-cracking, cyclic loading simulation was conducted prior to stable tearing analyses. Experimental and predicted results showed that a higher applied stress during the fatigue tests increased the resistance to stable crack growth initiation. Predicted residual strengths under plane stress conditions were within 4% of experimental results for 3.0 and 11.8 inch wide MT specimens. However, the plane stress analyses over-predicted crack extension prior to limit load while the plane strain analyses under-predicted crack extensions.

The above studies raised two important questions:

1. What is the governing mechanism that causes higher $CTOA_c$ values during crack initiation?
2. What is the governing mechanism that causes the discrepancy between 2D predictions and test results?

Dawicke and Sutton [Dawicke 1994b] examined the higher values of measured $CTOA_c$ observed during crack initiation, i.e., question 1. Two independent techniques, optical microscopy (OM) and digital image correlation (DIC) were used to measure surface $CTOA_c$ during crack growth. The results of the two methods agreed very well. Fatigue marker loads and a scanning electron microscope were used to examine the fracture morphology and sequences of crack front profiles. For specimens under low magnitude of fatigue stress prior to tearing, crack surfaces underwent a transition from flat-to-slant crack growth. A schematic of the transition is shown in Figure FAC-4.4. During the transition period, the $CTOA_c$ values were high and significant tunneling occurred. After an amount of crack growth equal to about the specimen thickness, $CTOA_c$ reached a constant value. After crack growth equal to about twice the thickness, crack tunneling stabilized. For specimens that were pre-cracked under a high magnitude of fatigue stress, a 45-degree, slant, through-thickness initial crack was formed prior to tearing. During the crack initiation period, the $CTOA_c$ values of specimens with high fatigue stress were lower than the ones with low fatigue stress. But the same constant $CTOA_c$ value was observed after crack growth equal to about the specimen thickness.

The discrepancy between 2D predictions and test results, i.e., question 2, was thought to be related to the 3D constraint effect. Although thin-sheet structures behave essentially in plane stress, the constraint due to the finite thickness of the specimens can cause the regions local to the crack tip to approach plane strain conditions [Hom 1990]. To investigate the constraint effect, 2D and 3D analyses were conducted. In the 2D analyses, a core of elements above and below the crack path were assigned as plane strain while all other elements were assigned as plane stress. The plane strain core concept is illustrated in Figure FAC-4.5.

In their first attempt, Dawicke *et al.* [Dawicke 1995; Newman 1993] used 2D finite element analyses with a 6.0 degree $CTOA_c$ computed at 0.02 inch behind the crack tip and a plane strain core height equal to 0.2 inch to simulate fracture behavior with the constraint effect. They showed that the use of a plane strain core was essential to

accurately model crack growth. The predicted residual strengths were within 2% for 3 and 12 inch wide, 0.09 inch thick MT specimens and within 4% for 6 inch wide, 0.09 inch CT specimens. For 20 inch wide, 0.04 inch thick MSD specimens, 2D analyses with a 5.1 degree $CTOA_c$ showed excellent agreement of link-up and residual strength between predictions [Newman 1993] and test results [Broek 1994].

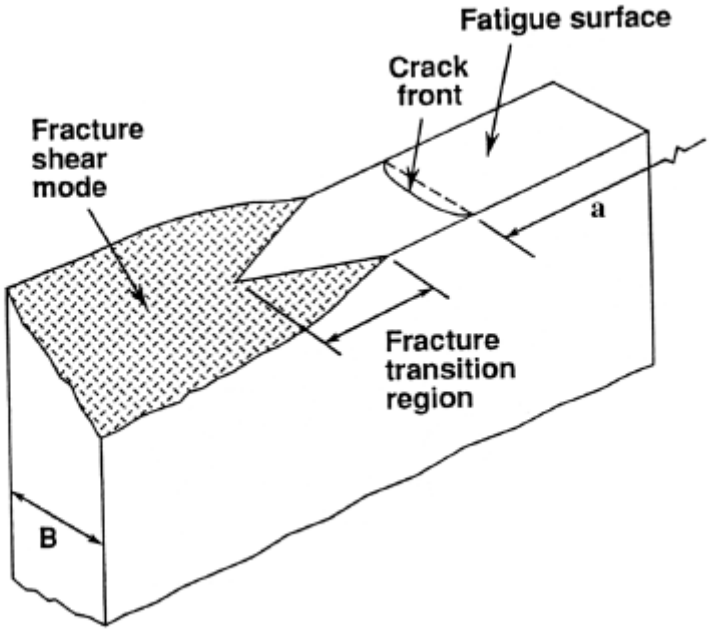

Figure FAC-4.4. Schematic of fracture surface indicating transition from a flat to a slant crack plane (after [Newman 1992]).

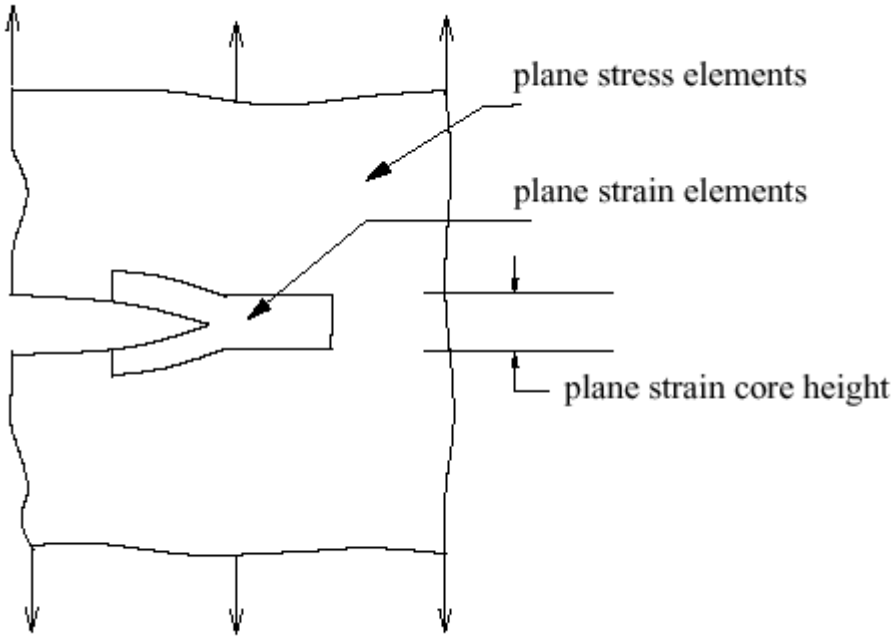

Figure FAC-4.5. Schematic of the plane strain core.

Dawicke et al. [Dawicke1996, 1998] further studied the constraint effect using 3D finite element analyses with a 5.25 degree $CTOA_c$ computed at 0.04 inch behind the crack tip. The 3D analyses successfully simulated fracture behavior of 2.0, 4.0, 6.0, and 8.0 inch wide CT specimens, 1.2, 3.0, 6.0, 12.0, 24.0, and 60.0 inch wide MT specimens, and 12.0 inch wide MSD specimens made of 0.09 inch thick, 2024-T3 aluminum alloy. A plane strain core height of 0.12 inch was required for 2D analyses to match the measured results and the 3D fracture predictions.

Computational Models

In the following examples, tests on MT and MSD specimens are simulated. The FRANC3D/STAGS system [www.cfg.cornell.edu] is used to simulate fracture behavior and to predict residual strength using the guidelines derived from the 2D and 3D studies just described.

Fracture tests of MT specimens were conducted by the Mechanics of Materials Branch at NASA Langley Research Center [Dawicke 1994a, 1996,1998]. The test specimens were made of 0.09-inch thick 2024-T3 aluminum alloy. All specimens were fatigue pre-cracked in the L-T orientation with a low stress level that results in a stress intensity factor range of $\Delta K = 7$ ksi $\sqrt{\text{inch}}$. For specimens with a single crack, different widths of panels equal to 3 inch, 12 inch, and 24 inch with a crack-length to width ratio equal to 1/3 were tested, Figure FAC-4.6. For cases with multiple cracks, only the 12-inch wide specimens with two to five near collinear cracks as illustrated in Figure FAC-4.7 were tested. All tests were conducted under displacement control with guide plates to prevent

out-of-plane buckling. Both OM and DIC techniques were used to measure the $CTOA_c$ during stable crack growth [Dawicke 1994]. Experimental results for MT and CT specimens are shown in Figure FAC-4.8. The $CTOA_c$ rapidly reaches a constant value with a scatter band about ± 1 degree.

Numerical Simulations of MT Specimens

Fracture processes in the MT specimens are simulated first. To investigate panel size effects, numerical simulations of 60-inch wide panels with the same crack-length-to-width ratio are also performed. Elastic-plastic finite element analyses based on incremental flow theory with the von Mises yield criterion and the small strain assumptions are used to capture the active plastic zone and the plastic wake during stable crack propagation. A piecewise linear representation is used for the uniaxial stress-strain curve for 2024-T3 aluminum, Figure FAC-4.9. The $CTOA_c$ used in this study was 5.25 degrees measured 0.04 inch behind the crack tip. This particular value was provided by Dawicke and Newman [Dawicke 1996, 1998] based on 3D simulations of CT specimens. Upon satisfaction of the fracture criterion, nodal release and load (or displacement) relaxation techniques are employed to propagate the crack. Because of the double symmetry of the geometry and loading, only one-quarter of the specimen with imposed symmetry boundary conditions is modeled. Out-of-plane displacements are suppressed. Displacement-based, four-noded and five-noded quadrilateral shell elements having C_1 continuity are used [Rankin 1991]. These elements are intended to model thin shell structures for which transverse shear deformation is not important. Each node of the element has six degrees of freedom including three translations and three rotations.

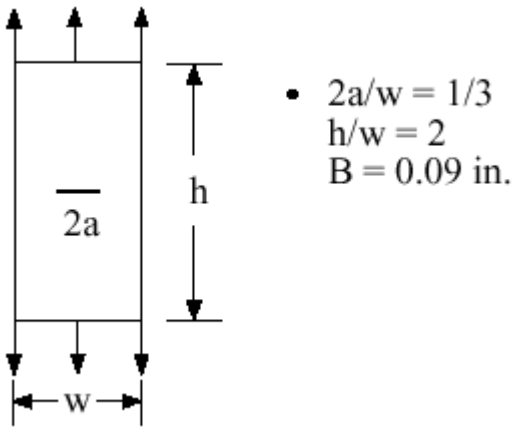

Figure FAC-4.6. Test configuration for MT specimens.

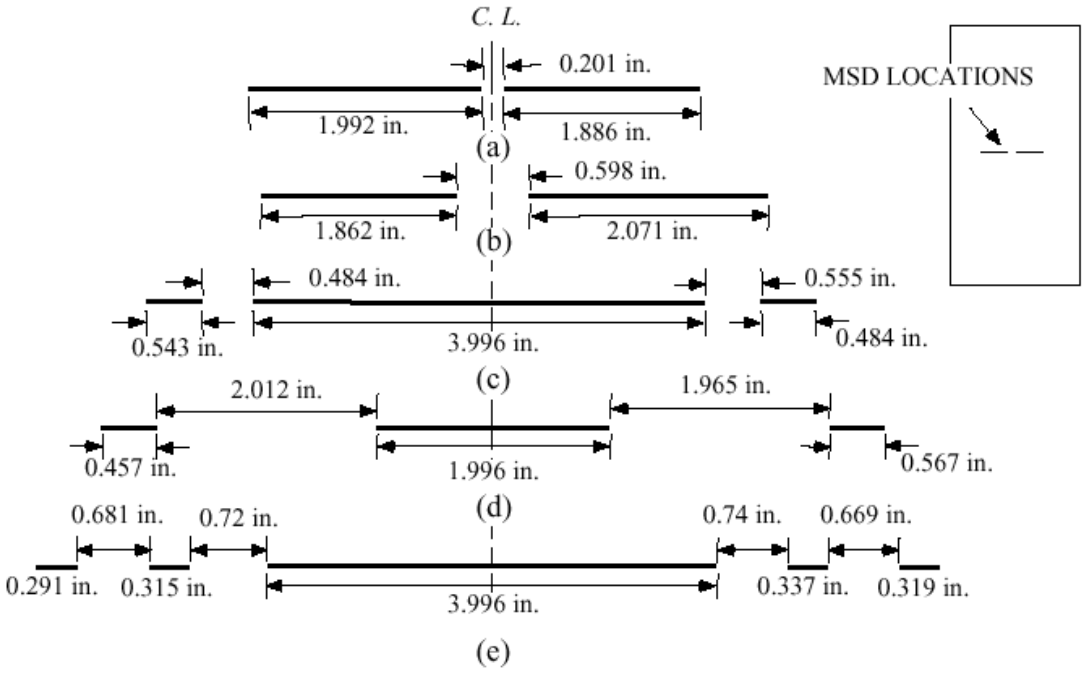

Figure FAC-4.7. Schematic of crack configurations for12- inch MT specimens.

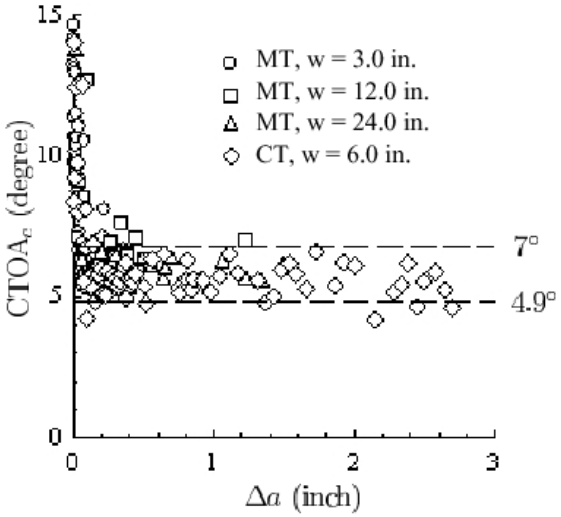

Figure FAC-4.8. Surface measurements of CTOA$_c$ [from Dawicke1998]

A special five-noded shell element, formulated by combining two four-noded elements and using linear constraint along the edge to eliminate the dependent node, is used to transition from locally refined zones around the crack path to a coarse mesh away from the crack.

A convergence study was conducted to determine the sensitivity of the predicted residual strength to the element size along the crack extension path. Three meshes for the 24-inch wide panel were created with crack tip element sizes of 0.04-inch, 0.02-inch, and 0.01-inch. For all crack growth and residual strength analyses, the CTOA is evaluated at 0.04-inch behind the crack tip to be consistent with experimental measurements. A finite element mesh with 0.04-inch square crack tip elements for the 24-inch wide panel is shown in Figure FAC-4.10. Predicted crack growth results for cases with 0.04-inch and 0.02-inch crack tip elements as well as predicted residual strengths for all three cases are shown in Figure FAC-4.11. Although some discrepancy is observed at the early stage of stable tearing, the predicted results exhibit little influence of mesh size after a relatively small amount of stable crack growth. More importantly, the predicted residual strength is very insensitive to crack tip element size. Thus, all the remaining meshes used in this example have 0.04 inch crack tip elements.

Figure FAC-4.12 shows two predicted crack opening profiles for the 24-inch wide panel. The angles are computed immediately after propagation (i.e., $CTOA_a$, see Figure FAC-4.2) with relaxation procedures completed and before increasing the applied displacement. The two $CTOA_a$ values correspond to (1) the angle after the first increment of crack growth, and (2) the angle after the specimen reaches its residual strength. As shown in the figure, $CTOA_a$ is much smaller than the critical angle after the first crack growth increment. This clearly demonstrates the permanent plastic deformation effects on stable crack growth in the elastic-plastic material. As the crack propagates, $CTOA_a$ increases. Since the analyses are conducted under displacement control, the $CTOA_a$ at residual strength is less than, but approaching its critical value.

Comparisons between numerical results and experimental measurements for the applied stress versus half crack extension are shown in Figure FAC-4.13. Results of predicted residual strength are comparable to experimental measurements, but as the width of the panel increases, the relative difference between experimental measurements and numerical predictions increases. Figure FAC-4.14 depicts the predicted plastic zone as the specimens reach their ultimate strength.

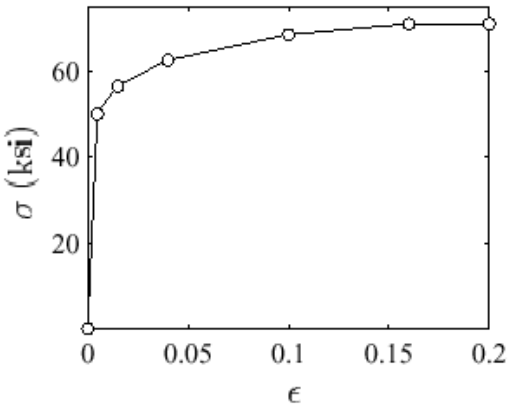

σ (ksi)	ϵ
0.0	0.0
50.0	0.00483
56.5	0.015
62.5	0.040
68.5	0.1
71.0	0.16
71.0	0.2

E = 10350 ksi
ν = 0.3

Figure FAC-4.9. Piecewise linear representation of uniaxial stress-strain relationship for 2023-T3 aluminum alloy used in the present example.

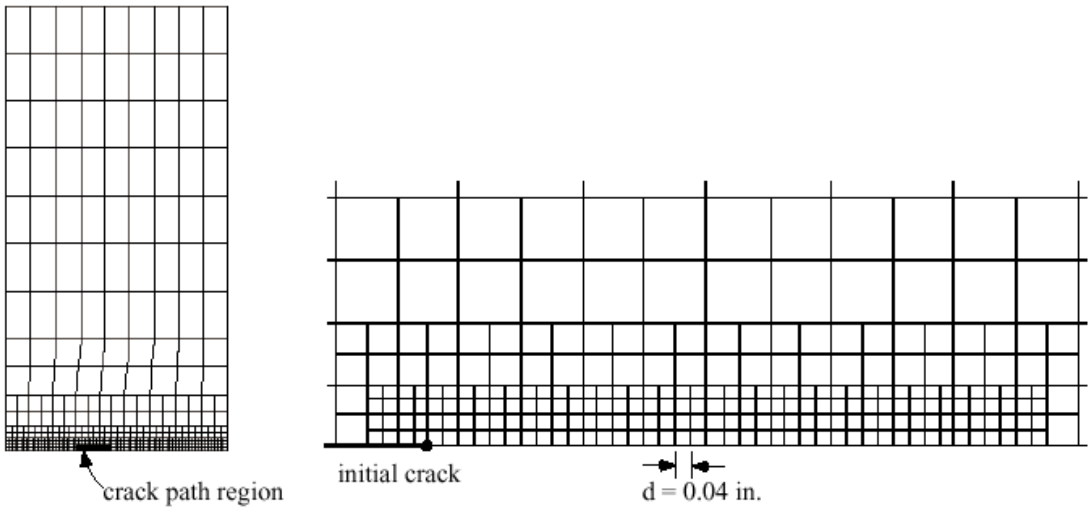

Figure FAC-4.10. Finite element mesh for 24- inch wide MT specimen and detail along crack path.

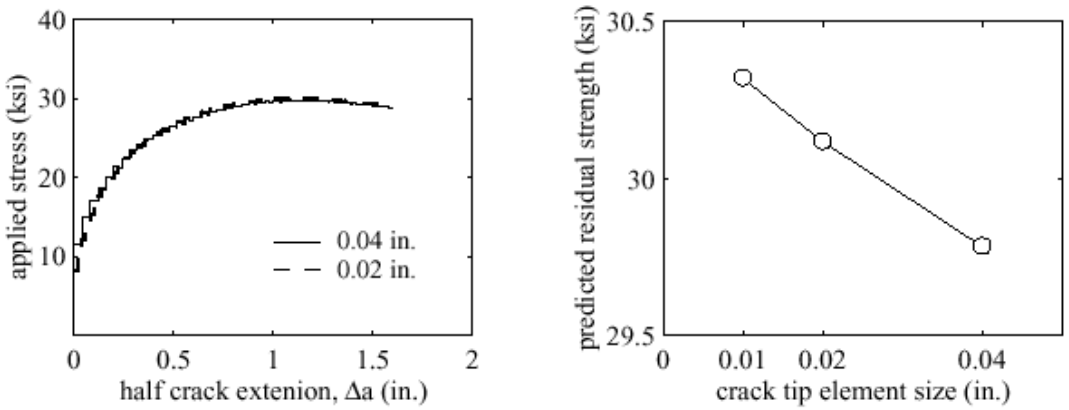

Figure FAC-4.11. Results from convergence study: predicted crack growth and predicted residual strength for 24- inch wide panel with different crack tip element sizes.

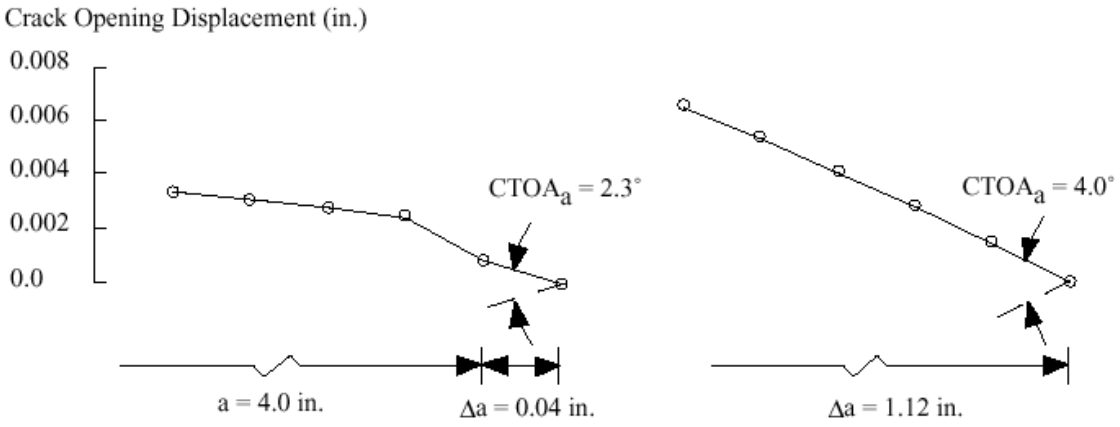

Figure FAC-4.12. Crack opening profiles and CTOA a after the first crack growth increment and after reaching the residual strength for 24 inch wide panels.

Two distinct phenomena are observed. For small specimens, plastic zones reach the free edge and the limit load is attained due to net section yielding. In contrast, for large specimens, plastic zones are well-confined by the elastic region and residual strength is reached near the fracture instability of the specimens.

As shown in Figure FAC-4.13, the relative difference in residual strength between experimental and numerical results increases as the width of the panel increases. This discrepancy is believed to be due to the three-dimensional nature of the stresses around the crack tip, a result of constraint effects due to the finite thickness of the panels [Hom 1990; Dawicke 1995]. Numerical results using plane strain, plane stress with a plane strain core height (see Figure FAC-4.5) equal to 0.12 inch, and three-dimensional finite

element analyses obtained from [Dawicke 1996, 1998] were studied to further demonstrate constraint effects on residual strength predictions. Predicted results shown in Table FAC-4.1 and Figure FAC-4.15 suggest that:

- Thin shell finite element analysis, behaving essentially in plane stress, tends to over-predict the residual strength as the width of the panel increases;
- Plane strain analysis over-predicts the residual strength of small specimens, but under-estimates it for large specimens;
- 2D plane stress analysis with a plane strain core and 3D analysis properly account for constraint effects. The predicted results follow the trend of experimental measurements even for wide panels.

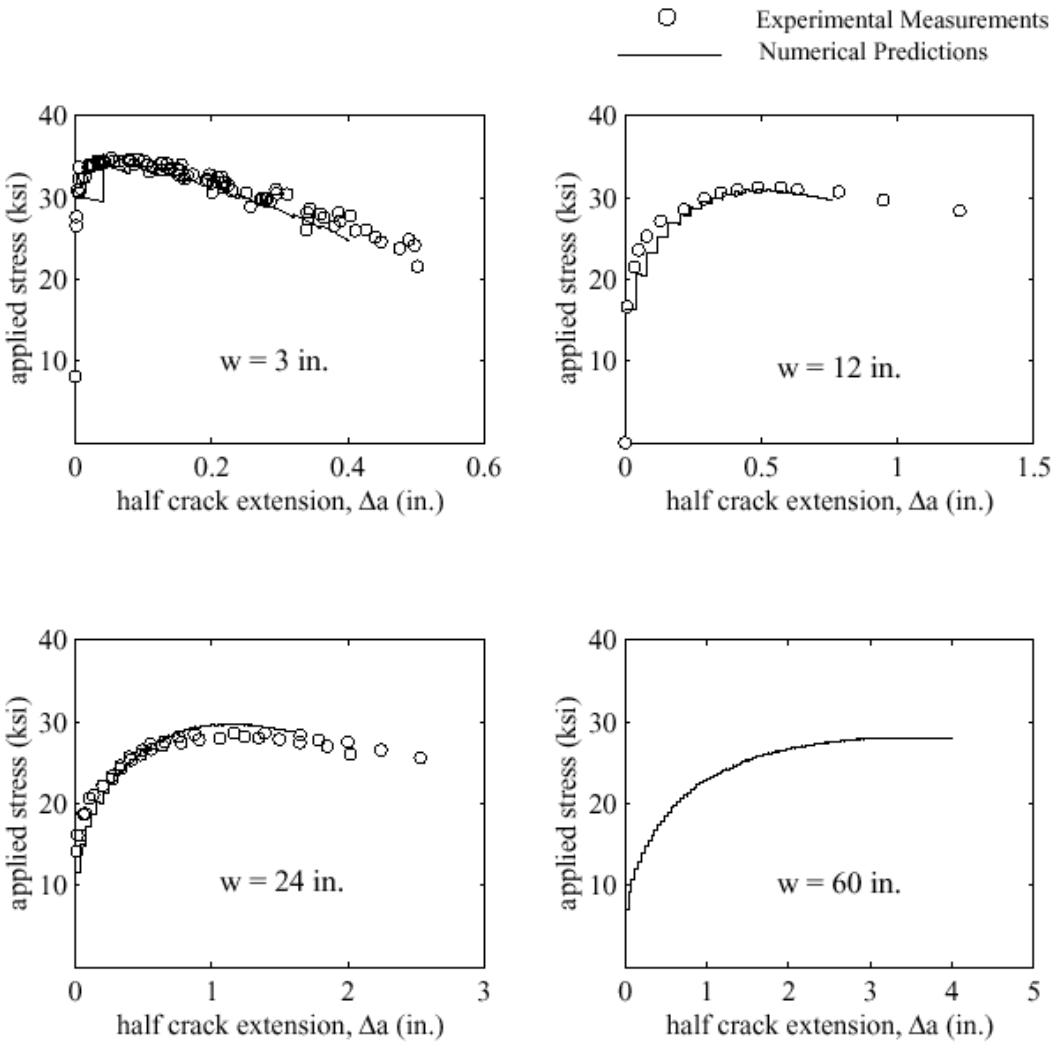

Figure FAC-4.13. Comparisons between experimental measurements and numerical predictions of applied stress versus half crack extension for various sizes of specimens.

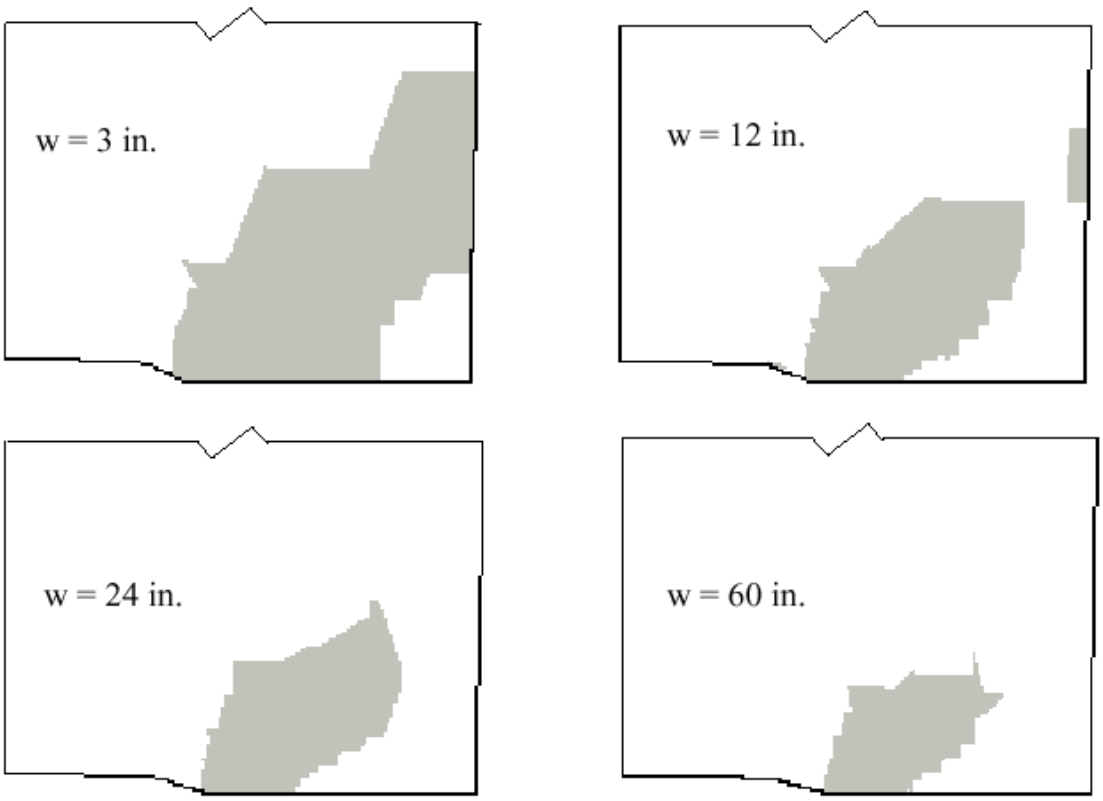

Figure FAC-4.14. Numerical predictions of plastic zone for various sizes of specimens reaching their residual strength.

Table FAC-4.1 Comparisons of Residual Strength Predictions (ksi) for MT Specimens

Plate Width	Thin Shell	Plane Strain	Plane Strain Core	3D	Experiment
3 in.	34.0	38	33.6	34.3	34.5
12 in.	30.7	32.7	30.7	30.8	31.3
24 in.	29.6	26.3	29.1	29.1	28.4
60 in.	28.1	16.6	26.7	26.3	N/A

The cross-over between plane stress and plane strain in predicting residual strength as the specimen size increases is an interesting topic. Based on the predicted plasticity distribution in Figure FAC-4.14, the net section yielding mechanism seems to dominate the residual strength prediction of small specimens. This may explain why the plane strain analysis predicts a higher residual strength for small specimens because the effective yield stress in plane strain is larger than that in plane stress. Thus, a further increase of remote stresses under plane strain conditions is needed for specimens to reach the point of net section yielding. For larger specimens, residual strength is governed by

stable crack growth and fracture. As one would expect from the thickness effects on K_c in LEFM, materials in plane stress have higher fracture toughness than materials in plane strain. Recent micromechanics-based, 3D analysis of ductile crack growth in a thin plate with a Gurson-type model also showed that, although the crack growth resistance at first increases with increasing plate thickness, the resistance to crack growth decreases after a small amount of crack extension [Mathur 1996]. For CTOA-driven ductile crack growth, stresses and strains under plane stress and plane strain conditions have not been studied in sufficient detail to clarify the issue. A possible cause of higher crack growth resistance in plane stress may be related to the residual plastic deformation effects. Based on asymptotic solutions for cracks growing in an incompressible elastic-perfectly plastic material under Mode I loading, larger residual plastic deformations would occur under plane stress than plane strain conditions leading to higher crack growth resistance.

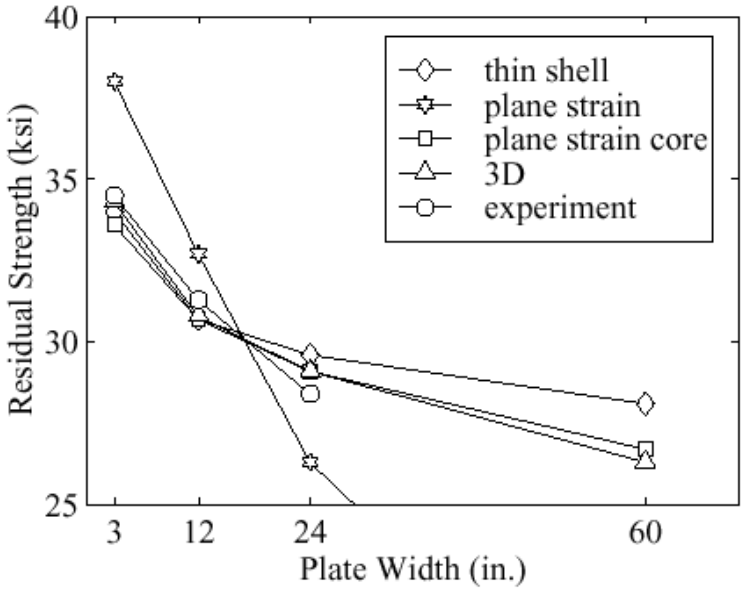

Figure FAC-4.15. Predicted results of thin shell, plane strain, plane stress with a plane strain core, and 3D analyses compared with experimental measurements.

Numerical Simulations of Specimens with Multiple Cracks

Numerical simulations of tests with multiple cracks using the CTOA fracture criterion are straightforward extensions of single crack specimen simulations. The same criterion ($CTOA_c$ = 5.25 degrees measured 0.04-inch behind the crack tip) is used to simulate stable crack growth and the link-up of multiple cracks, and to predict residual strength. No supplementary criterion is needed. Multiple crack test configurations as shown in Figure FAC-4.7 are modeled and the fracture processes are simulated. Note that the symmetry conditions along the vertical central line of the specimens are no longer valid due to the various lengths of fatigue pre-cracks; thus, at least one half of the specimen needs to be modeled. An example finite element mesh for test configuration b is shown in

Figure FAC-4.16. Mesh patterns around the multiple cracks are similar to those of the single crack models.

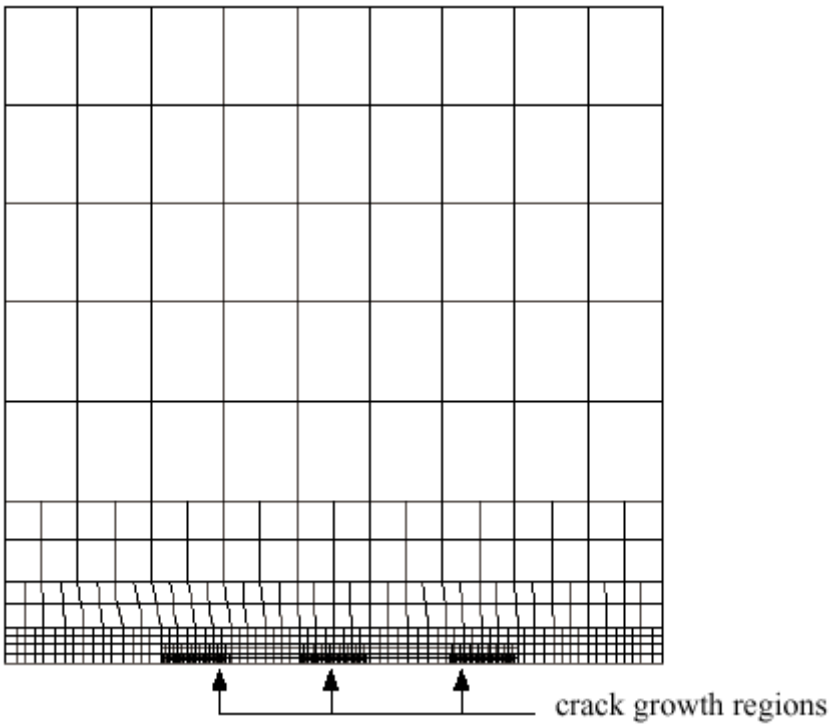

Figure FAC-4.16. Finite element mesh for the test configuration b (12-inch wide specimen with two cracks).

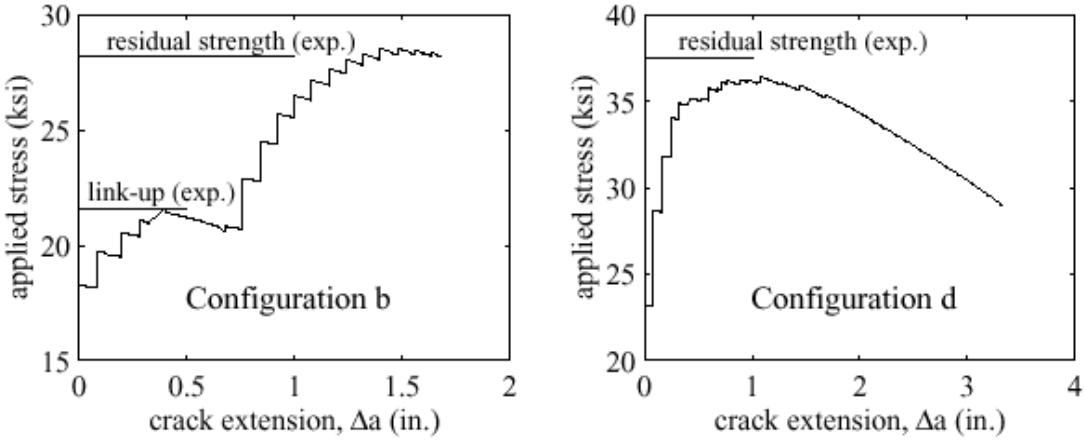

Figure FAC-4.17. Predicted applied stress versus crack extension for test configurations b and d.

Numerical results and experimental measurements for the applied stress versus half crack extension for test configuration b and d are shown in Figure FAC-4.17. Two distinct applied load versus crack growth history curves are predicted. For test configurations a, b, and c, link-up of cracks happens before the specimens reach their residual strength. For test configurations d and e, the limit load is attained before link-up. These numerical predictions agree with observations from the fracture tests. Again, plastic deformation plays an important role in the fracture process. Figure FAC-4.18 shows the plastic zone evolution of test configuration b during stable crack growth. The inherent residual plastic deformations during crack growth are clearly demonstrated through the deformed shapes.

Figure FAC-4.19 summarizes the relative difference between predicted results and experimental measurements. The predicted residual strength of all five MSD simulations agrees very well (within 3%) with experimental data. The predicted link-up load is comparable to experimental measurements, but the difference is larger than that for the residual strength. Reasons for the discrepancy may be related to the difficulty in measuring link-up load during the fracture tests. It is of practical importance to characterize the reduction in residual strength caused by MSD. Figure FAC-4.20 plots numerical predictions of residual strength versus lead crack length for cases with and without small cracks. A loss of residual strength due to the presence of multiple small cracks is observed.

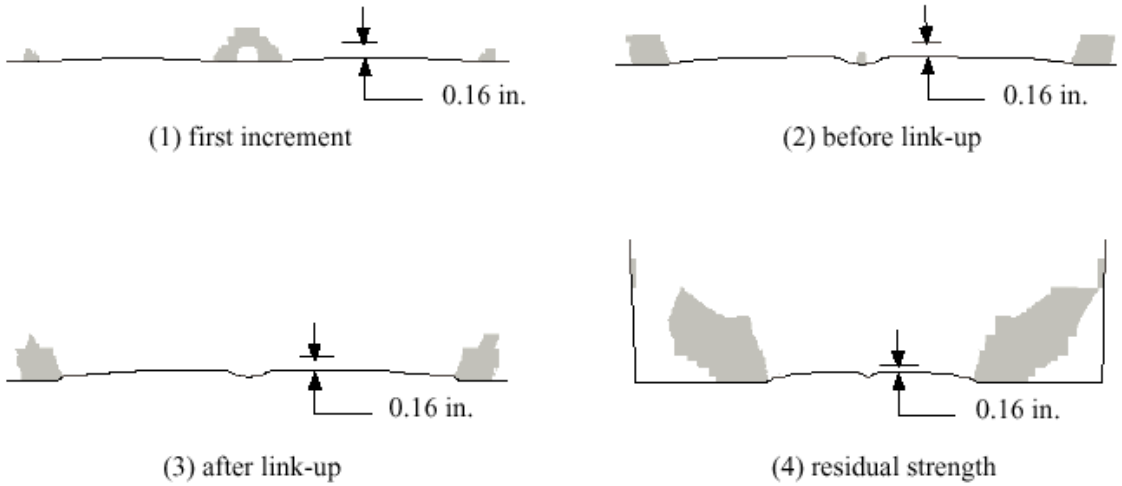

Figure FAC-4.18. Crack opening profile(s) and plastic zone evolution of test configuration b during crack growth: (1) at the first increment, (2) before link-up, (3) after link-up, and (4) reaching residual strength.

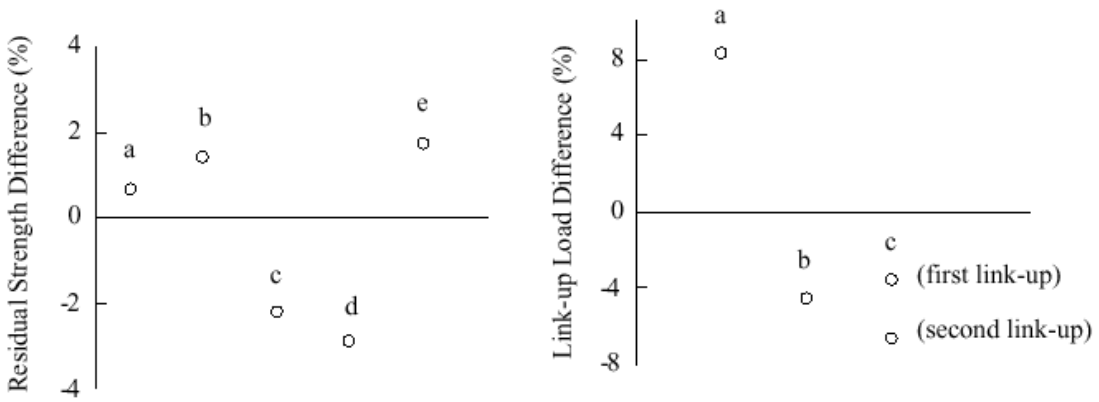

Figure FAC-4.19. Relative difference of residual strength and link-up load between predicted results and experimental measurements for specimens with multiple cracks.

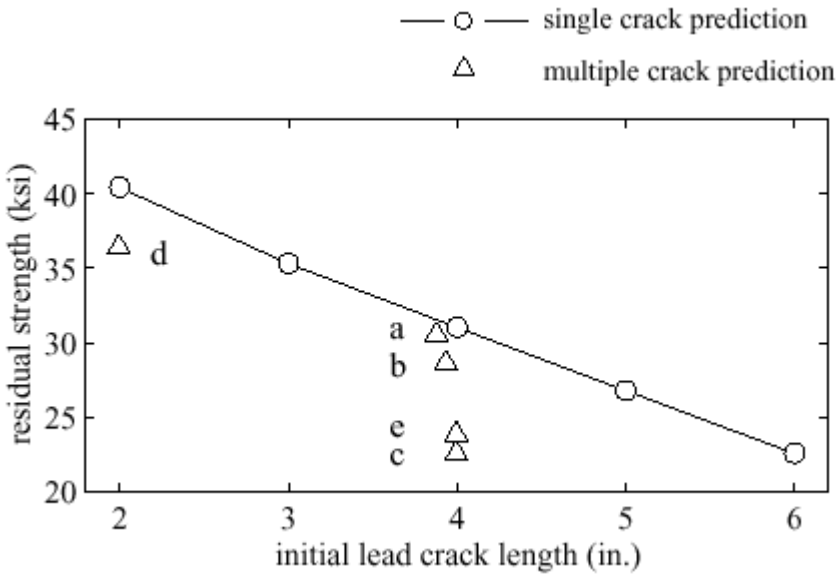

Figure FAC-4.20. Loss of residual strength due to the presence of small cracks.

References

D. Broek, D. Y. Jeong, and T. P. Forte. Testing and Analysis of Flat and Curved Panels with Multiple Cracks. In *Proceedings of the FAA-NASA Sixth International Conference on the Continued Airworthiness of Aircraft Structures*, pp 85-98, Atlantic City, New Jersey, 1994.

C.-S. Chen, P. A. Wawrzynek, and A. R. Ingraffea. Simulation of Stable Tearing and Residual Strength Prediction with Applications to Aircraft Fuselages. In *Proceedings of*

the FAA-NASA Symposium on Continued Airworthiness of Aircraft Structures, pp 605-618, 1996.

C.-S. Chen, P. A. Wawrzynek, and A. R. Ingraffea. Recent Advances in Numerical Simulation of Stable Crack Growth and Residual Strength Prediction. In *Proceedings of the Sixth East Asia-Pacific Conference on Structural Engineering & Construction*, pp 1773-1778, 1997.

C.-S. Chen, P. A. Wawrzynek, and A. R. Ingraffea. Elastic-Plastic Crack Growth Simulation and Residual Strength Prediction of Thin Plates with Single and Multiple Cracks. In *Fatigue and Fracture Mechanics: 29th Volume, ASTM STP 1332*, 1998.

D. S. Dawicke, M. Sutton. CTOA and Crack-tunneling Measurements in Thin Sheet 2024-T3 Aluminum Alloy. *Experimental Mechanics*, Volume 34, pp 357-368,1994a.

D. S. Dawicke, J. C. Newman, Jr., M. A. Sutton, and B. E. Amstutz. Influence of Crack History on the Stable Tearing Behavior of a Thin-Sheet Material with Multiple Cracks. In *Proceedings of the FAA-NASA Sixth International Conference on the Continued Airworthiness of Aircraft Structures*, pp 193-212, Atlantic City, New Jersey, 1994b.

D. S. Dawicke, M. A. Sutton, J. C. Newman, Jr., and C. A. Bigelow. Measurement and Analysis of Critical CTOA for an Aluminum Alloy Sheet. In *Fracture Mechanics: 25th Volume, ASTM STP 1220,* Philadelphia, pp 358-379, 1995.

D. S. Dawicke. Residual Strength Predictions Using a Crack Tip Opening Angle Criterion. In *Proceedings of the FAA-NASA Symposium on the Continued Airworthiness of Aircraft Structures*, pp 555-566, Atlanta, Georgia, 1996.

D. S. Dawicke, R. S. Piascik, and J. C. Newman, Jr. Prediction of Stable Tearing and Fracture of a 2000-Series Aluminum Alloy Plate Using a CTOA Criterion. In *Fracture Mechanics: 27th Volume, ASTM STP 1296*, Philadelphia, pp 90-104, 1997a.

D. S. Dawicke and J. C. Newman, Jr. Evaluation of Various Fracture Parameters for Predictions of Residual Strength in Sheets with Multi-Site Damage. In *Proceedings of the First Joint DoD/FAA/NASA Conference on Aging Aircraft*, Ogden, Utah, July 1997b.

D. S. Dawicke and J. C. Newman, Jr. Residual Strength Predictions for Multiple Site Damage Cracking Using a Three-Dimensional Analysis and a CTOA Criterion. In **F***atigue and Fracture Mechanics: 29th Volume, ASTM STP 1332*, 1998.

A. U. de Koning. A Contribution to the Analysis of Quasi-Static Crack Growth in Steel Materials. In *Fracture 1977, Proceedings of the 4th International Conference on Fracture*, Volume 3, pp 25-31, 1977.

C. L. Hom and R. M. McMeeking. Large Crack Tip Opening in Thin Elastic-Plastic Sheets. *International Journal of Fracture*, Volume 45, pp 103-122, 1990.

M. F. Kanninen and C. H. Popelar. *Advanced Fracture Mechanics*. Oxford University Press, New York, 1985.

K. K. Mathur, A. Needleman, and V. Tvergaard. Three Dimensional Analysis of Dynamic Ductile Crack Growth in a Thin Plate. *Journal of the Mechanics and Physics of Solids*, Volume 44, pp 439-464, 1996.

J. C. Newman, Jr. Finite-Element Analysis of Fatigue Crack Propagation-Including the Effects of Crack Closure. Ph.D. Thesis, Virginia Polytechnic Institute, 1974.

J. C. Newman, Jr. An Elastic-Plastic Finite Element Analysis of Crack Initiation, Stable Crack Growth, and Instability. In *Fracture Mechanics: Fifteenth Symposium, ASTM STP 833*, Philadelphia, pp93-117, 1984.

J. C. Newman, Jr. An Evaluation of Fracture Analysis Methods. In *Elastic-Plastic Fracture Mechanics Technology, ASTM STP 89***6**, Philadelphia, pp5-96, 1985.

J. C. Newman, Jr., D. S. Dawicke, and C. A. Bigelow. Finite-Element Analysis and Fracture Simulation in Thin-Sheet Aluminum Alloy. In *Proceedings of the International Workshop on Structural Integrity of Aging Airplanes*, 1992.

J. C. Newman, Jr., D. S. Dawicke, M. A. Sutton, and C. A. Bigelow. A Fracture Criterion For Widespread Cracking in Thin-Sheet Aluminum Alloys. In *International Committee on Aeronautical Fatigue, 17th Symposium*, Stockholm, Sweden, 1993.

C. C. Rankin and F. A. Brogan. The Computational Structural Mechanics Testbed Structural Element Processor ES5: STAGS Shell Element, 1991. NASA CR-4358.

J. R. Rice. Elastic-Plastic Models for Stable Crack Growth. In *Mechanics and Mechanisms of Crack Growth*, May, M. J. ed., British Steel Corp. Physical Metallurgy Center Publication, Sheffield, England, pp14-39, 1975.

J. R. Rice and E. P. Sorensen. Continuing Crack-Tip Deformation and Fracture for Plane-Strain Crack Growth in Elastic-Plastic Solids. *Journal of the Mechanics and Physics of Solids*, Volume 26, pp163-186, 1978.

PROBLEM NO. MERC-1

Title: Crack Growth Prediction of Center Wing Component with Emphasis on β-Factor Determination

Objective:

To illustrate the process of applying finite element and boundary element analyses to the determination of β-factors for crack growth simulations

General Description:

This problem focuses on the determination of β-factors for crack growth analysis of a longeron in the center wing area. Both 2-D and 3-D numerical methods are applied in the analysis. FRANC2D/L, a 2-D finite element (FE) analysis program, is used for the β-factor determination of through cracks. FRANC3D, a 3-D boundary element (BE) program is used to determine β-factors of a corner crack.

Topics Covered: finite element analysis, boundary element analysis, β-factor calculation

Type of Structure: center wing, longeron

Relevant Sections of Handbook: Sections 2, 5, 11

Author: Robert D. McGinty

Company Name: Mercer Engineering Research Center
Structures Technology Group
Warner Robins, GA 31088-7810
478-953-6800
www.merc.mercer.edu

Contact Point: Robert D. McGinty

Phone: 478-953-6800

e-Mail: bmcginty@merc.mercer.edu

MERC MERCER ENGINEERING RESEARCH CENTER
An Operating Unit Of Mercer University

Critical Area

This problem focuses on a critical area of an angle longeron in a center wing. As shown in the finite element mesh below, the crack starts in, and grows across the horizontal leg of the angle longeron. It begins as a corner crack in a fastener hole where the longeron and upper splice bar are attached.

The dominant loading mode of the longeron is tension during banking and turning maneuvers, but due to the complex geometries and interactions of the components, the details of the stress state are more complicated than simple, uniform tension near the critical fastener. The determination of β-factors through analytical means can, therefore, introduce significant errors in the crack growth analysis. Numerical methods such as finite and boundary element analysis provide a powerful alternative to the analytical solutions.

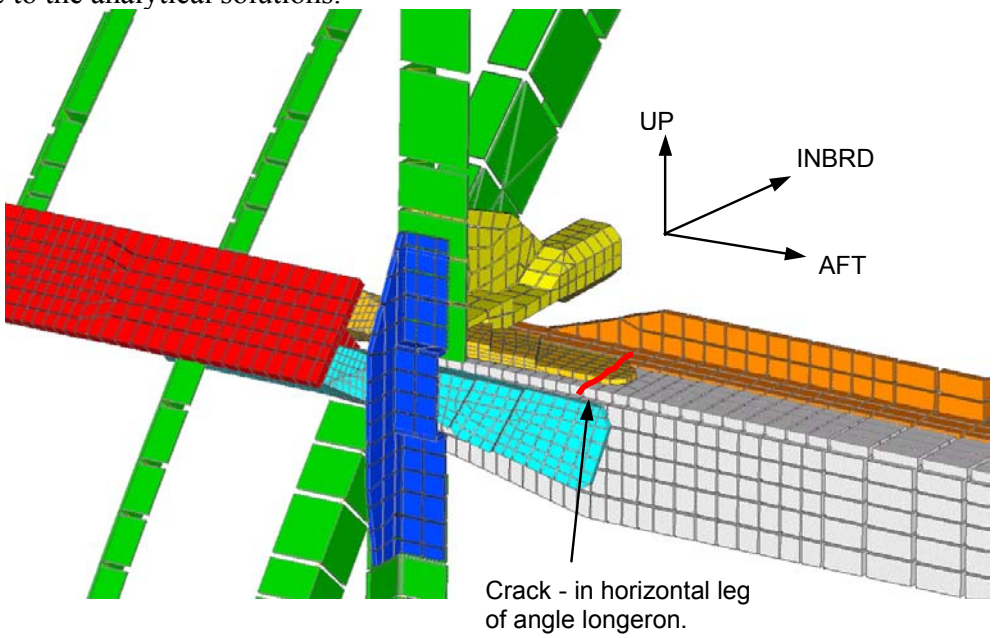

Figure MERC-1.1. Finite element mesh of center wing longeron and neighboring components. The crack location in the horizontal leg of the longeron is indicated.

Crack Growth Phases and Modeling Approach

As shown in Figure MERC-1.2 below, crack growth behavior can be divided into phases, usually alternating between "corner crack growth" and "through crack growth". The odd- numbered phases are corner cracks, and the even-numbered phases are through cracks. Also, it will be assumed here that the phases of crack growth take place sequentially. Corner crack growth starts in Phase 1 and continues until it grows through the part's thickness, at which point, through crack growth begins in Phase 2. Finally, Phase 3 does not begin until Phase 2 growth reaches the free edge of the longeron (Analysis has shown that the crack reaches critical length during Phase 3, therefore analysis of subsequent phases is not necessary.).

The β-factors for each phase of crack growth will be determined somewhat differently, due to the increasing complexity of each phase. Emphasis is placed on the numerical methods used for Phases 2 and 3.

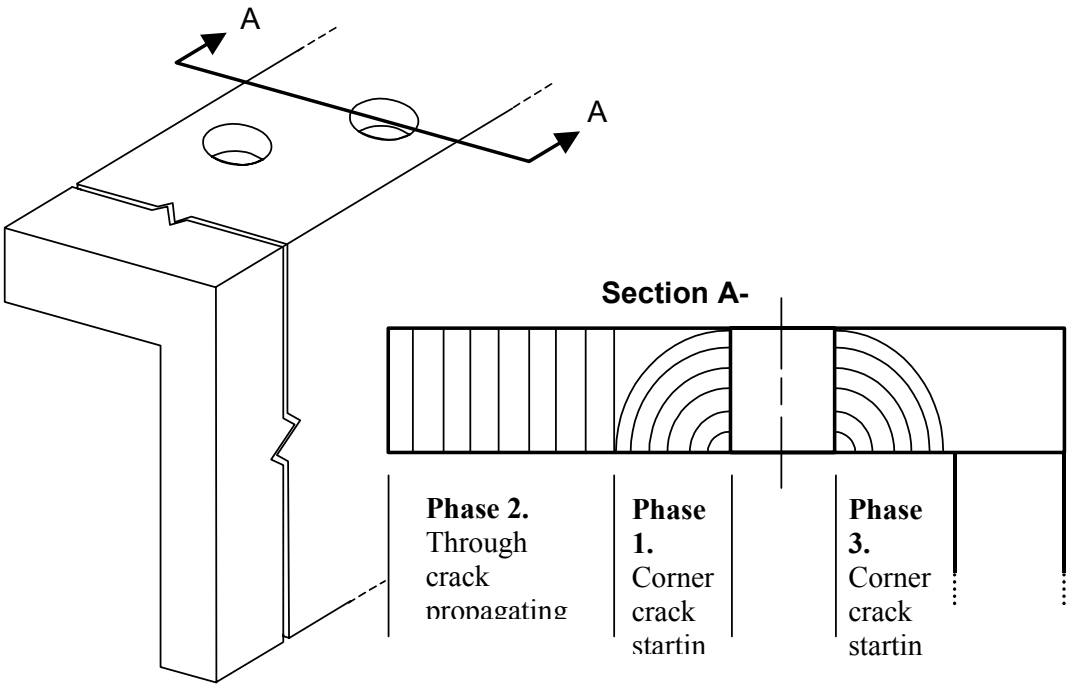

Figure MERC-1.2. Different Phases of Crack Growth in the Longeron are Shown

Phase 1 - Corner Crack at Fastener Hole

This represents a corner crack emanating from a loaded fastener hole that is offset from the center of the longeron leg. AFGROW provides pre-programmed solutions of β-factors for this case. Therefore, relatively little user expertise is required to obtain β-factors here, at least when compared to subsequent phases. Figure MERC-1.3 shows the AFGROW input form for defining part geometry, including the crack, from which AFGROW automatically computes β-factors.

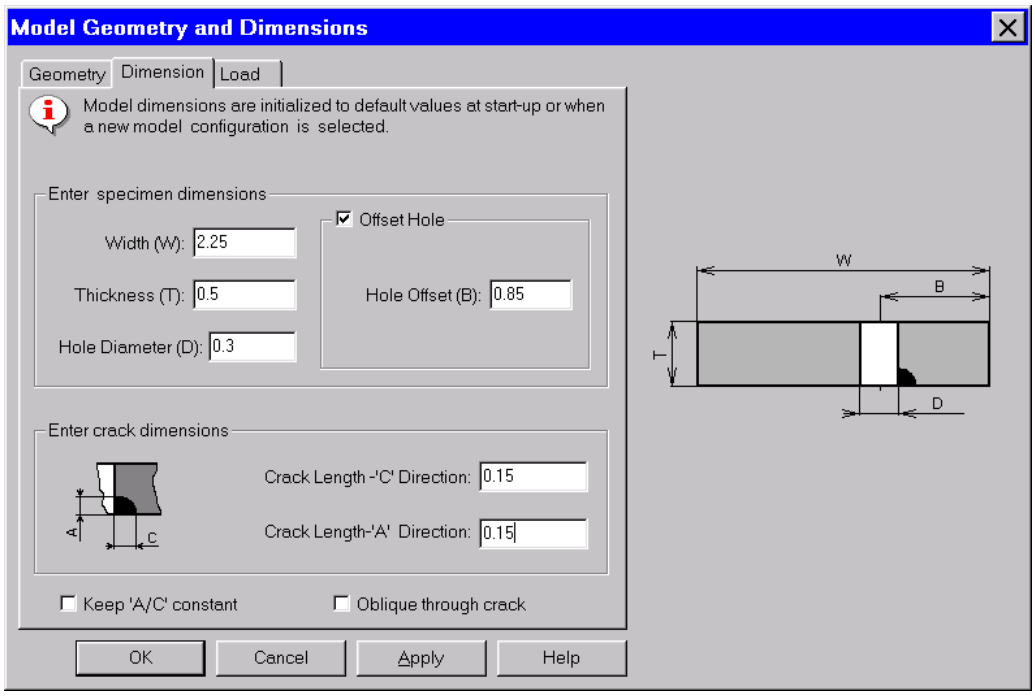

Figure MERC-1.3. AFGROW input form for defining part geometry, including the crack, from which AFGROW automatically computes β-factors.

Phase 2 - Through Crack Growing from Fastener Hole

Part geometry and loading conditions introduce complexities into the second phase of crack growth that are not fully incorporated into existing β-factor solutions. Therefore, numerical methods, i.e., finite elements, are used to estimate the β-factors. Figure MERC-1.4 shows a 2-D FE model of the longeron's horizontal leg developed in FRANC2D/L. FRANC2D/L is chosen because of its ability to automatically remesh while "growing" the crack. The boundary conditions, tractions and fastener forces, are determined from the NASTRAN FE model shown in Figure MERC-1.1. The crack path is also shown in Figure MERC-1.4. Note that it passes nearby a fastener whose presence introduces additional stress concentrations that further complicate the problem.

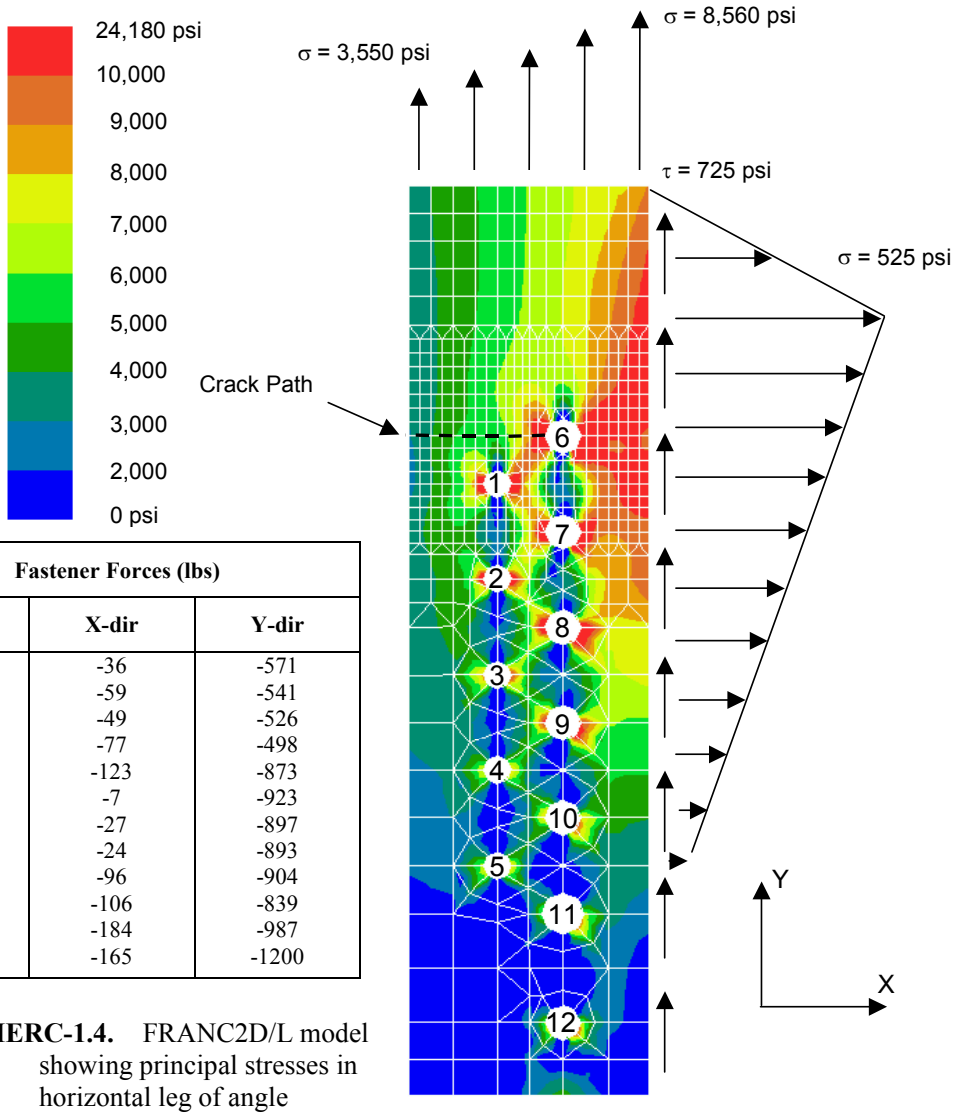

Fastener Forces (lbs)		
Number	**X-dir**	**Y-dir**
1	-36	-571
2	-59	-541
3	-49	-526
4	-77	-498
5	-123	-873
6	-7	-923
7	-27	-897
8	-24	-893
9	-96	-904
10	-106	-839
11	-184	-987
12	-165	-1200

Figure MERC-1.4. FRANC2D/L model showing principal stresses in horizontal leg of angle longeron

FRANC2D/L computes K values versus crack length as it automatically propagates the crack and remeshes. β-factors are determined by defining a reference stress, which is usually a remote tensile value, and solving for β in Eq. (1).

$$K = \sigma_{ref} \beta \sqrt{\pi a} \qquad (1)$$

where K is the stress intensity factor, a is crack length, and σ_{ref} is the reference stress, in this case 6,800 psi. Both K and β values are shown in the graph below.

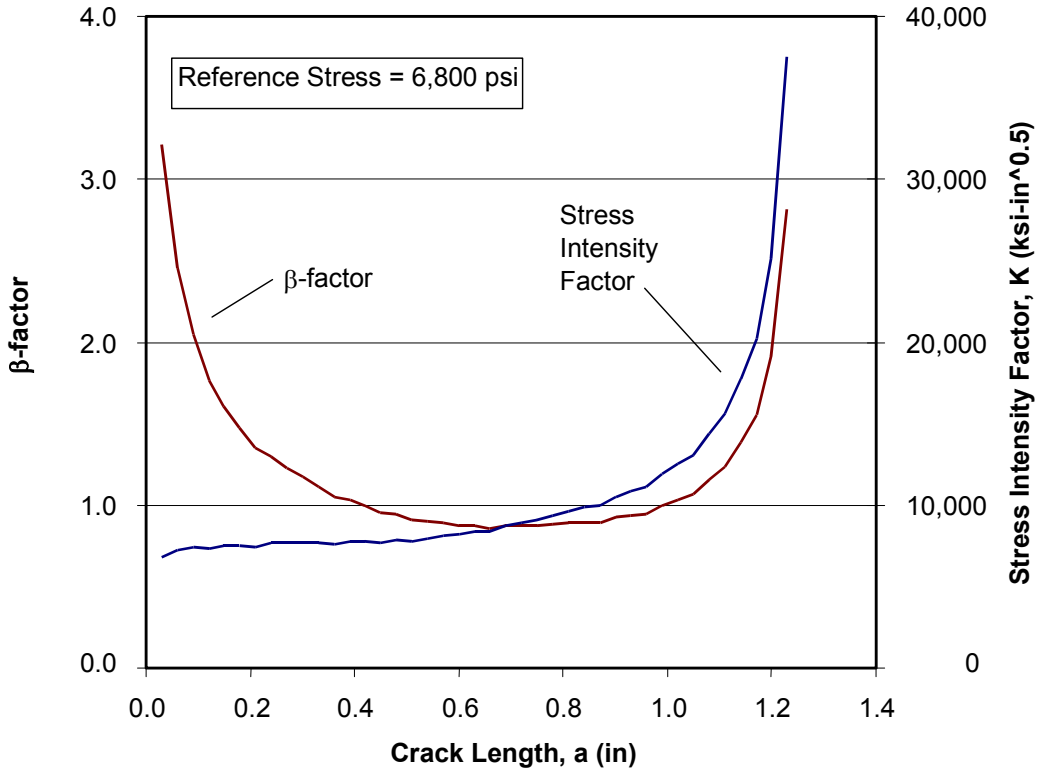

Figure MERC-1.5. β-factors and stress intensity values for Phase 2 of crack growth in the longeron. Values determined by FRANC2D/L

Phase 3 - Corner Crack Growing from Opposite Side of Fastener Hole

In Phase 3, a corner crack is assumed to grow from the opposite side of the fastener hole after the through crack reaches a free edge in Phase 2. But unlike Phase 1, AFGROW does not provide β-factor solutions for this situation. It is necessary to compute them numerically as in Phase 2. The process is substantially more involved because the problem is 3-D, however, it does begin just as the Phase 2 case. The NASTRAN and FRANC2D/L models are developed just as before, but the Phase 2 crack is present. The FRANC2D/L model is shown in Figure MERC-1.6 below.

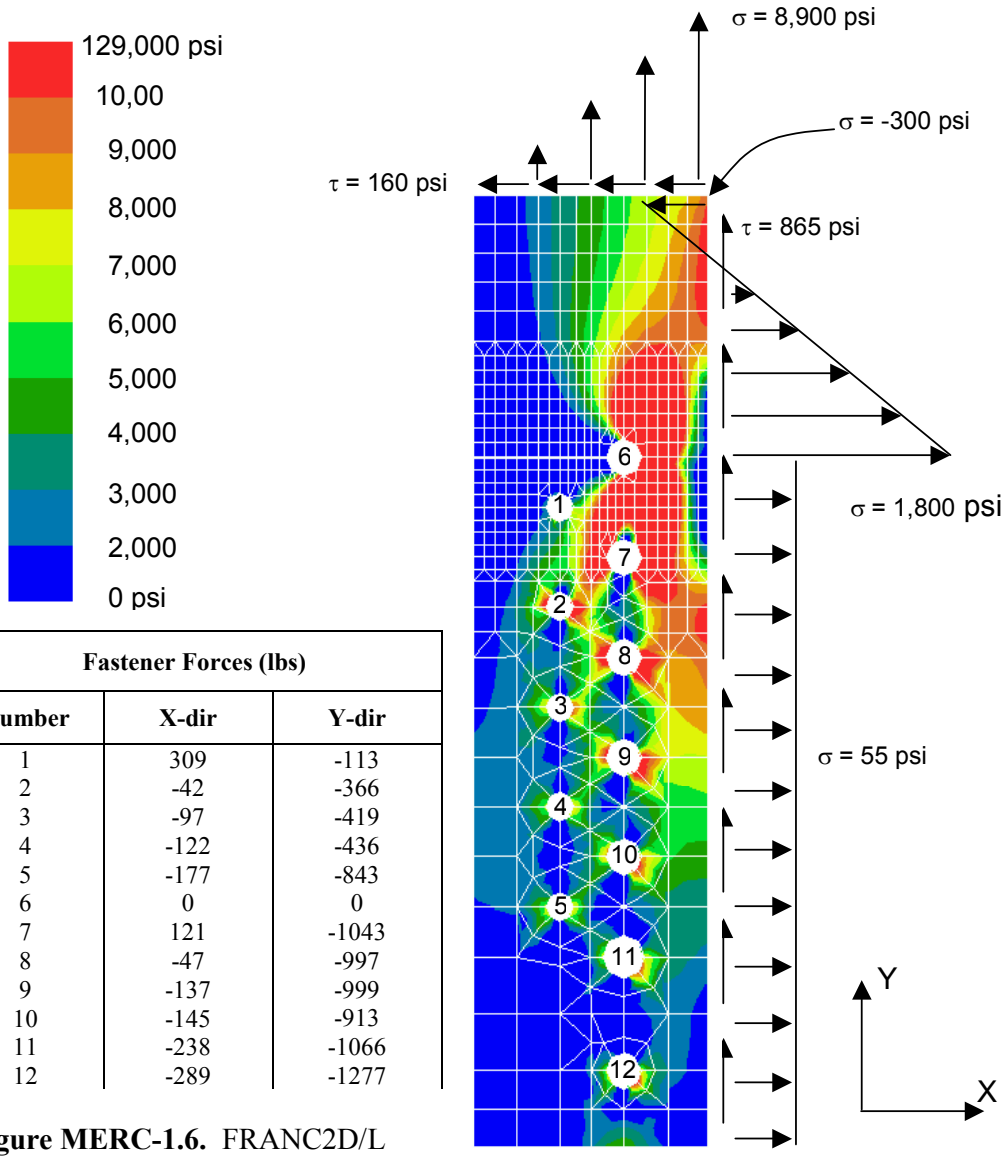

Fastener Forces (lbs)		
Number	**X-dir**	**Y-dir**
1	309	-113
2	-42	-366
3	-97	-419
4	-122	-436
5	-177	-843
6	0	0
7	121	-1043
8	-47	-997
9	-137	-999
10	-145	-913
11	-238	-1066
12	-289	-1277

Figure MERC-1.6. FRANC2D/L model showing principal stresses in horizontal leg of longeron with crack

The FRANC2D/L model results in Figure MERC-1.6 are used as boundary conditions for another, still more refined, numerical model. It is a 3-D boundary element model, developed in FRANC3D, of a corner crack at the fastener hole. This is shown in Figure MERC-1.7 below. FRANC3D reports *K* values along the corner crack front, and these are used to calculate β-factors using Eq. (1) just as in Phase 2.

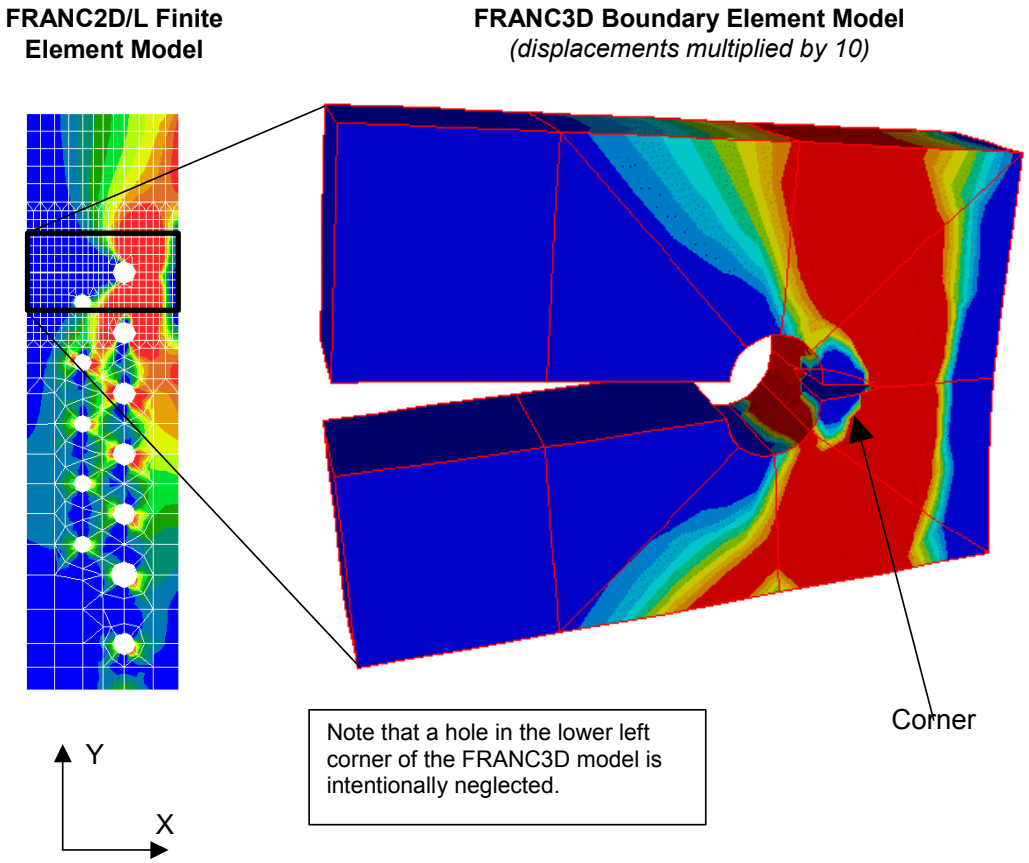

Figure MERC-1.7. FRANC3D model and principal stresses for Phase 3 corner crack at fastener hole. FRANC2D/L stresses serve as boundary conditions for the FRANC3D model

Several FRANC3D analyses are, in fact, necessary for each critical area in order to cover the possible combinations of thickness and surface lengths of the corner crack. As an example, Figure MERC-1.8 illustrates nine (3x3) corner cracks of various lengths that are analyzed in order to provide sufficient β-factor information for corner crack growth studies.

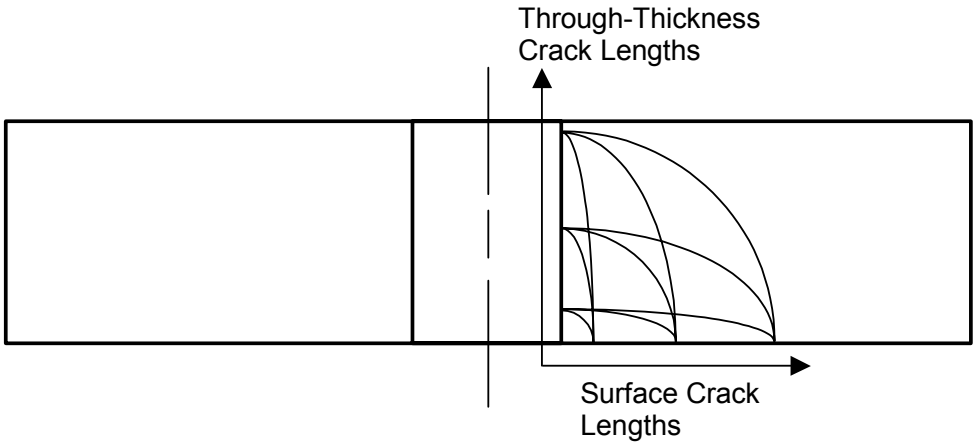

Figure MERC-1.8. Various Corner Crack Geometries that are Analyzed with FRANC3D

Tables MERC-1.1 and MERC-1.2 give β-factors for various corner crack geometries. Two tables are required to determine crack growth through the part thickness and along the part surface. Table MERC-1.1 gives β-factors that apply to crack growth through the part's thickness. Table MERC-1.2 corresponds to crack growth along the part's surface. AFGROW uses this information to independently predict growth rates along the two directions. Though independent, it is generally true that the growth rates produce a corner crack whose thickness length is approximately 50% greater than its surface length.

Table MERC-1.1. Beta Factors – Thickness Direction

		Thickness Crack Length (in)		
		0.05"	**0.264"**	**0.488"**
Surface Crack Lengths (in)	**0.05"**	9.739	4.715	3.219
	0.200"	11.26	8.172	7.940
	0.400"	11.30	11.48	14.62

Table MERC-1.2. Beta Factors – Surface Direction

		Thickness Crack Length (in)		
		0.05"	**0.264"**	**0.488"**
Surface Crack Lengths (in)	**0.05"**	7.590	12.88	14.03
	0.200"	1.381	6.824	11.25
	0.400"	1.211	3.813	10.57

Predicting Crack Growth

AFGROW is used to predict crack growth in the longeron using the β-factors presented here. The crack is assumed to start as a 0.05" radius corner crack at the fastener hole and grow according to the discussion above. Only surface crack length is plotted. Details of the stress spectra and material *da/dN* data are not presented. Note that Willenborg retardation is applied.

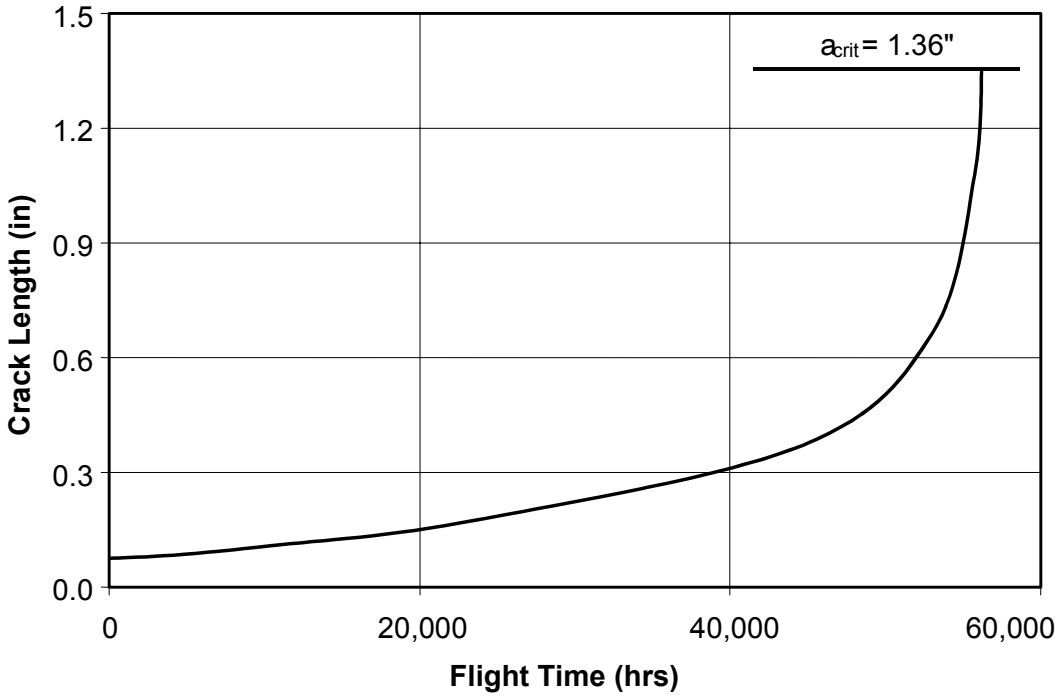

Figure MERC-1.9. Predicted crack growth versus flight hours for a crack growing across the horizontal leg of the longeron. Willenborg retardation is applied to the simulation

PROBLEM NO. MERC-2

Title: Damage Tolerance Analysis of Critical Area on Windshield Doubler

Objective:

To illustrate the process of estimating crack growth behavior, which is necessary for setting inspection intervals.

General Description:

This problem focuses on a damage tolerance analysis of the windshield doubler at the intersection of the upper windowsill and post of an airplane. The analysis goal is to estimate the crack growth behavior of the windshield doubler. A finite element model is developed, with extensive refinement in the window area, to determine stresses in the part. A stress spectrum and β-factors are used with AFGROW to predict crack length versus flight hours.

Topics Covered: Damage tolerance analysis, finite element analysis, crack growth analysis

Type of Structure: windows, windshield doubler

Relevant Sections of Handbook: Sections 2, 5, 7, 11

Author: Robert D. McGinty

Company Name: Mercer Engineering Research Center
Structures Technology Group
Warner Robins, GA 31088-7810
478-953-6800
www.merc.mercer.edu

Contact Point: Robert D. McGinty

Phone: 478-953-6800

e-Mail: bmcginty@merc.mercer.edu

MERC MERCER ENGINEERING RESEARCH CENTER
An Operating Unit Of Mercer University

Critical Area

This problem focuses on a critical area of the windshield doubler at the intersection of the upper window sill and window post #3. The doubler is shown in Figure MERC-2.1, with the expected crack path marked. It is fabricated from 0.091" thick 7075-T6 aluminum and is 1.5" wide at the crack location. The windows are fastened to the doubler in such a way that they "float", which means that the windows transfer only bearing loads to it. The fasteners do not exert tangential loads on the windshield doubler.

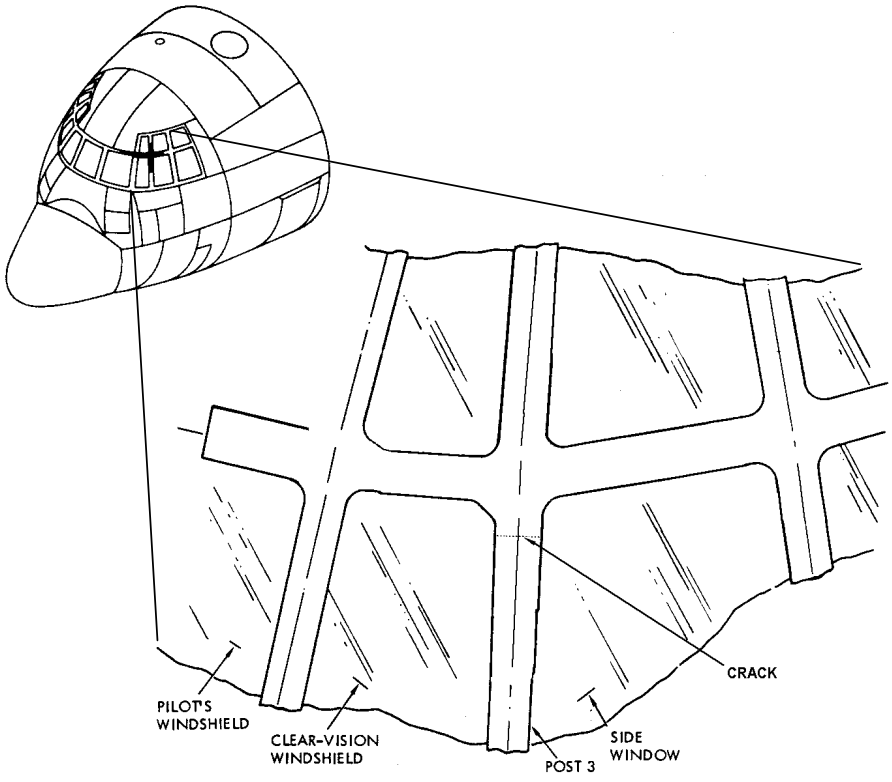

Figure MERC-2.1. Sketch of the Forward Fuselage and Windshield Doubler

Structural Finite Element Model

Geometry and Finite Element Mesh

A NASTRAN finite element model (FEM) of the forward fuselage was developed and is shown in Figure MERC-2.2. It is made up primarily of shell and beam elements. In general, joints are modeled by shared-nodes; fasteners are not explicitly modeled. However, fasteners that attach the windshield doubler to airframe structure and skin are explicitly modeled with beam elements. Rigid elements are used occasionally, such as to simulate floating windows that transfer only bearing loads to the windshield doubler.

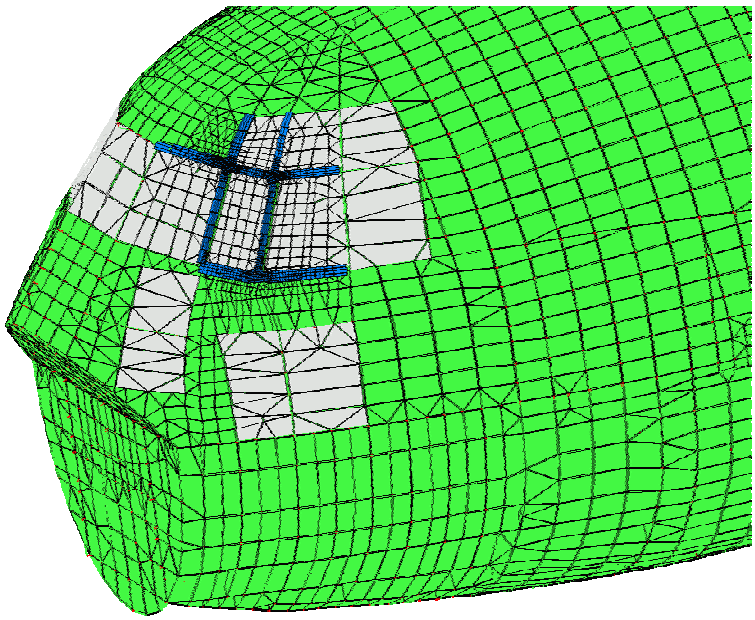

Figure MERC-2.2. Structural Finite Element Model of Forward Fuselage of the Aircraft With Mesh Refinement In Front Window Area

Loading Conditions and Stresses

Internal pressurization effects are the dominant cause of stresses in the window area. Loads due to maneuvers, landings, wind gusts, etc. are negligible in comparison. Internal pressurization actually refers to the case where the cabin is maintained at sea level pressure while flying at altitudes where atmospheric pressure is substantially less. The pressure differential is applied to the model as an internal pressure. Note that a release valve(s) in the plane prevents the pressure differential from exceeding 7.5 psi.

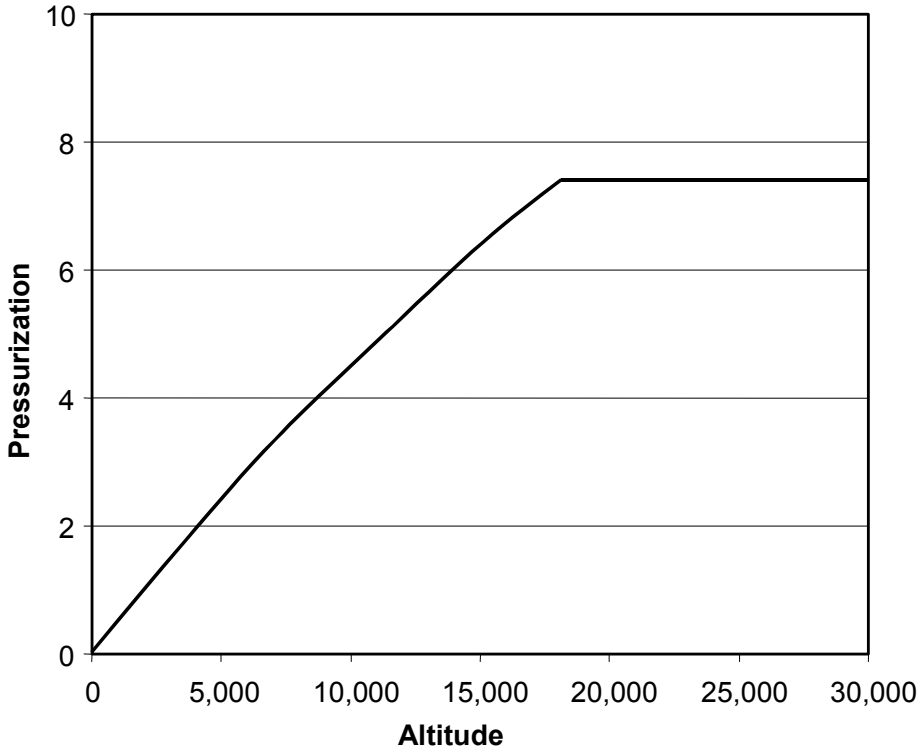

Figure MERC-2.3. Internal pressure versus altitude. A release valve prevents the pressure from exceeding 7.5 psi.

Mission profile data are combined with the pressurization information in Figure MERC-2.3 to give the frequency and amplitude of internal pressurization cycles that the plane will experience. Mission profile data consist of flight altitude data versus time. Figure MERC-2.4 shows a typical segment consisting of missions at several altitudes ranging from 1,000 ft to 25,000 ft. Combining the information in Figures MERC-2.3 and MERC-2.4 gives the internal pressurization cycles shown in Figure MERC-2.5.

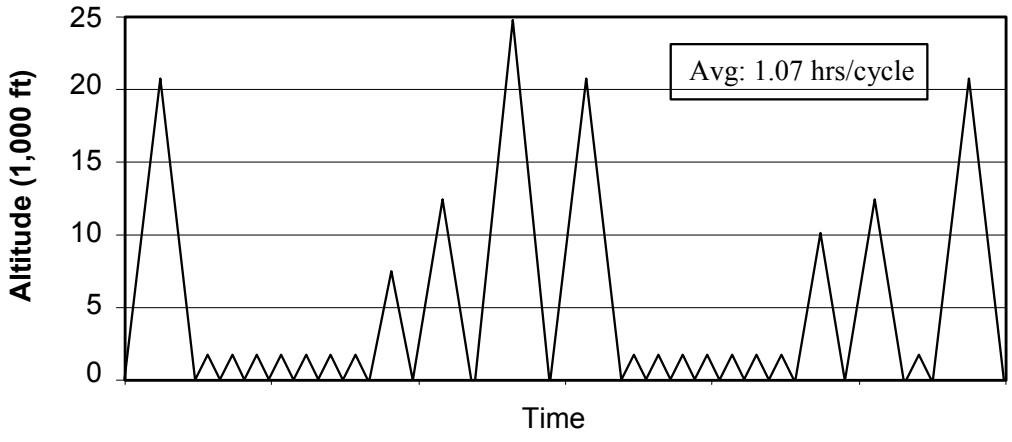

Figure MERC-2.4. Typical missions showing altitude versus time. Time spent at each altitude is not shown.

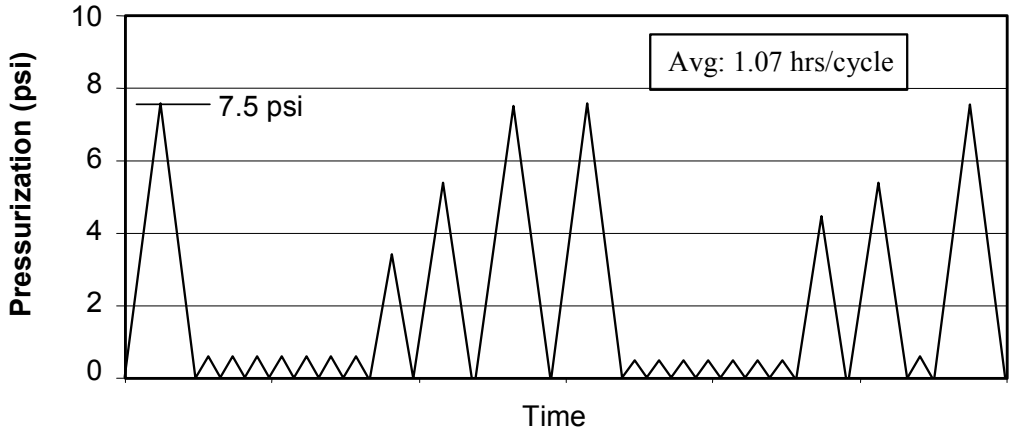

Figure MERC-2.5. Internal pressurization versus time for missions shown in Figure MERC-2.4.

Stresses in the forward fuselage and doubler for 1 psi pressurization are shown in Figure MERC-2.6 below. Stresses in the doubler are assumed to scale linearly with the imposed pressure. For example, the stress at any point in the doubler under 7.5 psi internal pressurization will be 7.5 times greater than its value in Figure MERC-2.6.

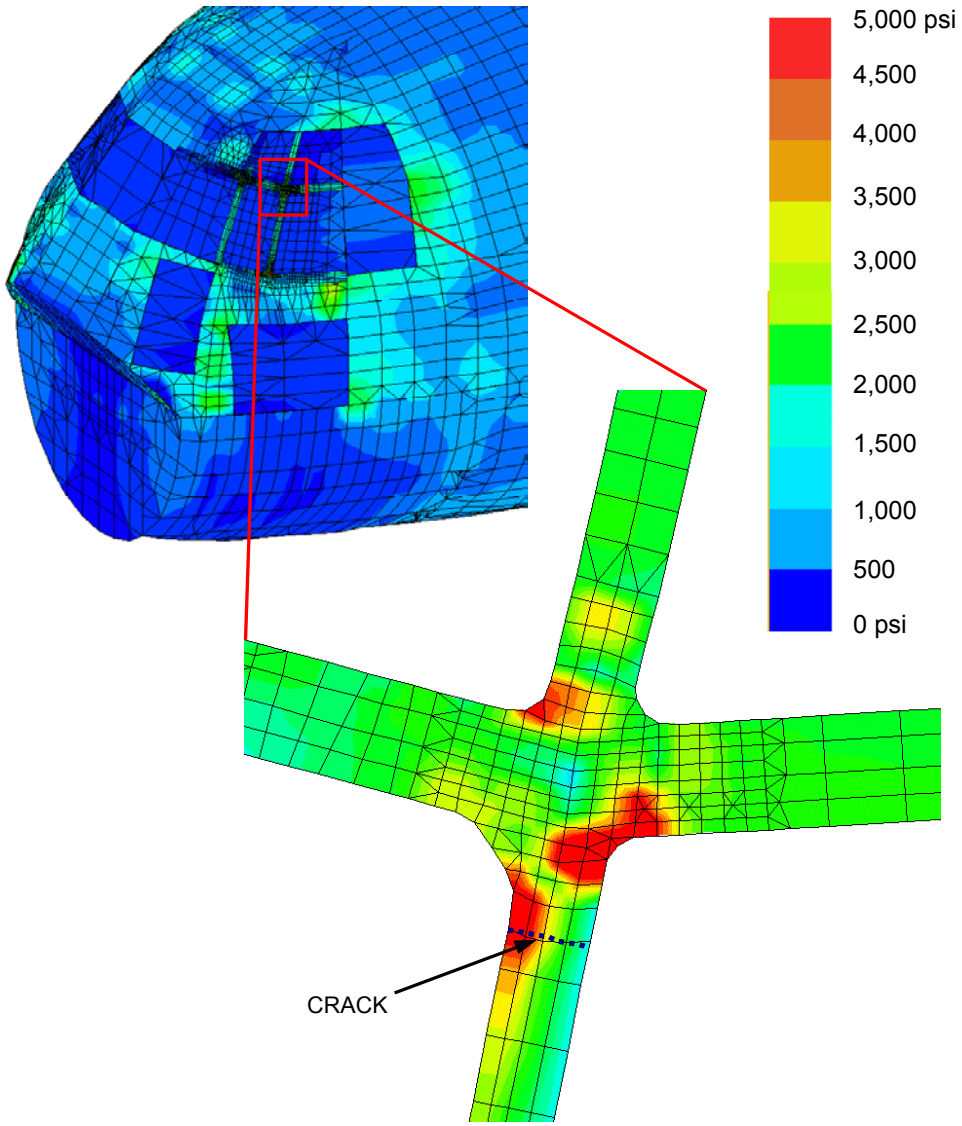

Figure MERC-2.6. Maximum principal stress in forward fuselage and window doubler due to 1 si pressurization of the fuselage. Typical crack location is shown.

Figure MERC-2.7 shows cycles of average tensile stress in the lower leg of the doubler. The values are the result of multiplying the pressure cycle data in Figure MERC-2.5 by the average tensile stress in the lower leg of the doubler predicted by the finite element analysis for 1 psi pressurization.

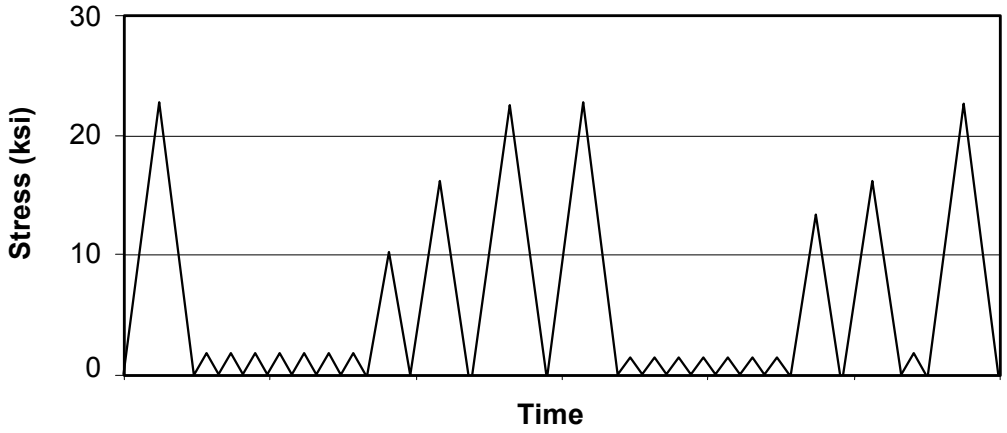

Figure MERC-2.7. Cycles of average tensile stress in lower leg of doubler. Stress cycles in the doubler are directly proportional to the pressurization cycles in Figure MERC-2.5.

Crack Growth Prediction

Critical Crack Length

Failure is defined as the time when the crack reaches a length, a_{crit}, such that further growth would be unstable under maximum loading conditions. This occurs when the stress intensity factor of the crack reaches its critical value, K_c. This value is 71 ksi$\sqrt{}$in for 0.091" thick Al 7075-T6. The tensile stress in the doubler at maximum loading conditions is σ_{limit}= 22.4 ksi. The critical crack length is determined by solving

$$K_c = \sigma_{limit}\,\beta\sqrt{\pi a_{crit}} \qquad (1)$$

for a_{crit}. This must be solved iteratively because β is a function of crack length, a. Solving the equation gives a_{crit}=0.7". Note that β-factors for this analysis were taken from the AFGROW library.

Predicting the Crack Growth

AFGROW was used to predict crack growth in the doubler due to the fuselage pressurization cycles. The crack is assumed to start as a 0.05" radius corner crack at a fastener hole, grow to a through crack, and then grow across the doubler until failure. Stress cycles (see Figure MERC-2.7), β-factors from AFGROW, and material *da/dN* data are combined to give the crack growth prediction in Figure MERC-2.8 below. Note that Willenborg retardation is applied.

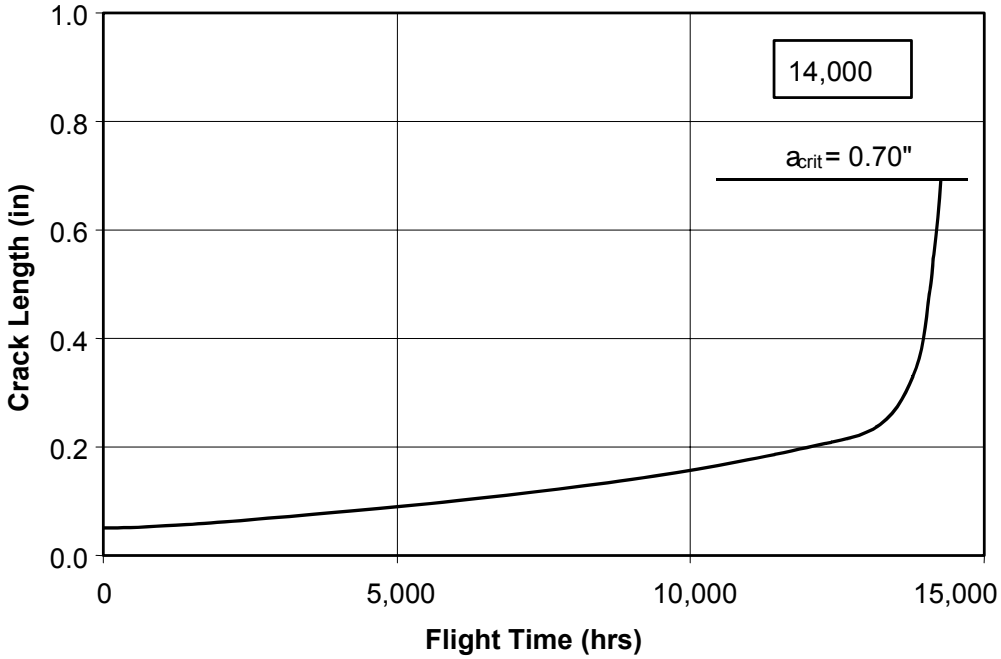

Figure MERC-2.8. Predicted crack growth versus flight hours for a crack growing across the lower leg of the doubler. Willenborg retardation is applied to the simulation.

PROBLEM NO. MERC-3

Title: Sensitivity of Fatigue Crack Growth Rates to Operating Conditions

Objective:

To quantify the sensitivity of fatigue crack growth rates and service life to various input parameters such as stress level and initial crack length.

General Description:

This problem focuses on quantifying the sensitivity of certain fatigue performance factors such as crack growth rate and operational service life to variations and/or uncertainties in input parameters such as cyclic stress amplitude and initial crack length. Simplified problems are first studied analytically. They are then followed by a complex application in the windshield area of a military airplane.

Topics Covered: Damage tolerance analysis, fatigue crack growth analysis, sensitivity analysis

Type of Structure: longeron

Relevant Sections of Handbook: Sections 2, 5

Author: Robert D. McGinty

Company Name: Mercer Engineering Research Center
Structures Technology Group
Warner Robins, GA 31088-7810
478-953-6800
www.merc.mercer.edu

Contact Point: Robert D. McGinty

Phone: 478-953-6800

e-Mail: bmcginty@merc.mercer.edu

MERC MERCER ENGINEERING RESEARCH CENTER
An Operating Unit Of Mercer University

Introduction

Damage tolerance analyses (DTA) of structures are often challenging and time consuming endeavors because of the types of data required and the sophistication of the techniques necessary to obtain it. Examples of required data include stress states in parts so complex that finite element (FE) analyses are necessary to obtain them. The fatigue crack growth behavior of materials may require lengthy experimental characterization.

The high demands of time and expertise can easily exceed the resources available. In such cases, it becomes necessary to prioritize the efforts devoted to obtaining various pieces of information according to each one's level of importance to the final analysis. Critical factors should receive large resources to enable their accurate determination. On the other hand, quick approximations may prove satisfactory for factors of secondary importance. But the question arises, "Which factors are critical, and which are secondary?" This example problem aims to address that question.

Mathematical Background: Sensitivity Analysis

Before one can determine what factors are and are not important in a DTA, one must choose a method of quantifying the qualitative term, *important*. Here, we have chosen to use a sensitivity analysis approach. It relates the percentage change in a system's input to the resulting percentage change in the system's output, the ratio of the two being the sensitivity parameter. As an example, consider the following equation

$$y = Ax^n \tag{1}$$

where x is the input, y is the output, and A and n are constants. The sensitivity of y with respect to x is therefore the ratio of the percentage change in y resulting from a given percentage change in x. The percentage change in the output y would be expressed as

$$100\%\left(\frac{\Delta y}{y}\right) \tag{2}$$

and likewise for the input variable x. Defining the sensitivity parameter, $S_{y/x}$, as the ratio of the percentage changes gives

$$S_{y/x} \equiv \frac{100\%\,(\Delta y / y)}{100\%\,(\Delta x / x)} \tag{3}$$

and taking the limit as $\Delta x \to 0$ gives the analytical definition of $S_{y/x}$.

$$S_{y/x} \equiv \frac{dy}{dx} \cdot \frac{x}{y} \tag{4}$$

Applying Eq. (4) to Eq. (1) gives the result

$$S_{y/x} = n \tag{5}$$

which states that the percentage change in y is simply n times the percentage change in x regardless of the values of A and x. So if n=3 and x is increased by 10%, then y would increase 30%. This is a very useful result because of its simplicity. It will be used extensively in the following applications of damage tolerance analysis. Of course many equations exist that are not in the form of Eq. (1). In these cases, Eq. (4) must be applied on an individual basis.

Applications to Damage Tolerance Analysis

Stress Intensity Factor

One of the most fundamental steps of any DTA is calculation of the stress intensity factor, K, using Eq. (6)

$$K = \beta\sigma\sqrt{\pi a} \tag{6}$$

where β is the geometry factor, σ is stress, and a is crack length. The sensitivity of K to the various parameters is then

$$S_{K/\beta} = 1 \qquad S_{K/\sigma} = 1 \qquad S_{K/a} = \tfrac{1}{2} \tag{7}$$

indicating that accurate values of β and σ are equally important to the calculation of K, and that the sensitivity to crack length is less.

Crack Growth Rates

The situation becomes more interesting when crack growth rates are analyzed. A Paris Law dependence on ΔK will be assumed as follows

$$\frac{da}{dN} = C(\Delta K)^n = C(\beta\Delta\sigma)^n(\pi a)^{n/2} \tag{8}$$

where N is the number of cycles, and C and n are Paris Law constants. Note that C and n are material properties with associated measurement uncertainties. Since the sensitivity of crack growth rate to the β-factor and stress is equal to n in both cases, it is worth reviewing typical values. Figure MERC-3.1 shows crack growth data for Al 7075-T6. The Paris Law forms a straight line on the logarithmic graph with n equal to the slope and C equal to da/dN at ΔK=1. It is seen that in this case, n=3.6. ($3 \le n \le$ for most materials) This value has critical implications on the accuracy of crack growth predictions. It means that a 10% error in the estimate of the β-factor results in a 36% error in the prediction of da/dN. The same sensitivity applies to the stress as well. It is this high sensitivity of da/dN to ΔK, reflected in the value of n, which presents a major challenge to the accurate prediction of crack growth rates.

What of the sensitivities to the Paris Law constants? The sensitivity to C is unity since that is its exponent in Eq. (8). It is necessary to apply Eq. (4) to Eq. (8) to determine the sensitivity to the exponent, n. Doing so gives

$$S_{\frac{da}{dN}/n} = n \ln(\Delta K) \tag{9}$$

Since ln(ΔK) is usually greater than one in engineering analyses, it is clear that the sensitivity of predicted crack growth rates to the accurate determination of the slope of the da/dN–ΔK data in Figure MERC-3.1 is even greater than to β-factors and stresses. In summary, the results are as follows

$$S_{\frac{da}{dN}/\beta} = n \qquad S_{\frac{da}{dN}/\sigma} = n \qquad S_{\frac{da}{dN}/a} = n/2$$

$$S_{\frac{da}{dN}/C} = 1 \qquad S_{\frac{da}{dN}/n} = n \ln(\Delta K) \tag{10}$$

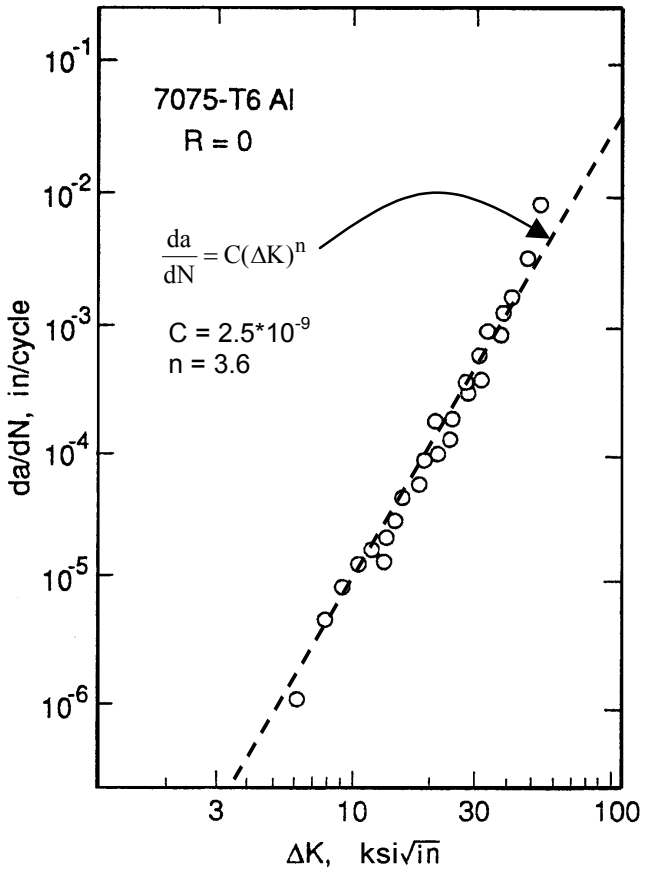

Figure MERC-3.1. da/dN – DK data for 7075-T6 Al and Paris Law curve fit.

Service Life – Cycles to Failure

The quantity of primary interest in a DTA is the service life of a component, measured in cycles to failure, N_{Life}. An analytical expression for N_{Life} can be obtained if one neglects crack retardation and assumes that the β-factor and stress range are both constant throughout a component's life. Integrating Eq. (8) and solving for N_{Life} gives

$$N_{Life} = \frac{a_f^{1-\frac{n}{2}} - a_o^{1-\frac{n}{2}}}{C\,(\beta\,\Delta\sigma\sqrt{\pi})^n\left(1-\frac{n}{2}\right)} \tag{11}$$

where a_o is initial crack length, and a_f is final crack length at which point failure takes place. From Eq. (11), it is seen that the sensitivity of N_{Life} to certain parameters is simply negative of the crack growth rate's sensitivity to them.

$$S_{N_{Life}/C} = -1 \qquad S_{N_{Life}/\beta} = -n \qquad S_{N_{Life}/\sigma} = -n \tag{12}$$

So a 10% increase in the β-factor or stress would produce a 36% decrease in service life assuming n=3.6. Eq. (4) must be applied to Eq. (11) to determine the sensitivity of N_{Life} to initial and final crack lengths. Doing so gives

$$S_{N_{Life}/a_o} = \frac{1-\frac{n}{2}}{1-\left(\frac{a_f}{a_o}\right)^{1-\frac{n}{2}}} \tag{13}$$

and

$$S_{N_{Life}/a_f} = \frac{1-\frac{n}{2}}{1-\left(\frac{a_o}{a_f}\right)^{1-\frac{n}{2}}} \tag{14}$$

Eqs.(13) and (14) are plotted versus a_o/a_f in Figure MERC-3.2 for three values of n. The sensitivity to initial crack length depends on both n and a_f, but is approximately –1 for common values of these factors. So a 10% increase in initial crack length results in a 10% reduction in predicted fatigue life. On the other hand, predicted life is relatively insensitive to final crack length, showing only ~10% sensitivity. So a 10% increase in a_f produces only ~1% increase in predicted life. Since a_f is usually chosen to equal the critical crack length, a_{crit}, this demonstrates that variations in a_{crit} have a small impact on N_{Life} estimates.

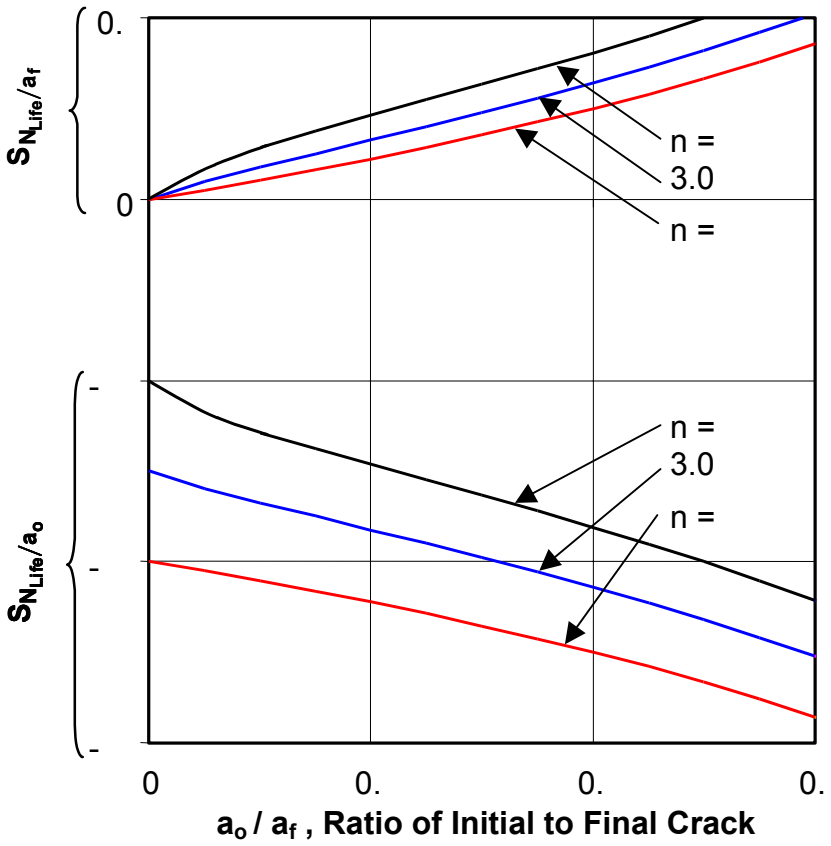

Figure MERC-3.2. Sensitivity of N_{Life} to initial and final crack lengths for three values of the Paris exponent, n. Paris law material behavior and constant β-factor and stress range are assumed.

Variable β-Factors – Numerical Example

The final example demonstrates that fatigue life sensitivity to a β-factor can depend on its relative value, with lower values being more critical than larger values. This analysis will be performed numerically rather than analytically because of the complexities of integrating non-constant β-factors. The horizontal leg of an aircraft longeron will be chosen for this example. A finite element model of it is shown in Figure MERC-3.3. The part is subjected to tension, bending, and fastener forces. The crack begins at the fastener hole and proceeds to the part edge as shown in the Figure. The β-factor is plotted in Figure MERC-3.4.

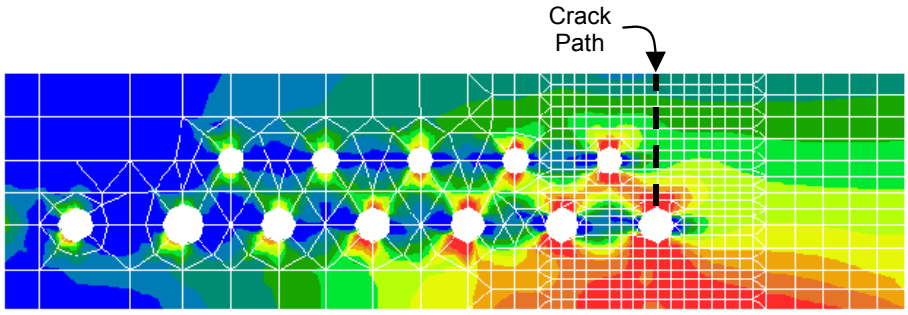

Figure MERC-3.3. Finite element model of horizontal leg of longeron. Crack originates at fastener hole and follows path shown.

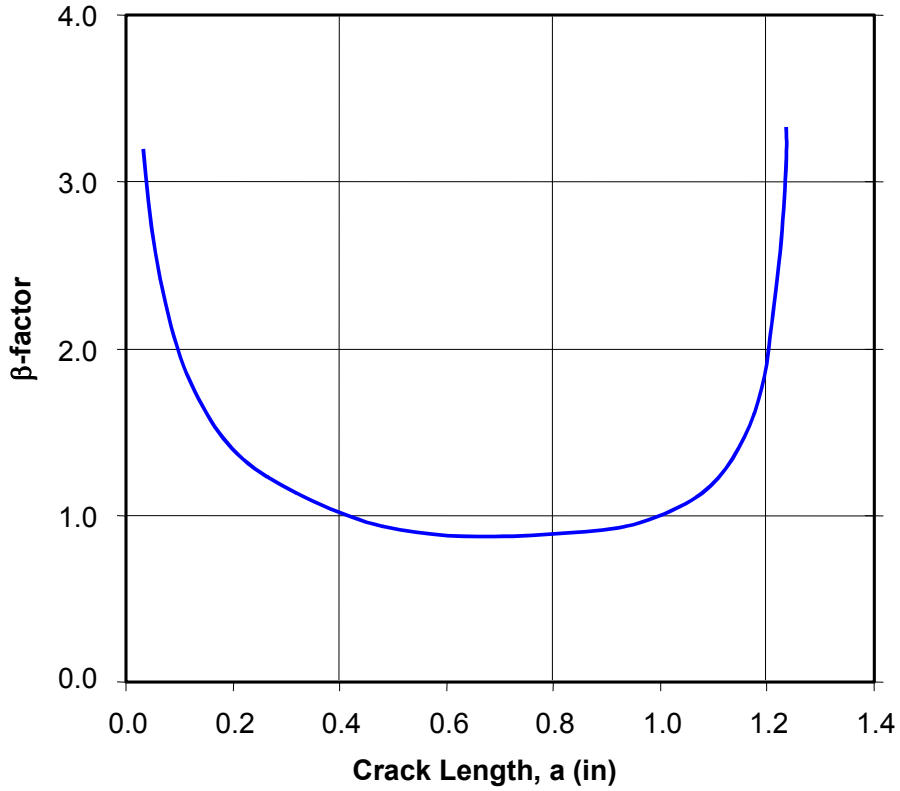

Figure MERC-3.4. β-factor versus crack length for crack starting at fastener hole in Figure MERC-3.3 and proceeding across part.

Figure MERC-3.4 shows that the β-factor is approximately three at short crack lengths because of the stress concentration at the fastener hole. The β-factor then decreases to approximately one with increasing crack length and then increases again as the crack approaches the free surface. The predicted life using the β-factor in Figure MERC-3.4 will be compared to two others having the following modifications.

Case 1. Large values of the β-factor increased. β values ≥3 were increased by 10%, β values ≤1 were not changed, intermediate values were scaled proportionately, i.e., β values = 2 were increased by 5%.

Case 2. Small values of the β-factor increased. β values ≤1 were increased by 10%, β values ≥3 were not changed, intermediate values were scaled proportionately, i.e., β values = 2 were increased by 5%.

AFGROW was used to predict the fatigue life of the part using the three different β-factor cases. Other inputs include: (1) $\Delta\sigma$=10ksi with R=0, (2) a_0=0.05 in. and a_f=1.25 in., (3) material da/dN–ΔK data taken from Figure MERC-3.1. Results are shown in Figure MERC-3.5.

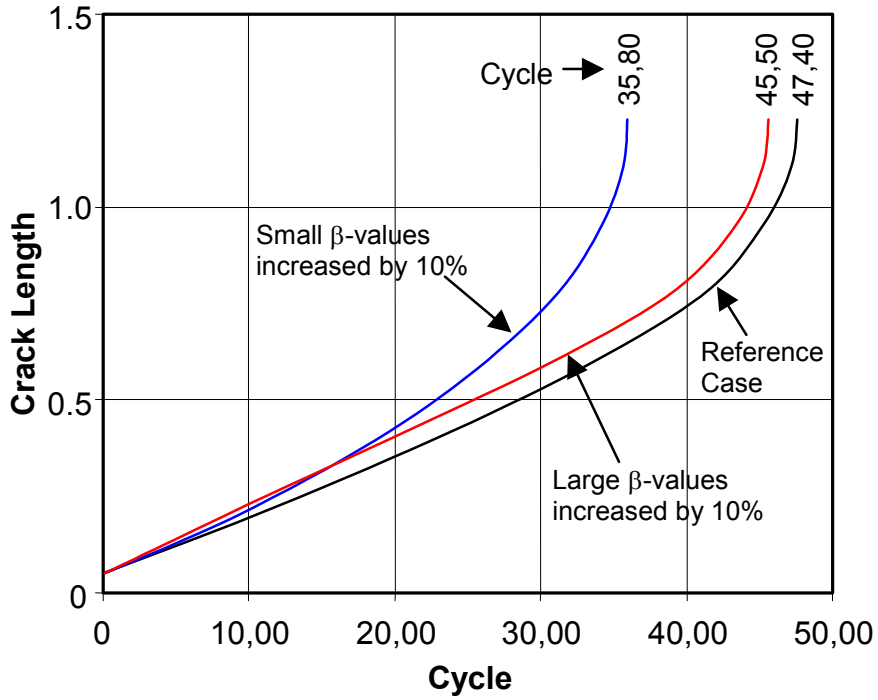

Figure MERC-3.5. Effects of β-factor variations on predicted fatigue life. Fatigue life is more sensitive to variations in small β-values than larger ones.

The 10% increase in small β-values produced a 25% decrease in predicted fatigue life, yielding a sensitivity of -2.5. The sensitivity to the increase in large β-values is -0.4. This demonstrates that fatigue life can be more sensitive to variations in small β-values than larger ones. It can therefore be more important to accurately determine small β-factor values than larger ones. This is a potentially counter-intuitive result since most analyses focus on large parameter values rather than small ones. This situation exists because cracks spend the majority of their life growing slowly at lengths with corresponding small β-factors.

Summary

A sensitivity analysis of factors affecting fatigue life predictions has been presented. It was demonstrated that certain factors have a large impact on predicted life, while others do not. Important factors include stress and β-factors. In most cases, a 10% increase in either one leads to ~35% decrease in predicted life. This high sensitivity is directly

related the high sensitivity of da/dN to ΔK, which is a material property. On the other hand, factors having a relatively small impact on predicted life are critical crack length and large β-values that occur when a crack approaches a free surface.

PROBLEM NO. MERC-4

Title: Influences of Retardation Models on Fatigue Crack Growth Predictions

Objective:

To illustrate the effects of the Willenborg and Wheeler retardation models on the prediction of fatigue crack growth behavior.

General Description:

This example problem focuses on a damage tolerance analysis of the windshield doubler at the intersection of the lower windowsill and post of an airplane. The goal is to predict the crack growth behavior of the doubler using two popular crack growth retardation models, Willenborg and Wheeler. The predicted crack growth rates are also compared to a reference case in which no retardation is applied. Stresses are obtained from a finite element model (FEM) and AFGROW is used to make the crack growth predictions.

Topics Covered: Damage tolerance analysis, crack growth analysis, retardation

Type of Structure: windows, windshield doubler

Relevant Sections of Handbook: Sections 2, 5

Author: Robert D. McGinty

Company Name: Mercer Engineering Research Center
Structures Technology Group
Warner Robins, GA 31088-7810
478-953-6800
www.merc.mercer.edu

Contact Point: Robert D. McGinty

Phone: 478-953-6800

e-Mail: bmcginty@merc.mercer.edu

MERC MERCER ENGINEERING RESEARCH CENTER
An Operating Unit Of Mercer University

Introduction

This example problem investigates the effects of two popular retardation models, Willenborg and Wheeler, on fatigue crack growth predictions. The part in question is a windshield doubler at the intersection of the upper windowsill and post of an airplane. The predicted crack growth rates are also compared to a reference case in which no retardation is applied. The retardation models will be briefly reviewed, followed by an example application to the windshield doubler. Stresses are obtained from a finite element model (FEM) of the forward fuselage and AFGROW is used to make the crack growth predictions.

Retardation Models

Retardation models address the case of reduced fatigue crack growth rates observed under variable amplitude loading conditions. They are important because fatigue crack growth measurements performed under variable amplitude loading can differ substantially from those under constant amplitude loading. During variable amplitude loading, a large loading cycle creates a large plastic zone that completely envelops the crack tip and surrounding region during subsequent smaller amplitude cycles. Retardation results from compressive residual stresses acting on the crack tip. It has been observed experimentally that crack growth is retarded as long as the plastic zone from the prior overload exceeds the plastic zone of current loading cycles. This is illustrated in Figure MERC-4.1.

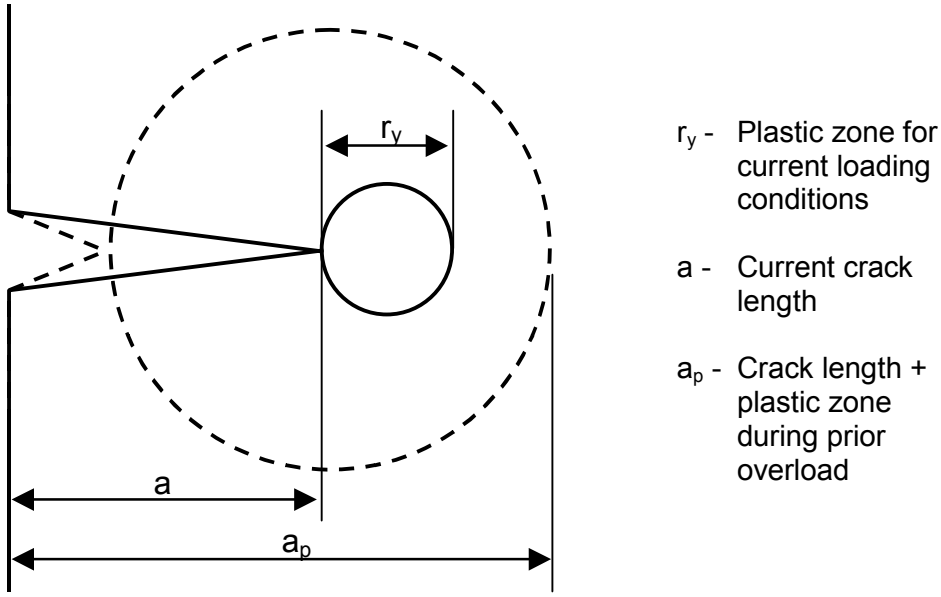

Figure MERC-4.1. Plastic zone size parameters used in crack growth retardation models.

The plastic zone size is given in Eq. (1)

$$r_y = \frac{1}{\alpha \pi}\left(\frac{K}{\sigma_y}\right)^2 \qquad (1)$$

where α=2 for plane stress and α=6 for plane strain, K is the stress intensity factor, and σ_y is the yield stress.

Willenborg Retardation Model

The Willenborg retardation model is based on the assumption that crack growth retardation is caused by compressive residual stresses acting on the crack tip. They are represented by a single stress value, σ_{cmp} , which is subtracted from both σ_{max} and σ_{min} to give corresponding effective values, σ_{max}^{eff} and σ_{min}^{eff}.

$$\sigma_{max}^{eff} = \sigma_{max} - \sigma_{comp} \qquad (2a)$$

$$\sigma_{min}^{eff} = \sigma_{min} - \sigma_{comp} \qquad (2b)$$

Either effective value is set equal to zero if it is negative. The compressive stress is defined as the difference between σ_{max} and the stress required to create a plastic zone extending to the edge of a plastic zone due to a prior overload. Equation (1) is used to calculate plastic zone size.

The effective stresses are used to calculate an effective stress intensity factor range

$$\Delta K^{eff} = \beta\left(\sigma_{max}^{eff} - \sigma_{min}^{eff}\right)\sqrt{\pi a} \qquad (3)$$

and an effective stress ratio

$$R^{eff} = \frac{\sigma_{min}^{eff}}{\sigma_{max}^{eff}} \qquad (4)$$

that are then used in the crack growth calculations.

Wheeler Retardation Model

The Wheeler model assumes that the retardation in the crack growth rate following an overload can be obtained by scaling the constant stress amplitude growth rate according to plastic zone size. The scaling parameter, C_p is defined as

$$C_p = \left(\frac{r_y}{a_p - a}\right)^p \qquad (5)$$

where p is an empirically determined constant and all other variables are defined in Figure MERC-4.1.

Fatigue Crack Growth Analysis

Critical Area

The retardation models will be applied to a fatigue crack growth analysis of the windshield doubler at the intersection of the upper windowsill and window post. The doubler is shown in the finite element models in Figures MERC-4.2 and MERC-4.3. It is fabricated from 0.091" thick 7075-T6 aluminum and is 1.5" wide at the crack location.

Finite Element Mesh

A NASTRAN finite element model (FEM) of the forward fuselage was developed and is shown in Figures MERC-4.2 and MERC-4.3. It is made up primarily of shell and beam elements. In general, joints are modeled by shared-nodes; fasteners are not explicitly modeled. However, fasteners that attach the windshield doubler to airframe structure and skin are explicitly modeled with beam elements

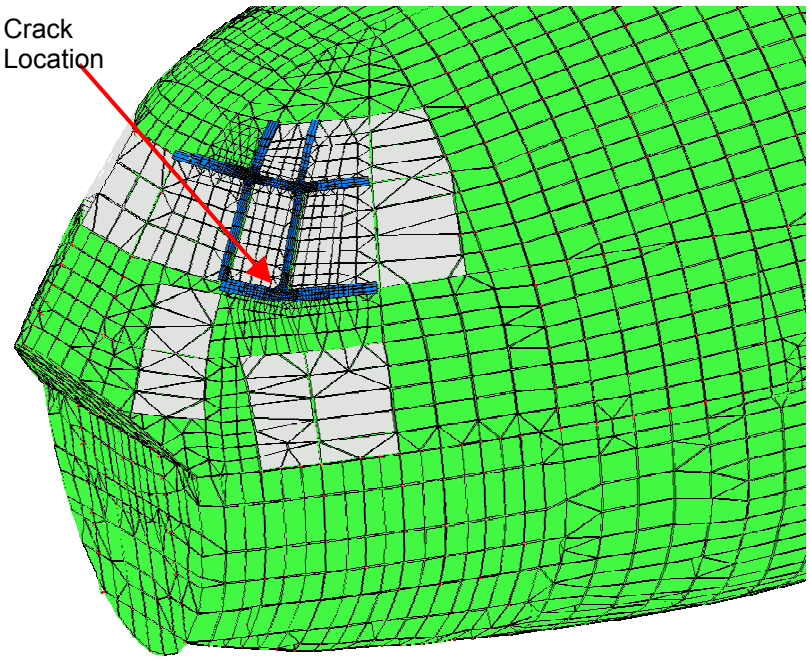

Figure MERC-4.2. Structural finite element model of forward fuselage of the aircraft with mesh refinement in front window area.

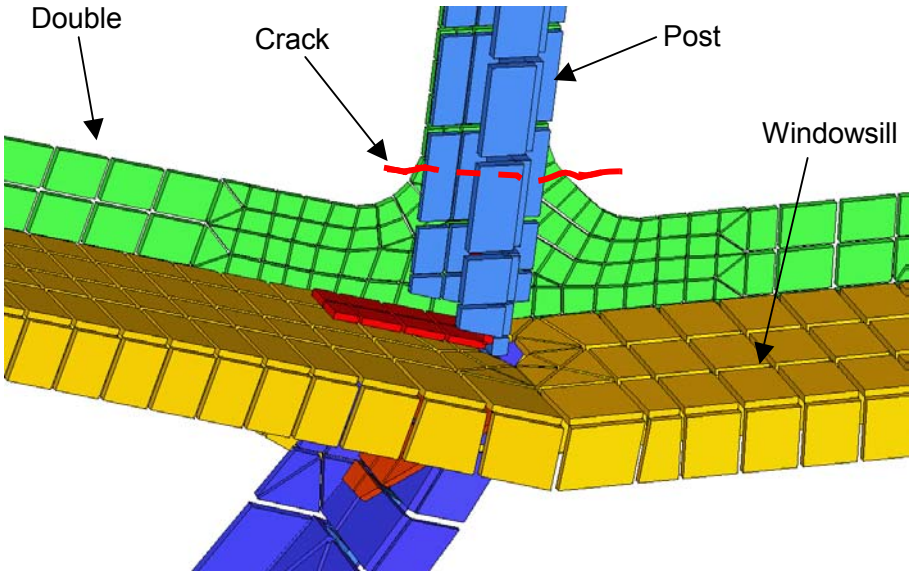

Figure MERC-4.3. Detail of structural finite element model showing mesh refinement in lower windowsill, post, and doubler. Windows are not shown. Crack occurs in doubler. View from inside of aircraft.

Stress Spectra

Internal pressurization effects are the dominant cause of stresses in the window area. Loads due to maneuvers, landings, wind gusts, etc. are negligible in comparison. Internal pressurization actually refers to the case where the cabin is maintained at sea level pressure while flying at altitudes where atmospheric pressure is substantially less.

Figure MERC-4.4 shows cycles of average tensile stress in the lower leg of the doubler. High stress cycles correspond to flights at high altitudes where large pressure differentials exist between the interior of the plane and the external atmosphere. Low amplitude stress cycles correspond to low altitude flights.

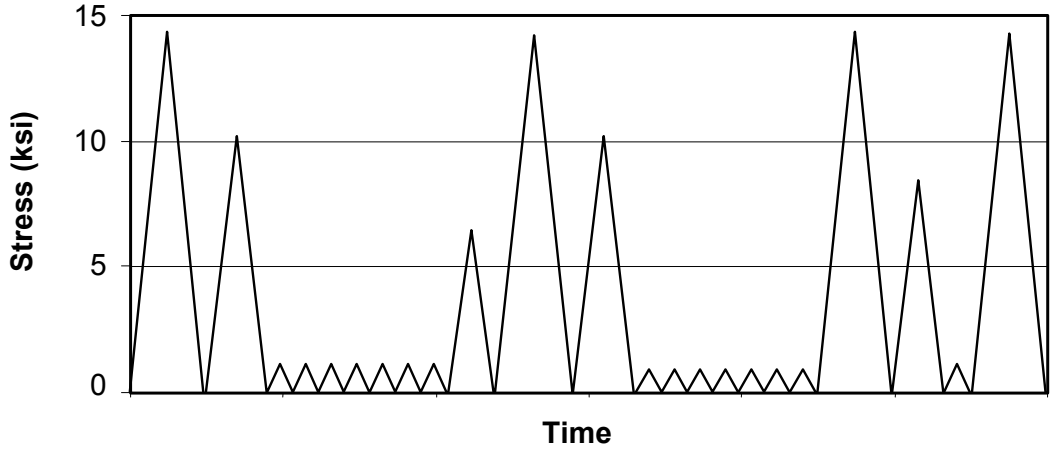

Figure MERC-4.4. Cycles of average tensile stress in lower leg of doubler.

Crack Growth Predictions and Retardation

The stress cycles in Figure MERC-4.4 are clearly not constant in amplitude. Therefore, crack growth retardation mechanisms are expected to be important and significantly affect the crack growth rates.

AFGROW was used to predict the crack growth in the doubler due to fuselage pressurization cycles. The crack is assumed to start as a 0.05" radius corner crack at a fastener hole, grow to a through crack, and then grow across the doubler until failure occurs. Stress cycles, β-factors from AFGROW and FRANC2D/3D, and material da/dN data are combined to give the crack growth predictions in Figure MERC-4.5 below.

Three predictions are shown on the graph. They correspond to the cases of (1) no retardation, (2) Willenborg retardation model, and (3) Wheeler retardation model with p=1.0. The Willenborg retardation model increases the predicted life by approximately 8% over the reference no-retardation case. The Wheeler retardation model yields an additional 8% predicted increase in fatigue life of the doubler. The retardation models do not appear to drastically alter the fundamental nature of the crack growth predictions. All

indicate that crack growth accelerates dramatically once the crack reaches approximately 0.3 inches in length.

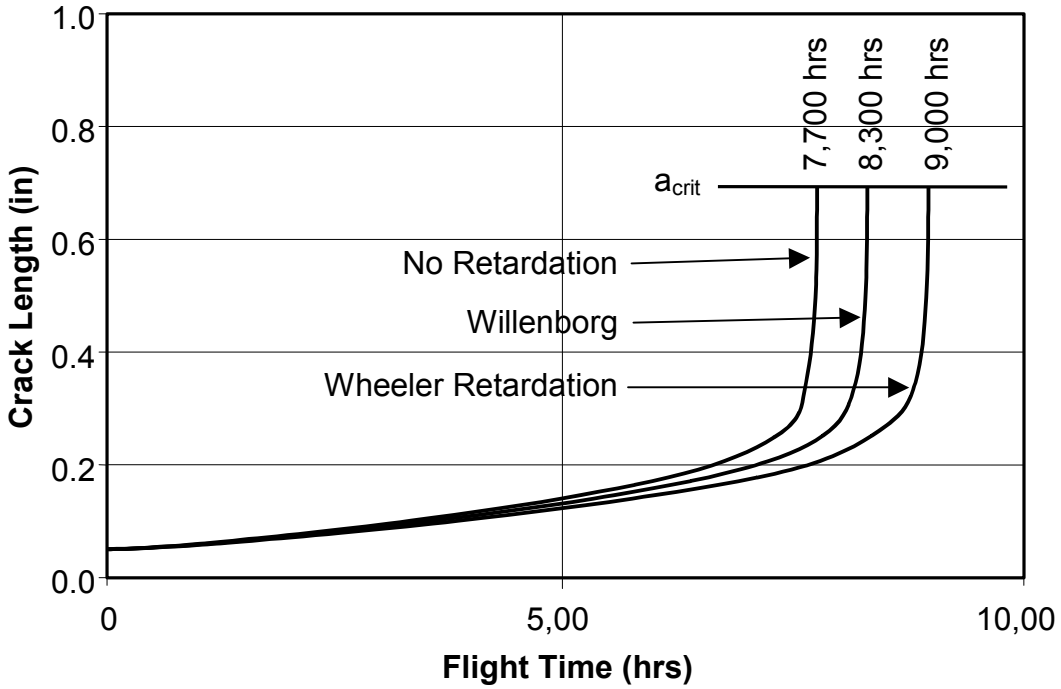

Figure MERC-4.5. Predicted crack growth versus flight hours for a crack growing across a lower portion of the windshield doubler. Effects of the Willenborg and Wheeler retardation models are compared to the reference case with no retardation.

Summary

This example problem focused on a damage tolerance analysis of the windshield doubler at the intersection of the lower windowsill and post of an airplane. The crack growth behavior of the doubler was predicted using two popular crack growth retardation models, Willenborg and Wheeler. The predicted crack growth rates were compared to a reference case in which no retardation is applied. Stresses were obtained from a finite element model and AFGROW was used to make the crack growth predictions.

PROBLEM NO. NRC-1

Title: Quantifying Corrosion in Fuselage Lap Joints

Objective:

(1) To show examples of the type of damage that can be present in corroded 2024-T3 lap joints and (2) to illustrate the process for determining the equivalent initial flaw sizes for corroded fuselage lap joints.

General Description:

This problem focuses on the methods to determine the equivalent initial flaw sizes that can be used to carry out a damage tolerance assessment of corroded fuselage lap joints. To differentiate the use of the EIFS concept in a corrosion fatigue situation, the phrase 'Equivalent Corrosion Damage' (ECD) is used. A study was carried out on dog-bone coupons fabricated from naturally and artificially corroded lap joints. These coupons were subjected to a cyclic load and the fracture surfaces were examined with the aid of a scanning electron microscope to determine the location and size of the nucleation site. Also, using x-ray techniques to map the thickness loss in these coupons as well as in corroded lap joints that were disassembled and cleaned of corrosion products, the coefficient of variation, which is a measure of the scatter, was determined.

Topics Covered: Corrosion, equivalent corrosion damage

Type of Structure: Fuselage lap joints

Relevant Sections of Handbook: Section 8

Author: Nicholas C. Bellinger

Company Name: National Research Council Canada
Institute for Aerospace Research
Montreal Road, Ottawa, Ontario Canada K1A 0R6
613-993-2410
www.nrc.ca/iar

Contact Point: Jerzy P. Komorowski

Phone: 613-993-3999

e-mail: jerzy.komorowski@nrc.ca

NRC · CNRC

Overview of Problem Description

This problem focuses on one of the critical areas in transport aircraft, lap joints, which can be of various designs usually consisting of two or more layers of material with two or three rows of rivets, Figure NRC-1.1. These joints are known to be susceptible to crevice corrosion, which is a form of attack that occurs when a corrosive liquid gains access to crevices in, or between components. Studies have shown that the corrosion products which form in lap joints fabricated from clad 2024-T3 aluminum material have a molecular volume of approximately 6.5 times greater than the aluminum alloy from which it originated (Bellinger et al., 1994). This increase in volume causes the skins between the rivets to bulge, an effect referred to as pillowing, Figure NRC-1.2, and is often used by inspectors to identify areas in lap joints affected by corrosion.

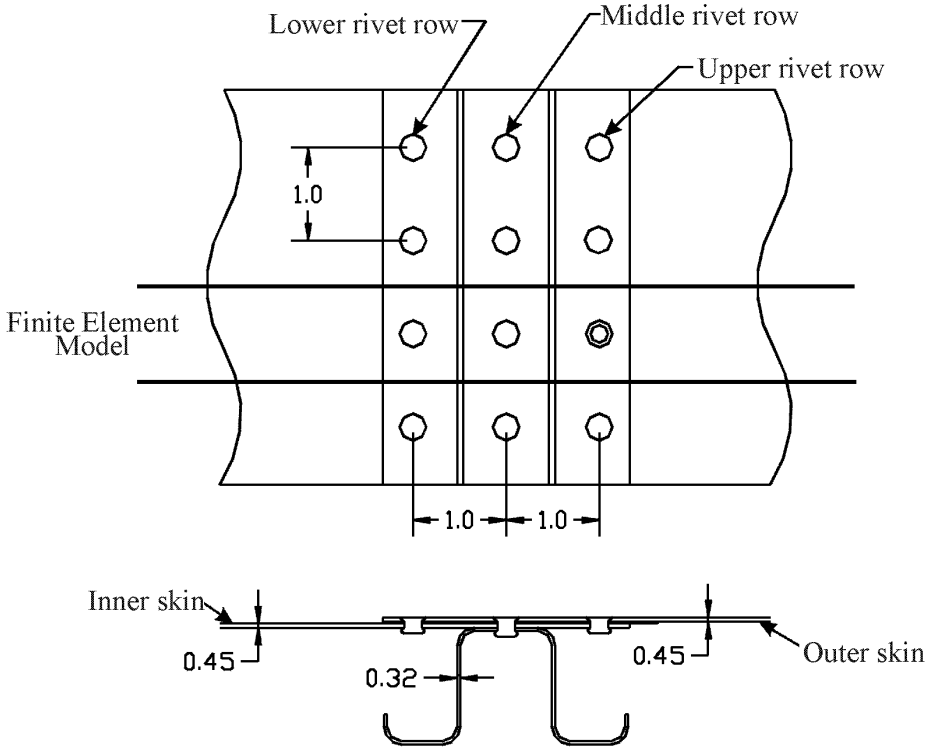

Figure NRC-1.1. Typical Fuselage Lap Joint

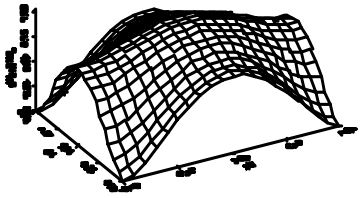

a) Rivet spacing ratio of 1.0

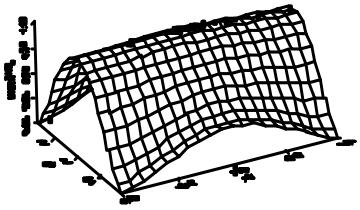

b) Rivet spacing of 1.50

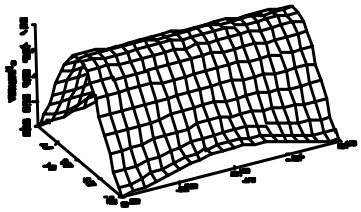

c) Rivet spacing ratio of 2.0

Figure NRC-1.2. Effect Of Rivet Spacing on Pillowing in Lap Joints

Damage Characterization of Faying Surface

Damage characterization studies that were carried out on naturally corroded lap joints have shown the presence of corrosion pits, exfoliation, intergranular corrosion and environmentally assisted cracking, which occurred in the presence of a sustained stress caused by corrosion pillowing, Figure NRC-1.3 (Bellinger et al., 1999). It should be noted that very few "large" pits were found in the lap joints that were studied although some areas had an average thickness loss of 20% or higher. Those large pits that were found occurred in an area that contained very little corrosion damage other than the pit. The presence of intergranular corrosion and exfoliation may explain why there were very few large pits given the high thickness loss. As the intergranular corrosion or exfoliation progressed causing pits to link-up to other edges, the material between the pits could be removed by way of flaking or dissolution decreasing the existing pit depths. This, in turn would cause the remaining damage to appear less severe although the average thickness loss would be higher.

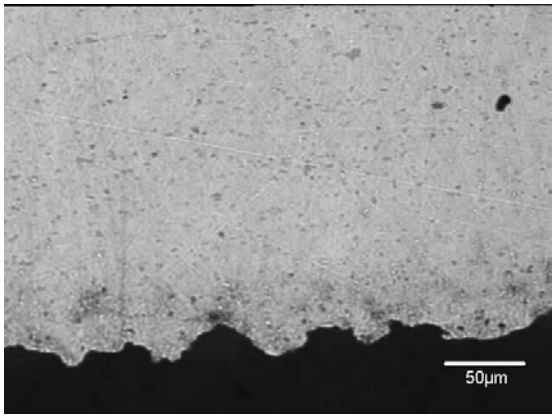

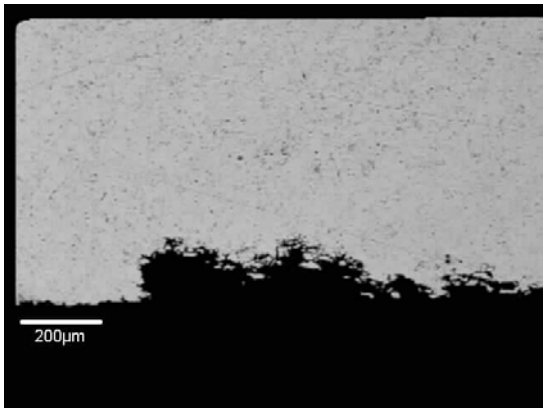

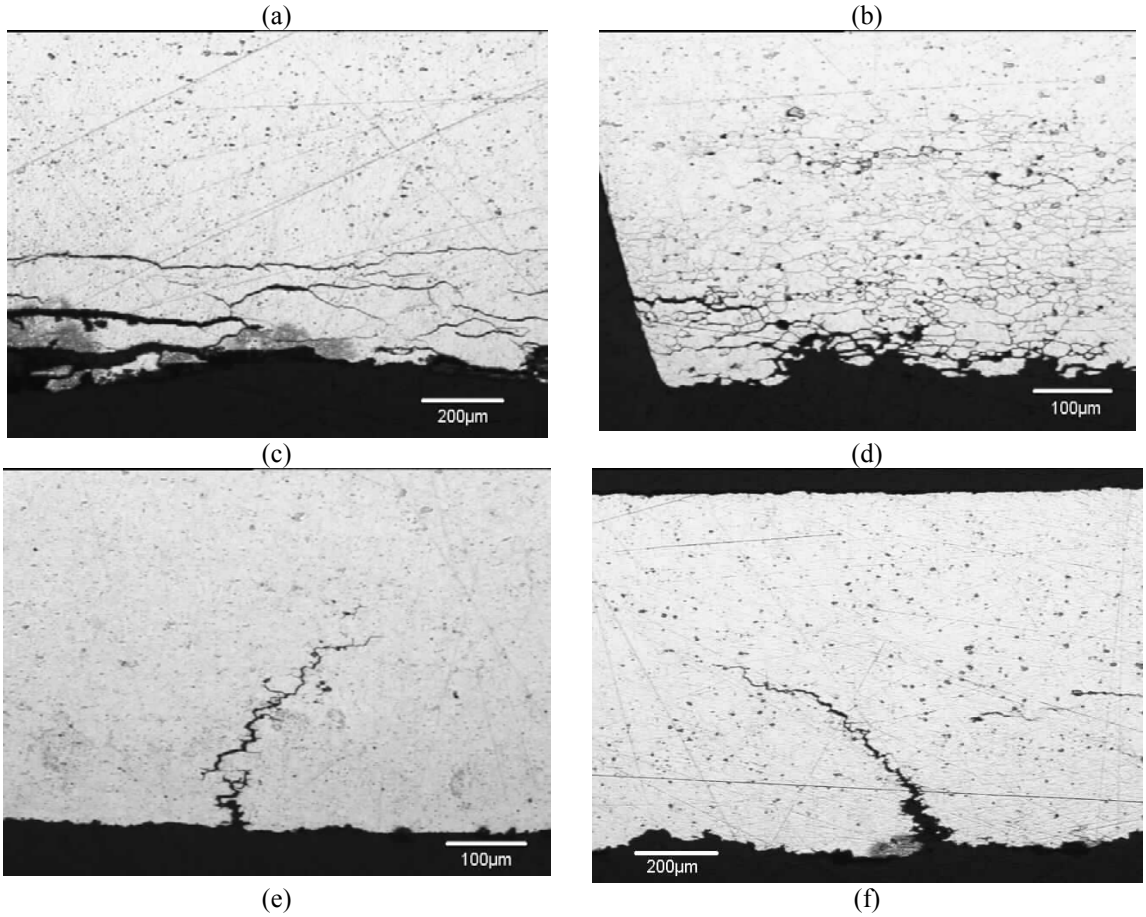

Figure NRC-1.3. Examples of damage present in corroded lap joints; (a), (b) pitting, (c) exfoliation along faying surface, (d) intergranular corrosion and (e), (f) environmentally assisted cracking that occurred near the rivet holes

Determination of ECD Values

ECD values can be determined either by examining failed corroded lap joints or by conducting tests on coupons fabricated from corroded lap joints taken from in-service or retired aircraft. Ideally, the tests should be carried out using stress levels similar to that experienced by lap joints in service. Prefabricated lap joints artificially corroded in a salt fog chamber may also be used if the resulting ECD values are similar to those determined from naturally corroded joints (that is the damage produced by the artificial process is similar to those produced by the natural process). This example addresses this issue (Bellinger et al., TBP; Bellinger et al., 1999a).

Artificial Process

Since ECD values are material dependent, any lap joint configuration can be used in the artificial process. However, it should be emphasized that only lap joints should be used and not just single sheets of material since crevice corrosion results in a more severe attack than just pitting corrosion. The fabricated joints were placed in a salt fog chamber and subjected to a modified copper assisted salt spray (CASS) process. The joints were

periodically removed and inspected using the enhanced optical inspection technique, D Sight™ and multi-frequency eddy current techniques to estimate the average thickness loss (Komorowski et al., 1991; Forsyth et al., 2000). Once the desired thickness loss was achieved, the joints were removed from the chamber, disassembled and the corrosion products removed using a chemical/ultrasonic process. Studies have shown that the damage produced by the artificial process was similar to that produced by the natural one (Eastaugh et al., 1999).

Test Coupon Design and Fabrication

One of the main problems in generating ECD values is the design of the test coupon since the majority of the lap joints consist of 2024-T3 clad aluminum material, 1.27 mm (0.05 inch) thick. The ASTM E466-96 standard was used to design a coupon since it did not place any restriction on the specimen dimensions. The coupons were machined such that the loading axis was perpendicular to the material rolling direction as shown in Figure NRC-1.4.

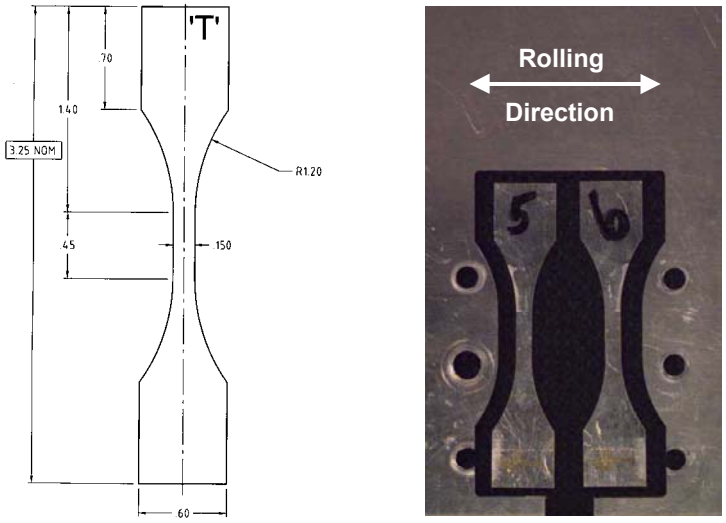

Figure NRC-1.4. Schematic Showing Test Coupon Configuration And Photograph Showing Orientation In Lap Joint Used For This Problem.

Using thickness maps developed from radiographs of the coupons, the thickness in the gauge length of each coupon was determined. Based on these results, ten coupons from the naturally corroded skins and twenty from the artificially corroded ones were machined such that the average thickness loss in the gauge length was approximately 2%. Coupons were also machined from both the naturally and artificially corroded skins so that the average thickness loss within the gauge length was 5%. Figure NRC-1.5 shows the x-ray thickness maps for the coupons fabricated from the naturally corroded lap joints.

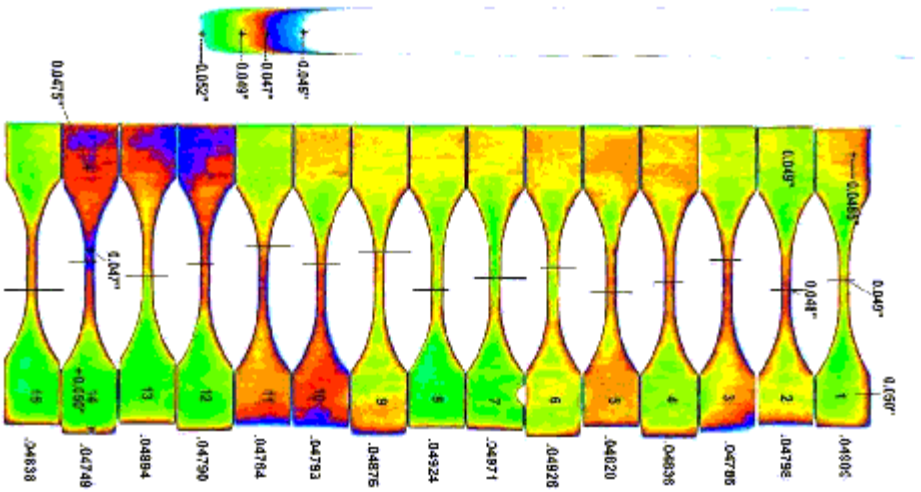

Figure NRC-1.5. X-Ray Thickness Maps Of Naturally Corroded Coupons

Experimental Procedures

All tests were carried out under load control in a servo-hydraulic load frame with hydraulic grips. Given the effect that humidity has on the fatigue life of aluminum alloys, the relative humidity was recorded throughout the duration of the test. Each coupon was subjected to cyclic loading until failure with a load ratio of 0.02 and a test frequency of 10 Hz. The maximum load was adjusted for each coupon to maintain a maximum stress level of 207 MPa (30 ksi) in the gauge length area. This stress was the approximate value that the lap joints experience in the vicinity of the critical rivet hole where multi-site damage occurs. To prevent premature failure at the corners, the edges of each coupon in the gauge length were 'broken' using a machinist sanding stone.

Experimental Results

The average number of cycles to failure and the standard deviation for each set of results is shown in Table NRC-1.1. The combined average number of cycles to failure for the 5% corroded test coupons is shown in this table along with the average value for the artificially and naturally corroded 5% results. The total number of coupons tested for each condition is also given.

To determine the ECD values for the different test condition, the majority of the fracture surfaces for the 2% artificial and natural coupons were examined with the aid of a scanning electron microscope (SEM) while values for the 5% coupons were determined by back-calculations. All the nucleation sites found using the SEM were semi-elliptical in shape and the majority of the sites were located along the corroded surface (faying surface of the joint). It should be pointed out that the coupons did not always fail at the thinnest area of the gauge length or at the maximum pit depth as shown in Figure NRC-1.5 by the black lines, which indicated where the coupons failed. For those coupons that did not have a single nucleation site, different scenarios were used to obtain the ECD value. The average semi-elliptical ECD values that were measured with the aid of a scanning electron microscope for the 2% artificial and natural coupons and the calculated

average semi-circular ECD value for the 5% combined coupons are shown in Table NRC-1.2.

Table NRC-1.1. Experimental Results Showing Average Number of Cycles To Failure

Percent Thickness Loss [number of coupons]	Average Number of Cycles to Failure	Standard Deviation
Artificial 2% [20]	237,679	25,734
Natural 2% [8]	231,086	30,729
Combine 5% [13]	212,248	21,998
Natural [4]	212,454	18,578
Artificial [9]	212,156	24,241

Table NRC-1.2. Experimental and Calculated ECD Values

Coupon	Experiment ECD Values (mm)		Equivalent Radius (mm)
	2c	a	
2% Artificial	0.1024	0.00610	0.05512
2% Natural	0.1215	0.05801	
5% Combine			0.06736

The resulting ECD numbers can then be used to predict the residual life of corroded lap joints, which is demonstrated in a separate example.

References

Bellinger, N.C., Krishnakumar, S. and Komorowski, J.P. (1994), "Modelling of Pillowing Due to Corrosion in Fuselage Lap Joints", CAS Journal, Vol. 40, No. 3, September 1994, pp. 125-130.

Bellinger, N.C., Komorowski, J.P. and Benak, T.J. (TBP), "Residual Life Predictions of Corroded Fuselage Lap Joints", to be published in the International Journal of Fatigue.

Bellinger, N.C., Cook, J.C. and Komorowski, J.P. (2000) "The Role of Surface Topography in Corroded Fuselage Lap Joints", to be published in the proceedings of the 2000 USAF Aircraft Structural Integrity Program Conference, December 5 to 7, 2000, San Antonio, Texas.

Bellinger, N.C., Benak, T.J., Chapman, C.E., Komorowski, J.P., Scarich, G., and Falugi, M. (1999a), "Equivalent Corrosion Damage Methodology for Corroded Fuselage Lap Joints", Published in the proceeding of the 1999 USAF Aircraft Structural Integrity Program Conference, San Antonio, Texas, 30 November – 2 December 1999.

Bellinger, N.C., and Komorowski, J.P. (1999b), “Environmentally Assisted Cracks in 2024-T3 Fuselage Lap Joints”, Published in the proceeding of the Third Joint FAA/DoD/NASA Conference on Aging Aircraft, Albuquerque, New Mexico, September 20-23, 1999.

Eastaugh, G.F., Merati, A.A. and Simpson, D.L. (NRC), Straznicky, P.V., Scott, J.P., Wakeman, R.B. and Krizan, D.V. (Carleton University) (1999), “An Experimental Study of Corrosion/Fatigue Interaction in the Development of Multiple Site Damage in Longitudinal Fuselage Skin Splices”, RTO-MP-18 AC/323(AVT)TP/8 March 1999, proceedings NATO-RTO Air Vehicle Technology Panel Workshop on Fatigue in the Presence of Corrosion (Fatigue sous corrosion), Corfu, 7-8 October 1998.

Forsyth, D. S., Fahr, A., Chapman, C. E., Bellinger, N. C., Komorowski, J. P. (2000) “NDI Capabilities for Airframe Corrosion Damage Tolerance”, in the proceedings of the 2000 USAF Aircraft Structural Integrity Program Conference, December 5 to 7, 2000, San Antonio, Texas.

Komorowski J.P., Simpson D.L., Gould R.W. (1991), “Enhanced Visual Technique for Rapid Inspection of Aircraft Structures”, Materials Evaluation, December 1991, pp. 1486-1490.

PROBLEM NO. NRC-2

Title: Residual Life Assessment of Corroded Fuselage Lap Joints

Objective:

To illustrate the process for including the effects of corrosion in the residual life assessment of fuselage lap joints.

General Description:

This problem focuses on the methods that can be used to carry out a residual life assessment of corroded fuselage lap joints. The first method is based on the Equivalent Initial Flaw Size approach, which can be used for quick assessments of the impact of corrosion on the structural integrity. The second method based on the holistic life assessment approach can be used to carry out a corrosion damage tolerance analysis on environmentally sensitive components. Finite element techniques will be described to take into account the increased stress caused by the build-up of corrosion products between the different layers of skin, referred to as "corrosion pillowing". This change in stress is required for both methods. The AFGROW crack growth rate program is also used in the first method to calculate the number of cycles to failure.

Topics Covered: life assessment, equivalent corrosion damage, finite element analysis.

Type of Structure: fuselage lap joints

Relevant Sections of Handbook: Section 8

Author: Nicholas C. Bellinger

Company Name: National Research Council Canada
Institute for Aerospace Research
Montreal Road, Ottawa, Ontario Canada K1A 0R6
1(613) 993-2410
www.nrc.ca/iar

Contact Point: Jerzy P. Komorowski

Phone: 1 (613) 993-3999

e-mail: jerzy.komorowski@nrc.ca

NRC · CNRC

Overview of Problem Description

This problem focuses on the impact that corrosion has on the residual strength of transport fuselage lap joints, Figure NRC-2.1, as well as the techniques that can be used to determine this impact. This example will concentrate on using the Equivalent Initial Flaw Size (EIFS) approach to predict the fatigue lives of pre-corroded lap joint specimens that were subjected to constant amplitude loading. To differentiate the use of the EIFS approach in a corrosion fatigue situation, the phrase 'Equivalent Corrosion Damage' (ECD) is used. A new procedure, known as the holistic life assessment approach, currently being developed for implementation by the United States Air Force, will also be discussed.

The corrosion products contained in aircraft lap joints fabricated from 2024-T3 clad aluminum were analyzed and found to contain a mix of oxides, primarily aluminum oxide trihydrate. This type of oxide had a molecular volume ratio to the alloy from which it originated of 6.45 (Bellinger et al., 1994). It was this high molecular volume ratio that is responsible for the deformation of the riveted skins in a joint resulting in the appearance commonly referred to as "corrosion pillowing", Figure NRC-2.2.

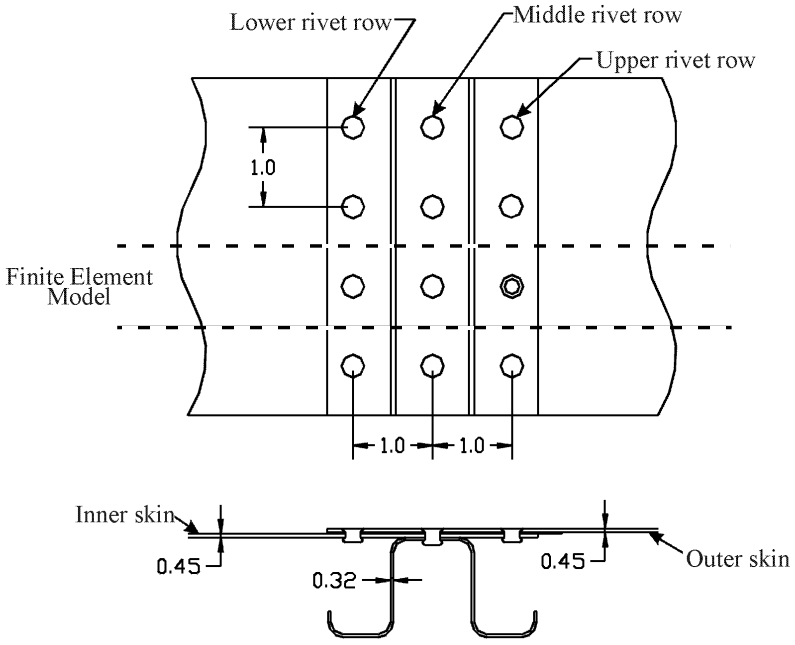

Figure NRC-2.1. Lap joint consisting of two skins and a stringer. All dimensions are in inches (1 inch=25.4 mm)

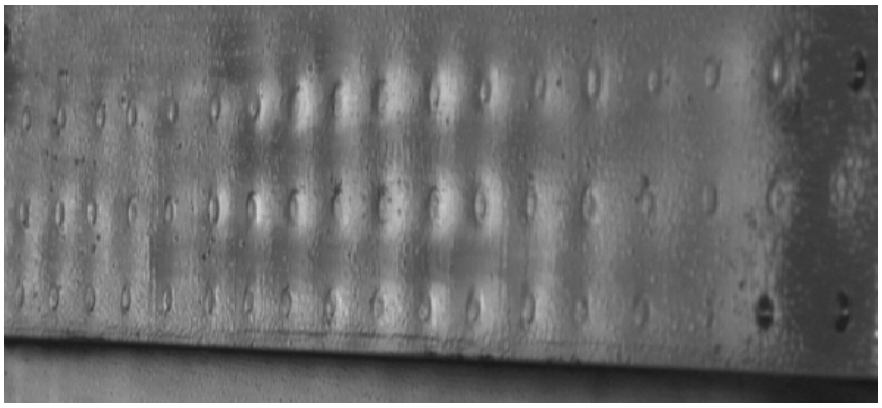

Figure NRC-2.2. D Sight™ Image Showing Pillowing Caused By Corrosion Product Accumulation

Analytical Predictions Using Experimental ECD Values

Experiments have been carried out at NRC Canada on lap joint specimens, Figure NRC-2.3, to determine the effect that corrosion has on the fatigue life. Three levels of corrosion were studied: 0%, 2% and 5% average material loss. The results from these tests, which will be used to verify the capability of the ECD concept to predict the effect that corrosion has on the residual life of corrosion lap joints are present elsewhere (Eastaugh et al., 1998a), (Eastaugh et al., 1998b), (Eastaugh et al., 2000). The majority of the crack nucleation sites for the specimens were located away from the rivet hole along the faying surface. The cracks were semi-elliptical in shape.

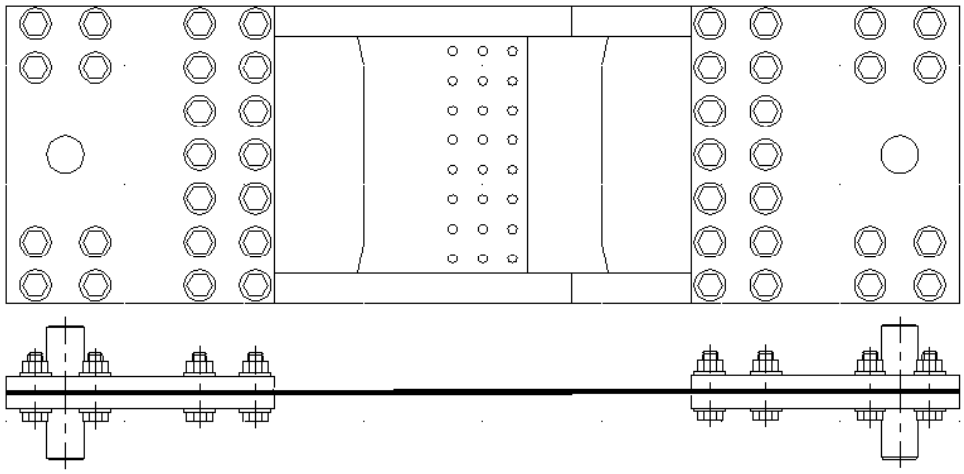

Figure NRC-2.3. Schematic of Lap Joint Specimen

Equivalent Corrosion Damage Values

The procedures to determine the equivalent corrosion damage from corroded (artificial and natural) lap joints are shown in another example problem within this Damage

Tolerance Design Handbook. In this example, coupons were machined from pristine and artificially and naturally corroded lap joints and tested to failure. The corroded lap joints contained different levels of material thinning, 2% and 5% thickness loss. Using scanning electron microscopy and back-calculations, ECD values were determined for the different corrosion levels. All the fatigue nucleation sites were semi-elliptical in shape.

As the cracking scenario that was present in the lap joint specimens (i.e. elliptical crack located away from the hole edge) is not present in crack growth rate programs, it was decided to calculate a semi-circular crack length with an equivalent area to the ECD values. These calculated crack lengths are plotted against the number of cycles to failure in Figure NRC-2.4.

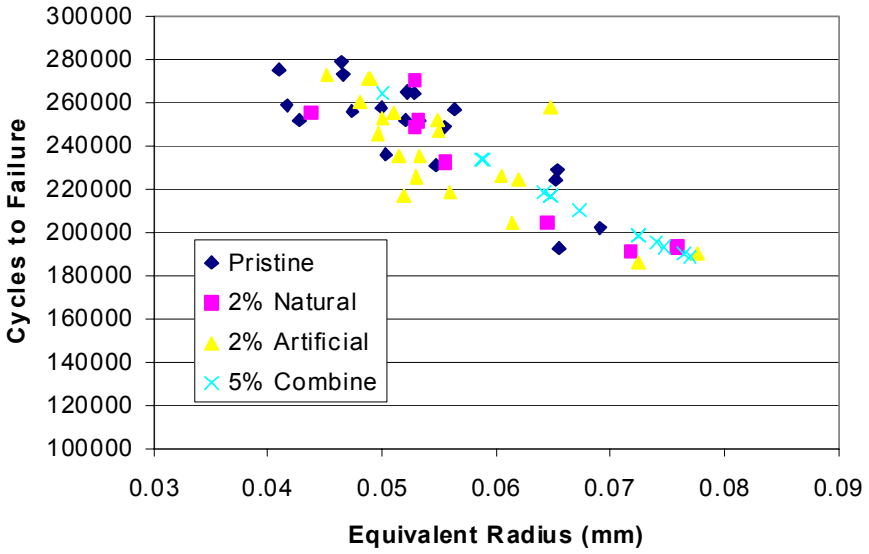

Figure NRC-2.4. Equivalent Circular Radius Versus Number of Cycles to Failure for Pristine, 2% Artificial and Natural and 5% Combined Coupons

Since the version of AFGROW that was used for this example was not capable of predicting a multi-site damage scenario, it was decided to concentrate on predicting the number of cycles to the first observed crack as well as the number of cycles to reach a specified crack length. This length was chosen to be small enough as to not be influenced by other cracks at the other rivets.

Finite Element Analysis

The critical rivet holes in fuselage lap joints are subjected to a complex stress state that is a result of different loading conditions. One load that has a strong influence on the stress state is the secondary bending, which is caused by the eccentric loading in the lap joints. Another one is the pre-stress that results from the rivet installation, which has a significant effect on the crack growth under the rivet head (Liao et al., TBP). Finally, for corroded joints, the out-of-plane displacements, or pillowing, have a very strong influence on the stress state along the faying surface of the lap joint.

Since the AFGROW program could not determine this complex stress state, stress correction curves had to be generated to take into account the different test conditions, 0%, 2% and 5% thickness loss as well as entered into the program. To generate such curves, three finite element models of the lap joint specimens were generated using the commercial finite element package MSC Patran/Nastran (Bellinger et al., 1994; Bellinger et al., 1997). Each model was generated consisting of two 1.02 mm (0.04 inch) skins joined together with three 100° countersink rivets as shown in Figure NRC-2.5.

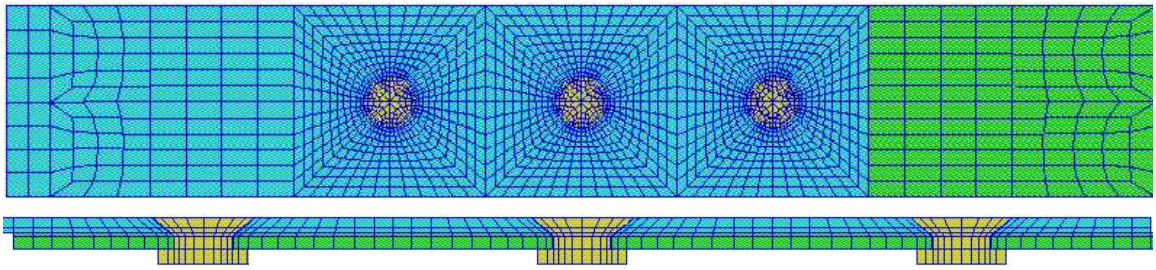

Figure NRC-2.5. Finite Element Mesh of MSD Specimen

All finite element models were generated with first-order brick elements to model the skins and rivets while nonlinear gap elements were used to model the skin/rivet interface. Symmetrical boundary conditions were applied along the edges of the joint and clamped boundary conditions were applied along one or both short edges, depending on the load case being modeled.

In the first model, the prestress caused by the rivet clamping force was simulated by applying a pressure to each rivet head. All the nodes were merged in this particular model to prevent the surfaces from overlapping. In the second model, a fixed displacement was applied along a skin edge to simulate the hoop stress while the opposing edge was fixed in all directions. The skins directly under the rivet heads were assumed to transfer some of the load, which was simulated by merging the nodes in these areas.

To simplify the third model (corrosion), it was assumed that the material loss due to corrosion was constant throughout the entire joint (Bellinger et al., 1994). An initial finite element run was carried out in which a pressure of 6.89 kPa (1 psi) was applied to the faying surfaces. The volume under the resulting deformed shape, V_{fem}, was determined using methods available in the Patran software. The actual volume required, V_{req}, to accommodate the corrosion products given a specific material loss was then calculated using:

$$V_{req} = abt_{lo}\left[\left(V_{mr}/2\right)-1\right] \qquad (1)$$

where, V_{mr} is the molecular volume ratio, 6.454 for 2024-T3 clad aluminum, and a and b are the rivet spacing. On the basis of the results from the chemical analysis, the corrosion products were considered to be incompressible (i.e. Young's modulus of the products was significantly higher than that of aluminum). Therefore, a linear relationship was assumed

to be present, and thus the pressure-to-volume ratios for the 6.89 kPa and the actual models were set equal:

$$\left(P_{req} / V_{req}\right) = \left(P_{fem} / V_{fem}\right) \quad (2)$$

From this equation, the pressure necessary to obtain the required volume was determined, which was then reapplied to the faying surfaces in the corrosion model and the corrosion finite element analysis was re-run. D Sight images of fuselage lap joints have shown that only a small amount of pillowing occurs at the free edges compared to the area between the rivets. D Sight is an enhanced visual inspection technique that is very sensitive to out-of-plane displacements (Komorowski et al., 1996). To accommodate this smaller volume, the pressure was progressively decreased from the rivets to the free edges in the finite element model (Bellinger et al., 1997).

To determine the resultant stress that would occur from a combination of the three load cases, the elemental stress values were combined (added together) within the Patran program.

To determine the effect that skin thickness loss has on the stress in a joint, four conditions were studied: 1) no corrosion, 2) corrosion simulated by decreasing skin thickness, 3) corrosion simulated by pillowing and 4) corrosion simulated by pillowing with effective skin thickness reduction. A 10% thickness loss was assumed to be present in all the corrosion models. For the effective thickness loss models, only the outer skin thickness was reduced. The resulting maximum principal stress was non-dimensionalized with respect to the remote stress and plotted in Figure NRC-2.6 for the critical river row (in terms of potential for cracking). As shown in this figure, pillowing has a greater influence on the stress as compared to the effective thickness loss alone and thus needs to be included in a residual life assessment analysis.

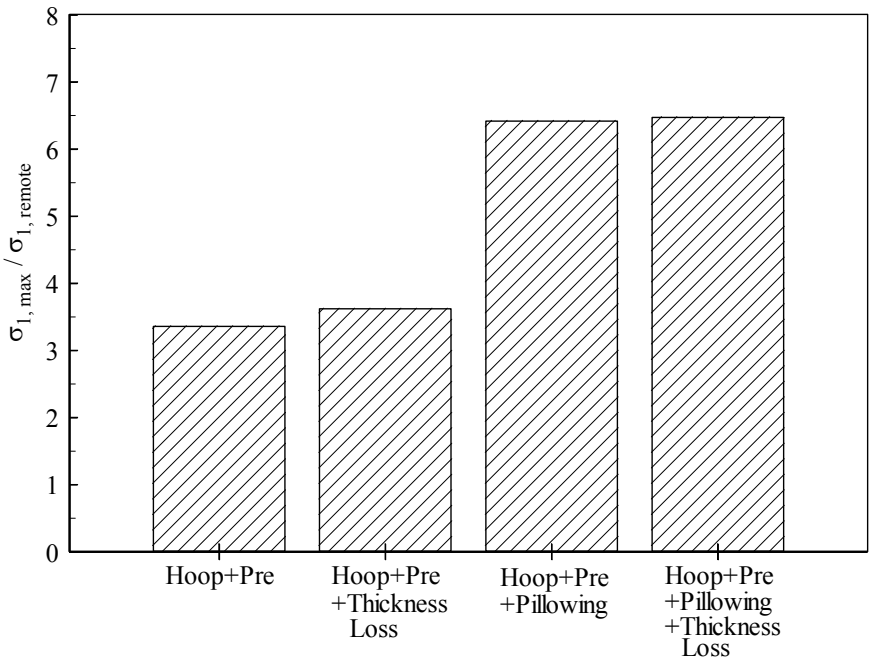

Figure NRC-2.6. Effect On Stress Caused by Reduction of Outer Skin Thickness as Compared to Pillowing (10% Thickness Loss)

The resulting stress plots for the outer faying surface at the critical rivet row area for the 2% thickness loss is shown in Figure NRC-2.7. As can be seen from this figure, the maximum stress in these joints did not occur at the location 90 degrees to the loading direction. To take this change into account, the stress values were determined along the two lines shown in this figure. These values were then non-dimensionalized with respect to the remote stress of 98.5 MPa (14.3 ksi) and the resulting stress correction curves are plotted in Figure NRC-2.8.

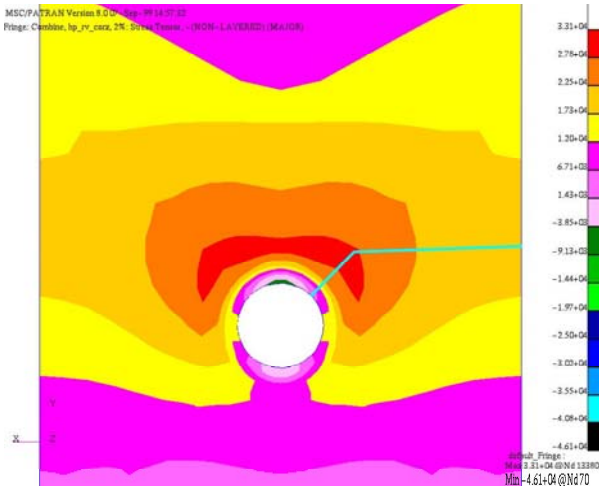

Figure NRC-2.7. Stress plot of maximum principal stress at critical rivet hole in 2% corroded specimen. The blue lines show the location where the stress

results were taken to obtain the stress correction factors that were used in the AFGROW program.

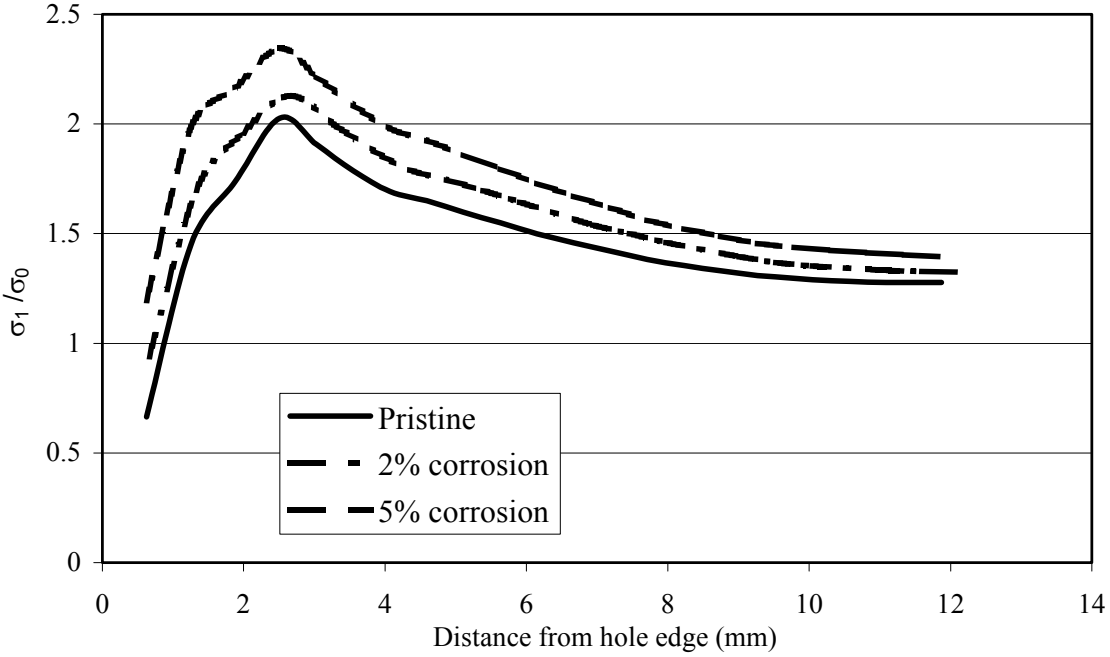

Figure NRC-2.8. Stress Correction Factors Used in AFGROW Program to Correct for Secondary Bending and Corrosion Pillowing Effects

Residual Life Predictions

A single corner crack located at a straight hole was used to predict the lap joint test results in addition to a constant amplitude loading with a load ratio of 0.02 and a maximum stress of 98.5 MPa (14.3 ksi). Short and long crack growth rate curves were used in the AFGROW program to predict the test results. For the 2% and 5% cases, the maximum stress was increased by the appropriate amount to take into account the stress increase caused by material thinning. The appropriate stress correction factors shown in Figure NRC-2.8 for the different test cases were used in the AFGROW program to take into account the secondary bending, rivet pre-load and corrosion pillowing. The results for the different test cases are presented in Table NRC-2.1 along with the average ECD value, the final crack length and the percent difference in the predicted versus observed cycles.

Table NRC-2.1. Predicted versus experimental cycles to failure

% Corrosion	ECD (mm)	Final Crack (mm)	Predicted # of Cycles	Experimental Results	% Diff
Pristine	0.05303	1.422	359600	332800	-8.1
		10.16	395700	375356	-5.4

2% Artificial	0.05512	4.313	172300	160770	-7.2
		10.16	190600	171500	-11.1
5% Combined	0.06736	8.974	104400	104107	-0.3
		12.70	106800	115409	7.5

-ve % differences indicate the predicted values over-estimated the number of cycles.

The final crack length shown in Table NRC-2.1 is the crack length at which the particular analysis was stopped. The smallest number presents the average first observed crack length. The other number gives the specified crack length that was chosen to prevent interaction with other cracks in the lap joint specimens. The experimental results are an average value of all the tests carried out at the specified average thickness loss. As can be seen from Table NRC-2.1, the majority of the predicted values give non-conservative results (over-estimate), which suggests that some of the areas near the critical rivet row had higher levels of corrosion than was first assumed. It should also be noted that the experimental results for the 5% case was based on only one test result. The remainder of the tests had either failed outside of the critical rivet hole at a large corrosion pit or a number of rivets had failed resulting in a stress redistribution that was not included in the finite element results.

Holistic Life Assessment Approach

In the lap joint specimens, corrosion and fatigue acted sequentially and thus were easier to model. Therefore it is no surprising that the calculated results were very close to the experimental ones. What was unexpected was that all the assumptions that were made (constant thickness loss, corner crack, etc.) did not appear to have a significant effect on the predicted results. It must be emphasized, however, that this particular sequence (corrosion then fatigue) would not be expected to occur in aircraft structures. Since in-service corrosion and its associated metrics, which include material thinning, surface topography (such as pits and intergranular attack) and pillowing, evolve, this implies that the ECD value would also change over time. Therefore this ECD approach could be only used to provide a quick assessment of the impact of corrosion on the remaining life of a particular component. Back-calculations could be carried out on failed components, or on samples fabricated from similarly damaged components and fatigue tested to failure, to estimate the ECD value. These calculated values could then be used to calculate the remaining life of the other components to determine if it could remain in-service until the next inspection interval.

The major disadvantage in the ECD approach is that it cannot take into account the fact that corrosion and fatigue act simultaneously in lap joints and also it is very test intensive. Another procedure known as the holistic life assessment approach, which is capable of predicting the progress of a discontinuity state in a material from cradle-to-grave (holistic) could be used to carry out a “corrosion damage tolerance” assessment of critical structural components. This approach allows for an evaluation of a change in state

during any time-slice in the holistic model. The terms that have been established to reflect these states include the Initial Discontinuity States (IDS) as well as the Modified Discontinuity States (MDS). IDS is a material characteristic that is related to the intrinsic material discontinuities or the intrinsic manufacturing and joining discontinuities that are present in pristine structures. However, once age degradation is considered then the effect time has on the discontinuity state must be taken into effect. Although IDS itself does not change over time, both cyclic and time domain mechanisms continue to evolve discontinuities.

IDS is used in the analysis to determine the effect that corrosion and cyclic loading has on a structure from the 'As-Built' to 'To-Be' condition. The 'To-Be' condition is the predicted state of the strucutre after a predetermined amount of time. MDS on the other hand is used in the analysis to determine the effect that corrosion and cyclic loading has from an 'As-Is' to 'To-Be' condition. For this time interval, nondestructive inspection techniques would be used to determine the damage state present in the structure and the results would then be used in the analysis to modify the stress state.

Once IDS data and verified holistic life models become available, this approach will be the preferred method of residual life assessment.

References

Bellinger, N.C., Krishnakumar, S. and Komorowski, J.P. (1994), "Modelling of Pillowing Due to Corrosion in Fuselage Lap Joints", CAS Journal, Vol. 40, No. 3, September 1994, pp. 125-130.

Bellinger, N.C., and Komorowski, J.P. (1997), "Corrosion Pillowing Stresses in Fuselage Lap Joints", AIAA Journal, Vol. 35, No. 2, February 1997, pp. 317-320.

Liao, Min and Xiong, Yeuxi, "Prediction of Fatigue Life Distribution of Fuselage Splices", to be published in the International Journal of Fatigue.

Eastaugh, G.F., Merati, A.A., Simpson, D.L., Straznicky, and Krizan, D.V. (1998a), "The Effects of Corrosion on the Durability and Damage Tolerance Characteristics of Longitudinal Fuselage Skin Splices", 1998 USAF Aircraft Structural Integrity Program Conference, San Antonio, 1-3 December 1998.

Eastaugh, G.F., Merati, A.A., Simpson, D.L., Straznicky, P.V., Scott, J.P., Wakeman, R.B. and Krizan, D.V. (1998b), "An Experimental Study of Corrosion/Fatigue Interaction in the Development of Multiple Site Damage in Longitudinal Fuselage Skin Splices", NATO-RTO Air Vehicle Technology Panel Workshop on Fatigue in the Presence of Corrosion, Corfu, Greece, 7-8 October 1998.

Eastaugh, G.F., Straznicky, P.V., Krizan, D.V., Merati, A.A. and Cook, J. (2000), "Experimental Study of the Effects of Corrosion on the Fatigue Durability and Crack Growth Characteristics of Longitudinal Fuselage Skin Splices", Published in the Fourth Joint DoD/FAA/NASA Conference on Aging Aircraft, St. Louis, MO, 15-18 May 2000.

Komorowski, J.P., Bellinger, N.C., Gould, R.W., Marincak, A. and Reynolds, R. (1996) "Quantification of Corrosion in Aircraft Structures with Double Pass Reflection", CAS Journal, Vol. 42, No. 2, June 1996, pp. 76-82.

PROBLEM NO. NRC-3

Title: Effect of Discontinuity States on the Risk Assessment of Corroded Fuselage Lap Joints.

Objective

To illustrate the effect that different discontinuity states (initial and modified) have on a risk assessment of fuselage lap joints.

General Description

This problem focuses on: (1) the methods that can be used to investigate the statistical characteristics of different discontinuity states (DS) and (2) a risk assessment of fuselage lap joints that contain multi-site damage (MSD) and corrosion. A statistical test for homogeneity will be described, which can be used to determine if a significant difference exists between the modified discontinuity states (MDS) present in naturally corroded fuselage lap joints and those found in artificially corroded joints. A goodness-of-fit test is applied to determine the best-fit distribution for the pristine and corroded DS data. The use of the best-fit distributions for the pristine and corroded DS data in a risk assessment analysis will be described. The risk assessment program PROF (PRobability Of Fracture) is used in this problem.

Topics Covered: Corrosion, Discontinuity States (DS), Statistical Methods, Risk Assessment.

Type of Structure: Fuselage Lap Joints

Relevant Sections of Handbook: 8

Authors: Min Liao and Nicholas C. Bellinger

Company Name: National Research Council Canada
Institute for Aerospace Research
Montreal Road, Ottawa, Ontario Canada K1A 0R6
1(613) 990-9812, Website: www.nrc.ca/iar

Contact Point: Jerzy P. Komorowski

Phone: 613-993-3999

e-mail: jerzy.komorowski@nrc.ca

NRC · CNRC

Overview of Problem Description

A new corrosion management approach has been proposed with the intent of anticipating, planning, and managing corrosion, which stands in sharp contrast to the present 'find and fix' philosophy (Peeler, 2000). This new philosophy uses the holistic ('cradle-to-grave') life assessment approach to address time and cyclic load issues (Brooks et al., 2000), and the cornerstone of this approach is the discontinuity state (DS) concept, which was described in detail in (Hoeppner, 1981). To characterize the different discontinuity states present in pristine (initial discontinuity state, IDS) and corroded (modified discontinuity state, MDS) fuselage lap joints, sections need to be taken from representative samples of the material, polished and the different discontinuity states that are present documented. Such a study was carried out on corroded fuselage lap joints to document the different modified discontinuity states present. The results from this study are presented in Example NRC-1 in this handbook. Experiments are also required in order to determine which of the different discontinuity states strain-energy fields (load spectrum) influence. Results from such tests are presented in Example NRC-1 in this handbook.

Due to the random nature of the different DS values, such as micro-porosity and inclusions (examples of IDS) and pit depth, intergranular cracks, exfoliation and environmentally assisted cracks (examples of MDS), a statistical analysis will be described in which a test for homogeneity and a goodness-of-fit test will be carried out. Using the results from the statistical analysis, the effect that the DS distribution has on a risk assessment of fuselage lap joints will be examined.

Coupon Test and Experimental DS values

As mentioned earlier, the experiments required to generate the DS data that will be influenced by strain-energy fields are described in Example NRC-1 in this handbook. To carry out these tests, coupons were machined from pristine, artificially and naturally corroded lap joints containing three levels of material thinning, 0%, 2% and 5% thickness loss. The holistic life approach recognizes four distinct phases of component life (nucleation, short crack, long crack, and final instability (Hoeppner and Chandrasekaran, 1998)), and requires physical discontinuity measurements and life modeling in the nucleation phase.

To determine the DS values for the different corrosion levels, the majority of the fracture surfaces from the pristine, 2% artificial and 2% natural coupons were examined with the aid of a scanning electron microscope (SEM). For the pristine coupons the nucleation sites were located along the non-machined edge while for the corroded coupons, they were located along the corroded faying surface edge. Although all the nucleation sites were semi-elliptical in shape, a semi-circular crack was used to describe the DS with an equivalent area to the initial semi-elliptical crack. It should be pointed out that the equivalent corrosion damage (ECD) defined in Example NRC-1 of this handbook corresponds to the MDS values in the holistic life assessment approach.

To verify the ability of the DS concept to predict the life of each coupon, the AFGROW crack growth program was used to predict the number of cycles to failure, which were then compared to the particular experimental result of the corresponding coupon (Bellinger et al., 2001). The results showed that all the predicted cycles to failure were within 10% of the experimental results (the largest error occurred when multiple nucleation sites were present in the coupons). This

good correlation indicated that the DS values could be back calculated from the number of cycles to failure of the coupons using the AFGROW program. Therefore, the DS data for the 5% corroded coupons, were determined by back calculations.

To compare the different DS data without knowing the best-fit distribution, each set of DS samples was ranked and their empirical distribution functions (EDFs) plotted as shown in Figure NRC-3.1. As can be seen from this figure, there is distinct difference between the EDFs of the 2% and 5% corrosion DS samples while for the pristine and 2% corrosion, the difference is relatively small. The mean and standard deviations of all the DS samples are presented in Table NRC-3.1.

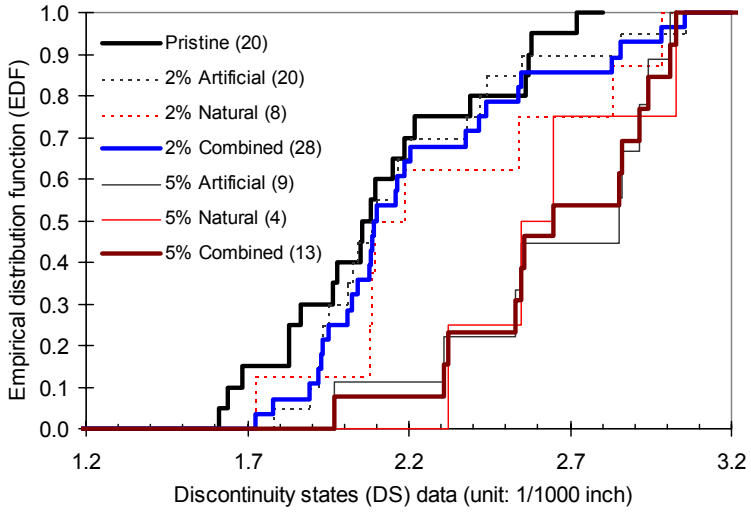

Figure NRC-3.1. Empirical distribution function (EDF) of DS data, ( ) denotes sample size.

Table NRC-3.1. IDS and MDS values.

	IDS Pristine (inch)	Artificial MDS 2% (inch)	Natural MDS 2% (inch)	Combined MDS 2% (inch)	Artificial MDS 5% (inch)	Natural MDS 5% (inch)	Combined MDS 5% (inch)
Mean	0.002103	0.002194	0.002314	0.002229	0.002659	0.002638	0.002652
Std. dev.	0.0003265	0.0003322	0.0004291	0.0003584	0.0003479	0.0002959	0.0003204
Coefficient of variation	15.52%	15.14%	18.54%	16.08%	13.08%	11.22%	12.08%
Sample size	20	20	8	28	9	4	13

Statistical Characteristics of DS data

Test for homogeneity of artificial and natural MDS samples

Although the sample size is small for each set of DS data generated, combining the natural and artificial results could increase it. However, before this can be accomplished, a test for homogeneity based on the k-sample Anderson-Darling statistic, which is recommended in MIL-HDBK-17 and 5 (Department of Defense, 1997, 1998) must first be carried out. This test is used

to determine whether a significant difference exists between two samples (in this case artificial and natural corrosion MDS samples) so that they could be pooled together to get a larger sample.

Table NRC-3.2 presents the k-sample Anderson-Darling test results for the artificial and natural MDS samples for the 2% and 5% corrosion levels. This table shows that the hypothesis that the artificial and natural MDS samples, either for the 2% or 5% corrosion, are from the same population was not rejected at a significance level (SL) of 5%. In addition, a previous study (Eastaugh et al., 2000) has shown that the physical appearance and microscopic topography of the damage from artificially and naturally corroded lap splices were similar. Based on these results, it was concluded that there was no significant difference in the damage resulting from the accelerated corrosion process as compared to the damage associated with the natural process. Therefore, the two MDS samples were combined, and the mean and standard deviation of the combined MDS data are also presented in Table NRC-3.1. Figure NRC-3.1 also shows the EDF of the combined MDS data for the 2% and 5% corrosion.

Table NRC-3.2. k-sample Anderson-darling test results.

Sample data	Homogeneity hypothesis	*ADK* (MIL-HDBK-17, 5)	Critical value of *ADK*	Conclusion
2% artificial and natural MDS samples	Two samples are from the same population	0.66	2.40	can not reject at SL=5%
5% artificial and natural MDS samples	Two samples are from the same population	0.49	2.30	can not reject at SL=5%

Best-fit distributions of DS data

Except for the 5% corrosion MDS data, the majority of the DS data were measured from the fracture surfaces with the aid of a SEM. Generally, in a material degradation process, failure may depend on the strength of the weakest element, or it may depend on the largest crack-like discontinuity present in the material. Therefore, it is reasonable to assume that the DS values used in this example are the largest values among all discontinuities. Based on the physical behavior of the DS, the mathematical simplicity as well as the usability in engineering (Liao et al., 2001b), six continuous distributions, presented in Table NRC-3.3, were selected as alternative (candidate) distributions to describe the DS data.

Table NRC-3.3. Alternative distributions.

No	Distribution form	Distribution function	Domain of variable
1	Normal	$F(x)=\Phi[(x-\mu)/\sigma]$	$x\in(-\infty,+\infty)$
2	Lognormal	$F(x)=\Phi[(\ln x-\mu)/\sigma]$	$x\in(0,+\infty)$
3	Weibull	$F(x)=1-\exp[-(x/\alpha)^{\beta}]$	$x\in[0,+\infty)$
4	Type-I extreme value distribution (EVD) of smallest values	$F(x)=1-\exp\{-\exp[(x-a)/b]\}$	$x\in(-\infty,+\infty)$
5	Gumbel (Type-I EVD of largest values)	$F(x)=\exp\{-\exp[-(x-a)/b]\}$	$x\in(-\infty,+\infty)$
6	Frechet (Type-II EVD of largest values)	$F(x)=\exp[-(\alpha/x)^{\beta}]$	$x\in[0,+\infty)$

In this example, all the alternative distributions were tested to fit the pristine, combined 2%, and combined 5% corrosion MDS data. Anderson-Darling goodness-of fit (A-D GOF) test (Department of Defense, 1997, 1998) was used to quantitatively examine which distribution

could provide the best fit to the DS data. All the parameters for the six alternative distributions were estimated using the maximum likelihood estimators (MLEs) (Liao et al., 2001b). The results showed that:

1. For the pristine IDS data, the Gumbel, Lognormal, Frechet, and Normal distributions were *highly acceptable* (significance level, SL>20%), the Weibull distribution was *acceptable* (5%<SL<20%), and only the Type-I EVD of smallest values was *unacceptable* (SL<5%);
2. For the combined 2% MDS data, the Frechet and Gumbel distributions were *highly acceptable*, and the other alternative distributions were all *unacceptable*;
3. For the combined 5% MDS data, Type-I EVD of smallest values, Weibull, and Normal distributions were *highly acceptable*, the Gumbel distribution was *acceptable*, and only the Frechet was *unacceptable*;
4. Only the Gumbel distribution was *acceptable* for all the DS data sets.

Another method to determine which distribution describes the data best is to plot the different distributions on a probability paper. This example plotted the six alternative distributions and the DS data on Normal probability papers, and the results are shown in Figures NRC-3.2 to NRC-3.4 for the pristine, combined 2%, and combined 5%, respectively. The symmetrical ranks (Shimokawa and Liao, 1999); i.e., $p_i=(i\text{-}0.5)/n$, were used as the plotting positions for the DS data. After carefully examining these plots, the same conclusions from the A-D GOF test could be drawn. It should be emphasized that the goodness-of-fit test and the probability plot are complementary to each other and both should be used to determine the best-fit distribution.

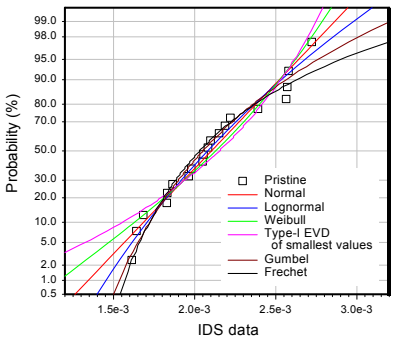

Figure NRC-3.2. Pristine IDS data plot on Normal probability paper

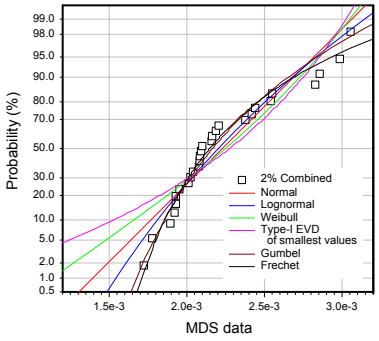

Figure NRC-3.3. Combined 2% MDS data plot on Normal probability paper.

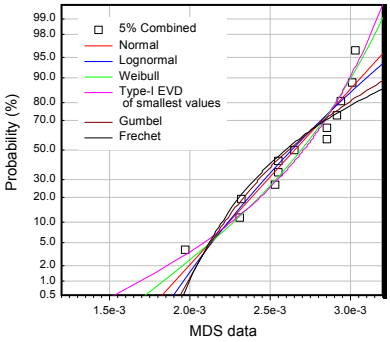

Figure NRC-3.4. Combined 5% MDS data plot on Normal probability paper.

Risk Analysis of Fuselage Lap Joints

MSD corrosion/fatigue test

Tests were carried out on multi-site damage (MSD) lap splice specimens to determine the effect that corrosion has on the fatigue life of a longitudinal fuselage lap joint (Eastaugh et al., 2000). Figure NRC-3.5 shows a schematic of the specimen, which was constructed of two 1.0 *mm* (0.040 *inch*) sheets of 2024-T3 clad aluminum with three rows of 4 *mm* (5/32 *inch*) 2117-T4 countersink rivets. Specimens were pre-corroded using an accelerated corrosion process. Three

corrosion levels were examined: 0%, 2%, and 5% average material loss. Fatigue tests were then performed by applying a constant amplitude loading such that the stress approximately one inch away from the critical rivet row was 98.5 *MPa* (14.3 *Ksi*) with a stress ratio of 0.02 and a frequency of 8 *Hz*.

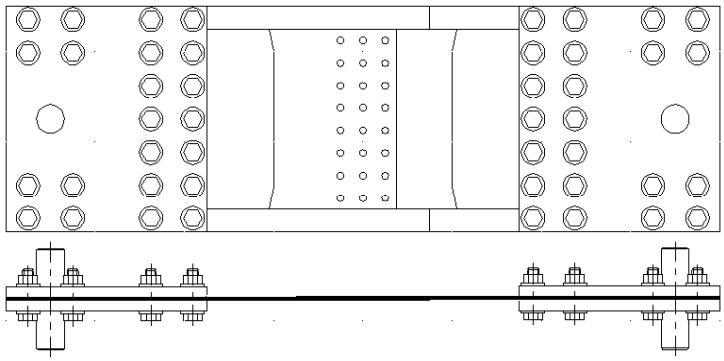

Figure NRC-3.5. Schematic of the MSD specimen.

Examinations of the failed specimens revealed that the majority of the crack nucleation sites were located away from the rivet hole along the faying surface and were semi-elliptical in shape. Although different MSD scenarios were observed in the pristine and corroded MSD tests, the onset of MSD, that is life to visible cracks, occupied over 80% of the total life and thus was used as the failure criteria for the risk analysis. The probability of failure (POF) for the onset of MSD in both the pristine and corroded specimens was predicted using the computer code, PROF (PRobability Of Fracture) (Berens et al., 1991) (Hovey et al., 1998). PROF has been used for quantifying risk and cost associated with inspection, replacement, and retirement of aging aircraft. The input data was found to play a key role in obtaining accurate POF predictions (Liao and Xiong, 2001a) (Liao and Xiong, 2000).

Input data preparation for PROF

Initial crack size distribution (ICSD) – To investigate the influence of the DS distributions on the POF predictions, all the *acceptable* distributions were used as ICSD in the risk analysis. Since PROF required a tabular format for the ICSD input, i.e., (a_i, $F(a_i)$), 1000 points of (a_i, $F(a_i)$) data were generated based on the distribution function and estimated parameters (Liao et al., 2001b).

Median crack growth curve – The crack growth analysis of pristine and corroded lap joints was accomplished earlier using the classic model of a corner crack at a straight hole in AFGROW (Bellinger et al., 2001). Stress correction factors, generated using a three dimensional finite element analysis, were used to take into account the bending, bearing, and corrosion pillowing that occur in non-corroded and corroded lap joints. Material thinning for the corroded joints was also taken into account by increasing the remote stress by the appropriate amount. Using the methods of (Bellinger et al., 2001), the median crack growth (*a*-*N*) curves for pristine and corroded lap joints were obtained, which are shown in Figure NRC-3.6. One hundred points of tabular (a_i, N_i) data were used in PROF.

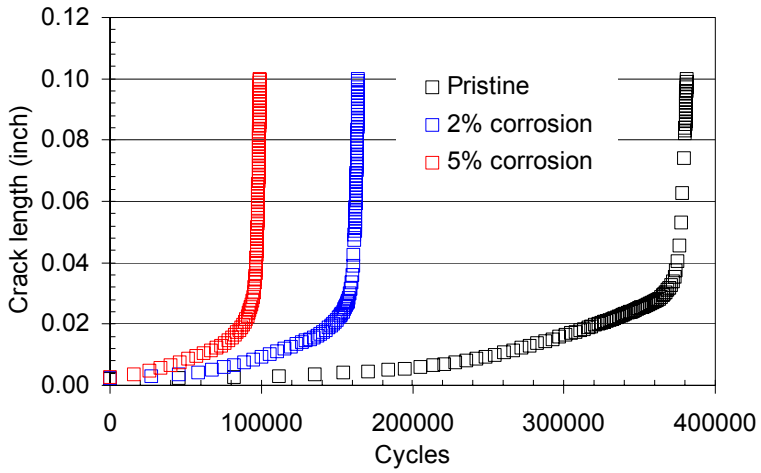

Figure NRC-3.6. Calculated *a-N* curves for pristine and corroded MSD specimens.

Critical crack length – In this example, a visible crack length of 2.54 *mm* (0.1 *inch*), i.e., the onset of MSD, was taken as the critical crack length for both the pristine and corroded specimens. This crack length was measured from the edge of the hole as it emerged beyond the rivet head on the outer skin of the specimen and was chosen because it was small enough not to be influenced by an adjacent crack.

Fracture toughness distribution and geometry factor – For the 1.0 *mm* (0.04 *inch*) sheet of 2024-T3 clad aluminum, the fracture toughness distribution was assumed to follow a normal distribution with a mean and standard deviation of 151.6 *MPa* $\sqrt{m}$ (138.0 *Ksi* $\sqrt{in}$) and 5.5 *MPa* $\sqrt{m}$ (5.0 *Ksi* $\sqrt{in}$), respectively (The Boeing Company, 1998). Since this analysis defined a small critical crack length, the fracture toughness criterion had no influence on the risk analysis. The input of the fracture toughness distribution was needed to run the software. For the same reason, the geometry factors were also arbitrarily set to be small values so that the fracture toughness criterion would not affect the calculated results.

Maximum stress distribution – The Gumble distributions with a mean at the constant amplitude level in the test and a small standard deviation were used for the maximum stress distribution. Using the method of (The Boeing Company, 1998), the Gumble parameters for the pristine and corroded specimens were calculated by taking into account the material loss due to corrosion. Since the critical crack length criterion was applied in this example, the maximum stress distribution had an insignificant effect on the risk analysis.

Probability of detection, POD(a), and repaired crack size distribution (RCSD) – Since this risk analysis does not involve any inspection or repair activities, arbitrary but reasonable data were used to define the *POD(a)*, and the *RCSD*.

Comparison of analytical and test results

Figures NRC-3.7 and NRC-3.8 show the results from the POF predictions for the pristine and corroded specimens. The experimental results, which were ranked and also plotted in these figures, used the symmetrical ranks as the plotting positions. The experimental results, which as mentioned earlier was the number of cycles to visible cracks, were observed from the central

four holes of the top rivet row and resulted in a sample size of 18, 7, and 1 for the pristine, 2%, and 5% corroded specimens, respectively.

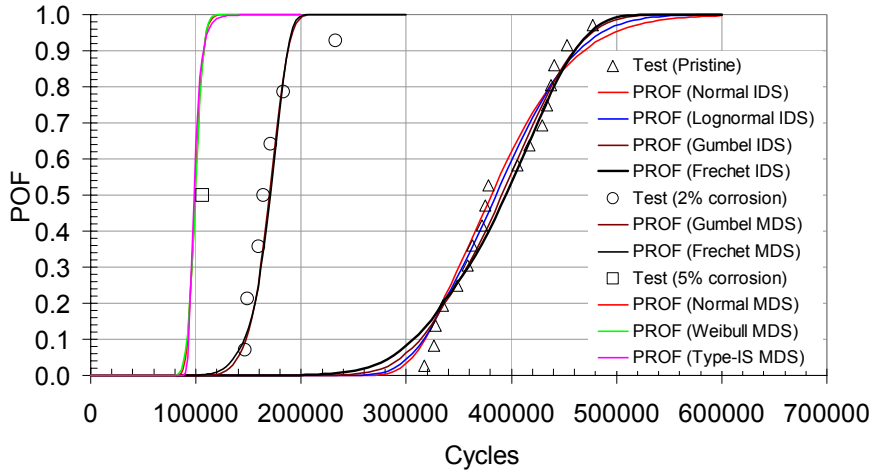

Figure NRC-3.7. POF predictions for pristine and corroded MSD specimens using the *highly acceptable* DS distributions.

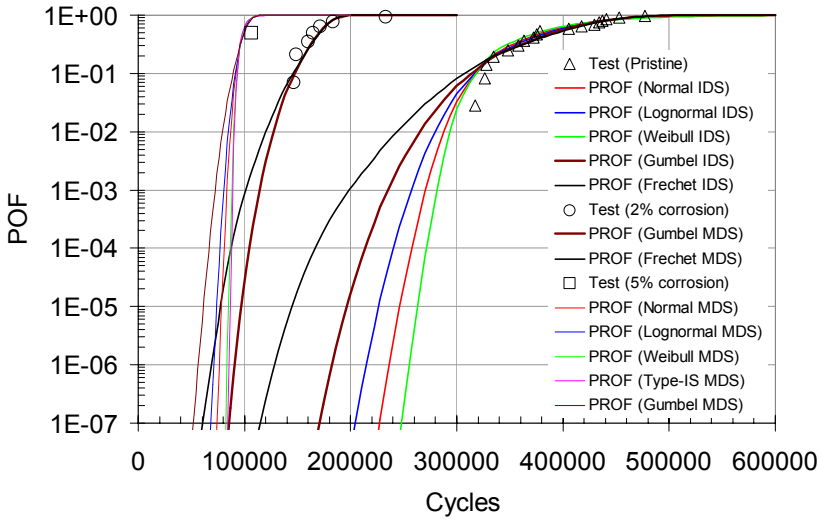

Figure NRC-3.8. POF predictions for pristine and corroded MSD specimens using the *acceptable* DS distributions.

Figure NRC-3.7 presents the POF predictions for the pristine and corroded specimens using different *highly acceptable* (best-fit) DS distributions. The results from Figure NRC-3.7 indicate that:

- For the pristine and 2% corroded specimens, predictions are close to the test results. Again A-D GOF tests (distribution free GOF test (Lawless, 1982)) were carried out and indicated that the predictions fit the test results very well (all SL>15%). All best-fit DS distributions produced close POF results to each other, especially for the corroded specimens;

- For the 5% corroded specimens, the prediction can't be compared to the test result since there is only one test datum available, however, the predicted mean life is close to this test datum;
- The POF results for the 2% corroded specimens are much higher than those for the pristine specimens, that is, corrosion in lap joints, even at low thickness loss levels, can result in a great increase of the POF. From the predictions, the POF difference between 2% and 5% is less than that between the pristine and 2%. This is consistent with the finding that the corroded surface topography at 5% may be "smoother" than that at 2% (Bellinger et al., 2000).

Figure NRC-3.8 presents the POF predictions for the pristine and corroded specimens using the *acceptable* DS distributions and is shown in logarithmic scale to more easily distinguish the results in the low probability zone (<0.1). Although the test data did not have a large enough sample size to verify the predictions in the low probability zone, Figure NRC-3.8 does reveal the following:

- For the pristine specimens, the different DS distributions produced significantly different POF predictions in the low probability zone. Assuming that 10^{-7} is an acceptable risk level for maintenance scheduling (Lincoln, 2000), the Frechet DS distribution gave the shortest time while the Weibull DS distribution gave the longest time and the time difference was about 130,000 cycles.
- For the 2% corroded specimens, the different MDS distributions also produced different POF predictions in the low probability zone, though the difference was not as significant as in the pristine case. However, the maintenance schedule could be significantly shortened due to prior corrosion even at this low thickness loss level. In this example, at a risk level of 10^{-7}, the time difference between the pristine and 2% corrosion cases was about 9,000 cycles, according to the POF predictions produced by the Gumbel DS distribution.

Figure NRC-3.8 also shows that the POF curves for the corroded specimens in the low probability zones are "steeper" than the curve for the pristine results, given the same type of DS distribution, for example the Gumbel distribution. This steeper curve would have a profound effect on the probability of failure if corrosion was missed during routine inspections. Figure NRC-3.9 illustrates an example, in which a risk assessment was carried out to maintain a POF level under 10^{-7} using the Gumbel DS distribution for both the pristine and corroded specimens and a log-logistic distribution (Berens et al., 1991) was assumed for the POD(a) with μ=0.01 and σ=0.1. To maintain the acceptable POF level for the pristine specimens, the first inspection would have to be carried out at 170,000 cycles, while the second inspection would be required at about 236,000 cycles. If during the first inspection, 5% corrosion was missed, this would significantly increase the POF at the second inspection interval by three orders of magnitude (10^{-4}). Figure NRC-3.9 also shows that a risk assessment can aid in scheduling the maintenance associated with corrosion. This assessment could allow a corroded lap joint to remain in service until the next scheduled maintenance while maintaining the acceptable POF level.

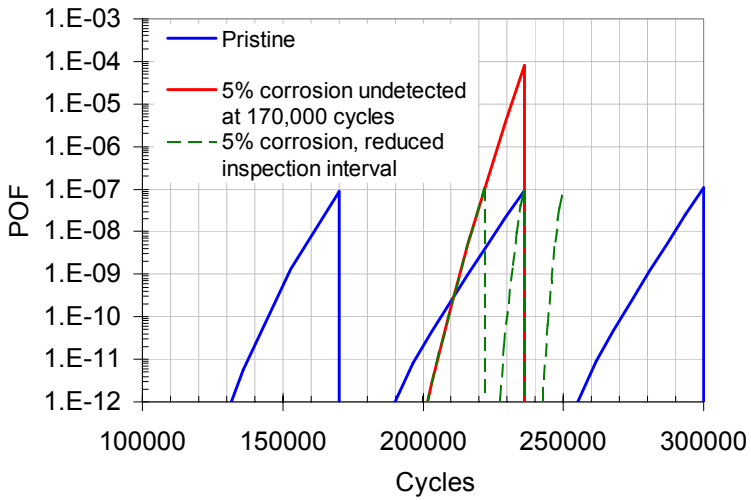

Figure NRC-3.9. Corrosion risk assessment example: what-if scenario predictions.

References

Bellinger, N.C., Cook, J.C. and Komorowski, J.P. (2000), "The Role Of Surface Topography In Corroded Fuselage Lap Joints", The proceedings of the 2000 USAF Aircraft Structural Integrity Program Conference, San Antonio, Texas, 2000.

Bellinger, N.C., Komorowski, J.P. and Benak, T.J. (2001), "Residual Life Predictions Of Corroded Fuselage Lap Joints", International Journal of Fatigue, Vol.23, No. 11, pp. 349-356, 2001.

Berens, A.P., Hovey, P.W. and Skinn, D.A. (1991), "Risk Analysis For Aging Aircraft, Vol.1—Analysis", WL-TR-91-3066, Air Force Research Laboratory, Wright-Patterson Air Force Base, Ohio, 1991.

The Boeing Company (1998), D500-13008-1, Corrosion Damage Assessment Framework, Seattle, W.A., 1998.

Brooks, C., Honeycutt, K., and Prost-Domasky, S. (2000), "Case Studies For Life Assessments With Age Degradation", The proceedings of the Fourth Joint DoD/FAA/NASA Conference on Aging Aircraft, St. Louis, Missouri, May, 2000.

Department of Defense (1997) MIL-HDBK-17E, Polymer Matrix Composites. Vol.1, U.S.A.

Department of Defense (1998) MIL-HDBK-5H, Metallic Materials and Elements for Aerospace Vehicle Structures, U.S.A.

Eastaugh, G.F., Straznicky, P.V., Krizan, D.V., Merati, A.A. and Cook, J. (2000), "Experimental Study Of The Effects Of Corrosion On The Fatigue Durability And Crack Growth

Characteristics Of Longitudinal Fuselage Splices", Proceeding of the Fourth DoD/FAA/NASA Aging Aircraft Conference. St. Louis, 2000.

Hoeppner, D.W., (1981), "Estimation of Component Life by Application of Fatigue Crack Growth Threshold Knowledge", Fatigue, Creep and Pressure Vessels for Elevated Temperature Service: presented at the Winter Annual Meeting of the American Society of Mechanical Engineers, Washington, D.C., edited by Carl W. Lawton, R. and Rodger Seeley, sponsored by the Metal Properties Council, Inc., the Materials Division, ASME, pp. 1-84, 1981.

Hoeppner, D.W. and Chandrasekaran, V. (1998), "Corrosion And Corrosion Fatigue Predictive Modeling State Of The Art Review", submitted as a part of the research program "*Modeling Corrosion Growth on Aircraft Structure*" subcontract Number NCI USAF 9061-008, April 30, 1998.

Hovey, P.W., Berens, A.P. and Loomis, J.S. (1998), "Update Of The PROF Computer Program For Aging Aircraft Risk Analysis, Vol.1- Modifications And User's Guide", UDR-TR-1998-00154, Air Force Research Laboratory, Wright-Patterson Air Force Base, Ohio, 1998.

Lawless, J.F. (1982), Statistical Models And Methods For Lifetime Data. John Wiley & Sons, New York, 1982.

Liao, M. and Xiong, X. (2000), "Risk Assessment Of Aging Aircraft Structures Using PRISM and PROF", Canadian Aeronautics and Space Institute Journal, Vol. 46, No. 4, pp. 191-203, 2000.

Liao, M. and Xiong, Y. (2001a), "A Risk Analysis Of Fuselage Splices Containing Multiple Site Damage And Corrosion", Journal of Aircraft, Vol. 38, No. 2, pp. 181-187, 2001.

Liao, M., Bellinger, N., and Komorowski, J.P. (2001b), "Statistical Characteristics Of Discontinuity States And Their Application To Corrosion Risk Assessment Of Aircraft Structures", Proceedings of ICAF 2001, Toulouse, France, June 2001.

Lincoln, J.W. (2000), "Effect Of Aircraft Failures On USAF Structural Requirements", Proceeding of ICAS 2000, England.

Peeler, D. (2000), "Managing The Impact Of Environment Degradation On The USAF Fleet", The proceedings of the Fourth Joint DoD/FAA/NASA Conference on Aging Aircraft, St. Louis, Missouri, May, 2000.

Shimokawa, T. and Liao, M. (1999) "Goodness-of-Fit Tests for the Type-I Extreme-Value and Two-Parameter Weibull Distributions", IEEE Transactions on Reliability, Vol. 48, No.1, pp. 79-86, 1999.

PROBLEM NO. SIE-1

Title: Crack Growth Analysis of Main Cargo Door Surround Doubler Attachment to Fuselage Skin with MSD Cracks

Objective:

To illustrate the process of estimating crack growth behavior to set inspection limits.

General Description:

This problem focuses on a damage tolerance assessment of a main cargo door surround doubler attachment to fuselage structure for the purpose of establishing inspection intervals for multi-site damage, MSD, conditions. The critical area includes the main cargo door surround doubler and the existing fuselage skin. The stresses acting at the doubler attachment at the upper edge are derived from a conservative loading spectrum based on pressure loading. The critical area was modeled using a standard NASGRO 3.0 stress intensity factor solution and crack growth model.

Topics Covered: Damage tolerance assessment, crack growth analysis, inspection intervals

Type of Structure: fuselage skin, main cargo door surround doubler

Relevant Sections of Handbook: Section 2, 5, 11

Author: Lesley Camblin

Company Name: Structural Integrity Engineering
9525 Vassar
Chatsworth, CA 91311
818-718-2195
www.sieinc.com

Contact Point: Matthew Creager

Phone: 818-718-2195

e-Mail: mcreager@sieinc.com

Overview of Problem Description

This problem focuses on the main cargo surround doubler attachment to the existing fuselage skin at stringers 2R and 26L. The skin is considered to be a single load path structure under the total hoop stress before the doubler attachment. The critical location is in the skin at the first row of fasteners because the skin sees both bypass and bearing stresses at this row, where as, at the other fastener rows the load is in both the doubler and the skin with each row having lower load transfer.

The fuselage skin was fabricated from 2024-T3 aluminum. The fasteners are 0.188 in diameter, and join the skin and surround doubler.

The specific area is shown in View A of Figure SIE-1.1, with the specific details and MSD crack path shown in Figure SIE-1.3. Note that the skin at this first row of fasteners is a single load path as shown in Figure SIE-1.2.

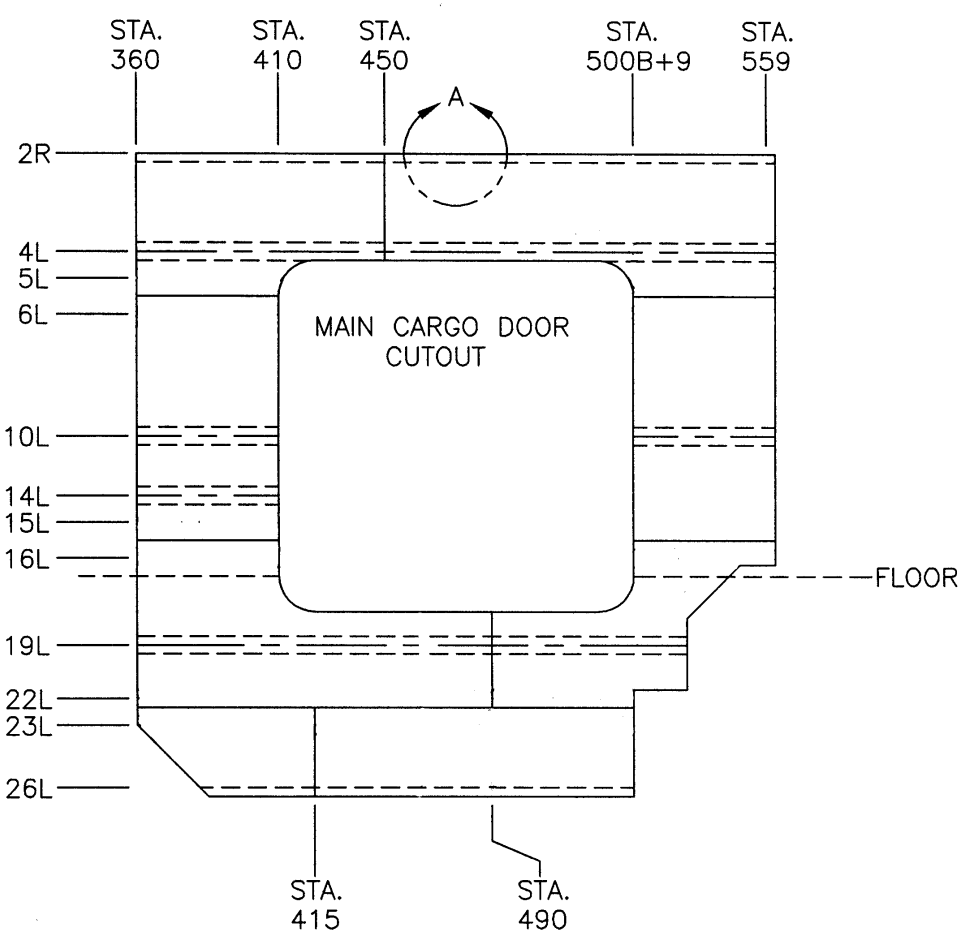

Figure SIE-1.1. Main Cargo Door Doubler Installation

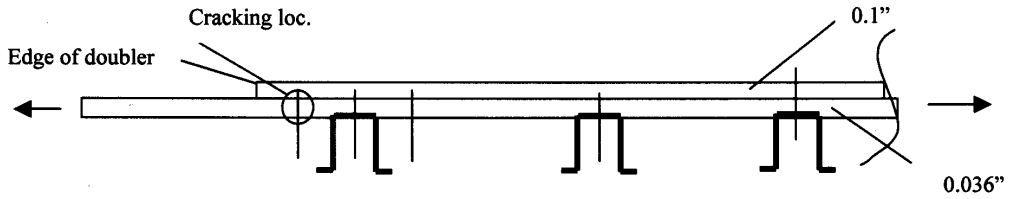

Figure SIE-1.2. Structural Detail for Critical Area

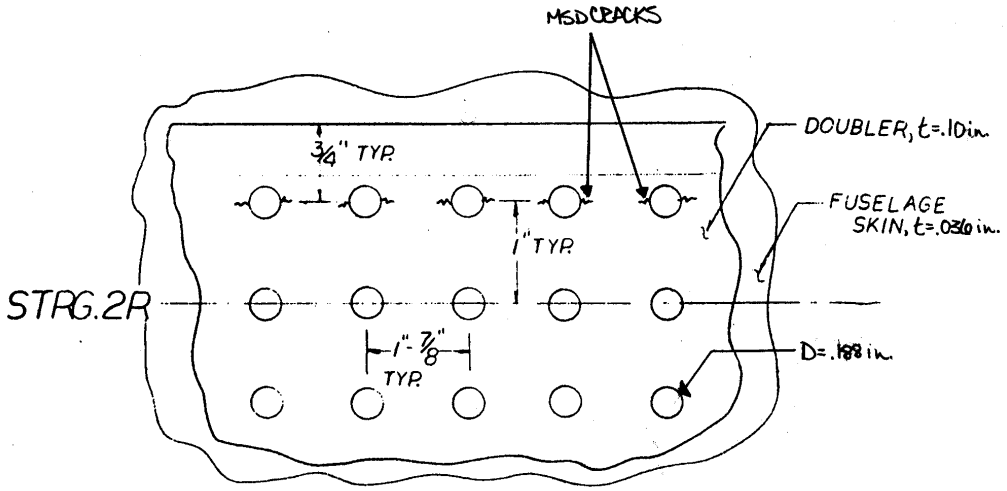

Figure SIE-1.3. Detail Geometry of Critical Location, View A.

Model Geometry Description

The crack growth analysis is based on the Fatigue Crack Growth Computer Program NASGRO3.0. This computer program calculates crack growth for a single crack for several standard crack cases. Crack growth rate calculations use the "NASGRO" equation with elements developed by Forman, Newman, de Koning, and Henriksen (see NASGRO reference manual). This is a modified Paris equation to account for fatigue crack closure, stress ratio effects, and upper and lower fatigue crack growth rate asymptotes for threshold and critical crack growth.

The analysis uses the NASGRO3.0 material libraries for the crack growth rate equation constants. Non-interaction of loads and constants for the Forman crack growth rate equation are used.

Since the standard crack models in NASGRO3.0 are for crack growth of single cracks, no influence of one crack upon another is calculated in NASGRO3.0 for these standard cases. MSD scenarios involve fatigue damage at multiple locations. This causes the potential of crack interactions. The analysis presented here includes these crack interaction effects by iterating though a series of NASGRO3.0 computer runs tracking the growth of multiple cracks and modifying the stress intensity factors appropriately. The increased stress intensity factors are based on the crack sizes of the interacting cracks from the previous iteration and correction factors based on the compounding of analytical stress intensity solutions.

This iteration procedure is accomplished in an Excel® Spreadsheet utilizing Visual Basic Programming to submit a NASGRO3.0 computer run for each crack at each iteration. The spreadsheet reads the NASGRO3.0 output files for cycles and current crack lengths. Based on these crack lengths, correction factors are calculated and input into the NASGRO3.0 input file for the next iteration, which is automatically submitted by the spreadsheet.

The correction factors are accounted for by increasing the stress scaling factors input into NASGRO3.0. These correction factors for crack interaction account for the condition of interactions of cracks in parts that are analyzed for multiple site damage. These increased stress scaling factors can be input based on the following:

$$K = S\beta_{CF}\beta_N\sqrt{\pi a} = S'\beta_N\sqrt{\pi a}$$

where,

$\beta_N =$ Beta for the standard NASGRO crack model

$\beta_{CF} =$ Beta calculated from the correction factor

$S' = S\beta_{CF} =$ increased stress scaling factor input into NASGRO

The correction factors for crack interaction are based on compounding of analytical stress intensity solutions. Two correction factors are used in this analysis. The first correction factor is termed "Bowie" and is for equal length cracks growing from opposite sides of a hole. The second correction factor is termed "Periodic" and is used for equal length cracks emanating from holes approaching one another.

Compounding of the first and second correction factors is done, and is termed "Bo + Bp'. This product of the "Bowie" and the "Periodic" correction factors is what is used for typical MSD situations where there are multiple fastener holes in a row and assumed imperfection flaws equal in size growing from opposite sides of each hole towards one another.

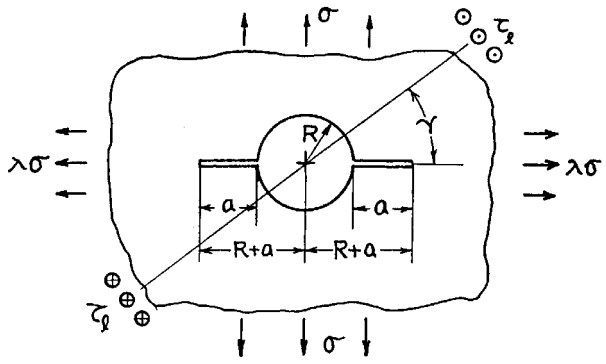

Figure SIE-1.4. Bowie Correction Factor

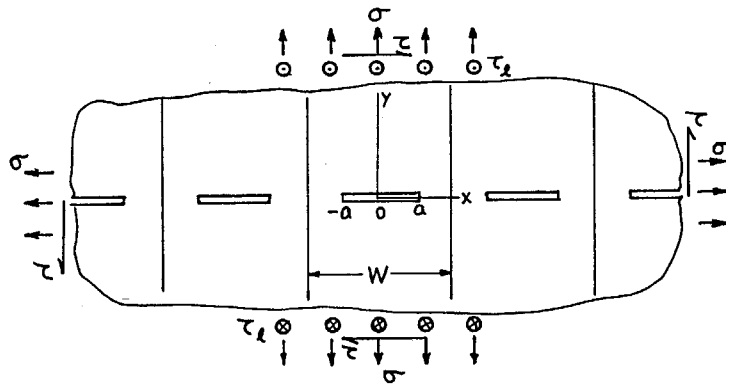

Figure SIE-1.5. Periodic Correction Factor

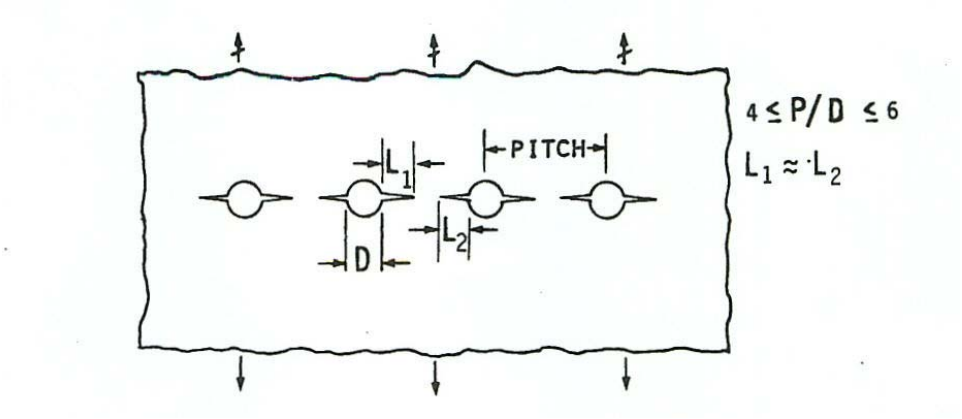

Figure SIE-1.6. Bowie + Periodic Correction Factor

These correction factors are based on through the thickness cracks. They are used for part through cracks when defined with an equivalent crack length. The equivalent crack length is based on equating the area of a part through crack as a quarter ellipse to that of an equivalent through crack as a rectangular area with thickness, t:

$$A_{pc} = A_{eq} = \frac{\pi ac}{4} = a_{eq}t \Rightarrow a_{eq} = \frac{\pi ac}{4t}$$

Note the correction factors are used in conjunction with standard crack models in NASGRO3.0. Therefore, to obtain a correction factor, the ratio of an analytical solution for a specific crack problem to a solution approximating the standard crack model is calculated. The analytical solutions used in deriving these correction factors are taken from H. Tada, P Paris, and G. Irwin, "The Stress Analysis of Cracks Handbook", Third Edition.

The "Bowie" correction factor is derived by comparing Bowie's solution for equal length cracks from both sides of a hole to the solution of a single crack from one side of a hole. The ratio of these solutions, from pages 19.1 and 19.2 of the Handbook, respectively yield the "Bowie" correction factor:

for,

$\lambda = 0$

$$s = \frac{a}{R+a}$$

$$\beta_{bowie} = \frac{K_{19.1}}{K_{19.2}} = \frac{\sigma F_{19.1}(\lambda, s)\sqrt{\pi a}}{\sigma F_{19.2}(\lambda, s)\sqrt{\pi a}} = \frac{F_{19.1}(0, s)}{F_{19.2}(0, s)} = \frac{F_{0,19.1}(s)}{F_{0,19.2}(s)}$$

$$\beta_{bowie} = \frac{0.5(3-s)[1+1.243(1-s)^3]}{[1+.2(1-s)+.3(1-s)^6](2.243-2.64s+1.352s^2-.248s^3)}$$

The "Periodic" correction factor is derived from the ratio of the beta factor for a periodic array of cracks from page 7.1 of the Handbook to the solution of a crack in an infinite width plate. Note the solution for a periodic array of cracks is an exact solution. Including the diameter of the hole in the crack length and defining the pitch of the hole spacing to be the pitch of the crack spacing yields the "Periodic" correction factor:

$a_{7.1} = D/2 + a$

$W = pitch = P$

$$\beta_{periodic} = \frac{K_{7.1}}{\sigma\sqrt{\pi a}} = \sqrt{\frac{W}{\pi a_{7.1}} \tan\frac{\pi a_{7.1}}{W}} = \sqrt{\frac{P}{\pi(D/2+a)} \tan\frac{\pi(D/2+a)}{P}}$$

Note the periodic correction factor is based on the solution of an infinite width plate, while the standard crack model in NASGRO3.0 is for a finite width plate. The use of this correction factor is conservative based on the following calculations.

A comparison of the stress intensity factor calculated for a finite width plate with that of a periodic array of cracks in an infinite plate is made to estimate the effects on crack growth as cracks approach one another. Note that the cracks are analyzed with a finite width plate using the width equal to the pitch of the fastener spacing. Solutions for both problems are taken from H. Tada, P Paris, and G. Irwin, "The Stress Analysis of Cracks Handbook", Third Edition.

Koiter found the exact limit for the beta factor for the finite width plate at a/b=1 as:

$$\beta_{fw} = \frac{2}{\sqrt{\pi^2 - 4}} \frac{1}{\sqrt{1-a/b}}$$

For the periodic array of cracks in an infinite plate, the beta factor is:

$$\beta_P = \sqrt{\frac{2b}{\pi a} \tan\frac{\pi a}{2b}}$$

Using the following expansion on the tan(x) , taking the limit of a/b $\rightarrow$1 and representing the second and higher terms of the series as the constant C_1:

$$\tan x = 8x\left[\frac{1}{\pi^2 - 4x^2} + \frac{1}{9\pi^2 - 4x^2} + \frac{1}{25\pi^2 - 4x^2} + \frac{1}{49\pi^2 - 4x^2} + \ldots\right] = 8x\left[\frac{1}{\pi^2 - 4x^2} + C_1\right]$$

$$\lim_{a/b \to 1} \tan\frac{\pi a}{2b} = \frac{8\pi a}{2b}\left[\frac{1}{\pi^2 - 4(\frac{\pi a}{2b})^2} + C_1\right] = \frac{4a}{\pi b}\left[\frac{1}{1 - \frac{a^2}{b^2}} + C_2\right]$$

$\therefore$

$$\beta_P = \sqrt{\frac{2b}{\pi a}\frac{4a}{\pi b}\left[\frac{1}{1 - \frac{a^2}{b^2}} + C_2\right]} = \frac{2}{\pi}\sqrt{\frac{2}{(1 - \frac{a}{b})(1 + \frac{a}{b})} + C_3}$$

Comparing the beta factors for both solutions as a/b $\to$1 and noting that the constant term is multiplied by zero:

$$\lim_{a \to b} \frac{\beta_P}{\beta_{fw}} = \lim_{a \to b} \frac{2}{\pi}\sqrt{\frac{2}{(1 - \frac{a}{b})(1 + \frac{a}{b})}}\frac{\sqrt{\pi^2 - 4}}{2}\sqrt{1 - \frac{a}{b}} + C_4\frac{\sqrt{\pi^2 - 4}}{2}\sqrt{1 - \frac{a}{b}}$$

$$\lim_{a \to b} \frac{\beta_P}{\beta_{fw}} = \lim_{a \to b} \frac{2}{\pi}\sqrt{\frac{2}{(1 + 1)}}\frac{\sqrt{\pi^2 - 4}}{2} = \frac{\sqrt{\pi^2 - 4}}{\pi} = 0.771$$

Based on this comparison, it is conservative to approximate the beta factor of a periodic array of cracks in an infinite plate with that of a finite width plate of the same dimension. Note that this comparison is at the limit as a/b $\to$1. This ratio increases to 1.0 as a/b $\to$0.

Therefore, the crack growth model for the main cargo door surround doubler attachment to the fuselage skin at stringer 2R employs the NASGRO3.0 corner crack from a hole centered in a plate, CC02, with the correction factors for both the influence of cracks growing from opposite sides of a hole , “Bowie”, and the influence of a periodic array of cracks approaching one another, “Periodic”.

These correction factors are used along with the NASGRO3.0 standard crack growth model CC02. The following dimensional values are used for the CC02 crack growth model.

$t = 0.036$ *in.*

$W_{typ} = 5.0$ *in.*

$D = 0.188$ *in.*

$B_{typ} = 2.50$ *in.*

$Pitch_{typ} = 0.94$ *in.*

$a_C = 0.005$ *in.*, multi-site damage crack

$$\beta_P = \sqrt{\frac{W}{\pi a}\tan\frac{\pi a}{W}} = \sqrt{\frac{p}{\pi(D/2+L1)}\tan\frac{\pi(D/2+L1)}{p}}$$

for,

$p = 0.94$ *in.*

$D = 0.19$ *in.*

$a_A = a_B = L1 = L2 = 0.005$ *in.*

.

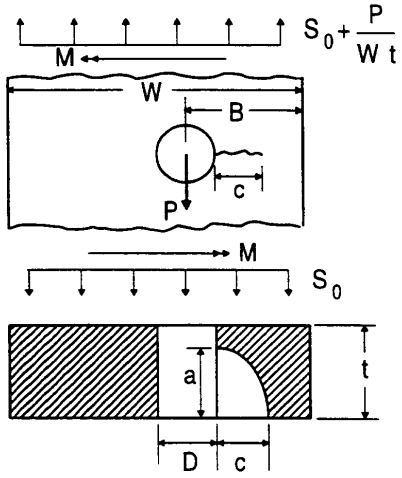

Figure SIE-1.7. NASGRO3.0 Crack Model, CC02.

Two identical NASGRO files are created for the multiple site damage cracks and submitted to the Excel interaction spreadsheet. The spreadsheet accesses NASGRO and grows both cracks for 100 flights. The β correction factors are calculated for the crack lengths at that time and the resulting increased stress scaling factors are plugged back into the NASGRO files. The interaction spreadsheet grows the two cracks until there is a 10% change in crack length (this could also be done in increments of flights), recalculates the β correction and stress scaling factors, and continues to grow the cracks until they become critical or the edge of the plate is reached, whichever occurs first.

Inspection Capabilities and Crack Limits

The holes in the fuselage skin at the attachment of the first row of the surround doubler attachment at 2R (and 26L) are directly accessible from the inside. Therefore, these areas are inspected by HFEC surface probe. With a HFEC inspection, the minimum detectable crack size in the field is assumed to be a 0.0625 inch crack past the fastener head.

Structural Loading and Stress History Description

The stress spectrum is considered to have a remote stress due to cabin pressurization. Cabin pressurization primarily causes hoop tension in the fuselage. The GAG pressurization load is based on FAR25.571. The pressure condition is comprised of a 7.8 psi normal operating differential pressure and an additional 0.5 psi external aerodynamic

pressure. A factor of 1.1 is only applied to the normal operating pressure for residual strength.

$$P = 7.8 + 0.5 = 8.3 \ psi$$

$R = 74$ *in.* (radius of fuselage)

$$S_r = \frac{PR}{t_{skin}} = \frac{8.3(74)}{0.036} = 17.061 \ ksi$$

The bypass and bearing load at the critical fastener row is calculated using a displacement compatibility analysis as described by Swift ("Repairs to Damage Tolerant Aircraft," presented to the International Symposium on Structural Integrity of Aging Airplanes, Atlanta, Georgia, USA, 1990). Layer "a" is the fuselage skin and an existing bonded doubler. Layer "b" is the main cargo door surround doubler. The surround doubler becomes fully effective after the first three rows. This analysis shows the most critical fastener location is the first row of fasteners.

Table SIE-1.1. Fastener Transfer Calculations.

DISPLACEMENT COMPATIBILITY ANALYSIS USING SWIFT'S FASTENER STIFFNESSES

(Note: If there are n fastener rows, there are n+1 segments.
However, stiffnesses of last segment do not affect solution)

INPUT — See bottom for sketch (expand view for clarity)

Copy last two columns for additional fastener rows

SEGMENT	1	2	3	4	5	6	7	8	9	10
FASTENER										
STEEL? 1=yes, 0 = no	0	0	0	0	0	0	0	0	0	
ALUMINUM? 1= yes, 0= no	1	1	1	1	1	1	1	1	1	
D	0.188	0.188	0.188	0.188	0.188	0.188	0.188	0.188	0.188	
ta	0.072	0.072	0.072	0.072	0.072	0.072	0.072	0.072	0.072	
tb	0.1	0.1	0.1	0.1	0.1	0.1	0.1	0.1	0.1	
Esheet	10000000	10000000	10000000	10000000	10000000	10000000	10000000	10000000	10000000	
PLATES										
L	1	1	1	9.5	9.5	9.5	9.5	9.5	9.5	
Aa	0.072	0.072	0.072	0.072	0.072	0.072	0.072	0.072	0.072	
Ea	10000000	10000000	10000000	10000000	10000000	10000000	10000000	10000000	10000000	
Ab	0.1	0.1	0.1	0.1	0.1	0.1	0.1	0.1	0.1	
Eb	10000000	10000000	10000000	10000000	10000000	10000000	10000000	10000000	10000000	
CALCULATIONS										
Ca		1.389E-06	1.389E-06	1.319E-05	1.319E-05	1.319E-05	1.319E-05	1.319E-05	1.319E-05	
Cb	0.000001	0.000001	0.000001	0.0000095	0.0000095	0.0000095	0.0000095	0.0000095	0.0000095	
Cf	4.5707E-06	4.571E-06	4.571E-06	4.571E-06	4.571E-06	4.571E-06	4.571E-06	4.571E-06	4.571E-06	
Cf*Pf		7.322E-07	4.541E-07	6.663E-08	1.001E-08	3.067E-09	1.136E-08	7.605E-08	5.183E-07	
Pa	1	0.6952251	0.5350271	0.4356777	0.4210997	0.4189104	0.4182393	0.4157542	0.3991162	0.285714
Pb	0	0.3047749	0.4649729	0.5643223	0.5789003	0.5810896	0.5817607	0.5842458	0.6008838	0.714286
Pf	0.30477492	0.160198	0.0993494	0.014578	0.0021893	0.0006711	0.0024851	0.016638	0.1134022	
Cumulative load transfer a to b	0.30477492	0.4649729	0.5643223	0.5789003	0.5810896	0.5817607	0.5842458	0.6008838	0.714286	0.714286
% Pf load transfer of segment 1 Pa	30.48%	16.02%	9.93%	1.46%	0.22%	0.07%	0.25%	1.66%	11.34%	0.00%

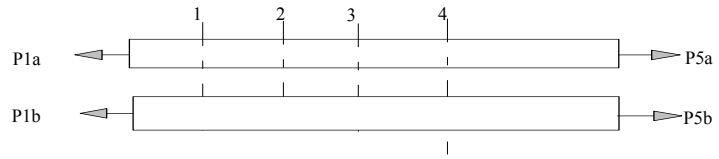

Based on these results, 30% of the load is taken through bearing in the first row of fasteners. This first row of fasteners therefore has 30% as a bearing load and the remaining 70% as a bypass load.

The axial stress and bearing stress acting on this section are:

$$\sigma_{bypass} = S_0 = (1-0.305)S_r = 0.695S_r = 0.695(17.061) = 11.857 \ ksi$$

$$\sigma_{brg} = S_3 = \frac{P}{Dt} = \frac{0.305S_rWt}{Dt} = \frac{0.305S_rW}{D} = \frac{0.305(17.061)0.94}{.188} = 26.018 \ ksi$$

The limit stress used for residual strength purposes in this scenario is calculated as stated earlier according to FAR25.571.

$$P = 1.1*7.8 + 0.5 = 9.1 \ psi$$

$$R = 74 \ in.$$

$$S_r = \frac{PR}{t} = \frac{9.1(74)}{0.036} = 18.706 \ ksi$$

The residual strength axial stress and bearing stress acting on this section are:

$$\sigma_{bypass} = S_0 = (1-0.305)S_r = 0.695S_r = 0.695(18.706) = 13.0 \ ksi$$

$$\sigma_{brg} = S_3 = \frac{P}{Dt} = \frac{0.305S_rWt}{Dt} = \frac{0.305S_rW}{D} = \frac{0.305(18.706)0.94}{.188} = 28.527 \ ksi$$

Material Property Description

The outer skin and doubler are made from 2024-T3 IAW QQ-A-250/5. The material properties from the NASGRO3.0 libraries are used for the fracture toughness and the crack growth rate properties. The material properties used are for 2024-T3; Clad, Plate and Sheet; T-L; LA & HHA NASGRO material code M2EA12AB1.

Table SIE-1.2. Material Properties and Growth Rate Data.

MATL 1: 2024-T3
Clad Plt & Sht; L-T; LA & HHA

Material Properties:

Matl No.	UTS	YS	K1e	K1c	Ak	Bk	Thk	Kc	Keac
1	66.0	53.0	46.0	33.0	1.00	1.00	0.036	66.0	

Matl No.	Crack Growth Eqn Constants C	n	p	q	DKo	Cth+	Cth-	Rcl	Alpha	Smax/SIGo
1	0.829D-08	3.284	0.50	1.00	2.90	1.50	0.10	0.70	1.50	0.30

Solution Technique

This type of problem is conveniently solved using NASGRO3.0 with the crack growth interactions previously discussed. The input files for the equal length cracks growing from opposites sides of a hole are identical for the NASGRO3.0 analysis shown in Table SIE-1.3. The spectrum is included as a constant amplitude GAG cycle with 100 flights per block, with a single block applied per schedule.

Table SIE-1.3. NASGRO Input File for Problem SIE-1.

Data	Description
71fc1-2cout	Output file name
1	1=US units
D	D=direct
71fc1-2 skin at upper and lower doubler edges	Problem name
CC	Crack model type
2	Crack model no.
0.036	Thk, t
5	W
0.188	D
2.5	Hole center to edge
0.33	Poisson's Ratio
U	U=User defined crack
0.005	Initial a
1	Initial a/c
1	Number of materials
N	Non Interaction
1	Matl input choice
w	File input choice
M	Material Category
2	Material type
EA	Material alloy
1	Material heat treat information
Stress on skin at upper/lower edged	Spectrum name
N	Flag for identifying steps
100000	No. times to apply schedule
1	No. distinct blocks
N	Don't display spec blocks
1	Num steps/block
3	Schedule option
1	Load step number
100	Number of cycles
0	FMIN(1) t1 S_0
11.857	FMAX(1) t2 S_0
0	FMIN(2) t1 S_1
0	FMAX(2) t2 S_1
0	FMIN(3) t1 S_3
26.018	FMAX(3) t2 S_3
0	End manual input
1	Scaling Factor S_0
1	Scaling Factor S_1
1	Scaling Factor S_3
Y	Reference stress input
13	REFACT(1,1,1) S_0
2	Ref Stress at t2
0	REFACT(2,1,1) S_1
2	Ref Stress at t2

28.527	REFACT(4,1,1) S_3
2	Ref Stress at t2
N	Do not enter schedule from file
1	Sblock case
1	Number of times to apply
0	End Spectrum input

Results

Critical crack size/Residual Strength

This case is considered to address an MSD case where 0.005 inch cracks are grown from both sides of a fastener hole over an effective width to represent multiple fastener holes with cracks growing from both sides. There is potential for these crack to link prior to failure. The following calculations estimate this potential.

The half distance between the edges of adjacent holes is:

$$e = \frac{H - D}{2} = \frac{0.94 - 0.188}{2} = 0.376 \ in.$$

The plastic zone size of the MSD type cracks is estimated to be:

$$r_p = \frac{1}{2\pi}\left(\frac{K_I}{\sigma_{ys}}\right)^2 = \frac{1}{2\pi}\left(\frac{30}{54}\right)^2 = 0.049 \ in.$$

If fast fracture failure does not occur first, the two MSD type cracks approaching one another will link at a crack length of:

$$c_L = e - r_P = 0.376 - 0.049 = 0.327 \ in.$$

Life:

Based on the calculations for growing the crack in NASGRO and the MSD crack growth interactions, the life from initial crack size to failure is determined to be 52,161 flights. The results of crack length and crack depth versus life are shown in Figure SIE-1.8. The life is given in numbers of flights.

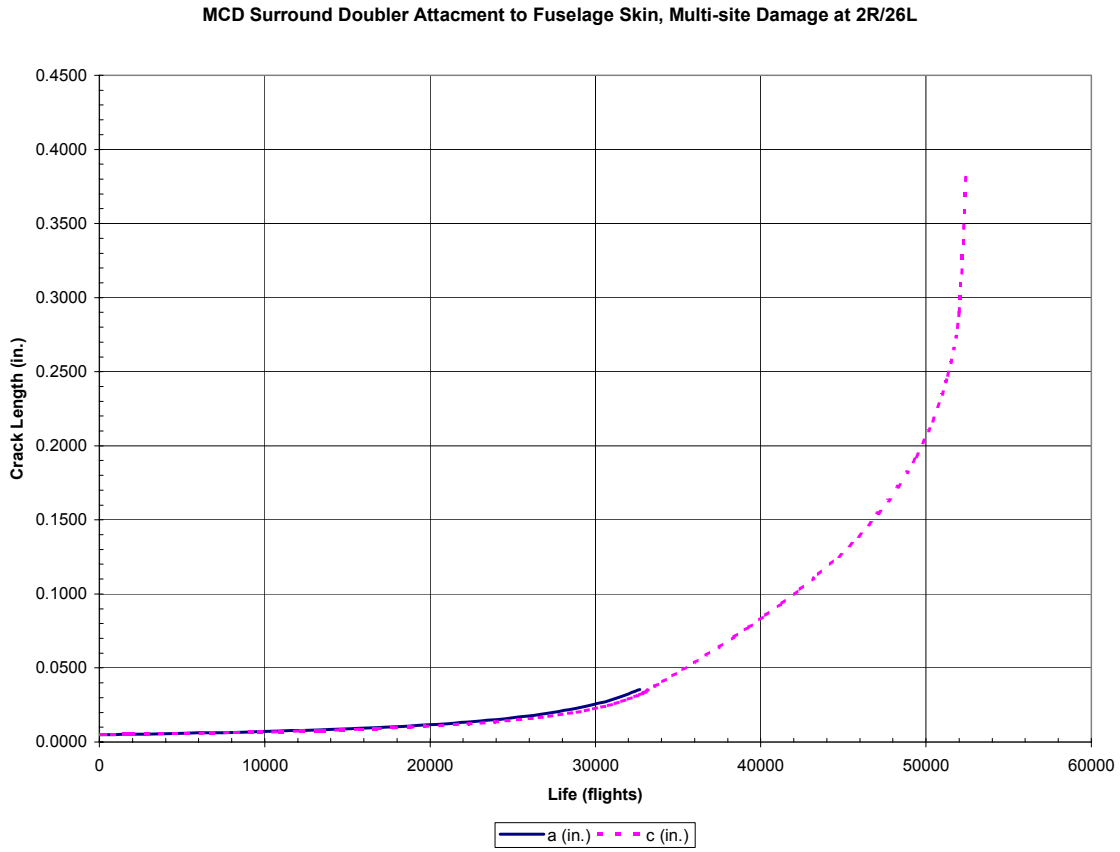

Figure SIE-1.8. Crack Growth Life for Problem SIE-1.

Inspection Intervals

The threshold and repeat intervals are calculated using the life reduction factors shown below.

Life Reduction Factors:
$K_1 = 2.0$
$K_2 = 3.0$, MSD crack scenario

Detectable crack length (HFEC around fastener head):

$$c_{\det} = a_{\det} = \frac{(D_{head} - D)}{2} + 0.0625 = \frac{(0.3016 - 0.188)}{2} + 0.0625 = 0.1193\,in.$$

Number of flights @ detectable crack length, N_{det} = 44,085 flights

Critical crack length: c = 0.327 in.
Number of flights @ critical crack length, N_{crit} = 52,161 flights

$$\text{Threshold Interval} = \frac{N_{crit}}{K_1} = \frac{52161}{2.0} = 26,081 \text{ flights}$$

$$\text{Repeat Interval} = \frac{N_{crit} - N_{\text{det}}}{K_2} = \frac{52161 - 44085}{3.0} = 2,692 \text{ flights}$$

PROBLEM NO. SIE-2

Title: Damage Tolerance Analysis of Wing Main Spars for Residual Strength

Objective:

To illustrate the process of estimating crack growth behavior to set inspection limits.

General Description:

This problem focuses on a damage tolerance assessment of cracks in a main wing spar, emanating from stringer cutout hole #13 in the center web between W.S. 8.5 and W.S. 17.5. The methodology used to analyze these cracks utilized Franc2DL (a layered finite element program) to propagate the crack(s) to obtain 'K vs. a' values and fastener transfer loads, NASGRO to compute the life of the cracked structure and 2024-T3 Crack Growth Resistance curves to verify residual strength at ultimate load.

Topics Covered: Damage tolerance assessment, stress intensity solutions using finite element analysis, crack growth analysis, crack growth resistance curves, residual strength, and inspection intervals

Type of Structure: wing main spar webs

Relevant Sections of Handbook: Section 4, 5, 9, 11

Author: Lesley Camblin

Company Name: Structural Integrity Engineering
9525 Vassar
Chatsworth, CA 91311
818-718-2195
www.sieinc.com

Contact Point: Matthew Creager

Phone: 818-718-2195

e-Mail: mailto:mcreager@sieinc.com

Overview of Problem Description

This problem focuses on the ability of a wing main spar to carry residual strength with the center web cracked at the stringer cutouts. The geometry of the main wing spar in the area between W.S. 8.5 and W.S. 27 is a built-up structure consisting of a center web, upper cap, lower cap, and a pressure plate fore and aft. The center web and pressure plates are connected via steel angles that are fastened to the upper and lower caps and a 'zee', both fore and aft, that is fastened directly to the web and pressure plates at W.S. 17.5. The specific area is shown in Figures SIE-2.1 and SIE-2.2 with the expected crack path marked. Note that Figure SIE-2.2 shows the crack trajectory as calculated by Franc2DL.

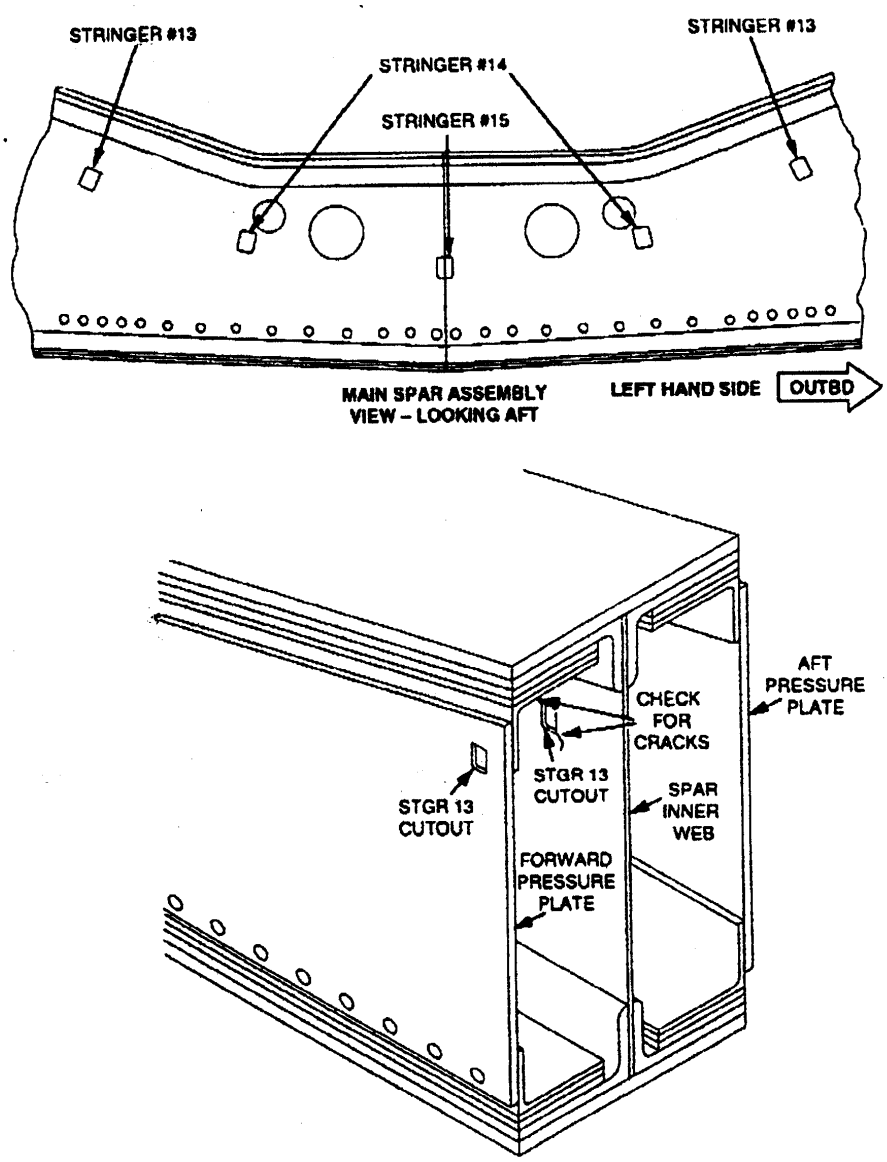

Figure SIE-2.1. Main Spar Assembly

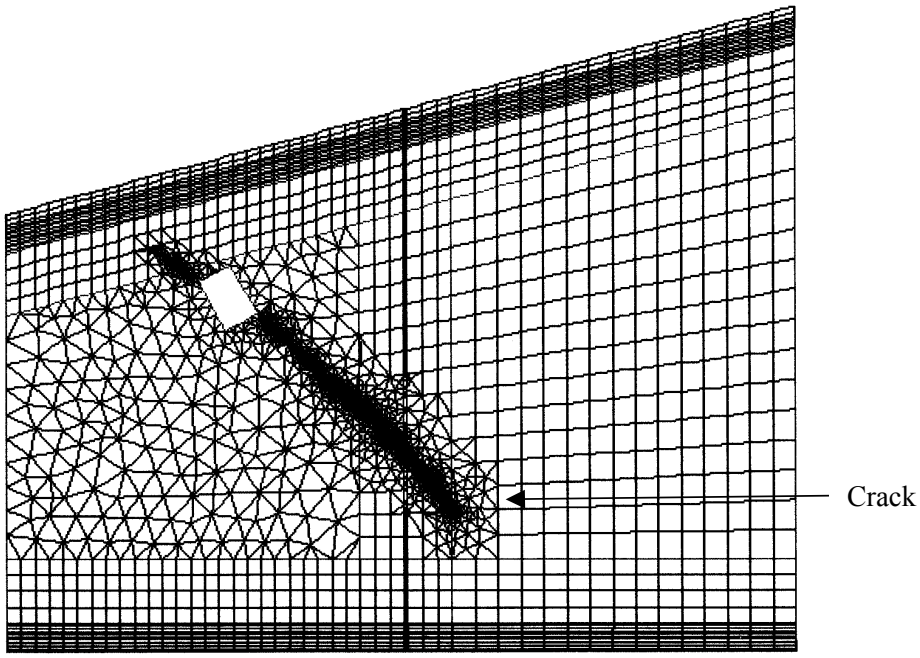

Figure SIE-2.2. Cracked Center Web as Calculated by Franc2DL.

Structural Model

Franc2DL models two-dimensional geometries with multiple layers fastened together. Therefore, the geometry of the Franc2DL finite element model involves the creation of multiple layers, each with equivalents areas as that of the structure being modeled. These layers and geometry are created in a meshing program, 'Casca', which are then incorporated via a conversion program, 'Casca to Franc', into Franc2DL.

Franc2DL limits the user to ten layers so a complex geometry such as this wing spar must be simplified in order to fit within that parameter. The final model has nine layers as shown in Figure SIE-2.3. These layers include a fore and aft pressure plate, a fore and aft, upper and lower steel 'reverse' angle which incorporate the adjacent straps, a center web which incorporate the steel angles along with the upper cap and lower cap and straps and a fore and aft 'Zee'.

The material properties for each element within a layer are defined individually to account for changes in material type and thickness. Layers are fastened together via rivets, which are actually finite element springs for which the user must define the stiffness.

Note that Franc2DL is used to propagate the crack(s) to obtain ‘K’ vs. ‘a’ values and fastener loads. This is input as tabulated data into NASGRO3.0 to compute crack growth life.

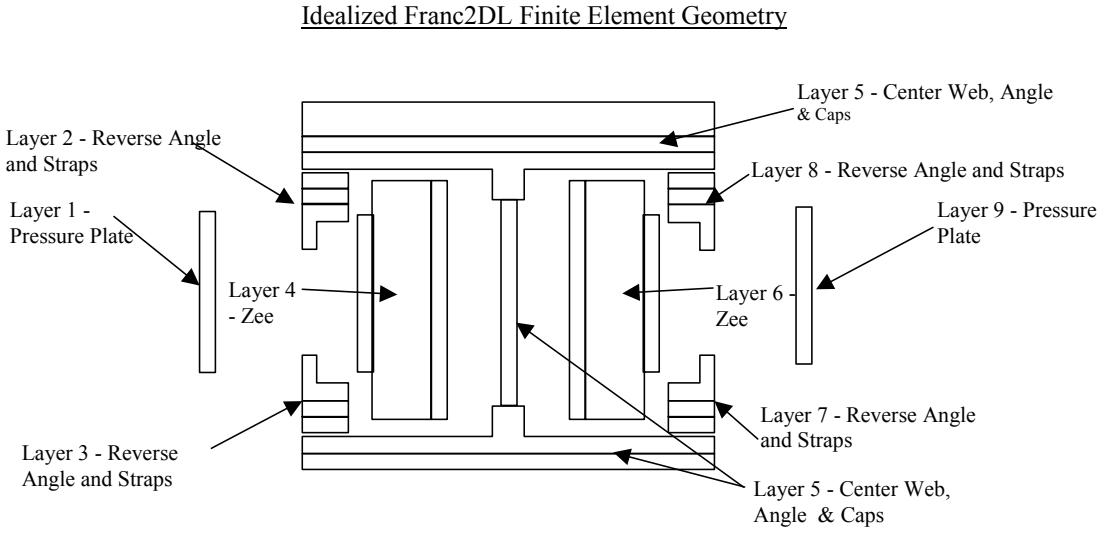

Figure SIE-2.3. Detail Geometry of Critical Location Shown in Figure 2.1.

Model Geometry Description

The crack growth analysis is based on the Fatigue Crack Growth Computer Program NASGRO3.0. This computer program calculates crack growth for a single crack for several standard crack cases. Crack growth rate calculations use the "NASGRO" equation. This is a modified Forman equation to account for stress ratio effects, and upper and lower fatigue crack growth rate asymptotes. The NASGRO3.0 material libraries are used for the material data in the analysis.

Stress intensity factors, K, and corresponding crack lengths are taken from the Franc2DL model and are used for the calculation of crack growth life. The K values from Franc2DL are converted into α values via the equation:

$$K = \beta\theta\sqrt{\pi a}$$

$$\alpha = \beta\theta$$

$$K = \alpha\sqrt{\pi a}$$

$$\alpha = \frac{K}{\sqrt{\pi a}}$$

The α and crack length values are input into NASGRO3.0 using the data tables option for a one-dimensional data table for through cracks, DT01, with a unit stress. Table SIE-2.1 shows the crack lengths, corresponding K values, and calculated α values for the outboard crack.

Table SIE-2.1. NASGRO Input Values for DT01.

a, in.	K, ksi√in.	α
0.05	11.45	28.89
0.1194	20.13	32.87
0.3194	21.48	21.44
0.5194	20.99	16.43
0.7194	22.03	14.65
0.9194	22.23	13.08
1.0194	22.94	12.82
1.2194	23.62	12.07
1.4194	24.47	11.59
1.6194	24.66	10.93
1.8194	25.91	10.84
2.0194	26.52	10.53
2.2194	27.14	10.28
2.5194	28.73	10.21
2.7194	28.26	9.67
3.0194	29.55	9.59
3.2194	29.95	9.42
3.5194	30.92	9.30
3.7194	31.65	9.26
4.0194	32.07	9.02
4.2194	32.77	9.00
4.4194	32.88	8.82
4.6194	33.41	8.77
4.8194	32.94	8.47
5.0194	34.41	8.67

Inspection Capabilities and Crack Limits

The wings will be inspected for cracking using visual techniques. To maintain a generous margin on the residual strength requirement, as well as avoiding the potential for alternate load path concurrent damage, crack lengths of two (2) inches or less were prudently selected to define tolerable limits. At the fastest crack growth rate, the proposed limitation of a 370 hrs/550 flights would allow for further propagation to a length of 2.5 inches. The proposed limitations furthermore require five intervals of repetitive crack monitoring inspections during this interval.

Structural Loading and Stress History Description

Initial loads reflect loads at W.S. 27 and 1.5g's for use in this analysis. The 1.5g loads represent an initial estimate at the simplified equivalent ground-air-ground flight spectrum for every flight. The 1.5g loads were then converted into shear stress using V/A and bending stress using the flexure formula Mc/I. The shear stresses were applied to layers 1,5, and 9 (layers with webs) while the bending stresses were applied to all layers except layer 4 and 6 (Zee's).

All loads were applied at W.S. 27. Subsequent tuning of these loads to bound the fatigue test crack growth rates in the 2-3 inch crack length regime led to factoring them up to 1.5g x 1.05 = 1.575g's or approximately 1.6g values.

An additional factor of 1.433 was applied to account for the apparent increase in the service spectrum severity beyond that of the test. This factor was derived by applying a fourth power law to the maximum difference between the test-to-field crack life. The calculation may be found in the Verification of Life Analysis Section.

The final GAG cycle used was then 1.433 x 1.575g = 2.26g's per flight. Since the K versus a data from the Franc2DL runs were already at 1.5g's, the combined total bump factor of 1.505 (1.505 x 1.5 = 2.26) was implemented via the stress scaling factor in the NASGRO runs.

In order to avoid operation at crack lengths promoting significant load redistribution and therefore possible concurrent damage or overloading of the secondary load paths, fastener transfer loads were monitored throughout the analysis. The change in fastener transfer loads was shown to be minimal, especially in tolerable crack length regime of less than or equal to 3.0 inches.

It is noted that the critical fasteners (lower spar cap tensile field) are somewhat relieved until the long crack lengths are generated. The subordinate fasteners (upper cap compressive field), which do feel the immediate detrimental effect of the cracking, are still well within their shear allowable at ultimate load; and furthermore, they transfer their load into the structure which is in overwhelming compression.

Material Property Description

In Franc2DL, materials can be assigned to each element individually. Material properties that are user defined for the models in this analysis are as follows; Young's modulus, Poisson's Ratio, and thickness. The values used are shown below for the various Young's modulus and Poisson's ratio.

Table SIE-2.2. Material Properties and Growth Rate Data.

Material	Young's Modulus	Poisson's Ratio
2024-T3 Aluminum	10.3E+06	0.35
Steel	29.0E+06	0.30
Titanium	17.4E+06	0.36

The material properties from the NASGRO3.0 libraries are used for the fracture toughness and the crack growth rate properties for the crack growth life determination. The material properties used are for 2024-T3; Clad, Plate and Sheet; T-L; LA & HHA NASGRO material code M2EA12AB1.

Table SIE-2.3. Material Properties and Growth Rate Data.

MATL 1: 2024-T3
Clad Plt & Sht; L-T; LA & HHA

Material Properties:

Matl: No.	UTS	YS	K1e	K1c	Ak	Bk	Thk	Kc	Keac
1	66.0	53.0	46.0	33.0	1.00	1.00	0.050	65.9	

Matl: No.	Crack Growth Eqn Constants C	n	p	q	DKo	Cth+	Cth-	Rcl	Alpha	Smax/SIGo
1	0.829D-08	3.284	0.50	1.00	2.90	1.50	0.10	0.70	1.50	0.30

Solution Technique

This type of problem is conveniently solved using Franc2DL and NASGRO3.0 as previously discussed. The cycles for the crack growth life will be converted into hours with the assumption of 0.67 hours per GAG cycle.

Results

Critical crack size/Residual Strength

The crack lives calculated by NASGRO were found to be 8,539 cycles (5,721 Hours) for the outboard crack. These lives correspond to initial crack lengths of 0.05 inches propagating to 5.03 inches. The maximum applied stress intensity was found to be 51.77 ksi√in. The fracture toughness, K_c for the material was computed to be in the range of 115 ksi√in. This is a typical value for wide panel data. Since the stress corresponding to 2.26g developed these applied stress intensities, the residual strength at ultimate load is verified. To maintain a generous margin on the residual strength requirement, the tolerable crack length regime of less than or equal to 3.0 inches was established.

Residual strength at ultimate load has been shown for the 3.0 inch crack length by superimposing the crack growth resistance ('R') curve for the 2024-T3 web onto the 4.5g ultimate crack curve anchored at the 3.0 inch crack length. It can be seen that the applied K curve is well below the crack growth resistance curve for cracks larger than 3.0 inches. Thus, no crack will run catastrophically and cause failure under the ultimate load.

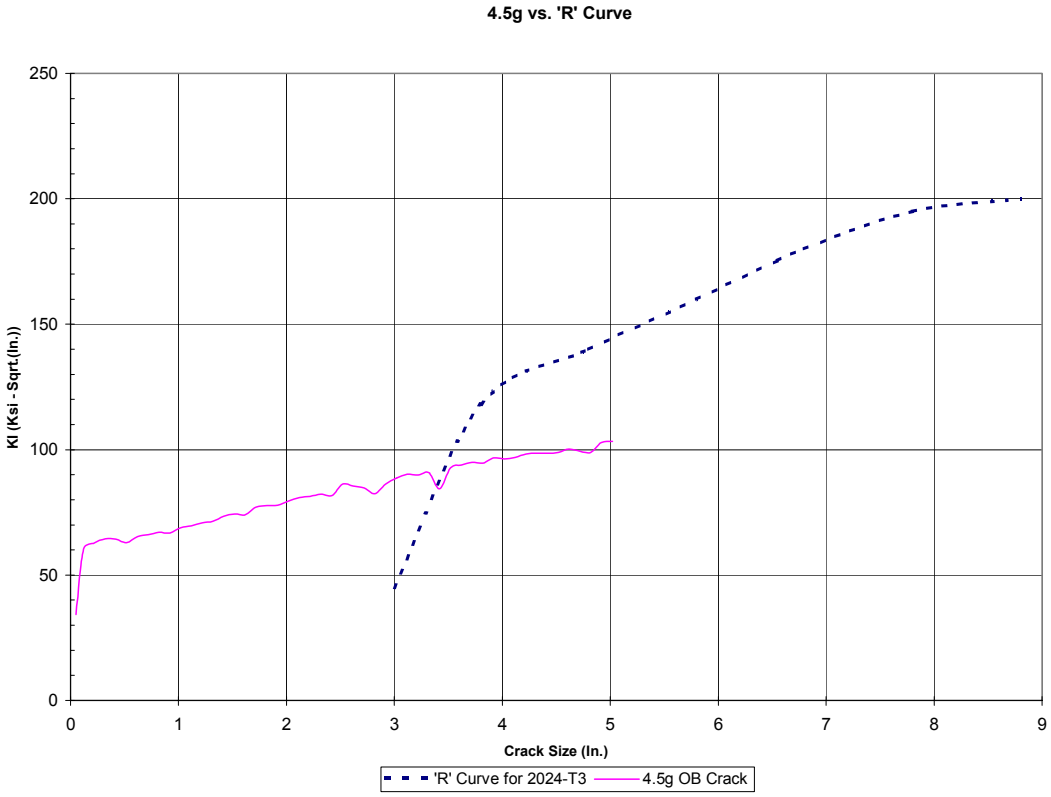

Figure SIE-2.4. Crack Growth vs. Resistance Curve.

Life:

Based on the calculations for growing the crack in NASGRO the life from initial crack size to failure is determined to be 8,539 cycles (5,721 Hours). The results are shown in Figure SIE-2.5. The life is given in numbers of cycles and hours.

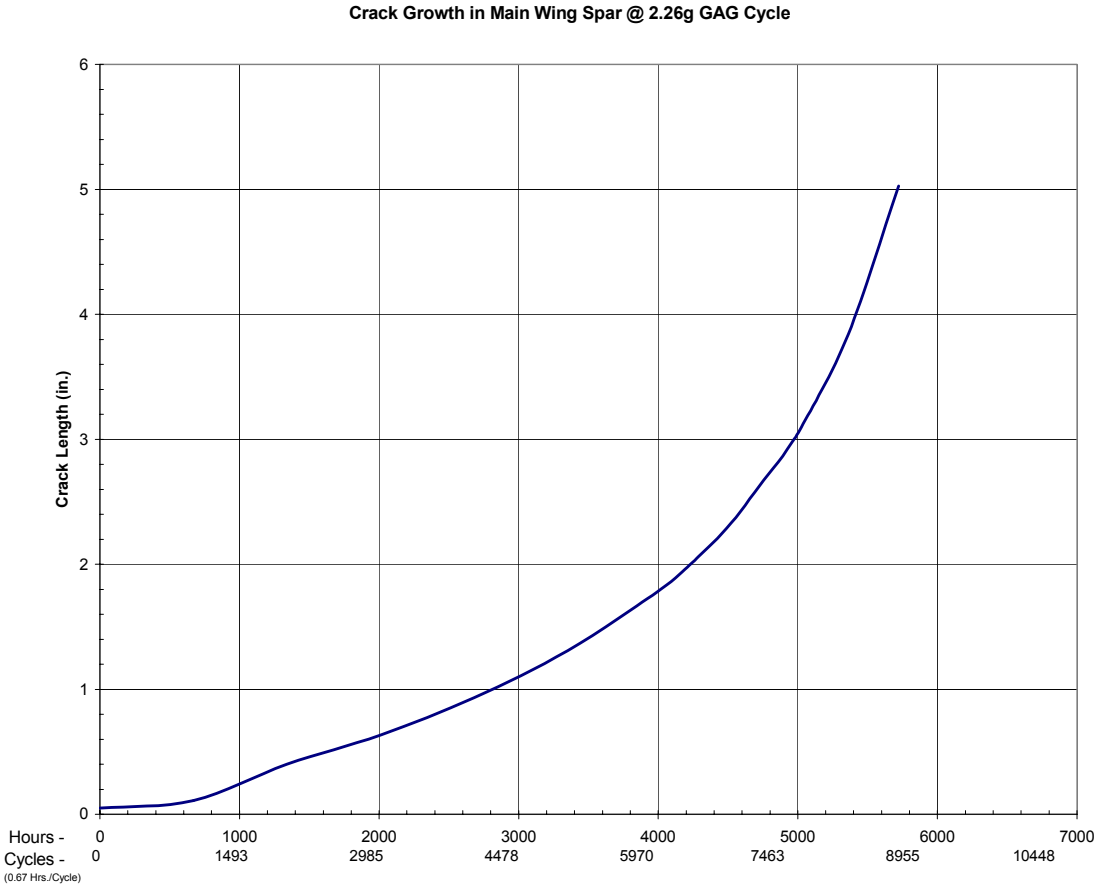

Figure SIE-2.5. Crack Growth Life for Problem SIE-2.

Verification of the Life Analysis

As mentioned previously, the following 4th power law calculation is used to derive a correlation factor between the fatigue test data and the field observations. The worst case (largest numerical correlation factor) is then used to scale the stress intensity factors input into NASGRO.

Table SIE-2.4. Test Data.

SWACO Test to Service Data Correlation Factor Derivation

226 Field Data	hrs	cycles	Field data crack size R IB	SWACO test cycles to field crack size	Test to Service correlation factor	Field data crack size R OB	SWACO test cycles to field crack size	Test to Service correlation factor	Field data crack size L IB	SWACO test cycles to field crack size	Test to Service correlation factor	Field data crack size L OB	SWACO test cycles to field crack size
TC 300	29769	46355	0.75	no data		4.00	130453	1.295	1.00	no data		4.25	74303
TC 358	23165	37219	1.75	63113	1.141	1.5	76184	1.196	2.5	68224	1.164	2.5	47276
TC 280	23577	30976	3.5	78362	1.261	4	130453	1.433	3.5	83749	1.282	4	66409

sample calculation of 4th power law correlation factor derivation:

test cycles/(field once-per-flt-stress/test once-per-flt-stress)^4 = field cycles

or (test cycles/field cycles) = (field once-per-flt-stress/test once-per-flt-stress)^4

or (130453/30976)^.25 = 1.433 for the worst case.

Worst Case : 1.433 (R. Outboard Crack from test and Outboard Crack from TC 280)

Inspection Intervals

A scatter factor of two (2) will be applied to all safe flight limits. The 2.0 inch crack would reach 3.0 inches in 740 hours/ 1100 flights; applying this scatter factor results in flight limits of 370 hours/ 550 flights (whichever occurs first). The repeat inspection intervals are determined according to the established limitation requiring five intervals of repetitive crack monitoring inspections. The repeat inspection intervals are calculated at 75 hours/110 flights, whichever occurs first.

PROBLEM NO. SIE-3

Title: Crack Growth Analysis of Main Cargo Door Surround Doubler Attachment to Fuselage Skin with Primary and Continuing Damage Cracks

Objective:

To illustrate the process of estimating crack growth behavior to set inspection limits.

General Description:

This problem focuses on a damage tolerance assessment of a main cargo door surround doubler attachment to fuselage structure for the purpose of establishing inspection intervals for crack growth with primary and continuing damage cracks growing from opposite sides of a hole. The critical area includes the main cargo door surround doubler and the existing fuselage skin. The stresses acting at the doubler attachment at the upper edge are derived from a conservative loading spectrum based on pressure loading. The critical area was modeled using a standard NASGRO 3.0 stress intensity factor solution and crack growth model.

Topics Covered: Damage tolerance assessment, crack growth analysis, inspection intervals

Type of Structure: fuselage skin, main cargo door surround doubler

Relevant Sections of Handbook: Sections 2, 5, 11

Author: Lesley Camblin

Company Name: Structural Integrity Engineering
9525 Vassar
Chatsworth, CA 91311
818-718-2195
www.sieinc.com

Contact Point: Matthew Creager

Phone: 818-718-2195

e-Mail: mcreager@sieinc.com

Overview of Problem Description

This problem focuses on the main cargo surround doubler attachment to the existing fuselage skin at stringers 2R and 26L. The skin is considered to be a single load path structure under the total hoop stress before the doubler attachment. The critical location is in the skin at the first row of fasteners because the skin sees both bypass and bearing stresses at this row, where as, at the other fastener rows the load is in both the doubler and the skin with each row having lower load transfer.

The fuselage skin was fabricated from 2024-T3 aluminum. The fasteners are 0.188 in diameter, and join the skin and surround doubler.

The specific area is shown in View A of Figure SIE-3.1, with the specific details and the primary and continuing damage cracks shown in Figure SIE-3.3. Note that the skin at this first row of fasteners is a single load path as shown in Figure SIE-3.2.

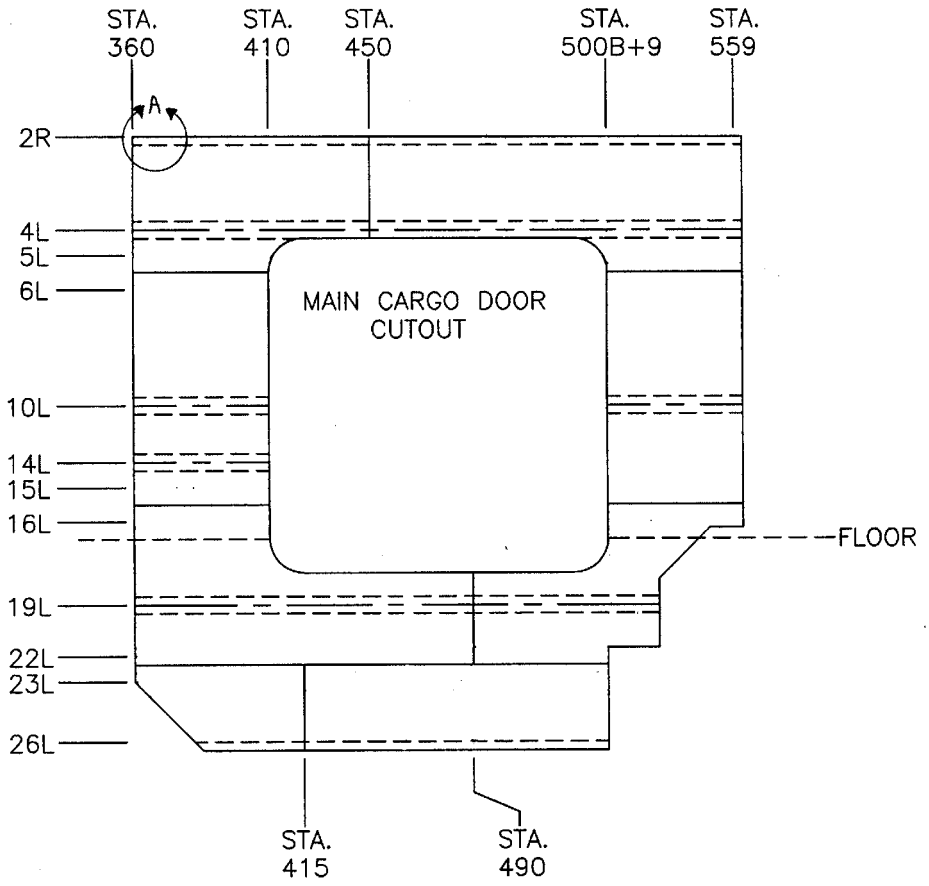

Figure SIE-3.1. Main Cargo Door Doubler Installation

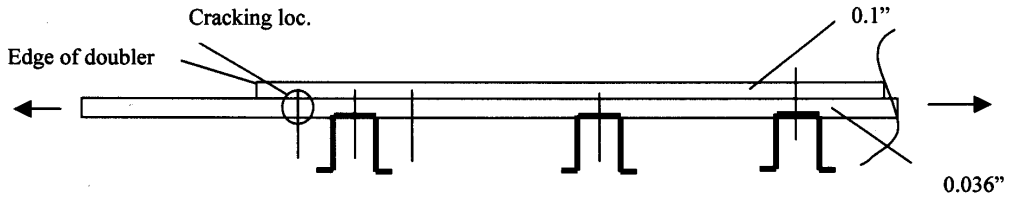

Figure SIE-3.2. Structural Detail for Critical Area

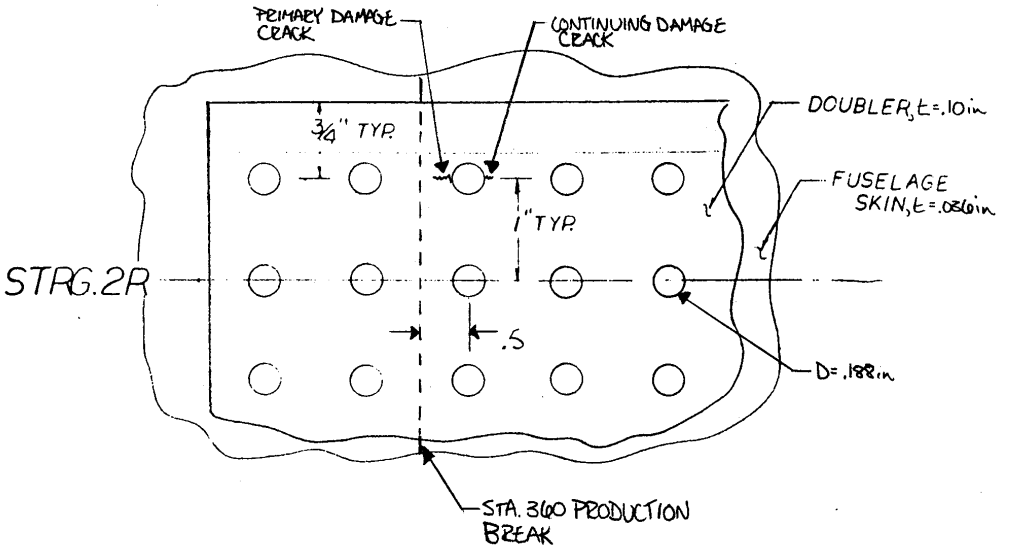

Figure SIE-3.3. Detail Geometry of Critical Location, View A.

Model Geometry Description

The crack growth analysis is based on the Fatigue Crack Growth Computer Program NASGRO3.0. This computer program calculates crack growth for a single crack for several standard crack cases. Crack growth rate calculations use the "NASGRO" equation with elements developed by Forman, Newman, de Koning, and Henriksen (see NASGRO reference manual). This is a modified Paris equation to account for fatigue crack closure, stress ratio effects, and upper and lower fatigue crack growth rate asymptotes for threshold and critical crack growth.

The analysis uses the NASGRO3.0 material libraries for the crack growth rate equation constants. Non-interaction of loads and constants for the Forman crack growth rate equation are used.

Since the standard crack models in NASGRO3.0 are for crack growth of single cracks, no influence of one crack upon another is calculated in NASGRO3.0 for these standard cases. The analysis presented here includes crack interaction effects between the primary damage crack and the continuing damage crack. This is accomplished by iterating though a series of NASGRO3.0 computer runs tracking the growth of both cracks and modifying the stress intensity factors appropriately. The increased stress intensity factors

are based on the crack sizes of the interacting cracks from the previous iteration and correction factors based on the compounding of analytical stress intensity solutions.

This iteration procedure is accomplished in an Excel® Spreadsheet utilizing Visual Basic Programming to submit a NASGRO3.0 computer run for each crack at each iteration. The spreadsheet reads the NASGRO3.0 output files for cycles and current crack lengths. Based on these crack lengths, correction factors are calculated and input into the NASGRO3.0 input file for the next iteration, which is automatically submitted by the spreadsheet.

The correction factors are accounted for by increasing the stress scaling factors input into NASGRO3.0. These increased stress scaling factors can be input based on the following:

$$K = S\beta_{CF}\beta_N\sqrt{\pi a} = S'\beta_N\sqrt{\pi a}$$

where,

$\beta_N =$ Beta for the standard NASGRO crack model

$\beta_{CF} =$ Beta calculated from the correction factor

$S' = S\beta_{CF} =$ increased stress scaling factor input into NASGRO

These correction factors for crack interaction account for interactions between the primary damage crack (rogue flaw) and the continuing damage crack. This is done assuming both cracks are in the same part.

Note that interactions between the rogue flaw and the continuing damage crack have historically not been done in crack growth analysis. This method of including these interactions from the onset of the crack growth of the rogue flaw is conservative since it does not account for any fatigue life due to the nucleation of the continuing damage crack.

As previously discussed, the correction factors for crack interaction are based on comparison of analytical stress intensity solutions. The correction factor for this analysis is termed “INT”, and is used for unequal length cracks growing from opposite sides of a hole.

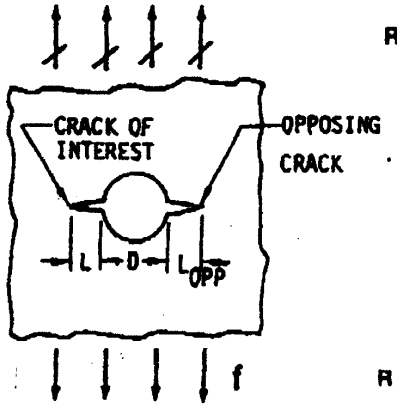

Figure SIE-3.4. INT correction factor

These correction factors are based on through the thickness cracks. They are used for part through cracks when defined with an equivalent crack length. The equivalent crack length is based on equating the area of a part through crack as a quarter ellipse to that of an equivalent through crack as a rectangular area with thickness, t:

$$A_{pc} = A_{eq} = \frac{\pi ac}{4} = a_{eq}t \Rightarrow a_{eq} = \frac{\pi ac}{4t}$$

The "INT" correction factor is derived based on comparing the stress intensity solution of a center cracked panel for two different crack lengths, a_1 and a_2. Including the diameter of the hole, D, in the total crack lengths, yields:

$$a_1 = D + a + a_{opp}$$

$$a_2 = D + a$$

$$INT = \frac{K_1}{K_2} = \frac{\sigma\sqrt{\pi a_1}}{\sigma\sqrt{\pi a_2}} = \sqrt{\frac{a_1}{a_2}} = \sqrt{\frac{D + a + a_{opp}}{D + a}} = \sqrt{1 + \frac{a_{opp}}{D + a}}$$

The crack growth model for the main cargo door surround doubler attachment to the fuselage skin at stringer 2R employs the NASGRO3.0 corner crack from a hole centered in a plate, CC02, with the correction factors for the influence of unequal length cracks growing from opposites sides of a hole. When the initial crack reaches the edge of the plate, the crack growth is continued in the opposite direction as a through crack from the edge of a plate, TC02.

The crack growth model CC02 was used with the following dimensional values.

$t = 0.036$ *in.*

$W_a = 220.0$ *in.*

$D = 0.188$ *in.*

$B_a = 0.5$ *in.*

$a_A = 0.050$ *in.*, primary damage crack

$a_B = 0.005$ *in.*, continuing damage crack

.

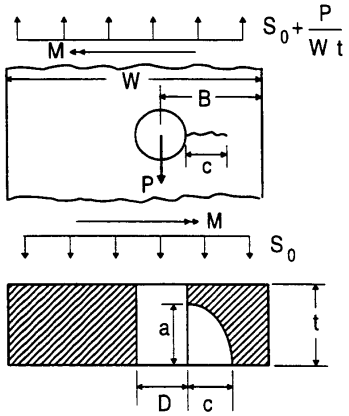

Figure SIE-3.5. NASGRO3.0 Crack Model, CC02.

Two NASGRO files are created for the primary damage crack and the continuing damage crack and submitted to the Excel interaction spreadsheet. The spreadsheet accesses NASGRO and grows both cracks for 100 flights. The β correction factors are calculated for the crack lengths at that time and the resulting increased stress scaling factors are plugged back into the NASGRO files. The interaction spreadsheet grows the two cracks until there is a 10% change in the primary damage crack length (this could also be done in increments of flights), recalculates the β correction and stress scaling factors, and continues to grow the cracks until the primary damage crack reaches the edge of the plate.

Once the primary damage crack reaches the edge and transitions into an edge crack growing in the opposite direction, the crack growth model TC02 was used with the following dimensional values.

$t = 0.036\ in.$

$W = 220.0 in.$

$$c = B_a + \frac{D}{2} + c_B = 0.5 + .094 + 0.1729 = 0.7669\ in.$$

where, c_B = surface length of continuing damage crack when primary damage crack reaches the edge.

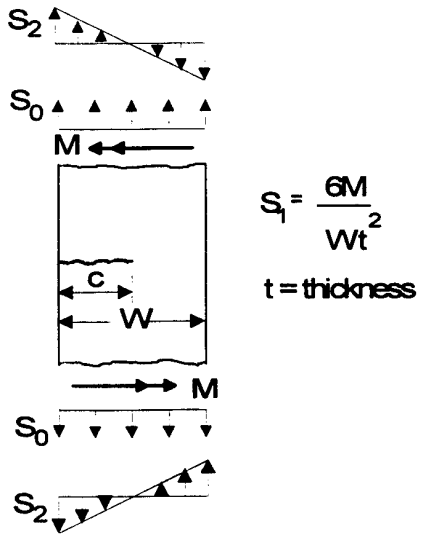

Figure SIE-3.6. NASGRO3.0 Crack Model, TC02

Inspection Capabilities and Crack Limits

The holes in the fuselage skin at the attachment of the first row of the surround doubler attachment at 2R (and 26L) are directly accessible from the inside. Therefore, these areas are inspected by HFEC surface probe. With a HFEC inspection, the minimum detectable crack size in the field is assumed to be a 0.0625 inch crack past the fastener head.

Structural Loading and Stress History Description

The stress spectrum is considered to have a remote stress due to cabin pressurization. Cabin pressurization primarily causes hoop tension in the fuselage. The GAG pressurization load is based on FAR25.571. The pressure condition is comprised of a 7.8 psi normal operating differential pressure and an additional 0.5 psi external aerodynamic pressure. A factor of 1.1 is only applied to the normal operating pressure for residual strength.

$P = 7.8 + 0.5 = 8.3 \ psi$

$R = 74 \ in.$ (radius of fuselage)

$$S_r = \frac{PR}{t_{skin}} = \frac{8.3(74)}{0.036} = 17.061 \ ksi$$

The bypass and bearing load at the critical fastener row is calculated using a displacement compatibility analysis as described by Swift ("Repairs to Damage Tolerant Aircraft," presented to the International Symposium on Structural Integrity of Aging Airplanes, Atlanta, Georgia, USA, 1990). Layer "a" is the fuselage skin and an existing bonded doubler. Layer "b" is the main cargo surround doubler. The surround doubler becomes fully effective after the first three rows. This analysis shows the most critical fastener location is the first row of fasteners.

Table SIE-3.1. Fastener Transfer Calculations.

DISPLACEMENT COMPATIBILITY ANALYSIS USING SWIFT'S FASTENER STIFFNESSES

(Note: If there are n fastener rows, there are n+1 segments.
However, stiffnesses of last segment do not affect solution)

INPUT — See bottom for sketch (expand view for clarity)

Copy last two columns for additional fastener rows

SEGMENT	1	2	3	4	5	6	7	8	9	10
FASTENER										
STEEL? 1=yes, 0 = no	0	0	0	0	0	0	0	0	0	
ALUMINUM? 1= yes, 0= no	1	1	1	1	1	1	1	1	1	
D	0.188	0.188	0.188	0.188	0.188	0.188	0.188	0.188	0.188	
ta	0.072	0.072	0.072	0.072	0.072	0.072	0.072	0.072	0.072	
tb	0.1	0.1	0.1	0.1	0.1	0.1	0.1	0.1	0.1	
Esheet	10000000	10000000	10000000	10000000	10000000	10000000	10000000	10000000	10000000	
PLATES										
L	1	1	1	9.5	9.5	9.5	9.5	9.5	9.5	
Aa	0.072	0.072	0.072	0.072	0.072	0.072	0.072	0.072	0.072	
Ea	10000000	10000000	10000000	10000000	10000000	10000000	10000000	10000000	10000000	
Ab	0.1	0.1	0.1	0.1	0.1	0.1	0.1	0.1	0.1	
Eb	10000000	10000000	10000000	10000000	10000000	10000000	10000000	10000000	10000000	
CALCULATIONS										
Ca		1.389E-06	1.389E-06	1.319E-05	1.319E-05	1.319E-05	1.319E-05	1.319E-05	1.319E-05	
Cb	0.000001	0.000001	0.000001	0.0000095	0.0000095	0.0000095	0.0000095	0.0000095	0.0000095	
Cf	4.57069E-06	4.571E-06	4.571E-06	4.571E-06	4.571E-06	4.571E-06	4.571E-06	4.571E-06	4.571E-06	
Cf*Pf		7.322E-07	4.541E-07	6.663E-08	1.001E-08	3.067E-09	1.136E-08	7.605E-08	5.183E-07	
Pa	1	0.6952251	0.5350271	0.4356777	0.4210997	0.4189104	0.4182393	0.4157542	0.3991162	0.285714
Pb	0	0.3047749	0.4649729	0.5643223	0.5789003	0.5810896	0.5817607	0.5842458	0.6008838	0.714286
Pf	0.304774916	0.160198	0.0993494	0.014578	0.0021893	0.0006711	0.0024851	0.016638	0.1134022	
Cumulative load transfer a to b	0.304774916	0.4649729	0.5643223	0.5789003	0.5810896	0.5817607	0.5842458	0.6008838	0.714286	0.714286
% Pf load transfer of segment 1 Pa	30.48%	16.02%	9.93%	1.46%	0.22%	0.07%	0.25%	1.66%	11.34%	0.00%

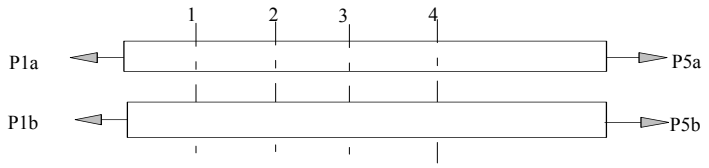

Based on these results, 30% of the load is taken through bearing in the first row of fasteners. This first row of fasteners therefore has 30% as a bearing load and the remaining 70% as a bypass load.

The axial stress and bearing stress acting on this section are:

$$\sigma_{bypass} = S_0 = (1-0.305)S_r = 0.695S_r = 0.695(17.061) = 11.857 \ ksi$$

$$\sigma_{brg} = S_3 = \frac{P}{Dt} = \frac{0.305S_rWt}{Dt} = \frac{0.305S_rW}{D} = \frac{0.305(17.061)0.94}{.188} = 26.018 \ ksi$$

The limit stress used for residual strength purposes in this scenario is calculated, as stated earlier, according to FAR25.571.

$$P = 1.1*7.8 + 0.5 = 9.1 \ psi$$

$$R = 74 \ in.$$

$$S_r = \frac{PR}{t} = \frac{9.1(74)}{0.036} = 18.706 \ ksi$$

The residual strength axial stress and bearing stress acting on this section are:

$$\sigma_{bypass} = S_0 = (1-0.305)S_r = 0.695S_r = 0.695(18.706) = 13.0 \ ksi$$

$$\sigma_{brg} = S_3 = \frac{P}{Dt} = \frac{0.305S_rWt}{Dt} = \frac{0.305S_rW}{D} = \frac{0.305(18.706)0.94}{.188} = 28.527 \ ksi$$

Material Property Description

The outer skin and doubler are made from 2024-T3 IAW QQ-A-250/5. The material properties from the NASGRO3.0 libraries are used for the fracture toughness and the crack growth rate properties. The material properties used are for 2024-T3; Clad, Plate and Sheet; T-L; LA & HHA NASGRO material code M2EA12AB1.

Table SIE-3.2. Material Properties and Growth Rate Data.

```
MATL 1: 2024-T3
        Clad Plt & Sht; L-T; LA & HHA

Material Properties:

:Matl:  UTS :  YS  :  K1e :  K1c :  Ak :  Bk :  Thk  :  Kc  : Keac :
: No.:      :      :      :      :     :     :       :      :      :
:----:------:------:------:------:-----:-----:-------:------:------:
:  1 :  66.0:  53.0:  46.0:  33.0: 1.00: 1.00:  0.036:  66.0:      :

:Matl:--------------- Crack Growth Eqn Constants -------------------:
: No.:    C    :  n  :  p :  q :  DKo : Cth+ :Cth- : Rcl:Alpha:Smax/:
:    :         :     :    :    :      :      :     :    :     :SIGo :
:----:---------:-----:----:----:------:------:-----:----:-----:-----:
:  1 :0.829D-08:3.284:0.50:1.00:  2.90:  1.50: 0.10:0.70: 1.50: 0.30:
```

Solution Technique

This type of problem is conveniently solved using NASGRO3.0 with the crack growth interactions previously discussed. The input files for the equal length cracks growing from opposites sides of a hole are identical for the NASGRO3.0 analysis shown in Table SIE-3.3. The spectrum is included as a constant amplitude GAG cycle with 100 flights per block, with a single block applied per schedule.

Table SIE-3.3. NASGRO Input File for Problem SIE-3.

Data	Description
71fc1-2cout	Output file name
1	1=US units
D	D=direct
71fc1-2 skin at upper and lower doubler edges	Problem name
CC	Crack model type
2	Crack model no.
0.036	Thk, t
220	W
0.188	D
0.5	Hole center to edge
0.33	Poisson's Ratio
U	U=User defined crack

0.05	Initial a
1	Initial a/c
1	Number of materials
N	Non Interaction
1	Matl input choice
w	File input choice
M	Material Category
2	Material type
EA	Material alloy
1	Material heat treat information
Stress on skin at upper/lower edged	Spectrum name
N	Flag for identifying steps
100000	No. times to apply schedule
1	No. distinct blocks
N	Don't display spec blocks
1	Num steps/block
3	Schedule option
1	Load step number
100	Number of cycles
0	FMIN(1) t1 S_0
11.857	FMAX(1) t2 S_0
0	FMIN(2) t1 S_1
0	FMAX(2) t2 S_1
0	FMIN(3) t1 S_3
26.018	FMAX(3) t2 S_3
0	End manual input
1	Scaling Factor S_0
1	Scaling Factor S_1
1	Scaling Factor S_3
Y	Reference stress input
13	REFACT(1,1,1) S_0
2	Ref Stress at t2
0	REFACT(2,1,1) S_1
2	Ref Stress at t2
28.527	REFACT(4,1,1) S_3
2	Ref Stress at t2
N	Do not enter schedule from file
1	Sblock case
1	Number of times to apply
0	End Spectrum input

Results

Critical crack size/Residual Strength

The primary damage crack, crack A, is assumed to grow from a hole to the edge, during which the continuing damage crack, crack B, is growing from the opposite side of the hole towards an adjacent hole. Once crack A reaches the edge it transitions into an edge crack with the crack tip at the tip of crack B.

Life:

Based on the calculations for growing the crack in NASGRO and the crack growth interactions, the life from initial crack size to failure is determined to be 41,412 flights. The results of crack length versus life are shown in Figure SIE-3.7. The life is given in numbers of flights.

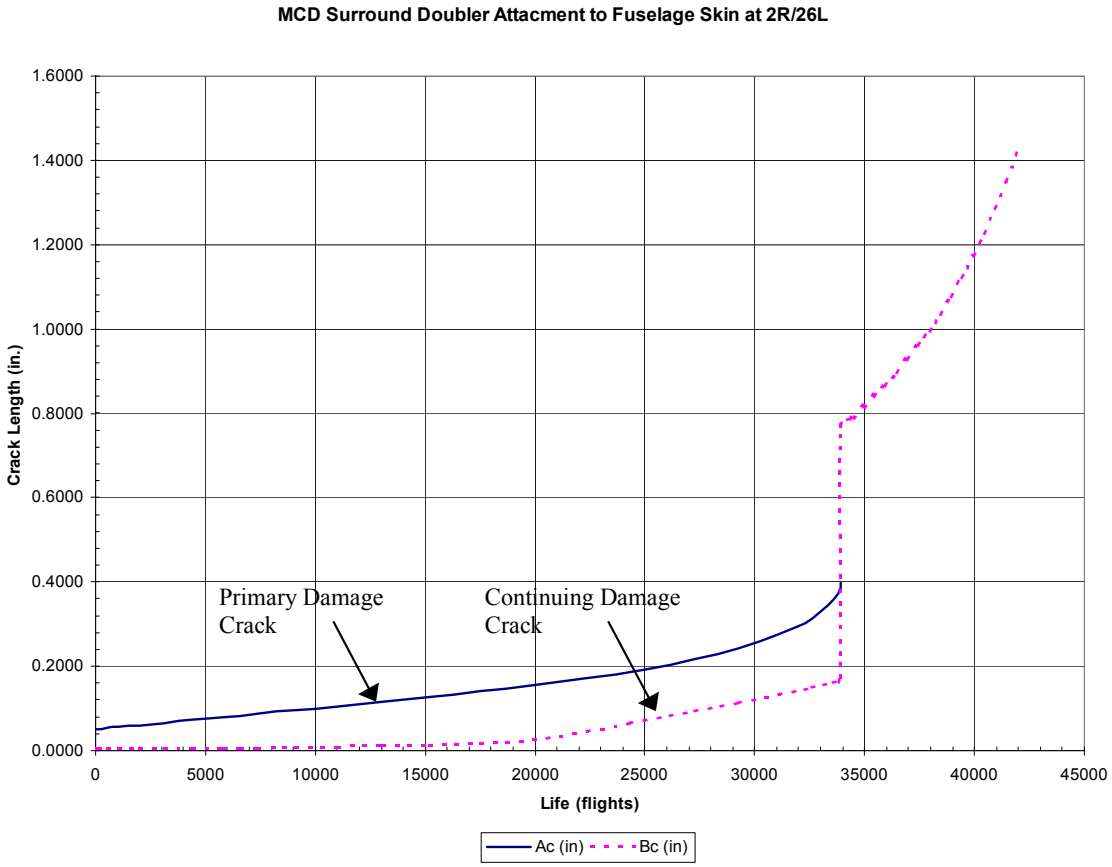

Figure SIE-3.7. Crack Growth Life for Problem SIE-3.

Inspection Intervals

The threshold and repeat intervals are calculated using the life reduction factors shown below.

Life Reduction Factors:
$K_1 = 2.0$
$K_2 = 3.0$

Detectable crack length (HFEC around fastener head):

$$c_{\det} = a_{\det} = \frac{\left(D_{head} - D\right)}{2} + 0.0625 = \frac{\left(0.3016 - 0.188\right)}{2} + 0.0625 = 0.1193\,in.$$

Number of flights @ detectable crack length, $N_{det} = 13{,}758$ flights

Critical crack length (distance to next adjacent hole):

$$c_{crit} = B_a + p - \frac{D}{2} = 0.5 + 0.94 - \frac{0.188}{2} = 1.346\,in.$$

Number of flights @ critical crack length, $N_{crit} = 41{,}412$ flights

$$\text{Threshold Interval} = \frac{N_{crit}}{K_1} = \frac{41412}{2.0} = 20{,}706 \text{ flights}$$

$$\text{Repeat Interval} = \frac{N_{crit} - N_{\det}}{K_2} = \frac{41412 - 13758}{3.0} = 9{,}218 \text{ flights}$$

PROBLEM NO. SIE-4

Title: Damage Tolerance Analysis of Rear Wing Spar Considering the Reinforcing Effect of the Wing Skin

Objective:

To illustrate the process of estimating crack growth behavior in a structure with reinforcement in order to set inspection limits.

General Description:

This problem focuses on a damage tolerance assessment of a rear wing spar. The methodology used to analyze this problem utilized a finite element model with cracked elements to generate stress intensity factors. This approach was used to account for the reinforcing effect of the wing skin. The analysis also utilized an in-house crack growth program to generate the crack growth life.

Topics Covered: Damage tolerance assessment, cracked finite element, crack growth analysis, load spectrum development, inspection intervals

Type of Structure: wing rear spar and skin

Relevant Sections of Handbook: Section 2, 5, 11

Author: Lesley Camblin

Company Name: Structural Integrity Engineering
9525 Vassar
Chatsworth, CA 91311
818-718-2195
www.sieinc.com

Contact Point: Matthew Creager
Phone: 818-718-2195
e-Mail: mcreager@sieinc.com

Overview of Problem Description

This problem focuses on the crack growth life of a rear wing spar accounting for the reinforcing effect of the wing skins. The rear spar is C shaped. The dimensions of the vertical web, top and bottom flanges, as well as the thickness change along the span of the spar are accounted for. The bottom flange is connected to the wing skin with two staggered rows of rivets. It is assumed that a crack will initiate from one of these attachments, since the specified loading spectrum causes this flange to be under the highest tension stress.

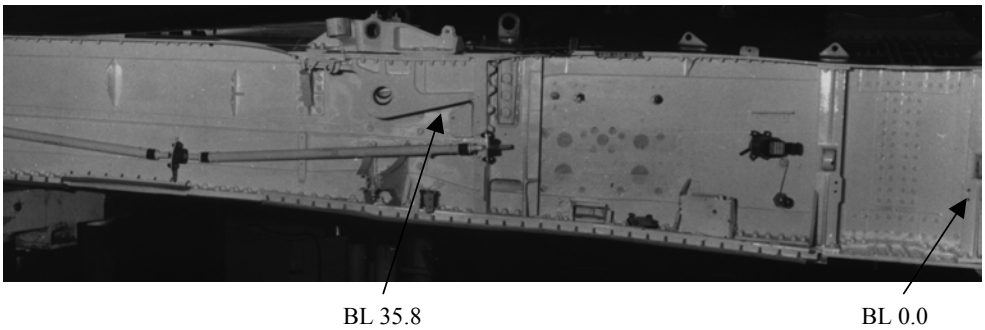

Figure SIE-4.1. Rear Wing Spar

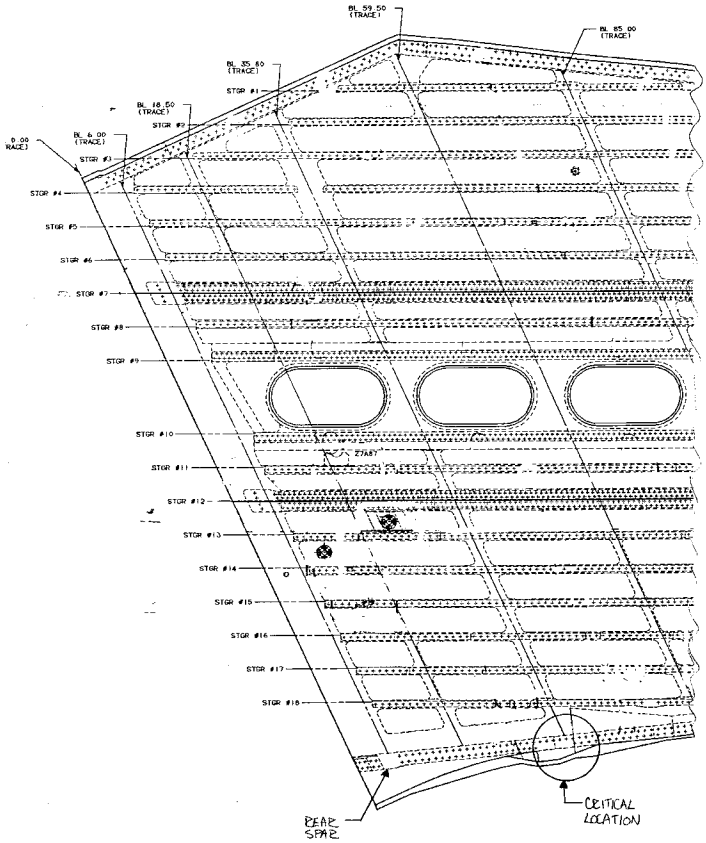

Figure SIE-4.2. Wing Lower Skin at Critical Location on Rear Wing Spar.

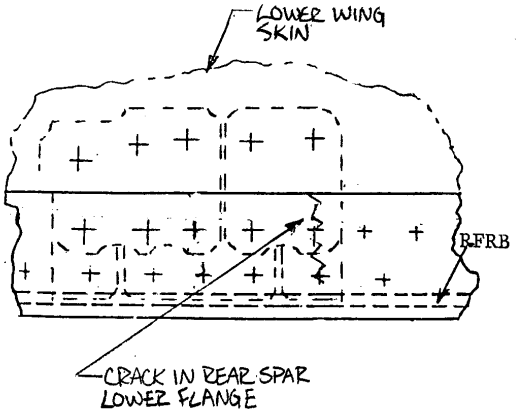

Figure SIE-4.3. View Looking Up at the Cracked Rear Spar.

Structural Model

The wing skins provide reinforcement to the assembly affecting the overall load transfer as the crack propagates. Where the overall load transfer is greatly affected by the crack, an established finite element approach is available. It is important to note that in these crack configuration cases, the crack will always be a through the thickness crack and thus a two dimensional model of the crack tip vicinity is appropriate.

The finite element approach that is used in this example employs a special cracked finite element that contains the crack tip singularity within it. A cracked finite element can be found in MSC/NASTRAN or other similar programs. The stress intensity factor is automatically generated and is uniquely defined. The overall mesh requirements are not demanding; relatively crude meshes give excellent results utilizing this element.

The proper singular behavior of stress and strain distributions from the near field solutions of linear fracture mechanics are embedded into the shape functions of the cracked element. The inter-element compatibility conditions of displacement and tractions are maintained through the use of Langrangian multiplier techniques. Consequently, the stress intensity factors are solved directly as unknowns in the final algebraic system of equations along with the nodal displacements. It has been shown that by using only 20 to 50 degrees of freedom, the stress intensity factor can be computed using the cracked element with accuracy of one percent or better.

Although this example uses a specific cracked element, the intent of this problem is to show how to incorporate these types of elements into a damage tolerance analysis. This is why the derivations of the specific element are not presented here.

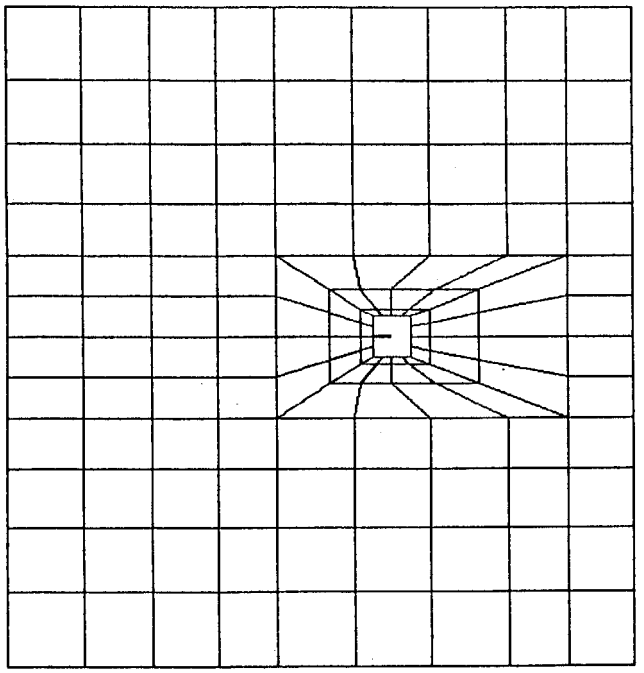

Figure SIE-4.4. Example of a Finite Element Mesh with a Cracked Element.

Model Geometry Description

For an initial crack at the rear spar to skin attachment, the fatigue crack propagation life is divided into two phases. The first phase, Phase 1, consists of a through the thickness crack starting from a rivet hole in the rear spar bottom flange in the row farthest from the web, and growing towards the edge of the flange. This is simulated as a crack emanating from an eccentric hole in a plate, as wide as the lower flange, subject to constant uniform stresses (W = 2.443 in., t = 0.25 in., D = 0.312 in.). In this first phase, the wing skin has negligible effects, and the crack growth analysis is performed using standard stress intensity solutions.

The second phase, Phase 2, occurs after the crack in Phase 1 reaches the edge of the flange. In this second phase, the crack becomes an edge crack growing towards the web of the spar. Phase 2 is analyzed as an edge crack in a semi-infinite plate subject to uniform stresses that change with crack length. This change in stress with crack length is due to the reinforcing effect of the wing skins.

This phase of crack growth in the rear spar was studied using the aforementioned finite element analysis with a cracked element to determine the stress intensity factor versus crack length.

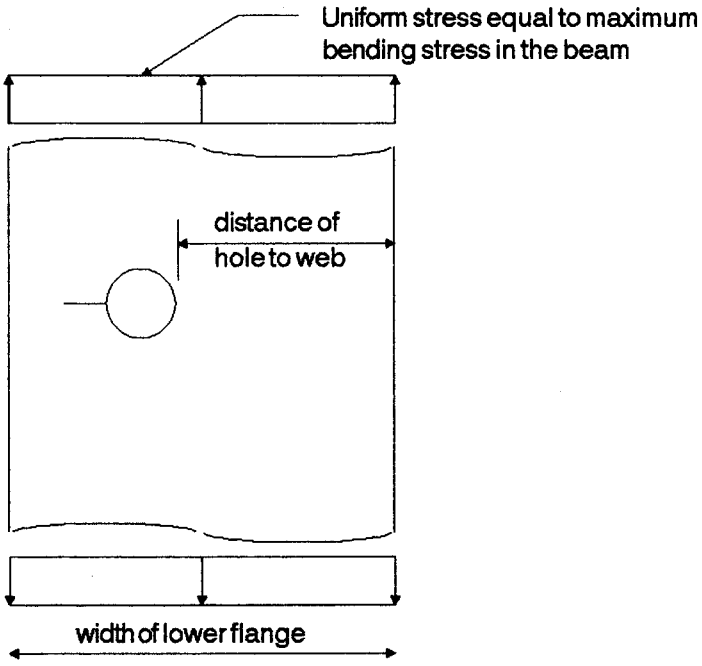

Figure SIE-4.5. Initial, Phase 1, Crack Growth Model.

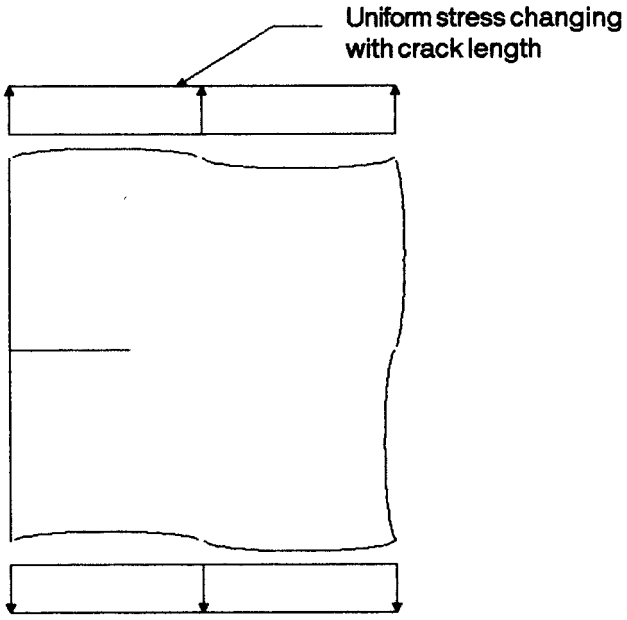

Figure SIE-4.6. Phase 2 Crack Growth Model.

In Phase 2, ten different finite element models representing the rear spar at BL35.8, each with a different crack length, were generated. The following figures show respectively the mesh for the case where the crack is partially along the flange and where the flange is fully cracked with the crack tip on the beam web.

These models utilize symmetry through the crack place and model the structure on one side of the crack with the appropriate boundary conditions along the crack plane.

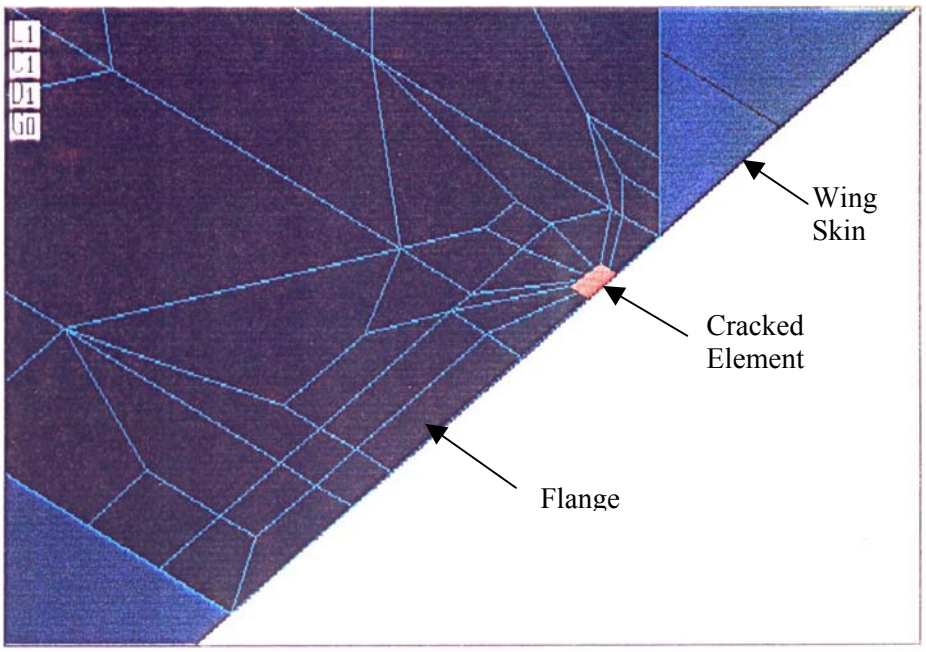

Figure SIE-4.7. Partially Cracked Flange.

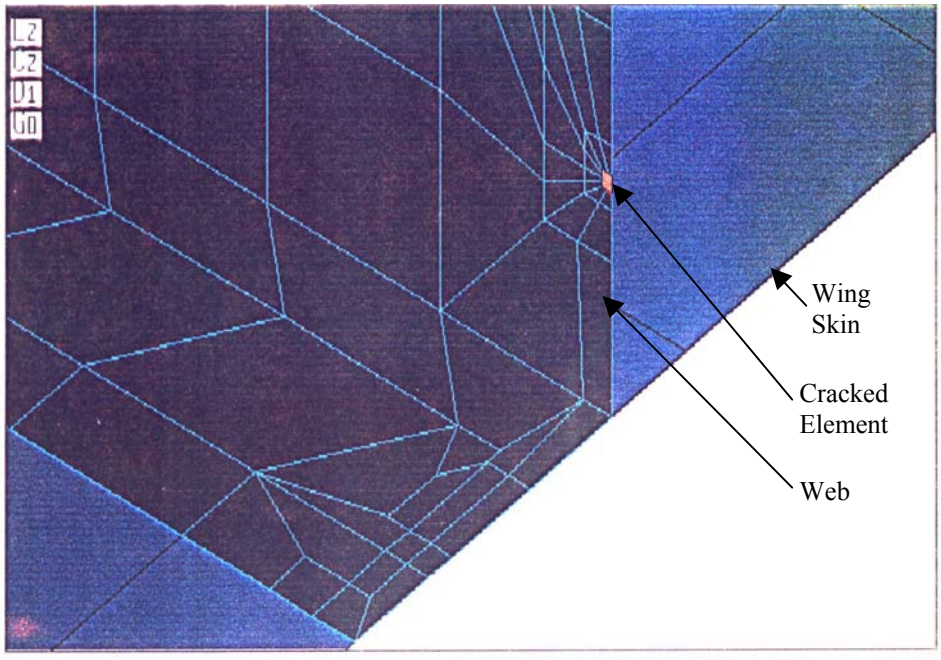

Figure SIE-4.8. Fully Cracked Flange.

The upper and lower skins were modeled as intact. It is appropriate to model these skins as intact as long as fatigue cracks will not be generated in the skins as the crack grows in the rear spar. The effect of the crack-stopper attached to the web was conservatively ignored. The applied load for the stress intensity factor analysis consisted of a unit moment applied at a distance of 24 inches from the crack. Table SIE-4.1 contains the obtained stress intensity factors for various crack lengths.

Table SIE-4.1. Stress Intensity Factors for Skin Intact.

CRACK LENGTH (in.)	STRESS INTENSITY FACTOR (ksi.sqrt(in.))
1.05	4.617E-03
1.25	4.493E-03
1.45	4.053E-03
1.65	3.542E-03
1.85	3.516E-03
2.443	3.654E-03
2.943	4.578E-03
4.443	5.166E-03
6.443	4.813E-03
8.443	4.037E-03

Figures SIE-4.9 and SIE-4.10 show the variation of β and K/σ with length. Note the reduction in K/σ as the crack progresses through the spar flange and then increases after it gets near the spar web.

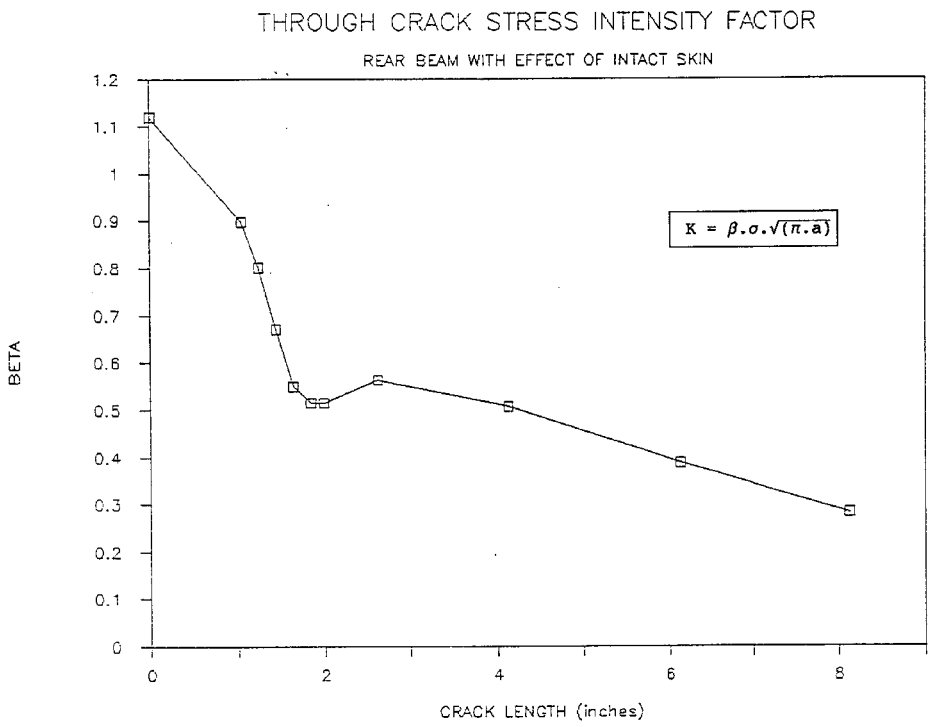

Figure SIE-4.9. Crack Length vs β.

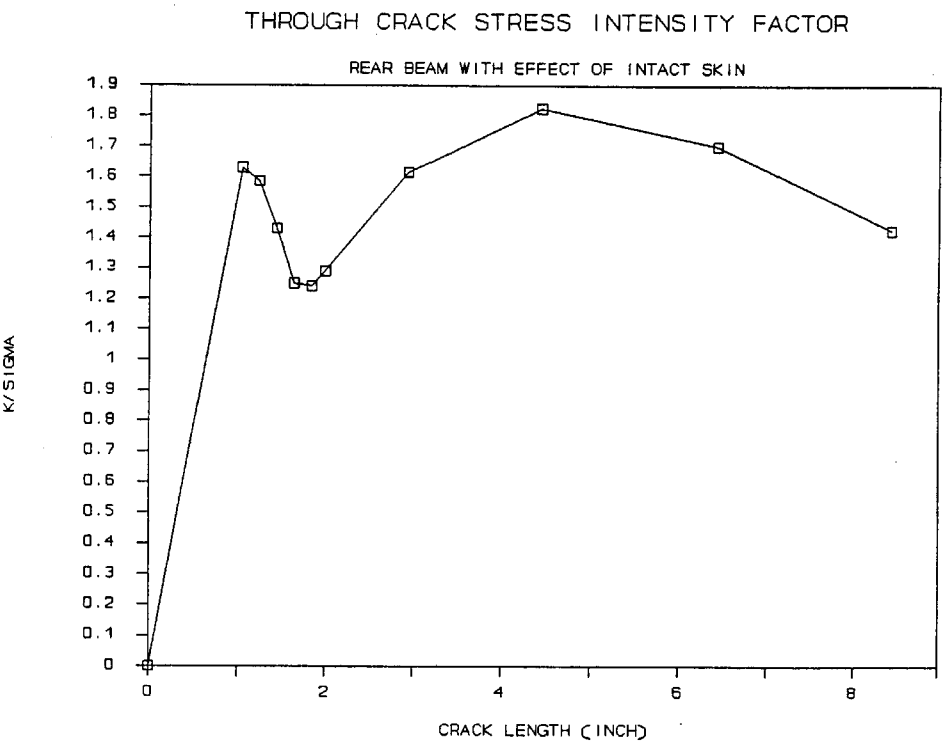

Figure SIE-4.10. Crack Length vs K/σ.

Inspection Capabilities and Crack Limits

The crack growth analysis was driven by the simple criteria that any fatigue damage is required to be discoverable prior to the failure of a critical element that could lead to the loss of the airplane. The goal of this analysis was to show that the rear wing spar and skin would have a crack growth life, with an initial through the thickness crack, greater than the design life of 20,000 hours and that the threshold inspection would be based on past experience and practice.

Structural Loading and Stress History Description

The design lifetime for the aircraft is 20,000 hours. Based on the Airplane flight profile combined with gust maneuver exceedance curves, and the stress profiles on the assembly, a stress spectrum is developed. This spectrum is defined in blocks for the analysis.

The spectrum block that was used for crack growth analysis is 500 hours long and repeated 40 times in a lifetime, so that the frequency of the highest load is 40 per lifetime. This is a conservative clipping level for the high loads, since less frequently applied loads would cause more crack growth retardation.

Based on a truncation study described below, a stress range truncation level of 1.6 ksi was used for the low loads. Due to the large number of cycles occurring in this spectrum block, first the cycles representing 100 flight hours were generated and then the 100 hour block was repeated five times with proper intermediate overloads to form the 500 spectrum block.

A truncation study was conducted for two locations located on the rear spar. Table SIE-4.2 shows the growth lives as a function of the spectrum truncation level.

Table SIE-4.2. Truncation Level.

Location	Truncation Level (ksi)	Life in Hours
1	0.8	28,000
1	0.85	29,000
1	0.9	30,000
1	1.0	34,000
2	0.7	746,000
2	0.8	782,000
2	0.9	953,500

For both locations, the growth lives stabilized at an amplitude stress level truncation value of 0.8 ksi. This corresponds to a stress range truncation value of 1.6 ksi. This truncation level was used for spectrum generation of the critical location.

There are four flight types in the mission mix. The following table shows the airplane life profile. For each flight, the duration and sequence of segments are indicated. The

last column represents the percentages of design life for each segment of a flight. There are twenty different segment types.

Table SIE-4.3. Airplane Flight Profile.

SEGMENT TYPE	DESCRIPTION	TIME (MINUTE)	% TOTAL TIME
SHORT TEST FLIGHT (18% of total flights)			
20	TAKEOFF	1.0	0.14723
1	CLIMB	0.9	0.13251
2	CRUISE	13.0	1.91402
3	DESCENT	2.4	0.35336
19	A & L	5.0	0.73618
SHORT RANGE FLIGHT (21% of total flights)			
20	TAKEOFF	1.0	0.17177
5	CLIMB	1.9	0.32636
6	CLIMB	2.8	0.48096
7	CLIMB	2.4	0.41225
4	CRUISE	18.0	3.09187
16	DESCENT	1.9	0.32636
17	DESCENT	3.6	0.61897
18	DESCENT	4.6	0.79015
19	A & L	5.0	0.85885
MEDIUM RANGE FLIGHT (46% of total flights)			
20	TAKEOFF	1.0	0.36808
5	CLIMB	2.0	0.73616
6	CLIMB	2.8	1.03062
7	CLIMB	3.4	1.25147
8	CLIMB	5.0	1.84040
9	CRUISE	90.0	33.12721
15	DESCENT	3.3	1.21466
16	DESCENT	2.5	0.92020
17	DESCENT	3.5	1.28828
18	DESCENT	4.5	1.65636
19	A & L	5.0	1.84040
LONG RANGE FLIGHT (18% of total flights)			
20	TAKEOFF	1.0	0.13087
10	CLIMB	2.5	0.32718
11	CLIMB	3.7	0.48423
12	CLIMB	4.5	0.58893
13	CLIMB	8.0	1.04698
14	CRUISE	300.0	39.26186
15	DESCENT	3.4	0.44497
16	DESCENT	2.6	0.34027
17	DESCENT	3.6	0.47114
18	DESCENT	4.7	0.61510
19	A & L	5.0	0.65436

Detailed exceedance curves for the take-off segment were not generated because it was simpler to use a slightly conservative ground load for all flights. Therefore, a total of 19 gust stress exceedance curves, 19 maneuver exceedance curves, and 19 1G stresses were supplied for the critical location.

The steps in generation of the 100 hour spectrum block are described below. In steps a and b, peak and valley stresses are generated without consideration of their sequence in the spectrum block. Step h describes the inclusion of fuselage pressure.

a. For each segment type (i.e. climb, cruise, descent, and approach and landing) the total number of excursions of positive and negative gusts and maneuvers in a spectrum block of 100 hours is determined. The total number of excursions is the product of the exceedances per flight hour at the stress truncation level and the number of blocks.

b. There are separate exceedance curves for maneuver peaks and valleys. Gust peaks and valleys are related in that their exceedances have the same absolute values but opposite signs. For each segment type, all gust peaks and maneuver peaks and valleys are picked from respective exceedance curves on a random basis and without replacement. The total number of excursions to be picked for each exceedance curve was generated in step a. Three files of stress values are generated for each of the nineteen segments.

c. The number of flights of each type (there are a total of four types) in the spectrum block is determined using their percentages of occurrence; their sequence is determined on a random basis.

d. For each segment of a flight, the numbers of cycles of gusts and maneuvers are determined from the duration of the segment within a flight (as compared to the total time in that segment in the design life).

e. For each segment of a flight, gust peaks are picked from the information generated in step b and in the order appearing there. The cycles for gust are formed by coupling each peak with its opposite value as a valley. The segment 1G stress is then added to the peaks and valleys. The stress cycles within the same segment for two flights of the same type are in general different.

f. For each segment of a flight, maneuver peaks and valleys are picked separately from the respective information generated in step b and in the order appearing there. The segment 1G stress is then added to the peaks and valleys. The gust cycles for a segment are placed before those of maneuver.

g. A ground stress (compression for the lower wing) is placed between each flight.

h. For reasons of simplicity, the stresses due to fuselage pressure for various flight conditions are taken to be equal to that of the most critical pressure condition (9.0 psi). It is added to all the spectrum peaks and valleys except to the ground stresses. In general, the net effect is to increase the mean stress by this stress value.

i. The highest peak in the block is then identified and the portion of the spectrum above it is moved to the end of the spectrum so that in the re-sequenced spectrum, the highest peak is at the beginning. In addition, the values in the spectrum not defining a peak or valley are eliminated. The re-sequencing is done to enable cycle pairing to be performed using the Rainflow method (this was accomplished with an in-house program). The cycle pairing is important to define the representative stress cycles for the crack growth analysis.

As discussed previously, a conservative clipping level is defined for the highest load. To calculate this, the combined exceedance curve of all 19 segments of gust and maneuver was generated and used to assemble a 500 hour block from the 100 hour block. The clipping level at a frequency of 40 per lifetime corresponds to the highest stress S_{500} occurring in a 500 hour spectrum; S_{500} is determined from the composite exceedance curve.

Composite exceedance curves were obtained by combining the 19 gust exceedance data, maneuver exceedance data, and 1G stress values for the 19 segment types using their associated percentage of occurrence. The composite exceedance curve was used to determine the stress level occurring 40 times in a lifetime. This was then used as the clipping level. The composite exceedance curve for the wing rear spar is shown below.

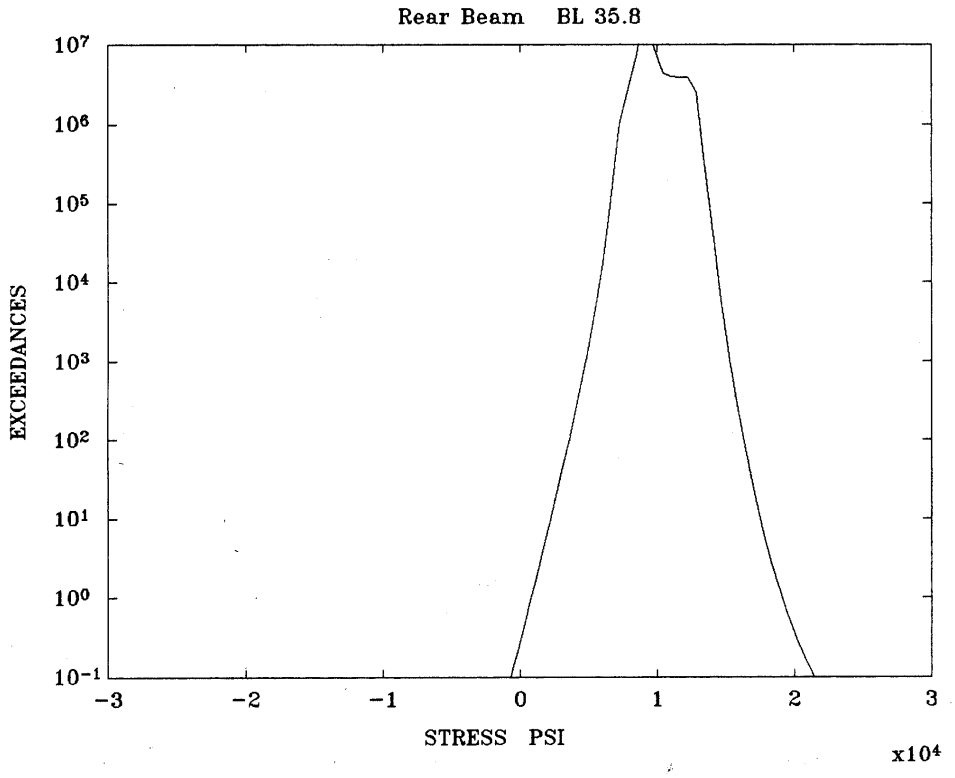

Figure SIE-4.11. Exceedance Curve for Wing Rear Spar.

S_{100} is the highest stress occurring in a 100 hour block; it can be determined either from the composite exceedance curve or from the 100 hour spectrum block. Four overloads, all larger than S_{100}, are used to extend the 100 hour block to a 500 hour block. The largest of these overloads is S_{500}. The other three overloads are determined by picking three equally distant values on logarithmic scale between S_{500} and S_{100}. The 500 hour block is formed by the following sequence:

$$S_1+S_5+S_3+S_5+S_2+S_5+S_4+S_5$$

Where S_1 through S_4 are the four overloads in decreasing order and S_5 is the 100 hour spectrum block.

Material Property Description

The material properties for the rear spar, 7075-T7351LS (long/short transverse), are given below. The in-house crack growth program used the modified Willenborg retardation model and the Chang acceleration option. For the alloys used in the wing, these models have been shown to be a reasonable representation of the crack growth retardation and acceleration that occurs due to the interaction of high and low loads in the loading spectrum. The bislope representation of the crack growth rate versus ΔK was opted for the aluminum alloys. The crack growth program uses a Walker stress ratio effect model.

Table SIE-4.4. Material Properties and Growth Rate Data.

Parameter	$\Delta K<12.1$	$\Delta K>12.1$
C	5.044×10^{-9}	2.584×10^{-7}
n	3.189	1.608
m	0.4	0.4
q	1.0	1.0
da/dn	1.42×10^{-5}	1.42×10^{-5}
K_C	61.5	61.5
K_{IC}	29.4	29.4
F_{ty}	58	58
ΔK_{th}	0.01	0.01

Solution Technique

Although the crack growth analysis for this problem was solved using an in-house computer program, NASGRO3.0 could be also be used. Using standard stress intensity factors for Phase 1 and the stress intensity factor versus crack length chart developed with the cracked finite element for Phase 2, the crack growth analysis for this type of problem is conveniently solved using NASGRO3.0. This would require a separate crack growth run for each phase. Note that for Phase 2, the stress intensity factors versus crack length can be input into NASGRO3.0 as a table. In this example, the cycles for crack growth life will be converted into hours with the assumption of 0.67 hours per ground-air-ground (GAG) cycle.

Results

Life:

Using the relationships for b, the crack growth rate data for 7075-T7351LS, and the appropriate stress spectrum, it was found that the total crack growth duration of parts 1 and 2 up to the crack stopper on the flange is 60,000 hours corresponding to three design lifetimes. Based upon this, the initial inspection should be based upon past experience and practice and is not impacted by the damage tolerance analysis.

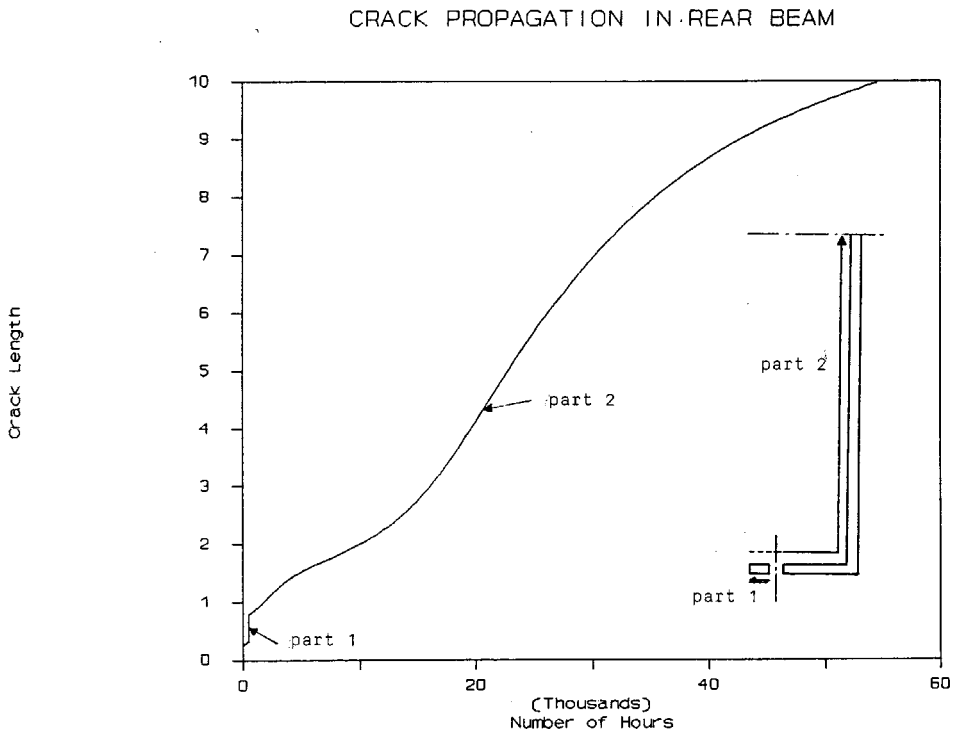

Figure SIE-4.12. Crack Growth Life for Problem SIE-4.

PROBLEM NO. SIE-5

Title: Crack Growth and Residual Strength Analyses of Cracks Under and Beyond a Main Cargo Surround Doubler at a Lap Joint

Objective:

To illustrate the process of estimating crack growth behavior to set inspection limits.

General Description:

This problem focuses on a damage tolerance assessment of skin lap joints underneath a main cargo door surround doubler for the purpose of determining multiple crack link up and establishing inspection intervals for a long crack growing from underneath the doubler. The critical area includes the main cargo door surround doubler and the existing fuselage skin. The stresses acting at the doubler attachments to the lap splices are derived from a conservative loading spectrum based on pressure loading. The critical area was modeled using Franc2DL for the long crack case to propagate the crack to obtain 'K' vs. 'a' values and NASGRO3.0 to compute the life of the cracked structure for both cases.

Topics Covered: Damage tolerance assessment, stress intensity solutions using finite element analysis, crack growth analysis, residual strength calculation, inspection intervals

Type of Structure: fuselage skin

Relevant Sections of Handbook: Section 2, 4, 5, 11

Author: Lesley Camblin

Company Name: Structural Integrity Engineering
9525 Vassar
Chatsworth, CA 91311
818-718-2195
www.sieinc.com

Contact Point: Matthew Creager

Phone: 818-718-2195

e-Mail: mcreager@sieinc.com

Overview of Problem Description

This problem focuses on the fuselage skin lap joints in transport aircraft when a main cargo door surround doubler is present. The doubler covers parts of the lap splices adjacent to the main cargo door cutout. The lap splices that are covered are 4L, 10L, 14L, and 19L. The doublers consist of patches of rectangular sheets butt spliced together. This problem addresses the potential for skin crack initiation at multiple locations and crack growth underneath the doubler.

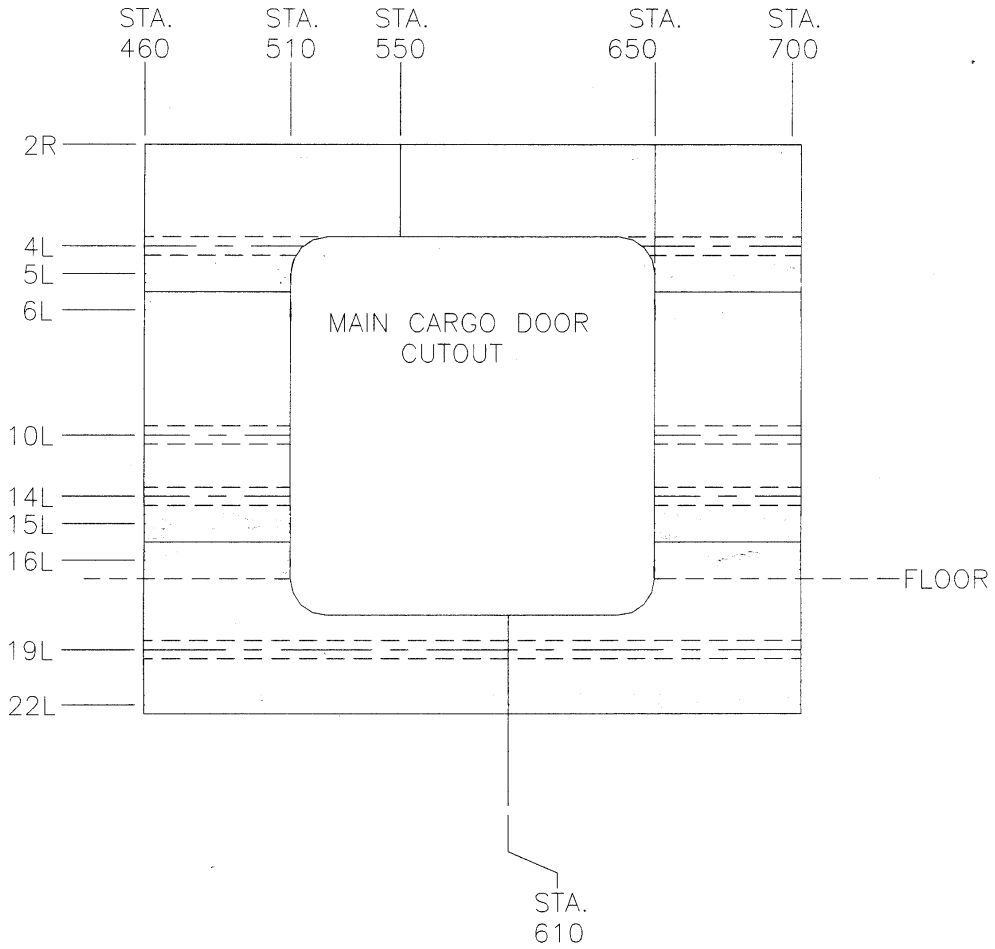

Figure SIE-5.1. Main Cargo Door Doubler Installation

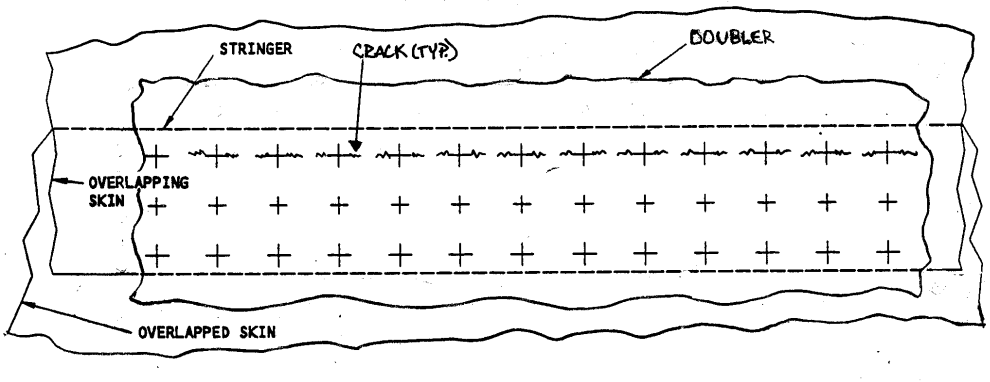

Figure SIE-5.2. Multiple Crack Linking Case.

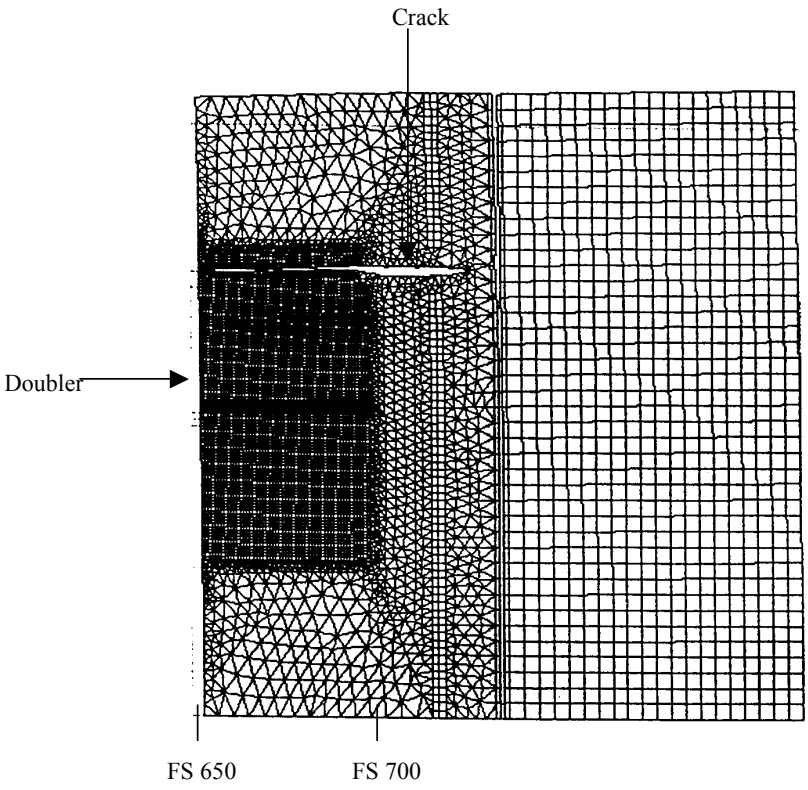

Figure SIE-5.3. Long Crack Case.

Structural Model

Franc2DL models two-dimensional geometries with multiple layers fastened together. Therefore, the geometry of the Franc2DL finite element model involves the creation of multiple layers, each with equivalent areas as that of the structure being modeled. These layers and geometry are created in a meshing program, 'Casca', which are then incorporated via a conversion program, 'Casca to Franc', into Franc2DL.

The basic model is as shown in Figure SIE-5.4. The layers include the 0.04 inch skin, 0.07 inch surround doubler, 0.05 inch tear strap, 0.07 inch doubler splice back up plate, and 0.07 inch skin circumferential splice. The fastener pitch in a row is 1.0 inch. The skin residual strength stress was used in the models.

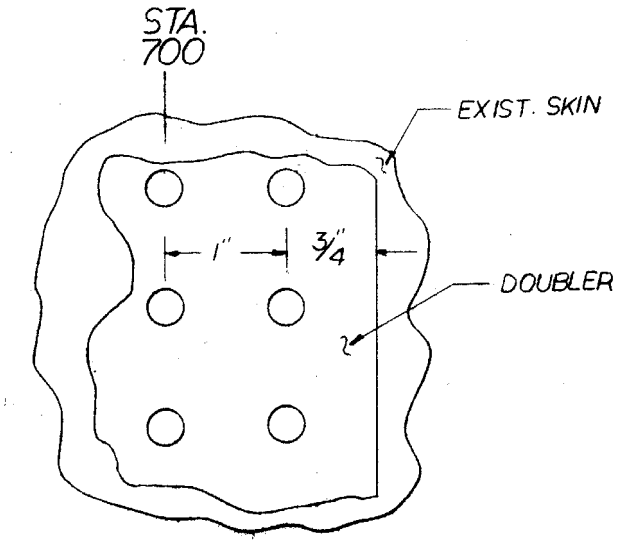

Figure SIE-5.4. Close Up View of Aft Doubler Edge

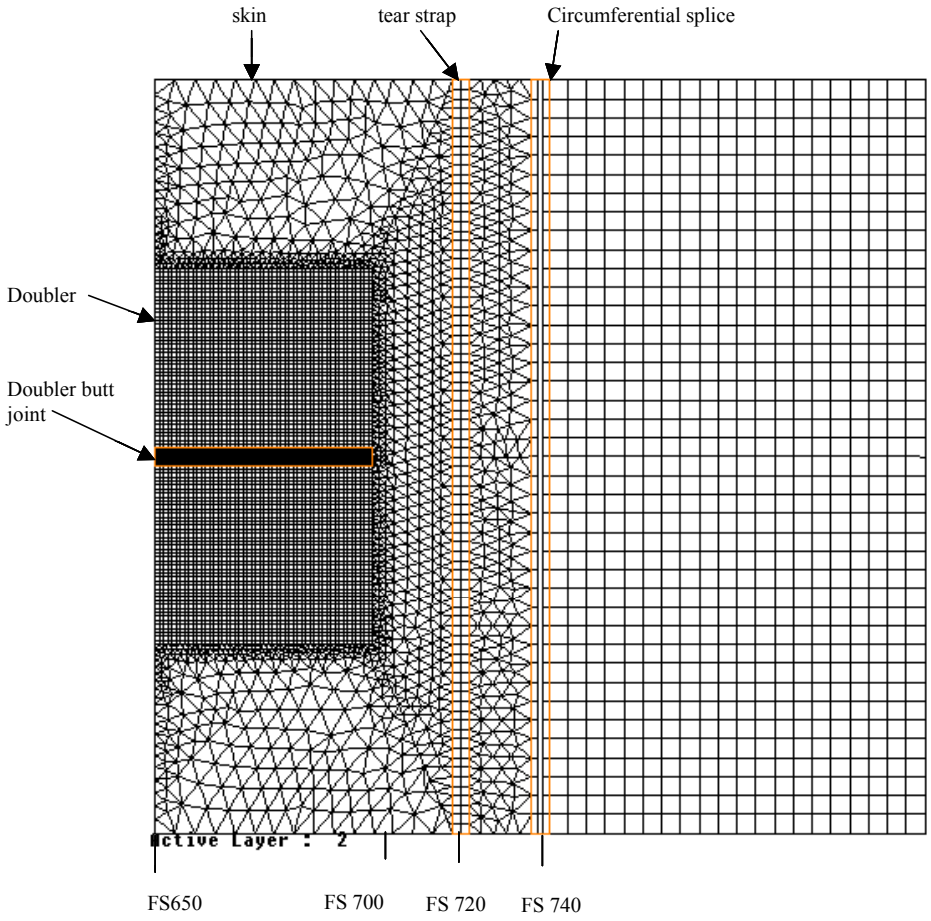

Figure SIE-5.5. Basic Franc2DL Model.

The material properties for each element within a layer are defined individually to account for changes in material type and thickness. Layers are fastened together with rivets, which are treated as finite element springs for which the user must define the stiffness.

If the skin cracks at the upper row of fasteners in a lap joint link underneath the doubler, a long crack completely covered by the doubler could be formed. Since the crack is covered, it is necessary to determine if the doubler can help maintain the residual strength of the skin lap splices. This is done by using a cracked element in Franc2DL as shown below.

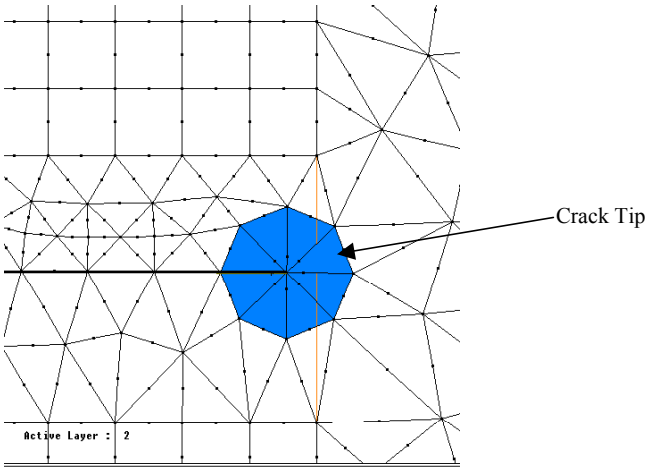

Figure SIE-5.6. Franc2DL Cracked Element.

The most critical location for a long crack is a crack growing from the edge of the door cutout towards the adjacent doubler edge (FS650-FS700). At lap splices 10L and 14L, a crack is located within one row of fasteners from the doubler edge.

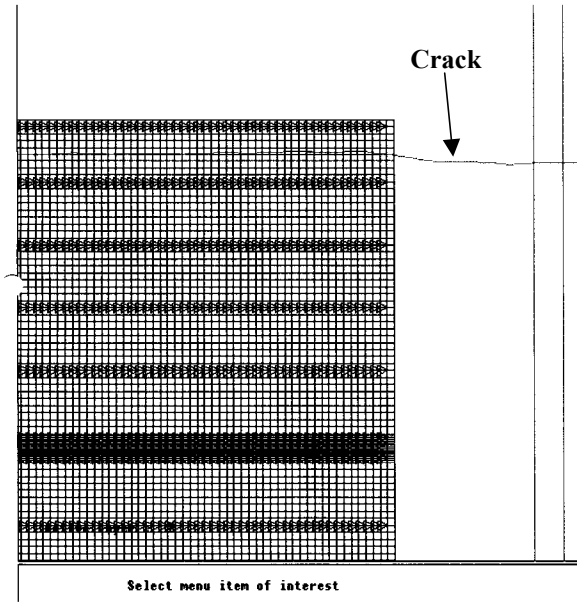

Figure SIE-5.7. Long Crack Model.

Note that Franc2DL is used to propagate the crack(s) to obtain 'K' vs. 'a' values. This is input as tabulated data into NASGRO3.0 to compute crack growth life.

Model Geometry Description

It is conceivable that cracks could have been present at most fastener holes in the top row of the lap splice at the time of the surround doubler installation. Since there were no inspections for cracks at the existing fastener holes prior to installation, it is necessary to establish the maximum crack size that could have been present. The largest multiple cracks that could have been present would have had crack lengths not quite long enough to cause failure under the standard operating loads. An ultimate strength failure criterion will be used for the ligament between two cracks emanating from adjacent holes and approaching each other (the applied K for the resulting crack size will be much smaller than the K_c for 2024-T3 thin sheet). For an applied cyclic stress of 16.8 ksi and a nominal ultimate strength of 66 ksi for 2024-T3, this will create a crack configuration as shown in Figure SIE-5.8 (L_i = (1-16.8/66)/2 = 0.373 in.).

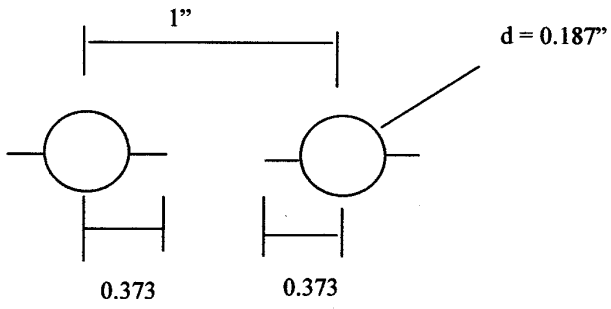

Figure SIE-5.8. Initial MSD Crack Length.

The cyclic stress for fatigue crack propagation after the 0.07 inch doubler installation on the 0.04 inch skin is (0.04/0.11)*16.8 = 6.11 ksi. For a 3/16 inch diameter hole, the initial crack length for crack growth is a_i = 0.373-3/32 = 0.279 inches. Note that this method of establishing the possible crack size of any cracks present is conservative since it assumes that the largest possible crack is present at all holes simultaneously.

The stress intensity factors for the case of cracks at adjacent holes, as shown in Figure SIE-5.9, were derived by combining several existing standard solutions.

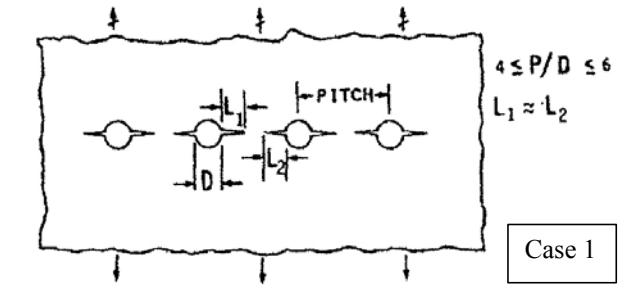

Figure SIE-5.9. Multi-Site Damage Crack Growth.

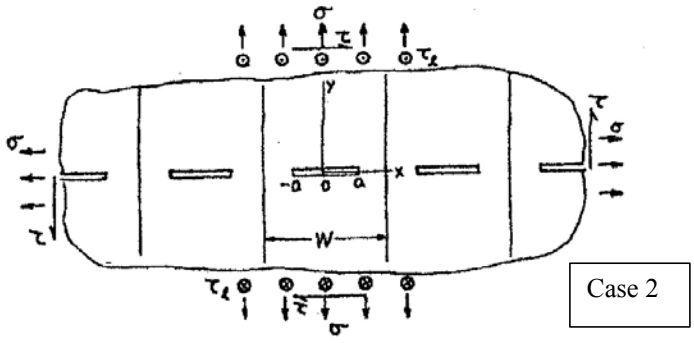

Figure SIE-5.10. Equally Spaced Cracks, Tada Case 7.1.

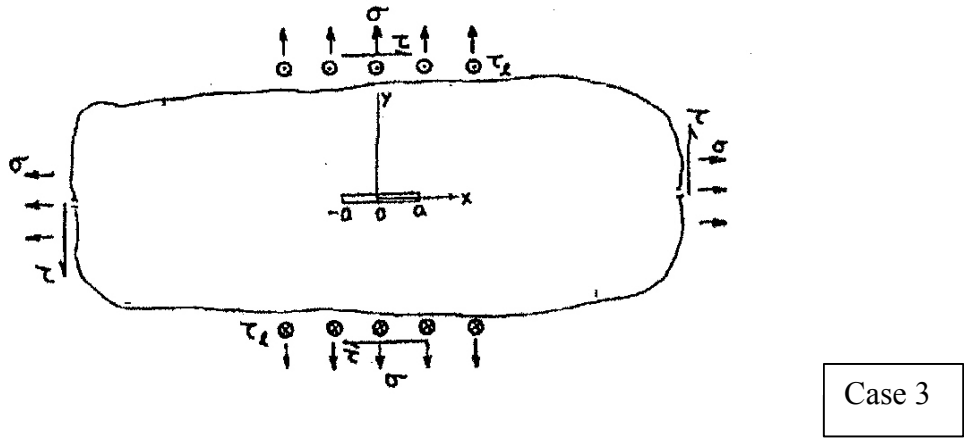

Figure SIE-5.11. Single Crack Solution, Tada case 5.1.

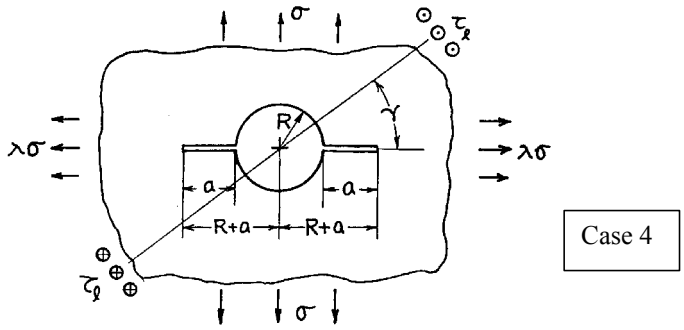

Figure SIE-5.12. Two Equal Cracks from a Hole, Tada case 19.1.

Combining the solutions and solving for K_1 gives:

$$K_1 = \frac{K_2}{K_3} K_4$$

$$K_2 = \sigma\sqrt{w \tan\frac{\pi(R+a)}{w}},\ w = 1.0\,in.\ \text{pitch}$$

$$K_3 = \sigma\sqrt{\pi(R+a)}$$

$$K_4 = \sigma\sqrt{\pi a} F_\lambda(s)$$

$$F_\lambda(s) = (1-\lambda)F_0(s) + \lambda F_1(s)$$

$$\lambda = 0,\ s = \frac{a}{R+a}$$

$$F_0(s) = 0.5(3-s)\left[1+1.243(1-s)^3\right]$$

After obtaining K_1, the crack growth analysis can be performed using the NASGRO3.0 data table option for a one-dimensional data table for through cracks, DT01, with a unit stress. The crack lengths and corresponding β values are shown below.

$$\beta = \frac{K_1}{\sqrt{\pi a}}$$

Table SIE-5.1. NASGRO Input Values for MSD DT01.

a (in.)	K_2	K_3	K_4	K_1	β
0.05	0.6964	0.6720	0.7068	0.7325	1.8481
0.1	0.8348	0.7802	0.7941	0.8498	1.5161
0.2	1.1494	0.9606	0.9563	1.1442	1.4434
0.25	1.3678	1.0392	1.0325	1.3589	1.5334
0.275	1.5120	1.0763	1.0690	1.5018	1.6157
0.28	1.5452	1.0836	1.0762	1.5347	1.6363
0.285	1.5802	1.0908	1.0834	1.5694	1.6586
0.29	1.6172	1.0980	1.0905	1.6062	1.6827
0.295	1.6564	1.1051	1.0976	1.6451	1.7089
0.3	1.6982	1.1122	1.1046	1.6866	1.7373
0.305	1.7427	1.1192	1.1116	1.7308	1.7682
0.31	1.7904	1.1262	1.1186	1.7783	1.8019
0.315	1.8418	1.1332	1.1255	1.8293	1.8389
0.32	1.8973	1.1401	1.1324	1.8845	1.8795
0.325	1.9576	1.1470	1.1392	1.9444	1.9243
0.33	2.0235	1.1538	1.1461	2.0099	1.9740
0.335	2.0959	1.1606	1.1528	2.0819	2.0293
0.34	2.1760	1.1673	1.1596	2.1616	2.0915
0.345	2.2655	1.1740	1.1663	2.2505	2.1617
0.35	2.3664	1.1807	1.1730	2.3508	2.2419
0.355	2.4814	1.1873	1.1796	2.4652	2.3343
0.36	2.6142	1.1939	1.1862	2.5972	2.4422
0.37	2.9569	1.2070	1.1993	2.9379	2.7250
0.38	3.4783	1.2200	1.2123	3.4564	3.1634
0.4	7.1360	1.2455	1.2379	7.0925	6.3270

The stress intensity factors, K, and corresponding crack lengths for the long crack case are taken from the Franc2DL model. This model was run with the skin residual strength stress of 18.426 ksi. The K values are converted into betas for a unit stress using the equation:

$$\beta = \frac{\left(\frac{K}{\sqrt{\pi a}}\right)}{18.246}$$

The β and crack length values are input into NASGRO3.0 using the same data table option as for the MSD case. Table SIE-5.2 shows the crack lengths, K values, and calculated β values for the long crack case.

Table SIE-5.2. NASGRO Input Values for Long Crack DT01.

a (in.)	K	β
48.066	35.49	0.1567
53.066	44.58	0.1874
58.066	58.57	0.2353
63.066	71.35	0.2751
68.066	81.82	0.3037
73.066	88.29	0.3163
78.066	93.84	0.3252
83.066	105.2	0.3534

Inspection Capabilities and Crack Limits

The long crack will be detectable once it grows out from underneath the surround doubler. The crack will be directly accessible externally and inspected for by using either HFEC or detailed visual techniques. With a HFEC inspection, the minimum detectable crack size in the field is assumed to be a 0.125 inch crack away from a fastener hole. With a detailed visual inspection, the minimum detectable crack size in the field is assumed to be a 3.0 inch uncovered crack.

Structural Loading and Stress History Description

The stress spectrum is considered to have a remote stress due to cabin pressurization. Cabin pressurization primarily causes hoop tension in the fuselage. The GAG pressurization load is based on FAR25.571. The pressure condition is comprised of a 8.6 psi normal operating differential pressure and an additional 0.5 psi external aerodynamic pressure. A factor of 1.1 is only applied to the normal operating pressure for residual strength.

$P = 8.6 + 0.5 = 9.1 \ psi$

$R = 74 \ in.$ (radius of fuselage)

$$S_r = \frac{PR}{t_{skin}} = \frac{9.1(74)}{0.04} = 16.835 \ ksi$$

The limit stress used for residual strength purposes in this scenario is calculated as stated earlier according to FAR25.571.

$P = 1.1*8.6 + 0.5 = 9.96 \ psi$

$R = 74 \ in.$

$$S_r = \frac{PR}{t_{skin}} = \frac{9.96(74)}{0.04} = 18.426 \ ksi$$

Material Property Description

In Franc2DL, materials can be assigned to each element individually. Material properties that are user defined for the models in this analysis are as follows; Young's modulus,

Poisson's Ratio, and thickness. The values used for the long crack case are shown in Table SIE-5.3.

Table SIE-5.3. Material Properties and Growth Rate Data.

Material	Young's Modulus	Poisson's Ratio
2024-T3 Aluminum	10.3E+06	0.35

The outer skin and doubler are made from 2024-T3 IAW QQ-A-250/5. The material properties from the NASGRO3.0 libraries are used for the crack growth rate properties. The material properties used are for 2024-T3; Clad, Plate and Sheet; T-L; LA & HHA NASGRO3.0 material code M2EA12AB1.

Table SIE-5.4. Material Properties and Growth Rate Data.

```
MATL 1: 2024-T3
        Clad Plt & Sht; L-T; LA & HHA

Material Properties:

:Matl:  UTS :  YS  :  K1e :  K1c :  Ak :  Bk :  Thk  :  Kc  : Keac :
: No.:      :      :      :      :     :     :       :      :      :
:----:------:------:------:------:-----:-----:-------:------:------:
:  1 :  66.0:  53.0:  46.0:  33.0: 1.00: 1.00:  0.036:  66.0:      :

:Matl:--------------- Crack Growth Eqn Constants -------------------:
: No.:    C    :  n  :  p :  q :  DKo : Cth+ :Cth- : Rcl:Alpha:Smax/:
:    :         :     :    :    :      :      :     :    :     :SIGo :
:----:---------:-----:----:----:------:------:-----:----:-----:-----:
:  1 :0.829D-08:3.284:0.50:1.00:  2.90:  1.50: 0.10:0.70: 1.50: 0.30:
```

The K_c value is conservative for the long crack case. This value was changed to 108.9 ksi√in. (Department of Defense Damage Tolerant Design Handbook) in order to better calculate the actual crack growth in a large panel.

Solution Technique

The multiple cracks case is conveniently solved using NASGRO3.0 with the crack growth interactions previously discussed, while the long crack case is solved using Franc2DL and NASGRO3.0. The spectrum is the same for both cases and is included as a constant amplitude GAG cycle with 100 flights per block, with a single block applied per schedule.

Results

Critical crack size/Residual Strength

The residual strength stress for the multiple cracks is (0.04/0.11)*18.4 = 6.7 ksi. This stress results in a critical crack geometry as shown in Figure SIE-5.13 (L_f = (1-6.7/66)/2 = 0.449 in.). The final crack length is a_f = 0.449-3/32 = 0.355 inches.

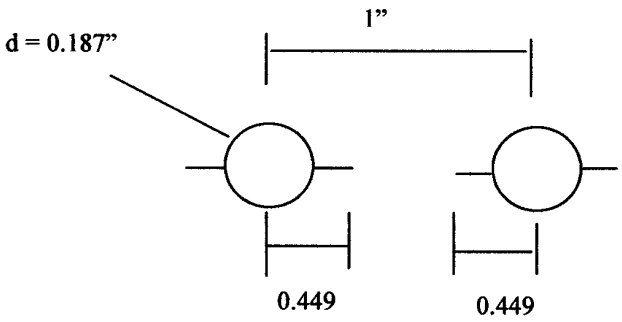

Figure SIE-5.13. MSD Critical Crack Length.

Life:

Based on the calculations for growing the crack in NASGRO3.0 and the MSD crack growth interactions, the life from initial crack size to failure is determined to be 16,868 flights. The results of crack length and crack depth versus life are shown in Figure SIE-5.14. The life is given in numbers of flights. These results show that there is ample time before multiple cracks present at the time of the surround doubler installation link up and become critical.

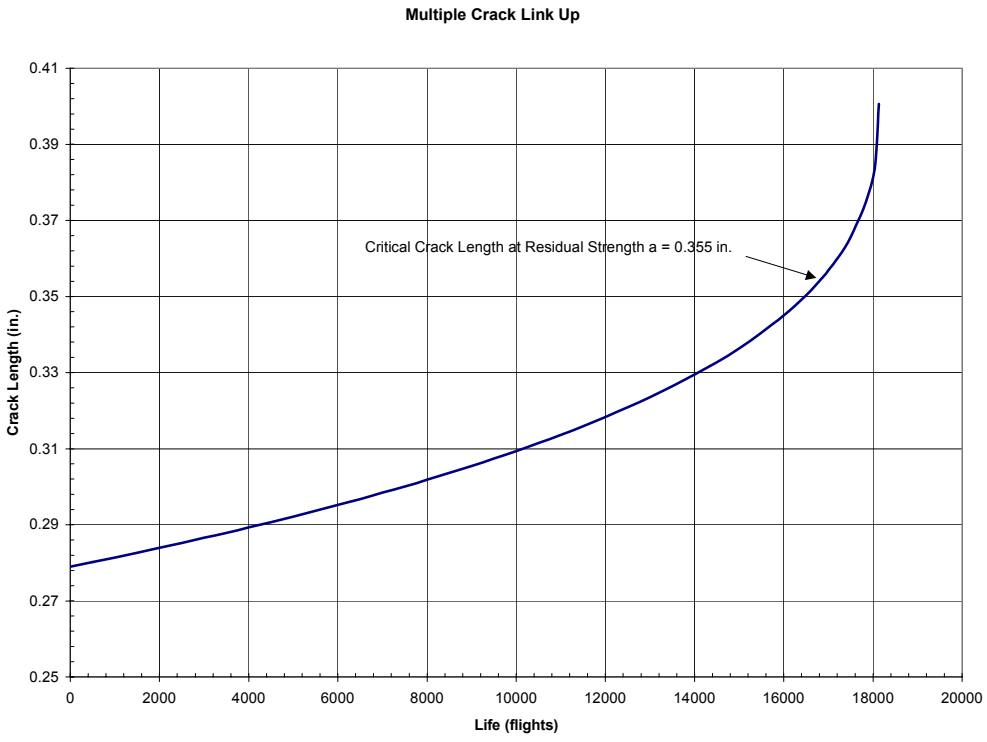

Figure SIE-5.14. Crack Growth Life for MSD Case.

Based on the calculations for growing the crack in NASGRO3.0 for the long crack case, the life from initial crack size to failure is determined to be 65,554 flights. The results of crack length and crack depth versus life are shown in Figure SIE-5.15.

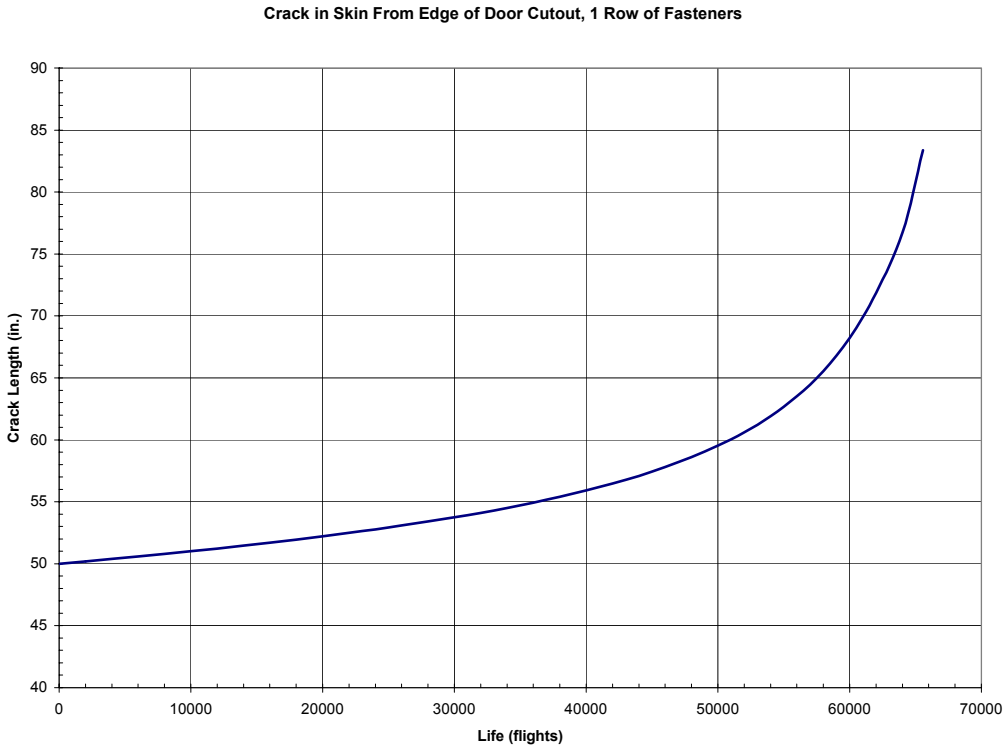

Figure SIE-5.15. Crack Growth Life for Long Crack Case.

Inspection Intervals

The threshold and repeat intervals for the long crack case are calculated using the life reduction factors shown below.

Life Reduction Factors:
$K_1 = 2.0$
$K_2 = 2.0$, Multiple load path structure

Detectable crack length (HFEC at edge of doubler):
$c_{det} = c_{dblr} + 0.125 = FS700 - FS650 + 1.75 + 0.125 = 51.75 + 0.125 = 51.875\,in.$
Number of flights @ detectable crack length, N_{det} = 17,400 flights

Detectable crack length (Detailed visual at edge of doubler):
$c_{det} = c_{dblr} + 3.0 = FS700 - FS650 + 1.75 + 3.0 = 51.75 + 3.0 = 54.75\,in.$
Number of flights @ detectable crack length, N_{det} = 35,200 flights

Critical crack length: c = 83.3659 in.
Number of flights @ critical crack length, N_{crit} = 65,554 flights

$$\text{Threshold Interval} = \frac{N_{crit}}{K_1} = \frac{65554}{2.0} = 32,777 \text{ flights}$$

$$\text{Repeat Interval, HFEC} = \frac{N_{crit} - N_{\text{det},HFEC}}{K_2} = \frac{65554 - 17400}{2.0} = 24,077 \text{ flights}$$

$$\text{Repeat Interval, Det. Visual} = \frac{N_{crit} - N_{\text{det},DV}}{K_2} = \frac{65554 - 35200}{2.0} = 15,177 \text{ flights}$$

References

Tada, H., P. Paris, and G. Irwin, "The Stress Analysis of Cracks Handbook," Third Edition.

PROBLEM NO. UDRI-1

Title: Crack Growth Analysis of Critical Area in Front Wing Spar and Verification of Model

Objective:

To illustrate the process of estimating crack growth behavior to set inspection limits and the process used to verify the analytical results.

General Description:

This problem focuses on a damage tolerance assessment of a critical area on a wing front spar for the purpose of establishing inspection intervals. The critical area includes both the spar cap and the wing skin. An airplane finite element model was developed to determine the stresses and the critical area was modeled using a standard AFGROW stress intensity factor solution. Verification testing was conducted to validate the life prediction model.

Topics Covered: Damage tolerance assessment, finite element analysis, crack growth analysis, inspection intervals

Type of Structure: wing skin, wing spar cap

Relevant Sections of Handbook: Sections 1, 2, 3, 4, 5, 7 and 11

Author: Peggy C. Miedlar

Company Name: University of Dayton Research Institute
Structural Integrity Division
Dayton, OH 45469-0120
937-229-4417
www.udri.udayton.edu

Contact Point: Peggy C. Miedlar
Phone: 937-229-4476
e-Mail: Miedlar@udri.udayton.edu

Overview of Problem Description

This problem focuses on a critical area on a wing front spar, shown in Figure UD-1.1 (photograph), and further described by the drawings of Figures UD-1.2 - UD-1.4. The critical area includes both the spar cap and the wing skin. The spar cap was fabricated from 2024-T3511 aluminum and the skin from 2024-T3 aluminum. The fasteners are 0.25 in diameter, and join the cap, skin and fitting. The specific area is shown in Figure UD-1.4, with the expected crack path marked.

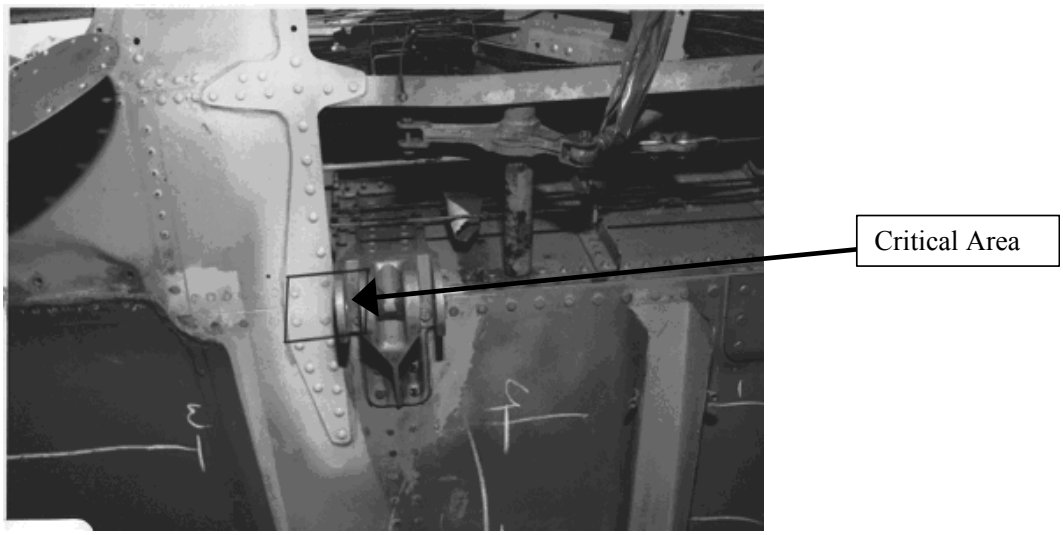

Figure UD-1.1. Photograph of Critical Area from Outside Wing.

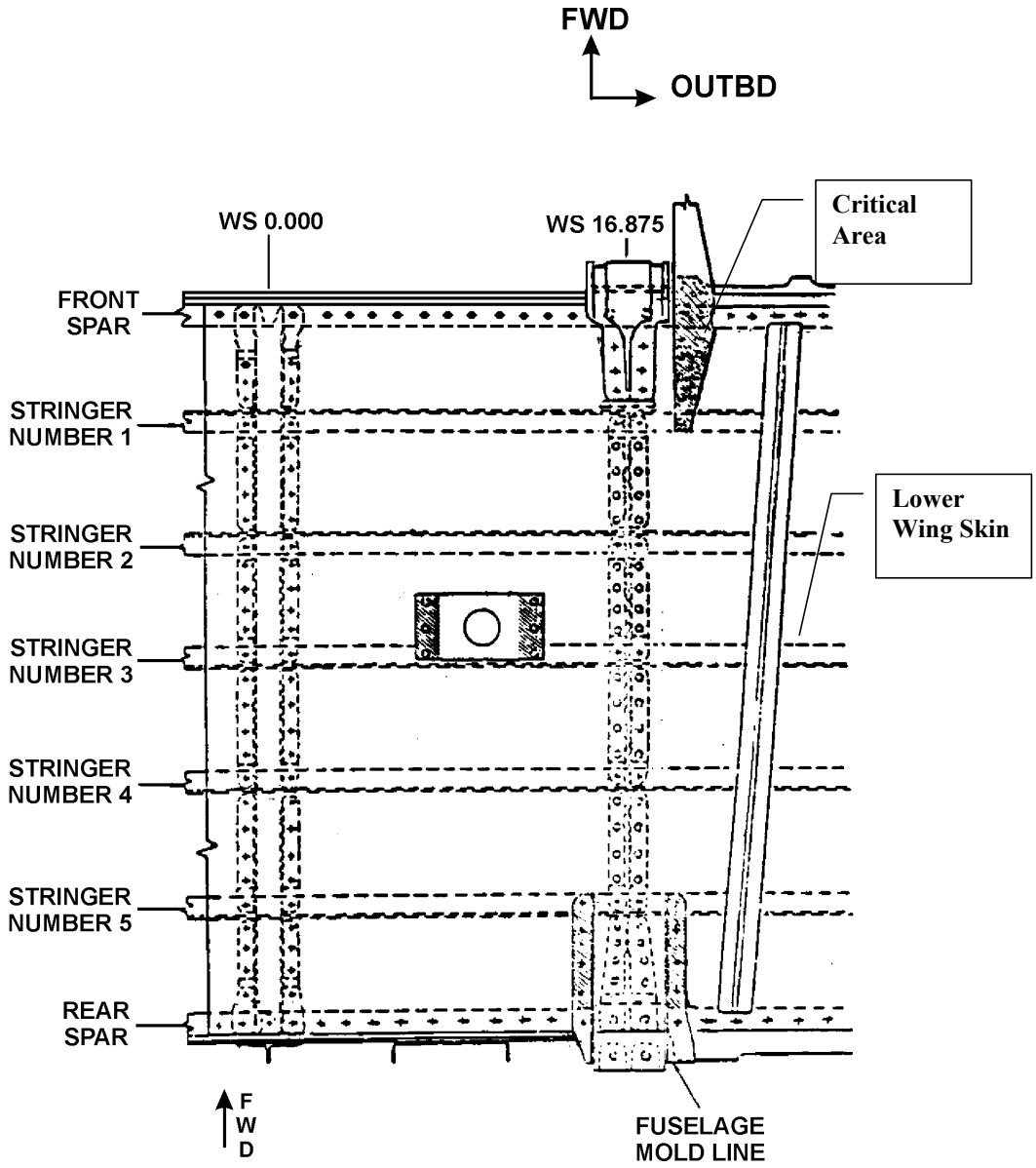

Figure UD-1.2. General Location of Critical Area.

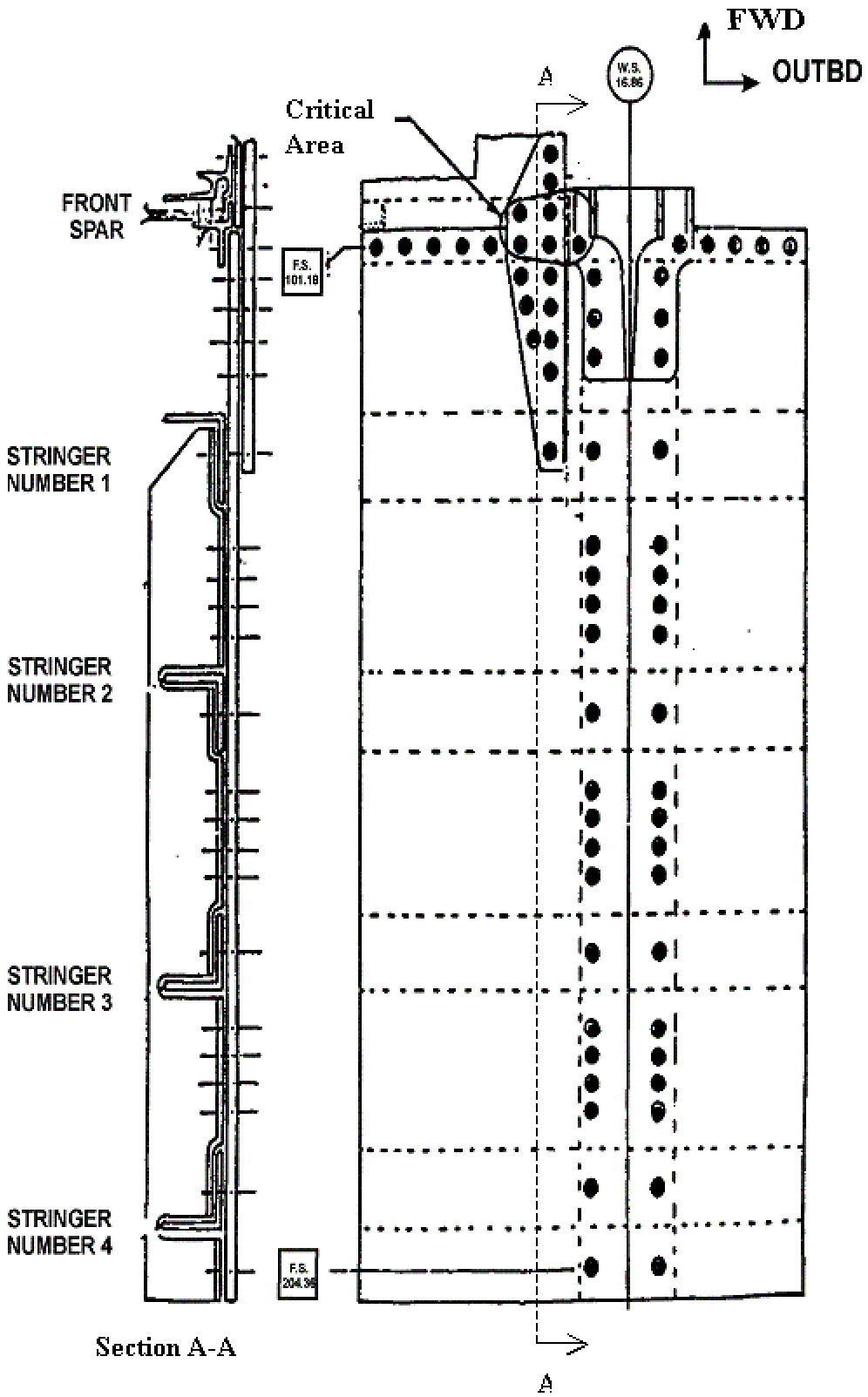

Figure UD-1.3. Structural Detail for Critical Area from Bottom of Wing Looking Up.

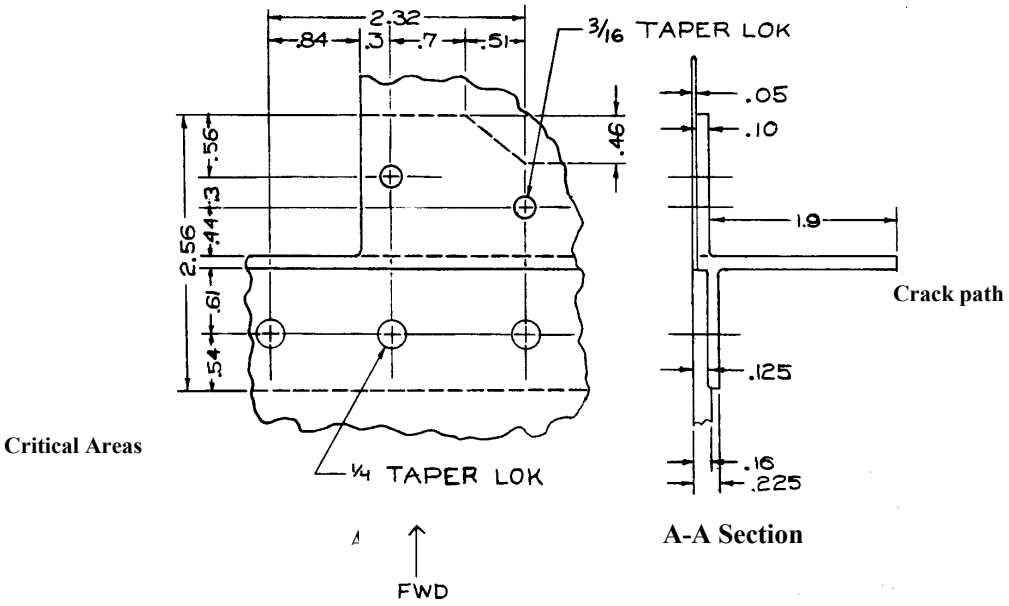

Figure UD-1.4. Detail Geometry of Critical Location Shown in Figure UD-1.3.

Structural Model

A finite element model was used for determining the level of stresses in the critical area. The loading for this geometry is tension.

Structural Model Details

If the details of the FE model are important to the problem, the model should be described here, using drawings to illustrate the model.

Model Geometry Description

The critical crack geometry was modeled as a corner crack from an off-centered hole, with the crack growing toward the short side. The corresponding AFGROW crack geometry model is called a single corner crack at a hole, as shown in Figure UD-1.5. A width (W) of 2.5 inches was assumed as representative of the distance from the plate edge to the next hole. The edge distance (B) is 0.61, thickness (t) is 0.125 and hole radius ($D/2$) is 0.125 inches.

Figure UD-1.6 describes the length direction beta factor (K/σ) for several a/c ratios.

Model Assumptions

Some assumptions were made for this analysis. Most of these assumptions are conservative, resulting in a shorter predicted life. These assumptions include: straight shank hole, open hole, no load transfer, no local residual stresses due to cold working, and no retardation.

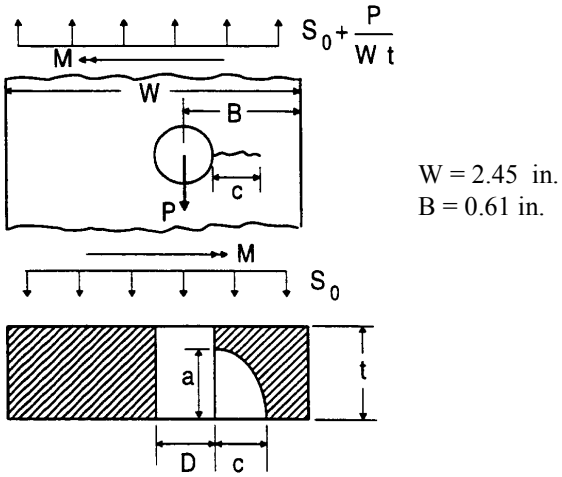

Figure UD-1.5. Crack Geometry Model for Stress Intensity Factor.

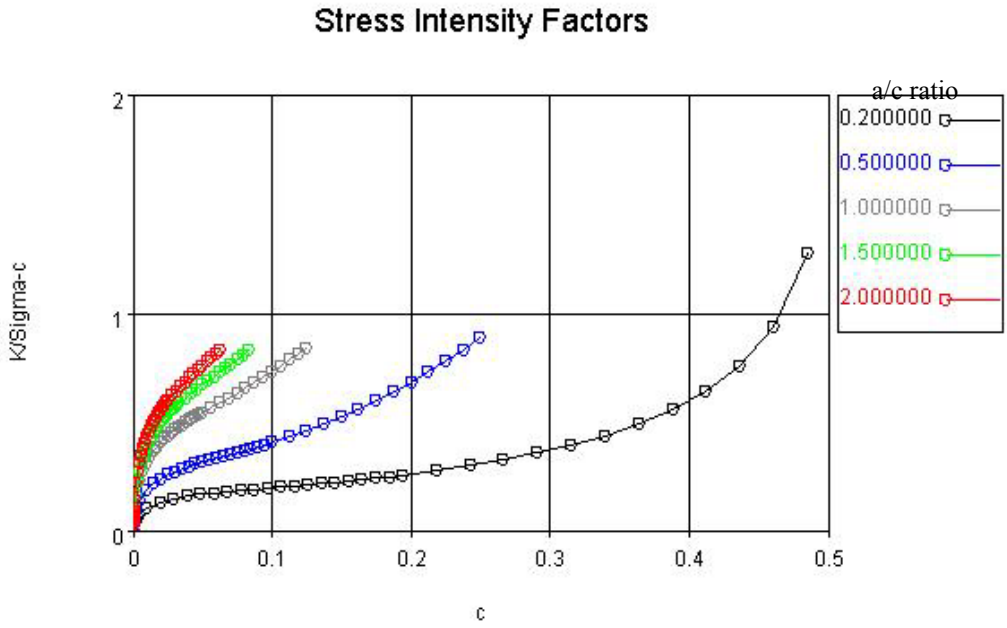

Figure UD-1.6. Surface Length Beta (K/σ) Factor for Corner Crack from a Hole for Several Different Crack Aspect Ratios (a/c).

Inspection Capabilities and Crack Limits

The holes in the flange and skin are covered by the wing-fuselage attachment fitting. With the fasteners removed, only the inside of the holes are visible. Therefore, these areas are inspected by X-ray. With X-ray inspection, the minimum detectable crack size in the field is 0.5 inch crack.

Structural Loading and Stress History Description

The stress spectrum is given in Table UD-1.1 where the flight history is presented as a fraction of the maximum spectrum stress (10.7 ksi). There are 1590 cycles in the spectrum, and this represents ten flights. Each flight is one hour.

Table UD-1.1. Flight History Data For Problem UDRI-1.

Step No.	Maximum Stress	Minimum Stress	Cycles
1	0.45	0.125	333
2	0.55	0.125	234
3	0.65	0.125	158
4	0.85	0.125	52
5	0.95	0.125	11
6	1.05	0.125	5
7	1.15	0.125	1
8	1.25	0.125	1
9	0.45	0.125	333
10	0.55	0.125	234
11	0.65	0.125	158
12	0.85	0.125	52
13	0.95	0.125	11
14	1.05	0.125	5
15	1.15	0.125	2

Material Property Description

The parameters for the Walker equation for the two aluminum alloys are given in Table UD-1.2, along with other material parameters. A detailed description as to how Walker constants were developed is presented in Section 5.

Table UD-1.2. Material Properties and Growth Rate Data.

Parameter	2024-T3	2024-T3511
Walker C	9.57×10^{-10}	9.57×10^{-10}
Walker n	3.7	3.7
Walker m	0.32	0.32
K_C	92.0	92.0
K_{IC}	35.0	46.0
σ_Y	48.0	54.0
ΔK_{th}	0.0	2.5

Solution Technique

This type of problem is conveniently solved using AFGROW. The input file for the AFGROW analysis is shown in Table UD-1.3.

Table UD-1.3. AFGROW Input File for Problem UDRI-1.

Data	Description
FAF012	
Example Problem	
~{Example problem using Walker equation and crack at off-centered hole }	Description of Problem
1030 0	
0.05	Geometry data
0.05 0	
0.05 0	
0.125	
2.5	
1 0 0 0	
0.25	
-1	
1 0.61	
10500	
0.33	
1.25e-005	
NOENVS	
NORETARD	
1	
1	
NOKMOD	
NOKRES	
WALKER_NEW	
2024-T3 example	Material Data
1	
9.57e-010 3.7 0.32	
92 2	
35 -0.3 0.99 48	
0	
NO_INITIATION	
10.7	
0	Spectrum data
SPFILE	
spectrum.sp3	

The spectrum is contained in a separate file named *spectrum.sp3*, and is shown in Table UD-1.4. Each repeat of the defined segment represents ten flights, and each flight represents one hour.

Using AFGROW terminology, the spectrum is entered as a blocked spectrum with one sub-spectrum. In this case, the sub-spectrum is the block of stresses given in Table UD-1.1.

Table UD-1.4. AFGROW Sub-Spectrum File for Problem UDRI-1.

Data	Description
1 15	Sub-spectrum number, number of levels
0.45 0.125 333	Maximum stress, minimum stress, number of cycles
0.55 0.125 234	
0.75 0.125 158	
0.85 0.125 52	
0.95 0.125 11	
1.05 0.125 5	
1.15 0.125 1	
1.25 0.125 1	
0.45 0.125 333	
0.55 0.125 234	
0.75 0.125 158	
0.85 0.125 52	
0.95 0.125 11	
1.05 0.125 5	
1.15 0.125 2	

Results

Critical crack size/Residual Strength

Using the Irwin Criterion for fracture, i.e.,

$$K_{\max} = \sigma\beta\sqrt{\pi c} = K_{Ic} = 92 \ ksi\sqrt{in}$$

This criterion is imbedded in the AFGROW code and is used to determine the critical thru-thickness crack size (c) = 0.458 inches. The corner crack transitions into a thru-thickness crack at about one-half of the life.

Life:

Based on the calculations for growing the crack in AFGROW, the life from initial crack size to failure is determined to be 3100 hours. The results of crack length versus life and crack depth versus life are shown in Figures UD-1.7 and UD-1.8, respectively. The life is given in flight hours.

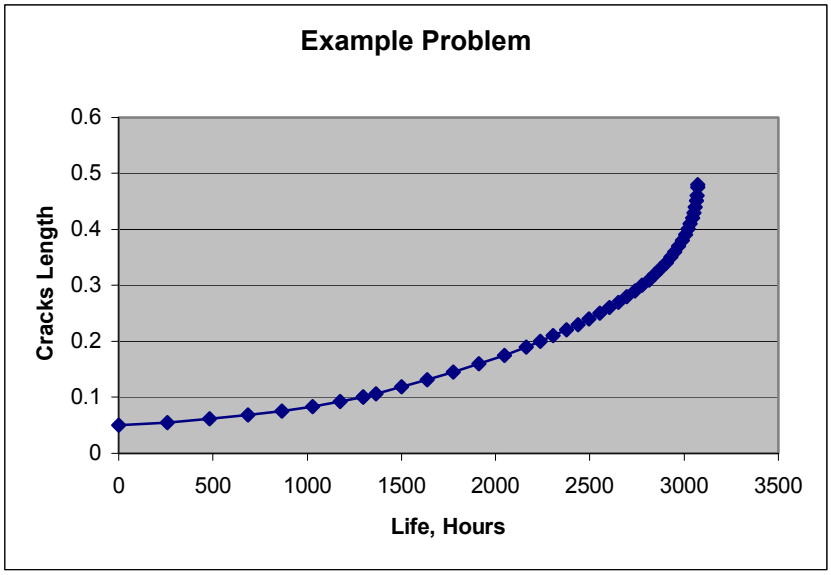

Figure UD-1.7. Crack Length versus Life for Problem UDRI-1.

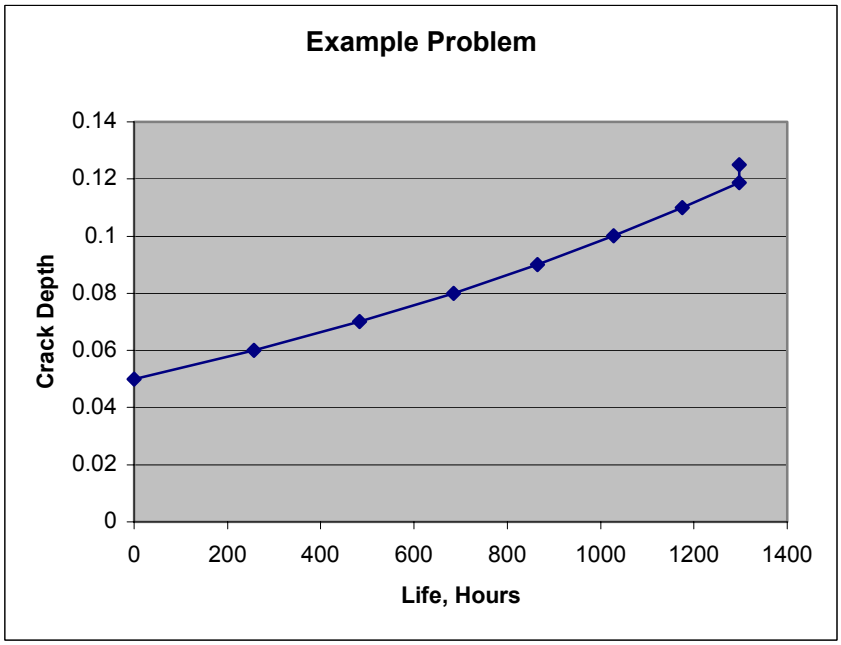

Figure UD-1.8. Crack Depth versus Life for Problem UDRI-1.

Verification of the Life Analysis

To verify the analysis procedure, four specimens were tested under the operational stress spectrum, and these results were compared to the analytical results. The test specimens were designed to represent the localized features that match the actual aircraft structure, seen in Figure UD-1.10. The operational spectrum is given in Table UD-1.1. The test results are summarized in Table UD-1.8.

The AFGROW program was used to predict the specimen lives. The results of the analysis are also shown in Table UD-1.8. The predicted results are compared to the analytical results with the ratio of predicted life divided by actual life (N_P/N_A).

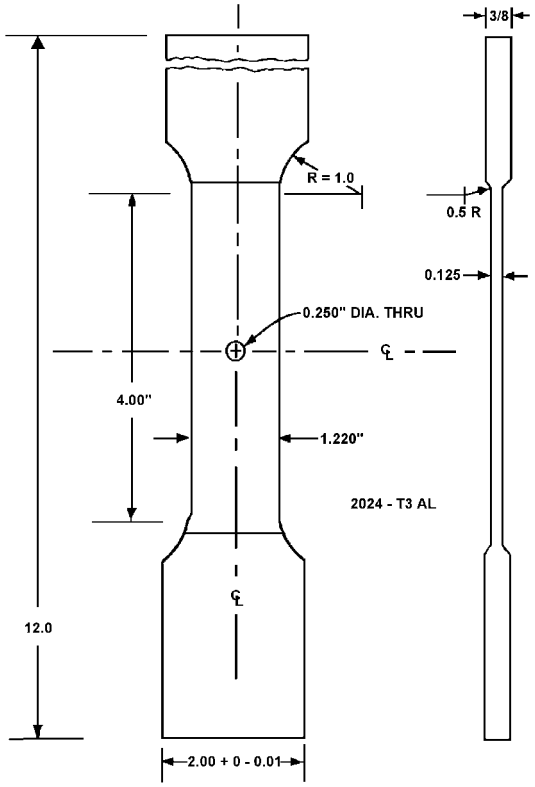

Note 3: Do not machine grip sections thickness.
Note 2: Do not undercut any radius adjacent to the gage section.
Note 1: All dimensions in inches unless otherwise noted.

University of Dayton Research Institute Structural Test Laboratory			
Title	*Specimen #2.*	Date	*5/2/90*
Project	*Spectrum Fatigue Study*	Draftsman	*IF*
Material	*2024-T3 Al. 3/8 TK*		
Drawing Number	*90EDD-B-401*		
Tolerances	*x.x = ± 0.1 x.xx = ± 0.01 x.xxx = ± 0.002*		

Figure UD-1.10. Test Specimen.

Table UD-1.8. Test Results for 2024-T351 C(T) Specimens.

Specimen ID	Width (in)	Thickness (in)	Hole Diameter (in)	Precrack Length (in)	Test Flights to Failure (N_A)	Predicted Flights to Failure (N_P)	$\frac{N_P}{N_A}$
5	1.220	0.123	0.250	0.050	2072	1616	0.78
8	1.221	0.124	0.249	0.050	1844	1697	0.92
11	1.220	0.124	0.250	0.049	1004	1626	1.62
12	1.220	0.125	0.250	0.048	2042	1736	0.85

Discussion of N_P/N_A

If the N_P/N_A ratio is equal to 1, then the analysis predicts the actual test results. If the N_P/N_A ratio is greater than 1, the analysis is unconservative. If the predicted life is less than the actual (N_P/N_A <1), the analysis is conservative.

If the ratio is too high or low, i.e. N_P/N_A=2 or N_P/N_A=0.5, then the analysis method and assumptions should be reviewed to rectify the differences between the experiment and analysis

For these tests, the N_P/N_A ratios show a good correlation between the test results and analysis. Three of the four tests show that the analysis is conservative.

Inspection Intervals

The initial inspection interval is at one-half of the life. For the predicted life of 3100 hours, the first inspection is set at 1550 hours.

Subsequent inspections are one half the life from NDI field detectable crack size to the critical crack size. However, for this problem, the failure occurs prior to the field detectable crack size.

Force Management Decisions

Since the critical crack size (a_f)= 0.458 inch is less than the NDE detectable size (a_{NDE} = 0.5 inch), the situation precludes the use of multiple inspections. And the structure must be classified as slow crack growth critical. This means that once the initial inspection period has been reached, the life limit of the structure has been reached, i.e., the life is 1550 flights (=3100/2). Alternately, one could use the results to assess different inspection and repair options. For example, if an inspection method can be found that will detect the presence of 0.005 inch long cracks, then the time between inspections becomes 6575 flights. Thus, if after pulling the fasteners from the holes for the first in-depth inspection, these holes are then coldworked, the lives can be extended tremendously, and subsequent inspections might not be required.

Complementary Sensitivity Studies

- Cold working of holes/compressive residual stresses due to taper-lok.
- Filled hole load transfer.

- Taper-lok holes – one method for accounting for fatigue rated fasteners systems is to start the analysis with initial crack size of 0.005 inches.
- Retardation model (currently using no retardation).

Problem No. UDRI-2

Title: **Structural Risk Assessment for a Discrete Source Damage Threat to the Fail Safety Capability of a Stringer**

Objective:

To illustrate the use of PROF for the calculation of the probability of failure due to discrete source damage at a stringer.

General Description:

This sample problem illustrates the use of the PROF risk analysis computer program for evaluating the fail-safe capability of a wing stringer given a discrete source damage event. The probability of failure as a function of flight hours given a two bay crack is calculated using data representative of a Boeing 707 JSTARS airframe. An equivalent initial flaw size distribution was used to model hole quality for the structure as it enters service. The initial flaw size distribution was grown using the crack growth life curve for an intact structure under normal operating conditions. Probability of failure was calculated using the stress distribution and residual strength of the stringer with the two bay discrete source damage event having occurred. The risk analysis was used to estimate the number of flight hours for the airframe to reach a probability of failure of 10^{-4}. In some applications, the 10^{-4} failure probability is the maximum acceptable risk for fail safety and the flight hours to reach this risk level is the time of the onset of widespread fatigue damage.

Topics Covered: Failure probability, discrete source damage, onset of WFD, residual strength, crack size distributions, crack growth life curves

Type of Structure: wing stringer

Relevant Sections of Handbook: Section 8

Author: Peter W. Hovey and Alan P. Berens

Company Name: University of Dayton Research Institute
Structural Integrity Division
Dayton, OH 45469-0120
937-229-4417
www.udri.udayton.edu

Contact Point: Alan P. Berens
Phone: 937-229-4475
e-Mail: Berens@udri.udayton.edu

Overview of Problem Description

The goal in analyzing the effect of widespread fatigue damage (WFD) in the discrete source damage (DSD) problem is to evaluate the ability of the structure to complete the current mission when a partial structural failure occurs. This analysis is aimed at one of two or more structural details that interact by providing a fail-safe capability in the event that one or more of the structural details has failed. The evaluation will use the conditional single-flight probability of failure, given that DSD is present as the measure of this ability. The prototype for this analysis is the ability of the structure to survive the sudden appearance of a two-bay crack in the fuselage or wing skin.

The two-bay crack is a crack that spans two bays in the skin, including the stringer or frame between the two bays. The size of two bays is considered an upper bound on the damage that would directly result from penetration of an engine blade thrown from the engine in an uncontained failure or from battle damage. The concern in this damage scenario is whether the crack-stopping structures on either side of the damage will hold through the remainder of the mission. The conditional probability that the crack-stopping structure will fail, given that the DSD has occurred, provides a measure of the ability of the structure to complete the mission.

Since the flaw size distribution changes in time, the PROF DSD analysis is calculated as a function of time. The presence of DSD only affects the structure during the flight in which it occurs. Therefore, the same model of the growing crack size population that is used in a standard PROF analysis can be used to assess the influence of aging on the conditional probability of failure given DSD. The details of the crack growth model are given in Berens, et al.[1991]. Because of its severity, DSD, will be detected and repaired before the next flight so that a model of crack growth in the presence of DSD is unnecessary.

Example Input Data

The data from the B-707 teardown inspection performed as part of the JSTARS assessment will be used to illustrate the procedures for an analysis of the impact of WFD on the fail safety in the presence of DSD using PROF. A detailed description of the data and the problems associated with using the B-707 for the JSTARS was given by Lincoln [1997]. The example presented here centers on the fail-safety capability of stringer 7 in the lower wing skin after stringer 8 and the adjacent wing panels have failed.

Figure UD-2.1 contains a schematic of the B-707 wing. The left half of Figure UD-2.1 shows the entire structure and the location of stringer 8 (S8). A cross-section of the skin and stringers is shown in the right half of Figure UD-2.1. The example will analyze the effect of a break in stringer 8 and the adjacent skins on the large adjacent stringer S7.

The data were collected and the structural analyses were performed by Boeing under an Air Force contract. The data and analysis results were delivered in a series of letter reports and in Excel spreadsheets. The data used for this example were extracted from the spreadsheets.

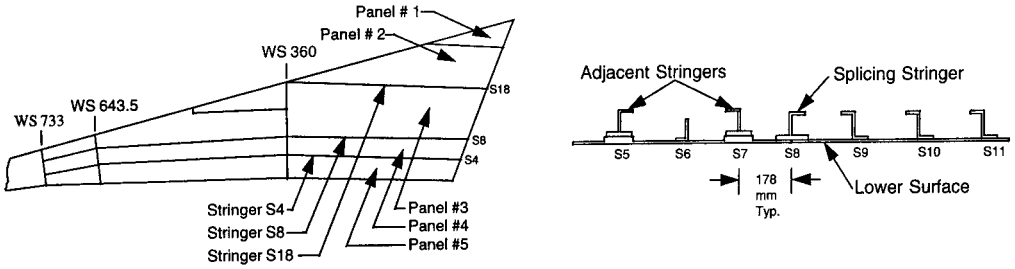

Figure UD-2.1. *Schematic of the B-707 Wing and Side View of the Skin and Stringer Structure [Lincoln, 1997].*

The structural analyses relevant to the DSD analysis include the crack growth curve, the stress exceedance data in the presence of DSD and the residual strength of stringer 7 in the presence of DSD. Figure UD-2.2 contains a plot of the crack growth curve; which was determined for intact structure under normal conditions. The DSD analysis is not concerned with crack growth in the presence of DSD because it is assumed that the DSD will be detected and repaired before the next flight.

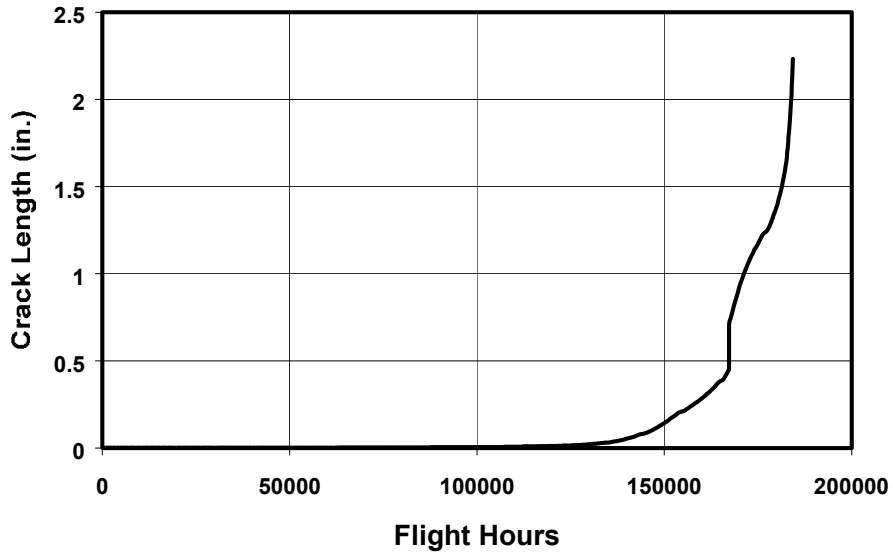

Figure UD-2.2. *Crack Growth Curve for Stringer 7 with All Structure Intact.*

Figure UD-2.3 illustrates the analysis of the peak load distribution from the exceedance data. The basis for the exceedance data is the spectrum used to generate the crack growth curve. The stresses were transformed to account for the damage to stringer 8 and the adjacent panels to get the empirical stress versus exceedance probability illustrated by the points in Figure UD-2.3. The straight line represents the Gumbel distribution that was fit to the data.

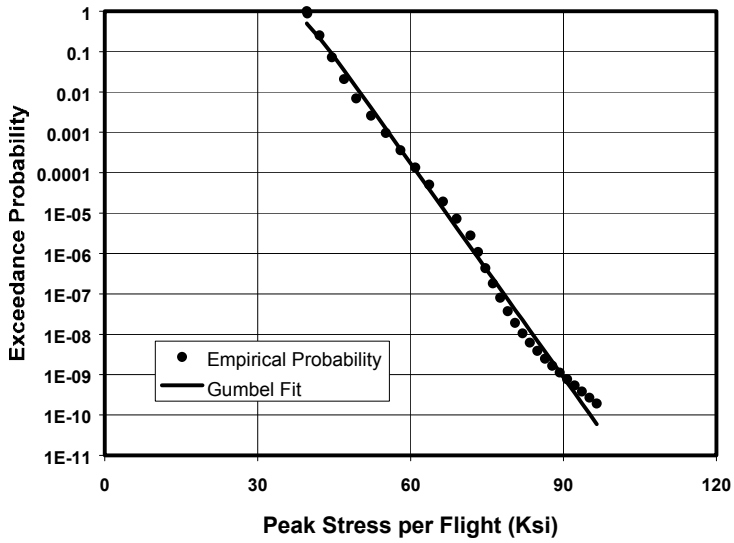

Figure UD-2.3. *Peak Stress Distribution with DSD Present.*

The residual strength function is plotted in FigureUD-2.4. The shape of the stringer is responsible for the flat region in the residual strength function. The residual strength function was derived primarily from the stress intensity curve for the stringer. Modifications from the Irwin criterion were required at low crack lengths and at the flat region in the middle of the curve. At low crack lengths, the Irwin criterion would push the residual strength to infinity, so it was necessary to truncate the residual strength function to the maximum material strength. The stress intensity factor actually dips between 0.5 and 1.5 inches because of the shape of the stringer. The residual strength does not, however, decrease, resulting in the flat region in the residual strength function.

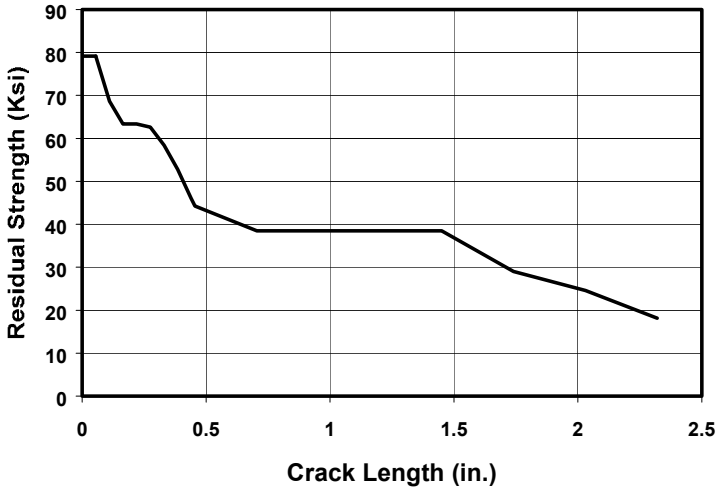

Figure UD-2.4. *Residual Strength as a Function of Crack Length in Stringer 7.*

The analysis was performed for two different initial crack length distributions. The crack length data were collected from an aircraft with 57,382 flight hours. The single-flight probability of failure is unacceptably high for the distribution seen in the teardown data. Since many of the JSTARS aircraft will have fewer hours, the distribution was adjusted to an age of 40,000 flight hours. The two-crack length distribution functions are

illustrated in Figure UD-2.5. A lognormal distribution was fit to the upper tail of the teardown data and the time adjustment was made by back extrapolating the percentiles from the 57,382 distribution using the crack growth curve.

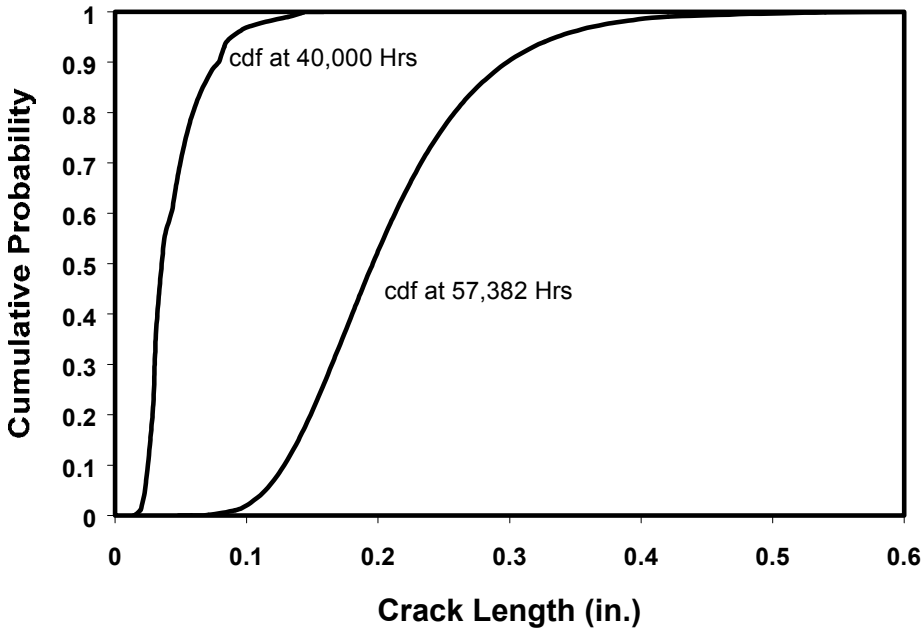

Figure UD-2.5. *Comparison of the Flaw Size Density Function at 40,000 Hours with the Density Function at 57,382 Hours.*

The results of two different PROF DSD analyses are plotted in Figure UD-2.6. The solid line represents the analysis using the flaw size distribution from the 57,382-hour aircraft as the starting point. The dashed line plots the results from using the flaw size distribution adjusted to a 40,000-hour aircraft. The two curves show close agreement in the overlap; however, some difference is expected since the time points at which calculations are made do not coincide from the two analyses.

Lincoln [1997] cited 10^{-7} as the desirable overall single-flight probability of failure and an estimated probability of DSD as 10^{-3}. The resultant requirement for the fail-safe capability of stringer 7 is 10^{-4}. Clearly, the aircraft at 57,382 hours does not meet this requirement. Starting at 40,000 hours, an aircraft will have approximately 16,000 hours before the conditional single-flight probability of failure exceeds the 10^{-4} requirement.

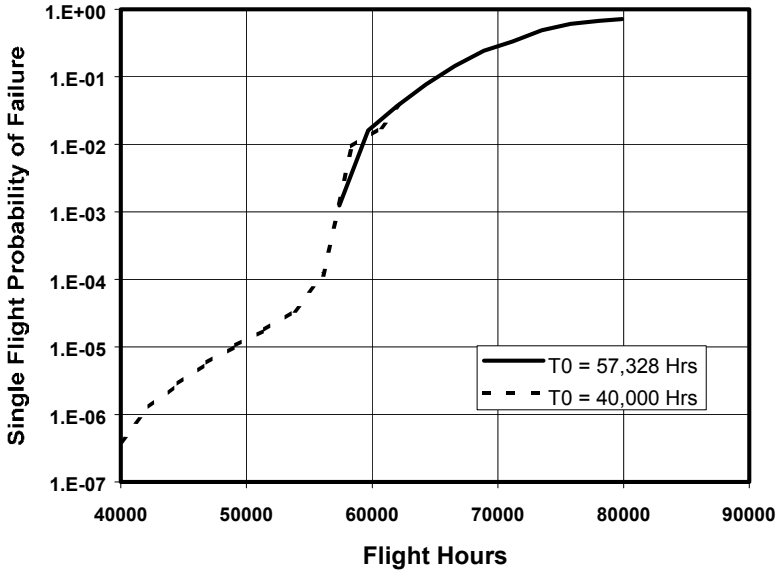

Figure UD-2.6. *Comparison of Single-Flight Probability of Failure Starting from 57,382 Hours versus 40,000 Hours.*

The use of the PROF DSD analysis module has been illustrated using data from the B-707 JSTARS aircraft. The problem of evaluating the fail safety capability of lower wing stringers in the B-707 is an example of the prototype DSD analysis. The essential elements that made the problem suitable for the PROF DSD module are:

a) interest in the conditional probability of failure, given that adjacent structural elements have failed,

b) likelihood of failure is increased by the presence of MSD,

c) prediction of the growth of MSD cracks with time being available, and

d) analysis of residual strength as a function of MSD crack size being available.

References

Berens, A.P., Hovey, P.W., and Skinn, D.A. (1991) *Risk Analysis for Aging Aircraft, Volume 1 – Analysis*, WL-TR-91-3066, Air Force Research Laboratory, Wright-Patterson Air Force Base, Ohio.

Lincoln, John W. (1997), "Aging Aircraft – USAF Experiences and Actions," *ICAF 97 – Fatigue in New and Aging Aircraft*, R. Cook, P Poole Eds., Proceedings of the 19th Symposium of the International Committee on aeronautical fatigue, Edinburgh Scotland.

Problem No. UDRI-3

Title: Structural Risk Assessment for a Multiple Element Damage Scenario

Objective:

To illustrate the use of PROF for the calculation of the probability of load path failure given a representative three element load path.

General Description:

This sample problem illustrates the use of the PROF risk analysis computer program for evaluating the probability of failure of the chordwise joint at WS407 of the C-141 airframe given the structural status of the adjacent beam cap and splice fitting. The failure probability of the chordwise joint as a function of flight hours from a reference time is calculated using representative crack growth data, stress distributions, and crack size distributions from inspections of C-141 airframes. Since the failure probability of the joint is conditioned on the failed or intact status of the beam cap and splice fitting, the probability of failure of these elements must also be calculated and the results combined.

Topics Covered: Failure probability, conditional probabilities, multiple element damage

Type of Structure: Wing chordwise joint, beam cap, splice fitting

Relevant Sections of Handbook: Section 8

Author: Alan P. Berens and Peter W. Hovey

Company Name: University of Dayton Research Institute
Structural Integrity Division
Dayton, OH 45469-0120
937-229-4417
www.udri.udayton.edu

Contact Point: Alan P. Berens
Phone: 937-229-4475
e-Mail: Berens@udri.udayton.edu

Overview of Problem Description

In the multi-element damage (MED) scenario, two or more structural elements bridge the same load path and the damage states of the elements can interact. In this scenario, failure of selected combinations of elements may not lead to system failure, but the effects of the failures may well lead to changes in the fracture mechanics (loads or geometry factors) of the remaining elements. Thus, the probability of system failure changes when the non-critical elements fail. To evaluate the failure risks of the complete structure, the functional interaction of the structural elements must also be taken into account. PROF can provide a reasonable approximation to this potentially complex calculation.

A fault tree type of analysis is first performed to identify all of the interactive states that have an affect on the conditions leading to system failure. This step is performed external to PROF and may prove to require extensive stress and fracture mechanics analyses. These states will represent structural conditions that can be modeled by deterministic crack growth analysis. PROF can then be used to calculate the conditional probability of failure, given the potential combinations of failed and intact states of the elements. The unconditional failure probability of the complete structure is a weighted average of the conditional probabilities in which the weights are the probabilities of being in each of the states, i.e., the probability that selected elements will have failed.

It is apparent that there are, potentially, a very large number of possible combinations of structural elements that would need to be considered in the analysis of a complex structure. From the viewpoint of structural interaction, it is judged that three or four elements will generally suffice. For two elements, there are only two basic combinations: the structure will fail if either element fails (the elements are in series), or the structure will not fail if one of the elements fails (the elements are in parallel). Note in the latter case, that the crack growth properties of either element will change upon failure of the other. Even this simple multi-element structure would require four PROF runs to be combined. If there are three interacting elements, there are a total of five basic combinations of series and parallel arrangements, and many more potential analysis combinations that could require PROF runs.

Problem Statement

Failure occurs at WS405 in the C-141 airframe when the chordwise joint fractures. Since the stress levels and crack growth behavior in the chordwise joint are dependent on the intact or failed status of both the splice fitting and the beam cap, the risk analysis for WS405 must combine conditional fracture probabilities for the relevant combinations of the states of the structural details. The probability of failure at this wing station under routine operations was previously calculated by Lockheed Aeronautical Systems Company (LASC) for a single inspection interval at 31,000 spectrum hours using a Monte Carlo analysis [Cochran, et al., 1991]. The data were re-analyzed to demonstrate using PROF to calculate the failure risks for the same scenario.

The input required by PROF was provided by LASC from their evaluation of the failure risks at WS405. The input data that were used in the analyses are presented in discussed in detail in Berens [1993] and Cochran et al. [1991].

LASC performed extensive finite element analyses of the chordwise joint, splice fitting and beam cap at WS405 of the C-141 airframe. The intact or fractured status of the beam cap affects the stress levels in both the splice fitting and the chordwise joint. The intact or fractured status of the splice fitting also affects the stress levels in the chordwise joint. Thus, different crack size versus flight hour relations and different maximum stress per flight distributions are needed for the various combinations of intact and fractured beam caps and splice fittings.

Since structural failure at WS405 of the C-141 airframe occurs when the chordwise joint fractures, LASC established a fault tree, Figure UD-3.1, which isolated the fracture events that need to be evaluated in the calculation of the probability of failure of WS405 [Cochran, et al., 1991]. The fault tree of Figure UD-3.1 was restructured to demonstrate that the WS405 failure probability can be modeled as a weighted average of the probability of fracture of the chordwise joint, given the intact or failed status of the splice fitting and the beam cap. The weighing factors are the probabilities of the intact or fractured status of the splice fitting and the beam cap. The chordwise joint fracture can also be visualized in terms of the Venn diagram of Figure UD-3.2 in which the event is partitioned four mutually-exclusive sub-events.

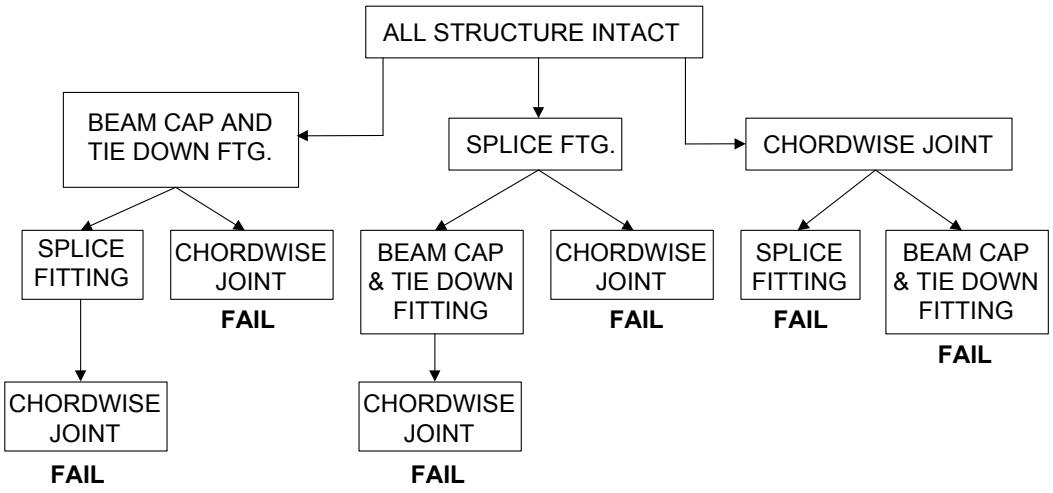

Figure UD-3.1. *WS405 Fault Tree.*

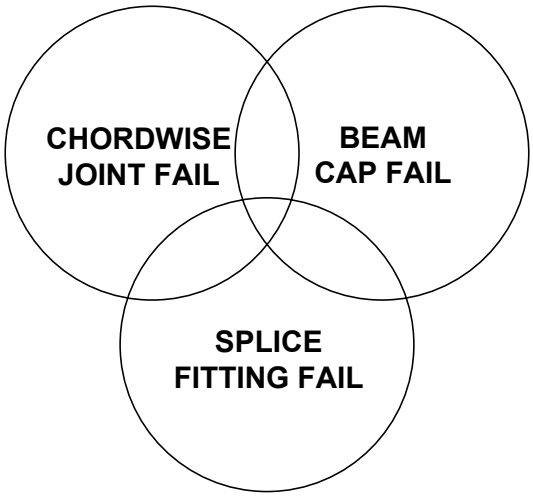

Figure UD-3.2. *WS405 Venn Diagram.*

Probabilistic Approach

The probability of failure at WS405 (POF) is given by:

$$\begin{aligned} POF &= P\{CSF,SFTAC,BCTAC\} + P\{CSF,SFTAC,BCF\} \\ &\quad + P\{CSF,SFF,BCTAC\} + P\{CSF,SFF,BCF\} \\ &= P\{CSF \mid SFTAC,BCTAC\} \bullet P\{SFTAC\} \bullet P\{BCTAC\} \\ &\quad + P\{CSF \mid SFTAC,BCF\} \bullet P\{SFTAC\} \bullet P\{BCF\} \\ &\quad + P\{CSF \mid SFF,BCTAC\} \bullet P\{SFF\} \bullet P\{BCTAC\} \\ &\quad + P\{CSF \mid SFF,BCF\} \bullet P\{SFF\} \bullet P\{BCF\}) \end{aligned} \qquad \text{(UD-3.1)}$$

where

CSF	= chordwise joint fracture
SFTAC	= splice fitting intact
SFF	= splice fitting fractured
BCTAC	= beam cap intact
BCF	= beam cap fractured
$P\{A,B,C\}$	= Probability of events A and B and C $= P\{A \mid B,C\} \bullet P\{B\} \bullet P\{C\}$
$P\{A \mid B,C\}$	= Conditional probability of event *A* given the events *B* and *C*

Note that because of the effect of the failed or intact effect of the beam cap on the splice fitting that

$$P\{SFF\} = P\{SF \mid BCTAC\} \bullet P\{BCTAC\} + P\{SF|BCF\} \bullet P\{BCF\} \quad \text{(UD-3.2)}$$

Further,

$$P\{SFTAC\} = 1 - P\{SFF\}$$
$$P\{BCTAC\} = 1 - P\{BCF\}. \quad \text{(UD-3.3)}$$

Time histories of the conditional probability of chordwise joint fracture given the intact or failed status of the splice fitting and beam cap were calculated using PROF (with the appropriate *a* versus *T* and maximum stress per flight distribution). Similarly, the time histories of the probability of the splice fitting and beam cap being in an intact or failed status were also calculated using PROF. These numbers were combined to calculate the unconditional probability of WS405 failure.

Selected WS405 Risk Analysis Results

PROF computed the single flight probability of fracture at ten approximately equally spaced times throughout each usage interval. The usage intervals were specified in terms of spectrum hours from the zero reference time (31,000 spectrum hours in this example) and define the times at which the inspection and repair actions are taken. In this risk evaluation at WS405 of the C-141, the analyses were performed over two usage intervals of 328-hour duration. The reported analyses were run assuming an inspection at the start of the analysis (Reference time $T = 0$ or 31000 spectrum hours).

PROF also calculates interval probability of fracture, but only at the end of a usage interval. For the structural elements and conditions of this example, the probability of fracture was dominated by cracks reaching unstable size (about 1 in.) as opposed to an encounter of a maximum stress in a flight. That is, the probability of fracture was determined primarily from the distributions of crack sizes. As a result, the single flight and interval probabilities of fracture were equal (to three significant figures) for the chordwise joint and the beam cap. The interval probabilities of fracture for the splice fitting were about five percent greater than the single flight fracture probabilities. Therefore, in this application, the single-flight fracture probabilities were used for the probabilities of intact and fractured status of the splice fitting and beam cap, Equation UD-3.1, in calculating the unconditional probability of failure at the ten times in a usage interval. This assumption is expected to occur in problems of interest because of the relatively small failure probabilities of risks in any realistic problem.

Sample results from the WS405 analysis are as follows. Figure UD-3.3 presents the probability of fracture as a function of spectrum hours for the splice fittings and the beam caps. This analysis assumed that maintenance (inspection and repair of detected cracks and failures) was performed at $T = 0$ (31,000 spectrum hours) and a subsequent maintenance was performed at 328 hours. The figure displays the relatively high fracture probabilities for the splice fittings, even after the maintenance cycle. In the original data, approximately 75 percent of the beam caps were in a failed crack size state and these were repaired before the failure probability calculations were started. The inspection capability assumed in the analysis was not sufficient to find and repair the cracks in the splice

fittings. The effect of the failed beam cap on the fracture probability of the splice fitting was relatively minor in comparison to other effects.

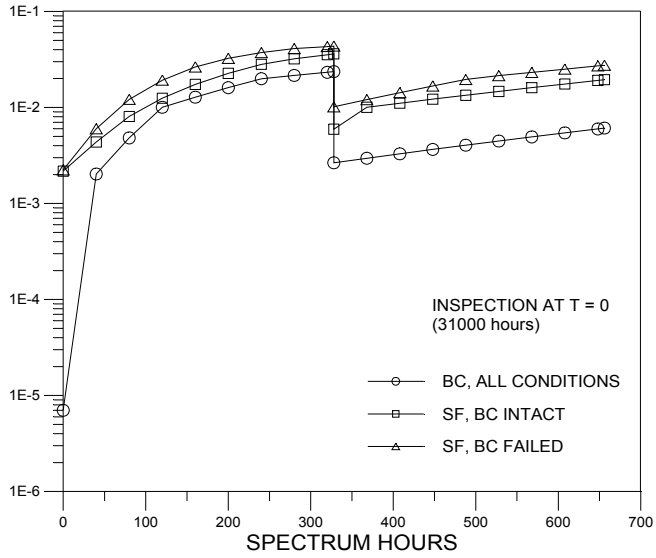

Figure UD-3.3. *Failure Probabilities of Splice Fitting and Beam Cap.*

Figure UD-3.4 presents the conditional probability of failure of the chordwise joint, given the intact or fractured status of the splice fitting and beam cap. The unconditional failure probability is a weighted average of these conditional probabilities, with the weights being determined by the proportion of intact and failed splice fittings and beam caps. Figure UD-3.5 displays the chordwise joint (system) unconditional failure probability along with the conditional failure probabilities. With the inspection at time zero, the intact or failed status of the splice fitting and beam cap had relatively minor effect on the failure probability of the system. Figure UD-3.6 compares system probabilities of failure for the analyses with and without an inspection at time zero. The effect of the maintenance action decreases the failure risks by about a factor of five.

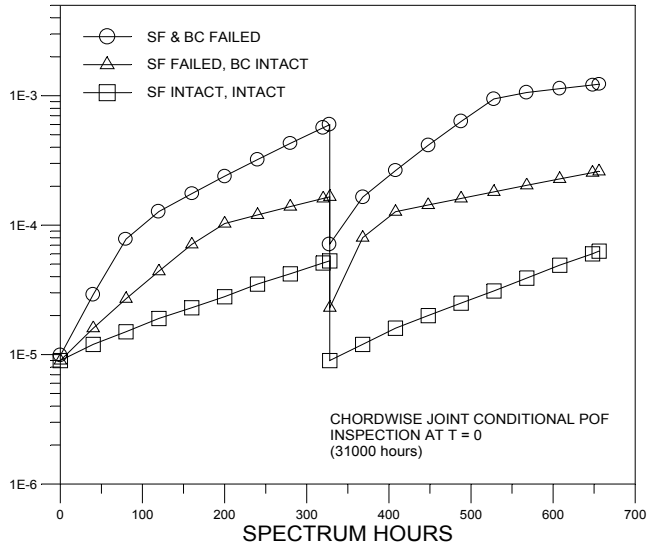

Figure UD-3.4. *Conditional Failure Probabilities of Chordwise Joint.*

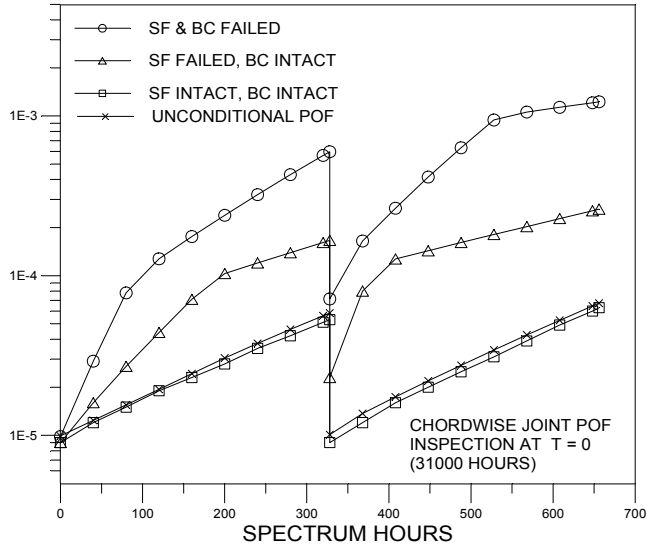

Figure UD-3.5. *Unconditional Probability of Failure of Chordwise Joint.*

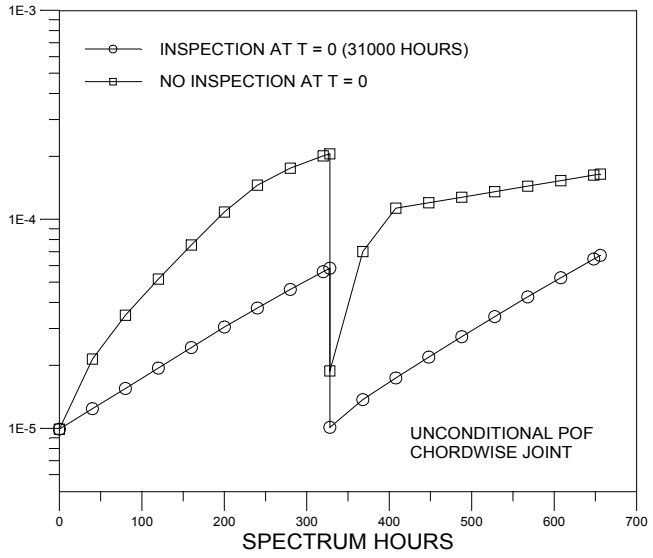

Figure UD-3.6. *Unconditional Probability of Failure of Chordwise Joint – With and Without Initial Inspection/Repair.*

Summary for Multi-Element Damage Example

The computer code PRobability Of Fracture, PROF, was used to evaluate the probability of failure at WS405 of the C-141 aircraft. Failure occurs at this location when the chordwise joint fails. The stress levels experienced by the chordwise joint are dependent on the failed or intact status of the splice fitting and the beam cap. This multi-element analysis was calculated in terms of the failure probability of the chordwise joint, given the status of the splice fitting and the beam cap, and the probabilities of the condition of the splice fitting and beam cap. The probability of failure at WS405 was calculated for a set of conditions comparable to those used in an independent analysis performed at LASC. For these conditions, the probability of a failure at WS405 in one wing was less than $2 \cdot 10^{-4}$ during a period of 656 hours of operational usage with an inspection/repair cycle at 328 hours.

References

Berens, Alan P. (1993), "Risk Analysis for C-141, WS405," UDR-TR-93-20, University of Dayton Research Institute, Dayton, OH, 45469-0120.

Cochran, J.B., Bell, R.P., Alford, R.E., and Hammond, D.O. (1991), "C-141 WS405 Risk Assessment," *Proceedings of the 1991 USAF Structural Integrity Program Conference*, San Antonio, Texas, December, 1991.

Problem No. UDRI-4

Title: Comparative Risk Assessment of the Thinning Effect of Corrosion in a Representative Lap Joint

Objective:

To illustrate the use of PROF for the calculation of the failure probability of a lap joint in the presence of various degrees of corrosive thinning.

General Description:

This sample problem illustrates the use of the PROF risk analysis computer program for evaluating the probability of failure of a lap joint with various degrees of corrosion and two different multi-site damage scenarios. The cracking scenarios are from test specimens but are considered representative of corrosion in lap joints. The analyses requires multiple runs of PROF with each given a different structural condition. The multiple runs are then combined based on the probability of occurrence on the conditions. Inspection intervals based on crack growth in pristine structure are compared with those assuming the presence of corrosion and multi-site damage.

Topics Covered: Failure probability, conditional probabilities, multiple element damage

Type of Structure: Wing chordwise joint, beam cap, splice fitting

Relevant Sections of Handbook: Section 8

Authors: Alan P. Berens and Peter W. Hovey

Company Name: University of Dayton Research Institute
Structural Integrity Division
Dayton, OH 45469-0120
937-229-4417
www.udri.udayton.edu

Contact Point: Alan P. Berens
Phone: 937-229-4475
e-Mail: Berens@udri.udayton.edu

Overview of Problem Description

The example risk analysis of a lap joint with MSD and corrosion is based on data from a specimen that is representative of a fuselage lap joint. The lap joint specimens had been used in a fatigue test program by Carleton University and the National Research Council (NRC) of Canada [Scott,1997; Eastaugh, et al., 1995]. Crack growth predictions for the specimens were performed as part of a program to develop an analytical corrosion damage assessment framework and the specimen test data were used to verify the predictions. The example is presented to demonstrate the risk analysis methodology.

The specimen, Figure UD-4.1, is constructed of two 1 mm sheets of 2024-T3 clad aluminum with three rows of 4 mm 2117-T4 rivets (MS20426AD5-5). The rivet pattern has 25.4 mm pitch and row spacing with an edge margin of 9.1 mm. The test specimens were 25.4 cm wide with eight fasteners in each row across the width.

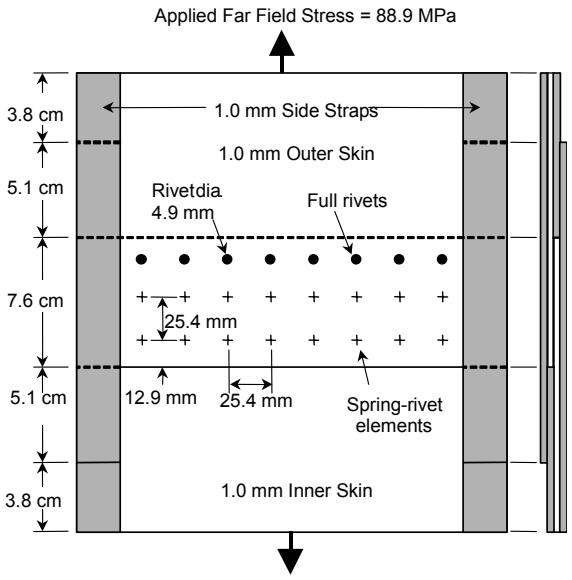

Figure UD-4.1. *Schematic of Lap Joint Specimen.*

Constant amplitude fatigue tests had been conducted at Carleton University on the lap joint specimens in non-corroded and corroded conditions with a constant amplitude far field stress of 88.9 MPa with $R = 0.2$. Details of the test procedure and resulting fatigue crack growth data are presented in Eastaugh, et al. [1995]. Nine non-corroded specimens were tested to failure to provide baseline data for comparison with corrosion specimens. Only data from these non-corroded baseline specimen tests are used in this example. Histories of crack size versus cycles for all cracks that initiated in the top row of rivet holes were recorded during the tests and were available for analysis. Examination of the histories showed that 95 percent or more of the joint life was expended when the lead crack reached about 9 mm and crack growth became unstable. Further, lead cracks initiated in accordance with two dominant scenarios. Scenario 1 is defined as a single crack originating from one side of a central hole. Scenario 2 is defined as approximately simultaneous, diametric cracks

originating from both sides of a central hole. Subsequent analysis showed significantly shorter lives for the double initial cracks. Analysis also showed that assuming both cracks were of equal size produced only 5 percent shorter lives than assuming one crack was twice the size of the second. Consequently, the assumptions were made that:

a) joint life is determined by the initiation and growth of lead cracks that originate by one of two scenarios,

b) cracks are of equal size in the double crack scenario, and,

c) panel is essentially failed when the lead crack reaches 9 mm.

Because first cracks were simultaneously discovered in different holes in four of the nine data sets, there were a total of 13 lead cracks. Eight were from Scenario 1 and five were from Scenario 2. For this population of structural elements, it was assumed that probability of a randomly selected lap joint having a Scenario 1 lead crack was 8/13 and the probability of a randomly selected lap joint having a Scenario 2 lead crack was 5/13.

Crack growth analyses were performed for both scenarios [Trego, et al., 1998]. Stress analysis was performed using FRANC2D/L, a finite element, fracture mechanics analysis code with crack propagation capability [Wawryznek & Ingraffea, 1994; Swenson & James, 1997]. The resulting crack tip stress intensity factor values as a function of crack size were then input to the crack growth code AFGROW [Boyd, et al., 1998] for selected degrees of corrosion severity. The no-corrosion, constant amplitude peak stress of the baseline fatigue tests and crack growth analyses was 88.9 MPa with an R ratio of 0.2. Predicted cyclic life from 0.25 mm to 9 mm averaged about 30 percent more than the test data.

Corrosion severity was modeled in terms of percent of thinning with the attendant increase in stress. To reflect corrosion severity, crack growth predictions were made for the somewhat arbitrarily selected levels of 0, 2, 5, 8, and 10 percent corrosive thinning by proportionate adjustments of the stress levels.

For the specimen conditions being modeled, the population of lap joint specimens has been divided into sub-populations based on combinations of two MSD scenarios and five corrosion severity levels. Cracking occurred in the two dominant MSD scenarios whose influence on crack growth was exhibited through the stress intensity factor. Corrosion severity was characterized by the metric of uniform thickness loss whose influence on crack growth is exhibited through the experienced stress levels. Each combination of MSD scenario and thickness loss produces a different crack growth analysis so that each combination must be individually analyzed in the risk analysis.

Figure UD-4.2 illustrates the partitioning of the total population of the lap joints into the ten sub-populations. Every lap joint must fit into one of the sets of conditions defined by MSD scenario and thickness loss. The probability that cracks will initiate under Scenarios 1 and 2 are p_1 (=8/13) and p_2 (=5/13), respectively. The probability that a randomly selected lap joint will have uniform thickness loss level j is q_j. $\mathrm{POF}(T/S_i,L_j) = \mathrm{POF}_{ij}(T)$ is the probability of fracture as a function of time for the combination of MSD Scenario i and thickness loss j. The calculation of the unconditional probability of failure for a random lap joint in the fleet for each corrosion severity level is shown in the last column. An analogous calculation could be performed across severity levels to obtain composite failure probabilities for each MSD scenario.

Corrosion Severity	Proportion of Joints	Dominant MSD		Composite over MSD
		Scenario 1 p_1	Scenario 2 p_2	
Thickness Loss 1	q_1	$POF_{11}(T)$	$POF_{21}(T)$	$p_1POF_{11}(T)+p_2POF_{21}(T)$
Thickness Loss 2	q_2	$POF_{12}(T)$	$POF_{22}(T)$	$p_1POF_{12}(T)+p_2POF_{22}(T)$
Thickness Loss 3	q_3	$POF_{13}(T)$	$POF_{23}(T)$	$p_1POF_{13}(T)+p_2POF_{23}(T)$
Thickness Loss 4	q_4	$POF_{14}(T)$	$POF_{24}(T)$	$p_1POF_{14}(T)+p_2POF_{24}(T)$
Thickness Loss 5	q_5	$POF_{15}(T)$	$POF_{25}(T)$	$p_1POF_{15}(T)+p_2POF_{25}(T)$

$POF_{ij}(T) = POF(T/S_i,L_j)$ = Probability of failure for Scenario i, Thickness Loss j

p = Proportion of lap joints with crack initiating under Scenario i

q_j = Proportion of lap joints with uniform thickness loss at level j

Figure UD-4.2. *Conditional Failure Probabilities for two MSD Scenarios and Five Levels of Uniform Thickness Loss.*

An interpretation of the corrosion effects can be made directly from the PROF output. If an estimate of the distribution of thickness loss in the fleet is also available, the results of the individual runs of PROF can be combined using Equation (UD-4.1) to provide an overall fracture probability for a randomly-selected detail.

$$POF(T) = \Sigma\ POF(T/C_i) \bullet P(C_i) \qquad \text{(UD-4.1)}$$

Further, the distribution of time to reach a fixed fracture probability can be inferred from the percentiles associated with the corrosion severity levels. These analyses will be demonstrated for corrosion in a representative lap joint.

It is realized that the risk analysis discussed herein does not account for the stress levels increasing as a result of increasing corrosion over the analysis period. At present, there are no accepted models for the corrosion damage growth (thickness loss) as a function of time so that the crack growth calculations are based on the state of corrosion at the beginning of the analysis interval. In reality, the stresses in the spectrum should be slowly increasing. If this effect could be accounted for in the deterministic analysis, the crack growth data input to PROF would reflect the change. However, the peak stress distribution would need to be made more severe at discrete increments. This added complexity could also be introduced by adding the additional level of conditioning and performing multiple PROF runs for each of the other ten conditions. This added level of conditioning provides insight into the total number of different runs that might be required to completely analyze a structure.

It might be noted that in the lap joint example of this paper, the peak stress distribution had no effect on the failure probability. The failure of the joint specimen was determined by reaching an unstable crack growth state when the lead crack reached 9 mm, a size far below the critical crack size for the applied far field stress.

PROF Input

The risk analysis for the lap joint corrosion example requires ten individual runs of PROF – two MSD scenarios and five stress levels for each of the MSD scenarios. The most significant inputs for the runs of this lap joint example are the crack growth projections and the initial crack size distribution. The other PROF inputs that reflect the changes between runs are the table of stress intensity factor divided by stress *(K/σ)* as a function of crack size and the distribution of peak stresses. These were changed between runs even though they had no affect on the results. K/σ came from the FRANC2D/L analysis. The peak stress distribution was estimated by a Gumbel extreme value distribution that had a mean at the appropriate constant amplitude level and a very small standard deviation to reflect the constant amplitude nature of the tests. Fracture toughness for the specimen was assumed to be normally distributed, with a mean and standard deviation of 152 and 11.4 Mpa√m, respectively. Because the example being modeled does not include inspection and repair cycles, reasonable, but arbitrary, data were used to define the inspection capability and the equivalent repair flaw size distributions.

The AFGROW crack growth curves for Scenarios 1 and 2 are presented in Figures UD-4.3 and UD-4.4, respectively. Each figure contains five crack growth curves reflecting the five levels of corrosion severity. The shorter crack growth lives from Scenario 2 are apparent from a comparison of these figures.

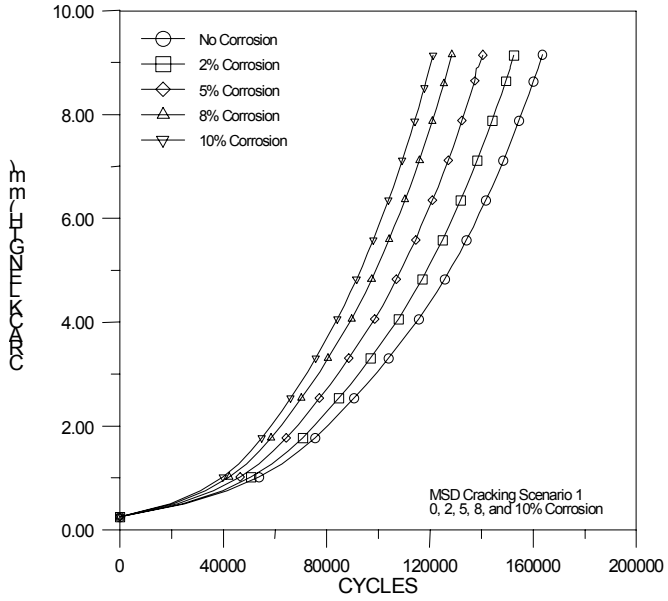

Figure UD-4.3. *Crack Size versus Cycles for Scenario 1.*

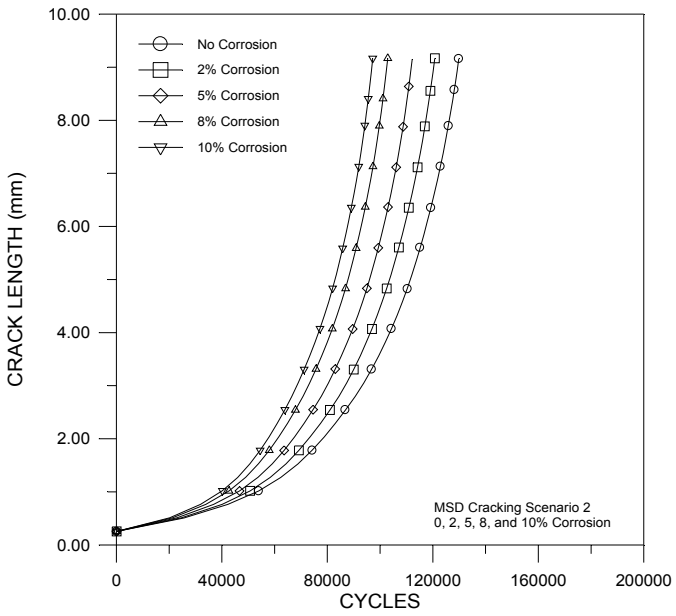

Figure UD-4.4. *Crack Size versus Cycles for Scenario 2.*

The initiating flaw size distribution was generated by back calculating from the sizes of the first observed lead cracks and their corresponding ages in the specimen test data. The back calculation was performed in two steps. First, the no-corrosion crack size versus cycles data of Figures UD-4.3 and UD-4.4 were used to determine the time at which each lead crack would have reached 0.25 mm. An exponential growth model was then fit to each lead crack to estimate an equivalent crack size at 50,000 cycles. Note that the inverse of this process returns each of the observed lead cracks to its original size and cycles.

The times to reach 0.25 mm for the cracks from the two MSD scenarios were statistically indistinguishable. Similarly, there was no statistical difference between the equivalent lead crack sizes from the two MSD scenarios at 50,000 cycles. The two sets of data were pooled to obtain the initiating flaw size distribution. The equivalent crack sizes at 50,000 cycles were fit with a mixture of two Weibulls as shown in Figure UD-4.5. Also indicated in Figure UD-4.5 are the MSD scenarios of origin of the lead cracks.

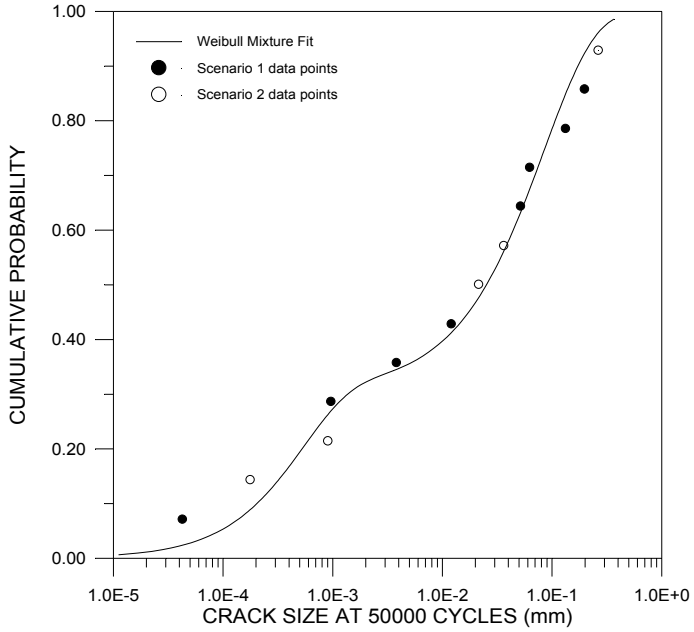

Figure UD-4.5. *Weibull Mixture of Initial Crack Sizes.*

PROF Risk Analysis Results

Probability of failure as a function of cycles was calculated for each of the ten combinations of cracking scenario and corrosion severity. Failure of the lap joint specimens was defined as the lead crack exceeding 9 mm, as previously discussed. Figures UD-4.6 and UD-4.7 present the failure probabilities as a function of experienced cycles for Scenarios 1 and 2, respectively. The failure probabilities behave as expected with increased risk of failure at a fixed age for Scenario 2 as compared to Scenario 1, and increasing risk of failure as the stress level increases due to corrosion material loss. These calculations do not account for any additional corrosive thinning after the start of the analysis.

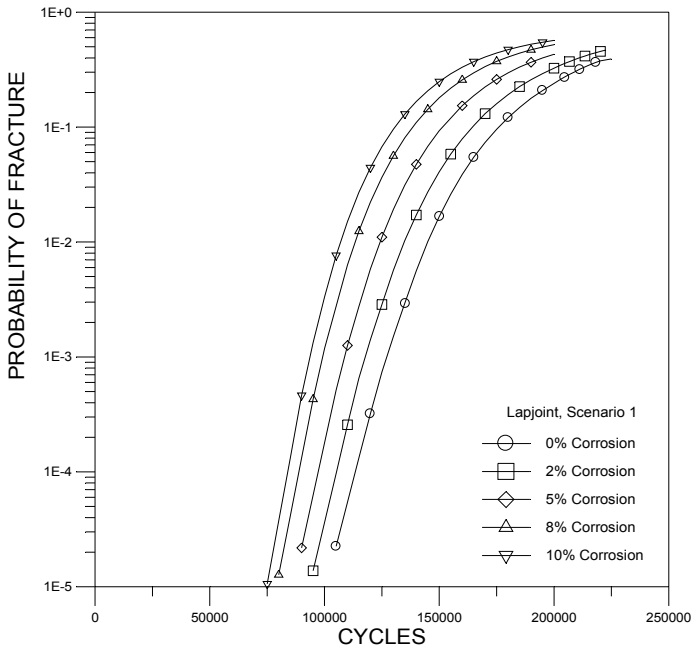

Figure UD-4.6. *POF versus Cycles for Scenario 1.*

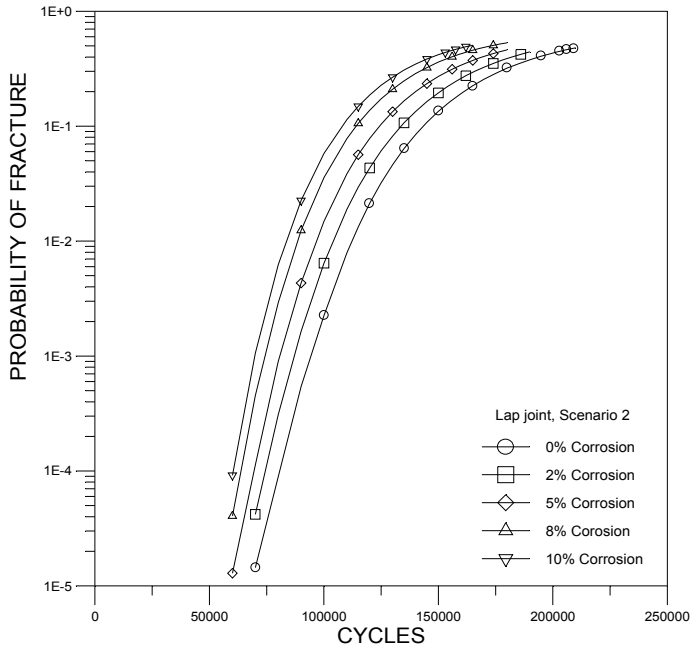

Figure UD-4.7. *POF versus Cycles for Scenario 2.*

As a gross check on the capability of the risk analysis methodology, Figure UD-4.8 compares the calculated probability of failure as a function of cycles for 0% corrosion for Scenarios 1 and 2 to the observed distributions of failure times. Superimposed on the predicted failure probabilities are the observed cumulative distributions of the cycles to

failure from the lap joints that were the basis of the analysis. The observed cumulative distribution function was obtained by ordering the cycles to failure and dividing the ranks of the ordered times by the sample size plus one. That is,

$$F(T_i) = i/(n+1) \qquad \text{(UD-4.2)}$$

where i is the rank for T_i, the time at which the i^{th} crack exceeded 9 mm, and n is the number of observed cracks that met the definition for the scenario. Sample sizes for Scenarios 1 and 2 were eight and five, as noted earlier. The differences between the observed and predicted probabilities of failure are most likely due to the conservative deterministic life predictions or the extrapolation of the crack-size-versus-cycles relation that was required to obtain the initiating distribution of crack sizes.

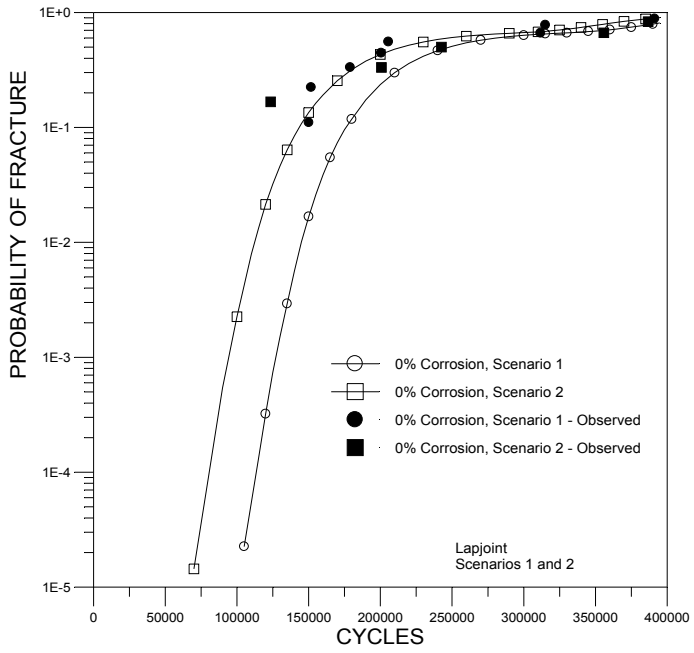

Figure UD-4.8. *POF versus Cycles for Scenarios 1 and 2 Showing Comparison with Observed Data.*

Figures UD-4.6 and UD-4.7 presented the conditional failure probabilities given the respective cracking scenario. The unconditional failure probability for a lap joint chosen at random from the population being analyzed is calculated as a weighted average of the conditional probabilities where the weighting factors are the proportion of specimens, which will initiate cracks in the two scenarios. See Equation UD-4.1 and Figure UD-4.2. The weighting factors were estimated from the lap joint data in which eight of the 13 lead cracks were from Scenario 1 (initial lead crack from one side of the hole) and five of the 13 were from Scenario 2 (initial lead crack from diametrically opposite sides of the hole). Thus, $p_1 = 8/13$ and $p_2 = 5/13$. Using these factors, a comparison of the observed and predicted cycles to failure for the composite of the two scenarios without corrosion is

shown in Figure UD-4.9. Again, the difference between the predicted and observed distributions of cycles to failure displays the somewhat non-conservative risks of the predicted failure probabilities.

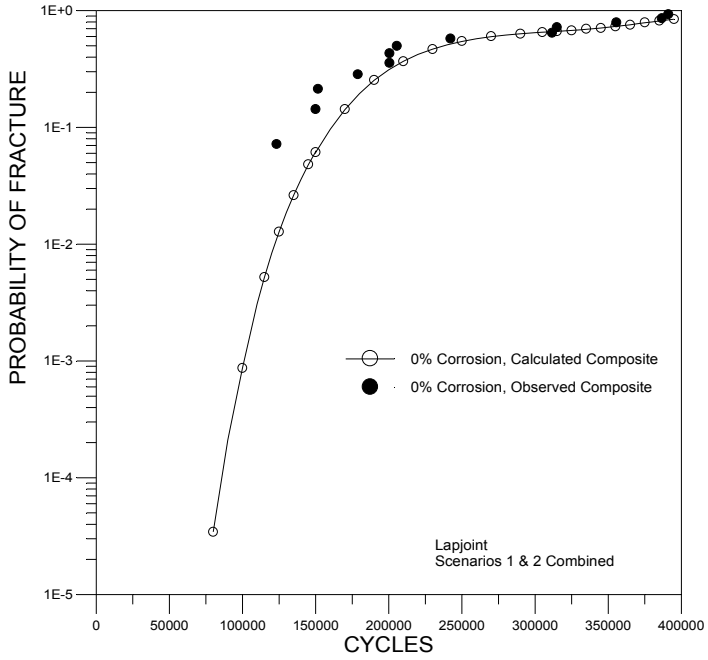

Figure UD-4.9. *POF versus Cycles for Composite of Scenarios 1 and 2 Showing Comparison with Observed Data.*

Figure UD-4.10 summarizes the probabilities of failure for a randomly-selected lap joint that can have either MSD scenario and is subject to the expected stress history for five levels of corrosion severity. These results will be interpreted both in terms of the times to reach a defined probability of fracture (POF) and in terms of the relative differences in POF at a fixed number of cycles.

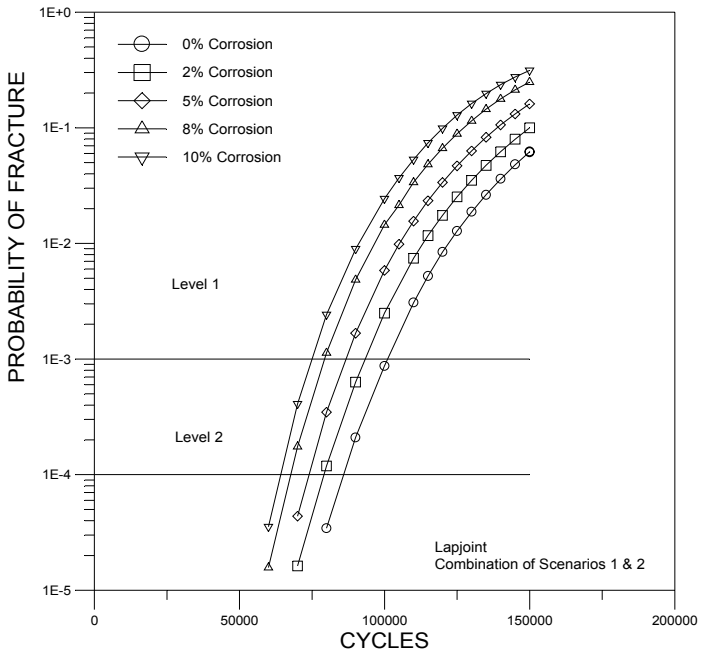

Figure UD-4.10. *POF versus Cycles for Scenario Composites.*

The cycles to reach a fixed POF for the different degrees of corrosion severity can be read from Figure UD-4.10 as indicated, for example, at POF equal to 0.001 and 0.0001. Assume that the proportion of lap joints in the population that contain each of the five degrees of corrosion is known. Then the distribution of the time to reach the POF levels can also be inferred.

To illustrate, three representative distributions of corrosion damage were assumed, as given in Table UD-4.1. Mix 1 is symmetric about a five percent material loss. Mix 2 is representative of a more severely corroded population. Mix 3 is representative of a less severely corroded population and is considered to be more representative of the corrosion that would be expected in aircraft.

Table UD-4.1. *Assumed Distributions of Corrosion Damage.*

Severity	Mix 1	Mix 2	Mix 3
0%	5	5	15
2%	25	15	40
5%	40	35	25
8%	25	35	15
10%	5	10	5

Figure UD-4.11 presents a histogram of Mix 3. The corresponding percentage of lap joints would be expected to reach the selected POF level in the indicated number of cycles. The histogram for cycles to reach POF = 0.0001 for severity Mix 3 is shown in Figure UD-4.12.

The cumulative distribution of time to reach the two POF levels for the three distributions of corrosion severity are shown in Figure UD-4.13.

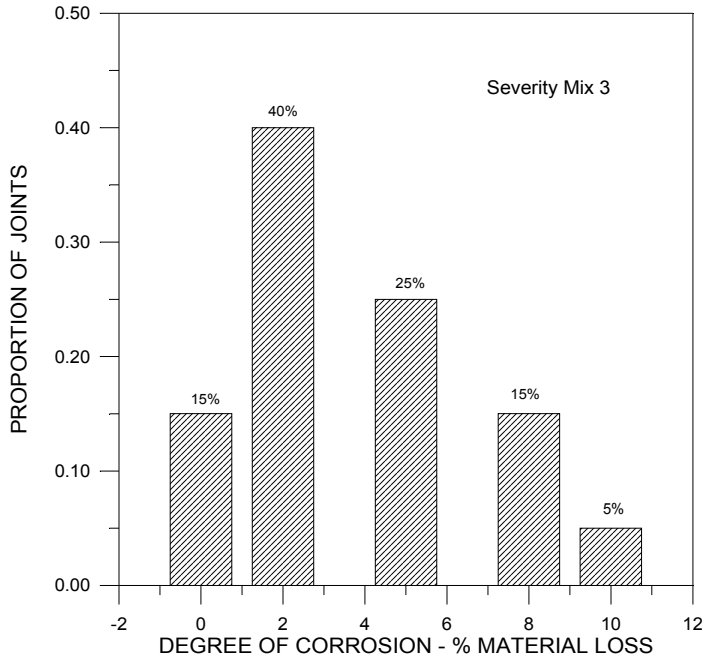

Figure UD-4.11. *Example Histogram of Levels of Corrosion Damage – Severity Mix 3.*

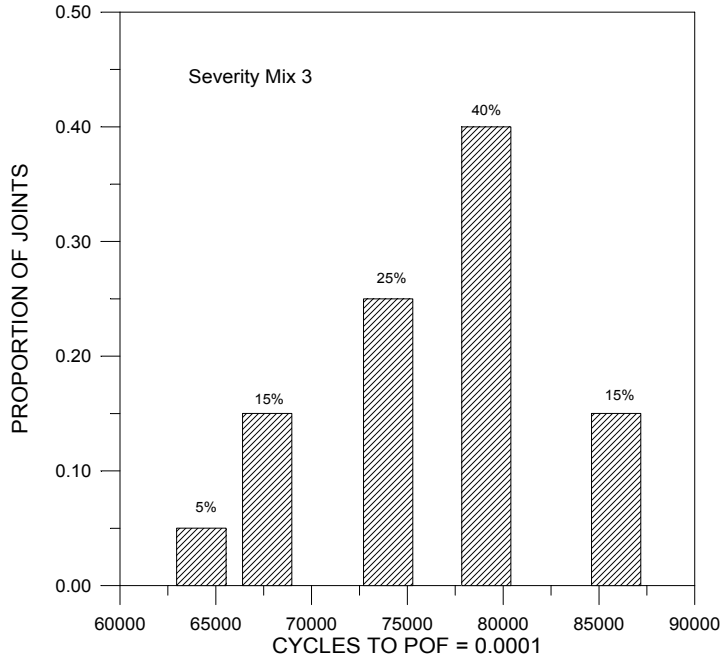

Figure UD-4.12. *Example Histogram of Cycles to POF = 0.0001 – Severity Mix 3.*

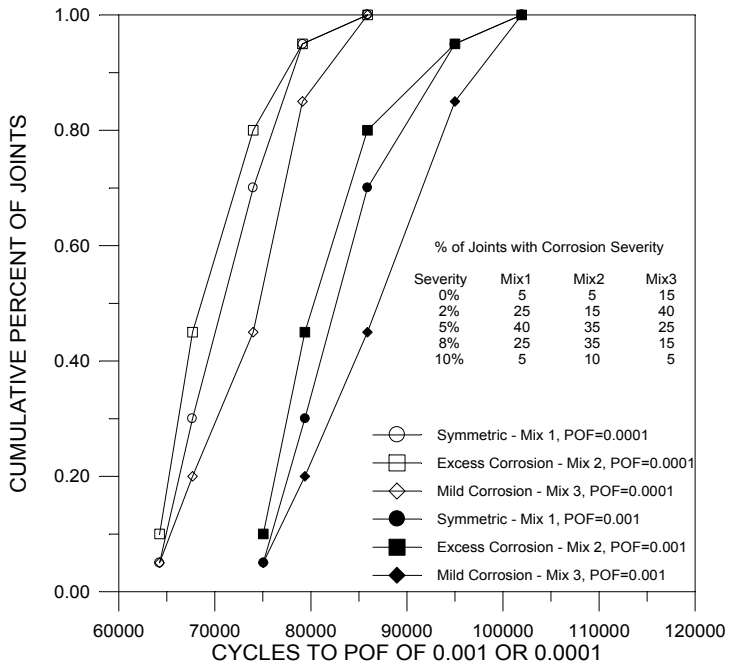

Figure UD-4.13. *Cumulative Distribution of Cycles to Selected POF – 3 Corrosion Severities.*

At a fixed number of cycles, the failure risk of a corroded lap joint can significantly exceed that of a non-corroded lap joint. To illustrate this difference, Figure UD-4.14 presents the ratio of failure probabilities for each of the four degrees of corrosion severity to that of the non-corroded lap joints. The ratios are presented as a function of the failure probability of the non-corroded lap joint. The lap joint failure probability for the severity characterized by ten percent thinning can be 70 times greater than that of a non-corroded lap joint. If maintenance scheduling were based on keeping the failure probability below about 0.0001 to 0.001, a lap joint with ten percent corrosion thinning would have a 25 to 50 times greater chance of resulting in fracture.

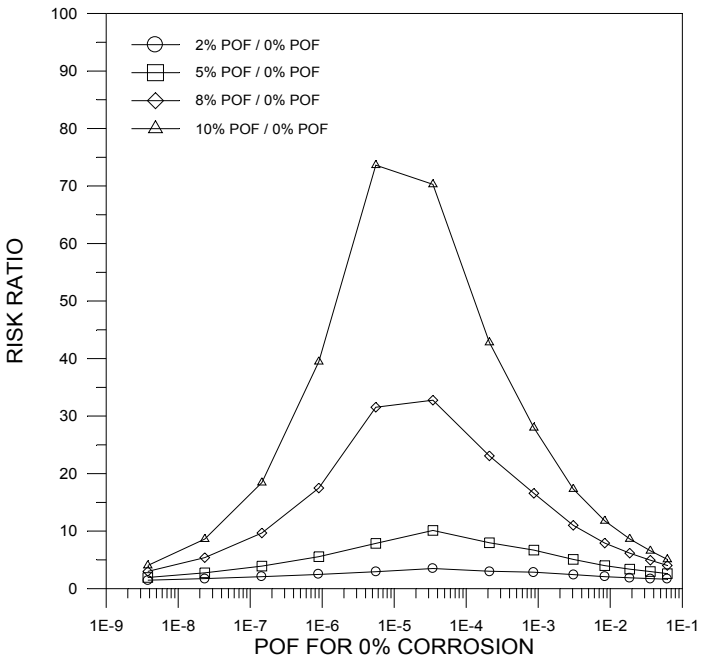

Figure UD4-14. *Risk Ratios Normalized to No Corrosion Condition.*

MSD/Corrosion Example Summary

This example demonstrates that it is possible to extend PROF to include probabilistic descriptions of the factors which influence fatigue life. In particular, a risk analysis was performed for fatigue failures in a representative lap joint in which the crack growth calculation was influenced by corrosion thickness loss and two scenarios of MSD. The basic approach to the analysis was to use deterministic crack growth calculations for different percentiles of the influencing factors in the probability of failure calculations, yielding conditional probabilities of failure. The full use of the analysis assumed that estimates of the proportion of Scenarios 1 and 2 and an estimage of the proportion of lapjoint with the discrete level of corrosive thinning were available, so that the conditional failure probabilities can be combined or otherwise interpreted.

In the lap joint example of this paper, the relative frequency of the two dominant MSD scenarios was estimated from data from a test program of the modeled specimen. Example distributions of thickness loss were assumed to demonstrate the calculations and interpretation. For this example, a ten percent thickness loss increased the failure probability by a factor of as much as 70 over the no-corrosion condition. Depending on the consequences of failure, inspection intervals based on the no-corrosion stress levels could pose a safety issue to corroded joints. The results were also used to demonstrate the generation of the distribution of time to a fixed risk.

References

Boyd, K., Harter, J.A., and Krishnan (1998), *AFGROW User's Manual Version 3.1.1*, WL-TR-97-3053, Air Force Research Laboratory, Wright-Patterson Air Force Base, Ohio.

Eastaugh, G.F., Simpson, D.L., Straznicky, P.V., and Wakeman, R.B. (1995), "A Special Uniaxial Coupon Test Specimen for the Simulation of Multiple Site Fatigue Crack Growth and Link-Up in Fuselage Skin Splices," National Research Council of Canada and Carleton University, AGARD-CP-568.

Scott, J.P. (1997), "Corrosion and Multiple Site Damage in Riveted Fuselage Lap Joints," Master's Thesis, Carleton University.

Swenson, D. and James, M. (1997) "FRANC2D/L: A Crack Propagation Simulator for Plane Layered Structures", Version 1.4 User's Guide, Kansas State University.

Trego, A., Cope, D., Johnson, P., and West, D. (1998) "Analytical Methodology for Assessing Corrosion and Fatigue in Fuselage Lap Joints," 1998 Air Force Corrosion Program Conference Proceedings, April 1998, Macon, Georgia.

Wawrzynek, P.A., and Ingraffea, A.R. (1994), "FRANC2D: A Two-Dimensional Crack Propagation Simulator, Version 2.7, User's Guide," NASA CR-4572.